Microphysics of Clouds and Precipitation

Second revised and expanded edition with an introduction to cloud chemistry and cloud electricity

Atmospheric and Oceanographic Sciences Library

18

H.R. Pruppacher
J.D. Klett

MyCopy powered by SpringerLink

MICROPHYSICS OF CLOUDS AND PRECIPITATION

ATMOSPHERIC AND OCEANOGRAPHIC SCIENCES LIBRARY

VOLUME 18

Editors

Lawrence A. Mysak, *Department of Atmospheric and Oceanographic Sciences, McGill University, Montreal, Canada*

Kevin Hamilton, *International Pacific Research Center, University of Hawaii, Honolulu, HI, U.S.A.*

Editorial Advisory Board

A. Berger	Université Catholique, Louvain, Belgium
J.R. Garratt	CSIRO, Aspendale, Victoria, Australia
J. Hansen	MIT, Cambridge, MA, U.S.A.
M. Hantel	Universität Wien, Austria
H. Kelder	KNMI (Royal Netherlands Meteorological Institute), De Bilt, The Netherlands
T.N. Krishnamurti	The Florida State University, Tallahassee, FL, U.S.A.
P. Lemke	Alfred-Wegener-Institute for Polar and Marine Research, Bremerhaven, Germany
A. Robock	Rutgers University, New Brunswick, NJ, U.S.A.
S.H. Schneider	Stanford University, CA, U.S.A.
G.E. Swaters	University of Alberta, Edmonton, Canada
J.C. Wyngaard	Pennsylvania State University, University Park, PA, U.S.A.

For other titles published in this series, go to
www.springer.com/series/5669

MICROPHYSICS OF CLOUDS AND PRECIPITATION

by

HANS R. PRUPPACHER

Institute for Physics of the Atmosphere
Johannes Gutenberg University, Mainz

and

JAMES D. KLETT

PAR Associates and
Department of Physics, New Mexico State University, Las Cruces

Second revised and expanded edition
with an introduction to
cloud chemistry and cloud electricity



H.R. Pruppacher
Universität Mainz
Institut für Physik der
Atmosphäre
Becherweg 21
55099 Mainz
Germany

Prof. J.D. Klett
Las Cruces
NM 88001
USA

ISBN 978-0-7923-4211-3 e-ISBN 978-0-306-48100-0
DOI 10.1007/978-0-306-48100-0
Springer Dordrecht Heidelberg London New York

Library of Congress Control Number: 2010924629

© Springer Science+Business Media B.V. 2010
No part of this work may be reproduced, stored in a retrieval system, or transmitted in any form or by any means, electronic, mechanical, photocopying, microfilming, recording or otherwise, without written permission from the Publisher, with the exception of any material supplied specifically for the purpose of being entered and executed on a computer system, for exclusive use by the purchaser of the work.

Printed on acid-free paper

Springer is part of Springer Science+Business Media (www.springer.com)

TABLE OF CONTENTS

PREFACE TO THE FIRST EDITION xv

PREFACE TO THE SECOND EDITION xvii

CHAPTER 1

HISTORICAL REVIEW 1

CHAPTER 2

MICROSTRUCTURE OF ATMOSPHERIC CLOUDS AND PRECIPITATION 10

2.1 Microstructure of Clouds and Precipitation Consisting of Water Drops .. 10
2.1.1 The Relative Humidity inside Clouds and Fogs 10
2.1.2 Microstructure of Fogs 12
2.1.3 Microstructure of Clouds 15
2.1.4 Formulations for the Drop Size Distributions in Clouds and Fogs 24
2.1.5 The Mean Distance between Drops in Clouds and Fogs 27
2.1.6 Microstructure of Rain 30
2.2 Microstructure of Clouds and Precipitation Consisting of Ice Particles ... 38
2.2.1 Shape, Dimensions, Bulk Density and Number Concentration of Snow Crystals 40
2.2.2 Shape, Dimensions, Bulk Density, and Number Concentration of Snowflakes, Graupel, and Hailstones 58

CHAPTER 3

THE STRUCTURE OF WATER SUBSTANCE 74

3.1 Structure of an Isolated Water Molecule 74
3.2 Structure of Water Vapor 77
3.3 Structure of Ice 78
3.4 Structure of Water and Aqueous Solutions 86
3.4.1 Structure of Water 86
3.4.2 Structure of Aqueous Solutions 98

CHAPTER 4

EQUILIBRIUM BETWEEN WATER VAPOR, WATER, AQUEOUS SOLUTIONS, AND ICE IN BULK **100**

4.1 Useful Thermodynamic Relations 100
4.2 General Conditions for Equilibrium 102
4.3 Phase Rule for Bulk Phases 104
4.4 Ideal versus Real Behavior of Dry Air, Water Vapor, and Moist Air 105
4.5 Chemical Potential of Water Vapor in Humid Air, and of Water in Aqueous Solutions 107
4.6 Equilibrium Between an Aqueous Salt Solution and Water Vapor 109
4.7 Latent Heat of Phase Change and its Temperature Variation 115
4.8 Clausius-Clapeyron Equation 116
4.9 Equilibrium Between an Aqueous Salt Solution and Ice 123

CHAPTER 5

SURFACE PROPERTIES OF WATER SUBSTANCE **126**

5.1 Surface Tension 126
5.2 Equilibrium Conditions 127
5.3 Phase Rule for Systems with Curved Interfaces 128
5.4 Water-Vapor Interface 129
5.4.1 Effect of Temperature on the Surface Tension of Water 130
5.4.2 Surface Tension of Aqueous Salt Solutions 130
5.4.3 Radius Dependence of Surface Tension 133
5.5 Angle of Contact 135
5.6 Adsorption of Water Vapor on Solid Surfaces 137
5.7 Ice-Vapor Interface 145
5.7.1 Surface Energy of Ice 145
5.7.2 Wulff's Theorem 147
5.7.3 Structure of Real Ice Surfaces 150
5.8 Adsorption of Reactive Gases on Ice Surfaces 155
5.9 Ice-Water Interface 157
5.10 Ice Aqueous Solution Interface 161
5.11 Condensation, Deposition, and Thermal Accommodation Coefficients .. 163

CHAPTER 6

EQUILIBRIUM BEHAVIOR OF CLOUD DROPS AND ICE PARTICLES **167**

6.1 General Equilibrium Relation for Two Phases Separated by a Curved Interface 167
6.2 Effect of Curvature on Latent Heat of Phase Change 168

6.3 Generalized Clausius-Clapeyron Equation 169
6.4 Equilibrium Between a Pure Water Drop and Pure Water Vapor or Humid Air 170
6.5 Equilibrium Between an Aqueous Solution Drop and Humid Air 172
6.6 Equilibrium Between Humid Air and an Aqueous Solution Drop Containing a Solid Insoluble Substance 175
6.7 Equilibrium Conditions for Ice Particles 178
6.8 Experimental Verification 184

CHAPTER 7

HOMOGENEOUS NUCLEATION 191

7.1 Homogeneous Nucleation of Water Drops and Ice Crystals from Water Vapor 192
7.1.1 Equilibrium Population of Embryos and Energy of Embryo Formation 192
7.1.1.1 Formal Statistical Mechanics Description 192
7.1.1.2 Molecular Model Method 194
7.1.1.3 The Classical Description 194
7.1.2 The Nucleation Rate J 199
7.1.3 Experimental Verification 204
7.2 Homogeneous Nucleation of Ice in Supercooled Water 205
7.2.1 The Nucleation Rate J 205
7.2.2 The Energy of Germ Formation 207
7.2.2.1 Classical Model 207
7.2.2.2 The Molecular Model 207
7.2.3 The Molar Activation Energy $\Delta g^{\ddagger}$ 209

CHAPTER 8

THE ATMOSPHERIC AEROSOL AND TRACE GASES 216

8.1 Gaseous Constituents of the Atmosphere 216
8.2 Atmospheric Aerosol Particles (AP) 225
8.2.1 Formation of Aerosol Particles by Gas to Particle Conversion (GPC) 226
8.2.2 Formation of Aerosol Particles by Drop Particle Conversion (DPC) 233
8.2.3 Formation of Aerosol Particles by Bulk to Particle Conversion (BPC) 240
8.2.3.1 BPC at the Solid Earth Surface 240
8.2.3.2 BPC at the Surface of Oceans 243
8.2.4 AP from Extraterrestrial Sources 247
8.2.5 Rate of Emission of Particulate Matter into the Atmosphere ... 248
8.2.6 Residence Time of AP 248

8.2.7 Water-soluble Fraction of AP 251
8.2.8 Total Mass and Number Concentration of AP 252
8.2.8.1 Number Concentration (except Polar Aerosols) 252
8.2.8.2 Mass Concentrations (except Polar Aerosols) 255
8.2.8.3 Total Mass and Number Concentration of Particles in Polar, Tropospheric Aerosols 260
8.2.9 Size Distribution of AP 261
8.2.10 Vertical Variation of the Number and Mass Concentration 270

CHAPTER 9

HETEROGENEOUS NUCLEATION **287**

9.1 Cloud Condensation Nuclei (CCN) 287
9.1.1 Number Concentration and Chemical Composition of CCN 287
9.1.2 Mode of Action of Water-Soluble and Mixed CCN 296
9.1.3 Nucleation of Drops on Water-Insoluble CCN 297
9.1.3.1 Nucleation on a Planar Substrate 298
9.1.3.2 Nucleation on a Curved Substrate 302
9.1.4 Experimental Verification of Heterogeneous Water Drop Nucleation 306
9.2 Ice Forming Nuclei (IN) 309
9.2.1 Number Concentration of IN 309
9.2.2 Sources and Chemical Composition of IN 317
9.2.3 The Main Requirements for IN 326
9.2.3.1 Insolubility Requirement 326
9.2.3.2 Size Requirement 326
9.2.3.3 Chemical Bond Requirement 328
9.2.3.4 Crystallographic Requirement 329
9.2.3.5 Active-Site Requirement 330
9.2.4 Theory of Heterogeneous Ice Nucleation 341
9.2.4.1 The Classical Model 341
9.2.4.2 Extensions of the Classical Model 344
9.2.4.3 The Semi-Empirical Statistical Mechanics Model 345
9.2.5 Heterogeneous Freezing of Supercooled Water Drops 347
9.2.6 Discrepancy Between the Concentrations of IN and the Concentration of Ice Particles 355

CHAPTER 10

HYDRODYNAMICS OF SINGLE CLOUD AND PRECIPITATION PARTICLES **361**

10.1 Basic Governing Equations 361
10.2 Flow Past a Rigid Sphere 364
10.2.1 Classification of Flows According to Reynolds Number 364

10.2.2 Steady, Axisymmetric Flow 366
10.2.2.1 The Stream Function 366
10.2.2.2 The Drag Problem 367
10.2.2.3 Analytical Solutions 369
10.2.2.4 Numerical Approach to the Navier-Stokes Equation .. 378
10.2.2.5 Comparison of Analytical and Numerical Solutions of the Navier-Stokes Equation with Experimental Results 379
10.2.3 The Fall Behavior of Rigid Spheres 384
10.2.4 Non-Steady Three-Dimensional Flow 384
10.3 Hydrodynamic Behavior of Water Drops in Air 385
10.3.1 Internal Circulation in Drops 386
10.3.2 Drop Shape 393
10.3.3 Drop Oscillation 400
10.3.4 Fall Behavior of Drops 409
10.3.5 Drop Instability and Breakup 410
10.3.6 Terminal Velocity of Water Drops in Air 415
10.4 Hydrodynamic Behavior of Disks, Oblate Spheroids, and Cylinders 421
10.4.1 Circular Disks and Oblate Spheroids 422
10.4.2 Circular Cylinders 428
10.5 Hydrodynamic Behavior of Snow Crystals, Snow Flakes, Graupel and Hailstones 433
10.5.1 Flow Field and Drag 433
10.5.2 Fall Velocity 438
10.5.3 Fall Pattern 444

CHAPTER 11

MECHANICS OF THE ATMOSPHERIC AEROSOL 447

11.1 Brownian Motion of Aerosol Particles 447
11.2 Particle Diffusion 449
11.3 Mobility and Drift Velocity 450
11.4 Sedimentation and the Vertical Distribution of Aerosol Particles 451
11.5 Brownian Coagulation of Aerosol Particles 454
11.6 Laminar Shear, Turbulence, and Gravitational Coagulation 463
11.6.1 Coagulation in Laminar Shear Flow 463
11.6.2 Coagulation in Turbulent Flow 465
11.6.2.1 Turbulent Shear Coagulation 467
11.6.2.2 Turbulent Inertial Coagulation 468
11.6.3 Gravitational Coagulation 469
11.7 Explanation for the Observed Size Distributions of the Atmospheric Aerosol 472
11.7.1 Quasi-Stationary Distributions (QSD) 472
11.7.2 Self-Preserving Distributions (SPD) 474
11.7.3 Quasi-Stationary Self-Preserving Distributions 480

11.7.4 Statistical Distributions 481
11.7.5 Power Law Solutions for a Source-Enhanced Aerosol 482

CHAPTER 12

COOLING OF MOIST AIR **485**

12.1 Water in the Atmosphere 485
12.2 Isobaric Cooling 488
12.3 Adiabatic Cooling of Unsaturated Air 488
12.4 The Thermodynamic Wetbulb Temperature 490
12.5 Lifting to Saturation and Beyond 490
12.6 Adiabatic Cooling of Saturated Air 492
12.7 Cooling with Entrainment 492
12.8 The Concept of Entrainment 493
12.9 The Air Parcel Model for a Convective Cloud 497

CHAPTER 13

DIFFUSION GROWTH AND EVAPORATION OF WATER DROPS AND SNOW CRYSTALS **502**

13.1 Laws for Diffusion of Water Vapor and Heat 502
13.1.1 Diffusion of Water Vapor 502
13.1.2 Diffusion of Heat 507
13.2 Growth of Aqueous Solution Drops by Diffusion of Water Vapor 509
13.2.1 Growth of an Individual Stationary Drop 509
13.2.2 Diffusional Growth of a Population of Solution Drops of Neglible Fall Velocity 512
13.2.2.1 Condensation Growth in Cumuliform Clouds 512
13.2.2.2 Condensation Growth in Stratiform Clouds and Fogs 531
13.2.3 Steady State Evaporation of Water Drops Falling in Subsaturated Air 537
13.3 Growth of Snow Crystals by Diffusion of Water Vapor 546
13.3.1 Growth of a Stationary Snow Crystal 546
13.3.2 Growth of a Ventilated Snow Crystal 550
13.3.3 Growth Rate of Snow Crystal Faces - Snow Crystal Habit Change 561

CHAPTER 14

CLOUD PARTICLE INTERACTIONS **568**

14.1 The Basic Model for Drop Collisions 568
14.2 Definition of Collision Efficiency 569
14.3 The Superposition Method 571

14.4 The Boundary Value Problem Approach 574
14.4.1 The Quasi-Stationary Assumption 574
14.4.2 Two Spheres in Steady Stokes Flow 575
14.4.3 The Slip-Flow Correction in Stokes Flow 577
14.4.4 Two Spheres in Modified Oseen Flow 579
14.5 Collision of Water Drops with Water Drops 581
14.5.1 The Case of Calm Air 581
14.5.2 The Case of Turbulent Air 584
14.5.3 Experimental Verification 591
14.5.4 Coalescence of Water Drops in Air 594
14.5.4.1 The Rebound Problem 595
14.5.4.2 Disruption Following Collision 598
14.6 Collision of Snow Crystals with Water Drops 599
14.6.1 Collision of Large Snow Crystals with Small Drops 599
14.6.2 Collision of Large Drops with Small Snow Crystals 606
14.7 Collision of Snow Crystals with Snow Crystals 607
14.8 Orientation Model for Particles in Turbulence 610
14.8.1 Turbulence Model 611
14.8.2 Orientation of Spheroids in Turbulent Air 611
14.8.3 Generalized Orientation Distribution 613

CHAPTER 15

GROWTH OF CLOUD DROPS BY COLLISION, COALESCENCE AND BREAKUP 617

15.1 Continuous Model for Collection Growth 617
15.2 Polynomial Approximations to the Gravitational Collection Kernel 620
15.3 Stochastic Model for Collisional Growth 622
15.3.1 Completeness of the SCE 624
15.3.1.1 Three Models for Collection Growth 625
15.3.1.2 Correlations in a Stochastic Coalescence Process 628
15.3.1.3 Monte Carlo Study of Stochastic Correlation 629
15.3.2 Exact Solutions to the SCE 630
15.3.3 Numerical and Approximation Techniques for the SCE 636
15.3.3.1 The Method of Berry (1967) and Reinhardt (1972) 637
15.3.3.2 The Method of Moments 639
15.4 Stochastic Model for Drop Breakup 645
15.5 Stochastic Drop Growth in Combination with Stochastic Drop Breakup 650

CHAPTER 16

GROWTH OF ICE PARTICLES BY ACCRETION AND ICE PARTICLE MELTING 659

16.1 Growth of Ice Particles by Accretion of Supercooled Drops 659

16.1.1 Growth Mode and Structure of Rimed Ice Particles, Graupel, and Hailstones 659
16.1.2 Structure and Growth Mode of Ice in Supercooled Water 663
16.1.3 Growth Rate of Ice in Supercooled Water 668
16.1.4 Freezing Time of Water Drops 674
16.1.5 Growth Rate of Graupel and Hailstones 679
16.1.6 Snow Crystal Multiplication by Riming 687
16.2 Growth of Snow Crystals by Collision with other Snow Crystals 689
16.3 Melting of Ice Particles 691
16.3.1 Melting of Graupel and Hailstones 692
16.3.2 Melting of Snow Flakes 697

CHAPTER 17

CLOUD CHEMISTRY **700**

17.1 Concentrations of Water Soluble Compounds in Bulk Cloud and Rain Water, and in Bulk Water of Melted Snow 701
17.2 Concentration of Water Insoluble Particles in Bulk Cloud and Rain Water and Bulk Water of Melted Snow 708
17.3 Concentration of Water Soluble Compounds in Individual Cloud and Raindrops 711
17.4 Scavenging of Aerosol Particles by Cloud Drops, Raindrops and Ice Particles 715
17.4.1 Nucleation Scavenging 716
17.4.2 Impaction Scavenging 720
17.4.2.1 Scavenging by Convective Brownian Diffusion 720
17.4.2.2 Scavening by Thermophoresis and Diffusiophoresis ... 724
17.4.2.3 Scavenging by Gravitational or Inertial Impaction 730
17.4.2.4 Scavenging by Turbulence 732
17.4.2.5 Combined Force Effects: the Trajectory and Flux Models 732
17.5 Scavenging of Gases by Cloud Drops, Raindrops and Ice Particles 744
17.5.1 Scavenging of Gases by Water Drops 749
17.5.1.1 Solution and Dissociation Equilibria 749
17.5.1.2 Diffusion Models for Gases 757
17.5.2 Asymmetry between Absorption and Desorption of Gases 775
17.5.3 Deviations from Equilibrium 777
17.5.4 Scavenging of Gases by Ice Particles 783
17.6 The Scavenging Parameters 784
17.7 Wet Deposition 787

CHAPTER 18

CLOUD ELECTRICITY **792**

18.1 Electrical State of the Cloudless Atmosphere 792

18.2 Electrical State of the Atmospheric Aerosol 795
18.3 Electrical Conductivity in Clouds 798
18.3.1 Diffusion and Conduction of Ions to Cloud Drops 798
18.3.2 Conductivity in Weakly Electrified Clouds 799
18.3.3 Conductivity in Strongly Electrified Clouds 802
18.4 Charge Distribution in Clouds 804
18.4.1 Weakly Electrified Clouds 804
18.4.2 Strongly Electrified Clouds 806
18.5 Cloud Charging Mechanisms 811
18.5.1 Requirements for a Cloud Charging Mechanism 811
18.5.2 The Major Cloud Charging Mechanisms 812
18.5.2.1 Charging by Diffusion of Ions 812
18.5.2.2 Convection Charging 812
18.5.2.3 Inductive Charging Mechanisms 816
18.5.2.4 Non-Inductive Charging Mechanisms Involving the Collision between Particles 821
18.5.2.5 Non-Inductive Charging Mechanisms Involving the Breakup of Precipitation Particles 824
18.5.2.6 Growth of the Electric Field 826
18.6 Effect of Electric Fields and Charges on Microphysical Processes 827
18.6.1 Drop and Ice Crystal Nucleation 827
18.6.2 Diffusional Growth of Ice Crystals 828
18.6.3 Drop Deformation, Disruption and Corona Production 829
18.6.4 Drop Terminal Velocities 835
18.6.5 Collisional Growth Rate of Cloud Particles 836
18.6.6 Scavenging of Aerosol Particles 846
APPENDICES 853
REFERENCES 874
LIST OF PRINCIPAL SYMBOLS 935
TABLE OF PHYSICAL CONSTANTS 944

INDEX **945**

PREFACE TO THE FIRST EDITION

Cloud physics has achieved such a voluminous literature over the past few decades that a significant quantitative study of the entire field would prove unwieldy. This book concentrates on one major aspect: *cloud microphysics*, which involves the processes that lead to the formation of individual cloud and precipitation particles.

Common practice has shown that one may distinguish among the following additional major aspects: *cloud dynamics*, which is concerned with the physics responsible for the macroscopic features of clouds; *cloud electricity*, which deals with the electrical structure of clouds and the electrification processes of cloud and precipitation particles; and *cloud optics* and *radar meteorology*, which describe the effects of electromagnetic waves interacting with clouds and precipitation. Another field intimately related to cloud physics is *atmospheric chemistry*, which involves the chemical composition of the atmosphere and the life cycle and characteristics of its gaseous and particulate constituents.

In view of the natural interdependence of the various aspects of cloud physics, the subject of microphysics cannot be discussed very meaningfully out of context. Therefore, we have found it necessary to touch briefly upon a few simple and basic concepts of cloud dynamics and thermodynamics, and to provide an account of the major characteristics of atmospheric aerosol particles. We have also included a separate chapter on some of the effects of electric fields and charges on the precipitation-forming processes.

The present book grew out of a series of lectures given to upper division undergraduate and graduate students at the Department of Atmospheric Sciences of the University of California at Los Angeles (UCLA), and at the Department of Physics of the New Mexico Institute of Mining and Technology at Socorro (New Mexico Tech.). We have made no attempt to be complete in a historical sense, nor to account for all the work which has appeared in the literature on cloud microphysics. Since the subject matter involves a multitude of phenomena from numerous branches of physical science, it is impossible to make such a book truly self-contained. Nevertheless, we have considered it worthwhile to go as far as possible in that direction, hoping thereby to enhance the logical structure and usefulness of the work. In keeping with this goal, our emphasis has been on the basic concepts of the field.

This book is directed primarily to upper division and graduate level students who are interested in cloud physics or aerosol physics. Since no specialized knowledge in meteorology or any other geophysical science is presumed, the material presented should be accessible to any student of physical science who has had the more or less usual undergraduate bill of fare which includes a general background in physics,

physical chemistry, and mathematics. We also hope the book will be of value to those engaged in relevant areas of teaching and research; also, we hope it will provide a source of useful information for professionals working in related fields, such as air chemistry, air pollution, and weather modification.

In the preparation of this book we have incurred many debts. One of us (H.R.P.) is extremely grateful to his long time associate Prof. A. E. Hamielec of McMaster University at Hamilton, Canada, whose generous support provided the basis for solving many of the hydrodynamic problems reported in this book. Gratitude is also gladly expressed to the faculty and research associates at the Meteorological Institute of the Johannes Gutenberg University of Mainz and at the Max Planck Institute for Chemistry at Mainz, in particular to Profs. K. Bullrich and C. Junge, and Drs. G. Hänel, F. Herbert, R. Jaenicke, and P. Winkler for the assistance received during two stays at Mainz while on sabbatical leave from UCLA. In addition, sincere thanks are extended to the Alexander von Humboldt Foundation for a U.S. Senior Scientist Award which made possible the second extended visit at Mainz. Also, one of us (J.D.K.) is grateful to Drs. C. S. Chiu, P. C. Chen, and D. T. Gillespie for informative discussions, and to Prof. M. Brook and Dr. S. Barr for providing time away from other duties. Appreciation is expressed also to the National Center for Atmospheric Research (NCAR) for the assistance provided during a summer visit.

A large number of figures and tables presented in this book have been adapted from the literature. The publishers involved have been most considerate in granting us the rights for this adaptation. In all cases, references to sources are made in the captions.

Our own research reported in this book has been supported over the years by the U.S. National Science Foundation. We would like to acknowledge not only this support, but also the courteous, informal, and understanding manner in which the Foundation's Officers, Drs. F. White, P. Wyckoff, E. Bierly, and F. Eden, conducted their official business with us.

Special thanks go also to the editors of the D. Reidel Publishing Company of Dordrecht, Holland, for providing a fruitful relationship with us.

Finally, we wish to express our sincere appreciation for the invaluable assistance of T. Feliciello, A. C. Rizos, and P. Sanders, who typed the manuscript, and to B. J. Gladstone who drew all the diagrams.

Los Angeles, H. R. PRUPPACHER

March 1978

Los Alamos, J. D. KLETT

PREFACE TO THE SECOND EDITION

In the intervening eighteen years since the appearance of the first edition, research in cloud microphysics has continued to expand at a rapid rate. In fact, we have found it necessary to consider for inclusion in this edition the contents of over 5,000 articles, as well as dozens of books and conference proceedings published since the first edition. Our approach to assimilating this material follows the philosophy of the first edition, namely to attempt a balance between providing a necessary body of descriptive and empirical knowledge, and a framework of theoretical generalities and principles with which to rationalize the otherwise unmanageable mountain of experimental facts. Such an effort naturally entails compromises and personal choices, as a truly exhaustive and completely coherent account of a subject this large cannot be confined within the bounds of a single volume of an acceptable length. Nevertheless, we feel that the present volume does accommodate the most significant advances that have occurred, and that it has been possible to close some of the gaps and answer some of the major questions which characterized the incompleteness of the subject at the time of the first edition.

As before, we have again attempted to enhance the appeal and clarity of the book by making it as self-contained as possible. Our success in this respect has been limited, not only because of the sheer volume of material, but also because of a shift in style of the theoretical approach to the subject. Now that nearly everyone has access to inexpensive desktop computers with more power than mainframes at the time of the first edition, and similar access to greatly improved and easily implemented numerical modeling software, a tendency has developed to address theoretical issues by constructing and then incrementally augmenting numerical models of great complexity, often of an ad hoc nature and with many adjustable parameters. The underlying assumption that more and more physics can successfully be encoded this way into larger and larger programs is sometimes subject to challenge; in any case, the resulting algorithms are often so complex that they and their results have to be accepted largely on faith by other researchers. It is obviously difficult to include an account of such theoretical work in a way that is truly self-contained and logically complete.

We have also had to continue to be extremely restrictive in treating fields intimately related to cloud microphysics. Thus, as in our first edition, we could touch only briefly on some simple concepts of cloud dynamics, and refer in places only to the results of cloud dynamic models which include detailed microphysics. (An excellent text on cloud dynamics is now available in the treatise by Cotton and Anthes (1989).) We also had to leave out the extensive field of the interaction between clouds and electromagnetic radiation, although we sometimes refer

to results derived from radar cloud studies and from studies on the effects of solar and terrestrial radiation on the microstructure of clouds. Also, in the chapter on cloud electricity we have had to omit many facets of clear weather electricity, and the subject of the physics of lightning. On the other hand, we have amplified the present edition by the inclusion of a chapter on cloud chemistry (Chapter 17). This was prompted by the seriousness with which worldwide ecological problems related to air, water, and ground pollution are viewed by the scientific community in general. Our treatment of the subject is restricted to some basic processes that must be considered in current pollution transport models.

Other changes in the book worth noting here include: (1) The descriptive material in Chapter 2 on the microstructural features of clouds has been updated and includes more diagrams to assist modelers, and much more information on cirrus clouds. (2) The section on the structure of water in Chapter 3 reflects our greatly improved knowledge of the specific heat, latent heat, and other properties of water, all the way down to $-40°C$; this supersedes previous extrapolations from the Smithsonian Tables. As an example, the new data on the activation energy for molecular transfer at the ice-water interface leads to homogeneous ice nucleation rates in much better agreement with cirrus observations (described in Chapter 7). Also, a distinct statistical mechanics theory for ice nucleation is now included, and it is shown that the thermodynamic data are consistent with the molecular data from ice physics research. (3) In Chapter 5 the values for surface tension and interface energy below $0°C$ are recomputed due to the new results in Chapter 3. (4) Size distribution measurements of the atmospheric aerosol now extend down to $0.01\,\mu m$ and lower. This new data, and enhanced discussions of gas-to-particle and drop-to-particle conversion, are included in Chapter 8. Also included is new information on aerosols over the North and South Polar regions, which is of relevance to the phenomenon of the Ozone Hole. (5) In Chapter 9, new statistical mechanics modeling results for the heterogeneous nucleation of ice on silver iodide and silicates supplement the previous thermodynamic approach. (6) Numerical simulations of flow about spheres at Reynolds numbers too high for steady axisymmetric flow, as well as for flow past cylinders and three types of snow crystal shapes, are now included in Chapter 10. This gives rise to new ventilation coefficients, hydrodynamic drag, and terminal velocities. Also, new data and modeling concerning drop breakup and oscillations are provided. As an application, improved non-equilibrium descriptions of oscillating drop shapes are given. (6) An amplified treatment of drop condensation growth in stratus clouds and fogs is given in Chapter 13. The chapter also includes new results on ventilation, and some sensitivity studies on the effects of drop collision and coalescence on the early stages of evolving spectra of cloud drops. (7) New parameterizations of experimental work on drop coalescence are given in Chapter 14. Also, the new flow fields described in Chapter 10 are used to determine collision cross-sections between various combinations of drops, finite-length cylinders, plates, and some other crystal shapes. The problem of turbulence is also revisited, including its effect on the orientation distribution of particles. (8) More complete simulations of stochastic drop breakup and growth are given in Chapter 15, along with an expanded treatment of the method of moments. (9) Chapter 16 has been enlarged with respect to parameteri-

zations of experimental data on graupel, rime, hailstones, and the polycrystallinity of frozen drops; there are also new theoretical modeling results on the growth rate of graupel, snow crystals, and hailstones in dry and wet regimes, on the evolution of ice particle size distributions taking various interactions into account, and on the melting of ice particles. (10) In Chapter 18, the description of strongly electrified clouds and cloud particles based on field studies has been updated and expanded considerably. The major cloud charging mechanisms are reviewed in light of new experimental data, and it is concluded that certain non-inductive mechanisms are dominant and primarily responsible for the tripolar thundercloud charge distribution often observed. The sections on the effects of electric fields and charges on drop shape and disruption, corona discharge, and the enhancement of collection and scavenging processes for various types of cloud particles have also been expanded and improved.

The overall scope and intended audience of the book remain unchanged. In particular, we hope it may provide for the upper division and graduate level student a quantitative survey of cloud microphysics, and that it will be a source of useful information for those engaged in related areas of teaching and research, including the fields of aerosol physics, cloud dynamics, climate modeling, air chemistry, air pollution, and weather modification.

In the preparation of this book, we have again incurred many debts. One of us (H.R.P.) is indebted to the German National Science Foundation (DFG) and to the German Ministry for Research and Technology (BMFT) for generously supporting the research carried out at the Institute for Physics of the Atmosphere at the Johannes-Gutenberg University of Mainz. He is particularly very grateful to his longtime associates Prof. Andrea Flossmann and Dr. Subir Mitra, and to Drs. Stefan Borrmann and Andreas Bott for fruitful and constructive criticism in preparing this text. He is thankful to them, as well as to Profs. K. V. Beard and P. K. Wang, for providing him with original figures, tables, and texts, in part still unpublished. Thanks go also to all his students, who have provided through their questions insights for clarifying many of the concepts presented in this book. He also warmly thanks his wife Monica and his son Lukas for bearing the many years of hardships with him. The second author (J.D.K.) would like to thank Prof. P. Chylek for many stimulating and wide ranging discussions, and Dr. R. A. Sutherland of the Army Research Laboratory of White Sands Missile Range, Dr. M. Farmer of Correa Enterprises Inc., and Mr. J. Serna of the Physical Sciences Laboratory of New Mexico State University for their indirect roles in providing financial support that facilitated the completion of this project. He also thanks his wife Cathy, and Mark, Lindsay, and Ali for keeping it all in perspective with love and good cheer. Finally, we wish to express our sincere gratitude to Mrs. K. Franke who typed the original manuscript, to Mr. Michael Lang for coordinating the text into LaTeX, to Mrs. Cornelia Schrörs who set the tables and the figure captions, to Mr. Werner Klaus Zangi who drew all the diagrams, and to Mrs. Renate Graf-Gries and Andrea Richter who were kind enough to coordinate much of the clerical work.

Again, a number of figures and tables in this book have been adapted from the literature. The publishers and authors involved have been most considerate in granting us the rights for this adaptation. In all cases, references to sources are

made in the figure and table captions.

Special thanks also go to the editors of Kluwer Academic Publishers, Dordrecht, in particular to Dr. Mariette de Jong, for providing a fruitful relationship with us.

Mainz, H. R. PRUPPACHER

March 1996

Las Cruces, J. D. KLETT

Hath the rain a father? or who has begotten
the drops of dew?
Out of whose womb came the ice? and the hoary
frost of heaven who has gendered it?
Canst thou lift up thy voice to the clouds,
that abundance of waters may cover thee?
Who can number the clouds in wisdom?
or who can stay the bottles of heaven?
Canst thou send lightnings, that they may go,
and say unto thee, here we are?
Knowest thou the ordinances of heaven? canst
thou set the dominion thereof in the earth?

Job **38**, 28-29, 34, 37, 35, 33

CHAPTER 1

HISTORICAL REVIEW

As one studies the meteorological literature, it soon becomes evident that cloud microphysics is a very young science. In fact, most of the quantitative information on clouds and precipitation, and the processes which are involved in producing them, has been obtained since 1940. Nevertheless, the roots of our present knowledge can be traced back much further. Although a complete account of the development of cloud physics is not available, a wealth of information on the history of meteorology in general can be found in the texts of Körber (1987), Frisinger (1977), Middleton (1965), Khrgian (1959) and Schneider-Carius (1955). Based on these and other sources, we shall sketch here some of the more important events in the history of cloud physics. In so doing we shall be primarily concerned with developments between the 17^{th} century and the 1940's, since ideas prior to that time were based more on speculation and philosophical concepts than scientific fact and principles. As our scope here is almost exclusively restricted to west European and American contributions, we emphasize that no claims for completeness are made.

It was apparently not until the 18^{th} century that efforts were underway to give names to the characteristic forms of clouds. Lamarck (1744-1829), who realized that the forms of clouds are not a matter of chance, was probably the first to formulate a simple cloud classification (1802); however, his efforts received little attention during his lifetime. Howard (1772-1864), who lived almost contemporaneously with Lamarck, published a cloud classification (1803) which, in striking contrast to Lamarck's, was well received and became the basis of the present classification. Hildebrandson (1838-1925) was the first to use photography in the study and classification of cloud forms (1879), and may be regarded as the first to introduce the idea of a cloud atlas. This idea was beautifully realized much later by the *International Cloud Atlas I* (1975), *II* (1987) of the World Meteorological Organization, the *Cloud Studies in Color* by Scorer and Wexler (1967) and the Encyclopedia *Clouds of the World* by Scorer (1972). In this last reference, excellent colored photographs are provided together with a full description of the major genera, species, and varieties of atmospheric clouds. An excellent collection of clouds, photographed from satellites, is found in another book by Scorer (1986).

Both Lamarck and Howard believed the clouds they studied consisted of water bubbles. The bubble idea was originated in 1672 by von Guericke (1602-1686), who called the small cloud particles he produced in a crude expansion chamber 'bullulae' (bubbles). Although he explicitly named the larger particles in his expansion chamber 'guttulae' (drops), the bubble idea, supported by the Jesuit priest Pardies (1701), prevailed for more than a century until Waller (1816-1870) reported in 1846 that the fog particles he studied did not burst on impact, as bubbles would have.

Although this observation was confirmed in 1880 by Dines (1855-1927), it was left to Assmann (1845-1918) to finally end the dispute through the authority of his more comprehensive studies of cloud droplets under the microscope (1884).

The first attempt to measure the size of fog droplets with the aid of a microscope was made by Dines in 1880. Some early measurements of the size of much larger raindrops were made by ingeniously simple and effective means. For example, in 1895 Wiesner (1838-1916) allowed raindrops to fall on filter paper impregnated with water-soluble dye and measured the resulting stains. A little later, Bentley (1904) described an arrangement in which drops fell into a layer of flour and so produced pellets whose sizes could easily be measured and related to the parent drop sizes.

The elegant geometry of solid cloud particles has no doubt attracted attention from the earliest times. Perhaps the first documentation of snow crystals that exhibit a six-fold symmetry was due to an author named Han Ying who made this observation in 1358 BC in China. It was not until centuries later that the same observation also became documented in Europe by means of a woodcut done in 1555 by Olaus Magnus, Archbishop of Uppsala in Sweden. Kepler (1571-1630) was also intrigued by the forms of snow crystals and asked 'Cur autem sexangula?' ('But why are they six-sided?'). Descartes (1596-1650) was perhaps the first to correctly draw the shape of some typical forms of snow crystals (1635). Hooke (1635-1703) first studied the forms of snow crystals under a microscope. Scoresby (1789-1857), in his report on arctic regions (1820), presented the first detailed description of a large number of different snow crystal forms and noticed a dependence of shape on temperature. A dependence of the shape of snow crystals on meteorological conditions was also noted by Martens (1675). Further progress was made when Neuhaus (1855-1915) introduced microphotography as an aid in studying snow crystals. Hellmann (1854-1939) pointed out in 1893 that snow crystals have an internal structure, which he correctly attributed to the presence of capillary air spaces in ice. The most complete collections of snow crystal photomicrographs were gathered by Bentley in the U.S. (published by Humphreys in 1931), and during a life's work by Nakaya (1900–1962) in Japan (published in 1954).

It was also realized early that not all ice particles have a six-fold symmetry. However, before the turn of the 18^{th} century, interest in the large and often quite irregular shaped objects we now call hailstones was apparently restricted to their outward appearance only. Volta (1745-1827) was among the first to investigate their structure, and in 1808 he pointed out that hailstones contain a 'little snowy mass' at their center. In 1814 von Buch (1774-1853) advocated the idea that hailstones originate as snowflakes. This concept was further supported by Waller and Harting (1853), who investigated sectioned hailstones under the microscope. In addition to finding that each hailstone has a center which, from its appearance, was assumed to consist of a few closely-packed snowflakes, they discovered that hailstones also have a shell structure with alternating clear and opaque layers, due to the presence of more or less numerous air bubbles.

All known observations of cloud and precipitation particles were made at ground level until 1783, when Charles (1746-1823) undertook the first instrumented balloon flight into the atmosphere. Although frequent balloon flights were made from

that time on, they were confined mostly to studies of the pressure, temperature, and humidity of the atmosphere, while clouds were generally ignored. The first comprehensive study of clouds by manned balloon was conducted by Wigand (1882-1932), who described the in-cloud shape of ice crystals and graupel particles (snow pellets or small hail) in 1903.

Attempts to provide quantitative explanations for the processes which lead to the formation of cloud particles came relatively late, well into the period of detailed observations on individual particles. For example, in 1875 Coulier (1824-1890) carried out the first crude expansion chamber experiment which demonstrated the important role of air-suspended dust particles in the formation of water drops from water vapor. A few years later, Aitken (1839-1919) became the leading advocate of this new concept. He firmly concluded from his experiments with expansion chambers in 1880 that cloud drops form from water vapor only with the help of dust particles which act as nuclei to initiate the new phase. He categorically stated that 'without the dust particles in the atmosphere there will be no haze, no fog, no clouds and therefore probably no rain'. The experiments of Coulier and Aitken also showed that by progressive removal of dust particles by filtration, clouds formed in an expansion chamber became progressively thinner, and that relatively clean air would sustain appreciable vapor supersaturations before water drops appeared. The findings of Coulier and Aitken were put into a more quantitative form by Wilson (1869-1959), who showed in 1897 that moist air purified of all dust particles would sustain a supersaturation of several hundred percent before water drops formed spontaneously. This result, however, was already implicitly contained in the earlier theoretical work of W. Thomson (the later Lord Kelvin, 1824-1907), who showed that the equilibrium vapor pressure over a curved liquid surface may be substantially larger than that over a plane surface of the same liquid (1870).

As soon as experiments established the significant role of dust particles as possible initiators of cloud drops, scientists began to look closer at the nature and origin of these particles. Wilson followed up his early studies with dust-free air and discovered in 1899 that ions promote the condensation process, a result which had been predicted theoretically in 1888 by J.J. Thomson (1856-1940). However, it was soon realized that the supersaturations necessary for water drop formation on such ions were much too large for them to be responsible for the formation of atmospheric clouds. It was again Aitken who noticed in 1881 that due to their different composition, some dust particles seem to be better nuclei than others. He even surmised that 'fine sodic chloride particles' would condense vapor before the vapor was cooled to the saturation point. This observation he attributed to the 'great attraction which salt has for water'. Aitken's observations were further extended by Welander (1897) and Lüdeling (1903), who suggested that Aitken's salt particles are injected into the atmosphere by the world oceans. The great importance of such salt particles to serve as condensation nuclei was also realized by Köhler (1888-1982) who pointed out that the presence of large numbers of hygroscopic particles generally should prevent large supersaturation from occurring in clouds. Also, Köhler was the first to derive a theoretical expression for the variation of vapor pressure over the curved surface of an aqueous solution drop (1921, 1922, 1927). His pioneering studies became the foundation of modern condensation

theory.

Although the sigificance of oceans as a souce of condensation nuclei was by now clearly recognized, Wigand's observations (1913, 1930) suggested that the continents, and not the oceans, are the most plentiful source. Wigand's conclusions (1934) were supported by the studies of Landsberg (1906-1985) and Bossolasco (1903-1981).

Lüdeling and Linke (1878-1944) were probably the first to determine the concentration of condensation nuclei in the atmosphere (1903, 1904). However, it was Wigand who, during balloon flights from 1911 to 1913, first carried out detailed studies of condensation nuclei concentrations at different levels in the atmosphere as a function of various meteorological parameters. He discovered that their concentration was related to the temperature structure in the atmosphere, and was significantly different inside and outside clouds. On comparing the concentrations of condensation nuclei and cloud drops, Wigand concluded that there are sufficient numbers of condensation nuclei in the amosphere to account for the number of drops in clouds.

Studies during the same period brought out the fact that dust particles also play an important role in the formation of ice crystals. Thus, those researchers who ascended into clouds with instrumented balloons, found ice crystals at temperatures considerably warmer than the temperatures to which Fahrenheit (1686-1736) had supercooled highly purified water in the laboratory in 1724. Nevertheless, Saussure (1740-1799) pointed out in 1783 that, despite the large number of condensation nuclei, cloud drops generally resist freezing to temperatures much below 0°C. This implied that apparently only a few of the dust particles present in the atmosphere act as ice-forming nuclei. Wegener (1880-1931) suggested that water drops form on water-soluble, hygroscopic nuclei while ice crystals form on a selected group of dust particles which must be water-insoluble. From his observations during a Greenland expedition (1912-1913), he concluded that ice crystals form as a result of the direct deposition of water vapor onto the surface of ice-forming nuclei. He therefore termed this special group of dust particles 'sublimation nuclei'. Wegener's mechanism of ice crystal formation by direct vapor deposition was also advocated by Findeisen (1909-1945). On the other hand, Wigand concluded from his balloon flights that ice crystal formation is often preceded by the formation of supercooled water drops, which subsequently freeze as a result of contact with water-insoluble dust particles. Other arguments against a sublimation mechanism for the formation of ice crystals were brought forward by Krastanow (1908-1977) who, in 1936, theoretically demonstrated that the freezing of supercooled drops is energetically favored over the formation of ice crystals directly from the vapor.

While all these studies provided some answers concerning why and how cloud particles come into being, they did not provide any clues as to how a cloud forms as a whole and why some clouds precipitate and others do not. One of the first precipitation theories was formulated in 1784 by Hutton (1726-1797). He envisioned that the cloud formation requisite to precipitation is brought about by the mixing of two humid air masses of different temperatures. The microphysical details of the apportioning of the liquid phase created by this cooling process were not considered. The meteorologists Dove (1803-1879) and Fitz Roy (1805-1865) evidently were in

favor of his theory, since it seemed to predict the observed location of rain at the boundary between 'main currents of air' (this is now interpreted as frontal rain). Therefore, Hutton's precipitation theory persisted for almost a century. When at last given up, it was not for apparent meteorological reasons but for the physical reason that, owing to the large amount of latent heat released during the phase change of water vapor to water, Hutton's process provides far too small an amount of condensed water to explain the observed amounts of rain.

It finally became clear that only cooling by expansion of humid air during its ascent in the atmosphere would provide clouds with sufficient condensed water to account for the observed rain. Thus, Hamberger (1662-1716) noted in 1743 and Franklin (1706-1790) in 1751 that air rises on heating. In turn, Ducarla-Bonifas (1738-1816) and de Saussure (1740-1799) formulated a theory which made use of this concept suggesting that warm moist air which rises will cool as it rises and produce precipitation at a rate which is proportional to the rate of ascent of the moist air. However, it was left to Erasmus Darwin (1731-1802) to clearly formulate in 1788 the connection between expansion, cooling and condensation. The first mathematical formulation of the cooling which is experienced by a volume of expanding air was given by Poisson (1781-1840) in 1823, thus providing the basis for understanding von Guericke's 'cloud chamber' experiments carried out 150 years earlier. Soon afterwards, the idea of cooling by adiabatic expansion, according to which there is no heat exchange between the rising parcel of air and the environment, was applied to the atmosphere by Espy (1785-1860). He deduced in 1835 from experiments and theory that, for a given expansion, dry air is cooled about twice as rapidly as air saturated with water vapor, owing to the heat released by condensing vapor. Also, Péclet (1793-1857) showed in 1843 that the rate of dry adiabatic cooling for a rising air parcel is larger than the cooling usually observed during balloon ascents in the atmosphere.

The first quantitative formulation of the 'saturation adiabatic process', according to which the condensation products are assumed to remain inside the water-saturated air parcel, was worked out by Lord Kelvin in a paper read in 1862 and published in 1865. Meanwhile, in 1864, Reye (1838-1919) independently derived and published formulations for the same process. A mathematical description of the cooling rate of a lifted air parcel from which the condensation products are immediately removed upon formation, a 'pseudoadiabatic process', was formulated in 1888 by von Bezold (1837-1907). In 1884, Hertz (1857-1894) further extended the thermodynamic formulation of a rising moist parcel of air. He suggested that if such a parcel rises far enough, it will pass through four stages: (1) the 'dry stage' in which air is still unsaturated, (2) the 'rain stage' in which saturated water vapor and water are present, (3) the 'hail stage' in which saturated water vapor, water, and ice coexist, and (4) the 'snow stage' in which only water vapor and ice are present.

In 1866, Renou (1815-1902) first pointed out that ice crystals may play an important role in the initiation of rain. Solely on the basis of the rather restricted meteorological conditions he observed, Renou suggested that for development of precipitation, two cloud layers are required: one consisting of supercooled drops and another at a higher altitude which feeds ice crystals into the cloud layer below.

More significant progress in understanding precipitation formation involving ice crystals was achieved by Wegener (1911), who showed through thermodynamic principles that, at temperatures below 0°C, supercooled water drops and ice crystals cannot coexist in equilibrium. Using this result, Bergeron (1891-1977) proposed in 1933 that precipitation is due to the colloidal instability which exists in clouds containing both supercooled drops and ice crystals. Bergeron envisioned that in such clouds the ice crystals invariably grow by vapor diffusion at the expense of the supercooled water drops until either all drops have been consumed or all ice crystals have fallen out of the cloud. Findeisen's cloud observations (1938) produced further evidence in favor of the Wegener-Bergeron precipitation mechanism.

Descartes (1637) had observed that hailstones often have a snowy globule in the middle. In suggesting a mechanism for the formation of hailstones, he therefore speculated that hailstones are the result of numerous snowflakes 'being driven together by wind'. Later, Ducarla Bonifas (1738-1816) proposed with considerable foresight in 1780 that 'columns of air, more strongly heated than the surrounding atmosphere, may violently rise to elevations where the temperature is sufficiently low that the condensation products freeze to become little snowy globules which further grow from the vapor and by collision with supercooled water drops until they are heavy enough to fall back to Earth'. Similarly, von Buch in 1814 and Maille (1802-1882) in 1853 suggested that hailstones originate as snow pellets and grow further by collision with supercooled water drops. Much later, Köhler (1927) applied the notion of collision growth to ice crystals, which he recognized might collect supercooled cloud drops. He also noted, but did not explain, his observation that both drops and crystals have to be of a minimum critical size before such growth may evolve.

The same basic idea of collisional growth, applied this time to cloud drops of different size and hence different fall velocities, was put forth independently in 1715 by Barlow (1639-1719) and by Musschenbroek (1692-1761) in 1739. Musshenbroek also proposed that drops growing by collision will not exceed a size of about 6 mm in diameter, due to the observed instability of drops larger than this size. Reynolds (1842-1912) expanded on the notion of collisional growth and showed by computation in 1877 that water drops above a certain size grow slower by vapor diffusion than by collision with other drops.

A subtle aspect of the collisional growth process was discovered by Lenard (1862-1947), who observed in 1904 that colliding drops do not always coalesce. This he attributed correctly to the difficulty of completely draining all the air from between the colliding drops. He also found (as had been noticed in 1879 by Strutt, later Lord Rayleigh, 1842-1919) that small amounts of electric charge residing on drops could build up attractive electric forces which are sufficiently large to overcome the hydrodynamic resistance to coalescence. In agreement with the expectations of Musschenbroek, Lenard concluded from his experiments that growth by collision-coalescence continues until drops grow to a critical size, after which they become hydrodynamically unstable and break up. He suggested that the fragment drops may then continue to grow in the same manner, producing a 'chain-reaction' effect of overall rapid growth.

Despite Lenard's experimental results, the mechanism of growth by collision

was paid little attention for a long time, since the Wegener-Bergeron-Findeisen mechanism dominated the thinking of meteorologists, most of whom studied storm systems at the middle and higher latitudes where the ice phase is quite common. Simpson (1878-1965) attempted to revive the collision mechanism in his presidential address to the Royal Meteorological Society in 1941. On the basis of reports from airplane pilots who flew over India through precipitating clouds with tops thought to be warmer than 0°C, and from some crude calculations made by Findeisen on the rate at which unequal size cloud drops coagulate, Simpson asserted that he found it untenable to assume that precipitation formation should be confined only to clouds which reach subzero temperature levels. However, convincing quantitative support for Simpson's position had to await the late 1940's, when radar observations and military flights finally led to a general consensus that clouds need not reach subzero temperature levels, and consequently need not contain ice crystals for precipitation to occur.

* * *

In striking contrast to the rather slow development of cloud physics prior to 1940, an abrupt and accelerating increase in research and knowledge has occurred since. A confluence of several factors has brought about this dramatic change. For example, a surge of interest in cloud physics was closely tied to the military-related research in meteorology which developed during the war years (1939-1945) and produced a great number of trained workers in meteorology. Also, several new observational techniques involving aircraft, radar, and other instruments became available to scientists at a time when both the necessary funding and support personnel were also relatively abundant. In addition, interest and support was stimulated by the demonstration of Schaefer and Langmuir in 1946 that it is possible to modify at least some clouds and affect their precipitation yield by artificial means. (They seeded supercooled stratus clouds with dry ice, which caused the formation and subsequent rapid growth of ice crystals. This induced colloidal instability led, in about 20 minutes, to a miniature snowfall.) Finally, the fast pace of general technological advances has had a continuing great impact on cloud physics, insuring an accelerated development by making available such important tools as computers, satellites, rockets, and accurately controlled climatic chambers and wind tunnels.

To a large extent, the rapid progress referred to above can be characterized as a fairly direct development of the ideas and discoveries which were made considerably earlier. As we shall see, the period of progress since the beginning of the 1940's has not been characterized by numerous conceptual breakthroughs, but rather by a series of progressively more refined quantitative theoretical and experimental studies of previously identified microphysical processes.

As we shall also see, much remains to be learned in spite of the significant advances of the past four decades. One principal continuing difficulty is that of incorporating, in a physically realistic manner, the microphysical phenomena in the broader context of the highly complex macrophysical environment of natural clouds. This problem was well expressed 35 years ago in the preface to the first edition of Mason's (1957a) treatise on cloud micrphysics.

Although the emphasis here is upon the *micro-physical* processes, it is important

to recognize that these are largely controlled by the atmospheric motions which are manifest in clouds. These *macro-physical* features of cloud formation and growth, which might more properly be called a *dynamics*, provide a framework of environmental conditions confining the rates and duration of the micro-physical events. For example, the growth or freezing of cloud droplets is accompanied by the release of great quantities of latent heat, profoundly influencing the motion of cloudy air masses, while the motions which ultimately cause evaporation of the cloud determine its duration, and will set a limit to the size which its particles can attain. Progress in cloud physics has been hindered by a poor appreciation of these interrelations between processes ranging from nucleation phenomena on the molecular scale to the dynamics of extensive cloud systems on the scale of hundreds or thousands of kilometers.

The problem of scale which Mason refers to provides a revealing point of view for appreciating the extent of the difficulties one encounters. Thus, stating the case in a very conservative manner, we are concerned in cloud microphysics with the growth of particles ranging from the characteristic sizes of condensation nuclei ($\geq 10^{-2}$ μm) to precipitation particles ($\leq 10^4$ μm for raindrops, $\leq 10^5$ μm for hailstone). This means we must follow the evolution of the particle size spectrum, and the attendant microphysical processes of mass transfer, over about seven orders of magnitude in particle size. Similarly, the range of relevant cloud-air motions varies from the characteristic size of turbulent eddies which are small enough to decay directly through viscous dissipation ($\geq 10^{-2}$ cm), since it is these eddies which turn out to define the characteristic shearing rates for turbulent aerosol coagulation processses, to motion on scales at least as large as the cloud itself ($> 10^5$ cm). Thus, relevant interactions may occur over at least seven orders of magnitude of eddy sizes. Also, in recent years it has become increasingly clear that a strong coupling may occasionally occur between the particle growth processes, including the development of precipitation, and the growth of the cloud electric field. Since in the atmosphere field strengths range from the fair-weather value ($\leq 10^2$ V m^{-1}) to fields of breakdown value (10^6 V m^{-1}), to understand the formation of highly electrified clouds, we must cope with about four orders of magnitude of electric field variation. At the same time, we also must be concerned with various electrostatic force effects arising from at least an eight order of magnitude range of particle charge, considering the observed presence of 1 to 10^8 free elementary charges (5×10^{-10} to 5×10^{-2} e.s.u.) on atmospheric particles. If the electrostatic contribution to the large-scale cloud energetics is also considered, a much larger charge magnitude range is involved. Recent studies have shown further that atmospheric clouds and precipitation significantly affect the chemical nature of the atmosphere in that they are able to incorporate aerosol particles as well as certain gaseous atmospheric constituents, which, once dissolved in the drops, allow chemical reactions to alter their chemical nature. Since observations show that the concentration of aerosol particles ranges from a few per cm^3 in remote background air to a few million per cm^3 in heavily polluted air over cities, while the concentration of pullutant gases range from a volume fraction of 10^{-10} to one of 10^{-4} in these same locations, we must follow the uptake of atmospheric chemical constituents by clouds and precipitation over about six orders of magnitude of concentration variation.

It is clear, therefore, that a complete in-context understanding of cloud microphysics including dynamic, electrical and chemical effects must await some sort of grand synthesis, an elusive and distant goal even from the point of view of presently available models. We should emphasize that such an approach to the subject is far beyond the scope of this book. Rather, our goal is to provide where possible a reasonably quantitative account of the most relevant, individual microphysical processes. In addition to whatever intrinsic interest and usefulness in other application the separate case studies of this book may hold, we also hope they may help provide a useful basis for an eventual integrated treatment of overall cloud behavior. As we shall see, however, even this restricted approach to the subject necessarily involves a degree of incompleteness, since many microphysical mechanisms are still not understood in quantitative detail. In this sense also cloud microphysics is still a developing subject, and so is characterized to some extent by inadequate knowledge as well as conflicting results and points of view.

CHAPTER 2

MICROSTRUCTURE OF ATMOSPHERIC CLOUDS AND PRECIPITATION

Before discussing the microphysical mechanisms of cloud particle formation, we shall give a brief description of the main microstructural features of clouds. Here we will be concerned primarily with the sizes, number concentrations, and geometry of the particles comprising the visible cloud.

2.1 Microstructure of Clouds and Precipitation Consisting of Water Drops

2.1.1 The Relative Humidity inside Clouds and Fogs

Although the relative humidity of clouds and fogs usually remains close to 100%, considerable departures from this value have been observed. Thus, reports from different geographical locations (Pick, 1929, 1931; Neiburger and Wurtele, 1949; Mahrous, 1954; Reiquam and Diamond, 1959; Kumai and Francis, 1962a,b) show that the relative humidity of fogs has been found to range from 100% to as low as 81%. Somewhat smaller departures from saturation are usually observed in cloud interiors. Warner (1968a) indirectly deduced values for the relative humidity in small to moderate cumuli from measurements of vertical velocity and drop size. From his results (shown in Figure 2.1), we see that in these clouds the relative humidity rarely surpasses 102% (i.e., a supersaturation of 2%), and is rarely lower than 98%. The median of the observed supersaturations was about 0.1%. Similarly, Braham (in Hoffer, 1960) found, during several airplane traverses through cumulus clouds, that in their outer portions the air generally had relative humidities between 95 and 100%, dipping to as low as 70% near the cloud edges where turbulent mixing was responsible for entraining drier air from outside the clouds. In the more interior cloud portions, the relative humidity ranged from 100% to as high as 107% (shown in Figure 2.2). More recently, Politovich and Cooper (1988) deduced from flights through 147 clouds over Miles City, Montana, that the supersaturation within these clouds ranged between -0.5 and 0.5% with an average of 0%.

Usually, the maximum supersaturation attained for a given updraft in a fog or cloud is inferred from a comparison between the observed number concentration of drops with the observed number concentration of aerosol particles which can form drops at a given supersaturation (Squires, 1952, Warner, 1968a; Hudson, 1980; Meyer *et al.*, 1980; Paluch and Knight, 1984; Austin *et al.*, 1985; Politovich and Cooper, 1988). Recently, however, instruments have become available which are able to measure the relative humidity in clouds more directly. Thus, the relative humidty inside fogs (Figure 2.3) was measured by Gerber (1981) by means of a spe-

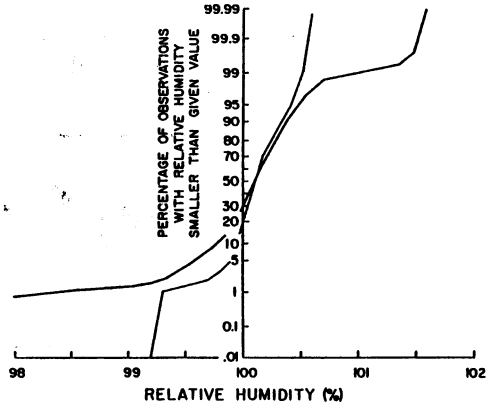


Fig. 2-1: Percentage of observations with relative humidity less than a given value for all samples (heavy line) and for samples taken within 300 m of cloud base (thin line). (From Warner, 1968a, by courtesy of *J. de Rech. Atmos.*, and the author.)

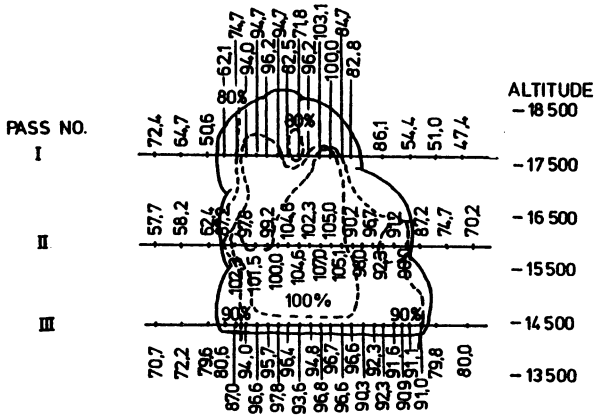


Fig. 2-2: Relative humidity across a small cumulus cloud, derived from flights at three levels. (From Hoffer, 1960, with changes.)

cial dew point hygrometer developed one year earlier to measure relative humidity above 100% (Gerber, 1980). We notice from Figure 2.3 that inside fogs the relative humidity varies rapidly between subsaturated and supersaturated conditions. We will show later in this chapter that the spatial and temporal non-uniformity of the humidity inside clouds and fogs results in a corresponding rapid spatial variation of the concentration of cloud drops and the cloud liquid water content.

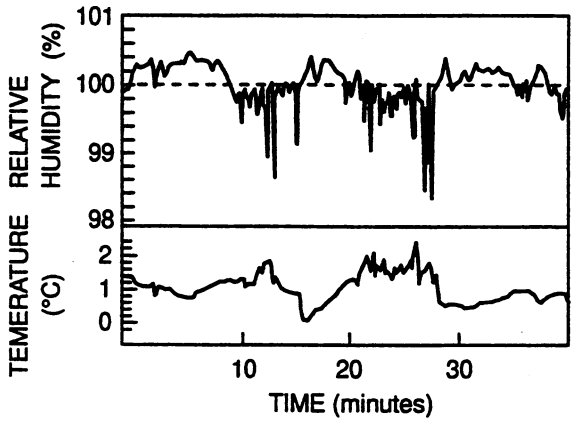


Fig. 2-3: Variation with time of the relative humidity and temperature in a radiation fog near Reston, Virginia. (From Gerber, 1981, with changes.)

2.1.2 Microstructure of Fogs

Observations by Houghton and Radford (1938), Kojima *et al.* (1952), Mahrous (1954), Reiquam and Diamond (1959), Kumai and Francis (1962a), Okita (1962), Meszaros (1965), and Garland (1971) show that fogs, unlike clouds, are characterized by relatively low water contents (generally less than 0.2 g m^{-3}), small drops (typically between 2.5 μm and a few tens of micrometers, with a typical mean diameter D between 10 and 20 μm), small number concentrations (1 to a few hundreds per cubic centimeter), and liquid water contents ranging between 0.05 to 0.5 g m^{-3}. More recent studies on fogs have been carried out by Low (1975), Roach *et al.* (1976), Pilie *et al.* (1975), Mack *et al.* (1980), Jiusto and Lala (1980, 1982), Stanev *et al.* (1987), Uyeda and Yagi (1984), and Kunkel (1982). From some of these more recent observations, Kunkel (1982) categorized the distributions of the drop number concentration $n(D)$ and liquid water content w_L of advection fogs as one of the three types shown in Figures 2.4 and 2.5, respectively. The common feature of the three types in Figure 2.4 is the high concentration of particles between 0.5 and 2.5 μm radius, which may be as large as several thousand per cm^3 (Garland, 1971). Kunkel suggests that these are haze particles consisting of moist aerosol particles which have not yet been activated to actual drops (see Chapters 6 and 13). Before the advent of optical particle counters, these smaller particles went virtually undetected since most other techniques available did not record droplets

smaller than 5 μm. However, using optical particle counters, this detection limit was eliminated. Hindman *et al.* (1977), Low *et al.* (1979), and Pinnick *et al.* (1978) also reported the presence of such haze particles in fogs. From Figure 2.4 we note that the type A drop size distribution is strongly bimodal, type B has a plateau, and type C shows a continuous simple decrease in number concentration which can be represented by a power law. In contrast, the variation of the liquid water content with drop size exhibits a single peak which appears either at a drop diameter near 10 μm (type A) or near 30 μm (type C). A double peak at these two diameters characterizes type B.

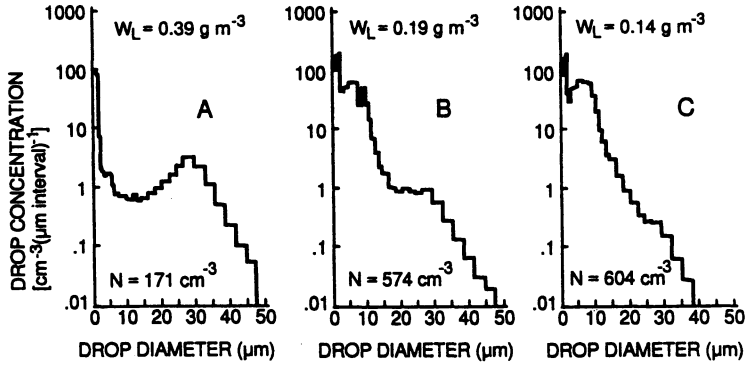


Fig. 2-4: Typical drop size spectra in advection fogs at Otis Air Force Base, Massachusetts. (From Kunkel, 1982, with changes.)

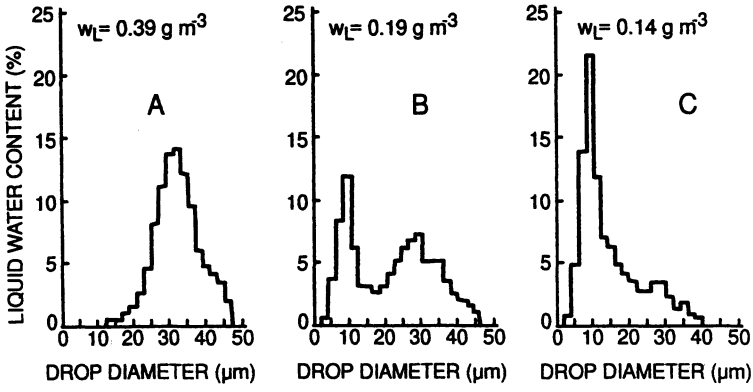


Fig. 2-5: Typical liquid water spectra in advection fogs at Otis Air Force Base, Massachusetts, corresponding to Figure 2-4. (From Kunkel, 1982, with changes.)

According to Kunkel (1982) and Low (1975), one may distinguish among three stages during a fog event. In the formative stage, the droplet number concentration increases with time resulting in increasing liquid water content, while the mean drop

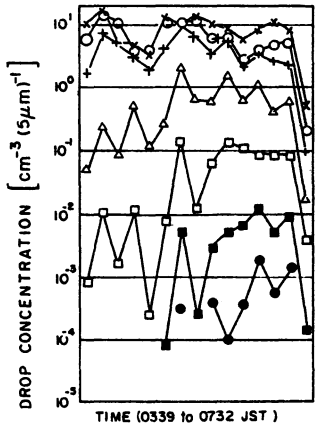


Fig. 2-6: Variation with time of the drop concentration in a fog at Asahikawa, Japan. × 5-10 μm; ○ 10-15 μm; △ 20-25 μm; ■ 35-50 μm; • 50-75 μm; JST is Japan standard time. (From Okita, 1962; by courtesy of *J. Meteor. Soc., Japan.*)

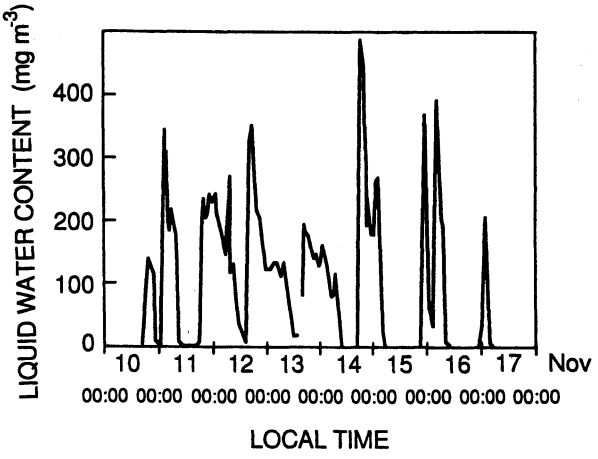


Fig. 2-7: Variation with time of the liquid water content, w_L, measured on the ground during successive fog events. (From Fuzzi *et al.*, 1992, with changes.)

size may remain the same or may increase slightly. During the mature stage, the number concentration, liquid water content, and mean drop size fluctuate rather strongly around generally constant values. The final dissipative stage is a period of decreasing drop concentration, drop size, and liquid water content. Figures 2.6 and 2.7 illustrate the large spatial variations of the drop number concentration and liquid water content during fog events, as noted as a function of time by an observer at a fixed observation site. The variation in time of the drop number concentration ranges up to two orders of magnitude for certain size categories. Analogously, the liquid water content may vary rapidly from near zero values up to 0.5 g m^{-3} (Fig. 2.7).

The vertical microstructure of fog is less well-known. Generally it is found that with increasing height in the fog, the drop spectrum narrows and the mean drop radius decreases slightly, while the liquid content rises to one or more maxima at some midlevel height in the fog.

2.1.3 Microstructure of Clouds

Turning now to the microstructure of clouds, we shall mainly be concerned with cumulus clouds as these have been studied most often. In contrast to fogs and also some stratiform clouds, the drop size distribution of cumulus clouds depend strongly on the development stage of the clouds, ranging from an early developing stage with no precipitation to the mature and eventually dissipating stage with large cloud drops and precipitation. This is exemplified by Figures 2.8a,b,c which show that non-precipitating fair weather continental cumuli have relatively narrow drop size spectra, while the spectra of continental cumuli which have reached the more mature stage of a cumulus congestus, cumulonimbus, or cumulus-complex, are much broader. Cumulus clouds which are embedded in a stratus layer have an even broader spectrum. However, we notice from these figures that at each development stage the drop spectra may vary considerably. In contrast to continental clouds, maritime clouds (Figure 2.9) have an even broader spectrum, and, in particular, have drop concentrations at the small drop size end which are one order of magnitude smaller than the concentration in continental cumuli. Figure 2.10 extends the spectrum for tropical cumuli in Figure 2.9 to larger sizes and illustrates a typical feature of cloud drop spectra in general: the concentration decreases sharply from a few tens to few hundreds per cubic centimeter at the small drop size end to between 1 l^{-1} and 1 m^{-3} for the large drops with diameters $> 500\,\mu$m.

Squires (1958a) has carried out detailed comparative studies of the drop spectra of different types of clouds. The observational sequence shown in Figures 2.11a,b,c illustrates the dependency of spectral shape on cloud type for situations in which the nuclei on which drops form are essentially the same in type and concentration, since a given air mass has spawned all three types shown. However, we can see that even though there is little variation in liquid water content, the drops become smaller, more numerous, and more homogeneous in size as one passes from the orographic to the stratus to the cumulus cloud types. Continental cumuli appear to represent an extension of this trend, in that the spectra are even narrower, the concentrations even higher, and the average drop sizes even smaller (Figure 2.11d).

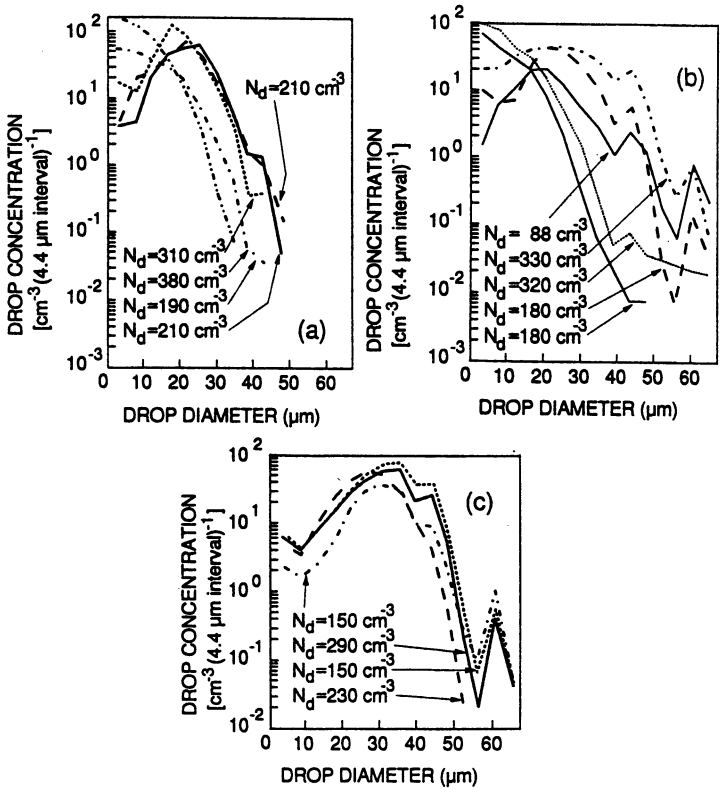


Fig. 2-8: Size spectra of cloud particles observed near the top of continental cumuliform clouds: (a) in six developing small cumuli, (b) in five cumulus complexes, (c) in four cumuli embedded in stratiform clouds. (From Hobbs *et al.*, 1980, with changes.)

For this case, a different air mass type with a correspondingly different aerosol particle content is involved, and this largely accounts for the change from the maritime spectrum. Squires' observations clearly express the trend that high drop concentrations in clouds are associated with narrow drop size spectra and small drop sizes. This is the pattern usually encountered in continental type clouds, while in maritime clouds low drop concentration are associated with broad size spectra and large drop sizes.

Individual drop size spectra often tend to be bimodal (Eldridge, 1957; Durbin, 1959; Warner, 1969a), as exemplified by Figure 2.12a. During his flights through clouds over the east coast of Australia, Warner (1969a) observed that the tendency of a size distribution to be bimodal increased with height above cloud base and with decreasing stability in the cloud environment (Figure 2.12b). The same tendency was found by Politovich and Vali (1983) in cap clouds over Elk Mt., Wyoming. Based on his observations, Warner suggested that bimodal drop size distributions are the result of a mixing process between the cloud and the environment. Since the drop size spectra were fairly uniform for a given level across a cloud and the

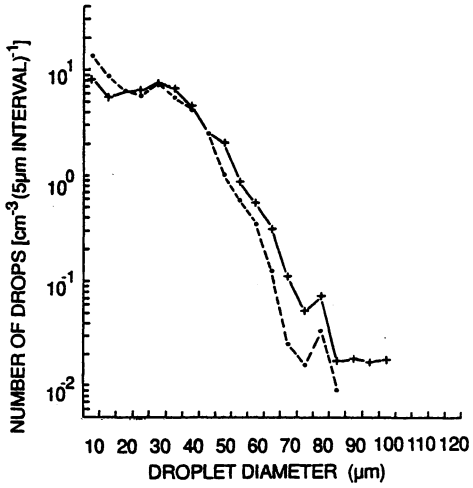


Fig. 2-9: Mean drop size distribution in maritime cumuli over the Gulf of Mexico, near the Bahama Islands, and near Puerto Rico. Average, total drop concentration in 11 clouds with echoes: 52 cm^{-3} (dashed line), in 26 clouds without echoes: 58 cm^{-3} (solid line). (From Battan and Reitan, 1957; by courtesy of Pergamon Press Ltd.)

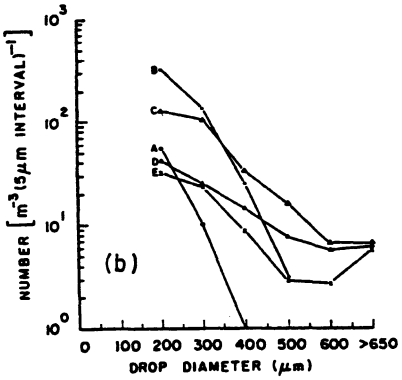


Fig. 2-10: Drop spectra for cumuli in the tropical trade wind region (Gulf of Mexico, Bahama Islds, Puerto Rico). Total concentration ranges: (A) 200 to 3000 drops m^{-3}, w_L = 1.0 to 33.1 × 10^{-3} g m^{-3}; (B) 3000 to 20000 drops m^{-3}, w_L = 32.0 to 213 × 10^{-3} g m^{-3}; (C) 3000 to 8000 drops m^{-3}, w_L = 33 to 163 × 10^{-3} g m^{-3}; (D) 1000 to 3000 drops m^{-3}, w_L = 3.3 to 116 × 10^{-3} g m^{-3}; (E) precipitation measurements. (From Brown and Braham, 1959; by courtesy of Am. Meteor. Soc., and the authors.)

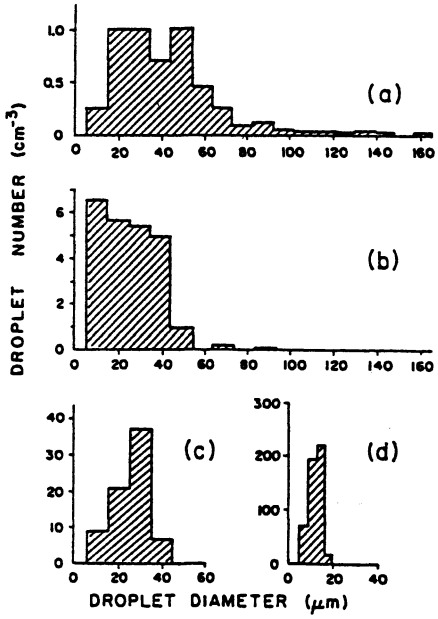


Fig. 2-11: Droplet spectra in clouds of various types. Cumulus samples are taken 2000 ft. above cloud base, orographic and dark stratus values are average. Note change in ordinate scale from figure to figure. (a) Orographic cloud over Hawaii, $w_L = 0.40$ g m^{-3}; (b) dark stratus over Hilo (Hawaii), $w_L = 0.34$ g m^{-3}; (c) tradewind Cumulus over Pacific off the coast of Hawaii, $w_L = 0.50$ g m^{-3}; (d) continental Cumulus over Blue Mts. near Sydney, Australia, $w_L = 0.35$ g m^{-3}. (From *The Physics of Rain Clouds* by N.H. Fletcher, copyrighted by Cambridge University Press, 1962a, redrawn by Fletcher after Squires, 1958a.)

bimodality was not confined to the cloud edges, Warner proposed that the mixing process producing the bimodality is due mostly to entrainment of drier air at the growing cloud top, and to a lesser degree, to entrainment at the cloud edges. Figure 2.12b shows further that the fraction of drops larger than 25, 30, and 35 μm diameter increased rapidly with height above cloud base, indicating that the size distribution experiences a broadening effect with increasing distance from cloud base. Spectra with double maxima have also been observed by McLeod (1976) in thunderstorm clouds over Alberta, by Meischner and Bögel (1988) in cumulus clouds over the Alps, by Slingo *et al.* (1982) in stratocumulus clouds over England, and by Ryan *et al.* (1972) in stratus clouds off the coast of California (Figure 2.13). Figure 2.14 for a continental cumulus and Figure 2.15 for a maritime stratocumulus, show that the relative size of the two maxima in the bimodal spectra varies with location in the cloud and with the stage of development.

If we consider the spatial distribution of the drop size, number concentration, and liquid water content, we find strongly inhomogeneous conditions. Thus, we notice from Figure 2.16 that w_L varies rapidly over short distances along a horizontal flight path in a manner which is closely related to the variation of the vertical

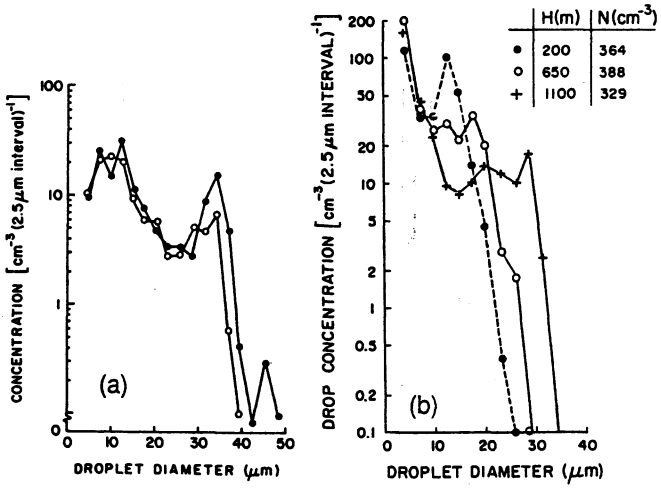


Fig. 2-12: a. Cloud drop spectra in isolated cumuli near the Eastern Australian coast. Adjacent samples taken 100 m apart near the top of a cloud 1400 m deep. (From Warner, 1969a; by courtesy of Am. Meteor. Soc., and the author.)

Fig. 2-12: b. Variation with height of cloud drop spectra in isolated cumuli near the Eastern Australian coast (based on two clouds). The height H above cloud base at which the samples were taken and the average total drop concentration N at that height are also shown. (From Warner, 1969a; by courtesy of Am. Meteor. Soc., and the author.)

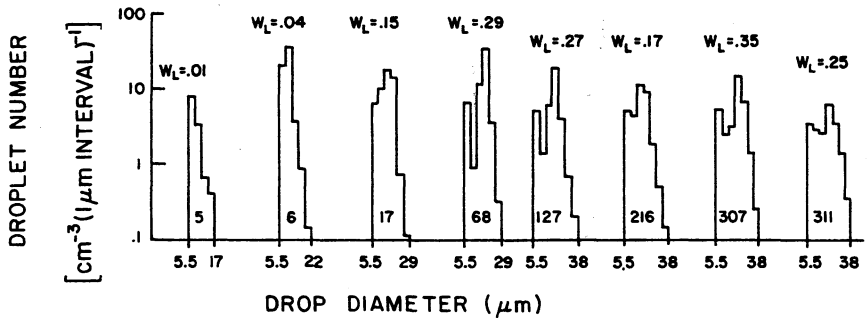


Fig. 2-13: Cloud drop spectra observed during a gradual ascent through a shallow non-precipitating maritime stratus off the Californian coast; N (cm^{-3}) is the total number of drops, w_L (g m^{-3}) is the liquid water content; number within the distribution represents elapsed time after penetration with aircraft. (From Ryan *et al.*; 1972, with changes.)

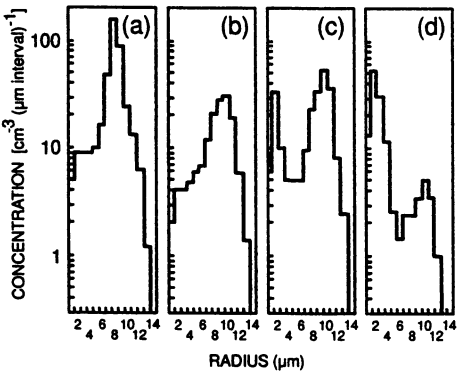


Fig. 2-14: Drop size spectra averaged over 100 m flight intervals inside a continental cumulus over Montana: (a) inside strongest updraft (W = 17 m sec^{-1}), (b) at larger altitude but in weak downdraft near cloud edges (W = -2.2 m sec^{-1}); (c), (d) two consecutive measurements in cloud (W = 11 m sec^{-1} , 8.8 m sec^{-1}). (From Paluch and Knight, 1984, with changes.)

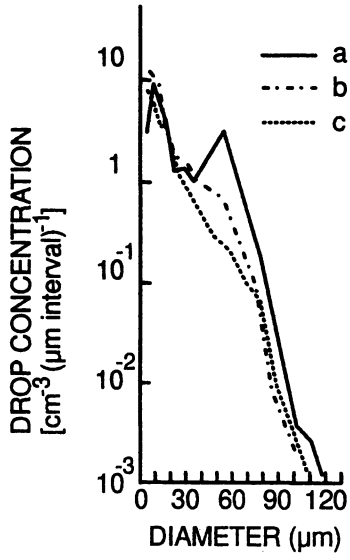


Fig. 2-15: Drop size distribution inside a maritime stratocumulus over Miyakojima Island, Japan. (a) developing stage, (b) intermediate stage, (c) decaying stage. (From Ichimura *et al.*, 1980, with changes.)

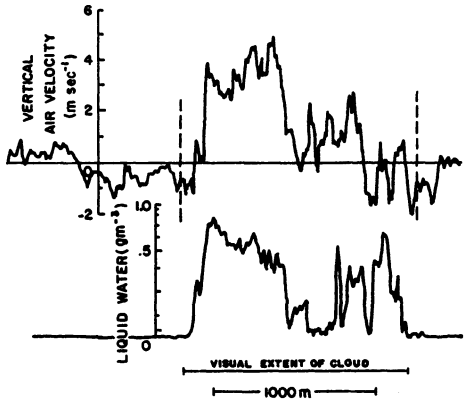


Fig. 2-16: Vertical air velocity and liquid water content in isolated cumuli near the Eastern Australian coast as a function of distance from the place the airplane entered the cloud. (From Warner, 1969a; by courtesy of Am. Meteor. Soc., and the author.)

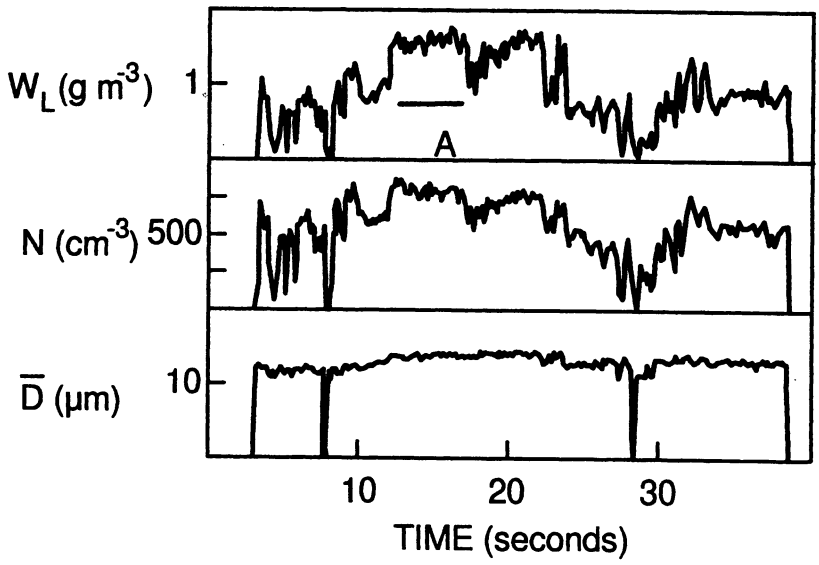


Fig. 2-17: Variation with time of the liquid water content w_L , total number concentration N, and mean diameter for drops of $D > 6\mu$m during the penetration of a cumulus cloud over Montana. A time period of 10 seconds corresponds to about 1 km flight distance. The region denoted by A indicates a steady updraft region. (From Blyth and Latham, 1990, with changes.)

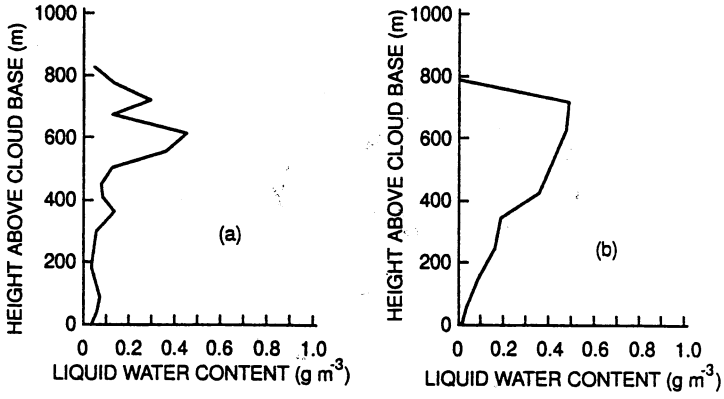


Fig. 2-18: Variation of the liquid water content, w_L , with height above cloud base inside: (a) an altocumulus-altostratus cloud layer, and (b) inside a stratus layer, both of negligible ice content above S. Germany. (From Hoffmann and Roth, 1988, with changes.)

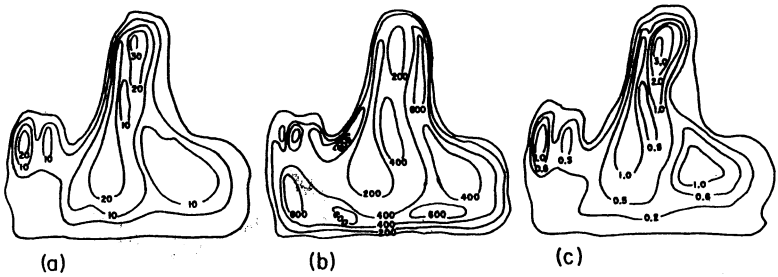


Fig. 2-19: Spatial distribution of microstructure parameters in cumulus cloud. (a) drop diameter (μm), (b) drop concentration (number cm^{-3}), (c) w_L (g m^{-3}). (From Huan, 1963; by courtesy of Air Force Geophys. Laboratory, Hanscom Air Force Base, Mass.)

velocity in the cloud. From Figure 2.17, we see that w_L varies essentially as the total number concentration of drops. On the other hand, the mean drop diameter $\bar{D}$ only reflects the two main strong dips in w_L. Notice also that there exist some 'steady' regions inside clouds with little variation in drop diameter.

The observations of Zaitsev (1950), Draginis (1958), Squires (1958b), Durbin (1959), Ackerman (1959, 1963), Huan (1963), Borovikov *et al.* (1963), Warner (1955, 1969a), Vulfson *et al.* (1973) demonstrate that the cloud water content typically increases with height above the cloud base, assumes a maximum somewhere in the upper half of the cloud, and then decreases again toward the cloud top. This is illustrated in Figure 2.18a for an alto-cumulus-alto-stratus cloud, by Figure 2.18b for a stratus cloud, both studied by Hoffmann and Roth (1988) in S. Germany, and by Figure 2.19 for a small continental cloud studied by Huan (1963) in China. We also notice from Figure 2.19 that, in contrast to the cloud in Figure 2.17, the distribution of the liquid water content parallels the distribution of the drop size

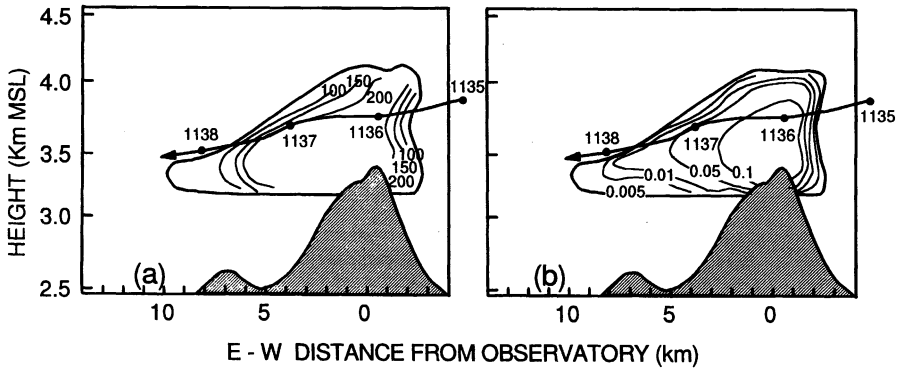


Fig. 2-20: Spatial distribution of microstruture parameters in a cap-cloud over Elk Mt. (Wyoming). (a) Droplet concentration (cm^{-3}), (b) liquid water content (g m^{-3}). The flight track (heavy line with mountain standard time) is also shown. (From Politovich and Vali, 1983, with changes.)

rather than the drop concentration. A rather symmetric distribution of the drop concentration and liquid water content is seen for the cap-clouds observed by Politovich and Vali (1983) (Figure 2.20a,b). The pronounced spatial variations of the cloud microphysical parameters in the vertical are exemplified in Figures 2.21a,b,c by the observations of Heymsfield *et al.* (1991) in an alto-cumulus layer.

Although the liquid water content of clouds varies strongly from cloud to cloud, one may use the following characteristic values (Borovikov *et al.*, 1963): Cumulus (early stage), 0.2 to 0.5 g m^{-3}; Cumulus (later stage), 0.5 to 1.0 g m^{-3}; dense cumulus congestus and cumulonimbus, 0.5 to 3 g cm^{-3}; alto-cumulus-alto-stratus, 0.2 to 0.5 g m^{-3}; stratus-stratocumulus, 0.1 to 0.5 g m^{-3}; nimbo-stratus, 0.2 to 0.5 g m^{-3}. In cumulus with very high updrafts, liquid water contents of up to 5 g m^{-3} and more have been observed (Poellot and Pflaum, 1989). Hobbs *et al.* (1980), Gayet *et al.* (1978) and Musil and Smith (1989) found in some thunderstorms liquid water contents up to 14 g m^{-3}, which amounted to twice the adiabatic value. They attributed this result to liquid water storage in accumulation zones inside the cloud. In most cases, however, a comparison between the observed cloud water content $(w_L)_{ad}$ computed on the basis of a saturated adiabatic ascent of moist air shows that generally $w_L < (w_L)_{ad}$. This fact is illustrated by Figure 2.22, which implies that, as a cloud builds, drier air is constantly entrained and subsequently saturated at the expense of some of the water released during ascent. In most cases, $w_L/(w_L)_{ad}$ is found to decrease with increasing height above cloud base but to increase with increasing cloud width. This implies that the entrainment is especially pronounced near the cloud top, while the net dilution effect by entrainment is less in wider clouds than narrower ones. Generally, $w_L/(w_L)_{ad}$ lies between 0.1 and 0.6, with near adiabatic values close to the cloud base, although near-adiabatic values may occasionally be found also higher up (Blyth and Latham, 1990; Heymsfield *et al.*, 1978; Jensen *et al.*, 1985).

Remote sensing with radar can provide useful information on the correlation

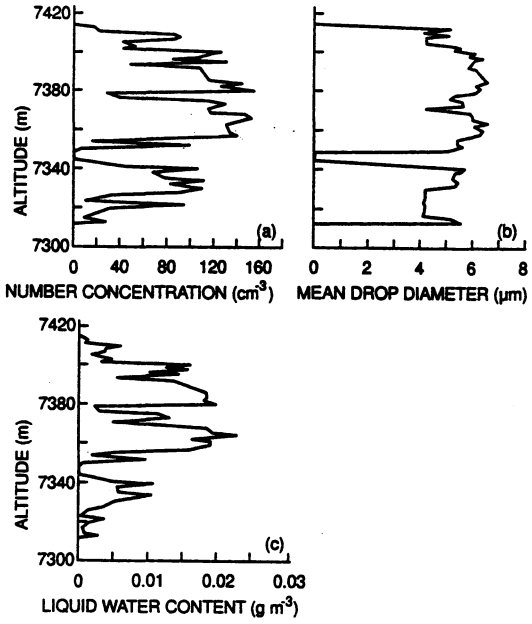


Fig. 2-21: Variation with altitude of the microstructure parameters inside a highly supercooled alto-cumulus cloud of negligible ice content over Green Bay (Wiscounsin) air temperature: $-28°C$ at 7100 m and $-30°C$ at 7500 m. (a) Droplet concentration, (b) mean drop diameter, (c) liquid water content. (From Heymsfield *et al.*, 1991, with changes.)

between the cloud microstructure and the overall development of precipitating clouds. Most of the early work was done with 10 or 3 cm radars which, in general, could only detect drops larger than a few hundred microns in diameter. More recent high power 3 cm radar, and most 1 cm radar, permit the detection of drops with diameters larger than a few tens of microns (Mason, 1971; Battan, 1973).

From radar studies of various types of cumuli, Battan and Braham (1956), and Morris (1957), found that the appearance of a radar echo is characteristically related to the cloud dimensions. Thus, Figure 2.23 shows that the probability of an echo developing in a cloud grows with its cloud top height and width. Notice that continental clouds need to build considerably higher than maritime clouds and must become considerably wider before a radar echo appears. Since higher clouds usually also have greater depths, we notice from Figure 2.24 that, as expected, the appearance of a radar echo is more likely the greater the cloud depth.

2.1.4 Formulations for the Drop Size Distributions in Clouds and Fogs

For many fog and cloud modeling purposes, it is necessary to be able to approximate the observed drop size distribution by an analytical expression. Fortunately, drop

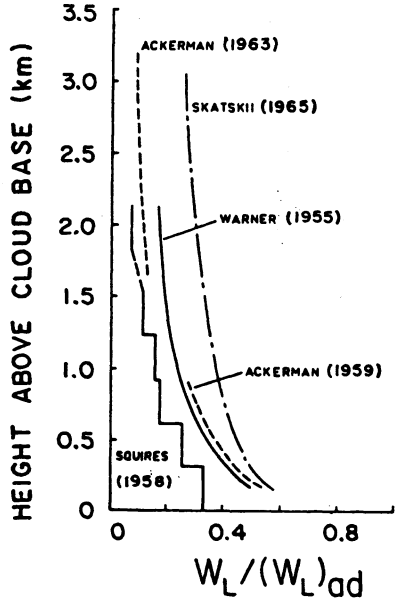


Fig. 2-22: Ratio of the observed mean liquid water content at a given height above cloud base to the adiabatic value, for non-precipitating clouds. (From Warner, 1970a; by courtesy of Am. Meteor. Soc., and the author.)

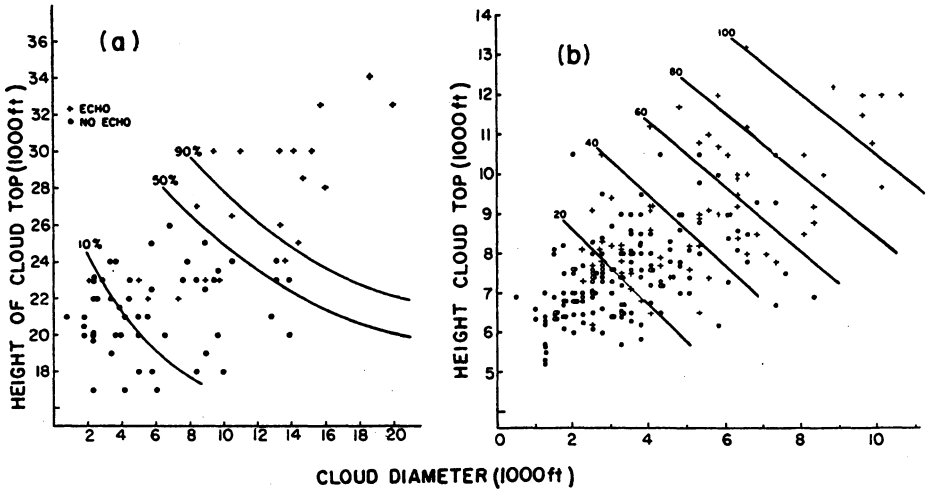


Fig. 2-23: Occurrence (+) or non-occurrence (o) of precipitation in cumuli as function of cloud-top height and cloud width derived from radar echoes. Lines of equal probability to find an echo are given. (a) Clouds over Arizona (from Morris, 1957; by courtesy of Am. Meteor. Soc., and the author). (b) Clouds over ocean near Puerto Rico (from Battan and Braham, 1956; by courtesy of Am. Meteor. Soc., and the authors).

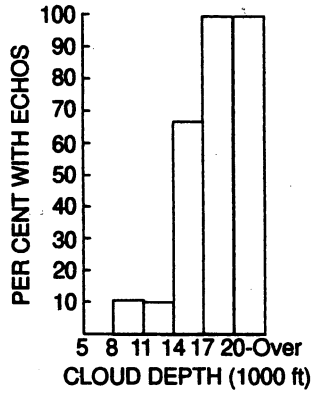


Fig. 2-24: Percentage of Arizona cumuli giving radar echo as a function of cloud depth. (From Morris, 1957; by courtesy of Am. Meteor. Soc., and the author.)

size distributions measured in many different types of clouds and fogs under a variety of meteorological conditions often exhibit a characteristic shape. Generally, the concentration rises sharply from a low value to a maximum, and then decreases gently toward larger sizes, causing the distribution to be positively skewed with a long tail toward the larger sizes. Such a characteristic shape can be approximated reasonably well by either a gamma distribution

$$n(a) = Aa^{\beta} \exp(-Ba^{\gamma}), \tag{2-1}$$

or a lognormal distribution

$$n(a) = \frac{N}{\sqrt{2\pi}(\log \sigma)a} \exp\left(-\frac{\left[\log \frac{a}{a_m}\right]^2}{2(\log \sigma)^2} \right), \tag{2-2}$$

where a is the drop radius, and $n(a)\mathrm{d}a$ is the number of drops cm^{-3} in the radius range $(a, a + \mathrm{d}a)$. Also, N is the total number of drops per unit volume, σ is the standard deviation of the distribution and a_m is the drop radius at the maximum of the distribution. The parameters A, B, β, and γ may be related to moments of the distribution. In order to describe a drop size distribution with two or more maxima, one or more unimodal distributions may be superposed. As an example, according to Khrgian and Mazin (in Borovikov *et al.* 1963) many drop size distributions with a single maximum may also be quite well represented by a gamma distribution for which $\gamma = 1$ and $\beta = 2$, i.e.,

$$n(a) = Aa^2 \exp(-Ba). \tag{2-3}$$

The parameters A and B can be related to any two moments of the distribution. For example, in terms of the total concentration N (the zeroth moment), and the

average radius $\bar{a}$ (the ratio of the first and zeroth moments) we find

$$N = \int_0^\infty n(a)\,\mathrm{d}a = \frac{2A}{B^3} \tag{2-4}$$

and

$$\bar{a} = \frac{1}{N}\int_0^\infty an(a)\,\mathrm{d}a = \frac{3}{B}\,. \tag{2-5}$$

Another related quantity of interest is the total mass concentration of liquid water. Since this often turns out to be about 10^{-6} g cm^{-3}, one defines the cloud liquid water content, $\mathrm{w_L}$, as follows:

$$\mathrm{w_L(g\ m^{-3})} \equiv 10^6 \left(\frac{4\pi}{3}\right) \rho_\mathrm{w} \int_0^\infty a^3 n(a)\,\mathrm{d}a\,, \tag{2-6}$$

where ρ_w is the density of water in g cm^{-3} and a is in cm. Then, for the Khrgian-Mazin distribution, we find

$$A \approx 1.45 \times 10^{-6} \left(\frac{\mathrm{w_L}}{\rho_\mathrm{w}\bar{a}^6}\right)\,, \tag{2-7}$$

and

$$N \approx 1.07 \times 10^{-7} \left(\frac{\mathrm{w_L}}{\rho_\mathrm{w}\bar{a}^3}\right)\,. \tag{2-8}$$

Stanev *et al.* (1987), Low (1975) and Meszaros (1965) also found that the size distributions of fog drops could be fitted by the Khrgian-Mazin distribution. Another convenient representation of the cloud drop size distribution is the empirical formula developed by Best (1951a):

$$1 - \mathrm{F} = \exp\left[-\left(\frac{D}{\mathrm{C}}\right)^\mathrm{k}\right]\,, \tag{2-9}$$

where F is the fraction of liquid water comprised of cloud drops with diameters smaller than D (μm). The characteristic parameters C and k vary with the liquid water content, the total drop concentration, and the maximum drop size in the cloud. Best found $1.92 \leq \mathrm{k} \leq 4.90$. $2 \leq \mathrm{C} \leq 29\,\mu$m. Of course, it must be remembered that these various analytical expressions only represent average distributions. As we have seen in the previous section, individual drop size spectra may be significantly different.

2.1.5 The Mean Distance between Drops in Clouds and Fogs

From the previous section, it is clear that microstructure inhomogeneities in clouds are rather pronounced. The question naturally arises as to whether such behavior

continues to hold down to the smallest scales of physical significance, such as distances of the order of the droplet separations. In general, given the many stochastic influences on drop growth and drop spacing in a complex natural system such as a cloud, one would indeed expect inhomogeneities, or fluctuations, to occur on all length scales, including the smallest. In fact, in one sense this is trivially so: If one measures the liquid water content over sample volumes of the order of average drop volumes, for example, the result is bound to reflect the fundamental dichotomy of being either inside or outside of a drop.

The more meaningful question is how to characterize the expected physical property fluctuations on the smaller scales within clouds. Let us address this problem briefly by focusing on the spacing of droplets in clouds. A simple estimate of the expected nearest-neighbor distance for droplets may be obtained as follows: The liquid water content of clouds, w_L, typically equal to 1 cm^3 of water per cubic meter of air, may be approximated by the ratio of the volume of the average cloud droplet (of radius $\bar{a}$) to the volume of a sphere whose radius is $\bar{d}$, the average distance between droplets; thus,

$$\frac{\bar{d}}{\bar{a}} \approx w_L^{-1/3} \approx 10^2 , \tag{2-10}$$

which shows that clouds are rather sparse aerosols. In terms of the concentration n, we note that $w_L = 4\pi/3\bar{a}^3 n$ and so also, $\bar{d} \approx 0.620 n^{-1/3}$. A more detailed analysis, given in Appendix A-2.1.5, shows that the above approximations are really quite good; e.g., we find

$$\bar{d} = \frac{0.554}{n^{1/3}} = \frac{0.893\bar{a}}{w_L^{1/3}} . \tag{2-11}$$

Given this mean spacing, and assuming droplets are randomly distributed in space, one can make various statistical predictions about the expected number of droplets in a particular volume of cloud. The basis for this is the Poisson discrete probability distribution function which defines the set of probabilities for encountering any given number of randomly placed droplets in a given volume, provided the mean number density is known, and that the process is truly random. (Further details of this distribution are not needed here; any text on probability theory may be consulted for more specifics. However, it may be noted that the derivation of (2-11) in Appendix A-2.1.5 provides an example of the reasoning characterizing Poisson statistics. Furthermore, Poisson statistics are used explicitly in the discussion of drop collection in Chapter 15.)

Given the above framework, one can now take advantage of the greatly enhanced measurement capability of recent years to search for possible deviations from the default Poisson statistics. For example, Baker (1992) attempted to analyze the arrival times of cloud droplets passing through the laser beam of a forward scattering spectrometer probe (FSSP) mounted on an aircraft. Although small departures from Poisson statistics were noted at scales between 0.5 and 5 cm, it was not possible to relate the measurements to actual inter-droplet distances. Similarly, Paluch and Baumgardner (1989) established with their FSSP measurements that non-uniformities in the drop concentration existed at scales below 10 cm, except deep inside a cloud where the drops were found to be randomly distributed.

A more definite conclusion was reached by Kozikowska *et al.* (1984), who conjectured, on the basis of holographic measurements in ground fog, that there appeared to be droplet clustering and systematic deviations from a random spatial droplet distribution. A quantitative study to test the conclusions of Kozikowska *et al.* was carried out by Borrmann *et al.* (1993) and by Uhlig (1995) using holograms taken inside stratus and stratocumulus clouds on Mt. Feldberg in Germany. An example of the local drop size distribution inferred from the holographic method is given in Figure 2.25.

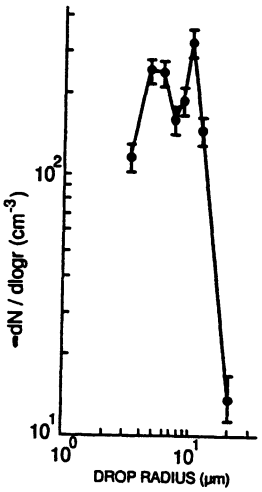


Fig. 2-25: Drop size spectrum in a fog on Kl. Feldberg (Germany) determined by holography. $N = (141 \pm 5)$ cm^{-3} , $w_L = 0.4$ g m^{-3}. (From Borrmann *et al.*, 1993, with changes.)

Analysis of the mean distance $\bar{d}$ derived from the holograms showed that within the experimental error, the drop size spatial distribution deviated from Poisson statistics, and hence from true randomness, by only a few percent. Thus, we deduce for example from Figure 2.25 and 2.11 that $\bar{d} = 1064 \pm 12\,\mu$m for $n = 141 \pm 5$ drops cm^{-3}. Comparison with the value of $1158\,\mu$m observed by Borrmann *et al.* shows agreement with the assumption of randomness to within 8%. Mean distances derived by Uhlig (1995) from her holograms, showed even smaller deviations from randomness. However, somewhat larger deviations were found if the formation of nearest-neighbor pairs was considered. Thus, in a previous theoretical and experimental study, Raasch and Umhauer (1989) determined that about 59% of particles, distributed randomly in an infinite volume, form nearest-neighbor pairs, in the sense that each droplet in a pair is the nearest-neighbor of the other. The field observations of Borrmann *et al.* showed, however, that only 51% of the particles in the observed collective formed such mutual nearest-neighbors, for a deficit of 14% from the expected value if randomness prevailed. Of course, from the mentioned tests on the mean distance, no conclusions can be drawn with regard to the deviation from Poisson statistics of the individual distances d between

the drops. Therefore, Uhlig (1995) and Borrmann *et al.* (1993) subjected their hologram data to additional tests which showed that for $d < 0.5n^{-1/3}$ the number of nearest-neighbor distances were up to 10% higher than the number predicted by Poisson statistics. The data also showed that a substantial fraction of the drops in the ensemble had nearest-neighbor distances of less than 100 drop radii. In fact, in the distribution given by Figure 2.25, Borrmann *et al.* found that 40% of the drops in the ensemble were closer to each other than 100 drop radii, 20% closer than 70 drop radii, 10% closer than 60 drop radii, and 3% even closer than 10 drop radii. This brings to mind the difficult matter of assessing how drop growth rates are affected by the proximity of other drops and by the proximity of walls around the drops (see also Sections 10.2.2.4, 13.2.2.1 and 14.2).

2.1.6 Microstructure of Rain

A small difficulty arises in attempting to describe the spectra of rain, since raindrops are large enough to have a size-dependent shape which cannot be characterized by a single length (see Section 10.3.2). The conventional resolution, which we adopt here, is to describe rain spectra in terms of the equivalent diameter D_0 defined as the diameter of a sphere of the same volume as the deformed drop. When falling at terminal velocity, drops are nearly perfect spheres if $D_0 \lesssim 280\,\mu$m. Larger drops are slightly deformed and resemble oblate spheroids if $280 \lesssim D_0 \lesssim 1000\,\mu$m. For $D_0 > 1000\,\mu$m, the deformation becomes large and the drops resemble oblate spheroids with flat bases (see Plate 1). Drops larger than about 10 mm in diameter are hydrodynamically unstable and break up, even in a laminar air stream (see Section 10.3.5).

In addition to the equivalent diameter D_0, there are three other quantities which are commonly used to characterize rain: (1) the size distribution $n(D_0)$, expressed here in terms of the number of drops per cubic meter of air per mm size interval; (2) the water content, w_L, given as

$$w_L(\text{g m}^{-3}) = \left(\frac{\pi}{6}\right) \times 10^{-3}\rho_w \int_0^\infty D_0^3 n(D_0)\,dD_0\,, \tag{2-12}$$

with D_0 in mm and ρ_w in g cm^{-3}, (3) the rainfall rate or intensity, R, usually expressed in mm hr^{-1}:

$$R(\text{mm hr}^{-1}) = 6\pi \times 10^{-4} \int_0^\infty D_0^3 n(D_0) U_\infty(D_0)\,dD_0\,, \tag{2-13}$$

with the drop terminal velocity U_∞ in m sec^{-1}.

As illustrated in Figures 2.26 and 2.27 for warm rains over Hawaii, such rain seldom includes drops larger than 2 to 3 mm in diameter (Blanchard, 1953, 1957). Larger drops are found to be very rare in rains with $R < 50$ mm hr^{-1} (Mason and Andrews, 1960; Diem, 1968; Blanchard and Spencer, 1970; Waldvogel, 1974; Hodson, 1986; Zawadzki and de Agostoino, 1988; Willis and Hallett, 1991). In

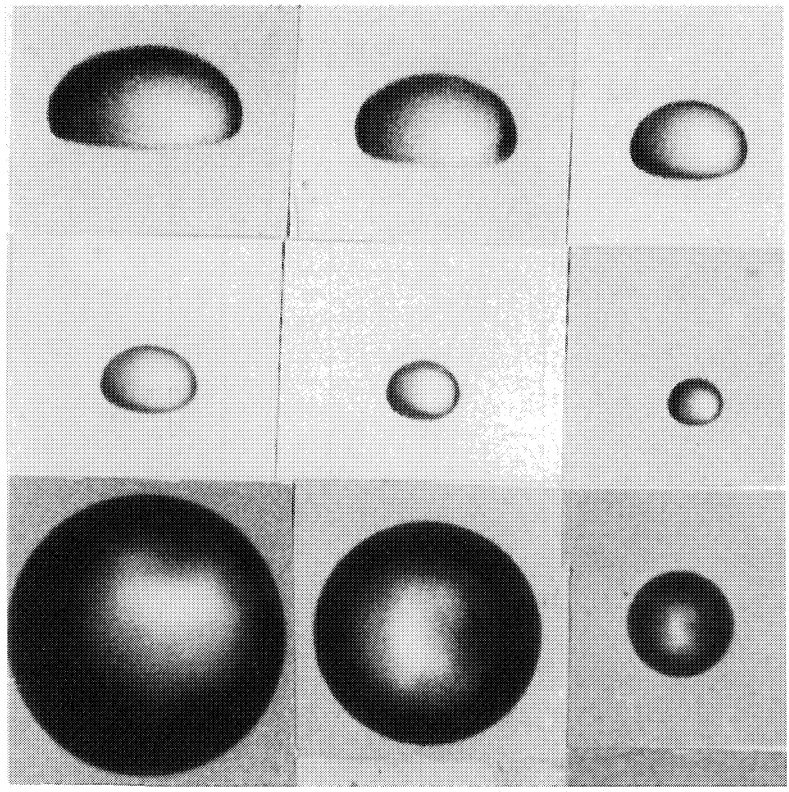


Plate 1. Shape of cloud and raindrops as determined from wind tunnel experiments. Equivalent radius of drops is given. Top row, from left to right: 4.00, 3.68, 2.90 mm; second row, from left to right: 2.65, 1.75, 1.35 mm; third row, from left to right 393, 354, 155 μm. Drops in third row were printed comparatively large to show sphericity. (From Pruppacher and Beard, 1970; by courtesy of *Quart. J. Roy. Meteor. Soc.)*

contrast, raindrops which exceed 2 to 3 mm in diameter are found in tropical storms and hurricanes with $R \gtrsim 50$ mm hr^{-1} (Willis, 1984; Willis and Tattelmann, 1989) and are common in thunderstorms, where large drops form from melting ice particles.

Recent studies on Hawaiian rainbands, however, by Johnson *et al.* (1986), Beard *et al.* (1986), and Rauber *et al.* (1991), confirm the existence of raindrops larger than 3 mm in diameter, despite relatively small rainfall rates (Figure 2.28). The largest drops recorded had diameters as large as 8 mm. Similar sizes were also detected in convective clouds over the SE U.S. by Illingworth (1988). These observations are quite surprising, since model and laboratory studies support the view that collisional break-up of drops rapidly destroys larger drops in natural clouds, and generally limits the drop diameter to less than 2 to 3 mm (McTaggart-Cowan and List, 1975; List and Gillespie, 1976; Gillespie and List, 1978; Takahashi, 1978c, Low and List, 1982a,b). Two mechanisms for the development of raindrops larger

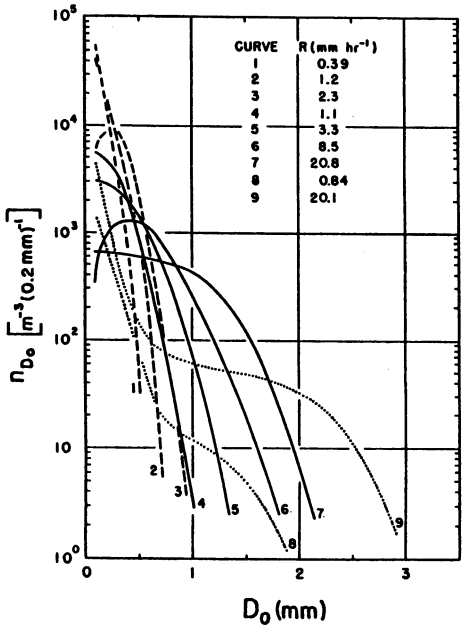


Fig. 2-26: Raindrop distribution at stations in Hawaii. Curves 1-3 are for measurements made at or near the dissipating edge of non-freezing orographic clouds. Curves 4-7 represent data taken at cloud base. Curves 8-9 are for non-orographic rains. (From Blanchard, 1953; by courtesy of Am. Meteor. Soc., and the author.)

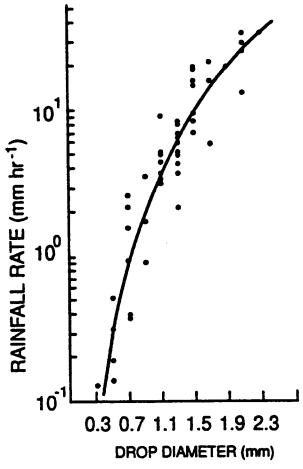


Fig. 2-27: Variation of the maximum rain drop size as a function of rainfall rate for rains over Hawaii at 2800 ft. elevation. (From Blanchard and Spencer, 1957, with changes.)

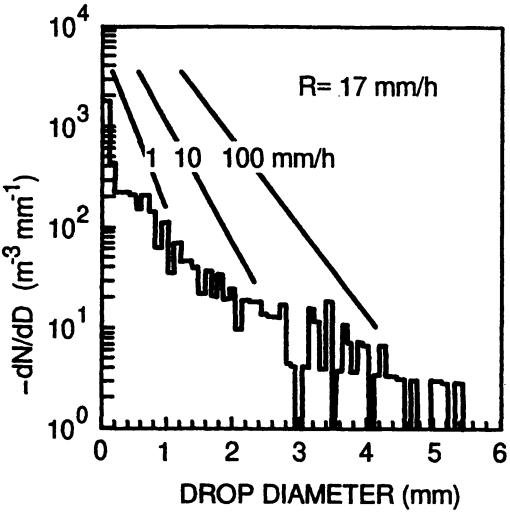


Fig. 2-28: Raindrop size spectrum of a rain shower near Hilo, Hawaii. Rain rate R = 17 mm hr^{-1}. For comparison exponential spectra are shown for 1, 10, and 100 mm hr^{-1}. (From Beard *et al.*, 1986, with changes.)

than 2 to 3 mm in diameter were suggested by Rauber *et al.* (1991). They envision that giant drops may develop in maritime air on exceptionally large aerosol particles acting as nuclei for the drops near cloud base (Johnson, 1982). These already large drops then grow further by accretion of smaller drops to reach giant size. Alternatively, they surmise that giant raindrops may develop when small raindrops re-circulate from the edge of the downdrafts in which they are contained into updrafts with large numbers of cloud drops but essentially no raindrops. Thus, fast growth occurs at the expense of the cloud drops without the encounter of raindrops, which otherwise would have induced collisional break-up. Eventually, as the updraft weakens, the giant drops fall to the ground through a relatively raindrop-free cloud channel.

Several factors influence the spectral shape of rain at the small size end. Since rain must fall against the cloud updraft, the strength of the latter tends by itself to truncate the spectrum at some minimum size. However, this effect is largely masked by the further processing of rain after it leaves the cloud. In particular, small drops continue to be produced by breakup and evaporation. Some of these are consumed by the latter process, while others are collected by larger drops. Also, near the beginning of a rainshower, the drop spectrum at ground level may be expected to be biased toward large sizes owing to the greater fall speeds of the larger drops, and possibly toward small sizes owing to an initially high evaporation rate. The overall shaping of the spectrum is obviously quite complicated, and determined in part by such meteorological variables as temperature, relative humidity, and wind in the subcloud region. Observations show that most precipitating drops which reach the ground have $D_0 > 200\,\mu$m.

Various empirical relations have been advanced to describe the size spectra of raindrops. One often used is the size distribution proposed by Best (1950a), which has essentially the same form as (2-9):

$$1 - F = \exp\left[-\left(\frac{D_0}{A}\right)^m\right], \tag{2-14}$$

where $m = 2.25$ and $A = 1.30R^{0.232}$, with R in mm hr^{-1} and D_0 in mm, and where F is the fraction of water comprised of raindrops with equivalent diameters smaller than D_0. Support for the Best distributions has been given by Shirvaikar *et al.* (1981).

Probably the most widely used description for the raindrop spectrum is the size distribution of Marshall and Palmer (MP) (1948), which is based on the observations of Laws and Parsons (1943). The Marshall-Palmer (MP) distribution is

$$n(D_0) = n_0 \exp(-\Lambda D_0), \tag{2-15}$$

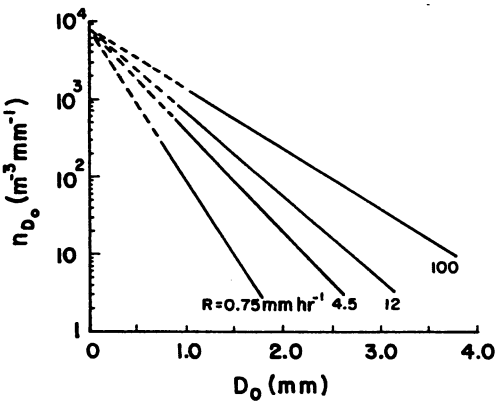


Fig. 2-29: Marshall-Palmer raindrop size distribution. (Based on Marshall and Palmer, 1948; by courtesy of Am. Meteor. Soc., and the authors.)

where $\Lambda = 4.1R^{-0.21}$ mm^{-1}, and $n_0 = 8 \times 10^3$ m^{-3} mm^{-1}. The parameter n_0 is obtained by extrapolation and is assumed to be a constant (Figure 2.29). Knowing Λ and n_0, the mean diameter D_0, the mass weighted mean diameter $D_{0,\mathrm{m}}$, the mass mode diameter $D_{0,\mathrm{mode}}$, the total number of drops N, and the liquid watter content $\mathrm{w_L}$ may be found from the definition of these quantities and (2-16), to give $D_0 = 1/\Lambda$; $D_{0,\mathrm{m}} = 4/\Lambda$; $D_{0,\mathrm{mode}} = 3/\Lambda$; $N = n_0/\Lambda$; $\mathrm{w_L} = \rho_\mathrm{w}\pi n_0 \times 10^{-3}/\Lambda^4$, with ρ_w(g cm^{-3}), D_0(mm), n(m^{-3}), $\mathrm{w_L}$(g m^{-3}) and Λ(mm^{-1}).

More detailed studies, including those by Blanchard (1953), Okita (1958), Mason and Andrews (1960), Caton (1966), and Blanchard and Spencer (1970), have demonstrated that the MP distribution is not sufficiently general to describe most observed raindrop spectra accurately. In particular, Joss *et al.* (1968), Joss and Waldvogel (1969), Strantz (1971), Diem and Strantz (1971), Sekhorn and Srivastava

(1971), Cerzwinski and Pfisterer (1972), and Waldvogel (1974) have pointed out that n_0 cannot be considered constant, but rather is a function of R. Also, the functional dependence on R varies. Thus, the observations of Sekhorn and Srivastava (1971) during thunderstorm rains near Cambridge, Massachusetts, led to a modified MP distribution wherein $n_0 = 7 \times 10^3 R^{0.37}$ m^{-3}mm^{-1} and $\Lambda = 3.8R^{-0.14}$ mm^{-1}.

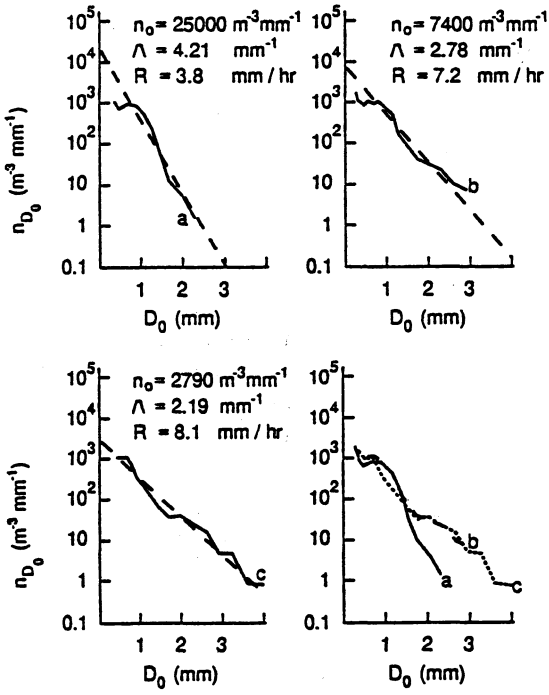


Fig. 2-30: Raindrop size spectra: (a) before, (b) after a 'n_0-jump' measured during a rainfall at a station in sourthern Switzerland. (From Waldvogel, 1974; by courtesy of Am. Meteor. Soc., and the author.)

On analysis of 46 rain spectra obtained in southern Switzerland with $0.3 \leq D_0 \leq 5.3$ mm, Joss *et al.* (1968) and Joss and Waldvogel (1969) found $3 \times 10^3 \leq n_0 \leq 10^5$ m^{-3}mm^{-1}. Also, Waldvogel (1974) discovered that during a particular rainfall, n_0 may suddenly change. Figure 2.30 gives an example of the variation of Λ and n_0 and of the raindrop distribution before, during, and after a sudden change in n_0 (termed 'n_0-jumps' by Waldvogel, 1974). The changes of n_0 were found to be related to changes in convective activity, i.e., air mass stability. However, 'n_0-jumps' were observed even during rainfalls of the same convective character with a continuous rainfall rate. For this condition, the 'n_0-jumps' must be attributed to changes in the microphysical processes occurring in the cloud system from which the rain fell, or in the air during the fall of the drops from cloud to ground. Examples of such 'n_0-jump' are given in Table 2.1.

Although n_0 and Λ varied considerably within each rainfall, and from one rainfall

TABLE 2.1
Examples for the variation of n_0 and Λ during different types of rain. CET is central European time. (Based on data of Waldvogel, 1974.)

	Type of Rainfall	n_0 (m^{-3} mm^{-1})	Λ (mm^{-1})	R (mm hr^{-1})
June 6, 1968	2205-2235 CET, thunderstorm	35 000	3.7	10.2
	2235-2310 CET, thunderstorm	4 000	2.5	5.8
June 19, 1969	0510-0540 CET, shower	16 000	3.8	4.0
	0550-0620 CET, widerspread rain	8 000	2.6	8.0

to another, at any particular moment, the raindrop-size distributions observed over southern Switzerland could be approximated in many cases by an exponential distribution of the MP type. Similarly, exponential type distribution were observed by Okita (1958), Müller (1966), Sekhorn and Srivastava (1971), Pasqualuci (1982), Willis (1984), Beard *et al.* (1986), Hodson (1986), Zawadzki and de Agostino (1988), Rauber and Beard (1991), and Willis and Hallett, (1991). A plot of Λ vs. R based on over 300 individual raindrop spectra is given in Figure 2.31. We note that Λ decreases with increasing rain intensity. This implies that with increasing rain intensity the raindrop spectra become broader.

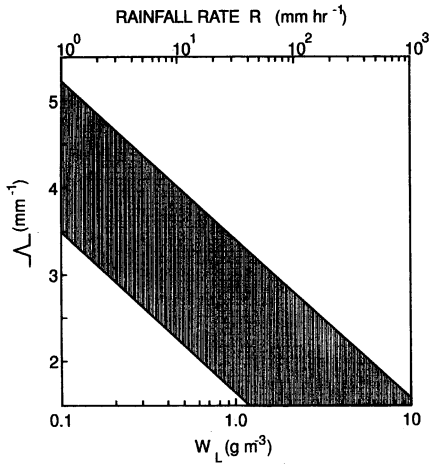


Fig. 2-31: Variation of Λ with rainfall rate and liquid water content based on 300 rainfall events over: Hawaii (Rauber & Beard, 1991; Beard *et al.*, 1986), Brazil (Zavadzki & de Agostino, 1988), Florida (Willis and Hallett, 1991), S. Africa (Hodson, 1986; Pasqualucci, 1982), Switzerland and S. Germany (Waldvogel, 1992), the US and Marshall Islds. (Müller, 1966; Sekhorn & Srivastava, 1971), and in tropical storms over the Atlantic (Willis & Tattelman, 1989; Willis, 1984). (From Hodson, 1986, with additions.)

Numerous studies (Baker and Hodson, 1985; Ulbrich, 1983, 1985; Willis 1984; Willis and Tattelman, 1989) have also used the gamma distribution (Equation

(2-1)) with $\gamma = 1$ to fit the observed raindrop spectra:

$$n(D_0) = n_0 D_0^{\beta} \exp(-\Lambda D_0). \tag{2-16}$$

As another alternative, Feingold and Levin (1986), Mueller and Sims (1966), Bradley and Stow (1974), and Markowiz (1976) have suggested using the lognormal distribution (Equation (2-2)) in the variable D_0.

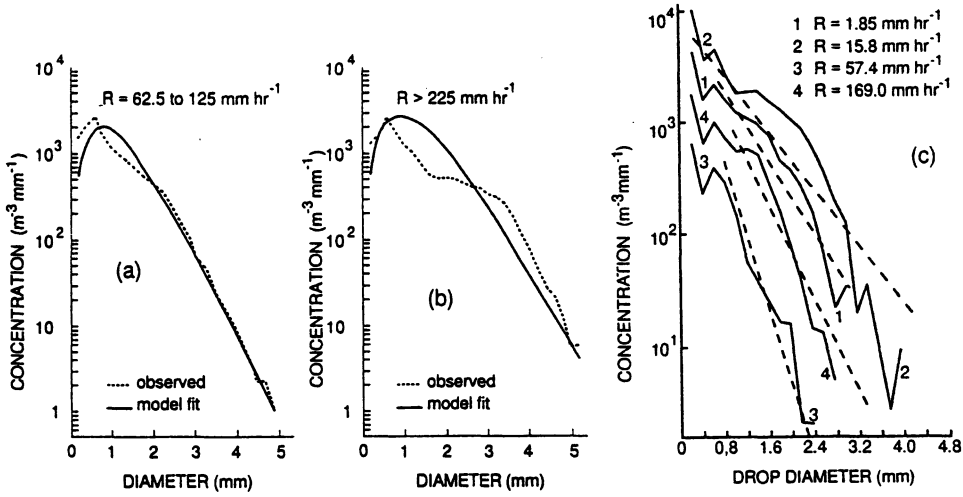


Fig. 2-32: Mean rain drop size distributions in tropical storms with various rain intensities. (a) (b) comparison to a Γ - function fit; (c) comparison to a MP distribution. (a: from Willis & Tattelman, 1986; b: from Willis, 1984, with changes.)

Detailed comparisons between the raindrop spectra actually observed and the distributions given by (2-15) and (2-16) show that in most cases only a partial fit can be acheived at best. This is demonstrated by Figures 2.32a,b,c showing a comparison with a gamma and a MP distribution for rains from tropical storms and hurricanes.

The observed raindrop spectra in Figures 2.30 and 2.32 also show, apart from a main mode, some secondary modes. Such modes have also been identified by du Toit (1967), Diem (1968), Diem and Strantz (1971), Strantz (1971), and Cerwinski and Pfisterer (1972), Willis (1984), de Beaville *et al.* (1988), Takahashi (1978), Battan (1977), Cataneo and Stout (1968), Steiner and Waldvogel (1987), Zawadzki and de Agostino (1988), de Beauville *et al.* (1988). We shall show in Chapter 15 that it is reasonable to attribute the main mode as well as the subpeaks to collisional drop breakup. In fact, inclusion of the collisional drop breakup mechanism in stochastic drop growth models produces distinct peaks in the theoretically predicted rain drop distribution which appear at drop sizes similar to those observed. Unexpectedly, these peaks are not present in all raindrop size distributions. One explanation for this may be that the breakup-induced peaks become masked due to turbulent and evaporative effects. Additional factors which complicate an interpretation of observed raindrop distributions are related to instrumental problems.

Thus, McFarquhar and List (1992) and Waldvogel (1993 pers. comm.), pointed out that the subpeaks found in raindrops distributions which were observed prior to 1992 are most likely due to an erroneous processing of data acquired from the raindrop spectometers. In fact, recent spectra for $R \lesssim 25$ mm hr^{-1} do not exhibit any prominent subpeaks (Waldvogel, pers. comm. 1993). An additional factor which makes data handling from raindrop spectrometers difficult is the fact that raindrops arrive at the ground in groups of similar sizes, alternating with groups of other sizes (Waldvogel, 1993, pers. comm.). Observations also show that rain often commences with the arrival of the largest drops which somewhat later gives way to a mix of large and small drops. This raindrop time-sorting of sizes causes the 'instant' spectra to be quite different from spectra obtained during longer exposure times (Joss and Gori, 1978, Gori and Joss, 1980).

In addition to the parameters n_0 and Λ, the liquid water content w_L of rains also depends on the rainfall rate. This dependence is usually expressed by a law of the form $w_L = AR^b$. Measurements at various locations have shown that A and b vary between $0.052 \leq A \leq 0.089$ and $0.84 \leq b \leq 0.94$. As is also the case for fogs and clouds, one finds that in rainschafts the spatial distribution of the liquid water varies considerably. Thus, Blanchard (1953) and Okita (1958) pointed out that w_L varies with distance from the cloud base, being higher just below the base than at the ground. They attributed this behavior to the existence of a much larger number of small drops at cloud base than at the ground, the drop depletion being caused by collision and coalescence and by evaporation. One might expect that due to drop breakup lower down in a rain shaft, the number of small drops may increase again and perhaps even surpass the concentration at the top of the shaft. However, the observations of Willis and Tattelman (1989) in rain shafts at 3000 and 450 m above ground show that drop growth by coalescence is sufficiently efficient to remove most of the small drops formed by drop breakup, so that they do not contribute significantly to the small drop size end of the spectrum.

2.2 Microstructure of Clouds and Precipitation Consisting of Ice Particles

Since water readily supercools, particularly in small quantities, water clouds as well as fogs are frequently found in the atmosphere at temperatures below 0°C. Figure 2.33, based on a large number of aircraft observations over various parts of the world, shows that supercooled clouds are quite a common occurrence in the atmosphere, especially if the cloud top temperature is warmer than −10°C. However, with decreasing temperature, the likelihood of ice increases such that at −20°C only about 10% of clouds consist entirely of supercooled drops. Nevertheless, on some occasions, supercooled clouds have been observed at temperatures as low as −35°C over Germany (Weickmann, 1949), −36°C over Russia (Borovikov *et al.*, 1963), and −40.7°C in wave clouds over the Rocky Mts. (Heymsfield and Miloshevich, 1993). Also, Heymsfield (1977), Heymsfield and Sabin (1989), and Sassen and Dodd (1988) reported frequent encounters of liquid drops even at the cirrus cloud level (−38°C). Rauber and Tokay (1991), Rauber and Grant (1986), and Hobbs and Rangno (1985) found that, quite unexpectedly, a narrow layer of

supercooled water often occurs at the top of both stratiform and convective clouds. This layer, which is approximately 30 m deep, sustains supercooled water as cold as −31°C. Rauber and Tokay showed that such layers develop as a result of an imbalance between the rate at which cloud water is produced by condensation and the rate at which vapor is depleted through the growth of snow crystals by vapor diffusion.

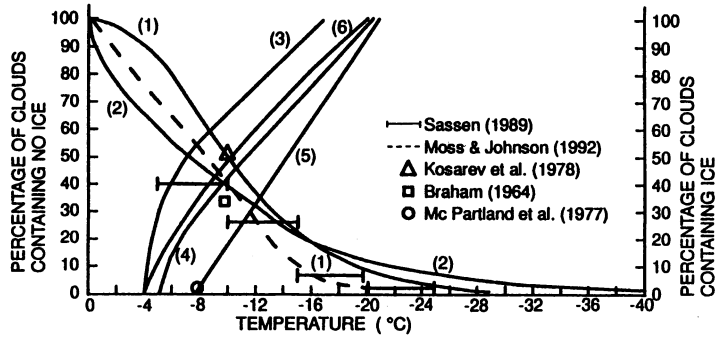


Fig. 2-33: Variation of the frequency of supercooled clouds and of clouds containing snow crystals. Curves (1) and (2) pertain to ordinate on the left; curves 3 to 6 pertain to ordinate on the right. (1) Peppler (1940) over Germany, (2) Borovikov *et al.* (1963) over the ETU, (3) Mossop *et al.* (1970) over Tasmania, (4) Morris & Braham (1968) over Minnesota, (5) Isaac & Schemenauer (1979) over Canada, (6) Hobbs *et al.* (1974b) over the northwest United States.

The mechanism which causes ice particles to grow by diffusion of water vapor is called *deposition.* If ice particles have grown by deposition, they are called *ice crystals* or *snow crystals.* Snow crystals may also grow by collision with supercooled drops which subsequently freeze. This growth mechanism is called *riming.* Snow crystals may also grow by collision with other snow crystals; this mechanism is referred to as *clumping* or *aggregation.* Aggregates of snow crystals are called *snowflakes.* Of course, riming and clumping ice particles may also grow simultaneously by deposition.

The terminology of ice particles formed as a result of riming is not very precise and has not been generally accepted. In the initial stages of riming, as long as the features of the original ice crystal are still well distinguishable, the ice particle is simply called a lightly or densely *rimed snow crystal.* When riming of an ice particle has proceeded to the stage where the features of the primary ice particle are only faintly or no longer visible, the ice particle is called a *graupel particle,* a *soft hail particle,* or a *snow pellet.* Such a particle has a white, opaque, and fluffy appearance due to the presence of a large number of air capillaries in the ice structure. It usually has a bulk density of less than 0.8 g cm^{-3} (List, 1958a,b; 1965). In the later stages of riming, such particles may have a conical, rounded, or irregular shape. An ice particle is called a *small-hail particle* or *type-b ice pellet* if it has originated as a frozen drop or ice crystal and has grown by riming to an irregular or roundish, semi-transparent particle (with or without a conical tip)

of bulk density 0.8 to 0.99 g cm^{-3} (List, 1958a,b; 1965). Such a particle may contain water in its capillary system. Hard, transparent, globular, or irregular ice particles consisting of frozen drops, or partially melted and subsequently refrozen snow crystals or snowflakes with bulk densities between the density of ice and 0.99 g cm^{-3} are called *type-a ice pellets* or *sleet* (List, 1958a,b; 1965). Such particles may also contain unfrozen water.

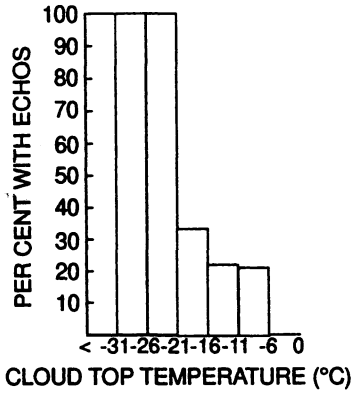


Fig. 2-34: Percentage of cumulus clouds which contained precipitation. Based on radar echoes from clouds over Arizona. (From Morris, 1957; by courtesy of Am. Meteor. Soc., and the author.)

Unrimed, single snow crystals usually have maximum dimensions less than 5 mm. Snowflakes may have maximum dimensions up to several centimeters, but they are usually less than 2 cm. Rimed snow crystals, graupel particles, and ice pellets usually have maximum dimensions of less than 5 mm. Ice particles grown by riming are called *hailstones* if their maximum dimensions are typically larger than 5 mm.

Since radar echoes indicate the presence of large cloud or precipitation size particles, and since these usually form once the temperature in a cloud is sufficiently low, one would expect the probability of a radar echo to be related to temperature. Indeed, in numerous clouds (Figure 2.34) the probability of an echo is often small as long as the cloud top temperature is warmer than or only a few degrees below 0°C. The probability then becomes much larger once the cloud top reaches −20°C, the temperature at which most clouds contain ice particles.

2.2.1 Shape, Dimensions, Bulk Density and Number Concentration of Snow Crystals

Casual observation shows that snow crystals appear in a large variety of shapes or 'habits'. More detailed studies, however, reveal that from a crystallographic point of view, snow crystals have one common basic shape, namely that of a six-fold symmetric (hexagonal) prism with two basal planes of type (0001) and six prism planes of type $(10\bar{1}0)$ (see Figure 2.35). Crystal planes of the type $(11\bar{2}0)$,

which would contribute to a dodecagonal shape, are metastable and occur very rarely. Crystal faces of the type $(10\bar{1}1)$, which would contribute to a pyramidal shape, also are metastable and rarely appear. This is also the case with faces of the type $(10\bar{1}2)$. The habit of a crystal is determined by the slowest growing faces. Metastable faces, such as $(11\bar{2}0)$, $(10\bar{1}1)$ and $(10\bar{1}2)$, grow quickly to become the crystal's edges and corners, while faces of the type (0001) and $(10\bar{1}0)$ grow slowly and become the bounding faces of the crystal.

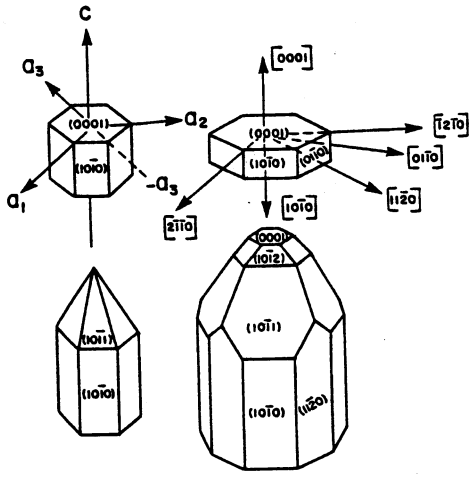


Fig. 2-35: Schematic representation of different habits of snow crystals. (Based on Wolff, 1957, with changes.)

Laboratory experiments reveal that the rate of propagation of the basal faces (growth along c-axis), relative to that of prism faces (growth along the crystallographic direction of type $[10\bar{1}0]$), varies with temperature and supersaturation in a characteristic manner (Aufm. Kampe *et al.*, 1951; Nakaya, 1954; Mason and Shaw, 1955; Kobayashi, 1957, 1958; Hallett and Mason. 1958). The results of these studies were consolidated by Kobayashi (1961), by Rottner and Vali (1974) and later by Kumai (1982). A more detailed experimental study in terms of the ratio of the height h to the diameter d of the crystals has been carried out by Fukuta (1985) and Wang (1987). Apart from minor deviations, these most recent measurements again corroborated the earlier results, which are summarized in Figures 2.36a,b. At a large vapor density excess or supersaturation with respect to ice the snow crystal shape changes with decreasing temperature from a plate to a needle, to a column, to a sector plate, to a dendrite, back to a sector plate, and finally back to a column. This cyclic plate-column-plate-column change in habit is due to a cyclic change of the preferential growth direction along the crystallographic directions of type $[10\bar{1}0]$ and [0001], the changes occurring at temperatures near $-4°C$, $-9°C$, and $-22°C$. While the former two transition temperatures are rather sharply defined, the latter is diffuse, i.e., habit change may take place in a temperature range of several degrees, centered around $-22°C$. In contrast, at very low vapor density

excess, the crystal shape changes between a short column and a thick plate near $-9°C$ and $-22°C$. Close to or at ice saturation, the ice crystal shape ceases to vary with temperature but rather assumes the equilibrium shape, which is a thick hexagonal plate with a height to diameter ratio of 0.8 (see Section 5.7.2).

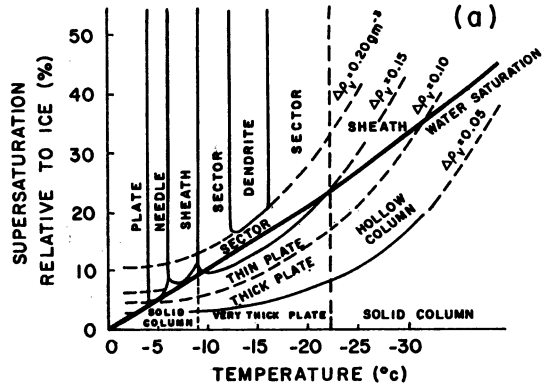


Fig. 2-36:a. Variation of ice crystal habit with temperature and supersaturation where $\Delta\rho_v = \rho_v - \rho_{v,\mathrm{sat},i}$ (Based on laboratory observations of Mason, 1971; Hallett & Mason, 1958; Kobayashi, 1961; and Weissweiler, 1969.)

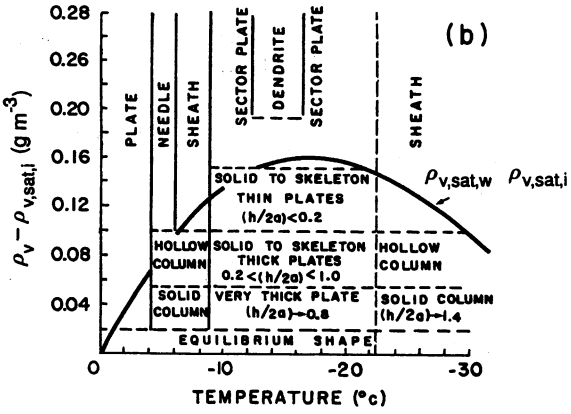


Fig. 2-36:b. Variation of ice crystal habit with temperature and vapor density excess. (Based on laboratory observations of Kobayashi, 1961; and Rottner & Vali, 1974.)

Thus, we see that although the temperature is the principal factor, humidity conditions in the environment also control the important growth features of snow crystals. For example, near $-15°C$, the snow crystal habit varies with increasing vapor density excess from a thick plate to a thin plate, to a sector plate, and finally to a dendrite for which preferential growth is along the crystallographic direction of type $[11\bar{2}0]$. Near $-5°C$, the ice crystal habit varies with increasing vapor density

excess from a short solid column, to a hollow column, to a needle with pronounced growth in the crystallographic direction [0001]. Laboratory observations of the ice crystal habit at temperatures between −22 and −50°C have revealed no essentially new habit features (Kobayashi, 1965a,b; Kumai, 1982). Long solid columns (sheaths) appear between −45 and −50°C at low supersaturations, and change into hollow columns as the supersaturation is raised.

Although the basic shape of ice crystals is hexagonal prismatic, laboratory observations have revealed a few snow crystals with other shapes. Trigonal prismatic plates and columns, trigonal dendrites, and rhombic and scalene pentagonal ice crystals were observed by Yamashita (1969, 1971, 1973) after seeding supercooled clouds with a very cold body. Aufm Kampe *et al.* (1951) and Mason (1953) also observed trigonal plates after seeding supercooled clouds with dry ice. Little is known of the detailed growth conditions of such rare ice crystal shapes. Ohtake (1970a,b) suspected that quasi-stable faces such as the pyramidal faces of type $(10\bar{1}2)$ or $(10\bar{1}1)$ may develop at rapid cooling rates when the time to complete a quasi-stable crystal face becomes comparable to the time for the completion of a stable face. Kobayashi (1965a,b) found that at temperatures between −50 and −90°C, pyramidal faces develop at the tip of prismatic columns.

So far, we have only considered snow crystals grown in the laboratory. It is essential to ask whether natural snow crystals exhibit the same characteristic changes in shape. Considerable uncertainties are involved in answering this question, due to the inherent difficulties of accurately establishing the actual temperature and humidity conditions of the locations at which the sampled snow crystals grew and acquired their shape. However, a large number of observations in different parts of the world have finally made a fairly definite conclusion possible. (Cloud observations have been made over Germany by Weickmann (1945, 1949, 1957a) and Grunow (1960); over Canada by Gold and Power (1952, 1954); over the U.S.S.R. by Bashkirova and Pershina (1956, 1964a,b); over Japan by Magono (1960), Nakaya and Higuchi (1960), Higuchi (1962a,b,c), Lee and Magono (1967), Magono *et al.* (1959, 1960, 1962, 1963, 1965, 1966), and Tazawa and Magono (1973); over Australia by Ono (1970); over Colorado and the Great Lakes region by Jiusto and Weickmann (1973), and Weickmann (1972); and over the Pacific northwestern U.S. by Hobbs *et al.* (1971a, 1972, 1974a).)

Observations prior to 1966 have been summarized in a diagram (Figure 2.37) prepared by Magono and Lee (1966). Observations made after 1966, have generally supported the Magono-Lee diagram. Comparison between Figures 2.36a,b and Figure 2.37 shows that laboratory experiments are in basic agreement with the Magono-Lee diagram.

The outstandingly beautiful photographs of snow crystals captured on the ground by Bentley (Bentley and Humphreys, 1931, 1962), Nakaya (1954), and Magono and Lee (1966), and of snow crystals captured during flights in cirrus clouds by Weickmann (1945), provide a comprehensive atlas of most snow crystal types found in atmospheric clouds. An attempt to bring order into this multiplicity of crystal forms has been made by Magono and Lee (1966). Although their classification (Figure 2.38) has not yet been formally accepted on an international basis, it has been found practical and is very widely used. Photographs of a few major snow

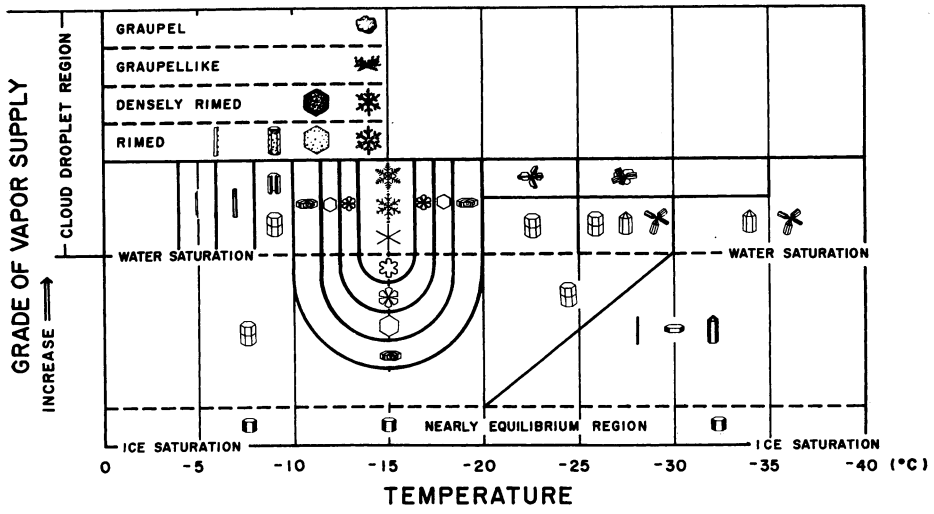


Fig. 2-37: Temperature and humidity conditions for the growth of natural snow crystals of various types. (From Magono and Lee, 1966; by courtesy of *J. Fac. Sci.*, Hokkaido University.)

crystal shapes are given in Plate 2.

A simple analytical model for approximating the major planar snow crystal shapes has been formulated by Wang and Denzer (1983) and Wang (1987). For the procedure to obtain these shapes, the reader is referred to the mentioned literature.

Let us now assume that a snow crystal of one particular habit, formed by growth at a particular temperature and humidity, is suddenly moved into a new environment of different temperature and humidity where it continues to grow by vapor diffusion. Under such conditions, the habit characteristic of the second temperature and humidity conditions becomes superimposed on the original habit. Thus, a columnar snow crystal suddenly surrounded by conditions characteristic of plate-like growth will develop end-plates (Figure 2.38, CPla). A stellar crystal suddenly surrounded by conditions characteristic of needle growth will develop needles on the branches, with the needles growing perpendicular to the plane of the crystal (Figure 2.38, CP3a). Although such snow crystals appear as combinations of different shapes, from a crystallographic point of view they are still *single ice crystals* since the crystallographic orientation of the c- and a-axes is still the same throughout the crystal.

While some ice particies in clouds originate on water-insoluble aerosol particles on which water vapor is deposited as ice, others originate as frozen drops. Various observers (e.g., Koenig, 1963; Braham, 1964) have studied frozen drops in atmospheric clouds. They are irregular in shape, often with bulges and protrusions formed during the freezing process. Ice particles formed from single-crystalline frozen drops are likely to turn into two-layered crystals (Figure 2.39). The conditions for the formation of such crystals were studied by Auer (1971, 1972a), Weick-

	N1a Elementary needle		C1f Hollow column		P2b Stellar crystal with sectorlike ends
	N1b Bundle of elementary needles		C1g Solid thick plate		P2c Dentritic crystal with plates at ends
	N1c Elementary sheath		C1h Thick plate of skelton form		P2d Dentritic crystal with sectorlike ends
	N1d Bundle of elementary sheaths		C1i Scroll		P2e Plate with simple extensions
	N1e Long solid column		C2a Combination of bullets		P2f Plate with dentritic extensions
	N2a Combination of needles		C2b Combination of columns		P3a Two-branched crystal
	N2b Combination of sheaths		P1a Hexagonal plate		P3b Three branched crystal
	N2c Combination of long solid columns		P1b Crystal with sectorlike branches		P3c Four-branched crystal
	C1a Pyramid		P1c Crystal with broad branches		P4a Broad branch crystal with 12 branches
	C1b Cup		P1d Stellar crystal		P4b Dentritic crystal with 12 branches
	C1c Solid bullet		P1e Ordinary dendritic crystal		P5 Malformed crystal
	C1d Solid bullet		P1f Fernlike crystal		C1d Solid bullet
	C1e Solid column		P2a Stellar crystal with plates at ends		P6e Plate with spatial plates

	P6b Plate with spatiel dendrites		CP3d Plate with scrolls at ends		R3c Graupellike snow with nonrimed extensions
	P6c Stellar crystal with spatial plates		S1 Side plans		R4a Hexagonal graupel
	P6d Stellar crystal with spatial dendrites		S2 Scalelike side planes		R4b Lump graupel
	P7a Radiating assemblage of plates		S3 Combination of side planes, bullets and columns		R4c Conelike graupel
	P7b Radiating assemblage of dendrites		R1a Rimed needle crystal		I1 Ice particle
	CP1a Column with plates		R1b Rimed columnar crystal		I2 Rimed particle
	CP1b Column with dendrites		R1c Rimed plate or sector		I3a Broken branch
	CP1c Multiple capped column		R1d Rimed stellar crystal		I3b Rimed broken branch
	CP2a Bullet with plates		R2a Densely rimed plate or sector		I4 Miscellaneous
	CP2b Bullet with dendrites		R2b Densely rimed stellar crystal		G1 Minute column
	CP3a Stellar crystal with needles		R2c Stellar crystal with rimed spatial branches		G2 Germ of skelton form
	CP3b Stellar crystal with columns		R3a Graupellike snow of hexagonal type		G3 Minute hexagonal plate
	CP3c Stellar crystal with scrolls at ends		R3b Graupellike snow of lump type		G4 Minute stellar crystal
					G5 Minute assemblage of plates
					G6 Irregular germ.

Fig. 2-38: The Magono-Lee classification of natural snow crystals. (From Magono and Lee, 1966; by courtey of *J. Fac. Sci.*, Hokkaido University.)

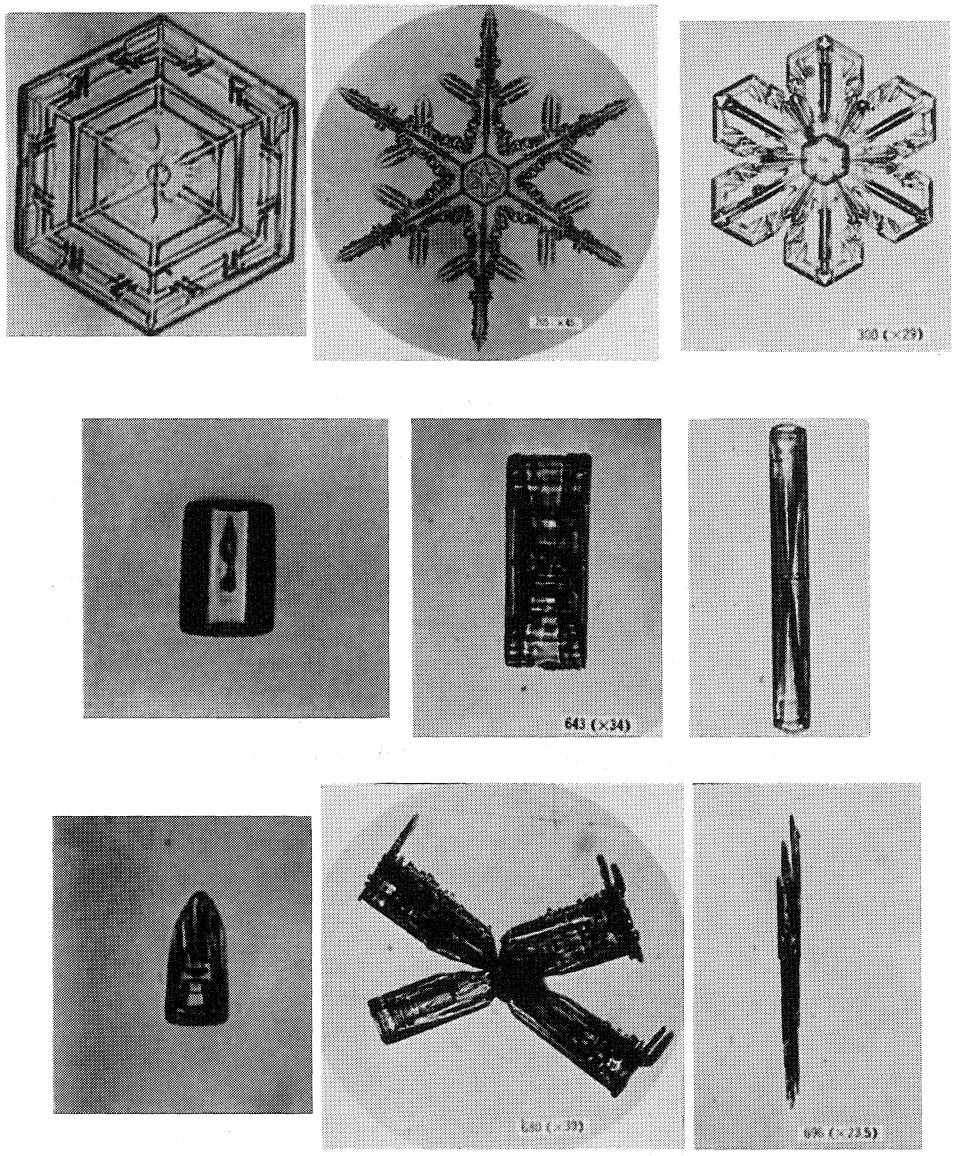


Plate 2. Major shapes of snow crystals: top row, from left to right: simple plate, dendrite, crystal with broad branches; second row, from left to right: solid column, hollow column, sheath; third row, from left to right: bullet, combination of bullets (rosette, Prismenbüschel), combination of needles. (From Nakaya, 1954; by courtesy of Harvard University Press, copyright 1954 by the President and Fellows of Harvard College.)

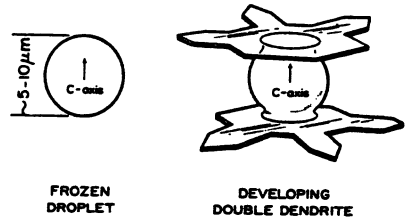


Fig. 2-39: Schematic drawing indicating the formation of a double star from a single-crystalline frozen drop. Note that competition for vapor causes irregular growth of opposing branches of the two crystals. (From Jiusto and Weickmann, 1973; by courtesy of Am. Meteor. Soc., and the authors.)

mann (1972), Jiusto and Weickmann (1973), Parungo and Weickmann (1973), and Hobbs *et al.* (1974b) who found that ice crystals with frozen drops in their centers were quite abundant. Auer's cloud studies indicated that at temperatures from -9 to $-10°C$, about 19% of the total snow crystal concentration could be attributed to crystals each with a frozen drop at the center. At -15 to $-16°C$, this fraction reached a maximum of 48%, and decreased to about 23% at temperatures between -1 and $-22°C$. The diameter of the frozen center-drop was found to range between 2.5 and 25 μm. Observations of Hobbs *et al.* (1974b) in clouds over the U.S. High Plains (see Fig. 2.40) showed that the most probable diameter of cloud drops ranged between 10 and 12 μm, while the diameter of the frozen drops in the center of double crystals was larger and ranged between 13 and 25 μm. This difference reflects the volume dependence of freezing, to be discussed in Chapters 7 and 9, where it will be shown that large drops are more likely to freeze than small ones.

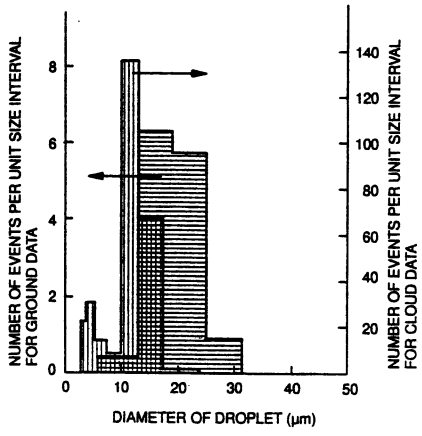


Fig. 2-40: Size distribution of frozen drops in the center of double crystals collected on the ground ($\equiv$). comparison is made to drop size distribution inside clouds (|||). Observed in continental clouds over the U.S. High Planes. (From Hobbs *et al.*, 1974b, with changes.)

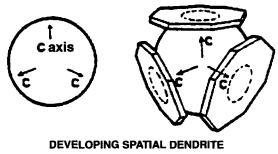


Fig. 2-41: Schematic drawing indicating formation of a spatial crystal from a polycrystalline frozen drop. (From Jiusto and Weickmann, 1973; by courtesy of Am. Meteor. Soc., and the authors.)

Drops which freeze polycrystalline and subsequently continue to grow by vapor diffusion form *spatial crystals* (Higuchi and Yoshiida, 1967; Magono and Suzuki, 1967; Lee, 1972; Kikuchi and Ishimoto, 1974). Figure 2.41 illustrates how, in principle, such a crystal develops. If, for example, such a frozen drop continues to grow by vapor diffusion near −15°C dendritic branches will emerge from the frozen drop at various angles (Figure 2.38, P7b). Since polycrystalline drops are more likely to occur at lower temperatures, they frequently develop into a combination of columnar crystals. Note that, due to competition for water vapor, the columns may have a conical or pyramidal shape (bullet-shape) pointing towards their common growth center which is the frozen drop (Figure 2.38, C2a). A snow crystal of this form is called a *combination of bullets* or a *rosette.* A single column broken off a rosette is simply called a *bullet* (Figure 2.38, Clc, Cld). A rosette may consist of 2 to 9 bullets but most frequently consists of 3 to 4 bullets (Kikuchi, 1968).

Spatial crystals may also develop as a result of supercooled drops colliding with a snow crystal. At temperatures of only a few degrees below 0°C, a drop colliding with a snow crystal turns into an ice-single-crystal with a crystallographic orientation which may be the same or different from the snow crystal it contacts. If the temperature is sufficiently cold, the colliding drop may turn into a polycrystalline mass of ice. Further growth of such polycrystalline frozen drops by vapor diffusion leads to a spatial snow crystal with two or more *c*-axis orientations (Figure 2.38, P6a-d, P7a).

Several peculiar snow crystal shapes not classified by Magono and Lee were encountered by Kikuchi (1970), Kikuchi and Yanai (1971), and Magono *et al.* (1971) at temperatures between −26 and −30°C during an Antarctic expedition; by Thuman and Robinson (1954), Kumai (1965, 1966a, 1969a), and Ohtake (1967, 1968, 1970a,b) at temperatures between −30 and −55°C during ice fog in Alaska; and by Itoo (1957) during a strong ground inversion at a station in central Mongolia. The ice crystals observed at the Antarctic station consisted mostly of combinations of bullets, columns, and side planes which very likely originated as a type of hoarfrost snow-covered surfaces. In ice fog, Thuman and Robinson observed irregular particles of 'block-shape' and polyhedral particles bounded by trapezoidal faces which were portions of a hexagonal bi-pyramid. Pyramidal planes of type $(10\bar{1}1)$ and higher-order planes were also observed by Itoo in 'diamond-dust' snow crystals.

Another group of peculiar crystal shapes which develop at temperatures below −25°C were discussed by Sato and Kikuchi (1989). These crystals, termed by the authors Gohei twins, seagull type or V-shaped crystals, and spearhead type

crystals result from an abnormal growth of their prism faces $(10\bar{1}0)$ induced by orientational faults during the ice nucleation of a supercooled drop.

Several theoretical models have been suggested to explain the origin of polycrystalline and peculiar types of snow crystals. Thus, Lee (1972) advanced a basal misfit theory, Iwai (1971) adopted a penetration twin theory, Kobayashi *et al.* (1976) and Furukawa (1982) used a generalized coincidence lattice site theory, and Kobayashi *et al.* (1976) proposed a cubic structure model.

In most cases, it is sufficient to characterize the size of a snow crystal by two dimensions: the crystal diameter (d) and the crystal thickness (h) in the case of plate-like crystals, and the crystal length (L) and the crystal width (d) for columnar type crystals. Detailed measurements of snow crystal dimensions have been carried out in several locations. The length of columnar crystals and the diameter of plate-like crystals were found to range typically between 20 μm and 2 mm. The thickness of plate-like crystals typically ranges from 10 to 60 μm, the width of the warm temperature columns from 10 to 200 μm, and the width of needles ranges from 10 to about 150 μm. Maximum dimensions reach several milllimeters.

Observations have shown further that the thickness and diameter of plate-like crystals, and the length and width of columnar crystals, are characteristically related to each other such that with increasing diameter of plate-like crystals their thickness increases, and with increasing length of columnar crystals their width also increases.

The significant fact is that a snow crystal, growing by vapor diffusion, distributes its mass in a fairly predictable manner which obeys certain dimensional relations. A comparison shows that, for a particular crystal type, the dimensional relationships proposed by various authors agree reasonably well, though they were derived from observations in clouds over different parts of the world. Davis (1974) combined observations of his own with those of Auer and Veal (1970), Ono (1969, 1970), Hobbs *et al.* (1974a), and Kajikawa (1972, 1973) to the best fit relationships given in Table 2.2a in terms of a set of power laws. Size relationships for additional snow crystal shapes are given in Table 2.2b.

Most ice crystals have a bulk density less than that of bulk ice. This is due to small amounts of air in capillary spaces, and to the tendency of snow crystals to grow in a skeletal fashion. In particular, columnar crystals often develop as hollow crystals with 'hour-glass' air spaces at either end. Heymsfield (1972), on combining his data with that of Ono (1970), determined relations between the bulk density and the crystal dimensions (Table 2.3). Somewhat lower bulk densities for columnar crystals were observed by Iwai (1973) and Jayaweera and Ohtake (1974). They found that short columns had bulk densities close to that of ice. With increasing L, however, the density decreased rapidly, reaching $\rho_c \approx 0.5$ for $\mathsf{L} \approx 1$ mm. For needles and sheaths, they found $\rho_c \approx 0.3$ to 0.4 g cm^{-3} if $\mathsf{L} > 1$ mm. Table 2.3 also implies that larger dimensions correlate with lower bulk densities.

For computations involving cloud models, it is often necessary to have relations available between the mass and size of snow crystals. Due to rather large uncertainties in the values for the bulk density of snow crystals, it is not advantageous to derive such relations based on size and density of the crystals; rather, one should obtain them from direct observation. Size-mass relationships for a few

TABLE 2.2 a

Dimensional relationships for various snow crystal types; $d(cm), \mathrm{L}(cm), V_c(cm^3)$. The form Plc-r refers to a simple 'daisy-type' dendrite; the form Plc-s refers to a dendrite with sector-type branches; d refers to the diameter of the circle circumscribed around the snow crystal. (From C.E. Davis, 1974; by courtesy of the author.)

Crystal type	Dimensional relationship d(cm), L(cm)	Volume of crystal, V_c (cm^3)	Range of major axis (μm)
Pla	$h = 1.41 \times 10^{-2}\ d^{0.474}$	$V_c = 9.17 \times 10^{-3}\ d^{2.475}$	10-3000
Plb	$h = 1.05 \times 10^{-2}\ d^{0.423}$	$V_c = 6.79 \times 10^{-3}\ d^{2.423}$	10-40
Plb	$h = 1.05 \times 10^{-2}\ d^{0.423}$	$V_c = 7.37 \times 10^{-3}\ d^{2.420}$	41-2000
Plc-r, Pld	$h = 9.96 \times 10^{-3}\ d^{0.415}$	$V_c = 6.47 \times 10^{-3}\ d^{2.415}$	10-90
Plc-r, Pld	$h = 9.96 \times 10^{-3}\ d^{0.415}$	$V_c = 1.096 \times 10^{-3}\ d^{2.045}$	91-1500
Plc-s	$h = 9.96 \times 10^{-3}\ d^{0.415}$	$V_c = 6.47 \times 10^{-3}\ d^{2.415}$	10-1000
Plc-s	$h = 9.96 \times 10^{-3}\ d^{0.415}$	$V_c = 2.09 \times 10^{-3}\ d^{2.175}$	101-1000
Clg	$h = 0.138\ d^{0.778}$	$V_c = 8.97 \times 10^{-2}\ d^{2.778}$	10-1000
Cle L/d 2	$d = 0.578\ \mathrm{L}^{0.958}$	$V_c = 0.217\ \mathrm{L}^{2.916}$	10-1000
Cle L/d 2	$d = 0.260\ \mathrm{L}^{0.927}$	$V_c = 4.39 \times 10^{-2}\ \mathrm{L}^{2.854}$	10-1000
Clf L/d 2	$d = 0.422\ \mathrm{L}^{0.892}$	$V_c = 0.116\ \mathrm{L}^{2.784}$	10-50
Clf L/d 2	$d = 0.422\ \mathrm{L}^{0.892}$	$V_c = 0.105\ \mathrm{L}^{2.765}$	51-1000
Clf L/d 2	$d = 0.263\ \mathrm{L}^{0.930}$	$V_c = 4.49 \times 10^{-2}\ \mathrm{L}^{2.860}$	10-50
Clf L/d 2	$d = 0.263\ \mathrm{L}^{0.930}$	$V_c = 4.06 \times 10^{-2}\ \mathrm{L}^{2.841}$	51-1000

TABLE 2.2 b

As Table 2-2a but for additional snow crystals types.

Crystal type h(cm), d(cm), L(cm)	Dimensional relationship	Author
Ple, Plf, P2c	$h = 9.022 \times 10^{-3}\ d^{0.377}$	Auer and Veal (1970)
P2g, P3c, P4b		
Nla	$d = 3.0487 \times 10^{-2}\ \mathrm{L}^{0.61078}$	Auer and Veal (1970)
Nle	$d = 3.527 \times 10^{-2}\ \mathrm{L}^{0.437}$	Jayaweera and Ohtake (1974)
Clc (L $\leq$ 0.3 mm)	$d = 0.1526\ \mathrm{L}^{0.7856}$	Heymsfield (1972)
Cld (L $\geq$ 0.3 mm)	$d = 0.0630\ \mathrm{L}^{0.532}$	Heymsfield (1972)

TABLE 2.3

Bulk density of various snow crystals (d and L in mm). (Based on data of Heymsfield, 1972.)

Crystal type	Bulk Density, ρ_c, (g cm^{-3}) d(mm), L(mm)	
hexagonal plate	$\rho_c = 0.9$	
plates with dendritic extensions	$\rho_c = 0.656\ d^{-0.627}$	($d \geq 0.7$ mm)
dendrites	$\rho_c = 0.588\ d^{-0.377}$	($d \geq 0.3$ mm)
stellar, broad arms	$\rho_c = 0.588\ d^{-0.377}$	($d \geq 0.3$ mm)
stellar, narrow arms	$\rho_c = 0.46\ d^{-0.482}$	($d \geq 0.24$ mm)
column, cold region	$\rho_c = 0.65\ \mathrm{L}^{-0.0915}$	(L ≥ 0.028 mm)
column, warm region	$\rho_c = 0.848\ \mathrm{L}^{-0.014}$	(L ≥ 0.014 mm)
bullet	$\rho_c = 0.78\ \mathrm{L}^{-0.0038}$	(L ≥ 0.1 mm)

TABLE 2.4a

Mass-size relationships for various types snow crystals. Data taken on Mt. Teine (1024 m, Hokkaido, Japan), based on data of Heymsfield & Kajikawa, 1987.

Crystal type	Mass-size relation m(g), d(cm)	Diameter range (mm)
C1h	$2.63 \times 10^{-2}\ d^{2.68}$	0.3-0.6
P1a	$3.76 \times 10^{-2}\ d^{3.31}$	0.3-1.5
P1b	$6.34 \times 10^{-3}\ d^{2.83}$	0.4-1.6
P1c	$3.76 \times 10^{-3}\ d^{2.79}$	0.5-2.8
P1d	$9.61 \times 10^{-4}\ d^{2.59}$	0.4-2.4
P1e	$6.12 \times 10^{-4}\ d^{2.29}$	0.6-5.3
P2a	$2.11 \times 10^{-3}\ d^{2.53}$	0.7-3.0
P2c	$2.66 \times 10^{-3}\ d^{3.12}$	1.3-5.6
P2e	$4.29 \times 10^{-3}\ d^{2.81}$	0.5-2.1
P2g	$4.68 \times 10^{-3}\ d^{2.94}$	0.7-2.8
P6c	$6.20 \times 10^{-4}\ d^{2.02}$	1.6-4.9
P6d	$9.23 \times 10^{-4}\ d^{2.55}$	2.0-6.5
P7b	$1.53 \times 10^{-3}\ d^{2.68}$	1.2-3.3

TABLE 2.4b

As in Table 2-4a but for data taken in the Sierra Nevada (2600 to 3000 m), based on data of Mitchell *et al.*, 1990.

Crystal type	Mass-size relations m (mg), L (mm)	Size range (mm)
N1a	$m = 0.0049\ \mathrm{L}^{1.8}$	0.6 - 2.7
N1e	$m = 0.012\ \mathrm{L}^{1.8}$	0.2 - 1.5
N2c	$m = 0.017\ \mathrm{L}^{1.8}$	0.2 - 2.6
C1e	$m = 0.064\ \mathrm{L}^{2.6}$	0.2 - 0.6
C2b	$m = 0.031\ \mathrm{L}^{1.9}$	0.4 - 1.4
C1f	$m = 0.037\ \mathrm{L}^{1.8}$	

selected rimed and unrimed snow crystals observed during winter storms over the Sierra Nevada by Mitchell *et al.* (1990), and for storms over Hokkaido (Japan) by Kajikawa (1989) are given in Tables 2.4 a,b.

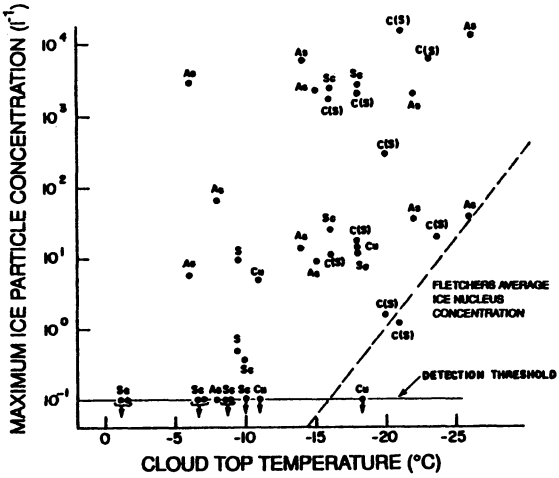


Fig. 2-42: Maximum ice particle concentration in clouds over the Cascade Mountains (State of Washington). Cloud types are indicated by As - altostratus, S - Stratus, Sc - stratocumulus, Cu - cumulus, C(S) - cumulus with stratified tops. (From Hobbs *et al.*, 1974b; by courtesy of the authors.)

Since the probability for the occurrence of the ice phase in clouds increases with decreasing temperature, we might expect a monotonic rise in the concentration of such particles with decreasing temperature. This behavior turns out to hold only in a minority of cases. More often, a rapid phase change to ice (*glaciation*) occurs, such that the ice particle concentration is not a sensitive function of further temperature lowering. We shall discuss this more fully in Section 9.2.7. At this point, we merely note the net effect of glaciation. Figure 2.42 summarizes measurements of Hobbs *et al.* (1974b) in clouds over the Cascade Mts. (Washington). It is seen that, in many cases at temperatures between -4 and -25°C, the range of number concentrations of ice particles varies little with cloud top temperature on the average, and that the concentrations may reach values as high as 10^4 liter^{-1}. Similar observations were made in clouds over Australia by Mossop (1970), in clouds over Missouri by Braham (1964) and Koenig (1963), and in clouds over the U.S. High Plains by Hobbs and Rangno (1985), Hobbs and Rangno (1990), Rangno and Hobbs (1991) and Hobbs and Atkinson (1976). In some cases, however, the number concentration of ice particles does depend somewhat on cloud top temperature. Thus, we find quite unexpectedly from Figure 2.43 that the largest ice crystal concentration does not appear at the lowest temperature but in the temperature range -12 to -14°C.

Once formed, snow crystals in lower tropospheric snowstorms exhibit a characteristic size distribution which for crystals smaller than 1 mm is highly peaked at the small size end, the concentration decreasing rapidly toward the large size end of the spectrum (Figure 2.44). The crystal shapes appearing in these storms are

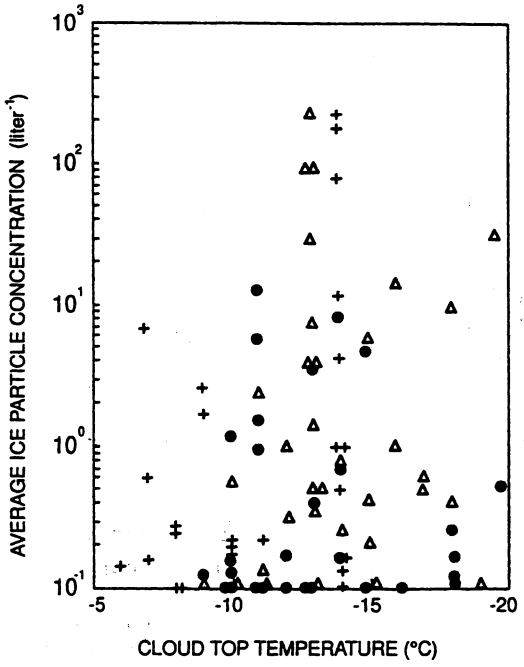


Fig. 2-43: Average ice particle concentration as a function of cloud top temperature in the updraft region of clouds sampled over Montana; (•) small cumulus, (△) convective complexes, (+) embedded cumulus. (From Hobbs *et al.*, 1980, with changes.)

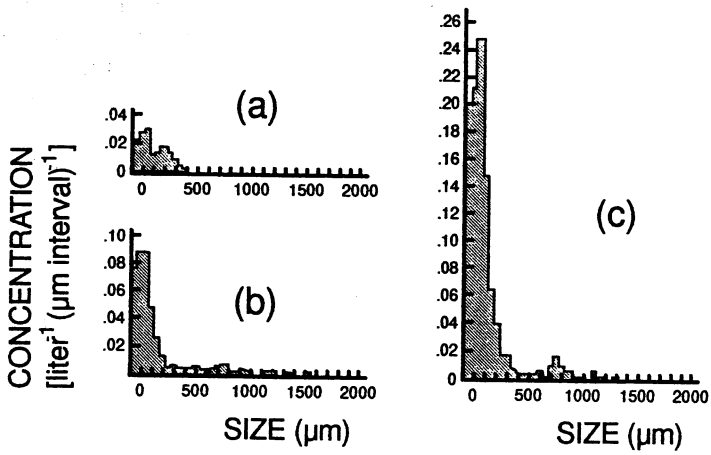


Fig. 2-44: Snow crystal size spectra at selected levels in wintertime snow storms over N. Colorado: (a) at 6694 to 6567 m, with temperatures −27.4 to −26.5°C, (b) at 5668 to 5504 m, −22.0 to −19.9°C, (c) at 5034 to 4898 m, −16.7 to −15.0°C. (From Rauber, 1987b, with changes.)

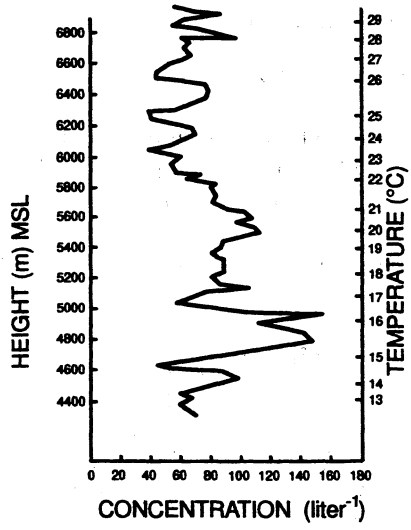


Fig. 2-45: Variation of snow crystal concentration with height in wintertime snow storms over N. Colorado. (From Rauber, 1987, with changes.)

typically those for temperatures warmer than −25°C. The variation with height of the snow crystal concentration in the cloud of Figure 2.44 is given in Figure 2.45).

The snow crystals in cirrus clouds which appear in the upper troposphere at temperatures typically between −25 to −60°C have characteristic shapes. Ice clouds at these levels typically consist of bullets, bullet rosettes, short hollow columns, thick plates, and aggregates. Most of the crystals in these clouds form by homogeneous ice nucleation in supercooled drops (see Section 7.2). Just prior to ice nucleation, the relative humidity reaches above 90% to decrease rapidly thereafter. Thus, in cirrus clouds over Wisconsin, Heymsfield *et al.* (1990) found dewpoints slightly above those for ice saturation, indicating that the air in the core of these clouds was ice supersaturated, decreasing rapidly to below ice saturation in the cirrus tails. Sassen *et al.* (1989) found near ice saturation in cirrus over Utah, Colorado and Wisconsin, while Heymsfield (1975a) measured ice subsaturation in cirrus over Illinois.

The microstructure of cirrus clouds has been studied by Weickmann (1945, 1949), Kikuchi (1968), Rosinski *et al.* (1970), Heymsfield (1972; 1975a,b,c; 1977; 1986), and Heymsfield and Knollellenberg (1972), Heymsfield and Platt (1984), Kajikawa and Heymsfield (1989), Heymsfield *et al.* (1990), Dowling and Radke (1990), and Stephens *et al.* (1990). From these studies, it is apparent that the concentration of ice particles in cirrus typically ranges between 50 and 500 liter^{-1}. The maximum dimension of the crystals typically ranged between 100 and 300 μm for thick plates and columns, between 200 and 800 μm for bullets and bullet rosettes, and between 400 and 1500 μm for aggregates. The ice water content w_i was found to range between 0.05 to 0.5 g m^{-3}, and to increase with increasing temperature,

i.e., decreasing altitude in the atmosphere according to the relation:

$$w_i(\text{g m}^{-3}) = 7 \times 10^{-4} \exp[0.41(T + 60)], \tag{2-17}$$

with T in °C (Stephen *et al.* 1990, based on data of Heymsfield and Platt, 1984). According to Heymsfield (1977), the mean length of columnar crystals relates approximately to the ice water content according to the data fit given by:

$$L_{i,\text{mean}} = 0.698 + 0.366(\log w_i) + 0.122(\log w_i)^2 + 0.0136(\log w_i)^3 . \tag{2-18}$$

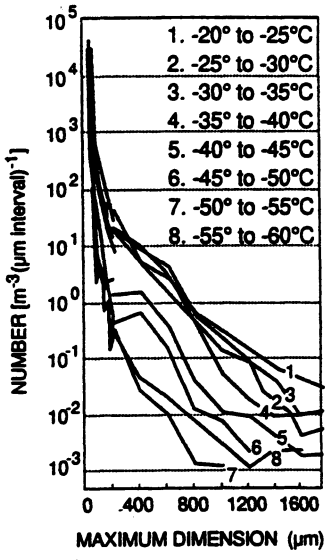


Fig. 2-46: Number concentration vs. maximum dimension of snow crystals in cirrostratus over the U.S. at various temperatures. (From Heymsfield & Platt, 1984, with changes.)

Equations (2-17) and (2-18) imply that the size of cirrus cloud crystals increases with increasing temperature, as can be seen also from Figure 2.46.

In Table 2.5, dimensional and mass relationships for columnar and bullet crystals at low temperatures are given according to the observation of Heymsfield (1975c). Heymsfield and Platt (1984) suggested that the size spectra for cirrus crystals larger than 20 μm may be parameterized by the relation

$$N = A w_i d^B , \tag{2-19}$$

where N is the total number concentration, d is the maximum dimension of the crystals, and w_i is again the ice water content of the cirrus cloud. The variation with height of the ice water content and ice crystal concentration inside a cirrus cloud is shown in Figure 2.47.

The microstructure of the anvil of cumulonimbus clouds was studied by Bennetts and Ouldridge (1984), Heymsfield and Knollenberg (1972), Hobbs *et al.* (1980),

TABLE 2.5

Dimensional- and mass-size relationships for cirrus crystals. Dimensional relation: d is the width of the crysal and L is its length, both in mm (data based on Heymsfield, 1972). Mass-size relations: L (lengths of bullet in rosette) in cm , mass in g (from Heymsfield, 1975c).

Type	Dimensional relationship	Range
Bullets	$d = 0.25\ L$	$L \leq 0.3$ mm
d (mm)	$d = 0.185\ L^{0.532}$	$L > 0.3$ mm
L(mm)		
Columns	$d = 0.5\ L$	$L \leq 0.3$ mm
d (mm)	$d = 0.1973\ L^{0.414}$	$L > 0.3$ mm
L(mm)		
Bullet-rosette	$m = 4.4 \times 10^{-2}\ L^3$	$L \geq 0.12$ cm
m(g)	$m = 8.8 \times 10^{-4}\ L^2$	$0.00187 \leq L \leq 0.02$ cm
L(cm)	$m = 4.71 \times 10^{-1}\ L^3$	$L \leq 0.00187$ cm

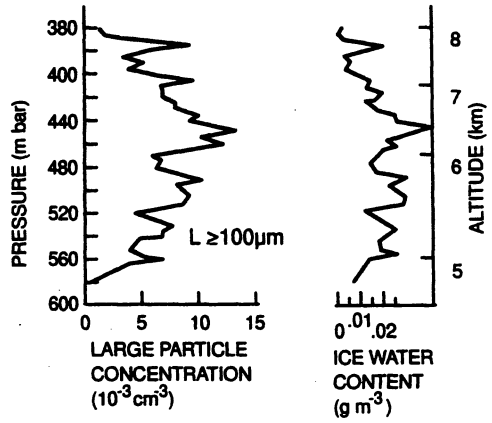


Fig. 2-47: Variation with altitude of ice particle concentration and ice water content inside cirrostratus during upward spiralling of airplane. (From Heymsfield and Platt, 1984, with changes.)

Heymsfield (1986), Heymsfield and Miller (1988), and Detwiler *et al.* (1992). Maximum ice particle concentrations and ice-water contents reached 300 liter^{-1} and 1 g m^{-3}, respectively. The ice particles in anvils consisted mostly of columns, bullet rosettes, and aggregates.

In closing this section we want to touch briefly on the microstructure of one additional form of ice cloud: the ice fog. Such a fog develops during a pronounced ground inversion at very low temperatures. Most of the studies on ice fogs were carried out in Fairbanks, Alaska by Thuman and Robinson (1954), by Ohtake (1967, 1968, 1970a,b), and by Kumai (1965, 1966a,b, 1969a,b). Strong ground inversions and winter temperatures between −30 and −55°C often develop at this location. Power plants, automobile exhausts, and exhausts from the heating systems of dwellings act as sources of moisture and dust particles. Under these conditions, ice crystals stay small and develop unusual forms. At −39 to −40°C, the crystals have diameters which range from 2 to 30 μm, with most frequent diameters near 10 μm. At warmer temperatures (−31 to −33°C) the size distribution broadens to diameters between 5 and 50 μm with a mode near 20 to 25 μm. The ice-water content is low and ranges between 0.09 g m^{-3} (at −40°C) and 0.02 g m^{-3} (at −30°C). The number concentration of ice crystals is very high, ranging between 100 and 200 cm^{-3}. Due to this high concentration, the visibility in ice clouds is severely reduced.

2.2.2 Shape, Dimensions, Bulk Density, and Number Concentration of Snowflakes, Graupel, and Hailstones

When certain conditions prevail in a cloud, snow crystals collide to form snowflakes (Plate 3). Air temperature and snow crystal shape play the dominant roles in such aggregation. Hobbs *et al.* (1974a,b) who studied cyclonic and orographic cloud systems over the Cascade Mts. (State of Washington), and Rodgers (1974b) who studied orographic cloud systems over Elk Mt. (Wyoming), established that the probability for the occurrence of snowflakes is highest if the air temperature at the site of their formation is near 0°C. With decreasing temperature, the probability of aggregation decreases with a secondary maximum near −15°C. Both observations show that the maximum dimensions of snowflakes are largest near 0°C. In addition to temperature, the snowflake size is strongly affected by the shape of the component crystals. Aggregates of columns and needles tend to stay small, while aggregates of dendritic crystals tend to become large. Although maximum snowflake diameters may be as large as 15 mm, most of the snowflakes have diameters between 2 and 5 mm.

Observations of Locatelli and Hobbs (1974) in the Cascade Mts. further demonstrated that, just as with single snow crystals, snow crystal aggregates tend to follow dimensional relationships during their growth by collision with other crystals. These relations are expressible in terms of power laws of the form $m = Ad^B$, where A and B are constants for an aggregate of component crystals of given shape, m is the mass of the snowflake, and d is its maximum dimension (Table 2.6a,b). Unfortunately, the above power law relation is supported only by the observations in clouds over the Cascade Mts. Considering the multitude of possible snow crystal

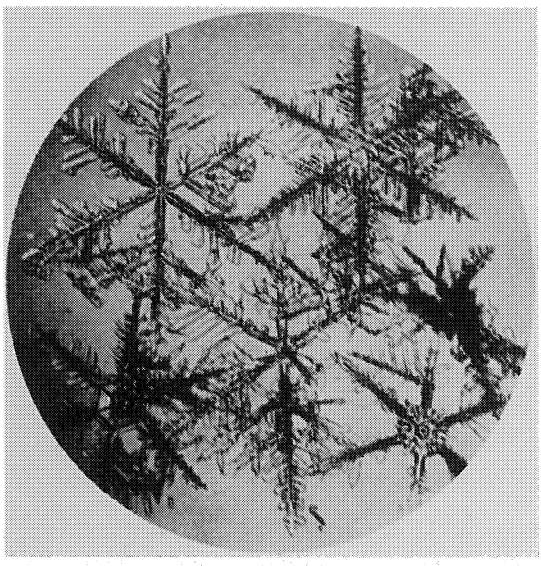


Plate 3. Snow flake consisting of dendritic crystals clinging together. (From Nakaya, 1954; by courtesy of Harvard University Press, copyright 1954 by the President and Fellows of Harvard College.)

combinations in a crystal aggregate, and the large variety of bulk densities associated with each crystal type, it is not yet possible to state whether the values for A and B given by these authors will apply to clouds over other regions as well.

The number of component crystals per snowflake was examined by Hobbs *et al.* (1974a,b), and Rodgers (1974a). Although the results of their studies scattered greatly, they indicate the expected trend that the number of component crystals increases with increasing snowflake size. This correlation is more pronounced, the smaller the component crystals (Figure 2.48).

The density of snow flakes was studied by Magono and Nakamura (1965), Matsuo and Sasyo (1981b) and Sasyo and Matsuo (1980). Typically, the density was found to range between 0.005 and 0.5 g cm^{-3}, with the most frequent values ranging between 0.01 and 0.2 g cm^{-3}.

A law for the size distribution of snowflakes, which is analogous to the Marshall and Palmer (1948) raindrop distribution, was proposed by Gunn and Marshall (1958). From an extensive field study, these authors suggested the relation

$$n(D_0) = n_0 \exp(-\Lambda D_0)\,, \tag{2-20}$$

where $\Lambda = 25.5R^{-0.48}$ mm^{-1}, $n_0 = 3.8\times10^3 R^{-0.87}$ $m^{-3}mm^{-1}$, D_0 is the equivalent diameter of the water drop to which the ice crystal aggregate melts, and R is the rate of precipitation in mm of water per hour (Figure 2.49). Observations by Sekhorn and Srivastava (1970) confirmed (2-20), although with somewhat different relations for the variation of Λ and n_0 with R.

Snowflake size distributions involving the actual size of the flakes were obtained by Braham (1990), Herzegh and Hobbs (1985), Passarelli (1978a,b), Lo and Pas-

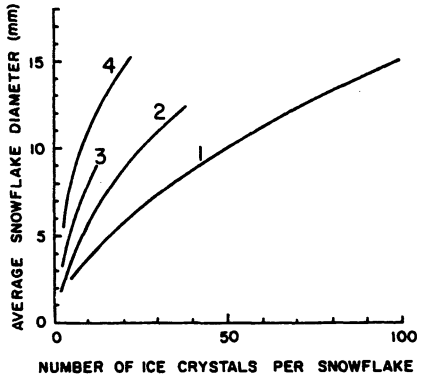


Fig. 2-48: Best fit lines for the relation between the number of component crystals per snowflake and snowflake diameter; average diameter of component crystals: (1) < 1.5 mm, (2) 1.5 to 2.5 mm, (3) 2.5 to 3.5 mm, (4) > 3.5 mm. (From Rodgers, 1974a; by courtesy of Am. Meteor. Soc., and the author.)

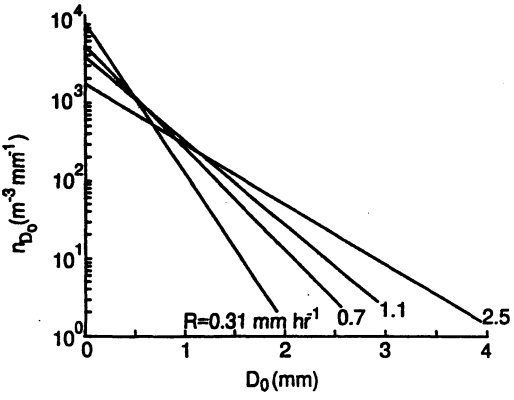


Fig. 2-49: Variation of the number concentration of snowflakes with drop diameter of melted snowflake. Data fitted to exponential distribution (solid line). (From Gunn and Marshall, 1958; by courtesy of Amer. Meteor. Soc., and the authors.)

TABLE 2.6a

Relationship between mass and maximum dimension of snow crystal aggregates. For aggregates collected on Cascade Mts. (750-1500 m, Washington), (based on data of Locatelli & Hobbs, 1974).

Type	Mass-size relation m(mg), D (mm)	Range of maximum dimensions (mm)
Aggregates of unrimed radiating assemblages of dendrites	$m = 0.073\ D^{1.4}$	2.0 - 10.0
Aggregates of unrimed radiating assemblages of dendrites	$m = 0.037\ D^{1.4}$	2.0 - 12.0
Aggregates of unrimed radiating assemblages of plates, side planes, bullets, and columns	$m = 0.037\ D^{1.9}$	1.0 - 3.0
Aggregates of unrimed side planes	$m = 0.04\ D^{1.4}$	0.5 - 4.0

TABLE 2.6b

As in Table 2-6a but for early snow flakes collected on Mt. Teine (1024 m, Hokkaido, Japan) (based on data of Kajikawa, 1989).

Type	Mass-size relation m(g), d (cm)	Range (cm)
P1e	$m = 4.82 \times 10^{-4}\ d^{1.97}$	0.08-0.68
P2a	$m = 8.30 \times 10^{-4}\ d^{2.09}$	0.14-0.70
P2e	$m = 3.96 \times 10^{-4}\ d^{1.40}$	0.08-0.46
P6d	$m = 1.02 \times 10^{-3}\ d^{2.22}$	0.16-0.66
R1d	$m = 5.28 \times 10^{-4}\ d^{1.76}$	0.16-0.58

sarelli (1982), and Houze *et al.* (1979). In many cases, the size distribution of flakes with dimensions larger than 2 mm could be fitted to an exponential law of the Marshall-Palmer type. For snowstorms over Lake Michigan, the parameter n_0 of this distribution ranged from 4×10^2 to 8.75×10^3 mm^{-1} m^{-3}, and the parameter Λ from 1.14 to 2.42 mm^{-1}. Often, however, significant deviations from the exponential distribution occurred. Thus, Herzegh and Hobbs (1985) observed subexponential distributions to be dominant in regions of weak stratiform clouds with low liquid water content, while superexponential distributions occurred in convective regions of clouds.

As snow crystals or snowflakes fall past the 0°C level they begin to melt (see Section 16.3). Due to the limited rate at which the released latent heat can be dissipated to the surrounding air, the flakes must fall over several hundred meters in order to melt, typically at the +5°C level. This 'melting layer' is detected by radar in terms of a 'bright band' caused by a sharp increase in reflectivity of the scattered electromagnetic radiation orginating from the radar (Figure 2.50a).

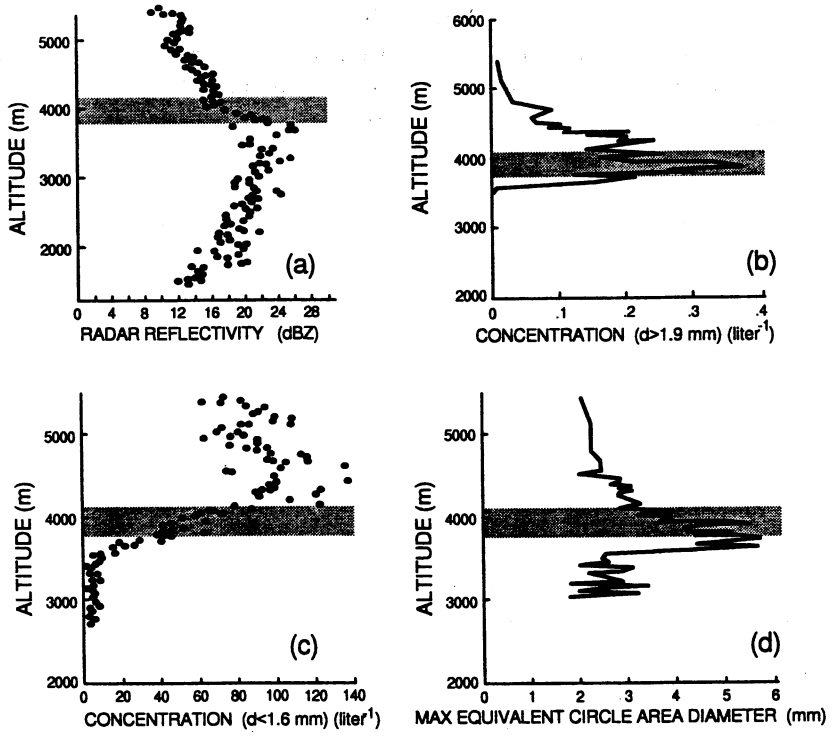


Fig. 2-50: Microstructure profiles through the melting layer of convective clouds over Oklahoma and Kansas: (a) radar reflectivity, (b) concentration of particle with $d > 1.9$ mm, (c) concentration of particles with $d < 1.6$ mm , (d) maximum size. The shading marks the extent of an isothermal layer of nearly 0°C. (From Willis & Heymsfield, 1989, with changes.)

Data on the bright band have been accumulated over almost five decades since the initial studies of Ryde (1946), who suggested that the bright band is associated with the melting layer in the cloud. Subsequent field studies have confirmed the early explanation (Cunningham, 1947; Hooper and Kippax, 1950; Marshall and Gunn, 1952; Austin and Bemis, 1950; Mason, 1955; du Toit, 1967; Atlas *et al.*, 1969; Ohtake, 1969, 1970a,b,c; Heymsfield, 1979; Leary and Houze, 1979; Houze *et al.* 1979; Stewart *et al.* 1984; Yokoyama and Tanaka, 1984; Yokoyama, 1985; Marwitz, 1987a,b; Willis and Heymsfield, 1989; Klaasen, 1988).

The bright band is the result of several microphysical mechanisms acting in sequence above, inside, and below the melting level. Between about −5 and 0°C, snow crystals of different sizes and fall velocities tend to grow rapidly by aggregation to form snow crystal aggregates (snowflakes) of rather similar fall velocities (1 to 2 m sec^{-1}), and sizes up to 5 to 10 mm. Of course, this growth, promoted by the quasi-liquid layer on ice (see Section 5.7.3), is associated with a reduction in the number concentration of the ice particles. As the flakes pass through the 0°C

level, they begin to melt and contain increased amounts of water with increasing fall distance. This in turn causes the dielectric constant of the particles to increase and to assume almost the value for water. Increased particle size and water content enhances the radar reflectivity to a maximum value. Upon completion of melting, the snowflakes collapse to raindrops of diameters typically between 1 and 2.5 mm, depending on the diameter of the original flake. The sudden change in shape and the associated reduction of the aerodynamic drag on the particle causes the fall speed of the precipitating particles to increase sharply up to 4 to 8 m sec^{-1}. This acts to decrease the concentration of the radar reflecting particles and hence the reflected radar signal. A typical variation with height of the radar reflectivity of a cloud bright band and the associated variation with height of the number concentration and size of the precipitating particles is given in Figures 2.50b,c,d.

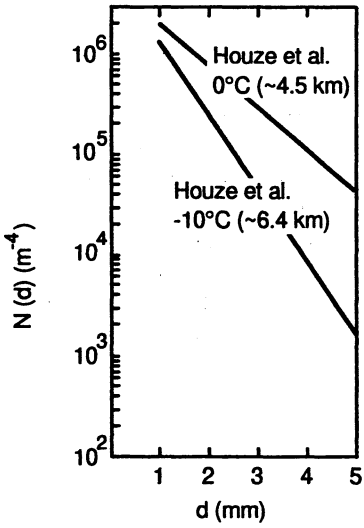


Fig. 2-51: Size distributions of ice particles above and at the top of the melting layer as reported by Houze *et al.* (1979). (From Leary and Houze, 1979, with changes.)

Studies of the size spectrum of precipitating particles falling through a melting layer were carried out by Lo and Liu (1990), Stewart *et al.* (1984), Lo and Passarelli (1982), Passarelli (1978a,b), Houze *et al.* (1979), Leary and Houze (1979), and Gordon and Marwitz (1983). For the case of exponential size distributions, they found that n_0 and Λ decrease as the 0°C level is approached (Figure 2.51), due to a broadening of the size spectra and a decrease in the number concentration. Once through the 0°C level n_0 changes little while a sudden increase in Λ takes place due to the sudden narrowing of the particle distribution when the snow crystal aggregates melt to smaller, faster falling drops.

From a comparison of the drop size spectrum just below the melting layer with the spectrum of the melted snow flakes just above it, Ohtake (1969, 1970a,b,c) concluded that snowflakes do not break up during their fall through the melting layer, confirming earlier observations of du Toit (1967). On the other hand, Magono

and Arai (1954), Gunn and Marshall (1958), Yokoyama and Tanaka (1984), Stewart *et al.* (1984) and Yokoyama (1985) found evidence from their radar studies that melting snowflakes do break up. Recent laboratory studies have finally settled the problem (see Chapter 16) and show that, under certain conditions, melting snow flakes do break up.

Rimed ice crystals and graupel are formed in clouds which contain both ice crystals and supercooled drops. Field studies have shown that in such clouds both snow crystals and frozen drops may serve as embryos for graupel formation. Thus, Harimaya (1976) carefully sectioned and disassembled natural graupel particles under the microscope to find both snow crystals and frozen drops as center particles. The importance of frozen drops to the formation of graupel has also been stressed by Pflaum *et al.* (1978), who experimentally studied the riming growth of frozen drops and of crystal plates while they were freely suspended in the vertical air stream of a wind tunnel. Considerable controversy exists in the literature with regard to the type of ice particle which may serve as an embryo for conically shaped graupel. Arenberg (1941) suggested that conical graupel originate on planar snow crystals which, while falling under gravity, primarily rime on their bottom side. Under such conditions, rime was assumed to build into a downward facing point, thus forming a conical graupel with its apex down. Holroyd (1964) proposed that conical graupel are the result of an aggregation of partially rimed needle crystals which continue to rime after aggregation. Nakaya (1954), List (1958a,b), and Knight and Knight (1973a), on the other hand, advocate the ideas of Reynolds (1876), who suggested that conical graupel are the result of planar ice crystals which preferentially rime on their bottom side, the rime fanning out into the wind rather than growing into a point. Such behavior causes the development of a conical graupel which falls with its apex up and has its embryo near the apex. Weickmann (1953, 1964) and Takeda (1968) suggested that conical graupel can also start on frozen drops. This suggestion was experimentally verified by the wind tunnel studies of Pflaum *et al.* (1978). A systematic overview (Figure 2.52) of the different formation mechanisms leading to graupel has been given by Harimaya (1976).

In studies of the initial stages of riming in various types of clouds, Ono (1969), Wilkins and Auer (1970), Hobbs *et al.* (1971a), Kikuchi (1972a), and Iwai (1973) found that both columnar ice crystals and ice crystal plates have to grow by diffusion to a certain critical size before they can grow further by riming. An example for this requirement is given in Figure 2.53 for planar crystals. We notice that with increased branching of the crystal, the onset of riming increases from about 150 μm for a single plate to about 800 μm diameter for a dendritic crystal. While the onset of riming for plate-like crystals only depends on the crystal's diameter, the onset for columnar crystals depends on their width as well as their length. Thus, their critical width has to be near 30 μm, and their critical length between 125 and 225 μm. Verification of these results has been presented by Reinking (1979), Borys (1983), and Auer (1970). Both Reinking (1979) and Bruntjes *et al.* (1987) have pointed out that capped columns and double plate crystals are especially good rimers. These crystals begin to rime at a diameter of 50 μm, and are heavily rimed at diameters of 150 to 200 μm. Harimaya (1975) and Kikuchi and Uyeda (1978) have shown that the onset of riming also depends on a critical drop size

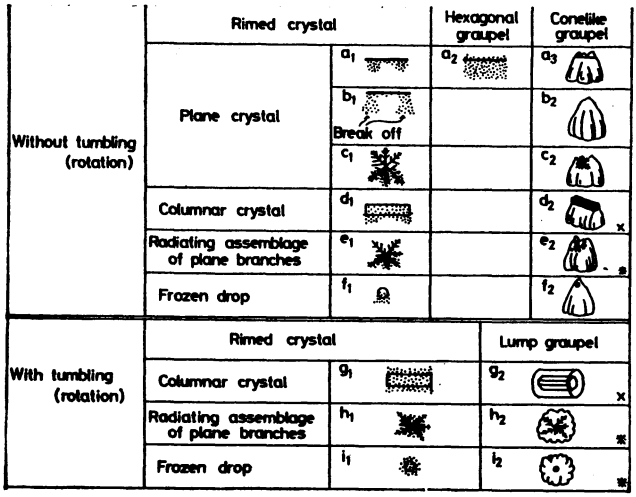


Fig. 2-52: Classification of graupel particles according to their formation mechanisms. X type not yet been found, ∞ type found but their embryos have not yet been detected. (From Harimaya, 1976, by courtesy of the Jap. Meteor. Soc., and the author.)

(Figure 2.54). One notices that drops of diameter less than 10 μm are unlikely to be involved in the riming process. The drops most likely to be found on rimed crystals have diameters between 10 and 80 μm. Drops having diameters larger than 80 μm are generally absent. The larger a crystal grows by riming, the wider is the size spectrum of the attached drops (Wilkins and Auer, 1970). Photographs of rimed crystals (Wilkins and Auer, 1970; Zikumda and Vali, 1972; Iwai, 1973; Knight and Knight, 1973a) show that plate-like and dendritic crystals are rimed most intensely at the crystal edges, with considerably fewer frozen drops attached to the interior surface portions of the crystal (Plate 4). Drops frozen onto simple columnar crystals are uniformly distributed over the crystal surface (Plate 5), and columns with end plates are most intensely rimed on the outer surface of an end plate, with few or no drops attached to the columnar stem of the crystal.

Observations show that, as in the case of snowflakes, rimed single snow crystals, rimed snow crystal aggregates, and graupel particles (Plate 6) also follow fairly definite size-mass relationships during their growth (Table 2.7).

The bulk density of rimed ice particles varies greatly, depending on the denseness of packing of the cloud drops frozen on the ice crystal. Table 2.8 shows that the bulk density of graupel particles ranges from about 0.05 g cm^{-3} to as high as 0.89 g cm^{-3}.

In clouds with sufficiently large updrafts, riming may continue until hailstones are produced. We have already given a description of the various shapes they may assume; some examples are shown in Plates 7 and 8. A variety of habits and surface textures have been observed, including: conical shapes (Hallett, 1965; List, 1958b; Mossop and Kidder, 1961), oblate spheroidal shapes (Carte and Kidder, 1961), apple shapes (Kidder and Carte, 1964; Spengler and Gokhale, 1972), hailstones

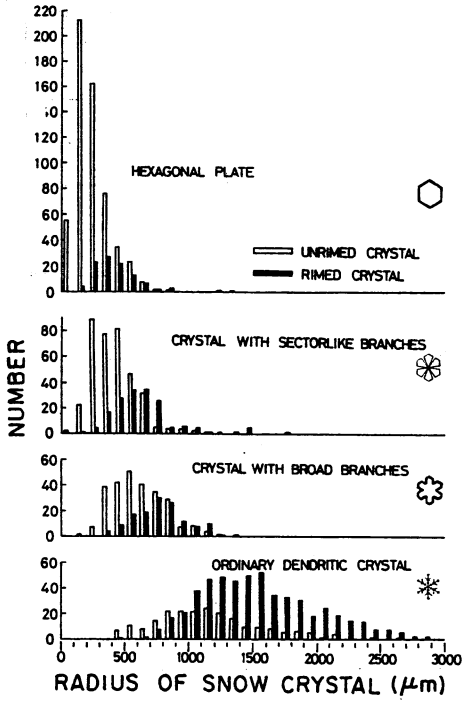


Fig. 2-53: Observed relationship between the onset of riming and the radius of planar snow crystals; open columns represent unrimed crystals; solid columns represent rimed crystals. (From Harimaya, 1975; by courtesy of the Jap. Meteor. Soc., and the author.)

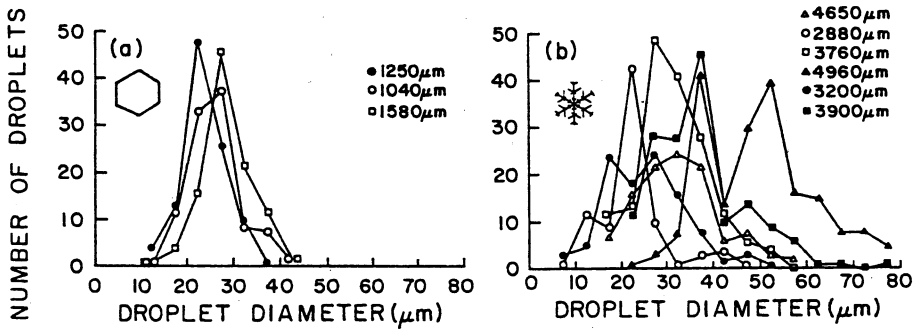


Fig. 2-54: Observed size distribution of cloud drops accreted on planar snow crystals. Number labeling curve is diameter of collector crystal; (a) planar crystal, (b) dendritic crystal. (From Harimaya, 1975; by courtesy of Jap. Meteor. Soc., and the author.)

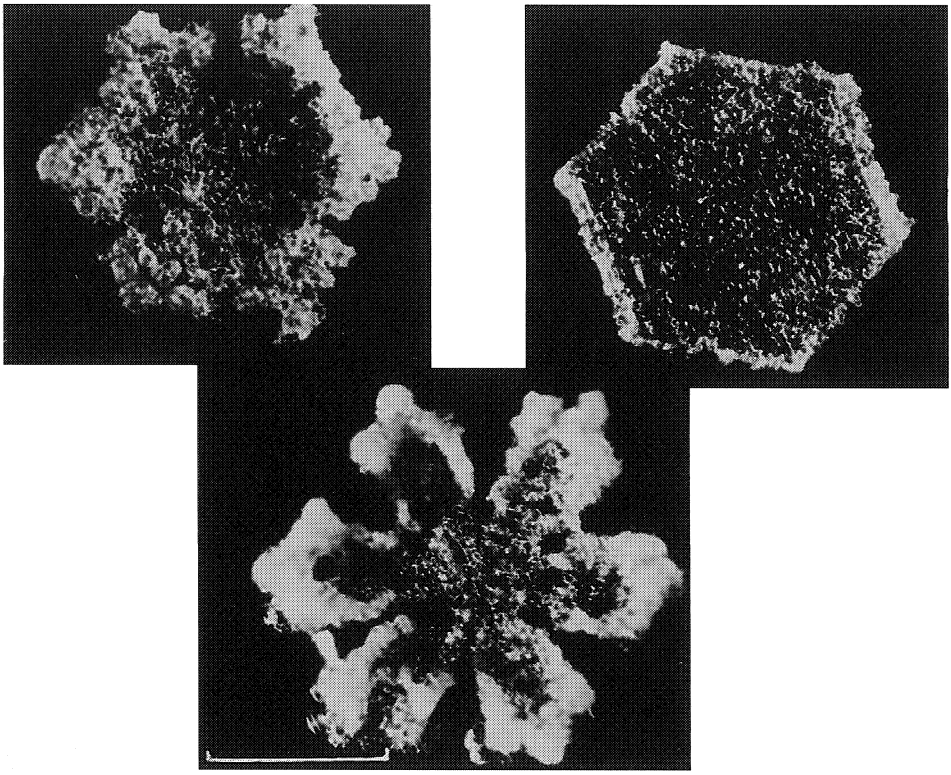


Plate 4. Rimed planar snow crystals of diameters between 2 and 3 mm. (From Hobbs et al., 1971; by courtesy of the authors.)

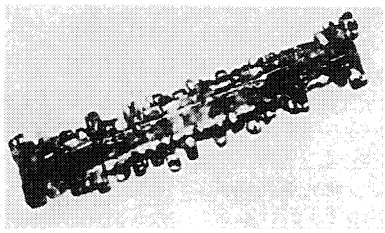


Plate 5. Rimed columnar snow crystal, magnification 31 times. (From Iwai, 1973; by courtesy of *J. Meteor.Soc., Japan*, and the author.)

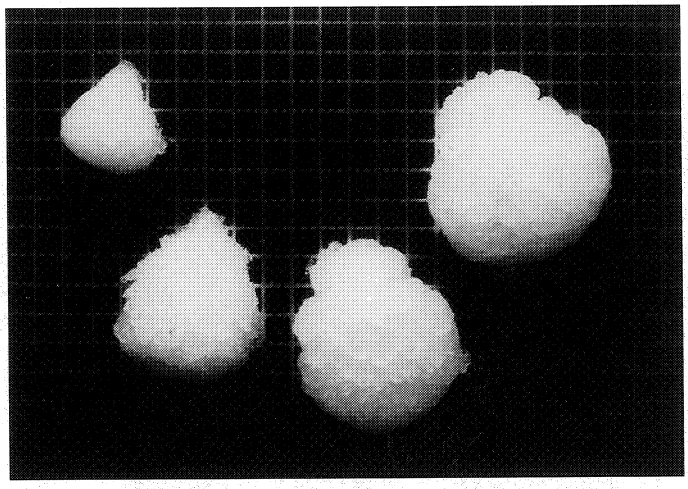


Plate 6. Graupel particles of various sizes collected during showers in Switzerland. Distance between lines on collection plate is 2 mm. (From Aufdermauer, 1963; by courtesy of the author.)

with spikes and lobes on the surface (Mossop, 1971a; Kidder and Carte, 1964; Briggs, 1968; Browning and Beimers, 1967; Knight and Knight, 1970a,c; Bailey and Macklin, 1968a; Browning, 1966), and irregular shapes (Rogers, 1971). Axis ratios of oblate spheroidal hailstones in storms over Oklahoma, Colorado and Alberta were measured by Knight (1986), Barge and Isaac (1973), and Matson and Huggins (1980). They found that the ratio of the short to the long axis varied from 0.95 for stones with 1 to 5 mm maximum dimension to about 0.6 to 0.7 for stones with 50 to 60 mm maximum dimension. Most stones had an axis ratio of 0.8.

Auer (1972b) and Auer *et al.* (1970) found that the size distribution of graupel and hailstones often fits a relation of the form

$$n(d) = Ad^B\,, \tag{2-21}$$

where d is the diameter of the ice particle, $A = 561.3$ and $B = -3.4$ (Auer, 1972b) for storms over the High Plains, and $A = 254$ and $B = -2.8$ for storms over northeastern Colorado. However, most studies showed that the size distribution for graupel and hailstones are fitted best by an exponential distribution of the Marshall-Palmer type (Figure 2.55a) (Xu, 1983; Cheng and English, 1983; Cheng *et al.*, 1985; Balakrishnan and Zrnic 1990; Douglas, 1964; Ziegler *et al.*, 1983; Ulbrich, 1978; Federer and Waldvogel, 1975; Smith *et al.*, 1975, 1976). For hailstorms over Alberta (Canada), Cheng and English, (1983) found for the size distribution of hailstones

$$n(d) = n_0 \exp(-\Lambda d)\,, \quad \text{with} \quad n_0 = A\Lambda^b\,, \tag{2-22}$$

where $A = 115$ and $B = 3.63$, with $n_0(\mathrm{m}^{-3}\ \mathrm{mm}^{-1})$ and $\Lambda(\mathrm{mm}^{-1})$. Hailfall rates R_H for storms over Switzerland (Federer and Waldvogel, 1975) ranged from 2.6 to

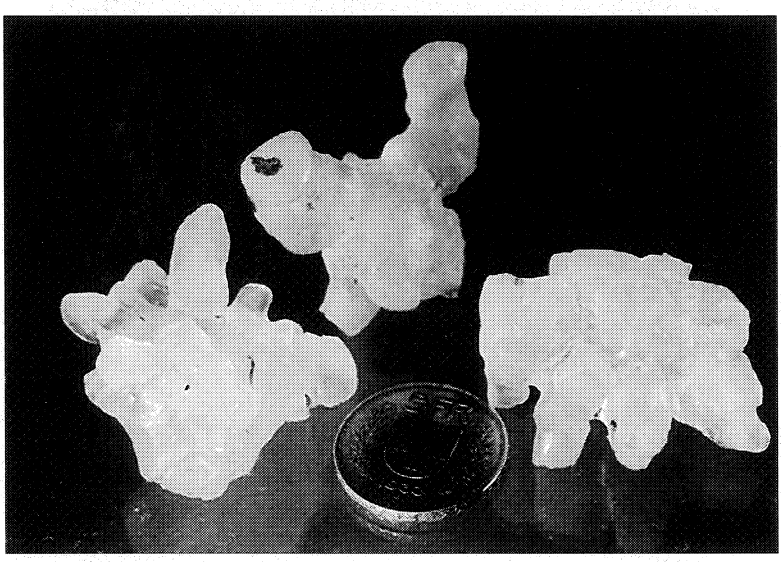


Plate 7. Hailstones collected during hailstorms in Switzerland. (From Levi *et al.*, 1970b, by courtesy of *Amer. Meteor. Soc.*, and the authors.)

TABLE 2.7

Mass-size relation for various type graupel particles. For all except R1a, R1b m in g and d in cm, (based on data of Heymsfield & Kajikawa, 1989) for graupel collected on Mt. Teine (1024 m, Hokkaido, Japan). Graupel types R1a and R1b collected on Sierra Nevada (2600-3000 m) for m in mg and d in mm (based on data of Mitchell *et al.*, 1990).

Type	Mass-size relation	Range
R1c	$m = 4.21 \times 10^{-3}\ d^{2.36}$	0.8 - 2.7
R1d	$m = 2.03 \times 10^{-3}\ d^{2.58}$	0.7 - 5.3
R2a	$m = 9.53 \times 10^{-2}\ d^{3.80}$	0.7 - 2.2
R2b	$m = 7.55 \times 10^{-3}\ d^{3.04}$	1.1 - 4.7
R2c	$m = 7.25 \times 10^{-4}\ d^{1.74}$	3.0 - 6.2
R4b	$m = 1.07 \times 10^{-1}\ d^{3.10}$	0.4 - 9.0
$T \geq 0.5°C$	$m = 7.61 \times 10^{-2}\ d^{2.38}$	0.5 - 4.7
$T < 0.5°C$	$m = 9.78 \times 10^{-2}\ d^{3.21}$	0.5 - 9.0
R4c	$m = 9.42 \times 10^{-2}\ d^{3.06}$	1.1 - 7.5
$T \geq 0.5°C$	$m = 1.76 \times 10^{-1}\ d^{3.06}$	1.1 - 7.5
$T < 0.5°C$	$m = 5.74 \times 10^{-2}\ d^{2.88}$	0.8 - 8.6
R1a	$m = 0.0060\ \mathrm{L}^{2.1}$	0.5 - 2.8
R1b	$m = 0.023\ \mathrm{L}^{1.8}$	0.2 - 2.4

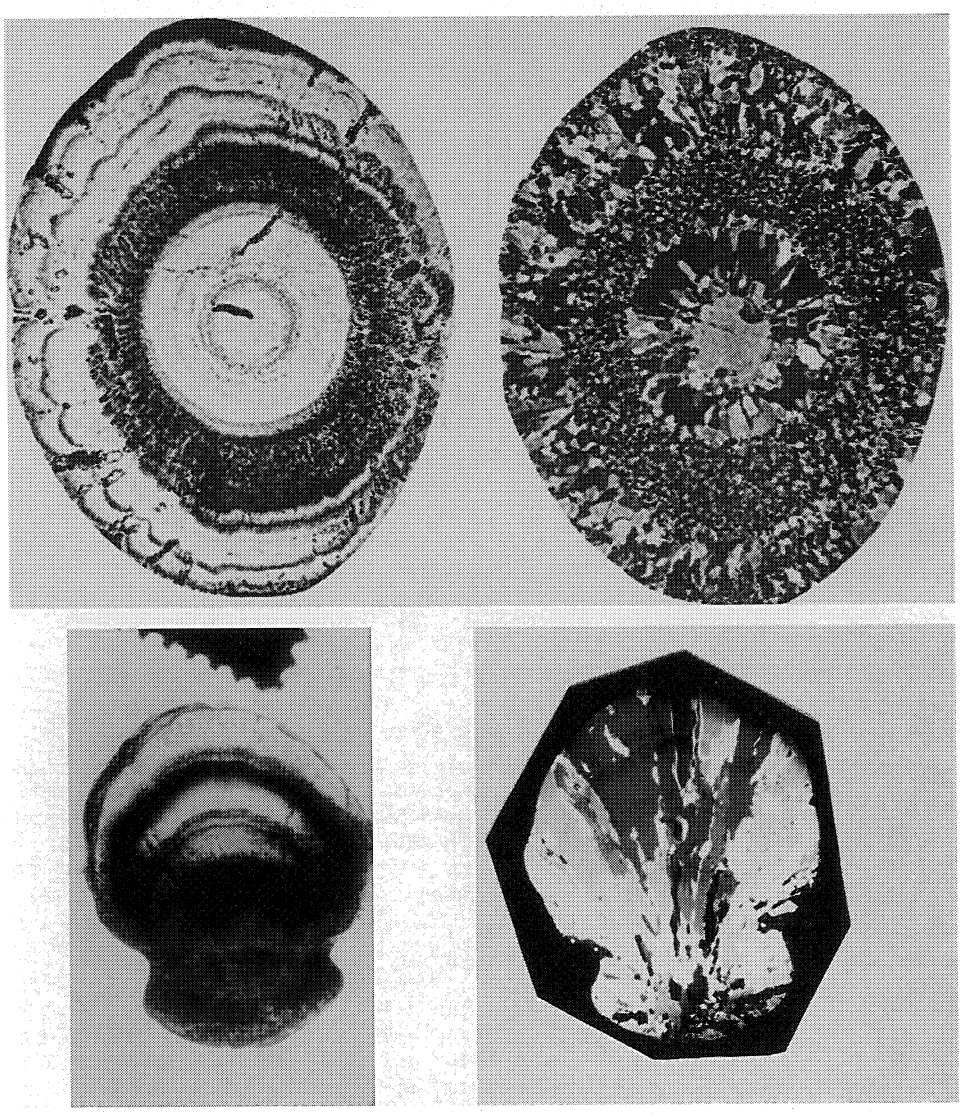


Plate 8. Thin sections of hailstones. Pictures on the left: section observed under the microscope in normal transmitted light; pictures on the right: section observed in polarized transmitted light. Plates on top row: from Knight & Knight, 1968a; by courtesy of *Am. Meteor. Soc.*, and the authors. Plates on second row: from Federer, 1977, (pers. comm.). Maximum diameter of hailstone on top row: 4 cm; maximum diameter of hailstone on second row: 1.8 cm.

TABLE 2.8
Densities of graupel particles

Observer	Size range (mm)	Density (g cm^{-3})
Locatelli and Hobbs (1974), Washington	0.5 - 3	0.05 - 0.45
Zikmunda and Vali (1972), Wyoming	0.5 - 1	0.45 - 0.7
Zikmunda and Vali (1972), Wyoming	1 - 2	0.25 - 0.45
Bashkirova and Pershina (1964a,b), U.S.S.R.	0.4 - 3	0.08 - 0.35
Braham (1963), Missouri	0.5 - 3	0.85 - 0.89
List (1958a, b), Switzerland	0.5 - 6	0.5 - 0.7
Magono (1953), Nakaya and Tereda, (1935), Japan	0.8 - 3	0.13

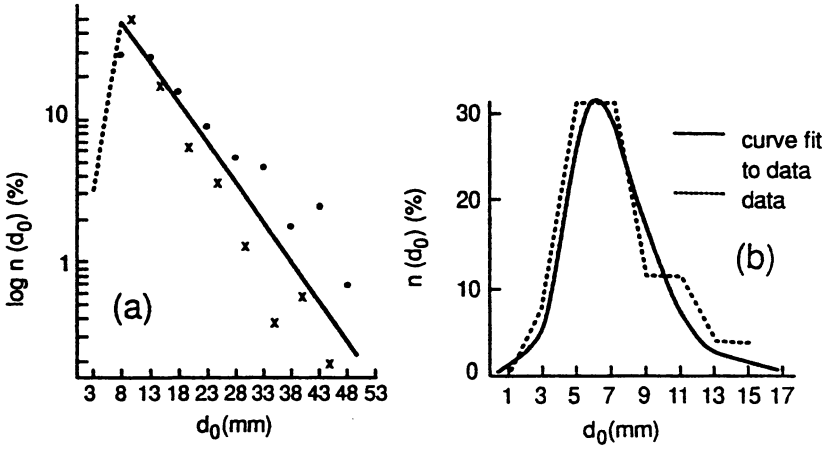


Fig. 2-55: Size distribution of hailstones (a), and their embryos (b), during a storm on June 4, 1976 over China. Data fit: $n(d_0) = 115\ \exp(-0.125\ d_0)$, for $d_0 \geq 6$ mm , d_0 = equivalent sphere diameter. (From Xu, 1983, with changes.)

152 mm hr^{-1}, with ice contents w_H ranging between 0.05 to 2.64 g m^{-3}, where w_H could be related to R_H by $w_H = 1.74 \times 10^{-2} R_H$. The size distribution parameters n_0 and Λ varied between $1.5 \leq n_0 \leq 52$ m^{-3} mm^{-1}, $0.33 \leq \Lambda \leq 0.64$ mm^{-1}, agreeing quite well with the values found by Smith *et al.* (1976) for hailstorms over N.E. Colorado.

While hailstones usually have diameters of a few centimeters, observations show that large hailstones may have a major axis length as large as 6 to 8 cm. Hailstones of even larger sizes have been observed by Browning (1966), and by Roos (1972), who described a hailstone which weighed 766 g and had a circumference of 44 cm, equivalent to a sphere radius of 7 cm.

Hailstones collected at the ground are usually hard ice particles. In early studies on hail growth, this observation led to the assumption that hailstones always grow as solid ice particles. However, in more recent experimental studies during which hailstone growth was simulated in wind tunnels, List (1958a,b; 1959; 1960a,b)

and Macklin (1961) discovered that hailstones are not always hard particles but, depending on the regime of growth, may also be 'soft' particles which consist of ice-water mixtures, termed *spongy ice* by List. Such ice-water mixtures are produced when the latent heat released during growth is not exchanged efficiently enough between the hailstone and its environment to allow all the water collected by the hailstone to freeze. That portion of the collected water which immediately freezes produces a skeletal framework or mesh of dendritic ice crystals (see Chapter 16), in which the unfrozen portion of the collected water is retained as in a sponge whose surface temperature is at 0°C.

A few field studies have verified the spongy growth mode of hailstones in clouds. Thus, Summers (1968) reported on the collection of soft or slushy hailstone samples which fell during hailstorms in Alberta, Canada. Gitlin *et al.* (1968) and Browning *et al.* (1968) used calorimetric methods to analyze freshly fallen hailstones at various geographic locations. They found that water comprising up to 16% of the total mass was embedded in the ice structure of some hailstones. In a more definitive study, Knight and Knight (1973b) analyzed natural hailstones by the quenching technique, and concluded that while some hailstones experience spongy growth at times, this growth mode is not the rule for all hailstones.

Studies of hailstones by the thin section technique (List, 1961) reveal that usually a hailstone has one distinct central growth unit or growth embryo (Knight and Knight, 1970b). Hailstones with two centers of growth exist but are extremely rare (Rogers, 1971). Considerable controversy exists in the literature concerning the nature of this central growth unit. List (1958a,b; 1959; 1960a,b), and Knight and Knight (1976, 1981) found that about 80% of the hailstones which fell in Switzerland and in Colorado, respectively, had a graupel embryo which, in turn, may have originated on a snow crystal or on a small frozen drop. Similarly, Mossop and Kidder (1964) and Carte and Kidder (1966) found that a large percentage of the hailstones collected during hailstorms in South Africa originated as graupel particles. In contrast, however, Macklin *et al.* (1960) found that most hailstones collected in England had clear growth centers, and they interpreted this to mean that these hailstones originated as large frozen drops. Both types of growth centers were found by Knight and Knight (1970b) and by Federer and Waldvogel (1978), who examined a large number of hailstones which fell in the U.S. and in Switzerland, respectively. They observed embryos of a few millimeters to 1 cm in diameter. Some of these were more or less opaque and had conical shapes, while others were clear or bubbly and had spherical shapes. Thus, present evidence indicates that hailstones may originate either as graupel or frozen drops depending considerably on geographic location. After analyzing a large number of hailstones to determine the effects of regional differences on their embryo structure, Knight (1981) surmised that for South Africa (Lowveld) 62 to 83% of the embryos were frozen drops. For other locations, the percentages were the following: for Colorado, 6 to 27%, for Switzerland 63%, for Oklahoma, 70% and for South Africa (Highveld) 35 to 54%. An analysis of the size distribution of hailstones and their embryos observed during a hailfall 4 June 1976 in China is given in Figures 2.55a and 2.55b, respectively. We note that the hailstone embryos on that day had a most frequent size of 7 mm.

The bulk density of hailstones tends to vary radially from surface to core with

alternating concentric layers of lower and higher density. The density of such hailstone shells has been found to vary usually between 0.8 and 0.9 g cm^{-3}, but shell densities as low as 0.7 g cm^{-3} have also been observed (List, 1958a,b, 1959; Macklin *et al.*, 1960; Mossop and Kidder, 1961; Prodi, 1970; List *et al.*, 1970a). The density variations are a reflection of varying amounts of trapped bubbles (Plate 8, left side). Many of these bubbles are quite regularly grouped within concentric layers, which alternately contain larger and smaller numbers. Hailstone shells with a large number of bubbles appear quite opaque, while shells with only a few bubbles appear as clear ice.

The size and number concentration of air bubbles in hailstones have been studied by List (1958b), Macklin *et al.* (1970), List *et al.* (1972), and List and Agnew (1973). From an examination of planar cuts through the stone centers, List and his co-workers found that the bubble size distribution was lognormal. The planar number concentration of bubbles varied across the slice surface by more than two orders of magnitude, from about 50 to 5000 cm^{-2}. Opaque shells consisted of numerous smaller bubbles, while clear, transparent shells contained fewer and larger bubbles. In hailstone layers deposited in the dry growth regime, Carras and Macklin (1975) found a volume air bubble concentration of 10^6 to 10^8 cm^{-3}, with air bubble sizes ranging from 2 to 8 μm in diameter. In layers deposited in the wet growth regime, the air bubble concentration was 10^5 to 10^6 cm^{-3}, and the bubbles had diameters between 20 and 100 μm.

When thin sections of graupel particles and hailstones are studied by means of polarized light, a second interesting structural feature is revealed: One finds that the ice of the sections is polycrystalline, with large and small individual crystallites (single ice crystals) in alternating layers (Plate 8, right side). Most crystallites tend to assume preferred orientations (List, 1958a,b; 1960a,b). Detailed studies of the size and orientation of crystallites in natural hailstones have been made by Aufdermauer *et al.* (1963), Knight and Knight (1968a,b), List *et al.* (1970), Levi *et al.* (1970a,b), Macklin *et al.* (1970), and Macklin and Rye (1974). These have shown that transparent layers relatively free of air bubbles tend to consist of fairly large crystallites, while opaque layers with relatively high air bubble concentrations tend to consist of numerous small crystallites. List *et al.* (1970) determined that in the slice-plane, crystallites have surface areas which range between 1×10^{-3} and 8×10^{-2} cm^2 (0.1 to 8 mm^2). Macklin *et al.* (1970) and Rye and Macklin (1975) found that the crystallite length decreases from 8 to 0.25 mm and the width from 1 to 0.2 mm as the ambient temperature decreases from -5 to -30°C.

Although hailstone crystallites are randomly oriented in some shells, they assume a preferred orientation in others. Aufdermauer *et al.* (1963), Knight and Knight (1968), and Levi *et al.* (1970a,b) found that in some shells crystallites have their crystallographic *c*-axis generally either parallel or at right angles to the hailstone's radial growth direction. List *et al.* (1970a,b) found crystallites with preferred *c*-axis orientation parallel to the radial growth direction in the clear shells of the hailstones, and with rather random orientations in opaque shells. A discussion of the reasons for the polycrystallinity of hailstones and the preferred orientation of crystallites under certain growth conditions is given in Chapter 16.

CHAPTER 3

THE STRUCTURE OF WATER SUBSTANCE

In the previous chapter, we described the observed variety of shapes, sizes, and concentrations of the solid and liquid particles which comprise clouds and precipitation. The remaining chapters will be devoted to exploring how such particles come into being and how they grow. Understanding these processes depends, to a large extent, on knowledge of the physical properties of water vapor, water, ice, and, ultimately, on the physical characteristics of the water molecule itself. Therefore, as a prelude to what will follow, this chapter will describe briefly some of the relevant structural features of individual water molecules and their various combinations in water vapor, bulk water, and ice.

For a detailed study of subjects covered in this chapter, the reader may refer to the texts of Hobbs (1974), Ben-Naim (1974), Whalley *et al.* (1973), Horne (1972), Franks (1972), Fletcher (1970a), Robinson and Stokes (1970), Eisenberg and Kauzmann (1969), Riehl *et al.* (1969), Kavanau (1964), and Dorsey (1940).

3.1 Structure of an Isolated Water Molecule

Measurements of the heat capacity C_{pv}(IT cal mole^{-1} °C^{-1}) of water vapor at constant pressure near room temperature yield a value of approximately 4k per molecule, where k is, the Boltzmann constant. For meteorological conditions of interest, the specific heat $c_{pv} = C_{pv}/M_{\mathrm{w}}$ of water vapor varies between 0.44 and 0.46 cal g^{-1} °C (Smithsonian Meteorological Tables, 1968; Landolt-Börnstein 1988).

Since quantum statistical mechanics shows that the vibrational degrees of freedom are frozen-in at these temperatures, we must interpret the heat capacity measurements in terms of a contribution of (1/2)k from each of the three translational degrees of freedom, and a contribution of (1/2)k from rotation about each of the three axes for which the molecule has an appreciable moment of inertia. This interpretation implies that the water molecule cannot have its three atoms arranged in a linear fashion. The same conclusion is reached by investigating the electrical properties of the water molecule. Since such measurements reveal a large electric dipole moment of $\mu = 1.83 \times 10^{-18}$ e.s.u. cm (see Hobbs, 1974; Eisenberg and Kauzmann, 1969), a linear molecule is once again ruled out.

The geometry of the water molecule can be deduced accurately from studies of the infrared spectrum of water vapor. On the basis of such measurements, Mecke (1933) concluded that the three atoms are situated at the vertices of a triangle, the geometry of which is given in Figure 3.1. Recent experiments show that the equilibrium O—H bond length is 0.95718 Å and that the equilibrium H—O—H bond angle is 104.523° (see Fletcher, 1970a; Hobbs, 1974).

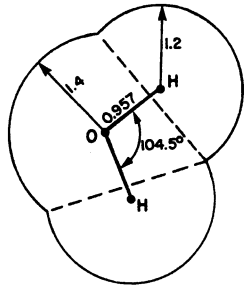


Fig. 3-1: Two dimensional geometry of a single water molecule. The O-H distance (in 10^{-8} cm) and the H-O-H angle are indicated, as are the radii of the hydrogen and oxygen atoms. (From *Water and Aqueous Solutions* by A. Ben Naim, copyrighted by Plenum Press, 1974.)

The structure of the water molecule is importantly affected by the electron configuration around the oxygen atom.* In its ground state, an oxygen atom has two electrons in the spherical 1s orbital, where they are bound tightly to the atomic nucleus, and two electrons, less tightly bound, in the spherical 2s orbital. In addition, two electrons can be considered to occupy the $2p_x$ orbital, one electron the $2p_y$ orbital, and one electron the $2p_z$ orbital. This electron configuration is illustrated in Figure 3.2. Since the $2p_y$ and $2p_z$ orbitals may contain two electrons each, these orbitals are incomplete. The electrons in these orbitals are therefore free to couple with the electrons in the 1s orbital of the two hydrogen atoms, allowing them to form two O—H bonds.

If these orbitals exactly described the O—H bond of a water molecule, one would expect water to have a bond angle of 90°. Experimentally, however, one finds that the bond angle is some 15° larger. One might try to explain this on the basis of the fact that the O—H in a water molecule is not truly covalent but is partly ionic; i.e., the electrons are not evenly shared by the oxygen atom and a hydrogen atom. Since oxygen is more electronegative than hydrogen, oxygen exerts a greater force on the shared electron pair than does the hydrogen. Consequently, the electrons spend a greater portion of their time in the outer shell of the oxygen atom than in the hydrogen shells, and so the positive charge of the hydrogen nuclei is incompletely shielded by the electrons. Electrostatic repulsion between the two hydrogen atoms must, consequently, lead to an increase of the bond angle.

*Generally, an atom's ground state electron configuration is described by specifying the number of electrons in each energy level or 'shell', characterized by the principal quantum number n and the angular momentum quantum number ℓ. In listing these electrons, it is customary to use the spectroscopic notation in which the numbers $\ell = 0, 1, 2, 3$ are replaced by the respective letters s, p, d, f. The number of electrons in a shell is indicated by a superscript; e.g., $2p^6$ means there are 6 electrons in the shell characterized by $n = 2$, $\ell = 1$. Each electron is said to occupy an 'orbital' corresponding to given values of n, ℓ, and the quantum number m describing the z-component of the electron's angular momentum. By the Pauli exclusion principle, there is room in each orbital for two electrons, necessarily with opposite spins. It is the outermost, *valence* electrons in incomplete orbitals which are responsible for *covalent* and *ionic* chemical bonds. For further information, see any standard reference on quantum mechanics, e.g., Schiff (1968).

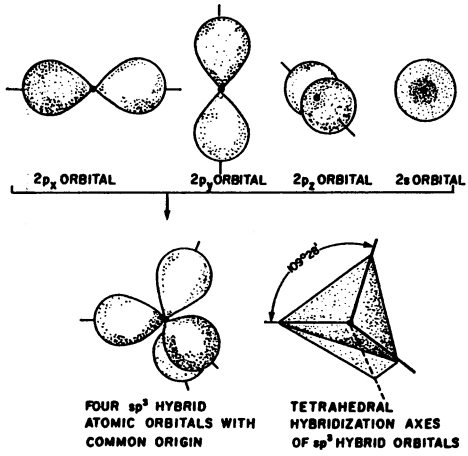


Fig. 3-2: Hybridization of orbitals of oxygen atom. (From *Organic Chemistry* by D.J. Cram and G.S. Hammond, copyrighted by McGraw-Hill, 1955.)

However, Heath and Linnett (1948) showed that this repulsion is insufficient to account for the experimentally found bond angle. They suggested that a more significant factor in opening up the bond angle is the mixing or 'hybridization' of the 2s orbital of the oxygen atom with its $2p_y$ and $2p_z$ orbitals, resulting in the formation of four sp^3-hybrid atomic orbitals. Two of these overlap with the hydrogen orbitals, while the two remaining orbitals form two lobes on the side of the oxygen atom away from the hydrogen atoms (Figure 3.2). These lobes, called *lone-pair hybrids*, are symmetrically located above and below the molecular plane and form roughly tetrahedral angles with the bond hybrids (exact tetrahedral angle, 109.467°). It is this tetrahedral character of the water molecule which gives rise to a tetrahedral coordination of water molecules in water and ice.

Duncan and Pople (1953) and Bader and Jones (1963) have carried out quantum mechanical ('molecular orbital theory') calculations of the electron density distribution around a water molecule. Their results confirm the distribution shown in Figure 3.2, and show that there are four locations in the water molecule with high electron density: close to the oxygen atom, close to each hydrogen atom, and at the location of the lone pair orbitals which appear as an electron density bulge 'behind' the oxygen atom.

The charge distribution around a water molecule may also be approximated by 'electrostatic' or point charge models. In these models, point charges are assigned whose sign, magnitude, and location are such that the molecule as a whole is electrically neutral, and the electric dipole moment is equal to that experimentally measured. Such models have been worked out by Bernal and Fowler (1933), Verwey (1941), Rowlinson (1951), Bjerrum (1951), Pople (1951), Campbell (1952), and Cohen *et al.* (1962). Although such models are convenient, in some cases they generally do not correctly predict the higher electric moments (Kell, 1972a).

3.2 Structure of Water Vapor

Experiments indicate that water molecules in water vapor tend to interact and form clusters, in contrast to ideal gas behavior. Dimers as well as higher-order polymers are considered to be present in water vapor, though in small concentrations only. Recent experiments involving molecular beam techniques (Lin,, 1973; Searcy and Fenn,1974) suggest that in highly supersaturated water vapor, clusters of up to 180 water molecules may be present. Clusters of 21 water molecules seemed to exhibit particularly large stability. It is interesting to note that 21 water molecules can be arranged in the form of a pentagonal dodecahedron with a molecule at each corner and a single molecule in the center of the 'cage'.

However, no conclusive evidence of the actual geometric arrangement, if any, of water molecules in such clusters in vapor is available at present. Studies on the possible and more likely cluster types have been reviewed by Rao (1972) and Kell (1972a). Theoretical studies of the formation of water clusters have been carried out by Kistenmacher *et al.* (1974a,b) and Abraham (1974a). Kistenmacher *et al.* found two possible stable configurations for the dimers, a cyclic form and an open form which was more stable. For the trimers and tetramers, the cyclic forms seemed to be somewhat more stable than the open structures. For the large clusters, the authors suggested not a single structure, but a statistical distribution of different configurations, since many configurations with significantly different geometry were found to possess nearly the same energy. The potential energy of interaction, U, between a pair of water molecules has the general character of being strongly repulsive at very close separations and weakly attractive at longer range. One widely used and relatively simple expression for it is due to Stockmayer (1941):

$$U = -\frac{\mu^2 f}{r^3} - \frac{c}{r^6} + \frac{c\sigma^{18}}{r^{24}}, \tag{3-1}$$

where r is the separation of the molecules, μ is the dipole moment of an isolated water molecule, σ is the collision diameter (the molecular separation at which $U = 0$ if $\mu = 0$), c is an adjustable constant, and f is a known function of the mutual orientation of the two molecules.

The first term on the right side of (3-1) is just the dipole-dipole contribution to the interaction energy, and may be attractive or repulsive, depending on the dipole orientations. The second term represents contributions from: (1) the interaction energy between a permanent dipole of one molecule and the dipole it induces in the other (dipole-polarization or induction interaction), (2) the net energy arising from momentary, fluctuating dipoles interacting with the corresponding induced dipoles (polarization-polarization or dispersion interaction). Even though the time average of these dipole fiuctuations may be zero, the energy contribution is proportional to their mean square, which is finite and positive. Both (1) and (2) are usually referred to as *van der Waal's interaction*, which by its nature can be seen to bring about an attractive force between the molecules. The third term in (3-1) represents the short-range repulsive forces, which may be loosely ascribed to the overlap of electronic orbitals which are incompatible according to the Pauli exclusion principle.

There is little doubt that the Stockmayer potential or similar ones, such as Rowlinson's (1949, 1951) potential, portray with fair accuracy the interaction between

pairs of water molecules at large separations in dilute water vapor. This is evidenced by the fact that values for the second virial coefficient computed via (3-1) can be made to fit experimental values. On the other hand, the same potential functions yield values for the third virial coefficient of water vapor which disagree substantially with experiment. Partly, this is due to the approximate nature of (3 -1), and partly because three-body interactions should also be included, since other molecules in the system can significantly modify the interaction of a given pair. In particular, the Stockmayer potential is insufficiently 'directional' in character to account for the geometry of cluster formation in water vapor. A recent, more complicated potential function which has proven to be of predictive value in this respect is described briefly in Section 3.4.

3.3 Structure of Ice

At atmospheric pressures and at temperatures between about -80 and $0°C$, water substance crystallizes from its gaseous or its liquid state to form a sixfold-symmetric or hexagonal solid called ice-I_h. At different temperatures and pressures ice assumes other crystalline modifications which are discussed, for example, in Fletcher (1970a) and Hobbs (1974). We shall concern ourselves here only with ice-I_h, henceforth referred to simply as 'ice'.

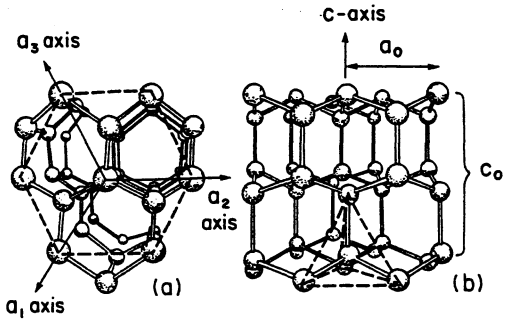


Fig. 3-3: Position of oxygen atoms in ice-I_h: (a) view along c-axis, (b) view perpendicular to c-axis.

X-ray diffraction studies demonstrate that, in ice, each oxygen atom is surrounded by four nearest-neighbor oxygen atoms at a distance of about 2.76×10^{-8} cm. These four atoms form an almost regular tetrahedron. In turn, oxygen tetrahedrons are joined together to form a hexagonal lattice (Figure 3.3). The hexagonal space group is denoted by D^4_{6h} or $P6_3/mmc$, and is characterized by 1 sixfold axis of rotation perpendicular to 1 mirror plane, (3 + 3) twofold axes of rotation perpendicular to (3 + 3) mirror planes, and a center of symmetry.

Near $0°C$, any given oxygen atom in ice also has 12 second nearest-neighbors at a distance of about 4.52 Å, 1 third nearest-neighbor at 4.59 Å, 6 fourth nearest-neighbors at 5.26 Å, 3 fifth nearest-neighbors at 5.31 Å, 6 sixth nearest-neighbors at 6.36 Å, 6 seventh nearest-neighbors at 6.46 Å, 9 eighth nearest-neighbors at 6.69 Å, 2 ninth nearest-neigbors at 7.36 Å, and 18 tenth nearest-neighbors at 7.81 Å.

Each water molecule in ice is hydrogen bonded to its four nearest-neighbors. (Generally, a hydrogen bond may be defined as a valence linkage joining two electronegative atoms through a hydrogen atom.) This is brought about through the formation of two hydrogen (O····H—O) bonds by each water molecule, each bond being directed towards a lone electron pair of a neighboring water molecule. This manner of bonding leads to an open lattice structure, as illustrated in Figure 3.3. Perpendicular to the c-axis, the ice lattice consists of open-puckered hexagonal rings (with oxygen atoms alternately raised and lowered). Along the c-axis are vacant shafts. Comparison shows that the arrangement of oxygen atoms in ice is isomorphous with the wurtzite structure of ZnS and the tridymite structure of SiO_2.

Each unit cell of ice, a four-sided prism set on a rhombic base, contains four water molecules and is characterized by the lattice constants a_0 and c_0 (Figure 3.4). X-ray data for a_0 and c_0 (Blackman and Lisgarten, 1957; Lonsdale, 1958; La Placa and Post, 1960; Brill and Tippe, 1967; Kumai, 1968) are summarized in Figure 3.5 as a function of temperature. These measurements show that a_0 and c_0 decrease with decreasing temperature such that $(c_0/a_0) = 1.629$ for all temperatures. Using the values for a_0 and c_0 given in Figure 3.5, the volume of a unit cell of ice, $V_{uc} = 2(a_0^2\sqrt{3}/4)c_0$ varies from 1.305×10^{-22} cm^3 (0°C) to 1.281×10^{-22} cm^3 (−180°C). Thus, the number of water molecules cm^{-3} varies from 3.06×10^{22} (0°C) to 3.12×10^{22} (−180°C), considering four water molecules per unit cell.

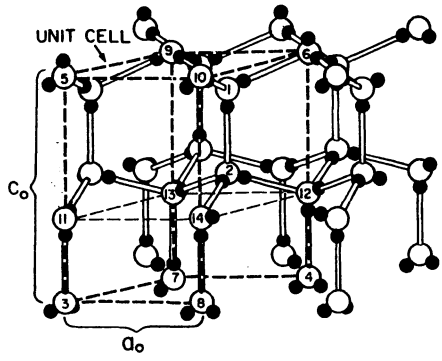


Fig. 3-4: Typical disordered arrangement of protons in the ice-I_h structure; oxygens (1) and (2) contribute 12/12 each, oxygens (3), (4), (5), (6) contribute 1/12 each, oxygens (7) to (12) contribute 2/12 each, and oxygens (13) and (14) contribute 4/12 each, for a total of 48/12 = 4 oxygens per unit cell. (From Fletcher, 1970a, with changes.)

The variation with temperature of ice density can either be determined from measurements of the temperature variation of the unit cell of ice via the relation $\rho_i = 4M_w/N_A V_{uc}$, or directly from observations (Ginnings and Corruccini, 1947; La Placa and Post, 1960; Lonsdale, 1958). These fit the relation

$$\rho_i = \sum_{n=0}^{2} a_n T^n , \qquad (3\text{-}2)$$

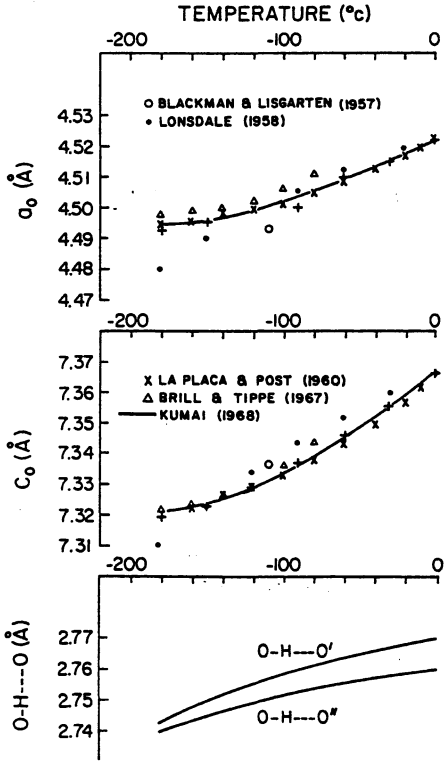


Fig. 3-5: Temperature variation of the lattice parameters of ice-I_h.

with T in °C and ρ_i in g cm^{-3}, for $a_0 = 0.9167$, $a_1 = -1.75 \times 10^{-4}$, and $a_2 = -5.0 \times 10^{-7}$, for the temperature range 0 to −180°C.

The positions of the hydrogen atoms in ice are subject to the *Bernal-Fowler* (BF) *rules* (Bernal and Fowler, 1933). These require that: (1) each water molecule is oriented such that its two hydrogen atoms are directed approximately towards two of four oxygen atoms which surround it tetrahedrally, (2) there is only one hydrogen atom on each O—O linkage, and (3) each oxygen atom has two nearest-neighboring hydrogen atoms such that the water molecule as a structural unit is preserved.

An ice structure which obeys the BF rules is termed ideal. Natural ice, however, does not behave ideally. Numerous experiments imply that a natural ice lattice contains defects which violate the BF rules. The following major *atomaric defects* are found in natural ice: stacking faults, chemical defects, molecular vacancies (Schottky defects), interstitial molecules (Frenkel defects), ionized states, and orientational defects (Bjerrum defects).

By means of regular oxygen tetrahedrons, one may build up a cubic as well as a hexagonal lattice. If the arrangement is cubic, a diamond-type ice lattice is

formed. *Stacking faults* occur when layers of cubic ice are intermixed in otherwise hexagonal ice. Such faults are particularly prone to occur in ice formed from vapor below about −80°C. *Chemical defects* result if foreign ions are built into the lattice during ice growth in an aqueous solution. Salt ions are either built into lattice voids or at regular lattice positions. *Molecular vacancies* denote the omission of water molecules from regular ice lattice positions. *Interstitial molecules* are water molecules occupying irregular positions in the ice lattice. Fletcher (1970a) estimates the energy necessary for the formation of a mole of vacancies to be about 12.2 kcal, whereas the energy necessary to form interstitial sites is about 14 to 15 kcal $mole^{-1}$. He further estimates that in natural ice at −19°C, the concentration of vacancies is about 10^{12} cm^{-3}.

Various authors (see Fletcher, 1970a; Hobbs, 1974) have shown that neither molecular nor interstitial molecules are capable of, producing changes in the hydrogen configuration of ice. (These defects, therefore, cannot explain the electrical properties of ice.) Rather, such changes are produced by ionic states and orientational defects. Ice, like water, exhibits *ionized states* (H_3O^+, OH^-) in violation of the third BF rule. Such a state is created by the motion of a proton from one neutral water molecule to another. According to Jaccard (1971), the concentration of ionized states in ice at −10°C is $C_{H^+} = C_{OH^-} \approx 3 \times 10^{11}$ cm^{-3}. He estimates the energy necessary for the formation of pairs of such states to be about 17.5 kcal $mole^{-1}$. Comparable figures for ionized states in water are $C_{H^+} = C_{OH^-} \approx 1.0 \times 10^{-7}$ mole $liter^{-1} = 6 \times 10^{13}$ ion pairs cm^{-3}, with a pair formation energy of 13.6 kcal $mole^{-1}$. *Orientational* or *Bjerrum defects* violate the first and second BF rules. Bjerrum defects consist either of a bond occupied by two protons instead of one (doubly occupied bond: O—H····H—O, D-defect), or of a bond which contains no proton at all (empty bond: O····O, L-defect). According to Jaccard (1971), these defects occur in concentrations of $n_D = n_L \approx 6 \times 10^{15}$ cm^{-3}, requiring an energy for pair formation of about 15.5 kcal $mole^{-1}$.

Pauling (1935, 1960) has pointed out that an ordered hydrogen arrangement in ideal ice would conflict with the experimental fact that ice possesses zero-point entropy. That is, from the relation $S = k \ln W$, wherein the entropy S is related to the number of distinguishable microstates W, an ordered hydrogen arrangement along with the restrictions of the BF rules would lead to $W_0 = 1$ and, thus, $S_0 = 0$ at $T = 0$ K. Consequently, Pauling proposed a disordered hydrogen arrangement, subject to the BF rules.

In Pauling's model, the zero-point entropy of ice may be deduced directly by counting the allowed microstates. For this purpose, we assume a perfect ice lattice which contains N_A (Avogadro's number) water molecules. There are then $2N_A$ OH····O bonds, on each of which the proton has two possible positions. This allows $(2)^{2N_A}$ possible arrangements in ice if we assume, with Pauling, that all arrangements are equally probable, and if we consider the first and second BF rules. However, many of these arrangements are not consistent with the third BF rule. To account for this, let us count all the possible arrangements of the hydrogens in the immediate vicinity of a particular oxygen atom. One finds 16 such arrangements: one OH_4^{2+}, four OH_3^+, six OH_2, four OH^-, and one O^{2-}. Only 6 out of these 16 arrangements are compatible with the third

BF rule. Assuming, again with Pauling, that all the arrangements are equally probable, the probability of a given oxygen atom having the correct arrangement around it is 6/16. Assuming further that all N_A oxygen atoms in ice are independent, the total number of possible configurations is reduced by a factor of $(6/16)^{N_A}$. Hence, $W_0 = (2^{2N_A})(3/8)^{N_A} = (3/2)^{N_A}$, from which $S_0 = \mathrm{k} \ln W_0 = \mathscr{R} \ln(3/2) = 0.805$ cal mole^{-1} (K)$^{-1}$. More detailed computations (Nagle, 1966) lead to S_0(theor.) $= 0.8145 \pm 0.0002$ cal mole^{-1} (K)$^{-1}$, in good agreement with the experimentally found value of S_0(expt.) $= 0.82 \pm 0.05$ cal mole^{-1} (K)$^{-1}$.

One may challenge this result on the grounds that defects are present in a real ice lattice, and energy differences exist between the various hydrogen arrangements. (Gränicher *et al.*, 1957; Gränicher, 1958). As the temperature of a real ice lattice is reduced, all molecules lose energy and tend to exist in the arrangement in which the energy of the system is lowest. Now, thermodynamic equilibrium is achieved only if opportunity is provided for the molecules to have free passage to all permitted energy states. One may argue that in real ice such free passage is provided by means of the migration of atomic defects, e.g., ionized states and Bjerrum defects which alter the atomic arrangement during migration. Such a mechanism would lead to just one spatial arrangement at 0 K and, thus, to $S_0 = 0$, which is contrary to observation.

Gränicher *et al.* (1957) and Gränicher (1958) also supplied a way out of this dilemma. Their experimental studies on the electrical behavior of ice showed that configurational changes due to the migration of atomic defects become negligible below a temperature of about 75 K. Below this temperature, both the concentration and diffusion rate of defects, which exponentially decrease with decreasing temperature, are suficiently small that one may consider the hydrogen configuration to be 'frozen-in'. In addition, computations by Pitzer and Polissar (1956) showed that above this freeze-in temperature, the energy differences between the various possible hydrogen arrangements in ice are small compared to the thermal energy kT. They become comparable to or larger than kT only if $T < 60$ K. These results imply that real ice is disordered with respect to the hydrogen arrangement, since the hydrogen arrangement freezes-in in any of the possible configurations at temperatures where the difference between the configurational energies is still smaller than kT.

Since in the Pauling-Bernal-Fowler model for ice each hydrogen atom has two equally likely positions along a given O—O linkage, theirs may be regarded as a 'half-hydrogen' model for ice. This model has been confirmed by the neutron diffraction studies of Wollan *et al.* (1949) and Peterson and Levy (1957). The model reflects explicitly the idea that the structure of ice is independent of the positions of the hydrogen atoms.

Peterson and Levy also found the H—O—H valence angle to be nearly equal to the corresponding O—O—O angle. The latter is nearly tetrahedral ($\approx 109.5°$) and, therefore, about 5° larger than that of an isolated water molecule. This result was questioned by Chidambaram (1961), who argued that since the O—H----O bond is more easily bent than the H—O—H valence angle, the latter angle should not increase during solidification. On the other hand, he showed that the data of Peterson and Levy are consistent with an ice structure in which the water mole-

cules keep the valence angle which they have in the vapor state, but in which the O—H----O bonds are slightly bent. In this structure, each H is about 0.04 Å off the O----O axis. This means that the O—H----O bonds are bent by an average of 6.8°. In support of his model, Chidambaram cited the small change of frequency for the H—O—H bending mode when water vapor changes to ice, and the H—O—H angle of water molecules in hydrated crystals, which deviates very little from 104.5°. Chidambaram's views are supported by nuclear magnetic resonance studies (see Hobbs, 1974).

According to Eisenberg and Kauzmann (1969), three points of view may be taken to define the molar hydrogen bond energy $E_{H,i}$ in ice. First, one may assume that $E_{H,i}$ is given by the lattice energy E_L of one mole of ice (the difference in energy between one mole of isolated water molecules and one mole of ice, both at 0 K and with motionless atoms), divided by the number of hydrogen bonds in a mole. Since both hydrogen atoms of a water molecule participate in one H-bond (excluding the molecules at the surface of ice), one may estimate $E_{H,i} = E_L/2 = 6.7$ kcal (mole of bond)$^{-1}$ at 0 K (Eisenberg and Kauzmann, 1969, based on values given by Whalley *et al.*, 1973). More appropriately, one may define $E_{H,i}$ in terms of the molar sublimation enthalpy $(\Delta h)_s$ of ice. According to Eisenberg and Kauzmann (1969) $(\Delta h)_s = 11.32$ kcal mole^{-1} (0 K), and $(\Delta h)_s = 12.20$ kcal mole^{-1} (0°C) according to the experiments of Rossini *et al.* (1952). With this definition we find $E_{H,i}(0K) = 5.66$ kcal (mole of bond)$^{-1}$ and $E_{H,i}(0°C) = 6.10$ kcal (mole of bond)$^{-1}$. In both of these definitions, we ascribe the entire intermolecular energy in ice to hydrogen bonding. We therefore include in $E_{H,i}$ the effects of dispersion and short-range repulsive forces which are present not only in ice but also in crystals of non-hydrogen bonded substances. Therefore, a third definition of $E_{H,i}$ is based on the premise that the contribution to $(\Delta h)_s$ from hydrogen bonds is distinct from that of other forces and one may set $E_{H,i} = [(\Delta h)_s - E_{other}]/2$, where E_{other} represents the intermolecular energy associated with the other forces. This definition suffers from the fact that E_{other} is not an observed quantity, and cannot presently be accurately calculated.

An accurate theoretical calculation of a single hydrogen bond in ice should include at least the effects of nearest-neighbors. To date, most investigators have avoided detailed computations for these effects. Generally, the approach taken has been to assume the total hydrogen bond energy as given by the sum of the four component energies (dipole-dipole, dipole-polarization, polarization-polarization, and short-range interactions), and to evaluate each of these by approximate methods for two neighboring water molecules at the relative positions found in ice. For this purpose, various models for the charge distributions in a water molecule have been assumed. For some component energies, rough estimates for the effect of neighboring molecules have also been made. The results of the most pertinent calculations on this subject have been summarized by Hobbs (1974) and Eisenberg and Kauzmann (1969). Other theoretical calculations have been carried out by Rahman and Stillinger (1971), Stillinger and Rahman (1978), Morse and Rice (1982) and Deutsch *et al.* (1983a,b). The values computed for $E_{H,i}$ range from 4 to 8 kcal mole^{-1}.

In another study, Morgensen and Eldrup (1978), Eldrup (1976) and Eldrup *et*

al. (1978) were able to determine the hydrogen bond energy in ice experimentally. Using a positron annihilation method, they found for the activation enthalpy $(\Delta h)^f_{v,i}$ to form (f) a vacancy (v) in ice, $(\Delta h)^f_{v,i} = (6.44 \pm 1.15)$ kcal mole^{-1}. Since this energy involves breaking two hydrogen bonds, it follows that the energy of a hydrogen bond is given by $E_{H,i} = 3.22$ kcal (mole of bond)$^{-1}$. Thus, $E_{other,i} = 12.20 - 6.44 = 5.76$ kcal mole^{-1}. Considering only the bond contribution to the nearest-neighbors of a given molecule in ice, we may express $E_{other,i} = (z_i/2)E_i$ (Nemethy and Sheraga, 1962a,b) where z_i is the number of nearest-neighbors and E_i is the bond energy due to forces other than the hydrogen bond. For $z_i = 4$ we find $E_i = 2.88$ kcal (mole of bond)$^{-1}$. For the sublimation enthalpy of ice, we have then the relationship

$$(\Delta h)_s = 2E_{H,i} + E_{other} = 2(E_{H,i} + E_i)\,. \tag{3-3}$$

Although the value of $E_{H,i}$ obtained by Eldrup *et al.* (1978) is considerably lower than the values previously published in the literature, we shall show later in this chapter that this value is consistent with the enthalpy of melting for ice.

Lattice vacancies in ice allow water molecules to diffuse through the ice lattice. Ramseier (1967) experimentally studied the self-diffusion mechanism of H_2O through ice. He found for the diffusivity

$$D_i = D_0 \exp\left(-\frac{(\Delta h)_{act,i}}{\mathscr{R}T}\right)\,, \tag{3-4}$$

with $D_0 = 9.13$ cm^2 sec^{-1}, and with the activation enthalpy for self-diffusion given by $(\Delta h)_{act,i} = 14.26$ kcal mole^{-1}. Two energies contribute to $(\Delta h)_{act,i}$: the activation enthalpy to create a lattice vacancy, $(\Delta h)^f_{v,i}$, and the activation enthalpy required for a lattice vacancy to migrate, $(\Delta h)^m_{v,i}$. Together with the experimentally determined values for $(\Delta h)^f_{v,i}$ and $(\Delta h)_{act,i}$, Morgensen and Eldrup (1978), Eldrup *et al.* (1978), and Eldrup (1976) deduced the value $(\Delta h)^m_{v,i} = (7.82 \pm 1.61)$ kcal mole^{-1}.

The experimentally observed value for D_0 in Equation (3-4) may now be used to justify indirectly the value obtained for $(\Delta h)^f_{v,i}$ and for $(\Delta h)^m_{v,i}$. For this purpose, we follow Shewmon (1963) and Ramseier (1967) and write for the diffusivity of a water molecule in ice

$$D_i = \frac{1}{6}\frac{\langle r^2\rangle}{t}\,, \tag{3-5}$$

where $\langle r^2\rangle$ is its mean square displacement in time t (see Section 11.1). In terms of the total number of diffusional 'jumps' n which the molecule carries out and the jump length approximated by the nearest-neighbor distance $\lambda = 2.76 \times 10^{-8}$ cm, we may express $\langle r^2\rangle$ as

$$\langle r^2\rangle = n\lambda^2 f\,, \tag{3-6}$$

where the correlation factor $f \approx 1 - 2/z_i = 0.5$, with $z_i = 4$, is a correction for the random walk of the molecule in a direction which is dependent on the direction of the previous jump. Now the number of jumps per second, $\Gamma = n/t$, depends on

the number z_i of jump directions, the frequency ν with which a molecule jumps into an adjacent vacancy, and the number of vacancies N_v as compared to the total number of molecules N:

$$\Gamma = z_i \nu \frac{N_v}{N} . \tag{3-7}$$

Considering (3-5) to (3-7), we then obtain for the diffusivity in ice

$$D_i = \frac{1}{6} f z_i \lambda^2 \nu \frac{N_v}{N} . \tag{3-8}$$

Now the relative number of vacancies N_v/N depends exponentially on the enthalpy and entropy of vacancy creation according to

$$\frac{N_v}{N} = \exp\left(-\frac{(\Delta h)^f_{v,i}}{\mathscr{R}T}\right) \exp\left(\frac{(\Delta s)^f_{v,i}}{\mathscr{R}}\right) . \tag{3-9}$$

On the other hand, the jump frequency ν depends on the enthalpy and entropy of vacancy migration according to

$$\frac{\nu}{\nu_0} = \exp\left(-\frac{(\Delta h)^m_{v,i}}{\mathscr{R}T}\right) \exp\left(\frac{(\Delta s)^m_{v,i}}{\mathscr{R}}\right) , \tag{3-10}$$

where $\nu_0 \approx 5 \times 10^{12}$ sec^{-1} is the frequency of oscillation of a water molecule in the ice lattice (Hobbs, 1974; Zajac, 1958; Compaan and Haver, 1956). Comparing (3-4) with (3-8) to (3-10) we find

$$D_0 = \frac{1}{6} f z_i \lambda^2 \nu_0 \exp\left[\frac{(\Delta s)^f_{v,i} + (\Delta s)^m_{v,i}}{\mathscr{R}}\right] . \tag{3-11a}$$

Inserting (3-11a) into (3-4) we see that the diffusion of water molecules through ice, being a constant pressure-constant temperature process, depends exponentially on the molar activation energy $(\Delta g)_{act,i} = (\Delta h)_{act,i} - T(\Delta s)_{act,i}$, with $(\Delta h)_{act,i} = (\Delta h)^f_{v,i} + (\Delta h)^m_{v,i}$ and $(\Delta s)_{act,i} = (\Delta s)^f_{v,i} + (\Delta s)^m_{v,i}$. Thus,

$$D_i = \frac{1}{6} f z_i \lambda^2 \nu_0 \exp\left(-\frac{(\Delta g)_{act,i}}{\mathscr{R}T}\right) . \tag{3-11b}$$

According to Zehner (1952), $(\Delta s)_{v,i} \approx 0.34[(\Delta h)_{v,i}/T_m]$ is applicable to the formation and migration process. Inserting now the values for $(\Delta h)^f_{v,i}$, $(\Delta h)^m_{v,i}$, ν_0, z_i, and f into (3-11) we obtain $D_0 = 9.10$ cm^2 sec^{-1}, in excellent agreement with the experimental value of 9.13 cm^2 sec^{-1}, given the approximations made in deriving (3-11).

In passing, it may be illustrative to determine how many vacancies are involved in the diffusion of water molecules through ice. On evaluating (3-9) for this purpose, we find for 0°C: $(C_v/C) = (N_v/N) \approx 4 \times 10^{-4}$, and for −40°C $(N_v/N) \approx 5 \times 10^{-5}$.

Thus, since for ice $C \approx 3 \times 10^{22}$ molecules cm^{-3}, it follows that the concentration of vacancies is 12×10^{18} cm^{-3} (0°C) and 15×10^{17} cm^{-3} (−40°C).

We have already noted above that water molecules in ice may carry out oscillations with an average period $\tau_0 = 1/\nu_0 = 2 \times 10^{-13}$ sec. In addition, as we have just seen, water molecules also undergo translational displacements with a frequency, obtained from (3-7) and (3-10), of $\Gamma \approx 6 \times 10^5$ sec^{-1} (0°C) and $\approx 6 \times 10^3$ (−40°C) and, thus, displacement periods of about $\tau_D \approx 2 \times 10^{-6}$ sec (0°C) and 2×10^{-4} sec (−40°C), in good agreement with the observed dielectric relaxation time for ice of $\tau_D = 2 \times 10^{-5}$ sec (−5 to −30°C) (Hobbs, 1974). In addition to vibration and translation, water molecules in ice also undergo reorientation. According to Eisenberg and Kauzmann (1969), a water molecule in ice waits about 5×10^{-5} sec for an orientational defect to arrive at its lattice site but then re-orients very rapidly in about 10^{-11} seconds.

In closing this section, we want to touch briefly on the specific heat of ice, which is a manifestation of the intermolecular vibrations of water molecules as hindered translation and hindered rotation (Eisenberg and Kauzmann, 1969). The measurements of Giauque and Stout (1936) and of Flubacher *et al.* (1960) show that one may express the specific heat of ice between 0°C and −40°C by the relation

$$c_i = 0.503 + 0.00175T, \tag{3-12}$$

with T in °C and c_i in IT cal g^{-1}(°C)$^{-1}$.

3.4 Structure of Water and Aqueous Solutions

3.4.1 Structure of Water

As ice melts, the bulk density of water substance abruptly increases by about 9.1%. Contrary to what might be expected, X-ray measurements show that during melting the intermolecular distance between first nearest-neighbors in water does not decrease, but rather increases over that found in ice by about 3% at 0°C. Consequently, the density increase must be attributed to a 'filling-in' of space by water molecules which leave regular lattice positions to move into what were cavities in the ice lattice. The X-ray findings are in accordance with this view, and show that the number of first nearest-neighbors in water increases from 4.0 in ice to 4.4 at 1.5°C, reaching 4.9 at 83°C. But despite this 'filling-in,' water has a very open structure and a density lower than that of an ideal liquid with a close-packed arrangement of molecules. This can be readily seen if we consider that the observed density of water is $\rho_w = 1.0$ g cm^{-3}, and that therefore in water the average volume of a water molecule, $\dot{v}_w = M_w/\rho_w N_A$, is 30×10^{-24} cm^3. On the other hand, if we were to regard a water molecule as a rigid sphere of radius equal to 1/2, the closest approach distance of two nearest-neighbor water molecules, which is 1.38×10^{-8} cm, the volume of a water molecule would be 11×10^{-24} cm^3, which is 2.7 times less than that observed. If these spherical molecules were arranged in water in a hexagonal close-packed arrangement (in which case a fraction 0.74 of space is filled with mass), the density of water would have a value of $\rho_w = 0.74 M_w/N_A = 2$ g cm^{-3}, or twice the value observed.

Experiments show that the density of water exhibits a maximum at about +4°C. Above this temperature, ρ_w decreases with increasing temperature due to an increase in amplitude of the molecular vibrations which causes a general expansion of the water volume. Below this temperature, ρ_w is found to decrease with decreasing temperture due to an increasingly ice-like structural arrangement of the water molecules.

According to Kell (1972a), at $p = 1$ atm, the best experimental values for the density of water can be fitted to

$$10^3\rho_w = \frac{A_0 + A_1T + A_2T^2 + A_3T^3 + A_4T^4 + A_5T^5}{1 + BT}, \tag{3-13}$$

with ρ_w in g cm^{-3}, with $A_0 = 999.8396$, $A_1 = 18.224944$, $A_2 = -7.922210 \times 10^{-3}$, $A_3 = -55.44846 \times 10^{-6}$, $A_4 = 149.7562 \times 10^{-9}$, $A_5 = -393.2952 \times 10^{-12}$, $B = 18.159725 \times 10^{-3}$, and T in °C. Equation (3-13) is applicable to the temperature interval $0°C \leq T \leq 100°C$.

For temperatures below 0°C, values for ρ_w are available from Dorsch and Boyd (1951) to −10°C, and from Hare and Sörensen (1987) down to −33°C. According to Hare and Sörensen (1987)

$$\rho_w = \sum_{n=0}^{6} a_n T^n, \tag{3-14}$$

with ρ_w in g cm^{-3} and T in °C, with $a_0 = 0.99986$, $a_1 = 6.690 \times 10^{-5}$, $a_2 = -8.486 \times 10^{-6}$, $a_3 = 1.518 \times 10^{-7}$, $a_4 = -6.9484 \times 10^{-9}$, $a_5 = -3.6449 \times 10^{-10}$, and $a_6 = -7.497 \times 10^{-12}$. This expression applies in the temperature range 0 to −33°C.

An extrapolation of ρ_w to lower temperature (Figure 3.6) suggests a dramatic decrease of ρ_w with decreasing temperature below −30°C, plunging rapidly to the density of ice as −45°C is approached. Of course, such a low temperature could only be reached if ice nucleation would not intervene. We shall show in Chapter 7 that in fact such low temperatures can be reached if experiments are carried out with sufficiently small droplets of pure water. Angell (1982) suggested that the dramatic plunge of ρ_w at low temperature is due to an increased short-range order in water.

In ascribing 'structure' to a fluid such as water, the time periods τ_0 and τ_D mentioned near the end of the previous section become especially relevant. In fact, we must consider three different time scales: times $t \ll \tau_0$, times intermediate to τ_0, and τ_D, and times $t \gg \tau_D$. Assuming we were equipped with a camera which had shutter speeds less than τ_0, we could obtain a relatively sharp picture of the actual position of a water molecule at any given instant. This would reveal the instantaneous water structure called the I-Structure (Eisenberg and Kauzmann, 1969). If the shutter speed were between τ_0 and τ_D, each molecule would complete many oscillations while the shutter was open, and the resulting somewhat blurred picture would provide information on the vibrationally averaged position of the water molecules in water, i.e., the V-Structure (Eisenberg and Kauzmann) of water.

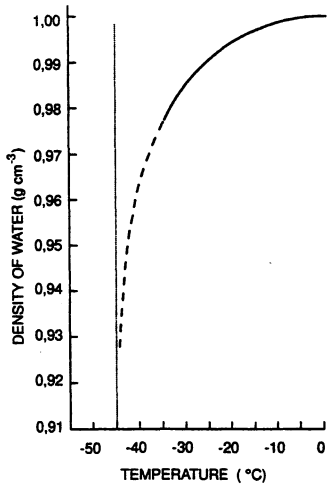


Fig. 3-6: Variation of the density of bulk water as a function of temperature, after Hare and Sorensen (1987), extrapolated to −45° C. (From Pruppacher, 1995; by courtesy of the Am. Meteor. Soc., and the author.)

If the shutter speed were larger than τ_D, the diffusionally averaged arrangement of the water molecules or D-Structure (Eisenberg and Kauzmann), could be found. No experimental techniques are available at present to obtain information on the I-Structure of a liquid. Experimental studies which employ infrared or Raman spectroscopy, or neutron scattering techniques, lead to information on the V-Structure, while X-ray studies determine the D-Structure.

Spectroscopic studies show that the frequency of oscillation for water molecules is slightly smaller in water than in ice, the period of vibration being $\tau_0 \approx 10^{-13}$ sec. Studies on self-diffusion, viscosity, dielectric relaxation, and nuclear magnetic resonance relaxation show that a water molecule in water has a characteristic displacement period near 0°C of $\tau_D \approx 10^{-11}$ sec.

From X-ray data (Narten *et al.*, 1967; Narten and Levy, 1969, 1970, 1971, 1972) one may derive the average number $\rho(\bar{r})$ of molecules in a volume element of water which is located at a distance from any given water molecule. Usually, however, one does not plot $\rho(\bar{r})$ but rather $g(\bar{r}) = \rho(\bar{r})/\rho_w$, where ρ_w represents the bulk density of water expressed as the number of molecules per unit volume of water. Thus, $g(\bar{r})$ is the factor by which the average local density $\rho(\bar{r})$ of water molecules differs at $\bar{r}$ from the density of water molecules in bulk water, and so at large distances from a given water molecule, $g(\bar{r}) = 1.0$. On the other hand, in the vicinity of the given molecule, the local density may differ considerably from bulk density. An example of the radial distribution function $g(\bar{r})$ for water of various temperatures is given in Figure 3.7. The first maximum near 2.9 Å must be attributed to the interactions between the oxygen atoms of nearest-neighbor water molecules. The broad maxima near 4.5 and 7 Å result from interactions between the oxygen atoms of second nearest and higher-order nearest-neighbor water molecules.

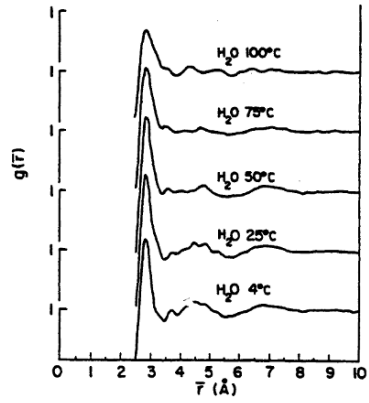


Fig. 3-7: Radial distribution functions $g(\bar{r})$ for water at various temperatures. (From Narten *et al.*, 1967, with changes.)

Figure 3.7 also shows that with decreasing temperature, the maxima become increasingly distinct, which implies that the number of water molecules participating in interactions at the distances of the intensity peaks increases. Thus, we see that with decreasing temperature, water becomes structurally more ordered. This trend continues, at temperatures below 0°C, with the scattering intensity peaks continuing to become increasingly pronounced and shifting toward the X-ray intensity maxima observed for ice (Dorsch and Boyd, 1951). We may conclude that, although the long-range order breaks down when ice melts, considerable local ordering persists in water. This implies that not all the hydrogen bonds which exist in ice become broken when ice melts. At any moment, a certain number of H-bonds are intact even though the location of the intact bonds in water rapidly fluctuates, since H-bonds break and reform in continuous succession. (It is interesting to note the correlation between the maxima shown in Figure 3.7 and the nearest-neighbor distances in ice; see Section 3.3.)

Information on the state of hydrogen bonds in water can also be obtained from infrared and Raman spectra (Walrafen, 1966; 1967; 1968a,b; 1972). Such spectra confirm that water molecules exist as entities in water. They also give evidence that some O—H groups in H_2O are hydrogen bonded and, therefore, point toward a free, lone electron pair of a neighboring H_2O molecule, while other O—H groups are non-directionally bonded to the surrounding water molecules and, hence, are disoriented with respect to neighboring lone electron pairs (Kell, 1972b; Eisenberg and Kauzmann, 1969). The latter are referred to as non-hydrogen bonded or 'broken' O—H groups. Estimates of the percentage of broken H-bonds in water as a function of temperature are summarized in Figure 3.8.

As expected, the number of broken bonds decreases with decreasing temperature, reaching about 12% at 0°C. An extrapolation to lower temperatures suggests that about 7% of the bonds are still broken at −20°C, while the percentage finally approaches zero near −45°C. Of course, these percentages are somewhat deceiving

in that even at $-40°C$ a concentration of only 1.5% broken bonds means that of the total number of bonds, $2N = 2N_A\rho_w/M_w = 642 \times 10^{20}$ cm^{-3} ($-40°C$) (where N is the total number of molecules), as many as 10×10^{20} bonds cm^{-3} are still broken, although this translates into a percentage of only 1.5%.

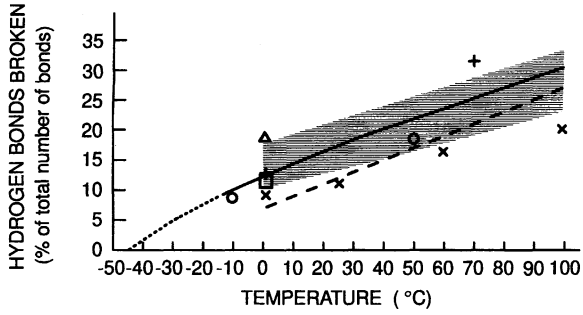


Fig. 3-8: Variation with temperature of the number of hydrogen bonds broken in water: - - - Walrafen (1972), × Hasted (1972), ○ Luck (1962, 1963, 1965; + from L_m/L_s, △ Davis and Litovitz (1965), ■ Luck (1967), □ Hindman (1966). Continuous line with dotted extrapolation: proposed variation consistent with the $-45°C$ limit. (From Pruppacher, 1995; by courtesy of the Am. Meteor. Soc., and the author.)

These experimental findings are supported by recent studies which attempted to simulate the molecular struture of water by purely theoretical methods (Rahman and Stillinger, 1971; Stillinger and Rahman, 1972; Popkie *et al.*, 1973; Kistenmacher *et al.*, 1974a,b). Stillinger and Rahman applied conventional molecular dynamics to a system of 216 water molecules which interacted via a potential function developed by Ben-Naim and Stillinger (1972) and Ben-Naim (1972). This pair potential function is considerably more complicated than the Stockmayer potential (3-1). It is based on Bjerrum's four-point charge model for a water molecule and incorporates the linear bonding tendency between neighbors in a tetrahedral pattern such as that found throughout the ice lattice, or locally around a given water molecule in water. It has been argued by Stillinger (1970) and Stillinger and Rahman (1972) that this potential function also incorporates the principal features of non-additivity; i.e., it takes into account the many-body aspect of the problem.

Another pair potential function has been developed by Clementi *et al.* (1973), Popkie *et al.* (1973), and Kistenmacher *et al.* (1974a,b) (see also Abraham, 1974a, and Fromm *et al.*, 1975). This function is based on an analytically fitted Hartree-Fock potential (Kern and Karplus, 1972), the Bernal and Fowler (1933) point charge model, and correlation energy corrections due to induced dipole interaction and short-range effects. It was used in conjunction with the Monte-Carlo simulation method of Barker and Watts (1969) to study a group of 125 water molecules. The computations of Clementi, Popkie, and Kistenmacher, as well as those of Stillinger and Rahman, yielded radial distribution functions for water molecules in water which are in fair agreement with X-ray results. In addition, the molecular dynamics study of Stillinger and Rahman (1972) predicted that the hydrogen bond rupture mechanism in water is characterized by an excitation energy of about

2.5 kcal (mole of bond)$^{-1}$. This is in good agreement with the Raman and infrared spectra of Walrafen (1966, 1967, 1968 a,b, 1972), Luck (1962, 1963, 1965), Worley and Klotz (1966), Davis and Litovitz (1965), Senior and Varrall (1969), and Buijs and Choppin (1963), who obtained 2.4 to 2.6 kcal (mole of bond)$^{-1}$ for the energy to rupture a hydrogen bond, or 4.8 to 5.2 kcal mole^{-1}, since there are 2 H-bonds per molecule. Bansil *et al.* (1982), Yeh *et al.* (1982), Hare and Sörensen (1990), d'Arrigo *et al.* (1981), and Scherer *et al.* (1974) obtained Raman spectra for water supercooled to as low as −30°C. Their values for the energy, required to break a hydrogen bond in water, tended to increase with decreasing temperature, and ranged between 2.6 to 3.1 kcal (mole of bond)$^{-1}$, or 5.2 to 6.2 kcal mole^{-1}, at temperatures between −20 and −30°C. Finally, Bucaro and Litovitz (1971) inferred from depolarized light scattering measurenments a value of 2.5 ± 0.1 kcal(mole of bond)$^{-1}$ to break a hydrogen bond in water.

Considerable uncertainties still exist as to how X-ray, infrared, and Raman studies should be interpreted in terms of the arrangement of the water molecules in water. Most modern theories of water assume that water has a 'structure' which can be described in terms of highly hydrogen-bonded, three-dimensional configurations of molecules. We shall now briefly describe just the main features of some of the more prominent models put forward for the water structure.

In the 'quasi-crystalline model', the water structure is assumed to resemble one of several possible forms: a broken down ice-I_h structure (Bernal and Fowler, 1933; Katzoff, 1934; Morgan and Warren, 1938), a quartz structure (Bernal and Fowler, 1933), a structure of octahedrally arranged molecules (Van Eck *et al.*, 1958), or a structural mixture of molecules arranged in a tridymite structure dispersed in a denser ice-*III* structure (Jhon *et al.*, 1966). In the 'interstitial model', the water is visualized as consisting of a highly hydrogen bonded structure inside of which non-bonded or partially bonded molecules occupy interstitial structure positions (Samoilov, 1946, 1957; Forslind, 1952; Namiot, 1961; Danford and Levy, 1962; Krestov, 1964; Gurikov, 1960, 1965). In the 'clathrate[†] model', water is assumed to have a structure similar to the clathrate structure of gas hydrates except that, instead of a gas molecule, a water molecule is held inside each cavity of a cage-like, hydrogen bonded framework of pentagonal dodecahedron cages (Pauling, 1959, 1960; Frank and Quist, 1961). The 'flickering cluster model' makes use of the partially covalent character of the hydrogen bond and assumes that H-bond formation in water is a cooperative phenomenon, in that the formation of a hydrogen bond between two water molecules reinforces the tetrahedral hybridization in the oxygen atoms. This in turn strengthens all existing bonds and promotes the formation of new bonds. Conversely, the breaking of an H-bond in water results in the almost simultaneous rupture of a whole group of bonds, thus leading to the formation and dissolution of water clusters in a 'flickering' manner (Frank and Wen, 1957 ; Frank, 1958a,b). The 'mixture model' pictures water as a mixture of 0-, 1-, 2-, 3-, and 4-bonded water molecules engaging in the formation of various sized clusters (Haggis *et al.*, 1952; Nemethy and Scheraga, 1962a,b, 1964; Walrafen, 1966, 1967, 1968a,b, 1972). Finally, the 'bent-bond model' assumes that few, if any, bonds

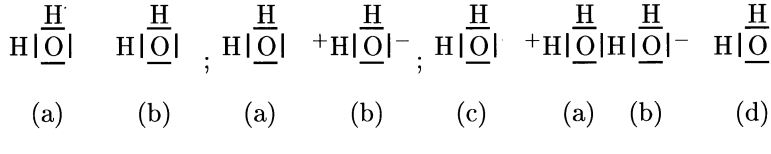
[†]A clathrate is a complex in which molecules of one substance are completely enclosed by molecules of another substance.

between water molecules are broken upon melting of ice, but instead become bent to various degrees (Pople, 1951).

Even though all of the models mentioned above were found to have certain attractive features from the point of view of their capacities to explain some of the observed physical properties of water, most of them suffer from a too highly idealized and overly rigid arrangement of the water molecules. This becomes particularly obvious if we compare these models with the results of the molecular dynamics model of Stillinger and Rahman (1972) mentioned above. Although the results of their computations support the 'mixture model' for water in which water molecules engage in a varying number of hydrogen bonds which locally tend to be tetrahedrally oriented, some bending away from bond linearity was also found to occur, especially at warmer temperatures. Furthermore, no clusters of molecules arranged in the manner of ice-I_h or in any other ice-like or clathrate structures were found for temperatures down to $-8°C$, and no obvious separation of water molecules into 'lattice'-molecules and 'interstitial'-molecules was detected. On the other hand, water molecules were frequently found to be arranged in polygons of 4 to 7 sides. Finally, a number of molecules exhibited 'dangling' O—H bonds which were not included in H-bond formation and persisted over times longer than the vibrational period of a water molecule.

The more recent studies of water at temperatures below 0°C of Hare and Sörensen (1990), Bansil *et al.* (1982) and Yeh *et al.* (1982), as well as the low angle X-ray scattering experiments of Bosio *et al.* (1981), Stanley and Teixeira (1980), and Rice and Sceats (1981), suggests that the hydrogen bond exhibits a strongly cooperative nature which results in the formation of a network of clusters of molecules with intact hydrogen bonds inside the cluster. Each cluster appears to be bonded to the surrounding clusters by mostly non-hydrogen bond forces. With decreasing temperature, these clusters grow increasingly larger. At the same time, the bond-links, which are bent at warm temperatures, become increasingly linear, resulting in an increase in bond energy.

According to Frank and Wen (1957), the cooperative nature of the hydrogen bond in water must be understood on the basis of a resonance among the following three bond structures:



This gives formal recognition to the fact that chemical hydrogen bond formation is an acid-base reaction. Thus, when a bond is formed, molecule (a) becomes more acidic and molecule (b) more basic than the unbonded molecule. In this way, the formation of an a—b bond makes molecule (a) capable of reacting with (c), and (b) capable of reacting with (d). This process of dipole induction is self-propagating and leads to cluster formation.

The tendency for cluster formation in supercooled water is reflected also in the temperature variation of the specific heat. At temperatures above 0°C, measure-

ments of the specific heat of water were made by Osborne *et al.* (1939). Between 0°C and +35°C their data fit the relation:

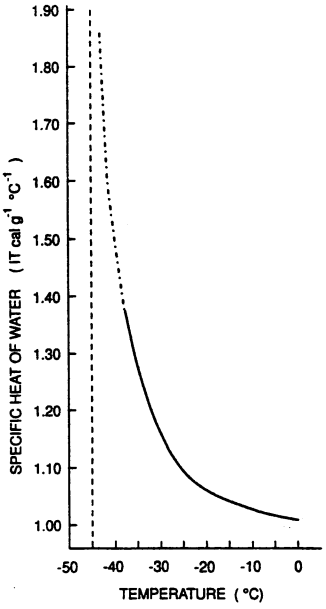


Fig. 3-9: Variation with temperature of the specific heat c_w of water (Angell *et al.* 1982), extrapolated to −45°C. (From Pruppacher, 1995; by courtesy of the Am. Meteor. Soc., and the author.)

$$c_w = 0.9979 + 3.1 \times 10^{-6}(T - 35)^2 + 3.8 \times 10^{-9}(T - 35)^4 , \tag{3-15}$$

with c_w in IT cal g^{-1}°C. Measurements of c_w below 0°C were made by Angell *et al.* (1982) down to −37°C. Their data fit the relation

$$c_w = \sum_{n=0}^{4} a_n T^n , \tag{3-16}$$

with c_w in IT cal g^{-1}°C^{-1} and T in °C, and with $a_0 = 1.000938$, $a_1 = -2.7052 \times 10^{-3}$, $a_2 = -2.3235 \times 10^{-5}$, $a_3 = 4.3778 \times 10^{-6}$, and $a_4 = 2.7136 \times 10^{-7}$. A plot of (3-16) demonstrates a strong rise of c_w with decreasing temperature below 0°C, which is particularly pronounced below −30°C (Figure 3.9), and reflects the increased structure in water. An analogous rise with decreasing temperature has been observed for the viscosity η_w of water by Hallett (1963a), White and Twinning (1913), Stokes and Mills (1965), Mills (1971, 1973) Bingham and Jackson (1918), Osipov (1977), and Kell (1972), as shown in Figure 3.10. Their data fit the relation:

$$\eta_w = a_0 \exp(a_1 T + a_2 T^2 + a_3 T^3) , \tag{3-17}$$

with η_w in centipoise, T in °C, and with $a_0 = 1.76$, $a_1 = -3.5254 \times 10^{-2}$, $a_2 = 4.7163 \times 10^{-4}$, and $a_3 = -6.0667 \times 10^{-6}$, for $T > 0$°C; and with $a_1 = -5.5721 \times 10^{-2}$, $a_2 = -1.3943 \times 10^{-3}$, and $a_3 = -4.3015 \times 10^{-5}$, for temperatures between 0 and −30°C.

We notice from Figures 3.9 and 3.10 that c_w and η_w increase exponentially with decreasing temperature, seemingly to infinity as the temperature limit of −45°C is approached, provided, of course, that ice nucleation does not intervene.

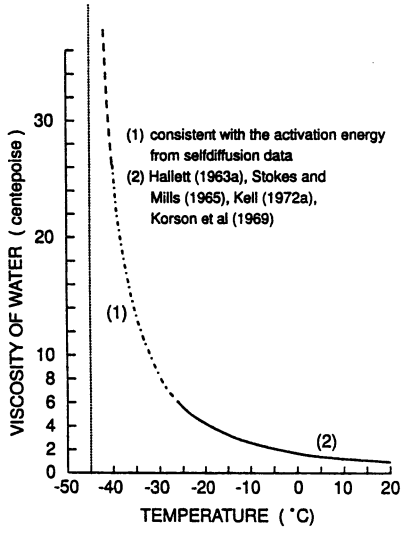


Fig. 3-10: Variation with temperature of the viscosity of water, extrapolated to −45°C. (From Pruppacher, 1995; by courtesy of the Am. Meteor. Soc., and the author.)

The repeatedly occurring limit of −45°C in the thermodynamic properties of water led Angell (1982) to speculate that this limit represents a singularity reminiscent of the exponential behavior observed for systems approaching phase transitions of higher order. As a reason for this behavior, he suggests the presence of a cooperative process among the water molecules which dominates the behavior at low temperature, as is, for instance, also observed for the ferromagnetic-paramagnetic transition. In analogy, he suggests that the anomalies of supercooled water might be described by an equation of the form

$$Y = A_y \left(\frac{T}{T_s} - 1 \right)^{-\lambda_y}, \tag{3-18}$$

well-known for critical phenomena, predicting a rapid increase of the property Y as T approaches T_s, where T_s is the singularity temperature and where A_y and λ_y are parameters chosen to fit the property Y as a function of T. Angell (1982) suggests that for water $T_s = 228 \pm 3$ K (-45 ± 3°C). It is also noteworthy (see Chapter 7 and Pruppacher (1995)) that T_s is within about 2 K of the lowest temperature to which the smallest observed water drops have been found to supercool.

Of course, as expected, the pronounced clustering in water also affects the diffusivity of water molecules in water. The self-diffusion coefficient D_w of water has been measured down to $-31°C$ by Gillen *et al.* (1972) and Pruppacher (1972), who show that D_w decreases progressively as the temperature decreases. Their results fit the relation

$$D_w = \sum_{n=0}^{3} a_n T^n , \tag{3-19}$$

with D_w in $cm^2\ sec^{-1}$, T in °C, and with $a_0 = 1.076 \times 10^{-5}$, $a_1 = 4.260 \times 10^{-7}$, $a_2 = 2.667 \times 10^{-9}$, and $a_3 = -2.667 \times 10^{-11}$, for temperatures between 0 and 50°C; and the relation

$$D_w = a_0 \exp(a_1 T + a_2 T^2 + a_3 T^3) , \tag{3-20}$$

with D_w in $cm^2\ sec^{-1}$, and $a_0 = 1.076 \times 10^{-5}$, $a_1 = 4.14 \times 10^{-2}$, $a_2 = 2.048 \times 10^{-4}$, and $a_3 = 2.713 \times 10^{-5}$, for temperatures between 0°C and −40°C.

One may easily convince oneself (Wang, 1951a,b; 1952) that viscous flow and self-diffusion of water is controlled by the same structure-breaking mechanism involving the formation and diffusion of vancancies. Therefore, both phenomena will have the same energy of activation. In fact, one finds (Wang, 1952) that

$$\frac{(\Delta g)_{act,w}}{\mathscr{R}} = \frac{d \ln(\eta_w / T)}{d(1/T)} = -\frac{d \ln D_w}{d(1/T)} . \tag{3-21}$$

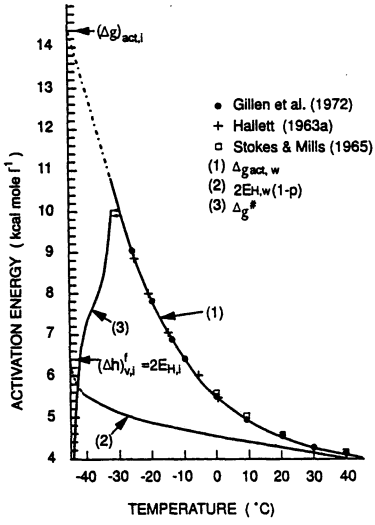


Fig. 3-11: Variation with temperature: (1) of the activation energy for viscous flow and self-diffusion of water extrapolated to −45°C, (2) of the variation of 2 $E_{H,W}(1-p)$, (3) of the activation energy for the transfer of water molelcular across the ice-water interface.

Plotting $(\Delta g)_{act,w}$ as a function of temperature using both the self-diffusion and the viscosity data, one obtains curve 1 in Figure 3.11. Note that in contrast to ice

TABLE 3.1

Vartiation with temperature of the H-bond energy $E_{H,w}$ between water molecules in water, of the percentage p of broken bonds, and of the enthalpy $\Delta h^f_{v,w}$ for vacancy formation in water.

T (°C)	$E_{H,\mathrm{w}}$ kcal (mole of bond)$^{-1}$	p (%)	$(1-p)$	$(\Delta h)^f_{\mathrm{v,w}} = 2(1-p)E_{H,\mathrm{w}}$ (kcal mole^{-1})
40	2.50	20	0.80	4.00
30	2.53	18	0.82	4.15
20	2.55	16	0.84	4.28
10	2.57	14	0.86	4.42
0	2.59	12	0.88	4.56
-10	2.61	10	0.90	4.70
-20	2.63	7	0.93	5.04
-30	2.71	5	0.95	5.15
-40	2.78	1.5	0.985	5.48

for which a plot of $\ln D_i$ vs $1/T$ is linear, implying one value for $(\Delta h)_{\mathrm{act},i}$ in the range -2 to -36°C, $(\Delta \mathrm{g})_{\mathrm{act,w}}$ increases rapidly with decreasing temperature. This trend can be described approximately by the relation

$$(\Delta \mathrm{g})_{\mathrm{act,w}} = \mathrm{a}_0 \exp(\mathrm{a}_1 T + \mathrm{a}_2 T^2 + \mathrm{a}_3 T^3)\,, \tag{3-22}$$

with $(\Delta \mathrm{g})_{\mathrm{act,w}}$ in kcal mole^{-1}, T in °C, and $\mathrm{a}_0 = 5.55$, $\mathrm{a}_1 = -8.423 \times 10^{-3}$, $\mathrm{a}_2 = 6.384 \times 10^{-4}$, and $\mathrm{a}_3 = 7.891 \times 10^{-6}$ for temperatures between +40°C and −40°C. We notice from Figure 3.11 that as the temperature approaches −45°C $(\Delta \mathrm{g})_{\mathrm{act,w}}$ approaches 14.26 kcal mole^{-1}, the value found experimentally by Ramseier (1967) for the activation enthalpy for self-diffusion in ice.

In Table 3.1, we have listed what seems to us the most reasonable experimentally derived values for $E_{\mathrm{H,w}}$ and p. In anology to ice, we find for the activation energy for vacancy formation in water $(\Delta h)^f_{\mathrm{v,w}} = 2(1-p)E_{H,\mathrm{w}}$, which also is plotted in Figure 3.11. We notice that as −45°C is approached $2(1-p)E_{\mathrm{H,w}}$ approaches a value of 6.44 kcal mole^{-1}, which is the value observed by Eldrup *et al.* (1978) for $(\Delta h)^f_{\mathrm{v},i}$. Of course, $(\Delta \mathrm{g})_{\mathrm{act,w}}$ is composed of the activation enthalpy of vacancy formation as well as the activation enthalpy of vacancy migration $(\Delta h)^m_{\mathrm{v,w}}$. The latter is simply given by the vertical difference of the curves $(\Delta \mathrm{g})_{\mathrm{act,w}}$ and $(\Delta h)^f_{\mathrm{v,w}}$ (in Figure 3.11), and approaches the value for ice, namely 7.82 kcal mole^{-1}, as −45°C is approached.

To check for consistency between the molecular parameters for water and ice and the macroscopic characteristics of water and ice, we shall follow a suggestion of Luck (1967) and Nemethy and Sheraga (1962a,b), and compute the molar enthalpies of evaporation and melting to compare them with values derived from observed specific heats given by (3-12), (3-15), and (3-16) (see also Section 4.7). For this purpose we shall use the following experimentally inferred values: $2E_{\mathrm{H},i} = 6.44$ kcal mole^{-1}; $2E_{\mathrm{H,w}} = 5.2$ kcal mole^{-1} (0°C), and 5.6 kcal mole^{-1} (−40°C); $p = 0.12$ (0°C) and 0.015 (−40°C); the number of nearest neighbor molecules $z_i = 4$, $z_{\mathrm{w}} = 4.3$ (0°C), and 4.0 (-40°C), according to Morgan and Warren (1938), Narten *et al.* (1967), and Danford and Levy (1962); and $E_{\mathrm{other},i} = (z_i/2)E_i = 5.76$ kcal mole^{-1},

with $E_i = 2.88$ kcal mole^{-1}. Assuming $E_i \approx E_w$ we obtain for water $E_{other,w} = (z_w/2)E_w = 6.20$ kcal mole^{-1} (0°C), and 5.76 kcal mole^{-1} (−40°C).

Based on bond energy considerations, the molar enthalpy of evaporation $(\Delta h)_e$ may be written (Luck, 1967)

$$(\Delta h)_e = pE_{other,w} + (1-p)(2E_{H,w} + E_{other,w})\,. \tag{3-23}$$

If we insert the above values into (3-23), we find $(\Delta h)_e = 10.77$ kcal mole^{-1} (0°C), and 11.28 kcal mole^{-1} (−40°C). Considering the uncertainties in the values used and the approximate nature of (3-23), we find excellent agreement of the computed values with the measurements of Osborne *et al.* (1939), who found $(\Delta h)_e = 10.75$ kcal mole^{-1} (0°C).

The results from (3-23) also agree with values for $(\Delta h)_e$ derived from (4-77) using observed values for the specific heat extrapolated to temperatures below −37°C. The values thus determined for the specific enthalpies of evaporation $(\Delta h)_e$ (IT cal g^{-1}) fit the relations

$$(\Delta h)_e = 597.3 - 0.561T\,, \quad -20 \le T \le 40°C\,; \tag{3-24a}$$

and

$$(\Delta h)_e = a_1 + a_2T + a_3T^2 + a_4T^3 + a_5T^4 + a_6T^5\,, \quad -44 \le T \le -20°C\,; \tag{3-24b}$$

with $a_1 = -1412.3$, $a_2 = -338.82$, $a_3 = -122.347$, $a_4 = -0.7256$, $a_5 = -1.1595 \times 10^{-2}$ and $a_6 = -7.313 \times 10^{-5}$. For example, these expressions give an enthalpy of evaporation of 11.25 kcal mole^{-1} at $T = -40°C$, and 10.75 kcal mole^{-1} at $T = 0°C$.

An analogous procedure may be used to compute the enthalpy of melting assuming $(\Delta h)_m = (\Delta h)_s - (\Delta h)_e$. Following Luck (1967), we then find

$$\begin{aligned}(\Delta h)_m &= 2E_{H,i} + \frac{z_i}{2}E_{H,i} - pE_{other,w} - (1-p)(2E_{H,w} + E_{other,w}) \\ &= 2(E_{H,i} - E_{H,w}) - \frac{1}{2}(z_w - z_i)E_w + 2pE_{H,w}\end{aligned} \tag{3-25}$$

If we insert the appropriate values in (3-25) we obtain $(\Delta h)_m = 1.43$ kcal mole^{-1} (0°C), and 1.01 kcal mole^{-1} (−40°C). This is in good agreement with the observations of Rossini *et al.* (1952) and Osborne *et al.* (1939) who found $(\Delta h)_m = 1.43$ kcal mole^{-1} (0°C), and also with the experiments of Dumas and Broto (1974), who determined for $T = -37.2°C$ that $(\Delta h)_m = (1.01 \pm 0.02)$ kcal mole^{-1}. The results from (3-25) also agree with values for $(\Delta h)_m$ deduced from (4-77) using observed values for the specific heat extrapolated to temperatures below −37°C. The values obtained in this way for the specific enthalpy of melting $(\Delta h)_m$ fit the relation

$$(\Delta h)_m = \sum_{n=0}^{4} a_n T^n\,, \tag{3-26}$$

with $(\Delta h)_m$ in IT cal g^{-1}, T in °C, and $a_0 = 79.7$, $a_1 = -0.1200$, $a_2 = -8.0481 \times 10^{-2}$, $a_3 = -3.2376 \times 10^{-3}$, $a_4 = -4.2553 \times 10^{-5}$. This expression gives $(\Delta h)_m = 1.43$ kcal mole^{-1} (0°C), and $(\Delta h)_m = 0.97$ kcal mole^{-1} (−40°C).

The variation of $(\Delta h)_e$ and $(\Delta h)_m$ with temperature is illustrated in Figure 3.12.

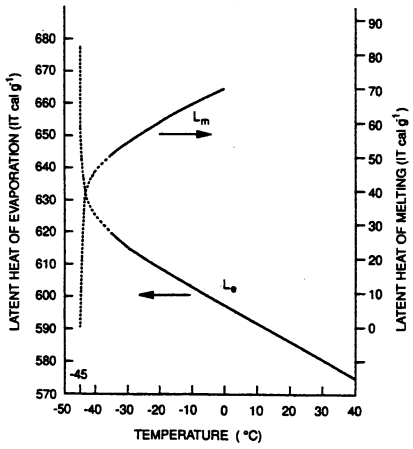


Fig. 3-12: Variation with temperature of the latent heat of melting and latent heat of evaporation of supercooled water based on values for the specific heat of water in Fig. 3-9, for the specific heat of ice from Lonsdale (1958) and Ginnings and Corrucini (1947), and based on Kirchoff's law. Extrapolation is done to be consistent with $-45°C$ limit.

3.4.2 Structure of Aqueous Solutions

Experiments show that the structure of water is altered when water-soluble salts, in part dissociated into ions, are dissolved in water. The aqueous solution resulting from dissolving a salt in water would be an ideal solution if the dissolved salt molecules or ions in no way affected the water molecules. In any real aqueous solution, this is not the case. For example, some of the salt molecules or ions do not fit into the water 'structure' and, therefore, distort it, causing a size effect. Second, solute ions are prone to interact with the water-dipoles which, depending on the size and electric charge of the ion, become grouped around the ion. This effect is called *hydration.* Since large ions have weaker local electric fields than small ions, the hydration effect is greater for small ions. In addition, hydration is more pronounced for positive ions than for negative ones, since a positive ion tends to interact with both lone electron pairs, which blocks the formation of two H-bonds. On the other hand, a negative ion tends to interact with just one H—O group of a water molecule, which blocks the formation of only one hydrogen bond.

Both the size and hydration effects cause hydrogen bonds in the vicinity of an ion to be broken. Such structure breaking and lessening of the four-coordination among the water molecules in water as a result of dissolved salts have been inferred from X-ray, nuclear magnetic resonance, and infrared and Raman spectra studies, as well as from studies on the dielectric properties, the viscosity, thermal conductivity, and heat capacity of aqueous solutions, and from studies on the diffusion of water and ions in aqueous solutions (Kavanau, 1964; Robinson and Stokes, 1970; Horne, 1972; Franks, 1973; Ben-Naim, 1974). According to these investigations, it is useful to visualize the arrangement of water molecules around an ion in the form of three regions: (1) a region close to the ion where the water molecules are immobilized

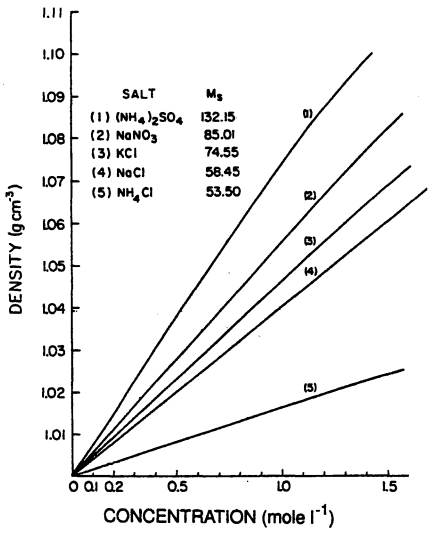


Fig. 3-13: Variation of the density of aqueous salt solutions with concentration of salt, at $T = 20°C$.

as a result of their electrical interaction with it, (2) a transition region further out in which the water is less ordered than ordinary water because of the structural disruption caused by the size and charge of the ion, and (3) the outermost region consisting of ordinary water.

Since ions generally have a structure-breaking effect on water, it is not surprising to find from experiments that salts dissolved in water lower its heat capacity. However, this lowering is small at high dilution and only becomes significant if the salt concentration is larger than 0.1 moles liter^{-1}. Since salts affect the specific heat of water, it is quite reasonable to expect that the latent heats are affected also. A quantitative assessment of the effect of salts is easily made by noting, that even at concentrations as large as 5 moles per liter, the enthalpy of mixing of water in an aqueous solution of NaCl affects the magnitude of the enthalpy of evaporation by less than 0.2% and the enthalpy of melting by less than 2%. Thus, for most purposes of atmospheric interest, we may assume that the specific enthalpies of evaporation and melting for aqueous solution are given by their values for pure water. Experiments show that dissolved salts also affect the density of water. As expected from the ability of salt ions to break hydrogen bonds, the density of aqueous solutions is found to increase with increasing salt concentration and with increasing molecular weight of the salt. This behavior is illustrated in Figure 3.13 for a few salts typically found in the atmosphere.

CHAPTER 4

EQUILIBRIUM BETWEEN WATER VAPOR, WATER, AQUEOUS SOLUTIONS, AND ICE IN BULK

In this chapter, we shall discuss the equilibrium thermodynamics of and between the bulk phases of water, ice and aqueous solutions. In addition to providing useful information on the behavior of water substance, this material, with surface effects included, will also serve as a basis for our later discussion on the phase changes which lead to cloud particle formation.

For background on the material covered in this chapter, the reader may wish to refer to texts on chemical thermodynamics and physical chemistry such as Kortüm (1972), Robinson and Stokes (1970), Prigogine and Defay (1967), Reiss (1965), Kirkwood and Oppenheim (1961), Lewis and Randall (1961), and Glasstone (1959), and the review acticles by Harrison (1965a,b) and Goff (1949).

4.1 Useful Thermodynamic Relations

Consider an open, homogeneous (single phase) thermodynamic system which may exchange heat, pressure work, and mass with the environment. For small reversible changes, the second law of thermodynamics tells us that the heat added may be expressed as $T\mathrm{d}S$, where T and S are respectively the temperature and entropy of the system; the incremental pressure work done on the system is $-p\mathrm{d}V$, where p and V are the pressure and volume of the system, respectively; and the incremental mass added is measured by $\mathrm{d}n_k$, $k = 1, 2, \ldots, c$, where n_k is the number of moles of chemical component k of the c components comprising the system. According to the first and second laws of thermodynamics, the incremental change in the internal energy $U = U(S, V, n_1, n_2, \ldots, n_c)$ of the system for reversible processes is

$$\mathrm{d}U = T\mathrm{d}S - p\mathrm{d}V + \sum_{k=1}^{c} \mu_k \mathrm{d}n_k \,, \tag{4-1}$$

where

$$\mu_k \equiv \left(\frac{\partial U}{\partial n_k} \right)_{S,V,n_{j \neq k}} \tag{4-2}$$

is called the chemical potential of component k.

Note that U and the independent state variables S, V, and n_k are extensive (proportional to n_k), in contrast to the intensive variables T, p, and μ_k. Let us denote the extensive and intensive variables by x_i and $y_i = \partial U / \partial x_i$, respectively. Then, for constant λ we have $U(\lambda x_1, \lambda x_2, \ldots) = \lambda U(x_1, x_2, \ldots)$, so that

$$U(x_1, x_2, \ldots) = \frac{\mathrm{d}}{\mathrm{d}\lambda} U(\lambda x_1, \lambda x_2, \ldots) = \sum_i \frac{\partial U(\lambda x_1, \lambda x_2, \ldots)}{\partial(\lambda x_i)} x_i = \sum_i y_i x_i \,, \tag{4-3a}$$

or

$$U(S,V,n_1,n_2,\ldots,n_c) = TS - pV + \sum_{k=1}^{c} \mu_k n_k \,, \tag{4-3b}$$

which is called *Euler's* equation.

If we subtract (4-1) from the differential of (4-3b), we obtain the *Gibbs-Duhem* relation

$$\sum_{k=1}^{c} n_k \mathrm{d}\mu_k = -S\mathrm{d}T + V\mathrm{d}p \tag{4-4a}$$

or

$$\sum_{k=1}^{c} x_k \mathrm{d}\mu_k = -s\mathrm{d}T + v\mathrm{d}p \,, \tag{4-4b}$$

where

$$x_k = \frac{n_k}{\sum_{i=1}^{c} n_i} = \frac{n_k}{n} \tag{4-5}$$

is the mole fraction of component k; and s and v are mean molar quantities. The result (4-4a) proves to be especially useful for exploring the relationships between phases in equilibrium.

The study of some processes is facilitated by introducing other thermodynamic potentials, in addition to the internal energy. We shall have occasion to use three: the enthalpy $H \equiv U + pV$, the Helmholtz free energy $F \equiv U - TS$, and the Gibbs free energy $G \equiv U + pV - TS = H - TS$. From (4-1), we see that

$$\mathrm{d}H = T\mathrm{d}S + V\mathrm{d}p + \sum_{k=1}^{c} \mu_k \mathrm{d}n_k \,, \tag{4-6}$$

$$\mathrm{d}F = -S\mathrm{d}T - p\mathrm{d}V + \sum_{k=1}^{c} \mu_k \mathrm{d}n_k \,, \tag{4-7}$$

$$\mathrm{d}G = -S\mathrm{d}T + V\mathrm{d}p + \sum_{k=1}^{c} \mu_k \mathrm{d}n_k \,, \tag{4-8}$$

Also, from (4-3b) and (4-8) we find that μ_k may be regarded as a partial molar Gibbs free energy, g_k, i.e.,

$$\mathrm{g}_k \equiv \left(\frac{\partial G}{\partial n_k}\right)_{T,p,n_j} = \mu_k \,; \quad G = \sum_{k=1}^{c} n_k \mu_k = \sum_{k=1}^{c} n_k \mathrm{g}_k \,. \tag{4-9}$$

Since $\mathrm{d}G$ is a perfect differential, we further conclude from (4-8) and (4-9) that

$$\left(\frac{\partial \mu_k}{\partial T}\right)_{p,n_{j\neq k}} = -\left(\frac{\partial S}{\partial n_k}\right)_{T,p,n_{j\neq k}} = -s_k \tag{4-10}$$

and

$$\mathrm{g}_k \equiv \left(\frac{\partial \mu_k}{\partial p}\right)_{T,n_{j\neq k}} = \left(\frac{\partial V}{\partial n_k}\right)_{T,p,n_{j\neq k}} = v_k \,, \tag{4-11}$$

where s_k and v_k are the partial molar entropy and volume of component k, respectively.

From (4-6), we see that if p and $n_1, n_2, \ldots, n_c$ are held constant, then $\mathrm{d}H$ measures the change in heat content in a reversible process. Therefore, the enthalpy is called the heat content of the system at constant pressure, and we may write

$$\left(\frac{\partial h}{\partial T}\right)_{p,n_k} = C_p = T\left(\frac{\partial s}{\partial T}\right)_{p,n_k}, \tag{4-12}$$

where C_p is the mean molar heat capacity at constant p, and $h = H/n, s = S/n$. Finally, useful relationships for evaluating the chemical potential from the enthalpy may be easily derived: $\mu_k = \mathrm{g}_k = h_k - Ts_k$, so that

$$\left[\frac{\partial(\mu_k/T)}{\partial T}\right]_{p,n_{j\neq k}} = -\frac{1}{T}\left[\frac{\mu_k}{T} - \left(\frac{\partial \mu_k}{\partial T}\right)_{p,n_{j\neq k}}\right] = -\frac{h_k}{T^2}, \tag{4-13a}$$

where we have used (4-10); and

$$\left[\frac{\partial(\mu_k/T)}{\partial p}\right]_{T,n_{j\neq k}} = \frac{1}{T}\left(\frac{\partial \mu_k}{\partial p}\right)_{T,n_{j\neq k}} = \frac{v_k}{T}, \tag{4-13b}$$

where we have used (4-11).

4.2 General Conditions for Equilibrium

The second law of thermodynamics provides, as a corollary, a quantitative criterion for thermodynamic equilibrium. Consider an isolated system which is not in equilibrium. In such a system irreversible processes evolve spontaneously. According to the second law, the entropy of such a system will increase until eventually it reaches a state where its entropy is a maximum. In such a state all irreversible processes will have stopped and only those processes, if any, will continue which are completely reversible. The system is then in a state of equilibrium. Thus, for such a system held at constant U, V, and $n_1, n_2, \ldots, n_c$, the criterion of equilibrium is

$$(\delta S)_{U,V,n_k} \leq 0, \tag{4-14}$$

where δS refers to the virtual variation in entropy with respect to neighboring states. An alternative expression for a system with constant S, V, and $n_1, n_2, \ldots, n_c$ is

$$(\delta U)_{S,V,n_k} \geq 0. \tag{4-15}$$

In addition, the equilibrium is stable if $(\delta^2 S)_{U,V,n_k} < 0$, unstable if $(\delta^2 S)_{U,V,n_k} > 0$, and conditionally stable or metastable if $(\delta^2 S)_{U,V,n_k} = 0$. Here $\delta^2 S$ is the second virtual variation in entropy with respect to neighboring states.

Unstable equilibrium states cannot be realized in nature since natural systems are continuously exposed to environmental perturbations which, even though very small, are always sufficient to prevent the system from remaining in such a state. On the other hand, metastable states frequently occur in nature. Supercooled

water in an environment of moist air saturated with water vapor is an example of such a system: while the supercooled water is in stable equilibrium with the water vapor surrounding it, it is in unstable equilibrium with respect to ice into which it would immediately transform if it came into contact with it.

Let us extend these equilibrium conditions to a heterogeneous isolated system containing c chemical components characterized by μ_k and n_k. By definition, a heterogeneous system consists of two or more phases which are separated from each other by planar surfaces of discontinuity in one or more of the intensive variables. Let us assume that all φ phases of a heterogeneous system are originally isolated and each phase is in internal equilibrium. We may now ask what conditions on the intensive variables are necessary and sufficient to insure equilibrium in the system after the restraint of isolation of the phases has been removed. In seeking these conditions, we shall assume that no chemical reactions occur and that the heterogeneous system itself remains isolated. After removing the restraint of isolation of the φ phases of the system, each phase (α) constitutes a homogeneous open system for which the condition of equilibrium is given by (4-15). Also, since extensive variables are additive, we may write

$$U = \sum_{\alpha=1}^{\varphi} U^{(\alpha)}; \quad S = \sum_{\alpha=1}^{\varphi} S^{(\alpha)}; \quad V = \sum_{\alpha=1}^{\varphi} V^{(\alpha)}; \quad n_k = \sum_{\alpha=1}^{\varphi} n_k^{(\alpha)}. \tag{4-16}$$

Then, from (4-1), the condition of equilibrium may be expressed as

$$\delta U = \sum_{\alpha=1}^{\varphi} \left[T^{(\alpha)} \delta S^{(\alpha)} - p^{(\alpha)} \delta V^{(\alpha)} + \sum_{k=1}^{c} \mu_k^{(\alpha)} \delta n_k^{(\alpha)} \right] \geq 0, \tag{4-17}$$

where S, V, and n_k are held constant, according to

$$\delta S = \sum_{\alpha=1}^{\varphi} \delta S^{(\alpha)} = 0; \quad \delta V = \sum_{\alpha=1}^{\varphi} \delta V^{(\alpha)} = 0; \quad \delta n_k = \sum_{\alpha=1}^{\varphi} \delta n_k^{(\alpha)} = 0. \tag{4-18}$$

For simplicity, let us momentarily consider a system of just two phases which we denote by $(')$ and $('')$. Then, from (4-17) and (4-18), we may express the equilibrium condition as

$$(T'' - T')\delta S'' - (p'' - p')\delta V'' + (\mu_k'' - \mu_k')\delta n_k'' \geq 0. \tag{4-19}$$

The constraints of (4-18) have all been incorporated into this equation so that $\delta S''$, $\delta V''$, and $\delta n_k''$ can be chosen independently. Therefore, the equation can be satisfied only if the coefficients of each of the variations are equal to zero. Since the same analysis could be applied to any pair of phases in a more complex system, we conclude that the conditions for thermodynamic equilibrium of a heterogeneous system in which all interface surfaces are perfectly deformable, heat conducting, and permeable to all components are

$$T' = T'' = \ldots = T^{(\alpha)}, \tag{4-20}$$

$$p' = p'' = \ldots = T^{(\alpha)}, \tag{4-21}$$

$$\mu_k' = \mu_k'' = \ldots = \mu_k^{(\alpha)}, \quad k = 1, 2, \ldots, c. \tag{4-22}$$

These three equations express the conditions of thermal, mechanical, and chemical equilibrium, respectively.

4.3 Phase Rule for Bulk Phases

The discussion of systems in equilibrium is facilitated by what is known as the *Gibbs phase rule*. This rule enables us to determine the *variance* of a system, i.e., the number of intensive variables which may be freely specified without causing the system to depart from equilibrium. To derive the phase rule, let us consider again the heterogeneous, isolated system of the previous section. As we have seen, in equilibrium the system is characterized by a common T and p and by a number of mole fractions in the various phases. Let us denote the mole fraction of the k^{th} component in the j^{th} phase by $x_k^{(j)} (= n_k^{(j)} / \sum_k n_k^{(j)})$. Then, for a system of φ phases and c components, there will be φc mole fractions altogether, giving us a total of $2 + \varphi c$ intensive variables at equilibrium. However, not all of these are independent. Thus, for every phase we have the simple mass conservation constraint that $\sum_{k=1}^{c} x_k = 1$, for a total of φ constraints. In addition, we have the condition (4-22) on the chemical potentials, which constitute another $\varphi - 1$ constraints for every k, for a total of $c(\varphi - 1)$ constraints. Therefore, at equilibrium the total variance, or number of thermodynamic degrees of freedom, is

$$w = 2 + \varphi c - \varphi - c(\varphi - 1) = 2 + c - \varphi \,, \tag{4-23}$$

which is the Gibbs phase rule for bulk phases. (As we shall see in Section 5.3, the phase rule assumes a substantially different form if phases with curved interfaces are present in a system.)

Let us consider some simple applications of (4-23). For a homogeneous fluid in equilibrium, we have $\varphi = 1$, $c = 1$, and so $w = 2$. This is consistent with the familiar circumstance that the equation of state of such a system provides one connection among three thermodynamic state variables (e.g., ρ, T, p). For a mixture of two gases, $c = 2$, $\varphi = 1$, and therefore $w = 3$; obviously, this is like the previous example, except that now we can also freely choose the relative concentration of the gases. For water in equilibrium with its vapor, $c = 1$, $\varphi = 2$, and therefore $w = 1$; the system is monovariant, and the vapor pressure is a function only of temperature. For water in equilibrium with its vapor and ice, $c = 1$, $\varphi = 3$, and therefore $w = 0$; equilibrium is possible only for a single choice of T and pressure, which defines the *triple point* temperature T_{tr} of the system. If this system is now exposed to the atmosphere, $c = 2$ (water substance and air), $\varphi = 3$, and therefore $w = 1$. However, if we make the reasonable assumption that the total gas pressure remains constant, the system can have no further variance if it is to remain in equilibrium. The system is now said to be at its *ice point* temperature T_0. Thus, we see that the ice point temperature is a function of pressure. By convention the concept of the ice point is restricted further by specifying that the pressure on the system should be exactly one atmosphere (see Section 4.9).

4.4 Ideal versus Real Behavior of Dry Air, Water Vapor, and Moist Air

Let us now consider some of the equations of state we will need in order to apply the equilibrium conditions (4-20) to (4-22). If we assume that water vapor behaves as an ideal gas of non-interacting molecules, its equation of state may be written in the following familiar forms:

$$\mathrm{e}v_{\mathrm{v},0} = \mathscr{R}T\,; \quad \mathrm{e} = \rho_{\mathrm{v}} R_{\mathrm{v}} T\,; \quad \mathrm{e} = N\mathrm{k}T\,, \tag{4-24}$$

where e denotes the water vapor pressure, $v_{\mathrm{v},0}$ is the molar volume of pure water vapor, $\mathscr{R} = N_A\mathrm{k}$ is the universal gas constant, N_A is the Avogadro number, k is the Boltzmann's constant, $N = N_A/v_{\mathrm{v},o}$ is the number concentration of vapor molecules, ρ_{v} is the vapor density, $R_{\mathrm{v}} = \mathscr{R}/M_{\mathrm{w}}$ is the specific gas content for water vapor, and M_{w} is the molecular weight of water.

A similar equation of state may be written for dry air if we regard it as a mixture of ideal gases. Then, in a fixed volume V we have for the partial pressure p_k of the k^{th} component, $p_k V = n_k \mathscr{R}T = m_k \mathscr{R}T/M_k$, where m_k is the mass of the k^{th} component. Applying Dalton's law, $p = \sum_k p_k$, we obtain

$$p_{\mathrm{a}} v_{\mathrm{a},0} = \mathscr{R}T\,; \quad p_{\mathrm{a}} = \rho_{\mathrm{a}} R_{\mathrm{a}} T\,, \tag{4-25}$$

where p_{a}, denotes the pressure of dry air, $v_{\mathrm{a},0} = V/\sum_k n_k$ is its molar volume, ρ_{a} its density, and $R_{\mathrm{a}} = \mathscr{R}/M_{\mathrm{a}}$, its specific gas constant, with

$$M_{\mathrm{a}} = \frac{\sum\limits_k m_k}{\sum\limits_k n_k} = \frac{\sum\limits_k m_k}{\sum\limits_k (m_k/M_k)}\,. \tag{4-26}$$

It is important to assess the extent of deviations from ideality owing to molecular interactions of the sort we discussed in the previous chapter. This problem has been considered in detail by Goff (1942, 1949) and Goff and Gratch (1945, 1946), who found that a virial expansion of the equation of state truncated at the fourth term could be used to represent the behavior of real air and water vapor. Thus, the real gas equations of state can be expressed adequately in the following form:

$$\mathrm{e}v_{\mathrm{v},0} = \mathscr{R}T - \mathsf{A}_{\mathrm{ww}}\,\mathrm{e} - \mathsf{A}_{\mathrm{www}}\,\mathrm{e}^2\,, \tag{4-27}$$

$$p_{\mathrm{a}} v_{\mathrm{a},0} = \mathscr{R}T - \mathsf{A}_{\mathrm{aa}}\,p_{\mathrm{a}} - \mathsf{A}_{\mathrm{aaa}}\,p_{\mathrm{a}}^2\,. \tag{4-28}$$

Values for the virial coefficients (A) may be determined experimentally from accurate measurements of the state variables. Alternatively, they may be computed theoretically, at least in principle, by using the methods of statistical mechanics (e.g., Hirschfelder *et al.*, 1954). Of course, in order to do this, one must model the intermolecular forces. Both routes have encountered great difficulties for the case of water vapor (e.g., Kennard, 1938; Harrison, 1965a; Kell *et al.*, 1968; Eisenberg and Kauzmann, 1969; Ben-Naim, 1974). The presently accepted values for A_{aa}, $\mathsf{A}_{\mathrm{aaa}}$, A_{ww}, and $\mathsf{A}_{\mathrm{www}}$ are tabulated in Goff (1949), Harrison (1965a) and the Smithsonian Meteorological Tables (SMT).

TABLE 4.1
Deviation of dry air, pure water vapor, and moist air from ideality in terms of the compressibility factor. (Based on data from Harrison, 1965a.)

	C_a		C_v	C_v	C_m
Temperature	1100 mb	300 mb	Water vapor saturated with respect to water	Water vapor saturated with respect to ice	100 % Relative humidity 1100 mb
−30°C	0.9988	0.9997	0.9999	0.9999	-
0°C	0.9994	0.9998	0.9995	0.9995	0.9993
30°C	0.9997	0.9999	0.9982	-	0.9995

It is customary to express the deviation from ideal gas behavior in terms of what is known as the compressibility factor, $C \equiv pv/\mathscr{R}T$, values of which may be computed once the virial coefficients are known. A few selected values for C_a, and C_v are given in Table 4.1. These show that the ideal gas law for both dry air and water vapor is in error by less than 0.2% throughout the range of meteorological interest. Fortunately, therefore, the simple expressions (4-24) and (4-25) can be used with confidence.

In view of these results, it is perhaps almost obvious that moist air can also be treated as an ideal gas (see Table 4.1). We say almost, because there remains the possibility that the forces of interaction between water molecules and some species of air molecules might be much greater than the water-water or air-air interactions. A partial explanation of why this, in fact, does not occur may be given by considering the example of the van der Waal's interaction (see Chapter 3): the strength of this force depends on the mean square fluctuation of the electric dipole moment and the molecular polarizability. Neither of these parameters shows an extremely wide range in nature and so, accordingly, the van der Waal's interaction is relatively insensitive to the molecular species involved.

The ideal gas law for moist air may be written in analogy to (4-25) as

$$pv_m = \mathscr{R}T\,; \quad p = \rho R_m T\,, \tag{4-29}$$

where R_m is determined in the same fashion as R_a. However, it is customary and more convenient to write the equation of state in the form used for dry air, with the moisture correction associated with the temperature. Proceeding in this way, we have for the pressure and density of moist air, $p = p_a + e$ and $\rho = \rho_a + \rho_v$. Then, from (4-24) and (4-25), we find $\rho = (M_a p_a + M_w e)/\mathscr{R}T = M_a[p - (1 - \varepsilon)e]/\mathscr{R}T$, with $\varepsilon = M_w/M_a = 0.622$, or

$$p = \rho R_a T_v\,, \tag{4-30}$$

where T_v, called the virtual temperature of moist air, is given by

$$T_v = T[1 - (1 - \varepsilon)e/p]^{-1}\,. \tag{4-31}$$

Physically, T_v is the temperature which dry air would have to have in order for its density to match that of the actual air. Since $M_w < M_a$, moist air has a lower

density than dry air at the same temperature, so that $T_v > T$ always. However, the extent of the difference is not large: a reasonable upper bound for e is the saturation value at 30°C, which is only about 4% of standard sea level pressure; hence $T_v - T \lesssim 5°C$.

We have now introduced two quantities, the virtual temperature T_v and the water vapor density or *absolute humidity* ρ_v, which provide a measure of the water vapor content of air. There are, in addition, several other such 'moisture variables' in common use. Among the most important are the *mixing ratio* w_v, the *specific humidity* q_v, the *relative humidity* ϕ_v, the mole fraction of water vapor x_v, the *saturation ratio* S_v, and the *supersaturation* s_v. These are defined as follows:

$$w_v \equiv \frac{m_v}{m_a} = \frac{\rho_v}{\rho_a} \quad (4\text{-}32); \quad q_v \equiv \frac{m_v}{m_m} = \frac{\rho_v}{\rho} \quad (4\text{-}33); \quad \phi_v \equiv \frac{w_v}{w_{v,sat}}, \tag{4-34}$$

$$x_v \equiv \frac{n_v}{n_a + n_v} \quad (4\text{-}35); \quad S_v \equiv \frac{e}{e_{sat}} \quad (4\text{-}36); \quad s_v \equiv \frac{w_v}{w_{v,sat}} - 1, \tag{4-37}$$

where the subscript sat refers to the maximum possible saturated value. Air for which $\phi_v = 1$ (100%) is saturated; if $\phi_v > 1$ (>100%), it is said to be supersaturated, corresponding to $s_v > 0$; if $\phi_v < 1$ (<100%), air is said to be subsaturated. The moisture variables are also connected by various relationships, such as

$$w_v = \frac{q_v}{1 - q_v}; \quad q_v = \frac{w_v}{1 + w_v}, \tag{4-38}$$

$$x_v = \frac{e}{p} = \frac{w_v}{w_v + \varepsilon}, \tag{4-39}$$

$$w_v = \varepsilon \frac{x_v}{1 - x_v} = \varepsilon \frac{e}{p - e} \approx \varepsilon \frac{e}{p} \tag{4-40}$$

and

$$T_v = T\left[\frac{1 + (w_v/\varepsilon)}{1 + w_v}\right] = T\left[1 + \left(\frac{1}{\varepsilon} - 1\right) q_v\right]. \tag{4-41}$$

4.5 Chemical Potential of Water Vapor in Humid Air, and of Water in Aqueous Solutions

We are now in a position to derive the chemical potential of water vapor and, through the equilibrium conditions, the chemical potential of water in aqueous solutions. From (4-11) we have, for an ideal gas k in a mixture of ideal gases, $(\partial \mu_k / \partial p_k)_{T, n_{j \neq k}} = v_k = \mathscr{R} T / p_k$, so that, upon integration,

$$\mu_k = \mu_{k,0} + \mathscr{R} T \ln p_k, \tag{4-42}$$

where the integration constant $\mu_{k,0}$ depends only on the temperature. For such a mixture, the partial pressure is $p_k = x_k p$, so that also

$$\mu_k = \mu_{k,0} + \mathscr{R} T \ln p + \mathscr{R} T \ln x_k. \tag{4-43}$$

Therefore, if we assume pure water vapor at pressure e is an ideal gas, its chemical potential is

$$\mu_{v,0}(e, T) = \mu^+_{v,0}(T) + \mathscr{R} T \ln e, \tag{4-44}$$

where $\mu^{+}_{\mathrm{v},0}(T)$ is the chemical potential at a standard state of unit pressure. Similarly, the chemical potential $\mu_{\mathrm{v}}(p,T)$ of water vapor in humid air at total pressure p is

$$\mu_(p,T,x_{\mathrm{v}}) = \mu^{+}_{\mathrm{v},0}(T) + \mathscr{R}T\ln p + \mathscr{R}T\ln x_{\mathrm{v}}\,. \tag{4-45}$$

From (4-44) with $\mathrm{e} = p$, we see that this last result may also be expressed as

$$\mu_{\mathrm{v}}(p,T,x_{\mathrm{v}}) = \mu_{\mathrm{v},0}(p,T) + \mathscr{R}T\ln x_{\mathrm{v}}\,, \tag{4-46}$$

which shows that $\mu_{\mathrm{v}} \leq \mu_{\mathrm{v},0}$ since $x_{\mathrm{v}} \leq 1$.

In contrast to pure gases whose chemical potentials vary logarithmically with pressure, the chemical potential of a pure liquid is proportional to pressure, to an excellent approximation. This is obvious from (4-11), on realizing that liquids are nearly incompressible. Thus, for water we have

$$\left(\frac{\partial\mu_{\mathrm{w},0}}{\partial p}\right)_T = v_{\mathrm{w},0} \approx \text{constant}\,, \tag{4-47}$$

from which the chemical potential is found to be

$$\mu_{\mathrm{w},0}(p,T) \approx \mu_{\mathrm{w},0}(0,T) + v_{\mathrm{w},0}p\,. \tag{4-48}$$

As we have seen, if a liquid and gas are in equilibrium, the chemical potential of a given component will be the same in both phases (Equation (4-22)). Consequently, from (4-42), the chemical potential of component k in a liquid solution, which is in equilibrium with its vapor at partial pressure p_k, is

$$\mu_{k,l} = \mu_{k,0} + \mathscr{R}T\ln p_k\,. \tag{4-49}$$

In addition, experiments show that for the so-called 'ideal' solutions, for which there are no interactions between the solvent and solute molecules, the equilibrium vapor pressure of any component is porportional to its mole fraction in the solution. (This is known as *Raoult's law*, about which more will be said in the following section.) Assuming Raoult's law, we then have $p_k = x_{k,l}p_{k,0}$, where $x_{k,l}$, is the mole fraction of component k in the solution, and $p_{k,0}$ is the partial pressure of component k in equilibrium with the pure liquid phase of k at the same temperature. Then, as a function of $x_{k,l}$, the chemical potential becomes

$$\mu_{k,l} = \mu^{\circ}_{k,l} + \mathscr{R}T\ln x_{k,l}\,, \tag{4-50}$$

where $\mu^{\circ}_{k,l}$ is a function of both temperature and total pressure, but is independent of the composition of the solution.

In clouds, the liquid phase is rarely present in the form of pure water, but rather is generally a dilute aqueous salt solution. Therefore, (4-50) is especially relevant to us, and we may use it to write the chemical potential for water in an ideal aqueous salt solution in the following form:

$$\mu_{\mathrm{w}}(p,T,x_{\mathrm{w}}) = \mu^{+}_{\mathrm{w}}(p,T) + \mathscr{R}T\ln x_{\mathrm{w}}\,, \tag{4-51}$$

where $x_w = n_w/(n_w + n_s) = 1 - x_s$ is the mole fraction of water, n_w and n_s, being, respectively, the number of moles of water and salt in the solution. By analogy, one would expect that the chemical potential of the salt component could be expressed in the same way, viz.,

$$\mu_s(p, T, x_s) = \mu_s^+(p, T) + \mathscr{R}T \ln x_s \,. \tag{4-52}$$

In passing, we may note that for $x_w = 1, \mu_w(p, T) = \mu_{w,0}(p, T) = \mu_w^+(p, T)$, the chemical potential of pure water at p, T. There is no analogous simple physical interpretation for the quantity $\mu_s^+(p, T)$. Experiments show that most dilute solutions of non-electrolytes are in conformity with (4-51) and (4-52). In general, however, real aqueous solutions depart from such ideal behavior. It is customary to account for non-ideal solutions through the replacement of the mole fraction x by the *activity*, $a \equiv fx$, where f is called the *rational activity coefficient.* Thus, for real aqueous salt solutions, we write

$$\mu_w(p, T, a_w) = \mu_{w,0}(p, T) + \mathscr{R}T \ln a_w \,; \quad a_w = f_w x_w \,, \tag{4-53}$$

$$\mu_s(p, T, a_s) = \mu_s^+(p, T) + \mathscr{R}T \ln a_s \,; \quad a_s = f_s x_s \,. \tag{4-54}$$

The importance of the activity to us is that it provides a direct measure of the equilibrium water vapor pressure over a real salt solution, or, in other words, the generalization of Raoult's law to real solutions. We now turn to a demonstration of this property.

4.6 Equilibrium Between an Aqueous Salt Solution and Water Vapor

Consider a system consisting of water vapor in equilibrium with an aqueous salt solution, both at temperature T and pressure e (here $e = e_{sat}$, but for brevity we omit the subscript in the development which follows). From (4-22), we have

$$\mu_{v,0}(e, T, a_w) = \mu_w(e, T, a_w) \,. \tag{4-55}$$

On substituting this equilibrium condition into (4-53) for $p = e$, we obtain

$$\mu_{v,0}(e, T, a_w) = \mu_{w,0}(e, T) + \mathscr{R}T \ln a_w \,. \tag{4-56}$$

According to the phase rule, the present system of two components and two phases is divariant ($w = 2$). Let us now fix T and investigate the variation of a_w with e. Then, from (4-55) and (4-56), we see that equilibrium can be maintained for variable e only if

$$\left(\frac{\partial \mu_w}{\partial e}\right)_T de = \left(\frac{\partial \mu_{v,0}}{\partial e}\right)_T de = \left[\left(\frac{\partial \mu_{w,0}}{\partial e}\right)_T + \mathscr{R}T\left(\frac{\partial \ln a_w}{\partial e}\right)_T\right] de \,. \tag{4-57}$$

Now, on substituting (4-11) and noting that $v_{w,0} \ll v_{v,0}$, (4-57) becomes

$$\left(\frac{\partial \ln a_w}{\partial e}\right)_T = \frac{v_{v,0}}{\mathscr{R}T} = \frac{1}{e} \,, \tag{4-58}$$

which, upon integration, yields

$$\ln a_w = \ln e_{sat} + g(T)\,, \tag{4-59}$$

where we have again recognized explicitly that $e = e_{sat}$, and where $g(T)$ is an unknown function of T. We may determine g by taking the limit $a_w \to 1$, which corresponds to the case, of pure water; i.e., $g(T) = -\ln e_{sat,w}$, where $e_{sat,w}$ is the saturation vapor pressure over pure water at temperature T. Therefore, (4-59) becomes

$$\frac{e_{sat,s}}{e_{sat,w}} = a_w(T)\,, \tag{4-60}$$

where we have now similarly replaced e_{sat}, by the more complete notation $e_{sat,s}$, which denotes the equilibrium vapor pressure over an aqueous salt solution at temperature T.

Equation (4-60) is the desired extension of Raoult's law. For an ideal solution, $a_w = x_w$, and we recover the original Raoult's law:

$$\frac{e_{sat,s}}{e_{sat,w}} = x_w \quad \text{(4-61a)}; \qquad \frac{\Delta e_{sat}}{e_{sat,w}} = x_s\,, \tag{4-61b}$$

where $\Delta e_{sat} = e_{sat,w} - e_{sat,s}$, and $x_w + x_s = 1$.

Let us now consider briefly the problem of finding values of a_w for use in (4-60). In the literature of cloud physics, the most commonly followed practice in expressing deviations from ideality has been to use the *van't Hoff factor* i, originally introduced by van't Hoff in his classic studies of osmotic pressure to account, in some poorly understood manner, for the degree of ionic dissociation in electrolytes. McDonald (1953a) effectively defined the factor i through the relation

$$a_w = \frac{n_w}{n_w + i n_s}\,. \tag{4-62}$$

This approach has been followed, for example, in the well-known cloud physics texts of Fletcher (1962a) and Mason (1971), who use this definition of i in their descriptions of the behavior of solution drops.

However, as pointed out by Low (1969a), the use of the van't Hoff factor has the practical disadvantage that relatively few values for it are available. Also, it is no coincidence that this approach is out of the mainstream of modern physical chemistry, which has largely ignored the van't Hoff factor altogether. Therefore, following Low (1969a,c), we shall now briefly introduce those parameters which are regarded by contemporary physical chemists as providing a more fundamental measure of non-ideality, and for which abundant tabulated data exist.

First of all, we introduce the *molality* concentration scale, in place of the mole fraction. The molality $\mathfrak{M}$ is defined as the number of moles of salt dissolved in 1000 g of water, so that

$$x_s = \frac{n_s}{n_s + n_w} = \frac{\mathfrak{M}}{\mathfrak{M} + (1000/M_w)}\,, \tag{4-63a}$$

or

$$\mathfrak{M} = \frac{1000 n_s}{n_w M_w} = \frac{1000 m_s}{M_s m_w}, \tag{4-63b}$$

where again, M refers to molecular weight and m to mass. It is convenient also to define the quantity

$$\hat{M} \equiv \frac{M_w}{1000}, \tag{4-64}$$

which, in combination with (4-63), gives

$$\hat{M}\mathfrak{M} = \frac{n_s}{n_w} = \frac{m_s M_w}{m_w M_s}. \tag{4-65}$$

For example, if the aqueous salt solution is present in the form of a drop of radius a and density ρ_s'', one finds

$$\hat{M}\mathfrak{M} = \frac{m_s M_w}{M_s \left(\frac{4\pi a^3}{3}\rho_s'' - m_s\right)}. \tag{4-66}$$

Now, whereas before we associated the rational activity coefficient f with the mole fraction x, we now associate a quantity called the *mean activity coefficient*, and denoted by $\gamma_\pm$, with the molality $\mathfrak{M}$. Then, in terms of $\mathfrak{M}$ and $\gamma_\pm$, the water activity of a solution of one salt in concentration $\mathfrak{M}$ turns out to be expressible in the form (e.g., Robinson and Stokes, 1970; Lewis and Randall, 1961; Low, 1969a):

$$\ln a_w = -\nu \hat{M}\mathfrak{M}\left(1 + \frac{1}{\mathfrak{M}}\int_0^{\mathfrak{M}} \mathfrak{M} d\ln\gamma_\pm\right), \tag{4-67}$$

where ν is the total number of ions a salt molecule dissociates into. This is a useful result, because extensive data for $\gamma_\pm(\mathfrak{M})$ exist.

Another quantity which appears often in the physical chemistry literature is called the *molal* or *practical osmotic coefficient*, Φ_s of the salt in solution. This is just the expression in parentheses in (4-67):

$$\Phi_s = 1 + \frac{1}{\mathfrak{M}}\int_0^{\mathfrak{M}} \mathfrak{M} d\ln\gamma_\pm, \tag{4-68}$$

and therefore also

$$a_w = \exp(-\nu \mathfrak{M} \hat{M} \Phi_s). \tag{4-69}$$

For aqueous solutions which contain several salts, and this is generally the case for cloud drops, the practical osmotic coefficient for the mixture is obtained by taking a weighted average over the molality of each component in the solution (Hänel, 1976; Thudium, 1978):

$$\Phi_{s,\mathrm{mix}}(a_w) = \frac{\sum_k \nu_k \mathfrak{M}_k \Phi_{s,k}(a_w)}{\sum_k \nu_k \mathfrak{M}_k}. \tag{4-70}$$

TABLE 4.2

Deviation of aqueous solutions from ideality at 25°C in terms of the activity a_w of water in an aqueous salt solution, the osmotic coefficient Φ_s, and the Van't Hoff factor i . For an ideal solution $a_w = 1$, $\Phi_s = 1$, $i = \nu$ (Based on data from Low, 1969a,b.)

	NaCl $\nu = 2$			$NaNO_3$ $\nu = 2$			$(NH_4)_2SO_4$ $\nu = 3$		
	a_w	Φ_s	i	a_w	Φ_s	i	a_w	Φ_s	i
0.1	0.99665	0.9324	2.65931	0.99669	0.921	1.84506	0.99586	0.767	2.30577
0.5	0.98355	0.9209	2.03730	0.98440	0.873	1.75980	0.98187	0.677	2.04969
1.0	0.96684	0.9355	1.90392	0.96980	0.851	1.72836	0.96600	0.640	1.95357
2.0	0.93162	0.9833	1.85737	0.94222	0.826	1.70215	0.93488	0.623	1.95357
5.0	0.80675	1.1916	1.86713	0.86766	0.788	1.69335	0.83080	0.672	2.26110

This result holds on the assumption that interactions between the salts in solution may be disregarded.

The parameter Φ_s was apparently first brought to the attention of cloud physicists by Byers (1965). As for sources of these various measures of non-ideality, we note that Robinson and Stokes (1970) have tabulated values for Φ_s and $\gamma_\pm$ as a function of $\mathfrak{M}$ for a large number of salts. Values for a_w and i have been computed and tabulated by Low (1969a,b) for some typical salts present in the atmosphere. (Incidentally, we should perhaps emphasize that the parameter i in Byers' description of solution drops is not the van't Hoff factor but rather is $i = \nu\Phi_s$.) In Table 4.2 we have provided values of Φ_s, a_w, and i for a few salts and concentrations. Note that for a solution to behave ideally, $\Phi_s = 1$, $i = \nu$, and $a_w = x_w$.

Significant departures from ideality are evident in Table 4.2 and in Figure 4.1. It is seen that the interaction of salt ions with water molecules results in a larger reduction of vapor pressure than is predicted by the original Raoult's law (4-61). Figure 4.2 illustrates this fact. It also shows the fairly strong dependence of vapor pressure reduction on the type of salt. This behavior may be used as a measure for the *hygroscopic* nature of salt. It has been customary to express the hygroscopicity of salts in terms of the relative humidity at which a dry salt changes ('deliquesces') into a saturated salt solution (see Table 4.3). Of course, this is also the relative humidity at which the saturated salt solution is in equilibrium with the environmental water vapor. Low (1969a) has proposed an alternative definition in which hygroscopicity is expressed in terms of the amount of salt required per 100 g of pure water to achieve a specified degree of vapor pressure lowering, i.e., a specified activity of water in solution. Low felt this definition to be somewhat more directly relevant to applications in weather modification experiments, where one generally wishes to obtain the maximum possible vapor pressure reduction for a given mass of hygroscopic salt. A comparison between the values given in Table 4.3 and Figure 4.3 shows that each of the two definitions leads to a different ranking for the hygroscopic salts.

Note also that, because of the temperature dependence of the saturation ratio through a_w (Equation (4-60)), the relative humidity at which salts deliquesce

TABLE 4.3

Critical values for the water activity a_w of water in an aqueous salt solution, for the relative humidity of moist air in equilibrium with a saturated aqueous salt solution, and for the relative humidity at which dry salt transforms into a saturated aqueous solution.

Salt	a_w of saturated salt solution (Stokes and Robinson, 1949; Robinson and Stokes, 1970) (25°C)	Relative humidity (%) for equilibrium between vapor and a saturated salt solution Robinson Stokes (1970) Admirat and Grenier, (25°C)	Relative humidity(%) for equilibrium between vapor and a saturated salt solution (Lagford, 1961; Roussel, 1968; (Twomey, 1953, 1954) 1975) (0°C)	(−20°C)	Relative humidity (%) for the transformation of 2 to 20 μm diameter salt particles to aqueous solution drops (20°C)
K_2SO_4	0.9740	97.40	-	-	97
KNO_3	0.9248	92.48	96	99	-
KCl	0.8426	84.26	88.5	96	86
$(NH_4)_2SO_4$	0.7997	79.97	-	-	80
NH_4Cl	0.7710	77.10	81	90	80.5
NaCl	0.7528	75.28	76.3	80	75-77
$NaNO_3$	0.7379	73.79	-	-	-
NH_4NO_3	0.6183	61.83	78	88	-
$Mg(NO_3)_2$	0.5286	52.86	-	-	56
$Ca(NO_3)_2$	0.4997	49.97	-	-	-
$MgCl_2.6H_2O$	0.3300	33.00	35	40	-
$CaCl_2.6H_2O$	0.2450	24.50	40	50	-

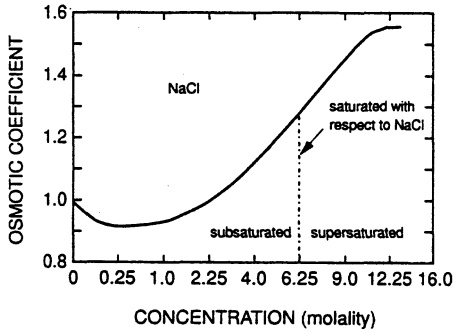


Fig. 4-1: Osmotic coefficient for NaCl as a function of molality in subsaturated, and supersaturated aqueous solution (saturation for $\mathfrak{M}$= 6.25 mole NaCl/1000 g water). (From Tang *et al.*, 1986b, with changes.)

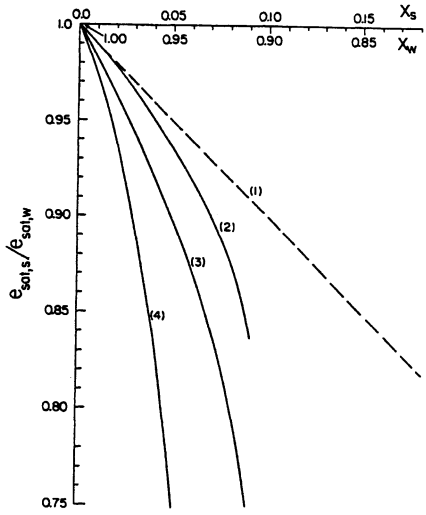


Fig. 4-2: Variation of ($e_{sat,s}/e_{sat,w}$) with mole fraction of salt in aqueous solution and with mole fraction of water in solution at 25° C, based on data of Low (1969b). (1) Equation (4-61), (2) sucrose solution, (3) NaCl solution, (4) $CaCl_2$ solution.

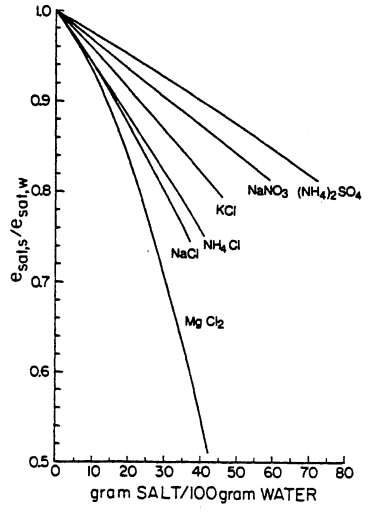


Fig. 4-3: Variation of $(e_{sat,s}/e_{sat,w})$ with concentration of salt in aqueous solution at 25° C, based on data of Low, (1969b).

changes noticeably with temperature. For example, experiments by O'Brien (1948), Lagford (1961), Hedlin and Trofimenkoff (1965), Roussel (1968), and Admirat and Grenier (1975) show that the relative humidity at which most salts in the atmosphere transform into a saturated salt solution increases by 2 to 30% as the temperature varies from +20 to −20°C. This, in part, reflects the experimental fact that the solubility of the salts studied decreases with decreasing temperature.

4.7 Latent Heat of Phase Change and its Temperature Variation

It is well-known that whenever a new phase appears, a certain amount of heat, the latent heat of phase change, is released or consumed. This latent heat can be defined in terms of the difference between the heat content (enthalpy) of the two phases involved in the phase change. Let us assume that inside a closed system consisting of two phases, a unit mass of water substance is reversibly transferred from phase ($''$), say water, of n'' moles to phase ($'$), say water vapor, of n' moles, during which time p and T of the system remain constant. The total enthalpy change must then be

$$\mathrm{d}H = \left(\frac{\partial H}{\partial n'}\right)_{T,p,n''} \mathrm{d}n' + \left(\frac{\partial H}{\partial n''}\right)_{T,p,n'} \mathrm{d}n'' . \tag{4-71}$$

But since the system is closed, $dn' = -dn''$. Therefore, denoting the partial molar enthalpies by $(\partial H/\partial n')_{p,T,n''} = h'$, $(\partial H/\partial n'')_{p,T,n'} = h''$ we find

$$\left(\frac{dH}{dn'}\right)_{p,T} = h' - h'' \equiv \mathscr{L}''^{/\prime}, \tag{4-72}$$

which defines the latent heat of phase change per mole in passing from phase ($''$) to phase ($'$). Also, since for a closed system at constant T and p we have $dh = T ds$, we may also write

$$\mathscr{L}''^{/\prime} = T(s' - s''). \tag{4-73}$$

Let us denote the molar latent heats of evaporation, sublimation, and melting for pure water substance by $\mathscr{L}_{e,0}$, $\mathscr{L}_s$ and $\mathscr{L}_{m,0}$, respectively. Then, simple conservation of energy (the first law of thermodynamics) applied to the triple point state where ice, vapor, and water are in equilibrium tells us that

$$\mathscr{L}_s = \mathscr{L}_{m,0} + \mathscr{L}_{e,0}. \qquad (T = 273.16\ \text{K}). \tag{4-74}$$

To find the temperature dependence of the latent heat, we may substitute (4-10) into (4-73) to obtain

$$\begin{aligned} \mathscr{L}''^{/\prime} &= T\left[\left(\frac{\partial \mu''}{\partial T}\right)_p - \left(\frac{\partial \mu'}{\partial T}\right)_p\right] \\ &= \left[\mu' - T\left(\frac{\partial \mu'}{\partial T}\right)_p\right] - \left[\mu'' - T\left(\frac{\partial \mu''}{\partial T}\right)_p\right], \end{aligned} \tag{4-75}$$

using (4-22). If we now take the total differential of this equation, and apply (4-10) through (4-12), we find

$$\frac{d\mathscr{L}''^{/\prime}}{dT} := (C_p' - C_p'') + \frac{dp}{dT}\left((v' - v'') - T\left[\left(\frac{\partial v'}{\partial T}\right)_p - \left(\frac{\partial v''}{\partial T}\right)_p\right]\right). \tag{4-76}$$

To a first approximation, we may ignore the second term and obtain Kirchoff's equations:

$$\frac{d\mathscr{L}_{e,0}}{dT} = C_{p,v} - C_w; \quad \frac{d\mathscr{L}_s}{dT} = C_{p,v} - C_i; \quad \frac{d\mathscr{L}_{m,0}}{dT} = C_w - C_i. \tag{4-77}$$

These turn out to be excellent approximations for most purposes. Observed values for the latent heats of evaporation $L_{e,0}$, of sublimation L_s, and of melting $L_{m,0}$ in IT cal/g and for the specific heats of water vapor $c_{p,v}$, of water c_w and of ice c_i in IT cal $(g°C)^{-1}$, and their variation with temperature, are given in Chapter 3.

4.8 Clausius-Clapeyron Equation

The conditions for equilibrium derived in Section 4.2 find a useful application in what is known as the *Clausius-Clapeyron equation.* In order to derive this equation,

consider a system of one component and two phases, ($'$) and ($''$). From the phase rule, we know there is one degree of freedom, so that, for instance, the pressure is a function only of temperature for those states corresponding to equilibrium between the two phases. The Clausius-Clapeyron equation provides an expression for the slope of this phase boundary curve in the $p - T$ plane. This may be obtained by noting that for small displacements along the curve, $\mathrm{d}\mu' = \mathrm{d}\mu''$, since $\mu' = \mu''$ along the curve (or, more accurately, on either side of the curve). Then, from (4-4b), we find

$$v'\mathrm{d}p - s'\mathrm{d}T = v''\mathrm{d}p - s''\mathrm{d}T \tag{4-78}$$

or

$$\frac{\mathrm{d}p}{\mathrm{d}T} = \frac{s' - s''}{v' - v''} = \frac{\mathscr{L}''/'}{T(v' - v'')}\,, \tag{4-79}$$

using (4-73). This is the Clausius-Clapeyron equation. As one direct application of its use note that it provides the expression for $\mathrm{d}p/\mathrm{d}T$ which is needed to integrate (4-76).

Considering the bulk phases to be water and water vapor, we thus find the saturation vapor pressure $\mathrm{e}_{\mathrm{sat,w}}$ is determined from the equation

$$\frac{\mathrm{de}_{\mathrm{sat,w}}}{\mathrm{d}T} = \frac{\mathscr{L}_{\mathrm{e},0}}{T(v_{\mathrm{v},0} - v_{\mathrm{w},0})} \approx \frac{\mathscr{L}_{\mathrm{e},0}}{Tv_{\mathrm{v},0}}\,, \tag{4-80}$$

since $v_{\mathrm{w},0} \ll v_{\mathrm{v},0}$. Analogously, if the bulk phases are ice and water vapor, or ice and water, we have

$$\frac{\mathrm{de}_{\mathrm{sat},i}}{\mathrm{d}T} = \frac{\mathscr{L}_s}{T(v_{\mathrm{v},0} - v_i)} \approx \frac{\mathscr{L}_s}{Tv_{\mathrm{v},0}} \tag{4-81}$$

and

$$\frac{\mathrm{d}p_m}{\mathrm{d}T} = \frac{\mathscr{L}_{m,0}}{T(v_{\mathrm{w},0} - v_i)}\,. \tag{4-82}$$

If we further assume the ideal gas law (Equation (4-24)), we obtain

$$\frac{\mathrm{d}\ln \mathrm{e}_{\mathrm{sat,w}}}{\mathrm{d}T} \approx \frac{\mathscr{L}_{\mathrm{e},0}}{\mathscr{R}T^2} \tag{4-83}$$

and

$$\frac{\mathrm{d}\ln \mathrm{e}_{\mathrm{sat},i}}{\mathrm{d}T} \approx \frac{\mathscr{L}_s}{\mathscr{R}T^2}\,. \tag{4-84}$$

If one includes the approximate temperature dependence given by (4-77), then (4-83) and (4-84) determine $\mathrm{e}_{\mathrm{sat,w}}$ and $\mathrm{e}_{\mathrm{sat},i}$, respectively, to an accuracy quite sufficient for applications in cloud microphysics. In addition, as a practical alternative, Lowe and Ficke (1974) have provided expressions which they feel are convenient for typical modern numerical simulations of cloud physical processes. Their expressions are given in Appendix A-4.8, Equation (A.4-1). They are curve fits based on the Goff (1942, 1949) integrations of the Clausius-Clapeyron equation, wherein the virial equation of state for water vapor was used. For practical purposes, the reader may also use the so-called Magnus Equation as given in the Landolt-Börnstein Tables (1988) (see Appendix A-4.8, Equations (A.4-2) and (A.4-3)). Goff's accurate

values are tabulated in the Smithsonian Meteorological Tables. Unfortunately, these suffer from the 1954 revision of the temperature scale (Stille, 1961). However, comparison shows that both the SMT values and the values subsequently revised by Goff (1957, 1965) agree to within 0.035% over the whole temperature range of meteorological interest (Murray, 1967a, 1970). According to Goff (1965), $e_{sat,w}(T_{tr} \equiv 0.01°C) = 6.1112$ mb, and $e_{sat,w}(T_0 \equiv 0°C\ p = 1\ atm.) = 6.1067$ mb. The former result is in excellent agreement with the experimental value obtained at the U.S. National Bureau of Standards by Guilder *et al.* (1975) who determined $e_{sat,w}(T_{tr}) = 6.11657$ mb (± 0.00010 mb, at the 90% confidence level).

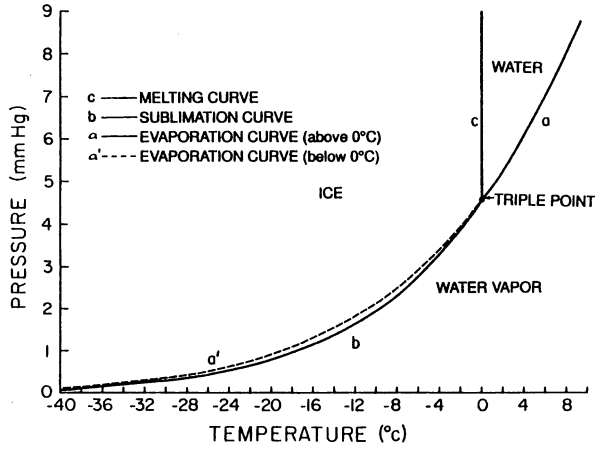


Fig. 4-4: p-T phase diagram for bulk water substance, based on data of the Smithsonian Meteorological Tables (1968).

The temperature variation of the saturation vapor pressures is shown in Figure 4.4. Note that $e_{sat,w} > e_{sat,i}$ for $T < 0°C$. This is also obvious on comparison of (4-80) and (4-81), since $\mathscr{L}_s > \mathscr{L}_{e,0}$. A closer inspection of Figure 4.4 reveals a single maximum for the difference $e_{sat,w} - e_{sat,i}$, which we can calculate by noting that the slopes of the curves are equal where the difference is a maximum. Therefore, on setting (4-83) and (4-84) equal for the temperature T_{max} which yields a maximum difference, we find

$$\left(\frac{e_{sat,w}}{e_{sat,i}}\right)_{T=T_{max}} = \left(\frac{\mathscr{L}_s}{\mathscr{L}_{e,0}}\right)_{T=T_{max}} . \tag{4-85}$$

Now, if we integrate the difference between (4-80) and (4-81) from T_{max} to $T_0 = 273.15$ K, holding $\mathscr{L}_{m,0}$ constant and taking into account that $e_{sat,i} = e_{sat,w}$ at $T = T_0$, we find that

$$\ln\left(\frac{e_{sat,w}}{e_{sat,i}}\right)_{T=T_{max}} = \frac{\mathscr{L}_{m,0}}{\mathscr{R}}\left(\frac{T_0 - T_{max}}{T_0 T_{max}}\right) . \tag{4-86}$$

Combining (4-85) and (4-86), we obtain the following expression for $T_{\max}$

$$T_{\max} = T_0 - \frac{T_0 T_{\max} \mathscr{R}}{\mathscr{L}_{m,0}} \ln \left(\frac{\mathscr{L}_s}{\mathscr{L}_{e,0}} \right)_{T=T_{\max}} . \tag{4-87}$$

Solving this equation by iteration gives $T_{\max} = 261.37$ K, or about $-11.8°$C. This agrees to within 0.1°C with the value found from the Goff expressions for e_{sat}, which again indicates the accuracy of the ideal gas law approximation. Finally, the variation of $e_{sat,w} - e_{sat,i}$ is illustrated in Figure 4.5.

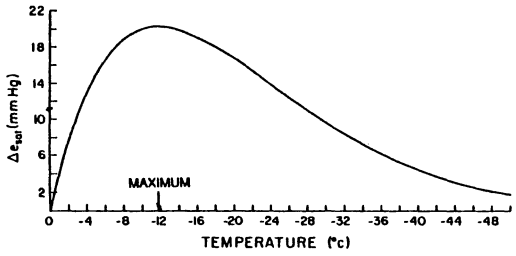


Fig. 4-5: Variation with temperature of $\Delta\, e_{sat} = (e_{sat,w} - e_{sat,i})$.

Of course, the interesting point to emphasize here is that air saturated with respect to ice is always subsaturated with respect to water, with the consequence that supercooled water drops and ice crystals cannot co-exist in equilibrium. As we mentioned in Chapter 1, this important fact, as first realized by Wegener in 1911, is the basis of the Wegener-Bergeron-Findeisen precipitation mechanism.

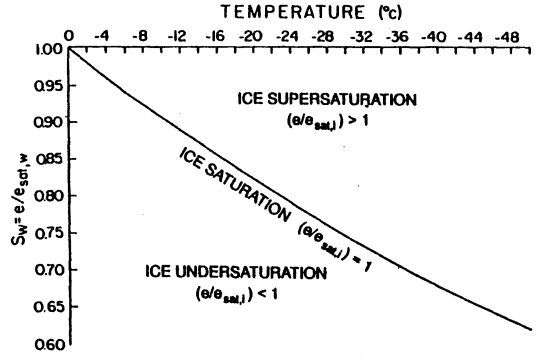


Fig. 4-6: Ice saturation as a function of saturation ratio with respect to water at temperatures below 0°C.

It is also worth emphasizing that at sufficiently low temperatures, air may be ice-supersaturated but water-subsaturated. This is illustrated in Figure 4.6. Similarly, Figure 4.7 shows the ice-supersaturations which are required for water-supersaturation to occur also.

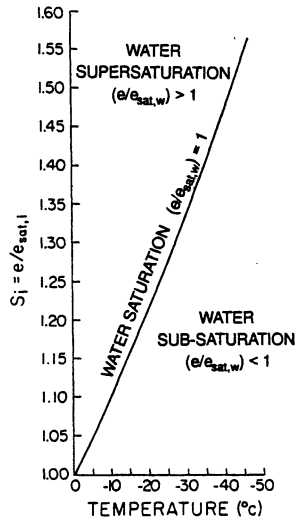


Fig. 4-7: Water saturation as a function of saturation ratio with respect to ice at temperatures below 0°C.

Let us now consider the equilibrium between bulk ice and water which is described by (4-82). No simplification can be made in this equation since $v_{w,0} \approx v_i$. Since at all temperatures below 0°C, $v_i > v_{w,0}$, we find that $(dp_m/dT) < 0$. In fact, experiments show that $(dp_m/dT) = -146.7$ atm $(°C)^{-1}$ at 0°C, which means that, at any given temperature, ice melts on applying sufficiently high pressures. The temperature variation of the melting pressure of ice is given in Figure 4.8. As an example, we note that at −10°C a very large pressure of 1100 atm. is required to melt ice. As we mentioned briefly earlier, it is a consequence of this melting pressure effect that the triple point of water substance is slighty higher than the ice point. Experiments have shown that by opening a vessel in which ice, water and water vapor are originally in equilibrium, and exposing it to air of 1 atm., the equilibrium temperature is reduced by 0.0098±0.0003°C, the pressure effect contributing 0.0075°C, while an additional 0.0023°C is due to the dissolved air. By international agreement, the total temperature difference between the triple point and ice point has been set equal to 0.0100°C, and the temperature of the triple point itself has been set equal to $T_{tr} = 273.16$ K (Stille, 1961). Therefore, the temperature of the ice point is $T_0 = (T_{tr} - 0.01)$ K $= 273.15$ K $\equiv 0.0$°C.

In addition to affecting the melting temperature of ice, pressure also affects its crystal structure. The phenomenon that a single chemical substance may appear in different crystallographic modifications is called *polymorphy.* At present, 11 polymorphic forms of ice have been found. Hobbs (1974) and Fletcher (1970a) have discussed in detail these crystallographic forms and the thermodynamic conditions for which they are stable and in equilibrium with each other. They are of little concern to us since they are not stable at typical atmospheric temperatures and pressures.

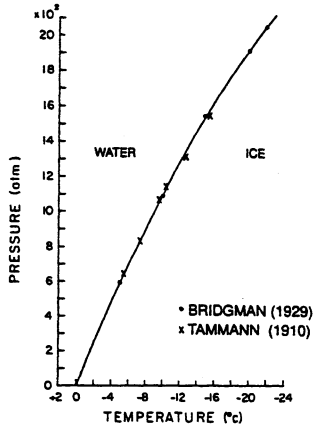


Fig. 4-8: The melting curve for ice-I_h.

Let us consider Figure 4.4 once more and note an interesting observation which can be made regarding the transformation of one phase into another. Suppose, for instance, that water vapor is cooled at constant pressure above the triple point. We see that eventually a temperature is reached at which the vapor is saturated (curve a). Upon further cooling, the evaporation curve is crossed and conditions are reached at which water is the stable phase. On cooling still further, the melting curve is crossed and conditions are reached at which ice is the stable phase. However, observations show that neither water nor ice appear at the temperatures predicted by the equilibrium phase diagram for bulk water substance. Unless suitable impurities are present in the vapor or on the walls enclosing the system, the water vapor *supersaturates* and water *supercools*. (By definition, the supersaturation of water vapor is described by (4-37), and the supercooling of water is defined by the quantity $\Delta T = T_0 - T$, where $T_0 = 273.15$ K.) The reason for this behavior (discussed in Chapters 7 and 9) rests in the fact that, during a phase change, the new phase always appears in the form of a small particle with a highly curved surface. The equilibrium conditions for such highly curved phases are not described by the Clausius-Clapeyron equation.

Another, similarly incorrect prediction is made by Figure 4.4. If water vapor is cooled isobarically below the triple point, the sublimation curve is crossed before the evaporation curve. This means that, upon cooling, those conditions are reached at which ice is the stable phase before water is; i.e., the phase diagram for bulk water predicts that ice will appear first at temperatures below the triple point. Observations, however, show that unless suitable impurities are present, the metastable phase, i.e., supercooled water, always appears before ice. The reason for this behavior again lies in the fact that phase change proceeds via the formation of new phase particles with highly curved surfaces. We shall show in Chapters 7 and 9 that, unless suitable impurities are present in the system, the formation of water drops is energetically favored at all temperatures over the formation of ice

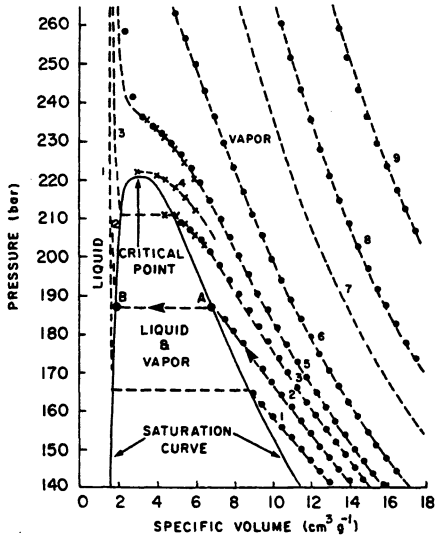


Fig. 4-9: p-V phase diagram for bulk water substance. Dashed lines represent isotherms: (1) 350 K, (2) 360 K, (3) 370 K, (4) 374 K, (5) 380 K, (6) 400 K, (7) 450 K, (8) 500 K, (9) 600 K; based on experiments of Bain (1964), and of Nowak *et al.* (1961). • based on Keyes's (1949) empirical formula. × based on Nowak and Grosh's (1961) empirical formula. (From *The Structure and Properties of Water* by D. Eisenberg and W. Kauzmann, copyrighted by Oxford Univ. Press, 1969.)

crystals directly from the vapor.

Thus far, we have displayed the equilibrium behavior of bulk water substance in the form of a $p - T$ phase diagram. Further information on the equilibrium behavior may be obtained from a $p - V$ phase diagram (Figure 4.9). Note that during isothermal compression, a state (e.g., state A) is reached at which water vapor is saturated with respect to water. If the walls enclosing the vapor are ideally rough, further compression results in the condensation of vapor to liquid. Along the line AB, $e = e_{sat,w}$ which remains constant as the specific volume decreases from that of pure vapor to that of pure liquid water. The small compressibility of liquid water is revealed by the steep excursion of the isotherm to the left of B.

At the top of the phase boundary curve is the *critical point* where the distinction between liquid and gas vanishes. At this extraordinary point, the surface tension or surface energy of the interface separating the phases becomes zero. Atmospheric water always lies far below the critical point, which occurs at $p_{cr} = 221$ bars (1 bar = 106 dynes cm^{-2} = 0.9869 atm.) and $T_{cr} = 374$°C. The concept of the critical point illuminates the distinction between water vapor and the other, permanent, atmospheric gases: the latter have critical temperatures far below atmospheric temperatures and, thus, never change phase. Note that this is not a consequence of an insufficiently massive atmosphere, as no amount of pressure can liquify them as long they remain above the critical temperature.

For completeness, in Figure 4.10 the *thermodynamic surface* of water in $p-V-T$

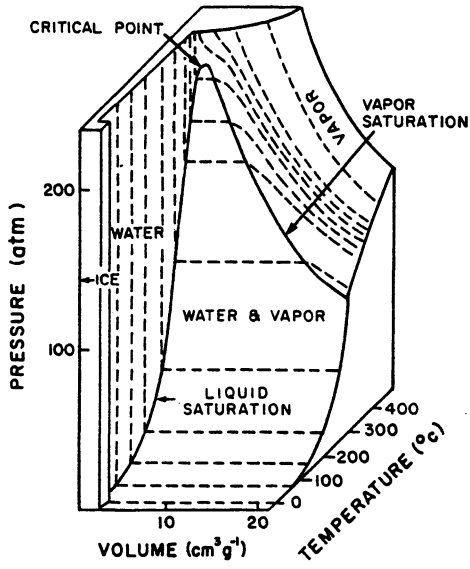


Fig. 4-10: Three-dimensional phase diagram for bulk water substance (dashed lines represent isotherms). (From *The Structure and Properties of Water* by D. Eisenberg and W. Kauzmann, copyrighted by Oxford Univ. Press, 1969.)

space is shown. The projection of this surface on the $p - T$ plane and the $p - V$ plane yields the phase diagrams shown in Figures 4.4 and 4.9, respectively.

4.9 Equilibrium Between an Aqueous Salt Solution and Ice

Experiments have shown that the equilibrium temperature between ice and an aqueous salt solution is lower than that between ice and pure water. This is a direct consequence of the lowering of vapor pressure over a salt solution, as illustrated in Figure 4.11. In order to derive an expression for this temperature lowering effect, consider a system open to the atmosphere, and consisting of air and an aqueous salt solution in equilibrium with ice (assumed to be free of salt) of chemical potential μ_i. The condition of chemical equilibrium between the pure ice and water in aqueous solution, assuming p and T to be uniform throughout the system, is just $\mu_i(p,T) = \mu_w(p,T)$, from (4-22). Therefore, on substitution from (4-53), we obtain

$$\mu_i(p,T,a_w) = \mu_{w,0}(p,T) + \mathscr{R}T \ln a_w \,. \tag{4-88}$$

From the phase rule, (4-23), we have $\varphi = 3$ (water, ice, air), $c = 3$ (salt, water, air) and, thus, $w = 2$. Let us assume the atmospheric air pressure is fixed at 1 atm., so that $w = 1$. Then, the equilibrium temperature becomes a function of the salt concentration, and we must therefore investigate the variation of a_w with T. Directly from (4-88), we see that equilibrium can be maintained for variable T

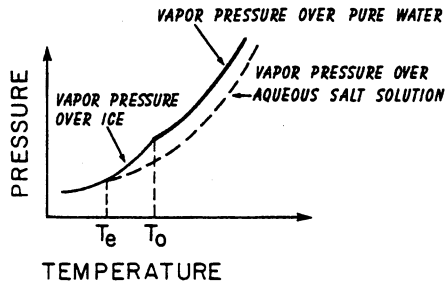


Fig. 4-11: Schematic to illustrate the temperature equilibrium between ice and aqueous salt solutions, and between ice and pure water.

only if

$$\left[\frac{\partial\left(\frac{\mu_i}{T}\right)}{\partial T}\right]_p = \left[\frac{\partial\left(\frac{\mu_{w,0}}{T}\right)}{\partial T}\right]_p + \mathscr{R}\left(\frac{\partial \ln a_w}{\partial T}\right)_p . \tag{4-89}$$

On substituting (4-13a) and (4-72), this becomes

$$\left(\frac{\partial \ln a_w}{\partial T}\right)_p = \frac{h_{w,0} - h_i}{\mathscr{R}T^2} = \frac{\mathscr{L}_{m,0}}{\mathscr{R}T^2} \tag{4-90}$$

which, upon integration, yields assuming $\mathscr{L}_{m,0}$ is independent of T,

$$\ln a_w = -\frac{\mathscr{L}_{m,0}}{\mathscr{R}T} + f(p) . \tag{4-91}$$

The unknown function $f(p)$ may be determined by noting that $a_w = 1$ for $T = T_0$; thus, the *equilibrium freezing temperature* T_e may be determined from the relation

$$\frac{\mathscr{L}_{m,0}}{\mathscr{R}}\left(\frac{T_0 - T_e}{T_0 T_e}\right) = -\ln a_w . \tag{4-92}$$

Since $a_w \leq 1$, we have $T_e \leq T_0$, as expected. The extent of the temperature lowering effect is generally measured by the *equilibrium freezing point depression*, defined as

$$(\Delta T)_{e,s} \equiv T_0 - T_e = -\frac{\mathscr{R}T_0T_e}{\mathscr{L}_{m,0}} \ln a_w \tag{4-93}$$

$$= \frac{\mathscr{R}T_0T_eM_w}{1000\mathscr{L}_{m,0}} \nu\Phi_s\mathfrak{M} , \tag{4-94}$$

using (4-69). Let us now suppose the solution is very dilute, so that $T_0T_e \approx T_0^2$ and $a_w \approx 1 - x_s$. Then, $\ln a_w \approx -x_s \approx -n_s/n_w$, and (4-93) becomes, using (4-65),

$$(\Delta T)_{e,s} \approx \frac{\mathscr{R}T_0^2 n_s}{\mathscr{L}_{m,0} n_w} = K_f\mathfrak{M} , \tag{4-95}$$

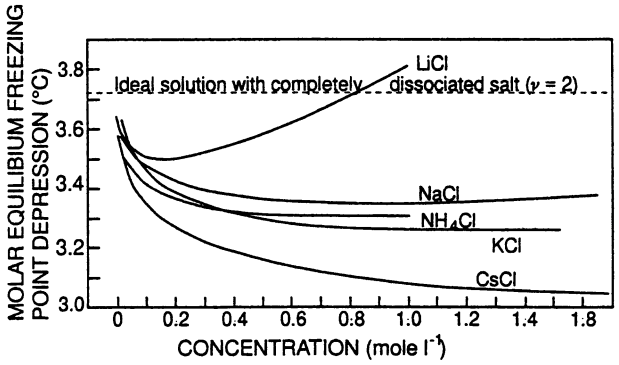


Fig. 4-12: Molar equilibrium freezing point depression for different aqueous salt solutions as a function of salt concentration.

where

$$K_f = \frac{\mathscr{R} T_0^2 M_{\mathrm{w}}}{1000 \mathscr{L}_{m,0}} \tag{4-96}$$

is the *molal equilibrium freezing point depression.* For water at 0°C, we find $K_f = 1.859°\mathrm{C\ mole}^{-1}$. For non-ideal or more concentrated solutions, (4-95) is inadequate. For these more realistic cases, $(\Delta T)_{\mathrm{e},s}$ depends noticeably on the nature of the dissolved salt, i.e., its degree of dissociation and the capability of its ions in solution for interacting with each other and the water molecules. The deviation of the molal equilibrium freezing point depression from ideality is illustrated in Figure 4.12 which shows experimental values for $(\Delta T)_{\mathrm{e},s}/\mathfrak{M}$. (In Figure 4.12 the small difference between the molal and molar units has been neglected.)

CHAPTER 5

SURFACE PROPERTIES OF WATER SUBSTANCE

In clouds, the liquid and solid phases of water are highly dispersed, with a large surface-to-volume ratio. As might be expected, this necessitates going beyond the bulk phase descriptions of the previous chapter, even for the most rudimentary understanding of the formation and growth of cloud particles. Therefore, in this chapter we shall consider briefly the essential distinctive surface properties of ice and water, and explore some of their more immediate consequences. Additional relevant material may be found in Hobbs (1974), Samorjai (1972), Bikerman (1970), Flood (1967), Reiss (1965), Osipow (1962), Defay *et al.* (1966), Davies and Rideal (1961), Adamson (1960), Ono and Kondo (1960), and Landau and Lifschitz (1958).

5.1 Surface Tension

Phases in contact are separated by a thin transitional region, generally only a few molecules thick; consequently, a useful abstraction is to regard such an interface as a geometrical surface. This permits a relatively simple and generally adequate description of surface effects via the usual straightforward machinery of macroscopic thermodynamics. Of course, this ceases to be a reasonable procedure when the bulk phases themselves have a similar microscopic thickness. In this chapter, we shall not consider such difficult circumstances. Such problems do arise, however, in the theory of homogeneous nucleation (Chapter 7); there we shall see how macroscopic thermodynamics must be supplanted, at least in part, by a detailed statistical mechanics approach in order that a satisfactory understanding of nucleation phenomena can be achieved.

The extension of our thermodynamic systems to include surface effects is conceptually simple: in complete analogy to the contribution $-p\mathrm{d}V$ of pressure-volume work to the internal energy, we now introduce a contribution $\sigma\mathrm{d}\Omega$, where Ω denotes the area of the *surface of separation*, and σ is the *surface tension*. The quantity σ is an intensive thermodynamic variable, and is seen to have the dimensions of energy per unit area, or force per unit length. The physical basis of this formulation is probably familiar to the reader from the example of a liquid drop: on average, molecules in the drop interior find themselves in a symmetrical, attractive force field, while molecules in the surface layer do not, and in fact experience a net attractive force toward the interior. As a consequence of this inward pull, the surface is in a state of tension, and it requires work to extend the surface further. On the molecular level, this work is seen to be that required to bring molecules from the interior to the surface, against the attractive forces.

The thermodynamic properties of the surface are so distinctive that it is conceptually useful to regard it as a separate phase, (σ), having its own entropy,

$S^{(\sigma)}$, adsorbed number of moles of chemical component k, $n_k^{(\sigma)}$, and so forth. Then, in accordance with the discussion above, the change in internal energy $U^{(\sigma)}(S^{(\sigma)}, \Omega, n_k^{(\sigma)})$ of the surface phase for reversible processes is (cf. (4-1)):

$$\mathrm{d}U^{(\sigma)} = T^{(\sigma)}\mathrm{d}S^{(\sigma)} + \sigma\mathrm{d}\Omega + \sum_{k=1}^{c} \mu_k^{(\sigma)}\mathrm{d}n_k^{(\sigma)}\,, \tag{5-1}$$

where the $\mu_k^{(\sigma)}$ are the surface chemical potentials.

5.2 Equilibrium Conditions

Let us now generalize our discussion in Section 4.2 of the equilibrium between two bulk phases ($'$) and ($''$), by also taking into account the surface phase (σ) which separates them. Proceeding as before, we imagine that each bulk phase is originally isolated and in internal equilibrium. After removing the constraint of isolation, we seek the conditions on the intensive variables which are necessary and sufficient to insure equilibrium throughout the system, which remains isolated as a whole. The independent extensive variables for the entire system are $V = V' + V''$, $S = S' + S'' + S^{(\sigma)}$, $n_k = n_k' + n_k'' + n_k^{(\sigma)}$, and Ω. Similarly, the total internal energy is $U = U' + U'' + U^{(\sigma)}$, and the generalized equilibrium condition which replaces (4-15) is

$$(\delta U)_{S,V,\Omega,n_k} \geq 0\,. \tag{5-2}$$

Then, from (4-1), (5-1), and (5-2), the expanded form of the equilibrium condition is

$$\begin{aligned}\delta U = \; & T'\delta S' + T''\delta S'' + T^{(\sigma)}\delta S^{(\sigma)} - p'\delta V' - p''\delta V'' + \sigma\delta\Omega \\ & + \sum_{k=1}^{c} \mu_k'\delta n_k' + \sum_{k=1}^{c} \mu_k''\delta n_k'' + \sum_{k=1}^{c} \mu_k^{(\sigma)}\delta n_k^{(\sigma)} \geq 0\,,\end{aligned} \tag{5-3}$$

where, from the constraint of isolation of the system as a whole, we have the additional conditions

$$\begin{aligned}\delta S &= \delta S' + \delta S'' + \delta S^{(\sigma)} = 0\,; \\ \delta n_k &= \delta n_k' + \delta n_k'' + \delta n_k^{(\sigma)} = 0\,; \\ \delta V &= \delta V' + \delta V'' = 0\,.\end{aligned} \tag{5-4}$$

None of these conditions is violated if we conceive a set of infinitesimal variations for which $\delta S' = 0$ and $\delta n_k' = 0$. Let us also suppose the bulk phase ($''$) is a sphere of radius a, so that $\mathrm{d}\Omega = 2\mathrm{d}V''/a$. With these specializations and (5-4), (5-3) becomes

$$(T'' - T^{(\sigma)})\delta S'' + \left(p' - p'' + \frac{2\sigma}{a}\right)\delta V'' + (\mu_k'' - \mu_k^{(\sigma)})\delta n_k'' \geq 0\,. \tag{5-5}$$

Since $\delta S''$, $\delta V''$, and $\delta n_k''$ represent independent and arbitrary variations, each coefficient must vanish. A similar result would have been obtained had we originally

chosen $\delta S'' = \delta n_k'' = 0$. Therefore, the condition of thermodynamic equilibrium leads finally to

$$T' = T'' = T^{(\sigma)}, \tag{5-6}$$

$$p'' - p' = \frac{2\sigma}{a}, \tag{5-7}$$

$$\mu_k' = \mu_k'' = \mu_k^{(\sigma)}, \qquad k = 1, 2, \ldots, c. \tag{5-8}$$

Comparison with (4-20) to (4-22) shows that only the condition of mechanical equilibrium has a new form; this is expressed by (5-7) and is called the *Laplace formula.* It may also be obtained by more elementary means, e.g., by equating the surface tension force along the circumference of a great circle of the sphere with the pressure difference acting across the great circle area.

The extension of these results to a more general system comprised of φ phases and χ spherically curved interfaces is obvious: for thermodynamic equilibrium to exist we must have uniform temperatures (thermal equilibrium) and uniform chemical potentials (chemical equilibrium) throughout the entire system. Additionally, a relation of the form of (5-7) (mechanical equilibrium) must hold for every pair of bulk phases, the greater pressure occurring on the concave side of the interface whose radius of curvature replaces a in (5-7).

5.3 Phase Rule for Systems with Curved Interfaces

Let us now consider the generalization of the phase rule (Section 4.3) to a system of φ bulk phases, c components, and χ curved surface phases. As before, we want to determine the number of intensive variables which may be altered independently without causing the system to depart from equilibrium. In this connection, therefore, we must consider what to use for the intensive variable corresponding to the quantity $n_k^{(\sigma)}$, the number of moles of component k adsorbed into the interface (σ). An obvious natural choice is the *adsorption,* defined by

$$\Gamma_k^{(\sigma)} \equiv \frac{n_k^{(\sigma)}}{\Omega^{(\sigma)}}, \qquad k = 1, 2, \ldots, c; \quad \sigma = 1, 2, \ldots, \chi, \tag{5-9}$$

where $\Omega^{(\sigma)}$ is the area of the interface (σ).

The number of intensive variables required to specify the state of the system in equilibrium must therefore include: (1) the common temperature T; (2) the $c\chi$ adsorptions $\Gamma_k^{(\sigma)}$ in the surface phases; (3) the $c\varphi$ mole fractions $x_k^{(\sigma)}$ in the bulk phases $(\alpha = 1, 2, \ldots, \varphi)$; (4) the φ pressures $p^{(\alpha)}$ of the bulk phases; and (5) the χ mean radii of curvature $a^{(\sigma)}$. This constitutes a total of $1 + (\varphi + \chi)(c + 1)$ intensive variables. Constraints among them include the following: (1) the mole fractions $\chi_k^{(\alpha)}$ must sum to unity for each bulk phase, leading to φ constraints; (2) the chemical potentials must be equal for all the phases for every k, leading to $c(\chi + \varphi - 1)$ constraints; (3) each interface gives rise to a conditional of mechanical equilibrium like (5-7), leading to χ constraints. This gives a total of $(\varphi+\chi)(c+1)-c$ constraints, and so we find for the variance of the system,

$$w = c + 1 \tag{5-10}$$

An interesting feature of this result is that the variance is independent of the number of bulk and surface phases.

Note that in the case that one of the components of the system is not present in one of the phases (e.g., humid air surrounding aqueous NaCl solution), one of the equations relating the chemical potentials disappears. On the other hand, for the phase in question, one must write $\sum_{k=1}^{c-1} x_k^{(\alpha)} = 1$, and add the relation $x_{i\neq k}^{(\alpha)} = 0$. This expresses the fact that component i is not present in the phase (α). Thus, the total number of relations remains the same and (5-10) does not change.

Let us now consider four simple examples which will illustrate the use of (5-10). First, consider a system of uniform temperature T in which a pure water drop of radius a is surrounded by pure water vapor of pressure e_a. From (5-10), w = 2 since $c = 1$. Thus, we may choose, for example, to hold T constant and study the dependence of e_a on a. Second, consider a system of uniform temperature T in which a drop of pure water of radius a is surrounded by humid air of total pressure p. From (5-10), w = 3; to study the dependence of e_a, on a we must hold both T and p constant. Third, consider a system of uniform temperature T in which an aqueous solution drop of radius a is surrounded by humid air of pressure p. Since $c = 3$ (water, salt, air), we find w = 4. However, since the total mass of salt in the drop does not change, even though the drop may change its radius by acquiring or losing water as a result of water vapor diffusion to or from the drop, the mole fraction of the water in solution becomes a function of the drop radius. This constitutes an additional relation not considered in (5-10). Thus, w = 3 as in the case of a pure water drop in humid air, and we may again choose to hold T and the total gas pressure p constant and study the dependence of e_a on a. Fourth, consider a system of uniform temperature T in which a pure water drop of radius a_w and a spherical ice crystal of radius a_i are surrounded by humid air of total gas pressure p. From (5-10), w = 3. We may choose to hold p constant and, thus, dispose of one of the intensive variables, so that the system at equilibrium is divariant. This is in contrast to a system of 3 bulk phases which, at equilibrium, is non-variant once p is fixed (Section 4.3). Thus, we may independently vary a_w and a_i and investigate the effect of their variation on the equilibrium temperature of the system. It is clear that if a_w and a_i are given, the system has no further variance at equilibrium.

5.4 Water-Vapor Interface

The difference between the pressure p_w inside a water drop of radius a and the pressure $e_{sat,w}$ of vapor with which it is in equilibrium is given by (5-7):

$$p_w - e_{sat,w} = \frac{2\sigma_{w/v}}{a}, \tag{5-11}$$

where now we have introduced the subscript w/v for the surface tension to emphasize that it is the water-vapor interface which is involved. Given that $\sigma_{w/v} \approx 76$ dyne cm^{-1} at 0°C, we see that the pressure difference is about 1.5 atm. for $a = 1\,\mu$m; smaller drops have correspondingly larger internal pressure.

For practical purposes, one may replace $\sigma_{w/v}$ in (5-11) by $\sigma_{w/a}$, the surface tension for a water-humid air interface. Experiments by Richards and Carver (1921) and Adam (1941) have shown that $\sigma_{w/a}$ increases by less than 0.05% if air at 1 atm. is replaced by pure water vapor at saturation pressure (at the same temperature).

Recent experimental studies and theoretical modeling involving molecular dynamics have shown that water molecules on the liquid side of the water interface tend to project both hydrogen atoms preferentially towards the liquid interior, exposing the oxygen atom to the vapor side. This arrangement yields a surface potential of +0.16 Volt at 300 K (Matsumoto and Kataoke, 1988; Wilson and Pokorille, 1987; Gok *et al.*, 1988).

5.4.1 Effect of Temperature on the Surface Tension of Water

As would be expected on consideration of the effects of thermal agitation, the surface tension of water decreases with increasing temperature. This behavior has been investigated experimentally by Dorsch and Hacker (1951) and Gittens (1969). Their results are shown in Figure 5.1. Although the measurements of Gittens have been carried out by a more refined experimental technique, we have preferred the values of Dorsch and Hacker, who extended their measurements into the regime of supercooled water, thus making possible an extrapolation to near $-40°C$. In order to be consistent with our discussion in Section 3.4, we have used as a criterion for the extrapolation the occurrence of sigularity behavior of liquid water near $-45°C$. The proposed values for the surface tension fit the relation

$$\sigma_{w/a} = \sum_{n=0}^{6} a_n T^n , \tag{5-12}$$

where $\sigma_{w/a}$ is in erg cm^{-2}, T in °C, and where $a_0 = 75.93$, $a_1 = 0.115$, $a_2 = 6.818 \times 10^{-2}$, $a_3 = 6.511 \times 10^{-3}$, $a_4 = 2.933 \times 10^{-4}$, $a_5 = 6.283 \times 10^{-6}$, $a_6 = 5.285 \times 10^{-8}$.

5.4.2 Surface Tension of Aqueous Salt Solutions

Let us now consider the effect of dissolved salts on the surface tension of water. Given that the liquid surface is in a state of strain owing to a residual force field, we expect that the adsorption onto the surface layer of some chemical component to concentrations higher than that which appears in the bulk phase will occur if such behavior will serve to lower the state of strain, and vice versa. Therefore, we expect that if a solute can lower the surface tension, it will appear in a greater relative concentration at the interface than in the bulk solution. Materials which cause this to happen to a marked degree are called *surface active.* Conversely, solutes which can increase the surface tension should appear in a relatively weaker concentration at the interface; this behavior is known as *negative adsorption.*

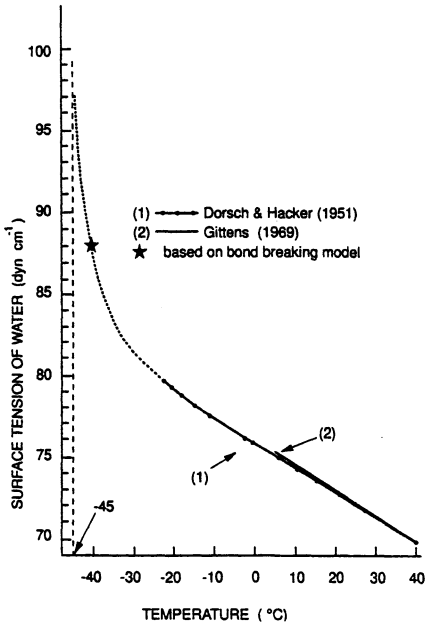


Fig. 5-1: Variation with temperature of the surface tension of water, extrapolated to be consistent with the $-45°C$ limit. (From Pruppacher, 1995; by courtesy of the Am. Meteor. Soc., and the author.)

An expression relating surface tension to adsorption may be derived most easily by integrating (5-1) in the same manner that led to (4-3). The result is

$$U^{(\sigma)} = T^{(\sigma)}S^{(\sigma)} + \sigma\Omega + \sum_{k=1}^{c} \mu_k^{(\sigma)} n_k^{(\sigma)} . \tag{5-13}$$

Now, on subtracting (5-1) from the differential of this equation, we obtain the surface phase form of the Gibbs-Duhem equation (cf. (4-4)):

$$S^{(\sigma)}\mathrm{d}T + \Omega\mathrm{d}\sigma + \sum_{k=1}^{c} n_k^{(\sigma)}\mathrm{d}\mu_k^{(\sigma)} = 0 \tag{5-14}$$

or

$$\mathrm{d}\sigma = -s^{(\sigma)}\mathrm{d}T - \sum_{k=1}^{c} \Gamma_k^{(\sigma)}\mathrm{d}\mu_k^{(\sigma)} , \tag{5-15}$$

where we have used (5-9) and $s^{(\sigma)} = S^{(\sigma)}/\Omega$ is the surface specific entropy. For constant T, (5-15) reduces to the *Gibbs adsorption isotherm* equation:

$$\Gamma_k^{(\sigma)} = -\left(\frac{\partial\sigma}{\partial\mu_k^{(\sigma)}}\right)_{T,\mu_j^{(\sigma)}} , \quad j \neq k . \tag{5-16}$$

Let us apply this result to the case of a binary solution of a salt in water. Denote the chemical potential of the salt in the solution-vapor interface by $\mu_s^{(s/v)}$. For equilibrium changes, we have $d\mu_s^{(s/v)} = d\mu_s$ from (5-8), where μ_s is the chemical potential of the salt in the bulk phase. For the latter, however, we have the form (4-54); therefore, at constant T and p, the adsorption of the salt is described by

$$\Gamma_s^{(s/v)} = -\left(\frac{\partial \sigma_{s/v}}{\partial \mu_s}\right)_{T,p} = -\frac{1}{\mathscr{R}T}\left(\frac{\partial \sigma_{s/v}}{\partial \ln a_s}\right)_{p,T} . \tag{5-17}$$

Also, from 4-4a we have $n_s d\mu_s = -n_w d\mu_w$,. therefore, on substituting (4-53) and (4-54) for μ_w and μ_s into this expression, and introducing (4-69), we obtain another form for $\Gamma_s^{(s/v)}$:

$$\Gamma_s^{(s/v)} = -\frac{\mathfrak{M}}{\mathscr{R}T\nu\Phi_s}\left(\frac{\partial \sigma_{s/v}}{\partial \mathfrak{M}}\right)_{p,T} . \tag{5-18}$$

In order to interpret this result, we must consider more closely the meaning of the quantity $n_k^{(\sigma)}$ in (5-9). Implicit in our abstraction of the transition zone between bulk phases to a geometric surface of separation has been the assumption of the homogeneity of these adjacent phases up to their contact with the surface. Thus, in the expression $n_k^{(\sigma)} = n_k - n_k' - n_k''$, where n_k is the total number of moles of component k in the real system, the quantities n_k', n_k'' are the corresponding number of moles in the homogeneous phases ($'$) and ($''$), assumed to retain their bulk properties up to the geometric interface. Referring now to the present example of a solution drop, we see therefore that if $n_s^{(s/v)} > 0$ (i.e., $\Gamma_s^{(s/v)} > 0$), there must be a higher concentration of salt in the transition region than in the interior of the drop, and vice versa. Consequently, the result (5-18) does support our qualitative expectations: for positive (negative) adsorption, the surface tension decreases (increases) with increasing concentration.

For most salts which are present in clouds, it has been found experimentally that if $\mathfrak{M} \lesssim 10^{-3}$ mole $(1000\ g)^{-1}$, then $(\partial\sigma_{s/v}/\partial\mathfrak{M}) < 0$, i.e., $\Gamma_s^{(s/v)} > 0$; at larger concentrations, $(\partial\sigma_{s/v}/\partial\mathfrak{M}) > 0$, meaning $\Gamma_s^{(s/v)} < 0$ (Jones and Ray, 1937). If we evaluate (5-18) for a 1 molal NaCl solution at 0°C ($\nu = 2$, $\Phi = 0.9355$, $\mathfrak{M} = 1$), we obtain $\Gamma_s^{(s/v)} = -3.82 \times 10^{-11}$ mole $cm^{-2} = -23 \times 10^{12}$ salt molecules cm^{-2}. This implies that the surface of such a solution lacks 23×10^{12} salt molecules cm^{-2} to make the surface phase homogeneous with the bulk. Let us now consider a spherical drop of aqueous NaCl solution and seek the drop size below which the error due to omitting the surface salt deficiency is less than 1%. This condition can be expressed by the inequality $\mathfrak{M}(4\pi/3)a^3\rho_s'' \geq 100(4\pi a^2)\Gamma_s^{(s/v)}$. For $\rho_s'' \approx \rho_w$ and $|\Gamma_s^{(s/v)}| = 3.82 \times 10^{-11}$ mole cm^{-2}, we find $a \geq 1.15 \times 10^{-5}$ cm. Thus, a drop consisting of one-molal sodium chloride solution can be considered a homogeneous salt solution if its radius is larger than about 0.1 μm. We shall see that this criterion is fulfilled by most cloud drops during the condensation process (see Chapter 13).

This estimate is also in accord with a detailed study by Tsuji (1950) of the effect of salt adsorption at the surface of a solution drop, formed by condensation of a salt particle, on the equilibrium vapor pressure over the drop. The results of his

computations show that the inhomogeneity due to adsorption at the drop surface is negligible for salt masses (NaCl) larger than 10^{-17} g, but becomes increasingly significant for smaller salt masses. As we shall see in Chapter 6, only salt particles of masses larger than 10^{-17} g contribute importantly to the formation of cloud drops by condensation. The effect of solution inhomogeneity may, therefore, be neglected in studying the condensation process.

Just as one may replace $\sigma_{w/v}$ by $\sigma_{w/a}$, a negligible error results on substituting $\sigma_{s/a}$, the surface tension of an aqueous salt solution exposed to humid air, for the quantity $\sigma_{s/v}$. Experimental values for $\sigma_{s/a}$ of a few selected salts are given in Figures 5.2a,b. These values are in good agreement with those of Low (1969b). We note that for the monovalent as well as the bivalent salts, $\sigma_{s/a}(m)$ is approximately linear. Since the slopes of these curves have a negligible dependence on temperature over the range of meteorological interest, Hänel (1970) suggested the following empirical relation:

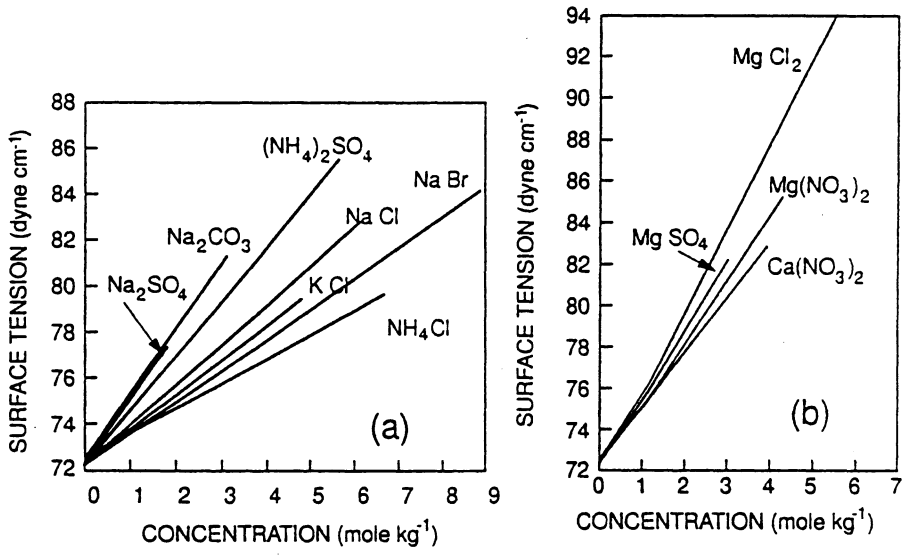


Fig. 5-2: Surface tension of various electrolyte solutions as a function of salt concentration; (a) monovalent cations, (b) bivalent cations. (From Jarvis and Scheimann, 1967, with changes.)

$$\sigma_{s/a}(m,T) = \sigma_{w/a}(T) + Bm\,, \tag{5-19}$$

where the first term on the right is given by (5-12), and B in the second term can be obtained from the slopes of the curves in Figure 5.2.

5.4.3 Radius Dependence of Surface Tension

A last relevant consideration for this section is the possible dependence of $\sigma_{w/v}$ (or $\sigma_{w/a}$) on the curvature of the water phase. Given that the surface tension

arises from attractive forces between molecules near the surface, we might expect that only an alteration of the average geometrical configuration of these molecules on a size scale comparable to the effective range of the attractive forces would significantly affect the surface tension. Thus, we would expect a dependence of $\sigma_{w/v}$ on size only for extremely small drops consisting of merely a few tens or hundreds of water molecules.

Several investigations of this problem have been carried out. Tolman (1949a,b) and Koenig (1950) suggested finding the answer on the basis of a quasi-thermodynamic approach. Kirkwood and Buff (1949) and Buff (1951, 1955) utilized statistical mechanics methods. Benson and Shuttleworth (1951) based their study on molecular interactions. Although all three approaches qualitatively predict that the surface tension of water decreases with decreasing radius of curvature of the water surface, there is little quantitative agreement among them. Tolman estimated that $\sigma_{w/v}$ for a drop which consists of 13 water molecules (equivalent to a drop radius of 4.6×10^{-8} cm, based on $\dot{v}_w = 30 \times 10^{-24}$ cm^3 and $\rho_w = 1.0$ g cm^{-3}) is 40% smaller than that for a plane water surface. In contrast, Benson and Shuttleworth computed the surface tension of a small group of water molecules by counting the number of bonds which had to be broken in order to cut off the group of molecules from the bulk water structure. In order to estimate the interaction energy between water molecules in water, Benson and Shuttleworth assumed that only the first and second nearest neighbors had to be considered. In this manner they predicted that the surface tension for a drop of 13 water molecules is only about 15% smaller than that for a plane water surface. Since the quasi-thermodynamic approach is not rigorous for such small water drops, one would tend to prefer the result of Benson and Shuttleworth. However, the success of the molecular interaction method obviously depends on the accuracy with which the structure of water can be described. In this context, our discussion in Chapter 3 suggests that a hexagonal, close-packed structure such as that used by Benson and Shuttleworth can hardly describe the actual water structure accurately. Therefore, both the thermodynamic and molecular methods must be treated with caution.

No trustworthy experimental determination of $\sigma = \sigma(a)$ is available for any liquid except for the measurements of Sambles *et al.* (1970), who experimentally tested the Kelvin law (see Chapter 6) for evaporating lead droplets. They concluded that the surface tension of these droplets did not deviate from the values over a flat surface, even if the drops were as small as 10^{-7} cm.

We shall now present a simple, approximate, quasi-thermodynamic derivation of the radius dependence of σ, following Defay *et al.* (1966). From (5-11) we have, for a displacement at equilibrium,

$$\frac{2\mathrm{d}\sigma_{w/v}}{a} + 2\sigma_{w/v}\mathrm{d}(1/a) = \mathrm{d}p_w - \mathrm{d}e_{sat,w} \,. \tag{5-20}$$

Also, from (4-4b) we find, at constant T, $\mathrm{d}\mu_v = v_v \mathrm{d}e_{sat,w}$, and $\mathrm{d}\mu_w = v_w \mathrm{d}p_w$. But here $\mathrm{d}\mu_v = \mathrm{d}\mu_w$; consequently, we may express the right side of (5-20) in the form $(v_v - v_w)\mathrm{d}p_w/v_v$. Then, on substituting from (5-15), $\mathrm{d}\sigma_{w/v} = -\Gamma_w^{(w/v)}\mathrm{d}\mu_w =$

$-v_w\Gamma_w^{(w/v)}dp_w$, (5-20) becomes

$$\frac{d\sigma_{w/v}}{\sigma_{w/v}} = -\frac{2\Gamma_w^{(w/v)}}{(2\Gamma_w^{(w/v)}/a) + \rho_w - \rho_v} d(1/a) . \tag{5-21}$$

Assuming $\Gamma_w^{(w/v)}/(\rho_w - \rho_v)$ is independent of a, we may integrate (5-21) to obtain

$$\sigma_{w/v} = \frac{(\sigma_{w/v})_\infty}{1 + (2/a)[\Gamma_w^{(w/v)}/(\rho_w - \rho_v)]} , \tag{5-22}$$

where $(\sigma_{w/v})_\infty$ is the surface tension of a plane water surface.

The adsorption $\Gamma_w^{(w/v)}$ may be estimated in the following manner. Our thermodynamic formalism requires for complete consistency that we choose the surface of separation between phases to be the same as the *surface of tension* in which the net surface forces appear to lie. Only for this choice can we be sure that the bulk volumes defined by the position of the dividing surface are identical with those appearing in the equation for mechanical work on which (5-1) and (5-3) are based. Of course, in practice it is essentially impossible to know exactly where the surface of tension is and, fortunately, for most purposes it turns out not to be necessary. Nonetheless, in the present instance there is some predictive value in realizing that the surface of tension, which is our reference surface for measuring adsorption, must lie slightly below the free surface of a mass of water molecules comprising a drop. Since the forces of attraction between the molecules in the first layer act nearly along the lines connecting their centers, we may suppose that the surface of tension is about half a molecular thickness below the free surface. Therefore, the amount of water adsorbed on the dividing surface may be estimated as half the mass of the first molecular layer. Then, taking 9.6 $(Å)^2$ to be the area occupied by each water molecule at the surface (Defay *et al.*, 1966), their surface density is 1.7×10^{-9} mole cm^{-2}, and we find that $\Gamma^{(w/v)}$ is approximately 0.87×10^{-9} mole cm^{-2}. This is in fair agreement with estimates made by Tolman (1949a,b).

Table 5.1 lists results for $\sigma_{w/v}(a)$ computed from (5-22), using the above value for $\Gamma_w^{(w/v)}$, and the approximation $\rho_v \ll \rho_w = 1$ g cm^{-3}. It is seen that the radius dependence becomes important for $a \lesssim 10^{-6}$ cm, as expected. It is clear from the derivation and discussion that these values are not likely to be very accurate for such small sizes; nevertheless, they should be adequate for our purposes. Unfortunately, more rigorous values are presently not available.

5.5 Angle of Contact

So far, we have considered water or solution drops which are surrounded by vapor or moist air only. Let us now consider a drop of water which is bounded by two phases: moist air and a solid phase on which the drop is resting (Figure 5.3). If the water only partially wets the solid, it will form a 'cap' which makes contact with the underlying surface at an angle Θ, the *contact angle* for water on this surface. If the water wets the solid completely, $\Theta = 0$. A surface which is readily wetted

TABLE 5.1
Variation of surface tension of water (against air) with radius of curvature of various size water drops; $(\sigma_{w/v})_\infty$ is the surface tension of water (against air) for a planar interface (computed from Equation 5-22).

a(cm)	$\sigma_{w/v}/(\sigma_{w/v})_\infty$	$(\sigma_{w/v})_\infty - (\sigma_{w/v})/(\sigma_{w/v})_\infty$ (%)
∞	1.0	0
10^{-4}	0.9997	0
10^{-5}	0.9969	0.3
10^{-6}	0.9697	3.0
10^{-7} (140 molecules)	0.7622	23.8
4.6×10^{-8} (13 molecules)	0.5959	40.4

TABLE 5.2
Contact angle of water on selected solid substances. (Based on data of Head, 1961a,b; Letey *et al.*, 1962; Koutsky *et al.*, 1965; Zettlemoyer, 1968; Mayamoto and Latey, 1971; Isaka, 1972.)

Substrate	Contact angle Θ (angular degrees)	$m_{w/a} = \cos\Theta$
Polyvinylformal (Formvar)	50	0.64
Polyethylene terphtalate (Therpane)	70	0.34
Polymethylmetacrylate (Plexiglass)	80	0.17
Polyethylene (Tedlar)	94	-0.07
Teflon	100 to 117	-0.17 to -0.45
Platinum (metal)	40	0.77
Gold (metal)	65.5	0.41
Silver (metal)	79.5	0.18
Cadmium iodide	0	1.0
Silver iodide	9 to 17	0.956 to 0.988
Silver chloride	50 to 55	0.57 to 0.64
Lead iodide	64 to 80	0.17 to 0.64
Surface soil	65.2 to 68.9	0.36 to 0.42
Quartz, beach sand	43 to 52	0.62 to 0.73

by water is called *hydrophilic*; a surface which is not is called *hydrophobic*. The contact angle for water on various solid surfaces is given in Table 5.2.

The contact angle is determined by the condition of mechanical equilibrium: there must be no net force component along the solid surface. From Figure 5.3, this condition, known as Young's relation, is easily seen to be given by

$$\sigma_{w/a} \cos\Theta = \sigma_{N/a} - \sigma_{N/w} . \tag{5-23}$$

This relation, though quite useful, does rest on some idealizations which, of course, are not found in practice. Some difficulties which complicate its use include: (1) the roughness of the substrate (Osipow, 1962); (2) the presence or absence of hydrophilic sites embedded in the surface (Zettlemoyer *et al.*, 1961); (3) the saturation state of the surrounding vapor (Corrin, 1975; also see Section 5.6); (4) the

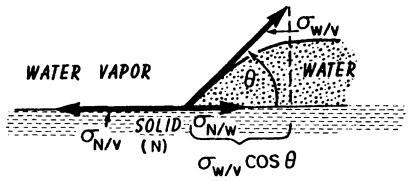


Fig. 5-3: Mechanical equilibrium conditions for a drop on a horizontal solid surface. Tension $\sigma_{N/a}$ balances the sum of tension $\sigma_{N/w}$ and $\sigma_{w/a} \cos\theta$.

TABLE 5.3

Specific interface energy for a few solids against air and against water.

Solid	Surface energy against air (erg cm^{-2}) (20°C)	Surface energy against water (erg cm^{-2}) (20°C)
Teflon	18	30.3 to 50.5
PbI_2	130	83.7 to 117.7
AgI	128	56.6 to 58.9
AgCl	190	143.7 to 147.8
soil, sand	21 to 43	0 to 17

dependence on whether the cap is advancing or receding ('contact angle hysteresis') (Osipow, 1962). A few values for $\sigma_{N/v}$ and $\sigma_{N/w}$ are presented in Table 5.3.

It is customary in the cloud physics literature to speak of the 'wetting coefficient', or 'compatibility parameter'; this is just the quantity $m_{w/a} \equiv \cos\Theta$, apparently introduced by Fletcher (1958). In analogy to the case of water on a solid substrate, Fletcher also defined compatibility parameters for ice on a solid substrate. These definitions are as follows:

$$m_{i/a} \equiv \frac{\sigma_{N/a} - \sigma_{N/i}}{\sigma_{i/a}} \quad (5\text{-}24a), \qquad m_{i/w} \equiv \frac{\sigma_{N/w} - \sigma_{N/i}}{\sigma_{i/w}}. \quad (5\text{-}24b)$$

Of course, formally identical defining equations can be set up for the case of an environment of pure water vapor and, in fact, one finds $m_{i/a} \approx m_{i/v}$, and $m_{w/a} \approx m_{w/v}$.

5.6 Adsorption of Water Vapor on Solid Surfaces

Most solids, especially in highly dispersed form, adsorb water vapor onto their surfaces. This reflects the tendency toward spontaneous reduction of surface energy, in the same way as was discussed in Section 5.4 in the context of the adsorption of dissolved salts onto the surface of tension.

Two main types of forces attract molecules to a solid surface: physical forces (*physical adsorption*) and chemical forces (*chemical adsorption* or *chemisorption*). The former are due to dispersion forces (attractive), forces caused by the presence

of permanent dipoles (attractive), and short range repulsion forces. The latter are due to a transfer of electrons between the solid surface and the adsorbed water molecules and, thus, involve valency forces.

If the binding force between the molecules in the first adsorbed layer and the newly arriving molecules is larger than the binding force between the molecules in the first adsorbed layer and the surface of the solid, a higher vapor pressure is required for formation of the first layer than for any subsequent layer. On such walls, called *hydrophobic walls*, a critical supersaturation is required to form the first adsorbed layer, and then subsequent layers are formed spontaneously. On the other hand, if the water molecules in the first layer are more strongly bonded to the solid surface than to the newly arriving molecules, the wall becomes covered with molecules at relative humidities below 100%. However, for the completion of the first and all subsequent adsorbed layers, the relative humidity in the environment must continuously be raised. On such walls, termed *hydrophilic walls*, the thickness of the adsorbed layer of water moleculcs increases as the relative humidity of the environment increases, and may be several molecular layers thick before a relative humidity of 100% is reached.

The adsorption behavior of a solid surface is generally characterized by a plot of the amount of gas adsorbed as a function of the gas pressure at constant temperature. The contour which describes such a functional variation is called an *adsorption isotherm.* For physical adsorption, Brunauer *et al.* (1967) distinguish five main types of adsorption isotherms (see Figure 5.4). Type I represents monolayered adsorption; types II and III represent monolayered adsorption at low pressures, followed by the adsorption of further layers with increasing pressure; types IV and V represent mono- and multilayered adsorption which occurs in the presence of condensation, at subsaturation pressures, in the capillary pores of the solid surface.

Various theories have been advanced to describe the processes of adsorption of gases and vapors onto solid surfaces. Since the physics of adsorption is a large and quite complicated subject in its own right, we must refrain from treating it here in great detail. However, since studies of the adsorption of water vapor on solid surfaces have frequently and very successfully been used to characterize the nucleating properties of these surfaces, it is important that we at least become familiar with the basic features of the most widely used models for the adsorption phenomenon. For further information, the reader may refer to sources such as Bowers (1953), Meyer (1958), Pierce (1960), Osipow (1962), Flood (1967), Dunning (1967), Clark (1970), and Samorjai (1972).

The three most widely used theoretical adsorption isotherms are those of Langmuir (1918) (*L-equation*); Brunauer, Emmett, and Teller (1967) (*BET-equation*); and Frenkel (1946), Halsey (1948), and Hill (1946, 1947, 1949, 1952) (*FHH-equation*). Because of its simplicity and because it serves as a prototype for the others, we shall now sketch a derivation of the Langmuir isotherm. Langmuir (1918) was the first to realize that adsorbed films are often just molecular monolayers, owing to the very short range of intermolecular forces. Accordingly, he treated adsorption in terms of a dynamic balance between molecules entering and leaving a unimolecular layer. Proceeding in this way, let $w^{\downarrow}$ denote the magnitude of the gas particle flux,

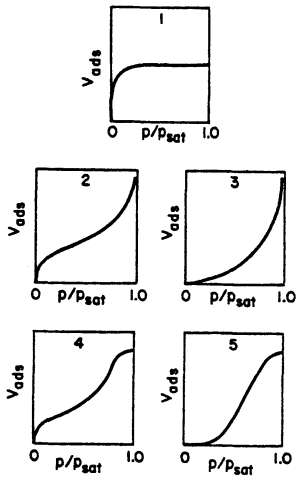


Fig. 5-4: The five principal isotherms for physical adsorption, after Brunauer *et al.* (1967).

i.e., the number of molecules striking the surface per unit area and time. Suppose a fraction α of these adhere, and that the fraction of the surface covered by molecules is f. Then, the rate of evaporation of gas molecules per unit area can be expressed as βf, where β is a constant, while the rate of deposition of molecules per unit area is $w^{\downarrow}\alpha(1-f)$. For a condition of dynamic equilibrium, these rates are equal and so $f = w^{\downarrow}\alpha/(\beta + w^{\downarrow}\alpha)$. But $w^{\downarrow}$ is proportional to the gas pressure (see (5-51)), and for a monolayer, $f = V/V_m$, where V is the volume of gas adsorbed at the equilibrium gas pressure p, and V_m is the gas volume necessary to form a complete monolayer. Therefore, for T = constant the balance may be expressed in the form

$$V = V_m bp/(1 + bp)\,, \tag{5-25}$$

where b is a constant for the given adsorbing material. This is the L-equation.

At low pressures, (5-25) predicts that adsorption is proportional to gas pressure; this is known as Henry's law. The type-I isotherm in Figure 5.4 is of the Langmuir form. An experimental example of this type is the adsorption of O_2 or CO onto silica at 0°C.

The BET theory extends the Langmuir theory to include the adsorption of two or more molecular layers. The BET-equation can be written as

$$\frac{p}{V(p_{\text{sat}} - p)} = \frac{1}{V_m c} + \frac{c-1}{V_m c}(p/p_{\text{sat}})\,, \tag{5-26}$$

or

$$\frac{V}{V_m} = \frac{n_{\text{ad}}}{n_m} = \frac{c(p/p_{\text{sat}})}{[1-(p/p_{\text{sat}})][1+(c-1)(p/p_{\text{sat}})]}\,, \tag{5-26a}$$

where n_{ad} is the number of vapor molecules adsorbed on the surface, n_m is the number of adsorption sites available on the solid surface, c is a constant for a given

solid, T = const., and p_{sat} is the saturation vapor pressure for the vapor being adsorbed. The BET theory assumes: (1) that all adsorption sites on the adsorbing surface are equivalent; (2) that each molecule adsorbed in a particular layer is a possible site for adsorption of a molecule in the next layer; (3) that no horizontal interaction between adsorbed vapor molecules takes place; (4) that the heat of adsorption is the same for all molecules in any given adsorbed layer; and (5) that the heat of adsorption is equal to the latent heat of evaporation for the condensed gas in bulk for all adsorbed layers except the first. Of course, assumptions (1), (3), and (4) also apply to the L theory.

If V/V_m is plotted against p/p_{sat}, a type-II isotherm is obtained if $c < 2$. Such an isotherm is obtained, for instance, if nitrogen is adsorbed on an ice surface (Figure 5.5). A type-III isotherm results if $0 < c < 2$. If $p/V(P_{\text{sat}} - p)$ is plotted against p/P_{sat}, (5-26) yields a straight line with a slope of $(c-1)/cV_m$ and an intercept of $1/V_m c$, from which c and V_m can be determined. The total surface area of the adsorbing solid can be computed from a known value of V_m and of the area occupied by one molecule adsorbed on the surface. From this, one can compute the specific surface area per unit mass of the adsorbing solid. Nitrogen, argon, and krypton turn out to be the gases best suited for such surface area determinations.

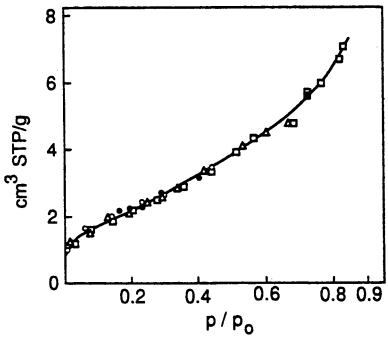


Fig. 5-5: Adsorption isotherm for nitrogen on non-annealed ice at 77 K; ○ original run; △ after 5 days at 77 K; □ after 14 days at 77 K. (From Adamson *et al.* 1967, with changes.)

At pressures close to saturation, the adsorbate consists of multilayers and has properties similar to the condensate in bulk. For such conditions, the adsorption mechanism is probably best described by the FHH theory, which can be expressed by the relation

$$\ln(p_{\text{sat}}/p) = \frac{\text{A}}{(V/V_m)^{\text{B}}}, \tag{5-27}$$

where A and B are constants for any particular adsorbing solid for T = const. Thus, a plot of V/V_m vs. $\ln(p_{\text{sat}}/p)$ on a doubly logarithmic scale exhibits a linear variation from which A and B can be determined.

Of course, the Gibbs adsorption isotherm (5-16) may also be used to study the adsorption behavior of a solid surface. As an example of its use, we shall now

determine the dependence of the contact angle for water on a solid on the environmental vapor pressure, following Corrin (1975). The reasoning is straightforward: the higher the vapor pressure e, the greater the adsorption $\Gamma_w^{(N/v)}$ of water on a given solid surface; from (5-15), a change in surface tension must result if T = constant. This, in turn, alters the contact angle. Proceeding in this manner, we have $d\mu_w^{(N/v)} = d\mu_v = \mathscr{R}T d\ln e$ for equilibrium changes, and assuming ideal gas behavior. Then, from (5-15) we have, at constant T,

$$d\sigma_{w/v} = -\mathscr{R}T\Gamma_w^{(N/v)} d\ln e\,, \tag{5-28}$$

which upon integration yields

$$\Pi(e) \equiv \sigma_{N/v}(0) - \sigma_{N/v}(e) = \mathscr{R}T \int_0^e \Gamma_w^{(N/v)} d\ln e\,. \tag{5-29}$$

The quantity $\Pi(e)$ is known as the *spreading pressure.*

If in a particular experiment the mass $m_{v,ad}$ of adsorbed water vapor is measured as a function of e in an environment of pure water vapor, then $\Gamma_w^{(N/v)} = m_{v,ad}/M_w\omega m_N$, where m_N is the mass of the adsorbing solid (N), and where ω is its specific surface area (determined by a separate experiment); with this information, $\Pi(e)$ may be found from (5-29).

For two different pressures e_1, and $e_2 > e_1$, we have

$$\Pi(e_2) - \Pi(e_1) = \sigma_{N/v}(e_1) - \sigma_{N/v}(e_2) = \mathscr{R}T \int_{e_1}^{e_2} \Gamma_w^{(N/v)} d\ln e > 0\,. \tag{5-30}$$

Consequently, the corresponding contact angles determined from (5-23) will also be different, and in fact

$$\cos\Theta_2 = \cos\Theta_1 - [\Pi(e_2) - \Pi(e_1)]/\sigma_{w/v}\,. \tag{5-31}$$

This shows that the contact angle for water on a solid substrate increases with increasing vapor pressure. For example, Barchet and Corrin (1972) studied the adsorption of water vapor onto pure silver iodide (AgI) at $T = -10°C$, and at an ice supersaturation of $e/e_{sat,i} = 1.025$; this led to $\Pi(e) - \Pi(e_{sat,i}) = 0.84$ erg cm^{-2}. From (5-31) one finds that $\Theta(e) - \Theta(e_{sat,i}) = 3°$, from which for $\Theta(e_{sat,i}) \approx 11°$, we find $\Theta(e) \approx 14°$. This trend is as expected; adsorption lowers the surface energy of the solid substrate, enabling the drop on the solid surface to pull itself together further.

Because of its ice nucleating properties, silver iodide has been the object of numerous adsorption studies in the recent past. It is seen in Figure 5.6a,b that the adsorption of nitrogen on a sample of powdered AgI is characterized by a type-II adsorption isotherm which can be fitted to give a straight BET adsorption curve. From such a curve one may determine V_m, the number of adsorption sites available to N_2 molecules, and the total surface area of the absorbing AgI sample. Knowing

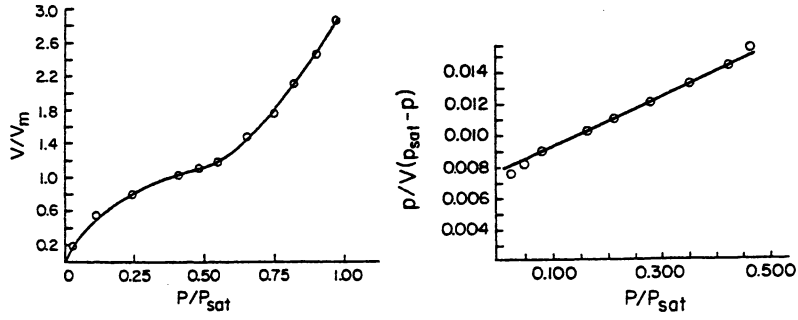


Fig. 5-6: Adsorption behavior of nitrogen on silver iodide at −196°C; (a) adsorption isotherm, (b) BET curve. (From Birstein, 1954; by courtesy of the Air Force Geophys. Laboratory, Hanscom Air Force Base, Massachussetts.)

the total surface area of the sample makes it possible to determine the amount of water adsorbed per unit surface area from the adsorption characteristics of the same sample for water vapor.

The adsorption chacacteristics of AgI for water vapor have been studied by Coulter and Candela (1952), Birstein (1955, 1956), Zettlemoyer *et al.* (1961, 1963), Tcheurekdjian *et al.* (1964), Corrin *et al.* (1964, 1967), Barchet and Corrin (1972), and Gravenhorst and Corrin (1972) using AgI of various purity. Type-II as well as type-III isotherms were observed, depending mainly on the method of preparing the AgI. Silver iodide samples, strongly contaminated with water-soluble impurities such as $AgNO_3$, and KI salts, characteristically gave type-III isotherms. Figure 5.7a illustrates the adsorption behavior of water vapor onto 'pure' AgI, and Figure 5.7b shows the adsorption behavior of water vapor on AgI of various purity. We notice that the amount of water vapor adsorbed increases with increasing vapor pressure, rising particularly strongly as saturation is approached, and that the presence of impurity ions such as K^+ and NO_3^- in the AgI lattice enhances the adsorption of water vapor.

Some AgI samples were found to give adsorption isotherms for water vapor which could be fitted to a linear BET curve from which the number of adsorption sites available to H_2O molecules could be determined. Other samples did not behave in this manner, requiring instead alternative methods to estimate the number of water adsorbing sites (Tcheurekdjian *et al.*, 1964; Corrin and Nelson, 1968). Comparison between the adsorption properties of AgI for water vapor and those for nitrogen demonstrated that the number of AgI surface sites available to water molecules is significantly less than the total number of sites present. This suggested that an AgI surface basically behaves like a *hydrophobic* surface with a few *water receptive*, i.e., *hydrophilic*, sites. Zettlemoyer and co-workers suggested that chemical impurity ions built into the AgI lattice may serve as such hydrophilic sites.

Since water molecules are rather weakly bonded to the AgI surface surrounding a site, they diffuse relatively easily towards the site to form a three-dimensional

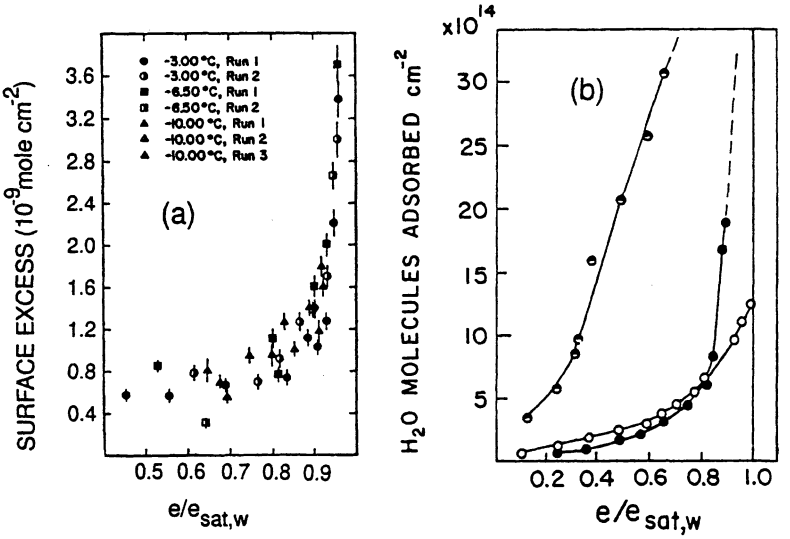


Fig. 5-7: Adsorption isotherms for water vapor on silver iodide, AgI. (a) pure silveriodide at various temperatures (from Barchet and Corrin, 1972; with permission from *J. Phys. Chem.* copyrighted by the Amer. Chem. Soc.), (b) comparison of pure AgI (○) with AgI doped with 0.1% KNO_3 (•) and with 1% KNO_3 (◓). (From Gravenhorst and Corrin, 1972; by courtesy of *J. de Rech. Atmos.*, and the authors.)

(3-D) water cluster. This results in the build-up of adsorbed multilayers before the completion of an adsorbed monolayer. The concept of water clusters was strongly advocated also by Corrin and co-workers. They too interpreted the adsorption behavior on impure AgI surfaces in terms of 3-D water clusters, which they found even at low relative humidities over highly localized surface impurity sites.

However, 'pure' AgI essentially free of impurity ions was found to behave differently. The studies of Corrin and co-workers suggested that on the surface of 'pure' AgI no 3-D water clusters build up at low relative humidities. Instead, the adsorption behavior suggests the formation of two-dimensional water patches in which the water molecules are distributed over a relatively wide area, exhibiting strongly cooperative, lateral interaction. Multilayers begin to build up only at high relative humidities.

Zettlemoyer (1968) found that, similarly to impure AgI, silica compounds doped with salt ions adsorbed considerably more water than undoped silica characterized by a fully hydroxylized surface. The larger adsorption was attributed to the doped ions acting as hydrophilic sites over which water clusters are built up. To confirm their results, Federer (1968) studied the adsorption behavior of water vapor on surfaces of silicon doped with boron and phosphorous. He noted a pronounced correlation between the amount of water adsorbed and the specific electric resistance of the adsorbens (see Figure 5.8a). Federer found that the samples of higher specific resistance (lower concentration of doping atoms) had a larger total den-

sity of adsorption sites, but that the sites on samples of lower specific resistance (higher concentration of doping atoms) were more active, and could adsorb more water. Through a study of the electrical surface potential of doped silicon, he concluded that the amount of charge exchanged between physically adsorbed water molecules and the substrate increases with an increase in doping. Since in giving up charge to the substrate, such molecules are chemisorbed, and since chemisorbed water molecules are preferred sites for subsequent further adsorption (Wanlass and Eyring, 1961), Federer interpreted the positive correlation noted between doping and adsorption in terms of a positive correlation between doping and the creation of active chemisorption sites.

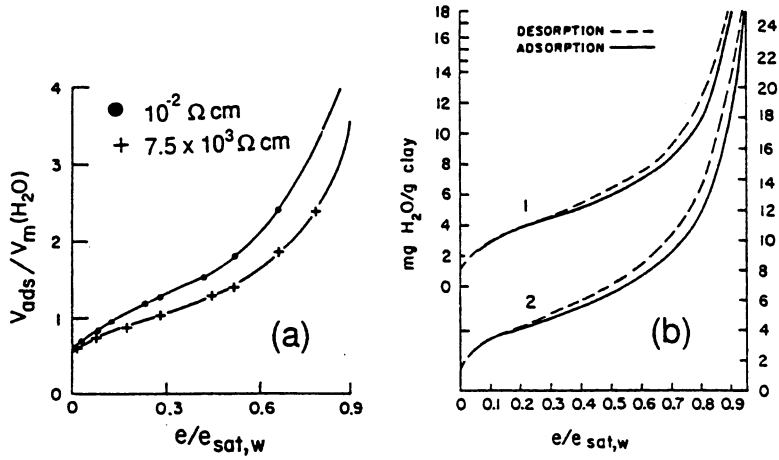


Fig. 5-8:a. Adsorption isotherms at −10°C for water vapor on p-type silicon doped with various amounts of boron. Specific electric resistance of sample: (•) 10^{-2} Ω cm, (+) 7.5×10^{3} Ω cm. (From Federer, 1968; by courtesy of *Z. Angew. Math. Phys.* and the author.)

Fig. 5-8:b. Adsorption isotherms at 25.5°C for water vapor on: (1) potassium kaolinite (pertains to ordinate on left), (2) lithium kaolnite (pertains to ordinate on right). Both ordinates have same units. (From Martin, 1959, with changes.)

A type of cluster-forming active site quite different from those mentioned above was photographically studied by Pruppacher and Pflaum (1975) on single crystals of $BaTiO_3$. Their studies showed that the tendency for water cluster formation strongly correlated with the location of the ferroelectric domains in $BaTiO_3$, and was particularly favored in regions where the electric dipole in the surface was oriented horizontally, and on the boundaries separating ferroelectric domains.

Experiments indicate that clays (a significant component of the atmospheric aerosol (see Chapter 8)) are uniformly hydrophilic and strongly adsorb water molecules over their entire surface. Nuclear magnetic resonance (NMR) studies by Wu (1964) at temperatures down to −10°C verified that water molecules are very tightly bound to clay surfaces, where they are arranged close to the surface in a structure significantly different from that of ice. His observations showed that these

strongly adsorbed water molecules experience a considerable loss of translational and rotational degrees of freedom. A similar observation was made by Morariu and Mills (1972) who found that at a coverage of one statistical monolayer, the diffusivity of water molecules on clay surfaces was almost one order of magnitude smaller than water diffusivity in bulk. Extrapolation of their data to higher coverage showed that the bulk value of the water diffusivity was approached only after the formation of about 15 monolayers. Expressed in another way, in the temperature interval between -22 and $+15°C$ the activation energy for self-diffusion of water molecules on a clay surface was found to be higher by about 1.6 kcal mol^{-1} than the corresponding value for bulk water.

In accordance with NMR and diffusivity studies, measurements by Palmer (1952) showed that the static dielectric constant for water adsorbed on clays varies between 4 and 3.14. This is considerably below the value of about 81 for water in bulk, and is indicative of a reduction of the freedom of movement of the adsorbed water molecules, so that the degree of dipole alignment in an applied electric field is lessened.

Figure 5.8b illustrates the adsorption behavior of two typical samples of clay. One notices that in the BET classification, both depicted adsorption curves are type-II isotherms.

5.7 Ice-Vapor Interface

5.7.1 Surface Energy of Ice

By the surface energy of ice we mean the energy required to form a unit area of new surface. For ideal crystalline ice, this energy may be identified with one half the energy per unit area, W_c, which is needed to split an infinite crystal parallel to a particular crystallographic plane and separate the two parts by an infinite distance. (The factor $1/2$ accounts for the fact that by cleaving the crystal, two new surfaces are created.) It is then natural to take $W_c/2$ as the surface tension or interfacial energy, $\sigma_{i/v}$, between the particular ice crystal face and water vapor or air, assuming the presence of such gases does not significantly affect the surface energy. Owing to the structure of the crystal lattice, it is clear that $\sigma_{i/v}$ will generally be different for different surface orientations with respect to the crystallographic axes, in contrast to the behavior of liquids.

To obtain W_c one must determine the binding energy, or work of cohesion; for a molecule on the crystal surface. Now for a cut perpendicular (parallel) to the crystallographic c-axis, a water molecule which is hydrogen bonded across the cleavage plane loses one nearest neighbor molecule and three (four) next nearest neighbor molecules. A water molecule which is not hydrogen bonded across the cleavage plane loses three (two) next nearest neighbor molecules. Therefore, a water molecule may be regarded as losing one nearest and six next nearest neighbors by cutting along a basal or prism plane. If we disregard the forces of interaction due to third and higher order nearest neighbors the energy per bond required for cleavage of an ice crystal can therefore be expressed as

$$E_m = U_1 + 6U_2\,, \tag{5-32}$$

where U_1, and U_2 are the average interaction potentials between the molecules in the first and second interaction zones. The interaction potentials U_1 and U_2 for intermolecular spacings of 2.76×10^{-8} cm and 4.51×10^{-8} cm, respectively, were computed by Reuck (1957) on the basis of Rowlinson's (1951) force constants, which take account of the multipole electrostatic interaction forces, induction forces, and repulsion forces. As a result, Reuck found, for 0 $E_m = 4.24 \times 10^{-13}$ erg bond^{-1} or 8.48×10^{-13} erg molecule, i.e., 12.15 kcal mole^{-1} since there are two bonds per molecule. This theoretical estimate is quite close to the experimetally determined value for the sublimation enthalpy of ice, $\mathscr{L}_s = 12.20$ kcal mole^{-1} (see Section 3.3). In order to estimate the surface energy of ice, we prefer to use the experimental value for the sublimation energy and consider $\mathscr{L}_s/2 = 6.10$ kcal (mole of bond)$^{-1}$ or 4.26×10^{-13} erg bond^{-1} as the interaction energy between a water molecule and its neighbors in ice.

All that remains now to estimate the surface energy of ice is to count the areal density of bonds at the basal and prism faces of the unit cell of ice (Figure 3.4). For a basal plane, the area is $\sqrt{3}a_0^2/2$. Since this area is occupied by $2(1/3 + 1/6) = 1$ bond the density of bonds in the basal plane is $2/\sqrt{3}a_0^2$. For $a_0 \approx 4.52 \times 10^{-8}$ cm, the bond density is 5.65×10^{14} cm^{-2}. Similarly, for a prism plane, the area of the unit cell is $c_0 a_0$, and the occupancy is $(4 \times 1/4) + (2 \times 1/2) = 2$ bonds. Since $c_0 \approx 7.36 \times 10^{-8}$ cm at -20°C, we obtain a bond density of 6.00×10^{14} bonds cm^{-2} for the prism plane.

Multiplying now these bond densities by the energy per bond, we arrive at the estimates $W_c^{(B)} = 241$ erg cm^{-2} for the basal face of ice and $W_c^{(P)} = 256$ erg cm^{-2} for the prism face. The corresponding values for the surface energies are $\sigma_{i/v}^{(B)} = 120$ erg cm^{-2} and $\sigma_{i/v}^{(P)} = 128$ erg cm^{-2}. Similar estimates were made by Mason (1952, 1954a) and McDonald (1953b).

McDonald (1953b) has pointed out, however, that the surface energies thus computed pertain to a 'fresh' surface. Since molecules in a freshly cleaved surface will not remain in their original position but will relax into new equilibrium positions, the surface energy of an 'aged' surface is somewhat less than that of 'fresh' surface.

The significance of such relaxation can be appreciated if we calculate $\sigma_{w/a}$ for water at 0°C in the same manner as was just done for ice, and compare results with the experimentally determined values of surface tension. Proceeding in this manner, but now considering evaporation rather than sublimation enthalpy, we suppose that $N_A E_m = \mathscr{L}_e/2$; i.e., as before, we assume that for a molecule to get from the interior to the surface requires breaking roughly half the bonds which must be severed for a complete escape. Thus, using the fact that $\mathscr{L}_e/2 = 5.375$ kcal mole^{-1} $= 3.75 \times 10^{-13}$ erg (bond)$^{-1}$ at 0°C and 5.61 kcal mole^{-1} $= 3.92 \times 10^{-13}$ erg (bond)$^{-1}$ at -40°C, and assuming at these temperatures a structural similarity between water and ice so that the areal bond density is approximately 5.8×10^{14} bonds cm^{-2}, we obtain a hypothetical cleavage energy for the water surface of 217 erg cm^{-12} (0°C) and 227 erg cm^{-2} (-40°C). However, from experiments we know that $\sigma_{w/a,obs}(0°C) \approx 76$ erg cm^{-2}, with an extrapolated value of 87.5 erg cm^{-2} at -40°C. Thus, for water at least, the real, 'relaxed' surface has less than half the surface energy predicted for a hypothetical 'freshly cut' surface.

In order to arrive at a suitable correction for the ice surface energy calculation, McDonald suggested subtracting $(\sigma_{\mathrm{w/a,fresh}} - \sigma_{\mathrm{w/a,obs}})$, from the $\sigma_{i/\mathrm{v}}$ which we obtained from our cleavage computation. However, McDonald realized this might over-correct because of the difference between $\mathscr{L}_{\mathrm{e}}$ and $\mathscr{L}_s$. Therefore, he suggested reducing the correction by the factor $\mathscr{L}_{\mathrm{e}}/\mathscr{L}_s = 0.88$ (0°C) and 0.92 (−40°C); for the corrected surface energies $\sigma_{i/\mathrm{v}}^{(\mathrm{B})}$ of ice this yields the final values of 100 erg cm^{-2} (0°C), i.e., 102 erg cm^{-2} (−40°C), and $\sigma_{i/\mathrm{v}}^{(\mathrm{P})} = 109$ erg cm^{-2} (0°C), i.e., 111 erg cm^{-2} (−40°C).

The values deduced above for $\sigma_{i/\mathrm{v}}$ corrected for the disposition of the water molecules at the ice surface, agree well with the experimental estimate of Ketcham and Hobbs (1969) who found $\sigma_{i/\mathrm{a}} = (106 \pm 3)$ erg cm^{-2}.

In deducing these surface energies we have only considered elastic relaxation. Still neglected is the fact that the ice surface exhibits a quasi-liquid layer to temperatures considerably below 0°C (see Section 5.7.3). This layer further reduces the surface energy of ice, as suggested by Furukawa *et al.* (1987) and Beaglehole and Nason (1980). Unfortunately, no quantitative corrections for this effect are available at present.

5.7.2 Wulff's Theorem

Wulff's theorem (Wulff, 1901) provides a description of the equilibrium shape of a crystal from a knowledge of the variation of surface tension with crystal face orientation. It should be emphasized that this equilibrium shape is not often oserved, since actual crystal geometries are strongly influenced by thermal and diffusion gradients, and other kinetic effects associated with active growth (see Section 13.3.3).

Because work is required to form new surface, the equilibrium shape must be the one which minimizes the total surface energy for a given volume. For a concise treatment of the problem along these lines, the reader is referred to Landau and Lifschitz (1958). Here we shall outline a simpler, more heuristic derivation following Dufour and Defay (1963).

Consider a crystal which has a volume V'' and is bounded by (σ) faces, each of which has a surface area $\Omega^{(\sigma)}$. Let the crystal be surrounded by its own vapor (or melt) of volume V' and pressure p', and suppose the whole system is contained in a cylinder whose volume $V = V' + V''$ can be varied by a piston. By moving this piston, the work $đW = -p'\mathrm{d}V$ may be done on the system; this may also be written as

$$đW = -p'V' - p''\mathrm{d}V'' + \alpha\mathrm{d}V'', \tag{5-33}$$

where $\alpha = p'' - p'$ and where we have assumed a uniform pressure p'' within the crystal. But $\mathrm{d}V'' = \Sigma_\sigma \Omega^{(\sigma)}\mathrm{dh}^{(\sigma)}$, for normal outward displacement of the faces $\Omega^{(\sigma)}$ by $\mathrm{dh}^{(\sigma)}$ (see Figure 5.9). Furthermore, the volume of the crystal is $V'' = (\Sigma_\sigma \mathrm{h}^{(\sigma)}\Omega^{(\sigma)})/3$, and on differentiation, this yields

$$3\mathrm{d}V'' = \Sigma_\sigma \mathrm{h}^{(\sigma)}\mathrm{d}\Omega^{(\sigma)} + \Sigma_\sigma \Omega^{(\sigma)}\mathrm{dh}^{(\sigma)},$$

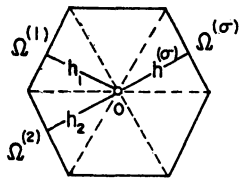


Fig. 5-9: Schematic of a hexagonal crystal to illustrate Wulff's relations.

so that

$$\mathrm{d}V'' = \frac{1}{2}\sum_{\sigma} \mathsf{h}^{(\sigma)}\mathrm{d}\Omega^{(\sigma)} \,. \tag{5-34}$$

Therefore, the work done on the system may also be expressed as

$$(đW)_{\text{cryst.}} = -p'\mathrm{d}V' - p''\mathrm{d}V'' + \frac{\alpha}{2}\sum_{\sigma} \mathsf{h}^{(\sigma)}\mathrm{d}\Omega^{(\sigma)} \,. \tag{5-35}$$

Now consider a system just like the above except that the crystal is replaced by a drop of the same volume. The work done may again be expressed as in (5-33). However, on invoking the condition of mechanical equilibrium, (5-7), we can write the last term in (5-33) in the form $2\sigma\mathrm{d}V''/a = \sigma\mathrm{d}\Omega$, where Ω is the area of the drop; therefore,

$$(đW)_{\text{drop}} = -p'\mathrm{d}V' - p''\mathrm{d}V'' + \sigma\mathrm{d}\Omega \,. \tag{5-36}$$

Comparison of (5-35) and (5-36) shows that a complete analogy between the two systems can be maintained by setting

$$\sigma^{(\sigma)} = \frac{\alpha}{2}\mathsf{h}^{(\sigma)} \,, \tag{5-37}$$

so that also

$$(đW)_{\text{cryst.}} = -p'\mathrm{d}V' - p''\mathrm{d}V'' + \sum_{\sigma} \sigma^{(\sigma)}\mathrm{d}\Omega^{(\sigma)} \,. \tag{5-38}$$

From (5-37), we have

$$\frac{\sigma^{(1)}}{\mathsf{h}^{(1)}} = \frac{\sigma^{(2)}}{\mathsf{h}^{(2)}} = \ldots = \frac{p'' - p'}{2} = \text{constant.} \tag{5-39}$$

This constitutes Wulff's theorem: In equilibrium, the distance of any crystal face from the center of the crystal is proportional to the surface tension of that face.

Let us use Wulff's theorem to estimate the equilibrium crystal shape for ice. From (5-39) we have

$$\frac{\mathsf{h}^{(\mathrm{B})}}{\mathsf{h}^{(\mathrm{P})}} = \frac{\sigma_{i/\mathrm{v}}^{(\mathrm{B})}}{\sigma_{i/\mathrm{v}}^{(\mathrm{P})}} \approx 0.92 \,, \tag{5-40}$$

inserting our previously determined values for the surface tensions. Referring to Figure 5.10, we see that $\mathsf{h}^{(\mathrm{P})} = a'$, where a' is the radius of the circle inscribed in

the basal plane, and that $\mathsf{h}^{(B)} = \mathsf{H}/2$, where H is the height of the ice prism. Also, $a' = a\sqrt{3}/2$, where a is the radius of the circle circumscribed in the basal plane. Inserting the values for $\mathsf{h}^{(P)}$ and $\mathsf{h}^{(B)}$ into (5-40), we find

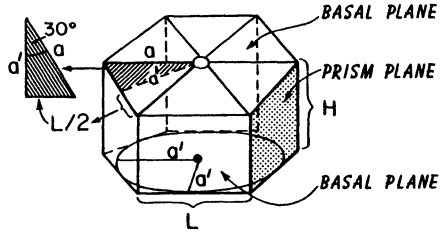


Fig. 5-10: Schematic of an ice crystal to illustrate the determination of the shape factor.

$$\frac{\mathsf{H}}{2a} \approx 0.80\,. \tag{5-41}$$

The equilibrium form is thus predicted to be a hexagonal prism with a ratio of axial length to hexagonal diameter (the observed 'diameter' of an ice crystal is usually given in terms of the diameter of the circle circumscribed within the basal plane of the crystal) of about 0.8 (Krastanow, 1943; Higuchi,1961).

This result is in excellent agreement with the observations of Kobayashi (1961) who found that at very low excess vapor pressures $(\mathsf{H}/2a) \to 0.8$ for ice crystals grown at $-22°\mathrm{C} \leq T \leq -10°\mathrm{C}$. However, at warmer temperatures, no trend to a limiting habit could be observed, while at $T < -22°\mathrm{C}$, $(\mathsf{H}/2a) \to 1.4$. These latter results could be explained if it is assumed that Kobayashi's experimental arrangement could not reproduce equilibrium conditions outside the studied temperature interval. Another possibility is that $\sigma_{i/\mathrm{v}}$ is temperature dependent in a way which is different for the basal and prism faces. This could possibly arise from temperature dependent behavior of surface defects, for example. However, at present no information on this point is available. On the other hand, at temperatures warmer than $-10°\mathrm{C}$, the equilibrium shape is controlled by the quasi liquid layer on the ice surface (see Section 5.7.3) which causes the prism faces to disappear from the equilibrium form. Colbeck (1985) experimentally found that in this temperature range the equilibrium form is a rounded plate with a thickness to diameter ratio of 0.4.

In computations of the rate of homogeneous and heterogeneous ice nucleation, one generally assumes that ice particles of spherical shape are nucleated. It is, however, more realistic to suppose that the nucleated ice particles have hexagonal shape. To take this into account, Dufour and Defay (1963) defined the shape factor of a Wulff type crystal ((5-39), (5-40)) by the relation $s \equiv 3V''/(a')^3$. Using Figure 5.10, we find $V'' = 6(a')^2\mathsf{H}/\sqrt{3}$, where from (5-40) $\mathsf{H} = 1.84a'$. We then obtain for the shape factor $s = 19.12$ (Dufour and Defay obtained $s = 20.78$ by assuming $\sigma_{i/\mathrm{v}}^{(B)} = \sigma_{i/\mathrm{v}}^{(P)}$; of course, for a sphere: $s = 4\pi$).

5.7.3 Structure of Real Ice Surfaces

Surface energies characterize the average conditions on a surface. For understanding the detailed behavior of an ice crystal during growth and evaporation by vapor diffusion, we must consider in addition the microscopic, topographic surface features which are typically present.

Experimental studies show that crystalline solids have rough surfaces, i.e., they contain molecular, microscopic, and even macroscopic *steps*. Such steps often are the result of crystallographic dislocations induced in the crystal by mechanical stresses, thermal stresses, and/or accidental assimilation of foreign solid particles during the crystal's growth. These may cause lattice layers to slip along definite boundaries called *dislocations*. There are two main types of dislocation: *edge dislocations* and *screw dislocations*. In a crystal with the former, the boundary between slipped and unslipped regions extends perpendicular to the slip direction. An edge dislocation may thus be thought of as being caused by inserting an extra plane of atoms into the crystal. In a crystal with a screw dislocation, the boundary between the slipped and unslipped regions extends parallel to the slip direction, and so a screw dislocation may be thought of as being caused by cutting part way through a crystal with a knife, then shearing it parallel to the plane of cutting by one atomic spacing. Steps from screw dislocations transform successive atom planes into a helical or screw-type surface, hence the name (Figure 5.11).

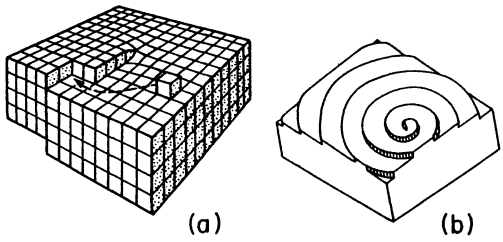


Fig. 5-11: Schematic of an emerging screw dislocation: (a) Schematic of formation, (b) schematic of a well developed screw dislocation 'staircase'. (From Lamb and Scott, 1974, with changes.)

Several studies have shown that molecular steps resulting from dislocations can be made visible at the ice surface by the method of *thermal etching* (see, e.g., Hobbs, 1974). During this process, the ice surface is subjected to slow evaporation. Since a surface molecule at a topographic imperfection is surrounded by fewer molecules than a molecule elsewhere in the surface, it is less strongly bonded to the surface. Topographic surface imperfections are therefore the location of preferred evaporation. As water molecules are removed preferentially from such locations, topographic imperfections are made visible in the form of *etch-pits* (Figure 5.12). Thermal etching is thus capable of revealing the location of dislocations in the crystal. During thermal etching screw dislocations 'unwind' in a screw-type manner, causing the formation of etch-pits with spirally stepped walls. Step heights have been found to vary between 0.01 and 0.2 μm. It has been suggested that micro-

scopically visible spiral step heights of as much as several tenths of a micron do not represent the original step height of an emerging screw dislocation, but rather result from a *bunching* of monomolecular layers (Frank, 1958). The number density of etch-pits has been found to range between 10^4 and 10^6 cm^{-2}, as expected from the number density of dislocations estimated on the basis of other methods.

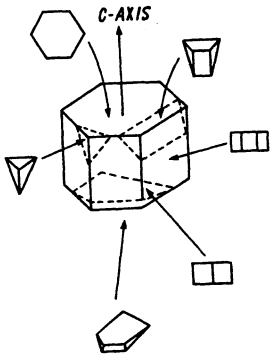


Fig. 5-12: Schematic of various types of etch-pits on the surface of ice. (From Higuchi, 1958a; by courtesy of Pergamon Press Ltd.)

In analogy to the etch-pits which appear at the locations of emergent crystallographic dislocations during very slow evaporation of an ice surface, small raised surface features termed *hillocks* have been observed to appear on a nascent, slowly growing ice surface at the site of emergent dislocations. This demonstrates that sites of emergent crystal dislocations are not only sites of preferred evaporation but also sites of preferred ice crystal growth. The reason for such a site serving as a preferred growth center lies in the fact that considerably less energy is involved in the propagation of an ice crystal face by the addition of water molecules to steps and ledges already present on the ice surface than by nucleation of new growth layers on a perfectly smooth ice surface.

At conditions where an ice crystal freely grows or evaporates in air, the submicroscopic surface roughness is found to manifest itself in the form of *facetted* surfaces. Such crystals are said to have a *hopper structure* (Figure 5.13). For surface ridges to be visible, the ice crystal diameter needs to exceed a few hundred microns. The ridges are considered to result from the bunching of much thinner growth layers.

The bunching mechanism of growth layers at the surface of ice crystals which grow in a vapor environment was studied by Mason *et al.* (1963). According to these authors, the bunching of monolayers on a growing ice surface is the result of interference between propagating steps. At the low supersaturations typical for atmospheric clouds, new layers on an ice surface originate at topographical surface imperfections and at the edges and corners of ice crystals. There the vapor concentration gradient which constitutes the driving force for diffusional growth, as well as the temperature gradient which controls the dissipation of the latent heat released during growth, are high relative to the center of an ice crystal face. Once a

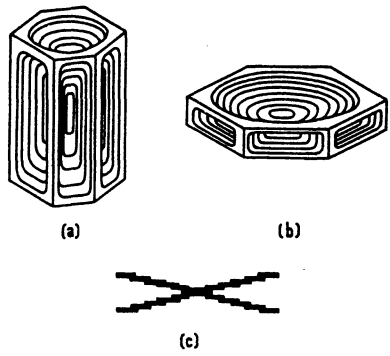


Fig. 5-13: Hopper structure at the surface of ice crystals grown freely in a supersaturated environment: (a) hollow, hexagonal prismatic column, (b) dish-shaped, hexagonal plate, (c) vertical section through center of (b). (From Mason *et al.*, 1963; by courtesy of Phil. Mag., and the authors.)

step is formed, it advances chiefly by the addition of water molecules brought to the step by surface diffusion. In isolation, each layer moves across the ice crystal surface with the same speed v_0. However, if two layers have originated sufficiently close to each other, competition for adsorbed water molecules tends to slow down both steps. If an additional layer originates some distance behind the pair of interfering steps, it will initially travel at the speed of an isolated step until it catches up with the interfering step pair, when it too will slow down, and so on. Eventually, the pile-up or bunching of monolayers will produce a microscopically visible step.

In order to estimate the time required for the bunching of monolayers, we let d_s denote the average migration distance which an adsorbed molecule travels by surface diffusion before re-evaporating. Then, assuming that direct arrival of molecules to the step front from the vapor is negligible in comparison to the surface diffusion flux, we see that steps grow by collecting molecules from a diffusion zone of width $2d_s$. Furthermore, two such fronts can be expected to experience considerable interference when their separation becomes less than this amount. We therefore expect the time needed for the two fronts to merge to be proportional to $2d_s$, and inversely proportional to the characteristic step speed v_0. In this manner, or simply by strict, dimensional analysis, given that d_s and v_0 are the only relevant parameters, we estimate the time t required for the formation of a step of N unit heights to be within an order of magnitude of the quantity $2d_sN/v_0$. A detailed calculation by Mason *et al.* (1963) provides a more quantitative estimate, viz.:

$$t = 4 \ln 2d_sN/v_0 \,. \tag{5-42}$$

This expression agrees well with their observations, giving sufficient evidence that surface diffusion is, in fact, the dominant process behind the bunching mechanism.

Since, as mentioned, the formation and propagation of layers is favored at the edges and corners of the ice crystal, as compared to its face center where the growing layers slow down, freely growing ice crystals preferentially thicken at the crystal's

periphery, leading to the observed hopper structure depicted in Figure 5.13. More details on the growth rate of individual crystal faces and its effect on the crystal shape will be given in Section 13.3.3.

In studying the adhesive properties of ice, Faraday (1860) conjectured that a 'quasi-liquid' layer exists at the interface between ice and air, and that this layer solidifies only when sandwiched between two ice surfaces. Although this possibility obviously has considerable bearing on the feasibility of the collection growth of ice crystals in clouds, it was not until much later that the idea was pursued more quantitatively. In support of Faraday's quasi-liquid film hypothesis, Nakaya and Matsumoto (1953, 1954) and Hosler *et al.* (1957), who measured the force required to separate two ice spheres brought into contact while hanging side by side, noted that the adhesive force was relatively large close to 0°C, but decreased with decreasing temperature and humidity of the surrounding air. In an ice saturated atmosphere, Hosler *et al.* (1957) found that the adhesive force decreased to zero if the ambient temperature decreased below −25°C. This result was taken to mean that quasi-liquid films on ice may be stable down to this temperature.

Further indirect evidence for the presence of a quasi-liquid layer at the ice-air interface has been provided by Bullemer and Riehl (1966), Jaccard (1967), Ruepp and Kass (1969), Maidique *et al.* (1971), and Maeno (1973), Caranti and Illingworth (1983), who showed that the surface electrical conductivity of ice increased significantly at temperatures warmer than −10°C, and particularly at temperatures warmer than −4°C, by Kvlividze *et al.* (1970, 1974) and Mizuno and Hanafusa (1987), who studied the layer using a nuclear magnetic resonance method, by Mantovani *et al.* (1980), who measured the surface viscosity of ice, by Beaglehole and Nason (1980), who determined the extent of the layer by means of a He-Ne laser light reflected from the ice surface, and by Goleki and Jaccard (1978), who probed the ice surface by a proton back-scattering technique.

An early attempt at a physical explanation for the existence of a disordered, quasi-liquid layer at the ice-air interface was provided by Weyl (1951), who suggested that it can be explained in terms of the tendency of any system to minimize its surface energy. A rearrangement of water molecules to provide such a minimization of surface energy is easily possible in liquid water where the molecules are highly mobile. On the other hand, in ice the long-range order of water molecules prevents an easy rearrangement of the molecules. However, according to the views of Weyl, breakdown of this long-range order may still occur near 0°C inside a thin layer at the ice-air interface. Weyl's conjectures were followed up more quantitatively by Fletcher (1962b, 1963, 1968, 1973). By taking into account the structure of a real ice crystal lattice and considering all the defects which occur in such a lattice (see Chapter 3), Fletcher (1973) developed a molecular thermodynamics model, from which it was possible to compute the lowering of the surface energy of ice when a quasi-liquid layer is present, and the temperature range for which such a film is stable. The thickness h of the quasi-liquid layer could not be expressed rigorously in a simple manner as a function of temperature T, but the following approximate relation was derived graphically from the computed variation of h vs. T:

$$\mathrm{h} = \mathrm{A} - \mathrm{B}\log(T_0 - T)\,, \tag{5-43}$$

where h is in 10^{-8} cm, T in K, $T_0 = 273$ K, A = 20 to 50, and B = 25. In fair agreement with Fletcher, Mazzega *et al.* (1976) found from experiments that A = 37 and B = 25. Some additional support for Fletcher's values for the thickness of the quasi-liquid layer came from the recent theoretical model of Chen and Crutzen (1994) who adapted the transition layer concept of Lacman and Stranski (1972) as modified by Kuroda and Lacman (1982). On the other hand, the results of Fletcher and of Mazzega *et al.* have been criticized by Goleki and Jaccard (1978), who found experimentally that the thickness of the disordered layer at the ice surface is about 10 times thicker than the value obtained by Mazzega *et al.* (1976) approaching about 0.1 μm at $-1°$C, and becoming near zero at $-55°$C, with A = (940 ± 170) and B = (540 ± 140). The thickness of the layer at $-1°$C agrees well with the thickness derived from measurements of the dielectric constant by Lagourette *et al.* (1976), and with Jellinek's (1967) and Weyl's (1951) estimate derived from mechanical work of adhesion. Goleki and Jaccard suggested that the differences between the various literature values for the thickness of the surface layer on ice are perhaps due to the different nature of the experimental techniques used, and also due to the lack of reliable values for the parameters in the theoretical models.

Direct evidence for the presence of highly mobile water molecules at the surface of ice has been presented by Bryant *et al.* (1959), Hallett (1961), and Mason *et al.* (1963). They found that water molecules at the surface of ice migrate for considerable distances before they become part of the ice crystal lattice. Quantitative measurements on the surface diffusion of water molecules on ice have been carried out by Mizuno and Hanafusa (1987) using a nuclear magnetic resonance technique. These showed that the diffusivity increases with increasing temperature from 1.35×10^{-9} cm^2 sec^{-1} at $-20°$C to 3.08×10^{-9} cm^2 sec^{-1} at $-1.5°$C, indicating increased mobility of the molecules with increasing temperature. We note from these values that the diffusivity is a few orders of magnitude smaller than the diffusivity of water molecules in water (3-19 and 3-20) but about two orders of magnitude larger than the diffusivity in bulk ice (see Section 3.3). As expected, the energy of activation for surface diffusion of 5.56 kcal mole^{-1} lies in between that for diffusion in water and in ice. It is interesting to note that the NMR signal indicated mobile molecules at the surface even at temperatures as low as $-100°$C. This result, however, should not be taken to mean that the mobile molecules form a quasi-liquid layer down to these low temperatures. Rather, as Goleki and Jaccard suggest, they form a 'disordered' or 'amorphous' layer due to oxygen atoms exercising large amplitude vibrations which are transmitted into the interior of the crystal by the directionality of the hydrogen bonds. Stillinger and Rahman (1972), Hale *et al.* (1981), and Kiefer and Hale (1977) have a somewhat different view, and suggest from their theoretical models that the surface diffusion of water molecules proceeds in the form of vascillating tours of molecules in a force field of a constantly changing network pattern rather than via occasional jumps between discrete binding sites in the ice lattice.

The work of Kuczynski (1949), Kingery (1960a,b), Kuroiwa (1961, 1962), Hobbs and Mason (1964), Hobbs and Radke (1967), Itagaki (1967), and Kikuchi (1972) showed that the quasi-liquid layer mechanism is not the only one which can explain the sticking together of two ice surfaces. The formation of a 'neck' joining two ice

surfaces in contact may proceed in four additional ways: (1) by viscous and plastic flow of water substance under surface tension forces, (2) by evaporation of water substance from the convex surface portion of the ice system, its transfer through the environment and subsequent condensation onto the strongly concave neck joining the two ice surfaces, (3) by volume diffusion of water substance resulting from a local excess of ice lattice vacancies which arise from the deficit in pressure produced by the surface tension forces in the neck region, and (4) by surface diffusion of water substance arising from the difference in concentration of adsorbed molecules existing in the neck and the rest of the ice system, again set up by the surface tension forces. Theoretical expressions for the growth rate of the neck by each of these four mechanisms have been derived by Kuczynski (1949). His theoretical considerations, as well as the experiments carried out by the authors mentioned above, demonstrated that the growth rate of the neck joining the two surfaces is of the general form

$$\left(\frac{\Delta}{a}\right)^n = \frac{\mathrm{A}(T)}{a^m} t\,, \tag{5-44}$$

where $\mathrm{A}(T)$ is a function of temperature and the type of neck-forming ('sintering') mechanism, 2Δ is the width of the neck after time t, and a is the radius of curvature of the two surfaces in contact. For the case of spherical particles of radius a in contact, $n = 2, m = 1$ for process (1); $n = 3, m = 2$ for process (2); $n = 5, m = 3$ for process (3); and $n = 7, m = 4$ for process (4).

In an experimental study and re-analysis of earlier work, Hobbs and Mason (1964) concluded that the adhesion of spherical ice particles is mainly the result of the evaporation-condensation mechanism (2). Later, however, Hobbs and Radke (1967) and Kikuchi (1972b) showed that volume diffusion of water molecules (mechanism 3), caused by the existence of a large concentration of molecular vacancies in ice just beneath the concave surfaces of the neck, contributes almost equally to its growth. While these two mechanisms may jointly determine the rate of growth of the neck, the initial 'bridging' between the two ice particles in contact is, according to Hobbs (1974), most likely the result of a quasi-liquid layer.

5.8 Adsorption of Reactive Gases on Ice Surfaces

We have already shown in Section 5.6 that at $-196°C$ (77 K) the surface of ice is solid and acts towards gases such as nitrogen and argon as a low-energy and rather inert adsorbent (Adamson *et al.*, 1967). The adsorption isotherm for N_2 on ice at this temperature has been plotted in Figure 5.5. Considering that near 0°C a quasi-liquid layer exists on the ice surface, one expects that, with increasing temperature, the adsorption behavior of ice changes progressively. In verification of this, Orem and Adamson (1969) showed that the adsorption behavior of non-polar hydrocarbons such as n-hexane and n-pentane on ice changes noticeably at a temperture near $-35°C$. They suggested that at temperatures above $-35°C$ the ice surface becomes actively involved in the adsorption process by forming a clathrate with the adsorbed molecules. A similar behavior was found by Adamson and Jones (1971) and by Ocampo and Klinger (1982, 1983) who studied the adsorption of CO_2 on ice at temperatures between $-78°C$ (195 K) and 0°C. They found that the

variation of the molecular coverage with relative pressure becomes rapidly steeper at temperatures above $-35°C$. They also showed that at any given temperature, the surface coverage spontaneously changes from a weakly covered surface for a non-polar adsorbent to that of a very polar, strongly adsorbing surface if the relative pressure rises above a critical value. In explaning their results, they pointed out, as did Orem and Adamson for the n-alkanes, that the CO_2 molecules become trapped and form a clathrate after striking the highly mobile water moleclules in the quasi-liquid layer on ice.

Reactive gases such as HCl, HNO_3, SO_2, exhibit a more complicated behavior. The uptake of such gases by planar ice surfaces, ice spheres and dendritic snow crystals has been studied by Sommefield and Lamb (1986), Clapsdale and Lamb (1989), Valdez *et al.* (1989), Mitra *et al.* (1990), Conklin and Bales (1993), Conklin *et al.* (1993), Diehl *et al.* (1995), Dominé and Thiebert (1995) and by Laird and Sommerfeld (1995). As expected, these observations show that the amount of gas taken up by an ice surface increases with increasing gas partial pressure in air and with increasing time of exposure to the gas. On the other hand, the observations demonstrate that the gas uptake is dependent on the type of gas, the temperature, the crystalline structure of the ice, and on whether the uptake takes place on a growing or non-growing ice surface. Thus, Mitra *et al.* (1990) and Diehl *et al.* (1995) showed that during its growth from the vapor near $-15°C$, a dendritic snow crystal takes up SO_2, HNO_3, and HCl in proportion to the amount of water vapor converted to ice. Whether or not the gas molecules become incorporated in the ice lattice during the growth of the crystal could not be determined. The uptake of reactive gases on non-growing ice sufaces is somewhat better understood, although a quantitative description of the uptake mechanism is still not available. From the presently available experimental results, the following conclusions may be drawn: (1) The quasi-water layer at the surface of ice plays a significant role in the uptake of such gases. (2) Gas uptake is largest at temperatures near $0°C$ where the quasi-water layer is thickest. This implies that the quasi-water layer is able to 'dissolve' a gas in a manner similar to bulk water. (4) Once 'dissolved', a highly concentrated quasi-aqueous solution layer is formed above which the vapor pressure is reduced below that over the intrinsic quasi-water layer. This has been verified by Diehl *et al.* (1995) who showed that ice spheres, exposed to HNO_3 vapor prior to evaporation, exhibit an evaporation rate which is considerably smaller than the rate from spheres of a pure ice. (5) A vapor pressure reduction is associated with a depression of the equilibrium melting temperature (see Section 4.9). This behavior is quantitatively expressed in the phase diagrams for the systems HCl/H_2O and HNO_3/H_2O provided by Hanson and Mauersberger (1988a,b). These diagrams delineate the conditions for the stability of the ice phase and the liquid phase in terms of the saturation water vapor pressure (i.e., temperature) and the partial pressure of the gas. As an example, the phase diagram for the system HCl/H_2O is given in Figure 5.14. From this diagram we note that at a given temperature there exists a critical partial pressure of the gas above which the liquid will be the stable phase. At such pressures, the quasi-solution layer is expected to continuously thicken with time, allowing additional gas to be dissolved which in turn promotes further melting. These expectations were verified by Mitra *et al.* (1990) and Diehl

et al. (1995) for HCl (see Figure 5.15). A similar result was found by these authors for HNO_3, except that the amount of gas taken up by the ice surface was found to be considerably larger than the amount taken up by HCl. (6) At a temperature and partial gas pressure at which ice is the stable phase, no melting will be induced by the dissolved gas and the quasi-liquid layer will have the thickness of the intrinsic quasi-water layer. This case was documented by Dominé and Thiebert (1995) who determined the uptake of HCl by single-crystalline bulk ice for partial gas pressures below the critical values. As expected, significantly less gas was taken up under these conditions, even considering that the ice samples of Dominé and Thiebert were exposed to HCl for 3 weeks. (7) In the quasi-liquid layer, HCl, HNO_3, and SO_2 in the presence of H_2O_2, dissociate into ions. Experiments of Diehl (1995) showed that these gases do not desorb when exposed to a stream of ice-saturated nitrogen gas. Desorption only occurs if, simultaneously, the ice sublimates in ice sub-saturated air. (8) Gases such as HF, HCl, HNO_3, and SO_2 in the of presence of H_2O_2, enter bulk ice. This has been verified by a number of experimental studies in which the diffusion coefficent for these gases in ice has been determined. Thus, Wolff *et al.* (1989) reported an apparent diffusion coefficient for HCl in ice of $D_{\mathrm{HCl}} < 10^{-10}$ cm^2 sec^{-1} at 185 K and $D_{\mathrm{HCl}} > 10^{-13}$ cm^2 sec^{-1} at 253 K. More specific values have been obtained by Krishnan and Soloman (1969) $D_{\mathrm{HCl}} = 2.2 \times 10^{-8}$ cm^2 sec^{-1} at -18°C, 4.9×10^{-8} cm^2 sec^{-1} at -11°C and 1.6×10^{-7} cm^2 sec^{-1} at -4°C, by Haltenroth and Klinger (1969) $D_{\mathrm{HF}} = 1.1 \times 10^{-7}$ cm^2 sec^{-1} at -10°C, 8.2×10^{-8} cm^2 sec^{-1} at -20°C and 4.5×10^{-9} cm^2 sec^{-1} at -85°C, by Barnaal and Scotfeld-Ellingson (1983) $D_{\mathrm{HCl}} \approx D_{\mathrm{HNO_3}} = 4 \times 10^{-9}$ cm^2 sec^{-1} at -15°C, by Chu *et al.* (1993) $D_{\mathrm{HCl}} = 2 \times 10^{-13}$ cm^2 sec^{-1} at -85°C, by Diehl (1995) $D_{\mathrm{HCl}} \approx D_{\mathrm{HNO_3}} \approx 5 \times 10^{-9}$ cm^2 sec^{-1} at -19°C. These values suggest that the diffusivity of the mentioned gases is considerably larger than the diffusivity of H_2O in ice (see Chapter 3).

Although during freezing of aqueous solutions, certain ions, such as F^- and NH_4^+ , may be trapped in the ice crystal lattice at lattice positions, and other ions at lattice interstitial locations, Hallenorth and Klinger (1969) suggested that the diffusion of a gas rather proceeds via existing grain boundaries in polycrystalline ice, and via dislocations and small angle boundaries in single crystals of ice. Thus, according to Truby (1955a), ice single crystals are composed of an immense number of hexagonal prisms. Some of these are not exactly parallel to the crystallographic axis of the crystal but deviate by a few minutes of arc. Hallenorth and Klinger suggested that these mosaic boundaries may have a considerable influence on the diffusion of a gas in ice.

5.9 Ice-Water Interface

Let us now consider a system consisting of an ice crystal surrounded by supercooled water. As we shall see in the next chapter, for sufficiently small particles of ice such a system can be in stable equilibrium, so that it is again possible to speak of the interface energy of the boundary separating the phases.

Intuition tells us that the interface energy between ice and supercooled water, $\sigma_{i/\mathrm{w}}$, must be considerably less than $\sigma_{i/\mathrm{v}}$ simply because the forces between water

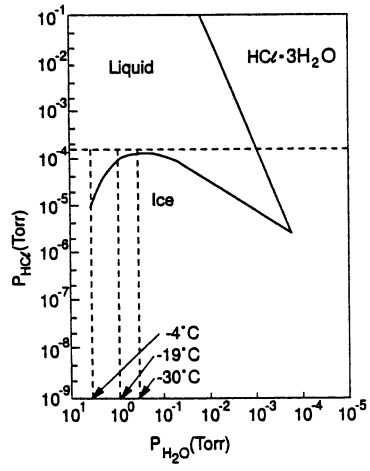


Fig. 5-14: Phase diagram for the system HCl/H_2O. The horizontal dashed line corresponds to 224 ppbv HCl. (From Hanson and Mauersberger, 1988b, with changes.)

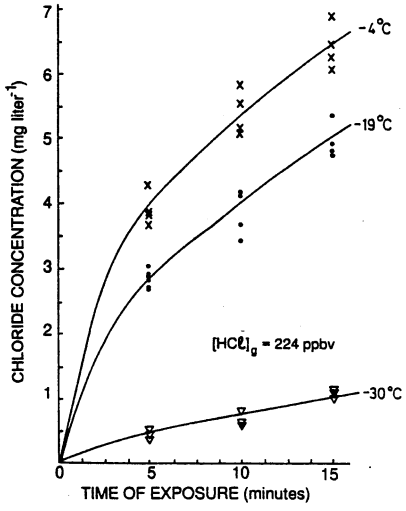


Fig. 5-15: Variation with time of the chloride concentration in dendritic snow crystals exposed to HCl at 224 ppbv and at various temperatures. (From Diehl *et al.*, 1995, with changes.)

molecules and the spatial arrangement of molecules in supercooled water are not too different from those in ice (Chapter 3). Unfortunately, it is very difficult to determine $\sigma_{i/w}$ by experimental techniques, and the results of numerous attempts show considerable spread (Figure 5.16). Nevertheless, all measurements agree on the fact that $\sigma_{i/w}$ decreases with decreasing temperature. This is to be expected since the structure of water becomes increasingly ice-like as the temperture decreases below 0°C (see Chapter 3). In Figure 5.16, the extrapolation to temperatures below −35°C was carried out by considering the results of experiments carried out near −40°C, as well as by forcing agreement with the singularity behavior of water near −45°C (see Section 3.4).

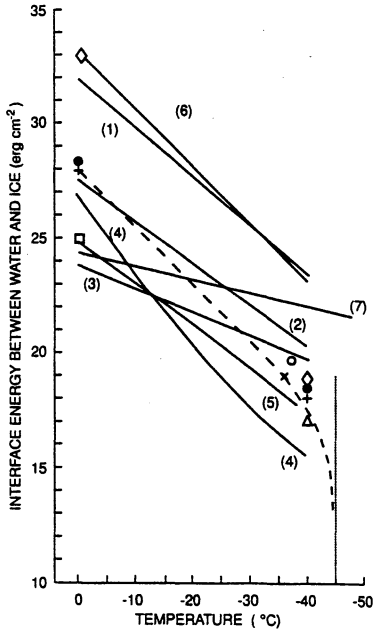


Fig. 5-16: Variation with temperature of the interface energy between water and ice. (1), (2) Wood and Walton (1970); (3) Dufour and Defay (1963); (4) Rasmussen and MacKenzie (1972); (5) Pruppacher (unpublished), based on data of Kubelka and Prokscha (1944); (6) Pruppacher (unublished), based on data of Turnbull (1950); (7) Eadie (1971); × Hoffer (1961); ○ Kuhns and Mason (1968); △ Mason (1957a,b); Coriel *et al.* (1971); ◇ Ketcham and Hobbs (1969); + Pruppacher (unpublished), based on Antonovs rule; and • Pruppacher (unpublished), based on latent heat of melting. The dashed line is the proposed variation, consistent with the −45°C limit.

In addition to the experimental results plotted Figure 5.16, two indirect methods for estimating $\sigma_{i/w}$ deserve attention. The first method is based on Antonoff's rule (Antonoff, 1907), which states that the interfacial tension between two mutually saturated liquids (l_1, l_2) is given by the absolute difference between their respective

surface tensions against the gas surrounding them, i.e.,

$$\sigma_{l_1/l_2} = \mid \sigma_{l_1/g} - \sigma_{l_2/g} \mid , \tag{5-45}$$

where g indicates the gas in contact with the liquid. This can be interpreted as a limiting form of Young's relation, (5-23). Antonoff's rule has been successfully applied to the three phases of water substance, assuming that they are mutually saturated. The analogous equation for ice, water and vapor is

$$\sigma_{i/\mathrm{w}} = \sigma_{i/\mathrm{v}} - \sigma_{\mathrm{w}/\mathrm{v}}. \tag{5-46}$$

It should be emphasized that this relation is largely just a plausible conjecture for the behavior of $\sigma_{i/\mathrm{w}}$, with some additional indirect empirical support coming from the success of Antonoff's rule in other applications. Using for $\sigma_{i/\mathrm{v}}$ a mean between the values for the basal and the prism face, i.e., $\sigma_{i/\mathrm{v}} \approx 104$ erg cm^{-2} (0°C) and 106 erg cm^{-2} (−40°C), together with $\sigma_{\mathrm{w}/\mathrm{v}} \approx 76$ erg cm^{-2} (0°C) and 88 erg cm^{-2} (−40°C), (5-46) predicts $\sigma_{i/\mathrm{w}} = 28$ erg cm^{-2} (0°C) and 18 erg cm^{-2} (−40°C).

A second method for estimating $\sigma_{i/\mathrm{w}}$ is based on knowledge of the latent heat of fusion, $\mathscr{L}_m$. To make this estimate, let us imagine that we 'cut' both a body of ice and a body of water, each surrounded by water vapor, into two halves. In so doing, the energy $W_{\mathrm{c},i} \approx \mathscr{L}_s/2$ is necessary to cut N_A bonds in the surface of the ice, and the energy $W_{\mathrm{c,w}} \approx \mathscr{L}_\mathrm{e}/2$ is expended to 'cut' N_A bonds in the surface of the water. On joining one water-half to one ice-half, we may roughly assume that the ice-half gains back the energy $\mathscr{L}_\mathrm{e}/2$. The net energy expended in cutting the ice body is therefore approximately $\mathscr{L}_s/2 - \mathscr{L}_\mathrm{e}/2 \approx \mathscr{L}_m/2$, which amounts to 5.0×10^{-14} erg bond^{-1} (0°C), and 3.40×10^{-14} erg bond^{-1} (−40°C). Therefore on taking into account the same bond coverages on the basal and prism planes as used in Section 5.7.1, we obtain for the basal plane $\sigma_{i/\mathrm{w}} = 28.3$ erg cm^{-2} (0°C), and 19.2 erg cm^{-2} (−40°C) and for the prism plane $\sigma_{i/\mathrm{w}} = 30$ erg cm^{-2} (0°C), and 20.5 erg cm^{-2} (−40°C).

Comparison of the results derived from these two semi-empirical methods with experiment reveals an overall consistency. Unfortunately, however, the theoretical estimates are insufficiently accurate for discriminating among the wide scatter of experimental values. They do guide us, however, in making the following educated guess as to a reasonable relation for the variation of $\sigma_{i/\mathrm{w}}$ with temperature.

$$\sigma_{i/\mathrm{w}} = 28.0 + 0.25T; \quad -36 \leq T \leq 0°\mathrm{C}, \tag{5-47a}$$

$$\sigma_{i/\mathrm{w}} = \mathrm{a}_1 + \mathrm{a}_2 T + \mathrm{a}_3 T^2 + \mathrm{a}_4 T^3; \quad -44 \leq T \leq -36°\mathrm{C}, \tag{5-47b}$$

with $\sigma_{i/\mathrm{w}}$ in erg cm^{-2} and T in °C, and $\mathrm{a}_1 = 189.081$, $\mathrm{a}_2 = 13.1625$, $\mathrm{a}_3 = 0.3469$, and $\mathrm{a}_4 = 3.125 \times 10^{-3}$. Note that (5-47) does not descriminate between basal and prism faces of the ice crystal lattice.

In closing this section, we shall briefly look at the structure of the ice-water interface. As expected from the surface structure of ice crystals growing from the vapor, one finds that ice crystals growing in supercooled water do not have a smooth surface.

Direct photographic evidence of the presence of steps at a growing ice-water interface has been provided by Ketcham and Hobbs (1968) and Hobbs and Ketcham (1969). Some of the observed steps had spiral forms appearing at a number concentration of about 10^2 cm^{-2}, with step heights between 0.1 and 4 μm, and spacings between the steps of 5 to 20 μm. These observed step heights are enormous considering that they probably originated on screw dislocations. No explanation for this observation is currently available except to say that, as in the case of step formation at the ice-air interface, some sort of bunching mechanism may be operating.

Bryant and Mason (1960) have investigated the etched surfaces of ice grown from supercooled water. Shallow etch-pits of about 100 μm diameter and having a number density of 10^3 cm^{-2} were observed on all crystal faces. Inside a large, shallow pit, small pyramidal etch-pits of 5 to 10 μm diameter were found in a number of concentration of up to 10^5 cm^{-2}. Pyramid heights and base diameters were about equal. The sides of the pyramidal pits were facetted in the form of concentric steps, each of which had a height of a few tenths of a micron. In some larger pyramidal pits, the concentric spiral steps reached heights of up to 1 μm.

A similar etch pattern had been observed earlier by Truby (1955a,b). He noted pyramidal etch-pits which were 0.2 to 0.5 μm in depth and 0.5 to 20 μm in width. At the pit walls, concentric steps of up to 0.05 μm height were observed. Often the pits had cores of up to 20 μm in depth.

These observers have suggested that the etch pattern at the surface of an ice crystal grown from supercooled water is the result of dislocations introduced into the ice during the freezing process by mechanical or thermal stresses. Gentile and Drost-Hansen (1956), elaborating on this mechanism, have suggested that an ice crystal represents a 'socially unhappy arrangement' of water molecules. The 'unhappiness' is caused by the necessity for 'opening up' the bond angle of a water molecule in order to conform to the tetrahedral lattice structure of ice. Such a forced, bond angle opening introduces into the ice lattice a strain which is not uniformly distributed over the entire crystal volume. Rather, the strain energy tends to be concentrated near lines parallel to the c-axis, thereby causing strain cores. According to Gentile and Drost-Hansen, the strain energy may be relieved through the incorporation of suitably-sized, foreign salt ions in optimal concentrations. This may explain the observations of Truby (1955a,b), who noted that ice crystals grown from 10^{-3} molar fluoride solutions did not exhibit any microstructure.

5.10 Ice Aqueous Solution Interface

Since cloud drops consist of weak aqueous salt solutions, it is worthwhile to describe briefly some of the processes which take place at the ice-solution interface. Experimental observations such as those by Jaccard and Levi (1961), de Micheli and Iribarne (1963), Gross (1967, 1968), Kvajic and Brajovic (1971) and Gross *et al.* (1975, 1987) demonstrate that at the ice-aqueous solution interface, a segregation process takes place which allows a small percentage of salt to enter the ice, while the rest remains dissolved in solution. Salt ions do not enter the ice in stoichiometric proportions. Rather, the experiments show that the interface behaves as a semi-permeable membrane, allowing certain types of salt ions to pass

through and enter the ice lattice more readily than others. This phenomenon has been found to be strongly dependent on the type of salt, the concentration of the salt in solution, and the rate at which the ice-solution interface advances. Work on this subject has been reviewed by Drost-Hansen (1967), Gross (1965, 1968), Pruppacher *et al.* (1968), Cobb and Gross (1969), Shewchuk and Iribarne (1971), Iribarne (1972), and Seidenstricker (1972).

The more recent studies have attempted to obtain information on the amount of salt segregation at the interface between ice and an aqueous salt solution by determining what is known as the *segregation* or *partition* coefficient, in some work also called the *retention* coefficient. This coefficient is generally defined as the ratio of the amount of foreign species in ice to the amount of this species in the aqueous solution (Iribarne *et al.*, 1990, 1983; de Michelis and Iribarne, 1963; Lamb and Blumenstein, 1987; Snider *et al.*, 1992; Iribarne and Pyshnov, 1990; Brill and Ender, 1955; Jaccard and Levi, 1961; Gross, 1967, 1968; Gross *et al.*, 1975, 1987).

In comparing the results of these studies, we find considerable agreement which allows the following conclusions: (1) The amount of salt trapped in ice increases with an increasing rate at which the ice solution interface advances implying that salt segregation is most efficient if the interface advances slowly. Nevertheless, at freezing rates of several centimeters per second, which are typical during the spontaneous growth of ice crystals in supercooled aqueous solutions, segregation is still significant. (2) The amount of salt trapped in ice increases with increasing supercooling of the solution. This is partly due to the increased growth rate of ice at lower temperatures, and also, for gases, due to their higher solubility in water at lower temperatures. (3) The amount of foreign species trapped in ice is a function of the type of species dissolved in water, and in particular of the type of ions into which the species is dissociated in the solution. As expected from our discussion in Chapter 3, generally negatively charged ions (anions) are more acceptable within the ice lattice than are positively charged ions (cations). (4) Small ions are more readily built into the ice lattice than are large ions or ions of complicated structure. (5) The two ions most readily accepted by the ice lattic are F^- and NH_4^+. F^- is preferred because of its electronegativity and because of its ionic radius, which is similar that of the oxygen atom in a water molecule. Although NH_4^+ does not conform well with points (3) and (4), it is nevertheless preferred because of its tetrahedral moleculear structure, which is analogous to the tetrahedral structural units in ice, and because of its ionic radius, which is similar to that of O^{2-}, thus making NH_4^+ isomorphous with H_3O^+. (6) Segregation of salts and ions is most effective at concentrations in solution between 10^{-5} and 10^{-3} mole liter^{-1}. In this concentration range, segregation usually exhibits a maximum. At higher concentrations, segregation is progressively less effective. Generally, the partition coefficient for salts varies between 10^{-2} and 10^{-4}. (7) Due to ion separation at the ice-solution interface, an interesting electrical effect occurs, known as the *freezing potential.* Owing to the low conductivity of ice, the incorporated ions, distributed throughout the ice volume, behave as a 'frozen-in' space charge. The charge of opposite sign which remains in solution is distributed as a surface charge at the ice-solution interface. This arrangement of charge results in the development of an electrical potential between the ice and the aqueous solution. Typical freez-

ing potentials range from several volts to several tens of volts, for some salts even as much as a few hundred volts may be realized (Heinmetz, 1962; Workman and Reynolds, 1950; Lodge *et al.*, 1956; Pruppacher *et al.*, 1968). Those interested in freezing potentials may wish to consult, in addition to the previously mentioned references, the theoretical explanations presented in Gross (1954), Le Febre (1967), Chernov and Melnikova (1971), and Jindal and Tiller (1972). (8) Numerous studies have shown that also gases dissolved in water may be transferred into the ice phase during the freezing of supercooled water containing dissolved gas. However, as expected from the uptake of salt ions by ice, only a small percentage of the gas present in supercooled water turns out to be actually transferred into the ice phase. Thus, Snider *al.* (1992) found that the retention coefficient Γ (defined as the ratio of the gas concentration in the ice phase to the concentration of the gas in the water in equilibrium with the surrounding gas) for a ventilated ice particle growing by collision with water drops which contain H_2O_2, is $\Gamma = 0.24 \pm 0.07$, a value much lower than the value found for H_2O_2 by Iribarne and Pyshnov (1990) for an unventilated ice surface. Jaccard and Levi (1960) found for NH_3 and HF, $10^{-4} \lesssim \Gamma \lesssim 10^{-2}$, depending on the concentration of the gas. For SO_2, Iribarne *et al.* (1990, 1983) found at $-15°C$ $\Gamma = 0.25$ for $[SO_2]_g = 19$ ppmv and $\Gamma = 0.9$ for $[SO_2]_g = 190$ ppbv, while Lamb and Blumenstein (1987) found $\Gamma = 0.01$ near 0°C and 0.12 near $-20°C$ for, $[SO_2]_g = 700$ ppbv.

5.11 Condensation, Deposition, and Thermal Accommodation Coefficients

There are some important gas kinetic relations pertaining to surfaces which we shall need in our discussions of nucleation and diffusion growth. Since they are of an elementary nature, for the most part we wish only to record them here, without derivations, for our future use.

Let $\dot{c}$ denote the concentration of molecules and $\bar{v}$ the mean molecular speed in a Maxwell-Boltzmann gas. Then, the number of molecules crossing per unit time to either side of an arbitrarily oriented planar unit area in this gas is

$$\mathrm{w}^{\downarrow} = \dot{c}\bar{v}/4\,. \tag{5-48}$$

Also for such a gas, the relation between $\bar{v}$ and temperature is

$$\bar{v} = \left(\frac{8\mathrm{k}T}{\pi\dot{m}}\right)^{1/2}, \tag{5-49}$$

where $\dot{m}$ is the molecular mass. And, if we may assume the gas is ideal, the gas pressure is

$$p = \dot{c}\mathrm{k}T\,. \tag{5-50}$$

Let us now consider the water-vapor interface. On combining (5-48) to (5-50), we find that the molecular flux of water vapor to the surface can be expressed as

$$\mathrm{w}^{\downarrow} = \mathrm{e}/(2\pi\dot{m}_{\mathrm{w}}\mathrm{k}T_g)^{1/2}\,, \tag{5-51}$$

TABLE 5.4
Accommodation coefficient (condensation coefficient) α_c , for water molecules on water surface.

Observer	α_c	Observer	α_c
Alty (1931)	0.006 to 0.016	Chodes *et al.* (1974)	0.033
Alty and Nicole (1931)	0.01 to 0.02	Golub *et al.* (1974)	0.12
Alty (1933)	0.04	Rogers and Squires (1974)	0.065
Alty and Mackay (1935)	0.036	Narusawa and Springer (1975)	0.038
Baramaev (1939)	0.033	Sinarwalla *et al.* (1975)	0.026
Pruger (1940)	0.02	Bonacci *et al.* (1976)	> 0.7
Yamamoto and Miura (1949)	0.023	Neizvestnyy and Onishekenko (1979)	> 0.3
Hammeke and Kappler (1953)	0.045	Neizvestnyy *et al.* (1979)	> 0.3
Kappler and Hammeke (1955)	0.1	Wagner (1982)	1.0
Delaney *et al.* (1964)	0.0415	Fujikawa *et al.* (1983)	0.04
Jameson (1964)	> 0.3	Garnier *et al.* (1987)	0.01
Kiriukhin and Plaude (1965)	0.019	Salk *et al.* (1988)	0.2 -1.0
Maa (1967)	≈ 1.0	Hagen *et al.* (1989a)	
Ahoy (1971)	0.8	clean drops	1.0
Levine (1973)	1.0	aged drops	0.01

where $p = \mathrm{e}$ is the vapor pressure, and T_g is the vapor temperature. For example, for saturated conditions at 20°C, $\mathrm{w}^{\downarrow} = 8.5 \times 10^{21}$ cm^{-2} sec^{-1}. Of these impinging molecules, only a fraction α_c, called the *mass accommodation* or *condensation coefficient*, actually is retained by the water surface. Under equilibrium conditions then, the rate $\mathrm{w}^{\uparrow}$ at which molecules leave the surface must satisfy the relation

$$\mathrm{w}^{\uparrow} = \alpha_c \mathrm{w}^{\downarrow} \quad \text{at equilibrium.} \tag{5-52}$$

Experimental values for α_c are listed in Table 5.4 based on a recent review of the subject by Mozurkewich (1986). The data listed were derived from observations with a quiescent or quasi-quiescent water surface, and from observation of growing aerosol particles. We notice that these values scatter over a wide range from about 0.01 to 1.0. Mozurkewich concludes from his survey that for pure water and water containing polar species, α_c may be approximately taken as near unity.

The mean residence time τ_s of a molecule in the water surface is given by

$$\tau_s = n/\mathrm{w}^{\uparrow}, \tag{5-53}$$

where $n \approx 10^{15}$ cm^{-2} is the equilibrium number of water molecules present in one cm^2 of water surface. Assuming $\alpha_c = 0.04$, we then find $\mathrm{w}^{\uparrow} = 3.4 \times 10^{20}$ cm^{-2} sec^{-1} and $\tau_s \approx 3\,\mu$ sec at 20°C. This very short lifetime of a water molecule before it evaporates from the water surface implies an extremely violent agitation; however, because of the strong cohesion in the liquid surface this agitation is confined to a layer of only a few molecular thicknesses. Note that this rapid exchange of molecules applies only at equilibrium. Of course, $\mathrm{w}^{\uparrow}$ should not be interpreted as a net evaporation rate. Drop evaporation rates are discussed in Chapter 13.

We shall assume now that the flux of molecules leaving the water is independent of the flux entering it, and that it is equal to the flux of molecules which would enter the water if it were in equilibrium with the vapor phase for which $\mathrm{e} = \mathrm{e}_{\mathrm{sat,w}}$; i.e.,

TABLE 5.5
Accommodation coefficient (deposition coefficient) α_d, for water molecules on an ice surface.

Observer	Temperature (°C)	α_d
Delaney *et al.* (1964)	-2 to -13	0.014
Vulfson and Levin (1965)	-6 to -7	0.04
Vulfson and Levin (1965)	-10 to -11	0.7
Fukuta and Armstrong (1974)	-25	0.12
Davy and Somorjai (1971)	-45	0.36
Kramers and Stemerding (1951)	-40 to -60	0.93
Tschudin (1945)	-60 to -85	0.94
Davy and Somorjai (1971)	-85	1.0
Koros *et al.* (1966)	-115 to -140	0.83

$w^{\uparrow} = \alpha_c e_{sat,w}/(2\pi \dot{m}_w k T_a)^{1/2}$, where T_a, is the temperature of the water surface. Assuming $T_g \approx T_a = T$, we find for the net flux of molecules into the surface,

$$w_{net,w} = \alpha_c (e - e_{sat,w})/(2\pi \dot{m}_w k T)^{1/2} . \tag{5-54}$$

Analogously, for the net flux of water molecules to an ice surface, we write

$$w_{net,i} = \alpha_d (e - e_{sat,i})/(2\pi \dot{m}_w k T)^{1/2} , \tag{5-55}$$

where α_d is called the *deposition coefficient.* Equations (5-54) and (5-55) are different forms of what is known as the Hertz-Knudsen equation.

More recently, Schrage (1953) and Patton and Springer (1969) have modified this equation to account for the effect of net bulk vapor motion of the molecular velocity distribution. According to these authors, a better representation for w_{net} is

$$w_{net,w} = \frac{\alpha_c}{1 - B\alpha_c} (e - e_{sat,w})/(2\pi \dot{m}_w k T)^{1/2} , \tag{5-56}$$

where B = 0.5, according to Schrage.

Experimentally determined values for α_d are listed in Table 5.5. We see from this table that the deposition coefficient for water molecules on ice exhibits a trend from values near unity at very low ice surface temperatures near 0°C. This result may be interpreted as evidence for the quasi-liquid film which has been postulated to exist on an ice surface.

Conceptually, one expects that water molecules striking a water or ice surface suffer inhibited accommodation with respect to heat as well as mass flow. In order to take this effect into account, one introduces a *thermal accommodation coefficient.* In the context of interest to us, this coefficient is defined as the ratio of water vapor molecules which on collision with a (macroscopic) water drop or ice particle achieve thermal equilibrium with it, to the total number of water vapor molecules striking the surface. This definition may also be expressed as

$$\alpha_T \equiv \frac{T' - T_2'}{T' - T_2} , \tag{5-57}$$

where T' and T are the kinetic temperature of the gas molecules incident on, and reflected by, the surface of the body with which the environment attempts thermal equilibrium, and T_2 is the surface temperature of the body. From our verbal definition α_T, it is clear that (5-57) is simply a statement of the balance of thermal energy into and out of the surface. Experiments by Alty and Mackay (1935), which unfortunately are the only ones available, show that for a water surface, $\alpha_T \approx 0.96$. This indicates that most gas molecules thermally equilibrate with a water surface during their residence time on that surface. No measurements for an ice surface are available.

CHAPTER 6

EQUILIBRIUM BEHAVIOR OF CLOUD DROPS AND ICE PARTICLES

Having established some background for use in studying the bulk and surface properties of water and aqueous solutions, it is appropriate now to take a closer look at the equilibrium behavior of typical and/or idealized cloud particles of ice and water. In particular, we shall study the equilibrium of (1) a pure water or aqueous solution drop surrounded by water vapor or humid air, (2) an ice crystal in humid air, (3) an ice crystal and a separate solution drop in humid air, and (4) an ice crystal immersed in a solution drop in humid air. We shall see later that the relationships provided by these case studies are needed in order to formulate the conditions for which cloud drops and ice crystals are nucleated in the atmosphere (Chapters 7 and 9).

6.1 General Equilibrium Relation for Two Phases Separated by a Curved Interface

In this section, we shall return to the system first discussed in Section 5.2, in which a spherical bulk phase $''$ of radius a is imbedded in another bulk phase $'$. We suppose each phase contains component k and other components constituting a non-ideal mixture. Also, we allow mass transfers to occur between phases, but exclude chemical reactions. We further assume thermal equilibrium, and let T denote the common temperature.

Our goal is to obtain a single equation relating the differentials of T, p', σ, a, and the activities a'_k and a''_k for component k. There are, of course, several possible starting points for accomplishing this; here we shall follow a particularly efficient procedure suggested by Dufour and Defay (1963). We begin with the chemical potential of component k in either of the bulk phases (cf. (4-53)):

$$\mu_k(p, T, \mathrm{a}_k) = \mu_{k,0}(p, T) + \mathscr{R} T \ln \mathrm{a}_k \,. \tag{6-1}$$

On dividing this expression by T, forming the total difierential, and using (4-13a) and (4-13b), we find that for equilibrium changes

$$\mathrm{d}\left(\frac{\mu_k}{T}\right) = -\frac{h_{k,0}}{T^2}\mathrm{d}T + \frac{v_{k,0}}{T}\mathrm{d}p + \mathscr{R}\,\mathrm{d}\ln \mathrm{a}_k \,. \tag{6-2}$$

Now in equilibrium we have $\mu'_k = \mu''_k$ also; consequently, we may write

$$\mathrm{d}\left(\frac{\mu'_k}{T}\right) = \mathrm{d}\left(\frac{\mu''_k}{T}\right) \,. \tag{6-3}$$

Therefore, on combining this equality with (6-2) as applied to both bulk phases, we may eliminate direct reference to the chemical potentials and obtain

$$-\frac{(h'_{k,0}-h''_{k,0})}{T^2}\mathrm{d}T+\frac{v'_{k,0}}{T}\mathrm{d}p'-\frac{v''_{k,0}}{T}\mathrm{d}p''+\mathscr{R}\,\mathrm{d}\ln(\mathrm{a}'_k/\mathrm{a}''_k)=0\,. \tag{6-4}$$

Finally, we invoke the condition of mechanical equilibrium, (5-7), and introduce the latent heat $\mathscr{L}''/'$, from (4-72); the desired form is thereby obtained from (6-4):

$$-\frac{\mathscr{L}''_{k,0}/'}{T^2}\mathrm{d}T+\frac{(v'_{k,0}-v''_{k,0})}{T}\mathrm{d}p'-\frac{2v''_{k,0}}{T}\mathrm{d}\left(\frac{\sigma}{a}\right)+\mathscr{R}\,\mathrm{d}\ln(\mathrm{a}'_k/\mathrm{a}''_k)=0\,. \tag{6-5}$$

This result may well be regarded as the 'master equation' for this chapter, because special cases of it describe nearly every situation we discuss. It is obvious that (6-5) contains the Clausius-Clapeyron equation as a special case which is readily obtained by letting $\mathrm{a}'_k=1, \mathrm{a}''_k=1$, and $(1/a)=0$.

6.2 Effect of Curvature on Latent Heat of Phase Change

Perhaps the reader is disturbed by a bit of sleight-of-hand we used in arriving at (6-5): In substituting $\mathscr{L}''_{k,0}/'$ for the enthalpy difference in (6-4), we glossed over the fact that the pressures are not equal in phases $'$ and $''$; thus, (4-72) does not strictly apply. We shall now estimate the error incurred by ignoring this pressure difference.

Evidently, the error is measured by

$$\Delta h''_{k,0}\equiv h''_{k,0}(p'',T)-h''_{k,0}(p',T)=\int_{p'}^{p''}\left(\frac{\partial h''_{k,0}}{\partial p''}\right)_T\mathrm{d}p''\,. \tag{6-6}$$

But from (4-6) we see that $(\partial h/\partial p)_T=v+T(\partial s/\partial p)_T$, where s is the molar entropy, while from (4-10) and (4-11) we find $(\partial s/\partial p)_T$; consequently,

$$\left(\frac{\partial h''_{k,0}}{\partial p''}\right)_T=v''_{k,0}-T\left(\frac{\partial v''_{k,0}}{\partial T}\right)_{p''}\,. \tag{6-7}$$

For either water or ice, the second term in (6-7) is negligible in comparison with the first; furthermore, since the compressibilities of water and ice are very small (see Section 6.4), we may regard $v''_{k,0}$ as constant when inserted into (6-6), and so obtain

$$\Delta h''_{k,0}\approx v''_{k,0}(p''-p')=2v''_{k,0}\sigma/a\,. \tag{6-8}$$

Now, if we denote the latent heat of pure substance k in passing from phase $''$ to spherical phase $'$ of radius a by $(\mathscr{L}''_{k,0}/')_a$, we see that

$$(\mathscr{L}''_{k,0}/')_a=(\mathscr{L}''_{k,0}/')_\infty-\Delta h''_{k,0}\,. \tag{6-9}$$

Consequently, for the case of a pure water drop in equilibrium with water vapor, we can write

$$\frac{(\mathscr{L}_{\mathrm{e},0})_a}{(\mathscr{L}_{\mathrm{e},0})_\infty}=1-\frac{\Delta h_{\mathrm{w},0}}{(\mathscr{L}_{\mathrm{e},0})_\infty}\approx 1-\frac{2\sigma_{\mathrm{w/v}}M_{\mathrm{w}}}{\rho_{\mathrm{w}}(\mathscr{L}_{\mathrm{e},0})_\infty a}\,. \tag{6-10}$$

This demonstrates that the latent heat of evaporation decreases with decreasing radius of curvature of the water surface. At 0°C, the second term on the right side of (6-10) has the value $6.1 \times 10^{-9}/a$, for a in cm. Thus, the error in setting $(\mathscr{L}_{e,0})_a = (\mathscr{L}_{e,0})_\infty$ becomes less than 1%, as long as $a \gtrsim 6 \times 10^{-7}$ cm.

Analogously, we find for the latent heat of sublimation

$$\frac{(\mathscr{L}_s)_a}{(\mathscr{L}_s)_\infty} \approx 1 - \frac{2\sigma_{i,v} M_w}{\rho_i (\mathscr{L}_s)_\infty a}. \tag{6-11}$$

At 0°C, the second term on the right side of this equation has the value $7.7 \times 10^{-9}/a$, so that the error in setting $(\mathscr{L}_s)_a = (\mathscr{L}_s)_\infty$ is less than 1%, as long as $a \gtrsim 8 \times 10^{-7}$ cm. Considering (4-74), we find that it is also justified to set $(\mathscr{L}_{m,0})_a = (\mathscr{L}_{m,0})_\infty$ with an error of less than 1%, as long as $a \gtrsim 2 \times 10^{-7}$ cm.

6.3 Generalized Clausius-Clapeyron Equation

We noted in Section 6.1 that (6-5) contains, as a special case, the Clausius-Clapeyron equation for a pure substance in bulk phases of negligible curvature. We may now very easily derive its extended form for the case where the curvature matters. For this purpose, consider again a pure water drop in equilibrium with vapor at pressure $p' = e_{a,w}$. We have $a'_k = a''_k = 1$, and so we may rearrange (6-5) to read

$$\frac{de_{a,w}}{dT} = \frac{(\mathscr{L}_{e,0})_a}{T(v_{v,0} - v_{w,0})} + \frac{2v_{w,0}}{(v_{v,0} - v_{w,0})} \frac{d(\sigma_{w/v}/a)}{dT}. \tag{6-12}$$

According to the phase rule for curved phases, (5-10), the present system has two degrees of freedom. Let us hold the radius a constant and study the variation of $e_{a,w}$ with T. Then, substitution of (6-10) and (4-80) into (6-12) leads to the desired extension of the Clausius-Clapeyron equation:

$$\frac{de_{a,w}}{dT} = \frac{de_{sat,w}}{dT} - \frac{2[\sigma_{w/v} - T(d\sigma_{w/v}/dT)_a]}{aT[(v_{v,0}/v_{w,0}) - 1]}, \tag{6-13}$$

where we should recall that the equilibrium vapor pressure $e_{a,w}$ over a curved water surface actually has the physical meaning $(e_{sat,w})_a \equiv e_a$, and the equilibrium vapor pressure $e_{sat,w}$ over a plane water surface has the meaning $(e_{sat,w})_\infty \equiv e_{sat,w}$. Since $d\sigma_{w/v}/dT < 0$ for all T, curvature is seen to decrease the temperature variation of the saturation vapor pressure. On evaluating the terms in (6-13) at 20°C, we have

$$\frac{\left(\frac{de_{a,w}}{dT}\right)_a}{\left(\frac{de_{sat,w}}{dT}\right)} \approx 1 - \frac{10^{-8}}{a}, \tag{6-14}$$

for a in cm. Thus, the quantitative effect is quite small (less than 1% difference for $a \gtrsim 10^{-6}$ cm), as we might expect from our previous studies of the effects of curvature.

In the remainder of this chapter, we shall ignore the small influence of curvature on latent heat.

6.4 Equilibrium Between a Pure Water Drop and Pure Water Vapor or Humid Air

We may suppose a system comprised of a pure water drop ($''$) in an environment of humid air ($'$) contains just two components, air and water, since there is negligible selective adsorption of the gaseous constituents of air. Therefore, the system has a variance of three according to the phase rule. We shall keep the temperature T and the total gas pressure constant, and study the variation of the water vapor pressure $\mathrm{e}_{a,\mathrm{w}}$ with radius a. With $v''_{k,0} = v_{\mathrm{w},0}$, $\mathrm{a}'_k = \mathrm{a}_\mathrm{v}$, and $\mathrm{a}''_k = \mathrm{a}_\mathrm{w}$, (6-5) reduces to

$$-\frac{2v_{\mathrm{w},0}}{T}\mathrm{d}\left(\frac{\sigma_{\mathrm{w/a}}}{a}\right) + \mathscr{R}\,\mathrm{d}\ln \mathrm{a}_\mathrm{v} = 0\,, \tag{6-15}$$

since for a pure water drop $\mathrm{a}_\mathrm{w} = 1$. Assuming ideal gas behavior, we have $\mathrm{a}_\mathrm{v} = \mathrm{x}_\mathrm{v} = \mathrm{e}_{a,\mathrm{w}}/p$. Making this substitution and disregarding for the moment the compressibility of water, we may immediately integrate (6-15) between ∞ and a to obtain

$$\ln\frac{\mathrm{e}_{a,\mathrm{w}}}{\mathrm{e}_{\mathrm{sat,w}}} = \frac{2v_{\mathrm{w},0}\sigma_{\mathrm{w/a}}}{\mathscr{R}Ta} = \frac{2M_\mathrm{w}\sigma_{\mathrm{w/a}}}{\mathscr{R}T\rho_\mathrm{w}a}\,, \tag{6-16a}$$

or

$$\frac{\mathrm{e}_{a,\mathrm{w}}}{\mathrm{e}_{\mathrm{sat,w}}} = \exp\left(\frac{2M_\mathrm{w}\sigma_{\mathrm{w/a}}}{\mathscr{R}T\rho_\mathrm{w}a}\right)\,. \tag{6-16b}$$

This is the *Kelvin equation*, first derived by W. Thomson (later Lord Kelvin, 1870). It demonstrates that at any given temperature, the saturation vapor pressure over the surface of a water drop is larger than that over a flat surface, and increasingly so with decreasing radius. Accordingly, in the atmosphere large drops must grow by vapor diffusion at the expense of the smaller ones.

Since the Kelvin equation assumes equilibrium between the drop and its environment, we of course have $\mathrm{e}_{a,\mathrm{w}} = \mathrm{e}$, the partial pressure of vapor in the environment. Hence, we can also say that equilibrium requires an environmental supersaturation of $\mathrm{s}_{\mathrm{v,w}} = (\mathrm{e}_{a,\mathrm{w}}/\mathrm{e}_{\mathrm{sat,w}}) - 1 > 0$; also, the Kelvin equation may be expressed in terms of the saturation ratio $S_{\mathrm{v,w}} = \mathrm{e}_{a,\mathrm{w}}/\mathrm{e}_{\mathrm{sat,w}}$ in the form

$$\ln S_{\mathrm{v,w}} = \frac{2M_\mathrm{w}\sigma_{\mathrm{w/a}}}{\mathscr{R}T\rho_\mathrm{w}a}\,. \tag{6-17}$$

A numerical evaluation of (6-17) is plotted in Figure 6.1 for 20°C and −20°C. Note that the effect of curvature becomes important only for $a \lesssim 10^{-5}$ cm (0.1 μm), and that the temperature dependence is relatively weak.

Let us assume now that air is absent from the system and that the water drop is surrounded instead by pure water vapor. From the phase rule, it follows that this system has two independent intensive variables. Of these we shall keep T constant and again determine the variation of $\mathrm{e}_{a,\mathrm{w}}$ with a. Under these conditions, the first and last terms of (6-5) are zero ($\mathrm{a}'_k = \mathrm{a}_\mathrm{v} = \mathrm{x}_\mathrm{v} = 1$, assuming ideal gas behavior), and we obtain

$$\frac{v_{\mathrm{v},0}}{T}\mathrm{d}\mathrm{e}_{a,\mathrm{w}} - \frac{v_{\mathrm{w},0}}{T}\mathrm{d}\mathrm{e}_{a,\mathrm{w}} - \frac{2v_{\mathrm{w},0}}{T}\mathrm{d}\left(\frac{\sigma_{\mathrm{w/a}}}{a}\right) = 0\,. \tag{6-18}$$

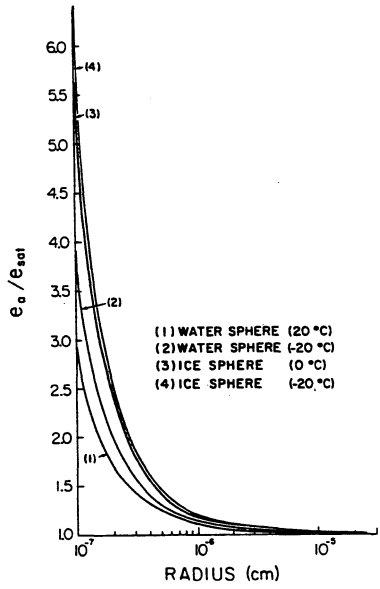


Fig. 6-1: Variation of the equilibrium vapor pressure over a water sphere and over an ice sphere with sphere size, for different temperatures. For curves (1) and (2), ordinate represents $e_{a,w}/e_{sat,w}$. For curves (3) and (4), ordinate represents $e_{a,i}/e_{sat,i}$

On substituting the ideal gas law for $v_{v,0}$ and integrating between ∞ and a (6-18) yields

$$\ln(S_{v,w})_{vapor} = \ln\left(\frac{e_{a,w}}{e_{sat,w}}\right)_{vapor} = \frac{2M_w\sigma_{w/v}}{\mathscr{R}T\rho_w a} + \frac{M_w}{\rho_w\mathscr{R}T}(e_{a,w} - e_{sat,w}), \quad (6\text{-}19)$$

which demonstrates that $(S_{v,w})_{vapor} > (S_{v,w})_{air}$. However, the difference is small: Comparison of (6-17) and (6-18) shows that

$$\frac{\ln(S_{v,w})_{vapor}}{\ln(S_{v,w})_{air}} - 1 \approx \frac{e_{a,w} - e_{sat,w}}{(2\sigma_{w/v}/a)} \ll 1, \quad (6\text{-}20)$$

for alI cases of interest.

Notice that in our derivation of the Kelvin equation, we assumed nowhere that the surface tension is independent of the curvature of the drop. However, we did assume that the compressibility of water is negligible. This latter assumption has been investigated by Dufour and Defay (1963), who found that the inclusion of compressibility leads to the following modification of (6-17):

$$\ln S_{v,w} = \frac{2\sigma_{w/a}v_{w,0}}{\mathscr{R}Ta}\left(1 - \frac{\kappa_{w,0}\sigma_{w/a}}{a}\right), \quad (6\text{-}21)$$

where $v_{w,0}$ is the molar volume of pure water in bulk, in contrast to $v_{w,0}$ in (6-17) which is actually the molar volume evaluated at the internal pressure of

the drop, and $\kappa_{w,0} = -(1/v_{w,0})(\partial v_{w,0}/\partial p_w)_T$ is the compressibility. Since in the temperature range +30 to −30°C $\kappa_{w,0}$ varies between 45×10^{-12} and about 70×10^{-12} cm^2 dyne^{-1} (Handbook of Chemistry and Physics), we readily find that $(\kappa_{w,0}\sigma_{w/a}/a) \ll 1$ for all drop radii encountered in clouds. We may therefore represent $v_{w,0}$ by its bulk value with negligible error.

6.5 Equilibrium Between an Aqueous Solution Drop and Humid Air

Let us now investigate the more interesting and realistic case of the equilibrium between a drop of an aqueous salt solution ($''$) and an environment of humid air ($'$). We assume that the dissolved substance has no vapor pressure of its own, and that its mass in the drop remains constant. The first of these assumptions holds for all salts typically found in the atmosphere. The second assumption holds for at least the early stages of cloud drop formation; during the later stages of growth, solutes may be added to the drop by means of various scavenging mechanisms.

According to (5-10), this system has three components, and so w = 4. However, the required constancy of salt mass in the drop introduces an additional relation between the drop radius and the mole fraction of water in solution, which makes w = 3. The volume of the solution drop is given by $4\pi a^3/3 = n_w v_w + n_s v_s$. Since $x_w = n_w/(n_w + n_s)$, where n_s, v_w, v_s are constants, the additional relation is

$$\frac{1}{x_w} = 1 + \frac{n_s}{n_w} = 1 + \frac{n_s v_w}{\frac{4\pi a^3}{3} - n_s v_s}\,. \tag{6-22}$$

Let us now determine the dependence of the saturation vapor pressure e_a on radius, subject to the conditions of constant T, n_s, and total air pressure p. This time only the last two terms of (6-5) survive, and since we now have $a_k' = a_v = e_a/p$ but $a_k'' = a_w \neq 1$, the following result is obtained:

$$-\frac{2v_{w,0}}{\mathscr{R}T}\mathrm{d}\left(\frac{\sigma_{s/a}}{a}\right) + \mathrm{d}\ln e_a - \mathrm{d}\ln a_w = 0\,. \tag{6-23}$$

On integration from a, e_a, a_w to $a \to \infty$, $e_a = e_{sat,w}, a_w = 1$ this equation yields

$$\ln\frac{e_a}{e_{sat,w}} = \ln a_w + \frac{2M_w\sigma_{s/a}}{\mathscr{R}T\rho_w a} \tag{6-24a}$$

or

$$\frac{e_a}{e_{sat,w}} = a_w \exp\left(\frac{2M_w\sigma_{s/a}}{\mathscr{R}T\rho_w a}\right)\,, \tag{6-24b}$$

where a_w is given by (4-68) and (4-69). For $a_w = 1$, (6-24) reduces to the Kelvin law, while for a flat water surface, the generalized Raoult's law, (4-60), is recovered.

Unfortunately, no information is available on the curvature dependence of the activity coefficient of water in an aqueous solution. However, in view of our previous discussion of the effects of curvature, it seems very reasonable to regard it as

negligible, and we shall do so here. Considering (4-69) and (4-66), we may replace a_w in (6-24b) by

$$a_w = \exp\left(-\frac{\nu\Phi_s m_s M_w/M_s}{(4\pi a^3/3)\rho_s'' - m_s}\right). \tag{6-25}$$

Therefore, for a drop in equilibrium with its environment ($e = e_a$), (6-24) may also be written in the form

$$S_{v,w} = \exp\left[\frac{2M_w\sigma_{s/a}}{\mathscr{R}T\rho_w a} - \frac{\nu\Phi_s m_s M_w/M_s}{(4\pi a^3\rho_s''/3) - m_s}\right] \tag{6-26a}$$

or

$$\ln S_{v,w} = \frac{2M_w\sigma_{s/a}}{\mathscr{R}T\rho_w a} - \frac{\nu\Phi_s m_s M_w/M_s}{(4\pi a^3\rho_s''/3) - m_s}. \tag{6-26b}$$

Now for a sufficiently dilute solution such that $m_s \ll m_w$, $\sigma_{s/a} \approx \sigma_{w/a}$, $\Phi_s \approx 1$ and $\rho_s'' \approx \rho_w$ (6-26b) reduces to the more convenient form

$$\ln S_{v,w} = \frac{A}{a} - \frac{B}{a^3}, \tag{6-27}$$

where

$$A = \frac{2M_w\sigma_{w/a}}{\mathscr{R}T\rho_w} \approx \frac{3.3\times 10^{-5}}{T}; \qquad B = \frac{3\nu m_s M_w}{4\pi M_w\rho_w} \approx \frac{4.3\nu m_s}{M_s}, \tag{6-28}$$

in cgs units and with T in K. Finally, if $e_a/e_{sat,w} \approx 1$, (6-27) reduces further to

$$S_{v,w} = 1 + \frac{A}{a} - \frac{B}{a^3}. \tag{6-29}$$

Equations (6-26) to (6-29) are different forms of the *Köhler equations* (Köhler, 1921a,b, 1922, 1927, 1936).

As we have seen, the vapor pressure over a pure water drop always obeys the inequality $e_{a,w} \geq e_{sat,w}$. In contrast, the vapor pressure over an aqueous solution drop may be larger or smaller than $e_{sat,w}$ depending on whether the solute term (the second term on the right side of (6-26) and (6-27)) is smaller or larger than the curvature term. This, in turn, implies that an aqueous solution drop may be in equilibrium with a subsaturated environment. Specifically, if $a^2A < B$, then $e_a < e_{sat,w}$.

The Köhler equations are plotted in Figure 6.2 for solution drops of two representative salts. The maxima in the curves are found from (6-29) to occur approximately at the *critical radius* $a_c = (3B/A)^{1/2}$, corresponding to $s_c = [(e_a/e_{sat,w}) - 1]_c = (4A^3/27B)^{1/2}$. (In the remainder of this chapter, we shall use the subscript c to denote conditions at the critical radius.) It is interesting to note that for $a > a_c$ the solution drop is in unstable equilibrium with its environment, just as a pure water drop is in unstable equilibrium at all sizes. For $a < a_c$ on the other hand, the solution drop is in stable equilibrium. This behavior can be understood on realizing the environment effectively provides an infinitely large reservoir of water vapor at constant pressure. For example, suppose the equilibrium state is given by

a point on the descending branch ($a > a_c$) of one of the equilibrium growth curves in Figure 6.2. Assume now that a small perturbation causes a few molecules of water to be added to the drop. At the slightly larger new radius, the equilibrium vapor pressure is lower; hence, vapor will continue to flow to the drop, and it will grow ever larger. Conversely, a small evaporation excursion will produce a slightly smaller radius for which the equilibrium vapor pressure is higher than that provided by the environment, and the drop will therefore continue to evaporate. If the drop is pure water, it will evaporate completely. On the other hand, if it is a solution drop, it will diminish in radius until it has reached a size which corresponds to an equilibrium state on the ascending branch ($a < a_c$) of the given equilibrium curve. Now it will be in stable equilibrium. For $da > 0 (< 0)$, we see that $de_a > 0 (< 0)$; i.e., the environmental vapor pressure is insufficient (excessive) for equilibrium at the new radius, and evaporation (condensation) will ensue to oppose the initial radius perturbation.

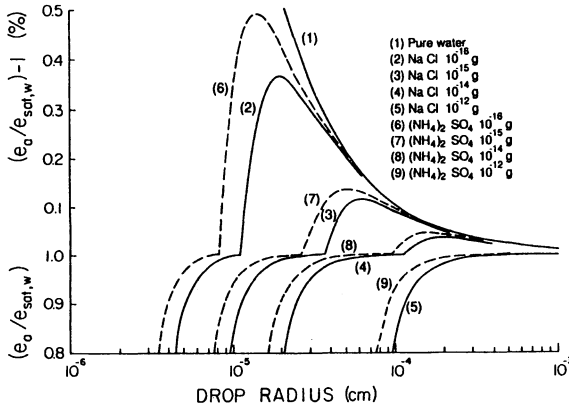


Fig. 6-2: Variation with drop size of the equilibrium vapor pressure over an aqueous solution drop; for NaCl particles (solid lines) and $(NH_4)_2SO_4$ particles (dashed lines) of various masses, and for 20°C and $\Phi_s = 1$. (Based on Equation 6-26 solved by Hänel, 1976.)

If the environment has reached a supersaturation equal to or larger than $[(e_a/e_{sat,w}) - 1]_c$, it is said to have reached the supersaturation needed to *activate* the drop. We note also that it is customary to call the radius of an aqueous solution drop which is in equilibrium with an environment of $S_{v,w} = 1.0$, the *potential radius* a_p; i.e., $a = a_p$ for $(e_a/e_{sat,w}) = S_{v,w} = 1.0$, from which $B = Aa_p^2$. Thus, we may write (6-27) in terms of a_p as

$$\ln S_{v,w} = A\left(\frac{1}{a} - \frac{a_p^2}{a^3}\right) . \tag{6-30}$$

This expression implies that aqueous solution drops which have the same potential radius exhibit the same equilibrium variation of $S_{v,w}$ with drop size.

Equation (6-26) shows how the equilibrium behavior of an aqueous solution drop depends on the total mass m_s, of salt in the drop, as well as on the type of salt (Φ_s, M_s, ν). This dependence is also illustrated in Figure 6.3, which shows that the smaller the mass of the salt in the drop, the higher the maximum, and the steeper the pre-maximum branch of the equilibrium curve for that drop. The effect of the type of salt in solution is also illustrated in Figure 6.2 for drops containing NaCl and $(NH_4)_2S0_4$. By comparing the figure with (6-27) and (6-28), we see that the dominant influence is the molecular weight of the salt, which is much larger for $(NH_4)_2SO_4$, than for NaCl, so that the equilibrium curves for a solution drop of $(NH_4)_2SO_4$ lie above the corresponding ones for NaCl.

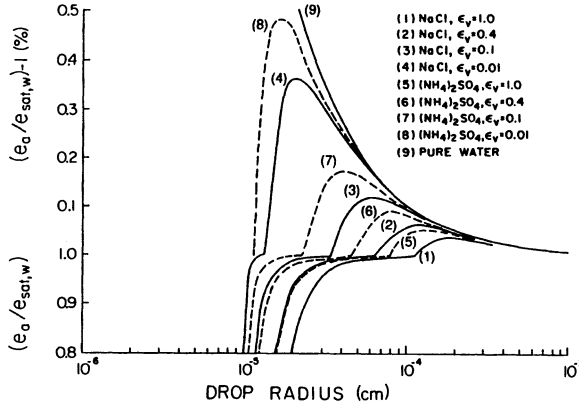


Fig. 6-3: Variation of the equilibrium vapor pressure over an aqueous solution drop formed from a mixed aerosol particle of radius $r_N = 0.1\mu$m containing various volume fractions ε_v NaCl and $(NH_4)_2SO_4$ and a water insoluble substance, for 20°C and for $\Phi_s = 1.0$. (Based on solutions to Equation 6-34, solved by Hänel, 1976.)

Temperature has only a small effect on the equilibrium conditions for solution drops, as Table 6.1 shows. The trend, such as it is, indicates that the supersaturation necessary to hold a given solution drop in equilibrium increases with decreasing temperature.

Table 6.2 lists the amount of water which is acquired and the salt dilution which is experienced during equilibrium growth of an aqueous solution drop of given salt content at different environmental equilibrium humidities. It is seen that the dilution of the salt solution is generally small, as long as the drop is in equilibrium with an environment of $S_{v,w} \lesssim 0.9$. However, the dilution increases quite rapidly as $S_{v,w}$ increases beyound 1.0 and approaches $(S_{v,w})_c$.

6.6 Equilibrium Between Humid Air and an Aqueous Solution Drop Containing a Solid Insoluble Substance

Most atmospheric aerosol particles are mixed, i.e., they are composed of water soluble and insoluble substances (see Chapter 8). The purpose of this section is

TABLE 6.1

Critical equilibrium radius a_c and critical equilibrium supersaturation $(s_{v,w})_c$ for aqueous solution drops containing different amounts of NaCl. $\rho_s(20°C) = 2.16$ g cm^{-3}, $\rho_s(-10°C) = 2.17$ g cm^{-3}, $\Phi_s = 1.0$. (Based on Low, 1969d, and of Hänel, 1976.)

m_N(g)		10^{-16}	10^{-15}	10^{-14}	10^{-13}	10^{-12}
r_N (cm)	20 °C	2.227×10^{-6}	4.797×10^{-6}	1.033×10^{-5}	2.227×10^{-5}	4.797×10^{-5}
	−10 °C	2.224×10^{-6}	4.792×10^{-6}	1.032×10^{-5}	2.224×10^{-5}	4.792×10^{-5}
$(s_{v,w})_c$ (%)	20 °C	3.660×10^{-1}	1.143×10^{-1}	3.578×10^{-2}	1.126×10^{-2}	3.558×10^{-3}
	−10 °C	4.738×10^{-1}	1.480×10^{-1}	4.628×10^{-2}	1.455×10^{-2}	4.595×10^{-3}
a_c (cm)	20 °C	1.947×10^{-5}	6.212×10^{-5}	1.988×10^{-4}	6.358×10^{-4}	2.012×10^{-3}
	−10 °C	1.783×10^{-5}	5.679×10^{-5}	1.819×10^{-4}	5.826×10^{-4}	1.844×10^{-3}

to study the effect of a solid insoluble substance within an aqueous solution drop on the equilibrium conditions for that drop. In this study, we shall assume that the insoluble particle does not take up any water by itself and does not adsorb salt ions, and that it is completely submerged.

Since the molality of the solution drop is unaffected by the addition of the insoluble particle, we may take (6-24) as our starting point. For a_w, we invoke (4-65) and (4-69) to obtain

$$\ln a_w = -\nu \Phi_s m_s M_w / m_w M_s \tag{6-31}$$

or

$$\ln a_w = -\frac{\nu \Phi_s M_w \varepsilon_m}{M_s} \frac{m_N}{m_w}, \tag{6-32}$$

where $\varepsilon_m = m_s/m_N$ is the mass fraction of water soluble material m_s in a mixed aerosol particle of mass in m_N and radius r_N. Assuming that the total drop volume V_d can be approximated by $V_d = V_w + V_N = (m_w/\rho_w) + (m_N/\rho_N)$, from which $m_N/m_w \approx (\rho_N/\rho_w)[(a/r_N)^3 - 1]^{-1}$, we find from (6-31) with (6-24)

$$\frac{e_a}{e_{sat,w}} = \exp\left[\frac{2M_w\sigma_{s/a}}{\mathscr{R}T\rho_w a} - \frac{\nu\Phi_s\varepsilon_m M_w \rho_N r_N^3}{M_s\rho_w(a^3 - r_N^3)}\right], \tag{6-33}$$

and with $\varepsilon_v = \varepsilon_m(\rho_N/\rho_s)$,

$$\frac{e_a}{e_{sat,w}} = \exp\left[\frac{2M_w\sigma_{s/a}}{\mathscr{R}T\rho_w a} - \frac{\nu\Phi_s\varepsilon_v M_w \rho_s r_N^3}{M_s\rho_w(a^3 - r_N^3)}\right], \tag{6-34}$$

where $r_N^3 = m_N/(4\pi/3)\rho_N$. Also, the densities ρ_N, ρ_s, and ρ_u of the aerosol particle and its soluble and insoluble fractions are related according to

$$\rho_N = \rho_s\varepsilon_v + \rho_u(1 - \varepsilon_v) \tag{6-35}$$

and

$$\rho_N = \frac{\rho_u}{1 - \varepsilon_m[1 - (\rho_u/\rho_s)]}. \tag{6-36}$$

TABLE 6.2

Amount of water gained during equilibrium growth of NaCl and $(NH_4)_2SO_4$ solution drops; 20° C . (Based on Low, 1969d, and of Hänel, 1976.)

		NaCl			$(NH_4)_2SO_4$		
mass m_N(g) of salt in solution		1.0×10^{-16}	1.0×10^{-14}	1.0×10^{-12}	1.0×10^{-16}	1.0×10^{-14}	1.0×10^{-12}
mass m_w(g) of water in solution at	$(S_{v,w}) = 0.80$	3.1×10^{-16}	3.2×10^{-14}	3.3×10^{-12}	1.05×10^{-16}	1.1×10^{-14}	1.1×10^{-12}
	$(S_{v,w}) = 0.90$	5.3×10^{-16}	5.8×10^{-14}	6.1×10^{-12}	2.1×10^{-16}	2.4×10^{-14}	2.4×10^{-12}
	$(S_{v,w}) = 1.00$	6.2×10^{-15}	6.8×10^{-12}	7.1×10^{-9}	2.5×10^{-15}	3.7×10^{-12}	3.8×10^{-9}
	$(S_{v,w}) = (S_{v,w})_c$	3.09×10^{-14}	3.29×10^{-11}	3.41×10^{-8}	1.20×10^{-14}	1.61×10^{-11}	1.80×10^{-8}
dilution m_w/m_N	$(S_{v,w}) = 0.80$	3.1	3.2	3.3	1.05	1.1	1.1
	$(S_{v,w}) = 0.90$	5.3	5.8	6.1	2.1	2.4	2.4
	$(S_{v,w}) = 1.00$	62	680	7 100	25	370	3 800
	$(S_{v,w}) = (S_{v,w})_c$	309	3290	34 100	120	1 610	18 000
Salt concentration in drop at $(S_{v,w})_c$	(g cm^{-3})	3.24×10^{-3}	3.04×10^{-4}	2.93×10^{-5}	8.34×10^{-3}	6.21×10^{-4}	5.55×10^{-5}
	(mol ℓ^{-1})	5.54×10^{-2}	5.20×10^{-3}	5.02×10^{-4}	6.30×10^{-2}	4.69×10^{-3}	4.19×10^{-4}
drop size (cm) at which salt concentration in drop is 1×10^{-3} mol ℓ^{-1}		7.42×10^{-5}	3.44×10^{-4}	1.59×10^{-3}	5.63×10^{-5}	2.62×10^{-4}	1.21×10^{-3}
a_c(cm)		1.95×10^{-5}	1.99×10^{-4}	2.01×10^{-3}	1.42×10^{-5}	1.57×10^{-4}	1.63×10^{-3}

Equations (6-32) to (6-34) are different forms of a relationship first derived by Junge (1950) and later refined by Junge and McLaren (1971).

Equation (6-34) has been solved by Hänel (1976) for aerosol particles of different masses m_N containing a water insoluble substance and $(NH_4)_2SO_4$ or NaCl in various volume proportions. The results of these computations are summarized in Figure 6.3 and Table 6.3. We notice that the water uptake by the aerosol particle increases with increasing water soluble fractions of the particle. For a given ε_v or ε_m the water uptake also increases with increasing total mass of the aerosol particle on which the drop forms.

The maxima in the curves of Figure 6.3 are found by differentiating (6-33) approximated as in (6-29):

$$s_{v,w} = \frac{A}{a} - \frac{Br_N^3}{a^3 - r_N^3}, \tag{6-37}$$

with

$$A = \frac{2M_w\sigma_{v,w}}{\mathscr{R}T\rho_w}; \qquad B = \frac{\nu\Phi_s\varepsilon_m M_w\rho_N}{M_s\rho_w}. \tag{6-38}$$

The result for the activation radius a_c is

$$a_c = -\frac{D}{2} + \left(\frac{D^2}{4} - E\right)^{1/2}, \tag{6-39}$$

with

$$D = \frac{2B^2A - 6BAs_{v,w}}{3Bs_{v,w}^2 - 3B^2s_{v,w}} \tag{6-40}$$

and

$$E = \frac{3BA^2}{3Bs_{v,w}^2 - 3B^2s_{v,w}}. \tag{6-41}$$

Expressing (6-37) in terms of r_N , we find for the critical radius $r_{N,c}$ of a dry aerosol particle which at a given supersaturation $s_{v,w}$ becomes activated at the radius a_c:

$$r_{N,c} = \left[\frac{a_c^3(A - s_{v,w}a_c)}{A + (B - s_{v,w})a_c}\right]^{1/3} \tag{6-42}$$

If the number concentration of aerosol particles as a function of their size is known, (6-42) permits determining the number of aerosol particles which become activated at a given super-saturation.

6.7 Equilibrium Conditions for Ice Particles

We now consider three equilibrium situations involving the ice phase: (a) an ice particle ($''$) in humid air ($'$), (b) an ice particle ($''$) and a separate supercooled solution drop ($''$) in humid air ($'$), and (c) an ice partide ($''$) in a supercooled solution drop ($'$) in humid air. These three cases are illustrated in Figure 6.4.

TABLE 6.3

Dilution $(m_W/m_N) = (\rho_W/\rho_N)[(a_c/r_N)^3 - 1]$ at $(S_{v,w})_c$, and critical supersaturations $(s_{v,w})_c$ at which aqueous solution drops form on an aerosol particle of mass m_N composed of NaCl and SiO_2 (water insoluble) in various proportions. (a) for 20° C, (b) for −10°C; $\rho_s = 2.16$ g cm^{-3} (20°C), $\rho_s = 2.17$ g cm^{-3} (−10°C), $\rho_u = 2.65$ g cm^{-3} (20°C), $\rho_u = 2.66$ g cm^{-3} (−10°C); $\Phi_s = 1.0$. (Based on data of Hänel, 1976.)

				m_N(g)			m_N(g)			m_N(g)		
				1×10^{-16}	1×10^{-14}	1×10^{-12}	1×10^{-16}	1×10^{-14}	1×10^{-12}	1×10^{-16}	1×10^{-14}	1×10^{-12}
	ε_v	ε_m	ρ_N(g cm^{-3})	m_w/m_N at $(S_{v,w})_c$			$(s_{v,w})_c$ (%)			salt concentration (mol ℓ^{-1}) in drop at $(s_{v,w})_c$		
(a)	1.0	1.0	2.163	309	3290	34 100	3.660×10^{-1}	3.578×10^{-2}	3.558×10^{-3}	5.5×10^{-2}	5.2×10^{-3}	5.0×10^{-4}
	0.4	0.35	2.455	53.5	560	5 880	6.597×10^{-1}	6.450×10^{-2}	6.389×10^{-3}	1.1×10^{-1}	1.1×10^{-2}	1.0×10^{-3}
	0.1	0.083	2.601	6.5	58.3	620	1.375	1.373×10^{-1}	1.355×10^{-2}	2.2×10^{-1}	2.4×10^{-2}	2.3×10^{-3}
	0.01	0.0082	2.601	0.87	2.7	19	3.214	4.130×10^{-1}	4.347×10^{-2}	1.6×10^{-1}	5.2×10^{-2}	7.4×10^{-3}
(b)	1.0	1.0	2.170	237	2520	26 240	4.738×10^{-1}	4.628×10^{-2}	4.595×10^{-3}	7.2×10^{-2}	6.8×10^{-3}	6.5×10^{-4}
	0.4	0.35	2.464	41.6	428	4 534	8.537×10^{-1}	8.351×10^{-2}	8.255×10^{-3}	1.4×10^{-1}	1.4×10^{-2}	1.3×10^{-3}
	0.1	0.083	2.611	5.1	44.9	476	1.770	1.778×10^{-1}	1.750×10^{-2}	2.7×10^{-1}	3.2×10^{-2}	3.0×10^{-3}
	0.01	0.0082	2.611	0.80	2.3	15	3.978	5.241×10^{-1}	5.599×10^{-2}	1.7×10^{-1}	6.1×10^{-2}	9.3×10^{-3}

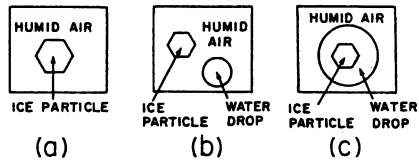


Fig. 6-4: The three basic equilibrium types involving ice crystals.

If we assume a spherical ice particle, the analysis of case (a) proceeds in strict analogy to the derivation of the Kelvin equation, (6-16), and we find the saturation vapor pressure over ice, $e_{a,i}$;, varies with radius according to

$$\frac{e_{a,i}}{e_{sat,i}} = \exp\left(\frac{2v_i\sigma_{i/a}}{\mathscr{R}Ta}\right) = \exp\left(\frac{2M_w\sigma_{i/a}}{\mathscr{R}T\rho_i a}\right), \tag{6-43}$$

and for the case of equilibrium between the ice particle and the environmental vapor $e = e_{a,i}$

$$\ln\frac{e_{a,i}}{e_{sat,i}} = \ln S_{v,i} = \frac{2M_w\sigma_{i/a}}{\mathscr{R}T\rho_i a}. \tag{6-44}$$

This result is plotted as curves 3 and 4 of Figure 6.1 (for 0 and $-20°C$). The behavior is seen to be very similar to that for a pure water drop, except that at small radii, $(e_{a,i}/e_{sat,i}) > (e_{a,w}/e_{sat,w})$. This is primarily a consequence of the inequality $\sigma_{i/a} > \sigma_{w/a}$.

If we abandon the requirement that the ice particle be spherical and, instead, make it a hexagonal prism which follows Wulff's relations (Section 5.7.2), then, in place of (6-38) we have

$$\frac{\mathscr{R}T}{2v_i}\ln\frac{e_{a,i}}{e_{sat,i}} = \frac{\sigma_{i/a}^{(P)}}{h^{(P)}} = \frac{\sigma_{i/a}^{(B)}}{h^{(B)}}, \tag{6-45}$$

where $h^{(P)}$ and $h^{(B)}$ are the perpendicular distances from the crystal center to the prism and basal planes, respectively. Thus, the conditions at equilibrium for the hexagonal prism which are compatible with Wulff's relations are formally similar to those which apply to the cases of a water drop and an amorphous sphere of ice.

We now turn to case (b) to study the equilibrium behavior of a system comprised of a spherical ice particle of radius a_i, and a separate aqueous solution drop of radius a_d, both surrounded by humid air. As in Section 6.5, we have three components, and we assume the constraint n_s = constant, so that w = 3. Let us hold the environmental pressure p constant and determine the independent variations of a_i and a_d with the equilibrium temperature.

On proceeding to specialize (6-5) in the appropriate, and by now familiar manner, we obtain for the solution drop

$$-\frac{\mathscr{L}_{e,0}}{T^2}dT - \frac{2v_{w,0}}{T}d\left(\frac{\sigma_{s/a}}{a_d}\right) + \mathscr{R}\,d\ln e_a - \mathscr{R}\,d\ln a_w = 0, \tag{6-46}$$

and for the ice particle

$$-\frac{\mathscr{L}_s}{T^2}\mathrm{d}T - \frac{2v_i}{T}\mathrm{d}\left(\frac{\sigma_{i/\mathrm{a}}}{a_i}\right) + \mathscr{R}\,\mathrm{d}\ln \mathrm{e}_{a,i} = 0\,. \tag{6-47}$$

These equations express the separate equilibrium balances between the drop and its environment and the ice particle and its environment. To put the drop and ice crystal in equilibrium with each other as well, requires that $\mathrm{e}_a = \mathrm{e}_{a,i}$. Imposing this condition, we may eliminate the vapor pressure term between (6-46) and (6-47) to obtain

$$\mathscr{L}_{m,0}\frac{\mathrm{d}T}{T} - \frac{2M_\mathrm{w}}{\rho_\mathrm{w}}\mathrm{d}\left(\frac{\sigma_{s/\mathrm{a}}}{a_\mathrm{d}}\right) + \frac{2M_\mathrm{w}}{\rho_i}\mathrm{d}\left(\frac{\sigma_{i/\mathrm{a}}}{a_i}\right) - \mathscr{R}T\,\mathrm{d}\ln \mathrm{a}_\mathrm{w} = 0\,. \tag{6-48}$$

An approximate integral of (6-48) between $T = T_0, a_\mathrm{d} \to \infty, a_i \to \infty, \mathrm{a}_\mathrm{w} = 1$ and $T = T_\mathrm{e}, a_\mathrm{d}, a_i, \mathrm{a}_\mathrm{w}$ is

$$\bar{\mathscr{L}}_{m,0}\ln\frac{T_\mathrm{e}}{T_0} = \frac{2M_\mathrm{w}\sigma_{s/\mathrm{a}}}{\bar{\rho}_\mathrm{w}a_\mathrm{d}} - \frac{2M_\mathrm{w}\sigma_{i/\mathrm{a}}}{\bar{\rho}_i a_i} - \frac{\mathscr{R}\bar{T}\nu\Phi_s m_s M_\mathrm{w}/M_s}{(4\pi a_\mathrm{d}^3\rho_s''/3) - m_s}\,, \tag{6-49}$$

where we have used (6-25) for a_w and employed an overbar to denote mean values over the temperature interval (T_0, T_e). For a pure water drop, this reduces to

$$\ln\frac{T_\mathrm{e}}{T_0} = \frac{2M_\mathrm{w}}{\bar{\mathscr{L}}_{m,0}}\left(\frac{\sigma_{\mathrm{w}/\mathrm{a}}}{\bar{\rho}_\mathrm{w}a_\mathrm{d}} - \frac{\sigma_{i/\mathrm{a}}}{\bar{\rho}_i a_i}\right)\,. \tag{6-50}$$

Inspection of these equations reveals that the presence of salts lowers the equilibrium temperature, as expected from the behavior of water in bulk. This effect is evident in Figure 6.5. However, we see that for NaCl the concentration has to be larger than about 10^{-3} mole liter^{-1} to cause a noticeable effect. The figure also indicates that, while for a pure drop of given size, the equilibrium temperature T_e decreases with decreasing ice particle size, T_e increases with decreasing drop size for a given ice particle size. This opposing behavior derives from the different dependencies of temperature with saturation vapor pressure over ice and supercooled water.

In Figure 6.6 we have plotted the separate solutions to (6-46) (for $\mathrm{a}_\mathrm{w} = 1$) and (6-47); the curve intersections therefore constitute states satisfying (6-48). This figure shows that for all drops and ice particles with $(a_\mathrm{d}, a_i) > 10^{-4}$ cm, the equilibrium temperature is essentially equal to the triple point for bulk phases (point A). The figure also reveals the contrary temperature dependence referred to above: for a drop of $a_\mathrm{d} = 10^{-4}$ cm and an ice particle of $a_i = 5 \times 10^{-6}$ cm, $T_\mathrm{e} = -3.8°\mathrm{C}$ (point B), while for $a_\mathrm{d} = 10^{-4}$ cm and $a_i = 10^{-6}$ cm, $T_\mathrm{e} = -18°\mathrm{C}$ (point D). On the other hand, for an ice particle of $a_i = 10^{-6}$ cm and a drop of $a_i = 10^{-6}$ cm, $T_\mathrm{e} = -12.5°\mathrm{C}$ (point C), a warmer temperature than for point D. Finally, we note that for $a_i = a_\mathrm{d}, \mathrm{e}_{a,i} < \mathrm{e}_{a,\mathrm{w}}$ for $T < 0°\mathrm{C}$, the same behavior as for ice and water in bulk $(a_i, a_\mathrm{d}) \to \infty$.

Let us now consider case (c) and determine the equilibrium temperature for a spherical ice particle inside a supercooled aqueous solution drop which is itself

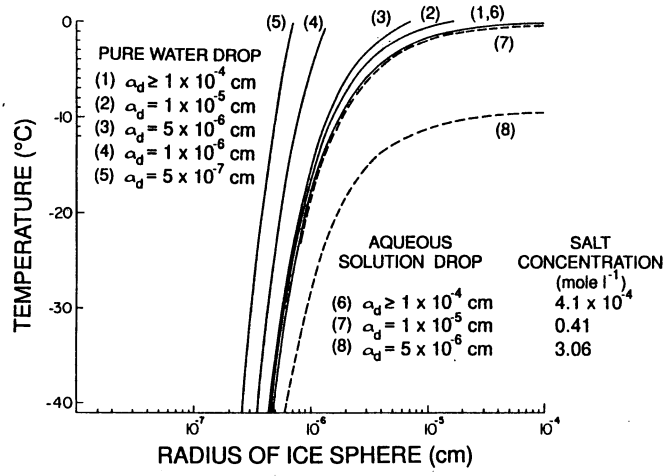


Fig. 6-5: Variation of the equilibrium temperature with drop size, ice particle size, and concentration of salt in solution, for a system which consists of a pure water or aqueous solution drop and an ice particle both surrounded by humid air, $m_s = 10^{-16}$ g NaCl. (Based on solutions to Equation 6-48.)

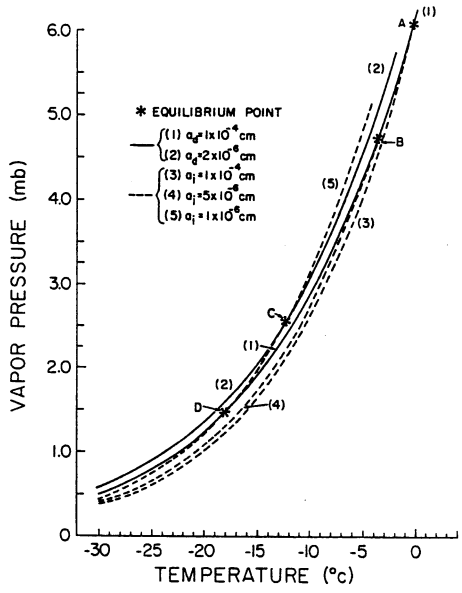


Fig. 6-6: Temperature variations of the vapor pressure over water drops and ice spheres of different sizes, and resulting equilibrium temperatures. (Based on solutions to Equations 6-46 and 6-47.)

in equilibrium with the environmental humid air. As in case (b), such a system has three independent variables. Of these, we shall keep the total gas pressure p constant and study the variation of the equilibrium temperature with the radii a_d and a_i.

For this case, (6-5) becomes with $a_i = 1$

$$-\frac{\mathscr{L}_{m,0}}{T}dT + (v_{w,0} - v_i)dp_w - 2v_i d\left(\frac{\sigma_{i/s}}{a_i}\right) + \mathscr{R}T d\ln a_w = 0\,, \tag{6-51}$$

or, on substituting the condition of mechanical equilibrium, (5-7),

$$-\frac{\mathscr{L}_{m,0}}{T}dT + 2M_w\left(\frac{1}{\rho_w} - \frac{1}{\rho_i}\right)d\left(\frac{2\sigma_{s/a}}{a_d}\right) - \frac{2M_w}{\rho_i}d\left(\frac{\sigma_{i/s}}{a_i}\right) + \mathscr{R}T d\ln a_w = 0\,. \tag{6-52}$$

Integrating as in case (b), we find

$$\bar{\mathscr{L}}_{m,0}\ln\frac{T_0}{T_e} = \frac{2M_w\sigma_{s/a}}{a_d}\left(\frac{1}{\bar{\rho}_i} - \frac{1}{\bar{\rho}_w}\right) + \frac{2M_w\sigma_{i/s}}{\bar{\rho}_i a_i} + \frac{\mathscr{R}\bar{T}\nu\Phi_s m_s M_w/M_s}{(4\pi/3)(a_d^3 - a_i^3)\rho_s'' - m_s}\,, \tag{6-53}$$

which for a pure water drop becomes

$$\ln\frac{T_0}{T_e} = \frac{2M_w\sigma_{w/a}}{\bar{\mathscr{L}}_{m,0}a_d}\left(\frac{1}{\bar{\rho}_i} - \frac{1}{\bar{\rho}_w}\right) + \frac{2M_w\sigma_{i/w}}{\bar{\mathscr{L}}_{m,0}\bar{\rho}_i a_i}\,. \tag{6-54}$$

If the drop is much larger than the ice crystal, this last equation reduces to

$$\ln\frac{T_0}{T_e} = \frac{2M_w\sigma_{i/w}}{\bar{\mathscr{L}}_{m,0}\bar{\rho}_i a_i}\,. \tag{6-55}$$

Finally, if T_e is close T_0, we may write

$$(\Delta T)_{e,a} \equiv T_0 - T_e = \frac{2M_w T_0\sigma_{i/w}}{\bar{\mathscr{L}}_{m,0}\bar{\rho}_i a_i}\,. \tag{6-56}$$

Equations (6-54) to (6-56) are different forms of a relation first derived by J.J. Thomson (1888).

For a solution drop, we may obtain a similar simplification of (6-53) for the case $a_d \gg a_i$ and assuming $\sigma_{i/s} = \sigma_{i/w}$:

$$(\Delta T)_e = \frac{2M_w T_0\sigma_{i/w}}{\bar{\mathscr{L}}_{m,0}\bar{\rho}_i a_i} + \frac{\mathscr{R}T_0\bar{T}\nu\Phi_s m_s M_w/M_s}{\bar{\mathscr{L}}_{m,0}[(4\pi a_d^3\rho_s''/3) - m_s]}\,. \tag{6-57}$$

The second term may be recognized as a combination of (4-94) and (4-66) and, thus, is the equilibrium freezing point depression, $(\Delta T)_{e,s}$, due to the presence of salts in bulk solution. Therefore, to the precision indicated in the derivations of (6-56) and (6-57), we may write

$$(\Delta T)_e = (\Delta T)_{e,a} + (\Delta T)_{e,s}\,; \tag{6-58}$$

i.e., the total equilibrium freezing point depression is simply the sum of contributions from the separate curvature and solute effects.

A numerical solution of (6-52) is displayed in Figure 6.7. In accordance with (6-56), the equilibrium freezing temperature is seen to decrease with decreasing size of the ice particle. This decrease becomes particularly pronounced for $a < 10^{-6}$ cm, and is further enhanced by the solute effect if the salt concentration is larger than about 0.1 mole liter^{-1}.

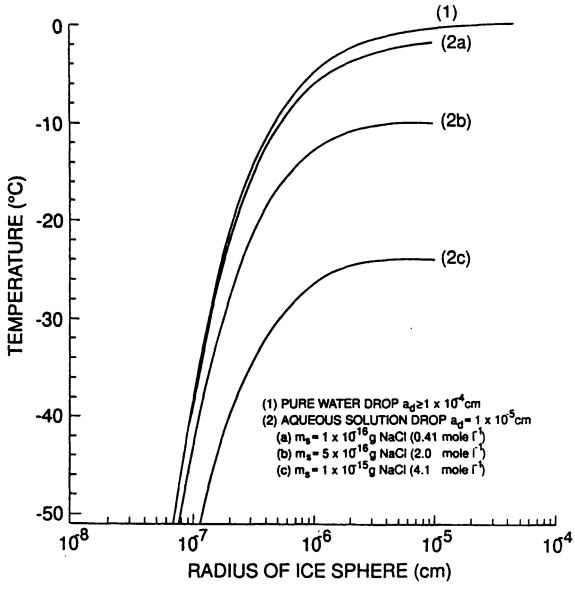


Fig. 6-7: Variation of the equilibrium temperature with drop size, ice particle size and concentration of salt in solution for a system which consists of an ice particle contained in a pure water or aqueous solution drop surrounded by humid air. (Based on solution to Equation 6-52.)

6.8 Experimental Verification

Several experimental difficulties have been encountered in attempting to verify the various equilibrium relationships discussed in the previous sections. The major difficulty in verifying the Thomson equation, (6-56), has arisen from a lack of accurate values for $\sigma_{i/w}$. Generally, therefore, the approach has been to assume the equation is correct and deduce values for $\sigma_{i/w}$; these in turn can be compared with other independently determined values for this quantity. Pawlow (1910), Meissner (1920), Tammann (1920), and Kubelka (1932) were among the first to verify experimentally that the melting temperature of a pure solid substance is dependent on whether the substance is present in bulk or in the form of small particles. Experiments for the ice-water system were first carried out by Kubelka and Prokscha (1944), Skapski *et al.* (1957), and Skapski (1959). These experiments involved

measuring the melting temperature of ice contained in pores and capillaries, or of ice in the form of thin wedges. Unfortunately, this method is subject to a considerable number of errors, and the interface energies obtained only agreed to within 20% with values derived from independent measurements. In subsequent years, more accurate techniques involving electron microscopy and electron diffraction have been developed and perfected (Wronski, 1967; Pocza *et al.*, 1969; Sambles, 1971). These more recent tests of the Thomson equation for tin, indium, lead, and gold particles of radii between 10^{-5} and 3×10^{-7} cm have yielded excellent agreement between experiment and theory.

Uncertainties concerning the Kelvin equation, (6-16), have been due mainly to the fact that the liquids tested were held in capillaries (see Skinner and Sambles, 1972). The first successful attempt to test the Kelvin equation for freely falling drops was carried out by Gudris and Kulikova (1924), who established its validity to within 10%. Subsequently, La Mer and Gruen (1952), experimenting with freely falling droplets in mixtures of dioctylphtalate and toluene, and of oleic acid and chloroform, verified the Kelvin equation to within 5% for drops larger than 0.1 μm radius. More recently, Sambles *et al.* (1970) and Sambles (1971), through electron microscope studies of the evaporation rates of small drops of lead, silver, and gold, established the correctness of the Kelvin law to within 5% for drops of sizes between 0.1 and 0.003 μm.

Quantitative experimental studies to verify (6-26) and (6-34) for increasing or decreasing relative humidity were carried out first by Junge (1936) and by Orr *et al.* (1958a,b) for Aitken sized particles, by Junge (1952a) for large and giant particles, and more recently by McMurry and Stolzenburg (1989) using differential mobility analyzers. An alternative method was used by Alofs *et al.* (1979), Gerber *et al.* (1977), Hoppel (1979) and Hoppel *et al.* (1981), who tested (6-26) and (6-34) by determining the critical supersaturation required to activate NaCl and $(NH_4)_2SO_4$ particles. The earlier as well as the later tests were found to agree well with (6-26) and (6-34). An example of this agreement is given in Figure 6.8 which compares the critical supersaturation for the activation of NaCl and $(NH_4)_2SO_4$ particles with (6-42).

Unfortunately, the experiments just described provide support for the equilibrium growth equations only as far as the average size of a large number of particles in a given size category is concerned. More definite experimental verification of the equilibrium growth equations was provided by Tang (1976), Tang and Muckelwitz (1978, 1984, 1994), Fung *et al.* (1987), Richardson *et al.* (1986a) and Tang *et al.* (1986) who studied the growth of *single* aerosol particles freely suspended by an elctrodynamic suspension technique in a humidified chamber. The resulting equilibrium growth and evaporation behavior of an $(NH_4)_2SO_4$ aerosol particle is shown in Figure 6.9a where comparison is made with the predictions of (6-26). We notice from this figure that, during growth, excellent agreement between theory and observation was obtained for relative humidities above the deliquescence point. In Figure 6.9b, the equilibrium growth and evaporation behavior of a mixed particle consisting of $NaNO_3$, Na_2SO_4, and $(NH_4)_2SO_4$ is shown. Comparing the relative humidity for the onset of deliquescence of this mixed particle with the onset of deliquescence for the pure components, given in Table 4.3, we notice that

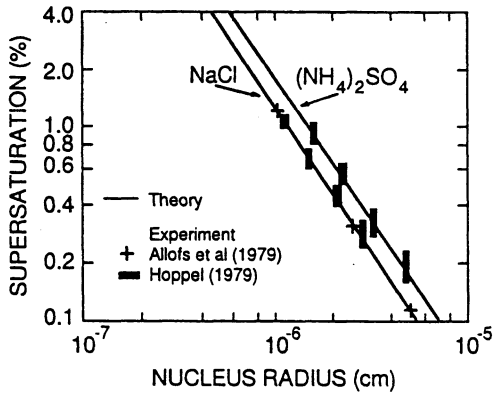


Fig. 6-8: Critical supersaturation to activate aerosol particles of $(NH_4)_2SO_4$ and NaCl. Comparison of experiment with theory. (Based on data of Alofs *et al.*, 1979, Gerber *et al.*, 1977, and Hoppel *et al.*, 1981.)

deliquescence of the mixed particle begins at a relative humidity which is lower than that required for any of the components. Note also from this figure that equilibrium growth and shrinking of a solution drop follows the same curve only above the deliquescence point. Below the relative humidity for deliquescence, a shrinking drop does not solidify as expected from its growth curve. Instead, the drop supersaturates with respect to the salt in it and continues to shrink at decreasing relative humidities in agreement with (6-26). At some unpredictable relative humidity, salt nucleation sets in inside the highly supersaturated drop. This behavior is illustrated in Figure 6.9a,b in terms of the 'hysteresis loop', which is described by the drops equilibrium growth and shrinking. These experiments suggest that during the evaporation of atmospheric clouds, some of the drops may be present in a metastable state consisting of a solution, highly supersaturated with respect to the salt contained in them. Such drops have been observed to exist in urban and rural atmospheres at relative humidities between 45 and 75% (Rood *et al.*, 1989).

A similar hysteresis behavior was noticed by Winkler (1967, 1968, 1970, 1973) and by Winkler and Junge (1972) during studies of the equilibrium growth and evaporation of aerosol particle deposits. Three such hysteresis curves are given in Figure 6.10 for deposits of pure salt particles of known chemical composition. As expected, observation and theoretical prediction are in good agreement for the equilibrium growth at relative humidities above the deliquescence point. The hysteresis behavior of natural aerosol deposits is exemplified in Figures 6.11 and 6.12. No comparison with theory could be made since the chemical composition of the deposits was not known. As expected from the equilibrium growth of pure salt particles, natural aerosol deposits begin to take up water at relative humidities well below the deliquescence point, although the actual amount of water taken up is small for relative humidities up to the deliquescence point. Above this point the water uptake rapidly increases. Note that the equilibrium growth curve for deposits of aerosol particles of continental type are smooth (Figure 6.11) while those

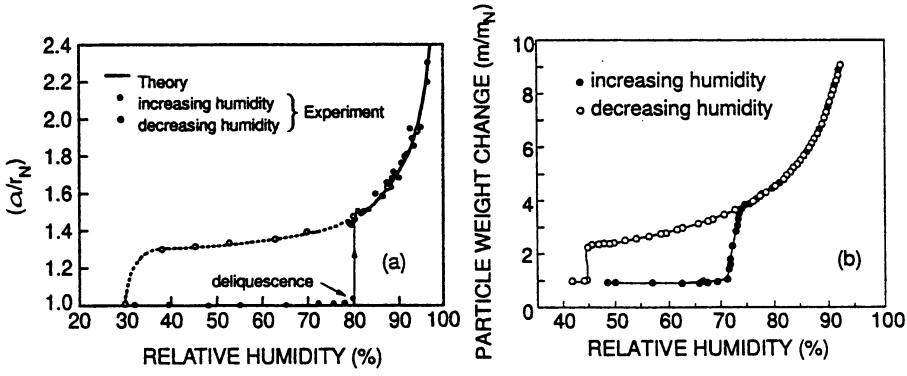


Fig. 6-9: Variation with relative humidity of the equilibrium size of an aerosol particle (a) of $(NH_4)_2SO_4$ at 25° C, and (b) of a mixture of NaCl, Na_2SO_4 and $NaNO_3$ at 17.5° C, freely levitated in air by an electrodynamic levitation technique. (From Tang and Munkelwitz, 1984, with changes.)

of maritime origin exhibit a characteristic near-discontinuity near 75% relative humidity (Figure 6.12). This 'sea-salt discontinuity' is due to the presence of NaCl in the deposit which has a deliquescence point near 75% relative humidity. We further note that at any given relative humidity maritime aerosol deposits take up considerably more water than continental aerosol deposits. This is due to the large portion of water-soluble, hygroscopic compounds in the former deposits, and also due to the stronger water uptake of NaCl as compared to the $(NH_4)_2SO_4$ prevalent in continental aerosols.

Three factors help explain why aerosol deposits take up water at a value of

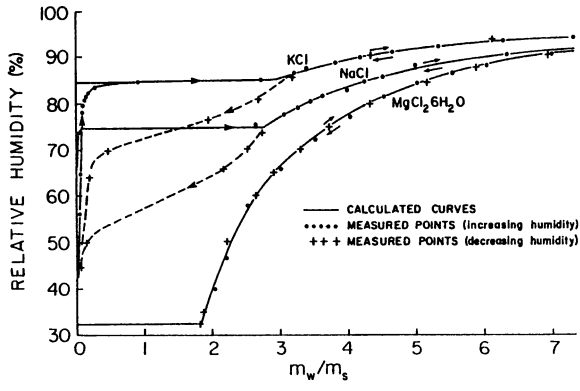


Fig. 6-10: Equilibrium growth curves of pure salt deposits (25°C). (From Winkler, 1967; by courtesy of the author.)

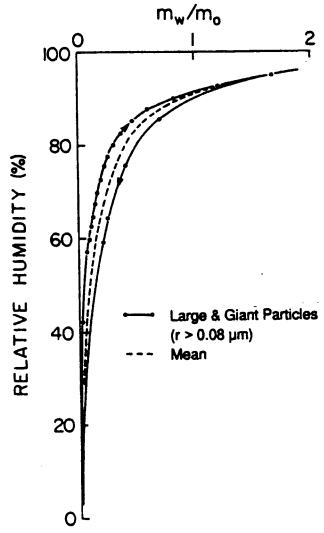


Fig. 6-11: Equilibrium growth curve of an urban aerosol deposit collected at Mainz, Germany during a north east wind. (From Winkler, 1967; by courtesy of the author.)

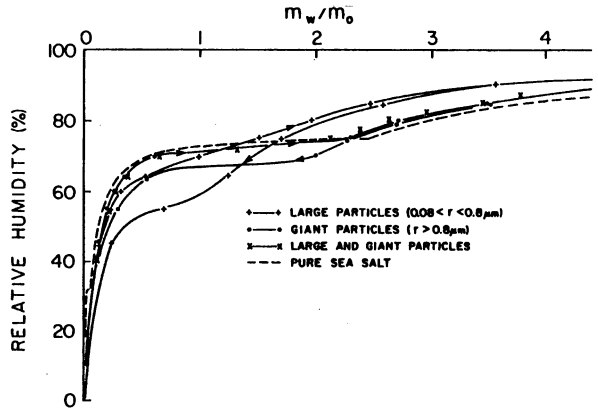


Fig. 6-12: Equilibrium growth of a maritime aerosol deposit collected at Helgoland Island, for west wind. (From Winkler, 1967; by courtesy of the author.)

$e/e_{sat,w}$ less than that necessary for equilibrium with a salt saturated solution. Firstly, the water solubility of any substance is a function of particle size. Solubility is enhanced especially if the particle size decreases below about 0.1 μm. This solubility enhancement was predicted qualitatively by Ostwald (1900) and Freundlich (1926) through a Kelvin law type analysis, and has been quantitatively established by the experiments of Dundon and Mack (1923), May and Kolthoff (1948), and Orr *et al.* (1958a,b). The experiments of Orr *et al.* showed that NaCl particles of 0.020 μm radius go into solution at a relative humidity of 69 to 70%, while NaCl particles of 1 μm radius need a relative humidity of 74%. Particles of $(NH_4)_2SO_4$ with radii of 0.015 μm were found to form a saturated solution drop at 68% relative humidity; KCl particles of 0.03 μm radius went into solution at 78% relative humidity. These values are considerably below the relative humidities necessary for salt in bulk, which are 75.3% for NaCl, 80% for $(NH_4)_2SO_4$, and 84.3% for KCl.

Secondly, aerosol particles contain air capillaries in which condensation of water vapor proceeds at a relatively low saturation ratio. This can be explained if we consider that the meniscus of water in a capillary with water wettable walls is concave, in contrast to the convex surface of a water drop. Therefore, instead of (6-16), we now have

$$\frac{e_{a,w}}{e_{sat,w}} = \exp\left(-\frac{2M_w\sigma_{w/a}}{\mathscr{R}T\rho_w a}\right), \tag{6-59}$$

which means that the smaller the radius of curvature a of the water surface in the capillary, the lower the equilibrium vapor pressure over it. For only partially wettable capillary walls characterized by a contact angle Θ, the argument of the exponential must be multiplied by $\cos\Theta$, but this does not change the qualitative effect of capillary spaces in the particle surface.

The third reason for the occurrence of deliquescence is simply that all solids show some affinity for water vapor and, thus, adsorb it onto their surfaces, as discussed in the previous chapter. The amount of adsorbed water vapor may be considerable, even at low relative humidities.

The development of a hysteresis loop in an equilibrium growth curve has three main causes. Firstly, evaporating salt solutions tend to supersaturate with respect to the salt in solution, as we stated earlier. This is due to the fact that the crystallization of salt requires surmounting an energy barrier unless suitable solid particles are present in the solution to serve as centers for crystallization. Thus, as the relative humidity decreases, the equilibrium growth curve is determined by the water vapor pressure over the supersaturated salt solution, until, at some undetermined relative humidity, the salt crystallizes. This behavior is in contrast to the growth during increasing relative humidity, which is assisted by the adsorption and deliquescence behavior of the substances in the aerosol deposit.

Secondly, air capillaries in aerosol particles behave differently during increasing relative humidity when they become filled, than during decreasing relative humidity when they are being emptied. Figure 6.13 demonstrates this hysteresis effect in a cylindrical capillary with an opening narrower than the body of the capillary. From

(6-59), it follows that such a capillary begins to fill at a higher relative humidity than that at which it begins to empty.

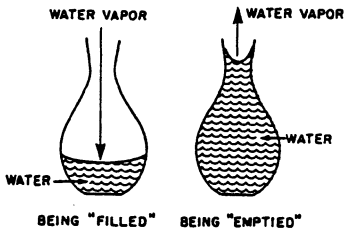


Fig. 6-13: Schematic behavior of a cylindrical bottle-type capillary during condensation and evaporation.

A third reason for the hysteresis loop is that water-insoluble substances such as clays behave differently during water adsorption than desorption, due to the presence of alkali ions in the silicate lattice. During increasing relative humidity (adsorption), the tendency of these ions to be bonded to the clay surface dominates their tendency to hydrate (to become surrounded by and weakly bonded to water molecules), particularly at low humidities. During the desorption which occurs with decreasing humidities, however, the silicate ions are already largely hydrated, and so their tendency to remain hydrated dominates the tendency to become bonded again to the clay surface.

CHAPTER 7

HOMOGENEOUS NUCLEATION

Our outline in the previous three chapters of the equilibrium thermodynamics of the phases of water is insufficient for an understanding of cloud particle formation, since we did not come to grips with the crucial question of how a new phase is initiated. Consider, for example, that on the basis of the Kelvin equation alone, the formation of a water drop from homogeneous water vapor would be precluded because the vapor pressure required to hold a microscopic quantity of newly formed phase in equilibrium would be quite enormous. This expectation is in disagreement with experimental observations which show that a large but finite supersaturation exists above which homogeneous phase change does take place. The reason for this behavior is that the formation of a new phase at the expense of a metastable original phase ('mother phase') does not begin in a continuous manner, but rather takes place spontaneously as a result of fluctuations in time and space of temperature and density in the original phase, provided that a critical supersaturation of the vapor or a critical supercooling of the water drops is exceeded. This spontaneous process is called *nucleation.*

From our studies of adsorption we might expect that nucleation could be greatly assisted if suitable solid surfaces were present. In fact, as we know from Chapter 1, such *heterogeneous nucleation* has long been recognized as being generally responsible for cloud formation. However, in order to clarify the physical principles involved in the nucleation process, we shall assume for now that all foreign substances are absent, and study *homogeneous nucleation* which occurs when only water substance is present. Homogeneous nucleation of drops in supersaturated vapor can only be realized under laboratory conditions and does not occur in the atmosphere. On the other hand, we shall see in Section 7.2 that homogeneous ice nucleation in supercooled water drops is the controlling mechanism for the formation of cirrus clouds in the atmosphere.

Some useful references for the material in this chapter include the texts by Abraham (1974b), Zettlemoyer (1969), Defay *et al.* (1966), Hirth and Pound (1963), Dufour and Defay (1963), Frenkel (1946), and Volmer (1939), and the review articles by Chalmers (1964), McDonald (1962, 1963a), Turnbull (1956), Dunning (1955), and Hollomon and Turnbull (1953).

7.1 Homogeneous Nucleation of Water Drops and Ice Crystals from Water Vapor

7.1.1 Equilibrium Population of Embryos and Energy of Embryo Formation

Within the metastable bulk phase of water vapor are small molecular clusters which result from the chance agglomeration of water molecules; these are generally referred to as *embryos* if the vapor pressure is below the critical value required for nucleation. Such embryos have small binding energies and are easily disrupted by thermal agitation. However, at a critical vapor pressure some embryos will reach a critical (*germ*) size, which are in unstable equilibrium with the mother phase. A germ will proceed to grow spontaneously and thereby produce a macroscopic phase change if, as a result of fluctuations in the mother phase, its size increases by even an infinitesimal amount.

Therefore, in order to understand the nucleation phenomenon, one must first learn something about the prenucleation embryos. For the sake of simplicity and on considering the relative populations of i-mers (embryos consisting of i molecules and denoted by A_i), it is generally assumed that these grow by the capture of single molecules (monomers). A further convention is to assume a state of dynamic equilibrium for the i-mers, which we may express in the form

$$A_{i-1} + A_1 \rightleftharpoons A_i\,, \quad i = 1, 2, \ldots \tag{7-1}$$

(the forward and reverse rates are assumed equal). On adding up a series of such equations, we have also

$$iA_1 \rightleftharpoons A_i\,. \tag{7-2}$$

As this represents an equilibrium situation, the corresponding statement in terms of chemical potentials is

$$i\mu_1 = \mu_i\,, \tag{7-3}$$

where μ_i is the chemical potential of an i-mer.

7.1.1.1 *Formal Statistical Mechanics Description*

Let us now proceed to determine the number N_i of i-mers in a volume V of vapor held at temperature T. As we are dealing in principle with a microscopic fluctuation phenomenon, it is appropriate to apply, insofar as possible, the machinery of statistical mechanics. For this purpose, we make the standard assumption that the vapor system consists of a mixture of non-interacting ideal gases; i.e., each collection of i-mers is considered to be an ideal gas of indistinguishable particles. Then, in view of the fact that we may expect small fluctuations in N_i, it is computationally convenient to determine N_i via the grand partition function of the grand canonical ensemble (see Appendix A-7.1). An alternative description in terms of the canonical ensemble has been given, for example, by Dunning (1969).

The grand canonical partition function for the component gases of i-mers is (A.7-15):

$$\mathcal{Q}_i = \sum_{N_i} [\exp(\mu_i N_i / \mathrm{k}T)] Q(N_i)\,, \tag{7-4}$$

where $Q(N_i)$ is the canonical partition function for the gas of i-mers:

$$Q(N_i) = \frac{q_i^{N_i}}{N_i!}, \tag{7-5}$$

from (A.7-6). In this expression, q_i is the partition function for a single i-mer. Then, from (A.7-12) and (A.7-14), the size distribution N_i is given as

$$N_i = kT \left(\frac{\partial \ln \mathscr{Q}_i}{\partial \mu_i} \right)_{T,V} . \tag{7-6}$$

The convenience of the grand partition function is that it can easily be rearranged in a manner which greatly simplifies the indicated calculation in (7-6). Thus, on substituting (7-5) into (7-4), we have

$$\mathscr{Q}_i = \sum_{N_i} \frac{[q_i \exp(\mu_i/\mathrm{k}T)]^{N_i}}{N_i!} = \exp[q_i \exp(\mu_i/\mathrm{k}T)] . \tag{7-7}$$

Consequently, we find immediately from (7-6) that

$$N_i = q_i \exp(\mu_i/\mathrm{k}T) . \tag{7-8}$$

By writing (7-8) once more for $i = 1$ and combining these two equations with (7-3), we can eliminate direct reference to the chemical potential to get

$$N_i = (N_1/q_1)^i q_i , \tag{7-9}$$

which is known as the 'mass action law'. This result may also be expressed in a form containing a Boltzmann factor, viz.,

$$N_i = N_{\mathrm{sat,w}} \exp[-\Delta\phi_i/\mathrm{k}T] , \tag{7-10}$$

where $\Delta\phi_i$ represents the energy required to form an embryo of i molecules. Comparing (7-10) with (7-9), for the energy of embryo formation, we find

$$\frac{\Delta\phi_i}{\mathrm{k}T} = i \ln(q_1/N_{\mathrm{sat,w}}) - \ln(q_i/N_{\mathrm{sat,w}}) - i \ln S_{\mathrm{v,w}} . \tag{7-11}$$

Here $N_{\mathrm{sat,w}}$ is the number of water molecules in V for conditions at saturation with respect to a flat water surface, and $S_{\mathrm{v,w}} = N_1/N_{\mathrm{sat,w}} = \mathrm{e}/\mathrm{e}_{\mathrm{sat,w}}$ is the saturation ratio of the system.

The determination of N_i has now been reduced to the problem of evaluating the partition function q_i for the i-mer. Unfortunately, however, no one has yet found an accurate *ab initio* way to do this. This is hardly surprising, since q_i depends on the complex structure of the i-mers which is largely unknown and on a realistic intermolecular interaction potential suitable for an arbitrary polymolecular aggregate, which is not available.

Consequently, at this point, a much more heuristic approach is necessary. Probably the most successful such procedure is that of Plummer and Hale (1972) and Hale and Plummer (1974a,b), who postulated certain allowed structures for the i-mers, and proceeded to work out the corresponding q_i's.

7.1.1.2 *Molecular Model Method*

As mentioned in the previous section, the procedure followed by Plummer and Hale is to assume certain structures for the embryo i-mers and to determine the corresponding q_i's. The size distribution is then available directly from (7-10) and (7-11). A direct determination of the partition function q_i would require a realistic description of the inter-action potential for the cluster-vapor system. Unfortunately, a realistic intermolecular potential which can be applied to an arbitrary number of water molecules in large clusters is not available. Therefore, Plummer and Hale assumed the following form for q_i:

$$q_i = q_{i,T} q_{i,R} q_{i,V} q_{i,B} q_{i,C} \,, \tag{7-12}$$

where $q_{i,T}$ and $q_{i,R}$ are the translational and the rotational partition functions of the i-mer, and where $q_{i,V} = q_{i,\text{intra}} q_{i,\text{lib}} q_{i,\text{inter}}$ is the vibrational partition function given in terms of the intramolecular, intermolecular, and librational contributions, $q_{i,B} = \exp(-E_{i,B}/\mathrm{k}T)$ is the contribution of the intermolecular binding energy $E_{i,B}$ to the partition function, and $q_{i,C}$ is the configurational contribution to the partition function.

Each of these quantities has been evaluated semi-empirically in a manner described by Plummer and Hale (1972), Plummer (1973), and Hale and Plummer (1974a). In these evaluations, it was assumed: (1) that i-mers have a well-defined structure, (2) that each structure has a lifetime sufficiently long to characterize its internal vibrational spectrum, and (3) that the internal structure of a water molecule is negligibly affected by cluster formation.

The assumed structure for water clusters in supersaturated vapor is that of closed or partially closed clathrates composed of five-membered rings (Pauling, 1962). An example of such a structure for a 20-mer is shown in Figure 7.1a. These cluster forms fulfill the imposed criteria that the molecules associate by hydrogen bonding with bond angles which are roughly tetrahedral, that the number of bonds be maximized, and that the forms possess near-spherical symmetry. This choice of geometry is supported by the studies of Lin (1973) and Searcey and Fenn (1974) (see Section 3.2).

However, these perfectly ordered clathrate structures cannot be used to represent arbitrarily large i-mers, since it becomes difficult to maintain the closed 'cages' without grossly distorting the bond angles and lengths. This results in the occurrence of considerable bond strain for $i \gtrsim 80$, the effect of which has been studied by Hagen (1973).

For the study of prenucleation embryos of ice in vapor, Hale and Plummer (1974a) assume an ice-I_h structure composed of rings containing six water molecules each (see Section 3.3). A typical structure with 20 molecules is shown in Figure 7.1b.

7.1.1.3 *The Classical Description*

Since we cannot rigorously proceed beyond (7-9) or (7-10) and (7-11), there arises the possibility that an earlier resort to intuition and approximate physical modeling

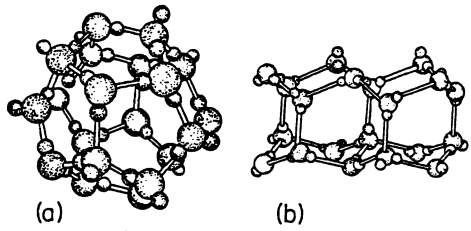


Fig. 7-1: Cluster models used in the theory of Hale and Plummer (1974a,b). (a) Cluster of 20 water molecules arraged in a clathrate structure forming a pentagonal dodecahedron. (b) Cluster of 20 water molecules arranged in an ice-I_h structure. (Based on Hale and Plummer, 1974a,b.)

might, in some respects, be more appropriate. Not surprisingly, this is the historical route of development of the subject (e.g., Volmer and Weber, 1926; Farkas, I927; Becker and Döring, 1935; and Zeldovich, 1942). These workers arrived relatively quickly at a complete description for N_i via two major assumptions: (1) the prenucleation embryos may be regarded as water spheres, characterized by the usual macroscopic densities and surface tensions, and (2) they are distributed according to the Boltzmann law.

The assumption of a Boltzmann distribution like (7-10) is quite reasonable: the i-mers are in thermal equilibrium, and the probability that they have a certain energy $(\Delta\phi)_i$ is just the probability for their existence, if we interpret $(\Delta\phi)_i$ as the energy of formation of the i-mer.

Let us therefore consider the energy of formation of a drop of radius a. We may assume the required phase change occurs at constant temperature. However, it is not a constant pressure process, according to (5-11). On the other hand, we may assume that the total volume V of the system considered (the mother phase plus the condensed phase) remains constant. Therefore, the Helmholtz free energy F is the proper thermodynamic potential to use in our description. (Elaborations of the point that F, rather than the traditionally used Gibbs function G, is the proper potential may be found in Abraham (1968) and Dufour and Defay (1963). For practical purposes, the resulting differences turn out to be negligible.)

Suppose the system to be comprised, after the phase change, of n_w moles of water within the drop, and n_v moles of water vapor. We neglect any adsorption of water onto the interface (σ); i.e., we assume $n_w^{(\sigma)} = 0$. The total system Helmholtz free energy at this time is thus given, considering (4-3b) and (5-13) and the definition $F \equiv U - TS$, by

$$F_2 = n_v\mu_{v,2} + n_w\mu_w - e_2(V - V_w) - p_wV_w + \sigma_{w/v}\Omega\,, \tag{7-13}$$

where we have used the subscript 2 to denote the post-phase change condition. Similarly, before the phase change we have

$$F_1 = (n_v + n_w)\mu_{v,1} - e_1V\,. \tag{7-14}$$

Further, we may assume that the small amount of new phase negligibly affects the vapor, so that $\mu_{v,1} = \mu_{v,2} = \mu_v$, and $e_1 = e_2 = e$; therefore, by subtraction we find for the energy of new phase formation

$$(\Delta F)_{T,V} \equiv F_2 - F_1 = n_w[\mu_w(p_w, T) - \mu_v(e, T)] - V_w(p_w - e) + \sigma_{w/v}\Omega . \quad (7\text{-}15)$$

On introducing the mechanical equilibrium conditions (5-11) and noting that $V_w = a\Omega/3$, we may express (7-15) as

$$(\Delta F)_{T,V} = n_w[\mu_w(p_w, T) - \mu_v(e, T)] + \sigma_{w/v}\Omega/3 . \quad (7\text{-}16)$$

We recall now that for T = constant, $d\mu_w = v_w dp_w$, so that on integration and ignoring the compressibility of water, this leads to

$$\mu_w(p_w, T) - \mu_w(e, T) = v_w(p_w - e) . \quad (7\text{-}17)$$

Substituting (7-17) into (7-15) and using $V_w = n_w v_w = a\Omega/3$ as well as (5-11), we obtain

$$(\Delta F)_{T,V} = n_w[\mu_w(e, T) - \mu_v(e, T)] + \sigma_{w/v}\Omega \quad (7\text{-}18)$$

$$= (\Delta F)_{vol} + (\Delta F)_{surf} , \quad (7\text{-}19)$$

where the first term is the volume or bulk free energy change and the second is the surface energy change.

Let us now express these results on a molecular scale, assuming that we may still employ macroscopic densities and surface tensions. Then, from (7-18), the energy of formation of an i-mer is

$$\Delta F_i = i[\dot{\mu}_w(e, T) - \dot{\mu}_v(e, T)] + \sigma_{w/v}\Omega_i . \quad (7\text{-}20)$$

This form has not made use of the assumption of spherical geometry; consequently, it will hold for complex i-mer shapes. (However, it may be necessary to generalize the surface term. See Section 5.7.) At equilibrium, we also have $\dot{\mu}_w(p_w, T) = \dot{\mu}_v(e, T)$, where p_w refers to the pressure in the water germ. Thus, (7-17) becomes

$$\dot{\mu}_w(e, T) - \dot{\mu}_v(e, T) = -\dot{v}_w(p_w - e) = -\frac{2\dot{v}_w\sigma_{w/v}}{a_g} . \quad (7\text{-}21)$$

In the last step, we have invoked mechanical equilibrium again. Going one step further, we may introduce the saturation ratio through the Kelvin law, (6-17), and arrive at the result

$$\dot{\mu}_w(e, T) - \dot{\mu}_v(e, T) = -kT \ln S_{v,w} . \quad (7\text{-}22)$$

Consequently, another form of (7-20) is

$$\Delta F_i = \sigma_{w/v}\Omega_i - ikT \ln S_{v,w} . \quad (7\text{-}23)$$

In terms of the i-mer radius, this is

$$\Delta F_i = 4\pi a_i^2 \sigma_{w/v} - \frac{4\pi a_i^3}{3\dot{v}_w} kT \ln S_{v,w} . \quad (7\text{-}24)$$

We have now reached our goal of describing the distribution of prenucleation embryos via the classical approach: the energy of formation ΔF_i has been determined as a function of embryo size, and so we now merely identify $\Delta F_i = \Delta\phi_i$ in (7-10) to obtain

$$N_i = N_{\text{sat}} \exp[-\Delta F_i/\text{k}T]\,, \tag{7-25}$$

or with $c_i = N_i/V$,

$$c_i = c_{\text{sat}} \exp[-\Delta F_i/\text{k}T]\,. \tag{7-26}$$

(For a highly detailed and quite different derivation of the same result, see Dufour and Defay, 1963.)

The behavior of ΔF_i as given in (7-24) is shown in Figure 7.2. We see that for vapor just saturated with respect to bulk water, the energy of i-mer formation rapidly increases with size (as a_i^2, from (7-24)). However, the behavior is seen to be quite different for supersaturated vapor. In this case, the curves each have a single maximum at some radius $a_{i,\max}$, so that i-mers of radius $a_i > a_{i,\max}$ require a work of formation which decreases with increasing size. Thus, $\Delta F_{i,\max}$ for $a_i = a_{i,\max}$ evidently represents the *energy barrier* to nucleation.

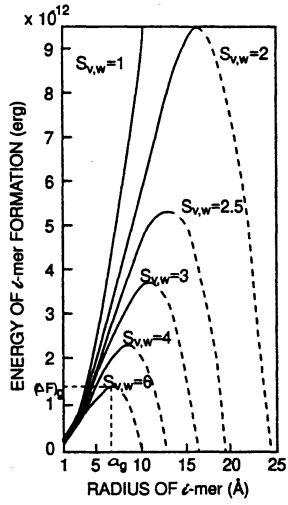


Fig. 7-2: Energy of i-mer formation as a function of i-mer size, for 0° C. (From *Elements of Cloud Physics* by H.R. Byers, copyrighted by University of Chicago Press, 1965.)

Consequently, through the classical approach we have available not only N_i, but also a description of the germ radius a_g as a function of supersaturation. This is given by $a_g = a_{i,\max}$; by differentiating (7-24) and setting the result equal to zero to obtain the maximum, we find

$$a_g = a_{i,\max} = \frac{2\dot{v}_{\text{w}}\sigma_{\text{w/v}}}{\text{k}T \ln S_{\text{v,w}}} = \frac{2M_{\text{w}}\sigma_{\text{w/v}}}{\mathscr{R}T\rho_{\text{w}} \ln S_{\text{v,w}}}\,; \tag{7-27}$$

i.e., the Kelvin law is obtained, as is necessary for consistency since the germ is in (unstable) equilibrium with the vapor. Furthermore, by inserting this result into (7-24), the energy barrier to nucleation, or the free energy of germ formation, is found to be

$$\Delta F_g = \Delta F_{i,\max} = \frac{\sigma_{\mathrm{w/v}}\Omega_g}{3} = \frac{16\pi M_{\mathrm{w}}^2 \sigma_{\mathrm{w/v}}^3}{3[\mathscr{R}T\rho_{\mathrm{w}}(\ln S_{\mathrm{v,w}})]^2}\,, \tag{7-28}$$

where $\Omega_g = 4\pi a_g^2$ is the surface area of the germ. This is the classical estimate of the amount of energy which must be supplied by fluctuations in the metastable mother phase in order for nucleation to occur.

With regard to Figure 7.2, Byers (1965) has stressed that physical reasoning does not suggest that embryos for $i > g$ are to be found in large numbers increasing with size, as we might expect from the negative exponent of ΔF_i (Equation (7-26)). After all, our physical concept of the nucleation event assumes that clusters which reach a size $i = g$ are in metastable equilibrium, which may lead spontaneously to the growth of a macroscopic new phase. Following Byers, we therefore have marked the curves beyond the maximum by a dashed line.

It is worthwhile at this point to record also the analogous expressions for homogeneous nucleation of ice in vapor. Obviously, (7-27) and (7-28) will also hold for a spherical ice germ in unstable equilibrium with water vapor, if we merely replace $\dot{v}_{\mathrm{w}}$ by $\dot{v}_i$, ρ_{w} by ρ_i, $\sigma_{\mathrm{v/w}}$ by $\sigma_{\mathrm{v}/i}$, and $S_{\mathrm{v,w}}$ by $S_{\mathrm{v},i}$.

As we shall see, these results of the classical theory provide a simple basis for predicting nucleation rates which are very similar to those actually observed. This is a much better outcome than we might have expected, in view of the first rather dubious assumption, referred to at the beginning of this section, which serves as half of the foundation for the classical description. Thus, it does not seem very likely that small clusters of molecules should exhibit macroscopic properties. And even if one could assume the macroscopic description is correct in principle, there would still arise conceptual difficulties in its application. In particular, it is not easy to decide where to locate the surface of separation between the phases, since the actual phase transition region may have a thickness comparable to the germ radius (see, for example, Ono and Kondo, 1960). Also, some size correction for the macroscopic surface tension would appear to be in order (recall Section 5.4.3 and Table 5.1).

We have already made some remarks in defense of the assumption of a Boltzmann distribution for the prenucleation embryos. However, here again conceptual difficulties arise in implementing the assumption. The difficulty this time is in describing accurately the contributions to the free energy of formation of the embryo. The classical account of ΔF_i assumes the embryos are at rest in the mother phase. This is obviously incorrect, but the error which results thereby is not obvious.

Nevertheless, some confirmation of the classical approach comes from the results of the molecular model. For this purpose, we identify ΔF_i from the classical model with $\Delta\phi_i$ from the molecular model, obtained according to the model calculations of q_i inserted into (7-11), and plot them together as a function of the number of molecules in a cluster. The values for the case of water embryos are shown in Figure 7.3. The effects of bond strain for the larger clusters is also indicated; this

causes only a small increase in the formation energy. The general good agreement with the classical model is most impressive and surprising, considering the theoretical deficiencies of the latter.

Before closing this section we should also mention another approach to the homogeneous nucleation problem, which is to use Monte-Carlo techniques to evaluate ΔF_i. The method is based on a stochastic process which generates a Boltzmann-weighted set of configurations for a given closed system containing a fixed number of molecules. For details, see Abraham (1974b). Though this method holds great promise for the future, it imposes a heavy computational burden on present generation computers, and it has so far been possible to simulate the growth of only small clusters. Consequently, we shall not consider it further here.

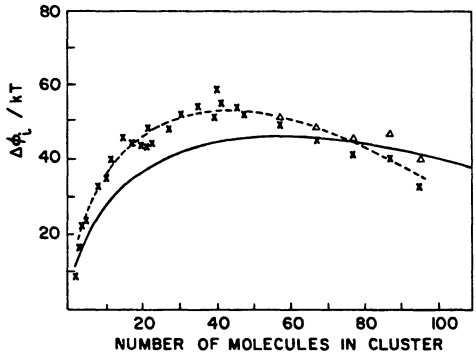


Fig. 7-3: Energy of embryo formation vs. embryo size (in number of molecules) at $S_{v,w} = 5$ and $T = 273°$ K for: (1) the classical liquid drop model, $(\Delta F)_i/\mathrm{k}\,T = 9.3\ i^{2/3} - 1.6i$ (solid line); (2) the molecular model, $(\Delta\Phi)_i/\mathrm{k}T$ (crosses); (3) the molecular model with strain (triangles); and (4) the least-squares fit to $(\Delta\Phi)_i/\mathrm{k}T = 12.8\ i^{2/3} - 2.40i$ (dashed line)). (From Hale and Plummer, 1974b; by courtesy of Am. Meteor. Soc., and the authors.)

7.1.2 The Nucleation Rate J

When homogeneous nucleation of water from the vapor occurs, what is observed is the (rather sudden) formation of a cloud of small drops. Thus, the experimental quantity of interest is the rate at which drops appear in the system as a function of the prevailing saturation ratio $S_{v,w}$. Let us denote this rate by J, measured as the number of drops appearing per unit volume and per unit time. We shall make the traditional assumption that J corresponds completely to the rate of germ formation; i.e., it is the *nucleation rate.*

A simple and direct way to estimate J has probably occurred to the reader: assume (7-26) holds for $i = g$, and determine J as the rate at which the $c_g = N_g/V$ germs per unit volume collect single molecules from the vapor; i.e., set

$$J = c_g \mathrm{w}^{\downarrow} \Omega_g \,, \tag{7-29}$$

where $w^{\downarrow}$, given by (5-48), specifies the flux of water molecules to the germs. The estimate (7-29) was first made by Volmer and Weber (1926). It is a quite reasonable first approximation, in that we are interested only in describing the onset of nucleation; for this purpose one might well expect the equilibrium distribution (7-26) for $i = g$ to provide an adequate basis for estimating J.

Let us reflect now on how we might improve our estimate. Two factors which we have so far neglected naturally suggest themselves for consideration. Firstly, germ evaporation as well as condensation should be accounted for. Secondly, we should recognize that as embryos flow through the phase-change 'bottleneck' created by the energy which is required to form a germ-sized embryo, their distribution will not, in principle, be the equilibrium distribution of (7-26), since it assumes no mass flux up the size spectrum.

An improvement which recognizes these features was first carried out by Farkas (1927) and Becker and Döring (1935); other refinements and extensions have been made by Volmer (1939), Zeldovich (1942), Turnbull and Fischer (1949), Farley (1952), and Frenkel (1946). The key simplifying assumption introduced by these authors is that the new size distribution may be regarded as being in a steady state. As we shall see, J can then be found without difficulty.

For this purpose, let us first estimate the time required to reach a steady state once a given vapor supersaturation is achieved. If we denote the time dependent concentration of embryos of size i by f_i', then, the generalization of (7-29) which includes the effect of evaporation is

$$J_i = f_{i-1}' w^{\downarrow} \Omega_{i-1} - f_i' w^{\uparrow} \Omega_i \,, \tag{7-30}$$

where $w^{\uparrow}$ is the flux of water molecules leaving the embryo surface. Here J_i is the number of embryos vol^{-1} sec^{-1} entering the size category i. A special case of this equation is the equilibrium situation for which $J_i = 0$; for this case we have

$$0 = c_{i-1} w^{\downarrow} \Omega_{i-1} - c_i w^{\uparrow} \Omega_i \,. \tag{7-31}$$

We may combine these two equations to eliminate $w^{\uparrow}\Omega_i$:

$$J_i = c_{i-1} w^{\downarrow} \Omega_{i-1} \left(\frac{f_{i-1}'}{c_{i-1}} - \frac{f_i'}{c_i} \right) . \tag{7-32}$$

From the definition of J_i, the first time variation of f_i' is given by

$$\frac{\partial f_i'}{\partial t} = J_i - J_{i+1} = -\frac{\partial J_i}{\partial i} \,. \tag{7-33}$$

Let us now pass over to an approximately equivalent continuous description. Then, in place of (7-32) we have $J_i \approx -c_i w^{\downarrow} \Omega_{i-1} \partial (f_i'/c_i)/\partial i$, and (7-33) becomes

$$\frac{\partial f_i'}{\partial t} \approx \frac{\partial}{\partial i} \left[c_i w^{\downarrow} \Omega_{i-1} \frac{\partial}{\partial i} (f_i'/c_i) \right] . \tag{7-34}$$

Assuming further that $c_i w^{\downarrow} \Omega_{i-1}$ is roughly constant, this equation reduces to a diffusion equation in f_i'/c_i with diffusion coefficient $w^{\downarrow}\Omega_{i-1}$:

$$\frac{\partial (f_i'/c_i)}{\partial t} \approx w^{\downarrow} \Omega_{i-1} \frac{\partial^2}{\partial i^2} (f_i'/c_i) \,. \tag{7-35}$$

Thus, the characteristic time to achieve the quasi-steady state germ concentration is just $\tau \approx (g^2/\mathrm{w}^{\downarrow}\Omega_{g-1})^{1/2}$ (Farley, 1952). For water germs in typical expansion chambers, $\tau \sim 10^{-6}$ to 10^{-5} sec, which is about 10^{-3} of the time during which the supersaturation remains essentially constant. Thus, the steady state assumption is consistent with usual experimental conditions.

Let us now proceed to find $J_i = J =$ constant, assuming a steady state concentration which we shall denote by f_i. Surprisingly, it turns out we do not have to determine f_i to find J. However, we do need to use boundary conditions on f_i, which we choose as follows: (1) $f_1/c_1 = 1$; this is reasonable since the monomer population is relatively enormous and need not deviate significantly from the equilibrium concentration in order to produce a substantial nucleation rate. (2) $f_G = 0$ for some $G \gg g$; the results are extremely insensitive to the choice of G, which makes this a reasonable working assumption.

From (7-32), we may now immediately obtain J by summing over i as follows:

$$\sum_{i=1}^{G-1} J/c_i \mathrm{w}^{\downarrow}\Omega_i = \sum_{i=1}^{G-1} \left(\frac{f_i}{c_i} - \frac{f_{i+1}}{c_{i+1}} \right) = \frac{f_1}{c_1} = 1 \tag{7-36}$$

or

$$J = \left(\sum_{i=1}^{G-1} \frac{1}{c_i \mathrm{w}^{\downarrow}\Omega_i} \right)^{-1}, \tag{7-37}$$

a result in which f_i does not appear. Now c_i will have a minimum near $i = g$ (recall (7-26) and Figure 7.2, and so the dominant contributions to J will come from terms in that neighborhood. Hence, we may approximate the sum in (7-37) as

$$\sum_{i=1}^{G-1} \frac{1}{c_i \mathrm{w}^{\downarrow}\Omega_i} \approx \frac{Z^{-1}}{\mathrm{w}^{\downarrow}\Omega_g c_g}, \tag{7-38}$$

where the factor Z^{-1} effectively counts the number of contributing terms; i.e., it measures the width of the minimum in the curve for c_i. From (7-37), we then obtain

$$J = Z \mathrm{w}^{\downarrow}\Omega_g c_g . \tag{7-39}$$

By comparing with (7-29), we see that (7-39) differs from the equilibrium approximations result only by the factor Z, called the *Zeldovitch factor* (Zeldovitch, 1942).

The Zeldovitch factor is obtained by expanding c_i about the minimum in a Taylor series through terms of the second order in i; this produces a Gaussian approximation to the curve in that neighborhood, and Z^{-1} is identified with the width (i.e., the standard deviation) of the Gaussian curve. Proceeding in this way, we write ΔF_i in (7-26) as

$$\Delta F_i \approx (\Delta F_g) + \frac{1}{2} \left[\frac{\mathrm{d}^2}{\mathrm{d}i^2} (\Delta F_i) \right]_{i=g} (i-g)^2 . \tag{7-40}$$

On abbreviating $B_g \equiv [(\mathrm{d}^2/\mathrm{d}i^2)(\Delta F_i)]_{i=g} (< 0)$ we find, with $c_g = c_{g,\mathrm{sat,w}} \times \exp[-\Delta F_g/\mathrm{k}T]$ from (7-26),

$$\frac{c_g}{c_i} = \exp\left[\frac{B_g(i-g)^2}{2\mathrm{k}T}\right] . \tag{7-41}$$

The Zeldovitch factor may then be found from (7-38)

$$Z^{-1} \approx \sum_i \frac{c_g}{c_i} \approx \int_{-\infty}^{+\infty} \exp[B_g \mathrm{x}^2/2\mathrm{k}T]\mathrm{d}\mathrm{x} , \tag{7-42}$$

where we have set $\mathrm{x} = i - g$. Evaluation of the integral gives

$$Z^{-1} = \left(-\frac{2\pi \mathrm{k}T}{B_g}\right)^{1/2} . \tag{7-43}$$

Using (7-23) and recognizing that $\Omega_i \propto i^{2/3}$, this leads to

$$Z = \left[\frac{\Delta F_g}{3\pi \mathrm{k}T g^2}\right]^{1/2} . \tag{7-44}$$

This expression is suitable for arbitrary geometries. Two additional forms which hold for spherical water germs are:

$$Z = \left(\frac{\ln S_{\mathrm{v,w}}}{6\pi g}\right)^{1/2} = \frac{2\dot{v}_{\mathrm{w}}}{\Omega_g}\left(\frac{\sigma_{\mathrm{w/v}}}{\mathrm{k}T}\right)^{1/2} , \tag{7-45}$$

where $g = (4\pi/3)a_g^3/\dot{v}_{\mathrm{w}}$. The mathematical approximations involved in passing from (7-37) to (7-39) and (7-44) produce an error of about 1% (Cohen, 1970), which is insignificant in comparison with the uncertainties in ΔF_i.

Numerical evaluation of (7-45) shows that Z is typically $\mathrm{O}(10^{-1})$. This result is in qualitative accord with our expectations: A finite rate of germ production should deplete the embryo population to something below the equilibrium level.

Collecting results, the nucleation rate of water germs from the vapor may be expressed as

$$J = c_{\mathrm{sat,w}} \mathrm{w}^{\downarrow} \Omega_g Z \exp[-\Delta F_g/\mathrm{k}T] . \tag{7-46}$$

This holds even for non-spherical germs, if (7-44) is used to describe Z. Other versions for spherical germs include

$$J = 2c_{\mathrm{sat,w}} \mathrm{w}^{\downarrow} \dot{v}_{\mathrm{w}} (\sigma_{\mathrm{w/v}}/kT)^{1/2} \exp[-\Delta F_g/\mathrm{k}T] , \tag{7-47}$$

using the second form of (7-45), and

$$J = \frac{\alpha_c}{\rho_{\mathrm{w}}}\left(\frac{2N_A^3 M_{\mathrm{w}} \sigma_{\mathrm{w/v}}}{\pi}\right)^{1/2} \left(\frac{\mathrm{e}_{\mathrm{sat,w}}}{\mathscr{R}T}\right)^2 S_{\mathrm{v,w}} \exp[-\Delta F_g/\mathrm{k}T] , \tag{7-48}$$

TABLE 7.1

Variation of the nucleation rate J as a function of saturation ratio over water and over ice for homogeneous nucleation of water drops and ice crystals in water vapor at $-12°$ C for $\alpha_c = \alpha_d = 1.0$. (Based on data of Dufour & Defay, 1963.)

$S_{v,w}$	2	3	4	5	6
$S_{v,i}$	2.249	3.374	4.499	5.623	6.748
J(drops cm^{-3} sec^{-1})	1.9×10^{-112}	7.0×10^{-31}	1.1×10^{-10}	7.1×10^{-2}	6.0×10^{3}
J (ice crystals cm^{-3} sec^{-1})	9.2×10^{-394}	2.7×10^{-163}	1.2×10^{-98}	4.4×10^{-69}	3.4×10^{-52}

using (5-51) for $w^{\downarrow}$ and the first form of (7-45), together with $\dot{v}_w = M_w/\rho_w N_A$, $c_{sat,w} = e_{sat,w}/kT$, and $k = \mathscr{R}/N_A$. Of course, equations exactly analogous to (7-47) and (7-48) hold for the nucleation rate of spherical ice germs from the vapor (with $c_{sat,w} \to c_{sat,i}$, $\dot{v}_w \to \dot{v}_i$, $\alpha_c \to \alpha_d$, $S_{v,w} \to S_{v,i}$, $\rho_w \to \rho_i$, $\sigma_{w/v} \to \sigma_{i/v}$, and $e_{sat,w} \to e_{sat,i}$).

Inspection of (7-46) to (7-48) and (7-28) shows that J is extremely sensitive to $S_{v,w}$, since the term in the exponent varies as $S_{v,w}^{-2}$. This is indicated further in Table 7.1, in which a numerical evaluation of (7-48) and its counterpart for ice are presented. We see, for example, that for water germs, J increases by 5 orders of magnitude as $S_{v,w}$ increases from 5 to 6. This behavior enables one to define, from an experimental point of view, a critical saturation ratio $(S_{v,w})_{crit}$ at which drops suddenly appear in the vapor; by convention, $(S_{v,w})_{crit}$ has been taken to correspond to $J = 1$ germ cm^{-3} sec^{-1}.

Table 7.1 also indicates that the nucleation rate of ice germs from the vapor remains near zero for all realizable supersaturations. This follows from the fact that $\Delta F_g \propto \sigma^3$; then, since $\sigma_{i/v} > \sigma_{w/v}$, we have $\Delta F_{g,ice} > \Delta F_{g,water}$ and, hence, $J_{ice} \ll J_{water}$ for a given $S_{v,w}$. This behavior apparently holds for T down to at least $-100°$C. This is in contrast to predictions based on the phase diagram for bulk water, which merely reinforces again the notion that surface effects dominate in nucleation phenomena. On the other hand, the nucleation prediction is in agreement with *Ostwald's rule of stages* (*Ostwalds Stufenregel*) (Ostwald, 1902) which states that a supersaturated phase (water vapor) does not directly transform into the most stable state (ice), but rather into the next most stable or metastable state (supercooled water). Although Krastanow (1940) proposed a reversal of this rule for water substance below about $-65°$C, Dufour and Defay (1963) have shown Krastanow's result to be erroneous, since it was based on incorrect values for $\sigma_{i/v}$ and v_i, and neglected the variation of $\sigma_{w/a}$ with temperature. A correct evaluation of the nucleation rate equations demonstrates that at temperatures warmer than $-100°$C no reversal of Ostwald's rule takes place. It must be stressed that this result is only applicable to *homogeneovs nucleation.* If nucleation is *heterogeneous*, Ostwald's rule does, indeed, reverse under certain conditions (see Chapter 9).

In Figure 7.4, a comparison is made between the classical model for a drop and ice crystal (for a crystal with a shape factor $s = 16$, see Section 5.7.2) with the clathrate and ice cluster model of Hale and Plummer. We notice excellent

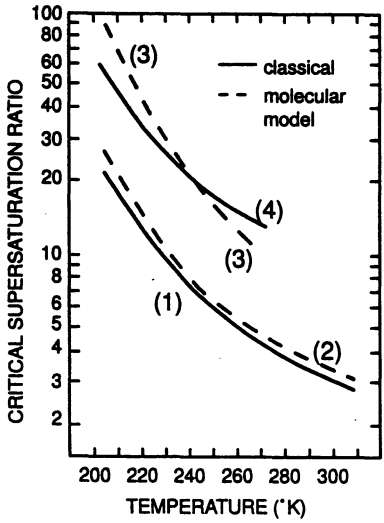


Fig. 7-4: Critical supersaturation for drop and ice nucleation (with respect to liquid water) predicted for $J = 1$ cm^{-3} sec^{-1} by the classical and the molecular model; for $\alpha_c = \alpha_d = 1.0$. Curves (3) and (4): for ice crystal nucleation in supersaturated vapor with s = 16. Curves (1) and (2): for water drop nucleation in supersaturated vapor. (From Hale and Plummer, 1974a, with changes.)

agreement between the classical drop model and the clathrate cluster model. The agreement is less satisfactory between the classical ice model and the ice cluster model. Nevertheless, the general agreement is quite surprising in view of the assumptions made in both theories: namely, the assumption in the classical theory that ρ_w, ρ_i and $\sigma_{w/v}$, $\sigma_{v,i}$ can be described by values which apply to macroscopic phases, and, for the molecular model, the assumption that the cluster takes on the shapes given in Figure 7.1a,b. It may be that the agreements are quite fortuitous and the result of compensating errors between the models as well as within a particular model. Thus, Lee *et al.* (1973) found from studies on spherical solid argon clusters, that the capillarity approximation overestimates the number of surface atoms in the cluster, but at the same time underestimates the surface free energy per surface atom. We further note from (7-28) that $\sigma_{v/w}$, or $\sigma_{v/i}$ appears in the numerator and ρ_w or ρ_i in the denominator, so that errors in σ and ρ due to the neglect of the cluster character of very small drops (or ice crystals) might compensate. We also note from Figure 7.4 that both models uphold the Ostwald rule of stages and predict that in homogeneous vapor at temperatures below 0°C ice appears via the freezing of supercooled water drops rather than directly from the vapor, as also expected from Table 7.1.

7.1.3 Experimental Verification

The various shortcomings inherent in the theories of homogeneous nucleation have made extensive comparison with experiment especially important. Following Wil-

son (1899), many experimenters have employed the expansion chamber technique to determine the onset of homogeneous water drop formation in supersaturated vapor. A review of many such studies has been given by Mason (1957a). Later, Katz and Ostermier (1967), and Heist and Reiss (1973) have used the diffusion chamber technique to study homogeneous water drop formation. Both experimental techniques have several major shortcomings and basic difficulties which are hard to overcome. Problems inherent in the diffusion cloud chamber technique have been discussed by Fitzgerald (1970, 1972), while difficulties of the expansion chamber technique have been discussed by Barnard (1953), Mason (1957a), Allard and Kassner (1965), Carstens *et al.* (1966), Carstens and Kassner (1968), Kassner *et al.* (1968a,b), and Allen and Kassner (1969).

In addition to the experimental problems of design and technique, Allen and Kassner (1969) and Hagen *et al.* (1982) gave evidence of the fact that the molecules of any carrier gas with which a cloud chamber is purged may act as nucleation centers to form clathrates. Under these conditions, nucleation is not truly homogeneous. Still another uncertainty arises from the fact that the condensation coefficient α_c is not accurately known (see Table 5.4).

In spite of these reservations, Figure 7.5 indicates a reasonably good agreement between experiment and both the classical theory and the molecular clathrate cluster theory of Hale and Plummer (1974b). This is particularly true for the expansion chamber studies of Kassner *et al.* (1971), Kassner *et al.* (1975, pers. comm.), Miller *et al.* (1983), and the diffusion chamber studies of Heist and Reiss (1973). From the discussion of Section 7.1.2, we must interpret the agreement between the classical theory and experiment as being partly fortuitous and due to compensating errors in the theory (see also Hale and Plummer, 1974a, and Lee *et al.*, 1973).

Some of the earlier experimental ice nucleation studies by Sander and Damköhler (1943), Cwilong (1947), and Pound *et al.* (1955) were interpreted to mean that, below a certain temperature, ice forms directly from the vapor. However, Fournier d'Albe (1949), Mason (1952a), Mossop (1955), Kachurin *et al.* (1956), Maybank and Mason (1959), Anderson *et al.* (1980), Hagen *et al.* (1981, 1982), DeMott *et al.* (1992) and DeMott and Rogers (1990) demonstrated conclusively that in supersaturated homogeneous vapor and at temperatures between 0 and $-70°C$, ice is always the result of the freezing of supercooled drops. Thus, present experiments support both the molecular ice cluster theory of Hale and Plummer (1974a,b) and the classical theory in their prediction that Ostwald's rule of stages indeed applies to the homogeneous phase change of water substance.

7.2 Homogeneous Nucleation of Ice in Supercooled Water

7.2.1 The Nucleation Rate J

In order to apply the nucleation rate equation to the nucleation of ice crystals in supercooled water, we must realize that the main difference between nucleation of ice embryos from supersaturated vapor and from supercooled water lies in the growth mechanism of the embryos. As we have seen, in the former case, the growth of an embryo is controlled by the monomer flux from the vapor. In the

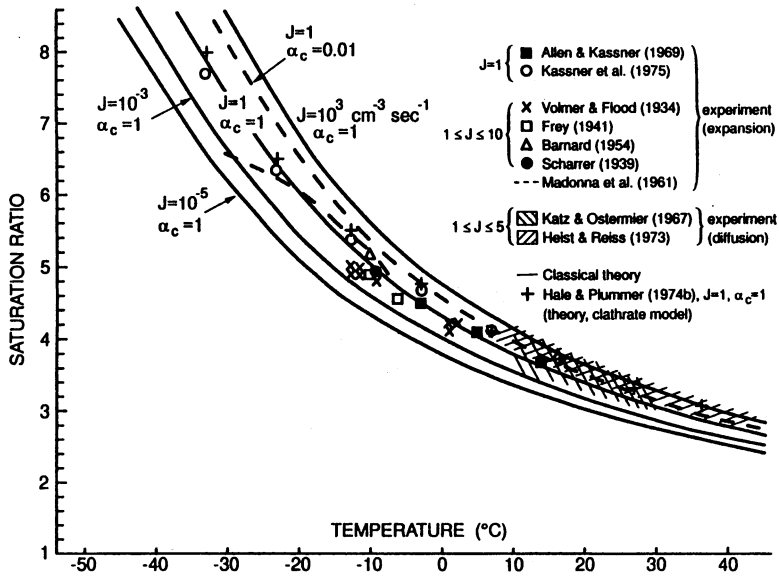


Fig. 7-5: Critical supersaturation for drop nucleation predicted by the classical and the molecular model for various values of J and α_c. Comparison of theory with experiment.

latter case, where water molecules are essentially already in contact with the ice-embryo, growth is a matter of molecular reorientation involving the breaking of water-to-water bonds and the formation of water-to-ice bonds. During this process, which proceeds at constant temperature and constant pressure, a water molecule must pass from its average equilibrium position of minimum potential energy in water to a new equilibrium position in ice, the two positions being separated by an energy barrier $\Delta g^{\ddagger}$. Expressed in another way, $\Delta g^{\ddagger}$ is the molar Gibbs free energy of activation for diffusion of water molecules across the water-ice boundary. Using the 'absolute reaction rate theory' (Glasstone *et al.*, 1941; Eyring and Jhon, 1968), Turnbull and Fischer (1949) have shown that this energy barrier leads to the following expression for the diffusive flux density of water molecules across the ice surface:

$$w_{\text{diff}}^{\downarrow} = \frac{N_c kT}{h} \exp(-\Delta g^{\ddagger}/\mathscr{R}T)\,, \tag{7-49}$$

where h is Planck's constant and N_c is the number of monomers of water in contact with unit area of the ice surface. Dufour and Defay (1963) estimate N_c to be about 5.85×10^{12} cm^{-2}, while Eady (1971) finds 5.30×10^{12} cm^{-2} using a molecular model. Using $w_{\text{diff}}^{\downarrow}$ in place of the factor $w^{\downarrow}$ in (7-46) or (7-47), we can immediately write down the homogeneous nucleation rate for ice germs in supercooled water in a form analogous to (7-47)

$$J = 2c_w w_{\text{diff}}^{\downarrow} \dot{v}_i \left(\frac{\sigma_{i/w}}{kT}\right)^{1/2} \exp\left[-\frac{\Delta F_g}{kT}\right], \tag{7-50}$$

or, with (7-49)

$$J = 2N_c \left(\frac{\rho_w kT}{\rho_i h}\right) \left(\frac{\sigma_{i/w}}{kT}\right)^{1/2} \exp\left[-\frac{\Delta g^{\ddagger}}{\mathscr{R}T} - \frac{\Delta F_g}{kT}\right]. \tag{7-51}$$

We note from (7-51) that, in contrast to ice nucleation from supersaturated vapor, ice nucleation in supercooled water has to overcome two energy barriers. We shall now discuss both barriers in sequence.

7.2.2 The Energy of Germ Formation

In order to evaluate (7-50) or (7-51), we must determine the work of ice germ formation ΔF_g. As in the case of nucleation from the vapor phase we may proceed along two avenues and use either the classical approach based on thermodynamic arguments or follow a molecular approach and apply statistical mechanics to supercooled water. We shall briefly touch on both of these approaches.

7.2.2.1 *Classical Model*

Using the classical approach, the energy of ice-germ formation in supercooled water is obtained following the same line of reasoning that applies to a water germ (cf. (7-28))

$$\Delta F_g = \frac{\sigma_{i/w}\Omega_g}{3} = \frac{4\pi(a_i)_g^3 \sigma_{i/w}}{3}, \tag{7-52}$$

where $(a_i)_g$ is found from (6-52) for the case that $a_d \ll a_i$ and no salts are in solution, and assuming that the supercooling required for ice nucleation to occur is sufficiently small so that average values for the latent heat of freezing and the density of ice may be used over the temperature interval of interest.

However, in the next few paragraphs it will be shown that homogeneous ice nucleation becomes significant only at supercoolings larger than 35°C. In this temperature range, the parameters ρ_w, ρ_i, $\mathscr{L}_m$ and $\sigma_{i/w}$ which appear in (7-52) and (6-52) vary significantly with decreasing temperature (see Chapters 3 and 5), thus prohibiting the use of average values over the temperature interval. Therefore, $(a_i)_g$ in (7-52) has to be computed by integrating the full equation (6-52) if ice is nucleated inside an aqueous solution drop of a given size. For $a_d \ll a_i$ and for pure water ($a_w = 1$), $(a_i)_g$ can be obtained by integrating (6-52) without the second and fourth term.

7.2.2.2 *The Molecular Model*

In an attempt to evade the assumptions of the classical theory, Eadie (1971) formulated an expression for the energy of ice germ formation in water by using a statistical approach similar to that employed later by Hale and Plummer (1974a,b) for the formation of water and ice germs in supersaturated vapor. Eadie based his approach on the statistical thermodynamic model of water by Nemethy and Sheraga (1962a,b) and Vand and Senior (1965a,b). In this model, it is assumed that the molecules in water can be partitioned into five classes according to the

number of H-bonds in which they participate, i.e., from none in the completely unbonded state to four in an ice-like state. In each of the five classes, the molecules undergo restricted translational, vibrational and rotational motions in the field of the nearest neighbor molecules. The canonical partition fuction for water consisting of i-bonded molecules can, in analogy to (7-5), be written as

$$Q = \sum_{(N_j)} N! \Pi_{j=0}^{4} \frac{q_j^{N_j}}{N_j!}, \tag{7-53}$$

where N_j is the number of molecules in the molecular class j of j-bonded molecules, (N_j) denotes summation over all distinct distributions of the $N = \sum_{j=0}^{4} N_j$ molecules of the system into the five molecular classes, and q_j is the j-bonded molecule partition function.

Eadie modified this expression by following a suggestion of Vand and Senior (1965a,b), wherein a *degeneracy* factor ω_j is included to account for the number of distinguishable ways in which the j hydrogen bonds in which a molecule in the jth molecular class participates can be distributed among the four possible directions with respect to the molecule:

$$\omega_j = \frac{4!}{(4-j)!j!} \tag{7-54}$$

With this adjustment the partition function becomes

$$Q = \sum_{(N_j)} N! \Pi_{j=0}^{4} \frac{(\omega_j q_j)^{N_j}}{N_j!}. \tag{7-55}$$

Next, the partition function is approximately evaluated by equating $\ln Q$ with the logarithm of the maximal term in the sum on the right-hand side of (7-55). Using Sterling's approximation for this purpose, the logarithm of a term in the sum over distinct distributions in (7-55) is

$$\ln T = N(\ln N - 1) + \sum_{j=0}^{4} N_j[\ln(\omega_j q_j) - (\ln N_j - 1)]. \tag{7-56}$$

The values of the N_j's for which $\ln T$ is a maximum subject to the constraint that the total number of molecules remains constant can be obtained by the method of Lagrange multipliers; the result is that the equilibrium value for the mole fraction of molecules in the jth class is given by

$$\frac{N_j}{N} = \frac{\omega_j q_j}{\sum_{j=0}^{4} \omega_j q_j}. \tag{7-57}$$

On substituting this result into (7-56), the canonical partition function is obtained:

$$\ln Q = N \ln \left(\sum_{j=0}^{4} \omega_j q_j \right). \tag{7-58}$$

Based on (7-58), Eadie assigned to a monomer in supercooled water the average partition function given by

$$q_1 = \sum_{j=0}^{4} \omega_j q_j \tag{7-59}$$

Then, considering the mass action law (7-9), the number of ice clusters (i-mers) consisting of i water molecules is

$$N_i = q_i' \left(\frac{N_1}{q_1}\right)^i , \tag{7-60}$$

where q_i' is the molecular partition function for an ice i-mer. As before, we may express this result in a form containing the Boltzmann factor:

$$N_i = N_1 \exp\left(\frac{-\Delta\phi_i}{\mathrm{k}T}\right) , \tag{7-61}$$

where $\Delta\phi_i$ represents the energy required to form an ice embryo of i-molecules. Combining (7-59) to (7-61), we find for the energy required to form an ice embryo of i-molecules. Combining (7-59) to (7-61), we find for the energy of ice embryo formation:

$$\frac{\Delta\phi_i}{\mathrm{k}T} = i \ln\left[\sum_{j=0}^{4} \omega_j q_j / N_1\right] - \ln(q_i'/N_1). \tag{7-62}$$

Eadie estimated q_i' by assuming an ice-like geometry for the i-mers, with molecules arranged in the form of a hexagonal prism with its height equal to the diameter of a basal face. He then determined the total number of molecules, the number of doubly (i_2), triply (i_3), and quadruply (i_4) bonded molecules in an i-mer, and the number of broken bonds on the surface of the i-mer. The required bookeeping is formidable and cannot be repeated here, but the result is that the ice i-mer partition function is obtained from the relation

$$q_i' = \frac{i_3!}{(i_3 - \bar{i}_{34})!\bar{i}_{34}!} \frac{2^{\bar{i}_{23}}}{(i_2 - \bar{i}_{23} - \bar{i}_{24})!\bar{i}_{23}!\bar{i}_{24}!} (q_I)^{i_4} (q_4)^{\bar{i}_{34}+\bar{i}_{24}} (q_3)^{i_3-\bar{i}_{34}+\bar{i}_{23}} (q_2)^{i_2-\bar{i}_{23}-\bar{i}_{24}} \tag{7-63}$$

where $q_I = \exp(-\dot{\mu}_I/kT)$ is the molecular partition function for the quadruply bonded molecules in the interior of an ice cluster given by the observed molecular chemical potential $\dot{\mu}_I$ fo ice, $\bar{i}_{24} = X_H^2 i_2$, $\bar{i}_{23} = 2X_H(1 - X_H)i_2$, $\bar{i}_{34} = X_H i_3$, and where X_H is the average fraction of hydrogen bonding between molecules in the liquid, given by $X_H = \sum_{j=0}^{4} (j/4)\omega_j q_j / \sum_{j=0}^{4} \omega_j q_j$. The energy of ice germ formation is then obtained as the maximum in a plot of $\Delta\phi_i$ versus i.

7.2.3 The Molar Activation Energy $\Delta g^{\ddagger}$

In most earlier work, $\Delta g^{\ddagger}$ has been identified with the experimentally determined activation energy $(\Delta g)_{act,w}$ for self-diffusion in water given by (3-21) (see also Section 5.9). Such identification led in the past to a serious underestimate of

the theoretical nucleation rate in comparison to the rate derived for temperatures between −43 to −33°C from cloud chamber studies (Butorin and Skripov, 1972; Hagen *et al.*, 1981; DeMott and Rogers, 1990), and from field experiments carried out at the cirrus cloud level (Sassen and Dodd, 1988; Heymsfield and Sabin, 1989; Heymsfield and Uriboshavich 1993). This discrepancy is evident from a comparison of curves (1) and (2) in Figure 7.6. The reason for this discrepancy lies in the fact that $(\Delta g)_{act,w}$ increases rapidly with decreasing temperature (see Figure 3.11), due to an increasingly bonded water structure (see Section 3.4). In contrast, cloud chamber studies of Hagen *et al.* (1981) suggest that below −32°C $\Delta g^{\ddagger}$ sharply decreases with decreasing temperature. They argued that the reason for this lies in the fact that, with decreasing temperature, the freezing process becomes an increasingly cooperative phenomenon where increasingly larger clusters of water molecules transfer across the ice-water interface by breaking only hydrogen bonds at the cluster periphery, but not in the interior of the cluster.

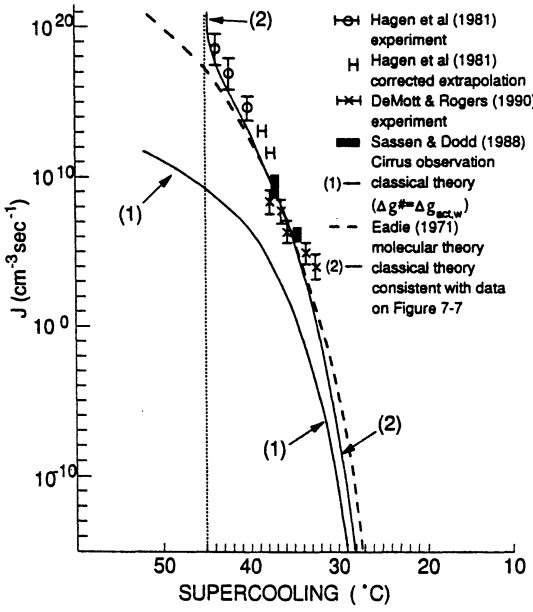


Fig. 7-6: Variation of the rate of homogeneous ice nucleation in supercooled water. (1) Classical theory based on values for $\sigma_{i,w}$, L_m, ρ_w, ρ_i available prior to 1978 and for $\Delta g^{\ddagger} = (\Delta h)_{act,w}$. (2) Classical theory based on recent values for $\sigma_{i,w}$, L_m and on $\Delta g^{\ddagger}$ given by curve 3 in Figure 3-11. Dashed line: molecular model of Eadie (1971). Cloud chamber experiments: ○ Hagen *et al.* (1981), H data of Hagen *et al.* (1981) extrapolated by author to warmer temperatures, × DeMott and Rogers (1990), and observations at the cirrus cloud level (Sassen and Dodd, 1988).

In order to arrive at a more realistic estimate for $\Delta g^{\ddagger}$, we may therefore follow Hagen *et al.* (1981) and solve (7-51) subject to observed values for J. In order to test whether the laboratory and field data given in Figure 7.6 are sufficiently

accurate for such computation, we shall compare them with the results from drop freezing experiments in the laboratory.

For this purpose, we note that J in (7-51) is given in terms of the number of germs in 1 cm^3 of supercooled water which is equivalent to a drop of 6.2 mm radius. Since the drops studied in the labortory and in the field are considerably smaller than this size, it is necessary to formulate an ice nucleation theory for smaller volumes of water. Let us follow first a heuristic approach and consider a population of N_0 isolated water drops, all having the same temperature T and the same volume V_d. We shall assume further that a nucleation event in any one drop is independent of that in any other drop. Given these conditions, we may express the number of ice-germs produced during the time dt in the volume $N_u V_d$ of unfrozen water as

$$N_{i,g}(t + dt) - N_{i,g}(t) = N_u V_d J(T)\, dt\,, \tag{7-64}$$

where N_u is the number of unfrozen drops and $J(T)$ is the rate of ice-germ formation.

We shall also assume that ice formation is the result of only one nucleation event per drop. This assumption is reasonable, since the growth velocity of ice is very large at the supercoolings where homogeneous ice-nucleation takes place. This makes it very likely that the first germ formed grows quickly enough to convert the drop into ice before any other germ is formed. The first germ receives additional protection from the fact that, during its growth, latent heat is released which immediately raises the temperature of water in the drop. This reduces the nucleation rate of other germs to a negligible value.

For these conditions the increase of ice-germs is given by dN_f, the increase in the number of frozen drops N_f. Also, since the total number N_0 of drops is constant, we have $dN_u = -dN_f$. Hence, we arrive at the simple differential equation

$$dN_u = -N_u V_d J(T)\, dt \tag{7-65a}$$

or

$$-\frac{1}{N_u}\frac{dN_u}{dt} = V_d J(T)\,. \tag{7-65b}$$

Integrating from N_0 at $t = 0$ to N_u at t, and assuming constant temperature T, we find

$$N_u = N_0 \exp[-V_d J(T) t]\,. \tag{7-66}$$

This indicates how, at constant temperature, the number of unfrozen drops decreases with increasing time.

Of course, we could have obtained (7-66) immediately by considering that ice nucleation, proceeding homogeneously in the drops, is a stochastic process. This implies that the freezing events are Poisson distributed (see, e.g., Melissinos, 1966). Therefore, the probability that, out of a population of N_0 drops, N_f drops have frozen during the time interval $t = 0$ to $t = t_f$ is

$$P(N_f, t_f) = \frac{(\lambda t_f)^{N_f} \exp(-\lambda t_f)}{N_f!}\,, \quad N_f = 0, 1, 2, \ldots \tag{7-67}$$

with $\lambda = V_d J(T)$. The probability that during the time interval $t = 0$ to $t = t_f$ no freezing events take place is then

$$P(N_f = 0, t_f) = \exp[-V_d J(T) t_f] . \tag{7-68}$$

Identifying $P(N_f = 0, t_f)$ with (N_u/N_0), i.e., with the ratio of the N_u drops which survived freezing to the whole population of drops, we recover (7-66). One readily also sees that half of the drop population has frozen after the time $t_{1/2} = 0.693/V_d J(T)$.

For a constant rate of cooling, $\gamma_c = -dT/dt$, we obtain, instead of (7-65b),

$$\left(\frac{1}{N_u}\frac{dN_u}{dT}\right)_{\gamma_c} = \frac{V_d J(T)}{\gamma_c} \tag{7-69}$$

or, after integration,

$$N_u = N_0 \exp\left[-(V_d/\gamma_c)\int_T^{T_0} J(T)dT\right] . \tag{7-70}$$

We notice from (7-69) that that the smaller the rate at which a drop is cooled or the larger the volume of a drop, the less it can be supercooled before it freezes.

These findings are physically reasonable if we consider that the larger the volume of a drop, the larger is the probability for a density fluctuation in the drop and, thus, the larger is the probability that an ice germ will be produced. It is also reasonable that, in a given volume of supercooled water, the probability for a density fluctuation and, thus, the probability for ice-formation, increases with increasing time during which the water is exposed to a certain change in temperature.

Frequently in the literature, the freezing temperature of a population of drops is characterized by the median freezing temperature T_m, i.e., the temperature where 50% of drops are still unfrozen, i.e., $N_u = N_0/2$. With this, (7-70) becomes

$$\int_{T_m}^{T_0} J(T)dT = 0.693\gamma_c/V_d . \tag{7-71}$$

Unfortunately, there is considerable scatter among experimentally derived values available in the literature for the median freezing temperature of water drop populations. This is not surprising, since water cannot easily be purified to such an extent that it consists almost entirely of water molecules, although some workers have gone far in devising techniques to reach such a desired state of purification (Mossop, 1955; Haller and Duecker, 1960; Pruppacher, 1963a). Additional uncertainties in providing homogeneous conditions arise from the need to support the water samples. Fortunately, a careful analysis of the lowest freezing temperatures recorded give a more consistent picture. These values are plotted in Figure 7.7 as a function of drop diameter, using letter symbols. Assuming now that at the lowest observed supercooling 99.99% of a population of equally sized water drops are frozen when cooled at a rate γ_c, we find, instead of (7-71),

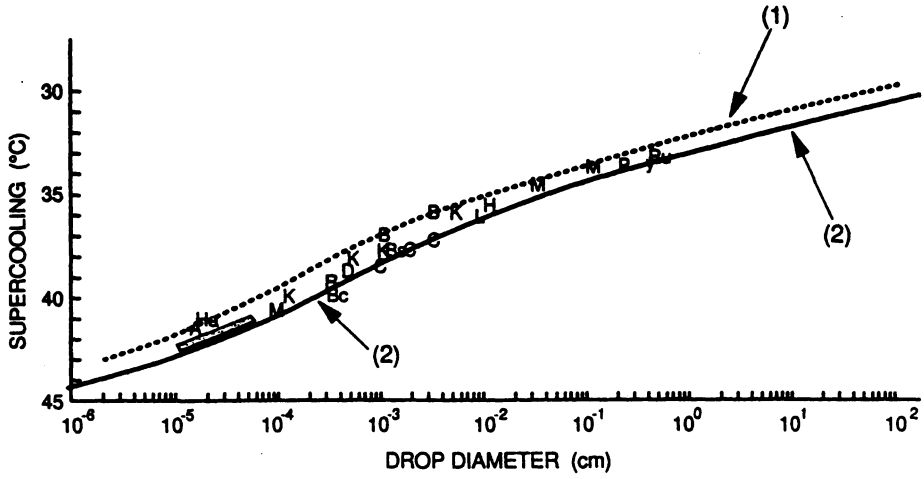


Fig. 7-7: Lowest temperatures to which pure water drops of given size and exposed to cooling rates between 1°C min^{-1} and 1°C sec^{-1} have been supercooled during laboratory experiments: H (Hoffer, 1961), M (Mossop, 1955), D (DeMott and Rogers, 1990), B (Bigg, 1953b), P (Pruppacher and Neiburger, 1963), L (Langham and Mason, 1958), Ha (Hagen *et al.*, 1981), Ru (Rouleau, 1958), K (Kuhns and Mason, 1968), Y (Bayardelle, 1955), R (Rasmussen, 1982), A (Anderson *et al.*, 1980), Bs (Butorin and Skripov, 1972), and Bc (Broto and Clausse, 1976). Curves 1 and 2: Temperature at which 99.99% of a population of uniform-sized water drops freezes when exposed to cooling rates of 1° C min^{-1} and 1° C sec^{-1}, respectively (from Equation 7-72, with J values consistent with curve 2 in Figure 7-6.)

$$\int_{T_{99.99}}^{T_0} J(T)\mathrm{d}T = 9.21\gamma_c/V_\mathrm{d}\,. \tag{7-72}$$

Equation (7-72) may be solved to obtain $T_{99.99}$ as a function of drop size for given values of J. Although we mentioned earlier that observational values for J are only available for the temperature range -44 to -33°C (see Figure 7.6), it turns out that J contributes only negligibly to (7-72) at temperatures warmer than -33°C, so that this contribution may safely neglected. One therefore may solve (7-72) by using J-values derived from a best fit to the observations between -44 and -33°C. The results of this computation for γ_c = 1°C sec^{-1} and 1°C min^{-1} are given by the continuous curves (1) and (2) in Figure 7.7. We notice from this figure that for a given drop size, $T_{99.99}$ is in excellent agreement with the largest drop supercooling observed in the laboratory. Assuming that this agreement can be taken as support for the J-values given as curve (2) in Figure 7.6, one may extrapolate curves (1) and (2) in Figure 7.7 to -27°C by requiring consistency with a similar extrapolation of curve (2) in Figure 7.6. The values for J thus obtained are listed in Table 7.2. We note from this table and curve (2) in Figure 7.6 that

TABLE 7.2
Variation of the nucleation rate J as a function of temperature for homogeneous nucleation ice in supercooled water.

Supercooling (°C)	J (cm^{-3} sec^{-1})	Supercooling (°C)	J (cm^{-3} sec^{-1})
29	46×10^{-11}	37	30×10^{7}
30	43×10^{-8}	38	50×10^{8}
31	15×10^{-5}	39	90×10^{9}
32	65×10^{-3}	40	10×10^{11}
33	15×10^{0}	41	20×10^{12}
34	30×10^{2}	42	10×10^{14}
35	20×10^{4}	43	50×10^{15}
36	10×10^{6}	44	20×10^{17}

TABLE 7.3
Variation with temperature of the activation energy for transfer of water molecule across the ice-water interface.

Temperature (°C)	Activation energy (kcal $mole^{-1}$)	Temperature (°C)	Activation energy (kcal $mole^{-1}$)
-29	10.00	-37	7.75
-30	10.00	-38	7.65
-31	10.00	-39	7.45
-32	9.60	-40	7.25
-33	9.20	-41	6.85
-34	8.60	-42	6.00
-35	8.20	-43	5.15
-36	7.90	-44	4.45

J rises strongly with increasing supercooling, rising eventually without bound as a supercooling of −45°C is approached. This tendency is a direct consequence of the singularity behavior observed for water at −45°C (Section 3.4). Finally, the values listed in Table 7.2 may be used to estimate $\Delta g^{\mp}(T)$ from (7-51). For this purpose, we compute ΔF_g from (7-52) with (5-47a,b) for $\sigma_{i/v}(T)$, (3-25) for $L_{m,0}(T)$, (3-2) for $\rho_i(T)$ and (3-14) for $\rho_w(T)$. The resulting values for $\Delta g^{\mp}(T)$ are listed in Table 7.3, and plotted as curve 4 in Figure 3.11. As anticipated by Hagen *et al.* (1981), $\Delta g^{\mp}(T)$ decreases rapidly with increasing supercooling, approaching zero as the temperature approaches the singularity temperature of −45°C. As seen in Figure 3.11, at temperatures warmer than −29°C, the transfer of water molecules across the water-ice interface is controlled by the self-diffusion of water molecules through bulk water, while at temperatures below −32°C, the controlling mechanism is the transfer of increasingly large clusters, as suggested by Hagen *et al.* (1981). At temperatures between −29 and −32°C, a transition regime exists in which the mechanism of growth of ice embryos is not well defined.

In order to check whether the semi-empirically derived values for $\Delta g^{\mp}$ are supported by the results from the molecular model of Eadie, we plotted in Figure 7.6

the J-values listed by Eadie. We notice a surprising good agreement between the molecular and the classical model for supercoolings between 33 and 42°C. Unfortunately, this agreement is purely accidental. A careful inspection of Eadie's molecular model shows that his computations of J was based on an estimate of the activation energy $\Delta g^{\ddagger}$ for transfer of molecules across the water ice boundary using values given by Dufour and Defay (1963) which, in turn, were based on Dorsey's (1940) data of the activation energy for viscous flow. These were significantly lower than the values derived from recent data of viscosity and self-diffusion given in Figure 3.11, resulting in an overestimate of J. At the same time, Eadie's molecular model significantly overestimates the interface energy $\sigma_{i/w}$ and therefore ΔF_g, when compared with the $\sigma_{i/w}$ values given in Figure 5.17. This causes an underestimate of J. Since these two errors tend to compensate each other, the apparent agreement between the J-values of the classical and of the molecular model cannot be used to substantiate the $\Delta g^{\ddagger}$ values derived from nucleation experiments via the classical model.

We finally may add that drops at cirrus level may contain dissolved salts which lower the temperature even further before homogeneous ice nucleation sets in. Unfortunately, values for $\Delta g^{\ddagger}$ and $\sigma_{i/s}$ are not known for solution drops.

CHAPTER 8

THE ATMOSPHERIC AEROSOL AND TRACE GASES

From Chapter 6, it is evident that an understanding of the cloud forming processes in the atmosphere requires knowledge of the physical and chemical characteristics of the atmospheric aerosol. In discussing this gaseous suspension of solid and liquid particles, it is customary to include all gases except water vapor, and all solid and liquid particles except hydrometeors, i.e., cloud and raindrops, and ice particles. In addition, it is the atmospheric aerosol with its gaseous and particulate constituents which also determines the chemical characteristics of the clouds and precipitation. This is simply a result of the fact that a considerable fraction of the atmospheric gases and aerosol particles become scavenged by clouds and precipitation, where they may partially dissolve and undergo chemical reactions (see Chapter 17). In the present chapter, we shall present a brief discussion of the physical and chemical characteristics of the gaseous constituents of the atmosphere, followed by a more detailed description of the main characteristics of the atmospheric aerosol particles. For background on the subjects covered, the reader is referred to the texts of Junge (1963a), Butcher and Charlson (1972), Hidy (1972), Rasool (1973), Twomey (1977), Friedlander (1977), Hidy (1984), Finlayson and Pitts (1986), Seinfeld (1986), Warneck (1988) and Jaenicke (1988). Most of the data on which this chapter is based are derived from these sources and from literature citations therein.

8.1 Gaseous Constituents of the Atmosphere

Up to an altitude of about 85 km, the composition of the atmosphere is essentially uniform. In this layer, called the homosphere, the gaseous constituents are present in quasi-constant proportions (see Table 8.1). Above about 85 km, the composition of the atmosphere begins to vary markedly due to gravitational separation of the chemical constituents, and due to solar radiation which dissociates some of the constituents and stimulates the formation of new chemical species. This outer portion of the atmosphere is called the heterosphere. For a discussion of the chemical characteristics of the higher atmosphere, the reader is referred to the texts of Brasseur and Solomon (1984), Shimazaki (1985), and Warneck (1988).

One may classify the gaseous constituents of the atmosphere according to their residence times. For quasi-constant constituents, the residence time is of the order of thousands of years or more; slowly varying constituents have residence times of a few months to a few years; and fast varying constituents have residence times of a few days or less.

The quasi-constant gaseous constituents of the atmosphere are N_2, O_2, Ar, He, Ne, Kr, and Xe. Slowly varying gaseous constituents include CH_4, O_3, N_2O, CO,

TABLE 8.1
Composition of clean, dry air. (Based on U.S. Standard Atmosphere, 1962)

Constituent gas	Content (% by vol.)	Constituent gas	Content (% by vol.)
Nitrogen, N_2	78.084	Helium, He	0.000524
Oxygen, O_2	20.9476	Krypton, Kr	0.000114
Argon, A	0.934	Hydrogen, H_2	0.00004
Neon, Ne	0.001818	Xenon, Xe	0.0000087

CO_2, and H_2. Fast varying gaseous constituents include SO_2, H_2S, NO, NO_2, NH_3, and radicals such as OH, HO_2, NO, NO_3. The only gases which can be considered 'permanent' are the nobel gases, Ne, A, Kr, Xe, since they have negligible sources or sinks in the atmosphere. All other gases, including O_2, N_2, He, and H_2, have sources and sinks and therefore a finite residence time.

Tables 8.2 summarizes the sources and sinks of the slowly and fast varying gases in the atmosphere. In Table 8.3, estimates are listed for some of the emission rates of these gases. These numbers are very rough and can only serve as a general guide. In Tables 8.4 and 8.5, we have selected from the wealth of observations on the trace gas concentrations a few typical values. Again, these data may only serve as a guide. Without considering the Arctic regions, we notice from Tables 8.4 and 8.5 that the trace gas concentrations are generally highest in urban air, less in continental rural air, and least in maritime air.

Observations show that, with the exception of ozone, the trace gas concentration generally decreases roughly exponentially with increasing height in the first 6 km of the atmosphere. This is also evident from some of the mountain stations listed in Table 8.5, and from Figures 8.1 to 8.5. In these figures, the concentration variation with height of a few selected trace gases is given.

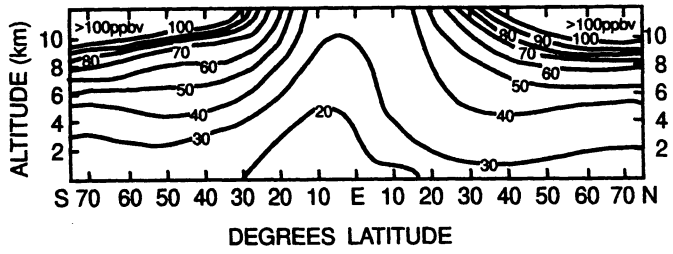


Fig. 8-1: Seasonally averaged meridional distribution of ozone. (From Fishman and Crutzen, 1978a,b, with changes.)

All tropospheric gases have sinks (see Table 8.2), since they undergo various chemical reactions, including chemical decomposition and photodissociation. They also are scavenged by cloud drops and rain drops due to their solubility in water.

TABLE 8.2

Sources and sinks for major atmospheric gases, other than N_2.

Gas	Sources	Sinks
CO	Combustion, biomass burning, biological activity in soil and in oceans, volcanoes, oxidation of CH_4	Oxidation in upper atmosphere, biological uptake by bacteria, uptake by soil-surface
CO_2	Combustion, cement production, volcanoes, burning of carbon compounds by animals and bacteria, respiration, biomass burning	Photosynthesis by biosphere, absorption by oceans
O_3	Dissociation of O_2 by solar radiation and subsequent collision of O with O_2, dissociation NO_2 by solar radiation and subsequent collision of O with O_2	Photochemical dissociation in upper atmosphere, collision of O_3 with O, NO, OH or HO_2
CH_4	Escape from oil wells and mines, bacterial decomposition of organic matter, biomass burning, exhalations from biosphere; solvent use, volcanoes	Photochemical reaction with NO, NO_2, and O_3 in upper atmosphere, dissociation by solar radiation at high altitudes
N_2O	Bacterial decomposition in soil and in oceans, in release from ocean artificial, combustion	Photodissociation in upper atmosphere, decomposition by biological activity in soil
NO_x	Bacterial activity in soil, combustion, volcanoes, lightning, biomass burning	Chemical reactions (with HC., oxidation to nitrates)
NH_3	Bacterial activity in soil, combustion, volcanoes, fertilzer loss, biomass burning	Chemical reactions (with SO_2, oxidation to nitrates)
H_2S	Decomposition of organic matter in soil and in stagnating water, volcanoes.	Chemical reactions (oxidation to sulfate), uptake by soil and oceans
SO_2	Combustion, volcanoes	Chemical reactions (oxidation to sulfate), uptake by soil and oceans
COS	Soil emission, ocean	Loss to stratosphere, hydrolysis in ocean water
DMS	Bacterial decomposition in ocean water	Chemical reactions (oxidation to sulfate)
HCHO	Biomass burning, emission from industry combustion, decomposition of CO	Collision of HCHO with OH radicals
OH	$O_3 \xrightarrow{h\nu} O(^1D) + O_2(^1\Delta g)$ $O(^1D) + N_2 \longrightarrow O(^3P) + N_2$ $O(^1D) + H_2O \longrightarrow 2OH$	$CO + OH \longrightarrow CO_2 + H$ $H + O_2 + M \longrightarrow HO_2 + M$ $HO_2 + NO \longrightarrow NO_2 + OH$
H_2O_2	$HO_2 + HO_2 \longrightarrow H_2O_2 + O_2$ $HO_2 + H_2O \rightleftharpoons HO_2 \cdot H_2O$ $HO_2 + HO_2 \cdot H_2O \longrightarrow H_2O_2 + O_2 + H_2O$	$H_2O_2 \xrightarrow{h\nu} OH + OH$ acting as oxidant
HO_2	$OH + CH_4 \longrightarrow H_2O + CH_3$ $CH_3 + O_2 + M \longrightarrow CH_3O_2 + M$ $CH_3O_2 + NO \longrightarrow CH_3O + NO_2$ $CH_3O + O_2 \longrightarrow HCHO + HO_2$	$HO_2 + HO_2 \longrightarrow H_2O_2 + O_2$ $HO_2 + NO \longrightarrow NO_2 + OH$ $HO_2 + O_3 \longrightarrow 2O_2 + OH$

TABLE 8.3
Anthropogenic- and natural emission rates for slow and fast varying trace gases (1 Tg = 10^{12} g).

Gas	Production rate (Tg/yr)	
CO_2	205×10^2	(1986)
CO	$15 - 28 \times 10^2$	
CH_4	225 - 854	
N_2O	17 - 69	(as N)
NO_x	19 - 99	(as N)
NH_3	22 - 83	
H_2S	75 - 122	(as S)
SO_2	50 - 100	(as S)
COS	12	(as S)
DMS	20 - 60	(as S)

TABLE 8.4
Background concentration of slowly varying trace gases in air of the troposphere.

Gas	Concentration	
CH_4	1.4 - 2.0	ppmv
CO_2	355	ppmv (1993)
CO	10 - 250	ppbv
O_3	20 - 300	ppbv
N_2O	300 - 400	ppbv

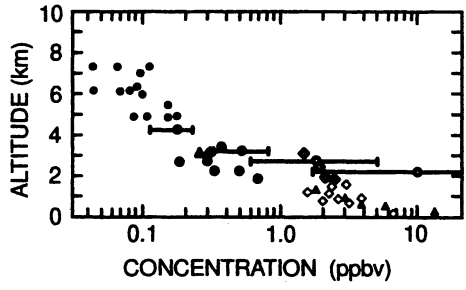


Fig. 8-2: Vertical distribution of NO_x in continental air. Dots: over wheatland (Wyoming), open circles: over Denver (Colorado), both based on Kley *et al.* (1981); open triangles and solid triangles: flights over Germany based on Georgii and Jost (1964). (From Warneck, 1988, with changes.)

TABLE 8.5

Surface concentration of fast varying trace gases in air.

(a) HNO_3, nitric acid

Continental air	ppbv	
Clermont, California, urban	4.4	Forrest *et al.* (1982)
Res. Triangle Park, N. Carol. rural	0.54	Shaw *et al.* (1982)
Abbeville, Luisiana, rural	0.72	Cadle *et al.* (1982)
Warren, Michigan, suburban	0.96	Cadle (1985)
Jülich, Germany, suburban, winter	1.02	Meixner *et al.* (1985)
Colorado, 3050 m.a.s.l	0.02 - 0.7	Parish *et al.* (1986)
Maritime air	**ppbv**	
Pacific	0.038 - 1.02	Huebert (1980)
Pacific	0.11	Huebert & Lazrus (1980a,b)
W. Pacific	0.14 - 0.90	Okita *et al.* (1986)
Bermuda	0.044 - 0.126	Wolff *et al.* (1986)
Marina Loa, Hawaii	0.018 - 0.09	Galasyn *et al.* (1987)

(b) NH_3, ammonia

Continental air	ppbv	
West Germany, winter	7.9 ± 5.3	Georgii & Müller (1974)
summer	22.4 ± 13.1	Georgii & Müller (1974)
Swiss Alps summer	0.26	Georgii & Lenhard (1978)
Netherlands	4.9 ± 2.5	Bos (1980)
Sweden	0.28	Ferm (1979)
Warren, Michigan, winter	1.05	Cadle *et al.* (1982)
Commerce City (Colorado), winter	4.5	Cadle *et al.* (1982)
Maritime air	**ppbv**	
Central Atlantic	0.26	Georgii & Gravenhorst (1972)
Saragasso Sea	7.9	"
N. Pacific	1.52	Tsunogai (1971)
Tropical Pacific	0.74	"
S. Pacific	0.17	"
Antarctica	0.02	Gras (1983)

(c) NO_x (NO, nitric oxide; NO_2, nitrogen dioxide)

Continental air	ppbv	
London	13 - 26	Williams *et al.* (1988)
Loop Head, Ireland	23 - 82	"
Claremont, California	48 - 62	Atkinson *et al.* (1986)
Deuselbach, Germany, rural	11.5 - 16.3	Broll *et al.* (1984)
England, rural	10 ± 82	Harrison & McCartney
White Water, rural	1.3 - 75	Atkinson *et al.* (1986)
Death Valley	< 0.3	"
Wank Peak (1780 m), Germany	2.5 - 7	Reiter *et al.* (1987)
Niwotridge (2910), Colorado	0.24 - 0.30	Bollinger *et al.* (1984)

TABLE 8.5 (continued.)

Maritime air	pptv	
Mid Pacific	30	Atkinson *et al.* (1986)
Atlantic	20 - 70	Broll *et al.* (1984)
Tropical Pacific	2.8 - 5.7	Liu *et al.* (1983)
Mauna Loa, Hawaii (2500 m)	30	Noxon (1981)

(d) SO_2, sulfur dioxide

Continental air	ppbv	
New York City	60.5 - 324	Greenburg & Jacobs (1956)
Frankfurt a.M	8.8 - 95.7	Georgii (1960)
England, rural	4.3	Meetham (1959)
Sweden, rural	1.3 - 9.1	Egner & Erikson (1955)
Colorado, rural	0.13 - 0.5	Georgii (1970)
Zugspitze (3000 m), Germany	8.6	" (1960)
US at 5-6 km	0.16	Maroulis and Bandy (1980)
Maritime air	**pptv**	
Atlantic	27 ± 8	Herrman & Jaeschke (1984)
N. Atlantic	87 ± 47	Nguyen *et al.* (1983)
Central Atlantic	51.5 ± 68.4	"
S. Indian Ocean	33.2 ± 38.8	"
Pacific	54 ± 19	Maroulis *et al.* (1980)

(e) H_2S, hydrogen sulfide

Continental air	pptv	
Bowling Green, Miss.; urban	290 - 340	Breeding *et al.* (1973)
Frankfurt a. M.	2 - 349	Bürgermeister (1984)
Toulouse	0 - 122	Delmas *et al.* (1980)
Loire Valley, France, rural	27.5 - 121	"
Pine forest, rural	38.5 - 51.2	"
Pic du Midi (2980 m), France	1.3 - 12.6	"
Ivory Coast, tropical forest	45.9 - 4253	"
Maritime air	**pptv**	
Wallops Islands	40 - 110	Maroulis & Bandy (1974)
Atlantic	0.7 - 31	Barnard *et al.* (1982)
Pacific	42 - 70	Andreae & Raemdonk (1983)

(f) CH_3SCH_3, dimethylsulfide (DMS)

Maritime air	pptv	
Equatorial Pacific	48 - 289	Andreae *et al.* (1988)
Cape Grim	25 - 354	"
Bahamas	4 - 494	"
N. Atlantic	2 - 302	"
Saragasso Sea	1 - 767	"

TABLE 8.5 (continued.)

Gulf of Mexico and Carribean	0 - 800	Salzman & Cooper (1988)
Flight over Puerto Rico	408 - 562	Carrol (1985)
S. Pacific Ocean	45 - 672	Bates *et al.* (1992)
(g) CS_2, Carbondisulfide		
	pptv	
Harewell, England	80 - 300	Sandalls & Penkett (1977)
Philadelphia, clean	27 - 47	Maroulis & Bandy (1980)
" polluted	76 - 304	"
Flight over Puerto Rico	11 - 166	Carrol (1985)
Free troposphere	≤ 3	Bandy *et al.* (1981)
(h) COS, Carbonylsulfide		
	pptv	
Troposphere	500	Khalil & Rasmussen (1984)
Pacific	500 - 525	Torres *et al.* (1980)
(i) HCHO, formaldehyde		
Continental air	ppbv	
Los Angeles	2 - 40	Grosjean *et al.* (1983)
New York City	2 - 40	Cleveland *et al.* (1977)
Osaka	1.6 - 8.5	Kuwala *et al.* (1983)
Deuselbach, Germany, rural	2.3 - 3.9	Schubert *et al.* (1984)
Warren, Mich., rural	1.3 - 6.3	Lipari *et al.* (1984)
Maritime air	ppbv	
Pacific	0.2 - 0.8	Fushimi & Miyake (1980)
Indian Ocean	0.8 - 11	"
Cape Point, S. Africa	0.2 - 1.0	Neitzert & Seiler (1981)
Pacific	0.4 - 0.6	Lowe & Schmidt (1983)
Atlantic	0.12 - 0.33	"
Mauna Loa Obs. (Hawaii)		
upslope	0.10	Heikes (1992)
downslope	0.19	
maximum	0.45	
(k) HCOOH, formic acid		
Continental air	ppbv	
Central Africal	0.5 - 3.7	Helas (1989)
urban	3	Dawson & Farmer (1988)
Austria, rural	0.9	Puxbaum *et al.* (1988)
semi-rural	1.4	"
Amazonas, rain forest	0.2 - 1.6	Helas (1989)

TABLE 8.5 (continued.)

Maritime air	ppbv	
N. Pacific	0.8	Arlander *et al.* (1990)
S. Pacific	0.22	"
N. Indian Ocean	0.75	"
S. Indian Ocean	0.19	"
(l) CH_3COOH, acetic acid		
Continental air	ppbv	
Central Africa	0.6 - 2.7	Helas (1989)
urban	4	Dawson & Farmer (1988)
Brazil, rain forest	0.2 - 2.2	Helas (1989)
Maritime air	ppbv	
N. Pacific	0.8	Arlander *et al.* (1990)
S. Pacific	0.28	"
N. Indian Ocean	0.69	"
S. Indian Ocean	0.29	"
(m) H_2O_2, hydrogen peroxide		
Continental air	ppbv	
numerous locations	0.05 - 4	Gunz & Hoffmann (1990) max. in summer
Arkansas summer	1 - 6	Ray *et al.* (1992)
winter	0 - 0.5	"
N. Carolina (at 2000 m)	0.63 ± 0.57	Claiburn & Aneja (1991)
Maritime air	ppbv	
Equatorial Atlantic	3.5	Jacob & Klockow (1992)
Mauna Loa Obs. (Hawaii)		
upslope	1.05	Heikes (1992)
downslope	0.9	
maximum	3.2	
N. Pacific average	0.4 - 0.5	Lind *et al.* (1987)
maximum	0.9	
N. Pacific off the coast of St. of Washington	0.3 - 1.0	Lee & Busness (1989)

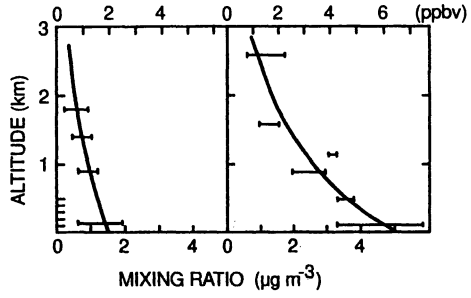


Fig. 8-3: Vertical distribution of gaseous ammonia and ammonium containing particles over Europe, based on data of Lenhard (1977) and Georgii and Lenhard (1978). (From Georgii and Lenhard, 1978, with changes.)

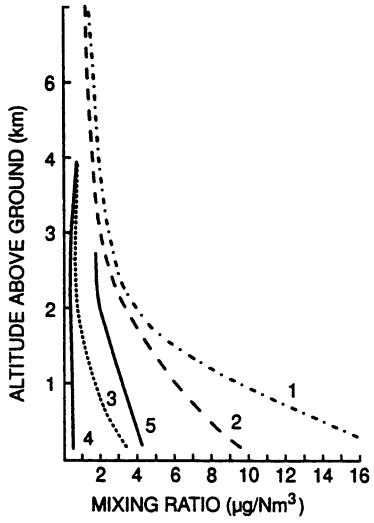


Fig. 8-4: Vertical distribution of SO_2 over various locations. (1) W. Germany in winter, (2) W. Germany in summer, (3) French coast, (4) Atlantic, (5) Sweden. Based on data of Jost (1974), Gravenhorst (1975) and Rodhe (1972). (From Georgii, 1982, with changes.)

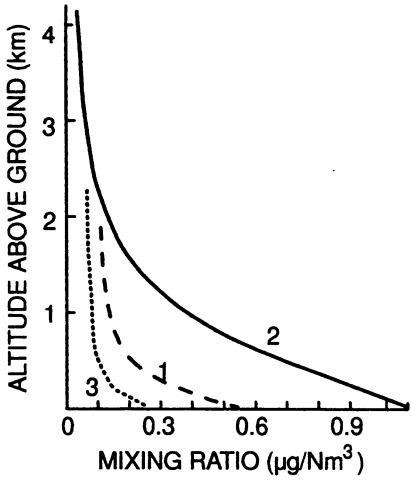


Fig. 8-5: Vertical distribution of H_2S over various locations. (1) Over Mainz-Nierstein, Germany, (2) over Aschaffenburg, Germany, (3) over the North Sea and Sylt. Based on data of Lenhard (1977).

TABLE 8.6

Residence time in the lower troposphere of various atmospheric trace gases.

Gas	residence time	
CO_2	4 - 10 yr	exchange with ocean mixed layer
	$\sim$ 20 yr	exchange with ocean deep sea
	15 - 75 yr	exchange with biosphere
COS	2 - 40 yr	
N_2O	10 - 100 yr	
CH_4	4 - 9 yr	
CO	2 - 6 months	
O_3	4 - 5 months	
SO_2, H_2S	few days	
CH_3SCH_3, CS_2	few days	
HNO_3, NO_x	few days	
NH_3	few days	

The various precipitation mechanisms subsequently lead to the permanent deposition (wet-deposition) of the scavenged gases. Trace gases also undergo chemical reactions and adsorption mechanisms on the Earth's surface. The mechanisms involved in this dry deposition of gases have been discussed by Warneck (1988), Seinfeld (1986), Finlayson and Pitts (1986), Hicks (1984), Pruppacher *et al.* (1983), and Georgii and Pankrath (1982). The mechanisms involved in wet deposition will be discussed in Chapter 17. The presence of sinks imply that the atmospheric gases have a definite residence time in the atmosphere. The residence times of some of these gases (other than those considered semi-permanent in Table 8.1) are listed in Table 8.6.

8.2 Atmospheric Aerosol Particles (AP)

Aerosol particles (AP) in the atmosphere have sizes which range from clusters of a few molecules to 100 μm and larger. Junge (1955, 1963a) suggested dividing the AP into 3 size categories. Particles with dry radii $r < 0.1\,\mu$m he called *Aitken particles* to pay tribute to Aitken who studied the behavior of these particles in great detail (see Chapter 1). Particles with dry radii $0.1 \leq r \leq 1.0\,\mu$m Junge called *large particles*, and particles with dry radii $r > 1.0\,\mu$m he called *giant particles*. More recently, it has become customary to follow Whitby (1978) and regard the AP with diameters $r < 0.1\,\mu$m as belonging to the *nuclei mode*, particles with $0.1 \leq r \leq 1\,\mu$m as belonging to the *accumulation mode*, and particles with $r > 1\,\mu$m as belonging to the *coarse mode*. In this classification, Whitby considers particles with $r \leq 1\,\mu$m as fine particles.

Particles are injected into the atmosphere from natural and anthropogenic or man-made sources. Most come from the Earth's surface, but some arise from the Earth's interior through volcanic action, while others enter the atmosphere from outer space. The concentration of AP varies greatly with time and location, and depends strongly on the proximity of sources, on the rate of emission, on the strength of convective and turbulent diffusive transfer rates, on the effficiency of the various removal mechanisms (see Chapter 17) and on the meteorological parameters which

affect the vertical and horizontal distributions as well as the removal mechanisms. Observations confirm that the concentration of AP decreases with increasing distance from the Earth's surface. This is expected from the atmospheric density profile, and also because the surface constitutes the major source of AP, while removal mechanisms operate continuously throughout the atmosphere. In fact, it is estimated that 80% of the total aerosol particle mass is contained below the lowest kilometer of the troposphere. The AP concentration also decreases with increasing horizontal distance from the seashore towards the open ocean, because the land is a more effficient source of particles than the ocean. Thus, it is estimated that 61% of the total AP mass is introduced in the Northern Hemisphere, as compared to the Southern Hemisphere which is covered with a smaller land mass. Within the Northern Hemisphere, most of the aerosol particle mass enters the atmosphere at latitudes between 30 and 60° N, since this latitude belt contains about 88% of all anthropogenic sources for particulates.

The removal rate of aerosol particles by self-coagulation is proportional to the square of the particle concentration, while the removal by interaction with cloud drops and raindrops is proportional to the first power of the particle concentration (see Chapter 11). Consequently, the removal rate of AP may become very small if their concentration is sufficiently small. Indeed, Junge (1957b, 1963a) and Junge and Abel (1965) have demonstrated the existence of a rather stable background AP population of a few hundred particles cm^{-3}. This fairly uniform atmospheric background aerosol exists over land at heights above about 5 km, and over the oceans far from shore above about 3 km (Junge,1969a).

Aerosol particles of terrestrial origin are formed by three major mechanisms: (1) gas-to-particle conversion (GPC), (2) drop-to-particle conversion (DPC) involving the evaporation of cloud and raindrops which contain dissolved and suspended matter, and (3) bulk-to-particle conversion (BPC) involving mechanical and chemical disintegration of the solid and liquid Earth surface.

8.2.1 Formation of Aerosol Particles by Gas to Particle Conversion (GPC)

Several pathways are possible to form AP by GPC. We shall briefly discuss three of these pathways. The first pathway involves the homogeneous nucleation of new particles in supersaturated vapors. Such nucleation may take place in plant exhalations, combustion products and in volcanic plumes, which include vapors that have low boiling point temperatures. These vapors readily condense to drops or directly to solid particles relatively close to their source. Some substances typically involved in this mechanism are soot, tars, resins, oils, sulfuric acid, sulfates, carbonates, and others. Most of these substances are the result of industrial operations and man-made or natural fires. AP formed in this manner cover a wide range of sizes, but the majority lay within the Aitken particle size range. Detailed discussions of this mode of AP formation are given by Dunham (1966), Sutugin and Fuchs (1968, 1970), and Sutugin *et al.* (1971).

The second pathway involves homogeneous nucleation of particles by gas phase chemical reaction. Many of these reactions are catalyzed by the ultraviolet portion

of the Sun's radiation. These effects have been discussed by Briccard *et al.* (1968, 1971), Mohnen and Lodge (1969), Vohra *et al.* (1969), Cox and Penkett (1970), Vohra and Nair (1970), Vohra *et al.* (1970), and Mohnen (1970, 1971). Thus, Gerhard and Johnstone (1955) proposed that sulfur trioxide (SO_3) may be the result of the following chain of reactions proceeding at the Earth's surface in bright sunlight:

$$SO_2 \xrightarrow{h\nu} SO_2^*\,, \tag{8-1}$$

$$SO_2^* + M \longrightarrow SO_2 + M\,; \quad SO_2^* + O_2 \longrightarrow SO_4\,, \tag{8-2}$$

$$SO_4 + SO_2 \longrightarrow 2SO_3\,, \tag{8-3}$$

where SO_2^* is an activated state of SO_2, and M is a chemically neutral gas molecule (e.g., N_2) that must be present for the reaction to proceed. In very polluted city air, Cadle and Powers (1966) suggested

$$SO_2 + O + M \longrightarrow SO_3 + M \tag{8-4a}$$

in competition with

$$O_2 + O + M \longrightarrow O_3\,, \tag{8-4b}$$

while Junge (1963a,b) proposed

$$SO_2 + O + M \longrightarrow SO_3 + O_2\,. \tag{8-5}$$

Warneck (1988) considered a two step reaction involving the radical OH

$$SO_2 + OH \longrightarrow HOSO_2\,, \tag{8-6a}$$

$$HOSO_2 + O_2 \longrightarrow SO_3 + NO_2\,, \tag{8-6b}$$

with a hydroxyl sulfur dioxide adduct ($HOSO_2$) as intermediate product. Once formed, SO_3 quickly hydrates to sulfuric acid according to

$$SO_3 + H_2O \longrightarrow H_2SO_4\,. \tag{8-7}$$

Sulfuric acid droplets then form by binary nucleation in the sulfuric acid-water vapor mixture. Nitric acid vapor may form according to

$$NO_2 + OH + M \longrightarrow HNO_3 + M\,. \tag{8-8}$$

Nitric acid droplets then form by binary nucleation in nitric acid-water vapor mixtures. At night time, nitric acid drops may form in a three step reaction

$$NO_2 + O_3 \longrightarrow NO_3 + O_2\,, \tag{8-9a}$$

$$NO_2 + NO_3 \rightleftharpoons N_2O_5\,. \tag{8-9b}$$

Due to its high solubility in water, nitrogen pentoxide N_2O_5 then quickly dissolves in water droplets to produce nitric acid droplets according to

$$N_2O_5 + (H_2O)_{liq} \longrightarrow HNO_3 . \tag{8-9c}$$

Other vapor reactions not involving water vapor which produce AP are

$$HNO_3 + NH_3 \rightleftharpoons NH_4NO_3 , \tag{8-10}$$

$$HCl + NH_3 \rightleftharpoons NH_4Cl . \tag{8-11}$$

On the surface of preexisting particles gas to particle conversion may cause the formation of new compounds. Thus, on the surface of sodium chloride particles, sodium nitrate may form according to

$$NaCl + HNO_3 \rightleftharpoons NaNO_3 + HCl . \tag{8-12}$$

The binary nucleation of sulfuric acid droplets in a mixture of H_2SO_4 vapor and water vaper has been theoretically studied by Kreidenweiss and Seinfeld (1988), Warren and Seinfeld (1985), Yue (1979), Yue and Hamill (1979), Stauffer (1976) and Mirabel and Katz (1974). The results predicted for the nucleation of sulfuric acid drops have been experimentally verified by Mirabel and Chavelin (1978). As another application of homogeneous nucleation theory discussed in Chapter 7, we will briefly outline the procedure needed to derive the rate of binary nucleation of sulfuric acid droplets in a H_2SO_4 - H_2O vapor mixture. For this purpose, we will follow Yue and Hamill (1979), and index the water vapor by 'A' and the acid vapor by 'B'. For $c_B \ll c_A$, where c is the concentration of a species in the mixture, and considering (7-46), the nucleation rate of acid droplets (as the number of drops cm^{-3} sec^{-1}) is given by

$$J = \Omega_g w_B^{\downarrow} c_A Z \exp(-\Delta F_g / kT) , \tag{8-13}$$

where Z is the Zeldovich Factor (see (7-39)), and $\Omega_g = 4\pi a_g^2$ if the sulfuric acid germ is assumed to be spherical. From (5-51) with $c = e/kT$, one finds for the molecular flux

$$w_B^{\downarrow} = \alpha c_B (kT/2\pi m_B)^{1/2} , \tag{8-14}$$

where α is the accommodation coefficient, m_B is the mass of one H_2SO_4 molecule, and ΔF_g is the free energy change associated with the formation of a sulfuric acid embryo in the binary vapor mixture. According to (7-28)

$$\Delta F_g = \sigma \Omega_g / 3 = 4\pi a_g^2 / 3 , \tag{8-15}$$

where σ is the surface tension of the binary nucleated droplet. The radius a_g of the germ may be computed analogously to the procedure outlined in Section 7.1.1.3. However, instead of (7-18), we have now

$$\Delta F(n_A, n_B) = n_A(\mu_A^l - \mu_A^g) + n_B(\mu_B^l - \mu_B^g) + 4\pi a^2 \sigma , \tag{8-16}$$

where μ is the chemical potential of the species and n the number of moles. Considering (6-24), ΔF can be expressd in a form analogous to (7-23):

$$\Delta F(n_A, n_B) = -n_A RT \ln \frac{S_A}{a_A} - n_B RT \ln \frac{S_B}{a_B} + 4\pi a^2 \sigma , \tag{8-17}$$

where a is the activity of the species, $S_A = e/e_{sat,w}$ is the saturation ratio for the water vapor, $S_B = p_B/p_B^0$ is the relative acidity, and $e_{sat,w}$ and p_B^0 are the equilibrium vapor pressures of water vapor and acid over a flat surface of the pure substance. Here a is obtained from $(4\pi/3)a^3\rho = n_A M_A + n_B M_B$, with ρ being the density of the liquid mixture, and M the molecular weight of the species. Analogous to Figure 7.2, ΔF vs n_A and n_B exhibit maxima at critical values of n_A and n_B at which $(\Delta F)_{max} = \Delta F_g$. These maxima are obtained from the conditions

$$\left(\frac{\partial \Delta F}{\partial n_A}\right)_{n_B} = 0 ; \quad \left(\frac{\partial \Delta F}{\partial n_B}\right)_{n_A} = 0 . \tag{8-18}$$

These two equations when solved simultaneously describe a saddle point in a three-dimensional system in which the ΔF-surface is plotted as a function of n_A and n_B. This saddle point represents the nucleation barrier ΔF_g which the embryos have to overcome in order to become stable and grow. The critical compositions which pertain to this condition are $n_{A,g}$ and $n_{B,g}$. On applying (8-18) simultaneously to (8-17), we find in place of (7-27) for water vapor alone the following generalized Kelvin equations:

$$a_g = \frac{2\sigma M_A}{\mathscr{R} T \rho \ln(S_A/a_A)} \left(1 + \frac{X_g'}{\rho}\frac{d\rho}{dX_g'} - \frac{3}{2}\frac{X_g'}{\sigma}\frac{d\sigma}{dX_g'}\right) \tag{8-19}$$

and

$$a_g = \frac{2\sigma M_B}{\mathscr{R} T \rho \ln(S_B/a_B)} \left(1 + \frac{X_g'}{\rho}\frac{d\rho}{dX_g'} - \frac{3}{2}\frac{(1-X_g')}{\sigma}\frac{d\sigma}{dX_g'}\right) , \tag{8-20}$$

where

$$X_g' = n_{B,g} M_B / (n_{A,g} M_A + n_{B,g} M_B) . \tag{8-21}$$

For given environmental conditions S_A, S_B, and T, the critical composition X_g', i.e., $n_{A,g}$, $n_{B,g}$, and radius a_g at the saddle point can be calculated from a simultaneous solution of (8-19) to (8-21). From this, ΔF_g can be obtained from (8-15). Knowing ΔF_g, the nucleation rate J can be computed from (8-13). An expression for the Zeldovich factor Z has been worked out by Kreidenweiss and Seinfeld (1988). The results of such a computation are given in Figure 8.6 for the nucleation of sulfuric acid drops in mixtures of H_2SO_4 and water vapor, and mixtures of MSA (methansulfonic acid, CH_2SO_3H) and water vapor. We notice that the nucleation rates are highly dependent on the environmental conditions. As a rule, higher concentrations of H_2SO_4 vapor and H_2O vapor and lower temperatures will lead to higher nucleation rates. Among these three parameters, the nucleation rate is most sensitive to the concentration of water vapor. It also is seen that nucleation of H_2SO_4 and MSA in the absence of water vapor, i.e., for zero relative humidity,

proceeds at very similar relative acidities. This is due to similar physical properties for the pure gases, most importantly for the surface tension. As the relative humidity increases, the differences in the nucleation rates of H_2SO_4 and MSA become increasingly noticeable. The reason for these differences are attributed by Kreidenweiss and Seinfeld to differences in the free energies of mixing as compared to a hypothetical ideal solution, and also to differences of the vapor pressures.

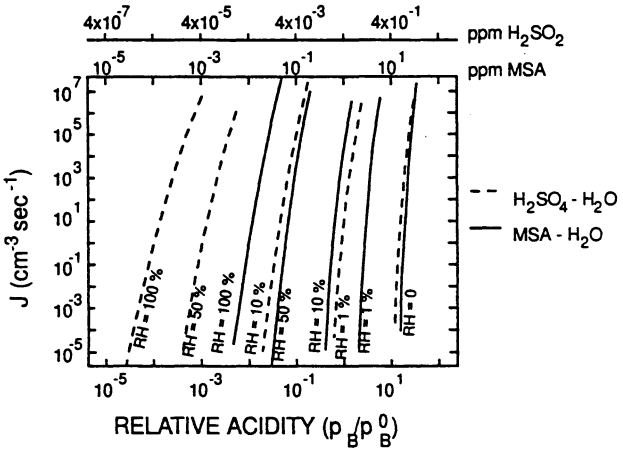


Fig. 8-6: Nucleation rates of aqueous acid droplets at 25°C and various relative humidities as a function of relative acidity. (From Kreidenweiss and Seinfeld, 1988, with changes.)

Hegg *et al.* (1990, 1992), applied the theory outlined above to the homogeneous nucleation of sulfate particles in the immediate surroundings of maritime clouds where he had observed large numbers of condensation nuclei. He assumed that H_2SO_4 forms from SO_2 via (8-6) to (8-8) and this, in turn, forms DMS (dimethylsulfide, CH_3SCH_3). Considering the observed DMS concentration of 85 pptv, an OH concentration of 5×10^6 molecules cm^{-3}, and the observed humidity at and above the cloud level, Hegg *et al.* computed the dashed line in Figure 8.7. We notice that the theoretical results predict well the observed enhanced concentration of aerosol particles (CN) just above the cloud top. Similar observations and computations on GPC in marine air have been carried out by Covert *et al.* (1992), Easter and Peters (1994) and Weber *et al.* (1995). Very recently, Bigg (1996) suggested that a binary nucleation of particles in sulfuric acid-water vapor mixtures may be aided by very sudden mixing events caused by breaking Kelvin-Helmholtz waves which occur preferentially in those regions where the nucleation process is most effective: in layers of strong thermal and moisture stratification, wind shear, and the presence of a gravity wave of longer period than the Kelvin-Helmholtz instabilities.

The third pathway for a gas to particle conversion involves pre-existing aerosol particles. According to Seinfeld and Bassett (1982) and Warren and Seinfeld (1985a,b), the rate-controlling step in this conversion is one or a combination of three mechanisms: the rate of diffusion of the vapor molecules to the surface of

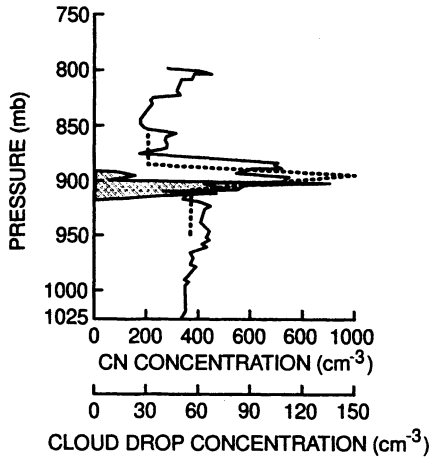


Fig. 8-7: Comparison of observed CN concentration off the Pacific NW Coast (solid line) with concentration of particles resulting from binary nucleation of sulfuric acid droplets from H_2O - H_2SO_4 vapor system (dashed line); shaded region represents the cloud layer. (From Hegg *et al.*, 1990; by courtesy of the authors, copyright Amer. Geophys. Union.)

the particles (diffusion controlled growth), the rate of surface reaction involving the adsorbed vapor molecules and the particle surface (surface reaction controlled growth), and the rates of reaction involving the dissolved species, which are assumed to be present uniformly throughout the volume of the particle (volume reaction controlled growth).

In diffusion controlled growth, the mass rate of change of a particle results from the diffusion of vapor molecules of a species A to the particle. Following Warren and Seinfeld (1985) and Seinfeld and Bassett (1982) this rate can be expressed (see Chapter 13) as

$$\frac{\mathrm{d}m}{\mathrm{d}t} = 4\pi r D_{\mathrm{A}}(c_{\mathrm{A}} - c_{\mathrm{A,S}}) f(N_{\mathrm{Kn}}), \tag{8-22}$$

$$= \left(\frac{48\pi^2 m}{\rho}\right)^{1/3} \frac{D_{\mathrm{A}} M_{\mathrm{A}}}{\mathscr{R}T}(p_{\mathrm{A}} - p_{\mathrm{A,S}}) f(N_{\mathrm{Kn}}), \tag{8-23}$$

where r is the radius of the particle, ρ is the density, m the mass, $c_{\mathrm{A}} = p_{\mathrm{A}} M_{\mathrm{a}}/\mathscr{R}T$ the concentration of species A, M_{A} the molecular weight, p_{A} the partial pressure of A in air, $p_{\mathrm{A,S}}$ the equilibrium vapor pressure of A just above the particle surface, D_{A} the diffusivity in air, $N_{\mathrm{Kn}} = \lambda_{\mathrm{a}}/r$ the Knudsen number, λ_{a} the free path length of air molecules, $p_{\mathrm{A},\infty}$ is the vapor pressure of species A over a flat surface, v_{A} is the molar volume of condensed A,

$$f(N_{\mathrm{Kn}}) = \frac{(1 + N_{\mathrm{Kn}})}{1 + 1.71N_{\mathrm{Kn}} + 1.33N_{\mathrm{Kn}}^2}, \tag{8-24}$$

and $p_{A,S}$, given by the Kelvin law (6-16), is

$$p_{A,S} = p_{A,\infty} \exp\left(\frac{2\sigma v_A}{r\mathscr{R}T}\right) = p_{A,\infty}\left[\left(\frac{32\pi}{3}\right)^{1/3} \frac{\sigma\rho^{1/3}v_A}{\mathscr{R}Tm^{1/3}}\right]. \tag{8-25}$$

Seinfeld and Bassett (1982) define the dimensionless time τ and particle mass μ by $\tau = (\mathrm{d}m/\mathrm{d}t)_r t/\rho\lambda_a^3$ and $\mu = m/\rho\lambda_a^3$. They further set $S = p_A/p_{A,\infty}$ and define a reference growth rate as $(\mathrm{d}m/\mathrm{d}t)_r = (48\pi^2)^{1/3}(\lambda_a D_A M_A p_{A,\infty}/\mathscr{R}T)$. With these, they obtain the dimensionless growth rate

$$\frac{\mathrm{d}\mu}{\mathrm{d}\tau} = \mu^{1/3}[S(\tau) - \exp(K\mu^{-1/3})]f(N_{Kn}), \tag{8-26}$$

where $K = (32\pi/3)^{1/3}(\sigma v_A/\lambda_a\mathscr{R}T)$, and $N_{Kn} = 3\mu/4\pi)^{-1/3}$. For perfect absorption, $p_{A,S}$ as well as the second term in the square brackets of (8-26) are zero.

In surface reaction controlled growth, we are concerned with the rate at which adsorbed species A become converted to another species B. Assuming that the concentration of adsorbed A on the surface is c_S and, further, that the rate of conversion to B is proportional to c_S with the rate constant k_S, the rate of mass growth of the particle is, according to Seinfeld and Bassett (1982),

$$\frac{\mathrm{d}m}{\mathrm{d}t} = 4\pi r^2 M_B k_S c_S . \tag{8-27}$$

The surface concentration c_S may be found for a steady state by equating (8-27) to (8-23), subject to (8-24) and (8-25) and with $p_{A,O} = H_S c_S$, where H_S is an equlibrium constant (see Chapter 17). When the rate determining step is the surface reaction, c_S may then be approximated by

$$c_S \approx \frac{p_A}{H_S} \exp\left[-\left(\frac{32\pi}{3}\right)^{1/3} \frac{\sigma\rho^{1/3}v_A}{\mathscr{R}Tm^{1/3}}\right]. \tag{8-28}$$

Substituting (8-28) into (8-27) and making the equation dimensionless as before, except now with $(\mathrm{d}m/\mathrm{d}t)_r = (36\pi)^{1/3} M_B k_S p_{A,O} H_S$, we obtain the dimensionless growth law

$$\frac{\mathrm{d}\mu}{\mathrm{d}t} = S\mu^{2/3}\exp(-K\mu^{-1/3}) . \tag{8-29}$$

For volume reaction controlled growth, the key rate is that for which dissolved species A is converted to another species B. If the concentration of dissolved A is c_v, and its rate of conversion to B is proportional to c_v with the rate constant k_v, the rate at which the particle gains mass due to the volume reaction is (Seinfeld and Bassett (1982))

$$\frac{\mathrm{d}m}{\mathrm{d}t} = \frac{4\pi}{3} r^3 M_B k_v c_v . \tag{8-30}$$

As before, Seinfeld and Bassett obtain c_v for steady state conditions by equating (8-30) to (8-23), subject to (8-24) and (8-25) and with $p_{A,O} = H_v c_v$ where H_v

is again an equilibrium constant. Assuming that the rate-determining step is the volume reaction, they therefore obtain the following for c_v:

$$c_v \approx \frac{p_A}{H_v} \exp\left[-\left(\frac{32\pi}{3}\right)^{1/3} \frac{\sigma \rho^{1/3} v_A}{\mathscr{R} T m^{1/3}}\right]. \tag{8-31}$$

Substituting (8-31) into (8-30) and making the equation dimensionless as before, but now with $(\mathrm{d}m/\mathrm{d}t)_r = \lambda_a^3 M_B k_v p_{A,O}/H_v$, they finally obtain the dimensionless growth law

$$\frac{\mathrm{d}\mu}{\mathrm{d}\tau} = S\mu \exp(-K\mu^{-1/3}). \tag{8-32}$$

For the purpose of comparing the above three growth mechanisms, Seinfeld and Bassett used measurements of power plant plume by Elgroth and Hobbs (1979) as the initial distribution $N_0(\mu)$. With this distribution, Seinfeld and Bassett evaluated the three growth laws by computing the dimensionless mass distribution $M(\log_{10} D_p, \tau)$, where $(\rho\lambda_a^3)^2 n_r M(\log_{10} D_p, \tau)\mathrm{d}\log_{10} D_p$ is the mass of particles having logarithm of diameter in the range $\log_{10} D_p$ and $\log_{10} D_p + \mathrm{d}\log_{10} D_p$, where $\log_{10} D_p$ is understood as $\log_{10}(D_p/1\,\mu\mathrm{m})$, and D_p is the particle diameter. M is related to N by $M(\log_{10} D_p, \tau) = 6.9\mu^2 N(\mu, \tau)$. For the initial distribution n_r was set to $1.645 \times 10^{14}\,\mu\mathrm{g}^{-1}\mathrm{cm}^{-3}$, a choice such that the maximum value of $M(\log_{10} D_p, \tau = 0)$ is 1.0. S was taken to be 2.878, corresponding to a critical diameter of $0.01\,\mu$m for a sulfuric acid-water aerosol particle at 25°C, and K was set to 0.1282. The results of these computations are plotted in Figure 8.8 for the time t at which the total mass added to the particulate phase was equal to seven times the initial aerosol mass. We notice from this figure that the mass added by diffusion controlled growth and surface growth is distributed over a very narrow size range, with a peak just below a particle diameter of $0.1\,\mu$m. In contrast, the mass added by volume reaction controlled growth is distributed over a broad diameter range with a main peak above 0.1μm diameter, indicating that by this mechanism particles are produced which are much larger than those produced by the two other mechanisms.

8.2.2 Formation of Aerosol Particles by Drop Particle Conversion (DPC)

Clouds and precipitation act as a sink for aerosol particles and atmospheric trace gases. Aerosol particles become incorporated into cloud drops and cloud ice crystals by acting as nucleation centers (see Chapter 9). Additionally, cloud drops, raindrops and ice particles pick up aerosol particles by various collision mechanisms (see Chapter 17). Since most gases are – at least to a certain degree – soluble in water, they will enter cloud and raindrops by diffusion. Inside the cloud and rainwater, the soluble aerosol particles and some of the gases will dissociate into ions. If a cloud drop or raindrop evaporates, all dissolved material will eventually crystallize to form a solid mass, of which the water insoluble particles which had entered the drops will be a part. In this manner, an aerosol particle results which has chemical and physical characteristics quite different from those possessed before entering the drop. Thus, Hegg *et al.* (1980) noticed, on passing from the

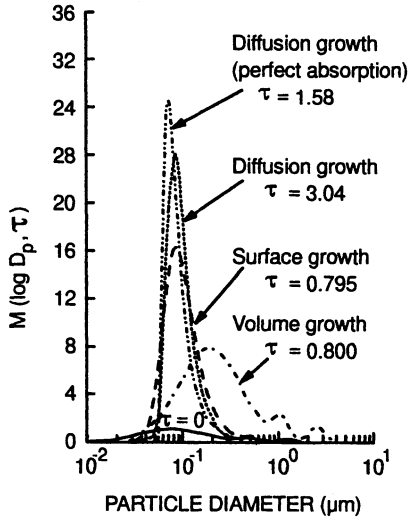


Fig. 8-8: Dimensionless mass distributions for three particle growth mechanisms for the case that the ratio of mass added by gas to particle conversion to initial mass is 7. (From Seinfeld and Bassett, 1982; by courtesy of the authors, copyright Amer. Geophys. Union.)

upstream to the downstream side of an altocumulus lenticularis, that the particle size spectrum had shifted towards larger sizes (Figure 8.9). They attributed this shift to DPC. A similar result was obtained by Flossmann (1993), who numerically simulated the growth and subsequent evaporation of a convective cloud which was allowed to scavenge both aerosol particles and gases. Heintzenberg *et al.* (1989) came to the same conclusion by comparing the size distribution (Figure 8.10b) of evaporated cloud drops of radii larger than 4 μm, sampled near the base of a stratocumulus cloud, with the size distribution of aerosol particles (Figure 8.10a) in nearby clear air. The pronounced shift of the size spectrum to larger sizes due to the 'processing' of the clear air particles and trace gases (not measured) by the cloud is clearly noticeable from Figure 8.10. In addition, Hoppel (1994) suggested that DPC be the cause for the double maximum found in maritime aerosol particle spectra. We thus conclude that clouds act as a source for atmospheric aerosol particles as well as a sink.

In Chapter 6 (see Figures 6.9 to 6.12), we have already shown that cloud drops which have formed on water soluble nuclei exhibit a hysteresis effect, in that they do not transform into the dry state at the same relative humidity at which their nuclei went into solution. For example, deliquescence of ammonium sulfate particles takes place at a relative humidity of about 80%. On the other hand, crystallization of this salt from a salt supersaturated solution drop requires a relative humidity as low as 35%. Similar low relative humidities were found to be required for the crystallization of other salts out of pure salt solution drops, and for the crystallization of dissolved material in drops grown on natural aerosol particles (Shaw and Rood, 1990; Orr *et al.*, 1958a,b; Tang and Munkelwitz, 1983; Spann and Richardson,

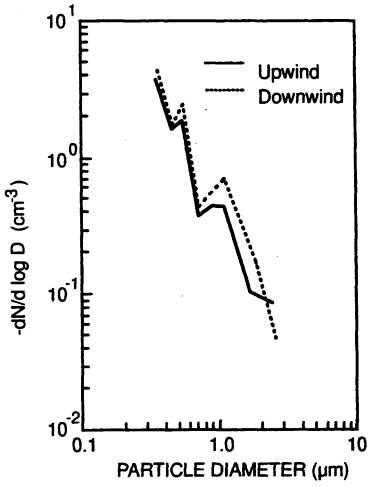


Fig. 8-9: Particle size spectra measured upwind and downwind of a wave cloud over Mt. Rainier (Washington). (From Hegg *et al.*, 1980, with changes.)

1985, and Cohen *et al.* 1987).

These observations appear to suggest that except in air over deserts and in subtropical high pressure systems, the DPC mechanism will rarely lead to dry aerosol particles. On the other hand, in the literature, the aerosol size distribution of atmospheric aerosol particles is generally presented as pertaining to dry particles. Three explanations for this apparent discrepancy may be offered: (1) The aerosol particles counted become dry as they pass through the particle counting system used. (2) Laboratory experiments overestimate the reduction in relative humidity necessary to initiate the crystallization of solution drops. Nucleation of salt in a supersaturated solution is a time dependent phenomenon. During an experimental situation in the laboratory, nucleation is 'forced' to take place over a time period

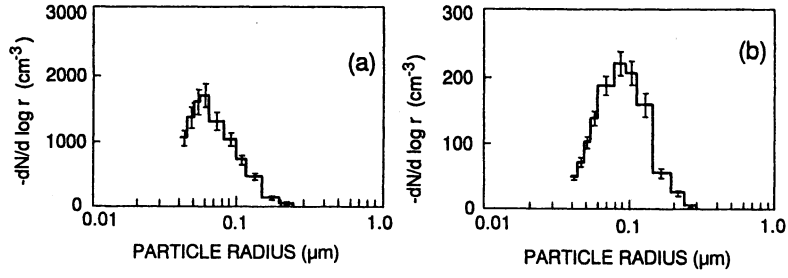
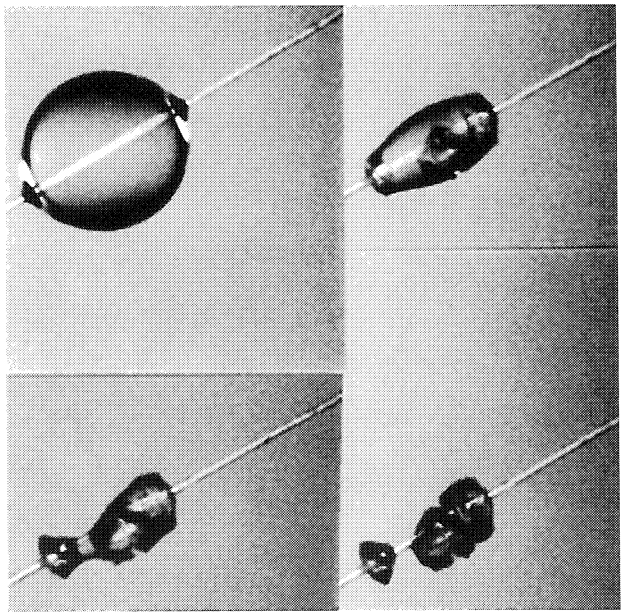


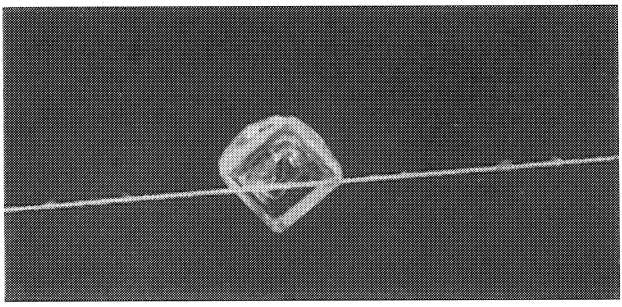
Fig. 8-10: Average size distribution of aerosol particles from evaporated cloud drops. (a) particles in cloudless air, (b) residual particles from evaporated cloud drops. (From Heintzenberg, 1989, with changes.)

much shorter than the time available for drop evaporation in the atmosphere. (3) During evaporation in the atmosphere, supersaturated drops may collide with water insoluble particles, which may initiate a heterogenous crystallization process at relative humidities much higher than those observed under clean laboratory conditions.

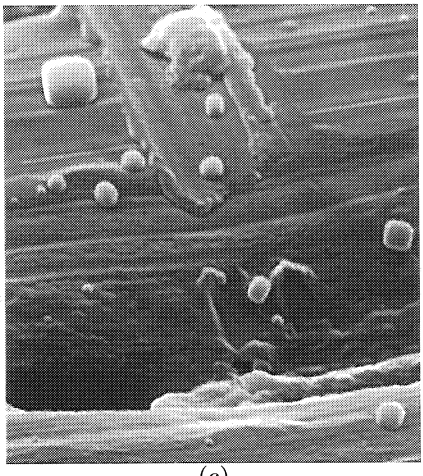
For a number of years, one assumed that salt particles which result from evaporating aqueous solution drops would break up into smaller portions due to stress which developed during the drying process. While Dessens (1946, 1947, 1949), Facy (1951), Twomey and McMaster (1955), Radke and Hegg (1972), and Cheng (1988) believed they had evidence for particle fragmentation during the drying of drops, Lodge and Baer (1954), Blanchard and Spencer (1964), Liu (1976), Pinnick and Auverman (1979), Tang and Munckelwitz (1984) and Baumgärtner *et al.* (1989) found no evidence for such fragmentation. The discrepancy between the results of the various investigators was resolved by Mitra *et al.* (1992a), who by wind tunnel experiments, showed that the drying process of freely air suspended aqueous solution drops is not accompanied by fragmentation of the drying salt particles. The presence of water insoluble particles inside the drying salt solution drop did not alter the result. One may, therefore, safely assume for cloud modeling purposes that the evaporation of a cloud drop results in the formation of one aerosol particle consisting of all the dissolved and undissolved matter which had entered the drop during its life time. However, solution drops drying on hydrophilic filaments (Plate 9a) do break up during the drying process, an effect which is prevented if a hydrophobic filament is used (Plate 9b). Fragmentation may also occur if salt particles, which resulted from the drying of salt mixtures such as ocean water, collide with solid surfaces since these particles are hollow and very fragile, as shown by Cheng *et al.* (1988), Baumgärtner *et al.* (1989) and Mitra *et al.* (1992), (see Plate 9i,k). Ranz and Marshall (1977), Charlesworth and Marshall (1960), Leong (1987 a,b, 1981), and Mitra *et al.* (1992a) concluded from their studies that the particle cavities shown in Plate 9k are not the result of a mass loss during the crystallization process, but rather are a result of the growth mode of the salt in the solution drop: crystallization begins at the upstream side of the solution drop and continues as a shell upward and inward. Since for typical salinities there is not sufficient salt to fill the whole volume of the drop, a hollow salt particle results with a cavity opening at the downstream side of the falling drop. Salt particles resulting from the drying of solution drops containing only one salt may at times also appear hollow, depending on the rate of drying. Generally, NaCl particles of diameters less than 1μm are single crystalline cubes (Mitra *et al.* 1992; Baumgärtner *et al.* 1989), while $(NH_4)_2SO_4$ particles are spherical (Plate 9c,f). Larger NaCl particles are single or polycrystalline with surface steps defining cubic forms (Plate 9d,e). $(NH_4)_2SO_4$ particles larger than $1\,\mu$m are always roundish (Plate 9g,h) with pronounced surface steps, and do not exhibit any features of the orthorhombic form a macroscopic ammonium sulfate crystal has.



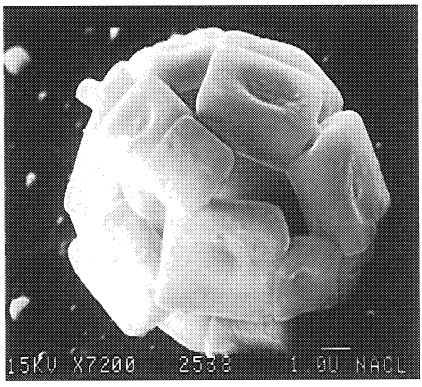
(a)



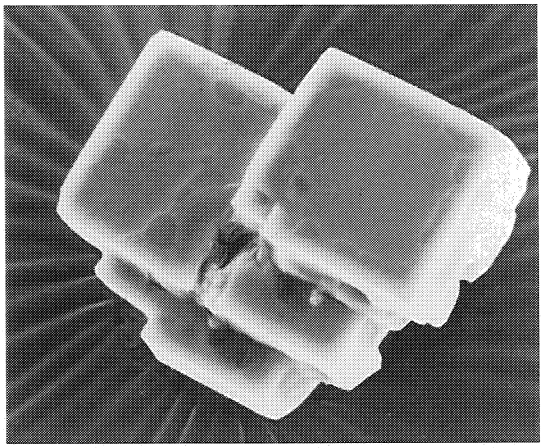
(b)



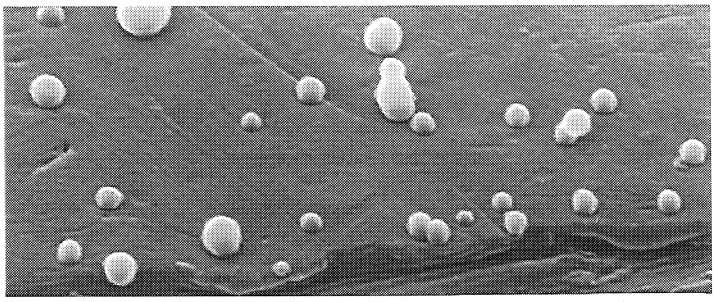
(c)



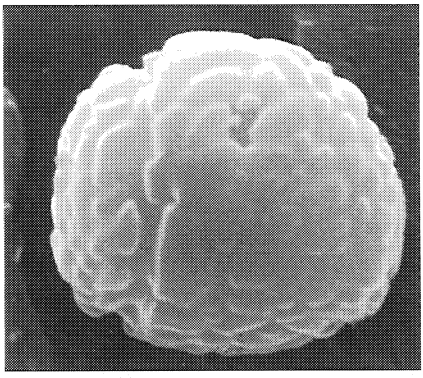
(d)



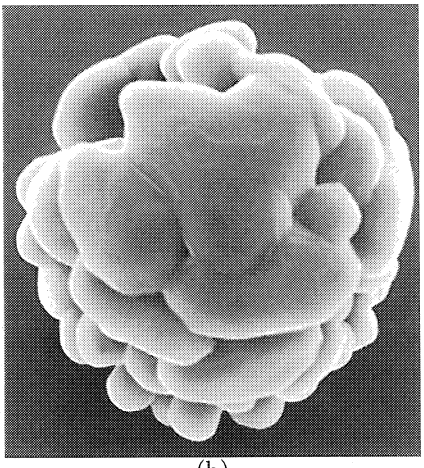
(e)



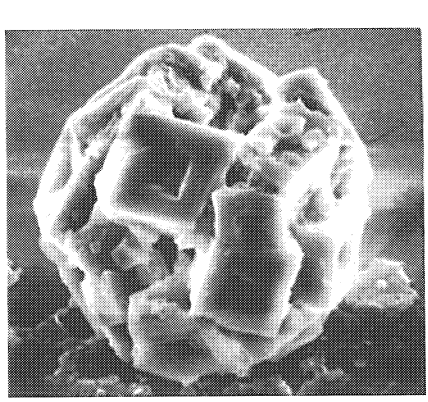
(f)



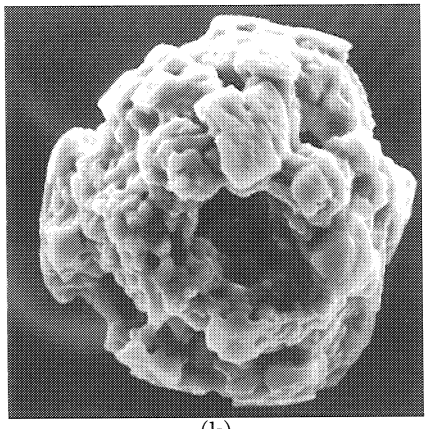
(g)



(h)



(i)



(k)

Plate 9. Examples of drop to particle conversion. (a) NaCl solution drop of 300 μm diameter drying on a hydrophilic filament; (b) NaCl particle of 150 μm diameter formed after drying of a NaCl solution drop on a hydrophobic filament. (c) NaCl particles of submicrom size formed after evaporation of NaCl solution drops freely falling in air; (d) NaCl particle of 6 μm diameter formed by evaporation of NaCl solution drop freely falling in air; (e) NaCl particle of 80 μm diameter formed by evaporation of NaCl solution drop freely falling in air; (f) $(NH_4)_2SO_4$ particles of submicron size formed after evaporation of $(NH_4)_2SO_4$ solution drop freely falling in air; (g) $(NH_4)_2SO_4$ particles of 10 μm diameter formed after evaporation of $(NH_4)_2SO_4$ solution drop freely falling in air; (h) $(NH_4)_2SO_4$ particle of 80 μm diameter formed after evaporation of $(NH_4)_2SO_4$ solution drop freely falling in air; (i) sea salt particle of 30 μm diameter formed after evaporation of ocean water drops freely falling in air; (k) sea salt particle of 80 μm diameter formed after evaporation of an ocean water drop freely falling in air. (a,b,c,e,f,g,h,k from Mitra and Brinkmann, by courtesy of the authors; d, from Prof. Krebs, Inst. of Radiochemistry, Techn. Univ. Münich, by courtesy of the author; i, from Dr. Roger Cheng, University of Albany, N.Y., by courtesy of the author.)

8.2.3 Formation of Aerosol Particles by Bulk to Particle Conversion (BPC)

8.2.3.1 *BPC at the Solid Earth Surface*

It is well-known that plants release various types of organic particulates, such as pollen, seeds, waxes, and spores which are distributed by air motions throughout the atmosphere (Gregory, 1961). A detailed study of the seasonal variation of pollen and spores was made by Grosse and Stix (1968), Stix (1969), and Stix and Grosse (1970). Diameters of these particles were found to range typically between 3 and 150 μm. It has also been shown that the atmosphere harbors large collections of microbial bodies, both living and dead (Gregory, 1967; Valencia, 1967; Parker,1968). Lodge and Pate (1966) reported that substantial amounts of organic materials rise from tropical forest floors into the atmosphere. They concluded that these particles were produced by aerobic bacterial decay of tree leaf litter. In related work, Parkin *et al.* (1972) found humus from vegetation, dark plant debris, and fungus debris on aerosol particles which were carried in the westerlies over the Atlantic from the eastern United States. Rasmussen and Went (1965) and Went *et al.* (1967) captured organic particles which originated from decaying mid-latitude forest litter. Went's studies showed that the number concentration of organic particles was largest during periods of rapid plant litter decay. A variety of organic compounds were also identified in snow and rain by Shutt (1907), Fonselius (1954), and Munzah (1960).

The mass concentration of a large variety of organic components were studied in the field by Ketseridis *et al.* (1976a,b, 1978), Ketseridis and Eichmann (1978), Doskey and Andren (1986), and Simonett and Mazurek (1982). Pollen, spores, microorganisms, seeds, bacteria, and molds were investigated by Rüden *et al.* (1978) and Gregory (1978) as a function of height above the ground. They also noticed a significant dependence of the concentration of these particles on the relative humidity, temperature, and the intensity of the solar radiation. The total biogenic fraction of the atmospheric aerosol particles of a radius larger than 2 μm found in air sampled at Mainz, Germany, was determined by Matthias (1992) to vary from a few % up to 40% with respect to the number concentration, and up to 15% with respect to volume. Organic particles in the air are also present as elemental carbon, i.e., soot particles, obviously resulting from combustion processes. Such particles have been studied at different locations by Meszaros (1984), Okita *et al.* (1986), and Heintzenberg and Covert (1984), Hansen and Rosen (1984), Rosen and Novakov (1983), Chylek *et al.* (1987). As expected, the largest concentration occurs in air over cities; but somewhat unexpectedly, measurable concentrations occur also in air over oceans. A summary of the role of organic materials in atmospheric aerosols has been given by Jaenicke (1978b), and Due *et al.* (1983). Some recent measurements of carbon rich (C-rich) particles in the upper troposphere and lower stratosphere were carried out by Sheridan *et al.* (1994). Two main classes of C-rich particles were observed: (1) a class consisting of soot particles with chain-like structure, each chain being composed of small spherules of 20 to 30 μm in diameter, and (2) non-chain type C-rich particle with elements of Ti, Fe, Ni, Cr inclusions. Similar observations were made by Blake and Kato (1995).

About one third of the Earth's land area is covered by rocks or soil devoid of vegetation (Meigs, 1953). The exposed silicate compounds are chemically and mechanically disintegrated by the combined action of wind, water, temperature variations, and gases such as oxygen, carbon dioxide, and others. This weathering forms particles which have diameters mostly larger than 0.1 μm. The loose silicate material, usually with considerable amounts of organic material attached, is then transported upward by air motions. Clays, which are layersilicates and consist mainly of SiO_2, Al_2O_3, Fe_2O_3, and MgO, are most easily disrupted by weathering. Frequently, they are present as kaolinite, montmorillonite, illite, attapulgite, halloysite, and vermiculite (for details on the chemical compositon and special properties of clays, see, e.g., Grim, 1953).

Airborne silicates emitted by the Sahara desert have been identified by Prospero and Bonati (1969), Prospero *et al.* (1970), Chester and Johnson (1971), Jaenicke *et al.* (1971), Parkin *et al.* (1972), Schütz and Jaenicke (1974), Schütz (1980), Prospero *et al.* (1981), d'Almeida and Schütz (1983), Talbot *et al.* (1986), Schütz (1989), and Fitzgerald (1991) in air over the Sahara and westward over the Atlantic; by Delany *et al.* (1967) and Prospero (1968) in air over the Isles of Barbados; by Abel *et al.* (1969) in air over the Island of Teneriffa; and by Rex and Goldberg (1958) and Ferguson *et al.* (1970) in air over the Pacific and Indian Oceans. The Saharan dust was found to occur preferentially at atmospheric levels of between 1.5 and 3.7 km (Pospero and Carlson, 1972). The size of the silicate particles ranged typically between 0.3 and 20 μm radius, with a mode (most probable radius) near 2 to 5 μm. Deserts and semi-arid regions in North China and Mongolia are another significant source of silicates. Isono *et al.* (1959) identified clay particles in air over Japan which originated in North China or Mongolia, where they became airborne during large dust storms. Similarly, Darzi and Winchester (1982) identified at Mauna Loa (Hawaii) silicate particles transported eastward from North China. Isono *et al.* (1970) have provided evidence that some of these clay minerals are transported by the upper level westerlies across the Pacific and deposited over the northwestern coast of the U.S. Dust outbreaks over the deserts of the Middle East were observed by Savoie *et al.* (1987) in terms of a sudden increase of the silicate content of aerosol over the North Indian Ocean. Aerosol particles sampled over the dusty High Planes in the U.S. contained between 45 to 83% siliceous material.

The mechanism by which clays and other soil or sand particles become airborne has been investigated by Chepil (1951, 1957, 1965), Chepil and Woodruff (1957, 1963), Owen (1964), Bagnold (1965), Gillette *et al.* (1972, 1974), Gillette and Walker (1977), Gillette (1978a,b), and by Borrmann and Jaenicke (1987). It is well-known that adjacent to a smooth surface and at wind speeds below some critical value, a laminar boundary layer exists, even if the air flow is otherwise turbulent. On the other hand, if the surface is rough due to the presence of irregular soil and sand particles, turbulent motion may prevail right down to the surface. Such turbulent flow can cause a rough soil or sand surface to be eroded either by direct aerodynamic pick-up of the particles, or as a result of the bombardment by particles performing a bouncing motion called *saltation.* Conditions for saltation derived by Owen (1964) are summarized in Figure 8.11. During saltation, individual grains follow distinctive trajectories determined by the size and shape of the particles.

The air in the saltation layer is strongly sheared. The lift force responsible for the particles' saltation ensues from the combined action of the particles' momenta and the environmental vorticity.

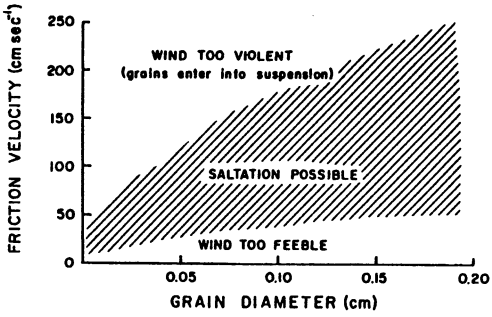


Fig. 8-11: Range of wind speed and grain size in which saltation of quartz grains can occur in the atmosphere. (From Owen, 1964; by permission of Cambridge University Press.)

According to observations by Chepil (1951), the minimum threshold wind velocity for direct aerodynamic pick-up of soil particles is a strong function of particle size. If particles were entrained by such a mechanism into the air layers adjoining the surface, one would expect greatly differing particle size distributions with height, owing to gravitational sorting and the effects of vertical wind shear. Such a dependence was not found by Gillette *et al.* (1974), Gillette and Walker (1977), Gillette (1978a,b) and Borrmann and Jaenicke (1987), who experimentally studied the size distribution of airborne particles from soil surfaces eroded by wind. Therefore, they concluded that sandblasting (saltation erosion) of the soil surface is the dominant mechanism by which particles become airborne. Wind tunnel experiments of Borrmann and Jaenicke (1987), and controlled field experiments of Gillette *et al.* (1974), and Gillette and Walker (1977) involving saltation-erosion on known soil and sand areas have allowed a determination of the vertical flux of soil particles and their mass distribution. These are consistent with the fluxes and mass distributions observed over the Libyan Desert (Schütz and Jaenicke, 1974; d'Almeida and Schütz, 1983).

After becoming airborne, silicate particles readily coagulate with other AP, thus becoming of mixed compositions. It is therefore not surprising that the bulk density of continental aerosol material varies over a range which may differ considerably from the bulk density of SiO_2 (quartz), which is $\rho(SiO_2) = 2.65$ to 2.66 g cm^{-3}. According to d'Almeida and Schütz (1983), some Sahara dust particles contain the elements Hf and Zr, and therefore have the much higher bulk density of approximately 4 g cm^{-3}. Hänel and Thudium (1977) found, for $0.05 \leq r \leq 5\,\mu$m, $\rho = 2.6$ to 2.7 g cm^{-3} (desert, Israel), $\rho = 1.8$ to 3.5 g cm^{-3} (urban, Mainz), $\rho = 2.9$ g cm^{-3} (Jungfraujoch, Switzerland), and $\rho = 1.8$ to 3.3 g cm^{-3} (rural, Deuselbach, Germany). Joshi (1988) observed $\rho = 1.24$ to 1.95 g cm^{-3} (Bombay, India). These

values are to be compared with the densities of NaCl ($\rho = 2.17$ g cm^{-3}), sea salt ($\rho = 2.25$ g cm^{-3}) and $(NH_4)_2SO_4$ ($\rho = 1.77$ g cm^{-3}).

Particles emitted by volcanoes also are often the result of a combination of both mechanical disintegration and gas-to-particle conversion. For example, during the eruptions of Krakatoa in 1883 in the East Indies and Gunung Agung in Bali in 1963, some of the emitted particles consisted simply of silicates from the crater walls, others consisted of finely divided solidified lava, while still others consisted of sulfates, fluorides, chlorides, and sulfuric acid. The particles, which ranged from submicron size to greater than 100 μm, were injected into both the troposphere and stratosphere. Similar results were found by Stith *et al.* (1978) who studied six volcanoes in Alaska and the State of Washington. More recently, Rose *et al.* (1982) and Hobbs *et al.* (1982, 1983) studied particles emitted by the Mt. St. Helens volcano (Oregon) in 1980. The particle sizes ranged from 0.001 to 2 μm. Also, the mass concentration showed a wide variation, ranging typically between a few tens to a few hundreds μg m^{-3} with a peak mass concentration of 11 829 μg m^{-3}, and a total particle number concentration of 10^3 to 10^6 cm^{-3}. Unfortunately, no direct measurements are available on the size distribution and chemical composition of the aerosol particles emitted during the eruption of Mt. Pinatubo (Phillipines) in June 1991, although significant changes in the particle size distribution of the stratosphere were noted by Wilson *et al.* (1993) and Borrmann *et al.* (1993).

Particles injected into the atmosphere by industrial processes are also often the result of mechanical disintegration and gas-to-particle conversion. Hobbs and Radke (1970) found, downstream of paper mill exhausts, particles of Na_2SO_4, NH_4HSO_3, $Ca(HSO_3)_2$, NaOH, Na_2SO_3, and H_2SO_4, which ranged from submicron size to several hundred microns, with a mode from 1 to 10 μm diameter. Serpolay (1958, 1959) and Soulage (1961) found a large number of metal and metal oxide particles downstream of steel foundries and electric steel mills.

8.2.3.2 *BPC at the Surface of Oceans*

Wind blowing across an ocean surface causes the formation of waves which produce spray drops at their crests. The finer of these drops remain airborne and eventually evaporate to give solid AP. A more important source of AP results from the bursting of bubbles produced by the entrainment of air at the wave crests.

Experimental studies of Woodcock *et al.* (1953), Kientzler *et al.* (1954), Knelman *et al.* (1954), Mason (1954b), Moore and Mason (1954), and Blanchard (1954) show that each air bubble which reaches the ocean surface develops a spherical cap which strains, thins, and then bursts. After the bubble cap has burst, fragments of the cap-film are thrown upward by the air which escapes from the bubble orifice. Now deprived of its cap, the bubble fills with water rushing down the sides of the cavity, which subsequently emerges from the center as a narrow jet. As the jet rises, it becomes unstable and eventually disintegrates into a few large and several small drops. Bubbles of 2 mm diameter project drops up to heights of nearly 20 cm above the ocean surface; drops from both larger and smaller bubbles generally reach lower heights (Blanchard, 1963; Hayami and Toba, 1958). Depending on the relative humidity and turbulence of the air, some of the drops formed by the

collapsing jet and by the shattered bubble cap fall back to the ocean surface. The remainder evaporate while airborne, leaving a small sea salt particle light enough to be carried aloft by air motions. The different stages in the production of sea salt particles by this *bubble-burst mechanism* are described schematically in Figure 8.12.

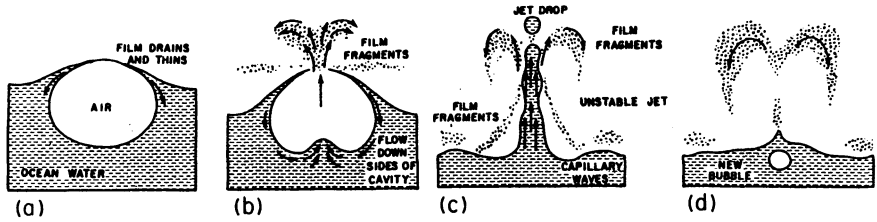


Fig. 8-12: Four stages in the production of sea salt particles by the bubble-burst mechanism. (a) Film cap protrudes from the ocean surface and begins to thin. (b) Flow down the sides of the cavity thins the film which eventually ruptures into many small fragments. (c) Unstable jet breaks into few drops. (d) Tiny salt particles remain as drops evaporate; new bubble is formed. (From Day, 1965, with changes.)

A sea salt particle is mainly composed of NaCl, the most abundant salt in ocean water. In addition, it often contains small amounts of CO_3^{2-}, SO_4^{2-}, K^+, Mg^{2+}, and Ca^{2+}. However, the chemical composition of sea salt particles deviates considerably from the composition of ocean water. Junge (1972b) suggested that this is partly a result of ion fractionation occurring during the bubble burst mechanism. Since organic materials often reside in the ocean surface, they too may become airborne and become part of the sea salt particles (Blanchard, 1964, 1968; Garret, 1965, 1969). Subsequent to its formation, a sea salt particle may change its composition further as a result of both chemical reactions with atmospheric trace gases and coagulation with other AP in the atmosphere. Thus, in air over the Atlantic near the Sahara Desert, sea salt particles may have silicates admixed. It is therefore not surprising that the bulk density of maritime aerosol material varies over a range which may differ considerably from the bulk density of the salt that crystallizes from evaporating ocean water. Such salt has a bulk density of 2.25 g cm^{-3}. In contrast, Hänel and Thudium (1977) observed $\rho_P = 1.93$ g cm^{-3} (West coast, Ireland), and Fischer and Hänel (1972) observed $\rho_P = 2.45$ to 2.64 g cm^{-3} (North Atlantic, near Sahara). Note that $\rho_P(NaCl) = 2.165$ g cm^{-3}.

During the bursting of a bubble of about 300 μm in diameter, the jet breakup produces on average 5 larger drops (Blanchard and Woodcock, 1980). With increasing bubble size, this number decreases to about 1 larger drop from bubbles of diameters larger than 3 mm (Cipriano *et al.*, 1983). These larger drops have diameters of about one tenth the diameter of the parent bubble. Assuming that the density of a sea salt particle is 2.25 g cm^{-3}, that the density of ocean water is 1.03 g cm^{-3}, and that its salinity is 35 g kg^{-1}, we find a bubble of 2 mm diameter produces a salt particle of 1.5×10^{-7} g, which is equivalent to a dry radius of about 25 μm. Similarly, bubbles of 100 and 20 μm diameter produce salt particles of 1.9×10^{-11} and 1.5×10^{-13} g, which are equivalent to dry radii of about

1.3 and 0.3 μm, respectively. In addition to these large drops, jet breakup bubbles of diameters larger than 2 mm also eject a group of smaller drops at low angles to the horizontal. These drops have diameters of 5 to 30 μm and produce sea salt particles of masses 2.4×10^{-12} to 5.1×10^{-10} g, corresponding to dry radii of 0.6 to 3.8 μm. There has been some speculation that salt particles of even smaller size are produced by the splintering of the drying remnants of solution drops (Mason, 1971). However, the wind tunnel studies of Mitra *et al.* (1992a) have disproven the existence of such a mechanism.

The bursting of the bubble cap produces a large number of smaller drops leading to salt particles of a mass smaller than those from jet breakup. Mason (1954b, 1957b) found that most of the salt particles from the bubble cap have masses less than 2×10^{-14} g, equivalent to a dry radius of less than about 0.1 μm. The largest particles had masses up to 2×10^{-13} g, equivalent to a dry radius of about 0.3 μm, while the smaller particles had masses as low as 10^{-15} g, equivalent to a dry radius of 0.07 μm. These results were essentially confirmed by Twomey (1960). Blanchard (1963) suggested, and Day (1964) and Cipriano and Blanchard (1981) confirmed, that the number of bubble cap droplets decreases with decreasing bubble size, and that bubbles in diameter smaller than 100 μm, produce no cap drops (see Figure 8.13). Thus, bubbles smaller that 100 μm in diameter produce sea salt particles only as a result of jet breakup. However, there also appears to be a lower size limit to the production of air bubbles. According to Woodcock (1972), Woodcock and Duce (1972), Resch and Avellan (1981), Johnson and Cooke (1979), and Wu (1981), who studied the size distributions of bubbles on the ocean surface, air bubbles smaller than 20 μm in diameter are unlikely to exist near the surface, since bubbles of such sizes rise extremely slowly in ocean water, providing sufficient time for them to be dissolved. Consequently, sea salt particles produced by jet droplets necessarily have masses larger than about 10^{-13} g. The bubble size distributions, studied by Resch and Avellan (1981), Wu (1981), Cipriano and Blanchard (1981), and Johnson and Cooke (1979) show further that the distributions have a definite maximum at bubble radii between 50 and 75 μm, the number falling off rapidly towards larger bubble sizes.

According to Blanchard and Woodcock (1957), the number of bubbles of radii R to $R + \mathrm{d}R$ bursting per cm^2 per sec in a foam patch on the ocean surface is given approximately by $3 \times 10^{-6}(\mathrm{d}R/R^4)$. Assuming that each bubble produces one jet drop which remains airborne, the rate of jet particle production in cm^{-2} sec^{-1} by bubbles of radii larger than R_0 is then $3 \times 10^{-6} \int_{R_0}^{\infty} \mathrm{d}R/R^4 = 1 \times 10^{-6}(1/R_0^3)$. One may assume this relation is applicable to bubble radii larger than 50 μm. Day (1964) determined that for bubbles of radii larger than 50 μm, the number of cap drops per bubble varies with bubble size as $10^4 R^2$. Mason (1971) deduced from this information that the rate of cap particle production (cm^{-2} sec^{-1}) by bubbles of radii larger than R_0 can be described by $3 \times 10^{-2} \int_{R_0}^{\infty} \mathrm{d}R/R^2 = 3 \times 10^{-2}(1/R_0)$, which is applicable to bubbles larger than 50 μm radius. Note that these results only apply to drop production by single bubbles. Experiments by Mason (1957b) and Twomey (1960) suggest that the rate of cap drop production is considerably larger if bubbles break in clusters.

Observations by Moore and Mason (1954) at a height of 10 m over the Atlantic

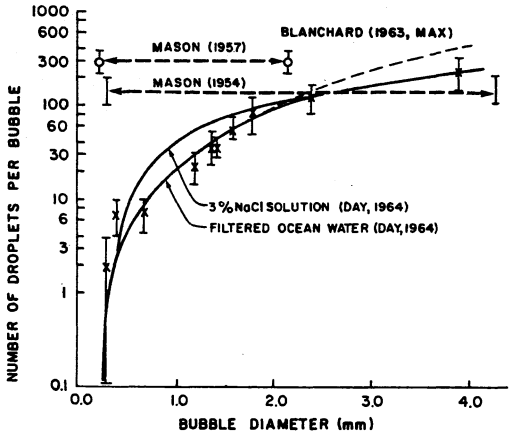


Fig. 8-13: Mean number of droplets resulting from the disintegration of an air bubble cap in salt water as a function of equivalent diameter of the air bubble. (From Day, 1964; by courtesy of *Quart. J. Roy. Meteor. Soc.*).

showed that sea salt particles of mass $m_s > 10^{-13}$ g are formed at a rate of 40 cm^{-2} sec^{-1}, particles of $m_s > 2 \times 10^{-15}$ g at a rate of 100 cm^{-2} sec^{-1}, and particles of $m_s > 10^{-15}$ g at a rate of 1000 cm^{-2} sec^{-1}, over areas where bubbles are bursting. Blanchard (1969) found, off the Hawaiian coast, the somewhat larger total particle number of 3000 cm^{-2} sec^{-1}. Using photographic observations of the state of the ocean surface at different times during a whole year, Blanchard (1963) estimated that, on a global average, 3.4% of the Earth's oceans are covered with breaking bubbles. Although Monahan (1968, 1969, 1971) and Williams (1970) argued that this figure was too large, Blanchard (1971a) upheld his original estimate by pointing out that the bubble-burst mechanism operates not only in the areas covered by white-caps, but also in the areas immediately adjacent to them. Thus, Blanchard (1969) suggested that the average sea salt particle production is $0.034 \times 3000 \approx 100$ cm^{-2} sec^{-1}, corresponding to a global production rate of about 10^{28} particles yr^{-1}. Assuming that on the average an airborne sea salt particle has a mass of 3×10^{-14} g, one estimates 300 Tg yr^{-1} for the global production rate of sea salt. This is in agreement with estimates by Erikson (1959), and by Peterson and Junge (1971).

Within this context, it is useful to test whether the flux of salt particles due to the bubble burst mechanism may account for the number of cloud condensation nuclei from which cloud drops are formed. Cipriano *et al.* (1983) used two routes of argumentation to explore this question. For the first argument they followed Twomey and Wojciechowski (1969), and assumed on global average a columnar concentration of cloud condensation nuclei of 5×10^7 cm^{-2} throughout the troposphere. Assuming a residence time for the salt particles of three days (2.6×10^5 sec), they deduced a nuclei flux of about 200 cm^{-2} sec^{-1}. If this flux of nuclei could be represented by a flux of salt particles only, and one assumes a 3% bubble coverage

of the oceans, the salt particle flux would need to be about 7×10^3 cm^{-2} sec^{-1}, or about seven times larger than the flux observed in the laboratory and in the field over breaking waves of 1000 cm^{-2} sec^{-1} (Moore and Mason, 1954; Cipriano *et al.* 1983; Cipriano and Blanchard, 1981). One concludes from this estimate that the data do not support a breaking wave origin for all the cloud condensation nuclei in the troposphere.

The second argument of Cipriano *et al.* (1983) tested whether the data support a breaking wave origin for cloud condensation nuclei at least in the maritime boundary layer. This boundary layer is typically 2 km (2×10^5 cm) deep (Blanchard and Woodcock, 1980). Assuming a typical droplet concentration in martime clouds of 50 cm^{-3} (Squires and Twomey, 1958; Jiusto, 1966), the columnar concentration of cloud condensation nuclei to support this drop condensation would be 100×10^5 cm^{-2}. Assuming again a three day residence time for aerosol particles, the required particle flux to support the observed drop concentration would be about 40 cm^{-2} sec^{-1}. If one requires that this nuclei flux be made up of salt particles from breaking waves, assuming again a 3% bubble coverage over the ocean, the required salt particle flux would need to be 1300 cm^{-2} sec^{-1}. The salt particle flux of 10^3 cm^{-2} sec^{-1} observed in the laboratory and in the field implies a cloud condensation nucleus flux of 200 cm^{-2} sec^{-1} at a supersaturation of 1% (see Table 9.3). Thus, we see that even in the maritime boundary layer, the observed sea salt particle flux falls short by a factor of about 6 from accounting for the maritime cloud formation.

Observations show that the ocean surface is not a source of inorganic salts only, but of organic materials as well. Wilson (1959), Blanchard (1964, 1968), Goetz (1965), and Garret (1967, 1970) found organic substances present in the ocean surface which become airborne through the bubble-burst mechanism. Goetz (1965) and Blanchard (1969) captured airborne, submicron-sized, organic particles which originated at the ocean surface. Zoebell and Matthews (1936) and Stevenson and Collier (1962) showed that air above oceans contained numerous micro-organisms indigenous to marine water. Studies of organic compounds in snow and rain also suggest a marine source for these materials (Wilson, 1959; Newmann *et al.*, 1959). Of course, significant amounts of surface active materials at the ocean surface also affects the bubble-burst mechanism through lowering the surface tension (Patterson and Spillane, 1968).

8.2.4 AP FROM EXTRATERRESTRIAL SOURCES

Extraterrestrial particles continuously enter the Earth's atmosphere at speeds great enough to produce strong frictional heating. The resulting light phenomenon is called a *meteor* and the particle itself is called a *meteoroid.* The vast majority of meteoroids are believed to be permanent members of the solar system. Meteoroids produce meteors at an average height of about 95 km, and nearly all of them completely disintegrate and their meteors disappear by the time they have reached an altitude of about 80 km. The small fraction which do survive the fall to Earth are termed *meteorites.* Some of these are quite large, one of the largest on display

in a single piece has a mass of 14 tons. This contrasts with an average meteoroid mass of a few grams or less.

Most meteorites are very small, having been nearly consumed before slowing sufficiently to reach temperatures below the burning point; such particles are called *micrometeorites.* Most of these are derived from a large pool of interplanetary dust which is concentrated in a lens-shaped volume located about the plane of the ecliptic. These particles move around the Sun in orbits similar to that of the Earth, and enter the Earth's atmosphere with small geocentric velocities. Their diameters range between about 1 and 1000 μm. Particles which result from the condensation of evaporated meteoroids are considerably smaller, ranging between 1 μm and a few Ångstrøms (Rosinski and Snow, 1961).

Chemically, meteorites are divided into four main groups: irons (siderites), stony irons (siderolites), stones with small spheroidal aggregates (chondrites), and stones without such aggregates (achondrites). Common minerals in meteorites include kamacite, taenite, troilite, olivin, orthopyroxene, pigeonite, diopside, and plagioclase. Elements typically found in meteoritic aerosol material are Fe, Si, Mg, S, Ca, Ni, Al, Cr, Mu, Cl, K, Ti, and Co (Cameron, 1981). Measurements in the upper troposphere and lower stratosphere by Sheridan *et al.* (1994) showed that metallic particles contained elements such as Fe, Ti, Al, Zu, Sn. Such particles appeared always as discrete particles which were not associated with detectable quantities of sulfate, commonly observed at these levels of the atmosphere.

8.2.5 Rate of Emission of Particulate Matter into the Atmosphere

Attempts to estimate the rate at which particulate matter is injected from the Earth's surface or from space into the atmosphere, have encountered considerable observational difficulties. Similar difficulties are involved in estimating the rate at which aereosol particles are produced inside the atmosphere. The estimates of Robinson and Robbins (1971) and of Peterson and Junge (1971) are summarized in the form of a table in SMIC (1971). This table has been extended by Jaenicke (1988) to include other authors. The values listed by Jaenicke are reproduced here as Table 8.7. Although the values given in this table are only rough estimates, they testify to the rather large amounts of material which enter the atmosphere. The data also suggest that the man-made contribution to the total particulate load in the atmosphere ranges between 5 and 65%, depending on the estimates of the source strength.

8.2.6 Residence Time of AP

It is considerably more difficult to estimate residence times for aerosol particles than for gaseous constituents of the atmosphere. The reason for the additional difficulty lies mainly in the fact that aerosol particles, particularly those at the smaller end of the size spectrum, undergo a continuous change in size and composition and, thus, lose their identity as a result of coagulating with other particles. Consequently, the term *residence time* is not only a measure of the time a species resides in a reservoir

TABLE 8.7

Estimates of the rate in Tg yr^{-1} at which aerosol material is emitted from various sources into the atmosphere; based on data of: (1) Peterson & Junge (1971), (2) Hidy & Brock (1971), (3) Schütz (1971), (4) Schütz (1971), Jaenicke (1978), Bach (1978). (From Jaenicke, 1988.)

	(1)	(2)	(3)	(4)
Natural sources				
Sea salt	500	1095	180	1000...2000
Mineral dust	250	7.....365	60.....300	60...1800
Volcanoes	25	4	15.....90	4
Forest Fires	5	146	3.....150	
Biological material				
Subtotal particles	780	1252...1610	258.....720	1144...2444
Converted sulfates	355	37.....365	130.....200	
Converted nitrates	60	600.....620	140.....700	160
Converted HC	75	182...1095	75.....200	154.....220
Subtotal GPC	470	819...2080	345...1100	1319
Total natural	1250	2071...3690	603...1820	2463...3763
Man-made sources				
Subtotal particles	30	37.....110	6.....54	54.....126
Converted sulfates	200	110	130.....200	
Converted nitrates	35	23	30.....35	
Converted HC	15	27	15.....90	
Subtotal GPC	250	160	175.....325	270
Total man-made	280	196...270	181.....379	324.....396

but it is also a measure of the spatial and temporal variation of the concentration of that species in the reservoir (Jaenicke, 1988).

The results of estimates made prior to 1970 have been summarized in SCEP (1970). More recent measurements have been obtained by using Pb^{210}, Po^{210}, Bi^{210}, Sr^{90}, Cs^{137}, and HTO isotopes (Martell, 1970, 1971; Poet *et al.*, 1972; Moore *et al.*, 1973; Ehhalt, 1973; Weickmann and Pueschel, 1973; Martell and Moore, 1974; Tsunogai and Fukuda, 1974). The more recent estimates have been collected by Jaenicke (1988) in Figure 8.14. From this figure it is seen that the residence time is longest for a particle in the size range 10^{-1} to 1 μm. The residence time decreases towards larger sizes due to the increased fall velocity of the particles and therefore their increased tendency to fall out. The residence time also decreases towards smaller sizes due to an increased tendency of a particle to coagulate with other particles. From Figure 8.15, the residence time of AP can also be seen to increase with height in the atmosphere. It ranges from a few days in the lower troposphere to a few weeks in the upper troposphere, to several weeks, months and even years at increasingly higher levels above the troposphere. This behavior is somewhat expected considering that clouds are most abundant below 6 km where they constitute a major sink for aerosol particles.

Of course, the residence time of an aerosol particle is also affected by its chemical composition, in particular its solubility in water. We will see in Chapter 9 that salt particles are preferred cloud condensation nuclei, so that they are rapidly removed from the atmosphere due to their involvement in forming cloud drops. Thus, Junge (1972b) showed that unrealisitic values for $\tau_{\text{sea salt}}$ are obtained if sedimentation is the only removal mechanism considered. He suggested that sea salt particles have

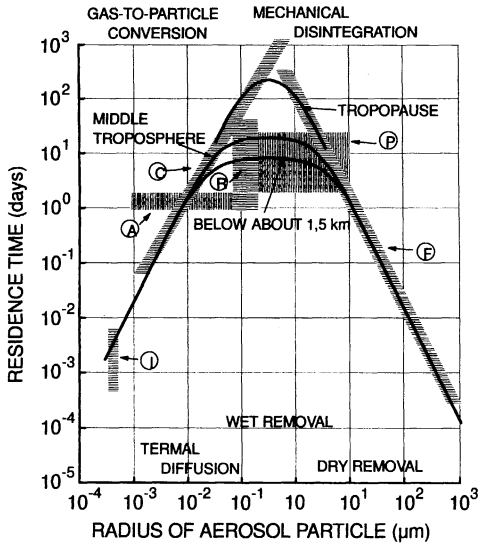


Fig. 8-14: Residence time of aerosol particles as a function of their radius. I: Small ions, A: Aitken particles, C: from thermal diffusion of aerosol particles, R: based on radioactivity data, P: removal by precipitation, F: removal by sedimentation. (From Jaenicke, 1978a, 1988, with changes.)

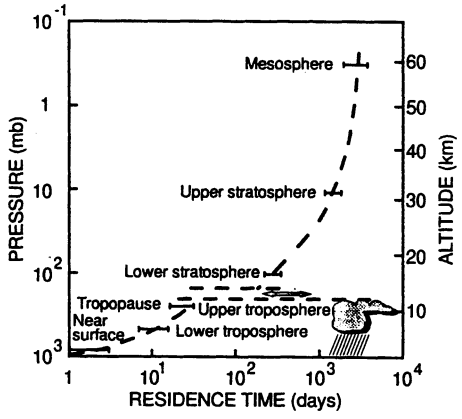


Fig. 8-15: Residence time of aerosol particles as a function of altitude in the atmosphere. (From Jaenicke, 1978c, 1988, based on Flohn, 1973, with changes.)

their major sink at the cloud level. Using his own estimates and those of Erikson (1959), Junge suggested $\tau_{\text{sea salt}} \approx 1$ to 3 days for $m_s > 10^{-9}$ g. This is the value we used earlier in Section 8.2.3.2 to show that the sea salt particle flux cannot account solely for maritime cloud formation.

8.2.7 Water-soluble Fraction of AP

Atmospheric AP have a wide range of water-solubilities. Compounds such as NaCl, $NaNO_3$, $(NH_4)_2SO_4$, NH_4NO_3, Na_2SO_4, and other salts typically found in the atmosphere are highly water-soluble, while substances such as silicates and metal oxides are practically water-insoluble. Substances such as $CaCO_3$ and $CaSO_4$ have a measurable but rather low solubility. In contrast to solid particulates, most gases exhibit measurable water-solubility. While SO_2, NO_2, NH_3, and CO_2 are highly soluble in water, where they dissociate into ions, other gases such as CO, N_2, and O_2 have a moderate solubility and are molecularly dissolved.

The water-solubility of any compound is temperature-dependent. Most salts suspended as particulates in the atmosphere dissolve by means of an endothermic (heat-consuming) process, so that their solubility increases with increasing temperature. On the other hand, gases such as N_2, O_2, CO_2, H_2S, CO, NH_3, NO, and SO_2 dissolve by means of an exothermic (heat-releasing) process, causing their solubility to increase with decreasing temperature. It is worth noting also that the solubility of a gas increases as its partial pressure increases (see Chapter 17).

The solubility of a salt (given in terms of the maximum mass of salt which can be dissolved in a given mass of water) is not directly related to its hygroscopicity or vapor pressure reducing power (see Chapter 4), but is a function of the interaction energy between the water molecules and the salt ions in water, and of the lattice energy of the salt crystal. Therefore, the solubility of a salt does not predict the relative humidity at which a particle of that salt changes into a solution drop; nor, once dissolved, does it predict the effect which the salt has on the equilibrium growth behavior of that drop.

Chemical analysis of AP shows that most individual AP are of a mixed chemical nature, and contain both water-soluble and water-insoluble substances. This fact was first pointed out by Junge (1950), who termed these AP *mixed particles* or *Mischkerne*. A mixed particle may be formed (1) by condensation or adsorption of foreign gases onto the surface of AP; (2) by coagulation of AP with other AP; (3) by solution of gases in cloud and raindrops followed by chemical reaction with other dissolved substances or insoluble particles in the water, and subsequent evaporation of the drop; (4) by coagulation of cloud drops with other cloud drops containing substances of a different chemical nature in dissolved form, and subsequent evaporation of the drops; and (5) as a result of the simultaneous condensation of vapors emitted during combustion processes. Most particles emitted into the atmosphere are also of a mixed type, such as sea salt particles, organic plant material, and soil derived particles.

According to Junge (1972c), one generally may assume that AP at the Earth's surface consist typically of about 50% water-soluble inorganic material, about 30% water-insoluble inorganic material, and about 20% organic material. However, ac-

cording to Table 8.8, the water soluble fraction ϵ_m in aerosol particles is quite variable. This is not surprising considering the large number of chemical compounds from which aerosol particles may be formed. Unfortunately, the chemical composition of the aerosol samples listed in Table 8.8 was not evaluated at the time at which the water soluble fraction was determined. Therefore, we do not know which chemical compounds contributed to the water soluble and the water insoluble portions of the particles. Also, only deposits of aerosol particles in given size intervals were studied, rather than single particles. The values for ϵ_m therefore reflect the 'inner mixture' of single particles as well as the 'outer mixture' of particles of different composition. Nevertheless, we may notice that maritime air generally consists of AP with $0.8 \leq \epsilon_m \leq 1.0$, while continental air contains AP with $\epsilon_m \leq 0.6$. Studying the water soluble fraction in aerosol particles of $r > 0.1\,\mu$m sampled at Mt. Feldberg (near Frankfurt/Main), Eichel (1994) found that the particles could be grouped into 3 solubility categories: a group with $\epsilon_m \approx 0.09$, a group with $\epsilon_m \approx 0.5$, and a group with $\epsilon_m \approx 0.88$.

8.2.8 Total Mass and Number Concentration of AP

8.2.8.1 *Number Concentration (except Polar Aerosols)*

Table 8.9 summarizes typical values for the number concentration of AP of all sizes, irrespective of their chemical type. The total particle concentration in air over land generally ranges between 10^3 and 10^5 cm^{-3}. In air over cities, the concentration may even be as large as 10^6 cm^{-3}, while in air over rural areas, near seashores, and at mountain stations, the concentration is usually only a few hundred to a few thousand cm^{-3}. Thus, Landsberg (1938) found an average minimum AP concentration of 1050 cm^{-3} over rural areas, while Auer (1966) reported 1000 cm^{-3} at the remote Yellowstone Park (Wyoming). Lower values were found by Landsberg at mountain stations, where the average minimum decreased to a few hundred cm^{-3}. Similarly, Junge *et al.* (1969) found at Crater Lake (Oregon, 1100 m) a total AP concentration of 700 cm^{-3} during subsidence conditions. However, under normal conditions, the concentration varied typically between 1000 and 2000 cm^{-3}. Bullrich *et al.* (1966) found a value of 600 cm^{-3} in air above the trade wind inversion over Hawaii on Mt. Haleakala (3050 m). These data imply that the number concentration of AP decreases with increasing distance from the aerosol particle source.

Let us now look at number concentrations of AP of a specific chemical type. Schütz and Jaenicke (1974) found near the ground over the Libyan Desert silicate particle concentrations of 260 liter^{-1} (0.2 mg m^{-3}), 9600 liter^{-1} (9.3 mg m^{-3}), and 8800 liter^{-1} (1.2 mg m^{-3}) at mean wind speeds of 7.6 m sec^{-1}, 8 m sec^{-1}, and 8.7 m sec^{-1}, respectively. d'Almeida *et al.* (1991) reported 250 to 2600 cm^{-3} for various locations in the Sahara. Schütz (1989) found for atmospheric conditions 80 to 600 cm^{-3} on the west coast of Africa at the latitude of the Sahara, and 800 to 2000 cm^{-3} during dust storms. Further west of the North African coast, the concentration of silicate particles varied between 400 and 900 cm^{-3} at various locations on the subtropical Atlantic.

TABLE 8.8

Water soluble mass fraction, ε_m, in atmospheric aerosol particle.

	ε_m	Observer
Nagoya and Yokkaichi (Japan)		Okada (1983a,b)
	0.95 - 1.0	$0.03 \leq r \leq 0.35\mu$m
Urbana (Illinois)		Ochs and Gatz (1980)
	0.3	$r > 4.6\mu$m
Los Angeles		McMurray & Stolzenburg (1989)
	0.7	$0.1 \leq r \leq 0.25\mu$m
Cairo (Egypt)	0.1 - 0.3	El Ghandour *et al.* (1983)
Deuselbach (Germany)		Winkler (1974, 1988)
	0.68	$r > 0.1\mu$m
	0.75	$0.1 \leq r \leq 1\mu$m
	0.46	$r > 1\ \mu$m
Mainz (Germany)		Winkler (1974)
	0.59	$r > 0.1\mu$m
	0.09 (Type I)	Eichel (1994) for
	0.50 (Type II)	$r = 0.43$; $r = 0.64$; $r = 2.31\ \mu$m
	0.88 (Type III)	
Rolla (Missouri)		Alofs *et al.* (1989)
	0.5	$0.2 \leq r \leq 0.4\mu$m
Tokyo (Japan)		Sekigawa (1983)
	0.3 - 0.5	$0.03 \leq r \leq 0.1\mu$m
Hamburg (Germany)		Winkler (1988)
Continental air	0.45	$r \leq 0.1\mu$m
"	0.64	$0.1 \leq r \leq 1\mu$m
"	0.47	$r > 1\mu$m
Maritime air	0.88 - 0.92	$r > 1\mu$m
Northe Bay (Ontario)		Isaac and Daum (1987)
	0.80; 0.57; 0.37	south, west, north wind
Po Valley (Italy)	0.64	Fuzzi *et al.* (1988)
U.S.S.R. (1500 - 4000 m)		Laktinov (1972)
	0.2	$r = 0.15\mu$m
	0.1	$r = 0.30\mu$m
Budapest (Hungary)		Meszaros (1968)
	0.17	$r \leq 0.14\mu$m
	0.07	$r > 0.14\mu$m
	0.02	$r > 0.3\mu$m
Chesapeake Bay (Maryland)		Twomey (1965, 1972)
Maritime	0.9 - 1.0	

TABLE 8.9

Number concentration of atmospheric aerosol particles at different locations at the Earth's surface. (Based on data of Landsberg, 1938.)

Locality	No. of places	No. of observations	Average concentrations (cm^{-3})	Average maximum (cm^{-3})	Average minimum (cm^{-3})
City	28	2 500	147 000	379 000	49 100
Town	15	4 700	34 300	114 000	5 900
Country inland	25	3 500	9 500	66 500	1 560
Country seashore	21	2 700	9 500	33 400	1 560
Mountain:					
500-1000 m	13	870	6 000	36 000	1 390
1000-2000 m	16	1 000	2 130	9 830	450
2000 m	25	190	950	5 300	160
Islands	7	480	9 200	43 600	460

Grosse and Stix (1968), Stix (1969), and Stix and Grosse (1970) found that in air over Darmstadt (Germany) the daily average concentration of pollen and spores ranged from a few hundred m^{-3} (maximum values of 1000 m^{-3}) during the months of December to April, to a few thousand m^{-3} (maximum values of a few ten thousand m^{-3}) during the months of May to October. During the months of October and November, intermediate values were found.

Rüden *et al.* (1978) observed micro-organisms in concentrations of 160 to 10^3 m^{-3}, bacteria in concentrations of 500 to 3500 m^{-3}, and molds up to 200 m^{-3}, at 20 m above ground. Gregory (1978) found spores and pollen in concentrations up to 10^6 m^{-3} during short periods, with averages of 12,000 m^{-3} at 2 m above ground. Matthias (1992) investigated the total number of biogenic particles in air over Mainz and found that the number concentration ranged between 300 and 6100 $liter^{-1}$. Soot particles were measured by Meszaros (1981, 1984) and Heintzenberg and Covert (1984). Meszaros observed the highest concentrations in air over Budapest, Hungary (1500 cm^{-3}), less in rural air of Hungary (260 cm^{-3}), and lowest numbers in air over the Atlantic (340 to 4800 $liter^{-1}$).

Particles containing sulfates, nitrates, chlorides, and calcium and ammonium compounds are found to be present in preferred size ranges. Junge (1953, 1954) found, from an analysis of air over Frankfurt/Main (Germany), over Round Hill near Boston (U.S.), at the Taunus Observatory (800 m, Germany), and at the Zugspitze Observatory (3000 m, Germany), that particles in the size range $0.08\,\mu m \leq r \leq 0.8\,\mu m$ seemed to consist mainly of ammonium sulfate. These results were supported by Georgii *et al.* (1971), who found that in air over West Germany more than 95% of the sulfate mass of AP was contained in particles with $r < 1\,\mu m$. Similarly, in air over Crater Lake (2200 m Oregon), 86% of the sulfur was contained in particles less than $1\,\mu m$ radius (Junge *et al.*, 1969). Junge (1953, 1954) also noticed that much of the NaCl was contained in particles of $0.8\,\mu m \leq r \leq 8\,\mu m$. In agreement with this, Junge *et al.* (1969) observed at Cape Blanco (Oregon) that 92% of the chloride was contained in particles larger than $1\,\mu m$ radius. According to Meszaros (1969), AP of purely continental origin contain most of the nitrate as ammonium nitrate in the 'large' AP range, while the water-soluble calcium is found primarily in AP of the Aitken size range. On the other hand, Junge (1954) found that in air near the east coast of the U.S., nitrate was predominant as $NaNO_3$ in AP of the 'giant' size range.

Table 8.10 illustrates that at locations over oceans, relatively remote from anthropogenic sources, the total concentration of AP generally ranges between 300 and 600 cm^{-3}, with minimum values close to 100 cm^{-3}. One would expect that in the air close to the ocean surface, sea salt particles would dominate the AP concentrations. However, this does not happen, and at average wind conditions, the concentration of such particles is found to be less than 10 cm^{-3}. Only in air over very agitated seas during storms does the concentration increase to a few tens cm^{-3}. During storm conditions off the coast of Denmark, Schmidt (1972) found sea salt particles with $m_s > 10^{-15}$ g in concentrations of 24 to 43 cm^{-3}. In air over the southern hemispheric Atlantic and Indian Oceans, Meszaros and Vissy (1974) found that the maximum concentration of sea salt particles varied between 4 and 23 cm^{-3}, accounting only for from 5 to 49% of the total number of particles,

TABLE 8.10
Number concentration of aerosol particles over the ocean.

	Number (cm^{-3})	Observer
Pacific	70 - 690 (290 mean)	Ohta (1951)
W. Atlantic	300 - 1000 (676 mean)	
N. Atlantic	445 - 703 (mean)	Moore (1952)
E. Atlantic	200 (mean)	Day (1955)
Atlantic (30°-40°N)	520 (mean)	Hogan (1968)
W. Atlantic (10°S-60°N)	510 (mean)	Jaenicke *et al.* (1971)
Atlantic and Indian Ocean	300 - 450	Meszaros and Vissy (1974)

TABLE 8.11a
Mass concentration of particulate matter in the troposphere; total particulate mass concentration.

	Mass concentration ($\mu g/m^3$)	Observer
Various cities	80 - 228	Cadle (1973)
Mainz, (Germany)	150	Ketserdis *et al.* (1976)
Various rural stations	23 - 44	Cadle (1973)
Deuselbach (Germany) rural	22	Ketserdis *et al.* (1976)
Jungfraujoch (3570 m), Switzerland	17.6	Hahn (1980)
North Atlantic	16.7	Eichmann *et al.* (1979)
Loop Head, Ireland	20.5	"
Cape Grim, Tasmania	31	"
West Pacific	13.3 - 27.3	Okita *et al.* (1986)
Gulf of Mexico	25	Parungo *et al.* (1990)

which ranged from 12 to 82 cm^{-3} for $r(\text{dry}) > 0.03\,\mu m$. On the other hand, the same authors found the concentration of $(NH_4)_2SO_4$ particles varied between 17 and 63 cm^{-3}, accounting for 36 to 74% of the total number of particles. This result is not surprising in light of our discussion in the previous section where we pointed out that the ocean is a significant source of organic sulfur in the form of DMS, which in marine air is converted to sulfate.

8.2.8.2 *Mass Concentrations (except Polar Aerosols)*

Table 8.11a summarizes typical values for the mass concentration of AP of all sizes irrespective of their chemical type. We notice that the total mass concentration generally ranges from 10 to a few hundred micrograms per cubic meter air. As expected from their number concentration, the mass load is highest in air over cities, less over rural areas, and lowest in air over oceans. Also, the mass load generally decreases with increasing elevation.

We shall now briefly turn to the mass concentration of AP of a specific chemical type. In Tables 8.11b and 8.11c, the mass concentrations of non-sea salt sulfate (NSS) and nitrate particles are listed for various urban, rural and ocean stations. We notice that the mass load of these particles typically ranges between 5 and

TABLE 8.11b

As Table 8-11a but for particulate non-sea salt sulfate (NSS) mass.

	Mass concentration ($\mu g/m^3$)	Observer
England, urban	8.1 - 14.6	Martin & Barber (1985)
Various U.S. cities, urban	6.1 - 23.0	Cadle (1973)
Various U.S. non-urban stations	1.9 - 6.5	Cadle (1973)
Continental US. outside B.L. (5-6 km)	0.13	Huebert & Lazrus (1980a, b)
Death Valley (remote)	0.09	Gillette & Blifford (1971)
Chacaltaya Mt. (5200 m), Bolivia	0.118	Adams *et al.* (1977)
Atlantic, near coast	2 - 5	Nguyen *et al.* (1974)
Virginia Key, Florida	2.8	Savoie *et al.* (1987)
Atlantic, open ocean	0.4 - 1.8	Nguyen *et al.* (1974), Fitzgerald (1991),
Bermuda	0.9	Savoie *et al.* (1987)
Spitzbergen	0.50 - 0.84	Heintzenberg *et al.* (1981)
West Pacific	0.8 - 1.5	Okita *et al.* (1986)
North Pacific	0.37 - 1.20	Prospero *et al.* (1985)
Pacific Ocean (5-6 km)	0.078	Huebert & Lazrus (1980a, b)
Indian Ocean	0.07 - 0.84	Horvath *et al.* (1981)
Mediterranean Ocean	8 - 9	Nguyen *et al.* (1974) Varhelyi & Gravenhorst (1983)
Gulf of Mexico	2.5	Parungo *et al.* (1990)

TABLE 8.11c

As Table 8-11a but for particulate nitrate mass.

	Mass concentration ($\mu g/m^3$)	Observer
Various U.S. cities, (urban)	2.2 - 9.4	Cadle (1973)
Claremont, California (urban)	12.5	Forrest *et al.* (1982)
Various U.S. (non-urban)	0.4 - 1.8	Cadle (1973)
N. Carolina (rural)	0.66	Shaw *et al.* (1982)
Abbeville, Louisana (rural)	0.9	Cadle *et al.* (1982)
free troposphere (continental air)	0.18	Huebert & Lazrus (1980a,b)
Pacific (tropical, equitorial)	0.11 - 0.29	Huebert (1980), Savoie *et al.* (1989)
West Pacific	0.2 - 1.3	Okita *et al.* (1986)
Bermuda (boundary layer)	0.6 - 0.9	Haste *et al.* (1988),
Bermuda (free troposphere)	0.2	Savoie *et al.* (1987)
Virginia Key (Florida)	1.9	Savoie *et al.* (1987)

TABLE 8.11d

As Table 8-11a but for particulate silicate mass.

	Mass concentration ($\mu g/m^3$)	Observer
Open Pacific	0.05 - 0.3	Fitzgerald (1991)
N. Atlantic with Sahara aerosol	0.01 - 8.0	"
Mauna Loa (3400 m)	8.6 (mean)	
(air trajectory from China)	28.6 (max)	Darzi and Winchester (1982)
N. Atlantic (Barbados)	400 (max)	Talbot *et al.* (1986)
Sahara and W. Coast of Africa		Schütz (1989)
Clear condition	50	
sand storm	10,000	
N.W. Indian Ocean with		Savoie *et al.* (1987)
aerosol from Middle Eastern deserts	7.6	
US High Planes		Hobbs *et al.* (1985)
av. soil particle load	5 - 10	
downwind dust storm	310	
in fringes of dust storm	625	

TABLE 8.11e

As Table 8-11a but for particulate organic carbon mass.

	Mass concentration ($\mu g/m^3$)	Observer
Various urban stations	1 - 110	Duce (1978)
Various rural stations	0.6 - 5.0	"
Bermuda	0.15 - 0.78	Hoffmann and Duce (1977, 1974)
Hawaii	0.36 - 0.43	Hoffmann and Duce (1977)
N. Atlantic (tropical)	0.33 - 0.93	Ketseridis *et al.* (1976)
N. Pacific (eastern tropical)	0.22 - 0.74	Barger & Garrett (1976)
S. Pacific (")	0.07 - 0.53	"
Loop Head, Ireland	0.28 - 0.80	Eichmann *et al.* (1979)
Mace Head, Ireland		
easterly winds	0.06 - 0.64	Jennings *et al.* (1993)
westerly winds	0.02 - 0.16	"
Urban site (France)	2.2 $\pm$ 1.3	Ducret & Cachier (1992)
Savannah (Ivory Coast)	0.36 $\pm$ 0.07	"
Mace Head (Ireland)	0.084 $\pm$ 0.065	"
Swedish Arctic	0.05 - 0.8	Noone & Clarke (1988)

TABLE 8.11f

As Table 8-11a but for particulate sea salt mass.

	Mass concentration ($\mu g/m^3$)	Observer
Atlantic (general)	1-55	Fitzgerald (1991)
N. Atlantic (central-north)	6.71 (mean)	Prospero (1979)
N. Atlantic (tropical-equatorial)	11.2 (mean)	"
S. Atlantic (tropical-central)	9.06 (mean)	"
Pacific (general)	8.44 (mean)	"
West Pacific	9.2 - 18.5	Okita *et al.* (1986)
Mediterranean Ocean	6.98 (mean)	Prospero (1979)
Indian Ocean	3.52 (mean)	"
Gulf of Mexico	8 (mean)	Parungo *et al.* (1990)

$20\,\mu g\ m^{-3}$ in air over cities, decreases to 1 to $5\,\mu g\ m^{-3}$ in air over rural stations, and assumes values between 0.1 and $1\,\mu g\ m^{-3}$ in maritime air.

Mass concentrations of AP separated according to the major size ranges and constituents have been determined by Junge (1956) for air over various continental and coastal stations (Figure 8.16). Note that with increasing proximity to oceans, the concentration of 'large' particles containing SO_4^{2-}, NH_4^+, NO_3^-, and Cl^- decreases. The same holds true for the concentration of 'giant' particles containing SO_4^{2-}, NH_4^+ and NO_3^-, while particles containing Cl^- in this size range become more frequent with increasing proximity to oceans. This trend has also been found by Rossknecht *et al.* (1973) in Oregon, Lodge (1955) in Puerto Rico, and Twomey (1955) in Australia.

In Table 8.11d, the mass concentration of silicate particles is listed for stations over desert areas and stations inside and outside the particle plumes downwind of deserts. We notice from this table that deserts are a significant source of aerosol particles. These may become transported downwind over considerable distances. Thus, according to Prospero and Bonatti (1969), Parkin *et al.* (1970, 1972), Jaenicke *et al.* (1971), Junge and Jaenicke (1971), Junge (1972b), and Prospero and Carlson (1972), the mass concentration of silicate particles in air over the Atlantic may range up to $100\,\mu g\ m^{-3}$ near the African coast within the Sahara dust layer typically located at about 3 km over the Atlantic. Outside this particle plume, the concentration is significantly lower, usually $0.05\,\mu g\ m^{-3}$ or less. The size of these silicate particles generally ranges between 0.3 and $20\,\mu m$ radius.

In Table 8.11e, the mass load due to particulate carbon in the atmosphere is given for a number of different stations. We notice that, contrary to expectation, these particles are widespread and not limited to the combustion sources of urban areas. We note that even over oceans, the mass load of particulate carbon ranges between 0.1 and $1\,\mu g\ m^{-3}$. Evidence for the dispersion of combustion aerosols in the global troposphere has also been provided by the presence of black carbon in remote areas such as Spitzbergen and the South Pole (Andreae, 1983a; Heintzenberg, 1982; Hanson *et al.*, 1988; Cachier *et al.*, 1990; Clarke, 1989).

Table 8.11f lists the mass concentration of sea salt particles found in air over

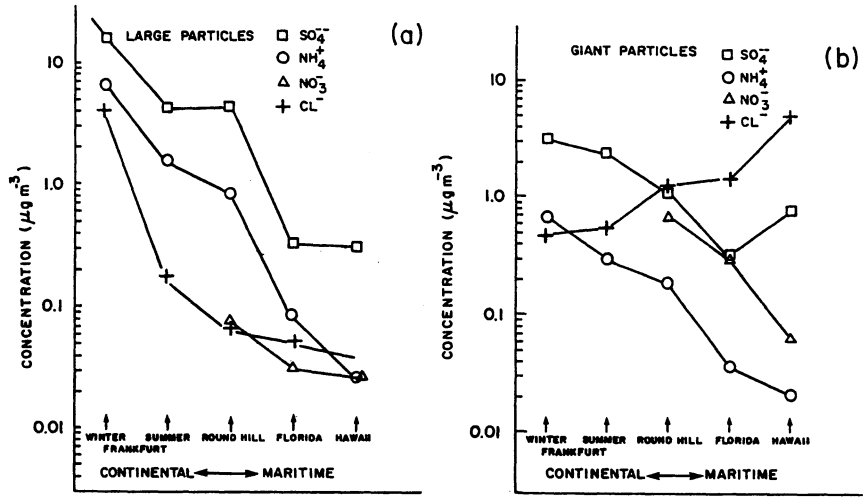


Fig. 8-16: Variation of the mass concentration SO_4^{2-}, NH_4^+, NO_3^-, and Cl^- in (a) 'large' particles, (b) 'giant' particles, captured at Frankfurt (Germany), at Round Hill near Boston, Mass., in Florida, and in Hawaii. (From Junge, 1956; by courtesy of *Tellus*.)

various oceans. As is the case with the number concentration, the total mass concentration of sea salt particles over oceans is found to be strongly dependent on the wind speed at ocean level. The observed dependence is summarized in Table 8.11g. We notice that the sea salt mass concentration increases exponentially with increasing wind speed. Using the values for A and B given by Lovett (1978) and Erikson *et al.* (1986) in Table 8.12, we find that the sea salt concentration varies from 4.5 μg m^{-3} with a light breeze (Beaufort 2) to 291 μg m^{-3} for full gale force winds (Beaufort 10).

TABLE 8.12

Variation of the mass concentration c of sea salt with wind speed U: $\ln c = AU + B$, for 15 to 600 m above the ocean.

A	B	Observer
0.16	1.45	Lovett (1978)
0.16	0.94	Woodcock (1953)
0.62	-8.01	Tsunogai *et al.* (1972)
0.16	1.45	Erikson *et al.* (1985b), $u \leq 15$ m sec^{-1}
0.13	1.89	Erikson *et al.* (1985b), $u > 15$ m sec^{-1}
0.13	1.77	Prodi *et al.* (1983)

8.2.8.3 *Total Mass and Number Concentration of Particles in Polar, Tropospheric Aerosols*

In conclusion, we shall consider briefly two types of aerosol of special significance: the Arctic aerosol, being the precursor of severe Arctic haze events, with an associated significant reduction in visibility, and the Antarctic aerosol, being of interest in conjunction with the observed ozone depletion events in the stratosphere.

A summary on the characteristics of Arctic air pollution has been provided in the text of Stonehouse (1986). Measurements of the chemical composition and of the mass and number concentration of Arctic aerosol particles have been carried out by Wilson *et al.* (1990, 1991), Hofmann (1990a,b), Barrie (1986), Barrie *et al.* (1981), Heintzenberg (1987), Radke *et al.* (1984), Bailey *et al.* (1984), Leaitch *et al.* (1984), Lazrus and Ferek (1984), and Hoff *et al.* (1983). These studies, which covered different Arctic regions such as Alaska, Arctic Canada, Arctic Norway, Sweden, Greenland, and Spitzbergen, have shown that air masses, despite their large distance from the main aerosol sources, are being polluted by man-made midlatitudinal emissions from fossil fuel combustion, smelting, and industrial processes. Arctic air pollution is most pronounced from December to April. The reason for this lies in the characteristics of the Arctic air mass, which exhibits subzero temperatures during much of the year, with the lowest values in winter. What little precipitation occurs mostly falls as drizzle from low stratus in the summer. Winter is characterized by very stable stratification and low levels of solar radiation. The absence of precipitating clouds and the pronounced temperature inversion associated with a strongly reduced vertical exchange of air during the winter half-year, favours the formation of a pronounced visibility-reducing haze layer. Also, during winter, the Arctic air mass extends sufficiently far south to allow the industrial regions to emit their pollution into this air mass. Most of the pollution mass is found to be located in the lowest 5 km of the troposphere. Chemically, sulfate is the most abundant compound found in the aerosol, its mass concentration ranging typically between 1.5 and 4.5 μg m^{-3}. In addition, nitrates, chlorides, and various metallic compounds, as well as combustion-generated carbon, were found. Most particles sampled had sizes ranging between 0.1 to 1.0 μm, with a maximum volume concentration near 0.3 μm diameter. They are present in concentrations ranging between 50 and 1000 cm^{-3}, with highest concentrations near the top (about 3 km) of the haze layer. These particles, foremost those containing graphitic carbon and sulfate, scatter and absorb visible radiation efficiently (Bodhaine *et al.*, 1981; Rosen *et al.*, 1981,) and appear to be responsible for the turbid Arctic haze. Apart from aerosol particles, gases such as SO_2, perfluorocarbons, and pesticides are also present in Arctic air. The acidic nature of Arctic pollution is reflected in the acidity of the cloud and precipitation water, of the snow pack, and of the glacier snow in the Arctic.

The aerosol over the ice sheet of the Antarctic has been studied by Hogan (1975), Hogan *et al.* (1979), Parungo *et al.* (1979), Ito (1985), Bodhaine *et al.* (1986), Ito *et al.* (1986), Shaw (1988), and Harvey *et al.* (1991). These studies all pertain to measurements close to the ground. Vertical variations will be discussed in Section 8.2.10. In air near the surface, Harvey *et al.* found at Buttler Point

station during summertime the total number concentration of 'large' and 'giant' particles typically range between about 9 and 90 cm^{-3}. The total number of Aitken particles ranged between a maximum of 6008 and a minimum of 39 cm^{-3} with a mean of 960 cm^{-3}. The total mass concentration ranged between about 0.1 and 3.7 $\mu g\ m^{-3}$. Aerosol particles were found to be made typically of crustal material, meteoritic compounds, NaCl, $(NH_4)_2SO_4$ and H_2SO_4. The mass concentration of sulfate ranged between 0.3 and 0.5 $\mu g\ m^{-3}$, that of nitrate between 0.14 and 0.19, and that of chloride between 0.26 and 0.32 $\mu g\ m^{-3}$. Particles with diameters less than 0.1 μm consisted entirely of sulfur compounds, while particles with diameters above 0.5 μm consisted of sea salt. These mass concentrations are similar to those reported by Bigg (1980) at the South Pole (0.14 $\mu g\ m^{-3}$) for particle sizes between 0.06 and 2 μm in diameter, and those reported by Radke and Lyons (1982) 90 m above the ice shelf (0.24 $\mu g\ m^{-3}$).

8.2.9 Size Distribution of AP

The size distribution of aerosol particles may be expressed in various ways. If $n(r)\mathrm{d}r$ denotes the number of AP cm^{-3} with radii between r and $r + \mathrm{d}r$, then the total concentration of AP of radii larger than r is

$$N(r) = \int_r^\infty n(r)\mathrm{d}r\,. \tag{8-33}$$

Accordingly, we also have

$$-\frac{\mathrm{d}N}{\mathrm{d}r} = n(r)\,. \tag{8-34}$$

Because of the wide range of particle sizes, it is often more convenient to express the size distribution in logarithmic form by defining $n^*(r)\mathrm{d}\log r$ as the number of AP cm^{-3} in the interval r, $r + \mathrm{d}\log r$. Then, the relation between N and n^* is

$$-\frac{\mathrm{d}N}{\mathrm{d}\log r} = n^*(r)\,. \tag{8-35}$$

It is customary to use logarithms to base 10. Adopting this convention and using the usual notation ln for the natural logarithm, we see that

$$n^*(r) = (\ln 10)rn(r)\,. \tag{8-36}$$

On the basis of his own observations and those of others, Junge (1952b, 1953, 1955, 1969a, 1972a,b,c, 1974) found that for $r > 0.1\,\mu m$ the concentration of AP decreases with increasing size such that $n^*(r)$ can be expressed approximately as a power law function of r, so that

$$n^*(r) = \frac{C}{r^\alpha}\,, \tag{8-37}$$

where C and α are constants. The other forms of this law become

$$n(r) = \frac{C}{(\ln 10)r^{\alpha+1}}\,, \tag{8-38}$$

and

$$N(r) = \frac{C}{(\alpha \ln 10) r^{\alpha}} . \tag{8-39}$$

The corresponding log radius volume (V) surface (s), and mass (m) distributions are

$$-\frac{\mathrm{d}V}{\mathrm{d}\log r} = -\frac{4\pi r^3}{3}\frac{\mathrm{d}N}{\mathrm{d}\log r} = \frac{4\pi}{3} C r^{(3-\alpha)} , \tag{8-40}$$

$$-\frac{\mathrm{d}S}{\mathrm{d}\log r} = -4\pi r^2 \frac{\mathrm{d}N}{\mathrm{d}\log r} = 4\pi C r^{(2-\alpha)} , \tag{8-41}$$

and

$$-\frac{\mathrm{d}m}{\mathrm{d}\log r} = -\frac{4\pi r^3}{3}\rho(r)\frac{\mathrm{d}N}{\mathrm{d}\log r} = \frac{4\pi}{3} C \rho(r) r^{(3-\alpha)} . \tag{8-42}$$

Note that in the special case of $\alpha = 3$, $\mathrm{d}V/\mathrm{d}\log r =$ constant.

Representative size distributions of AP over continents are given in Figures 8.17 and 8.18. The figures demonstrate that for $r > 0.1\,\mu$m, the concentration of AP decreases with increasing particles size, the decrease roughly following a power law with $3 \leq \alpha \leq 4$, on the average. Another example of a power law is shown in Figure 8.19 for the background aerosol in Nepal at 4900 m elevation (Ikegami *et al.*, 1978).

It has become customary in the literature to subdivide the aerosol in continental air masses into the categories urban, rural, remote continental, background, desert, and polar aerosol (Jaenicke, 1988). For each aerosol type, numerous measurements of the size distribution are available in the literature. Jaenicke (1988) has attempted to characterize these distributions by a 'typical' distribution applying to each category. These are given in Figure 8.20a,b in terms of the number and corresponding volume distributions. We notice from Figure 8.20a that the number distribution of each category can be approximated by a Junge power law for $r \geq 0.1\,\mu$m. A power law also fits the size distribution of Arctic aerosol particles of $r \geq 0.1\,\mu$m observed by Radke *et al.* (1984) at Barrow Alaska (Figure 8.21) and the size distribution of particles in Antarctica for $r > 0.05\,\mu$m observed by Ito (1985) (see Figure 8.22).

A power law also approximates the size distribution of particles of a specific chemical type. For silicate particles in air over the Libyan Desert, for instance, Schütz and Jaenicke (1974) found $\alpha \approx 2$ for $1 \leq r \leq 10\,\mu$m, and $\alpha \approx 3$ for $r > 10\,\mu$m, on the average. An example of such a distribution is given in Figure 8.23 based on the observations of d'Almeida and Schütz (1983). Gillette *et al.* (1974) found similar results near Big Spring, Texas. A power law was found to apply also to sulfate particles of $0.2 \leq r \leq 3\,\mu$m sampled by Georgii and Gravenhorst (1972) in continental air over Germany (see Figure 8.24); to biogenic particles of $r \geq 1\,\mu$m studied by Matthias (1992) in Mainz, Germany (see Figure 8.25); to soot particles of $r \geq 0.1\,\mu$m (Figure 8.26) observed by Meszaros (1984); and to NaCl and $(NH_4)_2SO_4$ particles of $r \geq 1\,\mu$m in maritime air (Figure 8.27) analyzed by Meszaros and Vissy (1974).

Inspection of all these figures show that near $r = 0.1\,\mu$m the AP concentration reaches a maximum. This might have been expected on the basis of the rapid

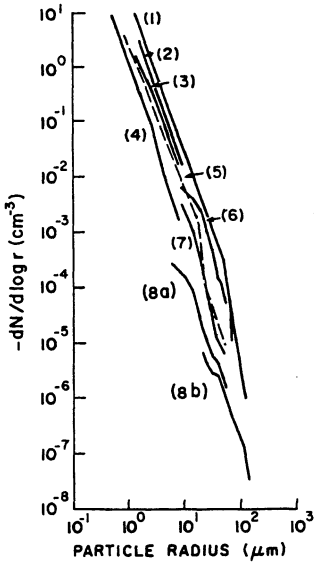


Fig. 8-17: Size distribution of aerosol particles (1 μm $\leq r \leq$ 100 μm) in air over various locations in Central Europe, Japan, and the U.S. (1) Data of Noll and Pilat (1971), Seattle, State of Washington. (2) to (8) Data of Jeanicke and Junge (1967): (2) Frankfurt (Germany), 1952; (3) Taunus (Germany), 800 m, 1952; (4) Zugspitze (Germany), 3000 m, 1952; (5) Yokomansbetsu (Japan) 1050 m (Okita, 1955); (6) Mainz (Germany), 1962; (7) Taunus, 1962; (8a,b) Jungfrauljoch (Switzerland), 3570 m, 1963.

attachment of particles smaller than 0.1 μm to larger ones by thermal (Brownian) coagulation, in a way which reduces their number concentration progressively with decreasing size (see Section 11.5). However, Junge (1972b) speculated that, following a local minimum caused by the coagulation effect, the AP concentration rises once more as result of continuous gas-to-particle conversion for particles $r < 0.01\,\mu$m. A local minimum and a second maximum was indeed observed by Junge (1972b) and Abel *et al.* (1969) over the North Atlantic. It is also implied by the measurements of Meszaros and Vissy (1974) over the oceans of the Southern Hemisphere, since the total concentration of Aitken particles they observed was larger by one order of magnitude than the concentration of AP with $r > 0.03\,\mu$m.

Maritime aerosol particles usually exhibit a bimodal size distribution. This feature, illustrated in Figures 8.28a,b, has been confirmed in numerous field studies over the Atlantic and Pacific by Hoppel *et al.* (1990, 1986, 1985) and Hoppel and Frick (1990). We notice from Figure 8.28a that the first mode in the number distribution occurs at a particle radius of 0.03 to 0.04 μm, separated from the second mode at about 0.1 μm by a minimum at a particle radius of about 0.06 μm. This feature is also well-documented by other observers, e.g., Haaf and Jaenicke (1980), and Meszaros and Vissy (1974) (see also Fitzgerald , 1991). Chemical analysis (Meszaros and Vissy, 1974), as well as analysis by heating the aerosol samples, shows that the particles in both modes of Figure 8.28 consist of $(NH_4)_2SO_4$, as the

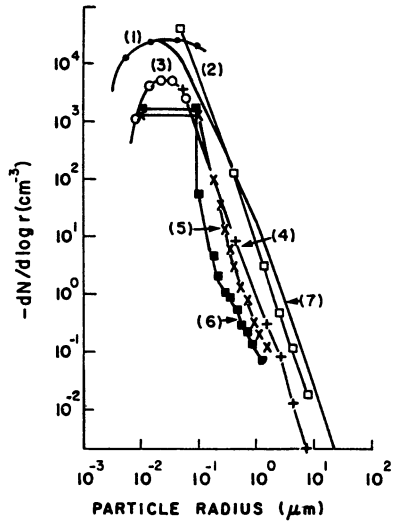


Fig. 8-18: Size distribution of aerosol particle (10^{-2} μm $\leq r \leq$ 10 μm) in air over various locations in Central Europe and the U.S. (Data of Junge, 1955): (1) Frankfurt, ion counter; (2) Frankfurt, nuclei counter and impactor; (3) Zugspitze, 3000 m, ion counter; (4) Zugspitze, 3000 m, nuclei counter and impactor. Data of Junge *et al.* (1969) with Royco counter and nuclei counter: (5) Crater Lake, 2200 m without subsidence; (6) Crater Lake, 2200 m with subsidence. Data of Noll and Pilat (1971) with impactor: (7) Seattle, State of Washington.)

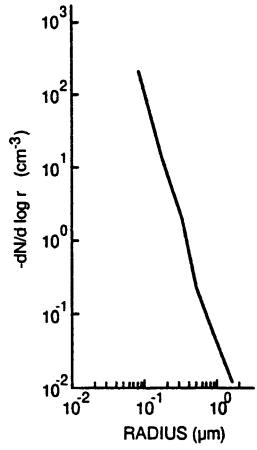


Fig. 8-19: Size spectrum of aerosol particles in a background aerosol, observed at Shorong Base Camp (Nepal, 4900 m). Average total particle concentration for $r > 0.05$ μm: 200 cm^{-3}. (From Ikegami *et al.*, 1978, with changes.)

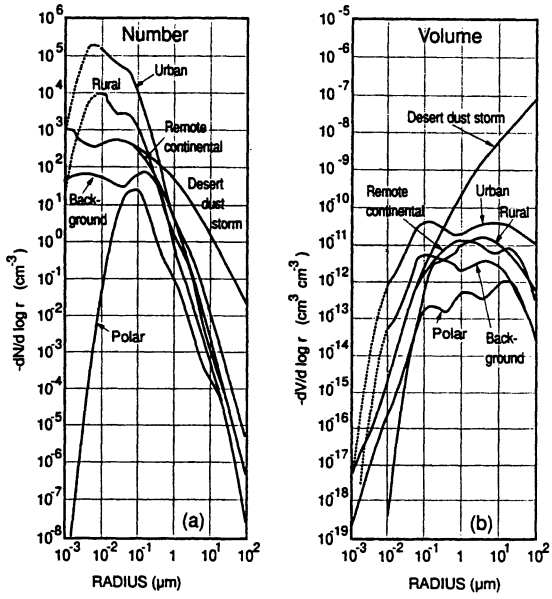


Fig. 8-20: Number size (a) and volume size (b) distribution of aerosol particles of various types. (From Jaenicke, 1988, with changes.)

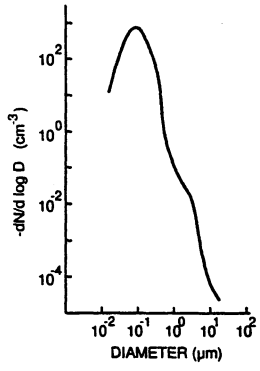


Fig. 8-21: Size spectrum of aerosol particles in an arctic aerosol, observed at Barrow, Alaska. (From Radke *et al.*, 1984, with changes.)

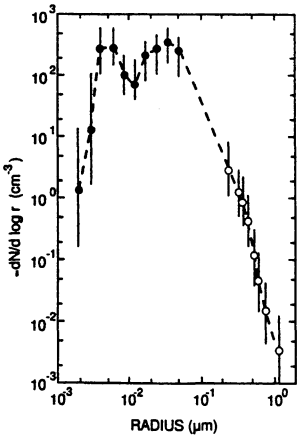


Fig. 8-22: Size spectrum of aerosol particles in an Antarctic aerosol observed at Syowa Station, Antarctica, September to December. • by diffusion decay technique, ○ by optical particle counter. (From Ito, 1985, with changes.)

particles are volatile when heated above 150°C (Twomey, 1968, 1971; Dinger *et al.*, 1970). The volatility of ammonium salts has also been documented by Pinnick *et al.* (1987), who experimentally determined that NH_4Cl and $(NH_4)_2SO_4$ sublime above 120 and 150°C, respectively, while NaCl does not sublime, but rather melts at 800°C and boils at 1400°C. Hoppel *et al.* (1990, 1986, 1985) and Hoppel and Frick (1990) have argued that the sulfate particles making up the first mode are due to GPC involving the conversion of DMS ($CH_3S\ CH_3$) to sulfate. The sulfate particles making up the second mode are considered to be the result of DPC involving drops of maritime stratus, stratocumulus and cumulus, which, during their life time, absorbed DMS-derived SO_2. After oxidation of the absorbed SO_2 in the cloud water, sulfate particles form subsequent to cloud evaporation (Hoppel, 1994). Assuming that during the approximate nine day residence time of atmospheric water vapor, about nine evaporation condensation cycles take place on the average, sufficient aerosol material would be produced by DPC to account for the second peak in the distribution (Hoppel *et al.* 1990, 1986, 1985).

An important feature exhibited by all the maritime volume spectra is the inflection point in the radius range 0.3 to 0.5 μm (see Figure 8.28b). Fitzgerald (1991) suggests that in this size range a transition takes place between two totally different sources of particles: (1) the bubble-burst mechanism producing sea salt particles, and (2) the various mechanisms producing sulfate particles. This result is also consistent with the conclusion of Junge (1963a) and the field observation of Parungo and Pueschel (1980), Savoie and Prospero (1982), Mamane and Mehler (1987) and Parungo *et al.* (1986a,b), who showed by chemical analysis that sulfate particles occur in the submicron size range, while particles in the supermicron size range consist of sea salt particles, some of which have become converted to $NaNO_3$ by reaction with HNO_3.

However, in the previous section, we noted that during the bubble-burst mech-

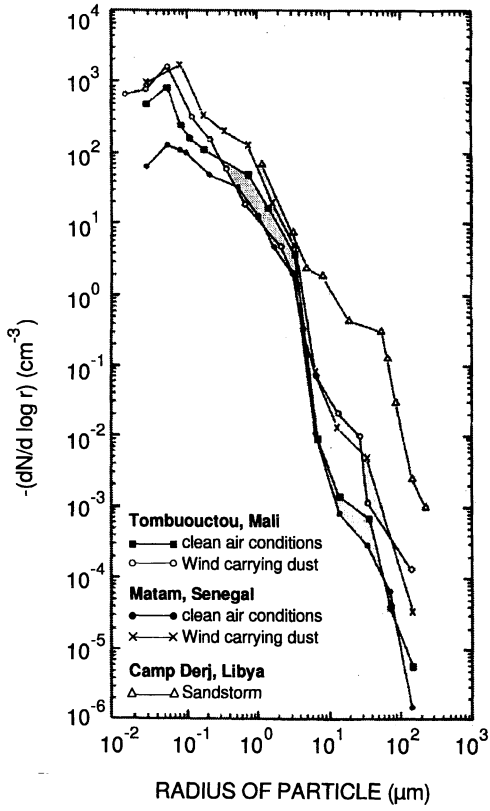


Fig. 8-23: Size spectrum of aerosol particle at various locations over the Sahara desert. (From d'Almeida and Schütz, 1983, with changes.)

anism, the disruption of the bubble cap produces sea salt particles of radius between 0.3 and 0.07 μm. We must therefore expect that sea salt particles are not only present in the supermicron size range, but also in the submicron size range. This expectation is well-documented by the observations of Meszaros and Vissy (1974), which are shown in Figure 8.26. We notice that the size distribution of NaCl particles ranges down to about 0.07 μm radius. This figure shows further that an inflection is also present in the number distribution of sea salt particles. Meszaros and Vissy suggested that this is due to a change in the particle production mechanisms. Thus, sea salt particles of $m_s > 2 \times 10^{-13}$ g ($r_{dry} = 0.28\,\mu$m) are due almost exclusively to jet drops formed during the bubble-burst mechanism, while particles of $10^{-15} \leq m_s \leq 2 \times 10^{-13}$ g ($0.07 \leq r_{dry} \leq 0.28\,\mu$m) result from the disintegration of the bubble cab. Woodcock and Duce (1972) and Woodcock (1972) independently drew the same conclusions from their observations of sea salt particles over the Pacific near Hawaii and over the Gulf of Alaska. Thus, we conclude that the transition from an ammonium sulfate dominated marine aerosol to a sodium chloride dominated one is regulated by the transition between the two

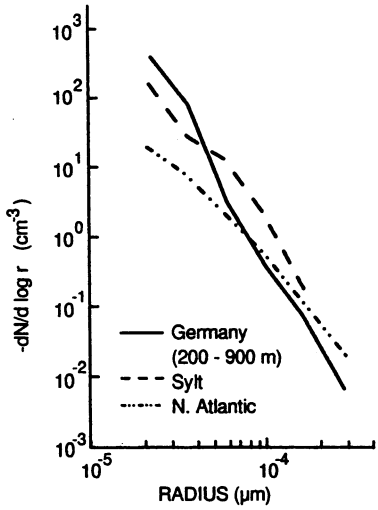


Fig. 8-24: Size spectrum of sulfate particles at various locations. Total concentration: 300 to 600 cm^{-3}. (From Georgii and Gravenhorst, 1972, with changes.)

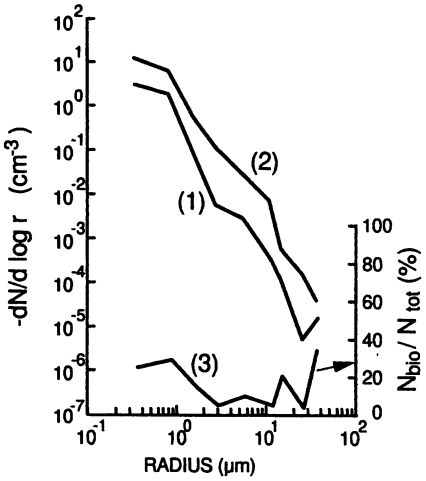


Fig. 8-25: Size spectrum of biological aerosol particles in air over suburbs of Mainz, Germany: (1) biological particles, (2) all particles, (3) biological fraction. (From Matthias, 1992, with changes.)

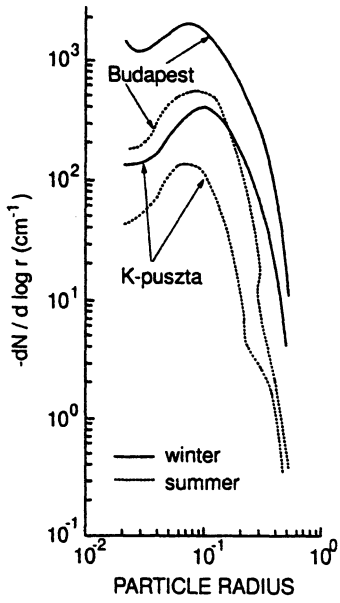


Fig. 8-26: Size spectrum of elemental carbon particles observed in air over Budapest and K-puszta (Hungary). (From Meszaros and Meszaros, 1989, with changes.)

sea salt production mechanisms.

The multimodal nature of the atmospheric aerosol demonstrates clearly that the Junge power law alone does not suffice to describe the size distribution. Better descriptions may be constructed through the superposition of analytical forms such as the gamma or lognormal distributions. For example, Jaenicke (1988) suggested to describe the aerosol size distribution by a relation of the form

$$-\frac{\mathrm{d}N}{\mathrm{d}\log r} = n^*(r) = \sum_{i=1}^{m} \frac{n_i}{(2\pi)^{1/2}\log\sigma_i} \exp\left[-\frac{\left(\log\frac{r}{R_i}\right)^2}{2(\log\sigma_i)^2}\right], \qquad (8\text{-}43)$$

where often it suffices to let $m = 3$, and where n_i is the total number of particles in mode i, R_i is the corresponding geometric mean aerosol particle radius, and σ_i is the standard deviation of the ith mode. Values for n_i, r_i and σ_i for the model distributions given in Figure 8.20 are listed in Jaenicke (1988) and in Table 8.13.

Some aerosol size distributions are too complex to be easily fitted by any simple theoretical distribution. Such an example is shown in Figures 8.29 for the size distribution of particles sampled relatively close to volcanic emission sites. Another complex distribution is given in Figure 8.30 for the case of an aerosol sampled near burns of forest slash.

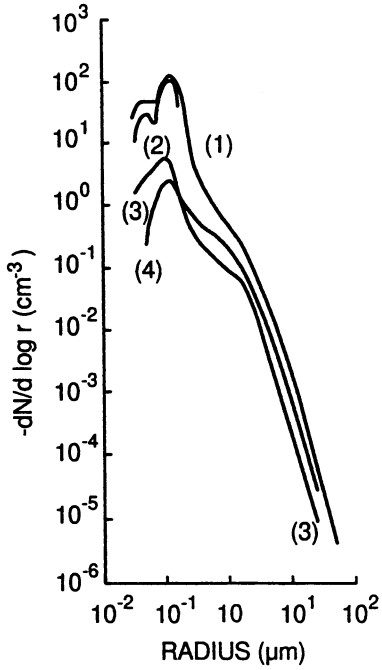


Fig. 8-27: Size spectrum of aerosol particles in air over Southern Hemispheric oceans at ship site during voyage of ship 0 to 20°S, wind speed 6 m sec^{-1}, total number of particles (Aitken) = 440 cm^{-3}, $N(r > 0.03\ \mu m) = 55$ cm^{-3}: (1) all particle, (2) $(NH_4)_2SO_4$, (3) long shaped particles, (4) NaCl, (5) non-cubic, crystalline particles. (From Meszaros & Vissy, 1974, with changes.)

8.2.10 Vertical Variation of the Number and Mass Concentration

From Tables 8.9 and 8.11a,b,c, which include observations at higher elevations, it is evident that the number and mass concentrations of aerosol particles decrease with increasing altitude.

More detailed studies of the variation of the total number concentration of aerosol particles with altitude have been made, e.g., by Isaac and Daum (1987) over Ontario, Canada, and by Selezneva (1966) over the continental U.S.S.R. The latter measurements are exhibited in Figure 8.31, and show that in the lowest 6 km of the atmosphere the number concentration decreases exponentially. A similar variation of Aitken particles with height was found in air over the mid and lower latitudes by Weickmann (1957b), Junge (1961, 1963b), and Junge *et al.* (1961a) in air over Germany, the eastern U.S., and India, and by Rosen *et al.* (1978) in air over Fairbanks (Alaska), Panama, and Laramie (Wyoming). We note from these observations, illustrated by Figure 8.32 of Junge (1963b) that, following an exponential decrease of the particle concentration in the lowest 5 to 6 km of the troposphere, the concentration in the upper troposphere remains nearly constant at a value between 50 to 500 cm^{-3}, with a most frequent value near 200 cm^{-3}.

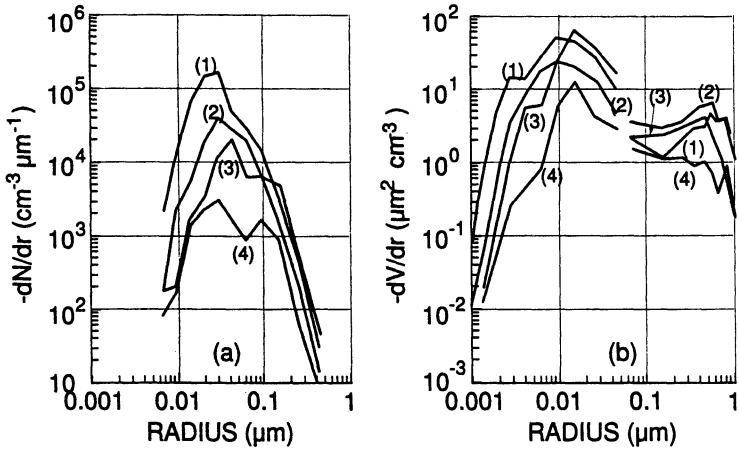


Fig. 8-28: Number-size (a) and volume-size (b) distribution of maritime aerosol particles in air over ocean at ship site during voyage of ship from Charleston, S. Carolina across the tropical N. Atlantic to Canary Islds. Transition from continental to maritime air masses. (1) $N = 5300$ cm^{-3}, (2) $N = 1740$ cm^{-3}, (3) $N = 1150$ cm^{-3}, (4) $N = 200$ cm^{-3}. (From Hoppel *et al.*, 1990, with changes.)

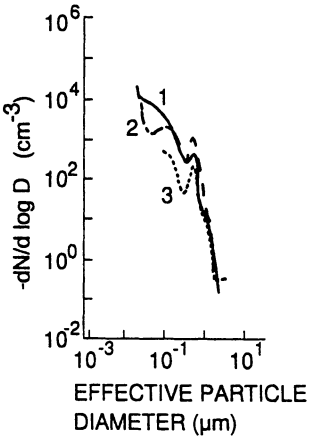


Fig. 8-29: Size spectrum of aerosol particles in different types of volcanic eruption plumes. (1) Mt. Mageik, Alaska, April 21, 1977, 2 km downwind; (2) Mt. Martin, Alaska, April 21, 1977, 2 km downwind; (3) Mt. Baker, Washington, June 30, 1975, 3.7 km downwind. (From Stith *et al.*, 1978, with changes.)

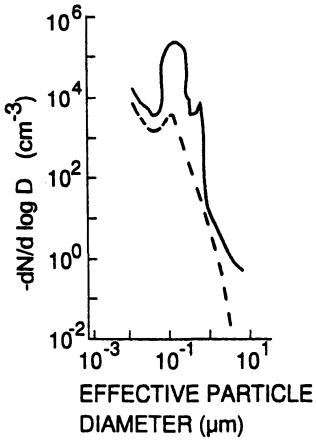


Fig. 8-30: Size spectrum of aerosol particles in plumes from burns of prescribed burning of forest slash, at 1825 m altitude 10 km downwind of burn (continuous line); dashed line: size distribution in ambient air. (From Stith *et al.*, 1981.)

TABLE 8.13

Parameters for the maritime, the remote continental, the rural, and the urban aerosol particle distribution as given by (8-43). n_i = total number of aerosol particles cm^{-3}, R_i = geometric mean particle radius in μm, σ_i = standard deviation in mode i. (From Jaenicke, 1988.)

Mode	Size interval (μm)	n_i (cm^{-3})	$R_i(\mu\text{m})$	log σ_i
Maritime				
1	$0.001 < r < 0.$	133	0.0039	0.657
2	$0.1 < r < 1$	66.6	0.1330	0.210
3	$0.1 < r < 1$	3.06	0.2900	0.396
Remote continental				
1	$0.001 < r < 0.1$	997	0.0010	0.328
2	$0.001 < r < 0.1$	842	0.0218	0.505
3	$r > 1$	0.00071	6.2400	0.277
Rural				
1	$0.001 \leq r \leq 0.1$	6650	0.00739	0.225
2	$0.001 \leq r \leq 0.1$	147	0.0269	0.557
3	$0.001 \leq r \leq 0.1$	1990	0.0419	0.266
Urban				
1	$0.001 < r < 0.1$	99300	0.00651	0.245
2	$0.001 \leq r \leq 0.1$	1100	0.00714	0.666
3	$0.001 \leq r \leq 0.1$	36400	0.0248	0.337

Aerosol particles of these concentrations constitute what is termed the tropospheric background. This background aerosol is clearly evident in the tropospheric distribution of number and mass load summarized in Figures 8.33 and 8.34 (Jaenicke, 1992).

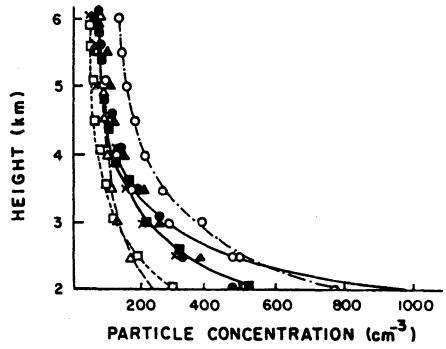


Fig. 8-31: Variation of the number concentration of Aitken particle with height over various cities of the U.S.S.R. (From Selezneva, 1966; by courtesy of *Tellus*.)

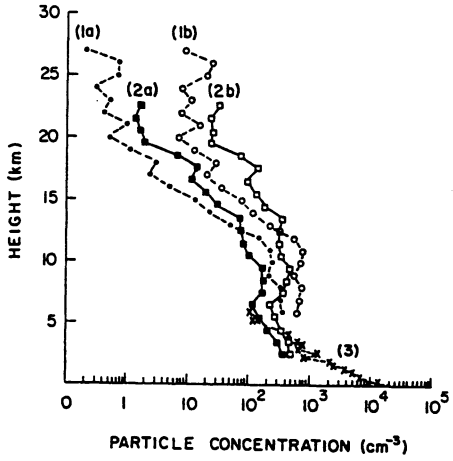


Fig. 8-32: Variation of the average number concentration of Aitken particles with height over various locations. (1a) Seven flights over Sioux Falls (S. Dakota, U.S., 44° N, June, 1959; July, 1960). Concentration in number cm^{-3} (ambient); data of Junge. (1b) Same as (1a) but concentration in number cm^{-3} (STP); data of Junge. (2a) Flights over Hyderabad (India, 17° N, March to April, 1961). Concentration in number cm^{-3} (ambient); data of Junge. (2b) Same as (2a) but concentration in number cm^{-3} (STP); data of Junge. (3) Data of Weickman (1957a,b) based on flights over Germany. (From Junge, 1963b; by courtesy of *J. de Rech. Atmos.*, and the author.)

In contrast to the total number concentration and mass load of AP, the vertical variation of AP of a specific chemical type often shows a quite irregular decrease

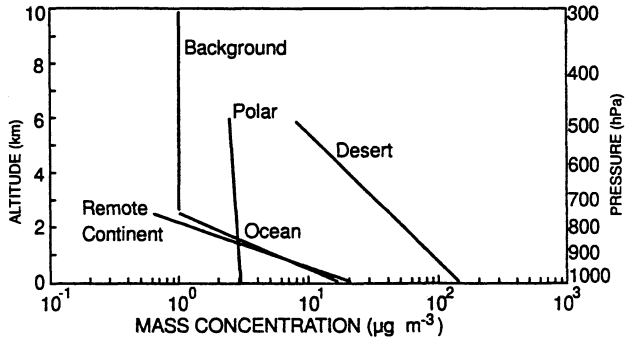


Fig. 8-33: Model for the vertical distribution of the aerosol mass concentration of aerosol particles in various aerosol types of the troposphere. (From Jaenicke, 1992; by courtesy of the author, copyright A. Deepak Publ. Co.)

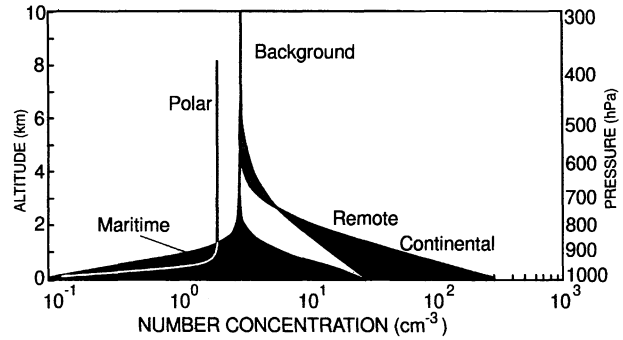


Fig. 8-34: Model for the vertical distribution of the number concentration of aerosol particles in various aerosol types of the troposphere. (From Jaenicke, 1992; by courtesy of the author, copyright A. Deepak Publ. Co.)

with altitude. These irregularities are mainly due to a specific sink mechanism for the particles. For example, water soluble particles act as cloud condensation nuclei and therefore will experience local minimum concentrations near the cloud level. The vertical variation of chloride particle concentrations has been measured by Twomey (1955) over Australia, by Byers *et al.* (1957) over various locations between central Illinois and the Gulf of Mexico, and by Podzimek and Cernoch (1961) over northern Bohemia. All three investigators agreed that chloride particles are very efficiently removed at cloud level.

Georgii *et al.* (1971) made a detailed study of the vertical variation of sulfate particles over various locations in Germany. Although the concentration varied strongly from day to day, average concentrations decreased with increasing height in a manner illustrated in Figure 8.35. Two additional observations of cloud physical significance were made by Georgii *et al.*: (1) Local maxima in the concentration of sulfate particles were found at cloud level and most often just below cloud

base. This observation was interpreted in terms of a sulfate-forming process taking place inside cloud drops. Further evidence for this effect was given by Radke and Hobbs (1969), and by Easter and Hobbs (1974). (2) The sulfate content of AP of a given size was found to increase with height while at the same time the size of particles containing a given percentage of sulfate was found to decrease with height (see Figure 8.36). Considerable structure in the vertical variation of the total particle concentration has also been found by Dreiling (1992) during flights over Germany. The results of one particular flight are given in Figure 8.37a,b in terms of the particle number distribution (a), and the particle surface distribution (b). We notice the very pronounced structure in the number and surface area distributions of AP which reflects the temperature inversion near 1400 altitude, as well as inhomogeneities in the aerosol concentration due to other causes.

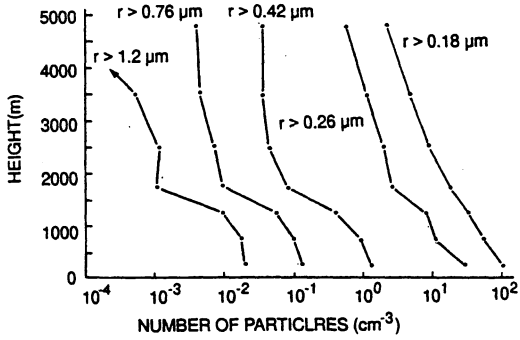


Fig. 8-35: Variation of the average concentration of sulfate particles with height over various locations in West Germany. (From Georgii *et al.*, 1971; by courtesy of the authors.)

The vertical variation of sea salt over the oceans was studied by Woodcock (1953, 1957) and Lodge (1955) over subtropical oceans, by Junge *et al.* (1969) over Cape Blanco (Pacific Coast, Oregon), and by Hobbs (1971) and Blanchard *et al.* (1984) over the Pacific. Although on individual days a vertical profile may look rather irregular (Lodge, 1955), in the mean an exponential decrease is observed above 0.5 km, suggesting that sea salt over the oceans is essentially confined to the lowest 2 to 3 km of the troposphere. This behavior is illustrated in Figure 8.38.

Figures 8.27 and 8.39a,b display some measurements of AP size distributions over the Northern and Southern Hemispheric oceans. It is evident that, for $r > 0.1\,\mu$m, the size distributions over oceans may be represented adequately by power laws with $3 \lesssim \alpha \lesssim 5$. As expected, the distributions shift towards lower concentrations with increasing height (compare Figures 8.39a and 8.39b). Note that Figure 8.39b describes the background aerosol. Figures 8.39b and 8.27 further indicate that the size distribution becomes steeper for $r > 20\,\mu$m, a trend also indicated in the continental distribution. Note that no clear upper limit in particle size can be seen. Although particles of $r > 20\,\mu$m are produced by the bubble-burst mechanism at the ocean surface, Toba's (1965a,b) theoretical estimates suggest that gravity prevents such particles from penetrating the turbulent boundary layer

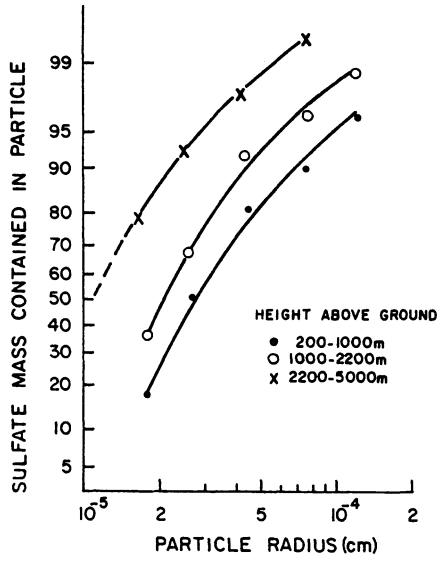


Fig. 8-36: Percentage of sulfate mass contained in atmospheric aerosol particles smaller than a given size at different heights. (From Georgii *et al.*, 1971; by courtesy of the authors.)

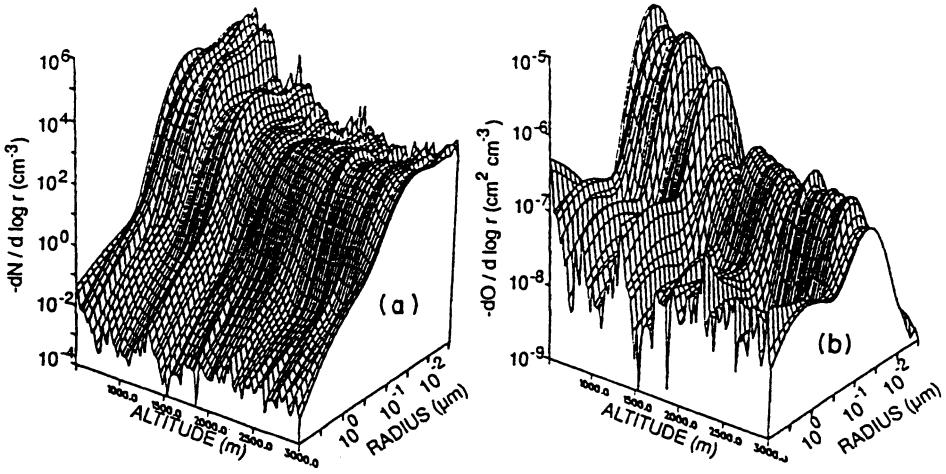


Fig. 8-37: Vertical variation of the number-size distribution (a), and the surface area size distribution (b), of aerosol particles observed over Germany. Inversion at 1400 m above ground. (From Dreiling, 1992, with changes.)

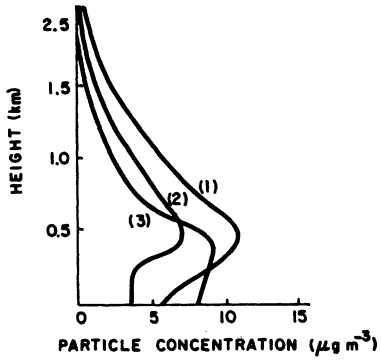


Fig. 8-38: Vertical variation of the mass concentration of sea salt in air (1) over the Pacific near Hawaii, (2) over the Atlantic near Florida, and (3) over the Caribbean. (From Erikson, 1959, based on data of Woodcock; by courtesy of *Tellus*.)

over the oceans to reach higher layers. As an explanation of their presence, Toba (1965a,b) and Junge (1963, 1972b) have suggested that these particles represent residues of evaporated drops.

Above the local tropopause, the total number concentration of AP decreases rapidly to reach values between 1 and 10 particles cm^{-3} (ambient) near 20 km altitude. The early observations of Junge *et al.* (1961a), and the later observations of Rosen *et al.* (1978) for mid and low latitudes, show that the concentration remains near this value at least up to about 30 km (see Figure 8.32). More recent observations in air over Arctic Kiruna (69°N), Sweden shows the same trend (Figure 8.40). A somewhat different trend is seen in Figure 8.41 for air over McMurdo Station (78°S), Antarctica. Here we notice that the total number concentration of AP reaches a broad minimum between 15 and 22 km and then increases again to reach concentrations between 50 and 100 cm^{-3} (ambient) near 25 km (Hoffmann and Deshler, 1991). According to these authors, this increase in particle concentration has a photochemical origin. Studies of the total particle concentration of the stratosphere by Rosen (1974), Podzimek *et al.* (1974, 1975), Käselau (1975), and Cadle and Langer (1975) have shown that immediately above the tropopause the concentration of Aitken particles may be subject to orders of magnitude variations. Podzimek *et al.* and Cadle and Langer suggested that these fluctuations in concentration may also be the result of gravity waves lifting particle-rich air masses from below.

In contrast to the vertical fall-off in the total number concentration of AP, the concentration of 'large' particles first decreases in the troposphere, but then increases again in the stratosphere to a broad maximum between 15 and 25 km (Figure 8.42). This aerosol layer was first observed by Junge *et al.* (1961a,b), Chagnon and Junge (1961) and Junge and Manson (1961). Following Junge's measurements, other researchers verified the existence of this layer and established it as a world-wide phenomenon (Rosen, 1969; Lazrus and Gandrud, 1974; Turco

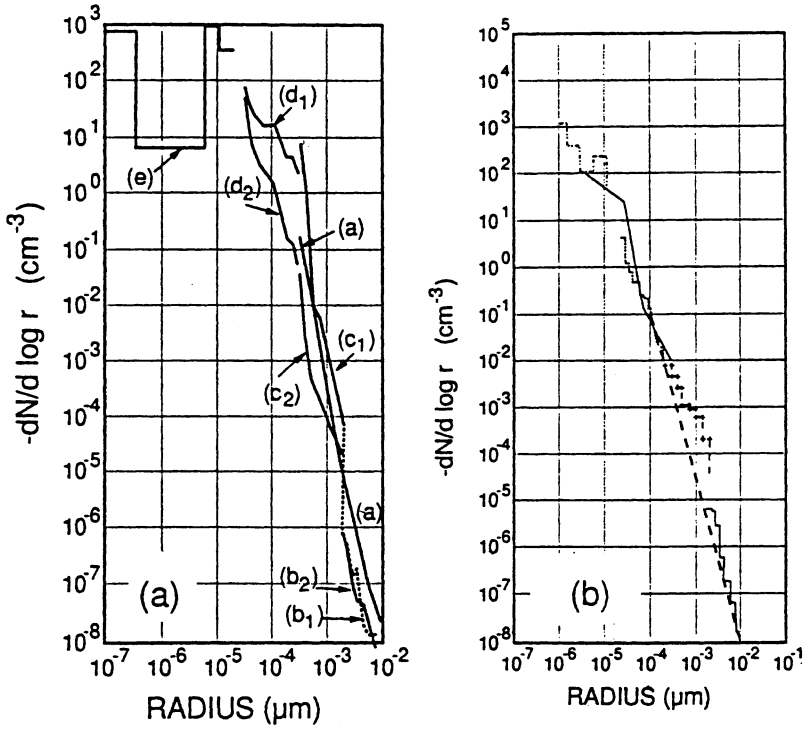


Fig. 8-39:a. Size distribution of aerosol particles in air over Atlantic taken during voyage of ship 'RV Meteor' along 30°W from 10°S to 60°N: (a) sea salt distribution, (b_1,c_1) data from impactors on days with Sahara dust, (b_2, c_2) data from impactors on days without Sahara dust, (d_1) data from Royco counter on days with Sahara dust, (d_2) data from Royco counter on days without Sahara dust, (e) data from a combination of a photographic nucleus counter, diffusion boxes, and electric denuders. (From Junge, 1972b, by courtesy of the author; copyrighted by Am. Geophys. Union.)

Fig. 8-39:b. Size distribution of aerosol particles in air over the N. Atlantic at Izana Obs., Teneriffa (2370 m). The straight dashed line represents the results of the theoretical model discussed in Section 11.7.5. Data taken with impactors, Royco counter, Scholz nucleus counter, and ion spectrometer. (From Abel *et al.*, 1969; by courtesy of *Meteor. Rundschau.*)

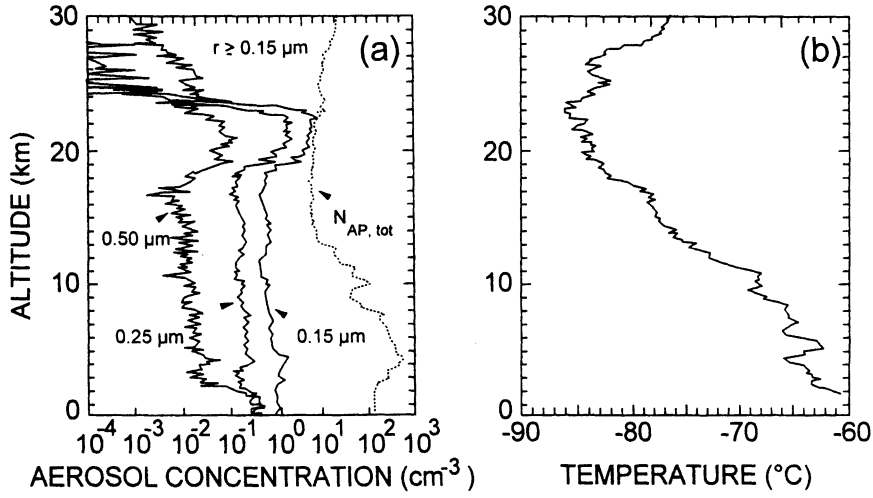


Fig. 8-40: Vertical variations of total aerosol particle concentration (a), and of temperature (b), in air over Kiruna (Sweden), January, 1990. (From Hofmann *et al.*, 1990, with changes.)

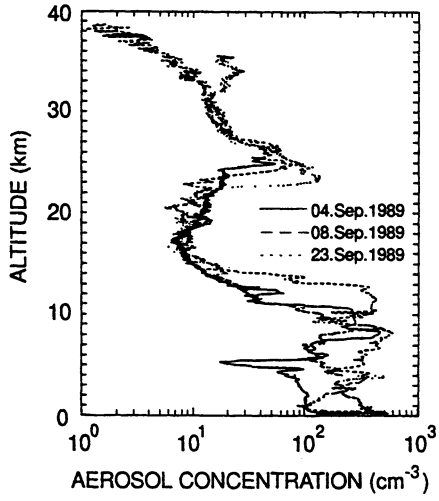


Fig. 8-41: Vertical variation of the concentration of condensation nuclei in air over McMurdo Station, Antactica during spring 1989. (From Hofmann and Deshler, 1991, with changes.)

et al., 1982; McCormick *et al.*, 1981; Hofmann, 1990a,b; Wilson *et al.*, 1992, 1993; Brock *et al.*, 1995).

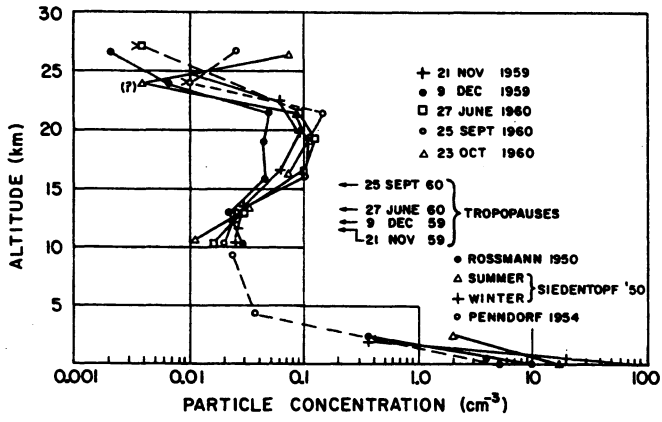


Fig. 8-42: Variation of the average number concentration (ambient) of 'large' particles ($r \geq 0.15$ μm) over Sioux Fall (S. Dakota). Data obtained by Junge over the U.S. are compared with data of Rossmann (1950), Siedentopf (1950), and Penndorf (1954) taken over Germany. (From Chagnon and Junge, 1961; by courtesy of Amer. Meteor. Soc., and the authors.)

The transport of 'large' particles from the troposphere to the stratosphere by turbulent diffusion through the tropopause, or by large-scale air exchange with the troposphere, has been considered as not a likely cause of the *Junge layer*, since such an explanation would not be consistent with the sharp decrease in the number of Aitken nuclei above the tropopause. Early attempts to study the chemical composition of particles in the Junge layer by Junge and Manson (1961), Junge *et al.* (1961a), Chagnon and Junge (1961), Friend (1966), Schedlovsky and Paisley (1966), Lazrus *et al.* (1971), and Cadle (1973) demonstrated that sulfur, present as SO_4^{2-}, is the predominant compound of these particles, with H^+ and NH_4^+ as the major cations. Since a large portion of these particles deliquesce to solution drops at a relative humidity of 72 to 80%, Junge and Manson (1961) and Cadle (1972) believed that $(NH_4)_2SO_4$ is the major constituent. Further evidence for the presence of sulfate particles in the stratosphere has been given by Bigg (1975) who analyzed stratospheric particles forced to impact on specially treated electron microscope screens. Bigg found that the submicron particles consisted predominantly of ammonium sulfate near the tropopause, and of sulfuric acid at higher altitudes. The acid particles were often, but not always, in a frozen state. The presence of free sulfuric acid was further confirmed by Rosen (1971), Bigg (1975), Arnold and Fabian (1980), and Arnold *et al.* (1980, 1981), who found that the sulfuric acid vapor in air was present in equilibrium with the aerosol at altitudes between 27 and 33 km.

Analysis of individual AP in and immediately above the Junge layer revealed further that numerous particles contained one or more water-insoluble, dense in-

clusions (Mossop, 1963a, 1965). Photographs with an electron microscope showed that some of the AP sampled above the Junge layer at 20 to 40 km, had the shape of compact spherules, while others looked like fluffy, highly branched chains, and still others had crystalline shapes (Bigg *et al.* 1970, 1971, 1972; Sheridan *et al.*, 1994). The observations of these authors had been interpreted to mean that the sulfate formation mechanism in the stratosphere is heterogeneous, in that insoluble particles, some possibly of extraterrestrial origin, and some possibly in situ produced by combustion from high flying aircraft, act as nuclei to initiate sulfuric acid drops. A heterogeneous nucleation mechanism for the sulferic acid droplets was also advocated by Turco *et al.* (1982).

Although volcanic eruptions were found to play a significant role in forming the sulfuric acid aerosol in the stratosphere by injecting sulfur dioxide to altitudes 20 to 25 km, where it is subsequently converted to sulfuric acid vapor and eventually to a sulfuric acid aerosol by GPC, observations demonstrate that a stable layer of sulfur containing particles persists in the stratosphere even during periods without major volcanic eruptions. In the upper troposphere, the concentration of SO_2 is low because of its reactivity and its water solubility. Thus, at the tropopause one finds SO_2 in concentrations of less than 100 pptv. Above the tropopause, the SO_2 concentration is found to rise again with altitude (Ockelmann, 1988; Meixner, 1981). Therefore, SO_2, originating in the troposphere, is not believed to be capable of producing the Junge layer. Crutzen (1976) suggested that a sulfur bearing compound which is chemically inert and water insoluble, such as carbonylsulfide (COS), may instead be responsible for the in situ production of the background aerosol in the Junge layer. As shown in Table 8.5h, the mixing ratio of COS in the troposphere is about 500 pptv, varying little with altitude in the troposphere. On the other hand, the observations of Inn *et al.* (1981) indicate a marked decrease of COS above 15 km, with a mixing ratio of only 10 to 20 pptv at 30 km. This has been taken as an indication that COS contributes substantially to the formation of the sulfate aerosol layer in the stratosphere. Also, carbon disulfide (CS_2), which becomes converted to COS in the troposphere, may act as a source for sulfate in the stratosphere. According to Brock *et al.* (1995), these gases oxidize in the stratosphere to H_2SO_4 vapor which subsequently condenses onto preexisting particles by heterogeneous nucleation. The sources of the nuclei on which this condensation proceeds are only poorly known. During non-volcanic periods the stratospheric degree of supersaturation with respect to H_2SO_4 is insufficient for particle formation via homogeneous nucleation. Thus, sources outside the stratosphere must provide the nuclei to maintain the Junge layer during volcanically quiescent periods. Meteoritic materials and in situ produced combustion particles have already been cited above as possible nuclei. On the other hand, evidence cited by Brock *et al.* (1995) suggests that the particles produced by homogeneous nucleation of H_2SO_4-H_2O particles in the upper troposphere of the tropics also constitute a possible source of nuclei upon which sulfur gases condense in the stratosphere.

Early measurements showed that at mid-latitudes, during 1959 and 1960, the concentration of 'large' ($r > 0.15\,\mu$m) particles in the troposphere decreased falling to a minimum between 0.01 to 0.02 cm^{-3} (ambient), and rose again to a pronounced

maximum of 0.05 to 0.2 cm^{-3} between 15 and 25 km, with a stable concentration of about 0.1 cm^{-3} (1.1 mg^{-1}) at 20 km (Penndorf, 1954; Junge *et al.* 1961a,b; Changnon and Junge, 1961; Junge and Manson, 1961; Mossop, 1963a, Friend, 1966).

However, on March 17, 1963, an event took place which altered substantially the stratospheric particle concentration between the early measurements and the measurements which followed later. These changes were due to the eruption of Mt. Agung on Bali, which increased the stratospheric loading by at least one order of magnitude in the Northern Hemisphere, and possibly even more in the Southern Hemisphere. In order to check for any long lasting effects of this and other volcanic eruptions, the vertical variation of the aerosol concentration in the upper troposphere and stratosphere were studied: (1) at mid-latitudes (Laramie, Wyoming 41°N) by Hofmann and Rosen (1981), Hofmann *et al.* (1975, 1976), and Rosen *et al.* (1975a,b) during a period of relative quiet volcanic activity in 1971 to 1973, before the eruption of Fuego in Gatemala in 1974; (2) during the quiet period of 1978 to 1979 before the eruption of Mt. St. Helens in Oregon, U.S.A. in 1980, and the eruption of El Chichon in Mexico in 1982; and (3) during the quiet period of 1988 to 1989 after the effects of the volcanic eruptions of El Chichon, Mt. St. Helens, and of Nevada del Ruiz in Colombia in 1985 had subsided.

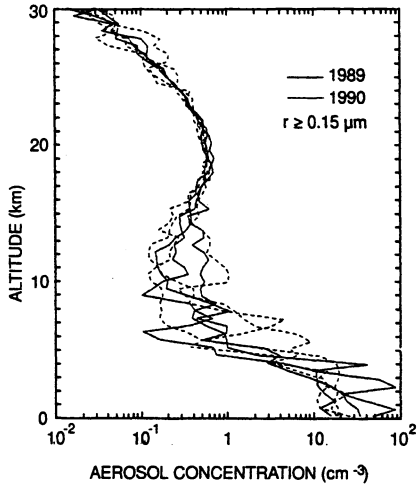


Fig. 8-43: Vertical variation of the concentration of aerosol particles with $r \geq 0.15$ μm in air over Laramie (Wyoming), summer, 1989 and 1990. (From Hofmann, 1993, priv. comm.)

We note from the observations of Hofmann (1993, priv. comm.) made in 1989 (Figure 8.43), that in comparison to the pre-1960 period (Figure 8.41), the whole vertical concentration profile of AP with $r \geq 0.15\,\mu$m had shifted to higher concentrations. This shift was already noted in 1972 and again in 1978 by Hofmann and Rosen (1981a,b) and Hofmann *et al.* (1975, 1976). While stable concentrations before 1960 were about 0.1 cm^{-3} for AP with $r = 0.15\,\mu$m, measurements, begun

in 1971 at Laramie (Wyoming), indicated a new stable concentration of 0.5 cm^{-3} (6 mg^{-1}) for these particle sizes. Comparison of these data with those of Junge led Hofmann and Rosen (1981a,b) and Hofmann (1990a,b) to conclude that the background or non-volcanic stratospheric sulfur particle concentration at mid-latitudes increased by (9 ± 2%) per year during the 20 years following 1959. Comparison of the AP mass concentrations between 1979 and 1989 indicated that at 20 km altitude a further increase of the aerosol mass mixing ratio by (5 ± 2%) per year may have had occurred. Due to a lack of appropriate data, it could not be determined whether the general increase of the stratospheric mass load of AP is due to anthropogenic or natural causes such as volcanic eruptions. Such eruptions have had, as expected, significant immediate effects on the aerosol population in the stratosphere, increasing their mass load, their number concentration, and shifting their size distribution to larger particle sizes. Measurements of the stratospheric aerosol just after volcanic eruptions were carried out by Hofmann and Rosen (1983, 1984), McCormick and Swissler (1983), Hofmann *et al.* (1985) and Snetsinger *et al.* (1987) following the eruption of El Chichon, by Hofmann and Rosen (1982) and Lezberg *et al.* (1982) following the eruption of Mt. St. Helens, and by Wilson *et al.* (1992, 1993) and Borrmann *et al.* (1993) following the eruption of Mt. Pinatubo. However, these measurements compared to those during volcanic quiet periods showed that, generally, the volcanic effects had subsided after a period of two to five years.

In the Arctic and Antarctic stratosphere, the temperature in their respective winters decreases to such low values that the aerosol particles of the Junge Layer (a typical size distribution of the unactivated AP in the Antarctic stratosphere is given in Figure 8.44) are able initiate polar stratospheric clouds (PSC's) by condensation. The formation of such clouds have been observed and studied, among others, by Hofmann and Deshler (1989, 1991), Ferry *et al.* (1989), Fahey *et al.* (1989), Gandrud *et al.* (1989), Arnold *et al.* (1989), Hofmann *et al.* (1990), Schlager *et al.* (1990), Dye *et al.* (1992), Pueshel *et al.* (1990, 1992), Carlslaw *et al.* (1994) and McKenzie *et al.* (1995). Examples for PSC formation observed in the Antarctic and Arctic stratosphere are given in Figures 8.40 and 8.45, respectively. The corresponding size distributions of the PSC particles are given in Figures 8.46 and 8.47, respectively. According to Hofmann and Deshler (1989), the development of a mono- or bimodal size distribution is controlled by the cooling rates occurring over a particular location.

Unfortunately, a detailed discussion of the various mechanisms which had been considered in the past for the formation of PSC particles would lead us much too far afield. However, since heterogeneous chemical reactions on the surface of PSC particles are believed to initiate the catalytic destruction of ozone in the polar lower stratosphere, we shall briefly summarize some considerations of McKenzie *et al.* (1995). For more details, the reader is referred to references cited by McKenzie *et al.* (1995) and Carlslaw *et al.* (1994).

According to McKenzie *et al.* (1995), two main classes of PSC exist, one of which (type I) forms at some temperature above the frost point, while the other (type II) forms near or below the frost point. While type-II particles mainly consist of ice, type-I PSC particles contain large amounts of nitric acid. Type-I particles

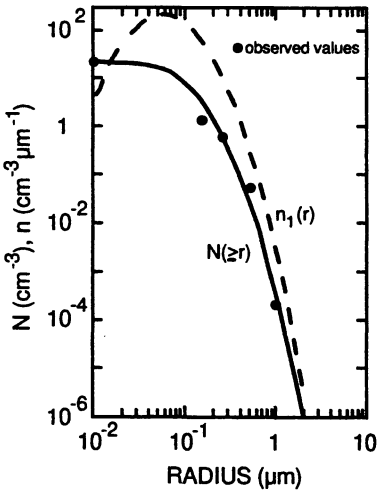


Fig. 8-44: Differential (dashed curve) and integral (continuous curve) size distribution of aerosol particles at 13.5 km, $-75,4°$C, on September 10, 1989 in air over McMurdo Station, Antarctica. Dots represent observed values for undisturbed sulfate layer; size distribution fitted to log normal distribution with $N_1 = 20$ cm^{-3}. (From Hofmann and Deshler, 1991.)

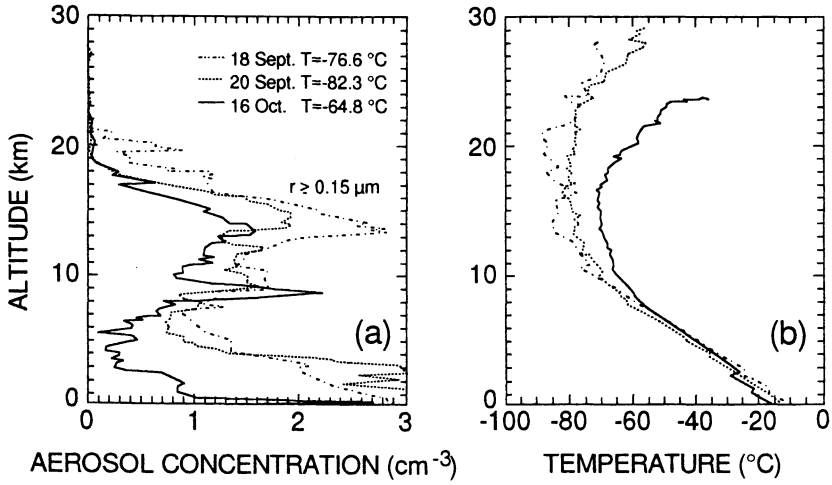


Fig. 8-45: Vertical variation of the concentration of aerosol particles with $r \geq 0.15$ μm for three temperature profiles in air over McMurdo Station (Antarctica). (From Hofmann and Deshler, 1991, with changes).

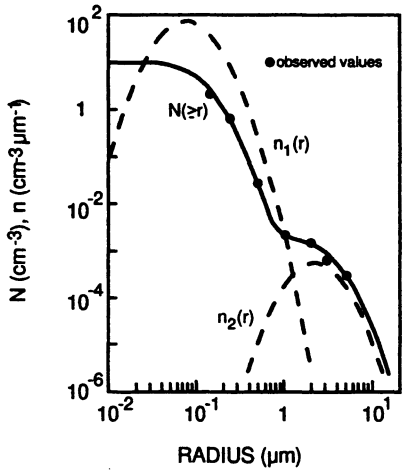


Fig. 8-46: Differential (dashed curve) and integral (continuous curve) size distribution of aerosol particles at 15.5 km, −82.3°C, on Sept. 20, 1989 in air over McMurdo Station, Antarctica, dots represent observed values. Size distribution of polar stratospheric cloud particles (PSC) fitted to two log-normal distributions $N_1 = 10.0$ cm^{-3}, $N_2 = 0.0019$ cm^{-3}). (From Hofmann and Deshler, 1991, with changes.)

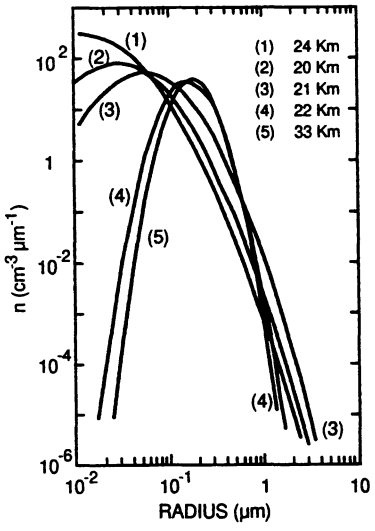


Fig. 8-47: Differential log-normal size distributions fitted to observations of polar stratospheric cloud particles in air at various altitudes over Kiruna (Sweden) on January 31, 1990. (From Hofmann and Deshler, 1990, with changes.)

are usually subdivided further into type Ia particles which are relatively large and anisometric, and type Ib particles which are smaller and more spherical.

The mechanisms for the formation of PSC particles have to allow for the following possible particle compositions: binary $H_2SO_4 \cdot H_2O$ solution, solid sulfuric acid tetrahydrate (SAT), ternary $HNO_3 \cdot H_2O \cdot H_2SO_4$ solution (STS), binary $HNO_3 \cdot H_2O$ solution, and solid nitric acid trihydrate (NAT). As a probable route for the formation of PSC particles, McKenzie *et al.* (1995) consider the following mechanisms: As a direct nucleation of nitric acid phases onto frozen sulfuric acid aerosol (SAT) has to be ruled out, it appears likely that PSC particles form via the condensation growth and subsequent freezing of ternary ($HNO_3 \cdot H_2O \cdot H_2SO_4$) solution droplets. Since a homogeneous nucleation of SAT or NAT does not occur from ternary solutions, formation of NAT and SAT must occur heterogeneously after the temperature of the air has fallen sufficiently low and enough nitric acid has been dissolved in the solution drops. Frozen particles, once formed, are then able to efficiently reduce the nitric acid vapor pressure in the air to the equilibrium vapor pressure for HNO_3 over NAT. If the temperature of the drops decreases further close to, or even below, the ice frost point, and the droplets are still in the liquid phase, water ice will be nucleated.

CHAPTER 9

HETEROGENEOUS NUCLEATION

Observations summarized and discussed in Chapter 2 show that supersaturations as high as several hundred percent, which would be necessary for drop formation in homogeneous water vapor (see Chapter 7), do not occur in the atmosphere, but that typically supersaturations remain below 10% and most often even below 1%. This indicates that drop formation in the atmosphere occurs via heterogeneous nucleation involving aerosol particles (AP). Aerosol Particles which are capable of initiating drop formation at the observed low supersaturations are called *cloud condensation nuclei* (CCN). All AP are eventually able to initiate drops provided that the supersaturation of the water vapor in their environment is high enough. Therefore, in air the total number of aerosol particles per unit volume is often measured in terms of the total number of drops per unit volume observed in a cloud chamber at supersaturations of several hundred percent. The aerosol particle concentration determined in this fashion is then simply called the concentration of *condensation nuclei* (CN).

Observations summarized in Chapter 2 show also that cloud glaciation generally begins at temperatures much too warm for homogeneous freezing of water. For example, on one occasion, Mossop *et al.* (1968) observed ice crystals in a long lived cumulus cloud whose top was probably never colder than $-4°C$, and which was not seeded with ice particles from clouds at higher altitudes. Such behavior indicates that some fraction of the local AP also can serve as *ice forming nuclei* (IN).

In this chapter, we shall discuss the atmospheric CCN and IN, including their modes of action, sources, concentrations, and other characteristic features.

9.1 Cloud Condensation Nuclei (CCN)

9.1.1 Number Concentration and Chemical Composition of CCN

The results of a comprehensive study by Twomey and Wojciechowski (1969) of CCN concentrations over various parts of the world are summarized in Figures 9.1a,b,c. We notice that the number of CCN increases with increasing supersaturation. This is expected from Figures 6.2 and 6.3, which show that as the supersaturation rises, increasingly smaller aerosol particles can be activated to form drops. We also notice from Figure 9.1 that no systematic latitudinal variation in concentration is evident. The observations also confirm previous conclusions that continental air masses are generally richer in CCN than are maritime air masses. Within a particular air mass, at flight level the variation of the median CCN concentration was surprisingly small. At supersaturations betwen 0.1 and 10%, the median concentration of CCN was

found to range from a few tens to a few hundred cm^{-3} in air over oceans, and from a few hundred to a few thousand cm^{-3} in air over the continents.

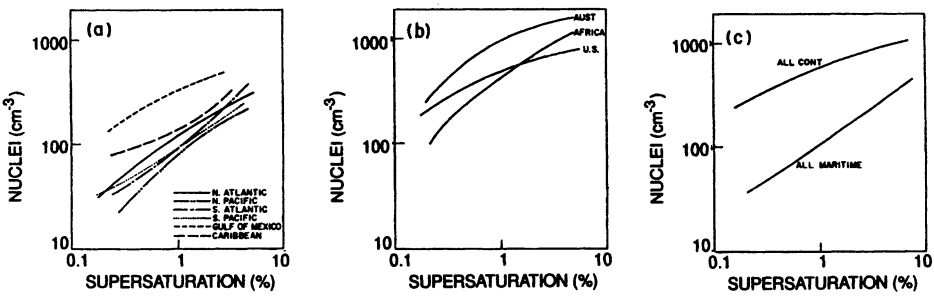


Fig. 9-1: Median world-wide concentration of CCN as a function of supersaturation required for activation; (a) in air over oceans, (b) in air over continents, (c) all observations. (From Twomey and Wojciechowski, 1969; by courtesy of Am. Meteor. Soc., and the authors.)

The concentration N_{CCN} of CCN can often be expressed adequately by a relation of the form

$$N_{\mathrm{CCN}} = C s_{\mathrm{v,w}}^{k} , \tag{9-1}$$

where $s_{\mathrm{v,w}}$ is the supersaturation (%) and C and k are constants for a given air mass. Then, by definition, C is also the CCN concentration at a supersaturation of 1%. Values for C and k at various maritime and continental locations are given in Tables 9.1 and 9.2. As expected, the values for C and k vary considerably depending on the type of airmass present at the particular observation site. According to Hegg *et al.* (1991a), the CCN spectra also vary with season, such that the values for C and k are generally larger in summer than in winter. In Table 9.3, ratios of $N_{\mathrm{CCN}}/N_{\mathrm{CN}}$ for maritime aerosols are given. These ratios range from 0.2 to 0.6, with a median value of 0.5. Hence, only about 50% of the aerosol particles in a marine atmosphere are commonly active as CCN at supersaturation of 1% or less (Hegg and Hobbs, 1992). Much lower values for $N_{\mathrm{CCN}}/N_{\mathrm{CN}}$ are found for continental aerosols due to much higher values for the CN (see Table 9.4). This implies that a large total concentration of AP does not necessitate a large number of CCN. In particular, we notice that for continental aerosols, the fraction of aerosol particles capable of serving as CCN may be as large as 0.1, but is typically 0.01 or less.

Generally, CCN concentrations in maritime and modified maritime air masses which have been over land less than two days rarely exceed 100 cm^{-3}, while concentrations in excess of 10^3 cm^{-3} are found in air which has been over land for several days (Twomey, 1959a, 1963; Jiusto, 1966, 1967; Jiusto and Kocmond, 1968; Radke and Hobbs, 1969; Wieland, 1956). The largest concentrations are usually found in air over cities or industrial complexes. This behavior is illustrated in Figure 9.2. The same behavior has been noticed for other geographic locations by Hoppel *et al.* (1973).

TABLE 9.1

Values for the empirical constants C and k in (9-1) for CCN at 1 % supersaturation in a maritime air mass (from Hegg & Hobbs, 1992).

C (cm^{-3})	k	Location	Observer
125	0.3	Australian Coast	Twomey (1959a)
53-105	0.5-0.6	Hawaii	Jiusto (1967)
100	0.5	North & South Atlantic Ocean, North & South Pacific Ocean, and Caribbean	Twomey and Wojciechowski (1969)
190	0.8	North & South Pacific Ocean	Dinger *et al.* (1970)
250	1.4	North Atlantic Ocean (1500 ft)	Dinger *et al.* (1970)
250	1.3	North & South Pacific Ocean	Hoppel *et al.* (1973)
145-370	0.4-0.9	North Atlantic Ocean	Saxena & Fukuta (1976)
100-1000	-	Arctic	Saxena and Rathore (1984)
140	0.4	Cape Grim, Australia	Gras (1990)
250	0.5	North Atlantic Ocean	Hoppel *et al.* (1990)
25-128	0.4-0.6	North Pacific Ocean	Hudson and Frisbie (1991)
27-111	1.0	North Pacific Ocean	Hegg *et al.* (1991a)
400	0.3	Polluted North Pacific Ocean	Covert (1992)
100	0.4	Equatorial Pacific Ocean	Covert (1992)
290	0.7	High Planes, Montana	Hobbs *et al.* (1978)

TABLE 9.2

Values for the empirical constants C and k in (9-1) for CCN at 1 % supersaturation in a continental air mass.

C (cm^{-3})	k	Location	Observer
600	0.5	Australia, Africa, U.S.A.	Twomey and Wojciechowski (1969)
2000	0.4	Australia	Twomey (1959a)
3500	0.9	Buffalo, N.Y.	Kocmond (1965)
300-4000	0.9	Alps	Stein *et al.* (1985)
3000-5000	0.8	Texas	Hobbs *et al.* (1985)
2000	0.9	High Planes, Montana	Hobbs *et al.* (1978)

TABLE 9.3

Ratios of the number concentration of CCN (at 1 % supersaturation) to the number concentration of CN in maritime air (from Hegg & Hobbs, 1992).

Location	N_{CCN}/N_{CN}	Observer
Pacific Ocean	0.6	Hoppel *et al.* (1973)
Arctic	0.5	Saxena and Rathore (1984)
Cape Grim, Australia	0.4 - 0.6	Gras (1989)
Cape Grim, Australia	0.4	Gras (1989)
Northeast Pacific Ocean	0.2	Hegg *et al.* (1991a)
Northeast Pacific Ocean	0.2	Hegg *et al.* (1991a)
Northeast Pacific Ocean	0.3	Hegg *et al.* (1991a)
East Pacific Ocean	0.6	Hudson and Frisbie (1991)

TABLE 9.4
Ratios of the number concentration of CCN (at 1 % supersaturation) to the number concentration of CN in continental air.

Location	N_{CCN}/N_{CN}	Observer
Washington (D.C)	0.025-0.14	Allee (1970)
Long Island (N.Y.)	0.004-0.021	Twomey & Severynse (1964)
Yellowstone Park	0.015	Auer (1966)

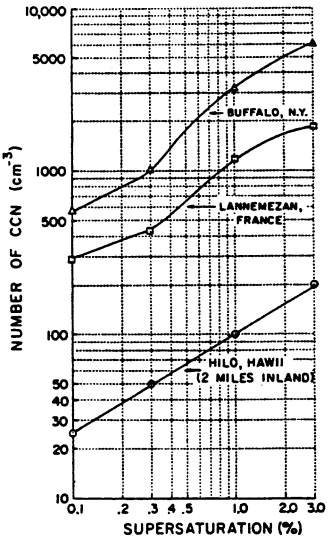


Fig. 9-2: Variation of the CCN concentration required for activation at various locations, as a function of supersaturation. (From Jiusto and Kocmond, 1968; by courtesy of *J. de Rech. Atmos.*, and the authors.)

In relatively pure air with close to 'background' AP concentrations at locations distant from sources, the concentration of CCN is very small. For example, at Yellowstone Park (Wyoming), Auer (1966) measured CCN concentrations at 1% supersaturation which ranged from zero to 78 cm^{-3}, with an average of 15 cm^{-3}. In 1968, Kikuchi (1971) observed at an Antarctic Station (69°S) CCN concentrations as low as zero, but generally near 100 cm^{-3} at 1% supersaturation. In flights over the North Atlantic, Iceland, and Greenland, Flyger *et al.* (1973) found at 1% supersaturation a CCN concentration which in 45% of the cases was less than 10 cm^{-3}, in 80% of the cases was less than 50 cm^{-3}, and in 92% of the cases was less than 100 cm^{-3}.

Most CCN spectra have been obtained for supersaturations found at cloud level typically ranging between 0.2 and about 2%. However, fogs form frequently at lower supersaturations, namely between 0.02 and 0.2%. CCN spectra for these supersaturation have been obtained by Hudson (1983, 1980) at three different lo-

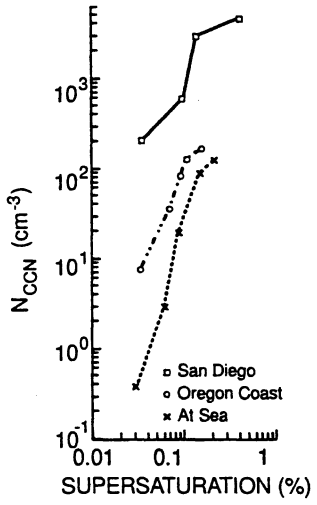


Fig. 9-3: Typical fog condensation nucleus spectra at two locations in California and one location over the Pacific Ocean (30 km off Oregon West). (From Hudson, 1980, with changes.)

cations (Figure 9.3). Aerosol particles which become activated to drops in this supersaturation range are sometimes termed *fog condensation nuclei.*

At a given location, the CCN concentration is found to vary with time over several orders of magnitude, depending on the proximity of sources and on meteorological factors such as wind direction, air mass type, precipitation, and decreasing or, increasing cloudiness (Twomey, 1959a; Jiusto, 1966; Radke and Hobbs, 1969). Figure 9.4 illustrates a typical time variation of the CCN concentration. Notice the effect of air mass changes, wind speed, and wind direction on the CCN concentration. Twomey and Davidson (1970, 1971) showed that at a given location, repeatable patterns can be detected in the diurnal variation of the CCN concentration. Thus, a noon maximum and a late evening maximum were observed consistently during a one year observation period at Robertson (N.S.W., Australia). Evidence for a long-range transport of CCN has been given by Borys and Rahn (1981) who studied the CCN concentration in Iceland.

Observations also show that the CCN concentration may vary significantly with increasing altitude. Accordingly, errors are expected if estimates of cloud microphysical properties are made from ground based CCN concentrations (Hobbs *et al.* 1978). Generally, the CCN concentration over continents decreases with height above ground (see Figure 9.5), reaching concentrations near the top of the mixing layer which are much lower than those near the ground (Squires and Twomey, 1966). Similar features were observed for continental air over Florida and Arizona by Hoppel *et al.* (1973), and by Hobbs *et al.* (1985) over Montana. Over oceanic regions, the CCN concentration often shows a different variation with height. The observations of Squires and Twomey (1966), Hoppel *et al.* (1973), Saxena and

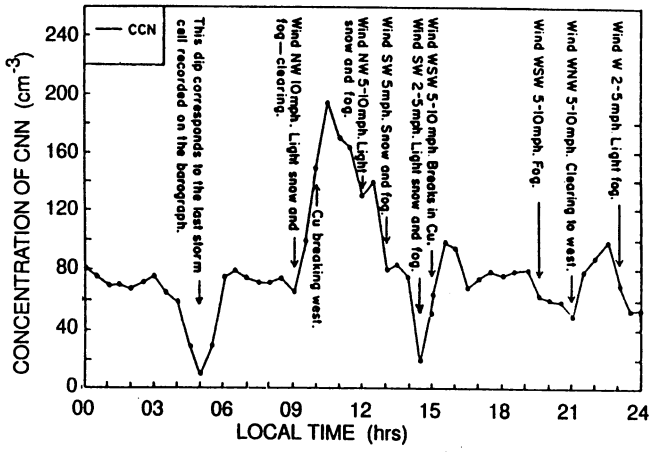


Fig. 9-4: Variation with time of the CCN concentration activated at 1 % supersaturation in air at a station (2025 m) on the Olympic Mts., Washington State. (From Radke and Hobbs, 1969; by courtesy of Am. Meteor. Soc., and the authors.)

Rathore (1984), Hegg *et al.* (1990a), and Hegg and Hobbs (1992) have established that over oceans the CCN concentration may remain fairly constant with height (as indicated in Figure 9.5) or even may increase with height, reaching a maximum value just above the mean cloud layer. Saxena and Rathore (1984) have attributed this behavior to incloud sulfate production. Hegg *et al.* (1990, 1991a) have suggested that a local maximum may occur due to an *in situ* photochemical gas-to-particle conversion, leading to the production of CN which subsequently continue to grow to CCN in the humid local environment of clouds. It is also worth noting that vertical variations in the CCN concentration are usually measured at one particular supersaturation, which may accentuate an over or underestimate of the decrease in CCN concentration with height. For example, Figure 9.6 shows that the decrease with height is much more pronounced when determined at 1.5% than at 0.2% supersaturation (Hobbs *et al.*, 1985).

Measurements by Radke (1970) at the downstream side of mountain 'cap' clouds and mountain lee wave clouds showed that increased CCN concentration at higher elevations may also be due to 'drop-to-particle conversion' (see Section 8.2.2). We notice from Figures 9.7a,b that the number concentration of CCN on the evaporating side of the mountain cap cloud or the mountain lee wave cloud is a factor two to three higher than the concentration on their upstream side.

From our discussions in Chapter 6, we expect that those AP which consist of water-soluble, hygroscopic substances are most suitable for initiating the formation of water drops from water vapor, and therefore will most likely act as CCN. It would seem reasonable, therefore, to assume that the oceans are the most significant source for CCN. However, we recall from Chapter 8 that even close to the ocean surface, the concentration of sea salt particles is too small by a factor of 10 (e.g., Hobbs, 1971). This conclusion is based on direct measurements of the

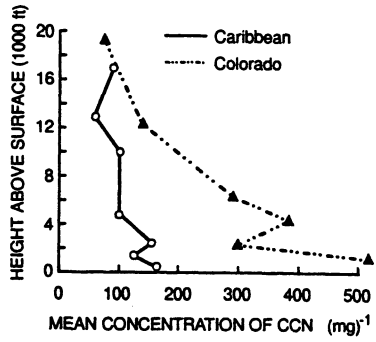


Fig. 9-5: Vertical variation of the CCN concentration in maritime air over the Caribbean), and in continental air over Colorado. (From Squires and Twomey, 1966, with changes.)

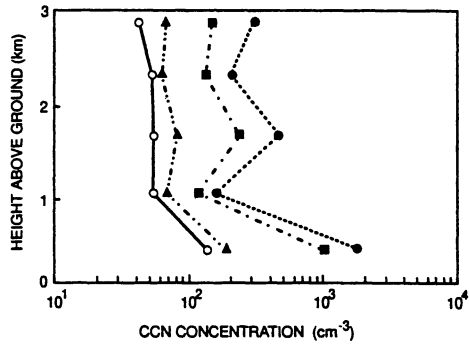


Fig. 9-6: Vertical variation of the CCN concentration over Miles City (Montana); effect of supersaturation: ○ 0.02 %, ▲ 0.5 %, ■ 1.0 %, • 1.5 % (From Hobbs *et al.*, 1985, with changes.)

sea salt particle concentration, as well as on indirect estimates from their rate of production and their residence time. For example, Twomey (1968, 1969, 1971) and Dinger *et al.* (1970) found that most soluble AP over both oceans and land were volatile when subjected to temperatures above 300°C and, thus, behaved analogously to $(NH_4)_2SO_4$ or possibly NH_4Cl. On the other hand, NaCl aerosols withstood temperatures of up to 500°C. Similarly, Dinger *et al.* (1970) measured the concentration of CCN activated at 0.75% supersaturation in air over the North Atlantic and over the east coast of Barbados (West Indies), and found that out of a typical population of 100 cm^{-3}, near the ocean surface as many as 50 to 90 cm^{-3} were volatile at 300°C and, thus, did not consist of NaCl. With increasing height, the percentage of volatile AP increased, reaching almost 100% above about 3 km. On the basis of these measurements, Twomey and Dinger *et al.* suggested that over the ocean only a small percentage of CCN consist of NaCl, while most are very likely composed of non-sea salt sulfate (commonly abbreviated NSS). This sugges-

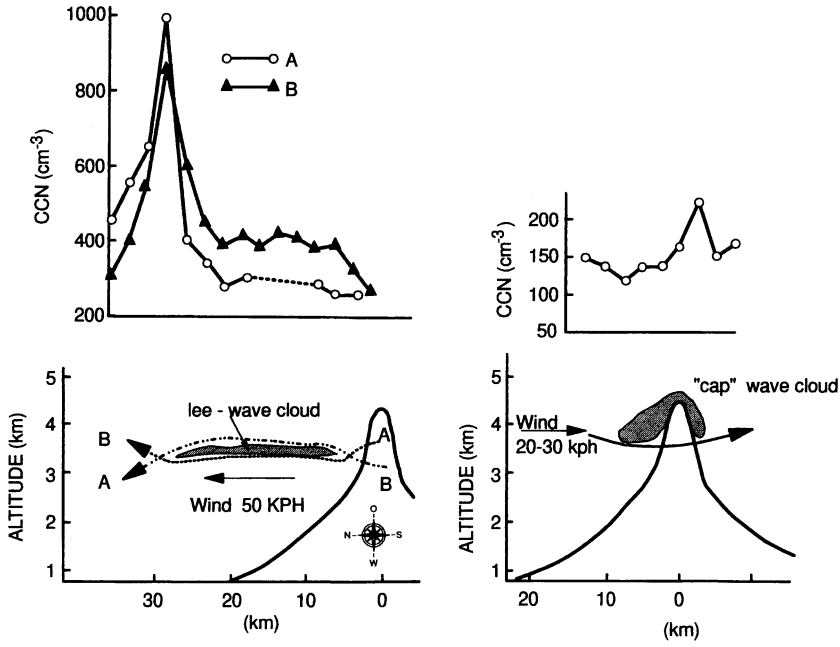


Fig. 9-7: Effect of cloud evaporation on CCN concentration: (a) on the windward and on the lee side of a mountain wave cloud, (b) on the windward and lee sides of a mountain cap cloud; during flights over Mt. Rainier (Washington). (From Radke, 1970, with changes.)

tion is in good agreement with the findings of Meszaros and Vissy (1974) discussed in Chapter 8, and with most more recent CCN studies (Bigg, 1986; Parungo *et al.*, 1986a,b; Clarke *et al.*, 1987; Ayers and Gras, 1991; Quinn *et al.*, 1990). These studies generally show that sea salt dominates the supermicron particle size range, while the NSS dominates the submicron size range.

Because the concentration of CCN is mainly determined by the submicron particles, these results suggests that it is the NSS that determines the CCN activation spectrum. This has led to the hypothesis (e.g. Charlson *et al.*, 1987) that the marine sulfur cycle modulates marine cloud structures and, thus, possibly, climate. Recent field studies revealed that sea salt particles at times may also be present in the submicron size range of marine air (Parungo *et al.*, 1986a,b; Hoppel *et al.*, 1990). This is somewhat expected on the basis of the fact that sea salt particles produced by the bubble burst mechanism include sizes which range between 0.3 and 0.1 μm, in agreement with the shipboard measurements of Parungo *et al.* (1986a,b).

In this context, one realizes rather quickly that the NSS could hardly be due to transportation from land sources alone. In search for other sources, many workers have suggested that organic sulfur emanated from the ocean surface is such a source. Indeed, several recent studies have revealed correlations between the CCN concentration and the concentration of dimethylsulfide (DMS) (Hegg *et al.*, 1991b;

Gras, 1990) and of methanesulfonic acid (MSA) (Ayers and Gras, 1991; Hoppel, 1987). For DMS, this is illustrated by the linear increase of the CCN concentration with increasing gas concentration of DMS (Figure 9.8). The significance of DMS as a source of CCN via gas-to-particle conversion is also hinted at by Nguyen *et al.* (1978), Andreae *et al.* (1985), Andreae and Raemdonck (1983), Bates *et al.* (1987) and Barnard *et al.* (1982), who have estimated that the total flux of DMS from oceans amounts to (40 ± 20) tg yr^{-1}. In addition to representing a source of organic gases which eventually are converted to CCN, the ocean surface has been shown also to be a direct source of organic particles which are introduced into the air by the bubble burst mechanism (Blanchard, 1971b; Spillane *et al.*, 1986).

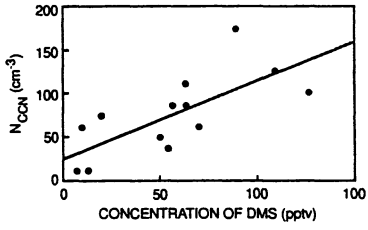


Fig. 9-8: CCN concentration at 1 % supersaturation as a function of mean concentration of DMS in the atmospheric boundary layer over the NE Pacific. Straight line is least-squares fit. (From Hegg *et al.*, 1991b; by courtesy of the authors, copyrighted by Am. Geophys. Union.)

The work of Winkler (1970) suggests that also over the land a considerable fraction of AP consists of volatile organic material. Further, Table 17.2 demonstrates that cloud and fog drop residues often contain combustion products and other organic material some of which are of biogenic origin, suggesting that they may also serve as CCN. This notion is supported by the observations of Twomey (1960), Twomey and Warner (1967), Warner and Twomey (1967), Warner (1968b), and Woodcock and Jones (1970), who observed a significant local increase in the concentration of CCN as a result of the burning of sugar cane leaves in Hawaii and Australia, and by Hobbs and Radke (1969), who observed a similar CCN increase as a result of forest fires.

Several studies have shown that combustion particles, which appear to be rather water insoluble, can nevertheless serve as CCN. Hallett *et al.* (1989), Hudson *et al.* (1991), Pitchford *et al.* (1991) and Hagen *et al.* (1989b) studied carbon particles with diameters between 0.02 and 0.1 μm derived from acetylene burners, from burning wood, and from aviation fuel. The supersaturations at which particles in this size range could be activated to drops ranged betweeen 0.7 and 9% and, according to Hagen *et al.* (1989b), were about 6 times as high as those required to activate NaCl particles of the same size. In contrast, Hallett *et al.* (1989) found that the critical supersaturation for an acetylene combustion aerosol did not differ much from that for $(NH_4)_2SO_4$ particles of the same size. They also found that the fraction N_{CCN}/N_{CN} for polydisperse aerosols was as high as 0.85 for particles derived from burning chaparral brush, 0.72 for particles from burning pine wood,

and 0.5 for particles from burning acetylene. Stith *et al.* (1981) studied the CCN formation during prescribed burns of forest slash. They found 10^{10} to 10^{11} CCN per gram of wood burned. The number of CCN in a fire plume reached 2000 to 8000 cm^{-3} at a supersaturation of 0.2% comparing to 100 CCN cm^{-3} at the same supersaturation in ambient air. However, Hallett *et al.* (1989) found that particles from jet exhaust appear to be relatively inactive as CCN. Nevertheless, a completely different situation arises at the rear of a jet engine at high altitudes, where the exhaust provides a high water supersaturated environment in which drops, and subsequently ice particles, form very prolifically. Weingärtner *et al.* (1993) studied the hygroscopic nature of combustion aerosols generated by a spark ignition engine using unleaded gasoline. The particles thus generated had diameters ranging between 29 and 111 nm and were found to begin growing at a relative humidity of 95%. Ambient combustion particles began their growth at a relative humidity of 85%, in agreement with the field observations of Svenningsen (1992). In contrast, pure graphite particles did not act as CCN up to 120% relative humidity.

Volcanic emissions of CCN have been investigated by Rogers *et al.* (1981). Using a U-2 aircraft at 13 to 19 km altitude during the eruption after Mt. St. Helens volcano, they found at 13.6 km CCN concentration up to 1000 cm^{-3} at 1% supersaturation; this is about one order of magnitude higher than the concentrations otherwise found at this altitude. Hobbs *et al.* (1982), who also studied particles in the plume of the Mt. St. Helens volcano, found that $554 \leq C \leq 26100$ and $0.49 \leq k \leq 1.85$ in (9-1).

Particles emitted into the atmosphere by the surface of deserts also serve as CCN. Thus, Desalmand (1987) found CCN concentrations up to 10 000 cm^{-3} at supersaturation between 0.3 and 0.8 during dust storms south of the Sahara desert. This is somewhat surprising as desert particles are generally assumed to be mostly water insoluble silicates.

Considering the definition of CCN, it is reasonable to assume that their concentration in a given air volume is to a large extent indicative of the drop concentration in a cloud which forms in that air volume. In fact, the concentrations would indeed be equivalent if the cloud updraft reached the particular supersaturation at which the CCN concentration was determined. The actual supersaturation reached in a given cloud will depend on the size distribution of AP present in the rising air, their chemical nature, the moisture content of the atmosphere, and its thermodynamic state which largely determines the updrafts that can develop (see Chapter 13). However, we may assume roughly that cloud supersaturations rarely exceed a few percent. At these values, the concentrations of CCN over continents typically range from 100 to 1000 cm^{-3}, while over oceans they range from a few tens to a few hundred cm^{-3} (Twomey and Wojciechowski, 1969). These values agree well with the drop concentrations found in continental and maritime clouds (see Chapter 2).

9.1.2 Mode of Action of Water-Soluble and Mixed CCN

The nucleation of water drops by water-soluble or mixed AP is controlled by the mass and chemistry of the water-soluble component. As we have seen, at a specific

relative humidity, which for most soluble compounds in the atmosphere is well below 100% (Table 4.3), the soluble components of the AP deliquesce into aqueous solution drops. As the relative humidity in the environment rises, such a drop will undergo a slow equilibrium growth by diffusion of water vapor until, if it reaches a critical supersaturation, it will become *activated* and, henceforth, grow freely and comparatively swiftly, again by vapor diffusion, into a macroscopic cloud drop.

In Chapter 6, we showed that the critical equilibrium supersaturation for activation can be computed from (6-26) and (6-33) for any given composition of the mixed aerosol particle. Junge and McLaren (1971) and subsequently Hoppel (1979) used similar equations to determine the critical equilibrium supersaturation as a function of aerosol particle size. While Junge and McLaren (1971) assumed NaCl for the water soluble portion of two typical size distributions for atmospheric mixed aerosol particles in various volume proportions, Hoppel actually determined the chemical composition (i.e., the quantity B in (6-29) and (6-38)) of the aerosol particles whose size distribution he had measured. From the known size distributions, their computations permitted the determination of the number of AP which become activated to drops (which is the number of CCN) at any specified supersaturation. Although Junge and McLaren's computations did not permit any rigorous comparison with observed CCN spectra, since they knew neither the size spectrum nor the composition of the particles which formed the CCN, their results allowed the conclusion that the chemical composition of AP has little effect on the shape of the CCN spectrums, although it strongly effects the CCN concentration at any given supersaturation. Also, they deduced that the shape of the CCN spectrum depended strongly on the AP size distribution. Similar results were obtained by Fitzgerald (1973, 1974). In contrast to the computations of Junge and McLaren (1971), the results of Hoppel (1979) allowed a direct comparison between the CCN spectrum computed from the aerosol size distribution (Figure 9.9a) and measured B, and the CCN spectrum observed by him using various experimental techniques (Figure 9.9b). We notice from Figure 9.9b that the CCN spectrum derived from the observed size distribution shows good agreement with the observed CCN spectrum, giving experimental suppport to the Köhler and Junge equations developed in Chapter 6.

9.1.3 Nucleation of Drops on Water-Insoluble CCN

Let us now consider AP which are wettable by water but completely water-insoluble. For the sake of simplicity, it is useful to assume that a water embryo or germ nucleated in supersaturated vapor on a water-insoluble, partially wettable surface assumes the shape of a spherical cap. Although no direct observations of the shape of water germs are available, some experimental justification for the spherical cap assumption has been provided by Gretz (1966a), who used an electron microscope to study the nature and appearance of silver embryos deposited from supersaturated silver vapor on a tungsten substrate.

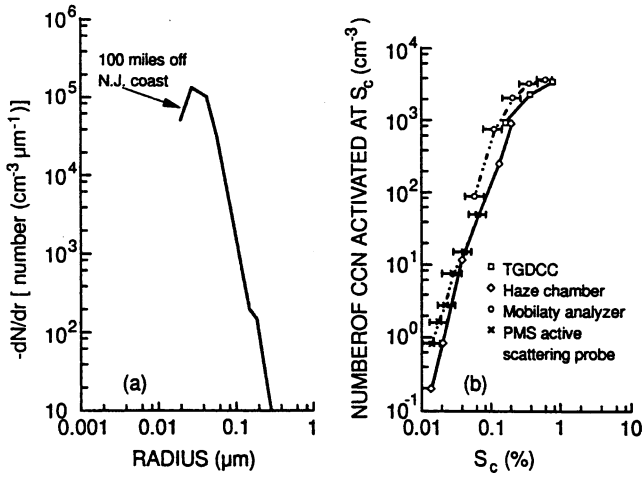


Fig. 9-9: Comparison of the CCN spectrum, derived from an observed aerosol particle size distribution and particle composition, with observed CCN spectrum. (a) Size distribution of AP in air over Norfolk (Virginia), 100 miles off the coast of New Jersey. (b) CCN spectrum observed at same location as in (a) (solid line); dotted line is spectrum calculated from size distribution and observed chemical composition of particles in (a). (From Hoppel, 1979, with changes.)

9.1.3.1 *Nucleation on a Planar Substrate*

Our present goal is to determine the rate at which water drops are nucleated on an insoluble AP surface. Let us first consider the simplest possible model for this process, and assume the surface on which the nucleation occurs is planar and energetically homogeneous.

We shall adopt the classical theory of nucleation (Chapter 7) for this problem. This procedure is amply justified in view of the success of the theory, its simplicity, and the ease with which it may be extended to new situations. In this and the next section, we follow most closely the works of Fletcher (1958, 1959a,b, 1962a), Hirth and Pound (1963), and Pound *et al.* (1954).

Let $c_{1,\mathrm{S}}$ be the concentration of single water molecules adsorbed on a surface and assume they are in metastable equilibrium with the new phase embryos residing there also. By invoking the classical theory of nucleation, we can express the i-mer embryo concentration on the surface in a form analogous to (7-26), viz.,

$$c_{i,\mathrm{S}} = c_{1,\mathrm{S}} \exp[-\Delta F_{i,\mathrm{S}}/\mathrm{k}T]\,, \tag{9-2}$$

where $\Delta F_{i,\mathrm{S}}$ is the energy of i-mer formation on the surface. Then, the rate J_{S} at which germs are formed per unit time and per unit surface area may be written, in analogy to (7-40), as

$$J_{\mathrm{S}} = Z_{\mathrm{S}} c_{g,\mathrm{S}} \mathrm{w}^{\downarrow} \Omega_{g,\mathrm{S}}\,, \tag{9-3}$$

where $Z_{\mathrm{S}} = [\Delta F_{g,\mathrm{S}}/3\mathrm{g}^2\pi\mathrm{k}T]^{1/2}$ is the Zeldovich factor for surface nucleation (see 7-45).

In this expression, $w^{\downarrow}\Omega_{g,S}$ may be taken to have the same meaning as in (7-40), if we assume the germs grow by direct addition of water molecules from the vapor. For this case, we have from (5-51), and assuming $\alpha_c = 1$, the result

$$w^{\downarrow}\Omega_{g,S} = \frac{\pi a_g^2 e}{(2\pi \dot{m}_w kT)^{1/2}}, \tag{9-4}$$

where we have approximated the cap surface area by πa_g^2.

On the other hand, if we assume that growth occurs primarily by surface diffusion of adsorbed water molecules to the germs, then the quantity $w^{\downarrow}\Omega_{g,S}$ must be interpreted as the product of the number of adsorbed water molecules in position to join the germ, and the frequency $\nu_S \exp[-\Delta G_{sd}/kT]$ with which such an adsorbed molecule will jump to join the germ; i.e., in this case we have

$$w^{\downarrow}\Omega_{g,S} = 2\pi\bar{\delta} c_{1,S} \nu_S a_g \sin\theta \exp[-\Delta G_{sd}/kT], \tag{9-5}$$

where $2\pi a_g \sin\theta$ is the circumference of the cap germ (see Figure 9.10a), ΔG_{sd} is the activation energy for surface diffusion of a water molecule on the substrate, ν_S is the frequency of vibration of an adsorbed molecule normal to the surface ($\approx 10^{13}$ sec^{-1}), and $\bar{\delta}$ is the average distance a molecule moves in a diffusion step or jump.

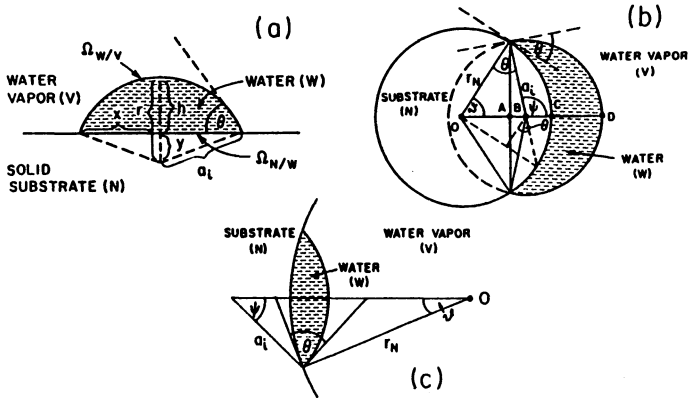


Fig. 9-10: Schematic for determining the volume and surface area of a spherical cap embryo of water: (a) on a planar, water-insoluble, partially wettable substrate, (b) on a spherically convex, water-insoluble, partially wettable substrate, (c) on a spherically concave, water-insoluble, partially wettable substrate.

The assumed steady concentration $c_{1,S}$ may be determined, in principle at least, by equating the flux density of water molecules to the surface with the outward flux of desorbed molecules; the latter is given by

$$w^{\uparrow} = c_{1,S} \nu_S \exp[-\Delta G_{des}/kT], \tag{9-6}$$

where $\Delta G_{\rm des}$ is the energy of desorption per molecule. On setting this result equal to (5-5), we obtain

$$c_{1,\rm S} = \frac{\rm e}{(2\pi \dot{m}_{\rm w} {\rm k} T)^{1/2} \nu_{\rm S}} \exp[\Delta G_{\rm des}/{\rm k}T] \,. \tag{9-7}$$

Therefore, on combining (9-3), (9-4), and (9-7), the rate of surface nucleation for the case of germ growth by direct vapor deposition is

$$J_{\rm S} = \frac{\pi Z_{\rm S} {\rm e} a_g^2}{(2\pi \dot{m}_{\rm w} {\rm k} T)^{1/2}} c_{1,\rm S} \exp[-\Delta F_{g,\rm S}/{\rm k}T] \tag{9-8a}$$

$$= \frac{Z_{\rm S} {\rm e}^2 a_g^2}{2\dot{m}_{\rm w} {\rm k} T \nu_{\rm S}} \exp[(\Delta G_{\rm des} - \Delta F_{g,\rm S})/{\rm k}T] \,. \tag{9-8b}$$

Similarly, combining (9-3), (9-5), and (9-7) gives the corresponding rate for the case of growth by surface diffusion of adsorbed molecules:

$$J_{\rm S} = \frac{Z_{\rm S} {\rm e}^2 \bar{\delta} a_g \sin\theta}{\dot{m}_{\rm w} {\rm k} T \nu_{\rm S}} \exp[(2\Delta G_{\rm des} - \Delta G_{\rm sd} - \Delta F_{g,\rm S})/{\rm k}T] \,. \tag{9-9}$$

If we assume $\bar{\delta} \sin\theta \approx a_g$ and compare (9-8) with (9-9), we find the surface diffusion nucleation rate is faster by the factor $\exp[(\Delta G_{\rm des} - \Delta G_{\rm sd})/{\rm k}T]$; experimental determination of the energy terms is difficult, but generally the qualitative, outcome is $\Delta G_{\rm des} > \Delta G_{\rm sd}$.

Let us now turn to the determination of the energy of germ formation, $\Delta F_{g,\rm S}$. As is always done in the classical approach, we shall assume macroscopic values of all relevant parameters. Then, on writing $\Delta F_{i,\rm S}$ in terms of bulk volume and surface contributions (recall (7-19)), we have only to cope with a simple geometry problem, namely that of finding the surface and volume of the cap embryo shown in Figure 9.10a. Proceeding in this manner, we write the energy of i-mer formation on the surface in the form

$$\Delta F_{i,\rm S} = V_i \Delta f_{\rm vol} + \sigma_{{\rm w},i} \Omega_{{\rm w},i} \,, \tag{9-10}$$

where V_i is the i-mer volume, $\Delta f_{\rm vol} = [\mu_{\rm w}({\rm e},T) - \mu_{\rm v}({\rm e},T)]/v_{\rm w}$ is the bulk energy change per unit volume $[= -\mathscr{R}T\rho_{\rm w}(\ln S_{\rm v,w})/M_{\rm w}$, from (7-21)], and the last term in (9-10) represents the total surface energy of the i-mer

$$\sigma_{{\rm w},i}\Omega_{{\rm w},i} = \sigma_{\rm w/v}\Omega_{\rm w/v} + (\sigma_{\rm N/w} - \sigma_{\rm N/v})\Omega_{\rm N/w} \,. \tag{9-11}$$

In terms of the lengths x, y, and h defined by Figure 9.10a, the i-mer volume is

$$V_i = \frac{a_i}{3}(2\pi a_i {\rm h}) - \frac{\pi {\rm x}^2 {\rm y}}{3} = \frac{\pi a_i^3}{3}(2 + m_{\rm w/v})(1 - m_{\rm w/v})^2 \,, \tag{9-12}$$

where $m_{\rm w/v} = \cos\theta$. Similarly, $\Omega_{\rm w/v} = 2\pi a_i {\rm h} = 2\pi a_i^2(1 - m_{\rm w/v})$, and $\Omega_{\rm N/w} = \pi {\rm x}^2 = \pi a_i^2(1 - m_{\rm w/v})$, with ${\rm h} = a_i - {\rm y}$, ${\rm y} = a_i m_{\rm w/v}$, and ${\rm x}^2 = a_i^2(1 - m_{\rm w/v})$, so that

$$\sigma_{{\rm w},i}\Omega_{{\rm w},i} = 2\pi a_i^2 \sigma_{\rm w/v}(1 - m_{\rm w/v}) + \pi a_i^2(\sigma_{\rm N/w} - \sigma_{\rm N/v})(1 - m_{\rm w/v}^2) \tag{9-13}$$

$$= \pi a_i^2 \sigma_{\rm w/v}(2 + m_{\rm w/v})(1 - m_{\rm w/v})^2 \,,$$

making use of Young's relation (5-23). Therefore, (9-10) becomes

$$\Delta F_{i,\mathrm{S}} = \left(\frac{\pi a_i^3}{3}\Delta f_{\mathrm{vol}} + \pi a_i^2 \sigma_{\mathrm{w/v}}\right)(2 + m_{\mathrm{w/v}})(1 - m_{\mathrm{w/v}})^2 . \tag{9-14}$$

As in the case of homogeneous nucleation, we identify the energy of germ formation as the maximum in the curve of $\Delta F_{i,\mathrm{S}}$ vs. a_i; i.e., we set $\partial(\Delta F_{i,\mathrm{S}})/\partial a_i = 0$ for fixed $m_{\mathrm{w/v}}$ to find the germ radius, which is

$$a_g = -\frac{2\sigma_{\mathrm{w/v}}}{\Delta f_{\mathrm{vol}}} = \frac{2M_{\mathrm{w}}\sigma_{\mathrm{w/v}}}{\mathscr{R}T\rho_{\mathrm{w}} \ln S_{\mathrm{w,v}}} . \tag{9-15}$$

This result, the same as for homogeneous nucleation, could have been written down immediately on realizing that the curved surface of the germ must be in equilibrium with the vapor. Substituting this result into (9-14) for $i = g$, the energy of germ formation is

$$\Delta F_{g,\mathrm{S}} = \frac{4\pi a_g^2 \sigma_{\mathrm{w/v}}}{3}[(2 + m_{\mathrm{w/v}})(1 - m_{\mathrm{w/v}})^2/4] \tag{9-16}$$

$$= \frac{16\pi M_{\mathrm{w}}^2 \sigma_{\mathrm{w/v}}^3}{3[\mathscr{R}T\rho_{\mathrm{w}} \ln S_{\mathrm{v,w}}]^2} f(m_{\mathrm{w/v}}) , \tag{9-17}$$

where

$$f(m) = (2 + m)(1 - m)^2/4 \tag{9-18}$$

(Volmer, 1939).

If the substrate is completely wettable by water, then $m = 1$, $f = 0$, and there is no energy barrier to nucleation. At the other extreme of a non-wettable surface $m = -1$, $f = 1$, and $\Delta F_{g,\mathrm{S}} = \Delta F_g$, the energy of germ formation for homogeneous nucleation. Of course, this last result is also as expected: The germ drop rests on the non-wettable surface, but does not otherwise interact with it. In, general, $0 \leq f(m) \leq 1$, confirming that the presence of a foreign surface serves to lower the free energy barrier to nucleation.

As we have seen, the rate of embryo growth by surface diffusion of adsorbed molecules dominates, to some extent, the rate of growth by direct deposition of molecules from the vapor. Unfortunately, however, the former process involves contributions which are not accurately known, and so we must be content to proceed with the latter process in order to arrive at a numerical evaluation of the nucleation rate. Thus, Fletcher (1962a) used (9-8a) to estimate J_{S}. The monomer concentration $c_{1,\mathrm{S}}$ was obtained by assuming adsorption yields essentially a monolayer at the supersaturations involved. In this manner, Fletcher estimated the prefactor to the exponential term in (9-8a) (the 'kinetic coefficient') to be of the order of 10^{24} to 10^{27} cm^{-2} sec^{-1}. Choosing 10^{25} cm^{-2} sec^{-1} as representative, he used (9-8a) and (9-17) to evaluate $(S_{\mathrm{v,w}})_{\mathrm{crit}}$ as a function of contact angle θ for $J_{\mathrm{S}} = 1$ cm^{-2} sec^{-1} and $T = 0°$C; the results are shown in Figure 9.11. It is seen that the critical saturation ratio for nucleation of water on a water-insoluble, partially wettable, planar substrate increases monotonically with contact angle. The increase is small at small and large wetting angles, and is almost linear for $60 \leq \theta \leq 120°$.

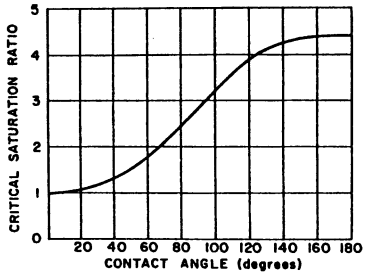


Fig. 9-11: Critical supersaturation for water nucleation (for $J_s = 1$ cm^{-2} sec^{-1}) on a planar insoluble substrate as a function of contact angle Θ, based on (9-8a) and (9-17).

9.1.3.2 *Nucleation on a Curved Substrate*

Fletcher (1958, 1959a) has extended the theory presented in the last section to include an account of the effects of the finite size of the nucleating particle. In this extension, the substrate is assumed to be a sphere of radius r_N. The determination of the energy of germ formation is carried out just as before; only the geometry has changed somewhat. Thus, from Figure 9.10b, if we let $\overline{AD} \equiv b = a_i(1 - \cos\psi)$ and $\overline{AC} \equiv c = r_N(1 - \cos\vartheta)$, then the volume of the embryo is $V_i = [\pi b^2(3a_i - b)/3] - [\pi c^2(3r_N - c)/3]$, and the surfaces bounding the embryo are $\Omega_{N/w} = 2\pi r_N c$ and $\Omega_{w/v} = 2\pi a_i b$. With these we find

$$V_i = \frac{\pi a_i^3}{3}(2 - 3\cos\psi + \cos^3\psi) - \frac{\pi r_N^3}{3}(2 - 3\cos\vartheta + \cos^3\vartheta) \tag{9-19}$$

and

$$\begin{aligned} \sigma_{w,i}\Omega_{w,i} &= \sigma_{w/v}(\Omega_{w/v} - \Omega_{N/w}\cos\theta) \\ &= 2\pi\sigma_{w/v}[a_i^2(1 - \cos\psi) - r_N^2\cos\vartheta(1 - \cos\vartheta)], \end{aligned} \tag{9-20}$$

where $\cos\vartheta = (r_N - a_i\cos\theta)/d$, $\cos\psi = -(a_i - r_N\cos\theta)/d$ and $d = (r_N^2 + a_i^2 - 2a_i r_N\cos\theta)^{1/2}$.

By substituting (9-19) and (9-20) into (9-10) we find, as before, that $(\Delta F_{i,S})_{max} = \Delta F_{g,S}$ occurs at $a_{i,max} = a_g$, where the latter is given by (9-15). Accordingly, the energy of germ formation becomes

$$\Delta F_{g,S} = \frac{16\pi M_w^2\sigma_{w/v}^3}{3[\mathscr{R}T\rho_w \ln S_{v,w}]^2} f(m_{v/w}, x), \tag{9-21}$$

where

$$2f(m,x) = 1 + \left(\frac{1 - mx}{\phi}\right)^3 + x^3\left[2 - 3\left(\frac{x - m}{\phi}\right) + \left(\frac{x - m}{\phi}\right)^3\right] + 3mx^2\left(\frac{x - m}{\phi} - 1\right), \tag{9-22}$$

with

$$\phi = (1 - 2m\mathrm{x} + \mathrm{x}^2)^{1/2}\,, \quad \mathrm{x} = r_N/a_g\,. \tag{9-23}$$

Let us consider the nucleation rate per particle, J'_S; to a first approximation, we simply have $J'_S = 4\pi r_N^2 J_S$, or

$$J'_S = \frac{4\pi^2 r_N^2 a_g^2 Z_{SE}}{(2\pi \dot{m}_w kT)^{1/2}} c_{1,S} \exp[-\Delta F_{g,S}/kT]\,, \tag{9-24}$$

using (9-8a). The kinetic coefficient in this equation has been estimated by Fletcher (1958, 1959a,b) to be about $10^{26} r_N^2$ (this assumes $r_N > a_g$). We also notice that for $m = -1$ (9-22) reduces to $f(m,\mathrm{x}) = 1$ and (9-21) to $\Delta F_{g,S} = \Delta F_g$, the energy required to form a drop germ homogeneously above a surface area of $4\pi r_N^2$.

Figure 9.12 presents a plot of the relations (9-21) to (9-24), giving the critical saturation ratio for $J'_S = 1$ germ (particle)$^{-1}$ sec^{-1} at 0°C, as a function of r_N for various contact angles. It is seen that for all values of $m_{w/v}$, $(S_{v,w})_{crit}$ increases rapidly if $r_N < 0.1\,\mu$m, and that for a given substrate particle size, $(S_{v,w})_{crit}$ increases monotonically with increasing contact angle. These results clearly indicate that water-insoluble, partially wettable, spherical AP must be large and exhibit low contact angles for water if they are to serve as CCN.

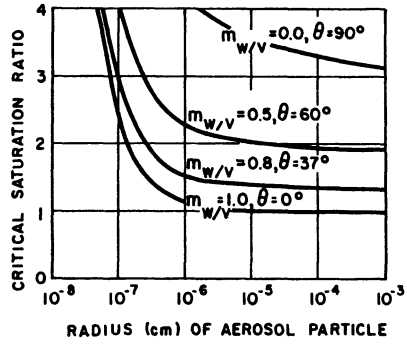


Fig. 9-12: Critical saturation ratio for water nucleation (for $J_s = 1$ sec^{-1} particle^{-1}) on a spherical, water-insoluble particle of radius r_N as a function of contact angle Θ, for 0°C, based on (9-25) and (9-22). (From *The Physics of Rain Clouds* by N.H. Fletcher, copyrighted by Cambridge University Press, 1962a.)

McDonald (1964) has extracted an approximate solution from (9-21) to (9-24) for the most interesting and relevant case of small contact angles and supersaturations; the result is

$$\cos\theta = 1 - \left(\frac{\mathrm{x}-1}{\mathrm{x}}\right)[0.662 + 0.022 \ln r_N]^{1/2} \ln(S_{v,w})_{crit}\,, \tag{9-25}$$

where $(S_{v,w})_{crit}$ corresponds again to $J'_S = 1$ germ (particle)$^{-1}$ sec^{-1} at 0°C, and where again $\mathrm{x} = r_N/a_g$. This equation is plotted in Figure 9.13, where comparison

is also made with the critical supersaturation required to activate mixed AP containing various volume proportions of NaCl. The figure reveals a strong dependence of $(S_{v,w})_{crit}$ on contact angle. For example, if we consider that the supersaturation reached in clouds is typically smaller than 3%, we must require that AP of radii $\gtrsim 0.01\,\mu$m have contact angles less than 12° if they are to serve as CCN in this supersaturation range.

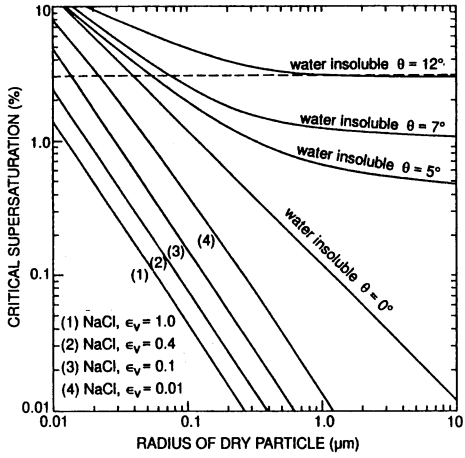


Fig. 9-13: Critical supersaturation for water nucleation (for $J_s = 1$ sec^{-1} particle^{-1}) on a spherical, water-insoluble substrate particle of radius r_N as a function of contact angle Θ; and critical supersaturation for activation of a mixed particle as a function of the volume fraction of NaCl in the particle: for 0°C, based on (9-26), and Equations. in Chapter 6.

Unfortunately, little is known about the contact angle for insoluble AP, except for some measurements of water against certain silicates (see Table 5.2). These values suggest that silicate particles are not likely to serve as CCN. Even if the contact angle on insoluble AP were zero, it would still be very unlikely that many such particles would become involved in the condensation process, because sufficient soluble, and mixed particles are generally available to nucleate at significantly lower supersaturations. Although continents release predominantly insoluble AP, many of these soon coagulate with soluble AP to become mixed particles, which are then competitive with CCN from the oceans.

Recently, Mahata and Alofs (1975) modified the heterogeneous nucleation theory of Fletcher to consider nucleation on an insoluble, partially wettable, spherically concave substrate of radius of curvature r_N (see Figure 9.10c). The only change from the previous theory is one of geometry. Thus, in place of (9-19) we now have

$$V_i = \frac{\pi a_i^3}{3}(2 - 3\cos\psi + \cos^3\psi) + \frac{\pi r_N^3}{3}(2 - 3\cos\vartheta + \cos^3\vartheta)\,, \qquad (9\text{-}26)$$

while the surface energy contribution still has the form of (9-20); however, in contrast to the convex case, we now have $\cos\vartheta = (r_N + a_i\cos\theta)/d$, $\cos\psi = (a_i +$

$r_N \cos\theta)/d$, and $d = (r_N^2 + a_i^2 + 2r_N a_i \cos\theta)^{1/2}$. The resulting free energy of germ formation is given by (9-21), where instead of (9-22) and (9-23), we have

$$2f(m,\mathrm{x}) = 1 - \left(\frac{1+m\mathrm{x}}{\phi}\right)^3 - \mathrm{x}^3\left[2 - 3\left(\frac{\mathrm{x}+m}{\phi}\right) + \left(\frac{\mathrm{x}+m}{\phi}\right)^3\right] + 3m\mathrm{x}^2\left(\frac{\mathrm{x}+m}{\phi} - 1\right), \tag{9-27}$$

and

$$\phi = (1 + 2m\mathrm{x} + \mathrm{x}^2)^{1/2}, \quad \mathrm{x} = r_N/a_g\,. \tag{9-28}$$

Mahata's computations, based on Fletcher's value of 10^{25} cm^{-2} sec^{-1} for the kinetic coefficient in (9-8a) (and with the minor change of setting $T = 23°$C instead of 0°C), are shown in Figure 9.14. The results indicate that concave surface features can significantly enhance the capacity of AP to serve as CCN.

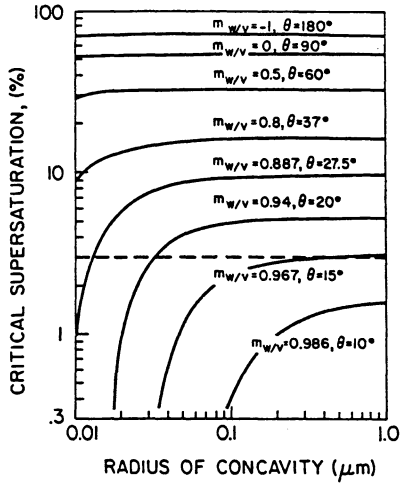


Fig. 9-14: Critical supersaturation for water nucleation (for $J_s = 1$ sec^{-1} cm^{-2}) on a concave, water-insoluble, partially wettable substrate, as a function of the radius of curvature and contact angle Θ, for 23°C. (From Mahata and Alofs, 1975; by courtesy of Am. Meteor. Soc., and the authors.)

Of course, one should realize that this enhancement results from an 'inverse Kelvin law' effect which must break down at some minimum radius. Mahata assumes, somewhat arbitrarily, that this cut-off should occur near 0.01 μm radius. The figure shows that surface roughness of this resolution has the effect, at 3% supersaturation, of inducing nucleation for contact angles $\theta \lesssim 30°$. This is considerably less stringent than the 12° figure for convex surface features, but is still insufficient to indicate that many insoluble AP could act as CCN.

9.1.4 Experimental Verification of Heterogeneous Water Drop Nucleation

Since water-soluble and mixed AP deliquesce and subsequently grow with increasing relative humidity, it is appropriate to test the theory of nucleation on such particles in two ways: (1) by experimentally determining the equilibrium growth of these particles, and (2) by determining the number of particles of given size and composition which become activated at a given supersaturation. The results of such equilibrium growth experiments, discussed in Chapter 6, have been found to be in good accord with theory. Observed CCN concentrations have been cited in Section 9.1.2, where it was pointed out that the agreement with theory is satisfactory as regards the shape of the CCN spectral curve and the actual concentrations of activated drops.

Attempts to verify experimentally the predictions of water drop nucleation on water-insoluble, partially wettable substrates have been made by Twomey (1959b), Koutsky *et al.* (1965), Isaka (1972), van de Hage (1972), and by Mahata and Alofs (1975). Their experiments were carried out in diffusion chambers where nucleation was forced to take place on plane substrates for which the contact angle of water had been measured separately. Unfortunately, the results derived from the experiments show considerable disagreement. While the critical supersaturations necessary for onset of drop nucleation were found by van de Hage and by Isaka to be significantly lower for all wetting angles than those predicted by theory, those measured by Twomey agree well with theory up to $\theta = 100°$.

In a critical review, Mahata and Alofs (1975) pointed out some serious experimental difficulties involved in such measurements, and expressed the opinion that these were the cause of the contradictory results. In an attempt to avoid the errors of previous investigators, they carried out new experiments, the results of which are reproduced in Figure 9.15. It is seen that their measured critical supersaturations as a function of contact angle agree fairly well with those of Koutsky *et al.* (1965) up to a supersaturation of about 10%, corresponding to a contact angle of about 25°. In this range, the experimental results also agree with the predictions of the classical theory, especially if a size correction for $\sigma_{w/v}$ is made, such as (5-22). Since the supersaturation in atmospheric clouds rarely exceeds 10%, the disagreement between experiment and theory at larger contact angles is of little significance.

The success of the classical nucleation theory in its simple extension to heterogeneous nucleation is surprisingly good, as it has several apparent deficiencies: (1) The theory assumes that a macroscopic contact angle and a macroscopic interfacial free energy and bulk density applies to submicron-sized water germs. (2) It treats the surface of a nucleating substrate as energetically homogeneous. (3) The theory, in Fletcher's version, assumes that a water embryo on the nucleating substrate grows by the addition of water molecules directly from the vapor.

Let us now elaborate on some of these criticisms. (1) The concept of a contact or wetting angle was discussed in Section 5.5. The angle is defined as the limiting angle of water toward the solid surface on which the drop rests, the system being in equilibrium with saturated vapor. As pointed out by Corrin (1975), contact angles

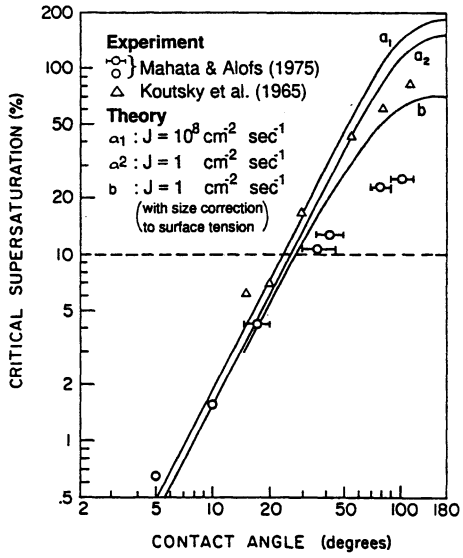


Fig. 9-15: Critical supersaturation for the onset of water nucleation on a plane, water-insoluble, partially wettable substrate, as a function of contact angle of water on substrate. Comparison of experiment with theory. (From Mahata and Alofs, 1975, with changes.)

are measured under the microscope with a linear resolution generally no better than 1 μm. This implies that the angle is not truly measured at the surface of the substrate, but is inferred by extrapolation from measurements of the drop profile well removed, on a molecular scale, from the surface. The phenomenon of hysteresis adds to the difficulties in measuring contact angles, making any measurement hard to reproduce. Even if contact angles could be measured accurately, the values would only apply to macroscopic systems and would have little meaning in the case of water-'caps' of germ-size. In addition, one has to recall that the contact angle is not only a function of the surface properties of the substrate, but is also a function of temperature and supersaturation.

Criticisms of the assumption of macroscopic interface free energies and bulk densities for small systems such as water germs have already been expressed in Chapter 7 in the context of homogeneous nucleation, and need not be repeated here.

(2) The classical theory assumes that the thermodynamic functions employed are independent of location on the nucleating substrate. This implies that the substrate surface is treated as energetically homogeneous. It is well-known, however, that surfaces are energetically heterogeneous. This behavior is well-documented by numerous adsorption studies, some of which were discussed in Chapter 5. These studies show that the surfaces of many solids do not adsorb water molecules uniformly, but rather preferentially at certain active sites. It is at these locations that phase changes are most likely to occur.

One may distinguish among three types of active sites for preferred adsorption

of water molecules from the vapor and, hence, preferred water drop formation. The first type of site is represented by a morphological surface inhomogeneity such as a step, crack, or cavity at the surface of the nucleating substrate. The second type is represented by a chemical inhomogeneity in the surface, generally caused by the presence of a foreign ion, which is hydrophilic relative to the rest of the solid surface. The third type of site is represented by electrical inhomogeneities other than ions in the surface of the nucleating substrate. Such sites may consist of sharply defined boundaries between surface regions of different electric field sign, or of locations where the electric field vector in the substrate surface is oriented parallel to the surface.

Morphological surface inhomogeneities are high energy sites where surface forces are available to effectively tie water molecules to the surface. Chemical inhomogeneities attract water molecules to the substrate surface by means of electric forces which develop between the dipole moment of the water molecule and the net dipole or charge on the foreign atom or ion. Growth of a water cluster at such a site is also aided by the relatively higher mobility of molecules on the substrate surface surrounding the hydrophilic site. Electric inhomogeneities other than ions attract water molecules to the substrate surface through interaction between local electric dipoles in the solid substrate and the dipole of a water molecule. Growth of water clusters at such sites can be aided if the diffusivity of water molecules on surface regions with either an inward-directed or an outward-directed electric field is high as compared to the diffusivity over the boundary between regions of electrically different sign, or as compared to the diffusivity over an area where the electric field vector in the substrate is oriented parallel to the substrate, since then both the positive and the negative ends of the water molecule are partially tied down.

(3) The adsorption studies of Corrin *et al.*, Zettlemoyer *et al.*, Federer, and Pruppacher and Pflaum referred to in Chapter 5 indicate that new phase embryos do not grow solely by the addition of water molecules directly from the vapor, but rather to a large extent as a result of surface diffusion of water molecules. (See also the statement immediately following (9-9).)

We recall that for the case of homogeneous nucleation, the deficiencies of the classical approach have been circumvented, in some instances, by the molecular model method of Hale and Plummer. Unfortunately, it is difficult to extend this method to a study of heterogeneous nucleation. This is because little is known of the mode and energy of interactions between clusters of water molecules and substrate molecules. The major problem in determining the interaction energy is that it is specific to each solid and to each crystallographic face of that solid. Furthermore, it is a function of position on each crystallographic face, due to the heterogeneous nature of the surface. In spite of the difficulties, some progress on applying the molecular method to heterogeneous nucleation has been reported in the literature and will be discussed in the next section, especially since this work applies to the heterogeneous nucleation of ice.

9.2 Ice Forming Nuclei (IN)

9.2.1 Number Concentration of IN

Ice forming nuclei exhibit four basic modes of action. In the first, water vapor at temperatures below 0°C is adsorbed directly from the vapor phase onto the surface of the IN where, at sufficiently low temperatures, it is transformed into ice. This mode, called the *deposition mode*, requires that the environment is supersaturated with respect to ice. Once water saturation is reached and surpassed, a second mode of action may take over: the *condensation freezing mode*. In this mode, an aerosol particle at temperatures below 0°C acts as a CCN to form a drop which freezes at some time during the condensation stage. In the third mode, the *immersion mode*, the IN becomes immersed into a drop at temperatures warmer than 0°C. Freezing is subsequently initiated whenever the temperature of the drop has become sufficiently low. In the fourth mode of action, the *contact mode*, the IN initiates the ice phase at the moment of its contact with the supercooled drop. Any of the scavenging mechanism discussed in Chapter 17 may provoke such a contact.

Aerosol particles which initiate the ice phase by the first mode of action are called *deposition* or *sorption-nuclei*, those acting by the second mode *condensation freezing nuclei*, those acting by the third mode *immersion nuclei*, and those acting by the fourth mode *contact nuclei*. An aerosol particle of given size and chemical composition may act as IN in one or possibly even in all of the four modes. In each mode the temperature at which ice is initiated is quite specific and may not be the same as the temperature characteristic of another mode. Unfortunately, none of the presently available devices which count the fraction of AP acting as IN is capable of allowing for the four different modes of action, nor can they realistically simulate the time scale over which temperatures and supersaturation vary in atmospheric clouds. Therefore, the IN concentrations quoted in the literature have to be treated with considerable caution.

In Figures 9.16 and 9.17, a selected number of IN concentration measurements are reproduced as a function of temperature and location. One notices that the mean or median IN concentration exhibits no systematic variation with geographic location. This suggests that, far from sources, the atmospheric aerosol is quite uniform with respect to its ability to initiate the ice phase. Figures 9.16 and 9.17 also show that the IN counts increase nearly exponentially with decreasing temperature. A convenient approximate statement of the behavior, due to Fletcher (1962a), is

$$N_{\mathrm{IN}} = A \exp[\beta \Delta T], \tag{9-29}$$

where $\beta = 0.6\ (^{\circ}\mathrm{C})^{-1}$, $A = 10^{-5}\ \mathrm{l}^{-1}$, where N_{IN} is the number of IN per liter active at a temperature warmer than T, and where $\Delta T = T_0 - T$. Bowdle *et al.* (1985) found for the High Planes (Montana). $A = 2 \times 10^{-4}\ \mathrm{l}^{-1}$ and $\beta = 0.3$.

For comparison with observations (9-29) has been included in Figures 9.16 and 9.17. The wide scatter of the IN counts in Figure 9.16 at any particular temperature can be attributed to a number of causes. Most obviously, the IN count at a particular station is closely coupled to the type of aerosol of the airmass present which, in turn, is a function of the immediate history of this airmass with

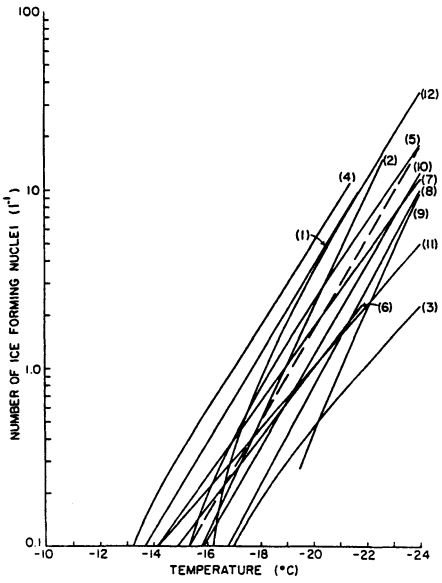


Fig. 9-16: Variation of the mean or median number concentration of IN with temperature and geographic location. (1) Bracknell (England), 51° N, 0° W; (2) Clermont-Ferrand (France), 46° N, 3° E; (3) Corvallis (Oregon), 44° N, 123° W; (4) Tokyo (Japan), 36° N, 140° E; (5) Tucson (Arizona), 32° N, 111° W; (6) Jerusalem (Israel), 32° N, 35° E; (7) Palm Beach (Florida), 27° N, 80° W; (8) Hawaii, 20° N, 158° W; (9) Swakopmund (S.Africa), 34° S, 14° E ; (10) Sydney (Australia), 34° S, 151° E; (11) Tasmania (Australia), 43° S, 147° E; (12) Antarctica, 78° S, 166° E. The dashed line represents N_{IN} (liter^{-1}) = 10^{-5} exp(0.6ΔT). (Data from Heffernan and Bracewell, 1959; Isono *et al.*, 1959; Carte and Mossop, 1960; Bigg and Hopwood, 1963; Kline, 1963; Soulage, 1964; Bigg, 1965; Droessler and Heffernan, 1965; Stevenson, 1968; and Mossop *et al.*, 1970.)

regard to its length of stay over aerosol sources. Thus, one finds pronounced day to day variations of the IN concentrations (see Figure 9.18). Similar observations were made by Bigg and Hopwood (1963) and Kikuchi (1971), who measured at an Antarctic station IN concentration maxima as high as 30 l^{-1} at $-20°C$ alternating with practically zero concentration. High concentration counts were found to last up to two days.

Short-term, positive anomalies in the IN concentration have also been found to occur at other latitudes. Such anomalies, termed *IN-storms*, are characterized by a sudden rapid increase of the IN concentration within a day or less, to values which may be several orders of magnitude larger than the typical average. After a few days, this rapid rise is followed by a similar rapid decrease in concentration.

Various explanations for these IN-storms have been offered. Bigg and Miles (1963, 1964), Droessler (1964), and Bigg (1967) attempted to explain this phenomenon on the basis of an extra-terrestrial source of IN. They hypothesized that local subsidence of air from a nucleus-rich stratosphere, occurring in the vicinity of jet streams, gives rise to layers in the troposphere which have relatively high concen-

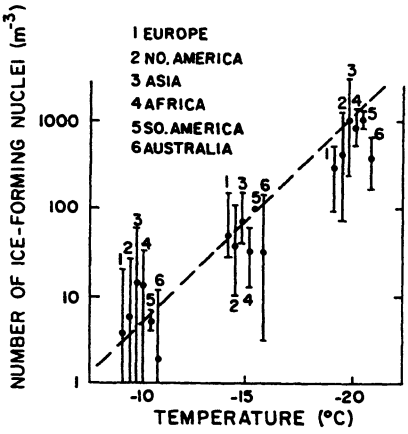


Fig. 9-17: Range of median number concentration of IN as function of temperature for various geographic locations: 44 stations, filter method. The dashed line represents N_{IN} (l^{-1}) = 10^{-5} exp (0.6 ΔT). (From Bigg and Stevenson, 1970; by courtesy of *J. de Rech. Atmos.*, and the authors.)

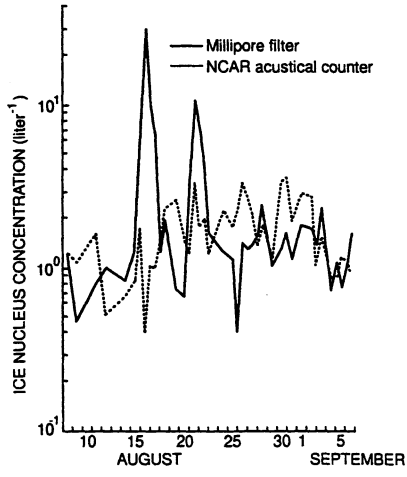


Fig. 9-18: Variation with time of the ice nucleus concentration at −20° C in air near Miles City (Montana); continuous line: millipor filter technique, dashed line: NCAR acoustical counter. (From Hobbs *et al.*, 1978, with changes.)

trations of IN. It was supposed that the particles in these layers are transported to the ground by vertical mixing. In support of this hypothesis, Droessler (1964) found that a pronounced IN-storm which occurred in December, 1963, in S.E. Australia was accompanied by a stable jet stream situation, stratospheric subsidence in the vicinity of the IN-storm area, and an associated unstable troposphere. Further support to this concept was given by Telford (1960), Bigg *et al.* (1961), and Bigg and Miles (1963), who found that the IN concentration was significantly higher in the upper troposphere and lower stratosphere than at the ground, and by Rosinski (1967b) who found the highest IN concentrations in the vicinity of jet streams. A second explanation for the phenomenon of IN-storms was given by Isono *et al.* (1959, 1970) and Hobbs *et al.* (1971b,c), based on air trajectory analysis. They concluded that local IN sources, such as vulcanic eruptions or dust storms in North China and Mongolia or in the Sahara Desert, inject IN which are advected over thousands of miles by strong tropospheric winds such as jet streams; intermittent vertical mixing and deposition should then follow. As a third alternative, Isono and Tanaka (1966), Georgii and Kleinjung (1968), and Ryan and Scott (1969) attributed IN-storms to the local formation of IN by evaporation of cloud and precipitation particles. A fourth explanation was given by Higuchi and Wushiki (1970) who noted that aerosols, sampled at Barrow (Alaska) at air temperatures between -20 and $-40°C$, and on Mt. Fuji (3776 m, Japan) at air temperatures between 0 and $-27°C$, contained IN concentrations which were considerably higher when the aerosol samples were kept below $0°C$ than when the samples were heated above $0°C$. They concluded, therefore, that terrestrial AP become activated at sufficiently cold temperatures, such as those found in the upper troposphere or in polar air masses.

A second cause for the wide scatter in the IN counts in Figure 9.16 lies in the measuring technique of the IN concentration itself. Thus, Hussain and Saunder (1984), Al Naimi and Saunders (1985), Cooper (1980), Rogers (1982) and Meyers *et al.* (1992) argued that the widely used static filter technique would underestimate the actual number of IN by as much as one order of magnitude as compared to the more recently developed continuous flow chamber technique which allows the aerosol particle to remain freely suspended in air. This is illustrated in Figure 9.19 which shows that, at any given temperature, a much larger number of AP act as IN in the contact mode than in the immersion or deposition mode. We note, in addition, the much higher IN counts in all three modes for air at Elk Mt. than for air at Laramie.

A third cause for the scatter in past IN measurements lies in the fact that the dependence of N_{IN} on relative humidities has been disregarded. Experiments by Bryant *et al.* (1959), Mason and Van den Heuvel (1959), Roberts and Hallett (1968), Gagin (1972), Matsubara (1973), Huffman (1973a,b), Schaller and Fukuta (1979), Hussain and Saunders (1984), Al Naimi and Saunders (1985), Stein and Georgii (1982), Rosinski *et al.* (1991), and Meyers *et al.* (1992) have shown that ice nucleation may proceed not only at water saturation (Weickmann, 1949), but also at relative humidities less than 100% with respect to water, as long as there is supersaturation with respect to ice. All of these investigators found that at any given temperature the number concentration of IN increases with increasing ice

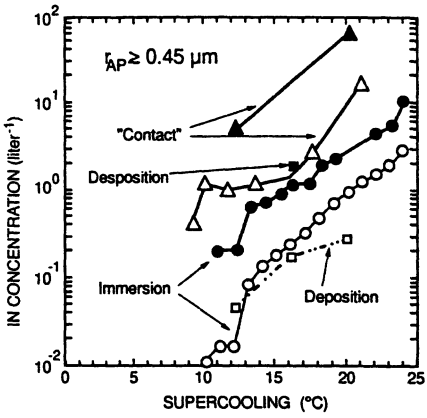


Fig. 9-19: Effect of ice nucleation mode on concentration of ice nuclei as a function of temperature. Open symbols observations at Laramie (Wyoming) in winter; solid symbols observations on Elk Mt. (3400 m, Wyoming). (From Cooper, 1980, with changes.)

supersaturation according to the relation

$$N_{\mathrm{IN}} = C^b s_{\mathrm{v},i}\,, \tag{9-30}$$

with N_{IN} in l^{-1} and $s_{\mathrm{v},i}$ in %, and where C and b are 'constants' for a given air mass. Thus, Huffmann (1973), Hussain and Saunders (1984), and Stein and Georgii (1982) found that $3 \leq b \leq 8$, with high values of b applying to the more polluted air masses. As long as $s_{\mathrm{v},i}$ remains below water saturation, the IN act in the deposition mode. Above water saturation the IN may continue to act in this mode or in the condensation freezing mode.

Unfortunately, without special equipment, it is not possible in practice to distinguish between the separate contributions of the deposition and condensation freezing modes when an air parcel becomes supersaturated with respect to water (Meyers *et al.*, 1992).

At any given temperature, the ice nucleus concentration generally increases as the saturation ratio $S_{\mathrm{v,w}}$ with respect to water increases. This increase is characteristic to each temperature (Figure 9.20a). However, if N_{IN}, as expressed in the form given in (9-30), is plotted as a function of ice supersaturation $s_{\mathrm{v},i}$ below water saturation the temperature dependence disappears (Figure 9.20b) and the increase of N_{IN} , becomes a single function of $s_{\mathrm{v},i}$ (Stein and Georgii, 1982; Huffman, 1973a,b). Using data from continous flow chambers, this has been expressed by Meyers *et al.* (1992) in the form

$$N_{\mathrm{IN}} = \exp(A + Bs_{\mathrm{v},i})\,, \tag{9-31a}$$

with N_{IN} in liter^{-1} and $A = -0.639$ and $B = 0.1296$, for the number of ice forming nuclei acting in the deposition and condensation freezing mode. Earlier, Cotton *et al.* (1986) combined the results of Fletcher and Huffman to give

$$N_{\mathrm{IN}} = A[s_{\mathrm{v},i}/(s_{\mathrm{v},i})_0]^b \exp(\beta \Delta T)\,, \tag{9-31b}$$

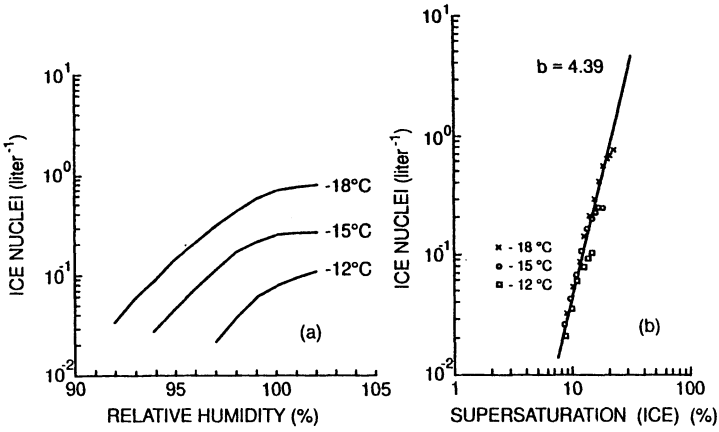


Fig. 9-20: Variation of ice nucleus concentration in air over St. Moritz (Switzerland) at 3 temperatures: (a) as a function of relative humidity with respect to water, (b) as a function of supersaturation with respect to ice. (From Stein and Georgii, 1982, with changes.)

with $A = 10^{-5}$ liter^{-1}, $\beta = 0.6(°C)^{-1}$ and $(s_{v,i})_0$ being the fractional ice supersaturation at ΔT. According to Meyers *et al.* (1992), (9-31b) underpredicts the number of ice nuclei and suggest that (9-13a) is more realistic. For the number of ice buclei acting in the contact mode, Meyers *et al.* (1992) suggested using

$$N_{IN} = \exp[a + b(273.15 - T_c)]\,, \tag{9-31c}$$

with $a = -2.80$ and $b = 0.262$, based on measurements of Vali (1974, 1976), Cooper (1980) and Deshler (1982).

In order to characterize the temperature and humidity conditions at which a given aerosol particle acts in one or another ice nucleation mode, Schaller and Fukuta (1979), confirming the earlier studies of Roberts and Hallett (1968) and of Isono and Ishizaka (1972), have demonstrated in their diffusion chamber that an aerosol particle of given chemical composition acts in the deposition mode only if the air temperature has fallen below a characteristic value. Thus, we see in Figure 9.21 that silver iodide particles act as condensation freezing nuclei above a characteristic temperature of $-9°C$. Below $-9°C$, they act as deposition nuclei if a critical ice supersaturation is surpassed. A much lower characteristic temperature of about $-18°C$, and a correspondingly higher critical supersaturation, are required for clay particles (kaolinite). These experiments demonstrate that, in contrast to the case of homogeneous nucleation (Chapter 7), Ostwald's rule of stages becomes inverted below the characteristic temperature. This implies that below this temperature the metastable phase, i.e., the supercooled water, is no longer prerequisite for the ice phase to appear.

The rapid increase in activity of aerosol particles as ice nuclei with increasing supersaturation, in particular as the humidity rises above water saturation

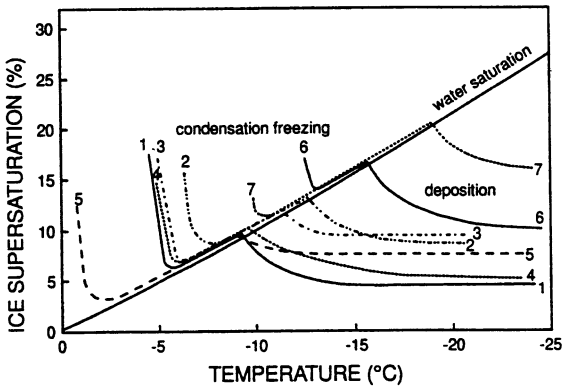


Fig. 9-21: Onset of ice nucleation as a function of temperature and ice supersaturation for various compounds. Conditions for condensation-freezing and deposition nucleation are indicated. Ice nucleation occurs above the indicated lines; (1) AgI, (2) PbI, (3) 1.5 Dihydroxynaphtalene, (4) Phloroglucinol, (5) Methaldehyde, (6) Soil, (7) Kaolinite. (From Schaller and Fukuta, 1979, by courtesy of Am. Meteor. Soc., and the authors.)

(e.g. Gagin, 1972; Rosinski *et al.*, 1975; Schaller and Fukuta, 1979; Hussain and Saunders, 1984; deMott and Grant, 1984; Gagin and Nozyce, 1984, Al Naimi and Saunders, 1985; Blumenstein *et al.*, 1987), prompts the question as to whether in atmospheric clouds the supersaturation with respect to water indeed may reach significantly above 100%. We have discussed this question in Section 2.1.1 and pointed out that accurate data derived from in situ measurements of the humidity in clouds are scarce. On the other hand, numerical modeling studies of atmosphere clouds suggest (Clark, 1973; Hall, 1980; Young, 1974; Ochs, 1978; Ahr *et al.*, 1989b) that pockets of high supersaturation may exist in cumuli-form clouds associated with the initiation of pronounced growth of cloud drops by collision and coalescence. As growth of drops by collision and coalescence sets in, the total drop number concentration abruptly falls, and the supersaturation rises due to a reduced total surface area of the drops onto which water vapor can condense.

In some studies (Dye and Hobbs, 1968; Nix and Fukuta, 1974; Rosinski *et al.*, 1975; Gagin, 1972; Gagin and Nozyce, 1984), it has been proposed that high supersaturation with respect to water may be reached in the vicinity of freezing cloud and precipitation drops, or growing graupel. However, Rangno and Hobbs (1991) and Baker (1991b) discounted such effects on the basis that freezing drops and growing graupel: (1) warm their immediate surrounding, thus counteracting any rise in supersaturation; (2) affect the humidity of only very small volumes of air; and (3) produce, if any, only very short lived effects due to the effective ventilation of their surface.

Considering that the AP concentration generally decreases with increasing height (Chapter 8), one might expect the same for the concentration of IN; however, we are also forewarned from the vertical variation of CCN to expect a more complex behavior. We notice from Figure 9.22 that for the indicated geographic location,

the IN concentration indeed varies with height as expected from the variation of the AP. On the other hand, Hobbs *et al.* (1978) found no variation with height up to 5 km in air over the High Plains (Montana). The general uniformity of ice nucleus concentration with height was also observed in the earlier airborne measurements of Murgatroyd and Garrod (1957) and Kassander *et al.* (1957). In addition, as we have noted already, Telford (1960), Bigg *et al.* (1961), and Bigg and Miles (1963) found that in air over Australia, the concentration of IN was significantly higher at 13 to 27 km altitude than at the ground. Analogously, Rosinski (1967b) found over Colorado that on some occasions the IN concentration was highest near the jet stream. In more detailed investigations, Bigg and Miles (1964) and Bigg (1967) found that at ground level in the Southern Hemisphere, high IN concentrations occurred in long strips of 100 to 300 km width, as well as inside elongated layers at 4 and 11 km altitude. These banded regions were narrower and had higher IN concentrations aloft than at the ground. Isolated smaller regions with high concentrations were also found. These regions of high concentration were found to be mostly confined to the latitude belt from 23 to 30°S. In addition to these anomalous regions, broad regions at 10 to 12 km altitude were found near the equator where the air was markedly deficient in IN.

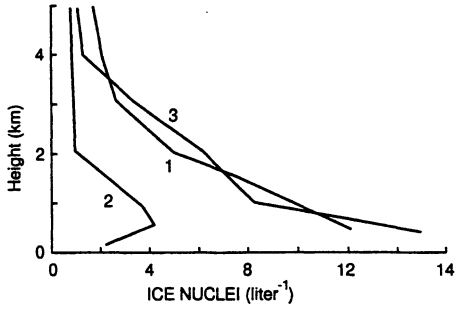


Fig. 9-22: Vertical variation of the ice nucleus concentration in air over the U.S.S.R.: (1) Foothills of N. Caucassus, (2) Black- and Caspian seas, (3) Kharkov region. (From Khorguany *et al.*, 1980, with changes.)

Huffman (1973b) observed that the vertical IN concentration profiles often exhibit a pronounced layer-structure even in the lowest few kilometers above ground. For example, a strong concentration maximum was observed during a few days of summertime sampling at about 500 m above ground over St. Louis and over north-east Colorado. No temperature inversion was present at the time over north-east Colorado, and the inversion over St. Louis was considerably above the IN concentration maximum; thus, the concentration maxima appear not to be correlated with the temperature inversion. It is likely that IN concentration maxima in the atmosphere and IN storms at the ground are closely related and have the same causes.

In some recent studies, Berezinski *et al.* (1988) concluded from a large number of aircraft flights over the European Territory of the U.S.S.R., that the IN

concentration decreases with height more slowly than the concentration of AP of corresponding sizes. This would imply an increase in the relative ice forming activity with increasing height. As reasons for such behavior, Berezinski *et al.* (1988) suggested (1) a shift of the AP size spectrum towards larger particles just underneath inversions, (2) an improvement of the ice-nucleability of AP, followed by drop-to-particle conversion during the evaporation of clouds, and (3) a decrease in the CCN portion of the AP spectrum during cloud formation, which generally leaves water insoluble particles unaffected.

9.2.2 Sources and Chemical Composition of IN

Some clues as to possible sources of IN are provided by the chemical identification of AP found at the center of snow crystals. Such studies were carried out by Kumai (1951, 1957, 1961, 1976), Isono (1955), Kumai and Francis (1962b), and Rucklidge (1965) using electron microscope and electron-diffraction techniques. Typically, one solid silicate particle, usually identified as clay, was found in the central portion of a snow crystal. The diameters of the particles ranged from 0.1 to 15 μm. These findings suggest that desert and arid regions of the Earth surface are a major source of IN. In support of this possibility, Isono *et al.* (1959, 1970) and Hobbs *et al.* (1971b,c) used an air mass trajectory analysis to show that high IN concentrations over Japan and the northwestern U.S. are often the result of local dust storms over arid regions of North China and Mongolia. During such storms, clay particles become airborne and are transported towards Japan and eastward to the U.S. continent via the jet stream.

A detailed analysis of the central particles of snow crystals is given in Table 9.5. We notice that the central particle consist of clay minerals such as illite, kaolinite, halloysite, and vermiculite, the last being the most abundant (Kumai, 1976), although some central particles may also be composed of hygroscopic materials, combustion products, and micro-organisms. In Table 9.6, the chemical composition of IN is separated according to three nucleation temperatures. Notice that the clay particles dominate the IN composition at temperatures between -12 and -20°C. Soulage (1955, 1957) dissected the residue of snow crystals and found that the larger particles consisted of a mixture of soluble and insoluble materials. Kumai (1966b, 1969b) found that about 2% of the central particles of his sample of ice crystals consisted of spherical particles (spherules) of diameter between 0.6 and 6 μm, some of which were identified as extraterrrestrial material. In addition to a large central particle, numerous smaller particles of diameters between 0.05 and 0.15 μm were found in the outer portions of the crystals. This led to the supposition that the central particle was instrumental in the nucleation of the snow crystal, while all other particles were subsequently captured.

The notion that surface soils act as an IN source is also strongly supported by laboratory experiments. The ice-forming capability of silicate particles collected at various parts of the Northern Hemisphere has been tested by Schaefer (1950), Pruppacher and Sänger (1955), Mason and Maybank (1958), Isono *et al.* (1959), Mason (1960a), Isono and Ikebe (1960), and Roberts and Hallett (1968). When these particles were allowed to function as IN in the deposition mode at water

TABLE 9.5
Composition of aerosol particles in the central portion of snow crystals.

Composition of center particle	Hokkaido (Japan) Number	%	Honshu (Japan) Number	%	Michigan (U.S.A) Number	%	Missouri (U.S.A) Number	%	Thule (Greenland) Number	%	Amundsen-Scott (South Pole) Number	%
Clay mineral	176	57	46	88	235	87	70	28	302	84	55	59.1
Hygroscopic particle	57	19	0	0	2	1	5	2	2	1	19	20.4
Combustion product	26	8	2	4	6	2	7	3	0	0	-	-
Micro-organism	3	1	0	0	0	0	3	1	0	0	-	-
Unidentified	30	10	4	8	25	9	100	40	39	11	5	5.4
Not observed	15	5	0	0	3	1	65	26	13	4	14	15.1
Total	307	100	52	100	271	100	250	100	356	100	93	100
Reference			Kumai (1961)				Rucklidge (1965)		Kumai and Francis (1962b)		Kumai (1976)	

TABLE 9.6
Composition of ice forming nuclei derived from aerosolized soil in Montana (from Rosinski *et al.*, 1981).

Chemical composition	Aerosol particles number	%	Ice-forming nuclei active at temperature −12°C number	%	−15°C number	%	−20°C number	%
Clay minerals:								
montmorillonite	194	24	28	18	17	13	41	28
feldspar	287	36	74	48	41	32	54	38
illite	163	20	37	24	39	31	28	19
miscellaneous	27	3	8	5	19	15	10	7
Organic particles	139	17	7	5	12	9	11	8
Number of particles: analyzed	810		154		128		144	
Mixed particles containing:								
NaCl	7		14	9	28	22	21	15
CuX	2		1		0		1	
$Fe0_x.nH_20$	-		7	5	12	9	11	8
Total	9		22	14	40	31	33	23

saturation, the threshold ice-forming temperature (which is conventionally taken as the temperature at which 1 particle in 10^4 produces an ice crystal) was found to range typically between −10 and −20°C. Clay particles, such as kaolinite, anauxite, illite, and metabentonite, have a threshold temperature as warm as −9°C (Mason, 1960a).

Surprisingly, clays such as kaolinite often exhibited varying ice nucleating abilities, or 'nucleabilities', depending on the location at which the clays were sampled. Similarly, soils from different parts of Australia were found to be generally less active than those from the Northern Hemisphere, the threshold temperature of Australian soils ranging between −18 and −22°C (Paterson and Spillane, 1967). The observations suggest that other substances admixed to soils in small quantities may importantly affect their ice nucleation behavior.

In an attempt to identify more quantitatively the chemical compounds in AP acting as IN, Parungo *et al.* (1976), Kikuchi *et al.* (1982), and Grosch (1978) carried out an analysis of the various elements contained in IN. They found that the elements particularly prevalent in IN were Si, Al, Mg Ca, K, Fe, S, and Cl. All but the last two are characteristic of silicate minerals.

Experiments by Roberts and Hallett (1968) showed that clay particles having been involved once in ice crystal formation, can exhibit a considerably improved nucleability. AP which behave in such a manner are termed preactivated. Roberts and Hallett showed that the IN activity spectrum for each of the tested clays, containing particles of diameters between 0.5 and 3 μm shifted by more than 10°C towards warmer temperatures (Figure 9.23) provided that the temperature of the air in which the clay particles were kept never rose above 0°C, and its relative humidity never fell below 50%.

Clays also seem to exhibit significant differences in their ice nucleating ability

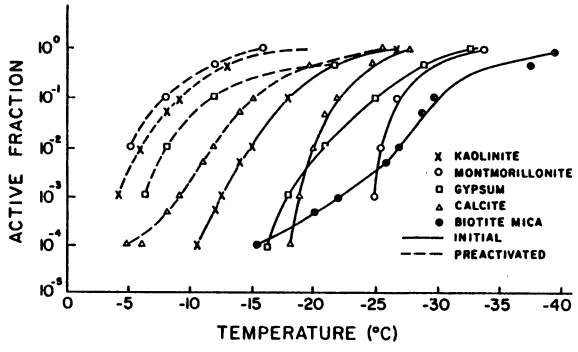


Fig. 9-23: Variation with temperature of the ice nucleating ability of clay mineral particles in the deposition mode: Initial ice nucleation ability and ice nucleation ability after preactivation. (From Roberts and Hallett, 1968; by courtesy of *Quart. J. Roy. Meteor. Soc.*)

according to their mode of action. Isono and Ikebe (1960), Mason (1960a), and Roberts and Hallett (1968) showed that kaolinite acting in the deposition mode has a typical activation temperature of about −9°C, and reaches full activity (1 to 1 ice crystal production ratio) near −20°C, while montmorillonite has an activation temperature of about −25°C, and reaches full activity near −30°C. In contrast, Hoffer (1961) found that the warmest freezing temperature of 50 to 60 μm radius drops containing kaolinite and montmorillonite was −13.5°C, and that the median freezing temperatures were −24.0 and −32.5°C, respectively. Gokhale and Spengler (1972), on the other hand, found that drops of 2 to 3 mm radius, freely suspended in the air stream of a wind tunnel, froze at temperatures as warm as −2.5°C, with full activity between −6 and −8°C, when contacted by red soil, sand, or clay particles. In agreement with the observations of Hoffer and of Gokhale and Spengler, Pitter and Pruppacher (1973) found from wind tunnel experiments that freely falling drops of 325 μm radius froze at temperatures below −14°C when freezing was initiated from within a drop by kaolinite or montmorillonite (freezing mode), with full activity being achieved below −28°C. On the other hand, the same drops froze at temperatures as warm as −4°C and with full activity near −14°C when contacted by dry clay particles (contact mode). These results are illustrated in Figure 9.24.

While monitoring the IN concentration in Japan, investigators detected another source of IN. Isono and Komabayasi (1954), Isono (1959b), and Isono *et al.* (1959) observed that pronounced IN storms arose following the eruption of volcanoes. As an example of this effect, the time variation of the IN concentration during the eruption of the volcano Asama is given in Figure 9.25. In support of the notion that volcanoes act as IN sources, Mason and Maybank (1958), Isono *et al.* (1959), and Isono and Ikebe (1960) found during laboratory experiments that volcanic ash and other volcanic materials were capable of serving as IN with threshold temperatures as warm as −7.5°C. A similar threshold temperature was found by Schnell *et al.*

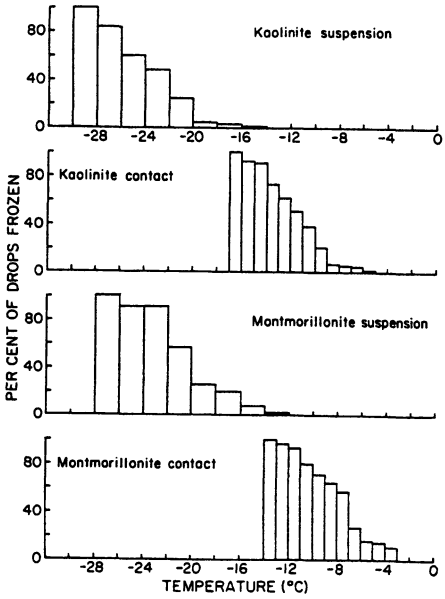


Fig. 9-24: Comparison between the freezing temperature of drops of 325 μm radius, frozen in the contact mode with clay particles, and the freezing temperature of drops frozen in the immersion mode by clay particles suspended inside the drops. Drops freely suspended in the air stream of a wind tunnel. (From Pitter and Pruppacher, 1973; by courtesy of *Quart. J. Roy. Meteor. Soc.*)

(1982) for AP in the effluent of Mt. St. Helen volcano (U.S.A.). However, in contrast to these findings, Price and Pales (1963) found no significant increase of the IN concentration during the eruption of volcanoes on the Hawaiian Islands, indicating that not all volcanic material has a high ice nucleability. Particles from the effluent of the Mt. Usu volcano (Japan) were found by Tanaka (1980) to act as IN following (9-29) with $A = 9.2 \times 10^{-4}\ l^{-1}$ and $\beta = 0.6\ (°C)^{-1}$. These particles also exhibited a remarkable increase in effectiveness above water saturation.

From Table 9.5, it is evident that some of the center particles consist of combustion products. This finding suggests natural or anthropogenic combustion sources for IN. In support of this notion, Hobbs and Locatelli (1969) observed a significant increase in the concentration of IN downwind of a forest fire, and Pueschel and Langer (1973) observed increased IN concentrations during sugar cane fires in Hawaii. In contrast, deMott (1990) and Hallett *et al.* (1986) found that soot particles from crude oil and acetylene burners were not active as IN at a temperature above $-15°C$. In fact, in most cases, the soot particles acted as CCN once the supersaturation with respect to water rose above about 2% and subsequently froze at temperature below $-20°C$ through the soot particles acting as immersion IN inside the drops.

Evidence for the effectiveness of other sources of anthropogenic IN has been provided by Soulage (1958, 1964), Telford (1960), Admirat (1962), Langer and

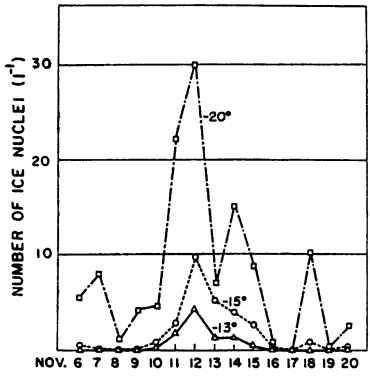


Fig. 9-25: Effect of the eruption of volcano Asama on November 10, 1958, in Japan on the concentration of IN. (From Isono, 1959b; by courtesy of *Nature*, and author.)

Rosinski (1967), and Langer (1968), who showed that certain industries, in particular, steel mills, aluminum works, sulfide works, and some power plants, release considerable amounts of IN into the atmosphere. The particles emitted from electric steel furnaces in France were found to be of particularly high effectiveness as IN, with a threshold temperature of about −9°C, Wirth (1966). Soulage (1966), and Georgii and Kleinjung (1968) showed that the mean IN concentration is comparatively high throughout heavily industrialized Europe. For example, the mean IN concentration observed during the summer of 1964, at 10 different locations in Europe ranged from 2.6 to 53.7 l^{-1} at −20°C. Similarly, Schnell *et al.* (1980) observed IN from steel mills to be active at temperatures as high as −6 to −8°C, and to appear in concentrations of up to 5 times ambient levels at temperatures between −10 to −12°C.

These high IN concentrations can be understood in part from the fact that some of the particles emitted during industrial processes consist of metal oxides, most of which are known to have a high nucleability. Thus, Fukuta (1958), Serpolay (1958, 1959), Mason and van den Heuvel (1959), Katz (1960), Pueschel (1978) found that the oxides Ag_2O, Cu_2O, NiO, CoO, Al_2O_3, CdO, Mn_3O_4, and Sb_2O_3 exhibit threshold temperatures between −5 and −12°C, while oxides such as CuO, MnO_2, SnO, ZnO, Fe_3O_4, MgO, NiO, Fe_2O_3, PbO, Y_2O_3, ZrO_2 and BaO have threshold temperatures of between −12 and −20°C. Also, particles of portland cement ($3CaO{\cdot}SiO_2$, $2CaO{\cdot}Si_2O$, $3CaO{\cdot}Al_2O_3$, $4CaO{\cdot}Al_2O_3{\cdot}Fe_2O_3$) were found to act as IN at temperatures as warm as −5°C (Murty and Murty, 1972).

Although some specific anthropogenic sources may emit IN, the anthropogenic emission from urban complexes as a whole is generally deficient in IN. Thus, studies by Braham (1974) and Braham and Spyers-Duran (1975) carried out in the area of St. Louis show that, on the average, fewer IN were found downwind of the city than upwind. This suggests that anthropogenic combustion products emitted into the air over urban areas are generally poor IN and, in addition, are capable of deactivating existing IN.

Two processes have been suggested by which IN become deactivated. Georgii (1963) and Georgii and Kleinjung (1967) showed that foreign gases such as SO_2, NH_3, and NO_2 severely reduce the ability of atmospheric AP to serve as IN. The higher the concentration of these gases, the stronger is the deactivation. A second mechanism of deactivation was proposed by Georgii and Kleinjung (1967). They suggested that in urban areas, where the concentration of Aitken particles may reach 10^6 cm^{-3} and higher, IN become deactivated as a result of coagulation with these particles, which are generally found to be poor IN. In support of this mechanism, Georgii and Kaller (1970) computed the time necessary for deactivation of IN of various sizes by coagulation with Aitken particles of various sizes and number concentrations. In these computations it was assumed (1) that coagulation is the result of Brownian diffusion, (2) that the effects of forced convection and turbulence can be neglected, (3) that an IN can be considered to be deactivated when covered with a monolayer of Aitken particles, (4) that the sticking efficiency is unity, (5) that the Aitken particles and the IN are spherical, (6) that the size of an IN remains constant, implying that the small size increase due to the added Aitken particles can be neglected, and (7) that there is no depletion of Aitken particles in the environment of an IN. Since some of these assumptions have opposite effects, it was considered that the over-all model should be fairly realistic.

The deactivation time determined by Georgii and Kaller is

$$t = \frac{2\nu^* \rho}{K_B(r_N, r)N(r)}, \tag{9-32}$$

where the coverage number $\nu^* = 2/(1 - [(r_N^2 + 2r_N r)^{1/2}/(r_N + r)])$, $\rho \approx 0.91$ is the packing density of the Aitken particles around the IN, r is the radius of the Aitken particle, r_N is the radius of the IN, $N(r)$ is the number concentration of Aitken particles, and K_B is the coagulation constant (see Chapter 11). The result of a numerical evaluation of (9-32) is given in Figure 9.26. It is seen that the time to deactivate IN decreases with increasing concentration of Aitken particles, with decreasing IN size for a constant Aitken particle size, and with increasing Aitken particle size for a constant IN size. Figure 9.26 implies that IN may become completely deactivated during 0.5 to 3 days, i.e., 12 to 72 hours (which is the residence time of AP in the lowest atmospheric layers) if the air is strongly polluted, i.e., $N \geq 10^6$ cm^{-3}. If N $< 10^6$ cm^{-3} partial coverage of the surface of IN may result in partial deactivation.

Laboratory and field studies also demonstrate that IN may have a biogenic source. Vali (1968a,b) noted during experiments that soils with a relatively high content of organic matter exhibited a higher ice nucleability than pure clays or sand. This observation led him to suggest that decaying plant material contributes to the IN content of the atmosphere. Subsequent detailed studies by Schnell (1972, 1974), Fresch (1973), Vali and Schnell (1973), Schnell and Vali (1976), and Vali *et al.* (1976) showed that some IN in soils are produced by decomposition of naturally occurring vegetation such as tree leaves. Leaf derived nuclei (LDN) were found to initiate ice by the freezing mode at temperatures typically between -4 and -10°C. The diameter of these particles ranged between 0.005 and 0.1 μm.

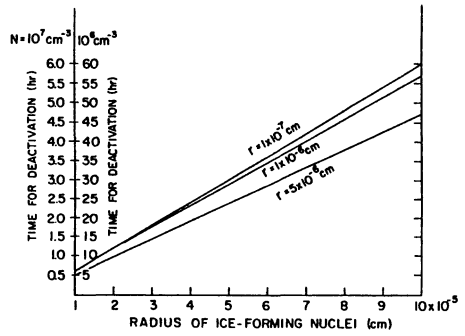


Fig. 9-26: Time for deactivation of IN by coagulation with Aitken particles of radius r and concentration $N = 10^6$ cm^{-3} and $N = 10^7$ cm^{-3}. (Based on data of Georgii and Keller, 1970.)

The global ubiquity of these biogenic IN was established by testing plant litter collected at various geographic locations in different climatic zones (Vali and Schnell, 1973). Highly active IN (active as immersion freezing nuclei at -1.3°C) were found to be present during the early stages of decay of aspen leaves. Fresch (1973) demonstrated that the ice forming capability of these decaying leaves is closely related to a single strain of aerobic bacteria (pseudomonas syringae), which by themselves act as IN. Similarly, the leaves of citrus plants were also found to carry bacteria which act as IN (Levin *et al.* 1980). Such nuclei were termed bacteria derived nuclei (BDN). Whether or not LDN and BDN are to be regarded as acting independently of each other has not been established. Schnell (1974, 1977) and Fall and Schnell (1984) also found that some organic material from the ocean surface, termed ocean derived nuclei (ODN), can be quite effective IN. Thus, marine phytoplankton at La Jolla, California, containing pseudomonas fluorescens bacteria, and sea water containing erwinia herbicola bacteria at the same site gave ice nucleation threshold temperatures of -2 to -3°C. These experiments showed that LDN, BDN, and ODN may act as IN in both the immersion freezing and deposition modes, being generally more efficient in the immersion freezing mode. Wind tunnel studies by Levin and Yankowski (1983) and Yankowski *et al.* (1981) with water drops freely suspended in the air stream of a wind tunnel and nucleated by dessicated bacterial cells, showed that these particles acted as IN both in the immersion freezing mode as well as in the contact mode at threshold temperatures between -2 and -5°C. Maki and Willoughby (1978) studied bacteria from various leaves, and showed that about one ice forming nucleus is formed among 20 to 100 bacteria cells, their ice nucleation activity being associated with properties of their cell wall.

Except for the ODN mentioned above, the world oceans are not a source of IN. Field observations by Mossop (1956), Georgii and Metnieks (1958), Georgii (1959a), Isono *et al.* (1959), Carte and Mossop (1960) and Murty (1969) have demonstrated that maritime air masses are consistently deficient in IN. The inverse

correlation between the concentration of sea salt particles and the IN concentration is illustrated in Figure 9.27. Laboratory studies carried out in cloud chambers by Hosler (1951), Birstein and Anderson (1955), Pruppacher and Sänger (1955), Fukuta (1958), and Sano *et al.* (1960) corroborate this notion. Their experiments showed that AP consisting entirely of NaCl, NH_4Cl, NH_4NO_3, $(NH_4)_2SO_4$ and $CaCl_2$ salts typically found in the atmosphere, did not act as IN at temperatures warmer than $-18°C$.

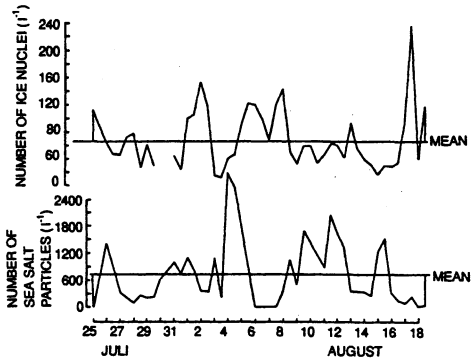


Fig. 9-27: Correlation between number concentration of ice forming nuclei active between 0 and $-30°C$ and sea salt particle concentration on the island of Valencia. (From Georgii, 1959a; by courtesy of *Ber. Deutsche Wett. Dienst., U.S. Zone.*)

Following a suggestion by Bowen (1953, 1956a,b), several researchers have advocated an extraterrestrial source of IN. Accounts of earlier arguments for and against the Bowen hypothesis have been given by Fletcher (1961, 1962a) and Mossop (1963b). Later evidence seems to be just as controversial. For example, Bigg (1963) and Bigg and Miles (1964) found a close correlation between the moon phase and the IN concentration, which was interpreted by them in terms of a lunar modulation of the extraterrestrial influx of IN. Bigg and Miles (1963, 1964) and Bigg (1967) suggested that an extraterrestrial influx of IN would explain the increase in the IN concentration with height, and the peculiar layered vertical structure in the concentration of IN which is often found over the Southern Hemisphere. Support for the Bowen hypothesis was also given by Maruyama and Kitagawa (1967), who gave evidence of a positive correlation between the IN concentration and the occurrence of meteorite showers. However, no such correlation was found by Georgii (1959b), Gagin (1965), or Isono *et al.* (1970). Reinking and Lovill (1971) also took issue with the Bowen hypothesis. They found at a high mountain observatory that a large IN concentration was not accompanied by a high ozone concentration, as would have been expected for a downward transport of extraterrestrial IN. Evidence against the Bowen hypothesis was also given by Mason and Maybank (1958) and by Qureshi and Maybank (1966), who tested the ice nucleating efficiency of ground meteorite materials. All samples tested by Mason and Maybank acted as IN below $-17°C$, while Qureshi and Maybank found three samples to be active between -13 and $-15°C$, and all others below $-16°C$. Bigg and Giutronich (1967), on

the other hand, criticized the early laboratory experiments as being unrealistic and showed that freshly condensed particles formed from artificially evaporated meteorite material acted as an abundant source of IN at $-10°C$ and water saturation. In contrast to these experiments, however, Gokhale and Goold (1969) found that particles of extraterrestrial material which were sampled at an altitude of 80 km, did not act as IN at $-20°C$.

However, as was pointed out somewhat earlier by Junge (1957a), even if clear evidence were available that certain types of meteorite materials possess ice forming capabilities at temperatures warmer than $-15°C$, it would remain physically and meteorologically quite unrealistic to assume that meteorite shower particles, which typically have a broad size distribution, could reach the troposphere as a sharply defined cloud, and then become responsible for world-wide rainfall anomalies after a time lag of 30 days between the meteor shower and the rainfall occurrence, as envisioned by the Bowen hypothesis. It is obvious from this controversy that more evidence is needed to settle the question of an extraterrestrial source of IN. Our present knowledge of the behavior of terrestrial AP seems, however, to suggest that no extraterrestrial source of significant strength needs to be invoked in order to explain the observed characteristics of atmospheric IN.

9.2.3 The Main Requirements for IN

If we compare the number concentration of IN with the total AP, it becomes clear that the ice forming process is very selective. Consider, for example, that at a temperature as low as $-20°C$, at which the atmosphere typically contains 1 IN l^{-1}, the ratio of the number concentration of IN to that of AP is as small as 10^{-6} for a total AP concentration of only 10^3 cm^{-3}. In polluted areas and at warmer temperatures, this ratio is even smaller. The reason for this selectivity lies in the fact that an aerosol particle must have a number of specific characteristics in order to serve as an ice forming nucleus. The most important of these will now be discussed.

9.2.3.1 *Insolubility Requirement*

In general, IN are highly water-insoluble. The negative correlation which is observed between the concentrations of IN and sea salt particles gives some evidence of this fact (Figure 9.27). The obvious disadvantage of a soluble substrate is that its tendency to disintegrate under the action of water prevents it from providing a rigid substrate needed for ice germ formation. In addition, the presence of salt ions causes a lowering of the effective freezing temperature (recall Section 6.7; also, see Section 9.2.5).

9.2.3.2 *Size Requirement*

Field studies have shown that AP of the Aitken size range are considerably less efficient IN than 'large' AP. For example, it can be seen from Figure 9.28a that the concentration of IN active at temperatures warmer than $-20°C$ is positively correlated with the concentration of large particles, but is uncorrelated with the

number of Aitken particles (Figure 9.28b). Although it is tempting to interpret such observations in terms of an IN size effect alone, they may partly reflect a dependence of AP chemistry on size (e.g., silicate particles, which are known to be good IN, are mostly confined to the 'large' size range).

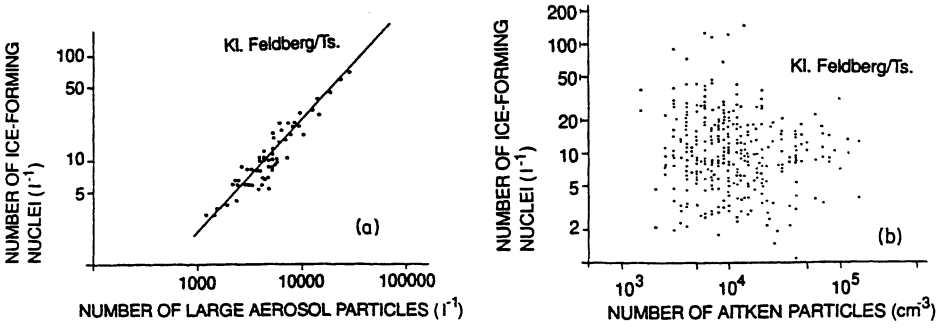


Fig. 9-28: a, b. Relation between the concentration of IN and aerosol particles on Mt. Kleiner Feldberg/Taunus (Germany): (a) large aerosol particles, (b) Aitken particles. (From Georgii and Kleinjung, 1967; by courtesy of *J. de Rech. Atmos.*, and the authors.)

However, there are other clear indications that IN size is important. For example, IN must have a size comparable to or larger than that of the critical ice embryo or germ. Estimates of the size cut-offs imposed by this requirement can be obtained from inspection of Figures 6.5 and 6.7. From the former figure, we see that in vapor at water saturation the radius of an ice germ is 0.035 μm at $-5°$C and 0.0092 μm at $-20°$C, while from the latter figure we find that inside a water drop at -5 and $-20°$C the ice germ radius is 0.010 and 0.0024 μm, respectively. For AP to act as IN at the temperatures indicated, they evidently must have radii larger than these. Observations show that, indeed, AP found in the center portions of ice crystals are considerably larger than the germ sizes indicated.

Such trends have been confirmed by several laboratory experiments. For example, Hosler and Spalding (1957), Sano *et al.* (1960), Edwards and Evans (1960), Edwards *et al.* (1962), and Gerber (1972) showed that below about 0.1 μm radius, the effectiveness of IN progressively decreases with decreasing size, becoming increasingly temperature dependent and negligibly small if the particle radius is less than about 0.01 μm (100 Å). However, the exact value of this cut-off seems to be dependent on the chemical composition of the IN and on its mode of action. For IN acting in the deposition mode, the cut-off seems to depend on the vapor supersaturation of the environment. IN acting in the freezing mode tend to be less affected by size. Unfortunately, no studies have been reported on the size effect of IN acting in the contact mode.

These observations suggest that IN typically have sizes larger than 0.1 μm. Indeed, Rosinski *et al.* (1980), Georgii and Stein (1981) and Stein and Georgii (1983) found from studies of the central particles of snow crystals, that the diameter of IN typically ranges between 0.1 and 15 μm, with a mode between 0.5 and 5 μm.

A size dependence quite different from that just described was found by Vali (1968a), who studied the freezing temperature of aqueous suspensions of surface soils which contained large quantities of organic material. By filtering these suspensions, Vali showed that organic particles attached to surface soil may initiate water freezing at temperatures as warm as $-8°C$, even though their diameters may be as small as $0.01\,\mu m$. These results were confirmed by Schnell (1972, 1974) who, as mentioned earlier, chemically isolated some organic, ice nucleation active materials. He found that organic particles such as those derived from tree leaf litter, could have diameters as small as 0.025 to $0.05\,\mu m$ and still be capable of initiating freezing at temperatures between -5 and $-8°C$.

Since the solubility of a substance increases with decreasing particle size (see Section 6.9), we might have expected, on this basis alone, to find that IN occur predominantly in the larger size ranges of AP. The existence of very small organic IN is consistent with the fact that such particles are known to be highly water-insoluble.

9.2.3.3 *Chemical Bond Requirement*

Numerous experimental studies show that the chemical nature of an IN, expressed in terms of the type and strength of the chemical bonds exhibited at its surface, also affects its nucleation behavior. Considering the fact that an ice crystal lattice is held together by hydrogen bonds (O—H----O) of specific strength and polarity, it is quite reasonable to assume that an IN must have similar hydrogen bonds available at its surface in order to exhibit good ice-nucleability. Fukuta (1966) found that, in addition to having similar bond strength and polarity, a hydrogen-bonding molecule at the IN surface should also possess rotational symmetry. While asymmetric molecules tend to point their active H-bonding groups inward to achieve minimum free energy at the solid surface, molecules with rotational symmetry cannot avoid exposing their active H-bonding groups, thus allowing maximum interaction with an oncoming water molecule.

In view of this bond requirement, it is not surprising that certain organic compounds have been found to behave as excellent IN. Head (1961a,b, 1962a,b) was one of the first to demonstrate experimentally that hydrogen-bonding groups such as —OH, $—NH_2$, =O, and their geometric arrangement at the surface of an organic substrate, are of importance to ice nucleation. Other experiments have shown that in the deposition mode metaldehyde $(CH_3CHO)_4$ has an ice nucleation threshold temperature as warm as $-0.4°C$ (Fukuta, 1963), cholesterol $(C_{27}H_{46}O{\cdot}H_2O)$ has a threshold of -1 to $-2°C$ (Fukuta, 1963; Fukuta and Mason, 1963), and phloroglucinol $(C_6H_3(OH)_3{\cdot}2H_2O)$ has a threshold temperature of -2 to $-4°C$ (Langer *et al.*, 1963; Fukuta, 1966). Many other organic compounds have also been found to be ice nucleation active at temperatures warmer than $-10°C$ (Komabayasi and Ikebe, 1961; Fukuta and Mason, 1963; Langer *et al.*, 1963; Barthakur and Maybank, 1963, 1966; Garten and Head, 1964; Parungo and Lodge,1965, 1967a; Evans, 1966; Fukuta, 1966).

9.2.3.4 *Crystallographic Requirement*

Experiments have also shown that the geometrical arrangement of bonds at the substrate surface is often of equal or greater importance than their chemical nature. Since ice nucleation on a foreign substrate may be regarded as an oriented (or *epitaxial*) overgrowth of ice on this substrate, it is quite reasonable to assume that this overgrowth is facilitated by having the atoms, ions, or molecules which make up the crystallographic lattice of the substrate exhibit, in any exposed crystallographic face, a geometric arrangement which is as close as possible to that of the water molecules in some low index plane of ice. In this manner, atomic matching across the interface between ice and the substrate particle may be achieved.

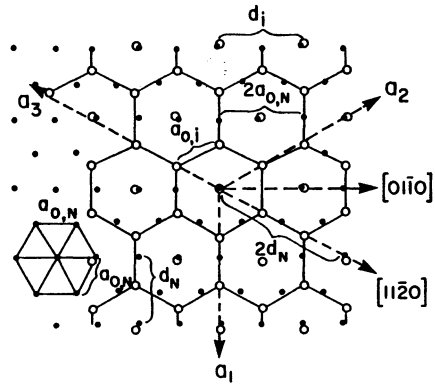


Fig. 9-29: Relative atomic position in the (0001) plane of CuS and ice. (•) Cu atoms, (◯) H_2O molecules; $d_N = a_{0N}/\sqrt{3}$, $d_i = a_{0,i}/\sqrt{3}$, where a_{0N} and $a_{0,i}$ are the lattice constants in the (0001) plane for CuS and ice, respectively, with $a_{0,i}$ = 4.52 A, $c_{0,i}$ = 7.36 A, a_{0N} = 3.8 A, c_{0N} = 16.43 A, and with $\delta(0\top0)$, [0001] = +11.6 % (2:1), and $\delta(0001)$, [10$\top$0] = -2.8 % (2:1). (After Bryant *et al.*, 1959, with changes.)

If there are but small crystallographic differences between ice and the substrate, either or both the ice lattice and the substrate may elastically deform so that they may join coherently. Thus, strain considerations suggest that the solid substrate should have an elastic shear modulus which is as low as possible in order to minimize the elastic strain energy. If there are large crystallographic differences between ice and the substrate, dislocations at the ice-substrate interface will result, leaving some molecules unbonded across the interface and causing the ice germ to be incoherently joined to the substrate. The interface may then be pictured as being made up of local regions of good fit bounded by line dislocations. These dislocations at the interface will raise the interface free energy. In addition, any elastic strain within the ice embryo will raise its bulk free energy. Both effects will reduce the ability of the AP to serve as an IN.

The apparent crystallographic misfit or *disregistry* is usually defined by

$$\delta \equiv \frac{na_{0,N} - ma_{0,i}}{ma_{0,i}}, \tag{9-33}$$

where $a_{0,N}$ is the crystallographic lattice parameter of a particular face of the nucleus, $a_{0,i}$ is the corresponding constant in the ice lattice, and n, m are integers chosen such that δ is minimal. An example of the crystallographic matching between the (0001) planes of ice and CuS is shown in Figure 9.29. In order to determine the actual crystallographic misfit, it is necessary to allow for strain. Assuming the embryo can be strained by the amount $\varepsilon = (a'_{0,i} - a_{0,i})/a_{0,i}$, where $a_{0,i}$ and $a'_{0,i}$ are the lattice parameters of the ice in the strain-free and the strained conditions, respectively, and assuming the substrate strain is negligible, the actual crystallographic misfit between the embryo and a particular face of the IN is given by $\delta - \varepsilon$. If $\delta = \varepsilon$, the embryo fits the surface element of the IN coherently. If the ice embryo cannot be strained by the full amount, then $\delta - \varepsilon > 0$ and the ice embryo joins the IN incoherently.

The effect of the crystallographic properties of IN on ice nucleation has been studied by a large number of investigators (see Mason, 1971). Some selected results of these studies are summarized in Table 9.7a,b where the threshold temperature for ice nucleation in the deposition mode is listed for various chemical compounds as a function of their crystallographic characteristics. Note, in particular, the relatively good ice nucleability of kaolinite. From Figure 9.30, this appears to be due to the pseudohexagonal arrangement of the hydroxyl (—OH) groups at the surface of the lattice. Other substances listed in Table 9.7a,b also seem to derive their warm ice nucleation threshold from a close fit of their crystal lattice to that of ice. An unequivocal proof of the necessity, although not of the sufficiency, for a substrate to meet certain crystallographic requirements for good ice nucleability, was given by Evans (1965). From a study of the effectiveness with which AgI nucleates ice-I_h and the high pressure modification ice-*III*, he was able to show that even under conditions where ice-*III* is the stable phase, ice-I_h, which has a closer crystallographic fit to AgI than ice-*III*, was consistently nucleated by Agl. However, despite the obvious importance of the crystallographic properties of a substrate to its ice nucleability, Table 9.7a,b demonstrates clearly that no unique correlation can be established between the ice nucleation threshold and any of the crystallographic characteristics such as symmetry or misfit. The main reason for this irregular behavior is the role played by active sites, which we will discuss next.

9.2.3.5 *Active-Site Requirement*

Experiments have established that ice nucleation, like heterogeneous water nucleation, is a very localized phenomenon in that it proceeds at distinct active sites on a substrate surface. Not surprisingly, it happens that sites which are capable of adsorbing water molecules are also sites at which ice nucleation is initiated. Therefore, our previous descriptions of the adsorption properties of active sites in Section 5.6, and of the character and types of water active sites given at the end of

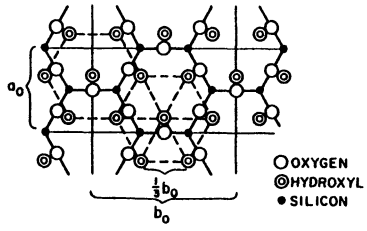


Fig. 9-30: Crystallographic structure of kaolinite. Projection on (001). (From *Clay Mineralogy* by R.E. Grim, copyrighted by McGraw-Hill Book Co., 1953.)

Section 9.1.4, both serve to describe the behavior of IN active sites as well. Consequently, for the most part, in the material which follows we will attempt merely to supplement our previous descriptions.

As expected, in laboratory studies one finds that at any given temperature only a fraction of the total number of available IN active sites is capable of initiating the ice phase. Since the nucleation sites active at a given temperature are not equally distributed among all the particles present, one then finds that only a fraction of the aerosol particles present form ice particles . Of course, as expected from Figures 9.16 and 9.17 the lower the temperature the larger the number of ice nucleation active sites and, thus, the larger the number of aerosol particles which can initiate an ice crystal. This expectation has been verified by the experiments of Serpolay (1959), Katz (1960, 1961, 1962), Edwards *et al.* (1962), Roberts and Hallett (1968), Edwards and Evans (1968, 1971), and Mossop and Jayaweera (1969) who showed that the ice nucleation active fraction of a population of AP of given size and chemical composition increases with decreasing temperature. This behavior is illustrated by Figure 9.31 for aerosol particles of various artificial chemicals and by Figure 9.32 for natural aerosol particles. It is noteworthy from Figure 9.32 that the ice-forming activity of each size fraction considered reaches 100% as a temperature of $-45°C$ is approached.

A reasonable interpretation of these results is that a given solid substance has a characteric area density of ice nucleation active sites of varying quality, which progressively become activated as the temperature is lowered. Eventually, freezing becomes independent of the substrate, and at sufficiently low temperatures, homogeneous nucleation takes over, leading to 100% ice nucleation efficiency at $-45°C$, the singularity temperature of water discussed in Section 3.4.1 and Section 7.2.3.

The discovery of ice nucleation active sites provides an explanation for the size effect discussed in Section 9.2.3.2. Thus, the smaller an aerosol particle the smaller also the probability that this particle contains an active site which is capable of initiating ice nucleation at a given temperature. However, the presence of active sites also implies that experiments on nucleation thresholds should be interpreted with caution, since the outcome may well depend on the area of the substrate under study. For example, the experiments by Mason and van den Heuvel (1959), Isono and Ishizaka (1972),and Bryant *et al.* (1959) typically involved fields of view

TABLE 9.7

Crystallographic misfit between various chemical compounds and ice, and its relation to the ice nucleability of these compounds. (Crystallographic data from Wyckoff (1963), Davis *et al.* (1975), and Burley (1963, 1964); data on nucleation threshold from references in text.)

Chemical Compound	Crystallographic Symmetry	Lattice constants (Å) a_0	b_0	c_0	Substrate plane	Ice Matching plane	Misfit between substrate lattice in directional ice (%)	Approx. ice nucleation threshold (°C)
Ice-I_h	D_{6h}^4 hex.	4.52(0 °C)		7.36(0 °C)				
β-$A_g I$	C_{6v}^4 hex.	4.592		7.510	(0001)	basal	$[10\bar{1}0]$ + 1.5(1 : 1); [0001] + 2.0(1 : 1); $[1\bar{2}10]$ + 1.5(1 : 1)	−3 to −6
γ-$A_g I$	T_d^2 cubic	6.496			(111)	prism basal	$[1\bar{2}10]$ + 1.5(1 : 1); [0001] + 8.1(1 : 1); $[1\bar{2}10]$ + 1.5(1 : 1)	−3 to −6
MgTe	C_{6v}^4 hex.	4.52		7.33	(0001)	basal	$[10\bar{1}0]$ 0.0(1 : 1); [0001] − 0.41(1 : 1); $[1\bar{2}10]$0.0(1 : 1)	−4 to −5
PbI_2	D_{3d}^1 trig.	4.54		6.86	(0001)	basal	$[10\bar{1}0]$ + 0.4(1 : 1); [0001] − 6.8(1 : 1); $[1\bar{2}10]$0.4(1 : 1)	−4 to −7
HgTe	T_d^2 cubic	6.36			(111)	basal	$[1\bar{2}10]$ − 0.4(1 : 1)	−4 to −7
CdTe	T_d^2 cubic	6.41			(111)	basal	$[1\bar{2}10]$ + 0.2(1 : 1)	−4 to −6
CuI	T_d^2 cubic	6.04			(111)	basal	$[1\bar{2}10]$ − 5.5(1 : 1)	−4 to −7
Cu_2O	T_h^5 cubic	4.25			(100)	basal	$[1\bar{2}10]$ − 6.0(1 : 1); $[10\bar{1}0]$ + 8.7(2 : 1); [0001] + 15.5(2 : 1)	−4 to −6
Mg_3Sb_2	D_{3d}^1 trig.	4.57		7.23	(0001)	basal	$[10\bar{1}0]$ + 1.1(1 : 1); [0001] − 1.8(1 : 1); $[1\bar{2}10]$1.1(1 : 1)	−4 to −5
CuS	D_{6h}^4 hex.	3.80		16.43	(0001)	basal	$[10\bar{1}0]$ − 2.8(2 : 1); [0001] + 11.6(1 : 2); $[1\bar{2}10]$ − 2.8(2 : 3)	−4 to −8
Ag_2S	C_{2h}^5 monocl.	4.20	6.93	9.50	(010)	basal	$[1\bar{2}10]$ − 7.1(1 : 1); $[10\bar{1}0]$ − 0.3(1 : 1); [0001] − 5.9(1 : 1)	−5 to −8
HgI_2	C_{2v}^{12} orthorh.	4.67	13.76	7.32	(010)	basal	$[1\bar{2}10]$ + 3.3(1 : 1); $[10\bar{1}\bar{0}]$ − 6.4(1 : 1); [0001] − 6.5(1 : 2)	−5 to −8
Ag_2O	T_h^5 cubic	4.72			(001)	prism	$[1\bar{2}10]$ + 4.4(1 : 1); $[10\bar{1}0]$ − 9.5(3 : 2); [0001] − 3.8(3 : 2)	−5 to −11
CdSe	C_{6v}^4 hex.	4.30		7.02	(0001)	basal	$[10\bar{1}0]$ − 4.9(1 : 1); [0001] − 4.6(1 : 1); $[1\bar{2}10]$ − 4.9(1 : 1)	−5 to −7
ZnSe	T_d^2 cubic	5.67			(111)	basal	$[1\bar{2}10]$ − 11.5(1 : 1)	−5 to −12

TABLE 9.7 (continued)

Chemical Compound	Crystallographic Symmetry	Lattice constants (Å) a_0	b_0	c_0	Substrate plane	Ice Matching plane	Misfit between substrate lattice in directional ice (%)	Approx. ice nucleation threshold (°C)
NiO	O_h^1 cubic	4.17(0 °C)			(100)	basal	$[1\bar{2}10] - 7.7(1:1)$; $[10\bar{1}0] + 6.6(2:1)$; $[0001] + 13.3(2:1)$	−6 to −11
CuO	C_{2h}^6 monoc.	4.65	3.41	5.11	(001) (010)	prism basal	$[1\bar{2}10] + 2.9(1:1)$; $[0001] - 7.4(2:1)$ $[1\bar{2}10] + 2.9(1:1)$; $[10\bar{1}0] - 2.0(3:2)$	−7 to −12
SnO_2	D_{4h}^{14} tetrag.	4.72		3.16	(010)	basal	$[1\bar{2}10] + 4.4(1:1)$; $[10\bar{1}0] - 14.2(2:1)$; $[0001] - 3.8(3:2)$	−8 to −14
CdO	O_h^1 cubic	4.69			(100)	basal	$[1\bar{2}10] + 3.8(1:1)$; $[10\bar{1}0] - 10.0(3:2)$; $[0001] - 4.4(3:2)$	−9 to −10
V_2O_5	D_{2h}^{13} orthorh.	11.48	4.36	3.55	(100) (001	basal prism	$[1\bar{2}10] - 3.5(1:1)$; $[10\bar{1}0] - 2.1(2:3)$; $[0001] - 3.5(2:1)$ $[1\bar{2}10] - 3.5(1:1)$; $[10\bar{1}0] - 2.1(2:3)$; $[0001] - 3.5(2:1)$	−11 to −15
I_2	D_{2h}^{18} orthorh.	4.78	7.25	9.77	(001)	basal prism	$[1\bar{2}10] + 5.8(1:1)$; $[10\bar{1}0] - 7.3(1:1)$; $[0001] - 11.3(2:3)$ $[1\bar{2}10] + 5.8(1:1)$; $[10\bar{1}0] - 16.6(2:3)$; $[0001] - 1.5(1:1)$	−12 to −14
MnO_2	D_{4h}^{14} tetrag.	4.44		2.89	(010)	basal	$[1210] - 1.8(1:1)$; $[10\bar{1}0] + 10.9(3:1)$; $[0001] - 9.5(3:2)$	−12 to −14
CdI_2	D_{3d}^3 trig.	4.24		6.84	(0001)	basal	$[10\bar{1}0] - 6.2(1:1)$; $[0001] - 7.1(1:1)$; $[1\bar{2}10] - 6.2(1:1)$	−12 to −15
Kaolinite $(OH)_8Si_4Al_4O_{10}$	C_1^4 triclin. (pseudohex. OH groups)	5.16 2.98	8.94	7.38 7.15	(001)	basal	$[1\bar{2}10] - 1.1(3:2)$; $[10\bar{1}0] - 1.1(3:2)$; $[0001] - 2.9(1:1)$	−9 to −11
Metaldehyde $(CH_3CHO)_4$	tetragonal	10.40		4.11	(110) $(1\bar{1}0)$ (001)	(0001) $(01\bar{1}0)$ $(\bar{2}110)$	c-axis 0.2 $[01\bar{1}0]$ 6.1 a-axis 9.1	−1
α-Phenacin $C_6H_4NC_6H_4N$	monoclinic	13.22	5.06	7.09	(001)	$(1\bar{1}00)$	a-axis 2.6 c-axis 3.0	−3 to −4
Phloroglucinol-dihydrate $C_6H_3(OH)_32H_2O$	orthorhombic	6.73	13.58	8.09	(011) (010) (001)	(0001) $(11\bar{2}0)$ $(10\bar{1}0)$	c-axis 8.7 a-axis 0.1 $[10\bar{1}0]$ 3.3	

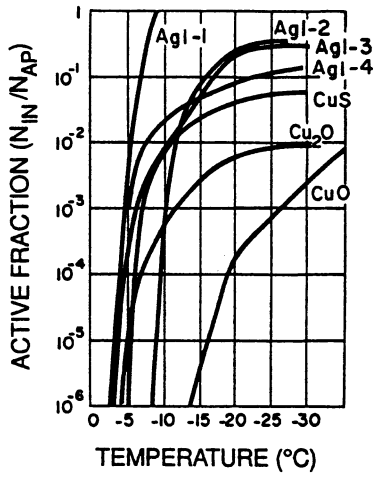


Fig. 9-31: Temperature dependence of fraction of particles active as IN for various substances. AgI-1: $r_N = 2$ μm, freezing mode; AgI-2: $r_N = 0.015$ to 0.2 μm (median, 0.045 μm), freezing mode;: AgI-3: $r_N = 0.2$ to 4 μm, deposition mode at water saturation; AgI-4: $r_N = 2$ μm, deposition mode at water saturation. (Based on data of Katz, 1961; Edwards and Evans, 1968; Mossop and Jayaweera, 1969.)

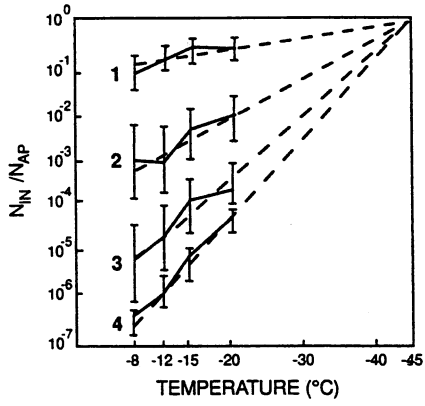


Fig. 9-32: Temperature dependence of active fraction of natural atmospheric aerosol particles active as ice nuclei at water saturation, sampled at high altitudes obs. Nalchik. U.S.S.R. Aerosol particle sizes: (1) 100 μm, (2) 10 μm, (3) 1 μm, (4) 0.1 μm. (From Berezinski *et al.*, 1988, with changes.)

under the microscope of about 5×10^{-3} cm^2, and led to observations of ice nucleation at water saturation (ice supersaturations of from 7 to 12%) for temperatures between -7.5 and -12°C, and at ice supersaturations of about 12% for temperatures between -12 and -20°C. In contrast to these results, Anderson and Hallett (1976), who observed considerably larger substrate areas, found that ice could be nucleated at ice supersaturations as low as 3% for temperatures between -7.5 and -20°C. These results are also consistent with the observations of Barchett (1971), who found from adsorption studies that the onset of ice nucleation in the deposition mode (1 ice germ per AgI sample of about 0.8 g, with a specific area of as large as 4900 cm^{2}g^{-1}) at temperatures between -4 and -10°C required an ice supersaturation, independent of temperature, of only about 3% (equivalent to a water-subsaturation of about 7% at -10°C and of about 3.3% at -6.5°C).

Numerous studies have attempted to characterize an active site. As is well-known, electron microscopy reveals that a solid surface is rarely completely smooth, but rather contains numerous topographic surface features. Experimental evidence for the effectiveness of topographic surface features to initiate the ice phase from the vapor has been given by Bryant *et al.* (1959), Fukuta *et al.* (1959), Fletcher (1960), Hallett (1961), and Kobayashi (1965a,b), who studied the ice nucleating properties of CuS, AgI, and PbI_2 in the depositional mode. Photographs taken during the course of these studies revealed that ice crystals appear preferentially at cleavage and growth steps, at cracks, and in cavities, and at the edges of the substrate surface (see Plate 10). These results are supported by the study of Hallett and Srivastava (1972), who showed that the ice nucleability of a AgI single crystal surface could be improved by etching or scratching. However, such behavior has not always been observed. For example, Federer (1968), working with single crystals of Si, GaAs, and GaSe, found that the area density of ice crystals formed by vapor deposition on these substrates was not closely correlated to the area density of steps caused by emerging dislocations.

Chemical impurities present at the surface of a solid constitute another type of active site. Indeed, adsorption studies by Gravenhorst and Corrin (1972) have established that particles from AgI samples containing impurity ion such as K^+ and NO_3^- have a considerably higher ice nucleation efficiency than 'pure' AgI. This behavior is shown in Figure 9.33. The lower nucleation efficiency of 'pure' AgI was attributed by Barchett an Corrin (1972) to the presence of relatively inactive physical adsorption sites at its surface, causing water molecules initially to be adsorbed in the form of extended water 'patches' within which the water molecules exhibit strong lateral interaction. Only on approaching water saturation do multilayers develop with an adsorbate-vapor interface which assumes the energetic properties of a liquid-like surface prior to nucleation.

We further recall from Section 5.6 that the efficiency with which a doped silicon surface adsorbs water molecules increases as the number of doped surface sites increases (i.e., it increases with decreasing electric conductivity of the sample). As expected, therefore, ice nucleation is most active on silicon particles with a large number of doped surface sites, or with a low electric conductivity (see Figure 9.34). The same effect was found by Stinebaugh *et al.* (1980) by doping silicon with atoms other than boron. The experiments with doped solid surfaces suggest that an ice

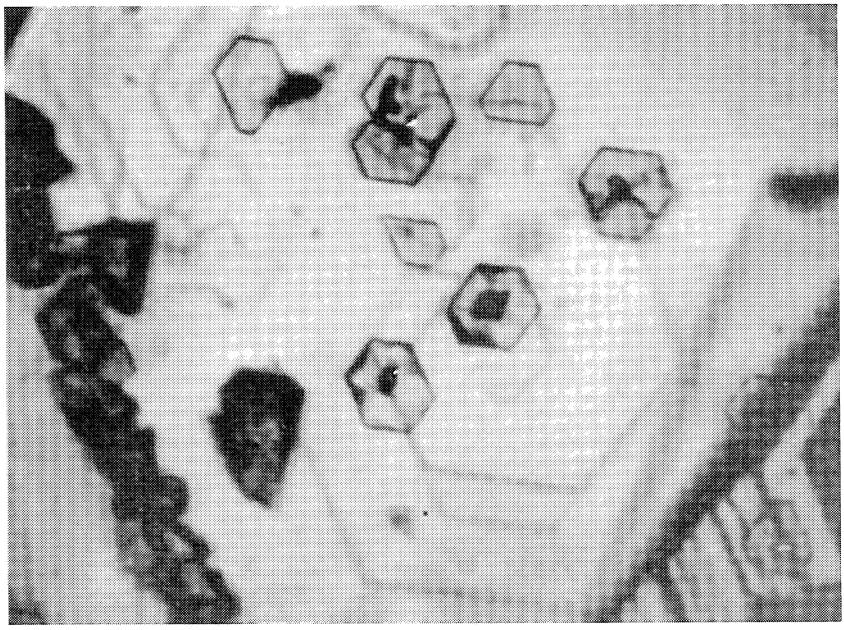


Plate 10. Epitaxial deposit of ice crystals growing at the steps of hexagonal growth spirals on a cadmium iodide crystal. (From Bryant *et al.*, 1959; by courtesy of *Pergammon Press Ltd.*)

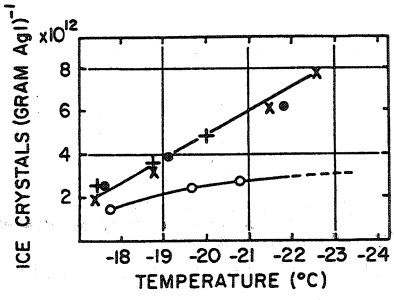


Fig. 9-33: Ice nucleation activity of AgI as a function of doping; (○) pure AgI, (●) AgI doped with 0.05 % KNO_3, (+) AgI doped with 0.1 % KNO_3, (×) AgI doped with 1 % KNO_3. (From Gravenhorst and Corrin, 1972; by courtesy of *J. de Rech. Atmos.*, and the authors.)

nucleation active site is hydrophilic, and surrounded by a hydrophobic region. One reason for this is that it is easier for water molecules to join a disordered water cluster on a low energy (hydrophobic) surface than to enter an oriented array of water molecules on a polar (hydrophylic) surface. Similarly, it is easier for a water cluster than an oriented film to achieve an ice-like structure. Also, as we have indicated previously, the growth of an ice embryo is facilitated by surface diffusion of weakly adsorbed molecules near the active site.

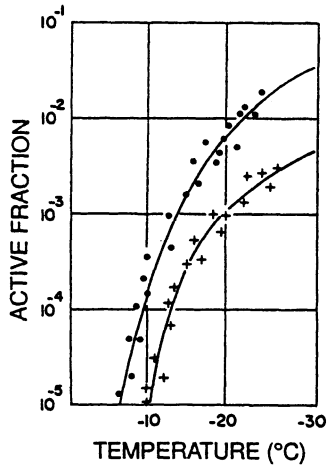


Fig. 9-34: Ice nucleation activity of p-type silicon as a function of doping with boron. Specific electric resistance of sample: (•) 10^{-2} Ω cm, (+) 7.5 x 10^{3} Ω cm. (From Federer, 1968, by courtesy of *Z. Angew. Math. Phys.*, and the author.)

The advantage of having a low energy, non-polar substrate was pointed out by Fletcher (1959b). As we know from Chapter 3, water dipoles in ice may assume a large number of orientations. Hence, Fletcher was able to demonstrate theoretically that a polar substrate can reduce the configurational entropy, and therefore raise the free energy of an ice embryo growing on it. In consequence, Fletcher predicted that AgI surfaces exposing either Ag^{+} or I^{-} exclusively should be poorer ice nucleation substrates than those where both ions are present.

Three additional effects which demonstrate the importance of active sites for nucleation in the deposition mode are worth mentioning. In order to discuss the first effect, let us recall from Figure 9.23 that, under certain conditions, IN may become activated (or 'trained'), and in this state exhibit a considerably improved ice nucleability (memory effect). To behave in this manner, the IN either must have been previously involved in an ice nucleation process and formed a macroscopic ice crystal, or they must have been exposed to temperatures below −40°C. Earlier explanations of this phenomenon conjectured the retention of ice remnants in small cavities or capillaries where they could survive relative humidities considerably below ice saturation due to the negative curvative effect, as long as the temperature of the environment remained below 0°C. However, the work of Roberts and Hallett

(1968) and of Edwards and Evans (1971) has shown that the observations are better explained in terms of the retention of patches of ordered, ice-like layers of water molecules at the surface of a substrate, where each patch can be considered to represent the remnant of a macroscopic ice crystal which developed over an active site.

The second effect involves the previously mentioned observation that foreign gases or vapors such as NO_2, SO_2, NH_3 strongly reduce the nucleability of IN (Georgii, 1963; Georgii and Kleinjung, 1967). Since the adsorption studies discussed in Chapter 5 have demonstrated that such foreign gases are adsorbed at active sites, we see that the observed suppression of nucleation is caused by the occupancy of active sites by molecules other than H_2O.

The third effect involves the characteristic time lag for the appearance of an ice crystal on the surface of a substrate once it has been exposed to supersaturated vapor at a temperature below 0°C. As shown for an AgI surface by Anderson and Hallett (1976), this time is longest at temperatures near 0°C and low excess vapor densities, but it rapidly decreases with decreasing temperature and increasing excess vapor density (Figure 9.35). Obviously, each active site on a surface requires a critical supersaturation which must be applied for a critical length of time for an ice embryo to form and to grow to a macroscopic crystal.

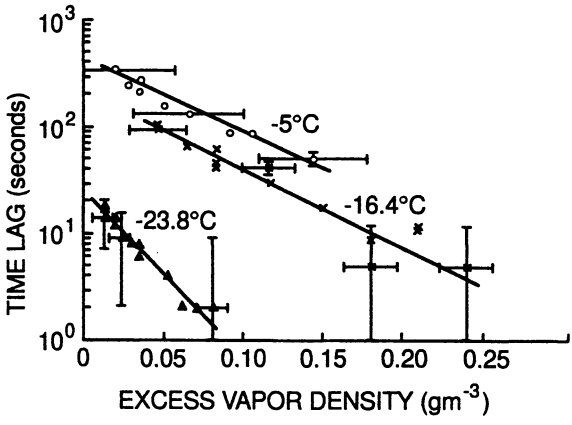


Fig. 9-35: Time lag for ice nucleation on AgI surfaces as a function of temperature and excess water vapor density. (From Anderson and Hallett, 1976, with changes.)

So far we have discussed the significance of active sites to ice nucleation in the deposition mode, and it remains for us to consider their significance in the freezing and contact modes. Unfortunately, no quantitative experiments are available to help elucidate this problem. One can merely speculate that the nucleation process proceeds somewhat differently in the freezing mode than it does in the deposition mode. Once a water-insoluble AP becomes submerged in water, it is surrounded by an abundance of water molecules. At any one moment, a large number of these molecules are linked together into small structural units in which some of them

tend to be tetrahedrally bonded, while other bonds seem to 'dangle' (Stillinger and Rahman, 1972; see also Section 3.4). Suppose now that the surface of the submerged solid particle is generally hydrophobic, but contains hydrophilic sites where water molecules are preferentially adsorbed. The molecules most likely to be adsorbed are those which exhibit 'dangling' bonds. In this manner, the already existing structural units become 'anchored' to the solid surface, causing them to be less vulnerable to destruction by the heat motion in the water. As the temperature of the water is lowered, more and more 'dangling' bonds become 'hooked' to the particle's surface, thus allowing individual structural units to be 'joined' together to form clusters in which individual water molecules have considerable freedom to move their dipoles into an orientation most favorable for a tetrahedral, ice-like arrangement. Eventually, the anchored 3-D cluster may reach germ size.

If, on the other hand, we consider a particle with a surface which has a strong, uniform affinity to water due to the presence of an array of strongly hydrating ions, polar groups, hydroxyl (OH^-), or oxygen (O^{2-}) atoms in the solid surface, water molecules will become adsorbed in a close array with most of the dipoles of individual molecules oriented more or less alike. Such an arrangement is not conducive to ice nucleation, due to the structural entropy penalty imposed on such an adsorbed layer. In this case, a second or even more adsorbed layers may be required before the freedom of orientation among the water molecules in the outermost adsorbed layer is sufficiently large for some of them to assume ice-like orientations while others remain anchored. Mechanisms similar to these have been proposed by Evans (1967a,b) and Edwards *et al.* (1970), based on their studies of heterogeneous ice nucleation in supercooled water.

There is also little known quantitatively about the importance of active sites to ice formation in the contact mode. Observations have shown that dry particles of many compounds such as clays, sand, soil, CuS, organic compounds, etc., are considerably better IN when acting in the contact mode rather than in the freezing or deposition modes (Rau, 1950; Levkov, 1971; Fletcher, 1962; Gokhale and Spengler, 1972; Pitter and Pruppacher, 1973). In an attempt to explain this effect, Fletcher (1970b) and Guenadiev (1970) pointed out that the observed differences between nucleation in the contact and freezing modes may be caused by the partial solubility of any solid, especially when in the form of small particles. Thus, it is reasonable to assume that active sites at the surface of a particle are especially vulnerable to erosion by dissolution after a particle has become immersed in water. In support of this notion, Hallett and Srivastava (1972) found that prolonged immersion in water reduced the nucleation effciency of AgI single crystals. However, although the erosion effect may account for some differences between the contact and freezing modes, it cannot explain the significant difference between the ice nucleability of some clays in the contact and deposition modes. In addition, the erosion effect is unable to account for the fact that in all three modes, AgI exhibits practically the same threshold temperature of $-4°C$ for particles of the same size.

A different explanation for contact nucleation was given by Evans (1970). He suggested that only those compounds initiate ice formation in the contact mode which exhibit a strong affinity for water, thus adsorbing water molecules from the liquid or vapor in a close array. In such a case, as mentioned previously,

ice nucleation is hindered due to a structural entropy penalty imposed on the adsorbed layer. However, during the initial brief moments of contact between a particle and a supercooled water drop, adsorption is incomplete and disordered despite the strong aflinity. Thus, during this period, the energy barrier to the formation of a more ordered, ice-like arrangement may be considerably lower and, thus, nucleation may be much more likely, than in an adsorbed and firmly attached oriented array. Although this explanation is attractive, it hinges on the assumption that the time required for building up an oriented water film is much longer than the time needed to form an ice germ in the disordered-adsorbed layer. Unfortunately, this assumption has not yet been justified.

A third explanation for contact nucleation has been given by Guenadiev (1972) and Cooper (1974). They conjectured that an IN acting in the contact mode must build up a critical ice embryo which is in equilibrium with the water of the supercooled drop, rather than with the surrounding water vapor. Since at any given temperature, the former requirement is less stringent, an IN may nucleate on contact with a supercooled drop even though the ice particle is of sub-germ size with respect to ice formation from the vapor. Although this mechanism can account for clay particles being better IN in the contact mode than in the deposition mode, it cannot explain, for example, why AgI exhibits the same nucleation threshold in both modes, nor can it explain why clay particles exhibit a better ice nucleability in the contact mode than in the freezing mode. In addition, computations by Grover (1978) show that the water vapor density decreases very rapidly with distance from the surface of a drop falling in sub-saturated air and reaches water saturation only at the drop surface itself. Thus, an AP which approaches a supercooled drop on a collision trajectory in a water subsaturated environment will not encounter a water saturated air layer, as was assumed by Cooper (1974), although it may be exposed to a thin layer of air which is ice supersaturated. The thickness of this layer depends strongly on the drop size and its fall speed, and on the relative humidity of the environmental air. One would therefore expect that contact nucleation is a function of drop size and of the relative humidity of the air. However, no dependence on either of these parameters was detected in the nucleation studies by Rau (1950), Gokhale and Goold (1968), Levkov (1971), Gokhale and Spengler (1972), and Pitter and Pruppacher (1973). Also, the question is left open as to whether the short time spent by a particle on its collision trajectory inside the region which is ice supersaturated is sufficient to build up ice embryos of germ size on its surface.

Another interesting explanation of the contact nucleation mechanism has been given by Fukuta (1975a,b), who studied the freezing behavior of supercooled drops frozen by contact with various organic substances. As other workers had found for inorganic substances, Fukuta observed that the drop freezing temperature via contact nucleation was significantly warmer than that of drops frozen by the same particles submerged within them. He interpreted his results to indicate that the reduction in ice-forming ability which the particles suffered when immersed in drops was not due to the dissolution of nucleation active sites. Rather, Fukuta suggested, on the basis of experiments carried out by Pruppacher (1963c), that the difference in freezing temperature was associated with the movement of the water-air interface relative to the solid substrate surface during contact. He suggested that the

mechanically forced rapid spreading of water along the hydrophobic solid surface forces its local wetting, and thereby temporarily creates local high interface-energy zones which can increase the likelihood of ice nucleation. Although the explanation of the creation of such zones seems somewhat incomplete, it is a simple matter to show that, should they exist, the consequence would be an enhanced nucleation efficiency. Thus, on adapting (9-9) and (9-10) to the case of ice nucleation inside the drop on the solid surface it contacts, we find the energy of embryo formation, assuming a planar substrate, is

$$\Delta F_{i,\mathrm{S}} = V_i \Delta f_{\mathrm{vol}} + \sigma_{i/\mathrm{w}} \Omega_{i/\mathrm{w}} + \Omega_{N/i}(\sigma_{N/i}) - \sigma_{N/\mathrm{w}}) \,. \tag{9-34}$$

The creation of a transient high energy zone would correspond to an increase in $\sigma_{N/\mathrm{w}}$, which (9-34) shows would lower the formation energy of ice embryos.

9.2.4 Theory of Heterogeneous Ice Nucleation

9.2.4.1 *The Classical Model*

Let us now turn to the classical theoretical model for heterogeneous ice nucleation. The treatment closely parallels that given previously in Section 9.1.3 for heterogeneous water nucleation. In view of the complex nature of IN, and our previous discussions of the limitations of the classical approach, we cannot expect too much of the following description. Nevertheless, it is the most comprehensive theory available and is capable of correctly predicting at least some of the observed features of ice nucleation.

We shall follow Fletcher (1958, 1959b, 1962a) and assume that an ice embryo on a curved solid substrate can be described by the spherical cap model. Then, the work of ice-germ formation from the vapor may, through arguments strictly analogous to those presented in Section 9.1.3.2, be expressed as

$$\Delta F_{g,\mathrm{S}} = \frac{16\pi M_{\mathrm{w}}^2 \sigma_{i/\mathrm{v}}^3}{3[\mathscr{R} T \rho_i \ln S_{\mathrm{v},i}]^2} f(m_{i/\mathrm{v}}, \mathrm{x}) \,, \tag{9-35}$$

where f is given by (9-22) and $m_{i/\mathrm{v}}$ by (5-24a). If the embryos are assumed to grow by direct vapor deposition, then the nucleation rate per particle, J'_{S} is given by combining (9-24) and (9-35).

For an environment which is saturated with respect to water, one may write $S_{\mathrm{v},i} = \mathrm{e}_{\mathrm{sat,w}}/\mathrm{e}_{\mathrm{sat},i}$, and therefore from (4-86b), $\ln S_{\mathrm{v},i} \approx (\overline{\mathscr{L}}_{m,0}/\mathscr{R} T_0^2)\Delta T$, with $\Delta T = T_0 - T$. For these conditions, and assuming $\sigma_{i/\mathrm{v}} \approx 100$ erg cm^{-2}, $J'_{\mathrm{S}} =$ 1 germ (particle)$^{-1}$ sec^{-1} and, further, that the kinetic coeffcient has a value of about $10^{26} r_N^2$, Fletcher has determined the variation of temperature with particle radius r_N and compatibility parameter $m_{i/\mathrm{v}}$ the results are shown in Figure 9.36. It is seen that there is little dependence on radii $r_N \gtrsim 0.1\ \mu$m for a given $m_{i/\mathrm{v}}$, but that below this size the ice nucleation efficiency decreases rather sharply. The nucleability also decreases rapidly with decreasing $m_{i/\mathrm{v}}$, i.e., with increasing interface free energy between ice and the substrate particle, for a given particle size.

Let us now turn to the case of heterogeneous ice nucleation in supercooled water. The rate J_{S} of germ formation per unit area per unit time may be obtained by

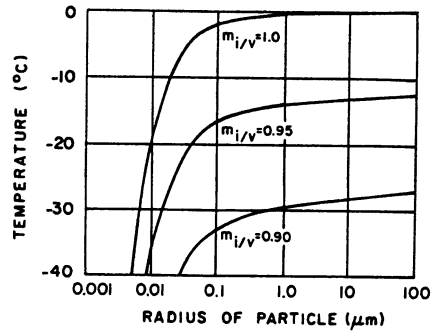


Fig. 9-36: Temperature at which a spherical aerosol particle will nucleate an ice germ in 1 second by the deposition mode at water saturation as a function of its radius and compatibility factor, from (9-24) and (9-35). (From *The Physics of Rain Clouds* by N.H. Fletcher, copyrighted by Cambridge University Press, 1962a.)

combining (9-2), (9-3), and (7-49):

$$J_{\mathrm{S}} = \frac{\mathrm{k}T}{\mathrm{h}} Z_{\mathrm{S}} N_c \Omega_{g,\mathrm{S}} c_{1,\mathrm{S}} \exp\left[-\frac{\Delta \mathrm{g}^{\ddagger}}{\mathscr{R}T} - \frac{\Delta F_{g,\mathrm{S}}}{\mathrm{k}T}\right] . \tag{9-36}$$

This equation may be simplified somewhat, since it happens that the factor $Z_{\mathrm{S}} N_c \Omega_{g,\mathrm{S}}$ is approximately unity under typical conditions. (One might have expected this to be so, since we have noted in Section 7.1.2 that $Z_{\mathrm{S}} \approx 10^{-1}$, while $N_c \Omega_{g,\mathrm{S}}$ counts the number of water molecules contacting the ice germ; an estimate that this count is O(10) is quite reasonable.) Therefore, an approximate description of the nucleation rate per particle is

$$J'_{\mathrm{S}} \approx \frac{\mathrm{k}T}{\mathrm{h}} 4\pi r_N^2 c_{1,\mathrm{S}} \exp\left[-\frac{\Delta \mathrm{g}^{\ddagger}}{\mathscr{R}T} - \frac{\Delta F_{g,\mathrm{S}}}{\mathrm{k}T}\right] . \tag{9-37}$$

Assuming a spherical cap germ as before, and following familiar arguments, the quantity $\Delta F_{g,\mathrm{S}}$ in (9-36) and (9-37) may be expressed as one-third the surface energy of the germ, multiplied by the geometric factor f of (9-22); using (6-55) for the germ radius, we have

$$\Delta F_{g,\mathrm{S}} = \frac{16\pi M_{\mathrm{w}}^2 \sigma_{i/\mathrm{w}}^3 f(m_{i/\mathrm{w}}, \mathrm{x})}{3[\overline{\mathscr{L}}_{m,0} \bar{\rho}_i \ln(T_0/T_{\mathrm{e}})]^2} , \tag{9-38}$$

where $m_{i/\mathrm{w}}$ is given by (5-24b). Computations of (9-37) and (9-38) have been carried out by Fletcher (e.g., 1959b, 1969) but, unfortunately, these do not include the temperature dependencies of $\sigma_{i/\mathrm{w}}, \overline{\mathscr{L}}_{m,0}, \bar{\rho}_i$, and $\Delta F_{g,\mathrm{S}}$. However, a suitably corrected computation (unpubl.), supports the essential results of Fletcher (1969). Their results are shown in Figure 9.37, where it has been assumed that $c_{1,\mathrm{S}} = 10^{28}$ cm^{-2} and $J_{\mathrm{S}} = 1$ germ (particle)$^{-1}$ sec^{-1}. It is seen from the figure that for

$r_N \geq 0.1\,\mu$m, the ice nucleation efficiency is relatively insensitive to r_N; however, it decreases rapidly for smaller sizes. For a fixed r_N, the required supercooling increases rapidly with decreasing $m_{i/w}$. Comparison with Figure 9.36 shows that the nucleability is less sensitive to the size and compatibility parameter of an IN in the freezing mode than in the deposition mode at water saturation. We also note from Figure 9.37 that by approaching homogeneous nucleation conditions, i.e., with decreasing radius of the aerosol particle and decreasing compatability factor, ice nucleation approaches the limiting value at $-45°$C, as expected from Sections 3.4, 7.2.3 and Figure 9.32.

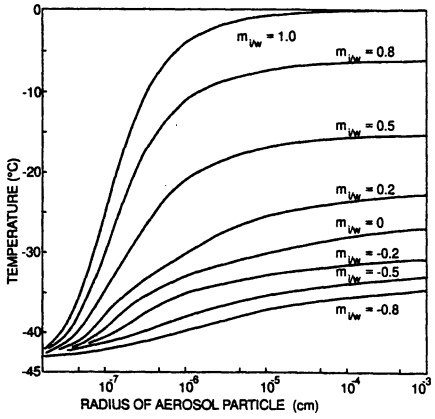


Fig. 9-37: Temperature at which a spherical ice germ will nucleate on an aerosol particle in supercooled water in one second by the freezing mode as a function of its values and compatibility factor; based on (9-38) and (9-39).

Recalling now the experimental observations discussed in the previous section, we find that the classical theory is successful in qualitatively predicting the observed decrease in ice nucleation ability with decreasing AP size. Quantitatively, however, observations show a considerably stronger size dependence, for small sizes in particular. The classical theory also qualitatively predicts the observed decrease in nucleability with decreasing m-factor, i.e., with increasing interface free energy between ice and the substrate. On the other hand, in practice it cannot discriminate among various aerosol particles, since $m_{i/v}$ and $m_{i/w}$ (i.e., $\sigma_{i/N}$) have not been determined for any substance. Even if these quantities were accessible to experimental determination, the derived values would pertain to an average, macroscopic behavior of the particular substrate face studied. Such values would clearly be unsatisfactory since heterogeneous ice nucleation occurs preferentially at the location of microscopic active sites, and is controlled by the nature of these sites rather than by the average behavior of the surface.

In view of these shortcomings, it is not surprising, for example, that the classical theory makes the seriously erroneous prediction that all AP of a given size and chemical composition will have the same ice nucleation efficiency. This prediction is in complete disagreement with observation which show that at any given temper-

ature, the nucleability varies from particle to particle, and that the ice nucleating active fraction of such a homogeneous set of particles increases with decreasing temperature (see Figures 9.31, 9.32, and 9.34). In addition, experiments do not substantiate the theoretical prediction that the nucleation efficiency is less dependent on the compatibility between ice and the substrate in the freezing mode than in the deposition mode.

9.2.4.2 *Extensions of the Classical Model*

Thus far, two attempts have been made to improve the classical theory. First of all, efforts have been made to include the effects of the elastic strain ε produced within an ice germ due to the misfit δ between the ice and substrate lattices. This gives rise to modifications in the interface energy, and so the m-factor, as well as the bulk free energy contribution Δf_{vol} of the ice germ. According to Turnbull and Vonnegut (1952), the concentration of dislocations at the interface depends linearly on $(\delta - \varepsilon)$, while the term $C\varepsilon^2$ has to be added to Δf_{vol}. In the case of coherent nucleation, i.e., $\varepsilon = \delta$, the concentration of dislocations at the interface zero, and the m-factor requires no correction. In most cases where $\delta \ll 1$, this is probably a reasonable approximation to make.

For the case of ice germ formation from the vapor, the only formal change required by these modifications is that $\mathscr{R}T\rho_i \ln S_{\text{v},i}$ in (9-35) must be replaced by $-\mathscr{R}T\rho_i \ln S_{\text{v},i} + C\varepsilon^2$, where C is a constant whose value depends on the elastic properties of ice. Similarly, for the case of ice germ formation in supercooled water, $-\overline{\mathscr{L}}_{m,0}\bar{\rho}_i \ln(T_0/T_e) + C\varepsilon^2$ replaces $\overline{\mathscr{L}}_{m,0}\bar{\rho}_i \ln(T_0/T_e)$ in (9-38). The effect is thus easy to interpret as a shift in $\ln S_{\text{v},i}$ or $\ln(T_0/T_e)$. As an example, the additional required depression of the ice nucleation threshold temperature as a function of ε is plotted in Figure 9.38, where the value for C is taken as 1.7×10^{11} erg cm^{-3}, following Turnbull and Vonnegut (1952). Granted that this refinement to the clasical theory is highly idealized, it is nevertheless encouraging to note the qualitative agreement of the figure with observation, namely that the temperature for the onset of ice nucleation is caused to decrease with an increase in the crystallographic misfit between ice and the nucleating substrate, in particular for misfits larger than 1%.

Fletcher (1969) has provided a second extension of the classical theory by constructing a simple model for the effect of active sites on the nucleating substrate. He supposed that, for the case of ice nucleation in the freezing mode on a particle of radius r_N, an active site could be represented by a patch of area αr_N^2 on which $m_{i/\text{w}} = 1$. The remainder of the surface was assumed to be characterized by $m_{i/\text{w}} < 1$.

The formulation is quite straightforward. Thus, without the active site, the total surface energy of the ice embryo $\sigma_{i,i}\Omega_{i,i}$ would be in strict analogy to (9-11) $\sigma_{i/\text{w}}\Omega_{i/\text{w}} + (\sigma_{N/i} - \sigma_{N/\text{w}})\Omega_{N/i} = \sigma_{i/\text{w}}\Omega_{i/\text{w}} - m_{i/\text{w}}\sigma_{i/\text{w}}\Omega_{N/i}$, using (5-24b). We may now take the presence of the active site into account by replacing the last term above with $-[m_{i/\text{w}}\sigma_{i/\text{w}}(\Omega_{N/i} - \alpha r_N^2) + \sigma_{i/\text{w}}\alpha r_N^2]$. In this manner, the expression analogous to (9-10) and (9-11) for the energy of i-mer formation is

$$\Delta F_{i,\text{S}} = V_i \Delta f_{\text{vol}} + \sigma_{i/\text{w}}(\Omega_{i/\text{w}} - m_{i/\text{w}}\Omega_{N,i}) - \alpha r_N^2 \sigma_{i/\text{w}}(1 - m_{i/\text{w}})\,. \qquad (9\text{-}39)$$

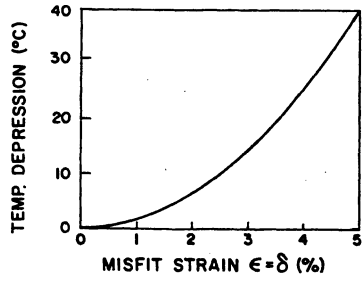


Fig. 9-38: Additional depression of the ice nucleation temperature as a function of misfit strain for coherent nucleation, $\epsilon = \delta$. (From Turnbull and Vonnegut, 1952; copyrighted by Am. Chem. Soc.)

The last term on the right side of this expression represents the correction due to the presence of the active site. Since it does not involve the geometry of i-mer, it is also not involved in the process of maximizing $\Delta F_{i,\mathrm{S}}$ to determine $\Delta F_{g,\mathrm{S}}$. Therefore, we have immediately the result

$$\Delta F_{g,\mathrm{S}} = \frac{4\pi a_g^2}{3}\sigma_{i/\mathrm{w}} f(m_{i/\mathrm{w}}, \mathrm{x}) - \alpha r_N^2 \sigma_{i/\mathrm{w}}(1 - m_{i/\mathrm{w}}) , \tag{9-40}$$

where a_g is given by (6-55) (it is assumed the germ still possesses the standard spherical cap geometry) and f is given by (9-22).

The solution of (9-37) together with (9-40) for $J_{\mathrm{S}}' = 1$ germ (particle)$^{-1}$ sec^{-1} is shown in Figure 9.39. It can be seen that, as expected, the larger α is for a given r_N, the warmer is the temperature at which the ice nucleation in the freezing mode is initiated. Thus, while a particle of $r_N = 1\,\mu$m bearing no active site ($\alpha = 0$) would initiate ice nucleation at -17°C, a particle bearing an active site of $\alpha = 2 \times 10^{-4}$, i.e., $\alpha r_N^2 = 2 \times 10^{-12}$ cm^2, is capable of initiating ice formation at -4°C, a truly potent effect. If $r_N = 1\,\mu$m and $\alpha = 2 \times 10^{-5}$, or $\alpha r_N^2 = 2 \times 10^{-13}$ cm, the particle is capable of initiating ice nucleation at a temperature near -12°C. Of course, a major drawback to this extension of the classical theory is that neither the area occupied by an ice nucleation active site nor the m-factor which characterizes the site is known *a priori*.

9.2.4.3 *The Semi-Empirical Statistical Mechanics Model*

Significant progress toward a quantitative description of the heterogeneous ice nucleation problem has been made by applying the ab initio approach of Hale and Plummer (see Chapter 7) using statistical mechanics in combination with an empirical molecular model (Ward *et al.*, 1982, 1983; Hale and Kiefer, 1980; Hale *et al.*, 1980). In analogy to (7-9) and (7-10), we may write for the heterogeneous formation of an ice embryo from the vapor

$$N_{i,\mathrm{S}} = (N_{1,\mathrm{S}}/q_{1,\mathrm{S}})^i q_{i,\mathrm{S}} , \tag{9-41}$$

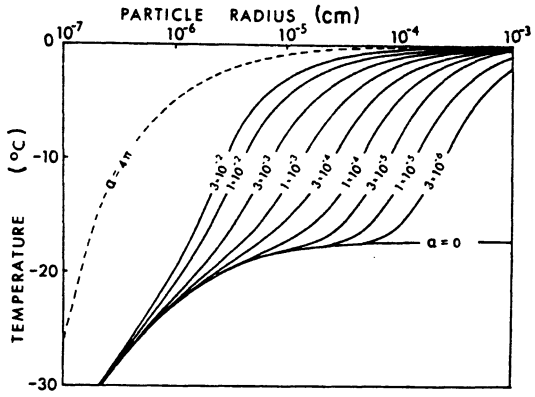


Fig. 9-39: Temperature at which a spherical aerosol particle with a compatibility factor $m_{i/N} = 0.5$ will nucleate an ice germ in one second as a function of its radius r_N and active site area αr_N. (From Fletcher, 1969; by courtesy of Am. Meteor. Soc., and the author.)

and

$$N_{i,\mathrm{S}} = N_{1,\mathrm{S}} \exp[-\Delta\phi_{i,\mathrm{S}}/\mathrm{k}T]. \tag{9-42}$$

Analogously to the homogeneous nucleation equation (7-11) follows

$$\frac{\Delta\phi_{i,\mathrm{S}}}{\mathrm{k}T} = i \ln\left(\frac{q_{1,\mathrm{S}}}{N_{1,\mathrm{S}}}\right) - \ln\left(\frac{q_{i,\mathrm{S}}}{N_{1,\mathrm{S}}}\right), \tag{9-43}$$

where now

$$N_{1,\mathrm{S}} = N_1^{(\mathrm{v})} q_{1,\mathrm{S}}/q_1^{(\mathrm{v})} \tag{9-44}$$

and

$$S_{\mathrm{v,w}} = N_1^{(\mathrm{v})}/N_{\mathrm{sat,w}}\,, \tag{9-45}$$

where $N_{i,\mathrm{S}}$ is the number of ice embryos on the substrate considered, $N_{1,\mathrm{S}}$ the number of water molecules adsorbed on the subtrate, $N_1^{(\mathrm{v})}$ the number of water molecules in the gas phase above the substrate, $N_{\mathrm{sat,w}}$ the number of water molecules in equilibrium with a plane water surface, $q_{i,\mathrm{S}}$ the partition function for an ice embryo of i-molecules on the substrate, $q_{1,\mathrm{S}}$ the partition function of the monomers on the substrate, and $q_1^{(\mathrm{v})}$ the partition function of water vapor. The formulation above assumes that the i-mers adsorbed on the substrate form a mixture of non-interacting ideal gases, that the system consists only of single molecules in the vapor phase, and that the total number of molecules in the vapor and in the surface clusters remain constant.

In order to evaluate $q_{i,\mathrm{S}}$ for a phase adsorbed on a solid surface, one cannot proceed in the manner that was possible in homogeneous nucleation, where we had only to consider the H_2O—H_2O interactions. In the present case, we have to consider, in addition, the interaction between the water molecules and the substrate.

In order to do this, Ward *et al.* (1982, 1983) proceeded in a semi-empirical fashion, assuming as before that the H_2O—H_2O interaction is described by the effective pair potential of Stillinger and Rahman (1978), while the interaction between the H_2O and the substrate is given by the semi-empirical effective pair potential of Hale and Kiefer (1980). Assuming further that the total number of bonds available for bonding to the substrate remains fixed and that the clusters on the substrate interact with the surface through bonds between the surface clusters and the surface monomers, a Monte Carlo method was used to let the molecules arrange themselves on the substrate. In this manner $\Delta\phi_i$ was determined as a function of cluster size, and from that followed $\Delta\phi_g$ and the critical cluster size g. Inserting this result into a formulation similar to (9-8) or (9-9), the steady state nucleation rate J_S on the model substrate was found. This procedure was applied to the basal plane of silver iodide (AgI), where the surface was modeled by an infinite array of point charge atoms. At $-8°C$ (265 K) and water saturation ($S_{v,w} = 1$), the critical cluster size was $g = 3$ and $J_S = 10^{23}$ cm^{-2} sec^{-1}, with a monomer concentration on the surface of $N_{1,S} = 10^{14}$ cm^{-2}. This large nucleation rate was taken to imply that a monolayer on the AgI surface forms rapidly, and that the nucleation of ice occurs after the deposition of just a few adsorbed layers. A closer look at the substrate surface shows that the AgI organized the adsorbed water molecules in the first and second monolayers in a solid-like plane of five and six membered rings centered on the iodine atoms. This is illustrated in Figure 9.40, which shows that the preferred adsorption sites for the H_2O on the AgI surface are the interstitial positions where no substrate atoms lie directly below in the first and second layers of the substrate, and that about 50% of the water molecules have positions which correspond to a perfect (0001) plane of ice. Reversing the temperature, this layer was shown to melt at about 300 K. The numerical simulation was found to be consistent with the experimental findings of Bakhanova and Kiselev (1972, 1974), who observed an ice-like IR absorption band for a thin film of H_2O on AgI at a temperature near 264 K. Using the same model, Hale *et al.* (1980) investigated the effect of atomic impurities and other defects in the AgI surface on the cluster formation. Thus, by replacing an Ag^+ in the surface of the AgI lattice by a K^+ impurity ion, or by creating a vacancy by removing an I^- ion in the surface of the AgI lattice, a stabilization of the formed clusters was observed.

A numerical study similar to that with a AgI substrate was later performed at 265 K by Raego (1986) with silica substrates including pure SiO_2, and a SiO_2 substrate doped with hydroxyl (OH) groups. As expected, the substrate organized the H_2O molecules on the (111) surface in the form of five and six membered rings. Also as expected, the OH groups were found to stabilize the clusters.

9.2.5 Heterogeneous Freezing of Supercooled Water Drops

Experiments with water drops containing various impurities have revealed that their freezing temperature (usually expressed in terms of the median freezing temperature T_{sm} of a population of drops of volume V_d) is a function of the drop volume. Such a dependence was first suggested by Heverly (1949) and subsequently verified in a quantitative manner by Dorsch and Hacker (1950), Levine (1950),

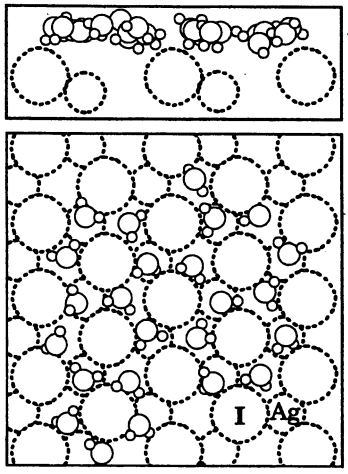


Fig. 9-40: Snapshot of the 24 water molecule situated on the basal face of a modelled silveriodide surface (iodine exposed), after 5×10^5 Monte Carlo steps at $-8°C$. The upper (lower) view is parallel (perpendicular) to the plane of the substrate. Large (small) dashed circles indicate iodine (silver) atoms in the substrate. The Ag atoms in the second layer are 0.94 Angströms below the surface plane. The area shown covers 400×10^{-16} cm^2. (From Ward *et al.*, 1982, by Courtesy of the authors, copyrighted by the Am. Inst. of Physics)

Bigg (1953b, 1955), Mossop (1955), Carte (1956, 1959), Kiryukhin and Pevzner (1956), Langham and Mason (1958), Barklie and Gokhale (1959), Stansbury and Vali (1965), Vali and Stansbury (1965, 1966), and Vali (1971). The experimentally derived volume relationship can be expressed as

$$T_{sm} = A - B \ln V_d \,, \tag{9-46}$$

where $T_{sm} = T_0 - T_m$ is the median freezing temperature in °C below $T_0 = 0°C$, T_m is the median freezing temperature in °C, and A and B are constants for a particular water sample. Figure 9.41 demonstrates this behavior for various water samples. In order to understand the physical basis of such a relationship, we shall consider two different points of view.

The 'classical' point of view was adopted by Bigg (1953a,b, 1955), Carte (1956, 1959), and Dufour and Defay (1963), who attempted to explain the freezing behavior of a population of water drops by assuming that at a given temperature all equal-sized ice embryos formed in a population of equal-sized supercooled water drops have an equal probability of reaching the size of a critical embryo or germ as a result of random fluctuations among the water molecules. Although these fluctuations were envisioned to form ice germs more efficiently in the presence of foreign particles, the effect of such particles in the water was considered non-specific, i.e., they were assumed to enhance the efficiency of the random nucleation process but not disturb its stochastic nature (*stochastic hypothesis*). Under these

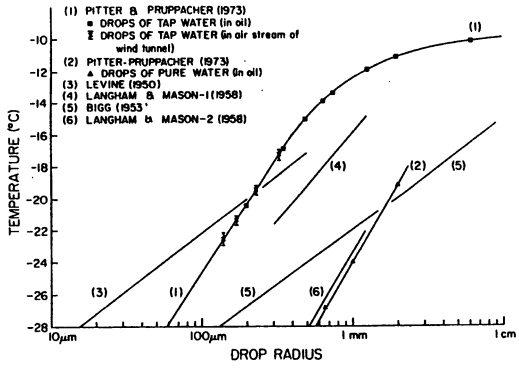


Fig. 9-41: Variation of the median freezing temperature of water drops as a function of their size. (From Pitter and Pruppacher, 1973; by courtesy of *Quart. J. Roy. Meteor. Soc.*)

conditions, the theory becomes equivalent to that given for homogeneous freezing in Section 7.2.3. In particular we may use (7-67) to express the relative change in the number of unfrozen drops during the time interval $\mathrm{d}t$ as

$$-\frac{\mathrm{d}N_\mathrm{u}}{N_\mathrm{u}} = V_\mathrm{d} J(T_s)\,\mathrm{d}t\,, \tag{9-47}$$

where $T_s = T_0 - T$. From his experiments, Bigg (1953b) deduced that

$$J(T_s) = B(\exp[\mathrm{a}T_s] - 1)\,, \tag{9-48}$$

where a is a constant of the order of unity. Therefore, for $T_s \gtrsim 5°\mathrm{C}$, we have from (9-47) and (9-48) the approximate result that

$$-\frac{1}{N_\mathrm{u}}\left(\frac{\mathrm{d}N_\mathrm{u}}{\mathrm{d}t}\right)_{T_s} = \frac{1}{N_\mathrm{u}}\left(\frac{\mathrm{d}N_\mathrm{f}}{\mathrm{d}t}\right)_{T_s} = BV_\mathrm{d}\exp(\mathrm{a}T_s) = \text{constant}\,, \tag{9-49}$$

since $\mathrm{d}N_\mathrm{u} = -\mathrm{d}N_\mathrm{f}$. Thus, the stochastic hypothesis leads to the prediction that at constant supercooling, the fraction of drops of volume V_d frozen per unit time interval is constant, and is larger, the larger the supercooling.

On the other hand, if the drop population is cooled at a constant cooling rate $\gamma_c = -(\mathrm{d}T/\mathrm{d}t) = \mathrm{d}T_s/\mathrm{d}t$, then, instead of (9-49), we find

$$-\frac{1}{N_\mathrm{u}}\left(\frac{\mathrm{d}N_\mathrm{u}}{\mathrm{d}T_s}\right)_{\gamma_c} = \frac{1}{N_\mathrm{u}}\left(\frac{\mathrm{d}N_\mathrm{f}}{\mathrm{d}T_s}\right)_{\gamma_c} = \frac{BV_\mathrm{d}}{\gamma_c}\exp(\mathrm{a}T_s)\,. \tag{9-50}$$

In other words, the fraction of drops of volume V_d frozen per unit temperature interval, while being cooled at a constant rate, increases exponentially with increasing supercooling, the fraction being smaller, the larger the cooling rate at any one supercooling.

The integral of (9-49) is

$$\ln \frac{N_0}{N_u(t)} = BV_d[\exp(aT_s)]t\,, \tag{9-51}$$

where $N_0 = N_u(t = 0)$. Thus, the number of unfrozen drops decays exponentially with time at a given supercooling. In terms of the time t_m needed to freeze one half of the drop population, i.e., $N_u(t_m) = N_0/2$, (9-51) states that

$$\ln t_m = A - aT_s\,, \tag{9-52}$$

where $A = \ln(\ln 2/BV_d) = \text{constant}$. We see that the median freezing time t_m decreases exponentially with supercooling.

Similarly, integration of (9-50) at constant γ_c yields

$$\ln \frac{N_0}{N_u(T_s)} = \frac{BV_d}{a\gamma_c} \exp(aT_s)\,, \tag{9-53}$$

so that for any given rate of cooling, the number of unfrozen drops decreases exponentially with increasing supercooling, and for any given supercooling, the number of unfrozen drops decreases with a decreasing rate of cooling. In terms of the median freezing temperature T_{sm}, where $N_u(T_{sm}) = N_0/2$, (9-53) becomes

$$T_{sm} = T_0 - T_m = C + \frac{\ln \gamma_c}{a}\,, \tag{9-54}$$

where $C = a^{-1} \ln(a \ln 2/BV_d) = \text{constant}$. Thus, the median freezing temperature lowers logarithmically, with increasing cooling rate. Given the form of C it is also clear that for fixed γ_c this relationship, namely

$$T_{sm} = T_0 - T_m = D - \frac{1}{a} \ln V_d\,, \tag{9-55}$$

is consistent with (9-46) in its account of the volume dependence of the drop freezing temperature, where $D = \ln(a \ln 2 \ln \gamma_c/B)/a$.

Bigg (1953a,b) used water of high purity and found $a = 0.82(°C)^{-1}$, $B = 2.9 \times 10^{-8}$ cm^{-3} sec^{-1}. Barklie and Gokhale (1959) used water of less purity and found $B = 2.0 \times 10^{-6}$ cm^{-3} sec^{-1} for distilled water, $B = 2.5 \times 10^{-4}$ cm^{-3} sec^{-1} for tap water, and $B = 2.0 \times 10^{-4}$ cm^{-3} sec^{-1} for rain water. The parameter a ranged between 0.57 and 0.75 $(°C)^{-1}$, with a mean of 0.65 $(°C)^{-1}$, independent of the type of water.

A second point of view was developed by Levine (1950) and Langham and Mason (1958), who attributed heterogeneous drop freezing entirely to the singular freezing characteristics of AP which have become incorporated in drops (*singular hypothesis*). They assumed that every particle contained inside a drop has one characteristic temperature at which freezing will be initiated in the drop. According to the singular hypothesis, then, the freezing temperature of a drop is determined by that particle in the drop which has the warmest characteristic temperature. It also implies that the number of ice germs formed in a drop volume V_d at a supercooling

T_s is given by the number of particles $n_P(T_s)$ inside the drop which become active as IN between 0°C and T_s; i.e., $n_P(T_s) = \int_0^t J(T_s)\mathrm{d}t$. Therefore, on intergrating (9-47), we have

$$\ln \frac{N_0}{N_u} = V_d n_P(T_s)\,. \tag{9-56}$$

For the distribution n_P, Langham and Mason assumed the empirical form of (9-29):

$$n_P(T_s) = n_{P_0} \exp(\mathrm{b}T_s)\,, \tag{9-57}$$

so that also

$$\ln \frac{N_0}{N_u(T_s)} = n_{P_0} V_d \exp(\mathrm{b}T_s)\,. \tag{9-58}$$

In contrast to the classical stochastic model, (9-58) predicts that the number of unfrozen drops is independent of the cooling rate. The equation also predicts that the number of frozen or unfrozen drops will not change with time for a given supercooling. In terms of the median freezing temperature, (9-58) states that

$$T_{sm} = T_0 - T_m = E - \frac{1}{\mathrm{b}} \ln V_d\,, \tag{9-59}$$

where $E = \mathrm{b}^{-1} \ln(\ln 2/n_{P_0}) =$ constant. Thus, we see further that the experimentally observed volume dependence is predicted both by the stochastic and the singular models, and so cannot be used to choose between them.

However, there are other corresponding predictions of the two models, such as (9-53) and (9-58), which may be checked against experimental data. Such comparisons have been made by Barklie and Gokhale (1959), Stansbury and Vali (1965), and Vali and Stansbury (1965, 1966). For drops of distilled water containing a large population of relatively small particles, it was found that, at a given cooling rate, the fraction of drops frozen per unit temperature interval increased exponentially with increasing supercooling (Figure 9.42), which is in accord with the dependence predicted by the classical stochastic model, and in direct conflict with the singular model, which predicts the fraction should be independent of γ_c. However, the variation with γ_c was found to be less than that expected on the basis of the stochastic model. Also, at a constant temperature, the fraction of drops frozen per unit time interval was found to decrease exponentially with time as $\exp(-t/T_s)$ (Figure 9.43), in contrast to both the stochastic model which predicts the fraction remains constant, and the singular hypothesis which predicts that the number of new freezing events is zero.

These studies suggest that the actual drop freezing mechanism is better represented by some combination of the stochastic and singular mechanisms than by either one acting alone. This observation is also more consistent with the known characteristic features of IN acting in the freezing mode, as discussed in Section 9.2.3. Thus, the singular characteristics of drop freezing can be attributed to the nature of the active sites on particles contained in the drop, and to the average chemical and crystallographic properties of the particles. On the other hand, the stochastic aspect of the drop freezing process can be attributed to the random

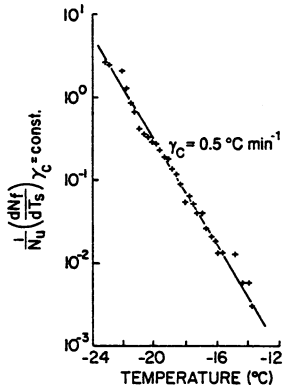


Fig. 9-42: Fraction of drops frozen per unit temperature interval as a function of temperature for distilled water; $V_d = 0.01$ cm^3. (From Vali and Stansbury, 1966; reproduced by permission of the Natl. Research Council of Canada.)

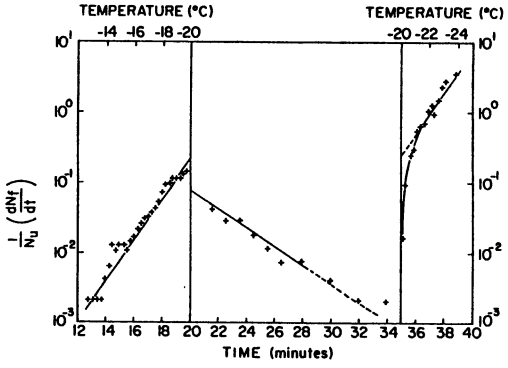


Fig. 9-43: Fraction of drops from distilled water, frozen per unit time interval as a function of time. $V_d = 0.01$ cm^3 , $t = 0$ at 0°C. At −20°C temperature was held constant for 15 min. (From Vali and Stansbury, 1966; reproduced by permission of the Natl. Research Council of Canada.)

manner in which, at any given supercooling, the water molecules in water join the clusters adsorbed at the active sites to eventually form an ice-like germ.

However, it should be recognized that the linear relationship between $\ln V_d$ and T_s in the singular model derives from a particular (exponential) size distribution for n_P. There is no reason to believe that such a functional dependence holds even approximately for all temperatures. Indeed, curve (1) in Figure 9.41 suggests that, for the particular water sample studied, the variation of the median freezing temperature of a population of water drops is not linear with $\ln V_d$ at temperatures warmer than $-15°C$. However, the behavior observed is physically reasonable since, on the basis of the singular hypothesis, one must expect that at temperatures approaching 0°C, the number of particles serving as IN in the freezing mode will rapidly decrease. This implies that above a certain temperature, the volume of a water sample which contains a particle that can nucleate ice will be progressively larger than that predicted by the $\ln V_d - T_s$ law.

We have pointed out in Chapter 8 that the major portion of aerosol particles consists of water-soluble substances. Hence, through various nucleation and scavenging processes, cloud water acquires both soluble and insoluble substances. The question then arises as to the effect of dissolved salts on the nucleating behavior of solid particles. This problem was studied by Pruppacher (1963a) and Pruppacher and Neiburger (1963), who also critically summarized relevant earlier work. Through experiments with drops of filtered solutions of various salts, they found that alkali- and earth alkali-halides, as well as other salts commonly found in the atmospheric aerosol, have a negligible effect on the freezing temperature of water drops if their concentrations are less than 10^{-3} mole l^{-1}. For larger concentrations, the salts studied invariably depressed the drop freezing temperatures. Their results can be summarized by the empirical relation

$$(\Delta T)_s = (\Delta T)_w + (\Delta T)_{e,s} + \delta T\,, \tag{9-60}$$

where $(\Delta T)_s$ is the median supercooling of a population of aqueous solution drops containing particles of a radius less than 0.01 μm, $(\Delta T)_w$ is the median supercooling of a population of drops of the same size and same water from which the solution was made, $(\Delta T)_{e,s}$ is the equilibrium freezing point depression of the particular salt in solution (see Section 4.9), and δT is a small temperature departure which varied between 0 and 2.5°C, being largest for solutions with salt ions which have a large tendency to disrupt the water structure and, hence, inhibit the formation of ice embryos.

Kuhns (1968), Parungo and Lodge (1967b), Pena *et al.* (1969), and Pena and Pena (1970) studied the effect of gases, in solution-equilibrium with pure water drops, on the freezing temperature of these drops. Kuhns found that the freezing temperature was affected by less than 1°C if the drops were in solution equilibrium with He, H_2, O_2, and air. Pena and Pena's observations supported Kuhns' results, but in addition they found that some organic gases such as CH_4, C_2H_6, and CH_4Cl slightly depressed the freezing temperature, while SO_2 depressed it strongly. Pena and Pena concluded that the clathrate structures which are induced by these gases at low temperatures are not conducive to ice formation. A similar conclusion

was reached by Pruppacher (1962), and Parungo and Wood (1968), who studied the effect of organic macromolecules in water. Parungo and Wood showed that the freezing temperature of water drops which contained macromolecules of dissolved substances such as agar, gelatin, citrus pectin, ovalbumin, bovin albumin, ribonucleic acid (RNA), and deoxyribonucleic acid (DNA) deviated by less than 1°C from that of pure water if the solute concentrations ranged between 0.01 and 1%. These results imply that water molecules, although immobilized by their interaction with macromolecules, are not arranged in an ice-like manner which would promote ice-germ formation, despite the fact that some macromolecules such as DNA have atomic spacings which closely agree with those present in ice (Jacobson, 1953; Watson and Crick, 1953).

Hoffer (1961) and Pruppacher and Neiburger (1963) suggested that the surfaces of insoluble particles of radii $> 0.01\,\mu$m in aqueous solution drops may be rendered ice nucleation active by physical adsorption of ions or by chemical reactions between the salt ions and the particle. However, Hoffer showed that the freezing temperature of drops which consisted of solutions of typical atmospheric salts such as $MgCl_2$ and Na_2SO_4, and containing typical aerosol insolubles, such as illite, kaolinite, montmorillonite, or halloysite, was not affected by the salt if its concentration was less than 10^{-3} mole l^{-1}, and was progressively lowered at larger concentrations. These results were essentially confirmed by Reischel (1972) and Reischel and Vali (1975), who found that salts present in the atmosphere affected the freezing temperature of water drops, which contained leaf-derived IN, by less than 1.5°C. A similar result was found for drops containing clay particles, except when $(NH_4)_2SO_4$ or NH_4Cl were present. In the latter case, the freezing temperature was shifted to warmer temperatures by up to 4°C at a salt concentration of about 10^{-2} mole l^{-1}, but by less than 1°C if the concentration was less than 10^{-3} mole l^{-1}. No explanation for the effects at larger concentrations was offered.

Junge (1952c) suggested that the freezing temperature of drops formed by condensation on mixed AP is affected by the presence of soluble material, particularly during the early stages of condensation, i.e., prior to activation of the drop. This fact is evident from Table 6.3, where the concentration of salt at the point of activation is listed for AP composed of NaCl and SiO_2 in various proportions. By comparing the results given in this table with the concentration requirement for a negligible effect on the freezing temperature of a solution drop, which is 10^{-3} mole l^{-1}, we learn that mixed particles have to have masses larger than 10^{-13} g, and have to contain more than 35% (by mass) salt in order for the drop to grow large enough so that the concentration of salt in solution is less than 10^{-3} mole l^{-1} at the point of activation of the drop. This requirement is not fulfilled for most atmospheric AP. Thus, prior to and at their point of activation, most atmospheric solution drops will consist of salt solutions too concentrated for ice nucleation. This implies, as Junge (1952, 1952c) suggested, that most mixed AP must form drops which have sizes beyond activation before the salt concentration is sufficiently low for a freezing or contact nucleus to initiate freezing.

9.2.6 Discrepancy Between the Concentrations of IN and the Concentration of Ice Particles

If one compares the concentrations of IN and ice particles at nearby locations in clouds, a rather unexpected discovery may be made. One finds that in many clouds, particularly at relatively warm temperatures, the concentration of ice particles may exceed by many orders of magnitude the concentration of IN determined at the cloud top temperature. Observations to this effect were made by Hobbs (1969) and Hobbs *et al.* (1974b) over the Cascade Mts. (State of Washington), by Auer *et al.* (1969) in stable cap clouds over Wyoming, by Isono (1965), Ono (1972), and Magono and Lee (1973) over Japan, by Mossop (1970, 1971, 1972), Mossop *et al.* (1967, 1968, 1970, 1972), Mossop and Ono (1969) in cumulus clouds over Australia and Tasmania, and by Braham (1964) and Koenig (1963, 1965) in cumulus clouds over Missouri.

These observations show that the ice *enhancement ratio* or *enhancement factor* R_M, defined as the ratio of the ice particle concentration to the IN concentration determined at the cloud top temperature, can be as large as 10^4 to 10^5 at temperatures near -5°C. With decreasing cloud top temperature, R_M tends to decrease reaching unity at cloud top temperatures near -20°C. Figure 9.44 presents some observations of R_M for a variety of clouds sampled over Montana. We notice that R_M varies approximately with the cloud top temperature T_c (in °C) as $\log R_M = 5.9 + 0.295T_c$, if we disregard some of the extraordinary high values for R_M at temperatures between -12 and -16°C. This 'local' maximum in R_M results from the maximum in the ice particle concentration of Figure 2.44 for that temperature region where delicate dendritic snow crystals are formed, and which can easily fragment.

The efficiency with which secondary ice particles are produced by mechanical

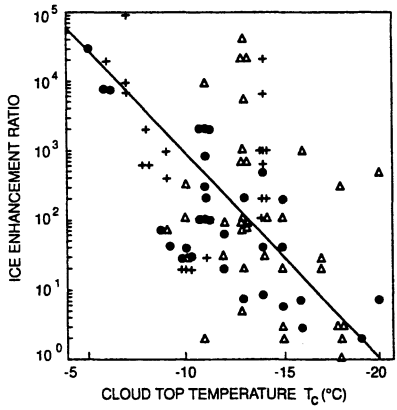


Fig. 9-44: Ice enhancement ratios, R_M, as a function of cloud top temperature determined in updraft regions of clouds over Miles City (Montana). (•) Small cumulus, (△) cumulus complexes, (+) embedded cumulus; line is given by: $\log R_M = 5.9 + 0.295T_c$, where T_c is the cloud top temperature in °C. (From Hobbs *et al.*, 1980, with changes.)

fracturing of fragile crystals, was studied by Hobbs (1969, 1972, 1974b), Hobbs and Farber (1972), Jiusto and Weickmann (1973), Vardiman (1974) and Vali (1980). These studies showed that the mechanical fracturing mechanism may, indeed, significantly enhance the ice particle concentration in these clouds. This conclusion was supported by the large number of ice crystal fragments collected in these clouds, and by the observation that over 50% of all stellar ice crystals collected at the ground had pieces (branches and portions of branches) missing. A similar observation was made on sector type crystals. Also, needles were often found fractured, especially at their tips. Ice crystals with spatial extensions and radiating assemblages of various crystal types often had portions missing. Similar observations were reported by Grant (1968) and by Vardiman and Grant (1972a,b) in clouds over the Colorado Rockies.

Figure 9.44 suggests that, in addition to mechanical fracture of fragile ice crystals formed at temperatures near -12 to $-16°C$, there must be other ice enhancing mechanisms. Mossop (1970, 1971) and Mossop *et al.* (1970, 1972) in their review articles, suggest that ice enhancement may also be the result of the fragmentation of relatively large individual cloud drops during freezing, or ice splinter formation during the riming of ice particles. We shall now discuss these in sequence.

Several observations have implied that the presence of large drops leads to efficient ice multiplication. Thus, observations by Ono (1972) in Japan, Mossop (1970, 1972), Mossop *et al.* (1968, 1970, 1972) in Australia, and Koenig (1963) and Braham (1964) in Missouri are consistent with the interpretation that drops of diameter $\gtrsim 250\,\mu m$ are required. These observations have been interpreted in terms of an ice multiplication mechanism involving the shattering or partial fragmentation of relatively large, freezing cloud drops.

Although earlier studies by Mason and Maybank (1960) suggested copious splinter formation during the freezing of supercooled drops, Dye and Hobbs (1966, 1968) demonstrated that Mason and Maybank's results were biased by the presence of abnormally large concentrations of CO_2. They showed that drops freezing at rest in ordinary air and in thermal equilibrium with their surroundings did not shatter, although the formation of cracks, spikes, and protuberances was frequent. This result was essentially confirmed by Johnson and Hallett (1968) and Pena *et al.* (1969).

However, Johnson and Hallett found that whether or not a freezing drop shattered also depended crucially on whether or not the drop rotated during freezing, thus allowing a more or less radially uniform dissipation of the latent heat. This finding raised some questions as to the realism of drop splintering and shattering experiments which are carried out with drops that freeze while being suspended in a fixed orientation on fibers and other mounts. Under such conditions, the lower or upstream side of a drop is colder than the upper or downstream side, since the former is much more effectively ventilated (see Section 13.2.3). Consequently, one would expect from the studies of Johnson and Hallett that the resulting asymmetric freezing would tend to inhibit shattering. Pitter and Pruppacher (1973), however, demonstrated by wind tunnel experiments that immediately after nucleation, a freezing supercooled water drop, which is freely falling at its terminal velocity in air, begins to tumble and spin as it falls along a helical path, thus providing for a

nearly radially symmetric heat loss from the drop to the environment during the initial stages of freezing. As expected from the findings of Johnson and Hallett, Hobbs and Alkezweeney (1968) observed, during experiments in which drops were allowed to fall freely in a long shaft, that a small but measurable fraction of drops with diameters between 50 and 100 μm shattered at temperatures between -20 and -32°C; similar results were obtained at -8°C. However, none shattered if the drop diameter was less than 50 μm. Similarly, Kuhns (1968) found no shattering for 10 to 50 μm diameter drops of very pure water frozen between -36 and -38°C, and Brownscombe and Goldsmith (1972) found no shattering for drops of 20 to 50 μm diameter frozen at -10 to -15°C. On the other hand, Brownscombe and Thorndyke (1968) observed that a small fraction of 40 to 120 μm diameter drops nucleated internally at temperatures between -5 and -15°C, shattered with 2 to 3 ice splinters being produced per drop. Similarly, a small fraction of 120 to 240 μm diameter drops shattered when nucleated at -5 to -15°C by contact with ice crystals.

From their observations, Brownscombe and Thorndyke deduced that the ice particle enhancement factor (defined by Mossop *et al.* (1970) as the ratio of ice particles produced to drops frozen) was finite but rather small, ranging between values of 1.12 to 1.30. Only on one occasion did they find an enhancement factor of 2.45. Similarly, Bader *et al.* (1974) observed for single free falling drops of 30 to 84 μm in diameter, an enhancement factor < 10. Takahashi and Yamashita (1969, 1970) deduced an enhancement factor of 1.74 near -15°C for drops of 74 to 350 μm in diameter. Both at colder and warmer temperatures, the enhancement factor was less. Pruppacher and Schlamp (1975) carried out wind tunnel studies with drops of 410 μm in diameter freely suspended in the air stream and nucleated by contact or freezing nuclei. They found an enhancement factor of 1.22 to 1.72 at temperatures between -7 and -23°C, the maximum enhancement occurring at temperatures between -11 and -15°C.

These observations suggest that shattering and splintering of freezing drops freely falling in the atmosphere results in an ice multiplication factor which at times surpasses a value of 2 but rarely, if ever, exceeds a value of 10. Further evidence that freezing drops at times do fragment in clouds has been provided by Knight and Knight (1974), who deduced from a photographic study of frozen drops preserved as hailstone embryos, that drop break-up during freezing is a fairly common occurrence.

A third promising mechanism to provide ice particle enhancement involves the riming of ice particles. Experiments by Latham and Mason (1961a) suggested that copious splintering accompanies the impaction of supercooled drops on an ice surface. However, Hobbs and Burrows (1966), Aufdermauer and Johnson (1972), and Brownscombe and Goldsmith (1972) failed to substantiate these findings. Later studies by Hallett and Mossop (1974), Mossop and Hallett (1974), and Mossop (1976) appear to have resolved this quandary by demonstrating that the process depends rather sensitively on several factors, such as the drop size distribution, the liquid water content, the velocity of the drops impacting on a riming ice particle, the air temperature, and the surface temperature of the riming ice particle. They made observations on a cloud characterized by a liquid water content of approxi-

mately 1 g m^{-3}, with drop diameters from 5 to 45 μm and total drop concentration of roughly 500 cm^{-3}, and found that ice splinter formation during riming was significant only for air temperatures between -3 and $-8°C$, drop diameters larger than 24 μm, and drop impact velocities between 1.4 and 3 m sec^{-1}. A pronounced maximum for splinter formation was found at a cloud air temperature of $-5°C$ and a drop impact velocity of 2.5 m sec^{-1}. For these conditions, the secondary ice particles appear as small columnar crystals. One may argue that after some growth by vapor deposition, these small crystals would then be scavenged by large cloud drops, which in turn would freeze and subsequently act as riming centers to produce new ice splinters, and so on.

To further define the conditions for secondary ice particle production, Mossop (1978) showed that the production rate of ice splinters is also dependent on the presence of drops of diameter less than 13 μm, which cover a riming ice particle. Additional information regarding the Hallet-Mossop mechanism came from Mossop (1985a,b,c) and Heymsfield and Mossop (1984), who demonstrated that what matters for the splinter formation mechanism is the surface temperature of the riming ice particle, rather than the air temperature. For a maximum ice production rate, the surface temperature of the riming ice particle needs to be near $-5°C$. Of course, this temperature, in turn, is controlled by combined effects of the temperature of the air, the liquid water content of the cloud and the relative velocity of the cloud drops with respect to the riming ice particle, since the latter two parameters determine the rate of release of latent heat at the surface of the riming ice particle. Under optimal conditions, 1 secondary ice splinter is produced per 100 to 250 drops of diameter larger than 24 μm impacting on the riming ice surface (Mossop, 1985a,b,c, 1976; Hallett and Mossop, 1974; Mossop and Hallett, 1974). Additional discussion on the ice multiplication mechanism is given in Section 16.1.6.

The sequence of events during ice splinter production by a riming ice particle has been recorded on motion picture film by Choularton *et al.* (1980) and Griggs and Choularton (1983, 1986). These films show that if a supercooled drop lands on an already frozen drop located on the surface of the riming ice particle (covered by drops of diameter less than 13 μm) at a temperature of $-6°C$, it freezes symmetrically as the ice front initiated at the small point of contact grows rapidly around the drop. When subsequently the supercooled water in the drop's interior also freezes, the ice shell breaks and an ice spike is produced which easily fractures. Although at $-8°C$ two growth fronts are initiated at the point of contact, ice shell formation followed by fracturing of the newly formed spikes still prevails. However, at $-10°C$, ice growth inward dominates ice growth around the drops so that ice shell formation and subsequent production of fragile spikes is prevented. On the other hand, at a temperature of $-3°C$, the impinging drop does not immediately freeze on contact with the riming ice particle, but rather spreads over the surface before it freezes. Also under these conditions, no ice shell formation is possible.

In order to interpret enhanced ice particle formation in clouds in terms of the Hallett-Mossop mechanism, it is necessary to check whether the specific conditions for this mechanism are met in these clouds. This was indeed the case for the convective clouds in Australia studied by Mossop (1970, 1972) and Mossop *et al.* (1968, 1970, 1972), for clouds in Japan studied by Ono (1971), clouds in Missouri

studied by Koenig (1963) and Braham (1964), clouds in Florida studied by Hallett *et al.* (1978) and Lamb *et al.* (1981), clouds associated with Atlantic hurricanes studied by Black and Hallett (1986), clouds in Texas studied by Jurica and Frey (1989), and for clouds in Oklahoma studied by Heymsfield and Hiemfelt (1984). On the other hand, no correlation between the ice particle content of the cloud and the Hallett-Mossop mechanism was found for the clouds studied by Paluch and Breed (1984), Vali (1992), and Rauber (1987a,b), while Hobbs and Rangno (1985) found that in the clouds they studied, the conditions for the Hallett-Mossop mechanism was only fulfilled in 75% of the cases. Gagin (1971) and Le Compte and Grant (1976) observed no ice enhancement in the clouds they studied, indicating that the ice particle concentration corresponded to the concentration of ice nuclei observed. Similarly, little or no ice multiplication was found in mid-level or low-level layer clouds in Australia (Mossop, 1972; Mossop *et al.*, 1972), nor in stratus clouds over Alaska (Jayaweera, 1972a). Negligible ice multiplication was also reported by Gagin (1971) in winter cumuli over Israel, the maximum enhancement ratio varying at most between 1 and 10.

We note from our discussion that none of the three ice enhancement mechanisms mentioned provides a unique explanation for the ice particle concentration found in clouds. In fact, it appears that all three mechanisms may contribute to the final ice particle concentration in clouds. In order to show this, we may follow Rangno and Hobbs (1988, 1991), and Hobbs and Rangno (1985,1990) who provided an inventory of the most significant stages during the evolution of cloud glaciation (valid at least for maritime type clouds). Accordingly, ice formation begins near the cloud top where even at an early stage, drizzle drops of diameter larger than 100 μm appear at concentrations of a few per liter as a result of collision and coalescence. In the next stage, the drizzle drops freeze and begin to rime by collecting cloud drops of diameters larger than 20 μm. This stage is followed by the appearance of small largely vapor grown ice crystals, in concentrations of 10 to 100 liter^{-1}. These crystals, in turn, nucleate the still unfrozen drizzle drops, turning them into rimers followed by more small crystals, and so on. Observations show that this ice enhancement may proceed extremely fast, such that within 10 minutes or so, the ice particle concentration at cloud top temperatures as warm as -8°C may increase from a few per liter to several hundred per liter. Rather than correlating with the cloud top temperature, the maximum ice particle concentration appears generally to be linked to the size of the drops in the clouds, following the relation

$$N_{\mathrm{IC,max}} = (D_T/D_0)^{\eta}\,, \tag{9-61}$$

with $D_0 = 18.5\,\mu$m and $\eta = 8.4$ for cumuliform clouds, $D_0 = 19.4\,\mu$m and $\eta = 6.6$ for stratiform clouds, and where D_T is a threshold diameter defined such that drops of $D_0 \geq D_T$ appear in a total concentration of 3 cm^{-3}. Superimposed on this general trend for the maximum ice particle concentration is a temperature dependent component at temperatures between -12 to -16°C, the region of the fragile dendrites. Thus, we see that the observed characteristics for cloud glaciation contain some of the features of all three ice enhancement mechanisms mentioned: large drops must appear and freeze, the frozen drops must rime by colliding with drops of a certain minimum size, and fragile dendritic snow crystals must appear.

One explanation for the observed discrepancy between IN and ice particles in clouds may certainly hinge on some deficiencies in counting the number of ice forming nuclei. In most previous IN measurements, the strong dependence of N_{IN} on ice supersaturation has not been considered sufficiently, and neither has the time lag for ice germs to grow to ice crystals. Also, the fact that aerosol particles may act as ice forming nuclei via the contact freezing mode has not yet been considered sufficiently in routine IN measurements. Given adequate instrumentation, it may be that the discrepancy between the IN and ice particle concentrations can be considerably reduced or even eliminated, and along with it the need for finding an adequate ice multiplication mechanism.

We shall conclude this section by saying a word on ice nucleation at the cirrus cloud level. We have already pointed out in Section 9.2.1 that only conflicting evidence is available in the literature regarding the vertical variation of IN in the atmosphere. On the other hand, field observations show that the concentration of ice crystals and therefore ice nuclei is rather low in the upper troposphere (Heymsfield, 1967; Rangno and Hobbs, 1986), and that liquid, supercooled drops are encountered at temperatures even as low as $-40.7°C$ (see Section 2.2). This prompted Heymsfield and Miloshewich (1993), Heymsfield and Sabin (1989) and Sassen and Dodd (1988) to conclude that homogeneous ice nucleation of supercooled drops are responsible for the occurrence of cirrus ice, a result consistent with the theory for homogeneous ice formation in drops formulated by Pruppacher (1995) and Eadie (1971). In contrast, Rogers (1994) and deMott *et al.* (1994) argue that even small numbers of heterogeneously nucleated ice crystals would lower the maximum ice crystals concentration as well as the maximum humidity reached. For such conditions, homogeneous ice nucleation would become irrelevant for the formation of cirrus clouds where the vertical motions are typically less than 30 cm sec^{-1}. Clearly then, more information on the quality and number of ice forming nuclei at the cirrus level is needed.

CHAPTER 10

HYDRODYNAMICS OF SINGLE CLOUD AND PRECIPITATION PARTICLES

Once formed, cloud particles immediately begin to move under the action of gravity and frictional forces, the latter arising from their motion relative to the air. Some fraction of these particles will undergo complex hydrodynamic interactions causing some to collide. The particles will experience growth if the collision results in a permanent union. Generally in clouds, the time during which two colliding particles interact to form a single particle is much shorter than the time during which they fall in isolation. We therefore will address ourselves in this chapter to the basic mode of isolated motion of cloud particles. The collison process will be discussed in Chapter 14. For simplicity, we also will defer to Chapter 18 the effects of electrical forces.

As we will see, the smallest of the cloud drops and ice crystals fall slowly, with speeds typically less than 1 cm $\sec^{-1}$, so that very gentle updrafts suffice to keep them suspended. On the other hand, large raindrops and hailstones have fall speeds of 5 m $\sec^{-1}$ and more, and generally cannot be supported by the prevailing updrafts.

In applying hydrodynamic theory to the motion of isolated cloud and precipitation particles, we will first restrict our attention to droplets small enough to be regarded as rigid impermeable spheres. Later, we will consider the phenomena of drop deformation, internal circulation, vibration, and breakup. The complicated shapes of ice particles makes a quantitative description of their hydrodynamic behavior extremely difficult. However, it turns out that the motions of simple plate-like ice crystals may be understood reasonably well through the expedience of studying flows past disks and thin oblate spheroids. Similarly, one may use circular cylinders and prolate spheroids as idealizations of simple columnar snow crystals. A discussion of the motion of more complex ice particles will follow at the end of this chapter.

10.1 Basic Governing Equations

The principle of mass conservation for a fluid in motion is shown in Appendix A-10.1 to lead to the continuity equation:

$$\frac{1}{\rho}\frac{\partial \rho}{\partial t} = -\nabla \cdot \vec{u}\,. \tag{10-1}$$

where ρ and $\vec{u}$ are the fluid density, and velocity, respectively. It is well-known that flow past an object may be regarded as incompressible ($d\rho/dt = 0$) whenever the

following conditions are met (see, for example, Chapter 1 of Rosenhead (1963)): (1) the characteristic flow speed U satisfies $U \ll c$, where c is the speed of sound in the fluid ($c \approx 340$ m sec^{-1} in air at 15°C and 1 atm.); (2) the dominant flow oscillation frequency f satisfies $f \ll c/L$, where L is the characteristic length scale for changes in $\vec{u}$ (in our context, L is the order of the size of the falling object); (3) $L \ll c^2/g$, where g is the magnitude of the gravitational acceleration (this is equivalent to the condition that the static pressure difference between two points separated in the vertical by length L must be very small compared to the absolute pressure; i.e., L is a small fraction of the atmospheric scale height H (≈ 10 km)); (4) the fractional temperature difference between obstacle and stream is small, i.e., $| T - T_\infty | \ll T_\infty$, where T and T_∞ are the characteristic temperature of the obstacle and streaming fluid, respectively. As these inequalities hold for all cloud particle motions, we will henceforth assume the flows under consideration are incompressible so that from (10-1).

$$\nabla \cdot \vec{u} = 0 \,. \tag{10-2}$$

For ordinary (Newtonian) fluids, of which air and water are examples, the momentum equation for incompessible flow in the presence of gravity acquires the form of (A.10-13):

$$\frac{\partial \vec{u}}{\partial t} + \vec{u} \cdot \nabla \vec{u} = -\frac{\nabla p}{\rho} + \nu \nabla^2 \vec{u} + \vec{g} \,, \tag{10-3}$$

where $\vec{g}$ is the local gravitational acceleration, p is the fluid pressure, and ν is the local kinematic viscosity, which like ρ is assumed constant over distances large compared to L. Equation (10-3) is known as the *Navier-Stokes equation.*

This system of equations must be supplemented with suitable boundary conditions. The most important of these recognizes that real fluids adhere to any material surface; this is known as the 'non-slip' boundary conditions. Thus, at any solid boundary surface (S), the fluid velocity must satisfy the condition

$$\vec{u} \,|_S = \vec{v}_S \,, \tag{10-4}$$

where $\vec{v}_S$ is the local surface velocity. If the boundary is a surface of separation between two immiscible fluids, then in addition to (10-4), we must require that the stresses the fluids exert on each other at the boundary are equal and opposite; at a free surface, for example, the stress must be zero.

If the fluid is at rest, (10-3) reduces to the equation for the static pressure, p_S:

$$\nabla p_S = \rho \vec{g} = -\nabla(\rho g z) \,, \tag{10-5}$$

assuming constant ρ and $| \vec{g} | = g$, and letting z denote the height above the Earth's surface. The total static pressure force on a particle of volume V and surface S may therefore be expressed as

$$-\int_S \vec{n} p_S \, dS = -\int_V \nabla p_S \, dV = \int_V \nabla(\rho g z) \, dV = \rho V g \hat{e}_z \,, \tag{10-6}$$

where $\vec{n}$ is the unit outward normal to dS and $\hat{e}_z$ is the unit vector in the z-direction. This result is just Archimedes' principle, which states that an object immersed in a fluid experiences a buoyancy force equal to the weight of the fluid it displaces.

Hence, we have an opportunity for another small simplification: We may hereafter ignore the gravity term in (10-3), as its only effect on the motion of the particle in the flow is to provide the simple buoyancy force given by (10-6). This may more conveniently be introduced separately later when considering the equation of motion of the falling cloud particle. (In any case, for practical purposes, the buoyancy force is negligible in comparison to the gravitational force on the particle, since $\rho_a/\rho_P \approx 10^{-3}$, where ρ_a is the density of air and ρ_P is the bulk density of the particle.) Formally, this simplification amounts to rewriting $-\nabla p/\rho + \vec{g}$ in (10-3) as $-\nabla p'/\rho$, where $p' = p - p_S$. The pressure profile obtained in this manner is called the dynamic pressure, since the static distribution due to gravity has been subtracted out. Dropping the prime for brevity (10-3) becomes

$$\frac{\partial \vec{u}}{\partial t} + \vec{u} \cdot \nabla \vec{u} = -\frac{\nabla p}{\rho} + \nu \nabla^2 \vec{u}. \tag{10-7}$$

Another simplification is possible for most of the applications considered in the present chapter. Suppose a particle of simple shape is released from rest in the atmosphere. If it is sufficiently small and therefore falls slowly enough, the fluid forces resisting its motion will eventually equilibrate with gravity, and a steady fall at some terminal velocity will result. During its acceleration to terminal velocity, the flow field past the particle will continuously change with time in accord with (10-7). At terminal velocity, the flow past such a particle will be steady so that the term $\partial \vec{u}/\partial t$ in (10-7) may be dropped, if we analyze the motion from the point of view of the particle past which the flow streams. As a result, the flow field is described by the steady state Navier-Stokes equation of motion:

$$\vec{u} \cdot \nabla \vec{u} = -\frac{\nabla p}{\rho} + \nu \nabla^2 \vec{u}. \tag{10-8}$$

The situation is quite different for larger particles of considerable fall speed and often quite irregular shape. Even at terminal velocity, such particles exhibit an intrinsically unsteady flow field which has no symmetry. To describe such flow fields, (10-7) has to be solved in three dimensions. In response to such unsteady flow, particles carry out a variety of secondary motions in addition to their main vertical fall mode. The oscillatory nature of these secondary motions also induces some unsteadiness into the vertical component of their fall velocity. Fortunately, the frequency of such oscillatory motions remains nearly constant in time, and is sufficiently high so that, if released from rest, they will eventually approach a constant, time-mean, terminal velocity. Since cloud and precipitation particles grow slowly compared to the relaxation time to achieve terminal velocity at a given size, they may generally be assumed to remain falling at terminal velocity throughout their life cycle.

We must emphasize at this point that the foregoing discussion applies to particles falling in calm air. In a turbulent atmosphere, the updraft speeds may vary

rapidly in time and space. Particles falling in such an evironment will experience fluctuating forces that may noticeably affect their fall behavior as well as their shape. The effects of such motions will be briefly touched upon in Sections 10.3.3 and 10.3.4 and in Chapters 14 and 15.

10.2 Flow Past a Rigid Sphere

10.2.1 Classification of Flows According to Reynolds Number

A glance at (10-8) warns of great difficulties, as the convective acceleration term $\vec{u} \cdot \nabla \vec{u}$ (also called the inertia term) is nonlinear. As a matter of fact, complete solutions to (10-2) and (10-8) have been found for only a very few special situations, among which the case of flow past a sphere, of great importance to cloud physics, is unfortunately not included. Nevertheless, useful approximate analytical and numerical solutions are available for a wide range of conditions.

For the problem of a falling sphere, the relative importance of $\vec{u} \cdot \nabla \vec{u}$ and the linear viscous acceleration term $\nu \nabla^2 \vec{u}$ may be assessed by simple dimensional arguments. Physically, the flow is characterized by the size of the sphere, for which we may take either the radius a or diameter d as a natural measure, and by the streaming velocity (or terminal velocity) U_∞. Therefore, we might expect $\vec{u} \cdot \nabla \vec{u}$ to be of the order U_∞^2/a, and $\nu \nabla^2 \vec{u}$ to be of the order $\nu U_\infty / a^2$. This leads to the estimate

$$\frac{| \vec{u} \cdot \nabla \vec{u} |}{| \nu \nabla^2 \vec{u} |} \approx \frac{U_\infty a}{\nu} \equiv R, \tag{10-9}$$

where R is the *Reynolds number.* (An alternative definition,

$$N_{\mathrm{Re}} \equiv \frac{U_\infty d}{\nu} = 2R, \tag{10-10}$$

also often appears in the literature and in this book.) Equation (10-9) implies that $\vec{u} \cdot \nabla \vec{u}$ may be omitted from (10-8) if $R \ll 1$.

A more precise way to come to almost the same conclusion is to introduce the dimensionless variables $\vec{r}' \equiv \vec{r}/a$ and $\vec{u}' \equiv \vec{u}/U_\infty$. Then, we have

$$\frac{| \vec{u} \cdot \nabla \vec{u} |}{| \nu \nabla^2 \vec{u} |} = R \frac{| \vec{u}' \cdot \nabla' \vec{u}' |}{| \nabla'^2 \vec{u}' |}, \tag{10-11}$$

where $\nabla' \equiv a \nabla$ is the dimensionless gradient operator. The factor multiplying R in (10-11) is a function only of $\vec{r}'$, and must be of order unity if (10-9) is to be consistent with (10-11). As we shall see below in Section 10.2.2.3, this is in fact not always the case. Nevertheless, it is generally correct to say that the inertia term becomes less important with decreasing R.

Many cloud particles indeed have Reynolds numbers much smaller than unity. For example, a cloud drop of $a = 10\,\mu$m has a fall velocity of about 1.2 cm sec^{-1} at $T = 20°$C and $p = 1000$ mb. Since under these conditions the kinematic viscosity for air is $\nu \approx 0.15$ cm^2 sec^{-1}, we find $R \approx 0.01$. Similarly, for a drop of $a = 30\,\mu$m, we have $R \approx 0.2$. To a good approximation the flow field, drag, and terminal

velocities for such drops are described by (10-7) without the $\vec{u} \cdot \nabla \vec{u}$ term. The resulting equation governs what is known as *Stokes flow.*

For larger drops, things are not as simple. Thus, a drop of $a = 50\,\mu$m has $R \approx 1$, while for $a = 150\,\mu$m, $R \approx 10$. For a raindrop of a few millimeter in radius, $R > 10^3$. As R increases, the flow becomes more complicated, reflecting the greater contribution of the nonlinear term. An additional complication is the change of shape with size for the larger drops, which by itself influences the flow pattern. Also, the larger the drop, the greater the tendency for development of a complex internal circulation, which contributes to its overall behavior.

In order not to unduly complicate matters at the outset, we shall restrict ourselves in this section to a discussion of the flows past drops small enough to be regarded as rigid spheres. As we shall see in Section 10.3.2, this is a good assumption for radii less than about $500\,\mu$m, corresponding to $R \lesssim 150$ ($N_{\mathrm{Re}} \lesssim 300$).

Before presenting any detailed results for the flow past a sphere, it is worthwhile to consider briefly the qualitative features to be expected at various Reynolds numbers. If we use a coordinate system in which the sphere is at rest, the no-slip boundary condition requires that the fluid velocity must decrease to zero at the surface. This causes the surface to act effectively as a source of fluid shearing motion and angular momentum. The latter may be measured by the vorticity $\nabla \times \vec{u}$ (it is easy to show that $\nabla \times \vec{u} = 2\vec{\omega}$, where $\vec{\omega}$ is the local fluid angular velocity). When $R \ll 1$ and fluid inertia is negligible, the flow is characterized by the diffusion of vorticity away from the sphere. This is easily seen by taking the curl of (10-8) without the $\vec{u} \cdot \nabla \vec{u}$ term, and recalling that $\rho =$ constant; the result is $\nabla^2(\nabla \times \vec{u}) = 0$, which is the steady state diffusion equation for vorticity. Such flow is relatively simple and has 'fore-aft' symmetry, i.e., symmetry with respect to the plane separating the sphere into upstream and downstream hemispheres.

As R increases to order unity (corresponding to increasing U_∞ for a given sphere), there is a tendency for part of the vorticity generated at the sphere surface to be convected downstream. This leads to an asymmetry in the flow, with most of the vorticity confined to the rear of the sphere in a roughly paraboidal region, known as the wake, with its vertex in the sphere and with symmetry about the axis of motion. If R increases to O(10), the wake becomes narrower and the vorticity within it more intense. At about $R = 10 (N_{\mathrm{Re}} = 20)$, a region of circulating fluid forms behind the sphere. This 'standing eddy' grows in size and strength with further increase in R. Incipient wake instability occurs near $R = 65 (N_{\mathrm{Re}} = 130)$; for larger R the flow thus becomes intrinsically unsteady. For $R > 150 (N_{\mathrm{Re}} > 300)$ the eddy oscillates while lumps of circulating fluid are torn away from it and travel downstream. This unsteadiness intensifies rapidly as the shedding frequency of eddies from the rear of the sphere increases with a further increase in Reynolds number (see Section 10.2.2.5).

Outside the wake there is little vorticity caused by the sphere, and since we assumed none upstream to begin with (the flow is assumed unbounded and undisturbed except for the sphere), the flow outside the wake tends to be irrotational ($\nabla \times \vec{u} = 0$), and increasingly so with increasing R. Viscosity has no effect where the flow is irrotational and nondivergent, since then $\nabla^2 \vec{u} = \nabla(\nabla \cdot \vec{u}) - \nabla \times (\nabla \times \vec{u}) = 0$. Therefore, such flow behaves like frictionless or inviscid irrotational flow, which

is called *potential flow.* This type of flow is especially simple since, as the name implies, its velocity field may be expressed in terms of the gradient of a potential: $\nabla \times \vec{u} = 0$ implies $\vec{u} = \nabla\Phi$, where $\nabla^2\Phi = 0$ since $\nabla \cdot \vec{u} = 0$.

Potential flow prevails almost everywhere when $R \gg 1$, and reflects the dominance of the fluid inertia. It cannot exist close to the sphere however, since there the no-slip condition creates large shears and viscous forces of the same magnitude or larger than the inertia forces. Neither can it exist in the vorticity-carrying wake. The thickness of the fluid layer adjacent to the sphere over which the transition from viscosity-dominated to inertia-dominated flow takes place, called the *boundary layer*, can be shown to vary as $R^{-1/2}$ (see Section 10.2.2.3). Outside the boundary layer and wake, the essentially potential flow possesses streamlines very much like those of low Reynolds number flow.

With this qualitative picture of the flow regimes as a background, we shall now look in more detail at the problem of flow past a sphere.

10.2.2 Steady, Axisymmetric Flow

The problem of a sphere falling in the $+z$ direction is the same as that of flow streaming in the $-z$ direction past a fixed sphere. The obvious advantage of the latter point of view, which we shall adopt here, is that the flow is steady relative to the sphere for Reynolds numbers small enough to preclude eddy shedding. In this case, the flow will also possess axial symmetry about the z-axis, meaning there is no azimuthal component of velocity, and that the motion is the same in every meridian plane (i.e., every plane containing the z-axis and defined by $\phi =$ constant, where ϕ is the azimuthal angle).

10.2.2.1 *The Stream Function*

As shown in Appendix A-10.2.2, the constraint of incompressibility on the two components of the velocity field makes it possible to describe the flow in terms of the derivatives of a single scalar function, ψ, called the *stream function.*

In spherical coordinates, with the polar angle θ measured from the $+z$ direction, the velocity field $\vec{u} = (u_r, u_\theta, 0)$ is given in terms of ψ by (A.10-17):

$$u_r = -\frac{1}{r^2 \sin\theta}\frac{\partial\psi}{\partial\theta}, \qquad \text{(10-12a)} \qquad u_\theta = \frac{1}{r\sin\theta}\frac{\partial\psi}{\partial r}. \qquad \text{(10-12b)}$$

Similarly, according to (A.10-22) and (A.10-26), the *vorticity* may be expressed as

$$\nabla \times \vec{u} = \hat{e}_\phi \zeta = \frac{\hat{e}_\phi E^2\psi}{r\sin\theta}, \qquad \text{(10-13)}$$

where $\zeta \equiv | \nabla \times \vec{u} |$ and

$$E^2 = \frac{\partial^2}{\partial r^2} + \frac{\sin\theta}{r^2}\frac{\partial}{\partial\theta}\left(\frac{1}{\sin\theta}\frac{\partial}{\partial\theta}\right). \qquad \text{(10-14)}$$

Finally, the steady state Navier-Stokes equation (10-8), is given in terms of the stream function by (A.10-25)

$$\sin\theta\left[\frac{\partial\psi}{\partial r}\frac{\partial}{\partial\theta}-\frac{\partial\psi}{\partial\theta}\frac{\partial}{\partial r}\right]\left(\frac{E^2\psi}{r^2\sin^2\theta}\right)=\nu E^4\psi\,, \tag{10-15}$$

where $E^4 \equiv E^2(E^2)$. The boundary condition that the velocity must vanish on the sphere surface leads from (10-12) to $\partial\psi/\partial r\,|_a = \partial\psi/\partial\theta\,|_a = 0$. If we choose to label the center streamline in the flow by $\psi = 0$, the surface boundary conditions are thus

$$\psi\,|_a = 0\,, \qquad \left.\frac{\partial\psi}{\partial r}\right|_a = 0\,. \tag{10-16}$$

Far from the sphere there is a uniform flow given by $-U_\infty\hat{e}_z$; hence, for $r \gg a$ we have

$$u_r = -U_\infty\cos\theta\,, \qquad u_\theta = U_\infty\sin\theta\,. \tag{10-17}$$

Since we want $\psi = 0$ for $\theta = 0$, an equivalent form for the boundary condition 'at infinity' is

$$\psi \longrightarrow \frac{U_\infty r^2\sin^2\theta}{2} \quad \text{as} \quad r\to\infty\,. \tag{10-18}$$

10.2.2.2 *The Drag Problem*

The components F_i of the hydrodynamic force on the sphere are given by

$$F_i = \int_S T_{ij}n_j\mathrm{d}S\,, \tag{10-19}$$

where the quantities T_{ij} denote the components of the stress tensor $\bar{\mathrm{T}}$ (see Appendix A-10.1), and n_j is the j^{th} component of the unit outward normal vector to the surface element $\mathrm{d}S$. By symmetry, there is only a z-component, F_z, which is generally referred to as the *drag* D.

For the calculation of D , it is appropriate to express $\bar{\mathrm{T}}$ in spherical coordinates. By the symmetry of the problem only T_{rr} and $T_{r\theta}$ are involved, as follows:

$$D = 2\pi a^2\int_0^\pi (T_{rr}\cos\theta - T_{r\theta}\sin\theta)_{r=a}\sin\theta\mathrm{d}\theta\,. \tag{10-20}$$

Unfortunately, the development of the components of $\bar{\mathrm{T}}$ in various coordinate systems is quite tedious, and so we will merely list the needed expressions for T_{rr} and $T_{r\theta}$:

$$T_{rr} = -p + 2\eta\frac{\partial u_r}{\partial r}\,, \quad \text{(10-21a)} \qquad T_{r\theta} = \eta\left(\frac{1}{r}\frac{\partial u_r}{\partial\theta}+\frac{\partial u_\theta}{\partial r}-\frac{u_\theta}{r}\right)\,. \quad \text{(10-21b)}$$

In these expressions, $\eta = \rho\nu$ is the dynamic viscosity. (For the interested reader, we mention what is probably the most elementary, though somewhat impractical, way

to obtain such results, which is to make direct use of the fact that the (r, θ) system is locally orthogonal. Consequently, we use the fundamental rule for transforming $\bar{\mathrm{T}}$ between two orthogonal systems S and S', i.e., $T'_{ij} = \gamma_{ik}\gamma_{jl}T_{kl}$, where γ_{ik} is the direction cosine between the i^{th} axis of S' and the k^{th} axis of S, and we have used the convention of summation over a double index. Thus, for example, $T_{rr} = \gamma_{ri}\gamma_{rj}T_{ij}$, which may be reduced directly to (10-21) on substituting the Cartesian form (A.10-10) for T_{ij}. A good source for more elegant and powerful methods is Aris (1962).)

On substituting (10-21) into (10-20), and simplifying through the use of the conditions $\nabla \cdot \vec{u} = 0$ and $\vec{u}\,|_a = 0$, we obtain

$$D = -2\pi a^2 \int_0^\pi \left[p\cos\theta + \eta\left(\frac{\partial u_\theta}{\partial r}\right)\sin\theta \right]_{r=a} \sin\theta \mathrm{d}\theta \tag{10-22}$$

$$= D_p + D_f\,, \tag{10-23}$$

where D_p, denoting the first term on the right side of (10-22), is called the *form* or *pressure* drag, and the second term, D_f, is called the *skin-friction* drag.

The dependence of D on U_∞, a, η, and ρ may be elucidated by writing the equations of motion in dimensionless form. Thus, on introducing $r' \equiv r/a$, $p' \equiv p/\rho U_\infty^2$, $\vec{u}' \equiv \vec{u}/U_\infty$, and $\nabla' \equiv a\nabla$ into (10-2) and (10-8), we obtain

$$\vec{u}' \cdot \nabla'\vec{u}' = -\nabla' p' + \frac{1}{R}\nabla'^2\vec{u}'\,, \quad \text{(10-24a)} \qquad \nabla' \cdot \vec{u}' = 0\,. \tag{10-24b}$$

The corresponding boundary conditions in dimensionless form are

$$\vec{u}'\,|_{r'=1} = 0\,, \quad \text{(10-25a)} \qquad \lim_{r'\to\infty} \vec{u}' = -\hat{e}_z\,. \tag{10-25b}$$

It is apparent that the solution to (10-24) and (10-25) must be functions only of $\vec{r}'$ and R. The same is therefore true of the dimensionless stress $T'_{ij} = T_{ij}/\rho U_\infty^2$, given by

$$T'_{ij} = -p'\delta_{ij} + \frac{1}{R}\left(\frac{\partial u'_i}{\partial x'_j} + \frac{\partial u'_j}{\partial x'_i}\right)\,. \tag{10-26}$$

In consequence, we see the drag must be of the form

$$D = a^2\rho U_\infty^2 \mathrm{f}(R)\,, \tag{10-27}$$

where $\mathrm{f}(R)$ is a function of the Reynolds number only.

This characteristic dependence of the drag on the Reynolds number is traditionally expressed in terms of the *drag coefficient* C_D, defined as

$$C_D \equiv \frac{D}{(\rho U_\infty^2/2)A_c}\,, \tag{10-28}$$

where A_c is the cross-sectional area exhibited by the body normal to the flow. Thus, C_D is a function of R only, and the drag problem for any ρ, U_∞, and A_c is solved once $C_D = C_D(R)$ is determined.

For a sphere ($A_c = \pi a^2$), we may combine (10-22) and (10-23) with (10-28) to obtain expressions for the form drag coefficient, $C_{D,p}$, and the skin friction drag coefficient, $C_{D,f}$. For this purpose, it is convenient to introduce another dimensionless pressure parameter, namely,

$$k \equiv (p - p_\infty)/(\rho U_\infty^2/2)\,, \tag{10-29}$$

and also the dimensionless vorticity magnitude

$$\zeta' \equiv \zeta a/U_\infty\,. \tag{10-30}$$

The constant p_∞ in (10-29) is the pressure far from the sphere. In terms of these quantities, we find $C_D = C_{D,p} + C_{D,f}$, where

$$C_{D,p} = \frac{D_p}{(\rho U_\infty^2/2)\pi a^2} = 2\int_0^\pi [k(\theta)]_{r'=1} \cos\theta \sin\theta \mathrm{d}\theta\,, \tag{10-31}$$

and

$$C_{D,f} = \frac{D_f}{(\rho U_\infty^2/2)\pi a^2} = \frac{8}{N_{\mathrm{Re}}}\int_0^\pi [\zeta'(\theta)]_{r'=1} \sin^2\theta \mathrm{d}\theta\,. \tag{10-32}$$

Equations (10-28), (10-31), and (10-32) demonstrate that the drag on a sphere can be found from a knowledge of the pressure and vorticity distributions on its surface. Furthermore, the surface pressure may be expressed in terms of the vorticity through the straightforward but lengthy process of integrating ∇p in (10-8) along the center streamline, recognizing that $\nabla^2 \vec{u} = -\nabla \times (\zeta \hat{e}_\phi)$. The result is

$$[k(\theta)]_{r'=1} = k_0 + \frac{4}{N_{\mathrm{Re}}}\int_0^\theta \left(\frac{\partial \zeta'}{\partial r'} + \zeta'\right)_{r'=1} \mathrm{d}\theta\,, \tag{10-33}$$

where

$$k_0 = 1 + \frac{8}{N_{\mathrm{Re}}}\int_{r'=1}^\infty \left(\frac{\partial \zeta'}{\partial \theta}\right)_{\substack{r'=1\\ \theta=0}} \frac{\mathrm{d}r'}{r'}\,. \tag{10-34}$$

In this manner, the drag coefficients can be determined solely from the surface vorticity distributions.

10.2.2.3 *Analytical Solutions*

1. *Stokes flow.* As we have said, Stokes flow is governed by (10-2) and (10-8) without the inertia term. In the stream function formulation, this term appears on the left side of (10-15) (note it is nonlinear in ψ), and so the governing form of the Stokes stream function ψ_S is

$$E^4 \psi_S = 0\,. \tag{10-35}$$

The boundary condition (10-18) motivates a trial solution of the form $\psi_S = f(r)\sin^2\theta$. This proves to be successful, and reduces (10-35) to an ordinary linear differential equation in r (for a detailed treatment of this and many other low Reynolds number problems, see Happel and Brenner, 1965). This can be integrated easily, and the constants of integration can be determined from (10-16) and (10-18). The result is

$$\psi_S = \frac{U_\infty a^2 \sin^2\theta}{4}\left(\frac{2r^2}{a^2} - \frac{3r}{a} + \frac{a}{r}\right), \tag{10-36}$$

which, upon substitution into (10-13), yields

$$\zeta_S = \frac{3U_\infty a \sin\theta}{2r^2} \tag{10-37}$$

for the vorticity. Similarly, the pressure may be recovered from (A.10-27):

$$p_S = p_\infty + \frac{3\eta a U_\infty \cos\theta}{2r^2}. \tag{10-38}$$

Therefore, from (10-31) and (10-32), the drag coefficients are

$$(C_{D,p})_S = \frac{8}{N_{\mathrm{Re}}}, \qquad (C_{D,f})_S = \frac{16}{N_{\mathrm{Re}}}, \qquad C_{D,S} = \frac{24}{N_{\mathrm{Re}}}. \tag{10-39}$$

Hence, from (10-28), the drag on a sphere in Stokes flow is (Stokes, 1851)

$$D_S = 6\pi a \eta U_\infty. \tag{10-40}$$

2. *Oseen Flow.* The Stokes approximation assumes $\vec{u}\cdot\nabla\vec{u}$ is negligible everywhere. One way to test this assumption is to form the ratio given in (10-11), using the Stokes velocity field for $\vec{u}$. The result is

$$\left(\frac{|\,\vec{u}\cdot\nabla\vec{u}\,|}{|\,\nu\nabla^2\vec{u}\,|}\right)_S \sim \frac{Rr}{a}. \tag{10-41}$$

This states that at sufficiently large distances ($r > a/R$) the assumption of negligible inertia breaks down, no matter how small R is. Therefore, the Stokes flow field is inaccurate at large distances. This ensures the failure of iteration attempts to improve upon Stokes flow past objects by using the Stokes solution to approximate previously neglected inertia terms in the equation of motion. (This predicament was puzzling to Whitehead (1889) and others who first tried such a procedure, and so became referred to as 'Whitehead's Paradox'.)

A way around this difficulty was proposed by Oseen (1910, 1927), who pointed out that a good approximation to $\vec{u}\cdot\nabla\vec{u}$ at large distances is $\vec{U}_\infty\cdot\nabla\vec{u}$, where $\vec{U}_\infty$ is the free stream velocity. He therefore suggested the following linear governing equations for the far field velocity distribution:

$$\vec{U}_\infty\cdot\nabla\vec{u} = -\frac{\nabla p}{\rho} + \nu\nabla^2\vec{u}, \quad \text{(10-42a)} \qquad \nabla\cdot\vec{u} = 0. \tag{10-42b}$$

Oseen solved (10-42) for flow past a sphere subject to the conditions $\vec{u}\,|_{\text{surface}} = 0$ and $\vec{u} \to \vec{U}_\infty$ as $r \to \infty$. He expressed his solution in terms of potential functions for p and $\vec{u}$ and obtained from it a new expression for the drag (D_0), including a term contributed by the fluid inertia:

$$D_0 = 6\pi a \eta U_\infty \left(1 + \frac{3}{16} N_{\text{Re}}\right) . \tag{10-43}$$

The corresponding drag coefficient is

$$C_{D,0} = \frac{24}{N_{\text{Re}}} \left(1 + \frac{3}{16} N_{\text{Re}}\right) = C_{D,S} + 4.5 . \tag{10-44}$$

It is not obvious whether these results constitute any real improvement over (10-39), and (10-40), since $\vec{U}_\infty \cdot \nabla \vec{u}$ misrepresents the convective acceleration close to the sphere. However, it has been proved that in fact the Oseen equations, (10-42a,b), do give the correct drag on bodies of arbitrary shape, to first order in N_{Re} (Brenner and Cox, 1962). The reason is that the first order contribution of fluid inertia to the drag depends on the inertia forces far from the body, where the Oseen equations provide a valid representation.

A more complete solution of the Oseen equations was obtained by Goldstein (1929) in terms of a series expansion. The drag coefficient obtained by him is

$$\begin{aligned} C_{D,G} \;=\; & \frac{24}{N_{\text{Re}}} \left(1 + \frac{3}{16} N_{\text{Re}} - \frac{9}{1280} N_{\text{Re}}^2 + \frac{71}{20\,480} N_{\text{Re}}^3 \right. \\ & \left. - \frac{30\,179}{34\,406\,400} N_{\text{Re}}^4 + \frac{122\,519}{550\,502\,400} N_{\text{Re}}^5 \cdots \right) . \end{aligned} \tag{10-45}$$

The last term is that corrected by Shanks (1955). Unfortunately, there are no theoretical reasons for regarding the extra terms supplied by Goldstein as providing an improved physical description. As we shall see in Section 10.2.2.5, however, comparison with experiment indicates (10-45) is slightly better than (10-44).

The stream function ψ_0 for Oseen flow past a sphere, valid to $O(N_{\text{Re}})$, is

$$\psi_0 \equiv \frac{U_\infty a^2 \sin^2\theta}{2} \left(\frac{r}{a} - 1\right)^2 \left[\left(1 + \frac{3}{16} N_{\text{Re}}\right)\left(1 + \frac{a}{2r}\right) + \frac{3}{16} N_{\text{Re}} \left(1 + \frac{a}{r}\right)^2 \cos\theta\right] . \tag{10-46}$$

It can be seen that $\psi_0 \to \psi_S$ as $N_{\text{Re}} \to 0$. A plot of streamlines, $\psi_0 =$ constant, from (10-46) reveals the presence of a wake for $N_{\text{Re}} \neq 0$. This is to be expected, since Oseen flow is characterized by both diffusive and convective transport of vorticity, as is evident from (10-42).

A simple argument shows that the wake has a paraboidal shape, i.e., its width ℓ varies as $z^{1/2}$, where z is the distance downstream of the sphere (the argument holds for any finite obstacle shape). Thus, an element of fluid containing vorticity generated at the sphere surface is convected downstream in the wake a distance $\sim U_\infty \delta t$ in time δt. If we imagine moving along with the element at the speed U_∞, its vorticity ζ will be seen to undergo a local transverse spreading by viscous diffusion; from our point of view, this will be characterized by the equation

$\partial\zeta/\partial t \sim \nu\nabla^2\zeta$. The boundary of this 'diffusive wave' must correspond approximately to the local boundary of the wake. Therefore, also in time δt the vorticity will change significantly over the distance ℓ, where $1/\delta t \sim \nu/\ell^2$. Hence, we find $\ell \sim (\nu z/U_\infty)^{1/2}$.

It is interesting to note also from (10-46) that $\psi_0 = 0$ on the sphere, along the center streamline where $\theta = 0, \pi$, and along the curve

$$\cos\theta = -\frac{16\left(1+\frac{3}{16}N_{\mathrm{Re}}\right)\left(1+\frac{a}{2r}\right)}{3N_{\mathrm{Re}}\left(1+\frac{a}{r}\right)^2}, \tag{10-47}$$

which may be interpreted as describing the boundary of a standing eddy. According to (10-47), the eddy first appears at the rear of the sphere ($\theta = \pi$, $r = a$) for $N_{\mathrm{Re}} = 3.2$, which correlates somewhat with observations giving $N_{\mathrm{Re}} \approx 20$. Even this limited success appears rather fortuitous, since one would expect (10-46) to be capable of meaningful predictions only for Reynolds numbers less than unity.

More recent research has confirmed the existence of Oseen flow eddies behind spheres. Thus, a numerical solution of the Oseen equations by Bourot (1969) for $N_{\mathrm{Re}} \leq 30$ has shown that a standing eddy develops at $N_{\mathrm{Re}} = 7.6$, and grows steadily with increasing N_{Re}. (This is in contrast to an earlier and less accurate numerical solution by Pearcey and McHugh (1955), who found no evidence of an eddy for $N_{\mathrm{Re}} \leq 10$.)

3. *Carrier's Modification.* Carrier (1953) proposed a simple semi-empirical modification of Oseen flow past obstacles. He argued that since the Stokes theory neglects inertia altogether, while the Oseen theory overestimates it, at least close to the body, perhaps a better representation might be found by some sort of compromise between the two approaches. Carrier suggested the inertial term in the Navier-Stokes equation be replaced by $c\vec{U}_\infty \cdot \nabla\vec{u}$, where c is a number between 0 and 1. Thus, the Stokes and Oseen approximations are given by $c = 0$ and $c = 1$, respectively. According to the idea that either of the classical approximations may be interpreted as replacing the factor $\vec{u}$ in $\vec{u}\cdot\nabla\vec{u}$ by a weighted average, Carrier conjectured a better weighting might be found. From an analytical study of flow past a flat plate, he proposed $c = 0.43$. (According to Murray (1967b), this value may be understood as a consequence of forcing the integral of the difference between the exact and approximate forms of the convective terms to vanish over the whole field of flow; i.e., for a plate in the plane $y = 0$, parallel to oncoming flow $U\hat{e}_x$, it happens that $\int_0^\infty (\partial u/\partial x) \times (u - 0.43U_\infty)\mathrm{d}y \approx 0$, where $0.43U\partial u/\partial x = \nu\partial^2 u/\partial^2 y$.) Carrier then found that this same value, if used to describe the drag on spheres and cylinders, produced fair agreement with experimental data for $N_{\mathrm{Re}} \leq 40$. This he took to imply that the theory describes general properties of the flow and is not strongly dependent on the geometry of the obstacles.

It is a simple matter to show that for a sphere the Carrier drag coefficient is related to Oseen's drag by

$$C_{D,C} = \frac{24}{N_{\mathrm{Re}}}\left(1+\frac{3c}{16}N_{\mathrm{Re}}\right). \tag{10-48}$$

4. *Matched Asymptotic Expansions.* As we have seen, the problem of obtaining an expansion of the flow at small N_{Re} is complicated by the existence of two flow

regimes: an inner regime where viscosity dominates; and an outer one where inertia forces are comparable to or larger than viscous forces. This difficulty has been surmounted, at least in principle, by the development of the method of matched asymptotic expansions (see, for example, Proudman and Pearson, 1957, and Van Dyke, 1964). The method employs two expansions in N_{Re}, one suitable for each regime. The no-slip boundary condition is used with the inner 'Stokes-type' expansion, and the uniform stream condition with the outer 'Oseen-type' expansion. Since the two expansions represent different forms of the same solution function, it is possible to complete the solution by matching the inner and outer expansions, term by term, in an intermediate region of common validity.

The first two terms of the inner expansion produce the following stream function in the vicinity of the sphere, valid to $O(N_{\mathrm{Re}})$ (Proudman and Pearson, 1957):

$$\psi_{\mathrm{PP},1} = \frac{U_\infty a^2}{4}\left(\frac{r}{a}-1\right)^2 \sin^2\theta \left[\left(1+\frac{3}{16}N_{\mathrm{Re}}\right)\left(2+\frac{a}{r}\right) + \frac{3}{16}N_{\mathrm{Re}}\left(2+\frac{a}{r}+\frac{a^2}{r^2}\right)\cos\theta\right]. \tag{10-49}$$

Like ψ_0, this stream function predicts a standing eddy for sufficiently large N_{Re}. In the present case, the boundary of the eddy is described by

$$\cos\theta = -\frac{16\left(1+\frac{3}{16}N_{\mathrm{Re}}\right)\left(2+\frac{a}{r}\right)}{3N_{\mathrm{Re}}\left(2+\frac{a}{r}+\frac{a^2}{r^2}\right)}, \tag{10-50}$$

so that an eddy is predicted to form when $N_{\mathrm{Re}} = 16$, in remarkably good agreement with the observed value of $N_{\mathrm{Re}} \approx 20$.

The next approximation to the stream function includes a term proportional to $N_{\mathrm{Re}}^2 \log N_{\mathrm{Re}}$:

$$\psi_{\mathrm{PP},2} = \frac{U_\infty a^2 \sin^2\theta}{4}\left(\frac{r}{a}-1\right)^2 \left[\left(1+\frac{3}{16}N_{\mathrm{Re}}+\frac{9}{160}N_{\mathrm{Re}}^2 \ln\frac{N_{\mathrm{Re}}}{2}\right)\left(2+\frac{a}{r}\right) + \frac{3}{16}N_{\mathrm{Re}}\left(2+\frac{a}{r}+\frac{a^2}{r^2}\right)\cos\theta\right] + O(N_{\mathrm{Re}}^2). \tag{10-51}$$

Unlike (10-49), this more accurate stream function (at least for $N_{\mathrm{Re}} \ll 1$) does not predict a standing eddy. It thus remains unclear why the prediction made by (10-49) should agree so well with experiment. It may simply be a fortuitous result, or the result of an effective cancellation of higher-order terms in N_{Re} for $N_{\mathrm{Re}} \gg 1$.

The stream function $\psi_{\mathrm{PP},1}$ reproduces the first-order Oseen drag, while from $\psi_{\mathrm{PP},2}$ Proudman and Pearson obtained the new result

$$C_{D,\mathrm{PP}} = \frac{24}{N_{\mathrm{Re}}}\left[1+\frac{3}{16}N_{\mathrm{Re}}+\frac{9}{160}N_{\mathrm{Re}}^2 \ln(N_{\mathrm{Re}}/2)\right]. \tag{10-52}$$

Finally, a further extension of the Proudman and Pearson analysis by Chester and Breach (1969) led to the inclusion of two more terms:

$$C_{D,\mathrm{CB}} = \frac{24}{N_{\mathrm{Re}}}\left[1+\frac{3}{16}N_{\mathrm{Re}}+\frac{9}{160}N_{\mathrm{Re}}^2 \ln(N_{\mathrm{Re}}/2)\right.$$

$$+\frac{9}{160}N_{\mathrm{Re}}^2\left(\gamma+\frac{5}{3}\ln 2-\frac{323}{360}\right)+\frac{27}{640}N_{\mathrm{Re}}^3\ln(N_{\mathrm{Re}}/2)\Bigg]\,, \quad (10\text{-}53)$$

where $\gamma = 0.57722\ldots$ is Euler's constant. The fourth term in (10-53) has been verified by Ockendon and Evans (1972), who used the method of matched asymptotic expansions in conjunction with Fourier transforms of the solution expansions.

5. *Potential Flow and Boundary Layer Theory.* There are no known analytical solutions capable of an accurate overall description of the flow past a sphere for intermediate or large Reynolds numbers, i.e., for $N_{\mathrm{Re}} \gtrsim 10$. However, as we have pointed out already in Section 10.2.1, for $N_{\mathrm{Re}} \gg 1$ the flow is such that viscous effects and vorticity are noticeable only within a thin boundary layer near the surface and in a downstream wake, and that elsewhere the flow is essentially potential. Fortunately, it turns out the flow in the boundary layer is amenable to analysis, and so it is possible to obtain an approximate, though somewhat incomplete, account of high Reynolds number flow by piecing together the properties of potential and boundary layer flow.

Let us first consider potential flow. This is described either in terms of a potential Φ, viz.,

$$\vec{u}_P = \nabla\Phi\,, \qquad \nabla^2\Phi = 0\,, \quad (10\text{-}54)$$

or in terms of a stream function ψ_P by

$$\vec{u}_P = \nabla\phi \times \nabla\psi_P\,, \qquad E^2\psi_P = 0\,, \quad (10\text{-}55)$$

from (A.10-18) and (A.10-22). To solve for potential flow past a sphere, we must also take into account its frictionless character and, hence, abandon the no-slip boundary condition (10-4), replacing it instead by the weaker condition that at the surface, (S) the flow must not penetrate the surface:

$$\vec{u}_P \cdot \hat{n}\,|_{\mathrm{S}} = 0\,. \quad (10\text{-}56)$$

As in the case of Stokes flow, the condition (10-18) of streaming flow at infinity suggests a trial solution of the form $\psi_P = f(r)\sin^2\theta$. Along with (10-55) and (10-56), this leads directly to the solution

$$\psi_P = \frac{U_\infty r^2}{2}\sin^2\theta\left(1-\frac{a^3}{r^3}\right) \quad (10\text{-}57)$$

and

$$\vec{u}_P = U_\infty\sin\theta\left(1+\frac{a^3}{2r^3}\right)\hat{e}_\theta - U_\infty\cos\theta\left(1-\frac{a^3}{r^3}\right)\hat{e}_r\,. \quad (10\text{-}58)$$

Since the convective acceleration term for potential flow can be expressed as $\vec{u}_P\cdot\nabla\vec{u}_P = \nabla(u_P^2/2) - \vec{u}_P\times(\nabla\times\vec{u}_P) = \nabla(u_P^2/2)$, the Navier-Stokes equation (10-8) reduces to $\nabla(p/\rho + u_P^2/2) = 0$, or

$$\frac{p}{\rho}+\frac{u_P^2}{2} = \text{constant}\,, \quad (10\text{-}59)$$

which is one version of *Bernoulli's law.* From (10-58) and (10-59), we find that the pressure distribution around a sphere in potential flow may be expressed, in terms of the dimensionless form of (10-29), as

$$k(\theta) = 1 - \frac{u_\theta^2(a,\theta)}{U_\infty^2} = 1 - \frac{9}{4}\sin^2\theta\,. \tag{10-60}$$

Now let us turn to an elementary discussion of the properties of boundary layer flow, of which the basic theory is due to Prandtl (1904). Consider a small region of the flow near the sphere surface where the boundary layer thickness δ_u is assumed to be well defined and much smaller than the sphere radius a. Let x denote distance along the drop surface in the direction of the local flow, and y denote distance normal to the surface. Then, using simple scaling arguments as in Section 10.2.1, we expect that in the region considered, $\vec{u}$ will experience changes of order U_∞ over a length a in the x direction, and over a length δ_u in the y direction. Hence, from the condition $\nabla \cdot \vec{u} = 0$, we immediately conclude that, in the boundary layer,

$$\frac{u_y}{u_x} \sim \frac{\delta_u}{a} \ll 1\,. \tag{10-61}$$

By the same logic, it is also obvious that $|\ \vec{u}\cdot\nabla\vec{u}\ | \sim U_\infty^2/a$ and $|\ \nu\nabla^2\vec{u}\ | \sim \nu U_\infty/\delta_u^2$ in the boundary layer. Moreover, since in this region the viscous and inertial forces are of comparable magnitude, we may set these two estimates equal to obtain $\delta_u^2 \sim a\nu/U_\infty$, or

$$\delta_u \sim \frac{a}{R^{1/2}}, \tag{10-62}$$

i.e., the boundary layer thickness decreases with increasing Reynolds number as $R^{-1/2}$. From (10-61) and (10-62), we also find

$$u_y \sim \frac{u_x}{R^{1/2}}\,. \tag{10-63}$$

Comparison of the x and y components of the equations of motion in the boundary layer shows that the respective terms involving $\vec{u}$ and, hence, generally the pressure terms as well, differ by a factor of order u_y/u_x, so that

$$\frac{\partial p}{\partial y}\left(\frac{\partial p}{\partial x}\right)^{-1} \sim \frac{u_y}{u_x} \sim \frac{1}{R^{1/2}} \ll 1\,. \tag{10-64}$$

Basically, this says that the pressure gradient normal to the boundary layer may be neglected because of its relativel small width, and that therefore the pressure in the layer is well approximated by the potential pressure profile just outside the layer. Then, from (10-59), we may also write $\partial p/\partial x \approx -\rho u_P \mathrm{d}u_P/\mathrm{d}x$, i.e., the pressure gradient in the layer may be approximated directly in terms of the potential velocity profile just outside the layer.

We are now in a position to write down the equations of motion for the assumed steady and laminar (i.e., non-turbulent) boundary layer flow. In view of our scale analysis, we see that we need be concerned only with the x-component of (10-8), and that in this equation only the $\partial^2 u_x/\partial x^2$ term in the Laplacian may be

neglected. Hence, if we assume for the moment that our x and y coordinates are strictly Cartesian, we obtain the following governing equations:

$$u_x \frac{\partial u_x}{\partial x} + u_y \frac{\partial u_x}{\partial y} - \nu \frac{\partial^2 u_x}{\partial y^2} = -\frac{1}{\rho}\frac{\partial p}{\partial x} = u_P \frac{\partial u_P}{\partial x}\,, \tag{10-65}$$

and

$$\frac{\partial u_x}{\partial x} + \frac{\partial u_y}{\partial y} = 0\,. \tag{10-66}$$

These equations are strictly valid only for rectilinear two-dimensional flow, but they turn out also to be very accurate for describing transverse flow past an infinite cylinder, so long as the boundary layer thickness is very small compared to the cylinder radius. However, it happens that the geometry of axisymmetric flow, of interest to us here, is a little more complicated: By taking into account the curvature of our choice of x-y coordinates for the sphere, we can show (e.g., Pai, 1956) that (10-65) is unaltered but that the continuity equation takes on the new form

$$\frac{\partial(\bar{\omega} u_x)}{\partial x} + \frac{\partial(\bar{\omega} u_y)}{\partial y} = 0\,, \tag{10-67}$$

where $\bar{\omega}$ is the distance from the flow symmetry axis to the sphere surface.

Let us now introduce the dimensionless variables $x' = x/a$, $y' = y/\delta_u$, $u'_x = u_x/U_\infty$, $u'_y = R^{1/2} u_y/U_\infty$, $\bar{\omega}' = \bar{\omega}/a$, and $u'_P = u_P/U_\infty$. Then, the boundary layer equations for a sphere acquire the form

$$u'_x \frac{\partial u'_x}{\partial x'} + u'_y \frac{\partial u'_x}{\partial y'} = \frac{\partial^2 u'_x}{(\partial y')^2} + u'_P \frac{\mathrm{d}u'_P}{\mathrm{d}x'} \tag{10-68}$$

and

$$\frac{\partial(\bar{\omega}' u'_x)}{\partial x'} + \frac{\partial(\bar{\omega}' u'_y)}{\partial y'} = 0\,. \tag{10-69}$$

Since neither these equations nor the boundary conditions which must be used with them ($u'_x = u'_y = 0$ at $x' = 0$; $u'_x = 1$ as $y' \to \infty$) involve the Reynolds number, we see that flows for different R are related by a simple similarity transformation; i.e., when R changes, the flow pattern changes only by having distances and velocities in the direction normal to the surface vary as $R^{1/2}$.

From our previous discussion of the standing eddies and wakes which exist behind spheres for even moderate Reynolds numbers, the question arises whether or not a well-defined boundary layer can exist over the entire sphere surface. In fact, it cannot; rather, at some location from the front of the sphere, the boundary layer detaches itself from the surface and flows into the main stream, carrying its load of vorticity with it. The occurrence of this phenomenon of *separation* can be understood qualitatively in terms of the potential pressure profile which is impressed on the boundary layer. From (10-60), we see that the potential pressure achieves a maximum at the front and rear of the sphere, and a minimum at the equator. Hence, over the back hemisphere there is a pressure force which acts to retard the flow. Of course, this adverse pressure gradient cannot reverse the free stream, but

it is sufficient to reverse the relatively weak flow in the boundary layer and, thus, cause separation.

When separation occurs, u'_y is evidently no longer small compared to u_x, as is assumed in the equations for the boundary layer. Nevertheless, one can use these equations to estimate the location of separation, which will be at the first angle θ (or ring) from the front of the sphere at which the flow parallel to the surface stops even for $y \neq 0$; i.e., separation occurs where $\partial u_x/\partial y = 0$, or where the shear stress falls to zero. According to (10-68) and (10-69), the separation position should also be independent of the Reynolds number, since there are no scale changes in the x-direction with changing R.

As might be expected, the flow and pressure profiles near the surface downstream of the ring of separation are relatively complicated, and the model of potential plus boundary layer flow breaks down. Even where their use is justified, the boundary layer equations, though vastly simpler than the original governing set, are still non-linear and, hence, quite formidable.

Nevertheless, some useful approximate analytical solutions for boundary layer flow past a sphere have been obtained. The better results take into account the fact that experimental observations show a marked difference between the actual pressure distribution at the surface and the theoretical potential distribution (Figure 10.1). Thus, an improvement in the description is possible by adopting the measured pressure profile as that which is impressed on the boundary layer. In one such study by Tomotika (1935), the pressure measurements of Flachsbart (1927) were used to obtain an approximate series solution for the velocity distribution in the boundary layer. Tomotika predicted the ring of separation should occur at $\theta = 81°$, which is in good agreement with Fage's (1934, 1937a,b) measured value of 83°. For the boundary layer thickness at the ring of separation, Tomotika obtained

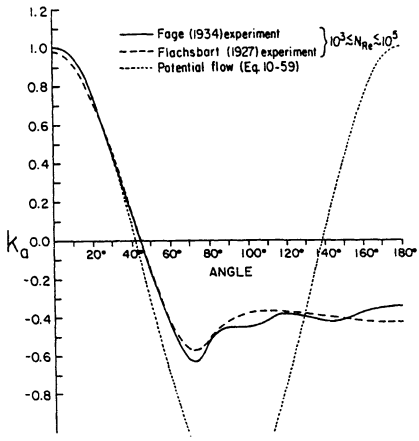


Fig. 10-1: Variation of the pressure at the surface of a rigid sphere with polar angle and Reynolds number for $N_{\mathrm{Re}} > 500$.

$$\delta_{u,\text{sep}} = \frac{6.8\nu}{u_{\text{sep}}} N_{\text{Re}}^{1/2}, \tag{10-70}$$

where u_{sep} denotes the tangential velocity just outside the boundary layer at the separation ring. Measurements show also that for $10^3 \lesssim N_{\text{Re}} \lesssim 10^5$, the surface pressure achieves a minimum near $\theta = 75°$ (see Figure 10.1); for this point Tomotika found

$$\delta_{u,75°} = \frac{3.8\nu}{u_{75°}} N_{\text{Re}}^{1/2}. \tag{10-71}$$

These last two expressions illustrate the fact that the boundary layer thickness increases with increasing θ. Qualitatively, this trend can be understood by the same kind of argument we used earlier to explain the parabolic shape of the downstream wake.

Several numerical solutions to (10-68) and (10-69) have also been obtained (e.g., Smith and Clutter, 1963; Wang, 1970; and Blottner and Ellis, 1973).

10.2.2.4 *Numerical Approach to the Navier-Stokes Equation*

The preceding discussions should serve to underscore the fact that the non-linear Navier-Stokes equation is tractable by analytical methods only for very special circumstances, and that often a great deal of effort is required for rather meagre results. Fortunately, however, the development of digital computers with increasingly large memories and fast execution times has provided an alternative approach of direct numerical solution, which has become progressively more attractive and fruitful.

The basic idea of the numerical approach is to represent the continuous flow field at only a finite number of points by means of a grid or lattice, and to approximate the solution of the governing differential equation by satisfying a finite difference version of it which relates function values at neighboring points. Since finite difference representations of second-order derivatives are simpler than those for fourth-order derivatives, it turns out to be advantageous, to write the fourth-order governing equation (10-15) as two coupled second-order equations. This is easily accomplished by using the vorticity as the second dependent variable. Thus, on substituting (10-13) into (10-15), and introducing for convenience the dimensionless variables $r' \equiv r/a$, $\psi' \equiv \psi/U_\infty a^2$, and $\zeta' \equiv \zeta a/U_\infty$, the two coupled equations suitable for numerical treatment may be expressed as

$$\sin\theta \left[\frac{\partial\psi'}{\partial r'}\frac{\partial}{\partial\theta} - \frac{\partial\psi'}{\partial\theta}\frac{\partial}{\partial r'}\right]\left(\frac{\zeta'}{r'\sin\theta}\right) = \frac{2}{N_{\text{Re}}} E'^2(\zeta' r' \sin\theta), \tag{10-72a}$$

and

$$\zeta' = \frac{E'^2\psi'}{r'\sin\theta}, \tag{10-72b}$$

where $E'^2 \equiv a^2E^2$. The boundary conditions to be used in conjunction with (10-72) include: (1) at the sphere surface ($r' = 1$), $\partial\psi'/\partial r' = \psi' = \partial\psi'/\partial\theta = 0$, $\zeta' = E'^2\psi'/\sin\theta$; (2) along the axis of symmetry ($\theta = 0, \pi$), $\psi' = \zeta' = 0$; (3) far from the sphere surface ($r' = r'_\infty$), $\psi' = (1/2)r'^2_\infty \sin^2\theta$, $\zeta' = 0$. To avoid wall

effects, Le Clair *et al.* (1970) showed from a numerical solution of the Navier-Stokes equation of motion for flow past a sphere of radius a, and Fidleris and Whitmore (1961) demonstrated experimentally, that r'_∞ must at least be $100 \times a$ for spheres with $N_{\mathrm{Re}} \gtrsim 1$ and as much as $1000 \times a$ for spheres with $N_{\mathrm{Re}} \approx 0.01$.

After the stream function and vorticity fields have been determined for a given Reynolds number, the surface pressure distribution can be found from (10-33) and (10-34) and, hence, the form and skin friction drag coefficients from (10-31) and (10-32). Numerical solutions following this formulation have been provided by Jenson (1959), Hamielec *et al.* (1967), Le Clair (1970), Le Clair *et al.* (1970), and Pruppacher *et al.* (1970).

10.2.2.5 *Comparison of Analytical and Numerical Solutions of the Navier-Stokes Equation with Experimental Results*

Let us now make a comparison between the characteristics of viscous, axisymmetric, steady state, incompressible flow past a sphere as determined by analytical and numerical solutions of the Navier-Stokes equation, and the flow characteristics determined experimentally. First consider the stream function and vorticity distribution determined numerically by Le Clair (1970), Le Clair *et al.* (1970), and Lin and Lee (1973, 1975). Le Clair found that the streamlines at $N_{\mathrm{Re}} = 0.01$ show fore-aft symmetry, while the vorticity contours clearly reveal that asymmetry in the flow exists even at this low Reynolds number, which is in pronounced disagreement with Stokes flow. At $N_{\mathrm{Re}} = 5$ (Figure 10.2a), the flow is already strongly asymmetric, as shown by both the streamlines and the vorticity contours. At $N_{\mathrm{Re}} = 20$ (Figure 10.2b) a standing eddy is present at the downstream end of the sphere and the flow asymmetry has increased further. At $N_{\mathrm{Re}} = 300$, the standing eddy extends over more than a sphere diameter downstream (Figure 10.2c).

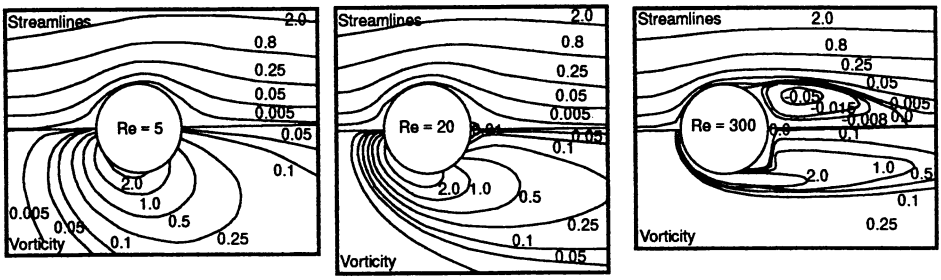


Fig. 10-2: Numerically computed stream function and vorticity distribution around a rigid sphere for steady state axisymmetric flow at $N_{\mathrm{Re}} = 5$ (a), $N_{\mathrm{Re}} = 20$ (b) and $N_{\mathrm{Re}} = 300$ (c). (From Lin and Lee, 1973, with changes.)

In Figure 10.3, comparison is made between the theoretically predicted and experimentally measured eddy lengths. It is seen that the length increases almost linearly with N_{Re} if $N_{\mathrm{Re}} > 50$. Extrapolation suggests that the eddy begins to develop at $N_{\mathrm{Re}} \approx 20$. Note that the experimental results are in good agreement

with the numerical predictions except at low Reynolds numbers where flow visualization, which suffers from the finite fall velocity of the tracer particles, slightly underestimates the eddy length. The simple analytical result (10-50) of Proudman and Pearson is again surprisingly successful, and only slightly overestimates the eddy length. The numerical solution of the Oseen equation by Bourot (1969), not shown in the figure, considerably overestimates the eddy length. Of course, the Stokes equations predict no eddy at all.

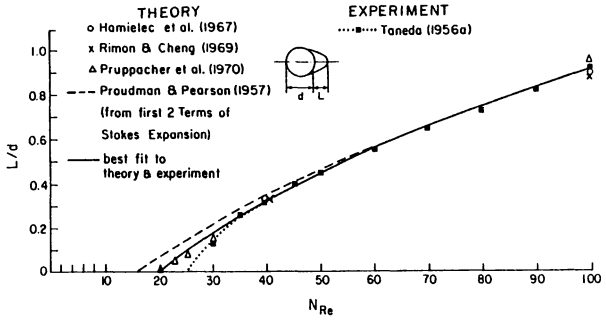


Fig. 10-3: Variation with Reynolds number of the length of the standing eddy at the downstream end of a rigid sphere. (From Pruppacher *et al.*, 1970; by permission of Cambridge University Press.)

The pressure distribution computed by Le Clair *et al.* for the sphere surface is exhibited in Figure 10.4. Note the large discrepancy between these results and the predictions of Stokes flow. Note, too, that on the front half of the sphere, the potential flow solution becomes acceptable for $N_{\mathrm{Re}} \gtrsim 400$. Comparison between the numerical results of Le Clair *et al.* (Figure 10.4) and the experimental measurements of Flachsbart (1927) and Fage (1937a,b) (Figure 10.1) shows that, for $500 \lesssim N_{\mathrm{Re}} \lesssim 10^5$, the normalized pressure distribution around a sphere remains essentially constant for $\theta \gtrsim 80°$.

Values for the drag force coefficients computed by Le Clair *et al.* are reproduced in Table 10.1. A best fit of C_D vs. N_{Re} for rigid spheres for $0.01 \leq N_{\mathrm{Re}} \leq 10^6$ is given by Clift *et al.* (p. 112, 1978). It is evident that there is a crossover in dominance from the skin friction to the pressure or form drag coefficient for Reynolds numbers between 100 and 300. The numerical solutions for C_D are in excellent agreement with experiment, as shown in Figure 10.5. On the other hand, the analytical solutions of Stokes (Equation (10-39)) and Oseen (Equation (10-44)) are seen to significantly underestimate and overestimate C_D, respectively, for $N_{\mathrm{Re}} \gtrsim 1$. Curve 3 of Figure 10.5 indicates that more complete solutions of the Oseen equation are somewhat more realistic than the solution to $O(R)$ found by Oseen; this was not anticipated theoretically.

Further comparisons are given in Figure 10.6, where the fractional deviation from the Stokes drag is plotted against the Reynolds number. The experimental data in this plot confirm the proof, mentioned earlier, that the Oseen drag is correct

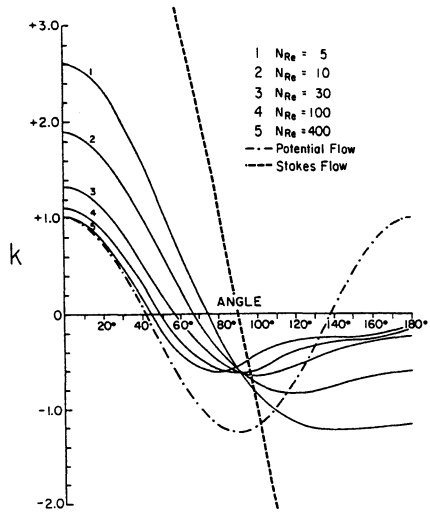


Fig. 10-4: Variation of the dimensionless pressure at the surface of a rigid sphere with polar angle and Reynolds number for $N_{\mathrm{Re}} < 500$. (Based on data of Le Clair *et al.*, 1970.)

TABLE 10.1

Comparison between the drag force coefficients for rigid spheres and for fluid, circulating spheres at various Reynolds numbers. (Based on data of Le Clair *et al.*, 1972.)

N_{Re}	$C_{d,f}$		$C_{D,p}$		C_D	
	rigid	liquid	rigid	liquid	rigid	liquid
10	2.77	2.71	1.52	1.51	4.29	4.23
30	1.30	1.29	0.81	0.81	2.11	2.10
57	0.88	0.88	0.63	0.63	1.51	1.51
100	0.59	0.59	0.51	0.49	1.10	1.08
300	0.28	0.29	0.35	0.34	0.63	0.63

to $O(R)$; i.e., the experimental curves approach zero for $N_{\mathrm{Re}} \to 0$ via the Oseen theory, rather than the Stokes theory.

It is interesting to note also that for small N_{Re} , the solution of Chester and Breach (1969) is inferior to that of Proudman and Pearson (1957), even though in principle the former is correct to a higher order in N_{Re} than the latter. Proudman 1969) attempted to remedy this problem of apparent poor convergence of successive solutions obtained through the method of matched asymptotic expansions. He suggested the poor convergence is due, at least in part, to the inappropriateness of the choice of the function D for expansion in terms of N_{Re}. Through semi-empirical arguments he recast the results of Chester and Breach in a new form involving a free parameter m. In Figure 10.6, his results are plotted as curve 6 for $m = 5$, the choice of which gives the best fit. The outcome is a fit to the experimental and numerical results which is roughly as good as that provided by Carrier (1953) (curve 5) (however, the Carrier theory has the advantage of being

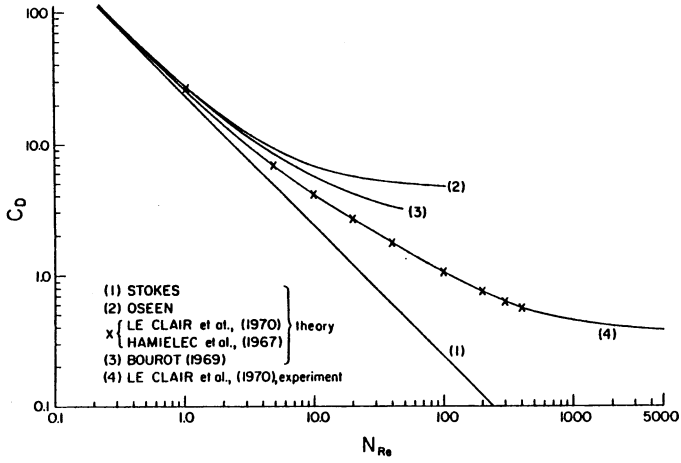


Fig. 10-5: Variation of the drag force coefficient as a function of Reynolds number for flow past a rigid sphere; comparison of various theories with experiment.

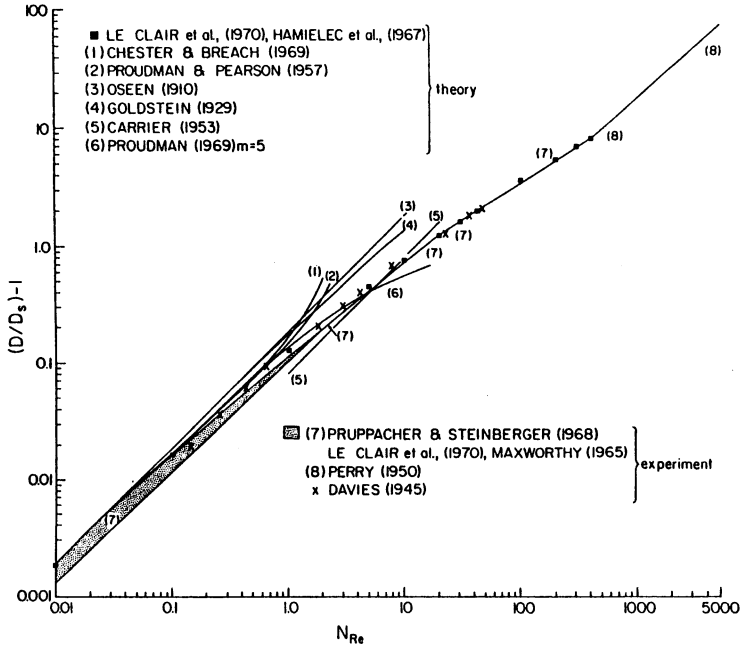


Fig. 10-6: Variation with Reynolds number of the dimensionless drag, (D/D_S), for rigid spheres. D_S is the Stokes drag. (From Le Clair *et al.*, 1970; by courtesy of Am. Meteor. Soc., and the authors.)

relatively simple). The other analytical results shown are not as good.

To summarize, we can say that the numerical solutions to (10-8) agree excellently with the experimental drag determinations for $0.01 \leq N_{\mathrm{Re}} \leq 400$. (An exception to this observation is provided by the results of Jenson (1959), whose flow fields suffer from step size and wall effect errors for $N_{\mathrm{Re}} < 20$.) The analytical solutions do not fare as well, and are generally limited in their applicability to low Reynolds numbers. Probably the best, and one of the simplest, of these for $N_{\mathrm{Re}} < 20$ is (10-48) with $c = 0.43$, due to Carrier. For the indicated range, this expression overestimates the drag on a sphere by a maximum of 13% (at $N_{\mathrm{Re}} = 20$). Finally, we should not lose sight of the fact that the simplest and most familiar analytical result, the Stokes drag given by (10-39) or (10-40), is quite adequate for many applications of interest in cloud physics. For example, it is accurate to within about 10% for $N_{\mathrm{Re}} \leq 2$, which, as we shall see below in Section 10.3.6, corresponds to drop radii $\lesssim 50\,\mu$m.

Close inspection of Figure 10.6 reveals another interesting feature, namely that there are three drag regimes. These are characterized by an almost constant slope over the Reynolds number intervals $0.01 \leq N_{\mathrm{Re}} \leq 20$, $20 \lesssim N_{\mathrm{Re}} \lesssim 400$, and $400 \lesssim N_{\mathrm{Re}} \lesssim 5000$. It is interesting to note that the change of drag regime at $N_{\mathrm{Re}} \approx 20$ coincides with the Reynolds number at which a standing eddy begins to form at the downstream end of the sphere, while the change of regime at $N_{\mathrm{Re}} \approx 400$ coincides with the Reynolds number at which vortex shedding begins (see below). This suggests that flow regimes make themselves felt as drag regimes, which is certainly a physically plausible relationship.

As we indicated earlier in our discussion of the classification of flows past spheres according to the Reynolds number, intrinsic unsteadiness sets in for $N_{\mathrm{Re}} \approx 130$. Close to this Reynolds number, the experiments of Möller (1938), Taneda (1956a), Goldburg and Florsheim (1966), Toulcova and Podzimek (1968), and Zikmunda (1970) have indicated the onset of faint, periodic, pulsative motions downstream of the standing eddy. These pulsations become increasingly pronounced as N_{Re} increases until finally, for some N_{Re} in the range $300 \leq N_{\mathrm{Re}} \leq 450$, the standing eddies begin periodically to shed lumps of rotating fluid. This behavior implies that numerical solutions for axially symmetric, steady state flow will have decreasing relevance for increasing N_{Re} beyond some maximum value. The comparisons given in Figure 10.6 imply that the observed instability which sets in near $N_{\mathrm{Re}} = 130$ causes a negligible departure from the strictly steady state drag. However, the observed change of the drag regime at $N_{\mathrm{Re}} \approx 400$ suggests this might be a resonable cut-off point for the steady state axisymmetric numerical approach.

The frequency f of vortex shedding from the downstream end of a sphere has been measured by Möller (1938) and Achenbach (1974). Their results are shown in Figure 10.7 as a plot of the *Strouhal number*, $N_{\mathrm{St}} \equiv 2fa/U_\infty$, versus N_{Re}. One finds, for example, that for water drops (considered to be rigid spheres) falling in air with $\nu_a = 0.15$ cm^2 sec^{-1}, the shedding frequencies are $f \approx 5.8 \times 10^2$ sec^{-1} for $N_{\mathrm{Re}} = 400$ ($a = 662\,\mu$m), $f \approx 1.1 \times 10^3$ sec^{-1} for $N_{\mathrm{Re}} = 1000$ ($a = 1.12$ mm), and $f \approx 1.9 \times 10^3$ sec^{-1} for $N_{\mathrm{Re}} = 2000$ ($a = 1.79$ mm).

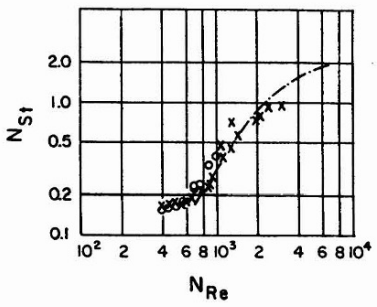


Fig. 10-7: Variation of the Strouhal number with Reynolds number for flow past a rigid sphere. (From Achenbach, 1974; by permission of Cambridge University Press.)

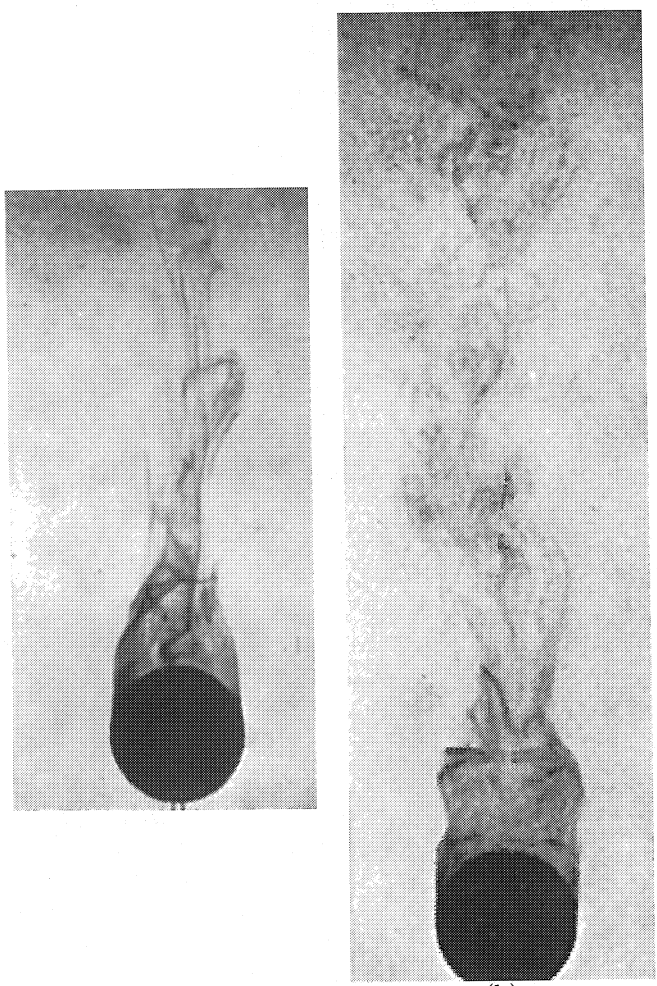
10.2.3 The Fall Behavior of Rigid Spheres

From our discussion in the previous section, we expect a freely falling rigid sphere to exhibit secondary motions in response to the unsteady flow past it for $N_{\mathrm{Re}} \gtrsim 130$ (Section 10.2.1). The experiments of Schmiedel (1928), Schiller (1932), Achenbach (1974), and Stringham *et al.* (1969) have verified the presence of such secondary motions. They observed faint deviations from a straight vertical fall mode at $N_{\mathrm{Re}} \approx 130$ and a pronounced helical fall mode for $N_{\mathrm{Re}} \gtrsim 300$. According to Achenbach (1974), this fall pattern results from a helical configuration of the sphere's wake in which the point of release of the vortices rotates around the sphere. Unfortunately, no data on the oscillation frequency and amplitude of smooth and rigid falling spheres have been recorded.

10.2.4 Non-Steady Three-Dimensional Flow

In Section 10.2.2 we assumed the flow past a sphere to be steady and axially symmetric, so that it can be described by the solutions to (10-15). Of course, the advantage of this treatment is that it reduces the number of dependent variables from two (the velocity components u_r, u_θ) to one (the stream function ψ). Unfortunately, no such simplification exists for the case of unsteady, incompressible, three-dimensional flow past a sphere with $N_{\mathrm{Re}} \gtrsim 300$ (Plate 11a,b). Although it is still possible to define a stream function (because of the incompressibility constraint), the function will no longer be a scalar as before but rather a vector consisting of three components. Thus, it would be necessary to solve for all three components of $\vec{\psi}$ in order to determine the corresponding three components of $\vec{u}$. There is no obvious advantage in following this route (Anderson *et al.* 1984). In fact, it turns out to be advantageous to consider the primitive Navier-Stokes equation of motion (10-7), and to solve it directly by numerical methods. Since the Navier-Stokes equations of motion cannot spontaneously generate asymmetric features in the flow field, the asymmetric flow has to be started by adding a strong shear flow to the steady state solution, which then, at the expected Reynolds numbers, produces a sustained shedding of vortices. Such an approach has been followed by Ji and Wang

(1990, 1991) and Ji (1991) who simulated the three-dimensional, non-steady flow past finite cylinders (see Section 10.4.2) and past planar snow crystals (see Section 10.5.1). Unfortunately, to date, no solutions using this method are available for the flow past spheres.



(a) (b)

Plate 11. Visualized turbulent flow in the rear of sphere exposed to an air stream. (a) $N_{Re} = 1340$ (b) $N_{Re} = 2020$. (From Möller, 1938, with changes.)

10.3 Hydrodynamic Behavior of Water Drops in Air

We must now consider the extent to which cloud and raindrops depart from the idealization of rigid spheres. Considerable information on this point is provided by the comparison shown in Figure 10.8 of the dimensionless drag on rigid spheres and

on water drops falling in air. It is seen that good agreement exists for Reynolds numbers corresponding to drop radii less than about 500 μm. At larger sizes, the drag on drops progressively increases above that for rigid spheres. In order to explain this behavior, we must consider three observed characteristics of falling drops: their internal circulation, their distortion from a spherical shape, and their oscillation.

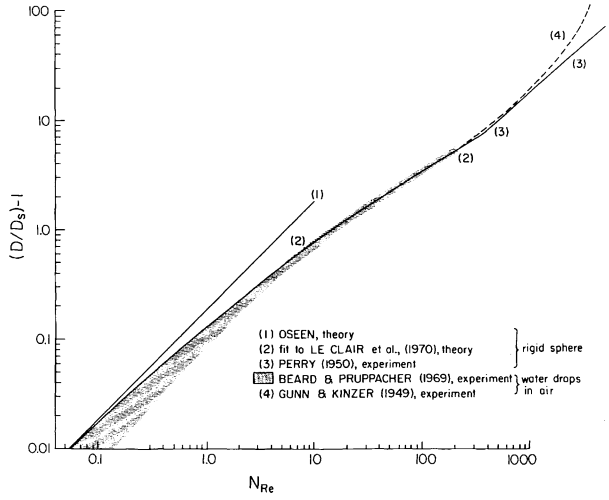


Fig. 10-8: Comparison between the Reynolds number dependence of the dimensionless drag, D/D_S, for rigid spheres and liquid circulating water drops.

10.3.1 Internal Circulation in Drops

The existence of an internal circulation inside drops falling through another immiscible liquid, or inside gas bubbles rising through a liquid, has been established by many experimenters (e.g., Spells, 1952; Savic, 1953; Garner *et al.*, 1954; Trinh and Wang (1982)). For water drops falling at terminal velocity in air, qualitative evidence for the presence of an internal circulation has been given by Blanchard (1949) and Garner and Lane (1959), and quantitatively by Pruppacher and Beard (1970) and Le Clair *et al.* (1972). Pruppacher and Beard, Le Clair *et al.*, and Diehl (1989) used a wind tunnel to determine the flow pattern and the average speed of the circulating water inside drops of 100 μm to 3 mm radius. Over the whole size range, the maximum internal velocity near the drop surface was found to be close to $u_{\mathrm{i}} \approx (1/25)U_\infty$, where U_∞ is the terminal velocity of the drop. A schematic representation of the observed flow pattern inside and outside a water sphere at $N_{\mathrm{Re}} = 140$ and $N_{\mathrm{Re}} < 1$ is given in Figure 10.9. For the case $N_{\mathrm{Re}} = 140$, the reverse circulation in the standing eddy at the downstream side of the drop is seen to cause a neighboring region of fluid within the drop to be stagnant, or to exhibit a weak reverse circulation.

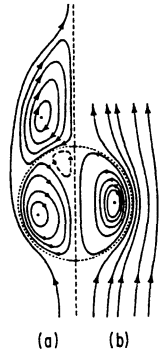


Fig. 10-9: Observed flow pattern inside and outside a water drop in air. Inside flow observed by Pruppacher and Beard (1970); outside flow observed by Taneda (1956a); for $N_{\mathrm{Re}} = 140$. (a) Observation, (b) Stokes flow. (From Pruppacher and Beard, 1970; by courtesy of *Quart. J. Roy. Meteor. Soc.*)

This observed behavior may be confirmed theoretically through a straightforward extension of our previous formulation of flow past a rigid sphere to the case of flow past and within a fluid sphere. Thus, if we use the vorticity-stream function approach, the exterior flow (ψ_0', ζ_0') will be governed by (10-72), as before, while the interior flow $(\psi_{\mathrm{i}}', \zeta_{\mathrm{i}}')$ will obey the same equation set, with the understanding that the relevant Reynolds number now depends on ν_{i}, the kinematic viscosity of the interior fluid. The boundary conditions which must supplement these equations are as follows: (1) the normal velocity components must vanish at the interface, so that $\psi_0' = \psi_{\mathrm{i}}' = 0$, $\zeta_0' = E^2\psi_0'/\sin\theta$, and $\zeta_{\mathrm{i}}' = E^2\psi_{\mathrm{i}}'/\sin\theta$ at $r' = 1$; (2) the tangential velocities must be equal at the interface, so that $\partial\psi_{\mathrm{i}}'/\partial r' = \partial\psi_0'/\partial r'$ at $r' = 1$; (3) the shear stress must be continuous at the interface, so that $(T_{r\theta})_0 = (T_{r\theta})_{\mathrm{i}}$ at $r' = 1$; (4) along the symmetry axis $(\theta = 0, \pi)$, $\psi_0' = \psi_{\mathrm{i}}' = \zeta_0' = \zeta_{\mathrm{i}}' = 0$; (5) far from the sphere surface $(r' = r_\infty')$, the flow streams freely, so that $\psi_0' = (1/2)r_\infty'^2 \sin\theta$ and $\zeta_0' = 0$.

After the stream function and vorticity fields have been determined, the pressure distribution at the surface of the fluid sphere can be found, as before, from (10-33) and (10-34), except that now the centrifugal term $-u_\theta^2$ must be added to the right side of (10-33). Finally, given the surface pressure and vorticity distributions, the drag force coefficients can be computed from (10-31) and, (10-32).

Numerical solutions to this problem have been obtained by Le Clair (1970) and Le Clair *et al.* (1972) for exterior flow Reynolds numbers $N_{\mathrm{Re}} \leq 400$ for water drops in air, with $\rho_{\mathrm{i}}/\rho_{\mathrm{o}} = \rho_{\mathrm{w}}/\rho_{\mathrm{a}} = 836$ and a viscosity ratio of $\eta_{\mathrm{i}}/\eta_{\mathrm{o}} = \eta_{\mathrm{w}}/\eta_{\mathrm{a}} = 55$ (assuming $\eta_{\mathrm{w}} = 1.00 \times 10^{-2}$ poise and $\eta_{\mathrm{a}} = 1.82 \times 10^{-4}$ poise at 20°C). In a later attempt, Oliver and Chung (1987) solved the Navier-Stokes equations for flow inside and outside of fluid spheres using a coupled finite element and series truncation method. Although this method appears to be very appealing, no comparison with the results of Le Clair *et al.* for water drops in air can be made since solutions were provided only for $\eta_{\mathrm{i}}/\eta_{\mathrm{o}} = 0.33$ and 3.0. The stream function distribution inside and

outside the circulating water sphere in air, as computed by Le Clair *et al.* (1972), is given in Figure 10.10. We see from the figures that, in its main features, the flow of air around a circulating water sphere strongly resembles the flow past a rigid sphere, a result which we might have expected from the fact that the viscosity of water is about 55 times larger than that of air. We further note that, as in the case of a rigid sphere, a standing eddy develops at the downstream end of the sphere at $N_{\mathrm{Re}} \approx 20$. However, while the length of this standing eddy differs little from that for a rigid sphere, its angular extent is significantly less. In particular, close to the fluid surface the eddy stream line $\psi = 0$ is shifted towards the rear stagnation point due to the effect of internal circulation. The general similarity between the gross hydrodynamic behavior of a liquid circulating sphere and that of a rigid sphere is further documented by the very small difference in values for the drag force coefficient. Comparison of the values listed in Table 10.1 shows that for $10 \leq N_{\mathrm{Re}} \leq 300$, C_D(fluid) differs from C_D(rigid) by less than $\sim 1\%$.

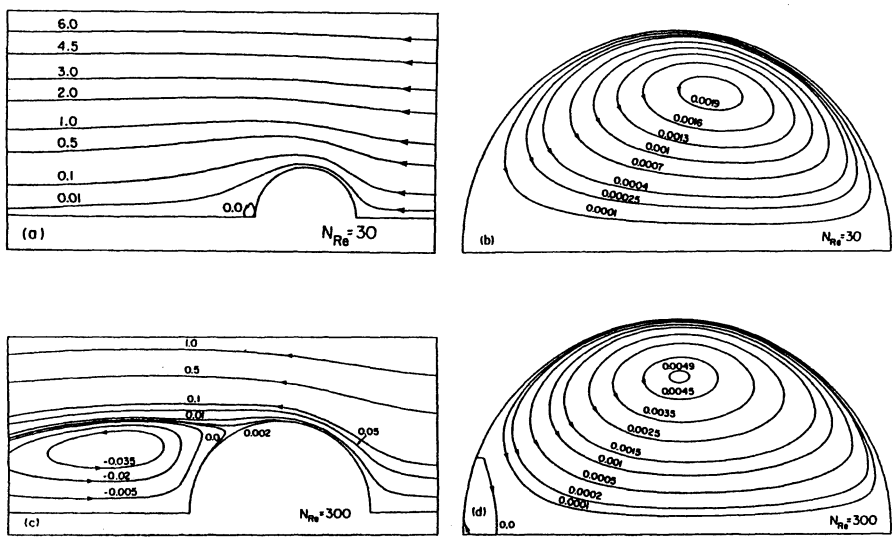


Fig. 10-10: Numerically computed distribution of stream function inside (b,d) and outside (a,c) a circulating spherical water drop in air, at $N_{\mathrm{Re}} = 30$ (a,b) and at $N_{\mathrm{Re}} = 300$ (a,c). (From Le Clair *et al.*, 1972; by courtesy of the Am. Meteor. Soc., and the authors.)

Le Clair's numerical solution for the flow within the liquid sphere is in good qualitative agreement with the flow patterns observed in wind tunnel experiments. The computations show that a water sphere falling in air has a vigorous internal circulation with a stagnation ring slightly upstream of the equator. Also, a reverse circulation toward the rear of the sphere develops for $100 < N_{\mathrm{Re}} < 300$, in agreement with observations. Le Clair *et al.* (1972) computed tangential velocities at the drop surface as a function of the polar angle θ for a variety of Reynolds numbers up to $N_{\mathrm{Re}} = 300$. Extrapolating to $N_{\mathrm{Re}} > 300$, Le Clair *et al.* showed that, at each angle θ, $u'_{i\theta}$ approaches a constant value. In other words, the dimensional

circulating velocity becomes proportional to the drop terminal velocity, with a proportionality that depends on θ. Using the tabulated values of Le Clair *et al.* and extrapolating them to larger Reynolds numbers, Diehl (1989) estimated the time needed by a fluid element at the drop surface to pass from the forward stagnation point of the drop to the point of flow separation by adding the average times required for the fluid element to move over angular distances of 5° under the effect of the local velocity. In this process actual drop terminal velocities were used, so that the effects of drop deformations on fall speed were included. This procedure allowed direct comparison of the computed velocities (Figure 10.11, curve 1) with those experimentally observed. We notice excellent agreement between theory and experiment for drop radii up to 500 μm, which is the size range where drop deformation is negligibly small and the drops do not oscillate. For drops which are deformed and oscillate the theory, which is based on a spherical geometry, provides an upper bound to the observations, which strongly scatter due to the oscillations. Diehl (1989) also noticed that in contrast to the doughnut shaped flow pattern for drops at radius smaller than 500 μm, the flow regime inside drops of radius larger than 500 μm alternates rapidly between a 4-looped flow pattern and completely turbulent flow.

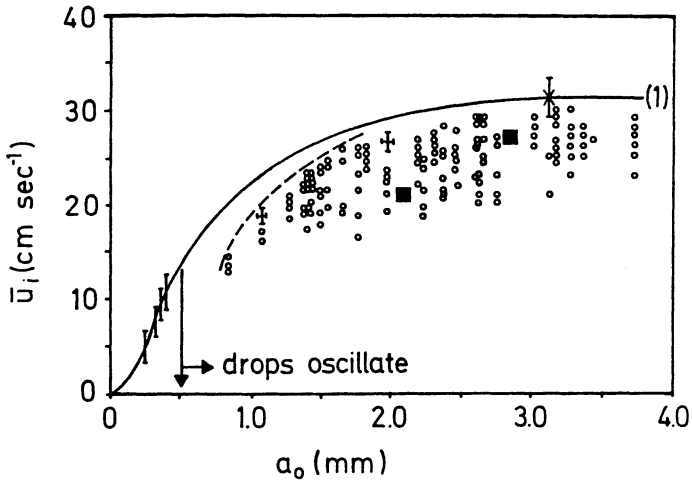


Fig. 10-11: Variation with drop radius of experimentally observed velocity of circulation inside water drops falling at terminal velocity in air. (I) Wind tunnel studies of Pruppacher & Beard (1970), and of Le Clair *et al.* (1972) from rotation frequency of tracer particles; (○, +) wind tunnel studies of Diehl (1989) from incomplete trajectories of tracer particles; (×) from wind tunnel studies of Schmidt (1995) from trajectories of tracer particles; (■) from wind tunnel studies of Garner and Lane (1959); line (1) based on numerical results of Le Clair *et al.*, 1972. (From Diehl, 1989, with changes.)

Analytical models for drop internal circulations exist for very small and very large Reynolds numbers. For the case $N_{\mathrm{Re}} \ll 1$, a simple analytical solution is available through the assumption of Stokes flow. The same form of trial solution as was invoked in Section 10.2.2.3 for the case of Stokes flow past a rigid sphere is

successful also for both the interior and exterior flows for a fluid sphere, and the following solutions may be obtained without difficulty:

$$\psi_0 = \frac{U_\infty \sin^2\theta}{4}\left[-3ar\left(\frac{1+\frac{2}{3}\gamma}{1+\gamma}\right) + 2r^2 + \frac{a^3}{r}\left(\frac{1}{1+\gamma}\right)\right] \tag{10-73}$$

and

$$\psi_i = \frac{U_\infty \sin^2\theta}{4}\left(\frac{\gamma}{1+\gamma}\right) r^2\left(\frac{r^2}{a^2} - 1\right), \tag{10-74}$$

where $\gamma = \eta_o/\eta_i$ is the ratio of the outside and inside dynamic viscosities (Hadamard, 1911; Rybczinski, 1911). From (10-74), one finds a stagnation ring (where $u_i = 0$) at $\theta = \pm\pi/2$ and $r = a/2^{1/2}$. The pattern of streamlines is shown in Figure 10.10b.

The Stokes tangential surface velocity for a falling water drop is

$$u_{i\theta}(a,\theta) = \frac{U_\infty \sin\theta}{2}\left(\frac{\gamma}{1+\gamma}\right) \approx \frac{\eta_a U_\infty \sin\theta}{2\eta_w} \approx 0.009 U_\infty \sin\theta, \tag{10-75}$$

using the previously quoted values for η_o and η_i. This expression predicts that the internal circulation of a small falling drop is only a small fraction of its terminal velocity, and is largest at $\theta = 90°$.

Applying to the Stokes surface velocities the same averaging procedure as was used to estimate surface velocities according to Le Clair *et al.* (given in Figure 10.12 as curve 1 with the open squares), Diehl (1989) obtained curve (2) marked with X's in Figure 10.12. We notice that in comparison to the experimental values in Figure 10.11, the Stokes surface velocities seriously underestimate the internal circulation in water drops falling in air.

The drag according to the Hadamard-Rybczinski (HR) theory is

$$D_{HR} = 6\pi a \eta U_\infty \left(\frac{1+\frac{2}{3}\gamma}{1-\gamma}\right). \tag{10-76}$$

For a falling drop in air at 20°C, $(1+\frac{2}{3}\gamma)/(1+\gamma) = 0.994$; thus, $D_{HR} \approx D_S$ and the drop behaves like a rigid sphere as far as the drag is concerned. For a gas bubble in a liquid, $D_{HR} \approx 2D_S/3$. Note there is no dependence of D_{HR} on surface tension. This is reasonable since surface tension only serves to alter the internal pressure by a constant amount and, thus, should have no dynamic effect. These results for the drag may become invalid if certain surface active impurities are adsorbed onto the drop interface (Levich, 1962).

It is interesting to note from (10-72b) that the vorticity corresponding to (10-74) has the form $\zeta_i = Ar\sin\theta$, where A is constant. Therefore, from (10-72a), it can be seen that this same vorticity would enable the equation of motion to be satisfied also for the case of negligible viscosity ($N_{Re} \to \infty$). In fact, the stream function (10-74) is an exact solution of the Navier-Stokes equation, and provides a description of a flow pattern which is possible for both the Stokes and inviscid limits. In the latter application, it is known as 'Hill's spherical vortex' (Hill, 1894).

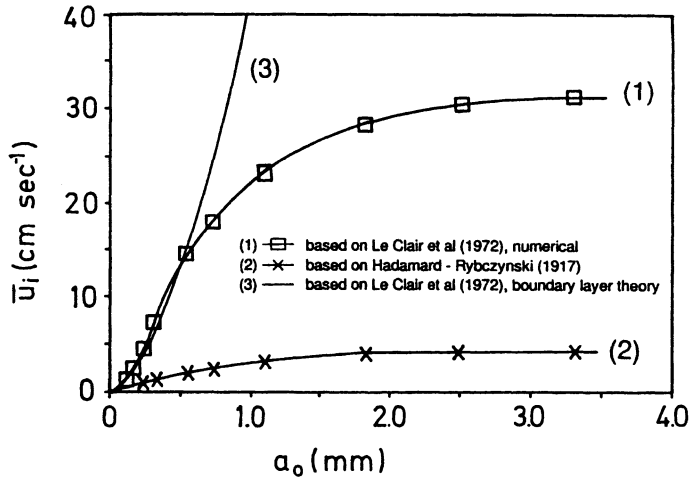


Fig. 10-12: Theoretically predicted variation of the circulation speed with drop radius in drops falling at terminal velocity in air. Comparison of three theoretical models. (From Diehl, 1989, with changes.)

In terms of the constant A, the stream function for Hill's spherical vortex is $\psi_i = -[A(a^2 - r^2)r^2 \sin^2\theta]/10$. If this is to describe inviscid flow, it is natural to fix A by assuming potential flow past the vortex. Therefore, for the exterior flow, we let $\psi_o = \psi_P$ as given by (10-57). If we now impose the condition of velocity continuity at $r = a$ (in this application conditions on shear stress do not apply), we obtain

$$\psi_i = -\frac{3U_\infty}{4a^2}(a^2 - r^2)r^2 \sin^2\theta\,. \tag{10-77}$$

The corresponding interior tangential velocity is

$$u_{i\theta}(r,\theta) = \frac{3U_\infty}{2a^2}(2r^2 - a^2)\sin\theta\,. \tag{10-78}$$

At the surface, this is $u_{i\theta}(a,\theta) = (3/2)U_\infty$ which matches the outer potential flow.

It is tempting to regard (10-77) and (10-78) as a model for the internal circulation at high Reynolds numbers. However, the predicted surface velocities are too large; e.g., $u_{i\theta}(a, 75°) = 1.46U_\infty$, which lie far above the experimental values in Figure 10.11. Of course, the failure of the model is due to the complete omission of viscous effects. As for the case of flow past a rigid object, one expects that for $N_{Re} \gg 1$ there will be a viscous bondary larger near the drop surface which will play a dominant role in the adjustment of the internal circulation to the exterior flow.

McDonald (1954) and Le Clair *et al.* (1972) have used boundary layer theory to estimate the shear stress which drives the internal circulation in a falling spherical drop. The results of Le Clair *et al.* are shown as curve 3 in Figure 10.12. The curve includes the effects of averaging the circulating velocity over a polar arc of 25° to

80°, although, as shown below, this has only a minor effect on the outcome. It can be seen that their boundary layer method, which is a refinement of McDonald's, drastically overestimates the true strength of the internal circulation for large drops.

The failure of the standard boundary layer model is due to the fact that it is based on the theory of flow past a rigid sphere, so that the boundary layer thickness varies as $N_{\mathrm{Re}}^{-1/2}$. Consequently, the shear stress at the drop surface and, hence, the internal circulation within it, are predicted to increase steadily with increasing N_{Re}. For example, the Le Clair *et al.* boundary layer model predicts that

$$u_{\mathrm{i}\theta}(a, 75°) \propto U_\infty N_{\mathrm{Re}}^{1/2} \propto a^{1/2} U_\infty^{3/2} . \tag{10-79}$$

Therefore, even if U_∞ becomes independent of size for large drops due to shape changes, as discussed below in Section 10.3.6, $u_{\mathrm{i}\theta}(a, 75°)$ and, hence, $u_{\mathrm{i}\theta}$ will still increase with a as $a^{1/2}$. This is in sharp contrast to the experimental trend evident in Figure 10.11.

The overestimation of drop circulating velocities according to the conventional boundary layer model can be corrected by noting that the drop surface can relieve stress by moving; hence the usual assumption of a fixed surface should be dropped. The surface motion will, in turn, tend to limit the thinning of the boundary layer. The neglect of this mechanism for stress reduction can therefore explain the failure of the standard boundary layer model. From the observation, referred to earlier, that the strength of the internal circulation becomes proportional to U_∞ for $N_{\mathrm{Re}} \geq 400$, an alternative boundary layer model suggests itself in which the boundary layer thickness approaches an asymptotic limit at $N_{\mathrm{Re}} = 400$ (Klett, 1977). This results in a direct linear coupling of the interior and exterior flows for all larger N_{Re}, which is consistent with the numerical trends found by Le Clair *et al.*. The results of the theory of Tomotika (1935) for a rigid sphere can be used to estimate the limiting thickness. Thus, from (10-71), we find $\delta_{75°,\infty} \approx 0.33a$, assuming the value $u_{\mathrm{o},75°} = 1.16U_\infty$ from the numerical solution of Le Clair *et al.*, and letting $N_{\mathrm{Re}} = 400$. Assuming further that the internal circulation has approximately the pattern of Hill's spherical vortex, the internal tangential velocity has the form

$$u_{\mathrm{i}\theta} = BU_\infty(2r^2/a^2 - 1)\sin\theta . \tag{10-80}$$

The constant B may be determined through the condition of continuity of shear stress at the interface. Thus, from (10-21b), the shear stress on the interior side of the interface is

$$(T_{r\theta})_{\mathrm{i}} = \eta_{\mathrm{i}} \left[r \frac{\partial(v_{\mathrm{i}}/r)}{\partial r} \right]_{a,\theta} = \frac{3BU_\infty \eta_{\mathrm{i}}}{a} \sin\theta . \tag{10-81}$$

If this is equated, at $\theta = 75°$, to the exterior shear stress, which on insertion of Tomotika's boundary layer profile corrected for the drop surface motion is

$$(T_{r\theta})_{\mathrm{o}} = \frac{2\eta_{\mathrm{o}}(u_{75°} - BU_\infty \sin 75°)}{\delta_{75°,\infty}} , \tag{10-82}$$

the constant B is found to be $B = 0.044$. Support for this model comes from the fact that the resulting predicted surface velocities for $0 \leq \theta \leq \theta_{\mathrm{sep}}$ agree closely with the computed values tabulated by Le Clair *et al.* for $N_{\mathrm{Re}} = 300$.

The fact that the internal tangential velocity varies essentially as $\sin\theta$ simplifies the comparison of theory with observed average circulating velocities. The observations concern the angular arc $\Delta\theta$ traversed over a given time interval Δt:

$$\Delta t = \int_{\theta_1}^{\theta_2} \frac{a}{u_{\mathrm{i}}(\theta)} \mathrm{d}\theta \,. \tag{10-83}$$

Therefore, the average circulating velocity is

$$\bar{u}_{\mathrm{i}} = \frac{a\Delta\theta}{a\int_{\theta_1}^{\theta_2} \frac{\mathrm{d}\theta}{u_{\mathrm{i}}(\theta)}} = BU_\infty \frac{(\theta_2 - \theta_1)}{\ln\left(\frac{\tan(\theta_2/2)}{\tan(\theta_1/2)}\right)} \,, \tag{10-84}$$

using (10-80). For example, substituting $\theta_1 = 25°$ and $\theta_2 = 125°$ to conform to the observations of Diehl (1989), (10-84) gives $\bar{u}_{\mathrm{i}} = 0.81BU_\infty$. Since $\sin 75° \approx 0.97$, we find $\bar{u}_{\mathrm{i}} \approx 0.84u_{\mathrm{i}\theta}(a, 75°)$. So the effect of averaging over the angular interval amounts only to about a 16% reduction from the values obtained by simply evaulating the circulating velocity at $\theta = 75°$, as was done earlier by Le Clair *et al.* in their comparisons of theoretical and observed circulating velocities. Finally, we note that $\bar{u}_{\mathrm{i}} \approx 0.037U_\infty$ according to the asymptotic boundary layer model. If one uses actual deformed drop terminal velocities for U_∞, then for $N_{\mathrm{Re}} \geq 400$ the results of this model lie essentially on curve 1 in Figure 10.12.

10.3.2 Drop Shape

Our discussion in the previous section suggests that internal circulation, although a marked characteristic of a water drop falling in air, contributes only neglibily to the drag on the drop. In the present section, we shall show that the observed drag increase exhibited by drops of $N_{\mathrm{Re}} \geq 300$ is primarily the result of a progressive change of their shape. Drops which have a steady flow field past them assume an equilibrium shape. Non-steady state flow fields induce drop oscillations which, in turn, cause periodic shape changes. We shall begin our discussion of drop shape by assuming that drops of all sizes relevant for atmospheric clouds have a steady flow field past them for which we compute their equilibrium shape. Subsequently we shall compare these equilibrium shapes with the observed shapes of falling drops and determine the effect of oscillation.

The equilibrium shape of a falling drop can be determined in principle from the condition that local interface forces must be in balance. Early accounts of this force balance were somewhat incomplete. For example, Lenard (1887, 1904) assumed the drop shape was controlled by an equilibrium between surface tension and the centrifugal force resulting from internal circulation. Somewhat later, Spilhaus (1948) attributed the flattening of large drops to the combined action of surface tension and aerodynamic pressure and, thus, ignored the effects of internal circulation and the hydrostatic pressure gradient within the drop.

To date, most purely analytical treatments of the drop shape problem have required a considerable sacrifice of physical realism, or a restricted scope in applications, for the sake of mathematical tractability. Thus, Imai (1950) assumed an

unrealistic unseparated potential flow past the drop, while the analysis of Taylor and Acrivos (1964) is restricted to very low Reynolds numbers and very small drop deformations. On the other hand, the analytical model of Green (1975), which ignores flow effects altogether, appears to yield results of surprising accuracy with respect to the observed maximum and minimum dimensions of a deformed drop, as we shall see below. However, Green's model is not capable of describing the complete drop shape.

We will now briefly outline the semi-empirical approach to the drop shape problem employed by Pruppacher and Pitter (1971), who based their work on the perturbation model proposed by Savic (1953). Their model, recently extended by Beard *et al.* (1989a), agrees well with observation for drops of equivalent diameters D_0 less than 5 mm.

First of all, we must obtain a generalization of the mechanical equilibrium condition (5-7) for a non-spherical drop shape. Consider a point on the surface where the principal radii of curvature are R_1 and R_2. Let the local area element $\mathrm{dS} = \mathrm{d}l_1 \mathrm{d}l_2$ undergo an outward displacement (away from the drop center) by a small distance $\delta\xi$, where $\mathrm{d}l_1$ and $\mathrm{d}l_2$ are the surface arc length elements associated with R_1 and R_2. Then, if the interior and exterior pressures are p_i and p_e, the pressure work done on dS by the displacement is $(p_\mathrm{e} - p_\mathrm{i})\delta\xi\mathrm{dS}$, neglecting the change $\delta(\mathrm{dS})$ in dS which the displacement brings about. On the other hand, this area change results in a change of surface energy in the amount $\sigma\delta(\mathrm{dS})$. Therefore, for a situation of static equilibrium in which the net energy change should be zero for an arbitrary small displacement, we find

$$(p_\mathrm{e} - p_\mathrm{i})\delta\xi\mathrm{dS} + \sigma\delta(\mathrm{dS}) = 0\,. \tag{10-85}$$

Now the first-order change in the area element is $\delta(\mathrm{dS}) = \delta(\mathrm{d}l_1)\mathrm{d}l_2 + \mathrm{d}l_1\delta(\mathrm{d}l_2)$, and the corresponding change in the arc length elements is $\delta(\mathrm{d}l_i) = \mathrm{d}l_i(\delta\xi/R_i)$, $i = 1, 2$. Consequently, (10-85) implies

$$(p_\mathrm{e} - p_\mathrm{i}) = \sigma\left(\frac{1}{R_1} + \frac{1}{R_2}\right), \tag{10-86}$$

which is the desired result (Laplace, 1806). Note that (10-86) reduces to (5-7) for a spherical surface with $R_1 = R_2 = a$.

The further generalization of (10-86) to the case of non-zero exterior and interior flows is achieved simply through the replacement of the static pressures by the full stress tensor components. Thus, the dynamic boundary condition of stress continuity at the drop interface, including the effect of surface tension stresses, becomes

$$(T_{ij}n_j)_\mathrm{exterior} - (T_{ij}n_j)_\mathrm{interior} = \sigma\left(\frac{1}{R_1} + \frac{1}{R_2}\right)n_i\,, \tag{10-87}$$

(cf. (10-19)).

In their drop shape study, Pruppacher and Pitter used (10-87) to describe the normal stresses acting on the surface, and ignored the viscous stress contribution. In terms of the notation in Figure 10.13, their final force balance equation reads as follows:

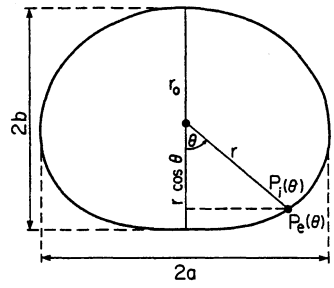


Fig. 10-13: Schematic of a deformed water drop.

$$\sigma\left(\frac{1}{R_1}+\frac{1}{R_2}\right)=g\rho_w(r_0+r\cos\theta)-[p_e(\theta)-p_\infty-p_{ic}(\theta)]+[p_i(\pi)-p_\infty]\,. \quad (10\text{-}88)$$

The first term on the right side represents the stress contribution due to hydrostatic pressure within the drop (ρ_w is the density of water, and the buoyancy of the air has been neglected). The second term, in which $p_{ic}(\theta)$ denotes the pressure due to internal circulation, Pruppacher and Pitter approximated by $(p_e(\theta)-p_\infty)_{\text{rigid sphere}}$, and then used the pressure measurements of Fage (1937a,b) and Le Clair *et al.* (1972) for this quantity.

The equation of the deformed drop surface of revolution may be expressed as follows:

$$r=a_0\left(1+\sum_{n=0}^{\infty}c_n\cos n\theta\right)\,, \quad (10\text{-}89)$$

where the c_n are coefficients representing the deformation. If the deformation is small, i.e., $r=a_0+\xi$ with $\xi\ll a_0$, we may express the curvature terms in (10-88) in terms of the c_n by means of (A.10-33), and obtain

$$\sigma\left[\frac{1}{R_1}+\frac{1}{R_2}\right]=\frac{\sigma}{a_0}\left[2+\sum_{n=0}^{\infty}(n^2-2)c_n\cos n\theta+\sum_{n=0}^{\infty}nc_n\sum_{m=1}^{m=n}\cos(n-2m)\theta\right]\,. \quad (10\text{-}90)$$

Finally, in order to exploit the orthogonality properties of the expansions (10-89) and (10-90), the (known) pressure field is also expressed as a cosine series, viz.,

$$[p_e(\theta)-p_\infty]_{\text{rigid sphere}}=\frac{\rho_a U_\infty}{2}\sum_{n=0}^{\infty}q_n\cos n\theta\,, \quad (10\text{-}91)$$

where ρ_a is the density of air.

By substituting (10-89) to (10-91) into (10-88), the c_n may be determined in terms of the q_n and the physical parameters of the problem. To avoid excessive computation, Pruppacher and Pitter truncated the infinite series at $n=9$.

They also bypassed the need to evaluate the constant terms in (10-88) by invoking the constraint of constant drop volume, which determines c_0 in terms of the other c_n. That is, on substituting (10-89) into the integral for the drop volume, $(2\pi/3)\int_0^\pi r^3 \sin\theta \mathrm{d}\theta$, and assuming small deformations, the condition of volume conservation becomes $\int_0^\pi \sum_{n=0}^\infty c_n \cos n\theta \sin\theta \mathrm{d}\theta = 0$, which leads to

$$c_0 = \sum_{n=1}^{\infty} c_{2n}/(4n^2 - 1)\,. \tag{10-92}$$

Pruppacher and Pitter also chose $c_1 = 0$, stating that it does not contribute to the drop distortions, but rather only causes bodily vertical displacement. However, Beard *et al.* (1989a) showed that for a distorted drop the fixed center of mass constraint, $c_1 = 3\sum c_n/(n^2-4)$ for $n = 3, 5, 7, \ldots$, is needed to prevent translation. Some meridional outlines of the drop shapes computed by Beard *et al.* (1989a) are presented in Figure 10.14.

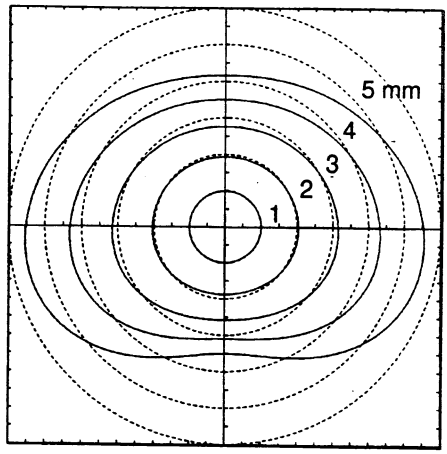


Fig. 10-14: Shape of water drops in air, computed by the perturbation method for equivalent drop diameters (D_0) of 1 to 5 mm; for 1 atm and 20°C. Shown for comparison are circles (dashed) with equivalent diameters 1 to 6 mm. (From Beard *et al.*, 1989a; by courtesy of the Am. Meteor. Soc., and the authors.)

Since the predictions of the perturbation model cannot be trusted for large drop deformations, Beard and Chuang (1987) carried out a drop shape analysis that omits the assumption of small departures from sphericity. Their model follows the approach of Bashford and Adams (1883), who used the static Laplace equation (10-86) to determine the equilibrium shape of sessile (base-supported) and pendant (hanging) drops due to the balance of hydrostatic and surface tension stresses. This can be accomplished by expressing the drop principal radii of curvature in terms of the differential relationships between the arc length along and at right angles to a distorted drop meridian, and some suitably chosen angle variable describing the local slope of the meridional curve. The result is a non-linear differential equation

for drop shape that can be integrated numerically to give the equilibrium form, for arbitrary deformation magnitudes.

Beard and Chuang (1987) extended this classical analysis to the dynamic case of (10-87) by including an aerodynamic supporting pressure. This was modeled by using Fage's (1937a,b) measurements of the pressure distribution around a sphere, just as was done in the perturbation models described above. However, in order to account approximately for the change in the pressure distribution due to departures from a spherical shape, Beard and Chuang assumed the required pressure adjustments were just those that would be appropriate for potential flow past corresponding oblate spheroids. Other, less critical, modeling assumptions included omitting any account of internal circulation, and scaling the magnitude of the pressure distribution to account for the fact that, since skin friction drag is ignored in the model, the form or pressure drag contribution must be boosted in order to compensate for this neglect (cf. (10-23)). For this purpose, they used an empirical formula relating form drag to total drag for a sphere in high Reynolds number flow, based on the measurements of Achenbach (1974, 1972).

The drop shapes computed by this method are shown in Figure 10.15. We notice that the meridional drop outlines do not exhibit a drop base as flattened as does the perturbation model, nor is the previously predicted concave depression present in the base of the largest drops. Beard and Chuang attribute such base depressions to a failure of the perturbation approach for large amplitude distortions. This plausible conjecture is supported further by the fact that Beard and Chuang clearly get better results for the axis ratio b/a as a function of drop size for $D_0 \geq 5$ mm than do Pruppacher and Pitter (1971), as shown in Figure 10.16. On the other hand, the perturbation method does agree with observations (Plate 12) in predicting drops with a flat base if $D_0 \geq 3.5$ mm ($N_{\mathrm{Re}} \geq 1965$), and a concave base depression if $D_0 \geq 4$ mm ($N_{\mathrm{Re}} \geq 2325$). In fact, this depression is thought to be responsible for the eventual hydrodynamic break-up of single drops in quiet air (Section 10.3.5). A resolution of these conflicting pieces of evidence may be brought about if we assume that the observed base depressions are in part a consequence of unsteady flow conditions, in contrast to the equilibrium conditions assumed in the theoretical models.

Unfortunately, it is not possible to derive the equilibrium shape of drops with equivalent diameters of several millimeters from wind tunnel data, since drops of such size oscillate vigorously. Therefore, observed shapes and axis ratios are either time-mean values, or the result of instantaneous snap shots of drops caught in a particular phase of their oscillatory motion. Generally, however, wind tunnel studies confirm that drops of $1\,\mathrm{mm} \leq D_0 \leq 3.5$ mm ($300 \leq N_{\mathrm{Re}} \leq 1965$) resemble oblate spheroids with curvature on the lower side less than that on the upper side. This curvature asymmetry decreases progressively with decreasing drop size so that drops of $280\,\mu\mathrm{m} \leq D_0 \leq 1$ mm ($20 \leq N_{\mathrm{Re}} \leq 300$) are almost perfect oblate spheroids. With further decrease in size, the drops become more and more spherical, and for $D_0 \leq 280\,\mu$m ($N_{\mathrm{Re}} \leq 20$) they may, for all practical purposes, be considered perfect spheres. An empirical fit (accurate to $\approx 1\%$) to the values for b/a computed by Beard and Chuang (1987) has been given by Andsager, Beard

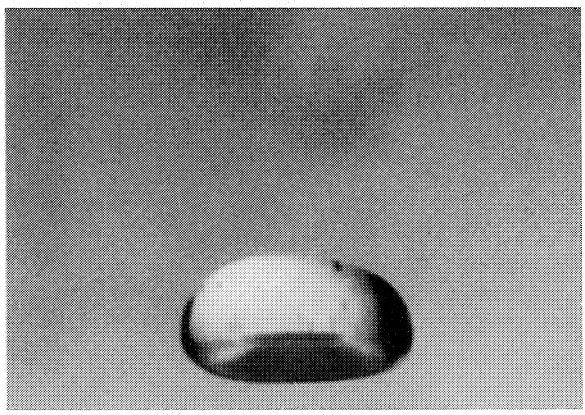


Plate 12. Oscillating water drops of $a_0 = 3.5$ mm, freely suspended in the vertical air stream of a wind tunnel; observation is taken from below the drop's equator.

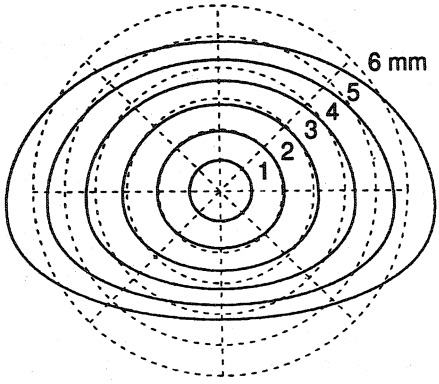


Fig. 10-15: Shape of water drops in air, computed by the method of Bashford and Adams, 1883, for equivalent drop diameters (D_0) of 1 to 6 mm, for 1 atm and 20°C. Shown for comparison are circles (dashed) of equivalent diameters 1 to 6 mm. (From Beard and Chuang, 1987; by courtesy of the Am. Meteor. Soc., and the authors.)

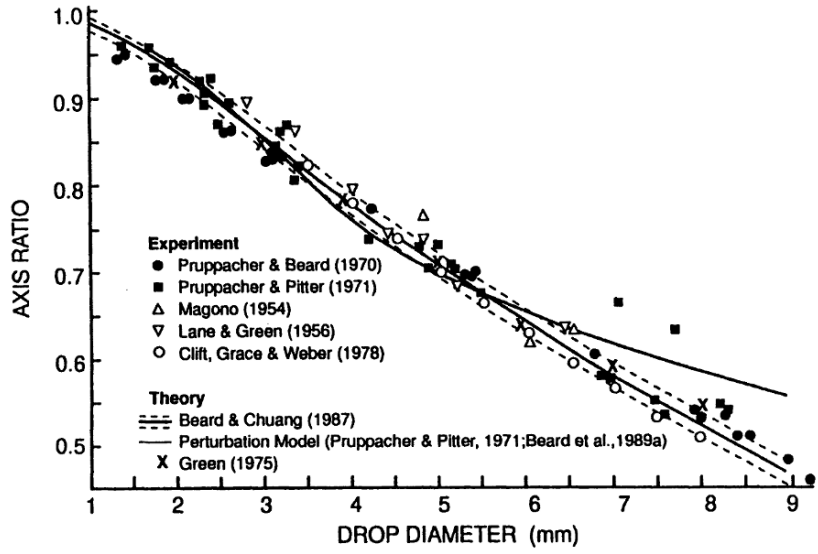


Fig. 10-16: Drop defomation, given by the axis ratio b/a , of water drops in air. Comparison of observations with theoretical results. (From Beard and Chuang, 1987, with changes.)

and Laird (1999) for $1 \leq D_0 \leq 9$ mm:

$$\frac{b}{a} = 1.01668 - 0.09806 D_0 - 2.52686 D_0^2 + 3.75061 D_0^3 - 1.68692 D_0^4 , \qquad (10\text{-}93)$$

with D_0 in cm.

Before leaving this section it is worthwhile to set forth the drop shape model of Green (1975) since, as noted previously, it has the appeal of both great simplicity and accuracy as regards the drop axis ratios. The model assumes the drop shape is oblate spheroidal for all deformations, and that hydrostatic and surface tension stresses alone are sufficient to determine the equilibrium shape. By applying (10-86) at the equator of the spheroid, Green's model yields

$$\sigma \left(\frac{1}{R_1} + \frac{1}{R_2} \right) = \sigma \left(\frac{a}{b^2} + \frac{1}{a} \right) = \frac{2\sigma}{a_0} + \rho_w g b , \qquad (10\text{-}94)$$

where a and b are the semi-major and semi-minor axes, respectively, and $a_0 = a^{2/3} b^{1/3}$ is the equivalent radius. Equation (10-94) may be solved for a_0 in terms of the axis ratio to obtain

$$a_0 = \left(\frac{\sigma}{g \rho_w} \right)^{1/2} \frac{[(b/a)^{-2} - 2(b/a)^{-1/3} + 1]^{1/2}}{(b/a)^{1/6}} . \qquad (10\text{-}95)$$

This result is plotted in Figure 10.16, where it can be seen to be about as accurate overall as the other, more elaborate theoretical models. For small drops, (10-95) tends to underestimate the equilibrium axis ratio slightly, while for very large drops of $D_0 \geq 5$ mm, it provides the best agreement with observations.

10.3.3 Drop Oscillation

It was noted, during early and subsequent experimental studies of falling drops, that oscillations set in once a critical size is exceeded (Lenard (1887, 1904), Flower (1928), Laws (1941), Best (1947), Blanchard (1948, 1950, 1955), Kumai and Itagaki (1954), Magono (1954a), Garner and Lane (1959), Cotton and Gokhale (1967)). Wind tunnel and fall chamber studies of single drops showed that such oscillation begins to be noticeable for drops of $a_0 \geq 500\,\mu$m ($N_{\mathrm{Re}} \geq 300$), in response to the unsteadiness of the flow past the drop. Although at this size the frequency of oscillation is quite high and the corresponding oscillation amplitudes almost unnoticeably small, the amplitudes grow rapidly with increasing drop size. Thus, it was noticed that the large raindrops which fall from vigorous cloud systems often exhibited large amplitude oscillations (Lenard, 1887, 1904; Schmidt, 1913; Jones, 1959). More recent field observations on the shape of oscillating raindrops were made by Jameson and Beard (1982), Jameson (1983), Beard (1984a), Chandrasekar *et al.* (1988), Sterlyadkin (1988), Beard *et al.* (1989b), Beard and Tokay (1991) and Tokay and Beard (1994). These field studies revealed that oscillating drops exhibit average axis ratios (the average over a large number of drops was taken as the time-mean axis ratio of a single drop) which are significantly larger than the equilibrium axis ratio. This effect was first noted by Jameson and Beard (1982), who analyzed the field observation of Jones (1959). Based on their finding, they pointed out that using equilibrium shapes would introduce significant errors in current models for computing rainfall rates from radar data. More recent field observations (see Figure 10.17, 10.18a) and laboratory studies (Figures 10.17, and 10.18b) have verified the earlier conclusions.

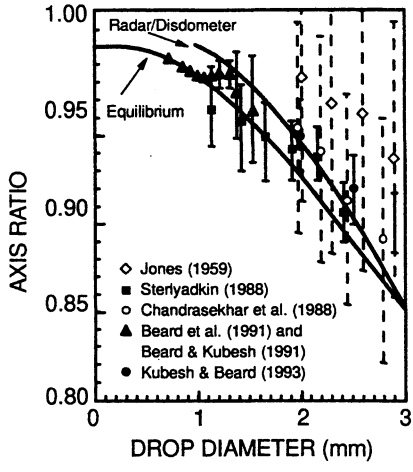


Fig. 10-17: Axis ratios of raindrops as a function of their equivalent diameter. Shown are mean axis ratios (symbols) and standard deviations (vertical lines) for various field observations and laboratory measurements. Curves indicate the equilibrium axis ratio computed from Beard *et al.* (1989a) and the radar-disdrometer derived axis ratios postulated by Goddard and Cherry (1984). (From Tokay and Beard, 1994, with changes.)

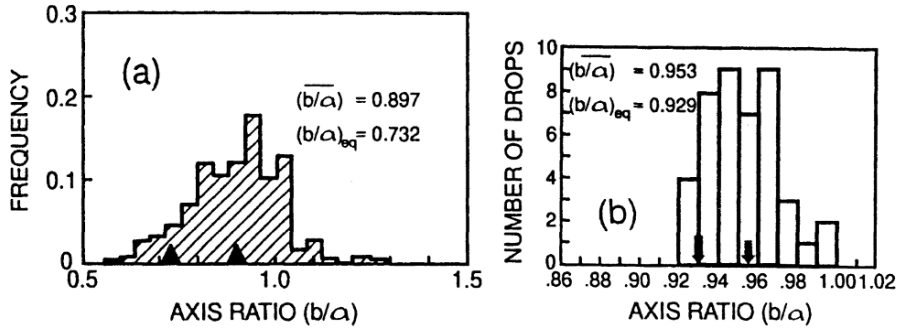


Fig. 10-18: Axis ratio histogram for raindrops of two equivalent diameters (D_0): (a) field study in rains over Miami (Florida), $D_0 = 4.8$ mm, (b) laboratory experiment in fall shaft, $D_0 = 2.0$ mm; arrow on the left in each diagram indicate the equilibrium axis ratio $(b/a)_{eq}$, arrow on the right in each diagram indicates the time mean axis ratio $\overline{(b/a)}$. (a: from Jameson, 1983, with changes; b: from Kubesh and Beard, 1993, with changes.)

Three questions need to be answered with regard to the laboratory and field observations mentioned: (1) what is the frequency at which the drops oscillate, (2) how does their oscillation affect their shape, and (3) what is the cause of their oscillation? We shall discuss these questions in sequence.

A simple estimate of the characteristic vibration frequency f is available through the use of dimensional analysis. If we ignore viscous effects and the weak coupling to the exterior medium (air), the only relevant characteristic physical parameters are the drop's surface tension σ, density ρ_w, and equivalent, radius a_0. Consequently, the necessity for dimensional consistency immediately tells us that

$$f \sim \left(\frac{\sigma}{\rho_w a_0^3} \right)^{1/2} , \tag{10-96}$$

A complete analysis of the problem, based on the assumption of potential flow and small amplitudes of vibration (Appendix A-10.3.3), shows that there is a discrete spectrum of allowed frequencies. From (A.10-38), these are

$$f_n = \left[\frac{n(n-1)(n+2)\sigma}{4\pi^2 \rho_w a_0^3} \right]^{1/2} . \tag{10-97}$$

This result was first derived by Rayleigh (1879). Each oscillation frequency allows $m = n + 1$ degenerate modes having unique spatial orientations, i.e. for each frequency, there is one axisymmetric mode $m = 0$ and $m = n$ physically distinct asymmetric modes. The choice $n = 0$ corresponds to radial oscillations, which are prohibited by the condition of incompressibility. The value $n = 1$ corresponds to the translatory motion of the drop as a whole. Therefore, the fundamental mode of drop oscillation occurs for $n = 2$, with the frequency

$$f_2 = f_{\text{Rayleigh}} = \left(\frac{2\sigma_{w/a}}{\pi^2 \rho_w a_0^3} \right)^{1/2} . \tag{10-98}$$

The first harmonic ($n = 3$) has the frequency

$$f_3 = \left(\frac{30\sigma_{w/a}}{4\pi^2 \rho_w a_0^3} \right)^{1/2} . \tag{10-99}$$

Thus, we see from (10-98) that the simple estimate (10-97) for the gravest mode is too large only by a factor of $\pi/\sqrt{2}$.

From (A.10-37), we see that drop oscillations occur in modes composed of spherical harmonic perturbations with the surface defined by

$$r_{n,m}(t, \theta, \phi) = a_0 + A \sin(\omega_{n,m} t) P_{n,m}(\cos\theta) \cos m\phi , \tag{10-100}$$

where a_0 is the undistorted drop radius, A is an arbitrary amplitude and $P_{n,m}$ are the associated Legendre functions. For axisymmetric oscillation ($m = 0$),

$$r_n = a_0 + A \sin \omega_n t P_n(\cos\theta) . \tag{10-101}$$

Equation (10-101) has been used in drop oscillation studies by Foote (1971), and (10-100) by Beard (1984b), by Beard and Kubesh (1991), and by Kubesh and Beard (1993). The drop shapes for $n = 2$ and 3 and $m = 0, 1$, and 2 are illustrated in Plate 13 and Figure 10.19.

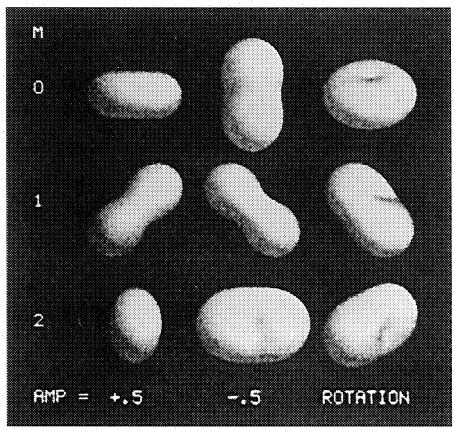


Plate 13. Three modes (m = 0,1,2) of the fundamental harmonic (n = 2) for an oscillating drop. Two relative amplitudes are shown in each row (± 0.5). In the third view of each row the shape is rotated: for m = 0 the rotation is 30° with respect to the horizontal plane; for m = 1 the rotation is about the vertical axis and 30° with respect to the horizontal plane. (From Beard, 1984b; by courtesy of the author, copyright by the *Am. Geophys. Union.*)

Beard and Kubesh (1991), Beard *et al.* (1991), and Kubesh and Beard (1993) argued that the strong *one-sided* scatter of the axis ratio of drops with $1.0 \leq D_0 \leq 1.3$ and $1.9 \leq D_0 \leq 2.6$ mm (see Figure 10.17) is due to oscillations in the transverse modes $(n, m) = (2, 1)$ and (3,1). The *two-sided* scatter of the axis ratios of drops with $1.4 \leq D_0 \leq 1.6$ mm., on the other hand, is thought to be due to the drops oscillating in the axisymmetric mode (2,0).

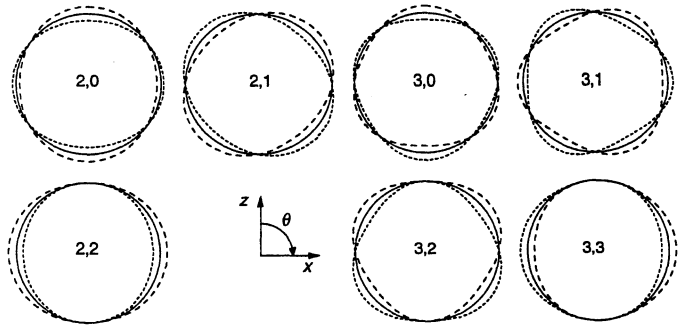


Fig. 10-19: Three modes of the spherical harmonics for $n = 2$ and $m = 0,1,2$, with perturbation maxima normalized to 10% of the undistorted radius viewed along the y axis (in the plane of maximum amplitude for the asymmetric modes where $\cos m\phi = \pm 1$.) The curves with large dashes are for positive amplitude ($\sin \omega t > 0$) and with small dashes are for negative amplitude. The solid curves show the undistorted sphere. (From Beard and Kubesh, 1991, with changes.)

According to Beard and Kubesh (1991), verification of these arguments follows directly from an analysis of (10-100) and (10-101). For a positive perturbation ($\sin \omega t > 0$), the axisymmetric mode (2,0) has an extension at the poles ($\theta = 0$) of $P_{2,0} = 1/2(3\cos^2 \theta - 1) = 1$, and an indentation of $P_{2,0} = 0.5$ at the equator ($\theta = 90°$) for all views around the z-axis. The axis ratio of a drop is found from the maximum vertical (b) and horizontal (a) chord for a particular horizontal view from

$$b(t) = 2(a_0 + \Delta v_{n,m} \sin \omega t)\,, \tag{10-102}$$

$$a(t) = 2(a_0 + \Delta h_{n,m} \sin \omega t)\,, \tag{10-103}$$

where the perturbation chords $\Delta v_{n,m}$ and $\Delta h_{n,m}$ are obtained for $n = 2$ and $m = 0$ from the appropriate vertical and horizontal components of $AP_{n,m} \cos m\phi$ in (10-100). Thus, we find for the axis ratio

$$\left(\frac{b(t)}{a(t)}\right)_{n,m} = \frac{a_0 + \Delta v_{n,m} \sin \omega t}{a_0 + \Delta h_{n,m} \sin \omega t}\,, \tag{10-104}$$

from which

$$\left(\frac{b(t)}{a(t)}\right)_{2,0} = \frac{a_0 + A \sin \omega t}{a_0 - 0.5A \sin \omega t}\,. \tag{10-105}$$

This axis ratio varies symmetrically above and below unity. The time average turns out also to be of order unity with a small secondary effect which shifts the axis ratio above unity by Aa_0^2/ω. Thus, the oscillation of drops in the mode (2,0) is expected to produce a two-sided scatter in the axis ratio with approximately equal amplitudes above and below the equilibrium value, in agreement with observations.

In contrast, in the transverse mode (2,1) the perturbation, when viewed from any angle around the z-axis, produces a vertical extension which varies in time as a

constant plus a rectified sine wave, $2[a_0 + \Delta v_{2,1} \mid \sin \omega t \mid]$, with maxima in the x-z plane at $\theta = 45, 135, 225$, and $325°$ (Fig. 10-19). In one principal view (along the y-axis perpendicular to the x-z plane), the horizontal chord perturbation at $\theta = \pm 45°$ is the same as the vertical chord perturbation, i.e. $\Delta h_{2,1} = \Delta v_{2,1}$. Thus, from (10-104) the axis ratio does not vary. Viewed along the x-axis, the perturbations are displaced $\pm 90°$ from the meridian. The maximum horizontal chord remains fixed at a_0 , whereas the maximum vertical chord is the same as in the orthogonal view. Therefore, from (10-104) $b(t)/a(t) = (a_0 + \Delta v_{2,1}) \mid \sin \omega t \mid / a_0$. Averaging the maximum horizontal chord over all views around the z-axis Beard and Kubesh (1991) find for the axis ratio

$$\left(\frac{b(t)}{a(t)}\right)_{2,1} = \frac{a_0 + \Delta v_{2,1} \mid \sin \omega t \mid}{a_0 + 0.5 \Delta v_{2,1} \mid \sin \omega t \mid} . \tag{10-106}$$

This implies that the axis ratio of drops oscillating in the transverse mode (2,1) will exhibit a one-sided scatter above unity because $b(t) \geq a(t)$, with a time-mean that is larger than unity to first order by $\Delta v_{2,1}/\pi a_0$, in agreement with observations.

Measurements of the oscillation frequency of various sized water drops in air have been carried out by numerous investigators in the laboratory and during field experiments. A selected number of the available experimental data are plotted in Figure 10.20, where they are compared with the Rayleigh frequency (10-98) and the theoretical computations of Feng and Beard (1991a,b), who used a multiparameter perturbation theory to derive a correction term to the Rayleigh frequency for $n = 2$ and $m = 0$, 1 and 2. We see from Figure 10.20 that the frequency of drop oscillation decreases by about one order of magnitude, from near 300 $\sec^{-1}$ to near 30 $\sec^{-1}$, if the drop diameter decreases from about 1 mm to about 5 mm. Considering the oscillation mode $n = 2$ and $m = 0$, one may approximate the oscillation frequency by the empirical relation

$$f_2 = 4.22 a_0^{-1.47} , \tag{10-107}$$

with a_0 in cm, f_2 in m $\sec^{-1}$, and b/a varied between 0.5 and 2 (Nelson and Gokhale, 1972).

The shedding of eddies from the rear of a falling drop can initiate drop oscillation. This mechanism was first pointed out by Gunn (1949), who noticed that the Rayleigh oscillation frequency for a drop of $a_0 \approx 500\,\mu$m falling at terminal velocity ($N_{\mathrm{Re}} \approx 300$) is close to the frequency of eddy shedding from the rear of a rigid sphere of the same Reynolds number (Möller, 1938). He concluded that the periodic detachment of eddies in the drop's wake excites drop vibration through induced pressure changes at the drop surface, resulting in resonance between the eddy shedding frequency and the natural oscillation frequency of the drop. From Figure 10.21, we notice that the shedding frequencies from rigid spheres and drops vary over quite a broad range, allowing resonance coupling to the fundamental frequency mode ($n = 2$) of drops in the range $1.0 \leq D_0 \leq 1.3$ mm. For drops of $1.4 \leq D_0 \leq 1.6$ mm, a match between the shedding frequency and the natural oscillation frequency exits for $n = 3$ and $n = 4$. The oscillation of larger drops is difficult to explain, since most drops of $2 \leq D_0 \leq 4$ mm are found to oscillate in the

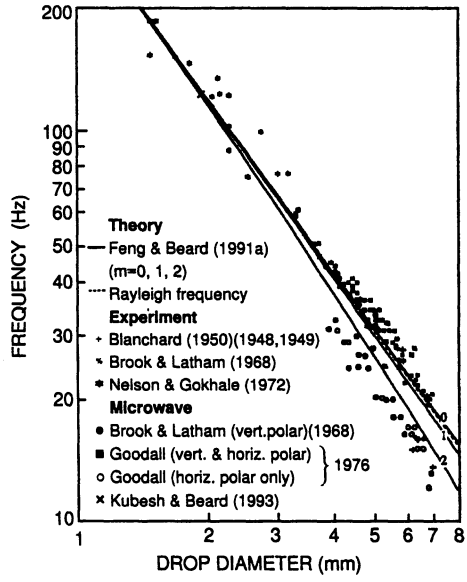


Fig. 10-20: Frequencies for two-lobed oscillations (n = 2) of water drops falling in air as functions of equivalent drop diameter. Data points are from observations. Solid lines are obtained from theory; curves 0,1 and 2 apply to the modes m = 0, 1 and 2; the dashed line is from Rayleigh's result for the degenerated two-lobed modes. (From Feng and Beard, 1991a, with changes.)

fundamental mode ($n = 2$) (Tokay and Beard, 1994), for which a large mismatch exists between shedding and natural oscillation frequency (see Figure 10.21).

Beard (1984b), Beard and Kubesh (1991), Beard *et al.* (1991a,b), Feng and Beard (1991), and Kubesh and Beard (1993) have suggested two mechanisms which cause the excitation of drop oscillation despite frequency mismatch: (1) Subharmonic resonance may occur if the eddy shedding frequency is equal to some integer multiple of f_2 or f_3; (2) Shape changes of the oscillating drop may induce a frequency feedback which shifts the shedding frequency towards the oscillation frequency such that they come into phase with each other.

Jones (1959) observed that raindrop oscillation was particularly pronounced if the drops fell through a strongly turbulent boundary layer. This observation suggests that in addition to eddy shedding from the rear of a drop, oscillations are also induced by wind shear and turbulence. To test the significance of this mechanism, we shall follow Tokay and Beard (1994) who used for their analysis the earlier finding of Beard *et al.* (1989a) that the equilibrium raindrop distortion is a known function of the *Weber number* $N_{\mathrm{We}} = \rho_{\mathrm{a}} D_0 \nu_\infty^2 / \sigma_{\mathrm{w/a}}$, and is given approximately by

$$\frac{b}{a} = \frac{1 - BN_{\mathrm{We}}}{1 + BN_{\mathrm{We}}}, \tag{10-108}$$

with $B = 0.11$. (The physical significance of the Weber number is discussed in

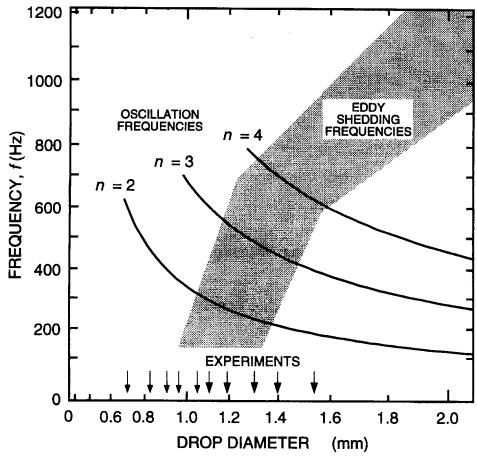


Fig. 10-21: Oscillation and eddy shedding frequency as a function of size of water drops falling in air. Curves are oscillating frequency of water drops in air. Eddy shedding frequencies (shaded region) are based on liquid tank experiments of Möller (1938), Achenbach (1974), Magarvey and Bishop (1961a,b) and Goldburg and Florsheim (1966), and plotted for water drops in air for the same Reynolds number and dimensionless frequency. The drop sizes studied are indicated by arrows. (From Beard *et al.* 1991, with changes.)

Section 10.3.5.) The change $N_{\rm We}$ in the Weber number due to a turbulent air velocity fluctuation u' in the direction of U_∞ is therefore

$$\frac{\Delta N_{\rm We}}{N_{\rm We}} = \left(1 + \frac{u'}{U_\infty}\right)^2 - 1 . \tag{10-109}$$

The corresponding change in axis ratio $\Delta(b/a)$ is then of the form

$$\Delta(b/a) = \beta[(1 + u'/U_\infty)^2 - 1]N_{\rm We} , \tag{10-110}$$

where $\beta = \mid \delta(b/a)/\delta N_{\rm We} \mid$ represents the change in axis ratio with Weber number from (10-108), and where $u' = [\bar{u}^2]^{1/2}$. For homogeneous, isotropic turbulence in the initial subrange, we have

$$\bar{u}^2 = c(\ell\epsilon/2\pi)^{2/3} , \tag{10-111}$$

where ϵ is the turbulence energy dissipation rate per unit mass (see Section 11.6.2), ℓ is the dominant eddy length scale, and $c = 1.5$ (Tennekes and Lumley, 1972; Hinze, 1959). For turbulence generated in the atmospheric boundary layer, ϵ may be estimated as

$$\epsilon = \frac{(u^*)^3}{kz} , \tag{10-112}$$

where $k = 0.35$ (Businger, 1973), and where the friction velocity u^* is

$$u^* = \frac{kU}{\ln(z - z_0)} . \tag{10-113}$$

In (10-113), U is the wind speed measured typically at a height $z = 10$ m; the roughness parameter $z_0 \approx 0.05$ m for a grass surface. In (10-112), Tokay and Beard set $z = 0.9\,\mathrm{m} + 0.5\ell_{\mathrm{oscil}}$, where 0.9 m was the height of their point of observation. The length ℓ_{oscil} is the fall distance of the drop during one period of oscillation. The eddy scale length ℓ in (10-111) can therefore be estimated from (10-99) as

$$\ell = \ell_{\mathrm{oscil}} = U_\infty^2 \pi / f_2 = (\pi/4) U_\infty / \rho_{\mathrm{w}} D_0^3 / \sigma_{\mathrm{w/a}})^{1/2} . \tag{10-114}$$

The change in axis ratio may then be determined from (10-110) together with (10-111) to (10-114).

A similar approach may be used to determine the effect of a horizontal shear on the axis ratio of a rain drop. Following Tokay and Beard, we shall assume that the shear is given by

$$\Delta u = u(z + \Delta z) - u(z) = (u^*/k) \ln \left(\frac{z + \Delta z}{z} \right) . \tag{10-115}$$

A vertically falling raindrop will then experience a change in air velocity of $(U_\infty^2 + \Delta u^2)^{1/2}$ and, therefore, a corresponding Weber number change of $\Delta u^2 / U_\infty^2$, in analogy to (10-109). The associated change in axis ratio is therefore

$$\Delta(b/a) = \beta (\Delta u / U_\infty)^2 N_{\mathrm{We}} . \tag{10-116}$$

A numerical evaluation of (10-110) and (10-116) was carried out by Tokay and Beard (1994) for $1 \leq U \leq 10$ m sec^{-1}, which occurred at their level of observation. The computed change in axis ratio was less than 0.02 for $D_0 \lesssim 4$ mm. From this result, Tokay and Beard concluded that turbulence and wind shear contributed negligibly to the large drop oscillation amplitudes observed under the conditions they encountered during their field experiment.

Let us now look at the significance of a third cause for drop oscillation. The large oscillation amplitudes of drops falling in intense rain suggests that drop collision may also excite oscillations. Laboratory studies in fall shafts and wind tunnels confirm that drop collisions cause large amplitude oscillations in newly coalesced drops, as well as in the drop fragments resulting from drop breakup. Collision induced oscillation has been modeled by Beard *et al.* (1983) and Johnson and Beard (1984), assuming that the raindrop agitiation may be computed from a balance between the kinetic energy imput resulting from drop collision, and viscous dissipation within the drops.

Following Beard *et al.* (1983) and Johnson and Beard (1984), the rate of imput of kinetic energy due to collision of a drop of diameter D_0 and mass M and velocity U_∞ with smaller drops of diameter d_i, mass m_i, velocity u_∞, and concentration $n(d_i)$ is given by

$$\frac{\mathrm{d}E_n}{\mathrm{d}t} = \sum_i C(D_0, d_i) E_k(D_0, d_i) , \tag{10-117}$$

where the collision rate C is

$$C(D_0, d_i) = \frac{\pi}{4} (D_0 + d_i)^2 [U_\infty(D_0) - u_\infty(d_i)] n(d_i) , \tag{10-118}$$

assuming a geometric collision cross-section (see Section 11.6.3). The excess kinetic energy E_k after collision of a D_0-drop with a small d_i-drop is by virtue of the conservation of momentum,

$$E_k(D_0, d_i) = \frac{1}{2}MU_\infty^2 + \frac{1}{2}m_i u_\infty^2(d_i) - \frac{1}{2}[MU_\infty + m_i u_\infty]^2/(M + m_i)\,. \quad (10\text{-}119)$$

According to Lamb (1932), the damping of a viscous sphere undergoing a small amplitude oscillation is given by

$$\frac{\mathrm{d}\epsilon}{\mathrm{d}t} = -\frac{2\epsilon}{\tau}\,, \quad (10\text{-}120)$$

where ϵ is the oscillation energy of the drop, and the decay time $\tau = D_0^2/20\nu_\mathrm{w}$, ν_w being the kinematic viscosity of water. A balance between the rate of collisional energy imput and dissipation of oscillation energy requires

$$-\frac{\mathrm{d}\epsilon}{\mathrm{d}t} = \left(\frac{\mathrm{d}E_k}{\mathrm{d}t}\right)\,. \quad (10\text{-}121)$$

Then, from (10-117) to (10-121), one finds the oscillation energy of a D_0-drop after collision with d_i-drops is given by

$$\epsilon = 0.5\tau \sum_i C(D_0, d_i) E_k(D_0, d_i)\,. \quad (10\text{-}122)$$

Beard *et al.* (1983), Beard and Johnson (1984) and Johnson and Beard (1984) evaluated (10-122) subject to the limitation (Low and List, 1982a,b) that $E_k \leq 0.5E_\mathrm{S}$, where E_S is the surface energy of a drop. This limitation implies that there is a 50% or larger probability of drop breakup when E_k exceeds half of the drop's surface energy. Assuming typical rainfall rates and the drop size distribution of Sekhorn and Srivastava (1971), the analysis of (10-122) led to three conclusions: (1) the oscillation energy ϵ is a maximum for collisions which take place between drops of $2 \leq D_0 \leq 5$ mm and drops of $d_0 \approx 0.5$ mm, for rainfall rates of $1 \leq R \leq 100$ mm hr^{-1}. (2) The fraction of drops having oscillation energies ϵ larger than 50% of their surface energy E_S is less than 15% for $R < 10$ mm hr^{-1} and $D_0 \leq 3$ mm. However, for large drops and large rainfall rates, this fraction increases rapidly, reaching 100% for $D_0 = 5$ mm and $R = 100$ mm hr^{-1}. (3) All drops having values of $(\epsilon/E_\mathrm{S}) \gtrsim 0.5\%$ experience axis ratio changes $\Delta(b/a) \gtrsim 10\%$ due to collisional forcing. In order to check whether collisional forcing of drop oscillation is significant under atmospheric conditions, Tokay and Beard (1994) compared their computations with the observations during a field experiment. They found that the number of drops predicted to oscillate at a point of observation due to a collision in or above the air volume of observation was only a small fraction of the number of drops actually observed to oscillate. Thus, it appears that although collisional forcing may contribute to drop oscillation, it is not the main cause.

10.3.4 Fall Behavior of Drops

Early studies on the fall behavior of water drops were carried out in immiscible liquids by Magarvey and Geldart (1962), Magarvey and Bishop (1961a,b) and Magarvey and McLatchey (1965). More recently, Pruppacher *et al.* (unpubl.) and Vohl (1989) studied the fall behavior of water drops in air by suspending the drops in a vertical wind tunnel or allowing them to fall in a 33 m high fall shaft. As expected from the fall behavior of rigid spheres, drops of $N_{\mathrm{Re}} \gtrsim 300$, follow a helical fall path. Water drops in air with $1\,\mathrm{mm} \leq D_0 \leq 3$ mm execute large sideways excursions of 10 to 50 drop diameters, thus preventing their stable suspension in narrow observation sections of vertical wind tunnels. Note that this is also the size range in which drops may oscillate in a transverse mode (Section 10.3.3). With further increase in drop size, the sideways excursions decrease rapidly so that for drops of $D_0 \gtrsim 3$ mm, the excursion is only a few diameters, allowing these drops to be 'stably' suspended in the air stream of vertical wind tunnels. However, such suspension requires a rapid adjustment of the tunnel's vertical velocity to compensate for the drop's rapid fall velocity fluctuations caused by the oscillation-induced drag changes.

Wind tunnel observations as well as field experiments show further that drops, for which the flat lower side is parallel to the ground during fall in quiet air, tilt in the presence of shear (Saunders, 1971). This behavior, called 'canting', is thought to significantly affect microwave transmission (Thomas, 1971; Watson and Arabi, 1973; Chu, 1974). From a large number of measurements in thunderstorm rains, McCormick and Hendry (1974) found that the canting angles are distributed about an average of 0.48°, with a standard deviation of 1.77°. Over 82% of the measured angles were within ±2.25°. This result agrees with the theoretical expectation of Beard and Jameson (1983), who suggested, on the basis of drag considerations, that the quasi-steady response to constant vertical shear Γ is a canting angle α given by

$$\tan\alpha = \frac{\Gamma U_\infty}{g}(1 - e^{-t/\tau}) = \frac{\Gamma U_\infty}{g}(1 - e^{-\ell/\ell_\tau})\,, \tag{10-123}$$

where g is the acceleration of gravity, $\tau = U_\infty/g$ is the time required for a drop to adjust to an imposed air velocity (see Section 10.3.5), and $\Gamma = (u_1 - u_2)/\ell$, with u_1 and u_2 being simultaneous velocities separated by the length scale $\ell = U_\infty t$, and $\ell_\tau = U_\infty \tau$. For simple homogeneous, isotropic turbulence in the inertial subrange, we find for the shear, using (10-111),

$$\Gamma = \frac{(\bar{u}^2)^{1/2}}{\ell} = c^{1/2}(\epsilon/2\pi)^{1/3}\ell^{-2/3}\,, \tag{10-124}$$

where here we have $\bar{u}^2 = (u_1 - u_2)^2$ (e.g. Pasquill, 1962; Panchev, 1971). Numerical analysis of (10-123) together with (10-124) shows that within the range $\ell = \ell_{\mathrm{oscil}}$ ((10-114)) to $\ell = \ell_\tau$, the canting angle α increases with the strength of the velocity fluctuations, and reaches a maximum for $\ell = 0.76\ell_\tau$. For larger values of ℓ , the drop increasingly tends to follow the fluctuations. At the maximum α varies between 1.6° and 3.5° for a drop of $D_0 = 2$ mm, and between 1.4° and 3.1° for

a drop of $D_0 = 6$ mm, for $\epsilon = 2 \times 10^2$ cm^2 sec^{-3} and $\epsilon = 3 \times 10^3$ cm^2 sec^{-3}, respectively.

If a drop freezes, its fall behavior changes abruptly (Pitter and Pruppacher, 1973). During freezing, drops of $a_0 \leq 500\,\mu$m exhibit an erratic sailing motion. Once frozen, they may fall stably while spinning around a vertical axis, or they may tumble forward or backward. Knobs or spikes stabilize the motion about the knob or spike. Drops which are large enough to exhibit a flat base quickly turn over on freezing, and fall with their flat side up (Spengler and Gokhale, 1972).

10.3.5 Drop Instability and Breakup

Drop breakup may be the result of hydrodynamic instability of large single drops, or a result of the collision between two drops which results in only a temporary coalescence. In this section, we will consider the former mechanism, while the latter mechanism will be discussed in Chapter 14. Experiments carried out by Fournier d'Albe and Hidayetulla (1955), Blanchard and Spencer (1972), Alusa and Blanchard (1973), and Alusa (1975) with drops falling through a long column of air at rest, and by Blanchard (1948, 1950) and Beard and Pruppacher (1969) with drops suspended in low turbulence wind tunnels, have demonstrated that, in quiet air, drops may be as large as 4.5 mm in equivalent radius before breaking up. The mechanism of breakup of such drops is closely tied to the development of the previously mentioned concave depression in the base of the falling drop. At a critical drop size, this depression almost explosively deepens and develops rapidly into an expanding bag supported by an annular ring which contains the bulk of the water. As this bag-like drop bursts, the bag portion breaks into a large number of small drops while the annular ring breaks into a smaller number of larger drops. The different stages of breakup are schematically drawn in Figure 10.22. This *bag breakup mechanism* has been studied by Blanchard (1948, 1949, 1950), Magarvey and Taylor (1956), Mathews and Mason (1964), and Koenig (1965a).

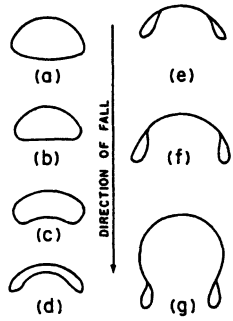


Fig. 10-22: Stages during the bag-breakup of a water drop in air. (From Matthews and Mason, 1964; by courtesy of Quart. J. Roy. Meteror. Soc.)

While a complete theoretical description of the growth of large amplitude drop distortions remains out of reach, the superficial aspects of the breakup process are

well-known. Probably the simplest order of magnitude estimate for the maximum stable drop diameter $d_{\max}$ is obtained through the statement that incipient instability occurs when the drag stress on the drop exceeds the surface tension stress. Thus, $d_{\max}$ may be estimated from the relation $C_D \rho_a U_\infty^2/2 \approx 4\sigma/d_{\max}$, or

$$d_{\max} \approx \frac{8\sigma}{C_D \rho_a U_\infty^2} . \tag{10-125}$$

An equivalent dimensionless statement of this is

$$\frac{\rho_a d_{\max} U_\infty^2}{\sigma} \equiv N_{\mathrm{We,max}} = \frac{8}{C_D} , \tag{10-126}$$

where N_{We} is the *Weber number*. The Weber number can be seen to be a measure of the relative strengths of the Bernoulli pressure (which is effective because of flow separation) and the stress due to surface tension. It is clear that if $N_{\mathrm{We}} \gg 1$, the surface tension stress, which tends to maintain a spherical shape, is negligible in comparison to the pressure, so that the latter can therefore strongly distort or disrupt the drop.

The value of C_D in (10-125) and (10-126) is unknown, but should lie between the values for a sphere (≈ 0.46) and a disk (≈ 1.17) at high Reynolds numbers. If we choose $C_D = 0.85$, (10-125) and (10-126) agree well with the experiments of Lane (1951), who found $U_\infty^2 d_{\max} = 6.1 \times 10^5$ (c.g.s. units). Thus, the critical Weber number for breakup (based on $d_{\max}$) is approximately 10. Estimates equivalent to (10-125) and (10-126) have been obtained, for example, by Dodd (1960), Levich (1962) and Mathews and Mason (1964).

Komabayasi *et al.* (1964) adopted a somewhat different approach to arrive at a similar estimate of the maximum stable drop size. They assumed that at the surface of a freely falling drop capillary and gravity waves are induced which, under certain conditions, become unstable and amplify. Thus, they consider drop breakup as a manifestation of the *Rayleigh-Taylor instability* of two superposed fluids of different density in a gravitational field. (An exhaustive treatment of this subject is available in Chapter 10 of Chandrasekhar (1961). A brief description, adequate for our purposes here, is given in Appendix A-10.3.5.)

Komabayasi *et al.* assumed the surface waves are plane parallel. From (A.10-48) we see that the critical wave number for instability is

$$k_c = \left[\frac{g(\rho_w - \rho_d)}{\sigma}\right]^{1/2} = 3.67\,\mathrm{cm}^{-1} , \tag{10-127}$$

assuming $\sigma = 72.8$ erg cm^{-2}. The corresponding minimum stable wave length is $\lambda_{\min} = 2\pi/k_c = 1.71$ cm. The critical maximum stable base width may therefore be estimated as $\lambda_{\min}/2 = 0.855$ cm, i.e., the base width is just sufficient to accommodate the fundamental standing wave corresponding to $\lambda_{\min}$.

When expressed in terms of a dependence on the relevant physical parameters, the estimate of Kombayasi *et al.* is

$$d_{\max} = \frac{\lambda_{\min}}{2} = \frac{\pi}{k_c} = \pi \left[\frac{\sigma}{g(\rho_w - \rho_a)}\right]^{1/2} . \tag{10-128}$$

This can be compared with the previous estimate (10-125) by noting that, at terminal velocity, the drag force balances the net gravitational force so that $4\pi a_0^3(\rho_w - \rho_a)g/3 = C_D(\rho_a U^2/2)\pi(d_{max}/2)^2$. Assuming an oblate spheroidal shape of axial ratio $x \equiv b/a$, where $a = d_{max}/2$, we have $4\pi a_0^3/3 = 4\pi a^2 b/3$, or $a_0 = x^{1/3} d_{max}/2$. Consequently, we may write

$$g(\rho_w - \rho_a) = \frac{3C_D \rho_a U_\infty^2}{4x d_{max}} . \tag{10-129}$$

Substitution of (10-129) into (10-128) gives

$$d_{max} = \frac{4\pi^2 x\sigma}{3C_D \rho_a U_\infty^2} , \tag{10-130}$$

which is the same as (10-125) except for a numerical factor. We may estimate $x = 0.55$ by extrapolation of the measurements of Pruppacher and Pitter (1971) to the case $a_0 = 0.45$ cm (see below); this gives $4\pi^2 x/3 = 7.2$. Given the approximate and disparate nature of the estimates, we conclude that (10-125) and (10-130) agree surprisingly well.

The above comparisons provide additional physical support for the use of the Rayleigh-Taylor instability mechanism as a means for estimating the maximum stable drop size. A further refinement of this technique is available by employing a model more compatible with the geometry of the drop (Klett, 1971a). The symmetry of a falling drop about a vertical axis through its center suggests it is appropriate to consider the stability of two-dimensional circular waves rather than one-dimensional plane parallel waves. Also, the curvature of the drop surface near the edge of its base will have a constraining effect on the wave motion. This influence may be modeled in an approximate manner by regarding the effect of the drop's walls on its stability as lying between two extreme cases: (1) There are no walls; i.e., the bottom surface of the drop behaves as if it were part of an infinite interface between two otherwise unbounded fluids. (2) There are rigid vertical walls such that the stability of the drop is the same as that of two superposed fluids contained in a vertical circular tube

As shown in Appendix A-10.3.5, if we assume inviscid flow, the velocity potentials in both cases have a radial dependence of the form $J_n(kr)$, where J_n is the Bessel function of the n^{th} order and k is the wave number. Also, in both cases, the instability condition (10-127) holds. Following the standing wave criterion described just before in (10-128), we see that for case 1 the radial distance from the z-axis to the lowest point on the drop bottom (half of what we call the base width $d_{c,1}$) must be the smallest of those distances r_{nm} such that $k_c r_{nm}$ is the m^{th} root of $J_n(x) = 0$. The smallest such root is $k_c r_{01} = 2.40$, so that $d_{c,1} = 2r_{01} = 1.31$ cm. The most unstable mode in case 1 is axisymmetric. In case 2, the velocity potential satisfies (A.10-39), so that the base width $d_{c,2}$ is twice the smallest of those distances r_{np} such that $k_c r_{np}$ is the p^{th} root of $\mathrm{d}J_n(x)/\mathrm{d}x = 0$. In this case, the smallest root is $k_c r_{11} = 1.84$, from which $d_{c,2} = 1.00$ cm. The most unstable mode in case 2 is seen to be asymmetric.

The preceding analysis thus suggests that the largest stable base width of a water drop falling in quiet air should lie between 1.00 and 1.31 cm, i.e., a value somewhat larger than that predicted by Komabayasi. Wind tunnel measurements by Pruppacher and Pitter (1971) have shown that the Iargest drops which are stable in quiet air have $a_0 \approx 0.45$ cm, and base widths ranging between 1.00 and 1.05 cm. This agreement with the refined but still very approximate Rayleigh-Taylor analysis is perhaps better than could be expected, since flow within and past the drop was ignored, and the effect of drop curvature was neglected except insofar as it determined boundary conditions at the 'edge' of the drop. A final comment in defense of the Rayleigh-Taylor instability model seems worth mentioning. By its nature, the model predicts that instability will occur on the bottom surface of the drop. This is in accord with wind tunnel observations.

Before leaving this section, let us briefly consider the question of whether or not atmospheric turbulence might have the capacity to disrupt drops. This is another nearly intractable problem, but again some estimates can be made on the basis of elementary arguments.

Let us assume the drop is immersed in homogeneous, isotropic turbulence in the inertial subrange and that its size is larger than the turbulent microscale length (see Section 11.6.2). Kolmogorov (1949) obtained an estimate of the maximum stable drop size under the further assumption that the dynamic pressure difference across the drop surface is due solely to turbulent fluctuations. When this is true, one may proceed as in the argument leading to (10-125), except that now U_∞ is to be replaced by Δu, the characteristic velocity fluctuation over the length $d_{\max}$; from (11-67) this is of order $(\epsilon d_{\max})^{1/3}$, where ϵ is the turbulent energy dissipation rate. On making the appropriate replacement in (10-125), it immediately follows that

$$d_{\max} \approx \left(\frac{8\sigma}{C_D \rho_a}\right)^{3/5} \epsilon^{-2/5} . \tag{10-131}$$

Unfortunately, however, the assumption that the dynamic pressure difference is caused solely by turbulent fluctuations does not hold for drops falling in air. It would be true only if the drop were essentially completely entrained by the turbulent eddies; i.e., (10-131) is applicable only for cases where drop and medium have comparable densities. Levich (1962) has obtained another estimate for the case where the density difference is large. However, his expression is also inapplicable in the context of interest to us, since he disregarded the effect of gravity on the drop motion.

For the case of water drops falling in air, it would seem reasonable to assess the influence of turbulence by comparing the pressure increment due to turbulent fluctuations with the Bernoulli pressure. The strength of the pressure fluctuations increases with eddy size, and the maximum relevant size should be of the order of the distance through which the drop falls during its relaxation time τ_{rel} for velocity fluctuations. Larger eddies are not felt as strongly, since the drop is able, to some extent, to move with them.

Since for $N_{\text{Re}} \gg 1$ the drag varies as the square of the velocity, the fall speed v of the drop may be estimated from the equation $\mathrm{d}/\mathrm{d}t = -Av^2 + g$, where $AU_\infty^2 = g$.

Letting $v = U_\infty + v'$, where the fluctuation $v' \ll U_\infty$, we thus have $\mathrm{d}v'/\mathrm{d}t \approx -2AU_\infty v'$, so that the relaxation time is

$$\tau_{\mathrm{rel}} \approx (2AU_\infty)^{-1} = \frac{U_\infty}{2g} . \tag{10-132}$$

Hence, the maximum effective eddy size is $\lambda \approx U_\infty^2/2g$, corresponding to the turbulent velocity fluctuation $v_\lambda \approx (\epsilon\lambda)^{1/3} \approx (\epsilon U_\infty^2/2g)^{1/3}$. Therefore, the ratio of the turbulent and Bernoulli pressures is

$$v_\lambda^2/U_\infty^2 \approx (\epsilon/2gU_\infty)^{2/3} . \tag{10-133}$$

For large drops, turbulent disruption should be significant only if this ratio is not much smaller than unity. A relatively large value of ϵ is 10^3 cm^2 sec^{-3}; assuming this value and $U_\infty \approx 10^3$ cm sec^{-1}, the magnitude of (10-103) is $\mathrm{O}(10^{-2})$. Hence, it appears that turbulence, if it is of the type assumed here, cannot be effective in breaking up drops that are not already close to the critical breakup size in absence of turbulence. This result is consistent with the conclusions of Tokay and Beard (1994), namely that turbulence and wind shear of the type encountered in the atmospheric boundary layer, with wind velocities up to 10 m sec^{-1}, do not noticeably alter the oscillation amplitude of raindrops (Section 10.3.3).

Experiments to determine the breakup probability of isolated water drops and the resulting size distribution of the drop fragments were carried out by Blanchard and Spencer (1970) in a large fall shaft, and by Komabayasi *et al.* (1964) and Kamra *et al.* (1991) in vertical wind tunnels. The simplicity with which the breakup of single drops can be incorporated in a stochastic drop growth model (see Chapter 15) motivates the inclusion of experimental data in current cloud models. Thus, Hall (1980), Flossmann *et al.* (1985, 1987), Flossmann and Pruppacher (1988) and Flossmann (1991, 1993, 1994) have assumed that all drops which have grown to a radius of $a_0 = 2580\,\mu$m will break up by hydrodynamic instability and produce the fragment distribution given by Hall who followed Danielsen *et al.* (1972), in using the observations of Blanchard and Spencer (1972) (see Table 10.2). In an earlier cloud model, Srivastava (1971) based his description of drop breakup on the wind tunnel data of Kombayasi *et al.* (1964), who found that the breakup probability for a parent drop of radius a_0^* is a function of the drop size and increases according to the relation

$$P(a_0^*) = 2.94 \times 10^{-7} \exp(3.4a_0^*) , \tag{10-134}$$

where $P(a_0^*)\mathrm{d}t$ is the probability for the a_0^*-drop to break up in time $\mathrm{d}t$. From the same wind tunnel data, Srivastava (1971) deduced for the distribution of the drop fragments the relation

$$Q(a_0^*, a_0)\mathrm{d}a_0 = \frac{AB}{a_0^*} \exp\left(-B\frac{a_0}{a_0^*}\right) \mathrm{d}a_0 , \tag{10-135}$$

where $Q(a_0^*, a_0)\mathrm{d}a$ is the number of drops of radii between a_0 and $a_0 + \mathrm{d}a_0$ formed during the breakup of one parent drop of radius a_0^*, $A = 623$, and $B = 7$. More

TABLE 10.2

Fragment mass distribution in per cent of the original mass of a drop of radius 2580 μm after it broke up by hydrodynamic instability. (From Hall, 1980, based on Daniels *et al.*, 1972, and on experiments of Blanchard & Spencer, 1970.)

Drop radius (μm)	%	Drop radius (μm)	%	Drop radius (μm)	%
143.7	0	406.4	5.5	1149.0	4.0
161.3	0.2	456.1	7.5	1290.0	2.5
181.0	0.3	512.0	9.0	1625.0	1.5
203.2	1.5	574.7	10.0	1825.0	1.0
228.1	1.0	645.1	12.0	2048.0	0.5
256.0	1.5	724.1	10.0	2299.0	0.3
287.4	2.0	812.7	9.0	2580.0	0.2
322.5	2.5	912.3	7.5	2600.0	0
362.0	4.0	1024.0	5.5		

recently, Kamra *et al.* (1991) derived from their wind tunnel data the alternative expressions

$$P(D_0^*) = 1.58 \times 10^{-4} \exp(0.773 D_0^*)\,, \tag{10-136}$$

and

$$Q(D_0^*, D_0)\mathrm{d}D_0 = 1.54 \times 10^{-2} (D_0^*)^3 \exp(-0.453 D_0)\mathrm{d}D_0\,, \tag{10-137}$$

for $D_0^* \geq 6.6$ mm. Both results agree reasonably well within the expected experimental error and for common drop sizes.

Finally, from Section 2.1.6, we realize that raindrops rarely reach sizes required for isolated drop breakup. It therefore appears that isolated drop breakup is not the predominant breakup mode in the atmosphere. Rather, evidence suggests that breakup is generally a consequence of collision and temporary coalescence between pairs of drops. As we mentioned in the beginning of this section, we shall discuss this breakup mode in Chapter 14.

10.3.6 Terminal Velocity of Water Drops in Air

In cloud physics studies, there is often a need to know the terminal velocities U_∞ of water drops at various levels in the troposphere. Of course, U_∞ is determined simply through the condition of balance between the buoyancy-corrected gravitation force and the drag force acting on the drop. Unfortunately, however, some complications arise in the attempt to describe the drag forces accurately. Some of these problems we have encountered already, while others we have avoided until now.

Consider first the case of small drops in air falling in the Stokes regime of negligible Reynolds numbers. Here matters seem especially simple: from (10-40) we write $6\pi a \eta_\mathrm{a} U_\infty = 4\pi a^3 g(\rho_\mathrm{w} - \rho_\mathrm{a})/3$, so that

$$U_\infty = U_S = \frac{2a^2 g(\rho_\mathrm{w} - \rho_\mathrm{a})}{9\eta_\mathrm{a}}\,, \tag{10-138}$$

where U_S is the *Stokes terminal velocity.* However, the Stokes drag description assumes continuum flow, and this assumption begins to break down for just those drops which are small enough to have negligible Reynolds numbers. Thus, for great accuracy, it is necessary to correct (10-138) for the effects of slip-flow (see also Section 14.4.3). The correction becomes more important with increasing height in the atmosphere, since the molecular mean free path λ_a increases with decreasing air density.

As we have seen, there is a second range of intermediate Reynolds numbers for which drops may be assumed to fall as rigid spheres in a continuum flow for which both inertial and viscous forces are significant. For this range, we may invoke the experimental and theoretical drag information which has been presented in Section 10.2.2.4. Finally, for larger sizes, the problem of drop shape, and possibly also the intrinsic flow unsteadiness, must be taken into account.

It is convenient and natural, therefore, to resolve the terminal velocity problem into three drag regimes. Of course, there is some latitude in the proper choice of the regime boundaries. In the sequel, we shall follow the classification and description of Beard (1976).

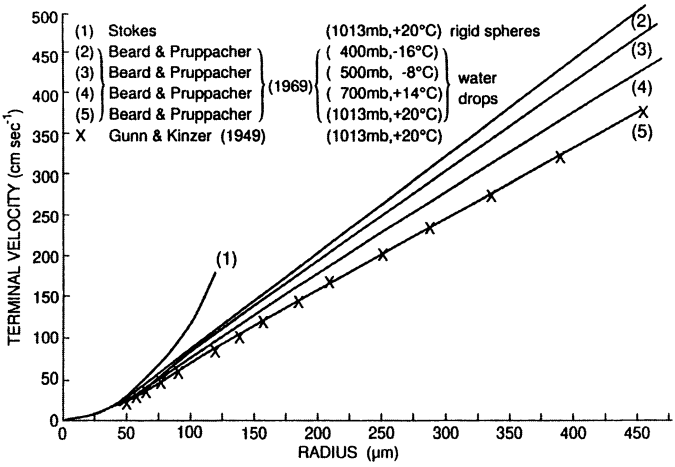


Fig. 10-23: Variation with size of the terminal fall velocity of water drops smaller than 500 μm radius in air. (From Beard and Pruppacher, 1969; by courtesy of Am. Meteor. Soc., and the authors.)

In regime 1: $0.5 \lesssim a \lesssim 10\,\mu$m ($10^{-6} \lesssim N_{\mathrm{Re}} \lesssim 10^{-2}$), the terminal velocity is

$$U_\infty = (1 + 1.26\lambda_a/a)U_S\,, \tag{10-139}$$

where U_S is given by (10-138). The slip flow 'Cunningham' correction factor (see (11-15)) multiplying U_S in (10-139) increases the terminal velocity above the Stokes value by about 1% for $a = 10\,\mu$m and 17% for $a = 1\,\mu$m, at standard conditions ($p_0 = 1013.25$ mb, $T_0 = 293.15$°K, $\lambda_{a,0} = 6.6 \times 10^{-6}$ cm). For other levels in the

atmosphere, the mean free path may be obtained from the expression

$$\lambda_a = \lambda_{a,0} \left(\frac{p_0}{p}\right) \left(\frac{T}{T_0}\right) . \tag{10-140}$$

Similarly, the dynamic viscosity for other than standard conditions is given with an accuracy of $\pm 0.002 \times 10^{-4}$ poise by

$$\eta_a(\text{poise}) = (1.718 + 0.0049T) \times 10^{-4} , \quad T(^\circ\text{C}) \geq 0^\circ\text{C} , \tag{10-141a}$$

$$\eta_a(\text{poise}) = (1.718 + 0.0049T - 1.2 \times 10^{-5} T^2) \times 10^{-4} , \quad T(^\circ\text{C}) < 0^\circ\text{C} . \tag{10-141b}$$

These expressions are based on data given by the Smithsonian Meteorological Tables. (Pressure does not affect η_a and atmospheric water vapor affects η_a negligibly; see Kestin and Whitelaw, 1965.)

In regime 2: $10 \lesssim a \lesssim 535\,\mu\text{m}$ ($10^{-2} \lesssim N_{Re} \lesssim 3 \times 10^2$), we may equate the drag and gravitational forces to obtain $6\pi a \eta_a U_\infty (C_D N_{Re}/24) = 4\pi a^3 g(\rho_w - \rho_a)/3$. When multiplied by ρ_a/η_a^2 , this yields for spherical drops

$$N_{Be} \equiv C_D N_{Re}^2 = \frac{32 a^3 (\rho_w - \rho_a) \rho_a g}{3\eta_a^2} , \tag{10-142}$$

which is sometimes referred to as either the *Davies* or *Best number*. On the other hand, from (10-28) and (10-40), we also have

$$\frac{D}{D_S} = \frac{C_D N_{Re}}{24} , \tag{10-143}$$

where D_S is the Stokes drag. Hence,

$$C_D N_{Re}^2 = 24 N_{Re} \frac{D}{D_S} = f(N_{Re}) , \tag{10-144}$$

since D/D_S is known as a function of N_{Re} from the data displayed in Figure 10.8. In fact, Beard has suggested the following empirical fit for the curves shown in Figure 10.8:

$$Y = B_0 + B_1 X + \ldots + B_6 X^6 , \tag{10-145}$$

where $B_0 = -0.318657 \times 10^1$, $B_1 = +0.992696$, $B_2 = -0.153193 \times 10^{-2}$, $B_3 = -0.987059 \times 10^{-3}$, $B_4 = -0.578878 \times 10^{-3}$, $B_5 = +0.855176 \times 10^{-4}$, $B_6 = -0.327815 \times 10^{-5}$, and where $X = \ln(C_D N_{Re}^2)$, and $N_{Re} = \exp(Y)$. Thus, for given a and atmospheric conditions ρ_a and η_a, $C_D N_{Re}^2$ is specified through (10-142), after which N_{Re} may be found from (10-145). Once N_{Re} is known, the terminal velocity may be determined from

$$U_\infty = \frac{\eta_a N_{Re}}{2\rho_a a} . \tag{10-146}$$

Some results for U_∞ versus a under different atmospheric conditions are shown in Figure 10.23. Notice that U_∞ increases almost linearly with radius for $100 < a <$

500 μm. Note also that U_S progressively overestimates the actual fall velocity; for $a = 30\,\mu$m ($N_{\mathrm{Re}} = 0.4$) the deviation is about 6%, while for $a = 42\,\mu$m ($N_{\mathrm{Re}} = 1.0$) it is 13%.

In regime 3: $535\,\mu\mathrm{m} \lesssim a_0 \lesssim 3.5$ mm ($3 \times 10^2 \lesssim N_{\mathrm{Re}} \lesssim 4 \times 10^3$), the drops can no longer be considered spherical (see Section 10.3.2). Foote and du Toit (1969) pointed out that the procedure outlined above for computing U_∞ is only justified for spherical drops, for only then are C_D and D/D_S a function of N_{Re} alone. If a drop is deformed, the drag and, thus, the terminal velocity are functions also of the amount of the drop's deformation. We have seen that the deformation is a function of ρ_{a}, which varies with height in the atmosphere, and also a function of σ and ρ_{w}, which vary with temperature and, therefore, also with height. Furthermore, the methods presented in Section 10.3.2 permit a determination of a drop's deformation only if its terminal velocity is known *a priori*. Therefore, the procedures of that section are inadequate to determine U_∞ at arbitrary heights, since the only measurements of U_∞ for drops have been carried out at pressures prevailing at the Earth's surface (Gunn and Kinzer, 1949; Beard and Pruppacher, 1969).

Methods to get around this problem have been proposed by Wobus *et al.* (1971), Dingle and Lee (1972), and Berry and Pranger (1974). Unfortunately, these attempts are based on the Gunn and Kinzer observations, which pertain to the Earth's surface and, thus, cannot be used to extrapolate C_D, $C_D N_{\mathrm{Re}}^2$ and, hence, U_∞ to other pressures and temperatures. Therefore, these methods do not correctly account for drop shape. Foote and du Toit (1969) recognized the need for including a pressure dependence, and used the data of Davies (as reported by Best, 1950b) and Sutton (1942), derived from measurements of U_∞ at reduced air densities. Unfortunately, however, a careful scrutiny of the data reveals that under the conditions used by Davies, the water drops did not reach terminal velocity and, thus, could not develop their equilibrium shape.

In order to remedy this situation Beard (1976) suggested following an approach originally proposed by Garner and Lihou (1965). These authors found from studies of drops of various liquids freely suspended in the air stream of a wind tunnel, that U_∞ depends on three independent dimensionless parameters: the Reynolds number $N_{\mathrm{Re}} = 2a_0 U_\infty \rho_{\mathrm{a}}/\eta_{\mathrm{a}}$, the *Bond number* $N_{\mathrm{Bo}} = g(\rho_{\mathrm{w}} - \rho_{\mathrm{a}})a_0^2/\sigma_{\mathrm{w/a}}$, and the *'physical property' number* $N_{\mathrm{P}} = \sigma_{\mathrm{w/a}}^3 \rho_{\mathrm{a}}^2/\eta_{\mathrm{a}}^4 g(\rho_{\mathrm{w}} - \rho_{\mathrm{a}})$. The Bond number can be seen to measure the relative strength of gravitational and surface tension force, i.e., the relative strength of the drag and surface tension forces for a drop at terminal velocity. The parameter N_{P} is formed by eliminating the radius between the Davies and Bond numbers. From their observations, Garner and Lihou established that

$$N_{\mathrm{Bo}} N_{\mathrm{P}}^{1/6} = f(N_{\mathrm{P}}^{-1/6} N_{\mathrm{Re}})\,. \tag{10-147}$$

Beard specified this functional relationship from a fit to the experimental results of Gunn and Kinzer (1949) for water drops in air. He found for drops of $535\,\mu\mathrm{m} \leq a_0 \leq 3500\,\mu$m that

$$Y = B_0 + B_1 X + \ldots + B_5 X^5\,, \tag{10-148}$$

with $B_0 = -0.500015 \times 10^1$, $B_1 = +0.523778 \times 10^1$, $B_2 = -0.204914 \times 10^1$, $B_3 = +0.475294$, $B_4 = -0.542819 \times 10^{-1}$, $B_5 = +0.238449 \times 10^{-2}$, and where $X =$

$\ln[(16/3)N_{\mathrm{Bo}}N_{\mathrm{P}}^{1/6}]$, and $N_{\mathrm{Re}} = N_{\mathrm{P}}^{1/6}\exp(Y)$. If we now specify the temperature and pressure of the atmosphere, ρ_{a}, η_{a}, ρ_{w}, and $\sigma_{\mathrm{w/a}}$ are determined and, thus, for a given drop size a_0, N_{Bo} and N_{P} are specified. Since these determine X, Y can be found via (10-148). From Y , the Reynolds number and, hence, U_∞ may be determined.

Some results of this computational scheme are shown in Figures 10.24 and 10.25, in which the respective plots of $N_{\mathrm{Re}} = N_{\mathrm{Re}}(a_0)$ and $U_\infty = U_\infty(a_0)$ are shown. As would be expected, in the latter figure the curve for 1013 mb and 20°C agrees with the experimental data of Gunn and Kinzer. It can be seen that the velocity of large drops increases noticeably with height in the atmosphere from about 9 m sec^{-1} at sea level to a value in excess of 12 m sec^{-1} at 500 mb.

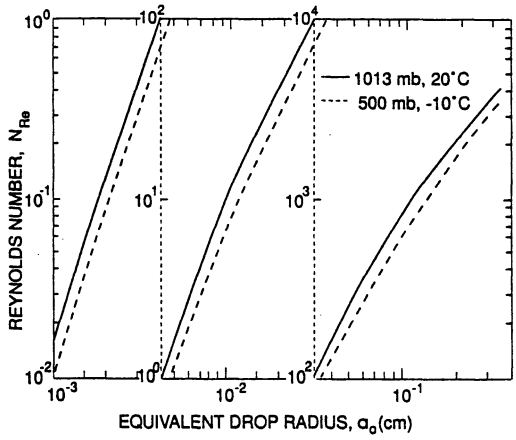


Fig. 10-24: Reynolds number as function of equivalent radius for water drops falling at terminal velocity in air. (Based on the relations of Beard, 1976.)

It is interesting to note from Figure 10.25 that U_∞ becomes independent of size for $a_0 \gtrsim 2.5$ mm. This indicates that the larger the drop, the more it is flattened and, thus, the larger is the cross-section presented to the flow. The consequent increased drag resistance compensates for the increase in gravitational force.

A prediction of a limiting, size-independent terminal velocity follows directly Rayleigh-Taylor instability analysis of the previous section. Thus, from (10-128) and (10-130), we immediately find that for drops of the maximums stable size,

$$U_\infty \approx \left(\frac{4\pi b}{3aC_D}\right)^{1/2}\left(\frac{\rho_{\mathrm{w}} g\sigma_{\mathrm{w/a}}}{\rho_{\mathrm{a}}}\right)^{1/4}, \qquad (10\text{-}149)$$

which is independent of size, except possibly for a weak dependence in the first factor. An equivalent expression was obtained in an entirely different manner by Levich (1962). Equation (10-149) predicts limiting velocity ratios for different levels which agree to within 10% with those displayed in Figure 10.25.

Because of drop vibrations which are excited by the shedding of vortices for $N_{\mathrm{Re}} \gtrsim 300$, one might also expect corresponding fluctuations in drop drag and,

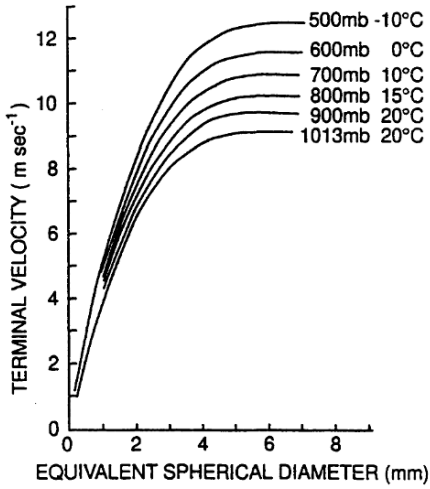


Fig. 10-25: Variation with size of the terminal fall velocity of water drops larger than 500 μm in air. (From Beard, 1976; by courtesy of Am. Meteor. Soc., and the authors.)

hence, terminal velocity. Indeed, as mentioned earlier, such variations in the terminal fall velocity have been observed by Vohl (1989), who studied the fall behavior of drops with $3 \leq D_0 \leq 8$ mm freely suspended in the air of a vertical wind tunnel. As we have seen in the previous section, the velocity response is limited by the relaxation time $\tau_{\rm rel}$ given by (10-132). In view of Figure 10.25, we see that for a drop of $D_0 = 4$ mm with a corresponding terminal fall velocity of 9 m sec^{-1} and an oscillation frequency of about 40 Hz, $\tau_{\rm rel} \approx 0.5$ sec, agreeing well with the relaxation time determined from wind tunnel observations by Vohl (unpubl.). For smaller drops, the vibration frequency rapidly becomes too large to result in a significant fluctuation of U_∞.

Finally, let us estimate the distances and times which are necessary for water drops of various sizes to reach terminal velocity after their release from rest. A completely rigorous treatment of this problem of accelerating motion is complicated by the need to include the $\mathrm{d}\vec{u}/\mathrm{d}t$ term in the equation of motion for the fluid (recall (10-3)). However, arguments presented in Section 14.4.1 demonstrate that the effect of local fluid acceleration is negligible, since $\rho_{\rm a}/\rho_{\rm w} \ll 1$. Hence, it is sufficient to use the steady state drag formulas to describe the hydrodynamic resistance experienced by the drops.

In view of the above remarks and (10-143), the equation of motion for a spherical drop of mass $m_{\rm d}$ and velocity v is

$$m_{\rm d}\frac{\mathrm{d}v}{\mathrm{d}t} = m_d g\left(1 - \frac{\rho_{\rm a}}{\rho_{\rm w}}\right) - 6\pi a\eta_{\rm a}\left(\frac{C_D N_{\rm Re}}{24}\right)v. \qquad (10\text{-}150)$$

In general, this equation must be solved numerically, since both C_D and $N_{\rm Re}$ are functions of v. However, an approximate analytical solution may be obtained for

very small drops falling in the Stokes regime. Then, $C_D N_{\mathrm{Re}}/24 = 1$ and the resulting linear equation may be integrated immediately to obtain

$$v(t) = U_\infty \left[1 - \exp\left(-\frac{6\pi a \eta_a}{m_d} t\right)\right] . \tag{10-151}$$

Thus, the viscous relaxation time for a spherical drop falling in Stokes flow is

$$\tau_S = \frac{m_d}{6\pi a \eta_a} = \frac{2a^2 \rho_w}{9\eta_a} \approx 1.3 \times 10^3 a^2 , \tag{10-152}$$

for $T = 0°\mathrm{C}$, a in cm and τ_S in sec. Similarly, the time required for the drop to reach a fraction β of its terminal velocity is seen to be $t_\beta = -\tau \ln(1 - \beta)$; e.g., $t_{99\%} = 1.02 a^2 \rho_w / \eta_a$. Integration of (10-151) gives for the distance s_β the drop must fall to reach a fraction β of its terminal velocity, the result

$$s_\beta = -\frac{m_d U_\infty}{6\pi a \eta_a} [\ln(1 - \beta) + \beta] . \tag{10-153}$$

For example, $s_{99\%} = 0.80 a^2 \rho_w U_\infty / \eta_a$. Thus, for a 30 μm radius drop falling in air at 20°C, we find $t_{99\%} \approx 5 \times 10^{-2}$ sec and $s_{99\%} \approx 4$ mm$\approx$ 133 drop radii.

Numerical solutions of (10-150) have been given by Wang and Pruppacher (1977a) for conditions under which the assumption of Stokes flow is not valid. The drag was represented by (10-145) or (10-148), depending on the drop size regime, and the atmospheric conditions assumed were $p = 700$ mb, $T = 10°\mathrm{C}$. For $a_0 = 100$, 200, 300, 400, 500 μm, 1.0 mm, and 2.0 mm, they found $s_{99\%}(m) = 0.18$, 0.90, 2.1, 3.6, 5.4, 12.6, and 19.8, respectively. Experimental confirmation of the numerical results has been provided by Sartor and Abbott (1975) and Wang and Pruppacher (1977a). It is clear from these results that in experiments on drop behavior in which drops are released from rest, some care must be taken to ensure a sufficient fall distance for terminal velocities to be achieved at the observation location.

10.4 Hydrodynamic Behavior of Disks, Oblate Spheroids, and Cylinders

We have devoted considerable attention to the hydrodynamic behavior of water drops, partly because they are the most abundant cloud particles and also because their approximately spherical geometry is relatively easy to deal with. We shall now turn to a discussion of the hydrodynamics of ice crystals, based largely on idealize metric models which approximate their shape. As might be expected, we shall find much behavior which is analogous to that of spherical particles. In such cases, therefore, where the differences in the descriptions are due mainly to mathematical details arising from differences in geometry, we shall provide only brief summaries of the essential results and refer the reader to the references for details.

We remarked in Chapter 2 that, to the casual observer, ice crystals appear in a variety of different shapes. Actually, however, these only represent variations of

two fundamental shapes: that of a columnar hexagonal prism and that of a plate-like hexagonal prism. One is tempted, therefore, to approximate the hydrodynamic behavior of ice crystals by that of finite circular cylinders, and of thin circular disks or oblate spheroids. Indeed, Jayaweera and Cottis (1969) have shown by model experiments that for simple columnar and plate-like ice crystals this analogy does hold (Figure 10.26). We shall therefore briefly discuss the relevant hydrodynamics of circular disks, oblate spheroids, and cylinders.

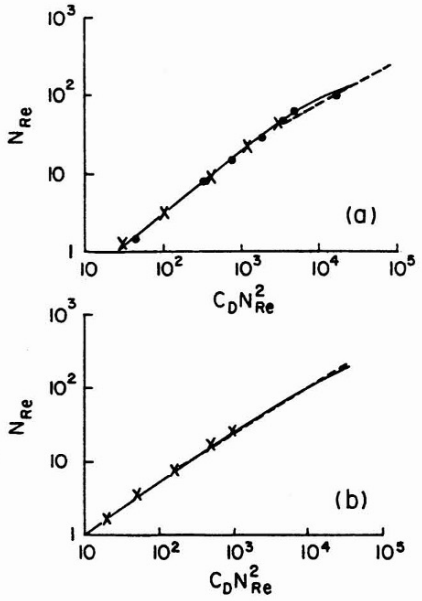


Fig. 10-26: Variation of $C_D N_{Re}^2$ vs. N_{Re} for disks and long, thin cylinders. (a) Schmiedel (1928), circular disks; • Willmarth *et al.* (1964), circular disks; - - - Podzimek (1968), hexagonal disks; × Jayaweera and Cottis (1969), hexagonal disks. (b) — Jayaweera and Mason (1965), long, thin, circular cylinders; - - - Podzimek (1968), hexagonal cylinders; × Jayaweera and Cottis (1969), hexagonal cylinders. (From Jayaweera and Cottis, 1969; by courtesy of *Quart. J. Roy. Meteor. Soc.*)

10.4.1 Circular Disks and Oblate Spheroids

An analytical solution to the Navier-Stokes equation for the (Stokes) flow past an oblate spheroid at negligible Reynolds numbers, parallel to its axis of revolution, was obtained by Oberbeck (1876) (see also Happel and Brenner, 1965). He found the drag to be given by the expression

$$D_{OB} = 8\pi\eta U_\infty \delta / [\lambda_0 - (\lambda_0^2 - 1)\cot^{-1}\lambda_0], \tag{10-154}$$

where $\delta = (a^2 - b^2)^{1/2}$, $\lambda_0 = b/\delta$ and where b and a are the minor and major axes, respectively, of the plate-like crystals. Since the cross-sectional area perpendicular

to the flow is πa^2, the corresponding drag coefficient is, from (10-28),

$$C_{D,\mathrm{OB}} = \frac{32\delta}{aN_{\mathrm{Re}}[\lambda_0 - (\lambda_0^2 - 1)\cot^{-1}\lambda_0]}, \tag{10-155}$$

where the Reynolds number is based on the major axis $2a$. If the oblate spheroid is infinitely thin, i.e.; $b \to 0$, $\lambda_0 \to 0$, $\delta \to a$, we obtain the drag expression for a disk:

$$\lim_{b\to 0} D_{\mathrm{OB}} = 16\pi a U_\infty, \qquad \lim_{b\to 0} C_{D,\mathrm{OB}} = \frac{64}{\pi N_{\mathrm{Re}}}. \tag{10-156}$$

An extension of these results to include first-order inertial effects was accomplished by Aoi (1955). From a study of Oseen flow past an oblate spheroid, he obtained the result

$$C_{D,A} = \frac{32}{N_{\mathrm{Re}}S}\left[1 + \frac{N_{\mathrm{Re}}}{S}\right], \tag{10-157}$$

where $S = a\delta^{-1}[\lambda_0 - (\lambda_0^2 - 1)\cot^{-1}\lambda_0]$. For the case of a disk, this reduces to an expression first obtained by Oseen (1915):

$$C_{D,O} = \frac{64}{\pi N_{\mathrm{Re}}} + \frac{32}{\pi^2}. \tag{10-158}$$

A further extension to include higher-order terms in N_{Re} was carried out by Breach (1961), who used the method of matched asymptotic expansions to obtain the result

$$C_{D,B} = \frac{8m}{3N_{\mathrm{Re}}}\left[1 + \frac{mN_{\mathrm{Re}}}{48} + \frac{m^2}{1440}N_{\mathrm{Re}}^2 \ln(N_{\mathrm{Re}}/2) + O(N_{\mathrm{Re}}^2)\right], \tag{10-159}$$

where $m = 12\mathrm{e}^3(\mathrm{e}(1-\mathrm{e})^{1/2} + (2\mathrm{e}^2 - 1)\tan^{-1}[\mathrm{e}/(1-\mathrm{e}^2)^{1/2}])$ and $\mathrm{e} = [1 - (b/a)^2]^{1/2}$. For a thin disk with eccentricity $\mathrm{e} \to 1$, (10-159) becomes

$$\lim_{\mathrm{e}\to 1} C_{D,B} = \frac{64}{\pi N_{\mathrm{Re}}}\left[1 + \frac{N_{\mathrm{Re}}}{2\pi} + \frac{2N_{\mathrm{Re}}^2}{5\pi^2}\ln(N_{\mathrm{Re}}/2) + O(N_{\mathrm{Re}}^2)\right]. \tag{10-160}$$

All of these results are quite analogous to those which hold for spheres, and so it should come as no surprise to learn they are accurate only for small values of N_{Re}. For moderate to large N_{Re} , one must again resort to numerical solutions of the Navier-Stokes equation. This can be done following procedures like those we discussed earlier for the case of steady state flow past a sphere (10-8), the only additional complication being the need to use oblate spheroidal coordinates (e.g., Rimon and Lugt (1969); Masliyah and Epstein (1970), and Pitter *et al.* (1973)).

As an example of the behavior of viscous flow past an oblate spheroid, the stream function and vorticity fields (as determined by Pitter *et al.*, 1973) are plotted in Figure 10.27 for the case of axial ratio $b/a = 0.05$ and for $N_{\mathrm{Re}} = 1$ and 20. Figure 10.27 shows that flow asymmetry is noticeable even at $N_{\mathrm{Re}} = 1$. A standing eddy develops at $N_{\mathrm{Re}} \approx 1.5$ and grows in length with increasing N_{Re}, reaching a length of $2a$ at $N_{\mathrm{Re}} \approx 30$. The larger the axis ratio of the spheroid, the smaller

the extent of the eddy and the higher the Reynolds number at which it begins to form. This is in good agreement with the experimental observations of Masliyah (1972). In Figure 10.28, the length of the standing eddy at the downstream end of the oblate spheroid is given as a function of N_{Re}. In Figure 10.29, comparison is made between the pressure distributions at the surfaces of a sphere and of oblate spheroids of various b/a. It is seen that with decreasing b/a the variation of the pressure with polar angle becomes increasingly pronounced.

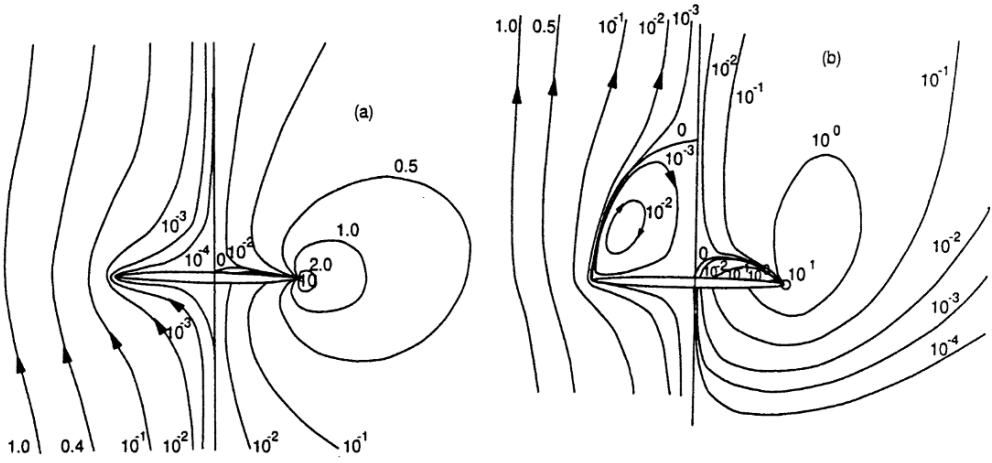


Fig. 10-27: Computed stream function (left) and vorticity distribution (right) around an oblate spheroid of $b/a = 0.05$ at: (a) $N_{\mathrm{Re}} = 1.0$, and (b) $N_{\mathrm{Re}} = 20$. From a numerical solution of the steady state axisymmetric Navier Stokes equation of motion. (From Pitter *et al.*, 1973; by courtesy of Am. Meteor. Soc., and the authors.)

The variation of C_D with N_{Re} for an oblate spheroid of $b/a = 0.05$ is plotted in Figure 10.30. Note that Oberbeck's low Reynolds number solution underestimates C_D on a disk progressively with increasing N_{Re}, while Oseen's solution progressively overestimates it. In Figure 10.31, the dimensionless drag $D/D_{\mathrm{OB}} = C_D/C_{D,\mathrm{OB}}$ is shown as a function of N_{Re}. This figure shows clearly that the analytical solutions are very accurate only for $N_{\mathrm{Re}} < 1$, while the numerical solutions agree excellently with experiments for $N_{\mathrm{Re}} \lesssim 100$. Also note from Figure 10.31 that, in analogy to flow past a sphere, the variation of D/D_{OB} reveals 'drag regimes' within which $\ln(D/D_{\mathrm{OB}} - 1)$ varies roughly linearly with $\ln(N_{\mathrm{Re}})$, and with rather pronounced changes in drag near $N_{\mathrm{Re}} = 1.5$ and $N_{\mathrm{Re}} = 100$. The experiments of Masliyah (1972) and the numerical results of Pitter *et al.* (1973) demonstrate that a standing eddy develops behind a thin oblate spheroid or disk at $N_{\mathrm{Re}} \approx 1.5$, while the experiments of Willmarth *et al.* (1964) show that at $N_{\mathrm{Re}} \approx 100$ the shedding of eddies begins from the downstream end of the disk. Thus, in further analogy to flow past a sphere, its drag regimes are a close manifestation of its flow field regimes.

Assuming that the variation of $C_D N_{\mathrm{Re}}^2$ with N_{Re} for oblate spheroids is only negligibly dependent on b/a for $b/a \leq 0.2$, and is given essentially by the ratio

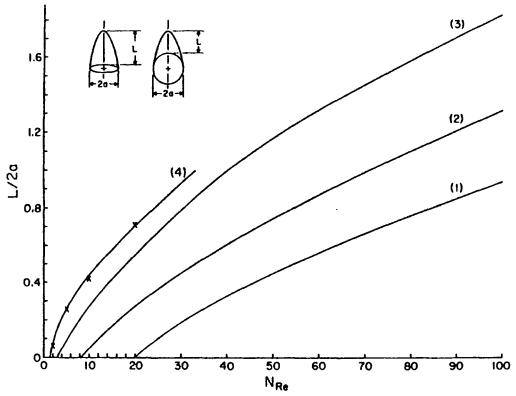


Fig. 10-28: Variation with Reynolds number of the length of the standing eddy at the downstream end of oblate spheroids of different axis ratios: (1) sphere, (2) oblate spheroid, $b/a = 0.5$ (Masliyah and Epstein, 1970), (3) oblate spheroid, $b/a = 0.2$ (Masliyah and Epstein, 1970), (4) oblate spheroid, $b/a = 0.05$. (From Pitter *et al.*, 1973; by courtesy of Am. Meteor. Soc., and the authors.)

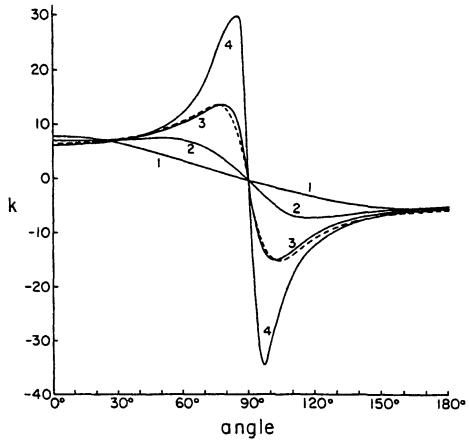


Fig. 10-29: Variation of the dimensionless Pressure with polar angle at the surface of oblate spheroids at $N_{\mathrm{Re}} = 1$; (1) sphere (Le Clair *et al.*, 1970), (2) oblate spheroid, b/a = 0.5 (Masliyah and Epstein, 1970), (3) oblate spheroid, $b/a = 0.2$ (Masliyah and Epstein, 1970), (4) oblate spheroid, $b/a = 0.05$. (From Pitter *et al.*, 1973; by courtesy of Am. Meteor. Soc., and the authors.)

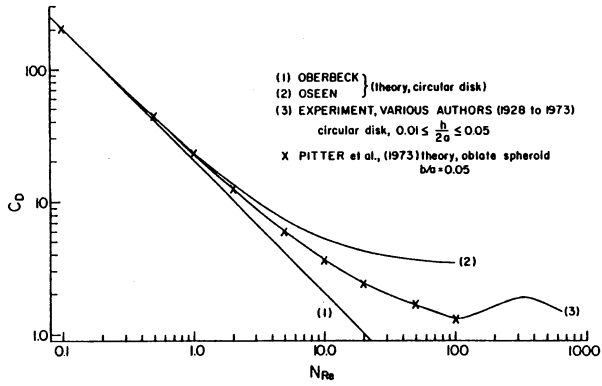


Fig. 10-30: Variation of the drag force coefficient with Reynolds number for thin circular disks and oblate spheroids of $b/a = 0.05$. The experimental results are those of Pitter *et al.* (1973), Jayaweera and Cottis (1969), Willmarth *et al.* (1964), and of Schmiedel (1928). (From Pitter *et al.*, 1973; by courtesy of Am. Meteor. Soc., and the authors.)

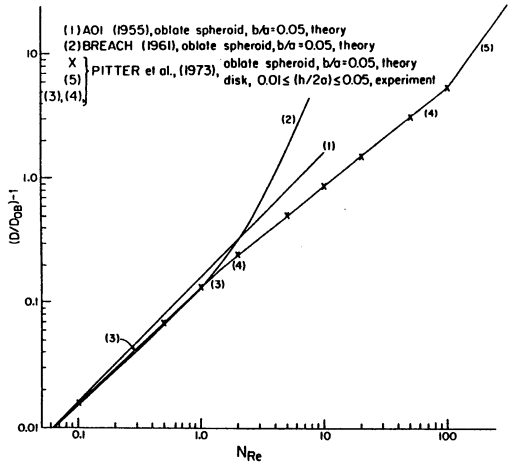


Fig. 10-31: Variation of the dimensionless drag with Reynolds number for thin disks and oblate spheroids of $b/a = 0.05$. The experimental results are those of the authors cited in Figure 10-30. (From Pitter *et al.*, 1973; by courtesy of Am. Meteor. Soc., and the authors.)

found for $b/a = 0.2$ (this is justifiable from the experiments of Jayaweera and Cottis 1969), we may express the functional relationship between $C_D N_{\mathrm{Re}}^2$ and N_{Re} as

$$\log N_{\mathrm{Re}} = B_0 + B_1 X + B_2 X^2 , \tag{10-161}$$

where $X = \log(C_D N_{\mathrm{Re}}^2)$, and $B_0 = -1.3300$, $B_1 = 1.0217$, $B_2 = -0.049018$. The corresponding expression for an oblate spheroid of $b/a = 0.5$ is

$$\log N_{\mathrm{Re}} = B_0 + B_1 X + B_2 X^2 + B_3 X^3 , \tag{10-162}$$

where $X = \log(C_D N_{\mathrm{Re}}^2)$, and $B_0 = -1.3247$, $B_1 = 1.0396$, $B_2 = -0.047556$, $B_3 = -0.002327$.

These relations may be used to approximate the terminal fall velocity of planar ice crystals. For this purpose, we may follow a procedure similar to that outlined in Section 10.3.6, and express $C_D N_{\mathrm{Re}}^2$ as a function of the relevant basic atmospheric parameters. Then, from (10-161) and (10-162), we have N_{Re} and, hence, U_∞ for given atmospheric conditions. The desired expression for $C_D N_{\mathrm{Re}}^2$ is found by equating the drag and gravitational forces; from (10-28) this leads to

$$C_D = \frac{2V_c(\rho_c - \rho_{\mathrm{a}})g}{A_c \rho_{\mathrm{a}} U_\infty^2} , \tag{10-163}$$

where V_c and ρ_c are the volume and density of the ice crystal, and A_c is its equatorial area oriented normal to the flow direction. Thus, for a circular disk of thickness h and radius a, it follows from (10-163) that

$$C_D N_{\mathrm{Re}}^2 = \frac{8a^2 \mathsf{h}(\rho_c - \rho_{\mathrm{a}})\rho_{\mathrm{a}} g}{\eta_{\mathrm{a}}^2} \approx \frac{8 m_c \rho_{\mathrm{a}} g}{\pi \eta^2} , \tag{10-164}$$

where m_c is the mass of the crystal (the small buoyancy force has been ignored in the last form of this equation). Similarly, for an oblate spheroid, we have

$$C_D N_{\mathrm{Re}}^2 = \frac{32a^2 b(\rho_c - \rho_{\mathrm{a}})\rho_{\mathrm{a}} g}{3\eta_{\mathrm{a}}^2} \approx \frac{8 m_c \rho_{\mathrm{a}} g}{\pi \eta_{\mathrm{a}}^2} . \tag{10-165}$$

In view of the close similarity between the motion of circular disks and plate-like hexagonal prisms (recall Figure 10.26), we may also include the case of a hexagonal plate of maximum (circumscribed) radius a and thickness h, for which

$$C_D N_{\mathrm{Re}}^2 = \frac{8a^2 \mathsf{h}(\rho_c - \rho_{\mathrm{a}})\rho_{\mathrm{a}} g}{\eta_{\mathrm{a}}^2} \approx \frac{16 m_c \rho_{\mathrm{a}} g}{3\sqrt{3}\eta_{\mathrm{a}}^2} . \tag{10-166}$$

Depending on the geometry of interest, any of the relations (10-164) to (10-166) may be used in conjunction with either (10-161) or (10-162) to estimate the terminal velocity of planar ice crystals.

This method is only applicable for $N_{\mathrm{Re}} \lesssim 100$, since only for these Reynolds numbers do such objects as thin disks fall stably with their broadest dimension normal to the direction of fall. For $N_{\mathrm{Re}} > 100$, oscillations occur which increase in amplitude with increasing N_{Re}, until eventually a glide-tumbling motion ensues. Finally, at still higher $N_{\mathrm{Re}} (= O(10^3))$, the objects simply tumble (Willmarth *et al.*, 1964; Stringham *et al.*, 1969; Schiller, 1932; Schmiedel, 1928).

10.4.2 Circular Cylinders

It is obvious from Figure 10.26b that the flow past certain columnar snow crystals may be idealized by that past a long, thin circular cylinder falling relatively slowly with $N_{\mathrm{Re}} \leq 45$.

Unfortunately, however, even this idealized geometry has proven overwhelmingly complicated, and there are no known solutions for the flow past such objects. Obviously, the difficulties are associated with the 'end' geometry. On the other hand, there is some empirical evidence which indicates that end effects are often not of great importance. For example, a glance at Plates 4 and 5 shows that while plate-like ice crystals rime preferentially at the edges, indicating a significant flow edge effect, columnar ice crystals rime rather uniformly over their entire length. This indicates that as far as the trajectories of drops past such crystals are concerned, end effects imposed on the streamlines are significant for plate-like crystals but less important for columns. Thus, for our idealization, we shall take one further step and assume the cylinder has infinite length.

At this point, the reader might well anticipate a description of the drag per unit length on a solid cylinder immersed in an otherwise unbounded Stokes flow moving at right angles to the cylinder axis. Curiously enough, such an analogy with our previous discussions cannot be provided, for there is no solution to this problem. A simple demonstration of this fact is possible using elementary dimensional arguments. Thus, if the free stream velocity is U_∞ and the cylinder radius is a, the force per unit length, f, can only depend on a, U_∞, and η. However, since the only dimensionless group that can be formed from these variables is $f/\eta U_\infty$ we conclude that $f = A\eta U_\infty$, where A is a dimensionless constant. This is clearly impossible, since the force per unit length must also depend on the radius a; e.g., we should have $f = 0$ if $a = 0$.

The resolution of this so-called 'Stokes paradox' requires recognition of the fact that the assumption of negligible fluid inertia everywhere cannot hold at infinity (see Section 10.2.2.3). Thus, one must turn to the Oseen equations for the simplest analytical estimate of the drag per unit length on an infinite cylinder in low Reynolds number flow. This was achieved by Lamb (1911) (also in Lamb,1945, §343), who found the drag coefficient per unit length to be given by

$$C'_D \equiv \frac{D}{(1/2)\rho U_\infty^2 d} = \frac{8\pi}{N_{\mathrm{Re}}[\ln(8/N_{\mathrm{Re}}) - \gamma + \frac{1}{2}]}, \tag{10-167}$$

where $\gamma = 0.57722\ldots$ is Euler's constant, and where d is the diameter of the cylinder. This expression progressively overestimates the drag for $N_{\mathrm{Re}} \gtrsim 0.2$.

Numerical solutions to the problem of flow past an infinite cylinder can be constructed, for example, by following a vorticity-stream function approach similar to that we discussed earlier for the case of a sphere. Numerical solutions have been obtained by Thom (1933), Kawaguti (1953), Hamielec and Raal (1969), Takami and Keller (1969), Griffin (1972), and Schlamp *et al.* (1975) and Schlamp and Pruppacher (1977). Some representative results are displayed in Figure 10.32, which shows the streamline and vorticity fields for $N_{\mathrm{Re}} = 1$ and 20. Note that, as was the case for disks and thin spheroids, the flow has fore-aft asymmetry even at

$N_{\mathrm{Re}} = 1$. At $N_{\mathrm{Re}} = 20$ a standing eddy of considerable length has developed at the downstream end of the cylinder. In Figure 10.33, a comparison shows excellent agreement between the theoretical and experimental eddy lengths. Note that the eddy begins to develop at $N_{\mathrm{Re}} \approx 6$ and subsequently grows linearly with increasing N_{Re}. Comparison with the case of flow past a sphere shows that, at a given N_{Re} , the standing eddy on a cylinder is considerably larger than that on a sphere. This result implies a longer range wake influence on cloud particles in the vicinity of a columnar ice crystal than would be the case for a spherical drop of comparable radius.

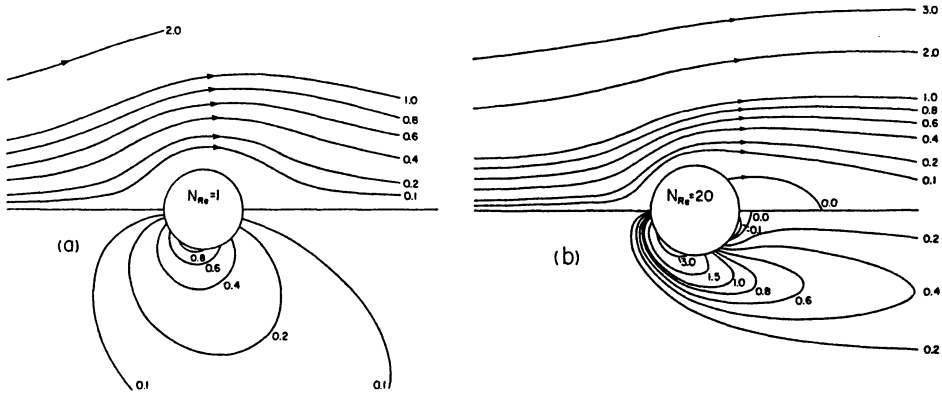


Fig. 10-32: Computed stream function (upper portion of figure) and vorticity distribution (lower portion of figure) around a circular cylinder at (a) $N_{\mathrm{Re}} = 1$ and (b) $N_{\mathrm{Re}} = 20$. From a numerical solution to the steady state axisymmetric Navier-Stokes equation of motion for an infinite cylinder.

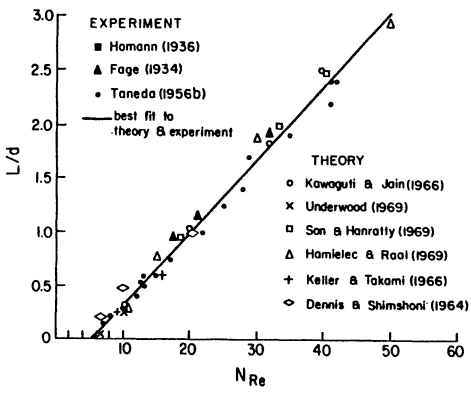


Fig. 10-33: Variation with Reynolds number of the length of the standing eddy at the downstream end of an infinitely long circular cylinder. (From Pruppacher *et al.*, 1970; by permission of Cambridge University Press.)

A comparison of drag coefficients as determined by theory and experiment is given Figure 10.34. The agreement for the case of 'infinite' cylinders is seen to be excellent. The figure also shows that C_D for a finite cylinder depends relatively strongly on the shape factor d/L, where L is the length and d the diameter of the cylinder. This is in contrast to the dependence of C_D on the axis ratio b/a for thin oblate spheroids and disks. It is obvious from these results that the numerical determinations of C_D for an infinite cylinder cannot provide an accurate description of the behavior of most columnar ice crystals.

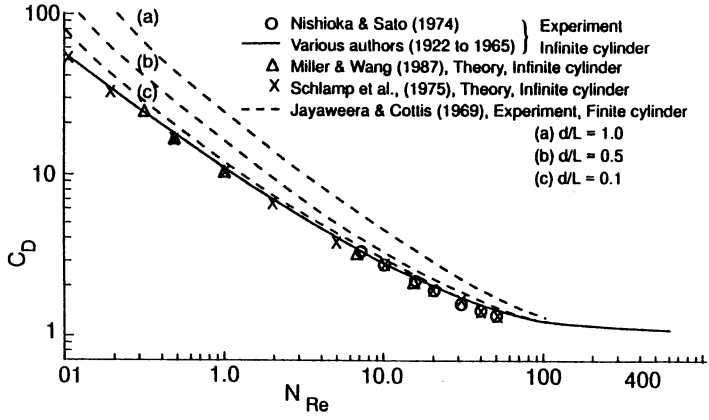


Fig. 10-34: Variation with Reynolds number of the drag force coefficient for circular cylinders of various diameter-to-length ratios. The experimental results for C_D on an infinite cylinder are those of Wieselberger (1922), Finn (1953, Tritton (1959), and Jayaweera and Mason (1965). (From Schlamp *et al.*, 1977, with changes.)

The experimental values of Jayaweera and Cottis for C_D shown in Figure 10.34 may be represented adequately by the following empirical expressions:

$$\log N_{\mathrm{Re}} = B_0 + B_1 X + B_2 X^2 + B_3 X^3 \,, \tag{10-168}$$

where $X = \log(C_D N_{\mathrm{Re}}^2)$. For $(d/\mathsf{L}) = 1.0$, $B_0 = -1.3100$, $B_1 = 0.98968$, $B_2 = -0.042379$, $B_3 = 0$. For $(d/\mathsf{L}) = 0.5$, $B_0 = -1.11812$, $B_1 = 0.97084$, $B_2 = -0.058810$, $B_3 = 0.002159$. For $(d/\mathsf{L}) = 0.1$, $B_0 = -0.90629$, $B_1 = 0.90412$, $B_2 = -0.059312$, $B_3 = 0.0029941$. For $(d/\mathsf{L}) = 0$ (infinite cylinder), $B_0 = -0.79888$, $B_1 = 0.80817$, $B_2 = -0.030528$, $B_3 = 0$. As we have done previously for spheres, spheroids, and disks, we may use (10-168) as a basis for estimating the terminal velocity of columnar ice crystals. Thus, from an elementary and by now familiar calculation, the Best or Davies number for a circular ice cylinder of length L, radius a, and mass m_c is

$$C_D N_{\mathrm{Re}}^2 = \frac{4\pi a^3(\rho_c - \rho_{\mathrm{a}})\rho_{\mathrm{a}} g}{\eta_{\mathrm{a}}^2} \approx \frac{4 m_c a \rho_{\mathrm{a}} g}{\mathsf{L}\eta_{\mathrm{a}}^2} \,. \tag{10-169}$$

Similarly, for a hexagonal cylinder of length L and radius a of the base circumscribed circle, we find

$$C_D N_{\mathrm{Re}}^2 = \frac{6\sqrt{3}a^3(\rho_c - \rho_a)\rho_a g}{\eta_a^2} \approx \frac{4m_c a \rho_a g}{L\eta_a^2} . \qquad (10\text{-}170)$$

Therefore, for a given columnar crystal geometry and atmospheric conditions, $N_{\mathrm{Re}}(= 2U_\infty a\rho_a/\eta_a)$ and, hence, U_∞ may be found by substituting (10-169) or (10-170) into (10-168).

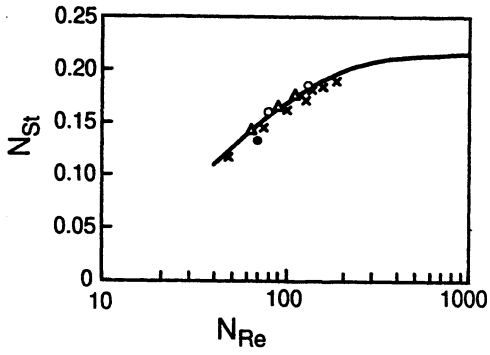


Fig. 10-35: Variation with Reynolds number of the dimensionless shedding frequency i.e. the Strouhal number, from the near of falling cylinders. (—) Experiments (Chillukuri, 1987), (×) experiments (Tritton, 1971), (△) experiments (Roshko, 1954), (○) theory (Chillukuri, 1987), (•) theory (Ji & Wang, 1991). (From Ji and Wang, 1991, with changes.)

Experiments of Jayaweera and Mason (1965) show (Plate 14) that the ends of cylinders with finite length and with $N_{\mathrm{Re}} < 40$ strongly affects the shape of the flow behind the falling cylinder. From Plate 14, we notice that the downstream flow is not uniform across the length of the cylinder, but instead has a pyramidal shape. Experiments of Homann (1936), Roshko (1954), Taneda (1956b), Tritton (1971) and Chillukuri (1987) have shown that the standing eddy at the downstream end of an infinite cylinder begins to 'shed' at $N_{\mathrm{Re}} \approx 40$. Measurements by Relf and Simmons (1924) and Jayaweera and Mason (1965) have demonstrated that the shedding frequency for a given N_{Re} is somewhat larger than that for a sphere (Figure 10.35). The three-dimensional, non-steady state flow past falling cylinders of finite length and $N_{\mathrm{Re}} > 40$ has been photographed by Jayaweera and Mason (1965) (see Plate 15).

In order to describe the flow past finite length cylinders, Ji and Wang (1991) solved the non-steady state Navier-Stokes equation of motion (10-7) in three dimensions using numerical methods analogous to those used to describe the three-dimensional, non-steady state flow past a sphere (Section 10.2.4). Notice from comparing Plates 14 and 15 with Figures 10.36 and 10.37 that excellent agreement with observed flows is obtained at $N_{\mathrm{Re}} = 40$ and $N_{\mathrm{Re}} = 70$.

As in the case for falling spheres and plate-like bodies, Jayaweera and Mason (1965) found experimentally that falling cylinders exhibit secondary motions in

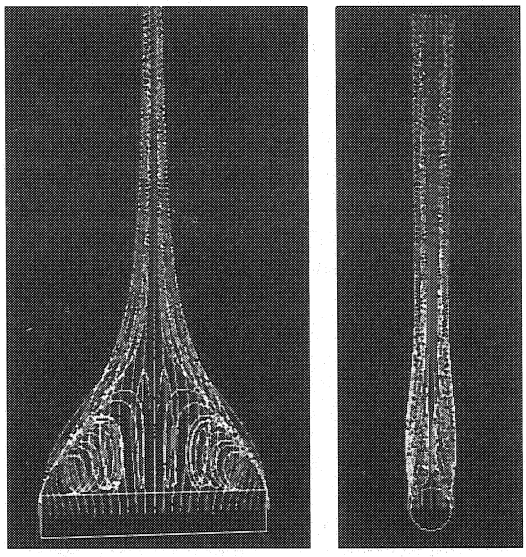


Fig. 10-36: Computed trajectories of massless marker particles for flow past a cylinder of finite length, for $(d/\mathsf{L}) = 0.18$ and $N_{\mathrm{Re}} = 40$. From a numerical solution of the time dependent three-dimensional Navier-Stokes equation of motion. Left: broad side view, right: end view. (From Ji & Wang, 1991; by courtesy of the authors, copyrighted by Springer-Verlag.)

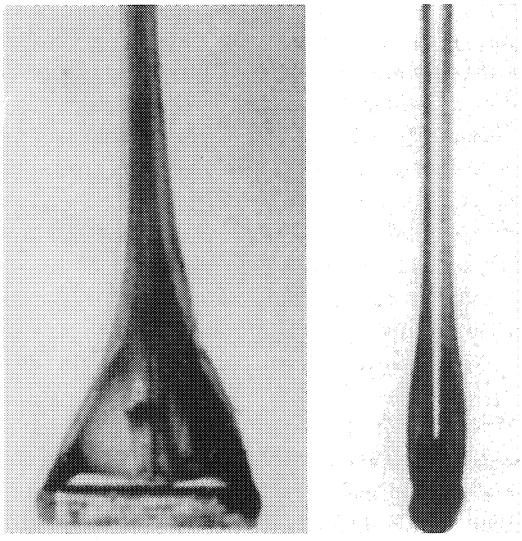


Plate 14. Visualized flow in the rear of a freely falling cylinder of finite length; for $N_{Re} = 40$; left: broad side-on, right: end-on; $(d/\mathsf{L}) = 0.18$. (From Jayaweera & Mason, 1965; by courtesy of the authors; copyrighted, 1965 by Cambridge University Press.)

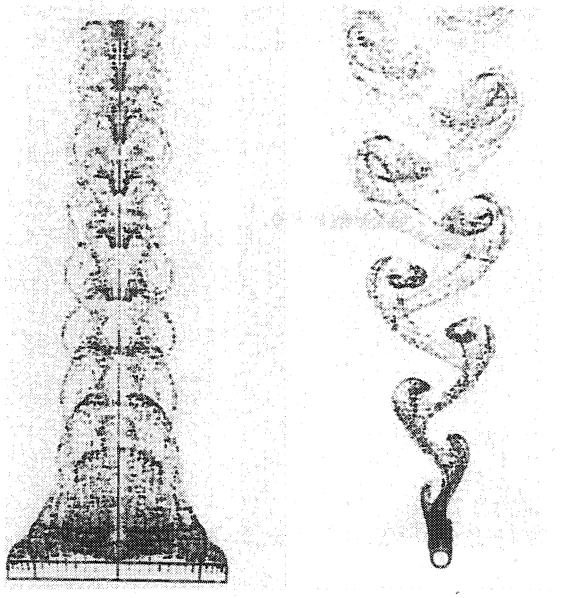


Fig. 10-37: Computed trajectories of massless marker particles for flow past a cylinder of finite lenght, for $(d/\mathsf{L}) = 0.07$ and $N_{\mathrm{Re}} = 70$. From a numerical solution of the time dependent three-dimensional Navier Stokes equation of motion. Left: broad side view, right: end view. (From Ji & Wang, 1991; by courtesy of the authors, copyrighted by Springer-Verlag.)

respond to the shedding of eddies from their rear. They showed that at $N_{\mathrm{Re}} < 40$ cylinders of all axis ratios d/L fall stably with their broadest extension oriented horizontally. For $N_{\mathrm{Re}} > 0$, the cylinders fluttered in a way that depended critically on the value of d/L. Thus, for $d/\mathsf{L} = 0.1$, fluttering was observed only if $N_{\mathrm{Re}} \gtrsim 100$. For $d/\mathsf{L} = 0.05$, fluttering required $N_{\mathrm{Re}} > 200$. With further decrease in d/L the Reynold number required for fluttering to occur increased rapidly, so that for $(d/\mathsf{L}) = 0.04$, i.e. for very long cylinder, no fluttering was observed even at $N_{\mathrm{Re}} = 1000$.

10.5 Hydrodynamic Behavior of Snow Crystals, Snow Flakes, Graupel and Hailstones

10.5.1 Flow Field and Drag

The complicated shapes of snow crystals make a theoretical determination of the flow field past them a very difficult task indeed. Recently, however, Ji and Wang (1990) and Ji (1991) succeeded in solving the non-steady state Navier-Stokes equation of motion (10-7) in three dimensions by numerical techniques (see Section 10.2.4) to determine the flow past two of the more simple crystal shapes, the simple hexagonal plate (type P1a), and the broad branched crystal (type P1c). The steady state velocity field of flow past a broad branched crystal at $N_{\mathrm{Re}} = 80$ is illustrated in

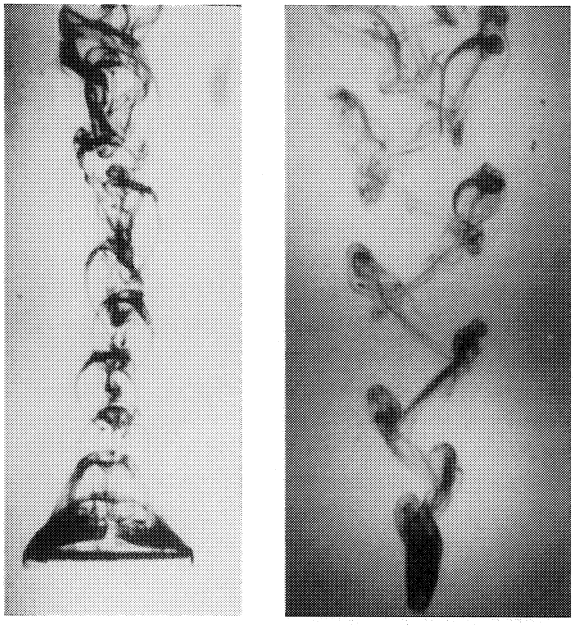


Plate 15. Visualized flow in the rear of a freely falling cyclinder of finite length; for N_{Re} = 70; left: broad side-on, right: end-on; $(d/\mathrm{L}) = 0.07$. (From Jayaweera & Mason, 1965; by courtesy of the authors; copyrighted, 1965 by Cambridge University Press.)

Figure 10.38a. In Figure 10.38b, the non-steady flow field past a simple hexagonal plate is illustrated for $N_{\mathrm{Re}} = 140$. We notice the symmetric eddies in the rear of the crystal at $N_{\mathrm{Re}} < 100$, and the asymmetric turbulent features in the rear of the crystal for $N_{\mathrm{Re}} > 100$. The length of the stationary eddy in the rear of the two crystal types is given in Figure 10.39 as a function of N_{Re}. We note that the eddy behind the hexagonal plate is larger than that behind a broad branched crystal and approximates well the length of the eddy behind an oblate spheroid of the same axis ratio (see Figure 10.28). The drag force coefficients C_D computed by Ji (1991) are plotted in Figure 10.40 where they are compared with C_D values for crystal models of the same and other shapes. We note from this figure that the more pronounced the dendritic shape features are, the larger is the drag force coefficient of planar crystal models at the same Reynolds number. This, of course, is a result of the larger surface area which dendritic crystals expose to a surrounding medium during their fall.

Values for the drag force coefficients of graupel models are also included in Figure 10.40. We note that for $N_{\mathrm{Re}} > 100$, C_D of a smooth conical graupel models is larger than that for a sphere at the same Reynolds number, while for $N_{\mathrm{Re}} \leq 100$, the values for C_D are approximately the same. Zikmunda and Vali (1972) determined C_D for natural graupel particles, and found that C_D was larger than for the smooth conical models, in particular at $N_{\mathrm{Re}} < 500$. This result was attributed to surface roughness of the natural graupel.

List *et al.* (1973) measured C_D for smooth oblate spheroidal hailstone models of

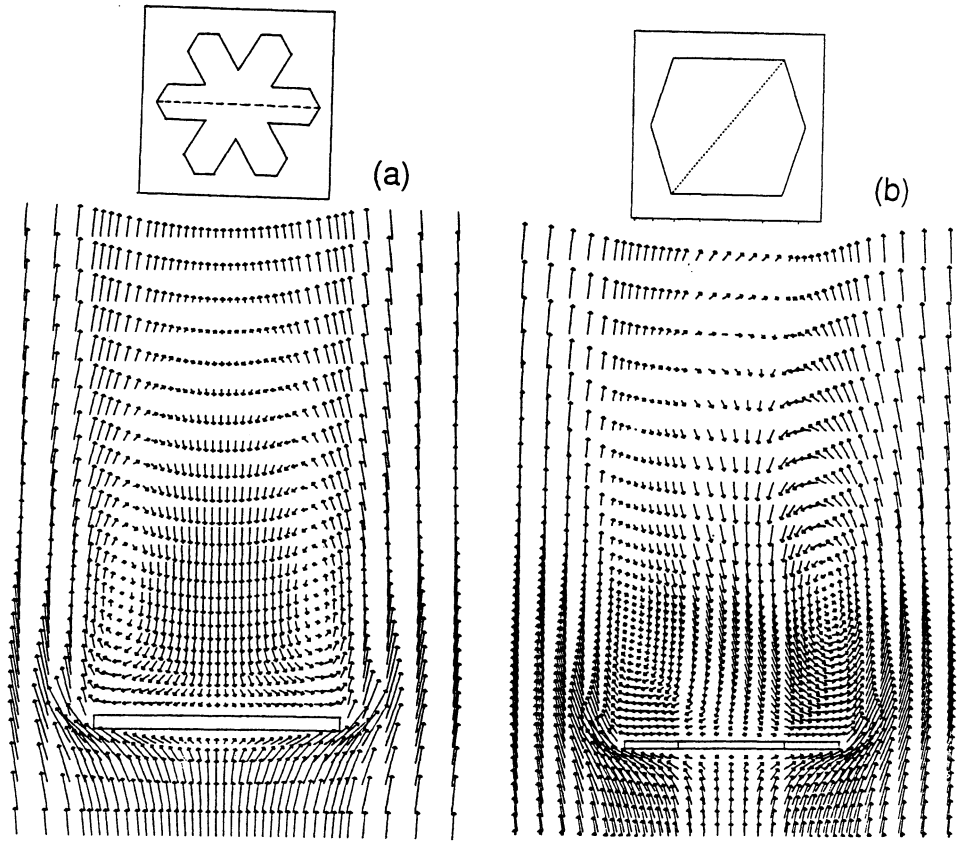


Fig. 10-38: Velocity fields around planar snow crystal models falling at terminal velocity in air. (a) broad-branched crystal, $N_{\mathrm{Re}} = 80$, $b/a = 0.05$, (b) simple hexagonal plate, $N_{\mathrm{Re}} = 140$, $b/a = 0.05$. From a numerical solution of the time dependent three-dimensional Navier Stokes equation of motion. (From Ji, 1991; by courtesy of the author.)

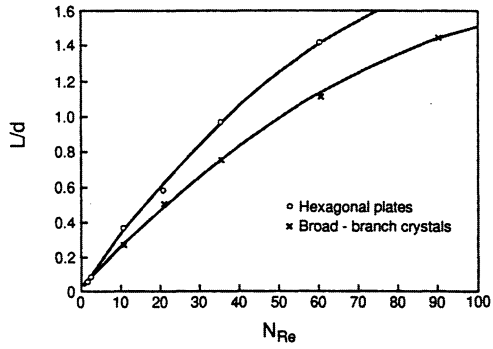


Fig. 10-39: Variation with Reynolds number of the length of the standing eddy at the downstream end of two snow crystal types; for $b/a = 0.046$ and 0.026. (From Ji, 1991, by courtesy of the author.)

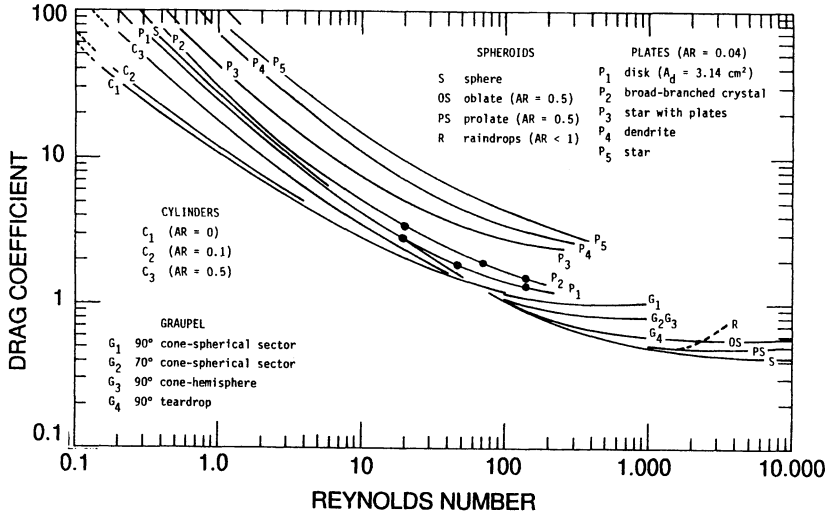


Fig. 10-40: Drag force coefficient of various shaped bodies as a function of Reynolds number based on laboratory studies. Comparison of P_1 and P_2 bodies with theoretical calculations of Ji and Wang (1990). (From Beard, 1980, with changes.)

various axis ratios and for $4\times10^4 \leq N_{\mathrm{Re}} \leq 4\times10^5$. Depending on the angle of attack ($\theta = 0°$ to $90°$) of the flow past the spheroid, C_D was found to vary between 0.2 and 0.85. The variation of C_D with N_{Re} for $\theta = 45°$ is illustrated in Figure 10.41, where comparison is made with C_D for a sphere. Note the sharp drop in C_D which occurs for large N_{Re}. Qualitatively, this 'drag crisis' corresponds to a transition from a laminar to a turbulent boundary layer. Turbulence in the boundary layer brings more fluid momentum closer to the boundary surface. This counteracts the effect of the adverse pressure gradient acting on the downstream side of the surface, so that the flow separation phenomenon is suppressed and, hence, the pressure drag is reduced (recall the discussion of separation in Section 10.2.2.3). Figure 10.41 shows that the drag crisis transition point is affected by the axis ratio of the oblate spheroid.

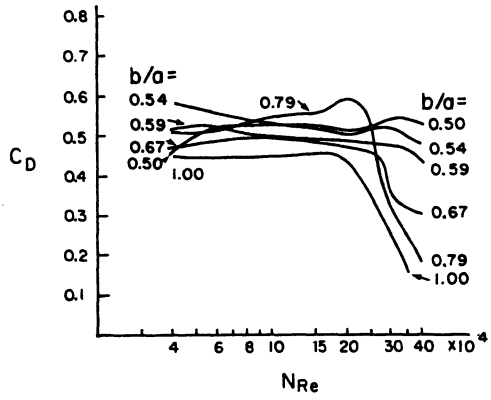


Fig. 10-41: Variation with Reynolds number of the drag force coefficient of oblate spheroids, for an angle of attack of 45° C. (From List *et al.*, 1973; by courtesy of Am. Meteor. Soc., and the authors.)

Young and Browning (1967) and List *et al.* (1969) used spherical hailstone models with close packed hemispherical roughness elements on their surfaces to study the effect of surface roughness on C_D of hailstones. Their observations showed that, except for uncommonly high surface roughness, the drag force coefficient varied unsystematically in value and sign, and differed by less than ±10% from that of a smooth sphere at the same Reynolds number. Both studies agreed, however, that with increasing surface roughness the transition to a turbulent boundary layer occurred at progressively lower Reynolds numbers.

List (1959), Macklin and Ludlam (1961), Bailey and Macklin (1968a), and Landry and Hardy (1970) measured C_D of natural and artificially grown hailstones. Depending on the angle of attack of the air flow, C_D was found to vary between about 0.3 and 0.8 for N_{Re} between 10^3 and 10^5. Knight and Heymsfield (1983) determined C_D for natural hailstones freshly fallen during a hailstorm in Colorado. These results may be summarized by $C_D = 18.1N_{\mathrm{Re}}^{-0.367}$ and $C_D = 0.77d_0^{-0.48}$. For soaked hailstones, they found $C_D = 0.191N_{\mathrm{Re}}^{0.173}$, and $C_D = 0.863d_0^{0.424}$, with the equivalent spherical diameter d_0 in cm.

10.5.2 Fall Velocity

The fall velocity of plate-like and columnar crystals may be estimated from drag data by idealizing their shape in terms of thin oblate spheroids or disks and hexagonal cylinders (see Figure 10.26). For example, from the thickness h, maximum radius a, and density ρ_c of a planar crystal, a value for $C_D N_{\mathrm{Re}}^2$ may be determined for given atmospheric conditions from (10-166). Then, from (10-161) or (10-162), one may compute N_{Re} for the equivalent circular disk, which is the disk with the same mass and thickness as the crystal. Since the radius of this disk is $a = (m_c/\pi \mathsf{h} \rho_c)^{1/2}$, the terminal velocity U_∞ may now be estimated from the relation $U_\infty = \eta_a N_{\mathrm{Re}}/2a\rho_a$.

This approach has been followed by Jayaweera and Cottis (1969), Jayaweera (1972b), Jayaweera and Ryan (1972), Kajikawa (1971, 1972, 1973), and Heymsfield (1972). Some selected results are summarized in Figure 10.42. We notice that the theoretical predictions are in satisfactory agreement with actually observed fall velocities. Figure 10.42 also indicates that the more pronounced are the dendritic shape features, the lower the fall velocity for a plate-type ice crystal of given maximum radius. For a given crystal size, this follows from the decrease of its mass and the increase of its drag with an increase in dendritic features.

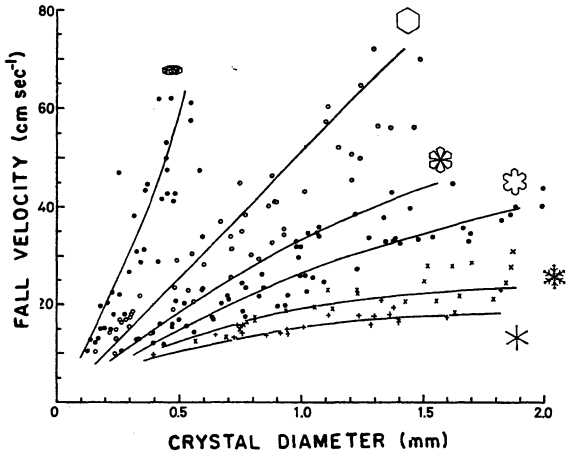


Fig. 10-42: Variation with size of observed terminal fall velocities (symbols) and velocities computed from drag data (lines) for ice crystals of various shapes, $-10°$C, 1000 mb. (From Kajikawa, 1972; by courtesy of *J. Meteor. Soc., Japan.*)

A similar approach may be used for computing the terminal velocity of columnar crystals idealized as hexagonal cylinders. Thus, from the crystal dimensions and atmospheric conditions $C_D N_{\mathrm{Re}}^2$ may be determined from (10-170). Then, from (10-168), N_{Re} may be computed. Once N_{Re} is known, U_∞ may be found from the definition of the Reynolds number, with $a = (2\sqrt{3} m_c/9\mathsf{L}\rho_c)^{1/2}$.

Similarly, studies of ice particles in cirrus clouds by Heymsfield (1972) have demonstrated that U_∞ for a bullet-shaped ice crystal may be determined from

its equivalent cylinder if one sets $(C_D N_{\mathrm{Re}}^2)_{\mathrm{bullet}} = 1.67(w/\mathrm{L})^{0.24}(C_D N_{\mathrm{Re}}^2)_{\mathrm{equiv.\ cyl.}}$, where w is the width of the bullet crystal.

By idealizing graupel particles and hailstones as spherical particles of diameter d, Rasmussen and Heymsfield (1987a) derived relations for $C_D N_{\mathrm{Re}}^2$ vs. N_{Re} from a large number of drag force coefficients C_D determined experimentally for natural hailstones and hailstone models. Their expirical relationships may be expressed as follows:

$$\log N_{\mathrm{Re}} = B_0 + B_1 Y + B_2 Y^2\,; \qquad 1 \le N_{\mathrm{Re}} \le 12.2\,, \tag{10-171a}$$

$$\log N_{\mathrm{Re}} = B_3 + B_4 Y + B_5 Y^2 + B_6 Y^3\,; \qquad 12.2 \le N_{\mathrm{Re}} \le 30\,, \tag{10-171b}$$

$$N_{\mathrm{Re}} = B_7 X^{B_8}\,; \qquad 30 \le N_{\mathrm{Re}} \le 2.4 \times 10^4\,, \tag{10-171c}$$

$$N_{\mathrm{Re}} = (X/B_9)^{1/2}\,; \qquad 2.4{\times}10^4 \le N_{\mathrm{Re}} \le 3{\times}10^5, \tag{10-171d}$$

with $B_0 = 1.7095$, $B_1 = 1.33438$, $B_2 = 0.11591$, $B_3 = -1.81391$, $B_4 = 1.34671$, $B_5 = -0.12427$, $B_6 = 0.0063$, $B_7 = 0.4487$, $B_8 = 0.5536$, $B_9 = 0.6$, and where $Y = \log X$, and $X = C_D N_{\mathrm{Re}}^2$. For a spherical hailstone or graupel particles of mass m_G,

$$X = C_D N_{\mathrm{Re}}^2 = 8 m_G g \rho_{\mathrm{a}} / \pi \eta_{\mathrm{a}}^2\,. \tag{10-172}$$

For an ice particle of a given mass and for given atmospheric conditions, x may thus be evaluated. N_{Re} can then be calculated from (10-171). Once N_{Re} is known, the terminal velocity follows from the definition of N_{Re}.

Despite the availability of values for C_D (and therefore $C_D N_{\mathrm{Re}}^2$) vs. N_{Re}, there is little justification for computing the terminal velocity of graupel particles and hailstones of a shape which deviates significantly from that of a sphere by using $C_D N_{\mathrm{Re}}^2$ values, since neither the volume of these particles nor their cross-sectional area perpendicular to the flow are well-defined in (10-163). The same conclusion applies also to snow crystal aggregates (or snow flakes). Additional complications arise further from the oscillatory spinning and tumbling motions of these ice particles. It is therefore necessary to resort to observations on natural particles to find U_∞. Such observations are also needed to verify the accuracy of computing U_∞ by means of the drag method.

Unfortunately, observations of U_∞ for natural ice particles apply only to the temperature and pressure level at which the observations were made. Since U_∞ is strongly dependent on both of these parameters, corrections are necessary to obtain U_∞ at other levels. A velocity adjustment for a particle of fixed shape has been suggested by Beard (1980) based on drag force coefficients obtained from experiments with models which simulate the shape of various ice particles. His studies suggest the velocity adjustment factor, $f = U_\infty / U_{\infty,o}$ may be computed from the relations

$$f = f_s + (f_\infty - f_s)(1.61 + \ln N_{\mathrm{Re},o})/8.52\,; \qquad 0.2 < N_{\mathrm{Re}} < 1000\,, \tag{10-173a}$$

$$f = f_\infty = (\rho_{\mathrm{a},o}/\rho_{\mathrm{a}})^{1/2}\,; \qquad N_{\mathrm{Re}} \ge 1000\,, \tag{10-173b}$$

$$f = f_s = (\eta_{\mathrm{a},o}/\eta_{\mathrm{a}})\,; \qquad N_{\mathrm{Re}} \le 0.2\,. \tag{10-173c}$$

Here the subscript 'o' represents the reference level at which the velocity was observed. In a later study, Beard and Heymsfield (1988) verified this velocity adjustment model by a slightly different technique.

Field studies of the terminal velocity of various types of ice particles have been carried out by Nakaya and Tereda (1935), Magono (1951, 1954b), Langleben (1954), Litvinov (1956), Bashkirova and Pershina (1964a,b), Magono and Nakamura (1965), Fukuta (1969), Brown (1970), Jiusto and Bothworth (1971), and Jawaweera and Ryan (1972). The most reliable values for the fall velocity of natural ice particles have been obtained by Kajikawa on Mt. Teine (1024 m MSL) on Hokkaido Isld. His velocities for unrimed, planar snow crystals are reported in Kajikawa (1972, 1975b). Best fit curves to some of these velocities are given in Figure 10.42. Fall velocites for unrimed columnar crystals are given in Kajikawa (1976), for various rimed snow crystals in Kajikawa (1975a,b), and for 'early' snow flakes consisting of 2 to 6 component crystals in Kajikawa (1989). Additional extensive sets of fall velocity measurements were provided by Locatelli and Hobbs (1974), whose observations were made in the Cascade Mts. (750-1500 m MSL, Washington), and by Zikmunda (1972) and Zikmunda and Vali (1972) on Elk Mt. (3350 m MSL, Wyoming). Best fit curves to the fall velocity of aggregates and graupel observed by Locatelli and Hobbs are given in Figures 10.43 and 10.44. We notice from these curves that the fall velocity increases with the maximum dimension of the ice particles in a manner which depends significantly on the degree of riming of the graupels, as well as on the type and number of component crystals in the aggregates.

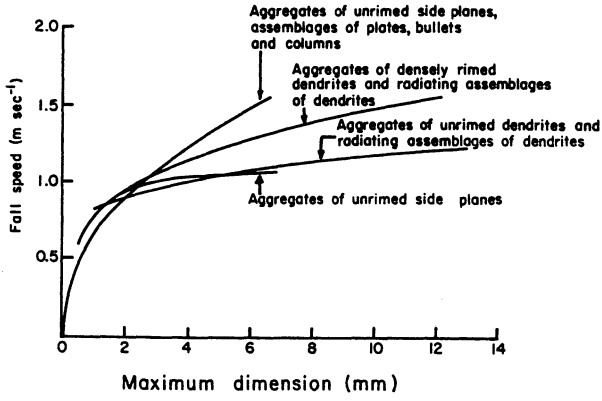


Fig. 10-43: Best fit curves for the fall velocity versus maximum dimension of various ice crystal aggregates; observed on the Cascade Mts. (750-1500 m, State of Washington). (From Locatelli and Hobbs, 1974; by courtesy of the authors; copyrighted by Am. Geophys. Union.)

Observations show that the size-mass relation for a given ice particle type varies significantly from one storm to another, and even during the life cycle of one particular cloud. It is therefore not surprising that one finds corresponding variations

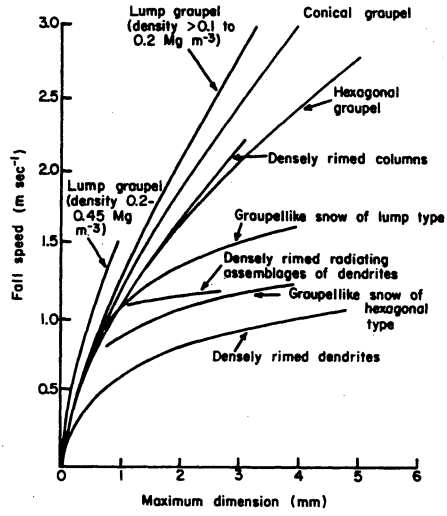


Fig. 10-44: Best fit curves for the fall velocity versus maximum dimension of graupel particles of various types. (From Locatelli and Hobbs, 1974; by courtesy of the authors; copyrighted by Am. Geophys. Union.)

also in the fall velocity of these particles. For these reasons, the empirical relations given in the literature for U_∞ (m_c or d_c) apply strictly only to the particular storm or cloud system for which the relation was obtained, and do not have general applicability. Nevertheless, to meet the need for such relations in contemporary cloud models, we have given some selected relations in Tables 10.3a,b, 10.4, 10.5, and 10.6, chosen such that they correspond to the mass-size relations in Chapter 2.

Terminal fall velocities of large graupel and hailstones have been determined by Bilham and Relf (1937), List (1959), Macklin and Ludlam (1961), Williamson and McCready (1968), Auer (1972b), and Roos (1972) from direct observations as well as from observed drag force coefficients. From (10-28), we find for a roughly spherical hailstone falling at terminal velocity,

$$U_\infty(\text{m sec}^{-1}) \approx 0.36(\rho_H d/C_D\rho_a)^{1/2}\,, \tag{10-174}$$

where ρ_H and ρ_a are the densities of the hailstone and the air, respectively, d(cm) is the average diameter of the hailstone, and we have assumed $g = 981$ cm sec^{-2}. Using appropriate values for ρ_H, C_D, and ρ_a, terminal velocities for hailstones can be computed from (10-174) which are in fair agreement with those directly observed. A summary of observed terminal velocities of hailstones and large graupel has been given by Auer (1972b). At the 800 mb level and 0°C, these values can be fitted to the relation

$$U_\infty(\text{m sec}^{-1}) \approx 9d^{0.8}\,, \tag{10-175}$$

for the range $0.1 \lesssim d \lesssim 8$ cm with d(cm).

TABLE 10.3a

Terminal fall velocity of unrimed snow crystals of various types; velocity-size relation for planar crystals. The corresponding mass-size relations are given in Tables 2-4a,b. (Based on data of Heymsfield & Kajikawa, 1987, and of Kajikawa, 1976.)

Habit designation	Diameter range (mm)	Terminal velocity range (cm s^{-1})	U_∞ (cm sec^{-1}) for 1000 mb
Clh	0.3 - 0.6	28 - 66	1457 $d^{1.09}$
Pla	0.3 - 1.5	14 - 71	297 $d^{0.86}$
Plb	0.4 - 1.6	15 - 45	190 $d^{0.81}$
Plc	0.5 - 2.8	15 - 46	103 $d^{0.62}$
Pld	0.4 - 2.4	10 - 35	58 $d^{0.55}$
Ple	0.6 - 5.3	13 - 43	55 $d^{0.48}$
P2a	0.7 - 3.0	33 - 61	72 $d^{0.33}$
P2c	1.3 - 5.6	30 - 59	54 $d^{0.20}$
P2e	0.5 - 2.1	19 - 56	129 $d^{0.68}$
P2g	0.7 - 2.8	23 - 69	160 $d^{0.80}$
P6c	1.6 - 4.9	36 - 57	57 $d^{0.21}$
P6d	2.0 - 6.5	31 - 58	60 $d^{0.37}$
P7b	1.2 - 3.3	28 - 57	137 $d^{0.83}$

TABLE 10.3b

As Table 10-3a but velocity-mass relation for columnar crystals.

Habit designation	U_∞ (cm sec^{-1}) at 1024 m
Nla	155 $m^{0.271}$
Clf	253 $m^{0.271}$

TABLE 10.4

Terminal fall velocity-mass relationships for early snow flakes consisting of 2 to 6 plate-like component crystals; observed on Mt. Tine (1024m), Hokkaido, Japan. The corresponding mass-size relations are given in Table 2-6b. (Data based on Kajikawa, 1989.)

Habit of component snow crystals	Ple	P2a	P2e	P6d	Rld
Diameter d(cm)	0.08 - 0.68	0.14 - 0.70	0.08 - 0.46	0.16 - 0.66	0.16 -0.58
Falling velocity U_∞ (cm sec^{-1})	102 $m^{0.11}$	94 $m^{0.089}$	68 $m^{0.053}$	135 $m^{0.13}$	286 $m^{0.18}$

TABLE 10.5

Terminal fall velocity-mass relations for snow crystal aggregates observed on Cascade Mts. (750-1500 m, Washington); m in mg. (Based on data of Locatelli & Hobbs, 1974.)

	U_∞ (cm sec^{-1})	Range of max. dimension (mm)
Aggregates of unrimed radiating assemblages of dendrites	$1.1\ m^{0.08}$	2-10
Aggregates of densely rimed radiating assemblages of dendrites	$1.3\ m^{0.15}$	2 - 12
Aggregates of unrimed radiating assemplages of plates, side planes, bullets, and columns	$1.2\ m^{0.07}$	0.2 - 3.0
Aggregates of unrimed side planes	$1.2\ m^{0.14}$	0.5 - 4.0

TABLE 10.6

Terminal fall veloctiy - mass relations for graupel particles of various types, based on observations on Mt. Teine (1024 m, Hokkaido, Japan). The corresponding mass-size relation are given in Table 2-7. (Data based on Heymsfield & Kajikawa, 1987.)

Habit	Diameter range (mm)	U_∞ (cm/sec) for 1000 mb
Rlc	0.8 - 2.7	$92\ d^{0.27}$
Rld	0.7 - 5.3	$79\ d^{0.36}$
R2a	0.7 - 2.2	$92\ d^{0.73}$
R2b	1.1 - 4.7	$162\ d^{0.53}$
R2c	3.0 - 6.2	$75\ d^{0.24}$
R4b	0.4 - 9.0	$733\ d^{0.89}$
$T \geq 0.5°$ C	0.5 - 4.7	$792\ d^{0.68}$
$T < 0.5°$ C	0.5 - 9.0	$614\ d^{0.89}$
R4c	0.8 - 8.6	$590\ d^{0.76}$
$T \geq 0.5°$ C	1.1 - 7.5	$689\ d^{0.66}$
$T < 0.5°$ C	0.8 - 8.6	$491\ d^{0.74}$

Lozowski and Beattle (1979) found for hailstones which fell in Alberta, Canada the relation

$$U_\infty(\text{m sec}^{-1}) = 12.43 d_{\max}^{0.5}, \tag{10-176}$$

with d(cm). Knight and Heymsfield (1983), who studied hailstones in Colorado storms distinguished between fresh hailstones for which

$$U_\infty(\text{m sec}^{-1}) = 8.445 d_0^{0.553}, \tag{10-177}$$

with d(cm), and soaked hailstones for which

$$U_\infty(\text{m sec}^{-1}) = 10.58 d_0^{0.267}, \tag{10-178}$$

for $0.5 \leq d_0 \leq 2$ cm. Note from (10-176) that giant hailstones may have terminal fall velocities of up to 45 m sec^{-1}. These large terminal velocities imply that comparable updraft velocities must exist inside clouds to permit the growth of such particles.

10.5.3 Fall Pattern

The fall pattern of unrimed, planar snow crystals has been studied in the field by Kajikawa (1992), and in the laboratory using planar crystal models, by Podzimek (1965, 1968, 1984) and by List and Schemenauer (1971). In response to the shedding of eddies from the rear of the falling crystals, secondary motions began to be noticeable at $N_{\text{Re}} \approx 100$ for simple hexagonal plates. Stellar and narrow branched crystal models fell stably up to $N_{\text{Re}} \approx 200$ due to their lower inertia, in agreement with the experiments of Willmarth *et al.* (1964), who also found increasing stability for circular disks with decreasing inertia. In contrast to the very symmetric crystal models, Kajikawa (1992) found that most natural planar crystals begin to exhibit secondary motions if $N_{\text{Re}} \approx 40$, due to differences between their center of gravity and their geometrical center. Essentially, three types of secondary motions were observed: a helical or spiral motion, an axial rotation, and a glide-pitch or swinging motion. For each of these motions empirical relations were obtained by Kajikawa (1992) to describe the non-dimensionalized frequency $n' = nd/U_z$, and the non-dimensionalized amplitude $a' = a/d$ of a crystal as a function of its mass.

Wind tunnel studies of Pflaum *et al.* (1978) showed that the glide-pitch amplitude of a riming planar crystal increased with the amount of rime deposited on the plate's lower side, until at some critical loading, the plate was observed to flip-over and begin riming on the plate's original upper side. Depending on the mass loading during riming, flip-over was observed to occur repeatedly, eventually resulting in the formation of a lump-type graupel. However, if growth continued only on the crystal's lower side, a conical graupel developed.

The fall attitude of conical models has been studied by Jayaweera and Mason (1965), Goldburg and Florsheim (1966) and List and Schemenauer (1971). The fall mode of these models depended on their mode of release and on the shape of the base of the cone. Natural graupel were observed by Zikmunda and Vali (1972) and Pflaum *et al.* (1978). Depending on the graupel's shape and mass-loading instability began at $15 \leq N_{\text{Re}} \leq 350$. Cones fell with apex up most frequently.

Three types of secondary motions could be identified: helical or spiral fall, axial rotation, and bell-swing motion about the apex of conical graupel (Pflaum *et al.*, 1978).

The fall attitude of columnar snow crystals was studied by Kajikawa (1976) and Zikmunda and Vali (1972). Typically, the crystals fell with their long axis horizontal. Three secondary motions were also observed: a helical fall motion, a rotational motion about one of the crystal's minor axes, and an oscillation of the major axis in the vertical plane. This behavior is consistent with the experiments of Jayaweera and Mason (1966) and of Podzimek (1968, 1969) with loaded cylinders.

The fall attitude of aggregates of various planar snow crystals was studied by Sasyo (1977), Kajikawa (1982, 1989), and Zikmunda (1972). Analogously to single planar snow crystals, three types of secondary motions were observed for aggregates, and their non-dimensional frequency and amplitude recored: a helical or spiral motion, an axial rotation, and a glide-pitch oscillation. Onset of secondary motions depended on the distance between the centers of the component crystals and on their size. For some of the most asymmetric configurations observed, instability set in at $N_{\mathrm{Re}} = 40$, while flakes with symmetric configurations fell stably for $N_{\mathrm{Re}} \leq 100$. Using a wind tunnel, Mitra *et al.* (1990c) showed that the fall attitude of snow flakes abruptly changes as soon as they begin to melt. Generally, large helical fall amplitudes resulted, since flakes melt asymmetrically. The fall velocity was found to change rather slowly until about 50% of the ice mass in the flake had melted. Subsequently, the fall velocity approached exponentially the fall velocity of a drop of the same mass as the flake.

Many observational difficulties have so far prevented direct quantitative studies of the fall mode of hailstones falling from hail-bearing clouds, although a number of field experiments have been carried out to simulate such fall. For example, Macklin and Lúdlam (1961) and Landry and Hardy (1970) dropped spheres and model hailstone in the free atmosphere, and tracked them with radar. Although these experiments yielded drag force coefficients, they could not resolve the detailed motion of the falling models. Knight and Knight (1970c) employed a skydiver to photograph freely falling oblate spheroids. It was found that these objects rotate preferentially around the major axis, which generally remains oriented horizontally. Unfortunately, little additional quantitative knowledge was gained.

Since large wind tunnels which are capable of freely supporting hailstones in an air stream are not yet available, laboratory studies have been confined to indirect determinations of the fall mode of hailstones, or to model experiments. For example, from water tank experiments, List (1959) determined that large, smooth oblate spheroids prefer to fall with the minor axis vertical. Browning (1966), Browning and Beimers (1967), and Knight and Knight (1970c) interpreted the observed structure of hailstones in terms of a constant fall attitude at some times and a random tumbling at others. List *et al.* (1973) used experimentally determined values for the drag force, lift force, and torque acting on a smooth oblate spheroid of $4 \times 10^4 \leq N_{\mathrm{Re}} \leq 4 \times 10^5$ to solve numerically for its motion. From their computations, they predicted that subsequent to a small perturbation on a spheroid's steady state fall attitude (major axis horizontal), damping may either restore the initial state, or coupling between rotational and horizontal translational

components of the spheroid's motion may give rise to amplification of the initial perturbation. Depending on the axis ratio and size of the spheroid, and on the magnitude of damping, such amplification was found to lead to either a constant amplitude oscillation or continuous tumbling around the horizontal major axis.

More recent theoretical and experimental studies (Kry and List, 1974a,b; Stewart and List, 1983; Lesins and List, 1986; List, 1990) have established that hailstones gyrate while freely falling. A gyrating hailstone spins about the hailstone's minor axis which remains approximately horizontal but wobbles to cause a precession and nutation so that the spin axis moves on the surface of a circular or elliptical cone. The free fall theory of Kry and List (1974a,b) and Stewart and List (1983) predict a spin frequency of 9.5 Hz and a nutation/precession frequency of 14 Hz in agreement with experiments which showed that lower or higher frequencies produce hailstone shapes which are not observed in nature.

While falling from cloud base to the ground, the terminal fall velocity of hailstones may change dramatically if they melt. A scheme which parameterizes this change has been provided by Rasmussen and Heymsfield (1987a).

CHAPTER 11

MECHANICS OF THE ATMOSPHERIC AEROSOL

The main purpose of this chapter is to outline the basic dynamic behavior of aerosols. We shall therefore discuss the phenomena of Brownian motion, diffusion, sedimentation, and coagulation of aerosol particles, including some effects of turbulence. (Possible electrical influences will be discussed in Chapter 18.) We shall also extend and/or apply the various formulations to the problems of explaining some observed features of the size distributions of atmospheric aerosol particles. This, in turn, will provide much of the mathematical framework which we shall subsequently use in our study of the individual or collective growth of cloud particles by diffusion (Chapter 13), by collision and coalescence (Chapters 15 and 16), and in our study of the mechanisms which remove aerosol particles from the atmosphere (Chapter 17).

Some useful references for this chapter include Rasool (1973), Hidy and Brock (1970, 1971, 1972), Davies (1966), Fuchs (1964), Greene and Lane (1964), Junge (1963a), Levich (1962), Bird *et al.* (1960), Friedlander (1977), Twomey (1977), Hidy (1984), and Seinfeld (1986).

11.1 Brownian Motion of Aerosol Particles

Let us first review briefly the classical theory of Brownian motion as it applies to the atmospheric aerosol. Brownian motion is the name given to the irregular motion ('random walk') of particles due to thermal bombardment with gas molecules. A satisfactory account of it may be deduced from a simple model which ignores the detailed structure of the participating particles and, more importantly, assumes that successive particle displacements are statistically independent. This latter assumption is often described by saying Brownian motion may be idealized as a *Markoff process*, which means a stochastic process in which what happens at a given instant of time t depends only on the state of the system at time t.

A direct consequence of the randomness of Brownian motion is that the mean square distance traversed by a Brownian particle is proportional to the length of time it has experienced such motion. One simple way to prove this and evaluate the constant of proportionality is by means of the form of Newton's second law known as *Langevin's equation* (see, for example, Chandrasekhar (1943), p. 20), which reads as follows:

$$\frac{\mathrm{d}\vec{\mathrm{v}}}{\mathrm{d}t} = -\beta\vec{\mathrm{v}} + \vec{\mathrm{A}}(t)\,, \tag{11-1}$$

where $\vec{\mathrm{v}}$ denotes the velocity of the particle. The first term on the right describes the continuous frictional resistance of the air to the motion of the particle, and the

second term denotes the fluctuating acceleration which is characteristic of Brownian motion. That the equation of motion can be broken up into continuous and discontinuous pieces like this is an *ad hoc* assumption which is justifiable in part because it is intuitively appealing, but more importantly because it is successful in predicting behavior.

The frictional term represents the loss of organized energy which contributes to the thermal energy responsible for the fluctuations. If we apply ordinary macroscopic hydrodynamic arguments, then, since the Reynolds number for an aerosol particle is quite small, we may assume the frictional retarding force is described adequately by Stokes' law (see Section 10.2.2.3). Obviously, for a particle with characteristic dimension r comparable to the mean free path λ_a of the air molecules, there will also be a dependence of the frictional force on the *Knudsen number* $N_{Kn} = \lambda_a/r$, but for now we will ignore this refinement. Then, for a spherical particle of radius r and mass m, we have

$$\beta = 6\pi r\eta_a/m\,. \tag{11-2}$$

If we now take the dot product of (11-1) with the position vector $\vec{r}$, and average the result over many trials or 'realizations' of the motion (denoting the averaging process by angular brackets), we find

$$\left\langle \vec{r}\cdot\frac{d\vec{v}}{dt}\right\rangle = \frac{d}{dt}\langle\vec{r}\cdot\vec{v}\rangle - \langle v^2\rangle = -\beta\langle\vec{r}\cdot\vec{v}\rangle + \langle\vec{r}\cdot\vec{A}\rangle\,. \tag{11-3}$$

Assuming the law of equipartition of energy holds, so that $\langle v^2\rangle = 3kT/m$, and considering that the complete directional isotropy of collisions implies $\langle\vec{r}\cdot\vec{A} = 0$, we find

$$\frac{d}{dt}\langle\vec{r}\cdot\vec{v}\rangle = \frac{3kT}{m} - \beta\langle\vec{r}\cdot\vec{v}\rangle\,, \tag{11-4}$$

which upon integration yields

$$\langle\vec{r}\cdot\vec{v}\rangle = \frac{3kT}{\beta m} + c\exp(-\beta t)\,, \tag{11-5}$$

where c is an arbitrary constant. The parameter β^{-1} is just the viscous relaxation time τ_S given by (10-152). Generally, τ_S is quite small for atmospheric aerosols; e.g., for a particle of $r = 1\,\mu$m and density $\rho_p = 1$ g cm^{-3} in air of 1 atm and 20°C, $\tau_S = 10^{-5}$ sec. For times $t \gg \tau_S$, any initial velocity disturbance will have decayed so that the stationary mean of $\vec{r}\cdot\vec{v}$, characteristic of Brownian motion, is

$$\langle\vec{r}\cdot\vec{v}\rangle = \frac{3kT}{\beta m}\,. \tag{11-6}$$

Since $\vec{r}\cdot\vec{v} = d(r^2/2)/dt$, one further integration immediately yields

$$\langle r^2\rangle = \frac{6kTt}{\beta m} = \frac{kTt}{\pi\eta_a r}\,, \tag{11-7}$$

or

$$\langle z^2 \rangle = \langle x^2 \rangle = \langle y^2 \rangle = \frac{\langle r^2 \rangle}{3} = \frac{\mathrm{k}Tt}{3\pi\eta_{\mathrm{a}} r} \,. \tag{11-8}$$

This basic result was derived originally by Einstein (1905) in a somewhat different manner. It has been confirmed experimentally in numerous ways, and has been used, for example, to determine the Boltzmann constant, k, and Avogadro's number, $N_A = \mathscr{R}/\mathrm{k}$, where $\mathscr{R}$ is the universal gas constant.

11.2 Particle Diffusion

The dependence $\langle z^2 \rangle \propto t$ of (11-8) is characteristic of a diffusion process, and in fact, we may describe the motion of a large number of particles undergoing random walks without mutual interference as a process of diffusion. We now turn to a brief discussion of the connection between these two points of view. According to the well-known macroscopic theory of diffusion, if $n(\vec{\mathrm{r}}, t)$ denotes the concentration of the diffusing aerosol particles at $\vec{\mathrm{r}}$ and at time t, then the current density in a stationary medium is given by 'Fick's first law', namely

$$\vec{\mathrm{J}} = -D\nabla n \,, \tag{11-9}$$

where D is the diffusion coefficient or diffusivity. Application of the equation of continuity for the diffusing substance

$$\frac{\partial n}{\partial t} = -\nabla \cdot \vec{\mathrm{J}}, \tag{11-10}$$

immediately results in the diffusion equation ('Fick's second law'):

$$\frac{\partial n}{\partial t} = D\nabla^2 n \,, \tag{11-11}$$

where we have assumed D is a constant.

Let us now determine the mean square displacement (second moment) of a distribution of diffusing particles, according to the foregoing equation. Let N identical aerosol particles per unit area be introduced at time $t = 0$ in an infinitesimally thick slab near $z = 0$ (we assume no dependence on x or y). The resulting diffusion corresponds to many simultaneous realizations of a single particle's random walk from the origin. Multiplying the diffusion equation by z^2 and integrating over z, we obtain

$$\int_{-\infty}^{+\infty} z^2 \frac{\partial n}{\partial t} \mathrm{d}z = N \frac{\partial \langle z^2 \rangle}{\partial t} = D \int_{-\infty}^{+\infty} z^2 \frac{\partial^2 n}{\partial z^2} \mathrm{d}z = 2DN \,, \tag{11-12}$$

where the right side of the equation has been integrated by parts twice, and where on the left hand side we have used the definition $\langle z^2 \rangle \equiv (1/N) \int_{-\infty}^{+\infty} z^2 n(z,t) \mathrm{d}z$. Consequently, the mean square displacement is

$$\langle z^2 \rangle = 2Dt \,, \tag{11-13}$$

which agrees with (11-8) if

$$D = \frac{kT}{\beta m} = \frac{kT}{6\pi\eta_a r} . \tag{11-14}$$

For particles in the submicron range, the Knudsen number correction referred to earlier becomes important. It has been found expreimentally (Cunningham, 1910) that a suitable form of the diffusion coefficient for small particles is

$$D = \frac{kT(1 + \alpha N_{Kn})}{6\pi\eta_a r} , \tag{11-15}$$

where $(1+\alpha N_{Kn})$ is termed the *Cunningham slip-flow correction.* For the parameter α, Knudsen and Weber (1911) proposed a relation of the form

$$\alpha = A + B\exp(-C/N_{Kn}) . \tag{11-16}$$

Unfortunately, there is some confusion in the literature on the values to be inserted for the 'constants' A, B and C. Thus, Flanagen and Taylor (1967) pointed out that A, B and C are not universal constants, but rather depend on the nature of the gas and the surface characteristics of the particles which move through the gas. Millikan (1924) found for oil drops in air $A = 0.864$, $B = 0.29$, $C = 1.25$. After correcting some systematic errors in the Millikan data, Flanagan and Taylor (1967) found $A = 0.866$, $B = 0.29$, and $C = 1.25$. In contrast, Knudsen and Weber (1911) found for glass beads in air $A = 0.772$, $B = 0.400$ and $C = 1.63$, and Matauch (1925) for oil drops in nitrogen $A = 0.898$, $B = 0.312$, $C = 2.37$. From an analysis of all the former experiments and using the definition for the mean free path due to Chapman and Enskog (see Kennard, 1938, p. 147), Davies (1945) found $A = 1.257$, $B = 0.400$, $C = 1.10$. These latter values have also been recommended by Junge (1963a), Friedlander (1977), Hidy (1984) and Seinfeld (1986). Table 11.1 lists a few representative values for D, computed from (11-15) and (11-16), and the corresponding values of $\langle r^2\rangle^{1/2}$ (from 11-7) multiplied by $(1+N_{Kn})$ after one minute of diffusion time. On the basis of the small and rapidly decreasing values of D and $\langle r^2\rangle^{1/2}$ with increasing particle size, one can reasonably anticipate that Brownian diffusion of aerosol particles in the troposphere becomes of secondary importance to other transport processes for $r \gtrsim 1\,\mu$m. It is also interesting to note that even for AP as small as $0.01\,\mu$m, D is still three orders of magnitude smaller than the diffusivity of foreign gases in air, which typically is of the order of 10^{-1} cm^2 sec^{-1}.

11.3 Mobility and Drift Velocity

Let us now generalize the Langevin equation (11-1) by letting an external force, $\vec{F}_{ext}$ act on the diffusing particle:

$$m\frac{d\vec{v}}{dt} = \vec{F}_{ext} - \beta m\vec{v} + m\vec{A} . \tag{11-17}$$

On taking mean values and assuming a steady state (which requires only that the characteristic time for a change in $\langle\vec{v}\rangle$ be large compared to β^{-1}), this yields

$$\langle\vec{v}\rangle = \frac{\vec{F}_{ext}}{\beta m} \equiv \vec{v}_{drift} . \tag{11-18}$$

TABLE 11.1

Diffusion coefficient D, Schmidt number N_{Sc}, root mean square distance $\langle r^2 \rangle^{1/2}$ travelled in 1 minute, and terminal fall velocity, for Brownian particles of radius r for 15°C, 1 atm, $\lambda_a = 7.37 \times 10^{-6}$ cm, $\eta_a = 1.78 \times 10^{-4}$ poise, $\nu_a = 0.148$ cm^2 sec^{-1}, $\rho_P = 2$ g cm^{-3}, (NACA Standard Atmosphere).

r (μm)	D (cm^2 sec^{-1})	$N_{Sc} = \nu_a/D$	$< r^2 >^{1/2}$ (μm, after 1 min)	U_S(cm sec^{-1})
0.01	1.56×10^{-4}	9.46×10^{2}	2333	3.1×10^{-5}
0.1	2.35×10^{-6}	6.28×10^{4}	290	4.3×10^{-4}
1.0	1.29×10^{-7}	1.14×10^{6}	68	2.7×10^{-2}
10	1.19×10^{-8}	1.24×10^{7}	21	2.5

This average response to an impressed force is called the *drift velocity.* It is customary to define the particle mobility, B_P , by the equation

$$\vec{v}_{drift} \equiv B\vec{F}_{ext} . \tag{11-19}$$

Therefore,

$$B = \frac{1}{\beta m} = \frac{1 + \alpha N_{Kn}}{6\pi\eta_a r} , \tag{11-20}$$

for a spherical particle obeying Stokes' law corrected for slip. Further, on combining (11-15) and (11-20), we obtain an intimate connection between the mobility and the diffusion coefficients, namely

$$D = BkT , \tag{11-21}$$

which is known as the Einstein relation.

11.4 Sedimentation and the Vertical Distribution of Aerosol Particles

The drift velocity of small particles falling under gravity is obviously just the terminal velocity in slip-corrected Stokes flow, V_S. Thus, for spherical particles of density ρ_p and $\vec{F}_{ext} = (4\pi/3)r^3(\rho_p - \rho_a)\vec{g}$, we have

$$| \vec{v}_{drift} | = V_S = \frac{2(1 + \alpha N_{Kn})r^2 g(\rho_p - \rho_a)}{9\eta_a} , \tag{11-22}$$

(cf. Section 10.3.6). This result is plotted in Figure 11.1 for $\rho_p = 2$ g cm^{-3}, which shows that the fall velocity of a particle increases rapidly with height, particularly above 10 km. Also, the velocities are seen to be quite small for $r \lesssim 1\ \mu$m; in fact, a time of the order of years is required for particles of $r < 0.1\ \mu$m to fall through a layer 1 km thick at altitudes less than 25 km.

In (11-22), we have assumed that the falling particles are spherical. However, dry atmospheric aerosol particles often have shapes other than that of a sphere.

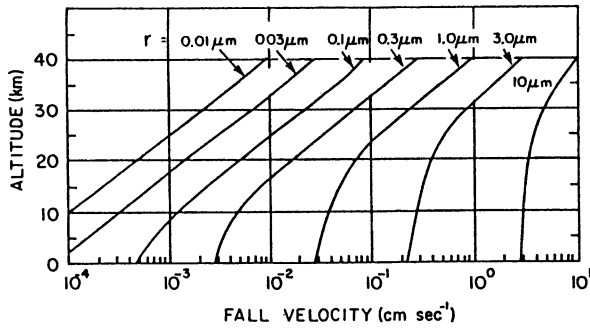


Fig. 11-1: Fall velocity of spherical particles of density $\rho_P = 2$ g cm^{-3}, as a function of particle radius and altitude in the NACA Standard atmosphere. (From Junge *et al.*, 1961a,b; by courtesy of Am. Meteor. Soc., and the authors.)

For example, dry NaCl particles are cubic, dry clay particles may be plate-shaped (kaolinite) or rod-shaped (halloysite), and soot particles may be present as chains of spheres. Many additional forms, including irregular shapes may be found. Obviously, the shape of a particle affects its mobility and, thus, its fall velocity. Effects of particle shape on fall velocity have been studied by Horvath (1974, 1979), Davis *et al.* (1987), Cheng *et al.* (1988a b), and Lee and Leith (1989). A variety of form factors have been defined in the literature. Some of these factors are based on the ratio of the actual aerodynamic drag to the Stokes drag; on the ratio of the actual fall velocity to the Stokes fall velocity; on the aerodynamic radius, which is the radius of a particle of arbitrary shape and density whose terminal velocity would be equivalent to that of a sphere of unit density; or on the radius of a spherical particle such that its terminal velocity (or its drag) is the same as that measured for the arbitrarily shaped particle. For these shape factors, the reader is directed to the appropriate original articles. As expected, the measured form factor becomes larger the more elongated the particle is, and the more sharp edges and corners it exhibits. Nevertheless, it is surprising to note from the observations that, except for extreme forms such as needles, very thin plates, or long chain aggregates, the shape effect is relatively small for typical atmospheric particles. In addition, we must remember that most of the atmospheric AP are mixed particles consisting of water insoluble and soluble compounds. From Table 4.3, we must therefore assume that at typical relative humidities in the atmosphere, the water soluble portion will have adsorbed significant amounts of water vapor, or even have gone partly into solution. Both processes tend to increase the particle's sphericity.

Let us now consider the problem of determining the distribution of particles undergoing simultaneous Brownian diffusion and sedimentation. In this case, we write the total particle current density $\vec{j}$ as the sum of the contributions from diffusion and drift in the gravity field:

$$\vec{j} = -D\nabla n + n\vec{v}_{\text{drift}} \,. \tag{11-23}$$

Application of the continuity equation for the particles, $\partial n/\partial t = -\nabla \cdot \vec{j}$, yields the governing ('Smoluchowski') equation for the concentration $n(r,t)$:

$$\frac{\partial n}{\partial t} = D\nabla^2 n + V_S \frac{\partial n}{\partial z}\,, \tag{11-24}$$

where we have assumed gravity acts in the $-z$ direction and that V_S = constant. If we suppose the plane $z = 0$ forms the bottom absorbing boundary of a semi-infinite homogeneous aerosol which was initially of uniform concentration n_0 for $z > 0$, then the solution for the vertical distribution $n(z,t)$ is

$$n(z,t) = \frac{n_0}{2}(1 - \mathrm{e}^{-V_S t/D}) + \frac{n_0}{2}\left[\mathrm{e}^{-V_S t/D}\mathrm{erf}\left(\frac{z - V_S t}{\sqrt{4Dt}}\right) + \mathrm{erf}\left(\frac{z + V_S t}{\sqrt{4Dt}}\right)\right], \tag{11-25}$$

where erf denotes the error function (see Appendix A-11.4 for details). The deposition rate $I(t)$ of particles on the surface $z = 0$ is therefore given by

$$I(t) = -\vec{j}(0,t)\cdot \hat{e}_z = D\left.\frac{\partial n}{\partial z}\right|_{z=0} = n_0\left[\frac{V_S}{2}\left(1 + \mathrm{erf}\sqrt{\frac{V_S^2 t}{4D}}\right) + \sqrt{\frac{D}{\pi t}}\mathrm{e}^{-V_S^2 t/4D}\right]. \tag{11-26}$$

According to (11-26), the diffusion current is infinite at $t = 0$. This happens because of the artificial specification of an infinite concentration gradient at $z = t = 0$. For $t \ll t_c = 4D/V_S^2$, (11-26) becomes $I(t) = n_0[(D/\pi t)^{1/2} + V_S/2]$, which is equal to the diffusion deposition rate which would occur in the absence of sedimentation, plus half of the pure sedimentation rate. For particles of radius 0.1 and 1 μm in air at $p = 1000$ mb and $T = 20°$C, t_c is about 40 sec and 4×10^{-3} sec, respectively, assuming a particle density of 2 g cm^{-3}. For $t \gg t_c$, the deposition rate is $I(t) = n_0 V_S$, so that Brownian motion no longer has any effect.

In reality, of course, the atmosphere is not motionless, nor is the surface of the Earth merely an aerosol sink. Generally, there will be an upward flux of material, usually by turbulent diffusion, which will tend to equilibrate with sedimentation and other processes over various time scales. If we assume a steady state balance of vertical turbulent diffusion and sedimentation, a crude account of the resulting vertical distribution of aerosol may be obtained by the following plausible modification of the particle current density in (11-23): let D be replaced by D_e, where D_e is an effective eddy diffusivity of aerosol particles describing the transport capability of turbulence within the framework of classical diffusion theory, and let $V_S \to V_S - W$, where W is the average updraft velocity of the air. Further, that part of the concentration gradient of particles which is due to the decrease in air density with height will not be effective in the turbulent transport. Therefore, in order to obtain results for heights comparable to the scale height of the atmosphere, we should replace n in (11-23) by $\sigma = n/n_a$, where $n_a = n_a(z)$ is the number concentration of air molecules at height z. Assuming the net particle flux is zero at all levels, the equation governing the mixing ratio σ becomes

$$\frac{\mathrm{d}\sigma}{\mathrm{d}z} = \frac{-(V_S - W)\sigma}{D_e}\,, \tag{11-27}$$

so that, with the ground at $z = 0$, the distribution is

$$\sigma(z) = \sigma(0) \exp(-z/z_e) , \tag{11-28a}$$

where

$$z_e = \frac{D_e}{V_S - W} , \tag{11-28b}$$

assuming constant z_e. If desired, the particle concentration may be recovered by noting that (11-28) may also be expressed in the form

$$\frac{n(z)}{n(0)} = \frac{n_a(z)}{n_a(0)} \exp(-z/z_e) , \tag{11-29}$$

where the first term in the product on the right side of (11-29) is given by

$$\frac{n_a(z)}{n_a(0)} = \frac{T(0)}{T(z)} \exp\left[-\frac{g}{R_a} \int_0^z \frac{dz}{T(z)} \right] , \tag{11-30}$$

using the ideal gas law and assuming hydrostatic equilibrium.

As we have discussed in Chapter 8, an exponential decrease of aerosol particle concentration with height, in qualitative conformity with (11-28), is often observed in the lower troposphere (recall Figures 8.31 and 8.32). However, the model used above leaves much to be desired. For example, we have neglected the effects of local sources and sinks, meteorological conditions of wind and stability, dilution by mixing with air of different properties, 'washout' or 'scavenging' by cloud and precipitation particles, and various coagulation processes operating in a heterogeneous aerosol. More complete models to describe the vertical distribution of aerosols have been formulated by Junge (1957b), Erickson (1959), Junge *et al.* (1961a), and Toba (1965a). Models for explaining the horizontal distribution of the atmospheric aerosol have been formulated by Toba (1965a), Tanaka (1966), Toba and Tanaka (1968), and Rossknecht *et al.* (1973).

11.5 Brownian Coagulation of Aerosol Particles

Particles undergoing relative Brownian diffusion have a finite probability of colliding and sticking to one another; i.e., they may experience thermal or spontaneous coagulation. The sticking probability or *sticking efficiency* of aerosol particles is a complicated function of their shape and surface conditions (roughness, absorbed vapors, etc.), the relative humidity of the air, the presence of foreign vapors in the air, and other factors. Although little is known quantitatively about the sticking efficiency of aerosol particles, the fact that the kinetic energy of the colliding particles is very small makes bounce-off unlikely. We shall therefore assume a sticking efficiency of unity in the sequel. (For a review of the topic of sticking efficiency, see Corn (1966).)

To formulate the coagulation process, we first need to find the diffusion coefficient D_{12} which characterizes the diffusion of particles of radius r_2 relative to those

of radius r_1, Suppose the particles experience displacements $\Delta\vec{r}_1$ and $\Delta\vec{r}_2$ in time Δt, respectively. Then, their mean square relative displacement is

$$\langle |\, \Delta\vec{r}_1 - \Delta\vec{r}_2 \,|^2 \rangle = \langle \Delta r_1^2 \rangle + \langle \Delta r_2^2 \rangle - 2\langle \Delta\vec{r}_1 \cdot \Delta\vec{r}_2 \rangle = \langle \Delta r_1^2 \rangle + \langle \Delta r_2^2 \rangle ,$$

since the motions are independent. Now from the meaning of D_{12} and the results (11-8) and (11-13), we have $\langle |\, \Delta\vec{r}_1 - \Delta\vec{r}_2 \,|^2 \rangle = 6D_{12}\Delta t$; on the other hand, we also have $\langle \Delta r_1^2 \rangle = 6D_1\Delta t$ and $\langle \Delta r_2^2 = 6D_2\Delta t$. Therefore, we obtain the simple result

$$D_{12} = D_1 + D_2 . \tag{11-31}$$

By the preceding argument, we may regard the r_1 particle as stationary and suppose the r_2 particles are diffusing toward it with diffusion coefficient D_{12}. Using the center of the r_1 particle as the origin of coordinates, we have by the isotropy of the process that the concentration n_2 of the r_2-particles is a function only of r, the distance from the origin, and time t. Further, the boundary condition of adhesion on contact may be expressed as

$$n_2(r_{12}, t) = 0 , \qquad r_{12} = r_1 + r_2 . \tag{11-32}$$

So we must solve

$$\frac{\partial n_2}{\partial t} = D_{12}\nabla^2 n_2 = \frac{D_{12}}{r}\frac{\partial^2}{\partial r^2}(r n_2) , \tag{11-33}$$

subject to (11-32) and the initial condition

$$n_2(r, 0) = n_{2,\infty} , \qquad r > r_{12} , \tag{11-34}$$

where $n_{2,\infty}$ is the ambient concentration of r_2-particles at the beginning of the coagulation process.

The solution to (11-32) to (11-34) is easily obtained, since (11-33) is just a one-dimensional diffusion equation in the dependent variable rn_2. It may be solved, for example, by application of the method presented in A-11.4, using the independent variable $z = r - r_{12}$. By this or other means, the solution is found to be

$$n_2(r, t) = n_{2,\infty}\left[1 - \frac{r_{12}}{r} + \frac{r_{12}}{r}\mathrm{erf}\left(\frac{r - r_{12}}{\sqrt{4D_{12}t}}\right)\right] . \tag{11-35}$$

The coagulation rate (loss rate) of the r_2-particles colliding with the r_1-particles is just the flux $(J_{r_2})_{r_{12}}$ of the r_2-particles 'through' the surface S_{12} given by $r = r_{12}$, in a direction opposite to the r-coordinate:

$$-(J_{r_2})_{r_{12}} = -\int_{S_{12}} \vec{j}\cdot d\vec{S} = D_{12}\int_{S_{12}} \frac{\partial n_2}{\partial r} dS = 4\pi r_{12} D_{12} n_{2,\infty}\left(1 + \frac{r_{12}}{\sqrt{\pi D_{12} t}}\right) . \tag{11-36}$$

We may generally ignore the time factor in this expression since $r_{12}^2/\pi D_{12}$ (i.e., the characterisitic time for diffusion over distances comparable to aerosol radii) is less

than $\approx 10^{-5}$ sec for $r \lesssim 0.1\,\mu$m and less than $\approx 10^{-2}$ sec for $r \lesssim 1\,\mu$m. For a steady state, (11-36) becomes

$$-(J_{r_2})_{r_{12}} = 4\pi r_{12} D_{12} n_{2,\infty}\,. \tag{11-37}$$

This result could have been obtained more readily from the steady state version of (11-33) (Laplace's equation):

$$\nabla^2 n_2 = 0\,, \tag{11-38}$$

subject to the boundary conditions (11-32) and (11-34). The result is

$$n_2(r) = n_{2,\infty}\left(1 - \frac{r_{12}}{r}\right)\,, \tag{11-39}$$

which is the large time limit of (11-35). Substitution of (11-39) into the second term on the right of (11-36) and evaluating the integral recovers (11-37).

Let us now take into consideration the fact that the ambient particle concentrations will in fact be functions of time owing to coagulation in a volume of acrosol. Until now we have denoted the ambient concentration of the r_2 particles as $n_{2,\infty}$; henceforth in this section we will simply use the notation n_2 or $n_2(t)$, if the explicit time dependence needs to be stressed; similarly for other aerosol particle concentrations. Suppose now that the concentration of particles of radius r_1 is n_1. Then, the total loss rate of r_2 particles per unit volume of aerosol is just (11-37) scaled up by the factor $n_1(\infty)$:

$$-\frac{\mathrm{d}n_2}{\mathrm{d}t} = 4\pi(r_1 + r_2)(D_1 + D_2) n_1(t) n_2(t). \tag{11-40}$$

Introducing (11-15) into this expression, we obtain

$$-\frac{\mathrm{d}n_2}{\mathrm{d}t} = \frac{2\mathrm{k}T}{3\eta_\mathrm{a}}(r_1 + r_2)\left[\left(\frac{1}{r_1} + \frac{1}{r_2}\right) + \left(\frac{\alpha_1\lambda_\mathrm{a}}{r_1^2} + \frac{\alpha_2\lambda_\mathrm{a}}{r_2^2}\right)\right] n_1(t) n_2(t)\,. \tag{11-41}$$

According to this equation, the rate of particle loss increases with increasing temperature, particle concentration, and mean free path with increasing altitude; it also increases with decreasing $\eta_\mathrm{a}(T)$, and with increasing polydispersity. This last effect is illustrated by letting $r_2 = xr_1$, from which $(r_1 + r_2)(1/r_1 + 1/r_2) = (1 + x)^2/x$. This function has a single minimum at $x = 1$, or $r_1 = r_2$.

Let us now assume an aerosol initially of uniform particle size, i.e., $r_1 = r_2$ and $D_1 = D_2$. Then, the loss rate of particles present in concentration n is, from (11-40),

$$-\frac{\mathrm{d}n}{\mathrm{d}t} = 16\pi D r n^2 = K_\mathrm{B} n^2\,, \tag{11-42}$$

where $K_\mathrm{B} = 16\pi D r = 8\mathrm{k}T/3\eta_\mathrm{a}$ is the *Brownian collection kernel* (without the slip correction) which, as will be described in more detail below, characterizes the process of aerosol coagulation. It is clear that this equation can only hold for a time interval which is small compared to that required for a significant buildup of coagulated multiple particles. We shall demonstrate below that when such particles are present, the decay of the single particles follows a different time dependence.

TABLE 11.2

Coagulation time $t_{1/2}$ for aerosol particles of given uniform size and given concentration, for 15°C and 1000 mb computed from (11-45); h = hours, d = days, m = minutes

$r(\mu m)$	1.0	1.0	0.1	0.1	0.01	0.01
$n(cm^{-3})$	10^4	10^3	10^4	10^2	10^5	10^4
$1 + \alpha N_{Kn}$	1.0926	1.0926	1.993	1.993	12.8	12.8
$t_{1/2}$	85.6 h	35.6 d	46.8 h	195.2 d	43.8 m	7.6 h

However, we can extend the validity of (11-42) through a minor adjustment and reinterpretation. This is based on the observation that for every pair of primary particles that coalesce, one double particle is produced. Therefore, if higher multiple particles are ignored, we can say that the net loss rate of the total concentration N is just one half of the rate specified in (11-42):

$$-\frac{dN}{dt} = 8\pi DrN^2 = \frac{K_B}{2}N^2. \tag{11-43}$$

On integration of (11-43), we find

$$\frac{1}{N} - \frac{1}{N_0} = 8\pi Drt \tag{11-44a}$$

or

$$N(t) = \frac{N_0}{1 + 8\pi DrN_0 t} = \frac{N_0}{1 + \frac{4kT}{3\eta_a}N_0 t}, \tag{11-44b}$$

where N_0 is the particle concentration at $t = 0$ (Smoluchowski, 1916, 1917). The total particle concentration is therefore reduced by a factor of one-half in a time $t_{1/2}$ given by

$$t_{1/2} = \frac{1}{8\pi DrN_0} = \frac{3\eta_a}{4kTN_0(1 + \alpha N_{Kn})}, \tag{11-45}$$

including the slip correction. As expected, the coagulation time $t_{1/2}$ decreases with decreasing size, increasing concentration, and increasing temperature of the aerosol. One may use $t_{1/2}$ to estimate the size range of tropospheric aerosols for which Brownian coagulation is important. As an example, we may assume aerosol particles of the size and concentration given in Table 11.2. We note that for Aitken particles, Brownian coagulation is the dominant loss mechanism.

In the early literature, (11-44a) was the basis for testing coagulation theory against observation by using the fact that, for a constant Brownian collection kernel K_B , a plot of $1/N$ against time t should be linear with a slope K_B. Experimental studies of aerosol coagulation, reviewed over a period of many years by Fuchs (1964), Green and Lane (1964), Whytlaw-Gray and Patterson (1932), Patterson and Cawood (1932), Whytlaw-Gray (1935), Artemov (1946), and Devir (1963), have shown that for many aerosol systems presumed to be coagulating by Brownian motion, $1/N$ does vary linearly with time, an observation which has been widely been used to evaluate K_B and to learn more about the ranges of applicability of Smoluchowski's theory for Brownian motion. However, comparison between theory

and experiment is complicated by the fact that the particles studied often have non-spherical shapes. This alters the collision distance which, for mass equivalent non-spherical particles, becomes larger than $r_1 + r_2$ (Lee and Leith, 1989). Additional factors which make a comparison of experiments with (11-44a) difficult are the polydispersity of the observed aerosol, electrical charges on the particles, wall effects and spurious air currents (Hidy and Brock, 1970).

We shall now generalize our coagulation model to account for the fact that coagulation changes the aerosol size distribution. Suppose initially we have a homogeneous aerosol of particles of volume v_1 in concentration $n_1(0) = n_0$. Coagulation sets in and soon there appear particles of volume $\mathrm{v}_2 = 2\mathrm{v}_1$ in concentration n_2, $\mathrm{v}_3 = 3\mathrm{v}_1$ in concentration n_3, etc. Then, to an excellent approximation, the rate of coagulation of v_i and v_j particles per unit volume of aerosol to form particles of volume $\mathrm{v}_{i+j} = (i+j)\mathrm{v}_1$ is given by $4\pi D_{ij} r_{ij} n_i n_j$ with $D_{ij} = D_i + D_j$ and $r_{ij} = r_i + r_j = (3/4\pi)^{1/3}(\mathrm{v}_i^{1/3} + \mathrm{v}_j^{1/3})$, where n_i and n_j are the ambient concentrations of the v_i and v_j particles at time t.

We can now write down the governing equation for coagulation. From our generalization above, the overall rate of formation of v_k particles per unit volume of aerosol is evidently given by $(1/2)\sum_{i+j=k} 4\pi D_{ij} r_{ij} n_i n_j$, where the factor of $1/2$ is included to avoid counting the same interaction event twice ($i + j = j + i$). Similarly, the loss rate of the v_k particles per unit volume of aerosol is given by $-\sum_i 4\pi D_{ik} r_{ik} n_i n_k$. Therefore, the equation which determines the discrete particle size distribution for binary collisions is

$$\frac{\mathrm{d}n_k}{\mathrm{d}t} = \frac{1}{2}\sum_{i+j=k} 4\pi D_{ij} r_{ij} n_i n_j - \sum_i 4\pi D_{ik} r_{ik} n_i n_k \,. \tag{11-46}$$

This is the discrete form of the kinetic coagulation equation for Brownian coagulation.

According to (11-14), the diffusion coefficient is inversely proportional to the radius, so that we may write

$$D_{ij} r_{ij} = Dr\left(\frac{1}{r_i} + \frac{1}{r_j}\right)(r_i + r_j)\,, \tag{11-47}$$

where D and r are the diffusion coefficient and radius of the primary particles. Since the Cunningham slip correction has been ignored, this expression applies only for $N_{\mathrm{Kn}} \lesssim 0.1$. For $0.5 \leq r_i/r_j \leq 2$, (11-47) may be approximated by $D_{ij} r_{ij} = 4Dr$, to within a maximum error of 12.5%. Since this approximation assumes $r_i = r_j$, it is said to ignore the aerosol polydispersity.

Smoluchowski (1916, 1917) obtained an approximate solution to (11-46) for the case of an initial homogeneous aerosol, assuming $D_{ij} r_{ij} = 4Dr$. If we introduce $f_k(\tau) \equiv n_k/n_0$ and $\tau \equiv 8\pi D r n_0 t$, (11-46) becomes

$$\frac{\mathrm{d}f_k}{\mathrm{d}\tau} = \sum_{i+j=k} f_i f_j - 2f_k \sum_i f_i \,. \tag{11-48}$$

Summing over k, we obtain

$$\frac{\mathrm{d}}{\mathrm{d}\tau}\left(\sum f_k\right) = \sum_{i=1}\sum_{j=1} f_i f_j - 2\sum_{k=1}\sum_{i=1} f_i f_k = -\left(\sum_k f_k\right)^2, \tag{11-49}$$

which upon integration yields

$$\sum_k f_k = \frac{1}{1+\tau}. \tag{11-50}$$

With this result, the solutions for f_k may be obtained successively. Thus, the equation for f_1 is

$$\frac{\mathrm{d}f_1}{\mathrm{d}\tau} = -2f_1\sum_k f_k = \frac{-2f_1}{1+\tau}, \tag{11-51}$$

which leads to $f_1 = (1+\tau)^{-2}$. By induction, one may easily show that for arbitrary k,

$$f_k = \frac{\tau^{k-1}}{(\tau+1)^{k+1}}, \tag{11-52}$$

which is Smoluchowski's solution.

It is interesting to note that since $\tau = 8\pi D r n_0 t$, the solution for the total concentration, given by (11-50), is entirely equivalent to (11-44b). This is a bit surprising, in view of the relatively weak arguments used to justify the latter equation. We also see that, according to (11-51), the decay law of the primary particles is of the form $f_1 = (1+\tau)^{-2}$, whereas from (11-42) we may obtain the approximate solution (indicated by a prime) $f_1' = (1+2\tau)^{-1}$. However, as expected, the two solutions merge for $\tau \ll 1$, and we obtain the first-order result $f_1 = f_1' = 1 - 2\tau$ for $\tau \ll 1$. Furthermore, for small τ , the solution for the total concentration becomes $\sum_k f_k = 1 - \tau + O(r^2)$. This shows that the early decay rate of the primary particles is in fact just twice the total concentration, as we anticipated earlier.

The most serious limitation of Smoluchowski's solution is that it assumes an initially homogeneous aerosol. In order to investigate the effect of Brownian coagulation on realistic aerosol spectra, Junge (1955, 1957b) and Junge and Abel (1965) have carried out numerical solutions of the kinetic coagulation equation, using measured tropospheric aerosol spectra for initial conditions and allowing for the dependence of the coagulation rate on particle size. For this purpose, they used a continuous form of the coagulation equation, involving the continuous size distribution function $n(r,t)$, where $n(r,t)\mathrm{d}r$ is the number of particles at time t with radius between r and $r + \mathrm{d}r$, per unit aerosol volume.

In order to derive the coagulation equation for $n(r,t)$, first note that (11-46) may be written in the form

$$\frac{\mathrm{d}n_k}{\mathrm{d}t} = \frac{1}{2}\sum_{i=1}^{k-1} K_{i,k-i} n_i n_{k-i} - n_k \sum_{i=1}^{\infty} K_{ik} n_i, \tag{11-53}$$

where

$$K_{ij} = 4\pi D_{ij} r_{ij} = K_{ji}. \tag{11-54}$$

The quantity K_{ij} is called the *collection kernel* for Brownian coagulation. An obvious continuous counterpart of this equation is obtained by making the changes

$$n_i(t) \to n(\mathrm{v},t)\mathrm{dv}\,, \qquad K_{ij} \to K(\mathrm{v},\mathrm{u}) = K(\mathrm{u},\mathrm{v})\,, \tag{11-55}$$

where $n(\mathrm{v},t)\mathrm{dv}$ is the number of v-particles at time t with volume between v and v + dv, per unit aerosol volume, and $K(\mathrm{u},\mathrm{v})n(\mathrm{u})\mathrm{du}$ is the coagulation rate of u-particles with a v-particle. The continuous form of involving the distribution function $n(\mathrm{v},t)$ is then

$$\frac{\partial n(\mathrm{v},t)}{\partial t} = \frac{1}{2}\int_0^{\mathrm{v}} K(\mathrm{u},\mathrm{v}-\mathrm{u})n(\mathrm{u},t)n(\mathrm{v}-\mathrm{u},t)\,\mathrm{du} - n(\mathrm{v},t)\int_0^{\infty} K(\mathrm{u},\mathrm{v})n(\mathrm{u},t)\,\mathrm{du}\,. \tag{11-56}$$

We may transform this directly into an equation for $n(r,t)$ by noting that

$$n(r,t)\mathrm{d}r = n(\mathrm{v},t)\mathrm{dv}\,,$$

which merely reflects the fact that more than one measure may be used to count the same particles. Therefore, if r, s, and $r' = (r^3 - s^3)^{1/3}$ are the radii corresponding, respectively, to v, u, and v − u, we have

$$\begin{aligned} n(\mathrm{v}-\mathrm{u},t)\mathrm{dv} &= n(\mathrm{v}-\mathrm{u},t)\,\mathrm{d}(\mathrm{v}-\mathrm{u})\,|_{\mathrm{u}=\text{const.}} \\ &= n(r',t)\,\mathrm{d}r'\,|_{s=\text{const.}} = \frac{n(r',t)r^2\mathrm{d}r}{(r^3-s^3)^{2/3}}\,, \end{aligned} \tag{11-57}$$

so that (11-56) becomes

$$\frac{\partial n(r,t)}{\partial t} = \frac{1}{2}\int_0^{r} K(s,r')\left(1-\frac{s^3}{r^3}\right)^{-2/3} n(s,t)n(r',t)\mathrm{d}s - n(r,t)\int_0^{\infty} K(r,s)n(s,t)\mathrm{d}s\,. \tag{11-58}$$

The collection kernel $K_{\mathrm{B}}(r,s)$ for Brownian coagulation is, from (11-41),

$$K_{\mathrm{B}}(r,s) = 4\pi(D_r + D_s)(r+s) = \frac{2kT}{3\eta_{\mathrm{a}}}(r+s)\left[\left(\frac{1}{r}+\frac{1}{s}\right) + \lambda_{\mathrm{a}}\left(\frac{\alpha_1}{r^2}+\frac{\alpha_2}{s^2}\right)\right]\,, \tag{11-59}$$

where we have again included the slip correction.

Equations (11-58) and (11-59) (with $\alpha_1 = \alpha_2$) were solved numerically by Junge (1957b, 1963a) and Junge and Abel (1965) for the case of an initial spectrum representative of average tropospheric conditions, and assuming that the aerosol particles colliding by Brownian motion have a sticking efficiency of unity and behave as droplets. The result of this computation is shown in Figure 11.2 in terms of the concentration $N(r,t)$ of particles with radii $\geq r$. It is seen that the modification of the size distribution due to Brownian coagulation is confined mainly to particles with radii less than 0.1 μm, i.e., the Aitken particle size range. With increasing time, particles of radii less than 0.1 μm rapidly disappear, while the maximum of the

original size distribution shifts to larger sizes, shifting less and less and centering over $r \approx 0.1\,\mu$m after a few days. From the computed corresponding particle volume changes, Junge and Junge and Abel also concluded that coagulation causes a steady flux of aerosol material from the Aitken size range into the 'large' particle size range, causing the formation of 'mixed' particles in the size range of 'large' particles.

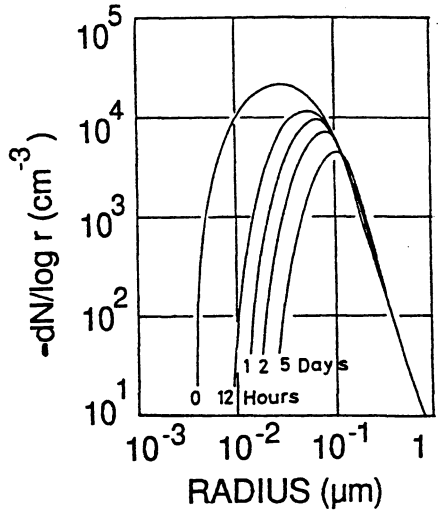


Fig. 11-2: Numerical calculation of the evolution of time of an average atmospheric aerosol particle distribution due to Brownian coagulation. (From Junge and Abel, 1965; by courtesy of the authors.)

Current atmospheric observations support the view (see Chapter 8) that tropospheric aerosols, particularly urban aerosols, show multimodal distributions due to mixing of primary sources and dissimilar formation processes. Assuming a spatially well-mixed aerosol, Suck and Brock (1979) showed that the effect of Brownian coagulation on an atmospheric bimodal aerosol size distribution is such that it will maintain its bimodal identity for long time periods (at least hours) unless meteorological changes, washout by rain or gravitational settling, occurs. This behavior is exemplified in Figure 11.3.

We mentioned in Section 8.2.9 that observations suggest that the aerosol particle concentration does not decrease to zero for particles of radii below $0.1\,\mu$m but, after a minimum for $0.01 \leq r \leq 0.1\,\mu$m, increases again to a second maximum for particles with $r \approx 0.001\,\mu$m. We indicated that it is reasonable to attribute this second maximum to a continuous production of primary particles by gas-to-particle conversion. In order to take this behavior into count, Walter (1973) solved the coagulation equation (Equations (11-58) and (11-59)) with a source-term included. Walter assumed an initially narrow normal distribution of primary aerosol particle sizes whose mean radius was 1.2×10^{-7} cm, and whose production rate GPC was 10^5 particles cm^{-3} sec^{-1}. Figure 11.4 shows that after only a

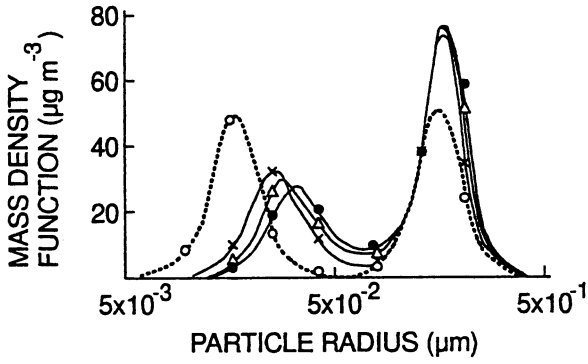


Fig. 11-3: Bimodal mass density function per logarithm radius interval, resulting from coagulation of aerosol particles after 3 elapsed times: (o) 0 min, (×) 20 min., (+) 40 min, (•) 60 min. (From Suck and Brock, 1979, with changes.)

short time, coagulation produces a secondary maximum of the size distribution. With increasing time, this maximum becomes more distinct and shifts to larger sizes until, after about 10^5 sec, the size distribution for r between 2×10^{-7} and 10^{-5} cm reaches a quasi-steady state, which means that in any size interval, as many particles are formed as are lost by coagulation.

The existence of a deep gap such as that appearing in Figure 11.4 contrasts with our knowledge of natural aersols (see Figure 8.20a). The curves in this latter figure display a shallow minimum in the number density for particles between 0.01 and 0.1 μm radius, but no cleft as in Figure 11.4. Jaenicke (1978a,b) suggested that the problem may be explained by considering simultaneous production of particles of different sizes. However, Seinfeld (1993, pers. comm.) does not expect that the size effect due to nucleation is significant, since the critical nucleus sizes would be too small. On the other hand, he suggests that the 'smearing' out of the sharp minimum in the observed AP size distribution is a result of the growth of AP by condensation following GPC. Such growth proceeds in the atmosphere under a wide variety of conditions and leads, therefore, to a wide variety of sizes within a given time. Seinfeld further points out that the time scales over which Brownian coagulation does affect the AP size distribution is long compared to the characteristic times for nucleation and condensational growth, so that one must assume that the role played by Brownian coagulation in shaping the AP size distributions is small relative to that from nucleation and condensational growth. The effect of nucleation and condensation on the evolution of an AP size distribution is illustrated in Figure 11.5. The curves in this figure are based on actual data from an outdoor smog chamber in which methylcyclohexane has reacted in the presence of sunlight, oxides of nitrogen, and primary $(NH_4)_2SO_4$ seed particles which grow from condensation of oxidation products. Note that at $t = 21$ min a new burst of particles from nucleation produces two modes, a nucleation mode at about 2 to 3×10^{-6} cm, and a condensation mode at about 1×10^{-5} cm diameter. Note also that the gap appearing at $t = 21$ min closes progressively as time progresses. The evolution of a particle size distribution

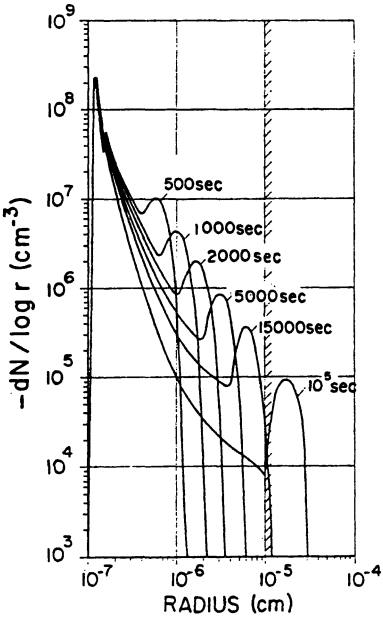


Fig. 11-4: Variation with time of an aerosol particle distribution affected by Brownian coagulation and a constant gas to particle conversion at a rate of 10^5 cm^{-3} sec^{-1}; total volume aerosol generated: 7.8 x 10^{-15} cm^{-3} sec^{-1}. (From Walter, 1973; by courtesy of Pergamon Press Ltd.)

due to homomolecular and heteromolecular nucleation, as well as condensational growth taking place simultaneously, have been studied theoretically by Seigneur *et al.* (1986) and Warren and Seinfeld (1985a,b).

11.6 Laminar Shear, Turbulence, and Gravitational Coagulation

In (11-53), (11-56), and (11-58), we have a framework for evaluating the effects on aerosol spectra of other processes besides Brownian coagulation, since any process which gives rise to a non-zero probability of particle interaction can be represented by some appropriate form of the collection kernel K_{ij} or K. In this section, we consider some possible influences of shear flows, turbulence, and relative motion under gravity.

11.6.1 Coagulation in Laminar Shear Flow

Velocity gradients in the air cause relative motion and may, as a result, induce collisions between aerosol particles. The simplest model for this collection process was worked out by Smoluchowski (1916). His model assumes a uniform shear field, no fluid dynamic interaction between the particles, and no Brownian motion. In order to determine the rate at which v_2-particles are collected by one v_1-particle,

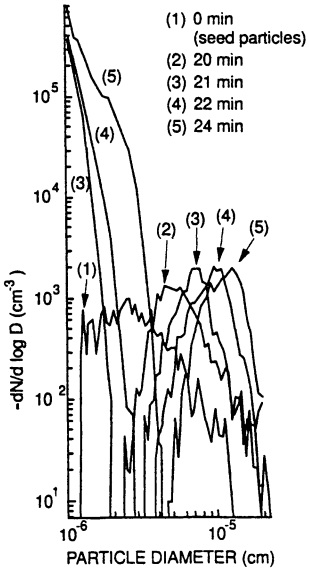


Fig. 11-5: Aerosol production by photo-oxidation of a methylcyclohexane/propane/NO_x mixture as a function of time. (From Seinfeld, 1993, pers. comm., by courtesy of Seinfeld, 1993).

we assume flow relative to the origin of v_1 in the $\pm z$-direction with the shear in the y-direction. The velocity field is then given by

$$\vec{u} = \Gamma y \hat{e}_z \,, \tag{11-60}$$

where Γ is the constant velocity gradient or shear rate. If we again use the general notation of the previous section, we can express the particle flux or current density vector relative to the v_1-particle as

$$\vec{j} = n_2 \Gamma y \hat{e}_z \,, \quad r > r_{12} \,, \tag{11-61}$$

and the collection rate is given by the positive flux J_{LS} of $\vec{j}$ into a sphere of radius r_{12} concentric with the origin:

$$J_{LS} = 2\Gamma n_2(\infty) r_{12}^3 \int_0^{\pi} \sin\phi \mathrm{d}\phi \int_0^{\pi/2} \sin^2\theta \cos\theta \mathrm{d}\theta = \frac{4}{3}\Gamma n_2(\infty) r_{12}^3 \,. \tag{11-62}$$

The collection kernel K_{LS} for laminar shear flow may therefore be expressed as $J_{LS}/n_2(\infty)$, or

$$K_{LS}(r,s) = \frac{4\Gamma}{3}(r+s)^3 \,. \tag{11-63}$$

One would expect that (11-63) might overestimate the actual shear collection rate, since viscous effects should tend to make the particles move around each

other, thus lowering the collision cross-section below the geometric value. However, at least one experimental study (Manley and Mason, 1952) showed that (11-63) is essentially correct for the case of large glass spheres (60 to 70 μm diameter) in a quite viscous fluid with $\Gamma = 0.4$ to 0.8 sec^{-1}.

The relative strength of laminar shear to Brownian coagulation for a homogeneous aerosol is given by the ratio

$$\frac{K_{LS}(r,r)}{K_{\text{B}}(r,r)} = \frac{2\Gamma r^2}{3\pi D}. \tag{11-64}$$

From the values of D given in Table 11.1, we find the shear rates required for the two processes to be comparable are rather high for particles smaller than a few microns: $\Gamma \approx 10^5$ sec^{-1} for $r = 0.1\,\mu$m; $\Gamma \approx 60$ sec^{-1} for $r = 1.0\,\mu$m; $\Gamma \approx 6 \times 10^{-2}$ sec^{-1} for $r = 10\,\mu$m. Accordingly, one would expect shear collection to become important only for particles larger than a few microns in radius. However, since in the atmosphere velocity gradients are generally associated with turbulent motions, one should hesitate to draw definite conclusions from a model based on laminar flow. Therefore, we now turn to a consideration of the collection rates in turbulent flow. However, in support of (11-63), it will be seen that the length and time scales over which particles interact are small enough so that the assumption of constant shear during the interaction does not lead to large errors.

11.6.2 Coagulation in Turbulent Flow

Since a comprehensive treatment of turbulent flow would go far beyond the scope of this book, we shall base our discussion in this section on a rather simple description using dimensional analysis. For more detailed information on the theory of turbulence, the reader is referred to such texts as Tennekes and Lumley (1972), Monin and Yaglom (1971), and Landau and Lifshitz (1959).

Turbulence is characterized in large part as a disordered vorticity field, which may be pictured qualitatively as a distribution of eddies of various sizes. The largest eddies have a size ℓ and characteristic fluctuating velocity Δu of the same order as the length and velocity characterizing the flow as a whole. The corresponding Reynolds number $N_{\text{Re},\ell} = \Delta u \ell / \nu$ is very large, indicating viscosity as a small effect on the dynamics of the large eddies.

The largest eddies contain most of the kinetic energy of the flow, which is passed on with little dissipative loss to eddies of smaller scale by some as yet poorly understood non-linear break-up process (the 'energy cascade'), until finally it is dissipated into heat by viscosity on the smallest scales of motion (see Figure 14.7). With a little dimensional analysis, this picture of turbulence leads to some interesting and useful predictions, which are considered to be correct to within an order of magnitude.

According to the above description, the rate of dissipation of kinetic energy per unit mass, ε, is controlled by the rate of break-up of the largest eddies, for which viscosity plays a negligible role. Thus, it is reasonable to assume that ε is not a direct function of ν, but instead can only be a function of the physical parameters characterizing the large scale flow, namely Δu, ℓ, and possibly ρ, the density of the

fluid. Then, dimensional consistency demands that

$$\varepsilon \approx \frac{\Delta u^3}{\ell} . \tag{11-65}$$

There is some evidence that ε is in fact a weak function of $N_{\mathrm{Re},\ell}$ and, hence, ν. A discussion of this point appears in Saffman (1968).

Note that (11-65) says the characteristic time for kinetic energy loss by the large eddies is $\ell/\Delta u$, i.e., the eddies lose a significant fraction of their energy by break-up in one revolution. On the other hand, the characteristic time for decay of the large eddies by diffusion is ℓ^2/ν. Therefore, the ratio of the diffusion dissipation time scale to the turnover time scale is $\ell\Delta u/\nu = N_{\mathrm{Re},\ell} \gg 1$, which is consistent with the assumption that viscous dissipation of the large eddies is unimportant.

Let us now introduce the concept of an eddy Reynolds number,

$$N_{\mathrm{Re},\lambda} \equiv \frac{v_\lambda \lambda}{\nu} , \tag{11-66}$$

where λ is the size and v_λ the fluctuating velocity which characterizes the eddy. Consider eddies with $N_{\mathrm{Re},\lambda} \gg 1$ but with $\lambda \ll \ell$. Since $N_{\mathrm{Re},\lambda} \gg 1$, it is natural to assume that the flow on this scale must also be independent of ν. However, since $\lambda \ll \ell$, the additional assumption may be made that the flow does not depend on ℓ or Δu (which means that the turbulence on scale $\lambda \ll \ell$ is isotropic), except insofar as ℓ and Δu determine ε. Then, the fluctuating velocity v_λ can depend only on λ, ρ, and ε. By dimensional reasoning, we then conclude that

$$v_\lambda \approx (\varepsilon\lambda)^{1/3} \approx (\lambda/\ell)^{1/3}\Delta u \tag{11-67}$$

(Kolmogorov, 1941). Combining (11-66) and (11-67), we may also write

$$N_{\mathrm{Re},\lambda} \approx \frac{\varepsilon^{1/3}\lambda^{4/3}}{\nu} . \tag{11-68}$$

Suppose now that λ_0 denotes the eddy size for which viscosity becomes important. A natural statement of this condition is $N_{\mathrm{Re},\lambda_0} \approx 1$, so that λ_0 may be estimated from (11-68) as

$$\lambda_0 \approx \left(\frac{\nu_a^3}{\varepsilon}\right)^{1/4} \equiv \lambda_K , \tag{11-69}$$

where λ_K is called the *Kolmogorov microscale length.* It may be found a little more directly from dimensional considerations on the assumption that the parameters governing the small scale motion include ρ, ε , and ν. In the same way, one may also write down the Kolmogorov microscales of time and velocity:

$$\tau_K \equiv (\nu/\varepsilon)^{1/2} \quad (11\text{-}70) , \qquad v_K \equiv (\nu\varepsilon)^{1/4} = (\lambda_K/\tau_K) . \tag{11-71}$$

The relative sizes of the large and small scales of length, time, and velocity are now easily determined as a function of the Reynolds number of the mean flow;

$$\frac{\lambda_K}{\ell} \approx N_{\mathrm{Re},\ell}^{-3/4} ; (11\text{-}72a) \qquad \frac{\tau_K}{\ell/\Delta u} \approx N_{\mathrm{Re},\ell}^{-1/2} ; (11\text{-}72b) \qquad \frac{v_K}{\Delta u} \approx N_{\mathrm{Re},\ell}^{-1/4} . \quad (11\text{-}72c)$$

Qualitatively, these relations indicate what is borne out experimentally, namely that the small scale structure of turbulence becomes finer with increasing Reynolds number. They also indicate the assumption of isotropic turbulence for eddies in the *inertial subrange*, $\lambda_K \ll \lambda \ll \ell$, becomes better with increasing $N_{Re,\ell}$.

Measurements of Ackermann (1967, 1968) under various conditions in cloudy air produced values of ε in the range $3 \leq \varepsilon \leq 114$ cm^2 sec^{-3}. Isaac *et al.* (1978) observed in well-developed cumuli a median value for ε of 207 cm^2 sec^{-3}, with a maximum value of 372 cm^2 sec^{-1}. Aleksandrov *et al.* (1969) and Rhyne and Steiner (1964) observed in strong cumulonimbi, values for ε as high as 2000 cm^2 sec^{-3}. Values in clear air generally are close to the low end of the range of values cited for clouds (Kitchen and Caughey, 1981; Merceret, 1976a,b). Therefore, from (11-69), we expect λ_K to vary typically between 4×10^{-2} and 2×10^{-1} cm in the troposphere, which means that almost all aerosol particles are smaller than the microscale length.

11.6.2.1 *Turbulent Shear Coagulation*

Velocity gradients in turbulent air should cause relative particle motion and possibly collisions in a manner analogous to the laminar shear process treated in the previous section. Since aerosol particles are much smaller than λ_K, it is the shearing motion on length scales $\lambda < \lambda_K$ which is relevant. Since such motion must be strongly affected by viscosity, it is clear that turbulent shear coagulation may be represented by an expression similar to (11-63). To find such an expression, we must obtain an estimate for the velocity gradients for $\lambda < \lambda_K$. On this scale, velocity causes the flow to vary relatively smoothly, so that we may expand the velocity fluctuation v_λ in powers of λ and retain just the first term. Thus, $v_\lambda \approx c\lambda$ where c is a constant. Such treatment should be applicable for $\lambda \leq \lambda_K$ so that we may also write $v_K \approx c\lambda_K$, or $v_\lambda/\lambda \approx v_K/\lambda_K = 1/\tau_K = (\varepsilon/\nu_a)^{1/2}$, which is the relevant characteristic shear rate. By analogy to (11-63), we may then estimate the collection kernel for turbulent shear as

$$K_{TS}(r,s) \approx (r+s)^3(\varepsilon/\nu_a)^{1/2}\,. \tag{11-73}$$

Note this result also follows from dimensional considerations and the assumption that the only characteristic length of the process is the geometric collision length, $r+s$: The dimensions of K_{TS} are (length)^3(time)$^{-1}$, and since τ_K is the characteristic time scale of the flow for $\lambda \lesssim \lambda_K$, (11-73) then follows. An elaborate model calculation by Saffmann and Turner (1956) provides a numerical coeffcient:

$$K_{TS}(r,s) = 1.30(r+s)^3(\varepsilon/\nu_a)^{1/2}\,. \tag{11-74}$$

Earlier, less detailed (but not necessarily less rigorous) calculations by Tunitskii (1946) and Levich (1954a,b) gave coefficients of 0.5 and 3.1, respectively. Ackermann's (1967, 1968) measured values of ε referred to earlier, correspond to turbulent shear rates τ_K^{-1} which vary between 4 and 28 sec^{-1}. This means the crossover in dominance from Brownian to turbulent shear coagulation usually occurs at a particle size of a few microns.

11.6.2.2 *Turbulent Inertial Coagulation*

A second mode of coagulation in turbulent flow is due to local turbulent accelerations, which produce relative particle velocities for particles of unequal mass. The characteristic acceleration, a_K, of eddies of size λ_K is

$$a_K = v_K^2/\lambda_K = \varepsilon^{3/4}/\nu_a^{1/4}. \tag{11-75}$$

For $\lambda < \lambda_K$, we find from the relation $v_\lambda/\lambda \approx v_K/\lambda_K$ that the acceleration is $v_\lambda^2/\lambda \approx (\lambda/\lambda_K)(v_K^2/\lambda_K) < a_K$. Also, from (11-67), the eddy accelerations are found to decay with size as $\lambda^{-1/3}$ when $\lambda > \lambda_K$. Therefore, (11-75) provides a reasonable estimate of the maximum turbulent acceleration experienced by particles smaller than λ_K.

For particle radii less than $10\,\mu$m, the viscous relaxation time β^{-1} is generally at least two orders of magnitude smaller than τ_K. Accordingly, we may estimate the magnitude v' of the velocity response of a particle of radius r and mass m to local turbulent accelerations by assuming a_K to be constant in time, so that by Stokes' law

$$v' \approx \frac{m\,a_K}{6\pi\eta_a r} = \beta_r^{-1} a_K, \tag{11-76}$$

from (11-2). Similarly then, the induced relative velocity of a pair of particles of radii r and s ($r > s$) in close proximity (separation less than λ_K, so that both particles experience the same acceleration) is $(\beta_r^{-1} - \beta_s^{-1})a_K$. Therefore, if we assume a geometric collision cross-section, the collection kernel for this process of turbulent 'inertial' coagulation is

$$K_{TI}(r,s) \approx \pi(r+s)^2(\beta_r^{-1} - \beta_s^{-1})a_K = \pi(r+s)^2(\beta_r^{-1} - \beta_s^{-1})\varepsilon^{3/4}\nu_a^{-1/4} \tag{11-77}$$

(Levich, 1954b). Essentially, the same result has been also obtained by Saffman and Turner (1956), with the slight difference that in their expression π is replaced by the numerical factor 5.7.

The relative strength of the two turbulent coagulation processes is given by the ratio

$$\frac{K_{TI}}{K_{TS}} \approx \frac{\rho_P(r-s)}{2\rho_a\lambda_K} \approx \frac{10^3(r-s)}{\lambda_K}. \tag{11-78}$$

The appearance of the factor $(r - s)$ emphasizes that, according to the models presented, collisions between equal sized particles may occur as a result of turbulent shear, but not as a result of turbulent accelerations. For a small particle size ratio, we find the two processes are comparable when $r \approx 10^3\lambda_K$; e.g., $r \approx 10^{-1}\,\mu$m for $\varepsilon = 5$ cm^2 sec^{-3}, and $r \approx 1\,\mu$m for $\varepsilon = 10^3$ cm^2 sec^{-3}. For larger particles the inertial coagulation process becomes dominant.

According to the model of Saffman and Turner, the proper way to describe the overall rate of turbulent coagulation due to the simultaneous action of turbulent accelerations and shearing motions is by taking the square root of the sum of the squares of the separate rates.

In deriving (11-73) and (11-77) for turbulent coagulation and (11-63) for laminar shear coagulation, we assumed that the viscous hydrodynamic interaction between

particles undergoing relative motion in close proximity is negligible. We now turn to a brief discussion of a coagulation mechanism, relative sedimentation under gravity, where it is known that such effects are quite important, and in fact reduce the effective collision cross-section below the geometric value by factors smaller than 10^{-1} for particle radii less than $10\,\mu$m. The implication of these results for the other models of coagulation is considered briefly in turn.

11.6.3 Gravitational Coagulation

To date, the most accurate estimates of the effective collision cross-section of small particles settling under gravity have been obtained by use of a slip-corrected Stokes flow model in which the mutual interference of the particles and fluid (air) are fully accounted for. This rather complicated approach is discussed in Chapter 14, especially in Section 14.4.3, in the context of drop collisions. In this section, we shall describe a much simpler and less accurate model for the process, but one which nevertheless is adequate for the purpose of illustrating the effects of the viscous interaction between small particles.

The model is due to Fuchs (1951) and Friedlander (1957). It involves the basic assumptions that (i) the flow is in the Stokes regime; (ii) the small particles near a large one move as if in a stream caused by the air flow around the large one in isolation ('superposition scheme' – see also Section 14.3). More precisely, the velocity of a small particle of radius r_2 relative to a larger one of radius r_1 is taken as $\vec{V}_{S,2} - \vec{u}_{S,1}(\vec{r})$, where $\vec{V}_{S,2}$ is the terminal velocity of the small particle in isolation, and $\vec{u}_{S,1}$ is the Stokes velocity field which would be induced at the location $\vec{r}$ of the center of the small particle if the large one was falling at its terminal velocity in isolation. The center of the large particle is taken as the origin for $\vec{r}$.

Therefore, in the notation of Section 11.5, the r_2-particle current density relative to the r_1-particle is

$$\vec{j} = (\vec{V}_{S,2} - \vec{u}_{S,1}(\vec{r}))n_2\,, \tag{11-79}$$

and, with the flow streaming past the r_1-particle in the positive z-direction, the rate of collection by the r_1-particle is given by the positive flux J_G of $\vec{j}$ into the lower hemisphere ($z \leq 0$) of radius r_{12} concentric with the origin:

$$J_G = -\int_{S_H} \vec{j}\cdot d\vec{S} = n_2 \int_{S_H} \vec{u}_{S,1}(\vec{r})\cdot d\vec{S} + n_2 V_{S,2} \int_{S_H} \hat{e}_z \cdot d\vec{S}\,, \tag{11-80}$$

where S_H denotes the lower hemisphere. The last term on the right side of (11-80) is simply $-\pi r_{12}^2 n_2 V_{S,2}$. The first term on the right side is due to motion following the lines, and is found most easily by using the Stokes stream function ψ_S, (10-35), which we write in the form

$$\psi_S = \frac{V_{S,1} r^2 \sin^2\theta}{2}\left(1 - \frac{3r_1}{2r} + \frac{r_1^3}{2r^3}\right)\,, \tag{11-81}$$

where $V_{S,1}$ is the terminal velocity of the r_1-particle and θ is the polar angle between $\vec{r}$ and the positive z-axis. The streamline which approaches to within a distance r_{12}

from the origin when $\theta = \pi/2$ is at a distance δ from the z-axis far upstream of the origin, where from (11-81) we must have $\delta^2 = r_{12}^2(1 - 3r_1/2r_{12} + r_1^3/2r_{12}^3)$. By the same kind of reasoning, the incompressibility of the flow requires that $\int_{S_H} \vec{u}_{S,1} \cdot d\vec{S} = \pi V_{S,1}\delta^2$, so that the first term in J_G is $\pi n_2 V_{S,1} r_{12}^2[1 - 3r_1/2r_{12} + r_1^3/2r_{12}^3]$. This represents the attachment rate by the effect known as *direct interception.* If we now combine the two contributions to J_G, and note that the corresponding gravitational collision kernel is $K_G = J_G/n_2$, we finally obtain

$$K_G(r,s) = \pi A(1+p)^2 r^4 \left(1 - \frac{3}{2(1+p)} + \frac{1}{2(1+p)^3} - p^2\right), \tag{11-82}$$

where $A = (2g/9\eta_a)(\rho_P - \rho_a)(1 + \alpha N_{Kn})$ (11-22), and we have introduced the 'p-ratio' defined by $p \equiv s/r$ (for $s < r$).

It is clear from the assumptions underlying the superposition scheme, that (11-82) is strictly valid only for $p \ll 1$; in that limit (11-82) reduces to

$$K_G(r,s) = \frac{\pi}{2} A r^4 p^2 = \frac{\pi}{2} s^2 V_{S,r} \qquad \text{for } p \ll 1, \tag{11-83}$$

which says the collection rate vanishes with the radius of the smaller particle. Of course, this is not a rigorous result since we have neglected Brownian motion, which becomes increasingly significant for the motion of the smaller particle as $s \to 0$. The function K_G should also vanish as s approaches r, since in that limit the Stokes terminal velocities are equal. In order to obtain an approximate form for K_G which exhibits the correct behavior for p near zero and unity, Friedlander (1965) generalized (11-83) to read as follows:

$$K_G(r,s) = \frac{\pi}{2} A r^4 p^2 (1 - p^2) = \frac{\pi}{2} s^2 (V_{S,s} - V_{S,r}). \tag{11-84}$$

It is apparent that if there were no hydrodynamic deflection of approaching particles, the collection rate would be controlled simply by the relative velocity of approach and the geometric collision cross-section. It is customary to describe the effect of the hydrodynamic interaction on the collection rate by use of the concept of *collision efficiency*, $E = E(r,s)$, defined to be the ratio of the actual cross-section to the geometric cross-section for a pair of interacting particles (see also Section 14.2). Then, we can also express K_G as follows:

$$K_G(r,s) = \pi(r+s)^2 E(r,s)[V_{S,r} - V_{S,s}]. \tag{11-85}$$

On comparing this with (11-84), we obtain

$$E(r,s) = \frac{p^2}{2(1+p)^2}, \tag{11-86}$$

for the collision efficiency according to the model of Fuchs (1951) and Friedlander (1957). Table 11.3 shows that this simple result agrees surprisingly well with the more elaborate computations referred to earlier. (Although in principle E depends on the absolute size of the particles as well as the p-ratio – see Section 14.2) – in

TABLE 11.3
Collision efficiency for spherical particles of radii less than 10 μm; from (11-86) and from values computed by M.H. Davis, 1972.

p	E Equation (11-86)	E Davis (1972)
0.2	1.4×10^{-2}	1.3×10^{-2}
0.4	4.1×10^{-2}	2.7×10^{-2}
0.6	9.9×10^{-2}	3.4×10^{-2}
0.8	9.9×10^{-2}	3.4×10^{-2}

practice, the size dependence becomes insignificant for $r \lesssim 10\,\mu$m. This is physically reasonable since, for sufficiently small particles, the motion is controlled by viscous forces, the role of particle inertia being negligible.)

Since Table 11.3 shows that for $r \lesssim 10\,\mu$m the effective collision cross-section for gravitational coagulation is generally less than three percent of the geometric value, it is appropriate to reconsider briefly the assumption that E = 1 for laminar shear, turbulent shear, and turbulent inertial coagulation. Particularly for this last process, the model used is close to the gravitational collision model, the only obvious difference being that the relative velocity of approach in the turbulent case is due to the terminal velocity difference of particles 'falling' in the constant acceleration field a_K instead of g. However, in the derivation leading to (11-77), a_K was regarded as constant only in the sense that $\beta_r^{-1} \ll \tau_K$. Besides β_r^{-1}, another relevant time scale is the characteristic time of hydrodynamic interaction. If this were much smaller than τ_K also, the analogy between the gravitational and turbulent models would be complete and we should then use values of E such as those in Table 11.3 for the case of turbulent coagulation also.

An estimate of the hydrodynamic interaction time t_i is given by dividing some representative interaction length by the relative velocity of approach, i.e., $t_i \propto n(p) r a_K^{-1} (\beta_r^{-1} - \beta_s^{-1})^{-1}$, where $n(p)$ is a number of order 1 to 10^2 which increases with increasing p (the mutual interference of particles and fluid becomes of longer effective range as the radii become comparable). Therefore, for small p we have $t_i/\tau_K \propto r\beta_r/\tau_K a_K = r\beta_r/v_K$, where v_K is the microscale of velocity, typically of order 1 cm sec^{-1}. Since $r\beta_r \approx 10^2$ cm sec^{-1} and 1 cm sec^{-1} for $r = 0.1\,\mu$m and $10\,\mu$m, respectively, we see that generally the particle relative velocities and accelerations will not remain constant in direction over the time of hydrodynamic interaction. This means the turbulent inertial coagulation process is similar to one of 'gravitational' coagulation in which gravity is allowed to vary randomly in strength and direction during interaction, at least over a limited range of values, with a characteristic frequency of order τ_K^{-1}. The consequences of such a model have not been worked out. (Sedunov (1960, 1963, 1964) has made a detailed study of the relative motion of small particles in turbulent flow, but this has not resolved the question of what is the effective collision cross-section.)

In Figure 11.6, a comparison is made of the collection kernels for Brownian, turbulent shear, turbulent inertial, and gravitational coagulation according to (11-59)

(with $\alpha = 0$), (11-74) (11-77), and (11-84), respectively. The dotted portions of the curves for turbulent shear and turbulent inertial coagulation indicate regions where the assumption of a geometric collision cross-section is not likely to be accurate. According to the figure, Brownian coagulaton is most important for particles of about one micron radius or smaller, while turbulence and especially gravity control the coagulation of particles larger than a few microns, assuming a modest energy dissipation rate of 5 cm^2 sec^{-3}.

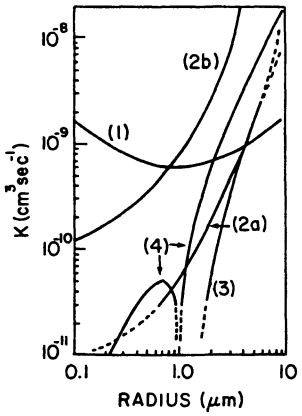


Fig. 11-6: Comparison of various collision modes for a spherical particle of density 1 g cm^{-3} and radius 1 μm interacting with a second spherical particle of radius r (dotted lines: regions where the assumption of a geometric collision cross-section is not likely to be accurate). (1) Brownian coagulation, (2a) turbulent shear coagulation ($\epsilon = 5$ cm^2 sec^{-3}), (2b) turbulent shear coagulation ($\epsilon = 1000$ cm^2 sec^{-3}), (3) turbulent inertial coagulation, ($\epsilon = 5$ cm^2 sec^{-3}), (4) gravitational coagulation (sedimentation). (Adapted from Klett, 1975 and from Hidy, 1973.)

11.7 Explanation for the Observed Size Distributions of the Atmospheric Aerosol

From our studies of the mechanics of aerosol particles, we are now in a position to consider some models which have been put forth to explain the observed regularities in the size distributions of tropospheric aerosols (recall Section 8.2.9).

11.7.1 Quasi-Stationary Distributions (QSD)

A physically appealing way of dealing with the problem of the steady state aerosol particle distribution $n(r)$ was introduced by Friedlander (1960a,b), who proposed the theory of *quasi-stationary distributions* (QSD). This theory is based on the assumption that, for $r \gtrsim 0.1\,\mu$m, the aerosol has attained a state of dynamic equilibrium between Brownian coagulation and gravitational sedimentation. The theory further assumes that the form of $n(r)$ is completely determined by the two parameters characterizing the process rates for coagulation and sedimentation, and by

the rate ε_m at which matter enters the upper end of the spectrum by coagulation of smaller particles. The QSD theory is somewhat analogous to the theory of turbulence in the inertial subrange, discussed in Section 11.6.2. There the assumption was made that $v_\lambda = v_\lambda(\lambda, \varepsilon)$, where ε measures the energy flow rate down the eddy size spectrum. Similarly, according to QSD, an aerosol in dynamic equilibrium is characterized principally by ε_m, the flow rate of matter passing up the aerosol size spectrum.

Friedlander delineates two subranges for n. At the lower end of the equilibrium range, the 'coagulation subrange' for which $0.1 \leq r \leq 0.5\,\mu$m, he assumes sedimentation to be negligible. Since the concentration of particles in this subrange is much larger than in the range $r > 1\,\mu$m, practically all the matter being transferred up the spectrum over the coagulation subrange will do so by Brownian coagulation rather than by inertial impaction with the larger sedimentation particles. Therefore, for the coagulation subrange it is reasonable to assume that $n = n(r, C, \varepsilon_m)$, where $C = 2kT/3\eta_a$ is the characteristic coagulation parameter (cf. (11-59). If L^3 denotes a characteristic air volume and ℓ denotes a characteristic spectral length (particle radius), then on dimensional grounds, one finds for the units of n, r, C, and ε_m: $[n] = L^{-3}\ell^{-1}$, $[r] = \ell$, $[C] = L^3t^{-1}$, $[\varepsilon_m] = \ell^3L^{-3}t^{-1}$, where t represents time. It therefore follows from the constraint of dimensional consistency that

$$n = B_1 \left(\frac{\varepsilon_m}{C}\right)^{1/2} r^{-5/2}, \quad 0.1 \leq r \leq 0.5\,\mu\text{m}, \tag{11-87}$$

where B_1, is a dimensionless constant.

The second subrange is considered to be confined to the upper end of the spectrum, $r \gtrsim 5\,\mu$m, where it may be assumed that Brownian coagulation is negligible. Thus, matter entering this subrange is lost by sedimentation without significant further transfer within the range by coagulation. Therefore, for this subrange n is assumed to be a function of r, ε_m, and the characteristic sedimentation parameter $A = (2/9)(g/\eta_a)(\rho_P - \rho_a)$ (cf. (11-22). Since $[A] = L\ell^{-2}t^{-1}$, by dimensional analysis, we find

$$n = B_2 \left(\frac{\varepsilon_m}{A}\right)^{3/4} r^{-19/4}, \quad r \gtrsim 5\,\mu\text{m}, \tag{11-88}$$

where B_2 is another dimensionless constant.

The physical basis of this second spectral form appears not be as sound as that for the coagulation subrange. Particle loss by sedimentation from an aerosol volume element requires a vertical gradient of particle concentration, and the characteristic length for this gradient will depend in part on some additional transport mechanism such as turbulent diffusion. The model leading to (11-88) misrepresents the physics of this situation by ignoring the possibility of such an additional independent characteristic length.

Although the power laws obtained for the two particle subranges agree qualitatively with aerosol spectra, it should be recalled from Section 8.2.9 that, in the lower troposphere, observed particle size spectra are usually better represented by $n \propto r^{-4}$, over a range as large as $0.1 < r < 100\,\mu$m (see Section 8.2.9).

In another attempt to check the QSD, Friedlander used the sedimentation subrange to obtain an estimate for ε_m. Assuming $B_2 \approx 1$, which is consistent with a

principle of dimensional analysis given by Bridgeman (1931), (11-88) gives

$$\varepsilon_m \sim A n^{4/3} r^{19/3} . \tag{11-89}$$

On substituting data given by Junge (1953) for n and r, Friedlander obtained $\varepsilon_m \approx 10^{-13}$ $\mathrm{cm^3 cm^{-3}}$ $\mathrm{sec^{-1}}$. Since ε_m represents approximately the rate at which matter enters the upper end of the spectrum by Brownian coagulation of Aitken particles, the time scale for 'processing' Aitken particles by coagulation ($\equiv$ mean residence time of matter in the Aitken range) may be estimated by dividing the volumetic concentration of Aitken particles by ε_m. From the data of Junge (1953), the volumetic concentration is of the order of 10^{-11} $\mathrm{cm^3 cm^{-3}}$ $\mathrm{sec^{-1}}$, corresponding to a characteristic residence time of the order of 10^2 sec. This is a very short time (for example, the half life for Aitken particles of $r = 0.01\,\mu$m coagulating by Brownian motion is one order of magnitude larger (recall Section 11.5)) and indicates that the estimate for ε_m is somewhat high. This result is not surprising considering the simplicity of the QSD theory. A numerical study by Storebo (1972) on steady state aerosol distributions indicates that the residence time may easily vary from several minutes to 10^2 hr for realizable conditions, depending primarily on the characteristics of the source of particles at the small size end of the spectrum.

Quasi-stationary distributions arising from a dynamic balance between two or more processes (such as Brownian and turbulent coagulation, gravitational sedimentation, gas to particle conversion, and interactions between aerosol particles and clouds) cannot occur in the atmosphere unless the aerosol source and sink processes operate with time scales which are short compared to meteorological time scales. Model calculations of Junge and Abel (1965) show that the time needed for establishing a steady state among the various aerosol source, modification, and removal processes on a large scale may be as much as 50 days. This is slow compared to the pace of changes induced by varying meteorological conditions, which may easily occur with a time scale of the order of 1 day. On this basis, Junge (1969b) concluded that the QSD theory cannot explain the observed r^{-4} dependency of aerosol concentration on size in the lower troposphere for $r > 0.1\,\mu$m.

However, under special conditions, it is presumably possible for QSD to exist. For example, aerosols in very clean air masses above the planetary boundary layer seem to show a tendency for concentrations to vary like r^{-k}, with $4.5 \lesssim k \lesssim 5$. This is close (11-88), which may thus approximately describe a global background QSD (see also Section 11.7.5). Also, the upper end of the sea salt particle spectrum within the planetary boundary layer over the ocean may be a QSD between salt particle production and vertical transport by sedimentation and turbulent diffusion (Toba, 1965a,b).

11.7.2 Self-Preserving Distributions (SPD)

Another plausible approach for explaining the observed regularities of size distributions for tropospheric aerosols involves the notion that they represent asymptotic solutions to the coagulation equation, rather than equilibrium solutions as in the QSD theory. It seems reasonable to expect that as time progresses, a coagulating aerosol might lose its 'birth marks' and acquire a size distribution independent of

its initial form. It is also reasonable to anticipate that such asymptotic solutions should have relatively simple forms, which might be investigated by the use of similarity transformations, i.e., a transformation of variables which will reduce the coagulation equation to an equation in only one independent variable. The single variable would then suffice to describe the form of the asymptotic distribution. Following the example of the self-preserving hypothesis used in the theory of turbulence (see, for example, Townsend,1956), Friedlander (1961) introduced a similarity transformation which forms the basis of his theory of *self-preserving distributions* (SPD). Further development and testing of the theory has been reported in a series of subsequent articles (Swift and Friedlander, 1964; Hidy, 1965; Friedlander and Wang, 1966; Wang and Friedlander, 1967, Friedlander and Hidy, 1969), Pick *et al.* (1970).

The similarity transformation for $n(\mathrm{v}, t)$ in the SPD theory is as follows:

$$n(\mathrm{v}, t) = g(t)\psi_1\left(\frac{\mathrm{v}}{\mathrm{v}_+(t)}\right), \tag{11-90}$$

where g and v_+ are functions of time, and it is assumed that the dimensionless 'shape' of the distribution does not change with time. The functions g and v_+ can be evaluated to within a constant from any two integral functions of n, such as the zeroth and first moments of the distribution (i.e., the total number of particles per unit volume of air, N, and the volumetric concentration or volume fraction of dispersed phase, ϕ). Thus, we have $N = \int_0^\infty n(\mathrm{v}, t)\mathrm{dv} = \mathrm{v}_+ g c_1$ and $\phi = \int_0^\infty \mathrm{v}n(\mathrm{v}, t)\mathrm{dv} = \mathrm{v}_+^2 g c_2$, where c_1, and c_2 are constants, since ψ_1 is assumed to be independent of time. On substituting the resulting expressions for v_+ and g into (11-90), we obtain

$$n(\mathrm{v}, t) = \frac{c_2 N^2}{c_1^2}\psi_1\left(\frac{c_2 N \mathrm{v}}{c_1 \phi}\right) = \frac{N^2}{\phi}\psi(\eta), \tag{11-91a}$$

where

$$\eta = \frac{N\mathrm{v}}{\phi}, \tag{11-91b}$$

and ψ is another suitable dimensionless distribution function. This representation also makes sense on dimensional grounds, since $\phi N \propto \ell^3$ is a characteristic spectral volume, namely the average particle volume.

The conjecture that (11-92) or (11-91) constitutes a solution can only be tested for a specific kernel K by substitution into the coagulation equation. The SPD theory was developed to apply to situations in which there is no addition or removal of aerosol mass in any elementary volume element (as for example, by sedimentation), so that a basic condition for the validity of (11-91) is that ϕ be constant in time.

Physically, it is obvious that (11-56) must satisfy the condition $\phi =$ constant. It can also be easily demonstrated by integrating (11-56) multiplied by v:

$$\frac{\mathrm{d}\phi}{\mathrm{d}t} = \frac{\mathrm{d}}{\mathrm{d}t}\int_0^\infty \mathrm{dv}\, \mathrm{v}n(\mathrm{v}, t) = \frac{1}{2}\int_0^\infty \mathrm{dv}\, \mathrm{v}\int_0^{\mathrm{v}} K(\mathrm{u}, \mathrm{v}-\mathrm{u})n(\mathrm{u}, t)n(\mathrm{v}-\mathrm{u}, t)\,\mathrm{du}$$

$$-\int_0^\infty \mathrm{dv}\, \mathrm{v} n(\mathrm{v},t) \int_0^\infty K(\mathrm{u},\mathrm{v}) n(\mathrm{u},t)\, \mathrm{du}\,.$$

If the order of integration is interchanged in the first integral on the right (i.e., $\int_0^\infty \mathrm{dv} \int_0^\mathrm{v} \mathrm{du}\, F(\mathrm{u},\mathrm{v}) = \int_0^\infty \mathrm{du} \int_\mathrm{u}^\infty \mathrm{dv}\, F(\mathrm{u},\mathrm{v})$), and this is followed by the substitution $\mathrm{v}' = \mathrm{v} - \mathrm{u}$, the two integrals on the right will cancel, so that $\phi =$ constant as expected.

We would now like to show that (11-91) represents a solution to (11-56) for the case that K is a homogeneous function of its arguments, i.e., $K(\mathrm{au},\mathrm{av}) = \mathrm{a}^b K(\mathrm{u},\mathrm{v})$. This includes the important cases of Brownian coagulation without the slip correction ($b = 0$) and laminar shear coagulation ($b = 1$). In order to facilitate our discussion here and again in Chapter 15 where more elaborate solutions and solution methods are presented, let us first introduce a dimensionless form of the coagulation equation. Following Scott (1968) and Drake (1972a,b), we write

$$\mathrm{u} \equiv \mathrm{v}_0 y,, \quad \mathrm{v} \equiv \mathrm{v}_0 x\,, \quad \tau \equiv K_0 N(0) t\,, \quad K(\mathrm{u},\mathrm{v}) \equiv K_0 \alpha(y,x)\,,$$

$$\mathrm{v}_0 n(\mathrm{v},t) \equiv N(0) f(x,\tau) \quad \mathrm{v}_0 n(\mathrm{v},0) = N(0) f(x,0) \equiv N(0) f_0(x)\,, \tag{11-92}$$

where $N(0)$ is the initial total number density, v_0 the initial mean particle volume ($\mathrm{v}_0 = \phi/N(0)$), K_0 a normalizing factor with dimensions of volume per unit time, τ the dimensionless time, $f(x,\tau)$ the dimensionless concentration, $\alpha(x,y)$ ($= \alpha(y,x)$) the dimensionless collection kernel, and x and y are dimensionless particle volumes. Substituting (11-92) into (11-56) gives, for the dimensionless coagulation equation,

$$\frac{\partial f(x,\tau)}{\partial \tau} = \frac{1}{2}\int_0^x \alpha(x-y,y) f(x-y,\tau) f(y,\tau) \mathrm{d}y - f(x,\tau) \int_0^\infty \alpha(x,y) f(y,\tau) \mathrm{d}y\,. \tag{11-93}$$

If we denote the moments of f by $M_n(\tau)$, i.e.,

$$M_n(\tau) \equiv \int_0^\infty x^n f(x,\tau)\, \mathrm{d}x\,, \tag{11-94}$$

we find from the condition of aerosol mass conservation ($\phi = \text{const.} = \mathrm{v}_0 N(0)$) that $M_1(\tau) = 1$. Therefore, a similarity transformation for $f(x,\tau)$ which is completely equivalent to (11-91), is as follows:

$$f(x,t) = M_0^2(\tau)\psi(\eta)\,, \quad \text{(11-95a)} \qquad \eta = M_0(\tau) x\,. \tag{11-95b}$$

Now let us proceed to show that this transformation is indeed a solution to the coagulation equation for homogeneous kernels. From (11-95a), we have

$$\frac{\partial f}{\partial t} = \left(2\psi + \eta \frac{\mathrm{d}\psi}{\mathrm{d}\eta}\right) M_0 \frac{\mathrm{d}M_0}{\mathrm{d}\tau}\,. \tag{11-96}$$

Evidently, an expression for $\mathrm{d}M_0/\mathrm{d}\tau$ is needed. An ordinary integro-differential equation for any of the moments is easily obtained by integration of the coagulation equation in the manner discussed above for the first moment. The result is

$$\frac{\mathrm{d}M_n}{\mathrm{d}\tau} = \frac{1}{2}\int_0^\infty\int_0^\infty [(x+y)^n - x^n - y^n]\alpha(x,y)f(x,\tau)f(y,\tau)\,\mathrm{d}x\,\mathrm{d}y\,. \tag{11-97}$$

Therefore, we have

$$\begin{aligned}\frac{\mathrm{d}M_0}{\mathrm{d}\tau} &= -\frac{1}{2}\int_0^\infty\int_0^\infty \alpha(x,y)f(x,\tau)f(y,\tau)\,\mathrm{d}x\,\mathrm{d}y \\ &= -\frac{M_0^{2-b}}{2}\int_0^\infty\int_0^\infty \alpha(\eta,\xi)\psi(\eta)\psi(\xi)\,\mathrm{d}\eta\,\mathrm{d}\xi\,,\end{aligned} \tag{11-98}$$

in view of the homogeneity of α. Similarly, the right side of (11-93) in similarity variables is

$$M_0^{3-b}\left(0.5\int_0^\eta \alpha(\eta-\xi,\xi)\psi(\eta-\xi)\psi(\xi)\,\mathrm{d}\xi - \psi(\eta)\int_0^\infty \alpha(\eta,\xi)\psi(\xi)\,\mathrm{d}\xi\right).$$

On combining these expressions, we see that the similarity transformation does work (i.e., it is successful in eliminating reference to τ), and reduces the coagulation equation to the following ordinary integro-differential equation:

$$\left(\eta\frac{\mathrm{d}\psi}{\mathrm{d}\eta} + 2\psi\right)\int_0^\infty\int_0^\infty \alpha(\eta,\xi)\psi(\eta)\psi(\xi)\,\mathrm{d}\eta\,\mathrm{d}\xi$$

$$= 2\int_0^\infty \alpha(\eta,\xi)\psi(\eta)\psi(\xi)\,\mathrm{d}\xi - \int_0^\eta \alpha(\eta-\xi,\xi)\psi(\eta-\xi)\psi(\xi)\,\mathrm{d}\xi \tag{11-99}$$

(Friedlander and Wang, 1966). Two accompanying integral constraints, corresponding to $M_0(0) = M_1(\tau) = 1$, are as follows:

$$\int_0^\infty \eta\psi(\eta)\,\mathrm{d}\eta = \int_0^\infty \psi(\eta)\,\mathrm{d}\eta = 1\,. \tag{11-100}$$

In order to gain some idea of the spectral shapes predicted by the SPD theory, let us now solve (11-99) for the simplest case of Brownian coagulation with a constant collision kernel. For α = constant (11-99) reduces to

$$\eta\frac{\mathrm{d}\psi}{\mathrm{d}\eta} = -\int_0^\eta \psi(\eta-\xi)\psi(\xi)\,\mathrm{d}\xi\,. \tag{11-101}$$

The convolution form suggests the use of Laplace transforms by which the following solution is readily obtained:

$$\psi = \mathrm{e}^{-\eta}\,. \tag{11-102}$$

This also satisfies (11-100). The corresponding spectrum function is

$$f(x,\tau) = M_0^2(\tau)\mathrm{e}^{-M_0(\tau)x}\,. \tag{11-103}$$

To proceed further, we must choose an explicit representation for τ, or, in other words, K_0 (see (11-92). From (11-59) the kernel is $K = 16\pi Dr = K_0\alpha$. In order to obtain the best correspondence with the notation for Smoluchowski's discrete solution, (11-52), we choose $K_0 = 8\pi Dr$, and $\alpha = 2$. Then, from (11-97), we have $\mathrm{d}M_0/\mathrm{d}\tau = -M_0^2$, or $M_0 = (1+\tau)^{-1}$ so that the spectrum function is

$$f(x,\tau) = \frac{\mathrm{e}^{-x/(1+r)}}{(1+\tau)^2}\,. \tag{11-104}$$

This result represents a particular asymptotic solution to the coagulation equation. It corresponds to the initial spectrum $f(x,0) = \exp(-x)$, but it is expected that any initial distribution would approach (11-104) for large τ. See Wang (1966) for a proof of this assertion for the case of constant α.

Actually, the solution (11-104) was obtained in a similar way some time ago by Schumann (1940), who also conjectured it would be approached asymptotically after a long time, no matter what the initial distribution might be. In support of his conjecture, he showed how an initially monodisperse distribution would, by a discrete growth process, adopt a form like (11-104) for small steps and large times. We can easily carry through a similar procedure here, and show that Smoluchowski's discrete solution (11-52) approaches the self-similar form of (11-104) for large times. It suffices for this purpose to find the limit of $f_k(\tau)/(\sum f_k)^2$ as $\tau \to \infty$ for fixed $\eta = k(\sum f_k)$ (recall (11-95) and note that $k = \mathrm{v}/\mathrm{v}_0 = x$). Proceeding in this manner, we find for fixed $\eta = k(1+\tau)^{-1}$ (recall (11-51)) that

$$\begin{aligned}\lim_{\tau\to\infty}\left[\frac{f_k(\tau)}{(\sum f_k)^2}\right] &= \lim_{\tau\to\infty}\left((1+\tau)^2\left[\frac{\tau^{k-1}}{(\tau+1)^{k+1}}\right]\right)\\ &= \lim_{\tau\to\infty}\left(\left(1+\frac{1}{\tau}\right)^{1-\eta}\left[\left(1+\frac{1}{\tau}\right)^{\tau}\right]^{-\eta}\right) = \mathrm{e}^{-\eta},\end{aligned} \tag{11-105}$$

in agreement with (11-102).

An interesting feature of (11-104) is the indication that SPD due to Brownian coagulation decline faster at large sizes than observed tropospheric spectra. The inclusion of size dependence and a slip correction for the Brownian kernel does not alter this conclusion, as shown by Hidy (1965). He carried out numerical calculations of $n(r,t)$ using (11-59) for $0 \le N_{\mathrm{Kn},0} \le 2$, where $N_{\mathrm{Kn},0}$ is the Knudsen number for initially uniform distributions, and for a variety of initial distributions without slip ($N_{\mathrm{Kn},0} = 0$). In all cases, the solutions converged toward SPD with the exact shape depending on $N_{\mathrm{Kn},0}$. In general, however, the self-similar shape

for size-dependent continuum Brownian coagulation was found to approach $e^{-\eta}$ for $\eta > 1$.

Evidently then, the shape of Brownian coagulation SPD does not conform well with tropospheric aerosol distributions. This point has been emphasized by Junge (1969b), who plotted Hidy's SPD for $N_{\mathrm{Kn}} = 1$, corresponding to particle radii near $0.1\,\mu$m; on a graph with coordinates $\partial N'/\partial \log_{10} r$ versus $\log_{10} r$, for various values of time. The quantity $N'(r,t)$ is the number of particles per unit volume with radii less than r, i.e., $N'(r,t) = \int_0^r n(r,t)\mathrm{d}r$. Therefore, we have $\partial N'/\partial r = n(r,t) = n(\mathrm{v},t)\mathrm{d}\mathrm{v}/dr = 4\pi r^2 n(\mathrm{v},t)$, or $\partial N'/\partial \log_{10} r = 3(\ln 10)\mathrm{v}n(\mathrm{v},t)$. Then, since $\mathrm{v}n(\mathrm{v},t) = N(0)xf(x,\tau) = N(t)\eta\psi(\eta)$, where $N(t) = N'(\infty,t)$ is the total particle concentration at time t (note also that $N'(r,t) = N(t) - N(r,t)$, where $N(r,t)$ is given by (8-33), the desired form for plotting is $\partial N'/\partial \log_{10} r \approx 6.9N(t)\eta\psi(\eta)$, where $\eta\psi(\eta)$ represents Hidy's numerical solution for the SPD. The result of this computation is shown in Figure 11.7, where it is assumed that at $\tau = 3$ and $r = 0.1\,\mu$m, $\partial N'/\partial \log_{10} r$ ($= 4.5 \times 10^3$ cm^{-3}) is maximal; this concentration is in accordance with observations under moderately polluted conditions. It is seen that the SPD is approached by $t = 13.4$ days and, subsequently, changes with time as indicated in the figure. It is interesting to note that the slope of the envelope curve for the SPD follows an r^{-3} law (which we recall from Chapter 8 is similar to the observed spectral shapes in the lower troposphere). This is a consequence of aerosol volume conservation (ϕ= const.), which causes radii for different times to vary as $N^{-1/3}$; i.e., for a time shift of δt the ordinate in Figure 11.7 shifts by $(\log_{10} N/\partial t)\delta t$, whereas since $\eta \propto r^3 N/\phi$, for constant ϕ the abscissa shifts by $-(\partial \log_{10} N/\partial t)(\delta t/3)$. From the figure, it is clear that the shape of the Brownian coagulation SPD differs from observed distributions, especially with respect to the steep slope beyond the maximum. Also, just as for QSD, the time for establishing Brownian SPD is long compared to meteorological time scales. Therefore, although there remains a need for research into the possibilities of SPD for other mechanisms, we may conclude that the occurrence of SPD for Brownian coagulation is unlikely in the tropospheric aerosol.

A similar conclusion was implicit in the earlier studies of in-cloud scavenging by Junge and Abel (1965). The results of their computations are displayed in Figure 11.8 in terms of the concentration $N(r,t)$ of particles with radii $\geq r$ (cf. (8-33) and (8-35)). These results are based on the assumptions (1) that the troposphere has a height of 8 km, is uniformly mixed, and is filled initially with an aerosol of size distribution specified by curve $t = 0$ in Figure 11.8; (2) that a uniform fraction 0.2 of the troposphere is filled with clouds which are composed of uniformly sized drops of radius $10\,\mu$m present in a number concentration of 200 cm^{-3}; (3) that the clouds have an average base height of 1.5 km and an average depth of 4 km ; (4) that all clouds evaporate after a time period of 1.5 hr, after which they reform; (5) that the troposphere undergoes 10 such evaporation-condensation cycles for each precipitation event; (6) that the mean annual global rainfall rate is 1000 mm, and (7) that rain is composed of raindrops of 0.8 mm in diameter. From their computations, Junge and Abel concluded that neither Brownian coagulation, nor condensation, nor interaction of aerosol particles with cloud and raindrops significantly affects the size distribution of aerosol particles of radii larger than $0.1\,\mu$m,

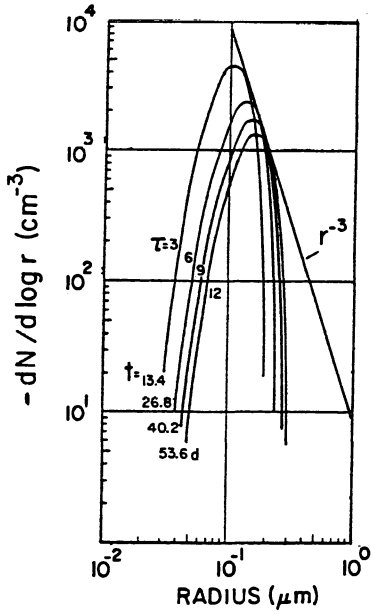


Fig. 11-7: Variation with time of aerosol size distribution; at $\tau = t = 0$ aerosol is monodisperse, $r = 0.04$ μm, and $N = 3.55 \times 10^4$ cm^{-3}; at $\tau = 3$ or $t = 13.4$ d the self-preserving particle distribution is approached and subsequently changes with time as indicated. (From Junge, 1969b; by courtesy of Am. Meteor. Soc., and the author.)

at least during time periods up to a week.

11.7.3 Quasi-Stationary Self-Preserving Distributions

Let us suppose the coagulation equation is extended to include possible sources and sinks of particles, so that in general ϕ is no longer constant. Liu and Whitby (1968) investigated the spectral form which could result in this situation if the following restrictions were to apply: (1) dynamic equilibrium exists within some subrange, so that $\partial n/\partial t = 0$; (2) in that subrange a self-similar form ψ for n exists, so that ϕ is constant or nearly so over the time interval of interest.

These strong constraints suffice to specify ψ and n to within a constant. Thus, the governing equation for ψ is simply

$$2\psi + \eta \frac{d\psi}{d\eta} = 0\,, \tag{11-106}$$

as can be seen from (11-96). The solution is $\psi = C_1 \eta^{-2}$, where C_1 is a dimensionless constant. The corcesponding solution for n is, from (11-91), $n(\mathrm{v}) = C_1 \phi \mathrm{v}^{-2}$, or

$$n(r) = \frac{C_1 \phi}{\mathrm{v}^2} \frac{d\mathrm{v}}{dr} = \frac{C_2 \phi}{r^4}\,, \tag{11-107}$$

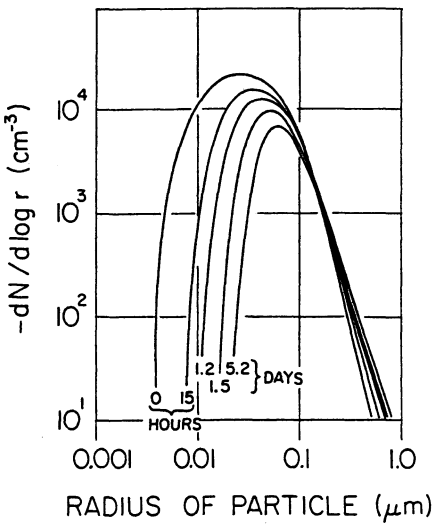


Fig. 11-8: Variation with time of an average atmospheric aerosol particle size distribution due to sedimentation, capture by cloud and raindrops, and due to their involvement in condensation. (From Junge and Abel, 1965; by courtesy of the authors.)

where C_2 is another dimensionless constant (Liu and Whitby, 1968).

Of course, this simple result is in good agreement with observations, and it is tempting to regard this as a demonstration that the tropospheric aerosol is a quasi-stationary self-preserving distribution. However, it must be remembered that the r^{-4} law is not rigorous experimentally, and that there is no proof of the existence of SPD for general coagulating mechanisms. The simple expression (11-107) is just the envelope curve of the assumed SPD (both time independent and self-preserving), and is a result of an almost over-determined formulation.

11.7.4 Statistical Distributions

Over portions of the spectrum where $n(r) \propto r^{-4}$, the volume distribution

$$\frac{\partial V}{\partial \log_{10} r} = \left(\frac{4}{3}\pi r^3\right) \frac{\partial N'}{\partial \log_{10} r}$$

is constant. Thus, one may say there is a tendency for atmospheric aerosols to form quasi-constant log volume distributions, which in turn may be approximated by broad log normal volume distributions. Noting that mechanical processes such as grinding form log-normal volume distributions, Junge (1969a,b) has suggested it is not unreasonable to expect that a large number of independent aerosol sources could produce log-normal distributions also, and that this could provide an explanation for the observations (1) that the r^{-4} distribution is only an approximation for average conditions with irregular deviations in individual cases, (2) that the r^{-4} distribution is usually best realized in polluted areas where the statistics are

better due to a large number of sources, and (3) that the deviations become more pronounced if one or only a few sources dominate, as in the case, for instance, of aerosols within the lowest 2 to 3 km over the ocean where sea salt particles dominate. These ideas are schematically illustrated in Figure 11.9. Although the statistical explanation for the form $n \propto r^{-4}$ seems quite plausible, it remains to be demonstrated quantitatively under what conditions log-normal distributions will result.

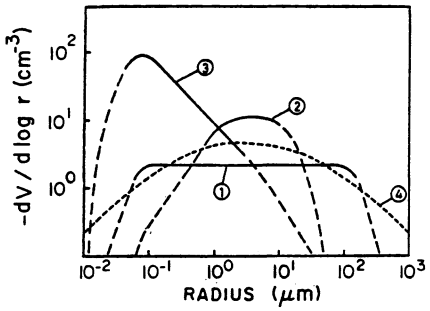


Fig. 11-9: Log-volume distributions for aerosol particle spectra of the form $n(r) \sim r^{-k}$. (1) Continental surface air, $k = 4$; (2) maritime surface air, $k \approx 3$, but not constant; (3) upper tropospheric air, $k = 5$; (4) log-normal distribution, $k \approx 4$, but not quite constant. (From Junge, 1969b; by courtesy of Am. Meteor. Soc., and the authors.)

11.7.5 Power Law Solutions for a Source-Enhanced Aerosol

Distributions somewhat like measured ones of the form $n(r) \propto r^{-k}$ (k= constant) have been obtained by numerical integration of the coagulation equation with sources (e.g., Walter (1973), Storebo (1972), Takahashi and Kasahara (1968), Mockros *et al.* (1967), Quon and Mockros (1965)), and by analytical solution of simple models based on a related growth equation (Brock, 1971). In addition, there is an analytical solution for the steady state case with a kernel of the form $K(\mathrm{u}, \mathrm{v}) \propto \mathrm{u}^{\beta}\mathrm{v}^{\beta}$, where β is a constant between 0 and 1 (Klett, 1975). Because it includes some cases considered by others and provides an illustrative exact solution, we will now turn to a brief discussion of this last theoretical model.

Let us modify the coagulation equation (11-56) by including a contribution to $\partial n/\partial t$ from a local particle source term, $I(\mathrm{v}, t)$, due to unspecified processes. For example, $I(\mathrm{v}, t)$ may describe gas-to-particle conversion; alternatively, if we are interested in describing n over some size interval where a particular coagulation mechanism is known to be dominant, $I(\mathrm{v}, t)$ can be regarded as describing the entry of particles into the lower end of this range, caused by other coagulation processes which are controlling for still smaller particle sizes. We shall assume a class of particle sources which can be represented by steady gamma distributions, i.e., $I = I_0 J(x)/\mathrm{v}_0$, where I_0 is a constant, v_0 is the average source particle volume,

$x = v/v_0$, and

$$J(x) = \frac{(p+1)^{p+1} x^p e^{-(p+1)x}}{\Gamma(p+1)}, \tag{11-108}$$

where $\Gamma(p)$ is the gamma function (given by A.15-18) and p is a positive real number. This represents a fairly wide range of reasonable unimodal distributions. In particular, we may note the limiting forms $\lim_{p\to 0} J(x) = e^{-x}$ and $\lim_{p\to\infty} J(x) = \delta(x-1)$, the Dirac delta function (corresponding to a constant feed rate of single particles of volume v_0).

In terms of the normalization of (11-92), the source-enhanced, dimensionless coagulation equation for the steady state and with $\alpha(x,y) = x^\beta y^\beta$ may be expressed as

$$x^\beta f(x) = \frac{v_0^\beta M_0}{2M_\beta} \int_0^x (x-y)^\beta y^\beta f(x-y) f(y)\, dy + \frac{I_0 J(x) v_0^\beta}{K_0 M_0 M_\beta} \tag{11-109}$$

(cf. (11-93) and (11-94). The convolution form suggests the use of Laplace transforms. Denoting the Laplace transforms of $g(x) \equiv x^\beta f(x)$ and $J(x)$ by $\bar{g}(s)$ and $\bar{J}(s)$, respectively, we find

$$\bar{g}(s) = \frac{M_\beta}{M_0 v_0^\beta}\left[1 - \left(1 - \frac{2I_0 v_0^{2\beta}}{K_0 M_\beta^2}\bar{J}(s)\right)^{1/2}\right] = \frac{1}{M_0}\left(\frac{2I_0}{K_0}\right)^{1/2}(1 - [1-\bar{J}(s)]^{1/2}). \tag{11-110}$$

The last step is possible since $2I_0 v_0^{2\beta} = K_0 M_\beta^2$, as can be seen by setting $n = 0$ and $dM_n/d\tau = 0$ in the source-enhanced moment equation, which is obtained by adding the term $(I_0 v_0^{2\beta}/K_0)\int_0^\infty x^n J(x)\, dx$ to the right side of (11-97). Since $\bar{J}(s) = (p+1)^{p+1}/(s+p+1)^{p+1}$, the radical in (11-110) may be expanded in a binominal series, which leads to the solution

$$f(x) = \left(\frac{2I_0}{K_0}\right)^{1/2} \frac{x^{-\beta}}{M_0}\left(\frac{J(x)}{2} + \sum_{k=2}^{\infty} \frac{(2k-3)!!}{2^k k!} L^{-1}[\bar{J}^k(s)]\right), \tag{11-111}$$

where

$$L^{-1}[\bar{J}^k(s)] = \frac{(p+1)^{(p+1)k} e^{-(p+1)x} x^{p+(k-1)(p+1)}}{\Gamma[k(p+1)]}, \tag{11-112}$$

and where $(2k-3)!! = (2k-3)(2k-1)\ldots 3\cdot 1$. A plot of this solution is given in Figure 11.10, where it can be seen that the influence of the source on the spectral shape soon becomes secondary to that of the collection kernel. The asymptotic form of $f(x)$ for finite p,

$$f(x) = \frac{1}{2M_0}\left(\frac{2I_0}{\pi K_0}\right)^{1/2} x^{-(\frac{3}{2}+\beta)}, \qquad x \gg 1, \tag{11-113}$$

is thus achieved for $x \gtrsim 6$ even for the rather sharply peaked source distribution shown in the figure.

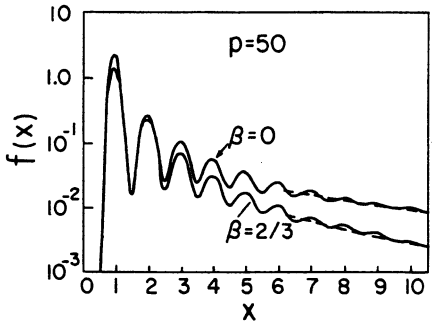


Fig. 11-10: Dimensionless size spectrum f(x) for $\beta = 0$ (constant collision kernel), $\beta = 2/3$ (gravitational collection), and for $p = 50$ (sharply-peaked source distribution). Dashed lines represent the corresponding asymptotic power-law forms of f(x), given by (11-115). (From Klett, 1975; by courtesy of Am. Meteor. Soc.)

From (11-113) and (11-92), we see that for $\beta = 0$ and $\mathrm{v} \gg \mathrm{v}_0$ the solution is $n(\mathrm{v}) \approx (\mathrm{v}_0 I_0 / 2\pi K_0)^{1/2} \mathrm{v}^{-3/2}$; this is equivalent to the numerical solution of Quon and Mockros (1965) for the case of a constant input rate of single particles. Since $n(\mathrm{v}) = 4r^2 n(\mathrm{v})$ and $\mathrm{v}_0 I_0 = \varepsilon_m$, the rate of aerosol particle volume input to the system the solution may also be expressed in the form $n(r) \approx (3/2\pi)(3/2)^{1/2}(\varepsilon_m / K_0)^{1/2} r^{-5/2}$, which is just Friedlander's QSD in the Brownian coagulation regime (cf. (11-87)). For $\beta = 2/3$, the kernel coincides with (11-83), so that the resulting solution, $n(r) \propto r^{-9/2}$, provides an approximate description of the effects of gravitational coagulation. The solution for this case is plotted in Figure 8.39b, and can be seen to conform reasonably well with the background aerosol spectrum in the upper troposphere, where such coagulation would be expected to dominate for $r \gtrsim 1\,\mu\mathrm{m}$.

CHAPTER 12

COOLING OF MOIST AIR

As mentioned in the historical review of Chapter 1, it has been known for over 150 years that only cooling by expansion of humid air during its ascent can provide clouds with sufficient condensed water to account for the observed amounts of precipitation. It is our main purpose in this chapter to describe the essentials of this thermodynamic cooling process. We shall also touch briefly upon isobaric processes. These formulations provide us with the necessary mathematical framework for describing in Chapter 13 the conditions of temperature, pressure, and humidity which control the rate of activation and subsequent diffusional growth of a representative population of cloud particles. Effects of radiative cooling, which are of significance to fog and stratus formation, will also be considered briefly in Chapter 13.

Some useful references for this chapter include the texts of Iribarne and Godson (1973), Turner (1973), Hess (1959), van Mieghem and Dufour (1948), Cotton and Anthes (1989), Wallace and Hobbs (1977), the survey articles of Simpson (1976), Cotton (1975), Turner (1969), and Simpson *et al.* (1965), and the reports of Dufour (1965a,b).

12.1 Water in the Atmosphere

As a prelude to our discussion of the basic thermodynamics of moist air, we shall touch here briefly on some of the more relevant characteristics of the atmospheric water cycle. Hopefully, this will set some of the later material in better perspective.

The amount of water vapor present in the atmosphere is a complicated function of (1) the amount which enters the atmosphere through evaporation and sublimation, (2) its transport by motions of various scales throughout the troposphere and lower stratosphere, and (3) the amount which leaves the atmosphere intermittently and almost exclusively as a flux of rain, hail, and snow. The fact that all three phases of water contribute to this cycle at the prevailing terrestrial temperatures and pressures is most fundamentally a consequence of the molecular structure of water, which permits the strong association of water molecules through hydrogen bonding (see Chapter 3). This is also the principal determinant for the relatively small amount of atmospheric water – only about 1.3×10^{16} kg or about 10^{-5} of the total surface store – in spite of the presence of extensive water surfaces for evaporation and sublimation. More specifically, the small store of atmospheric water is a consequence of the comparatively low water vapor pressure under saturated conditions at terrestial temperatures which, in turn, is a result of the unusually high latent heat of evaporation, which, in turn, is due to the molecular structure of

water controlled by the strong association of water molecules by hydrogen bonding (see Chapter 3).

At 55°C, which is close to the highest temperature ever recorded at a meteorological station, air could hold about 117 g of water vapor per kg of dry air at 1000 mb atmospheric pressure. This is equivalent to a mixing ratio w_v of 117×10^{-3} g g^{-1}. In actuality, much lower values for the atmospheric water vapor mixing ratio are observed. Although mixing ratios of up to 27×10^{-3} g g^{-1} have been observed over the Indian Ocean, at the mid-latitudes of the Northern Hemisphere, air is characterized by mixing ratios of only 2×10^{-3} g g^{-1} in winter and 10×10^{-3} g g^{-1} in summer. In polar regions, the typical water vapor content is of the order of 0.1×10^{-3} g g^{-1}.

Since the Earth's surface is the primary source of water vapor, we expect a decrease in the water vapor mixing ratio w_v with height. From a slightly different point of view, one may also attribute this expectation to the observed decrease in temperature with height in the troposphere: Since the maximum possible (saturation) mixing ratio $w_{v,sat}$ decreases with decreasing temperature (see Section 4.8), water is squeezed out of air parcels during their ascent. Thus, w_v is not a conservative quantity in the troposphere but, in fact decreases with height. An example of the observed vertical distribution of the mixing ratio of water vapor in the lower troposphere is shown in Figure 12.1a,b and can be seen to be approximately exponential.

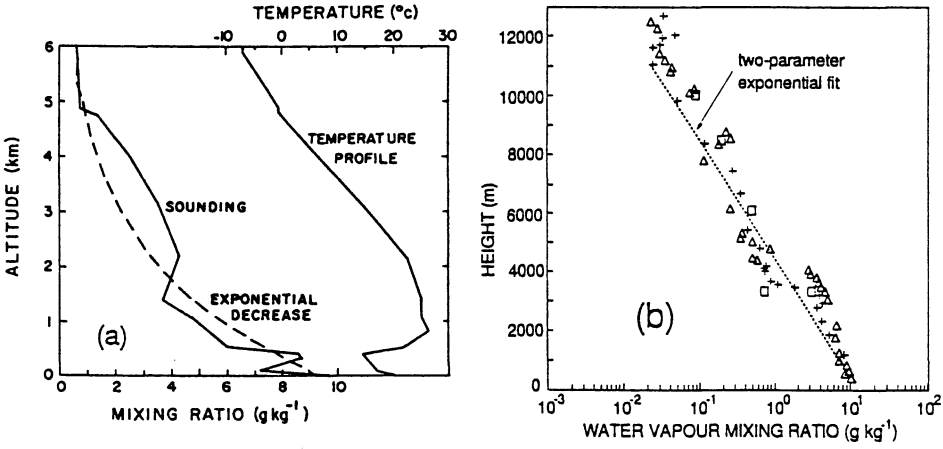


Fig. 12-1: Variation with height of the water vapor mixing ratio in the lower troposphere. (a) Radiosonde data taken over San Diego (California). (From Wang, 1974; by courtesy of Am. Meteor. Soc., and the author.) (b) Data taken over Munich (Germany): (*) Radiosonde data, (□) data taken with air plane. (From Hauf, 1995, with changes.)

Many measurements have been made of the distribution of water vapor above the tropopause. Some earlier observations of Mastenbrook (1961, 1968, 1974), McKinnon and Morewood (1970) and others have been reviewed by Harries (1976).

These observations showed that the stratosphere is generally very dry, exhibiting a fairly constant mixing ratio of about $w_v = (2.5 \pm 0.7) \times 10^{-6}$ g g^{-1} between 13 and 30 km altitude. This value is to be compared with a saturation mixing ratio of 1.4×10^{-6}g g^{-1} at 5 mb and -60°C. More recent observations of Kley *et al.* (1979, 1982) and Kelly *et al.* (1993) with more sophisticated measuring techniques agreed in essence with the earlier measurements, showed, however, that the water vapor mixing ratio is not constant with altitude but reaches a minimum (termed the *hygropause*) 3 to 4 km above the local tropopause. Thus, a minimum of 1.6×10^{-6} g g^{-1} was observed over tropical Brazil, 2.2×10^{-6} g g^{-1} over tropical Panama (see Figure 12.2), 2.3×10^{-6} g g^{-1} over Laramie (Wyoming), and 1.5×10^{-6} g g^{-1} over Darwin (Australia).

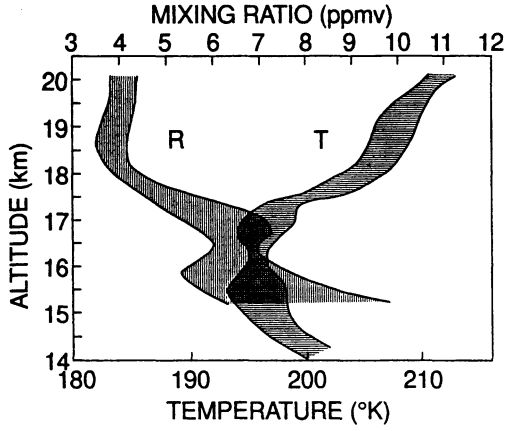


Fig. 12-2: Variation with height of the water vapor mixing ratio in the upper troposphere and lower stratosphere. Data taken over Panama. R: mixing ratio, T: temperature. (From Kley *et al.*, 1982; by courtesy of the authors, copyrighted by the Am. Geophys. Union.)

In accordance with its arid state, the stratosphere is generally cloudless. However, during the northern and southern polar winter, the temperature may decrease to values near and sometimes even below -80°C at a level of 50 mb. At these low temperatures, the mixing ratio w_v reaches or even surpasses saturation with respect to ice (e.g. $w_{v,sat} = 4.1 \times 10^{-6}$ g g^{-1} at 50 mb and -83°C). Such conditions prevail, for example, due to diabatic cooling in the Antarctic stratosphere during the south polar winter in association with its circumpolar vortex. A similar decrease in temperature is observed in the Arctic stratosphere during the northern polar winter, this time due to adiabatic cooling induced by orographic lifting of air during flows over mountain ranges in Scandinavia. As mentioned in Section 8.2.10, during such cooling, polar stratospheric clouds (PSC) form.

12.2 Isobaric Cooling

Although most cooling of moist air to saturation occurs via the expansion which accompanies lifting, there are also a variety of cooling mechanisms which can occur isobarically (at constant pressure). As these often lead to the formation of ground fogs and stratus clouds, isobaric cooling processes are of sufficient importance to be mentioned here in passing.

Consider a volume of moist air which is cooled isobarically. Assuming that we may neglect any exchange of air between the parcel and its environment, its mixing ratio w_v must remain constant during cooling. Therefore, after sufficient cooling $w_v = w_{v,sat}$, and the parcel will be vapor-saturated. Assuming that the proper condensation or ice forming nuclei are present, a phase change will thus commence. This occurs at the *dew point temperature*, T_d, if the condensate is in the form of water drops; if ice crystals appear, it is called the *frost point temperature*, T_f.

Dew or frost are often formed by the night-time radiational cooling of calm moist air in ground contact. The same cooling process may also produce ground fogs. Isobaric cooling leading to fog or stratus cloud formation may also occur when a mass of moist air moves horizontally over a colder land or water surface, or over a colder air mass.

An expression giving T_d as a function of the prevailing T and w_v, or relative humidity $\phi_v \equiv w_v/w_{v,sat}(T)$, may be obtained by recognizing that the vapor pressure $e = e_{sat,w}(T_d)$ when $T = T_d$. Then, from the Clausius-Clapeyron equation, (4-80), and noting that $w_v \approx \varepsilon e/p$ (Equation 4-40), we find, for $p =$ constant,

$$\frac{dT_d}{T_d^2} = \frac{R_v}{L_e}\frac{de}{e} \approx \frac{R_v}{L_e}\frac{dw_v}{w_v} . \tag{12-1}$$

Integration between T_d, w_v, and T, $w_{v,sat}(T)$ yields

$$T_d \approx R + R_v\frac{TT_d}{L_e}\ln\phi_v \approx T + \frac{R_vT^2}{L_e}\ln\phi_v . \tag{12-2}$$

An evaluation of (12-2) for $T = 20°C$ shows that a dew point temperature of $T_d = 10°C$ corresponds to a relative humidity $\phi_v = 52.8\%$. Similarly, if $T_d = -10°C$, then $\phi_v = 12.7\%$, and if $T_d = -20°C$, $\phi_v = 5.7\%$.

12.3 Adiabatic Cooling of Unsaturated Air

We shall now consider the expansion cooling of a rising parcel of dry air. Although heat $đQ$ may be added to the parcel through the effects of radiation, frictional dissipation, and mixing with the environment, in many situations the resulting temperature changes are of secondary importance to that arising from the expansion process. Hence, it is a reasonable and useful idealization to assume the expansion is strictly adiabatic, with no heat exchanges. We shall further assume it is reversible, so that $đQ = TdS = 0$, i.e., the process will be assumed isentropic ($S =$ constant).

We shall also assume the dry air is an ideal gas. Now a property of an ideal gas, which we have not made use of previously, is that its internal energy U is

a function of temperature only. (This is true because ideal gases have no intermolecular potential, so that U is just the total molecular kinetic energy, which is a function only of T.) Therefore, its enthalpy $H \equiv U + pV$ is also just a function of T, owing to the form of the ideal gas law. Consequently, from (4-12) the specific enthalpy h_a per unit mass of dry air satisfies the relation

$$dh_a = c_{pa} dT , \tag{12-3}$$

where c_{pa} is the specific heat of dry air at constant pressure ($c_{pa} \approx 0.240$ cal g^{-1}°C^{-1}). Alternatively, from (4-6), applied to a reversible adiabatic expansion of a closed parcel, we find $dh_a = \alpha_a dp$, from which with (12-3)

$$c_{pa} dT = \alpha_a dp , \tag{12-4}$$

where $\alpha_a \equiv 1/\rho_a$ is the specific volume of the dry air. Introducing the gas law (4-25) into (12-4) and integrating, we obtain for the dry adiabat

$$T = A p_a^{\kappa_a} , \tag{12-5}$$

where A is a constant and $\kappa_a \equiv R_a/c_{pa} \approx 0.286$. Logarithmic differentiation of this equation with respect to height z yields the temperature lapse rate of the parcel:

$$\frac{dT}{dz} = \frac{R_a T}{c_{pa} p_a} \frac{dp_a}{dz} . \tag{12-6}$$

Assuming $p_a = p'_a(z)$, the environmental pressure at level z, and that the latter is in hydrostatic equilibrium, so that $dp'_a/dz = -g\rho'_a = -gp'_a/R_a T'$, (12-6) can be written in the form

$$\Gamma_d \equiv -\left(\frac{dT}{dz}\right)_d = \frac{g}{c_{pa}} \left(\frac{T}{T'}\right) \approx \frac{g}{c_{pa}} \approx 9.76°\text{C km}^{-1} , \tag{12-7}$$

where Γ_d is the *dry adiabatic lapse rate*, and where g is the magnitude of the gravitational acceleration. Thus, a parcel of dry air cools by about 1°C for every 100 m of lift.

For moist unsaturated air, the only modification required in the above development is a recognition that the composition of the ideal gas under consideration is now slightly different, which must be reflected in the parameters κ and c_p. For example, the lapse rate of the parcel becomes $\Gamma_m = g/c_{pm}$ where c_{pm} is the specific heat of the moist air and Γ_m is termed the *moist adiabatic lapse rate*. Since air of mixing ratio w_v contains w_v grams of vapor for every gram of dry air, c_{pm} is determined from the balance condition $c_{pm}(1 + w_v)dT = (c_{pa} + w_v c_{pv})dT$ for arbitrary dT and where c_{pv} is the specific heat of water vapor; i.e., c_{pm} is a mass weighted average of the component specific heats. Since generally $w_v \ll 1$, we find $c_{pm} \approx c_{pa}$ and $\Gamma_m \approx \Gamma_d$, the small differences being negligible for all practical purposes. In a similar fashion, we can show that $\kappa_m \approx (1 - 0.23 w_v) \approx \kappa_a$.

12.4 The Thermodynamic Wetbulb Temperature

A water drop exposed to unsaturated air cools by evaporation, with heat being supplied by the environment. At a steady state, the drop assumes a surface temperature T_a which is below the temperature of the environment by an amount which depends on the relative humidity. An exact computation of this temperature will be given in Chapter 13. An approximate value for T_a to within $\pm 0.5°C$ is obtained in terms of the wetbulb temperature.

At the meeting of the Aerological Commission of the World Meterological Society in 1953 in Toronto, the *wetbulb temperature* T_w of moist air consisting of mass m_a of dry air and mass m_v of water vapor, initially at temperature T and pressure p, and of mass m_w of liquid water at temperature T_w, was defined as the temperature which the moist air assumes if liquid water at T_w = constant is evaporated isobarically and adiabatically into it until the moist air is saturated.

In order to find a mathematical formulation for T_w , we follow Dufour (1965a,b) and assume that the system considered is closed and the process is reversible; since it is also isobaric, the enthalpy of the system must be conserved. Therefore,

$$m_a h_a(T) + m_v h_v(T) + m_w h_w(T_w) = m_a h_a(T_w) + m_{v,sat} h_v(T_w) + m_{w,sat} h_w(T_w) . \tag{12-8}$$

Since mass is also conserved, i.e., $m_v + m_w = m_{v,sat} + m_{w,sat}$, we obtain

$$m_a[h_a(T) - h_a(T_w)] + m_w[h_v(T) - h_v(T_w)] = [m_{v,sat} - m_v][h_v(T_w) - h_w(T_w)] . \tag{12-9}$$

Introducing (4-12) and (4-72) into (12-9), we find, after arranging terms,

$$T_w = T - \frac{L_e(T_w)[w_{v,sat}(T_w) - w_v]}{c_{pa} + c_{pv} w_v} , \tag{12-10}$$

Dufour (1965a,b). In (12-9) c_{pa} and c_{pv} are the specific heats of dry air and water vapor, respectively, and L_e is the specific latent heat of evaporation. Comparing T_w with T_a obtained from (13-63), we find that for all relative humidities (RH), T_w is within about 0.5°C of T_a. Thus, for RH= 50%, $T_w = 5.54°C$ and $T_a = 5.19°C$ for $T_\infty = 10°C$, and $T_w = -11.68°C$ and $T_a = -11.88°C$ for $T_\infty = -10°C$.

12.5 Lifting to Saturation and Beyond

Let us now consider the height to which a parcel of unsaturated air would have to be lifted adiabatically to become saturated. This height is called the *lifting condensation level* (LCL). During the ascent, $w_v \approx \varepsilon e/p$ remains constant, so that from (12-5) we may write $T \sim e^{\kappa a}$. Hence, the temperature at the LCL is given in terms of w_v and the initial T and p by

$$T_{LCL} \approx T \left[\frac{e_{sat,w}(T_{LCL})}{e}\right]^{\kappa a} \approx T \left[\frac{\varepsilon e_{sat,w}(T_{LCL})}{w_v p}\right]^{\kappa a} . \tag{12-11}$$

This implicit relation for T_{LCL} may be solved iteratively, since $e_{sat,w}(T_{LCL})$ is known as a function of T_{LCL} and T from the integral of (4-83). Once T_{LCL} is

determined, the LCL itself can be found from the lift distance, which is $(T - T_{LCL})/\Gamma_a$.

In order to avoid tedious computations, one may use the following approximate, explicit, semi-empirical relations for the LCL (Inman, 1969), and for the 'lifting sublimation level' (LSL) (Chappel *et al.*, 1974) at which $e = e_{sat,i}(T_{LSL})$:

$$T_{LCL} = T_d - (0.212 + 0.001571T_d - 0.000436T)(T - T_d), \quad (12\text{-}12)$$

$$T_{LSL} = T_d - (0.182 + 0.00113T_d - 0.000358T)(T - T_d), \quad (12\text{-}13)$$

with T and T_d in °C. The use of T_d as a moisture variable follows standard practice. Finally, graphical solutions for the LCL are readily obtained by use of various thermodynamic diagrams (e.g., see Chapter 5 of Hess, 1959).

If the parcel at the LCL is warmer than the environment, it will continue its ascent, due to positive buoyancy, under conditions that are both adiabatic and saturated. This is described by saying the parcel follows a 'saturation' – or 'wet adiabat'. If the parcel is colder than the environment at the LCL, but is forced higher in spite of its negative buoyancy by frontal or orographic lifting, for example, it may eventually reach a level called the *level of free convection* (LFC), at which point it will again rise spontaneously. Under certain conditions, it is possible for the LCL and LFC to coincide at a height called the *convective condensation level* (CCL).

In the real atmosphere, a parcel lifted beyond the LCL will experience condensation (or deposition) of water vapor, as will be described in the next section. However, it is instructive to consider the hypothetical case in which no condensation occurs, owing to a complete lack of condensation nuclei. From the definition of saturation ratio given by (4-36), $S_{v,w} = e/e_{sat}(T)$, and the fact that for a parcel lifted adiabatically from level 1 to level 2 we have $e_2/e_1 = p_2/p_1$, it follows that if the parcel is just saturated at level 1, then at level 2 the saturation ratio is

$$S_{v,w} = \frac{e_{sat}(T_1)}{e_{sat}(T_2)} \frac{p_2}{p_1}, \quad (12\text{-}14)$$

T_2 may be computed from (12-5) and $e_{sat}(T)$ from (4-83). For $p_1 = 500$ mb, $p_2 = 495$ mb, $T_1 = 5°C$, and $T_2 = 4°C$, we find $S_{w,v} = 1.06$; i.e., after about a 100 m excursion, the adiabatically lifted parcel is 6% supersaturated. Lifting the parcel adiabatically from 500 mb and 5°C to 435 mb and −5°C , we find $S_{v,w} = 1.80$, so that vapor in the parcel is 80% supersaturated after an excursion of about 1000 m. Let us recall now from Chapter 7 that for homogeneous nucleation of water drops, a supersaturation between 400 and 500% is needed. Such supersaturations would evidently require adiabatic excursions of air parcels over unrealistic distances of several thousands of meters. It is also quite obvious that over such long distances, the concept of a closed identifiable air parcel is untenable; mixing with environmental air would destroy its identity. Hence, supersaturations sufficient for homogeneous nucleation are ruled out.

12.6 Adiabatic Cooling of Saturated Air

If we lift a parcel of moist air beyond the LCL, latent heat of condensation will be released. (For simplicity, we shall consider here only the onset of the liquid phase.) Thus, the parcel will cool at less than the dry adiabatic rate, the exact rate depending on whether part or all of the water remains inside the parcel. If it all remains, we continue to have a closed system, and the process can be carried out reversibly. This is called a *reversible saturated adiabatic process.* If all the water is assumed to fall out immediately upon formation, the process can be neither strictly adiabatic nor reversible; this extreme is called a *saturated pseudo-adiabatic process.* Fortunately, the heat capacity of the water is negligible relative to that of the parcel air, so that there is no significant difference between the two resulting cooling rates. Since the pseudo-adiabatic process requires less book-keeping, we shall use it exclusively in the sequel.

Let us calculate the cooling rate of a saturated parcel containing 1 gram of dry air and $w_{v,sat}$ grams of vapor. For a temperature change dT , the enthalpy change is $dh = (c_{pa} + w_{v,sat} c_{pv})dT = đQ + V dp$, while the incremental heat of condensation $đQ$ for the corresponding change $dw_{v,sat}$ is just $-L_e dw_{v,sat}$. Substituting the gas law for V, we thus obtain

$$(c_{pa} + w_{v,sat} c_{pv})dT + L_e dw_{v,sat} - (R_a + w_{v,sat} R_v)T\frac{dp}{p} = 0\,, \tag{12-15}$$

which describes the saturation pseudo-adiabatic process. Equation (12-15) is called the *saturation pseudo-adiabat* or *wet adiabat.* (Obviously, had we considered the reversible adiabatic process instead, the additional heat change $w_L c_w dT$ of the condensate water would have been added to (12-15), where w_L and c_w are the mixing ratio and specific heat capacity of the water, respectively. In this case, the resulting equation would be referred to as the *reversible saturation adiabat* or *cloud adiabat.* Since typically $w_L c_w / c_{pa} = O(10^{-2})$, the difference between the approaches is of no practical significance.) Usually, $w_{v,sat} < 2 \times 10^{-2}$ g g^{-1}, so that (12-15) may be simplified further to

$$c_{pa}\frac{dT}{T} + L_e\frac{dw_{v,sat}}{T} - R_a\frac{dp}{p} = 0\,. \tag{12-16}$$

Division by dz results in the expression for the saturation adiabatic lapse rate

$$\Gamma_s \equiv -\left(\frac{dT}{dz}\right)_s = \frac{g}{c_{pa} + L_e(dw_{v,sat}/dT)}\,, \tag{12-17}$$

where we have assumed the parcel is in hydrostatic equilibrium with the environment. This may be reduced further to an explicit function of T and $w_{v,sat}$ by substitution of (4-40) and (4-83) into the denominator. For 1000 mb and 0°C, (12-17) gives $\Gamma_s = 5.8$°C km^{-1}, or about 60% of the dry adiabatic lapse rate.

12.7 Cooling with Entrainment

Let us now abandon the fiction that a rising air parcel is a closed system. We have already discussed in Section 2.1.1 how the entrainment of relatively dry environmental air into convective clouds lowers their liquid water contents substantially

below that expected on the basis of a closed saturated ascent (recall Figure 2.22). Observations also show that updrafts in most cumulus clouds are warmer than the environment by only 1°C or less, rather than the 2 to 3°C temperature excess which is typical for computations of rising closed air parcels. In addition, observations demonstrate that the temperature gradient in clouds is larger, and the height reached by clouds is substantially less than that computed for adiabatically ascending air.

The description of the previous section may be easily extended to the case of an entraining parcel by following a procedure originated by Austin and Fleisher (1948). According to their scheme, we must add the following additional heat terms to (12-15) multiplied by the mass m of the saturated parcel under consideration: (1) a term $L_e(w_{v,sat} - w'_v)dm$ expressing the heat needed to evaporate sufficient water to increase the mixing ratio w'_v of mass dm, entrained during the parcel displacement dz, to the saturation value in the parcel, and (2) a term $c_{pa}(T - T')dm$, expressing the heat required to warm the entrained air from its original temperature T' to the temperature T of the parcel. With these additions, the generalization of (12-16) to include the effects of entrainment is

$$c_{pa}\frac{dT}{T} + \frac{L_e dw_{v,sat}}{T} - R_a\frac{dp}{p} + \frac{1}{T}\left[L_e(w_{v,sat} - w'_v) + c_{pa}(T - T')\right]\frac{dm}{m} = 0\,. \quad (12\text{-}18)$$

Similarly, in place of (12-17) we obtain the *cloud lapse rate* Γ_c:

$$\Gamma_c \equiv -\left(\frac{dT}{dz}\right)_c = \frac{g + \frac{1}{m}\frac{dm}{dz}\left[L_e(w_{v,sat} - w'_v) + c_{pa}(T - T')\right]}{c_{pa} + L_e(dw_{v,sat}/dT)}\,. \quad (12\text{-}19)$$

Since $dm/dz > 0$, we see that $\Gamma_c > \Gamma_s$. As an example (from Hess, 1959, p.108), if we suppose that $p = 700$ mb, $T = 0°C$, $T' = -1°C$, $w'_v/w_{v,sat} = 0.67$, and $d\ln m/dz = 0.25\ km^{-1}$, we find $\Gamma_c = 6.6°C\ km^{-1}$, compared to $\Gamma_s = 5.8°C\ km^{-1}$.

Note that in (12-19) the *entrainment rate*, μ, has the simple dimensional form

$$\mu \equiv \frac{1}{m}\frac{dm}{dz} = \frac{1}{l}\,, \quad (12\text{-}20)$$

where l is a length scale characterizing the mixing process. There is an extensive literature on buoyant convective processes, involving a variety of physical models of varying complexity, which yield estimates for l. We turn now to a brief summary of these models in the next section.

12.8 The Concept of Entrainment

Stommel (1947) was the first to note that cumulus clouds had to be significantly diluted by air from above the cloud base in order to explain their internal temperature and liquid water content. His lateral entrainment model, in which air was thought to mix homogeneously across the width of the updraft, was followed by other models of similar type, such as the jet or plume model of Morton (1957), Squires and Turner (1962) and Scorer (1957). Stommel's model was supported by Byers and Hull (1949), Byers and Braham (1949) and Malkus (1954) (Figure 12.3a).

The theory of similarity jets or plumes, pioneered by Priestly and Ball (1955), Morton *et al.* (1956) and Morton (1957), differed from Stommel's treatment of jets, although both featured lateral entrainment. A further modification of the jet or plume model was introduced by Turner (1962) who formulated the starting plume model (Figure 12.3c). The idea here was to provide a model which, along with the feature of a steady updraft and lateral entrainment of the jet model, also allows entrainment to occur through the front interface of the plume. Such a plume has a rounded cap with an internal circulation represented by a Hills spherical vortex (see Section 10.3.1). Below the cap is the supporting jet. Such a system was modeled by Levine (1959), Malkus (1960), and in a modified version by Simpson *et al.* (1965).

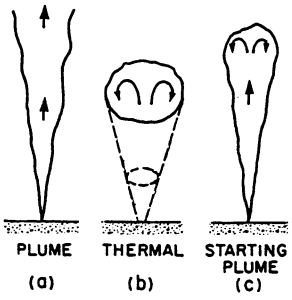


Fig. 12-3: Sketches of three basic convective phenomena. The arrows indicate the direction of motion. (From Turner, 1969; reproduced with permission, from 'Buoyant Plumes and Thermals', Annual Review of Fluid Mechanics, Volume 1. Copyrighted 1969 by Annual Reviews Inc. All rights reserved.)

In an alternative attempt to describe the entrainment, Scorer and Ludlam (1953) proposed the 'bubble' theory of convection, which describes the growth of a cumulus cloud in terms of a buoyant bubble (Figure 12.3b) which steadily erodes as it rises. In its early form, the model assumed that the mixed air was completely shed into the bubble's wake. However, laboratory studies of Scorer and Ronne (1956), Scorer (1957) and Woodward (1959) revealed that part of the entrained fluid was caught up in the internal motion of the bubble. Support for the bubble model came from the field observations of Saunders (1961), Malkus and Scorer (1955), Scorer (1957) and Glass and Carlson (1963) who observed that, analogously to jets or plumes, bubbles also broaden as they rise.

A corollary of the lateral entrainment models (jet or bubble) is that the fractional rate of entrained air into the updraft would vary inversely with the cloud radius. Some support for the inverse radius dependence of lateral mixing has come from the observations of McCarthy (1974) in clouds over the Gulf coast. Similarly, the inverse radius dependence of the entrainment rate in the model of Simpson and Wiggert (1969) correctly predicted the internal features of clouds observed by them over the Caribbean and over Florida.

The entrainment rate in all three models discussed above is represented by an empirical law which takes into account the inverse radius (R) dependence in the

form

$$\mu = \frac{C}{R}, \tag{12-21}$$

where C depends on the ratio of the length scale l (12-20) to R. Such a form is easily verified for a spherical bubble of radius R_B and mass $m_B = 4\pi R_B^3 \rho_a/3$, from which $dm_B = 4\pi R_B^2 \rho_a dR_B$. The entrainment rate for a bubble is therefore

$$\mu_B = \frac{1}{m_B}\frac{dm_B}{R_B} = \frac{2\alpha_B}{R_B} = \frac{C_B}{R_B}, \tag{12-22}$$

where the broadening angle $\alpha_B = dR_B/dz$. Similarly, for a plume or jet with radius R_J and vertical velocity U, the mass flux $F_m = \pi R_J^2 \rho_a U$, from which $dF_m = 2\pi R_J \rho_a U dR_J$. The entrainment rate for a jet is therefore

$$\mu_J = \frac{1}{F_m}\frac{dF_m}{dz} = \frac{2\alpha_J}{R_J} = \frac{C_J}{R_J}, \tag{12-23}$$

where α_J is the broadening angle of the jet. From laboratory studies, Morton (1959) and Squires and Turner (1962) found that the broadening angle was $\alpha_J \approx 0.1$ so that $C_J \approx 0.2$ and $l_J = 5R_J$. On the other hand, laboratory studies of Turner (1962, 1963) and Scorer (1957), and field studies of Simpson *et al.* (1965) and McCarthy (1974) showed that $\alpha_B \approx 0.2$, so that $C_B \approx 0.6$ and $l_B = 5R_B/3$. Generally, the thermal cap of a starting plume is regarded as only a small fraction of the 'cloud', so that the entrainment rate is taken to be the same as that for a steady state jet.

Warner (1972, 1975a,b) criticized the above entrainment parametrizations and their use in one-dimensional models on three grounds: (1) such models assume that entrainment occurs laterally, whereas in fact cumulus entrainment largely takes place at cloud tops; (2) such models are based on an inverse-radius law which implies that the entrainment decreases with height, in contradiction to observations (see Figure 2.22), which show that cloud dilution increases with height as exemplified by a decrease of liquid water content; (3) such models cannot simultaneously predict cloud top height and liquid water content. In fact, by adjusting the entrainment rate to obtain the proper cloud top height, one obtains a liquid water content which is far too large, while tuning the model to yield the correct liquid water content generates a cloud with too low a top.

Even before Warner's criticism, Squires (1958b) hypothesized that the observed structure of cumulus clouds can be described by the entrainment of dry air into the cloud top. He visualized this mechanism in terms of 'tongues' of dry air which become engulfed into the top and, by evaporative cooling, penetrate downwards into the interior of the cloud due to their negative buoyancy. Telford (1975) developed a vertical mixing model consistent with the suggestions of Squires (1958b). He assumed that mixing occurs at the cloud top and that parcels of air subsequently move vertically down to their level of neutral buoyancy. Support for this model came from Paluch (1979), Boatman and Auer (1983), Jensen *et al.* (1985), Pontikis *et al.* (1987), Blyth and Latham (1985), Blyth *et al.* (1988), Deardorff (1980), Randall (1980), and Emanuel (1981). In further support, Paluch (1979), and later

Betts (1985), used conservative variables (the total mixing ratio of water substance and the wet equivalent potential temperature) to diagnose the origin of air sampled at various levels in the cloud. Paluch (1979) concluded that air at a given observed level in an updraft could not have originated as a mixture of environmental air at that level or below. Instead, most of the air must have been entrained into the updraft several kilometers above the observational level near the cloud top. A cloud top entrainment process was also visualized by Rogers *et al.* (1985), Telford and Chai (1980), and Telford *et al.* (1984) who formulated an entity-type entrainment model in which various different but individually well-mixed entities or 'blobs' move to their respective levels of neutral buoyancy. Raymund and Blyth (1986) extended this approach to allow for a variety of mixing proportions between cloud top and cloud base air. Nevertheless, Betts (1982a,b) had already argued earlier that cloud top entrainment could not describe all the features of small cumuli.

Another attempt to describe entrainment followed a suggestion by Ludlam (1958), who proposed that cumulus clouds are composed of a succession of thermals. This suggestion was followed by Jonas and Mason (1974), Mason and Jonas (1974), and Rösner *et al.* (1990). Although Warner (1975a,b) showed that these models also would not solve the discrepancy regarding the liquid water content and cloud top height, they were able to compute realistic cloud drop size distributions (see Chapter 13).

Little further progress was made by abandoning the Lagrangian one-dimensional cloud models and formulating instead various one-dimensional time dependent models in an Eulerian frame. In these models, the lateral entrainment is expressed in terms of lateral eddy fluxes (Weinstein, 1971; Wisner *et al.*, 1972; Asai and Kasahara, 1967; Holton, 1973;, Cotton, 1972). The fact that these models still could not simultaneously predict correct liquid water contents and cloud top heights, prompted Cotton (1975) and Cotton and Tripoli (1978) to recall the suggestion of Simpson and Wiggert (1969) that shear in cloud environment may be important. This has been explored in numerical simulations by Cotton (1975) and Cotton and Tripoli (1978), in which eddy fluxes are made to depend on convective scale wind deformations. As a result, they were able to show that, as expected, sheared clouds entrain more than unsheared clouds. Since this type of dilution is a result of organized cumulus scale entrainment, it is commonly called 'dynamic entrainment'. However, the most significant result of the study of Cotton and Tripoli was that simulations applied to a stagnant environment predicted too large a liquid water content near the cloud top, exceeding the observed value by as much as a factor of three. In contrast, their three-dimensional simulation for an environment with the observed shear flow predicted liquid water contents in good agreement with observations, and not at the expense of accuracy in predicting the cloud top height. From their computations, Cotton and Tripoli (1978) drew the conclusion that cumulus cloud internal properties are controlled in part by the interaction of the cloud with an environment which exhibits vertical shear of the horizontal wind.

Recent work has provided some further insight into the small scale turbulent entrainment mechanism. This work was pioneered by Latham and Reed (1977), Baker and Latham (1979), and Baker *et al.* (1980), who introduced the concept of inhomogeneous mixing. Support for their results came subsequently from Blyth

et al. (1980), Broadwell and Breidenthal (1982), Baker *et al.* (1982), Baker and Latham (1982), Paluch and Knight (1984), Baker *et al.* (1984), Blyth and Latham (1985), Austin *et al.* (1985), Paluch (1979, 1986), Choularton *et al.* (1986), Bower and Choularton (1988), and Blyth and Latham (1990). In this mechanism, subsaturated air is entrained from outside the cloud as a series of discrete events each of which results in the total evaporation of some drops of all sizes. Subsequently, turbulent motions mix the droplet free air with cloud air on scales of 10 to 100 m. This causes a reduction of the total number of drops without affecting the drop size distribution and causes the supersaturation in the surroundings of the remaining drops to rise as the ascent of air continues, allowing these drops to be favored for further growth by diffusion. At the same time, entrained nuclei may become activated to drops. Both processes lead to an overall broadening of the drop spectrum in the cloud. Hill and Choularton (1985) and Blyth and Latham (1984) have shown that, despite their dilutions, the affected cloud portions are capable of rising due to the large updraft momentum in rapidly ascending cloud turrets.

According to Baker (1992), the initial mixing of clear and cloudy air, transport of the mixing regions from the cloud edges to the cloud interior, and the homogenization of the interior regions, all occur on similar time scales. Thus, Baker (1992) argues that for the largest scale motions, one may compute the time scale by dividing the characteristic cloud turret size of 100 to 1000 m by its characteristic velocity of several meters per second, giving a time scale of the order of several minutes. Mixing between cloud and air occurs initially at the cloud edges, in regions smaller in scale than the large eddy size, and therefore it proceeds on time scales shorter, but not very much shorter, than those for the large scale transport. Likewise, the time scale for homogenization of regions 10 to 100 m in size is again shorter, but not very much shorter, than that for cloud scale eddies; otherwise, larger homogeneous cloud regions should have been observed. For inhomogeneous mixing to proceed, the characteristic evaporation time of drops must be considerably smaller than the mixing time scales of a few minutes. However, computations of evaporation times for drops in cloud air environments show that this condition does not generally hold. For example, if one uses (13-64) to make such estimates, it is found that the evaporation time (i.e., the time to reach 1 μ radius) of drops of 20, 50, and 100 μm radius is, respectively, 0.8, 5, and 13 min. in air of 10°C and 90% humidity; for 80% relative humidity the times are 0.5, 2, and 7 min.

It would lead us too far afield to consider further the complex and rather unsettled state of entrainment modeling. Accordingly, in most of the sequel we shall use the homogeneously entraining air parcel model; inhomogeneous mixing will only be touched upon briefly in Section 13.2.2.1. The homogeneous model is adequate for our purpose of demonstrating microphysical behavior, and has the virtue of being relatively simple.

12.9 The Air Parcel Model for a Convective Cloud

In this section, we shall formulate the differential equations describing the properties of a vertically rising, entraining parcel of moist air in which cloud drops are allowed to form. In doing this, we must account for the presence of condensed

water, even though we have shown it has a negligible effect on the parcel cooling rate.

Suppose the parcel has mass m and density ρ (exclusive of liquid water), vertical velocity W, and liquid water mixing ratio w_L[‡]. Then, if we include body forces arising from buoyancy and the weight of the liquid water, the momentum equation for the parcel beecomes

$$\frac{\mathrm{d}(mW)}{\mathrm{d}t} = g(m' - m) - mg\mathrm{w}_L = gm\left(\frac{\rho' - \rho}{\rho} - \mathrm{w}_L\right), \tag{12-24}$$

where m' is the environmental mass of air displaced by the parcel. We have not included a drag force due to turbulent entrainment of momentum, on the assumption that the environmental momentum is small. However, the air outside the parcel must be accelerated to some extent by the parcel's motion. In order to account for the resulting reaction force on the parcel, we shall follow a suggestion of Turner (1963) and include an 'induced mass' acceleration term, $(m'/2)\mathrm{d}W/\mathrm{d}t$, on the left side of (12-24). With this addition, the parcel acceleration may be expressed as

$$\frac{\mathrm{d}W}{\mathrm{d}t} = \frac{g}{1+\gamma}\left(\frac{T - T'}{T'} - \mathrm{w}_L\right) - \frac{\mu}{1+\gamma}W^2, \tag{12-25}$$

where $\gamma \equiv m'/2m \approx 0.5$.

The time rate of change of temperature in the parcel may be written down immediately from (12-19), noting that $\mathrm{d}/\mathrm{d}t = W\mathrm{d}/\mathrm{d}z$. For our applications in the next chapter, we must take into account the slight supersaturations which develop from the lifting of air. Therefore, it is no longer sufficient to regard the parcel as just saturated, and so we must replace $\mathrm{w}_{\mathrm{v,sat}}$ in (12-19) by w_{v}. The result is

$$-\frac{\mathrm{d}T}{\mathrm{d}t} = \frac{gW}{c_{pa}} + \frac{L_{\mathrm{e}}}{c_{pa}}\frac{\mathrm{d}\mathrm{w}_{\mathrm{v}}}{\mathrm{d}t} + \mu\left[\frac{L_{\mathrm{e}}}{c_{pa}}(\mathrm{w}_{\mathrm{v}} - \mathrm{w}'_{\mathrm{v}}) + (T - T')\right]W. \tag{12-26}$$

An equation relating the time rates of change of w_{v} and the parcel supersaturation $s_{\mathrm{v,w}}$ is also needed. From (4-37) and (4-40), we have $\mathrm{w}_{\mathrm{v}} = (1+s_{\mathrm{v,w}})(\varepsilon \mathrm{e}_{\mathrm{sat,w}}/p)$. On differentiating this expression with respect to time, and assuming the environment is in hydrostatic equilibrium, i.e., $\mathrm{d}p'/\mathrm{d}z = \mathrm{d}p/\mathrm{d}z = -g\rho'$, it follows (with (4-25) and $\mathrm{w}_{\mathrm{v}} \ll 1$) that

$$\frac{\mathrm{d}p}{\mathrm{d}t} = -\frac{gpW}{R_{\mathrm{a}}T'} \approx -\frac{gpW}{R_{\mathrm{a}}T}. \tag{12-27}$$

Therefore, we find approximately

$$\frac{\mathrm{d}s_{\mathrm{v,w}}}{\mathrm{d}t} = \frac{p}{\varepsilon \mathrm{e}_{\mathrm{sat,w}}}\frac{\mathrm{d}\mathrm{w}_{\mathrm{v}}}{\mathrm{d}t} - (1 + s_{\mathrm{v,w}})\left[\frac{\varepsilon L_{\mathrm{e}}}{R_{\mathrm{a}}T^2}\frac{\mathrm{d}T}{\mathrm{d}t} + \frac{gW}{R_{\mathrm{a}}T}\right], \tag{12-28}$$

where we have used (4-83).

[‡]Note that w_L here has units of g water/g air, while in Chapter 2 the units assigned for w_L were g water/m^3 air.

The condensed water is related to w_v through an obvious statement of water conservation, viz., $m(w_v + w_L) + w'_v dm = (w_v + dw_v + w_L + dw_L)(m + dm)$. Neglecting products of differentials, this leads to

$$\frac{dw_v}{dt} = -\frac{dw_L}{dt} - \mu(w_v - w'_v + w_L)W . \tag{12-29}$$

We shall assume constant environmental profiles of T' and w'_v. Therefore, from the point of view of the parcel, the time variations in T' and w'_v are given by

$$\frac{dT'}{dt} = -\Gamma'_T W , \tag{12-30}$$

and

$$\frac{dw'_v}{dt} = -\Gamma'_v W , \tag{12-31}$$

where $\Gamma'_T = -dT'/dz$ and $\Gamma'_v = -dw'_v/dz$ are the observed height variations of the environmental T' and w'_v, respectively.

Entrainment will cause the parcel volume to increase with time. If we assume the convective element is a sphere or thermal bubble of radius R_B then, since $m = 4\pi\rho R_B^3/3$, we can relate the growth of the radius to the entrainment rate μ_B according to

$$\frac{d \ln R_B}{dt} = \frac{1}{3}\left[\mu_B W - \frac{d \ln \rho}{dt}\right] . \tag{12-32}$$

For a jet or plume of radius $R_J(z)$ and vertical velocity $W(z)$, entrainment is described in terms of a change in mass flux $F_m \equiv \pi R_J^2 \rho W$ along the vertical plume axis. Thus, the change in mass flux over Δz is $\Delta z(dF_m/dz)$, and by continuity this must equal the radial mass influx over Δz, viz., $2\pi R_J \Delta z \rho' U_R$, where $U_R(z)$ is the inward radial velocity. Therefore, for a jet the entrainment rate is

$$\mu_J = \frac{1}{F_m}\frac{dF_m}{dz} = \frac{C}{R_J} , \tag{12-33}$$

where $C = 2\rho' U_R/\rho W$ is the *entrainment parameter*; as we have indicated earlier, laboratory studies show that $C \approx 0.2$. Finally, the equation for the jet radius which is analogous to (12-32) is

$$\frac{d \ln R_J}{dt} = \frac{1}{2}\left[\mu_J W - \frac{d \ln \rho}{dt} - \frac{d \ln W}{dt}\right] , \tag{12-34}$$

where from the ideal gas law

$$\frac{d\rho}{dt} = \frac{1}{R_a T}\frac{dp}{dt} - \frac{p}{R_a T^2}\frac{dT}{dt} . \tag{12-35}$$

We must now establish a connecting link between the parcel properties and the microphysical drop growth processes. In order to do that we must initialize the model by an assumed or observed number distribution function $n'_{AP,a}(m_{AP})$ of dry aerosol particles of mass m_{AP} and known chemical composition. Unfortunately,

the growth of dry aerosol particles in a supersaturated environment would involve formulating an initial growth phase due to vapor adsorption on the surface of the particles (see Chapter 5). For practical purposes, one avoids this difficulty by computing from $n'_{AP}(m_{AP})$ via (6-33) the number distribution $n_{AP,\mathrm{a}}(m_{AP})$ of unactivated drops which are in equilibrium with an environmental relative humidity between 90 and 99% in order to insure the deliquescence of all soluble components in the AP in a time period which is short compared to the time over which significant changes occur in the atmosphere. Following Flossmann *et al.* (1985), we initially have $n_{AP,\mathrm{a}}(m_{AP}) = n'_{AP,\mathrm{a}}(m_{AP})$, where $n_{AP,\mathrm{a}}(m_{AP})$ is the number distribution of inactivated drops inside the air parcel at a time t. As the parcel rises and the relative humidity increases, $n_{AP,\mathrm{a}}(m_{AP})$ changes (1) due to entrainment of additional inactivated particles from the enviromental air, (2) the activation of some of the inactivated particles to drops, and (3) due to drops which by evaporation become inactivated particles again. These changes are expressed by the relation

$$\frac{\partial n_{AP,\mathrm{a}}(m_{AP})}{\partial t} = -\mu W[n_{AP,\mathrm{a}}(m_{AP}) - n'_{AP,\mathrm{a}}(m_{AP})] + \left.\frac{\partial n_{AP,\mathrm{a}}(m_{AP})}{\partial t}\right|_{\mathrm{act/deact}} . \tag{12-36}$$

In the beginning of a parcel's ascent, the change in $n_{AP,\mathrm{a}}$ is only due to the second term on the right of (12-36). As the parcel ascends $n_{AP,\mathrm{a}}$ decreases, so that for $n_{AP,\mathrm{a}} < n'_{AP,\mathrm{a}}$ the entrainment term of (12-36) also contributes to the change in $n_{AP,\mathrm{a}}$. Initially, the number distribution function $n_{\mathrm{d}}(m)$ of drops of mass m is zero in the parcel. As aerosol particles become activated to drops and these grow further by vapor diffusion, the number concentration of drops in the parcel changes according to

$$\frac{\partial n_{\mathrm{d}}(m)}{\partial t} = -\mu W n_{\mathrm{d}}(m) + \left.\frac{\partial n_{\mathrm{d}}(m)}{\partial t}\right|_{\mathrm{act/deact}} + \left.\frac{\partial n_{\mathrm{d}}(m)}{\partial t}\right|_{\mathrm{con/eva}} . \tag{12-37}$$

The change in drop concentration due to the activation of aerosol particles or deactivation of drops is given by

$$\left.\frac{\partial n_{\mathrm{d}}(m)}{\partial t}\right|_{\mathrm{act/deact}} = -\left.\frac{\partial n_{AP,\mathrm{a}}(m_{AP})}{\partial t}\right|_{\mathrm{act/deact}} , \tag{12-38}$$

and the change in drop concentration due to their diffusional growth or evaporation is

$$\left.\frac{\partial n_{\mathrm{d}}(m)}{\partial t}\right|_{\mathrm{con/eva}} = -\frac{\partial}{\partial m}\left[\left(\frac{\mathrm{d}m}{\mathrm{d}t}\right)_{\mathrm{con/eva}} n_{\mathrm{d}}(m)\right] , \tag{12-39}$$

where the mass growth or loss rate $\mathrm{d}m/\mathrm{d}t$ from vapor diffusion in (12-39) will be given in Chapter 13 by (13-28). If drops evaporate to sizes which are smaller than those at which the particles are considered to be activated, then they will contribute to the third term on the right of (12-36). The second term on the right of (12-36) is computed with the help of (6-42), so that the left-hand side of (12-38) becomes known and may be used in evaluating (12-37).

Finally, the change in the liquid water content of the parcel during the growth of drops by vapor diffusion is given by

$$\frac{\mathrm{d}w_L}{\mathrm{d}t} = \frac{\mathrm{d}}{\mathrm{d}t}\int_0^\infty m n_\mathrm{d}(m) = \int_0^\infty \left[n_\mathrm{d}(m)\left.\frac{\mathrm{d}m}{\mathrm{d}t}\right|_{\mathrm{con/eva}} + m\frac{\partial n_\mathrm{d}(m)}{\partial t}\right] \mathrm{d}t\,. \qquad (12\text{-}40)$$

We have now a complete set of governing equations to describe the changes taking place inside an entraining air parcel. For a specified size distribution of aerosol particles $n'_{AP,\mathrm{a}}(m_{AP})$ and their chemical characterisitics, for a given vertical variation of temperature and humidity Γ'_T, Γ'_v and entrainment parameter C, and using (12-39), (12-37), (6-42), and (13-26) we can determine the 13 quantities R, W, T, T', $\mathrm{w_v}$, $\mathrm{w'_v}$, p, $s_{\mathrm{v,w}}$, w_L, μ, n_d, and $n_{AP,\mathrm{a}}$ from the 13 equations, (12-25) to (12-31), (12-32) or (12-34), (12-33), (12-35), (12-36), (12-38) and (12-40). To model a closed (non-entraining) parcel, the only change required is to set $\mu = 0$ everywhere. We shall use the entraining parcel model in Chapter 13 to study the growth of a population of AP into cloud drops, and in Chapter 17 to study the rate at which aerosol particles and gases are scavenged by a population of growing cloud drops.

CHAPTER 13

DIFFUSION GROWTH AND EVAPORATION OF WATER DROPS AND SNOW CRYSTALS

Immediately following their formation through heterogeneous nucleation, cloud particles proceed to grow by the process of vapor diffusion. Later on they may also experience growth by the mechanisms of collision and subsequent coalescence or sticking. In the present chapter, we shall describe the individual and collective growth (and evaporation) of cloud particles by vapor diffusion; collisional growth (and breakup) are considered in Chapters 15 and 16.

13.1 Laws for Diffusion of Water Vapor and Heat

13.1.1 Diffusion of Water Vapor

In Section 11.2, we have applied Fick's first and second laws to the diffusion of aerosol particles. An adequate treatment of water vapor diffusion to drops or snow crystals can be based on a strictly analogous formulation. Thus, if we let $\vec{j}_v = \rho_v \vec{u}_v$ denote the flux density vector of water vapor mass, then for moist air moving with velocity $\vec{u}$ relative to the drop or crystal under study, $\vec{j}_v$ may be represented as the sum of contributions due to diffusion and convection:

$$\vec{j}_v = -D_v \nabla \rho_v + \rho_v \vec{u}\,, \tag{13-1}$$

where D_v is the diffusion coefficient or diffusivity for water vapor, and ρ_v is the water vapor density. Then, from the continuity equation (see A.10-3), $\partial \rho_v / \partial t = -\nabla \cdot \vec{j}_v$, and considering that $\nabla \cdot (\rho_v \vec{u}) = \rho_v \nabla \cdot \vec{u} + \vec{u} \cdot \nabla \rho_v$, we obtain the convective diffusion equation for water vapor:

$$\frac{\partial \rho_v}{\partial t} + \vec{u} \cdot \nabla \rho_v = D_v \nabla^2 \rho_v\,. \tag{13-2}$$

To obtain (13-2) we have made the usual assumption that $\nabla \cdot \vec{u} = 0$ (recall the discussion just before (10-2) and that D_v is constant over the region of interest (in applications, this means D_v must not vary over distances of the order of the size of the growing or evaporating drop or snow crystal). We have also made the implicit assumption that the total air density ρ is constant in the vicinity of the drop or crystal; otherwise we would have had to express the diffusive transport of vapor in terms of the concentration gradient of the mixing ratio $w_v = \rho_v / \rho_a$, or in terms of ρ_v / ρ.

The diffusivity D_v of water vapor in air has been experimentally determined only for temperatures warmer than 0°C, and in this range the experimental results

scatter quite strongly. The unreliability of past experimental values for D_v has also been stressed by Ranz and Marshall (1952), Reid and Sherwood (1966), Thorpe and Mason (1966), and Beard and Pruppacher (1971a), all of whom pointed out that the conventionally used values for D_v tabulated in the Smithsonian Meteorological Tables (1968) may be too high by as much as 10%. In a survey, Marreno and Mason (1972) pointed out that probably the best experimental values for D_v at temperatures above 0°C are those of O'Connell *et al.* (1969). Following an extrapolation procedure suggested by E. A. Mason (1975, private comm.), Hall and Pruppacher (1976) arrived at the following best estimate relation for the diffusivity of water vapor in air for temperatures between −40 and 40°C:

$$D_v = 0.211 \left(\frac{T}{T_0}\right)^{1.94} \left(\frac{p_0}{p}\right), \tag{13-3}$$

with $T_0 = 273.15°K$, $p_0 = 1013.25$ mb, and D_v in $cm^2\ sec^{-1}$.

For a fixed cloud particle surface (ignoring any tangential motion of the surface, and ignoring the rate of change of particle size due to evaporation or condensation), the usual flow boundary condition at the surface (S) taken to accompany (13-2) is $\vec{u}\ |_S = 0$. However, when we recognize that $\vec{u}$ is the mass-average velocity $(\rho_a \vec{u}_a + \rho_v \vec{u}_v)/\rho$ of the velocities of vapor ($\vec{u}_v$) and dry air ($\vec{u}_a$), we can appreciate that $\vec{u}_v$ does not vanish at the surface, and that the proper boundary condition is $\vec{u}_a\ |_S = 0$. This latter boundary condition leads, from (13-1), to the surface flux relation $\vec{j}_v\ |_S = \rho_v \vec{u}_v\ |_S = -[D_v(1-\rho_v/\rho)^{-1} \nabla \rho_v]_S$; this differs by a factor of $(1-\rho_v/\rho)^{-1}$ from the more familiar statement $\vec{j}_v\ |_S = -[D_v \nabla \rho_v]_S$, which arises from the former boundary condition $\vec{u}\ |_S = 0$. On the other hand, since usually $\rho_v/\rho = O(10^{-3})$, we are justified in ignoring this refinement and the complications it entails. Therefore, we shall henceforth employ the simpler formulation expressed by (13-1), (13-2), and the condition that the total air velocity (or its radial component for a drop with internal circulation) must vanish at the particle surface. Additional complications may arise if there are gradients in temperature or pressure. Then, the phenomena of thermal and pressure diffusion of vapor will also occur. Discussions of these effects may be found, for example, in Bird *et al.* (1960) and Hidy and Brock (1970). Fortunately, these effects are of negligible importance for circumstances of interest in cloud microphysics.

We shall now explore the possibility of simplifying (13-2) by dropping the $\partial \rho_v/\partial t$ term. For this purpose, let us consider the initial-value problem of radially symmetric diffusion from a motionless drop ($\vec{u} = 0$) of radius a, subject to the boundary condition $\rho_v(a,t) = \rho_{v,a} =$ constant, and the initial condition $\rho_v(r,0) = \rho_{v,\infty} =$ constant for $r > a$. This problem is mathematically equivalent to the one of particle diffusion to a sphere discussed in Section 11.5; in fact, the solution is given by (11-35) with the replacements $r_{12} \to a$, $D_{12} \to D_v$, $n_2 \to (\rho_v - \rho_{v,a})$, and $n_{2,\infty} \to (\rho_{v,\infty} - \rho_{v,a})$:

$$\rho_v(r,t) = \rho_{v,\infty} + (\rho_{v,a} - \rho_{v,\infty}) \frac{a}{r} \left[1 - \operatorname{erf}\left(\frac{r-a}{2\sqrt{D_v t}}\right)\right]. \tag{13-4}$$

From this expression, the vapor flux at the drop surface is found to be

$$j_{\mathrm{v},r}\,|_{r=a} = \vec{j}_{\mathrm{v}} \cdot \hat{\mathrm{e}}_r\,|_{r=a} = -D_{\mathrm{v}} \left(\frac{\partial \rho_{\mathrm{v}}}{\partial r}\right)_{r=a} = \frac{D_{\mathrm{v}}(\rho_{\mathrm{v},a} - \rho_{\mathrm{v},\infty})}{a} \left(1 + \frac{a}{\sqrt{\pi D_{\mathrm{v}} t}}\right). \tag{13-5}$$

Thus, it can be seen that the steady state description will be valid for times $t \gg t_c = a^2/\pi D_{\mathrm{v}}$; for $T = 0°\mathrm{C}$ and $p = 1$ atm., $t_c < 1.7 \times 10^{-6}$ sec for drops smaller than 100 μm radius. Since in the atmosphere significant changes in vapor density fields occur over times much larger than this, we may justifiably ignore the non-steady state contribution to the diffusional growth or evaporation of cloud particles under natural conditions. (We have ignored the intrinsic unsteadiness due to the rate of contraction or expansion of an evaporating or growing drop. This effect may also be shown to be generally negligible for $t \gg t_c$ (e.g., see Section 4.2 of Hidy and Brock (1970)).) For steady state (13-4) and (13-5) become, respectively,

$$\rho_{\mathrm{v}}(r,t) = \rho_{\mathrm{v},\infty} + (\rho_{\mathrm{v},a} - \rho_{\mathrm{v},\infty})\frac{a}{r} \tag{13-6}$$

and

$$(j_{\mathrm{v},r})_{r=a} = -D_{\mathrm{v}} \left(\frac{\partial \rho_{\mathrm{v}}}{\partial r}\right)_{r=a} = \frac{D_{\mathrm{v}}(\rho_{\mathrm{v},a} - \rho_{\mathrm{v},\infty})}{a}. \tag{13-7}$$

Of course, we could have obtained this result directly by simply solving Laplace's equation for conditions of radial symmetry:

$$\nabla^2 \rho_{\mathrm{v}} = \frac{1}{r}\frac{\mathrm{d}^2}{\mathrm{d}r^2}(r\rho_{\mathrm{v}}) = \frac{\mathrm{d}^2 \rho_{\mathrm{v}}}{\mathrm{d}r^2} + \frac{2}{r}\frac{\mathrm{d}\rho_{\mathrm{v}}}{\mathrm{d}r} = 0, \tag{13-8}$$

subject to the boundary conditions $\rho_{\mathrm{v}}(a) = \rho_{\mathrm{v},a}$ and $\rho_{\mathrm{v}} = \rho_{\mathrm{v},\infty}$ for $r \to \infty$. If we now identify the rate of change of the drop mass m for a motionless drop $(\mathrm{d}m/\mathrm{d}t)_0$ with the flux of vapor $-J_{\mathrm{v},a}$ through the drop's surface, we obtain

$$\left(\frac{\mathrm{d}m}{\mathrm{d}t}\right)_0 = -J_{\mathrm{v},a} = -\int_{\mathrm{S}} (j_{\mathrm{v},r})_{r=a}\,\mathrm{dS} = 4\pi a D_{\mathrm{v}}(\rho_{\mathrm{v},\infty} - \rho_{\mathrm{v},a}), \tag{13-9}$$

where $\mathrm{S}(= 4\pi a^2)$ denotes the drop surface area (Maxwell, 1890). An alternative expression in terms of vapor pressure e and temperature T may be obtained by substituting the equation of state (4-24) into (13-9):

$$\left(\frac{\mathrm{d}m}{\mathrm{d}t}\right)_0 = \frac{4\pi a D_{\mathrm{v}} M_{\mathrm{w}}}{\mathscr{R}} \left(\frac{\mathrm{e}_\infty}{T_\infty} - \frac{\mathrm{e}_a}{T_a}\right). \tag{13-10}$$

The description of diffusional growth or evaporation provided by (13-9) and (13-10) must break down for very small drops. This happens because the assumption that the vapor density in moist air is continuous right up to the drop surface, which is implicit in the formulation presented so far, becomes quite unrealistic for drops with radii comparable to the mean free path λ of air molecules. An intuitive, semi-empirical extension of the continuous description to account for this effect has

been carried out by Schäfer (1932) and later in much more detail by Fuchs (1959); both of these treatments follow Langmuir (1918), who pointed out the existence of a rapid change in vapor concentration at the surface of an evaporating drop. (An analogous discontinuity in temperature had been known to exist earlier (Lazarev, 1912).) Since Fuchs's method is often used and produces results of reasonable accuracy (see, e.g., Fuchs, 1959; Fukuta and Walter, 1970), we shall now present a version of it following Fitzgerald (1972). A discussion of more rigorous treatments of the discrete field problem may be found in Hidy and Brock (1970).

Fuchs assumed the diffusion equation and its solution are valid only for distances greater than the 'vapor jump' length $\Delta_v \approx \lambda_a$ from the drop surface. Within the layer $a \leq r \leq a + \Delta_v$, vapor transport is assumed to occur according to an elementary gas kinetic mechanism. The condition of continuity of vapor flux across the surface $r = a + \Delta_v$ may be invoked to complete the description. Proceeding in this manner for the region $r \geq a + \Delta_v$, we must again solve Laplace's equation for the case of radial symmetry, subject first to the boundary condition $\rho_v = \rho_{v,\infty}$ for $r \to \infty$. The appropriate solution is simply

$$\rho_v(r) = \rho_{v,\infty} + \frac{A}{r}, \tag{13-11}$$

where A is a constant to be determined.

For the region $a \leq r \leq a + \Delta_v$, we assume the vapor flux may be described according to the gas kinetic expressions presented in Section 5.11. If we assume the vapor density at $r = a + \Delta_v$ measures the concentration of molecules which strike the surface (which is reasonable since on the average these molecules will have suffered their last collision about one mean free path above the surface), then from (5-48) and (5-52), we estimate the condensation flux of vapor mass per unit area of the surface to be $\alpha_c \dot{m}_w N_v \bar{v}_v/4 = \alpha_c \bar{v}_v \rho_v(r = a + \Delta_v)/4$, where $\dot{m}_w$ is the mass of the water molecule, $\bar{v}_v$ is the average thermal velocity of vapor molecules, N_v is the concentration of vapor molecules at $r = a + \Delta_v$, and α_c is the condensation coefficient. Similarly, we estimate the evaporation flux per unit area of surface to be $\alpha_e \bar{v}_v \rho_{v,sat}(T_a)/4$, where α_e is the evaporation coefficient (we have ignored any effects due to temperature gradients or incomplete thermal accommodation). On setting $\alpha_e = \alpha_c$, which is justified by the absence of contrary experimental evidence, we may therefore express the net evaporation flux $J_v(a)$ of water mass from the drop surface as follows:

$$J_v(r = a) = \pi a^2 \alpha_c \bar{v}_v [\rho_{v,sat}(T_a) - \rho_v(a + \Delta_v)], \tag{13-12a}$$

which is another form of the Hertz–Knudsen equation (5-54). In (13-12a) $\rho_{v,sat}(T_a)$ is the equilibrium vapor density over the drop at the drop surface temperature T_a and $\rho_v(a + \Delta_v)$ is the vapor density at $r = a + \Delta_v$.

For a steady state, we must require that $J_v(r = a)$ in (13-12a) is equal to $J_v(a + \Delta_v)$ at $r = a + \Delta_v$. To determine the latter, we recall (13-7) and (13-9) to get

$$J_v(r = a + \Delta_v) = -4\pi(a + \Delta_v)^2 D_v \left(\frac{\partial \rho_v}{\partial r}\right)_{a+\Delta_v} = 4\pi D_v A, \tag{13-12b}$$

with $(\partial\rho_{\mathrm{v}}/\partial r)_{a+\Delta_{\mathrm{v}}} = -A/(a+\Delta_{\mathrm{v}})^2$, from (13-11). Equating now (13-12a) and (13-12b), and consider that $\rho_{\mathrm{v}}(r = a + \Delta_{\mathrm{v}}) = \rho_{\mathrm{v},\infty} + [A/(a+\Delta_{\mathrm{v}})]$ from (13-11), we find for the constant A

$$A = \frac{a(\rho_{\mathrm{v,sat}}(T_a) - \rho_{\mathrm{v},\infty})}{\left(\frac{a}{a+\Delta_{\mathrm{v}}} + \frac{4D_{\mathrm{v}}}{a\alpha_c \bar{\mathrm{v}}_{\mathrm{v}}}\right)} . \tag{13-13}$$

We may also express our result in the form of (13-9) or (13-10), where now D_{v} is replaced by a modified diffusivity given by

$$D_{\mathrm{v}}^* = \frac{D_{\mathrm{v}}}{\left[\frac{a}{a+\Delta_{\mathrm{v}}} + \frac{D_{\mathrm{v}}}{a\alpha_c}\left(\frac{2\pi M_{\mathrm{w}}}{\mathscr{R}T_a}\right)^{1/2}\right]} \tag{13-14}$$

(Okuyama and Zung, 1967; Fitzgerald, 1972). To obtain this result, we have used (5-49) for $\bar{\mathrm{v}}_{\mathrm{v}}$. Equation (13-14) coincides with an expression derived by Fukuta and Walter (1970) on setting $\Delta_{\mathrm{v}} = 0$; also, for the case that $\alpha_c = 1$ and $\Delta_{\mathrm{v}} = C\lambda_{\mathrm{a}}$, where $C \approx 0.7$ is the 'Cunningham constant', (13-14) reduces to a result obtained by Langmuir (1944).

Using (13-13), we obtain from (13-11)

$$\rho_{\mathrm{v}}(r) = \rho_{\mathrm{v},\infty} + \frac{a}{r}\left[\frac{1}{\left(\frac{a}{a+\Delta_{\mathrm{v}}} + \frac{4D_{\mathrm{v}}}{a\alpha_c \bar{\mathrm{v}}_{\mathrm{v}}}\right)}\right](\rho_{\mathrm{v,sat}}(T_a) - \rho_{\mathrm{v},\infty}) . \tag{13-15a}$$

Equations (13-9) and (13-10) become then

$$\left(\frac{\mathrm{d}m}{\mathrm{d}t}\right)_0 = 4\pi a D_{\mathrm{v}}^*(\rho_{\mathrm{v},\infty} - \rho_{\mathrm{v,sat}}(T_a)) = \frac{4\pi D_{\mathrm{v}}^* M_{\mathrm{w}}}{\mathscr{R}}\left(\frac{\mathrm{e}_\infty}{T_\infty} - \frac{\mathrm{e}_{\mathrm{sat}}(T_a)}{T_a}\right) . \tag{13-15b}$$

The magnitude of the correction to the diffusivity in (13-14) (and the corresponding correction to the thermal conductivity, which we shall discuss in the next section) can be seen from Table 13.1. The table indicates that the usual continuum theory of Maxwell strongly overestimates the growth rate for submicron particles. The difference in growth rates is illustrated further in Figure 13.1, which presents the results of a computation by Fukuta and Walter (1970) for the case of a single drop growing by diffusion at 10°C, 1000 mb, a supersaturation of 1%, and a thermal accommodation coefficient of unity. The figure shows that the ratio of droplet masses, $\mathrm{x}_m = m(D_{\mathrm{v}})/m(D_{\mathrm{v}}^*)$, computed from the Maxwell theory and the modified theory using D_{v}^* of (13-14) (with $\Delta_{\mathrm{v}} = 0$), reduces to $\mathrm{x}_m \approx 2$ within the first 20 sec after the start of growth. For longer times, x_m decreases until finally the difference between the predictions of the two models becomes negligible ($\mathrm{x}_m \approx 1$). Since, as we shall see below, growth times much longer than 20 sec are generally needed to establish the spectral characteristics of a drop population growing by diifusion, the results shown in Figure 13.1 suggest that the correction of the continuum diffusion model for gas kinetic effects is not likely to make a significant quantitative difference in the predictions of growth models for natural conditions. (Also, the practical advantages of the corrected model are further narrowed by the present uncertainties in the known values of Δ_{v}, D_{v} and α_c.)

TABLE 13.1

Modified diffusivity of water vapor and modified thermal conductivity of air computed from (13-14) and (13-20) for 10^5 C and 800 mb, assuming $\alpha_c = 0.036$, $\alpha_T = 0.7$, $D_v = 0.30$ cm^2 sec^{-1}, $k_a = 5.97 \times 10^{-5}$ cal cm^{-1} sec^{-1} (°C)$^{-1}$, $\lambda_a = 8 \times 10^{-6}$ cm, $\Delta_T = 2.16 \times 10^{-5}$ cm and $\Delta_v = 1.3\lambda_a$.

Drop radius (μm)	0.01	0.01	1.0	10.0	∞
D_v^* (cm^2 sec^{-1})	5.2×10^{-4}	5.2×10^{-3}	4.5×10^{-2}	0.19	0.30
k_a^* (cal cm^{-1} sec^{-1} °C^{-1})	1.9×10^{-6}	1.7×10^{-5}	5.2×10^{-5}	5.9×10^{-5}	6.0

13.1.2 Diffusion of Heat

Water vapor transport by diffusion to or from a cloud particle necessarily involves a substantial flow of heat as well, owing to the release or absorption of heat of phase change. The resulting temperature difference between the particle and its local environment causes a flow of sensible heat by the familiar process of thermal diffusion or heat conduction. The flux density vector $\vec{j}_h$ for heat transport by this process in given by Fourier's law:

$$\vec{j}_h = -k\nabla T\,, \tag{13-16}$$

where k is the thermal conductivity of humid air through which heat is transported.

From (13-16), and for the physical conditions of relevance in cloud microphysics, we may easily derive an equation for the diffusion of heat which is analogous to (13-2). From the meaning of $\vec{j}_h$, the conductive heat change experienced by a moving volume element δV of air in time dt is just $-\nabla \cdot \vec{j}_h \delta V \mathrm{d}t$. Since the heated or cooled air in the vicinity of a cloud particle is free to expand or contract, the heat exchange may be assumed to occur at constant pressure. Then, from (4-6), the corresponding enthalpy change of the considered volume element is just $\mathrm{d}(h\rho\delta V) = -\nabla \cdot \vec{j}_h \delta V \mathrm{d}t$, where h is the enthalpy of air per unit mass of air. Also, since $\mathrm{d}h = c_p \mathrm{d}T$ from (4-12), and considering that $\mathrm{d}(p\delta V) = 0$ by conservation of mass, we arrive at the desired result:

$$\frac{\mathrm{d}T}{\mathrm{d}t} = \frac{\partial T}{\partial t} + \vec{\mathrm{u}} \cdot \nabla T = -\frac{\nabla \cdot \vec{j}_h}{\rho c_p} = \kappa \nabla^2 T\,, \tag{13-17}$$

where $\kappa \equiv k/\rho c_p$ is called the thermal diffusivity, with p and c_p being the density and specific heat of humid air, and where (13-16) has been inserted for $\vec{j}_h$. To obtain (13-17), we have assumed k to be a constant over the region of interest (within a few radii of the given cloud particle). We have also ignored heat changes arising from radiation, and from frictional dissipation of air motion (or drop internal motion). Heating by frictional dissipation is always of negligible importance for individual cloud microphysical processes (see, for example, §55 of Landau and Lifschitz, 1959). Radiative heat exchange is also negligible in the context of interest in this chapter, since temperature differences between particles and the local environment are always quite small.

A survey of the best experimentally and theoretically determined values for the thermal conductivity of dry air, k_a, and water vapor, k_v, has been given by Beard

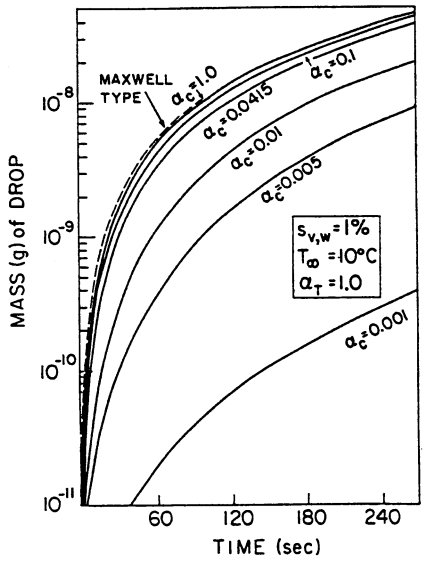


Fig. 13-1: Influence of kinetic effects on the diffusion growth of small drops, for various α_c. (From Fukuta and Walter, 1970; by courtesy of Am. Meteor. Soc., and the authors.)

and Pruppacher (1971a). They suggested that the temperature variation for k_a and k_v can be expressed adequately by the relations

$$k_a = (5.69 + 0.017T) \times 10^{-5}, \tag{13-18a}$$

$$k_v = (3.78 + 0.020T) \times 10^{-5}, \tag{13-18b}$$

with T in °C and k in cal cm^{-1} sec^{-1}°C^{-1}. One may then use the Mason-Sexena formula (Bird *et al.*, 1960) to find the thermal conductivity of moist air, viz.,

$$k = k_a[1 - (\gamma_1 - \gamma_2 k_v/k_a)x_v], \tag{13-18c}$$

where x_v is the mole fraction for water vapor in moist air and $\gamma_1 \approx 1.17$, $\gamma_2 \approx 1.02$. Since for typical atmospheric conditions $x_v \ll 1$, we see that $k \approx k_a$.

From the identical forms of (13-2) and (13-17), we can borrow the argument of the previous section concerning the validity of assummg a steady state; this will be permissible for times $t \gg t_c' = a^2/\pi\kappa$. Since $\kappa \approx D_v$, then $t_c' \approx t_c$ and so we can generally ignore the non-steady state contribution to the conductive heat flow to or from evaporating or growing cloud particles. Therefore, from the same mathematical arguments as used in the previous section, we conclude the rate of conductive heat transfer to a motionless drop may be expressed as

$$\left(\frac{dq}{dt}\right)_0 = -J_{h,a} = 4\pi a k_a (T_\infty - T_a) \tag{13-19}$$

(cf. (13-9)).

We may also correct k for gas kinetic effects in exactly the same manner as for the previous case of vapor diffusion. The only difference is in the replacement of the vapor mass flux per unit area, $\alpha_c \rho_v \bar{v}_v/4$, by the heat flux per unit area, $\alpha_T \rho \bar{v}_a c_{pa}/4$, where α_T is the thermal accommodation coefficient (see Section 5.11), and c_p is the specific heat of air. The modified form for the thermal conductivity is then given by

$$k_a^* = \frac{k_a}{\left[\frac{a}{a+\Delta_T} + \frac{k_a}{a\alpha_T \rho c_{pa}} \left(\frac{2\pi M_a}{\mathscr{R} T_a}\right)^{1/2}\right]} \tag{13-20}$$

(Fitzgerald, 1972) (cf. (13-15). The 'thermal jump' distance Δ_T is analogous to Δ_v in (13-14). If $\Delta_T = 0$ and c_p is replaced by $c_{pa} + R_a/2$, (13-20) coincides with an expression obtained by Fukuta and Walter (1970). It can also be made to agree with a result derived by Carstens (1972) and Carstens *et al.* (1974) by making the replacements $c_{pa} \to c_{pa} + R_a/2$ and $\alpha_T \to \alpha_T(1 - \alpha_T/2)^{-1}$. These differences arise from slightly different modeling approaches, and are of little consequence. An evaluation of (13-20) is given in Table 13.1. The previous discussion of the significance of the differences between D_v and D_v also applies to the present case of k' versus k.

13.2 Growth of Aqueous Solution Drops by Diffusion of Water Vapor

13.2.1 Growth of an Individual Stationary Drop

We shall now formulate a governing equation for the diffusional growth (or evaporation) of a single stationary drop in a motionless atmosphere. From (13-10), the rate at which such a drop changes its radius a may be expressed as

$$a\frac{da}{dt} = \frac{D_v^* M_w}{\mathscr{R} \rho_s''} \left(\frac{e_\infty}{T_\infty} - \frac{e_{sat}(T_a)}{T_a}\right), \tag{13-21}$$

where we have replaced D_v by D_v^* to include the correction for gas kinetic effects. An expression for the temperature T_a at the drop surface can be obtained by considering the coupling of the rates of change of heat and mass through latent heat release:

$$\left(\frac{dq}{dt}\right)_0 = -L_e \left(\frac{dm}{dt}\right)_0, \tag{13-22}$$

where L_e is the specific latent heat of evaporation. Then, on substituting (13-19) (with $k_a \to k_a^*$) into this equation, we find

$$T_a = T_\infty + \frac{L_e \rho_s''}{k_a^*} a \frac{da}{dt}, \tag{13-23}$$

where ρ_s'' is the density of the aqueous solution drop. As expected, we see that an evaporating drop ($da/dt < 0$) is predicted to be cooler than its environment, and vice versa.

To integrate (13-21), we also need an equation for the vapor pressure e_a at the surface of the solution drop. An adequate expression for this purpose, including both the drop curvature and solution effects, is given by (6-33):

$$e_{sat}(T_a) = e_{sat,w}(T_a) \exp\left[\frac{2M_w\rho_{s/a}}{\mathscr{R}T_\infty\rho_w a} - \frac{\nu\Phi_s\varepsilon_m M_w\rho_N r_N^3}{M_s\rho_w(a^3 - r_N^3)}\right]. \tag{13-24}$$

To close the system of equations, we must also invoke the Clausius-Clapeyron equation (4-83), in order to relate $e_{sat,w}(T_a)$ to $e_{sat,w}(T_\infty)$, which is a function only of the environmental temperature T_∞. On integrating (4-83), we obtain

$$e_{sat,w}(T_a) = e_{sat,w}(T_\infty) \exp\left[\frac{L_e M_w}{\mathscr{R}}\left(\frac{T_a - T_\infty}{T_a T_\infty}\right)\right], \tag{13-25}$$

where T_∞ is the temperature in the drop's environment (note: T_∞ is to be identified with the temperature T used in Chapter 12 for the temperature inside a rising air parcel). We see that the system consists of the four unknowns $a(da/dt)$, e_{sat}, T_a, and $e_{sat,w}(T_a)$ related by the four equations (13-21), (13-23), (13-24), and (13-25). In cloud models, this set of equations is solved numerically in order to determine the growth rate of a drop by diffusion of water vapor. The equations can also be combined into the single expression

$$\begin{aligned} a\frac{da}{dt} = \frac{D_v^* M_w e_{sat,w}(T_\infty)}{\rho_s''\mathscr{R}T_\infty}\Bigg(S_{v,w} - \frac{1}{(1+\delta)}\exp\Bigg[\frac{L_e M_w}{\mathscr{R}T_\infty}\left(\frac{\delta}{1+\delta}\right) \\ + \frac{2M_w\rho_{s/a}}{\mathscr{R}T_\infty(1+\delta)\rho_w a} - \frac{\nu\Phi_s\varepsilon_m M_w\rho_N r_N^3}{M_s\rho_w(a^3 - r_N^3)}\Bigg]\Bigg), \end{aligned} \tag{13-26}$$

in which we have set $(T_a/T_\infty) = 1 + \delta$, and $\delta = (L_e\rho_s''/T_\infty k_a^*)a(da/dt)$. For usual conditions of drop growth, $\delta \leq 10^{-5}$ (Neiburger and Chien, 1960), which means that the heat released by condensation is very efficiently dissipated by conduction. One might therefore expect that the heating of the drop by release of latent heat could be ignored, as was assumed in an early study by Houghton (1933). However, this turns out not to be the case; Neiburger and Chien showed that the neglect of temperature differences between the drop and its environment leads to large errors for all sizes of drops and condensation nuclei.

The result (13-26) is rather cumbersome and, worse yet, is an implicit equation due to the dependence of δ on da/dt. Fortunately, several simplifications are possible. Thus, since $\delta \ll 1$, we may expand (13-26) to $O(\delta)$, and write

$$\exp\left[\frac{L_e M_w \delta}{\mathscr{R}T_\infty(1+\delta)}\right] \approx 1 + \frac{L_e M_w \delta}{\mathscr{R}T_\infty}; \tag{13-27a}$$

also, on defining

$$y = \frac{2\sigma_{s/a}M_w}{\mathscr{R}T_\infty\rho_w a} - \frac{\nu\Phi_s m_s M_w/M_s}{(4\pi\rho_s'' a^3/3) - m_s}, \tag{13-27b}$$

we may write $\exp(y) \approx 1 + y$, since both the curvature and solute contributions to the equilibrium vapor pressure over a solution drop are generally small for $a \gtrsim 1\,\mu$m

(see Figure 6.2). With these approximations and on setting $\rho_s'' \approx \rho_w$, and $L_e \approx L_{e,0}$, (13-26) reduces to

$$a\frac{da}{dt} \approx \frac{s_{v,w} - y}{\frac{\rho_w \mathscr{R} T_\infty}{e_{sat,w}(T_\infty) D_v^* M_w} + \frac{L_{e,0}\rho_w}{k_a^* T_\infty}\left(\frac{L_{e,0} M_w}{T_\infty \mathscr{R}} - 1\right)}, \tag{13-28}$$

where the supersaturation $s_{v,w} + 1 = e_\infty / e_{sat,w}(T_\infty)$. Equation (13-28) with the replacements $D_v^* \to D_v$ and $k_a^* \to k_a$ is equivalent to one used by Howell (1949). For realistic conditions of growth, it agrees with (13-26) to within a few percent. (For the same diffusivities, Langmuir (1944) derived a similar equation, except for the omission of the solute effect, which is the second term in y.)

The growth histories of individual solution drops calculated from an equation almost identical to (13-28) are shown in Figure 13.2. It can be seen that there is a tendency for more dilute solution drops, of smaller initial radii, since they contain less salt, to catch up to the size of the more concentrated drops. This happens because both the curvature and solute effects rapidly become negligible with increasing a, so that approximately $y \approx 0$ and, hence, $da/dt \approx C/a$, or $a^2 \approx a_0^2 + Ct$, where C is a constant. The prediction of a parabolic growth law for relatively large and pure water drops has been verified by the experiments of Houghton (1933).

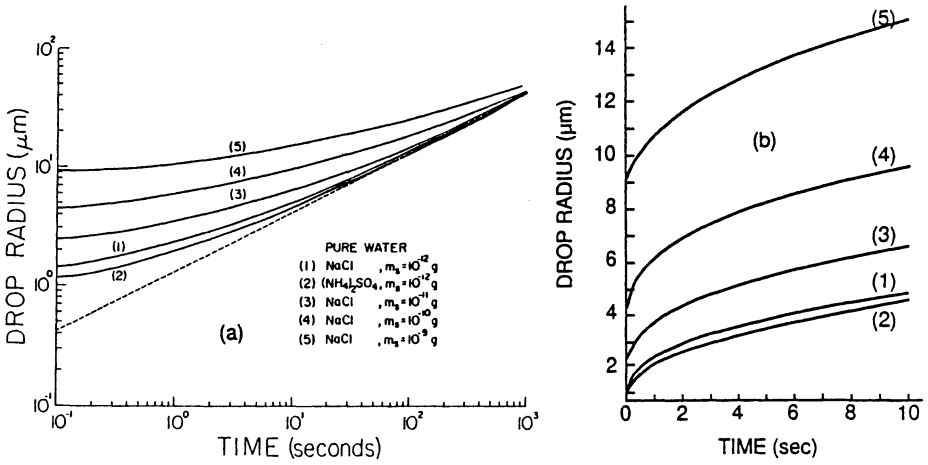


Fig. 13-2: Diffusional growth rate of individual aqueous solution drops as a function of time at 1 % supersaturation and 20° C; $\alpha_c = 0.045$; the initial drop radius corresponds to that of a salt saturated solution drop in equilibrium with the relative humidity at which the salt deliquesces. (a) On double-logarithmic scale, (b) on linear scale. (Based on data of Low (1971.)

Using an equation like (13-26), Woodcock (1978) and Woodcock *et al.* (1981) computed the growth of NaCl particles observed in a marine atmosphere and compared the size of drops formed after a growth time of 1 to 5 hours with those found

in marine advection fogs. The study showed that the drop sizes computed agreed well with those observed in fogs, and that they were roughly proportional to the salt particle sizes on which they grew.

13.2.2 Diffusional Growth of a Population of Solution Drops of Negligible Fall Velocity

The growth equations derived in the previous section may be used to describe the evolution in size of a given population of initially highly concentrated aqueous solution drops. For this purpose, we must make a distinction between drop growth in cumuliform clouds where vertical velocities are appreciable and where the rate of cooling can be described by a saturation adiabatic ascent corrected for entrainment (see Chapter 12), and stratiform clouds where the vertical velocities are small and cooling may be considered isobaric. We shall first consider diffusional drop growth in cumuliform clouds, since such a growth has been treated quite extensively in the literature. Subsequently, we shall briefly summarize the few studies that have been carried out on diffusional drop growth in stratiform clouds and fogs.

13.2.2.1 *Condensation Growth in Cumuliform Clouds*

As we shall show below in Section 13.3, the diffusional growth or evaporation of drops with $a \lesssim 50\,\mu$m falling at terminal velocity is essentially unaffected by the air flow around them. Hence, the characteristic shapes of drop spectra which evolve through diffusion growth can be established without considering ventilation effects. It is also reasonable to omit consideration of vapor field interactions between pairs of growing drops. This is justified mainly by the fact that the average distance between nearest neighbor drops is commonly $\gtrsim 10^2\bar{a}$, where $\bar{a}$ is the average drop radius, even for clouds which have already experienced substantial diffusion growth subsequent to nucleation (see Section 2.1.5). An experimental verification of this argument has been given by Szymanski and Wagner (1983).

Although a complete description of the evolution of a drop spectrum by diffusion growth in a cloud updraft is fairly complicated and requires the simultaneous numerical solution of several differential equations, some important features of the process are easy to understand, and are even amenable to a simple approximate analysis. As a parcel of air rises and cools by expansion, its humidity will increase rapidly (nearly in proportion to its upward velocity, as shown below). Eventually, the largest and most hygroscopic of the suspended condensation nuclei will deliquesce to solution drops, which will proceed to grow toward their critical radius for activation and subsequent rapid growth (see Section 6.5). The parcel supersaturation will continue to increase for a while longer as more nuclei are activated, until, finally, the growing drop population is able to absorb excess vapor as fast as it can be released by expansion. Beyond this point, the supersaturation will fall, the activated drops will tend to approach a fairly uniform size (since $\mathrm{d}a/\mathrm{d}t \sim 1/a$), and the unactivated solution drops will tend to evaporate.

From this physical picture we would expect to find a strong correlation between the concentration of drops produced by diffusion growth and the maximum supersaturation achieved in the expanding parcel. Approximate theoretical correlations

of this nature have been established by Squires (1958a) and Twomey (1959c). We shall now turn to a derivation of Twomey's equation, since this model serves as a good example to illustrate some of the physics of condensation growth. Furthermore, the results are widely used, owing to their simplicity and surprising accuracy (e.g. Johnson, 1981).

We first require a description of the rate of change of supersaturation with height. This is readily obtained by substituting (12-26) and (12-29) into (12-28) for the case $\mu = 0$ (entrainment effects are ignored in Twomey's model). The result is

$$\frac{\mathrm{d}s_{\mathrm{v,w}}}{\mathrm{d}t} = \left(\frac{\varepsilon L_{\mathrm{e}} g}{R_{\mathrm{a}} T^2 c_{pa}} - \frac{g}{R_{\mathrm{a}} T}\right) W - \left(\frac{p}{\varepsilon \mathrm{e}_{\mathrm{sat,w}}} + \frac{\varepsilon L_{\mathrm{e}}^2}{R_{\mathrm{a}} T^2 c_{pa}}\right) \frac{\mathrm{d}\mathrm{w}_L}{\mathrm{d}t}\,, \tag{13-29}$$

where we have made the approximation $1 + s_{\mathrm{v,w}} \approx 1$ on the right side of (12-28) (from Figure 2.1, we see that usually $s_{\mathrm{v,w}} \lesssim 10^{-2}$ in clouds). Equation (13-28) shows how the supersaturation increases nearly in proportion to W, in the absence of condensation, and how it is decreased by the production of liquid water. Although we could proceed directly with (13-29), a slightly modified form which replaces w_L (g water/g air) (see Chapter 12) by the density ρ_L (g water/m^3 air) of condensed water is more convenient. Since $\rho_L = \rho \mathrm{w}_L$, where ρ (g air/m^{3}air) is the density of moist air, we have $\mathrm{d}\mathrm{w}_L/\mathrm{d}t = \rho^{-1}(\mathrm{d}\rho_L/\mathrm{d}t - \mathrm{w}_L \mathrm{d}\rho/\mathrm{d}t) \approx \rho^{-1}\mathrm{d}\rho_L/\mathrm{d}t$; with this result and the ideal gas law, we obtain the desired result:

$$\frac{\mathrm{d}s_{\mathrm{v,w}}}{\mathrm{d}t} = A_1 W - A_2 \frac{\mathrm{d}\rho_L}{\mathrm{d}t}\,, \tag{13-30}$$

where

$$A_1 = \frac{\varepsilon L_{\mathrm{e}} g}{R_{\mathrm{a}} T^2 c_{pa}} - \frac{g}{R_{\mathrm{a}} T}\,, \qquad A_2 = \frac{R_{\mathrm{a}} T}{\varepsilon \mathrm{e}_{\mathrm{sat,w}}} + \frac{\varepsilon L_{\mathrm{e}}^2}{p T c_{pa}}\,. \tag{13-31}$$

We next make use of (13-28), ignoring the relatively small curvature and solute terms for activated drops by, setting $y = 0$:

$$a \frac{\mathrm{d}a}{\mathrm{d}t} \approx A_3 s\,, \tag{13-32}$$

where A_3 is the denominator in (13-28), and we have omitted the subscripts on $s_{\mathrm{v,w}}$ for brevity. Noting that the characteristic time for substantial drop growth is short compared to the time for significant changes in A_3, (13-32) may be formally integrated to yield

$$a^2(t) - a^2(\tau) \approx a^2(t) \approx 2A_3 \int_{\tau}^{t} s(t')\mathrm{d}t'\,, \tag{13-33}$$

where τ is the activation time for the considered drop. From (13-32) and (13-33), the rate of mass increase for the drop may be expressed as

$$\frac{\mathrm{d}m}{\mathrm{d}t} \approx 2\pi \rho_{\mathrm{w}} (2A_3)^{3/2} s(t) \left[\int_{\tau}^{t} s(t')\mathrm{d}t'\right]^{1/2}\,. \tag{13-34}$$

Now let $n(s)\mathrm{d}s$ denote the concentration of nuclei activated on the interval $(s, s+\mathrm{d}s)$; assuming (9-1), we thus have $\int_0^s n(s')\mathrm{d}s' = Cs^k$, so that

$$n(s) = kCs^{k-1}\,. \tag{13-35}$$

With (13-34) and $n(s)$, we can now express $\mathrm{d}\rho_L/\mathrm{d}t$ as follows:

$$\frac{\mathrm{d}\rho_L}{\mathrm{d}t} \approx 2\pi\rho_w(2A_3)^{3/2}s(t)\int_0^s n(s')\left[\int_{\tau(s')}^t s(t')\mathrm{d}t'\right]^{1/2}\mathrm{d}s'\,. \tag{13-36}$$

If (13-36) is substituted into (13-30), an approximate governing equation for s results which, unfortunately, cannot be solved analytically. However, from our previous description of the condensation process, we can expect to obtain a reasonable estimate of the final drop concentration by determining just the maximum supersaturation $s_{\max}$. And from (13-30) and (13-36) it is clear that an analytical lower bound approximation to $\int_\tau^t s\,\mathrm{d}t$ will yield an analytical upper bound for $s_{\max}$ (by the setting $\mathrm{d}s/\mathrm{d}t = 0$ in (13-30) for $s = s_{\max}$). Reasoning thus, Twomey obtained the following lower bound estimate:

$$\frac{(s^2 - s'^2)}{2A_1W} < \int_{\tau(s')}^t s(t')\mathrm{d}t'\,. \tag{13-37}$$

The basis for this choice can be seen from Figure 13.3, which illustrates schematically the curve of $s = s(t)$. In the absence of condensation, the supersaturation would follow the straight line $s = A_1Wt$ shown in the figure. The triangle ABC, with its hypotenuse parallel to $s = A_1Wt$, has an area $s^2/2A_1W$, and this is clearly less than $\int_0^B s\,\mathrm{d}t$; hence (13-37) follows.

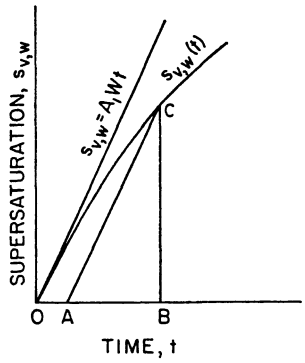


Fig. 13-3: Schematic variation with time of the supersaturation in a rising air parcel. (From Twomey, 1959c; by courtesy of *Geophys. Pura e Appl.*, and the author.)

On substituting (13-35) and (13-37) into (13-36), we see that we must calculate the integral I:

$$I = \int_0^s s'^{l-1}(s^2 - s'^2)^{1/2} \mathrm{d}s' \,. \tag{13-38}$$

Letting $y = (s'/s)^2$, I becomes

$$I = \frac{s^{k+1}}{2} \int_0^1 y^{(k/2)-1}(1-y)^{1/2} \mathrm{d}y = \frac{s^{k+1}}{2} B\left(\frac{k}{2}, \frac{3}{2}\right) , \tag{13-39}$$

where $B(u,v) \equiv \int_0^1 x^{u-1}(1-x)^{v-1}\mathrm{d}x$ is the beta function. Finally, on substituting (13-39) and (13-36) into (13-30) and setting $\mathrm{d}s_{\mathrm{v,w}}/\mathrm{d}t = 0$, we obtain the desired estimate of $(s_{\mathrm{v,w}})_{\max}$:

$$\begin{aligned} (s_{\mathrm{v,w}})_{\max} &\lesssim C^{1/(k+2)} \left[\frac{A_1^{3/2} W^{3/2}}{2\pi\rho_{\mathrm{w}} A_2 A_3^{3/2} k B\left(\frac{k}{2}, \frac{3}{2}\right)}\right]^{1/(k+2)} \\ &\approx C^{1/(k+2)} \left[\frac{6.9 \times 10^{-2} W^{3/2}}{k B\left(\frac{k}{2}, \frac{3}{2}\right)}\right]^{1/(k+2)} , \end{aligned} \tag{13-40}$$

where the numerical evaluation has been carried out for $T = 10°\mathrm{C}$ and $p = 800$ mb, W is in cm sec^{-1}, C is in cm^{-3}, and $(s_{\mathrm{v,w}})_{\max}$ is expressed as a percent. The corresponding estimate $N_{\max} \approx C(s_{\mathrm{v,w}})_{\max}^k$ of the cloud drop population is

$$N_{\max}(\mathrm{cm}^{-3}) \approx C^{2/(k+2)} \left[\frac{6.9 \times 10^{-2} W^{3/2}}{k N\left(\frac{k}{2}, \frac{3}{2}\right)}\right]^{k/(k+2)} . \tag{13-41}$$

The success of this model is illustrated in Figure 13.4, which exhibits a correlation coefficient in excess of 90% between the observed and computed values (from 13-41) for the drop concentration in the bases of small to moderate, nonparticipating cumulus clouds.

Although the above simple model is apparently capable of predicting quite well the total droplet population soon after the onset of diffusion growth, it tells us nothing about the variation of drop spectral shape with time. Such detailed behavior can be studied only through numerical solution of the full set of governing equations for a given cloud model. Several such studies using different models have been carried out.

A first step in calculations of this type is to specify the chemical composition and size distribution of the dry aerosol particles on which the drops condense. In this regard, it is important to recall from Chapter 6 that (13-28) does not describe the deliquescence of an aerosol particle, i.e., its transformation from a dry particle into a saturated solution drop of equilibrium size. In order to get around this problem, one generally assumes, as we have pointed out before at the end of the previous chapter, that each aerosol particle of the considered population of dry particles acquires its

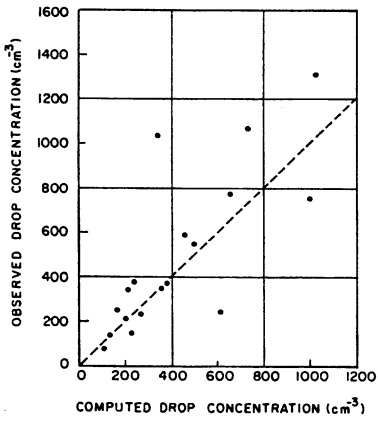


Fig. 13-4: Comparison of observed mean cloud drop concentration with cloud drop concentration computed from CCN spectra for an updraft of 3 m sec^{-1}. Dashed line represents exact agreement between observation and computation. (From Twomey and Warner, 1967; by courtesy of Am. Meteor. Soc., and the authors.)

equilibrium size at the specified initial ambient relative humidity (assumed to lie between 90 and 99% to insure deliquescence of all water-soluble components in the aerosol particle) in a time period which is short compared to the time over which significant changes occur in the atmospheric environment. This assumption has experimentally been verified by Zebel (1956), Orr *et al.* (1958b), and Winkler (1967), who also demonstrated that the rate determining (slower) step in this transformation is the growth of the saturated solution drop to its new equilibrium size, rather than the deliquescence of the dry aerosol particle. The time required for a saturated solution drop to grow to a new equilibrium size can readily be computed from (13-28). For NaCl dissolved in the drop, Lee and Pruppacher (1977) found that a solution drop in equilibrium with an environment, initially of 75% relative humidity, grows to within 10% of the equilibrium size corresponding to a suddenly imposed 99% humidity in about 2×10^{-4}, 2×10^{-2}, 3 and 13 sec for drops containing a salt mass equivalent to a NaCl particle of 0.01, 0.1, 1.0 and 2 μm radius, respectively, in good agreement with the experimental results of the authors mentioned above. Similar computations were made earlier by Zebel (1956). Such computations show that particles of sizes typically involved in the condensation process ($r \lesssim 1\,\mu$m) are transformed into solution drops of equilibrium size in times which are usually short even compared to the turbulence microscale time τ_k [from the discussion immediately following (11-74), we see that τ_k typically lies in the interval $4 \times 10^{-2} \lesssim \tau_k \lesssim 3 \times 10^{-1}$ sec]. Since τ_k provides a lower bound estimate of the quickest fluctuation the CCN can be subjected to by the environment, we see that the assumption of a negligible adjustment time for the conversion from a dry particle to an equilibrium drop is well-founded for AP with radii less than 1 μm, but not for larger paricles.

Let us now consider a vertically rising and, thus, cooling, air parcel in which a

population of aerosol particles of given composition and size distribution is contained. From the previous paragraph, we may assume that all water-soluble components go into solution when the relative humidity in the parcel reaches the critical value for deliquescence of the particular salts and that when the relative humidity has reached 99% , all solution drops will have reached their corresponding equilibrium size. If we divide the original spectrum of dry particles into small size intervals, we may readily compute the corresponding equilibrium size distribution of solution drops by using (6-26) if the aerosol particles consist of water-soluble material only, or by using (6-33) if the aerosol is mixed. The evolution in time of this drop size distribution may now be determined from (13-28) if the parcel's temperature, humidity, and vertical velocity are known as functions of time. Relations which describe the variation with time (and thus with height) of these parcel parameters have been given in Chapter 12 for both entraining as well as closed rising air parcels.

Studies of the diffusional growth of drops in closed, adiabatic parcels have been carried out by Howell (1949), Squires (1952), Mordy (1959), Neiburger and Chien (1960), Warner (1969b, 1970a), Bartlett and Jonas (1972), and Fitzgerald (1974). Of these, only Bartlett and Jonas included some effects of turbulence. Chen (1971) employed a parcel model which considered entrainment of air devoid of aerosol particles, while Mason and Chien (1962) and Warner (1973) allowed for the entrainment of air containing active CCN.

Following these early studies, the effects of entraining AP were studied more quantitatively by Lee and Pruppacher (1977), Lee *et al.* (1980), Flossmann *et al.* (1985), Ahr *et al.* (1989a,b), and Baumgarten (1990). In these studies, the three most often used versions of the parcel model were investigated: (1) a closed parcel in which the vertical velocity is one of the computed variables, (2) a closed parcel in which the vertical velocity is prescribed, and (3) an open parcel in which the vertical velocity is computed and cloud environmental air with aerosol particles is allowed to entrain. In addition, the effects of various initial size distributions and compositions of the aerosol particles on the development of the drop size distribution were studied. Before we give some results obtained with these models, we must emphasize that in atmospheric clouds the process of condensation cannot be separated rigorously from the process of collision and coalescence (see Chapter 14), since collision does not begin as a 'step function' after the drops have reached a critical size due to growth by diffusion of water vapor. Rather, collision sets in gradually as the collision efficiency (see Chapter 14) between the drops increases from very low but still finite values for drops below 10 μm radius, to values near unity for drops larger than 50 μm radius (see Figure 14.5). This is the reason why drop spectra calculated by cloud models cannot be compared with observed drop spectra unless the effects of collision and coalescence as well as condensation are included in the model.

If the collision-coalescence process is to be included in the parcel model, it is necessary to add the term $[\partial n_{\mathrm{d}}(m)/\mathrm{d}t]_{\mathrm{d,coal}}$ to (12-37). This term represents the change of the drop size distribution function n_{d} due to the collision and subsequent coalescence of drops. We find an expression for this term by rewriting (11-56) as a function of mass instead of the volume of the colliding particles

$$\left.\frac{\partial n_{\rm d}(m,t)}{\partial t}\right|_{\rm d,coal} = \frac{1}{2}\int_0^m K_{\rm d}(m', m-m')n_{\rm d}(m',t)n_{\rm d}(m-m',t){\rm d}m'$$

$$-n_{\rm d}(m,t)\int_0^\infty K(m,m')n_{\rm d}(m',t){\rm d}m' \,, \qquad (13\text{-}42)$$

where the collection kernel K_d for the for colliding drops of mass m and m' is given by (11-85). The first term in (13-42) expresses the production of m-drops by collision and coalescence of drops of mass $m - m'$ with drops mass m', while the second term describes the removal of m-drops by collision of drops of mass m with any other drop (a fuller discussion of this equation is given in Chapter 15). Once the drop size distribution function $n_{\rm d}(m,t)$ has been obtained the corresponding mass distribution function $g_{\rm w}(m,t) = mn_{\rm d}(m,t)$ can be determined.

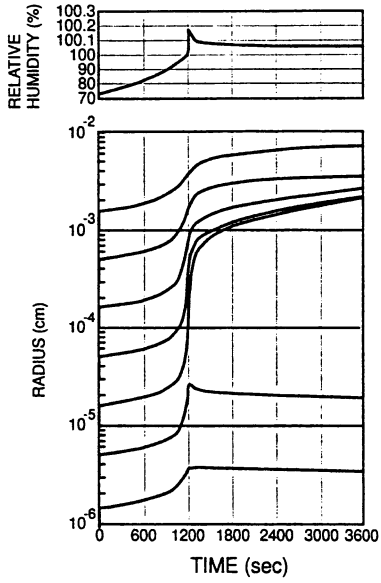


Fig. 13-5: Growth of aqueous solution drops inside an air parcel during its adiabatic ascent, after NaCl aerosol particles of $r = 0.01$, 0.03, 0.1, 0.3, 1.0, 3.0, 10 μm have been activated to drops at a relative humidity of 75 %. (From Neiburger and Chien, 1960, with changes.)

From the parcel model studies, the following main conclusions may be drawn: (1) As anticipated from our discussion in Chapter 6, the largest hygroscopic particles become readily activated to drops and grow quickly to visible-sized drops, while the smallest particles grow little and produce inactivated drops which even undergo partial evaporation after the peak in supersaturation has been reached. This behavior is illustrated in Figure 13.5. (2) Adiabatic condensation models

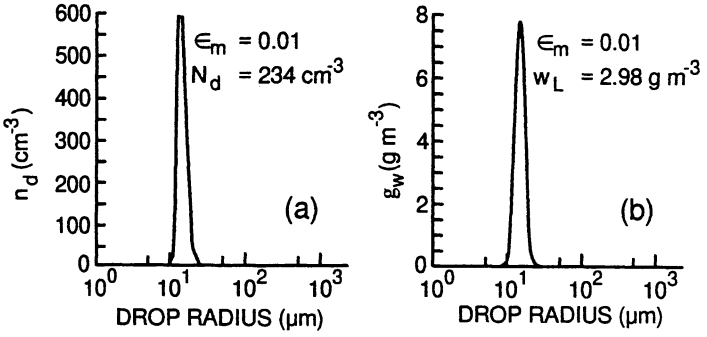


Fig. 13-6: Number distribution function (a) and mass distribution function (b) per logarithm radius interval for drops inside an air parcel after its adiabatic ascent to a height of 2600 m. Condensation only, no coalescence, no entrainment. For a rural aerosol spectrum (Jaenicke, 1988) of $(NH_4)_2SO_4$ particles with $N_{AP,a}$ = 8610 cm^{-3}, ϵ_m = 0.01 . (From Flossmann, 1993, pers. comm.; by permission of the author.)

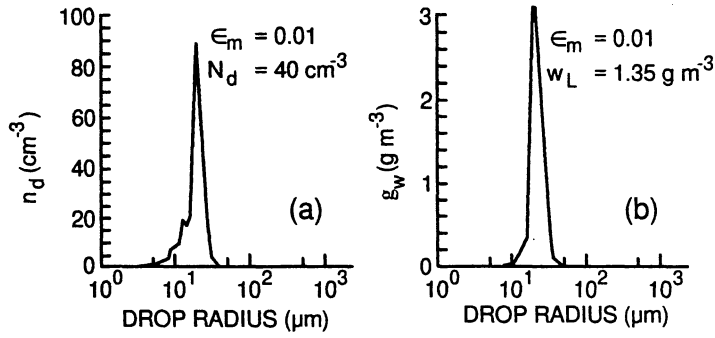


Fig. 13-7: Number distribution function (a) and mass distribution function (b) per logarithm radius interval for drops inside an air parcel after its ascent to 3000 m. Condensation with entrainment, no coalescence, aerosol spectrum as in Figure 13-6. (From Flossman, 1993, pers. comm. by courtesy of the author.)

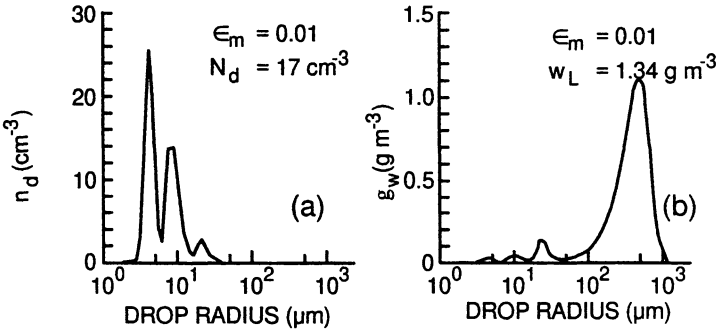


Fig. 13-8: Number distribution (a) and mass distribution function (b) per logarithm radius interval for drops inside an air parcel after its ascent to 3000 m. Condensation with entrainment and coalescence. Aerosol spectrum as in Figure 13-6. (From Flossmann 1993, pers. comm., by courtesy of the author.)

in which an air parcel remains closed to heat, water vapor, and aerosol particles predict updraft velocities U, liquid water contents w_L, supersaturations $s_{v,w}$, and numbers of AP activated to drops which are unrealistically large, while the predicted drop size distribution is unrealistically narrow and has only a single mode (e.g. Lee and Pruppacher, 1977). (3) Parcel models in which the ascent is adiabatic but its updraft velocity is prescribed predict more reasonable values for U, w_L and $s_{v,w}$. Also, the number of AP activated to drops is lower; however, the drop size distributions are still unrealistically narrow and singly peaked. This is illustrated in Figure 13.6 for a rural aerosol (Jaenicke, 1988), and for the temperature and humidity distribution given by Lee and Pruppacher (1977). (4) If entrainment is included in the condensation model, U, w_L and $s_{v,w}$ assume more realistic values, while the drop size distribution broadens and often develops a secondary mode (or even multimodes). This is illustrated in Figure 13.7 for the same conditions as in Figure 13.6. (5) Collision and coalescence between drops broaden the drop size distribution further even at an early stage in the cloud development, generally when the drops have reached radii larger than 15 μm. This is illustrated in Figure 13.8 for the same conditions as in Figures 13.6 and 13.7. We notice that, after 1600 sec model time, the concentration of drops smaller than 20 μm radius is much lower than when collision and coalescence is not present, multimodes have developed, and most of the water mass had shifted into precipitation-sized drops. (6) The composition ε_m and the total number concentration $N_{AP,a}$ of the aerosol particles present in air play an important role in shaping the drop size distribution. This is illustrated in Figures 13.9 to 13.11 for a given gamma distribution of AP consisting of $(NH_4)_2SO_4$ which grow by condensation with entrainment and collision and coalescence. We note from Figure 13.9 that, for $N_{AP,a} = 10^3$ cm^{-3} and $\varepsilon_m = 1.0$, no precipitation sized drops develop. On the other hand, for $N_{AP,a} = 10^3$ cm^{-3} but $\varepsilon_m = 0.01$ (Figure 13.10), drops larger than 100 μm in concentrations of 1 per liter have formed after 1400 seconds. Drops of such concentration have already formed after 1000 seconds for the case that $N_{AP,a} = 100$ cm^{-3} and $\varepsilon_m = 1.0$.

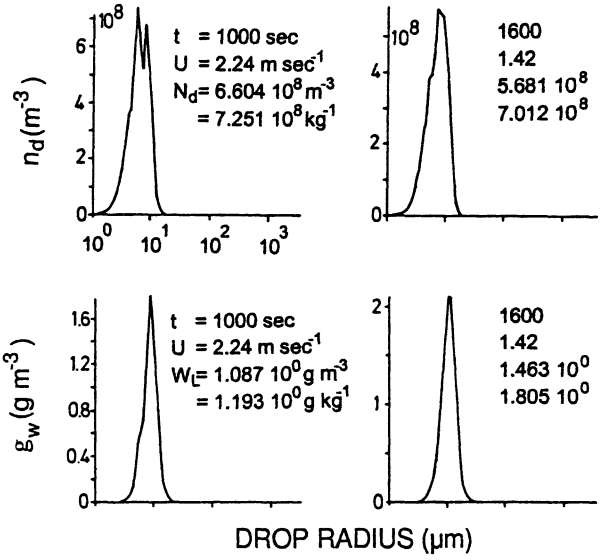


Fig. 13-9: Number and mass distribution function per logarithm radius interval for drops inside an air parcel after its ascent for 1000 and 1800 sec; for a gamma distribution of $(NH_4)_2SO_4$ particles growing by condensation with entrainment and by collision and coalescence, and for $N_{AP,a} = 10^3$ cm^{-3}, $\epsilon_m = 1.0$. (From Flossmann *et al.*, 1985, with changes.)

In our discussion of the evolution of a drop size spectrum, we have assumed that the chemical composition of the aerosol is uniform across the size spectrum. From Section 8.2.9 we know, however, that the size distribution of atmospheric aerosol particles is represented best by the superposition of at least three lognormal distributions, each of which may consist of AP of a different chemical composition. The effect of such an 'external' mixture of AP is illustrated in Figure 13.12 for a remote continental spectrum (Jaenicke, 1988) with $N_{AP,a} = 1366$ cm^{-3}, consisting of $(NH_4)_2SO_4$ with $\varepsilon_m = 1.0$ in the first mode, 50% $(NH_4)_2SO_4$ and 50% H_2SO_4 with $\varepsilon_m = 0.5$ in the second mode, and H_2SO_4 with $\varepsilon = 0.1$ in the third mode, and in Figure 13.13 for a maritime spectrum afterFigure 8.28a (curve 4) with $N_{AP,a} = 223$ cm^{-3} consisting of $(NH_4)_2SO_4$ with $\varepsilon_m = 1.0$ in the first and second modes, and of 90% NaCl and 10% $NaNO_3$ with $\varepsilon_m = 1.0$ in the third mode. We notice from these figures that the size spectrum of drops formed in a maritime aerosol broadens much more rapidly than does the spectrum of drops formed in a remote continental aerosol.

At this point, one pervasive and artificial feature of all the condensation computations discussed so far comes to mind, namely the fact that they basically involve the lifting of just a single mass of air. It is well-known from observations, especially those made with the aid of time lapse photography, that real convective clouds do not grow in this manner. Rather, their development is characterized, at least in the

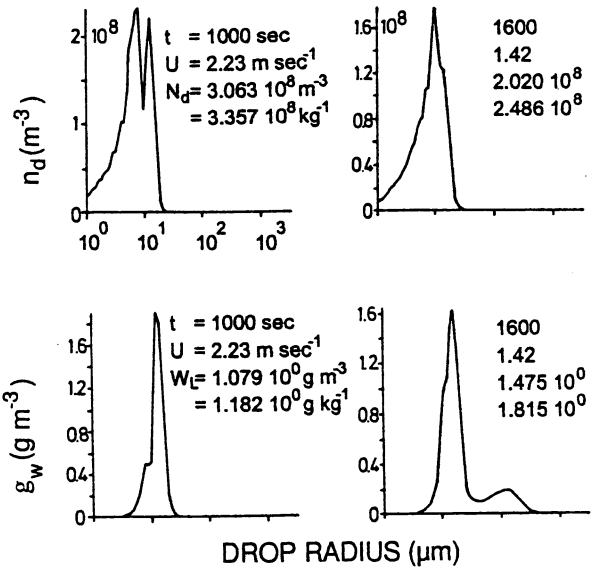


Fig. 13-10: Number and mass distribution function per logarithm radius interval for drops inside an air parcel after its ascent for 1000 and 1800 sec; for a gamma distribution of $(NH_4)_2SO_4$ particles growing by condensation with entrainment and by collision and coalescence; $N_{AP,a} = 10^3$ cm^{-3}, $\epsilon_m = 0.01$. (From Flossmann *et al.*, 1985, with changes.)

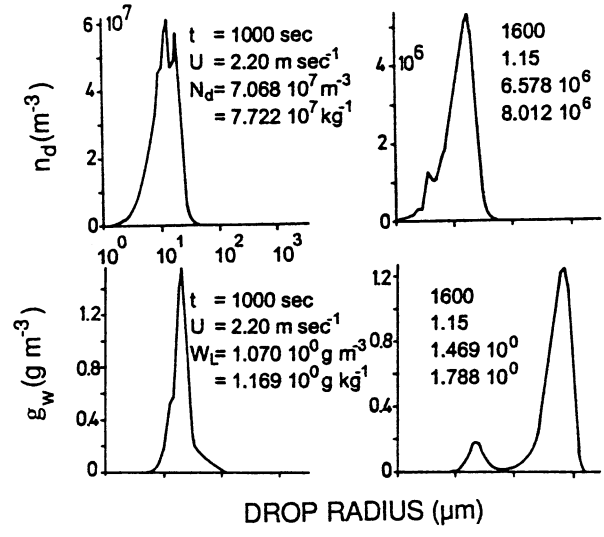


Fig. 13-11: Number and mass distribution function per logarithm radius interval for drops inside an air parcel after its ascent for 1000 and 1800 sec; for a gamma distribution of $(NH_4)_2SO_4$ particles growing by condensation with entrainment and by collision and coalescence; $N_{AP,a} = 10^2$ cm^{-3}, $\epsilon_m = 1.0$. (From Flossmann *et al.*, 1985, with changes.)

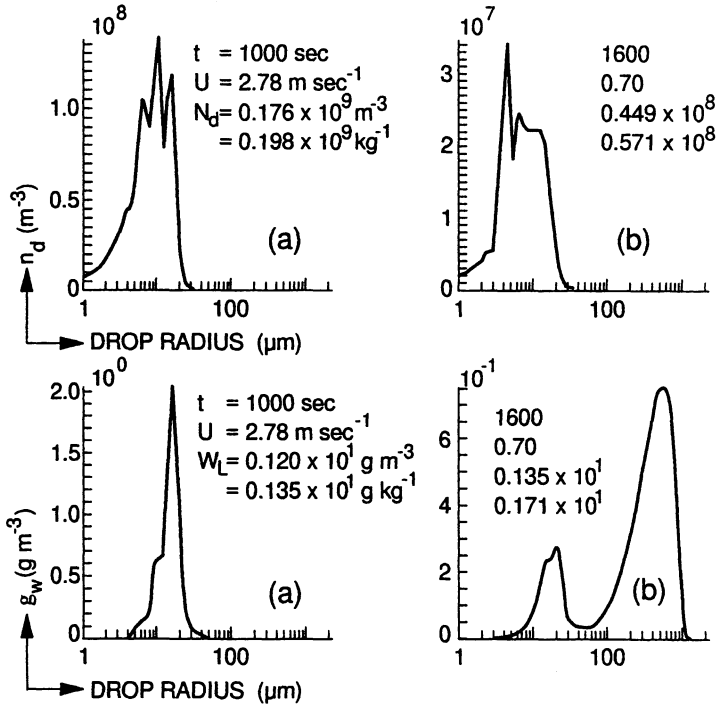


Fig. 13-12: Number and mass distribution function per logarithm radius interval for drops inside an air parcel after its ascent for 1000 sec (a) and 1800 sec (b). For a remote continental aerosol (Jaenicke, 1988) with a size distribution given by the superposition of 3 log-normal distributions consisting of: $(NH_4)_2SO_4$; $\epsilon_m = 1.0$ in the first mode; 50 % $(NH_4)_2SO_4$ and 50 % H_2SO_4, $\epsilon_m = 1.0$ in the second mode; H_2SO_4, $\epsilon_m = 1.0$ in the third mode; $N_{AP,a} = 1366$ cm^{-3}; for condensation with entrainment and collision-coalescence. (From Ahr, 1988, with changes.)

early stages, by a succession of lifting and sinking motions. It is reasonable to expect a strong cumulative effect of such percolating motion, with its cycles of mixing, evaporation, and further condensation, on the evolving cloud drop spectra. This expectation is borne out by the condensation model of Mason and Jonas (1974), which includes at least a simplified simulation of the observed percolating motion. (Unfortunately, the collision and coalescence process was not included.) Thus, in their model, a single spherical 'thermal' is allowed to rise and then sink back again under the influence of evaporative cooling resulting from the entrainment of drier environmental air. Following this, a second thermal is released to rise through the residue of the first. In consequence, though most of the droplets in the subsiding first thermal evaporate, a few of the largest survive to be caught up and experience further growth in the second thermal. In this way, it was possible to produce a few large drops without invoking the presence of large hygroscopic particles. Also, the subsidence of the first thermal boosts the relative concentration of small droplets

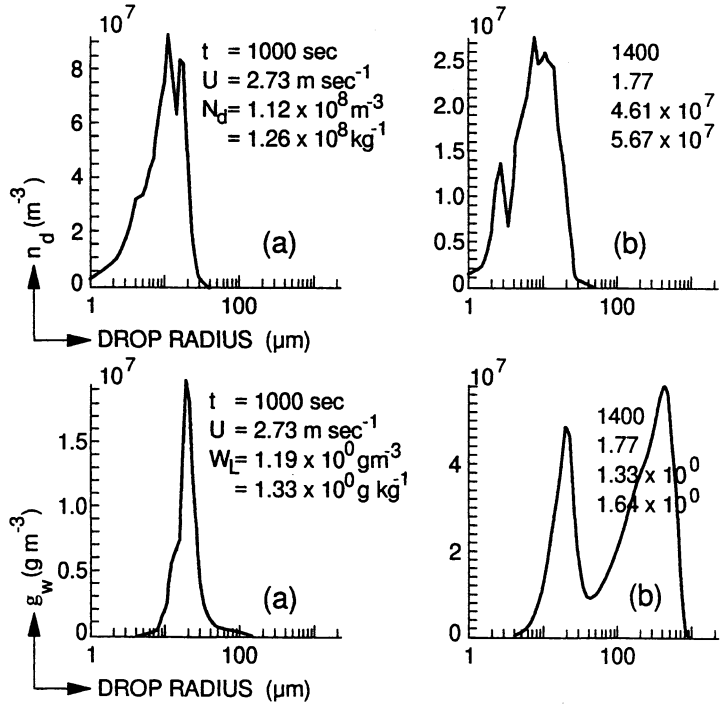


Fig. 13-13: Number and mass distribution function per logarithm radius interval for drops inside an air parcel after its ascent during 1000 sec (a) and 1400 sec (b). For a maritime aerosol (Figure 8-28a, curve 4) with $N_{AP,a} = 223$ cm^{-3}, given by the superposition of 3 log-normal distributions consisting of: $(NH_4)_2SO_4$, $\epsilon_m = 1.0$ in the first and second mode; and 10 % $NaNO_3$, 90 % NaCl, $\epsilon_m = 1.0$ in the third mode. For condensation with entrainment and collision coalescence. (From Wurzler, 1994, pers. comm., by permission of the author.)

to more realistic values.

The variations with height and time of $U, s_{v,w}, w_L$, and $w_L/w_{L,ad}$ (the ratio of the actual liquid water content to that which would be produced by the adiabatic lifting of a closed parcel) computed by Mason and Jonas (1974) are shown in Figure 13.14 for the case of a maritime cumulus cloud of the type observed by Warner (1969a,b) in Australia, assuming a maritime spectrum of NaCl particles. The computed drop spectra resulting after the ascent of the second thermal are given in Figure 13.15 for heights of 150 and 1400 m above cloud base. Also included in this figure are representative observed maritime spectra (Warner, 1969a,b) for clouds with total drop concentrations similar to those in the model cloud.

A comparison between Figures 13.15 and 2.23 shows that, according to the model, $w_L/w_{L,ad}$ is significantly larger than the observed values. This discrepancy has been emphasized by Warner (1972, 1975a,b), who also pointed out that the model results would only deteriorate in this respect if the number of successive

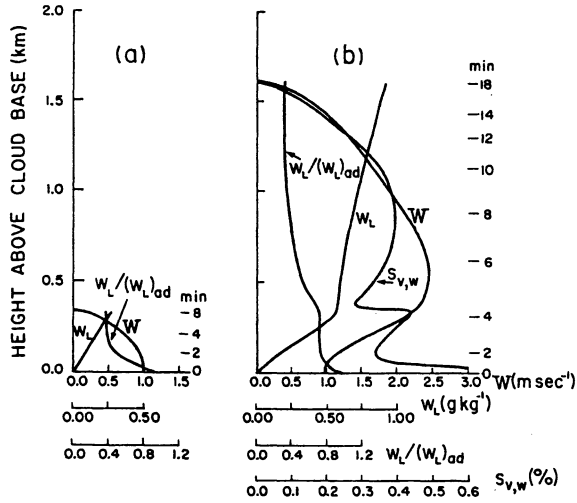


Fig. 13-14: Maritime cumulus case; multiparcel entrainment model. Variation of updraft W, supersaturation $s_{v,w}$, liquid water content w_L, and $w_L/(w_L)_{ad}$ with height above cloud base. (a) During ascent of first parcel, (b) during ascent of second parcel through residue of first parcel. Numbers on right of diagrams show the time elapsed since the start of each stage. (From Mason and Jonas, 1974; by courtesy of *Quart. J. Roy. Meteor. Soc.*)

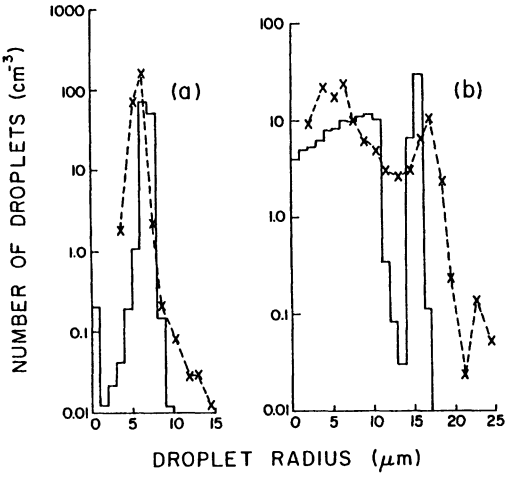


Fig. 13-15: Maritime cumulus case; multiparcel model. (a) Comparison of drop spectrum predicted by model after ascent of second parcel (150 m above cloud base) with drop spectrum observed by Warner at a similar height in a similar sized cloud of similar total drop concentration. (b) Comparison of computed drop size spectrum at 1400 m above cloud base with mean of two drop size spectra observed by Warner near top of a cloud 1.4 km deep, and of a similar total drop concentration. (From Mason and Jonas, 1974; by courtesy of Quart. J. Roy. Meteor. Soc.)

thermals were allowed to increase, since each of these would deposit additional moisture in the air to be traversed by the next in the series (for example, note from Figure 13.14b that $w_L/w_{L,ad} \approx 0.8$ in the lowest 400 m of the cloud, which can be seen from Figure 13.14a to be the height achieved by the first thermal). Against this criticism, Mason (1975) has argued that the observed values of $w_L/w_{L,ad}$ represent averages over cloud regions which are probably composed largely of the residues of earlier thermals, and that therefore one would expect $w_L/w_{L,ad}$ to be significantly larger in active growing thermals such as are simulated by the Mason-Jonas model.

In spite of the likelihood that the Mason-Jonas cloud is unrealistically wet, its microphysical properties seem to agree better with observations than do those of the other condensation models. Thus, we see from Figure 13.15 that the predicted droplet spectra agree quite well with observations. The model drop spectrum for the maritime cloud was found to broaden rapidly, and produced drops with $a \gtrsim 25\,\mu$m in concentrations of about 300 m^{-3}, and drops with $a \gtrsim 20\,\mu$m in concentrations of about 10 cm^{-3}, within 30 min; as we shall see in Chapter 15, this is sufficient to continue growth by collision and coalescence. It is particularly noteworthy that the production of these relatively large drops was accomplished without assuming as large a population of large and giant nuclei as has been found necessary in the other condensation models.

Similar model computations by Mason and Jonas for the case of a continental type cloud produced total drop concentrations of about an order of magnitude larger than for the maritime cloud, but with very few drops of even 20 μm radius. A more realistic broadening of the drop spectrum was only achieved by including growth by collision and coalescence (Jonas and Mason, 1974).

A similar outcome was obtained by Rösner *et al.* (1990) who constructed a parcel model in which three successive air parcels were allowed to rise in succession. Inside each parcel, the AP were allowed to grow by condensation and collision. Each of the three air parcels was assumed to start from just below the cloud base, having the same initial radius of 350 m, an updraught velocity of 1 m s^{-1}, and containing aerosol particles of the same composition and size distribution. The temperature excess of the first parcel over the undisturbed environment was assumed to be 0.3°C. The second and third parcels were assumed to have the same temperature excess, but now with respect to the environment left behind by the previous parcel. While rising, the air parcels were assumed to entrain air of zero vertical velocity. However, heat, water vapor, aerosol particles, and drops were assumed to be exchanged between the parcel and its environment. In the model, each parcel was followed to its level of neutral buoyancy at which, through mixing, it came to rest. The times of release of the second and third parcels were chosen such that a thermal would reach the previous one only at the time when the previous one had stopped ascending. The behavior of the first parcel was assumed to be determined by the given temperature and moisture distribution of the undisturbed ambient air; and as the parcel was rising, its thermodynamic and microphysical parameters varied with height. At each height, these values were taken to represent the environment for the second parcel. Since this rose higher than the first parcel, the original environmental conditions were applied as soon as the second parcel emerged from the environment of the first – and so on.

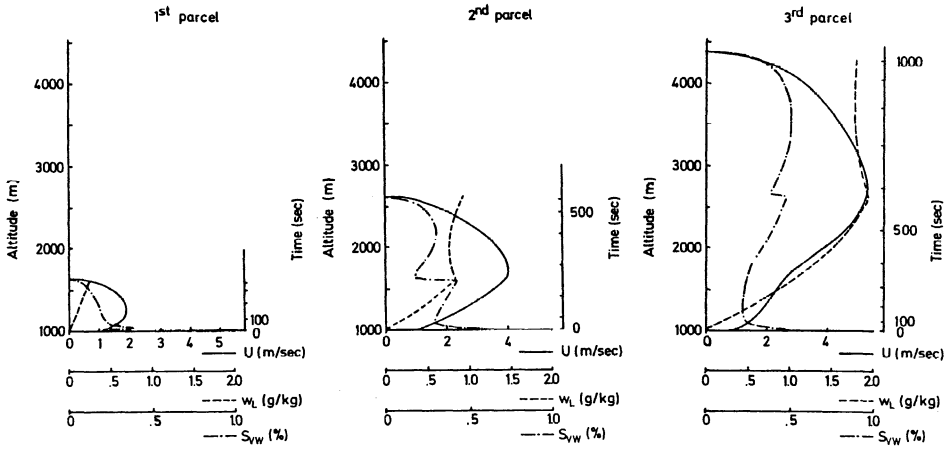


Fig. 13-16: Variation with height and time of the vertical velocity U, liquid water content w_L and supersaturation $s_{v,w}$ during the ascent of an entraining air parcel in an environment with a temperature and humidity profile given by Rösner *et al.*, (1990, Figure 3). (From Rösner *et al.*, 1990; by courtesy of the Roy. Meteor. Soc., and the authors.)

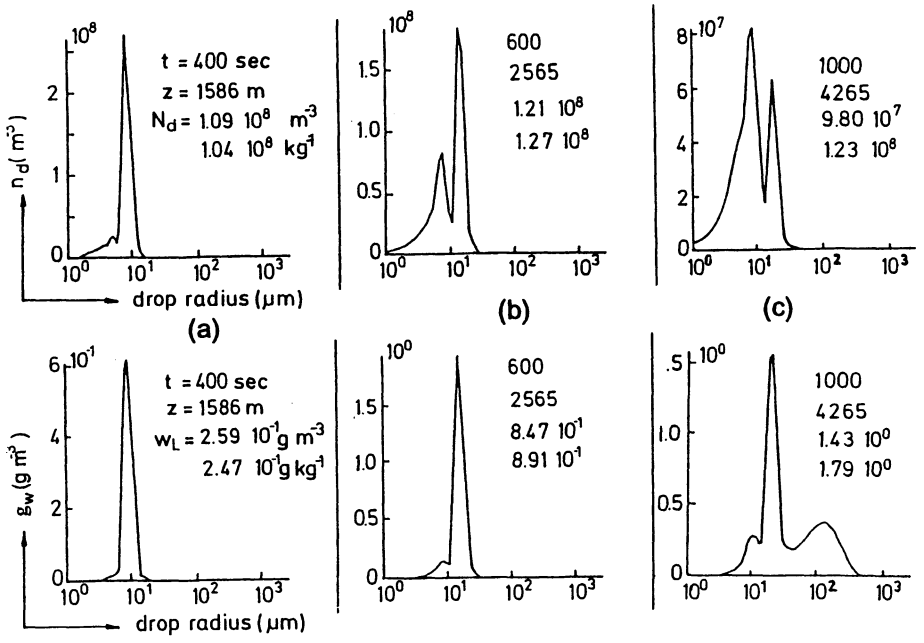


Fig. 13-17: Drop-size and drop-mass distribution per logarithm radius interval for (a) the first, (b) the second and (c) the third parcel, involving condensation on a remote continental aerosol (Jaenicke, 1988), and assuming growth by collision and coalescence. (From Rösner *et al.*, 1990, with changes.)

The variation with height (i.e. with time) of the vertical velocity U, the liquid water content w_L, and the supersaturation $s_{v,w}$ of the three successive parcels are displayed in Figures 13.16a,b,c. We note that the first parcel comes to rest after just a few hundred meters, and that each successive air parcel rises with a higher vertical velocity, and reaches a higher altitude than the previous one. The discontinuities in Figures 13.16b,c are the result of the different environmental conditions which a parcel experiences when it emerges from the environment of the air left by the previous parcel. The associated variation of the drop-size distribution function n_d, is given in Figures 13.17a,b,c. As expected, the first parcel produces only a narrow drop size distribution. Similarly, the second and third parcels do not develop a secondary maximum in the drop size distribution as long as the parcels are inside the air left behind by the previous parcel. However, as soon as the parcel emerges from the remnants of the previous parcel, thus allowing aerosol particles to be entrained from the undisturbed environment, a secondary maximum develops in the drop size distribution.

The variation of the mass distribution function g_w, which describes the location of the main water mass in the drop size spectrum, is also displayed in Figures 13.17a,b,c. The collision and coalescence of drops eventually form a second maximum in g_w representing the precipitation-sized drops. We notice that these drops do not develop until the third parcel ascends (Figure 13.17c). In Table 13.2a, the number of drops per m^3 larger than 30, 50, and 100 μm radius is given for various times during the ascent of the third parcel. Note that in the third parcel, precipitation drops develop by condensation and collision and coalescence after only about 600 seconds, or after an ascent of about 1700 m above cloud base. On the other hand, Table 13.2b shows that if the collision-coalescence mechanism is omitted, the broadening of the drop size distribution is insufficient to produce precipitation-sized drops, even in times as long as 800 seconds.

We have noted that simulations of the condensation growth alone, and especially those which involve the lifting of a single air mass, produce drop spectra which are still unrealistically narrow. It has been argued that this shortcoming may be due to their neglect of the existence of turbulence-induced fluctuations in the local supersaturation in updrafts, Warner (1970b). The notion that turbulence may significantly increase the dispersion in drop sizes has been pursued especially by Russian and Chinese workers (e.g., Belyayev, 1961; Mazin, 1965; Sedunov, 1965; Levin and Sedunov, 1966; Jaw Jeou-Jang, 1966; Wen Ching-Sung, 1966; Stepanov, 1975, 1976). As one representative result of these efforts, we note that Mazin (1965) predicted turbulence can produce in 5 min a standard deviation of 4 μm in the radius of drops initially centered about 10 μm radius.

On the other hand, quite different results have been obtained by Bartlett (1968), Warner (1969b), and Bartlett and Jonas (1972). They have found that the turbulence-induced spread in the radii of drops grown by vapor diffusion at any given level is quite small, in fact generally less than 0.2 μm. According to these authors, the key argument for understanding this result is based on the fact that the supersaturations and updrafts which a growing drop encounters are closely correlated to each other. Thus, a droplet which experiences a high supersaturation – and therefore grows rapidly – is at the same time likely to be in a strong up-

TABLE 13.2

Number of drops per m^3 air with radii larger than 30, 50 and 100 μm in the third air parcel as a function of time, for condensation on a remote continental aerosol and (a) coalescence included (b) coalescence not included; multiple air parcel model with entrainment. (Based on data of Rösner *et al.*, 1990.)

t (sec)	$a > 30\mu$m	$a > 50\mu$m	$a > 100\mu$m
(a) remote continental (coalescence included)			
400	1.6×10^{2}	0.3	3.6×10^{-8}
500	2.5×10^{3}	13	4.5×10^{-4}
600	3.7×10^{4}	5.6×10^{2}	0.5
700	1.6×10^{5}	9.8×10^{3}	34
800	3.7×10^{5}	4.9×10^{4}	1.0×10^{3}
(b) remote continental (coalescence not included)			
400	2.9×10^{1}	5.1×10^{-4}	1.4×10^{-14}
500	1.8×10^{2}	3.1×10^{-3}	3.7×10^{-13}
600	1.7×10^{3}	2.1×10^{-2}	6.3×10^{-12}
700	7.5×10^{3}	1.3×10^{-1}	4.9×10^{-11}
800	2.2×10^{4}	6.5×10^{-1}	2.8×10^{-12}

draft which restricts the drop's growth between any two given levels to a relatively short time. Conversely, low supersaturations are associated with small updrafts and longer growth times. It appears that the resulting significant distinction to be drawn between calculations of drop-size dispersions after a given time and those at a given level have generally been overlooked in the studies which have predicted large dispersions. For example, Sedunov (1965) obtained an estimate of the drop-size distribution at a given time, but refers to it as the distribution at a given level. Another fault of much of the Russian and Chinese work is that it generally involves linearized versions of the full governing equations, this being done to permit the extraction of analytical solutions. Unfortunately, some of the physics is unavoidably lost by such simplifications.

These results suggest that the observed growth of a population of drops by condensation cannot be explained by the effects of turbulent mixing within clouds but rather must be explained on the basis of turbulent entrainment of air from the environment into the clouds.

Although there are still doubts as to the detailed mechanism of entrainment (see Section 12.7), we shall briefly sketch the procedure necessary to obtain some numerical results from the model of inhomogeneous mixing of Baker *et al.* (1980) described in Section 12.7. For this purpose, we shall follow the authors and assume that unsaturated blobs of constant volume v_0 of 1/10 to 1/100 of the original ascending cloud volume V_0 are drawn into the cloud either at random intervals or regularly at a rate λ. The entrainment of such discrete air blobs is assumed to occur instantaneously at time $t = t_i$. The entrainment rate can then be written as $(1/V)(\mathrm{d}V/\mathrm{d}t) = (v_0/V)\sum_i \delta(t - t_i)$, where $\delta(x)$ is the Dirac delta function. Each entrained blob is assumed to completely evaporate a fraction F of droplets of all sizes until the relative humidity has risen to 100%. Along with the blob of drier

air, aerosol particles of a given chemical type and constant number concentration are also assumed to be entrained from the cloud environment and activated during the subsequent ascent. The rate of entrainment is adjusted such that the total number of drops, N_{d}, remains constant during the parcel's ascent. Incorporating the above entrainment rate into the thermodynamic relations of Section 12.9, and using an equation like (13-28) for the rate of growth of a drop of radius a_i, the rate of change of the drop spectrum can be computed as a function of time due to the combined effects of: (1) entrainment, from

$$\left.\frac{\mathrm{d}n(a_i,t)}{\mathrm{d}t}\right|_{\text{entrain}} = \sum_i \delta(t-t_i)n_0(r_i)[F+(v_0/V)][1+(v_0/V)]^{-1}\,; \tag{13-43}$$

(2) subsequent drop evaporation, from

$$\left.\frac{\mathrm{d}n(a_i,t)}{\mathrm{d}t}\right|_{\text{eva}} = -\sum_i \delta(t-t_i)n(a_i,t)F[1+(v_0/V)]^{-1}\,; \tag{13-44}$$

(3) and subsequent dilution of cloud air, from

$$\left.\frac{\mathrm{d}n(a_i,t)}{\mathrm{d}t}\right|_{\text{dil}} = -\sum_i \delta(t-t_i)n(a_i,t)(v_0/V)[1+(v_0/V)]^{-1}\,. \tag{13-45}$$

In (13-42) and (13-43) F is given by

$$F = \frac{v_0}{\mathrm{w}_L V}[\rho_{\mathrm{v,sat,w}}(T) - \phi_{\mathrm{v}}\rho_{\mathrm{v,sat,w}}(T')]\,, \tag{13-46}$$

where ϕ_{v} is the relative humidity of the air in the cloud's environment, and $n_0(\mathrm{a}_i)$ is the constant number density of the entrained aerosol particles of dry radius r_i in the environement. In order to compare the results of inhomogeneous mixing with the parameter for homogeneous mixing, $\mu = (1/V)(\mathrm{d}V/\mathrm{d}t)$, the frequency of ingestion of blobs λ is adjusted such that during the ascent of the parcel, the total mass of entrained air is the same in both models. In Figure 13.18, such a comparison is shown after the parcel had ascended for 1000 seconds. The drop spectrum calculated with the inhomogeneous model agrees well with the spectrum observed by Warner (1969a), whereas no agreement is found between Warner's observations and the predictions of the model for homogeneous entrainment. Baker *et al.* (1980) concluded from this exercise that, by inhomogeneous mixing, the growth of a small portion of droplets is several times faster than that predicted by the classical model with homogeneous mixing. Unfortunately, Baker *et al.* (1980) did not include the collision and coalescence process in their calculations.

Although air parcel models with homogeneous entrainment are very useful for studying detailed cloud microphysics, such models have three basic deficiencies (1) they cannot simultaneously predict liquid water content and cloud top height, as discussed earlier in Section 12.8; (2) they underestimate the entrainment progressively with increasing cloud top height due to the $1/R$ dependence of the homogeneous entrainment parameter μ; (3) they retain the drops grown in the air

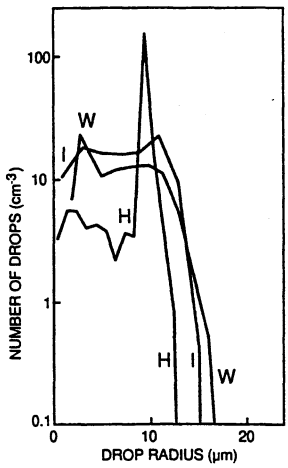


Fig. 13-18: Drop-size distribution per logarithm radius interval inside an air parcel during its ascent after 1000 sec. For an NaCl particle spectrum given by Lee and Pruppacher (1977). Comparison of homogeneous entrainment (H) and inhomogeneous entrainment (I) with observations (W) of Warner (1969a). For updraft speed = 1 m sec^{-1}, $1/\lambda$ = 10 sec., cloud base temperature = 15° C, environment lapse rate = 7.5° C km^{-1}, N_d = 200 cm^{-3}, $\mu = 10^{-3}$ m^{-1}, environmental relative humidity = 80 %, and w_L = 0.4 g cm^{-3}. (From Baker *et al.*, 1980, with changes.)

parcel because the model does not provide for drop settling; and (4) they overestimate the time necessary to produce drops large enough for growth by collision and coalescence.

In order to remedy the above deficiencies, dynamic frameworks are required which are more realistic than that provided by a Lagrangian cloud parcel. To meet this need, numerous one-dimensional time dependent, and two- and three-dimensional models have been formulated. Due to the vast literature on this matter, we cannot discuss these models in this context as it would lead us much too far afield. We shall simply refer the reader to the cloud dynamic texts of Agee and Asai (1982), Matveev (1984), Lilly and Gal Chen (1982), Cotton and Anthes (1989), and Houze (1992). However, we must emphasize that in many models a more realistic dynamic framework often is achieved only at the expence of an accurate description of the microphysical nature of the cloud. This is usually done by parameterizing the microphysical processes.

13.2.2.2 *Condensation Growth in Stratiform Clouds and Fogs*

A somewhat different overall theoretical approach from the previous section is needed if we attempt to describe the drop spectral evolution in stratiform clouds, since they generally have longer lifetimes and much weaker updrafts (and, hence, have smaller vertical extent) than cumuliform clouds. These characteristic features should especially enhance the role played by turbulent exchange of air between the cloud and its environment. Hence, it is perhaps not surprising that the closed parcel

model of Neiburger and Chien (1960), for which an equation similar to (13-26) was used, combined with an isobaric cooling law and the assumption of a Junge-type size distribution of NaCl particles, produced size distributions considerably narrower than those observed in stratiform clouds.

The first attempt to describe the drop spectra in stratus clouds in terms of a balance between condensation growth and turbulent transport of drops to the cloud boundaries, where they evaporate, was made by Best (1951b, 1952). In his first paper, Best obtained an order of magnitude estimate of the mean lifetime of cloud drops subjected to turbulent diffusion. To accomplish this, he applied a formula of Sutton (1932) for the standard deviation σ_P of airborne smoke particles from their mean path, namely $2\sigma_P^2 = c^2(ut)^m$, where u is the wind velocity, t denotes time, c has a value of about 0.08, and m is 1.75 (cgs units). By assuming σ_P can be taken to represent half the cloud thickness, and adopting the value $u = 10$ m sec^{-1}, Best found that the resulting values of t, interpreted as the mean lifetime of the drops, were consistent with their mean size as computed from an equation similar to (13-28) and assuming a constant supersaturation of 0.05%. In his second paper, Best claims to have accounted as well for the observed drop spectral shapes, but the mathematical development presented in the paper appears to be flawed by several errors.

A more detailed treatment of this diffusional transport model has been provided by Mason (1952b), 1960b). Mason assumed an idealized layer cloud with boundaries at $\pm z_0$, and with turbulent eddying motions on a scale $l \ll z_0$ so that classical diffusion theory could be applied. Then, in terms of the diffusion problem described in Section 11.2, the probability density $w(z,t) = n(z,t)/N$ for finding drops at distance z from the origin $z = 0$ at time t, assuming they were introduced at $z = 0$ and $t = 0$, is governed by the equation

$$\frac{\partial w}{\partial t} = D_e \frac{\partial^2 w}{\partial z^2}\,, \tag{13-47}$$

where D_e is the effective eddy diffusion coefficient. Drops which arrive at the boundaries are assumed lost, so that the boundary conditions for (13-46) are $w(\pm z_0, t) = 0$. Also, according to the above description the initial condition may be expressed as $w(z,0) = \delta(z)$, where δ is the delta function.

The solution to this problem may be obtained most easily by means of the procedure described in Appendix A-11.4, i.e., by simulating the boundary conditions with an extended initial distribution, so that the formal solution form of (A.11-7) may be applied. In this manner, Mason computed the probability that drops may be found somewhere in the cloud at time t. From that, he computed the fraction of drops which are removed from the cloud in a given time interval, assuming that the lost drops are replaced by an equal number of inactivated nuclei in order to maintain a constant total concentration. Thus, the drops present at the beginning of a time step will include those surviving previous time intervals plus those activated during the last time step. Corresponding to this time history of the drop population, a cumulative size distribution was computed by integrating an equation of the type given by (13-28) over the lifetimes belonging to each fraction of the total population. This was done under the assumptions of a constant supersaturation,

an initial NaCl particle size distribution, a half-life time of the drops based on the above-mentioned smoke dispersion formula of Sutton (1932), and a certain cloud thickness. The cumulative drop size distribution obtained in this manner agreed well with the drop spectrum observed by Neiburger (1949) near the middle of a California stratus cloud with similar total drop concentration.

Following these early attempts to describe the evolution of the cloud drop spectrum in fogs and stratus clouds, numerous improved models followed. In particular, it was realized that in a realistic condensation model for fog and stratiform clouds, the effects of radiation must also be included. This was not necessary for treating drop growth in convective clouds, because in such clouds the drops grow rapidly initially by condensation due to the much higher updraft velocities and supersaturations, and subsequently by collision and coalescence.

A correct description of the effects of radiation on the development of a fog or stratus would require a detailed description of the radiative interaction with all microphysical processes. However, the fog models formulated by Zdunkowski and Nielsen (1969), Zdunkowski and Barr (1972), Brown and Roach (1976), Oliver *et al.* (1978), Welch *et al.* (1986), and Forkel *et al.* (1987) as well as the stratus models of Duynkerke and Driedonks (1988), and Finger and Wendling (1990) in fact lack detailed microphysics. On the other hand, the stratus model of Nicholls (1987) contains some microphysics, but lacks the inclusion of detailed dynamics. Roach (1976) may have been the first to explicitly compute the effects of radiation on the growth of a drop by condensation, although he did not formulate a complete fog model. He showed that if a drop is cooled by radiation, it may even grow in a water subsaturated environment, while a radiatively warmed drop may evaporate even into supersaturated air. Assuming for the radiative heat imput per unit surface area of a drop a value of ± 30 Watt m^{-2}, he computed the growth rate of a drop at a supersaturation of 0.05%. The result of this calculation is shown in Figure 13.19. It can be seen from this figure that during radiative cooling, drop growth is enhanced, while it is retarded by radiative warming.

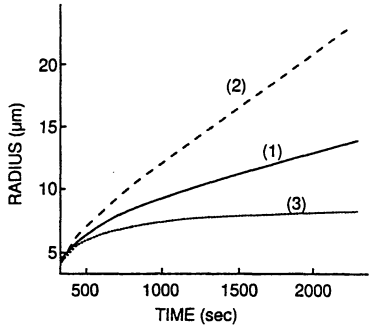


Fig. 13-19: Droplet growth on a nucleus of 10^{-12} g $(NH_4)_2SO_4$ at 0.05 % supersaturation. Solid curve (1): no radiative effects; dashed curve (2): radiative cooling of 30 Watt m^{-2}; dotted curve (3): radiative heating of 30 Watt m^{-2}. (From Roach, 1976, with changes.)

The effects of radiative cooling on the growth of a whole drop population in a fog was studied by Brown (1980). We notice from his results that radiative cooling increased the mean drop radius by about 30% if the nucleus concentration was low (Figure 13.20a). At the same time, the total drop concentration and liquid water content has decreased. In contrast, evaporative cooling had only a small effect on drop growth if the nucleus concentration is high, as seen in Figure 13.20b. The reason for this lies in the fact that with increasing nucleus concentration the drop concentration also increases, and with it the optical depth of the fog. At the same time, the size of the drop decreases. Both factors reduce the radiative loss. Unfortunately, Brown (1980) did not take into account droplet settling, which significantly affects the liquid water content of a fog and thereby the radiative cooling; and neither does it contain detailed dynamics.

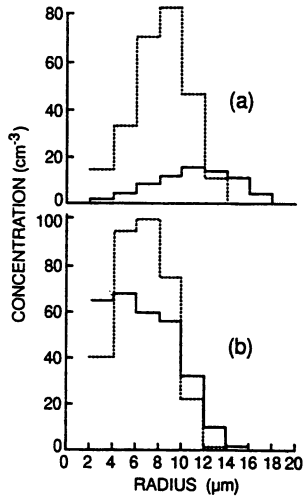


Fig. 13-20: Drop spectra inside a radiation fog, 2 m above ground, computed after 4 hours model time, for the case of condensation on an $(NH_4)_2SO_4$ aerosol particle size distribution of the Junge type with $\epsilon_m = 1.0$, and (a) $N_{AP,a} = 2320$ cm^{-3}, and (b) $N_{AP,a} = 11600$ cm^{-3}. Solid curve: radiative cooling included; dashed curve without radiative cooling. (From Brown, 1980, with changes.)

More recently, Bott (1991) and Bott *et al.* (1990) developed a one-dimensional fog model which includes a detailed description of the microphysical and dynamic processes, the transfer of radiation through the fog, and the effects of radiation on the microphysical structure of the fog. For calculating the radiative fluxes and the heating and cooling rates, a modified version of the δ-two stream approximation of Zdunkowski *et al.* (1982) was utilized in which the radiation parameters were calculated as time dependent functions of the actual aerosol/droplet size distribution. Following Forkel *et al.* (1987), the dynamic model consisted of a set of prognostic equations for the horizontal wind field, for the potential temperature and the specific humidity, including a description of the turbulent exchange coefficients for heat and momentum, as well as droplet settling.

Computations were made for the rural AP spectrum of Jaenicke (1988), of composition given by Shettle and Fenn (1979), and for the temperature, humidity, and wind conditions prescribed in Bott *et al.* (1990). The results of these computations are given in Figure 13.21a,b. The figures show that the particle spectrum is divided into two portions separated by a pronounced minimum. To the left of the minimum, the curve describes the size distribution of the slightly grown but inactivated aerosol particles. To the right of the minimum, the curve depicts the size distribution of the formed droplets. Comparison of Figure 13.21a with 13.21b shows that the total number concentration of activated AP is higher, the minimum between the inactivated and activated particles much lower, and the liquid water content higher, when one omits the radiative effects than when these effects are included. This is a result of the fact that the radiative effects favor the growth of the larger drops so that less water vapor is available for the activation of new small drops. Also, larger drops have a higher settling rate, thus reducing the liquid water content.

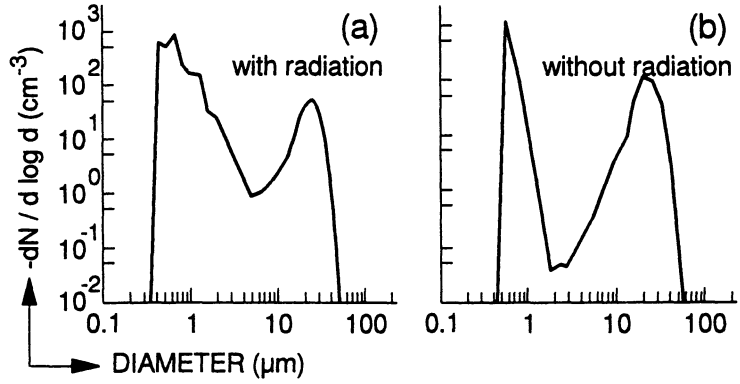


Fig. 13-21: Particle distribution in a fog simulated for an October situation at mid-latitudes at 6.45 a.m. local time (simulation began at 9 a.m. the day before) involving condensation on a rural aerosol (Jaenicke, 1988) of chemical composition given by Shettle and Fenn (1979). (a) radiation included, (b) without radiation. (From Bott *et al.*, 1990, with changes.)

In order to compare the effects of the initial aerosol particle spectrum and chemical composition, computations were made by Bott (1991) for an urban, a rural, and a maritime AP spectrum. The rural aerosol particles were assumed to be composed of $(NH_4)_2SO_4$, with ε_m varying linearly from 0.9 for $r = 0.01\,\mu$m to 0.5 for $r = 1\,\mu$m. The urban aerosol particles were assumed to consist of 80% rural aerosol and 20% soot-like material. The maritime aerosol particles were assumed to consist of $(NH_4)_2SO_4$ for $r \leq 0.5\,\mu$m and NaCl for $r > 0.5\,\mu$m, both with $\varepsilon_m = 1.0$. The temperature and humidity profile and the initial wind conditions were those prescribed by Bott (1991). We notice from Figure 13.22 that the particle distributions are again strongly bimodal, separating the cloud drops from the inactivated aerosol particles at a particle radius of 4 to 6 μm, and with a maximum value of the drop concentration located near a drop radius of 15 μm, independent of the initial

aerosol type. The location of the maxima, and minima, and the values for the drop concentration of the spectra in Figure 13.22 agree quite well with the spectra observed by Meyer *et al.* (1980), Jiusto and Lala (1982), and Kunkel (1982) (see Figure 2.4a in Chapter 2).

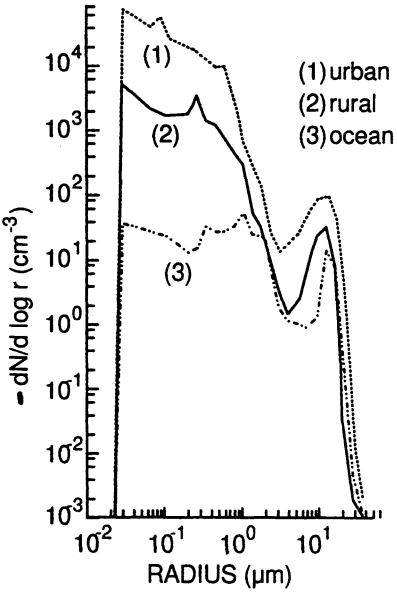


Fig. 13-22: Particle distribution in a fog simulated for an October sistuation at mid-latitude at 4 a.m. local time (simulation began at 8 a.m. the day before), for 3 different size distributions according to Jaenicke (1988), radiation effects included. (From Bott, 1991, with changes.)

Before leaving the subject of condensation, we hasten to emphasize that it is not always necessary to treat the condensation process by an ab-initio calculation, i.e. by beginning the computation with a distribution of dry aerosol particles. Rather, one may as well start the computation with a specification of the number of cloud condensation nuclei (CCN) as a function of supersaturation, usually given in terms of a power law in the form (9-1). However, Ahr *et al.* (1989a) have shown that for a correct description of drop spectra, the constants in the CCN-power law must pertain exactly to the air mass in which the cloud or fog grows. This can best be done by actually measuring the CCN spectrum of the air mass. Alternatively, if the CCN spectrum is not available, it can indirectly be obtained from the measured size distribution of the AP and their chemical characteristics using the method outlined in Section 9.1.2.

13.2.3 Steady State Evaporation of Water Drops Falling in Subsaturated Air

In this section we shall consider the ventilating effect of a drop's motion on its rate of diffusional growth or evaporation. The results presented here will justify our previous neglect of the ventilation effect for the small sizes which are involved in the early stages of evolution of cloud drop spectra.

From the discussions of Section 13.1.1, it is clear that our problem here is to solve the steady state convective diffusion equation

$$\vec{u} \cdot \nabla \rho_v = D_v \nabla^2 \rho_v \tag{13-48}$$

for a spherical drop of radius a past which moist air containing water vapor of density ρ_v flows with velocity $\vec{u}$. There are several conventional ways of describing the resulting convective enhancement of the diffusional growth or evaporation rates. Thus, in the cloud physics literature, one generally uses the *mean ventilation coefficient*, $\bar{f}_v$, defined as the ratio of the water mass fluxes to or from the drop for the cases of a moving and a motionless drop, viz.,

$$\bar{f}_v \equiv \frac{dm/dt}{(dm/dt)_0}, \tag{13-49}$$

where $(dm/dt)_0$ denotes the mass flux for the motionless case of pure diffusion, and is given by (13-9) for a growing drop (the same expression but with opposite sign applies to the case of an evaporating drop). A closely related quantity used in the chemical engineering literature (Bird *et al.*, 1960) is the *mean mass transfer coefficient*, $\bar{k}_v$, defined by

$$\bar{k}_v \equiv \frac{dm/dt}{4\pi a^2(\rho_{v,\infty} - \rho_{v,a})}. \tag{13-50}$$

On combining (13-9), (13-49) and (13-50), we also see that

$$\bar{k}_v = \frac{D_v \bar{f}_v}{a}. \tag{13-51}$$

Finally, another useful dimensionless measure found in the chemical engineering literature (Bird *et al.*, 1960) is the *mean Sherwood number*, $\bar{N}_{Sh}$, defined in terms of $\bar{k}_v$ as

$$\bar{N}_{Sh} \equiv \frac{2\bar{k}_v a}{D_v} = 2\bar{f}_v. \tag{13-52}$$

From this last result and (13-48), we see that $\bar{f}_v = 1$ and $\bar{N}_{Sh} = 2$ for a motionless drop. Substituting (13-51) or (13-52) into (13-50), we find for a moving drop

$$\frac{dm}{dt} = 4\pi a D_v \bar{f}_v(\rho_{v,\infty} - \rho_{v,a}) = 2\pi a D_v \bar{N}_{Sh}(\rho_{v,\infty} - \rho_{v,a}). \tag{13-53}$$

We see that for computing the growth rate of a moving drop, we must determine $\bar{N}_{Sh}$ or $\bar{f}_v$. To do this, we recall from (13-7) and (13-9) that $(dm/dt) =$

$D_v \int_S (\partial \rho_r / \partial r)_{r=a} dS$ so that we obtain from (13-53)

$$\bar{N}_{Sh} = \frac{\int_S [\partial \rho_r(\theta)/\partial r]_a \, dS}{2\pi a(\rho_{v,\infty} - \rho_{v,a})}, \tag{13-54}$$

assuming D_v to be constant over the diffusion path.

Considering that $dS = a^2 \sin\theta \, d\theta \, d\phi$, where ϕ is the azimutal angle, we find, after partial integration for an axisymmetric flow past the drop,

$$\bar{N}_{Sh} = \frac{a}{(\rho_{v,\infty} - \rho_{v,a})} \int_{\theta=0}^{\pi} \left[\frac{\partial \rho_v(\theta)}{\partial r}\right]_a \sin\theta d\theta, \tag{13-55}$$

where θ is the angle from the forward stagnation point of the flow. By defining the local enhancement of the vapor flux by what is known as the local Sherwood number, $N_{Sh}(\theta)$, as follows

$$N_{Sh}(\theta) \equiv \frac{2a}{(\rho_{v,\infty} - \rho_{v,a})} \left[\frac{\partial \rho_v(\theta)}{\partial r}\right]_a, \tag{13-56}$$

we may express the overall enhancement of the vapor transport by

$$\bar{N}_{Sh} = \frac{1}{2} \int_0^{\pi} N_{Sh}(\theta) \sin\theta d\theta. \tag{13-57}$$

In order to compute $\bar{N}_{Sh}$, we must find the vapor density distribution $\rho_v(r, \theta)$ around the moving drop from (13-48). This in turn allows us to determine the vapor density gradient at the drop surface and thus $N_{Sh}(\theta)$ from (13-56).

Of course, to solve (13-48) for ρ_v requires specifying $\vec{u}$, and generally this can be accomplished only through a numerical solution of the Navier-Stokes equation for $\vec{u}$; hence, for nearly all cases of interest, (13-48) must be solved by numerical methods. To do this, one generally first renders (13-48) dimensionless by introducing the variables $r' \equiv r/a$, $\rho'_v \equiv (\rho_v - \rho_{v,\infty})/(\rho_{v,a} - \rho_{v,\infty})$, and $\vec{u}' \equiv \vec{u}/U_\infty$; in terms of these (13-48) becomes

$$\vec{u}' \cdot \nabla' \rho'_v = \frac{2}{N_{Pe,v}} \nabla'^2 \rho'_v, \tag{13-58}$$

where $\nabla' = a\nabla$, $N_{Pe,v} = 2U_\infty a/D_v = N_{Sc,v} \times N_{Re}$ is the Péclet number for vapor transport, $N_{Sc,v} = \nu_a/D_v$ is the Schmidt number for vapor in air, and ν_a is the kinematic viscosity of air. An axially symmetric numerical solution of (13-58) may be carried out in spherical coordinate (r', θ) in conjunction with (10-72) by writing $\vec{u}' = \hat{e}_\phi \times (\nabla\psi'/r' \sin\theta')$ (cf. (A.10-18))), and by imposing the following boundary conditions: (1) On the sphere surface ($r' = 1$), $\psi' = 0$, $\zeta' = E'^2 \psi' \sin\theta$, and $\rho'_v = 1$; (2) along the symmetry axis ($\theta = 0, \pi$), $\psi' = 0$, $\zeta' = 0$, $\partial \rho'_v / \partial \theta = 0$; (3) far from the sphere surface ($r' = r'_\infty$, $\psi' = \frac{1}{2} r'^2_\infty \sin^2\theta$, $\zeta' = 0$, and $\rho'_v = 0$.

Numerical solutions as outlined above have been obtained by Woo (1971) and Woo and Hamielec (1971) for an evaporating drop in air with a Schmidt number

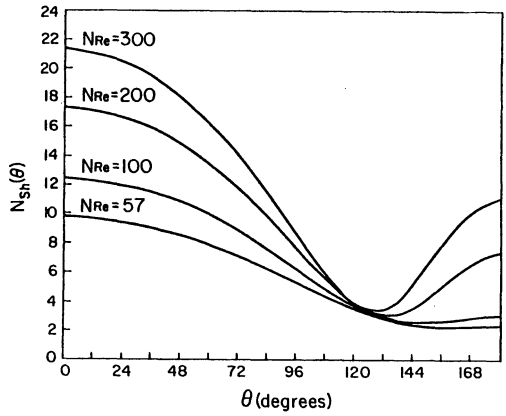


Fig. 13-23: Variation of local Sherwood number for a ventilated water sphere in air ($N_{Sc,v}$ = 0.71) as a function of angle Θ from foreward stagnation point on sphere. (From Woo and Hamielec, 1971; by courtesy of Am. Meteor. Soc., and the authors.)

$N_{Sc,v} = 0.71$. Some resulting plots of $N_{Sh}(\theta)$ versus θ are shown in Figure 13.23 for various $N_{Re} \gg 1$. It is seen that the effect of ventilation varies strongly with the angle θ from the forward stagnation point, and is smallest near the location of flow separation from the drop. Also, the ventilation effect and, hence, the rate of evaporation, is greatest on the upstream side of the drop, as would be expected.

We shall show in Chapter 17 that boundary layer theory leads to the prediction that the convective enhancement of the mass or particle flux to a sphere is proportional to $N_{Sc,v}^{1/3} N_{Re}^{1/2}$ for $N_{Re} \gg 1$. It has therefore been custormary to plot the values of $\bar{N}_{Sh}$ or $\bar{f}_v$ as a function of this quantity. The rate at which this asymptotic behavior is approached is indicated in Figures 13.24a,b. We note from Figure 13.24a,b that, for $N_{Sc,v} = 0.71$, the expected linear dependence of the ventilation coefficient begins near $N_{Re} = 3$. A linear dependence on $\bar{f}_v$ with $N_{Sc,v}^{1/3} N_{Re}^{1/2}$ was found experimentally by Ranz and Mashall (1952), Frössling (1938), Beard and Pruppacher (1971a), Wedding *et al.* (1986), Pruppacher and Rasmussen (1979), and from a numerical solution of the convective diffusion equation (13-58) by Woo and Hamielec (1971). The experimental values of Kinzer and Gunn (1951) deviate significantly from the expected behavior due to various experimental inaccuracies. For $N_{Sc,v}^{1/3} N_{Re}^{1/2} \leq 1.4$, we notice from Figure 13.24a that $\bar{f}_v$ no longer varies linearly with $N_{Sc,v}^{1/3} N_{Re}^{1/2}$ but approaches $\bar{f}_v = 1$ asymptotically as $N_{Re} \to 0$. This is, of course, what we would expect, since boundary layer theory becomes inapplicable for $N_{Re} \leq O(1)$. However, for such decreasing N_{Re} the flow becomes increasingly linear and simple so that various analytical approximations to $\bar{f}_v$ become possible. For example, (13-58) has been solved by the method of matched asymptotic expansions (see case 4 of Section 10.2.4) for small N_{Pe} and N_{Re} by Acrivos and Taylor (1962), Rimmer (1969), Gupalo and Ryazantsev (l972), and Sano (1972). The differences in these studies are due to the assumed form for $\vec{u}'$. Thus, Acrivos

and Taylor assumed Stokes flow; Rimmer, and Gupalo and Ryazantsev assumed 'Proudman-Pearson flow'; and Sano assumed potential flow. As one representative example, we shall quote the series expression obtained by Acrivos and Taylor:

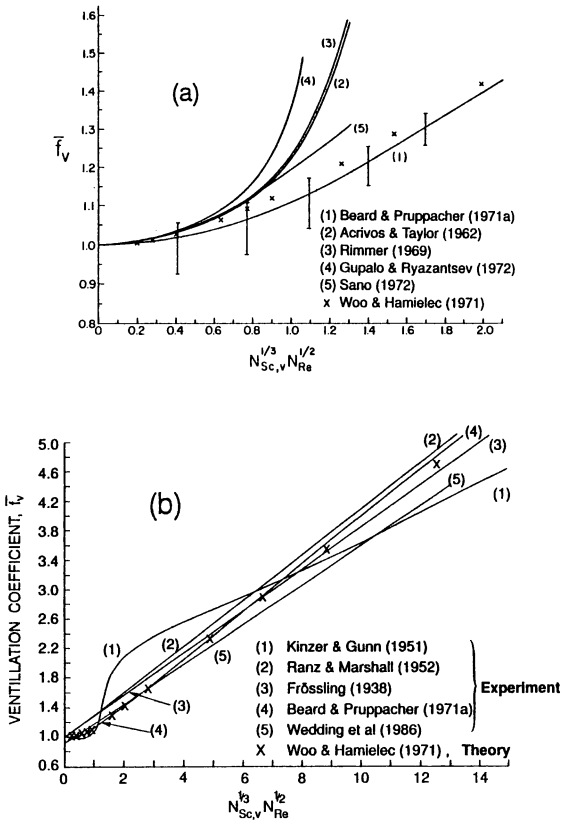


Fig. 13-24: Comparison of experimentally determined ventilation coefficients for water drops in air with numerical results of Woo and Hamielec (1971) and with various analytical results. (a) for low Reynolds numbers, (b) for moderate Reynolds numbers. (From Beard and Pruppacher, 1971a; by courtesy of Am. Meteor. Soc., and the authors.)

$$\bar{N}_{\mathrm{Sh}} = 2 + \frac{N_{\mathrm{Pe}}}{2} + \frac{N_{\mathrm{Pe}}^2 \ln N_{\mathrm{Pe}}}{4} + 0.03404 N_{\mathrm{Pe}}^2 + \frac{N_{\mathrm{Pe}}^3 \ln N_{\mathrm{Pe}}}{16} + \ldots . \qquad (13\text{-}59)$$

This result and some others are plotted in Figure 13.24a. Note that the experimental, numerical, and analytical results merge as $\bar{f}_v \to 1$ with $N_{\mathrm{Re}} \to 0$. Note also that the analytical results begin to diverge noticeably from the experimental and numerical results as $N_{\mathrm{Re}} \gtrsim 0.1$. The values of $\bar{f}_v$ obtained by Beard and Pruppacher (1971a) and Pruppacher and Rasmussen (1979) are closely approximated by the

following empirical expressions:

$$\bar{f}_v = 1.00 + 0.108(N_{Sc,v}^{1/3} N_{Re}^{1/2})^2 , \tag{13-60}$$

for $N_{Sc,v}^{1/3} N_{Re}^{1/2} < 1.4$, i.e. $a_0 \leq 60\,\mu$m with $N_{Sc,v} = 0.71$; and

$$\bar{f}_v = 0.78 + 0.308 N_{Sc,v}^{1/3} N_{Re}^{1/2} , \tag{13-61}$$

for $1.4 \leq N_{Sc,v}^{1/3} N_{Re}^{1/2} \leq 51.4$, i.e. for $60\,\mu\text{m} \leq a_0 \leq 1500\,\mu$m with $N_{Sc,v} = 0.71$. The whole range of values for $\bar{f}_v$ is plotted in Figure 13.25. The experimentally found behavior implies that the evaporation enhancement expected due to vortex shedding from the rear of large drops, and the evaporation reduction expected due to drop defomation (reducing the drop surface area effectively ventilated), approximately cancel each other.

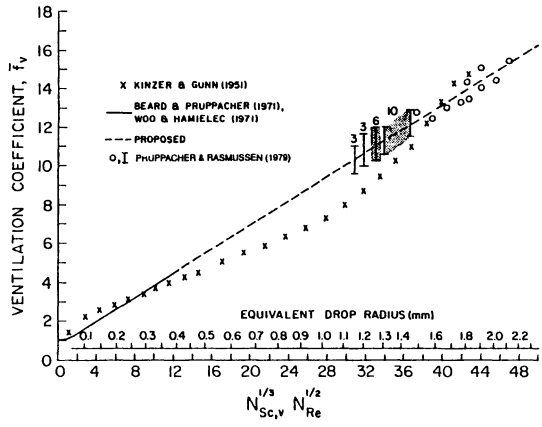


Fig. 13-25: Comparison of experimentally determined ventilation coefficients for water drops of large Reynolds numbers with an extrapolation of the theoretically computed ventilation coefficient for water drops at moderate Reynolds numbers. (From Pruppacher and Rasmussen, 1979, with changes.)

To determine the rate of evaporation of a falling drop, we must also take into account the convective-diffusional transfer of heat to the drop from the environment. Because of the complete mathematical analogy between problems of convective heat and mass transfer (cf. (13-2) and (13-17)), we may express the ventilation effect on heat transfer in terms of a mean ventilation coefficient for heat, $\bar{f}_h$, which is obtained from $\bar{f}_v$ merely by replacing D_v with κ_a i.e., $\bar{f}_h = \bar{f}_v(D_v \to \kappa_a)$. Similarly, corresponding to the mean Sherwood number for mass transfer, there is the *mean Nusselt number*, $\bar{N}_{Nu}$, for heat transfer, given by $\bar{N}_{Nu} = \bar{N}_{Sc}(D_v \to \kappa_a)$.

Because the ventilation effect shows a strong local variation over the drop surface (Figure 13.23), there must be a non-zero temperature gradient at the surface. This gradient will be degraded to some extent by the drop internal circulation, but unfortunately there are no computations available with which to estimate the

resultant steady state gradient. For lack of any information on this point, it is customary to assume the local cooling effect is negligible, so that the drop has an isothermal surface at temperature T_a. Simple order of magnitude estimates indicate this is probably a very good assumption, because of the large thermal conductivity of water and the expected small differences in the heat flux around the drop surface.

In order to determine T_a for an evaporating drop, we first write, in analogy to (13-22),

$$\frac{\mathrm{d}q}{\mathrm{d}t} = \bar{f}_h \left(\frac{\mathrm{d}q}{\mathrm{d}t}\right)_0 = -L_\mathrm{e}\frac{\mathrm{d}m}{\mathrm{d}t} = -L_\mathrm{e}\bar{f}_\mathrm{v}\left(\frac{\mathrm{d}m}{\mathrm{d}t}\right)_0 , \tag{13-62}$$

for the coupling of the rates of heat and mass exchange for the ventilated drop. Then, on substituting (13-10) and (13-19) into this equation, we find that

$$T_a - T_\infty - \frac{L_\mathrm{e}D_\mathrm{v}M_\mathrm{w}}{\kappa_\mathrm{a}\mathscr{R}}\left(\frac{\mathrm{e}_\mathrm{sat}(T_a)}{T_a} - \frac{\mathrm{e}_\infty}{T_\infty}\right)\left(\frac{\bar{f}_\mathrm{v}}{\bar{f}_h}\right) , \tag{13-63}$$

where $\mathrm{e}_\mathrm{sat}(T_a)$ is given by (13-24) and (13-25).

With T_a available, the drop evaporation rate may be determined from (13-53), which we now express in the form

$$a\frac{\mathrm{d}a}{\mathrm{d}t} = -\frac{M_\mathrm{w}D_\mathrm{v}}{\rho_\mathrm{w}\mathscr{R}}\left(\frac{\mathrm{e}_\mathrm{sat}(T_a)}{T_a} - \frac{\mathrm{e}_\infty}{T_\infty}\right)\bar{f}_\mathrm{v} . \tag{13-64}$$

Obviously, (13-64) may also be used to determine $\bar{f}_\mathrm{v}$ experimentally from observed drop evaporation rates. If $\bar{f}_\mathrm{v}$ is known, (13-64) allows the calculation of the variation in the radius of a water drop falling from the cloud base to the ground in subsaturated air. The results of such a calculation are illustrated in Figures 13.26a,b. As expected, we see that below the cloud base the future fate of a drop depends strongly on the humidity structure of the air below the cloud, on the original size of the drop, and on the height of the cloud base. Thus, in order for a 600 μm radius drop to arrive at the ground with a radius of 500 μm, the cloud base from which it falls may only be 1100 m above the ground if the air below the cloud base has a relative humidity of 60%; but it may be 2800 m above the ground if the relative humidity is as high as 80% (Figure 13.26a). Considering a fixed cloud base of 3000 m, the same figure tells us that the original radius of a drop falling from this cloud base must be as large as 700 μm in order to arrive at the ground with a radius of 500 μm if it falls through air of 60% relative humidity, while the drop can be as small as 560 μm if it falls from the cloud base through air of 90% relative humidity.

Supposing now that a drop makes a simple isothermal excursion of 300 m, Figure 13.27 shows that the probability of such a drop surviving the excursion, at 90% relative humidity and at $T = 0°\mathrm{C}$ and $p = 765$ mb, is a sensitive function of its initial size. Thus, a drop of $a > 150\,\mu$m experiences a negligible change in size, while drops of $a < 100\,\mu$m do not survive the excursion.

Another related quantity of interest is the time required for a falling drop to achieve its quasi-steady state temperature difference between itself and the environment. Let us consider this adaptation time for the case of a drop of initial

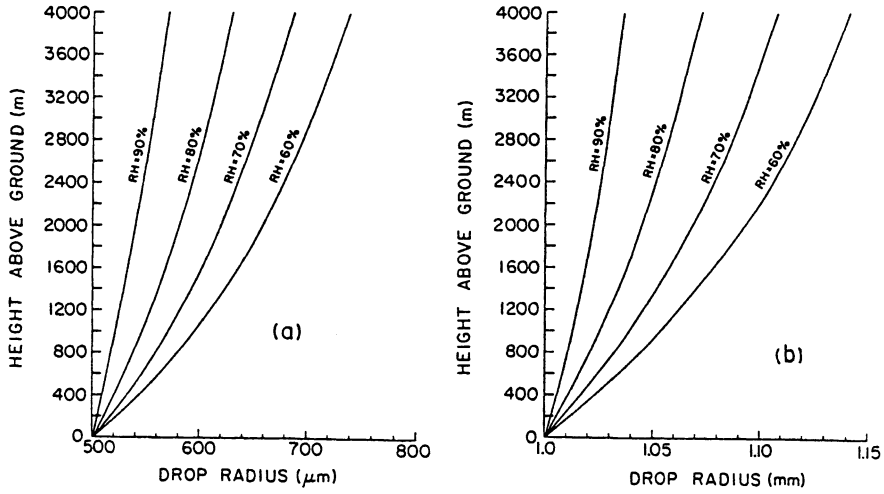


Fig. 13-26: Size variation of a water drop falling from the cloud base through subsaturated air of various relative humidities in a NACA standard atmosphere, and arriving at the ground with a final radius of : (a) 500 μm, (b) 1 mm. (From Pruppacher and Rasmussen, 1979, with changes.)

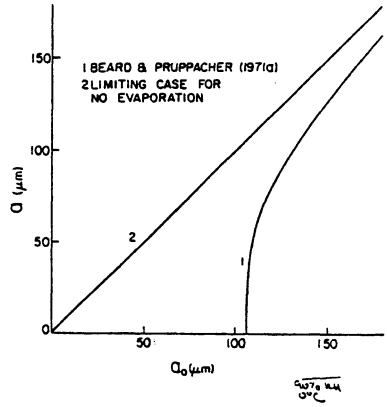


Fig. 13-27: Final size a of various drops of initial size a_0 after an isobaric and isothermal excursion of 300 m into air of 90 % relative humidity, at 0° C and 765 mb. (From Beard and Pruppacher, 1971a; by courtesy of Am. Meteor. Soc., and the authors.)

temperature $T_{a,0} = T_a(t = 0)$ placed abruptly in an environment at $T_\infty > T_{a,0}$ and with a relative humidity $\phi_v < 1$. Then, because of evaporative cooling, the instantaneous drop temperature $T_a(t)$ satisfies $T_a < T_\infty$, so that there is a conductive heat flux from the air to the drop given by $4\pi \bar{f}_h a k_a (T_\infty - T_a)$ (cf. (13-19)). At the same time, the rate at which heat is lost from the drop due to its evaporation is $-L_e dm/dt$ (> 0 since $dm/dt < 0$). Thus, we find that the total rate at which the drop gains heat is given by

$$\left(\frac{dq}{dt}\right)_{\text{total}} = 4\pi \bar{f}_h a k_a (T_\infty - T_a) + L_e \frac{dm}{dt} . \tag{13-65}$$

This total heat flux to the drop must cause the temperature difference between the drop and its environment to change at a rate determined by the obvious heat balance relation $(dq/dt)_{\text{total}} = m c_w d(T_a - T_\infty)/dt$, where c_w is the specific heat capacity of water and m is the mass of the drop. From this relation, (13-65), and (13-53) for dm/dt, we obtain the governing equation for temperature adaptation:

$$\frac{a^2 \rho_w c_w}{3} \frac{d}{dt}(T_\infty - T_a) = -k_a (T_\infty - T_a) \bar{f}_h - L_e D_v (\rho_{v,\infty} - \rho_{v,a}) \bar{f}_v . \tag{13-66}$$

Let us now assume that the water drop is sufficiently large that the curvature effects are negligible; then, we may set $\rho_{v,a} = \rho_{v,\text{sat}}(T_a)$. If we make the further approximation that $[\rho_{v,\text{sat}}(T_\infty) - \rho_{v,\text{sat}}(T_a)]/(T_\infty - T_a) \approx \overline{(d\rho_v/dT)}_{\text{sat}}$, which represents the mean slope of the saturation vapor density curve over the interval $T_a \le T \le T_\infty$, then (13-66) may be expressed in the form

$$\frac{d(T_\infty - T_a)}{dt} = -A(T_\infty - T_a) + B , \tag{13-67}$$

where

$$A = \frac{3}{a^2 \rho_w c_w} \left[k_a \bar{f}_h + L_e D_v \left(\overline{\frac{d\rho_v}{dT}} \right)_{\text{sat}} \bar{f}_h \right] , \tag{13-68}$$

and

$$B = \frac{3 D_v L_e \bar{f}_v}{a^2 \rho_w c_w} [(1 - \phi_v) \rho_{v,\text{sat}}(T_\infty)] , \tag{13-69}$$

where $\phi_v = \rho_{v,\infty}/\rho_{v,\text{sat}}(T_\infty)$. An approximate solution of (13-67) to (13-69) is

$$T_\infty - T_a(t) - \delta = (T_\infty - T_{a,0} - \delta) \exp(-t/\tau) , \tag{13-70}$$

where $T_{a,0} = T_a(t = 0)$ is the drop's initial temperature, $\delta = \bar{B}/\bar{A}$, and $\tau = 1/\bar{A}$ is the relaxation time given by

$$\tau = \frac{a^2 \bar{\rho}_w \bar{c}_w}{3 \left[k_a \bar{f}_h + \bar{L}_e \bar{D}_v \left(\overline{\frac{df_v}{dT}} \right)_{\text{sat}} \bar{f}_v \right]} . \tag{13-71}$$

(Kinzer and Gunn, 1951). The bars over A, B, ρ_w, c_w, L_e and D_v denote averages over the integration interval.

For a relative humidity of 100%, i.e, $\phi_v = 1.0, B = 0$ and, thus, $\delta = 0$, the temperature adaption of the drop is then given by

$$T_\infty - T_a(t) = (T_\infty - T_{a,0}) \exp(-t/\tau) . \tag{13-72}$$

Equation (13-72) implies that for $t \to \infty$, $T_a \to T_\infty$. In contrast, for an evaporating drop, (13-70) implies that for $t \to \infty$, $(T_\infty - T_a) \to \delta$. This means that an evaporating drop never reaches T_∞ but approaches the steady state temperature difference δ given by

$$\delta = \frac{\bar{B}}{\bar{A}} = \frac{\bar{D}_v \bar{L}_e \bar{f}_v [\rho_{v,sat}(T_a) - \rho_{v,\infty}]}{k_a \bar{f}_h} . \tag{13-73}$$

From (13-70), the e-folding time for $T_a - T_{a,0}$ is just $t_e = \tau$. A plot of $t_e = t_e(a)$ is given in Figure 13.28 for three different drop temperatures. To obtain these curves, it has been assumed that $\bar{f}_h = \bar{f}_v$; also, $\overline{(d\rho_v/dT)}_{sat}$ has been evaluated for $T = T_a$. It can be seen that, as expected, larger drops have larger adaptation times. The only experimental results which are available for comparison with the theoretical values are those of Kinzer and Gunn (1951). They studied drops of $a_0 = 1.35$ mm radius cooling from 22.4 to 14.9°C while falling in subsaturated air. The observed adaptation time was 4.4 sec, at which time the drop temperature was about 17.6°C. For these data, (13-71) predicts $t_e \approx 4.6$ sec, which is in surprisingly good agreement with the experimental value, considering the approximations involved in (13-68) and the uncertainties in Kinzer and Gunn's experiments. This good agreement suggests that the neglect of local unsteadiness (terms involving $\partial/\partial t$) in the derivation of (13-71) is of little consequence. This indication has been verified quantitatively by Watts and Farhi (1975), who solved for t_e including the effect of local time dependence. Kuhns and Mason (1968) also found good agreement between the relaxation times calculated by (13-71), and their observed values for drops of radii between 30 and 80 μm, for which t_e ranged between 50×10^{-3} and 200×10^{-3} sec.

Before leaving this section on the diffusional growth and evaporation of water drops, we hasten to add that surface active chemical compounds may significantly reduce the rate of evaporation of drops (Mihara, 1966; Ofani and Wang, 1984; La Mer, 1962; Derjaguin *et al.*, 1966; Eisner *et al.*, 1960; Snead and Zung, 1968; Garrett, 1971; Hoffer and Mallen, 1970; Hoffer and Bowen, 1972; Chang and Hill, 1980). Surface active agents also reduce the rate of drop growth by condensation (Thareau *et al.*, 1987; Ueno and Sano, 1971; Derjaguin *et al.*, 1971; Pilie, 1966; Kocmond *et al.*, 1972). Other effects caused by such agents include a reduction of the surface tension (Gal-Or and Waslo, 1968), an increase in drop deformation (Marty and Aliot, 1979), a dampening of drop oscillation (Huang and Kintner, 1969), and an enhancement of drop breakup (Ryan, 1976).

However, most of the experiments which led to these results were carried out with artificial surfactants (e.g. hexadecanol), with linear molecular configurations so that closed monolayers would form at the surface of drops. Studies were therefore needed to check whether atmospheric surfactants have similar characteristics.

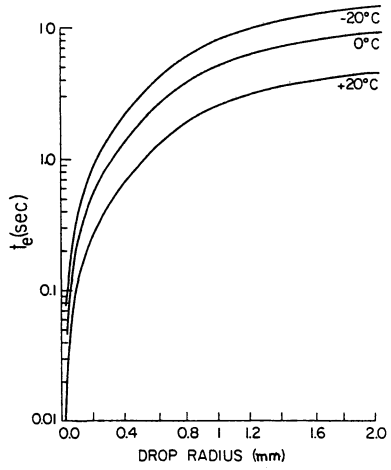


Fig. 13-28: Variation of the e-folding adaptation time t_e for evaporating, ventilated water drops of radius a falling at terminal velocity in subsaturated air; based on Eq. 13-71.

A search showed that film-forming chemical compounds do exist at the ocean surface, from where they are transported into the atmosphere by the bubble burst mechanism (Garrett, 1967; Blanchard, 1964; Blanchard and Syzdek, 1974; Barger and Garrett, 1970, 1976; Duce, 1972; Hardy, 1982), and to the surface of aerosol particles (Ketseridis *et al.*, 1976b; Ketseridis and Eichmann, 1978; Barger and Garrett, 1970; Neumann *et al.*, 1959). A review of surfactants in the atmosphere has been also given by Gill *et al.* (1983). However, these surfactants have mostly a non-linear molecular configuration, or are only weakly surface active, so that complete monolayers on drop surfaces are unlikely to be formed under atmospheric conditions.

13.3 Growth of Snow Crystals by Diffusion of Water Vapor

13.3.1 Growth of a Stationary Snow Crystal

The diffusional growth of simple snow crystals can be treated in the same manner as for drops, by making use of an analogy between the governing equation and boundary conditions for electrostatic and diffusion problems (Stefan, 1873; Jeffreys, 1918). To understand this approach, recall that the electrostatic potential function Φ outside a charged conducting body (assumed to be the only source for Φ) satisfies Laplace's equation, i.e., $\nabla^2\Phi = 0$, and that the boundary conditions on Φ are $\Phi = \Phi_S$ = constant on the conductor and $\Phi = \Phi_\infty$ = constant at infinity. Similarly, if we now consider a stationary growing or sublimating ice particle of the same geometry as the conducting body, then in the steady state, the vapor density field ρ_v also satisfies Laplace's equation and, if the particle surface is at uniform temperature T_S, the boundary conditions are similarly given by $\rho_v = \rho_{v,S} = \rho_{v,sat}(T_S)$ = constant on the particle (ignoring the dependence of $\rho_{v,sat}$ on local curvature) and $\rho_v =$

ρ_∞ = constant at infinity. Therefore, with this complete analogy, we can borrow known solutions for electrostatic problems and use them to describe the diffusional growth of ice articles of corresponding geometry.

In particular, the growth rate of the particle can be written down immediately if the capacitance C of the corresponding conductor is known. Thus, by integrating Gauss's law over the surface S of the conductor, we have, with the electric field $\vec{E} = -\nabla\Phi$,

$$\int_S \nabla\Phi \cdot \hat{n}\, dS = -4\pi Q = -4\pi C(\Phi_S - \Phi_\infty)\,, \tag{13-74}$$

where Q is the total charge on the conductor, and where the last form on the right side of (13-74) follows from the definition of capacitance. Then, from the analogy between the Φ and ρ_v fields and the physical meaning of $-D_v\nabla\rho_v\,|_S$ as the vapor mass flux vector at the ice particle surface, we immediately conclude that the growth rate of a stationary particle is given by

$$\left(\frac{dm}{dt}\right)_0 = \int_S D_v\nabla\rho_v \cdot \hat{n}\, dS = -4\pi D_v C(\rho_{v,s} - \rho_{v,\infty})\,. \tag{13-75}$$

A comparison of (13-75) and (13-74) shows that they are formally equivalent, with the capacitance of the particle or crystal replacing the radius of the sphere. Therefore, we may immediately write down a growth rate equation for the crystal in a form analogous to (13-28), but expressed in terms of dm/dt and with C replacing a; for negligible curvature and solute effects ($y \approx 0$), the result is

$$\left(\frac{dm}{dt}\right)_0 \approx \frac{4\pi C s_{v,i}}{\frac{\mathscr{R}T_\infty}{e_{sat,i}(T_\infty)D_v^* M_w} + \frac{L_s}{k_a^* T_\infty}\left(\frac{L_s M_w}{\mathscr{R}T_\infty} - 1\right)}\,, \tag{13-76}$$

where now the subscript i refers to the ice phase, and L_s is the specific latent heat of sublimation.

In order to apply (13-76) to a particular crystal form, we must specify C, which is a function only of the crystal geometry. For example, in the simplest case of a spherical particle of radius a, $C = a$ (in electrostatic units), and we recover the previous description for drops. As we recall from Section 10.4, the hydrodynamic behavior of many simple crystals can be described adequately in terms of the behavior of very simple geometric forms, such as finite circular cylinders, thin circular disks, and prolate or oblate spheroids. Similar idealizations work well in the present context also, and so we shall now quote the capacitances C_0 for some simple geometries (in e.s.u.). To model the shape of a simple thin hexagonal ice plate, we use the idealization of a circular disk of radius a, for which

$$C_0 = \frac{2a}{\pi}\,. \tag{13-77}$$

The shape of simple ice plates of various thicknesses may be modeled by an oblate spheroid of semi-major and semi-minor axes lengths a and b, for which, after McDonald (1963c),

$$C_0 = \frac{a\varepsilon}{\sin^{-1}\varepsilon}\,, \qquad \varepsilon = \left(1 - \frac{b^2}{a^2}\right)^{1/2}\,. \tag{13-78}$$

The shape of a columnar crystal may be modeled by a prolate spheroid of semi-major and minor axes a and b for which, after McDonald (1963b),

$$C_0 = \frac{A}{\ln[(a+A)/b]}, \qquad A = (a^2 - b^2)^{1/2}. \tag{13-79}$$

Finally, for $b \ll a$, (13-74) transforms into

$$C_0 = \frac{a}{\ln(2a/b)}, \tag{13-80}$$

which is applicable to a long, thin needle.

Measurements by McDonald (1963b) and Podzimek (1966) of the capacitances of metal models of snow crystals agree surprisingly well with the above theoretical values for the idealized forms. Thus, the capacitance of a simple hexagonal plate (snow crystal shape P1a in the nomenclature of Figure 2.39) is within 4% of the value for a circular disk of the same area. Similarly, Podzimek compared the capacitance C_0 of a prolate spheroid and that (C) of a hexagonal prism of the same maximum dimensions, and found that $C/C_0 = 1.116$ for a solid short prism, and $C/C_0 = 1.099$ for a short prism with hourglass-like hollow ends. The capacitances C of various dendritic models were found to be only a little less than that (C_0) of a hexagonal plate having the same maximum dimensions. For example, referring again to the crystal forms shown in Figure 2.39, McDonald found that: (1) for crystal shape P1c, $C/C_0 = 0.98$; (2) for shape P2a, $C/C_0 = 0.97$, decreasing to 0.91 with decreasing end plate size; (3) for shape P2g, $C/C_0 = 0.97$, decreasing to 0.80 with increasing openness of the dendrite; (4) for shape P1d, $C/C_0 = 0.77$. Similar values were also obtained by Podzimek. The observed insensitivity of C to such large variations in crystal surface area for crystals of the same maximum dimensions is apparently due to the increasing edge length with decreasing area; such edges of high curvature can store relatively large amounts of charge and, hence, compensate for the loss of surface. For typical cirrus cloud particles, Heymsfield (1975a,b,c) suggested $C = L$ for bullet rosettes, where L is the length of an individual bullet.

We shall now apply (13-76) to the growth of an snow crystal in an environment of supercooled cloud drops. In Section 4.8, we have already shown that at any temperature below 0°C, the vapor pressure over a supercooled water surface is larger than over an ice surface. Hence, if in a supercooled cloud snow crystals are present among drops, one would expect that the crystals will grow at the expense of the drops due to the flux of water vapor from the drops to the crystals. Such a situation would lead to a colloidally unstable cloud, as the snow crystals would grow until all water drops have disappeared or the crystals have fallen out of the cloud. As mentioned in Chapter 1, such a precipitation mechanism was first described by Wegener, Bergeron and Findeisen, and is therefore named accordingly. This process is illustrated by Plate 16 which shows a snow crystal of about 400 μm in diameter at rest and surrounded by micron-sized supercooled water drops. Note the absence of drops in the vicinity of the crystal, due their evaporation onto the crystal.

Newer cloud model calculations show, however, that in convective clouds with water-supersaturated updrafts, the snow crystals grow by virtue of the available

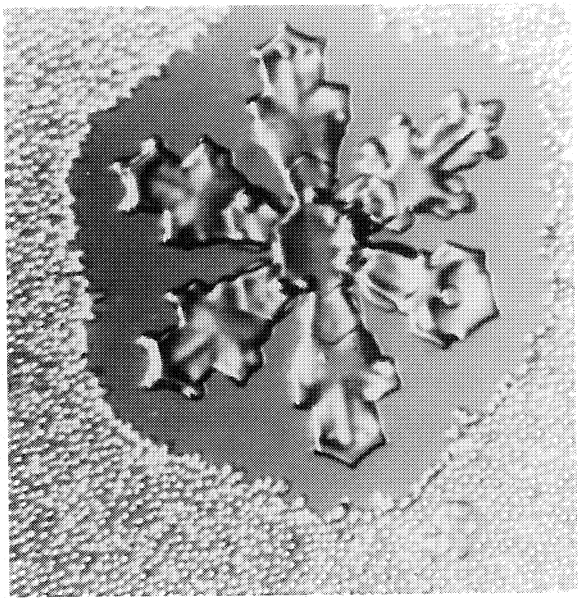


Plate 16. Bergeron-Findeisen process illustrated by means of a snow crystal of 400 μm diameter growing at the expense of surrounding, supercooled water drops. (Reproduced by courtesy of Dr. R.L. Pitter, Desert Res. Inst., Reno, Nevada, 1993.)

water vapor, rather than at the expense of the drops present in the cloud. The Wegener-Bergeron-Findeisen mechanism therefore does not contribute significantly to the growth of the snow crystals in such clouds. The mechanism may, however, proceed in stratus clouds with very low updrafts and associated low supersaturations. We proceed now to use (13-76) to determine the growth rate of an snow crystal in a water saturated environment, and thereby model the Wegener-Bergeron-Findeisen mechanism. The condition of water saturation specifies the supersaturation with respect to ice as a function of temperature according to the relation $s_{v,i} = (e_{sat,w}/e_{sat,i}) - 1 > 0$. The resulting mass growth rate, dm/dt, calculated from (13-76) with $C = 1/4\pi$, is displayed as a function of temperature in Figure l3.29 for two pressure levels. Note that the growth curves each have a single maximum, near $-14°C$ for the 1000 mb curve and $-17°C$ for the 500 mb curve. From our discussions in Section 4.8, we might have expected the maxima to occur near $-12°C$, since at that temperature the difference $e_{sat,w} - e_{sat,i}$ is a maximum (see Figure 4.5) The reason the actual maxima are shifted to lower temperatures is that local heating from latent heat release causes the vapor pressure difference between the crystal surface and its environment to be reduced slightly. The system must therefore cool below $-12°C$ before the vapor flux and, hence, the growth rate,

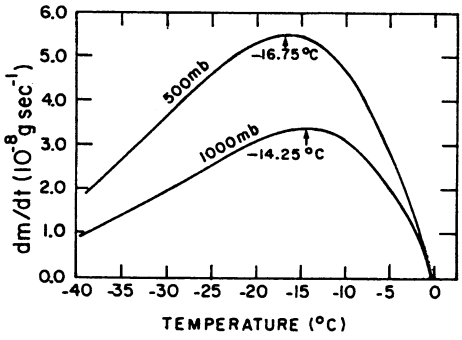


Fig. 13-29: Diffusion mass growth rate dm/dt of an ice crystal with C = $1/4\pi$ in a water saturated environment as a function of temperature. (From Elements of Cloud Physics by H.R. Byers, copyrighted by Univ. Chicago Press, 1965.)

can achieve its maximum value.

Finally, it should be recalled from Section 2.2 that the growth habit of snow crystals is strongly dependent on both temperature and vapor pressure. This implies that C is also indirectly a function of these variables, through its dependence on crystal geometry. Hence, (13-76) can provide a complete description of crystal growth only if $C = C(T, s_{v,i})$ is known (see also Section 13.3.3).

13.3.2 Growth of a Ventilated Snow Crystal

If a snow crystal has grown by vapor diffusion to a size at which it has an appreciable fall velocity, it is necessary to take into account the effect of ventilation on the diffusion of water vapor and heat. This may be done through methods which are entirely analogous to those we have discussed in Section 13.2.3 for the case of spherical water drops, the only additional complication in the present application being the more complex geometry of ice particles. Fortunately, however, experiments on heat and mass transfer from bodies of various shape (e.g., Pasternak and Gauvin, 1960; Brenner, 1963; Skelland and Cornish, 1963) have shown that most of the complications arising from the snow crystal geometry may be effectively circumvented if the ventilation effect is described in terms of a Sherwood number or ventilation coefficient which depends on a particular characteristic length, L^*.

The appropriate definition for L^* follows from a recognition of the physical fact that the degree of ventilation is controlled by that portion of the particle's area which is most directly exposed to the oncoming flow. Thus, we define L^* as the ratio of the total surface area Ω of the body to the perimeter P of its area projected normal to the flow direction:

$$L^* \equiv \frac{\Omega}{P}. \tag{13-81}$$

As a trivial example, we see that for a sphere, $L^* = 2a$. The corresponding mean

Sherwood number is (cf. (13-52)

$$N_{\mathrm{Sh},L^*} \equiv \frac{\bar{k}_{\mathrm{v},\Omega} L^*}{D_{\mathrm{v}}} , \tag{13-82}$$

where, in analogy with (13-50), the mean mass transfer coefficient is defined by

$$\bar{k}_{\mathrm{v},\Omega} \equiv \frac{\mathrm{d}m/\mathrm{d}t}{\Omega(\rho_{\mathrm{v},\infty} - \rho_{\mathrm{v},s})} . \tag{13-83}$$

(Note that $\bar{k}_{\mathrm{v},\Omega} \geq 0$ for particle growth or evaporation.)

From (13-81) to (13-83), the mass rate of change may be expressed in terms of the mean Sherwood number as

$$\frac{\mathrm{d}m}{\mathrm{d}t} = P D_{\mathrm{v}} (\rho_{\mathrm{v},\infty} - \rho_{\mathrm{v},s}) \bar{N}_{\mathrm{Sh},L^*} . \tag{13-84}$$

On comparing (13-84) with the corresponding expression for a stationary crystal, (13-75), we see that the ventilation coefficient, $\bar{f}_{\mathrm{v},L^*}$ defined as in (13-48), is

$$\bar{f}_{\mathrm{v},L^*} \equiv \frac{\mathrm{d}m/\mathrm{d}t}{(\mathrm{d}m/\mathrm{d}t)_0} = \frac{P}{4\pi C} \bar{N}_{\mathrm{Sh},L^*} . \tag{13-85}$$

From this equation, we see that for a stationary particle,

$$\bar{f}_{\mathrm{v},L^*} = 1 , \qquad (\bar{N}_{\mathrm{Sh},L^*})_0 = \frac{4\pi C}{P} . \tag{13-86}$$

In order to make use of (13-84), given $\bar{N}_{\mathrm{Sh},L^*}$, we need expressions for the perimeter P. For a sphere, $P = 2\pi a$; this is also the appropriate expression for a disk or oblate spheroid falling with its maximum dimension normal to the flow direction. For a prolate spheroid in the falling mode of a columnar ice crystal (with its longest extension, $L = 2a$, perpendicular to the direction of all), $P = \pi L y$ with $y = -0.25\varepsilon^2 - 0.0469\varepsilon^4 - 0.0195\varepsilon^6 - 0.0107\varepsilon^8 - 0.0067\varepsilon^{10} - \ldots$, where $\varepsilon = [(1-(b/a)^2]^{1/2}$ is the eccentricity of the spheroid. For an oblate spheroid $P = 2\pi a^2 + \pi(b^2/\varepsilon) \ln[(1+\varepsilon)/(1-\varepsilon)]$, where b and a are the minor and major axes of the spheroid, respectively, and $\varepsilon = [1 - (b/a)^2]^{1/2}$. The surface areas and perimeter of planar and columnar crystals may be computed from Table 2.2a. For bullet rosettes in cirrus clouds, Heymsfield (1975a,b,c) suggests $P = 2(L + \mathrm{w})$ and $\Omega = (\pi \mathrm{w}^2/4) + \pi \mathrm{w} L$, where L is the length of an individual bullet and w is its width.

It appears to be quite difficult to determine experimentally and under controlled conditions, the rate of evaporation of individual snow crystals of a given shape and freely suspended in an air stream. Theoretical studies, on the other hand, have the difficulty of finding an appropriate idealization for the actual shape of the crystal. Pitter *et al.* (1974) and Masliyah and Epstein (1971) idealized the shape of a planar crystal by a thin oblate spheroid and solved the convective diffusion equation (13-47) using another spheroidal coordinate system for Reynolds numbers

which were sufficiently small to justify axially symmetric flow. From an evaluation of ρ_v around the ventilated crystal, $\bar{f}_{v,L^*}$ was determined from

$$\bar{f}_{v,L^*} = -\frac{\int_S (\nabla \rho_v)_S \cdot d\vec{S}}{4\pi C(\rho_{v,s} - \rho_{v,\infty})}, \tag{13-87}$$

(see Eq. 13-54). A few results from these studies are plotted in Figure 13.30. We notice fair agreement between the numerical results of Masliyah and Epstein (1974) and Pitter *et al.* (1971) with the experiments of Thorpe and Mason (1966) for hexagonal plates. The numerical results are also seen to conform, for $\bar{f}_{v,L^*}$ near unity, with the analytical results of Brenner (1963), who solved the convective diffusion equation by the method of matched asymptotic expansions.

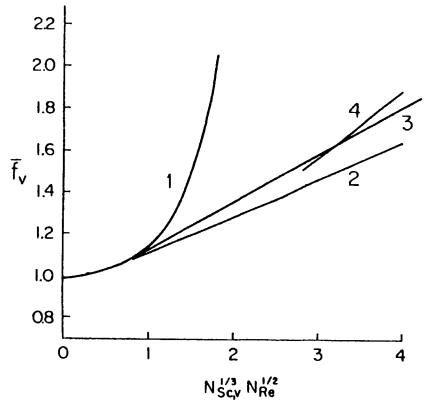


Fig. 13-30: Ventilation coefficient for an oblate spheroid of ice in air ($N_{Sc,v} = 0.71$). (1) Analytical result of Brenner (1963) for infinitely thin circular disk, (2) numerical results of Pitter *et al.* (1974) for spheroid of axis ratio 0.05, (3) numerical result of Masliyah and Epstein (1971) for spheroid of axis ratio 0.2, (4) experimental results of Thorpe and Mason (1966) for hexagonal ice crystals. (From Pitter *et al.*, 1974; by courtesy of Am. Meteor. Soc., and the authors.)

Hall and Pruppacher (1976) suggested that the ventilation coefficient for such idealized snow crystals may adequately be described by

$$\bar{f}_{v,L^*} = 1 + 0.14X^2, \qquad X = N_{Sc,v}^{1/3} N_{Re,L^*}^{1/2} < 1.0, \tag{13-88}$$

$$\bar{f}_{v,L^*} = 0.86 + 0.28X, \qquad X \geq 1.0, \tag{13-89}$$

where $N_{Re,L^*} = V_\infty L^*/\nu$. Subsequently, however, Wang *et al.* (1985) pointed out that the vapor density and temperature fields around falling snow crystals are not adequately described by idealizing their shape in terms of prolate and oblate spheroids, but that rather one has to consider their true shape for getting accurate ventilation coefficients.

Solving (13-2) with flow fields from a numerical simulation of the three-dimensional unsteady viscous flow (see Chapter 10) around two snow crystal types, Ji

(1991) and Wang and Ji (1992) determined the ventilation coefficient $\bar{f}_v$ from (13-87), to find for columnar crystals of $0.2 \leq N_{Re} \leq 20$

$$\bar{f}_v = 1.0 - 0.00668(X/4) + 2.39402(X/4)^2 + 0.73409(X/4)^3 - 0.73911(X/4)^4 ; \tag{13-90a}$$

for simple hexagonal plates Pla of $1.0 \leq N_{Re} \leq 120$

$$\bar{f}_v = 1.0 - 0.6042(X/10) + 2.79820(X/10)^2 - 0.31933(X/10)^3 - 0.06247(X/10)^4 ; \tag{13-90b}$$

and for broad branched crystals Plc $1.0 \leq N_{Re} \leq 120$

$$\bar{f}_v = 1.0 + 0.35463(X/10) + 3.55333(X/10)^2 . \tag{13-90c}$$

In these expressions, we have $X = N_{Sc,v}^{1/3} N_{Re}^{1/2}$, and $N_{Sc,v} = 0.632$. These results are plotted in Figure 13.31.

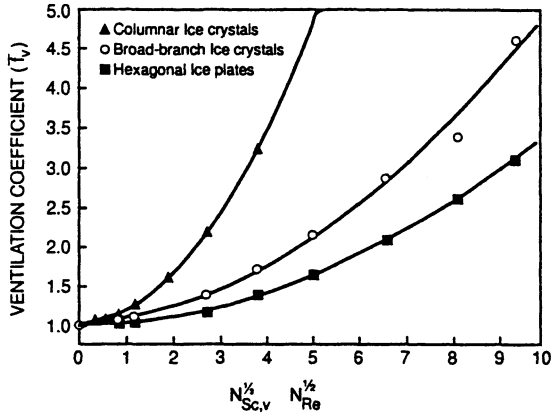


Fig. 13-31: Variation of the ventilation coefficients with Reynolds number as $N_{Sc,v}^{1/3} N_{Re}^{1/2}$ for three types of snow crystals from a solution of the complete non-steady state Navier Stokes equation of motion. (From Ji, 1991, with changes.)

For a falling snow crystal, we may now include the ventilation coefficient in (13-75), and determine its growth rate from

$$\frac{dm}{dt} = 4\pi D_v C \bar{f}_v (\rho_{w,\infty} - \rho_{v,s}) , \tag{13-91}$$

where $\rho_{v,s} = \rho_{v,sat,i}(T_s)$, and where the surface temperature of a ventilated crystal is given by

$$T_s = T_\infty - \frac{L_s D_v M_w}{k_a \mathscr{R}} \left(\frac{e_s}{T_s} - \frac{e_\infty}{T_\infty} \right) \frac{\bar{f}_h}{\bar{f}_v} . \tag{13-92}$$

Hall and Pruppacher (1977) used (13-90) and (13-91) together with (13-88) and (13-89) to determine the growth rate of various snow crystals falling at terminal velocity, on the assumption that the crystals obey the dimensional relationships specified by

Auer and Veal (1970) (see Section 2.2.1) for an environment at water saturation. The results, given in Figure 13.32, show that the differences in growth rates for the various crystal types are small for early growth times, but become increasingly significant with increasing growth time. This is in marked contrast to the case of water drop diffusional growth (recall Figure 13.2), and reflects the fact that the crystal geometry can increasingly 'assert itself' as the crystal size increases.

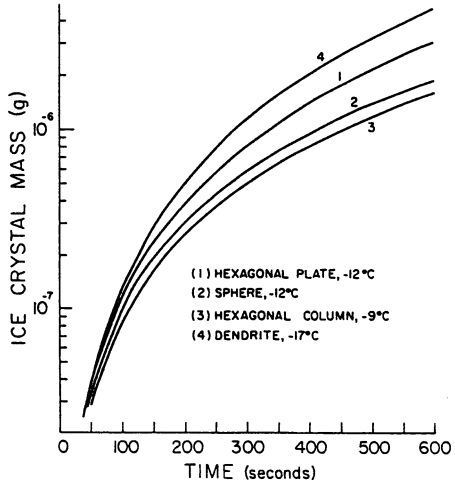


Fig. 13-32: Growth rate of snow crystals of various shapes by diffusion of water vapor in an atmosphere saturated with respect to water at constant temperature. Initial ice crystal radius: 3 μm; $\alpha_c = 0.1$, crystal density given in Table 2-3.

Numerous additional studies on the growth of snow crystals have been reported in the literature (Koenig, 1971; Jayaweera, 1971; Middleton, 1971; Houghton, 1950, 1972; Miller and Young, 1979; Redder and Fuktua, 1989; and Mason, 1994). Unfortunately, a close comparison of these studies is complicated by the different expressions used for the ventilation coefficients, the capacitances, and the different assumed dimensional relationships for the crystals. The growth rates determined theoretically by Middleton are given in Figures 13.33 and 13.34.

The experimental studies of Ryan *et al.* (1974, 1976), Takahashi and Fukuta (1988a,b), Takahashi *et al.* (1991), and the studies reported by Redder and Fukuta (1989) show generally reasonable agreement with the theory regarding both the mass growth as well as the growth of the major dimensions of crystals. However, some discrepancies appear near $-6°$C, a temperature at which needle crystals grow. In this temperature range, the theoretical predictions over-estimate the crystals' mass growth rate as well as the growth rate along crystal axes, perhaps by a factor of as much as three, due to uncertainties in the capacity, the ventilation coefficient, and the dimensional relationship for such crystals. This is particularly evident from a comparison of the experimental values of Takahashi *et al.* (1991) (Figures 13.35 and 13.36) with the theoretical predictions of Middleton (1971) (see Figures 13.33 and 13.34), who used Frössling's (1938) ventilation coefficient

for a sphere and Auer and Veal's (1970) formulae for the crystal dimensions, and with the predictions of Miller and Young (1979), who used (13-88) and (13-89) for computing the ventilation factor and a combination of various formulae for the crystal dimensions.

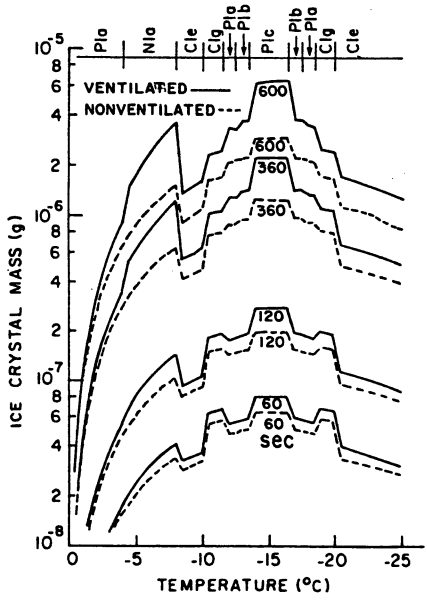


Fig. 13-33: Mass of ice crystals grown by vapor deposition in a water saturated environment computed as a function of growth time (sec) and temperature, including (solid line) and excluding (dashed line) ventilation, at 700 mb. (From Middleton, 1971; by courtesy of the author.)

Generally, we notice from Figures 13.33 to 13.36 that the growth rate is highest at temperatures where needles and dendrites form, while the slowest growth occurs at temperatures favoring the development of solid columns and plates (refer to Figure 2.27 for a translation of the symbols designating crystal type). These differences increase with time, since dm/dt increases with crystal size. Thus, after 10 minutes, a snow crystal growing dendritically at $-15°C$ has acquired a mass which is almost 10 times that of a crystal growing as a solid column near $-8°C$. Also, if we recall from Table 14.3 that planar and columnar snow crystals must grow, respectively, by diffusion to diameters of about $300\,\mu m$ and widths of about $50\,\mu m$ before they can commence riming, we see from Figure 13.35 that this implies a hexagonal plate of type P1a must grow by diffusion at water saturation and $-12°C$ for about 6 minutes before riming is possible. Similarly, a columar crystal must grow for about 3 minutes at water saturation and $-8°C$ before it may commence riming. The significiance of riming to the growth of ice particles has already been pointed out by Jiusto (1971) who showed that after a few minutes growth time by vapor diffusion, riming becomes the dominant growth process if the number of ice forming nuclei is less than a few tens per liter.

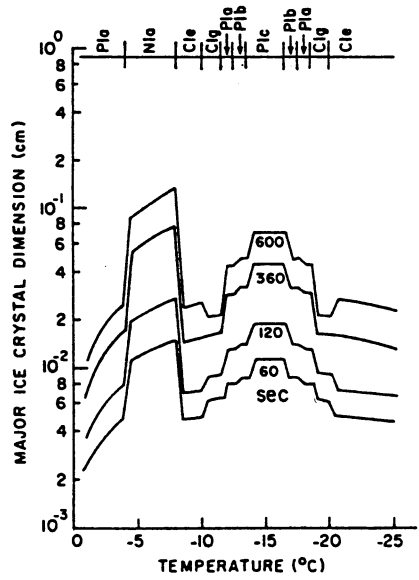


Fig. 13-34: Major dimension of ice crystals grown by vapor deposition in a water saturated environment computed as a function of growth time and temperature, at 700 mb. (From Middleton, 1971; by courtesy of the author.)

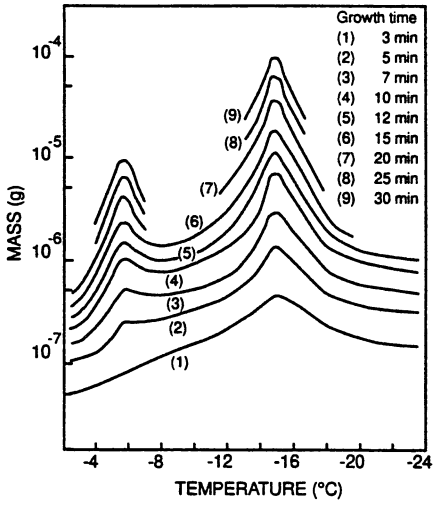


Fig. 13-35: Mass of ice crystals grown by vapor depositon in a water saturated atmosphere, observed as a function of growth time and temperature, at 1000 mb. (From Takahashi *et al.*, 1991, with changes.)

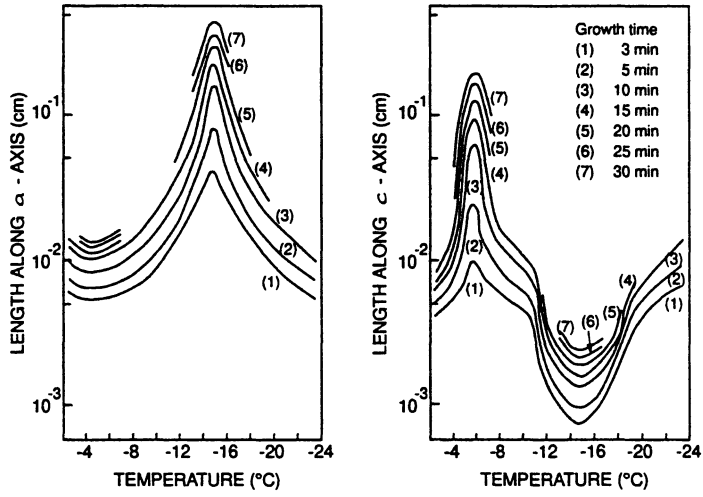


Fig. 13-36: Major dimension of ice crystals grown by vapor deposition in a water saturated atmosphere, observed as a function of growth time and temperature, at 1000 mb. (From Takahashi *et al.*, 1991, with changes.)

TABLE 13.3

Empirical relationships for the variation of the mass m and dimensionless a and c of snow crystals with growth time t. (From Takahashi *et al.*, 1991.)

T(°C)	t(min)	m (g)	a (mm)	c (mm)	Crystal shape
-3.7	< 20	$1.3\times10^{-8}t^{1.40}$	$3.1\times10^{-2}t^{0.46}$	$3.3\times10^{-2}t^{0.42}$	Thick plate (Clg)
-5.3	< 6	$8.4\times10^{-9}t^{2.00}$	$4.0\times10^{-2}t^{0.36}$	$9.7\times10t^{-3}t^{1.95}$	Hollow column (Clf)
	$6< t <30$			$3.6\times10^{-2}t^{1.16}$	Bundle of sheaths (Nld) to needle (Nla)
-8.6	< 15	$2.5\times10^{-8}t^{1.52}$	$3.7\times10^{-2}t^{0.54}$	$2.9\times10^{-2}t^{0.59}$	Thick plate (Clh)
-10.6	< 12	$3.3\times10^{-8}t^{1.51}$	$6.1\times10^{-2}t^{0.48}$	$2.3\times10^{-2}t^{0.53}$	Thick plate (Clh)
-12.2	< 7	$6.3\times10^{-8}t^{1.28}$	$1.2\times10^{-1}t^{0.37}$	$8.5\times10^{-3}t^{0.44}$	Plate(Pla)
	$7< t <20$	$1.1\times10^{-8}t^{2.16}$	$4.1\times10^{-2}t^{0.92}$		Sector (Plb)
-14.4	< 4	$6.4\times10^{-8}t^{1.63}$	$1.4\times10^{-1}t^{0.95}$	$4.4\times10^{-3}t^{0.52}$	Broad branch (Plc)
	$4< t <30$	$2.3\times10^{-8}t^{2.37}$	$1.3\times10^{-1}t^{1.02}$		Dendrite (Ple)
-16.5	< 5	$8.1\times10^{-8}t^{1.36}$	$1.3\times10^{-1}t^{0.54}$	$5.8\times10^{-3}t^{0.48}$	Sector (Plb)
	$5< t <20$	$3.5\times10^{-8}t^{1.91}$	$1.0\times10^{-1}t^{0.74}$		
-18.2	< 15	$4.2\times10^{-8}t^{1.49}$	$6.7\times10^{-2}t^{0.64}$	$1.7\times10^{-2}t^{0.21}$	Plate (Pla) to plate with simple extension (P2e)
-20.1	< 12	$3.8\times10^{-8}t^{1.44}$	$5.4\times10^{-2}t^{0.54}$	$2.6\times10^{-2}t^{0.44}$	Thick plate (Clh)
-22.0	< 12	$3.4\times10^{-8}t^{1.42}$	$4.0\times10^{-2}t^{0.49}$	$3.6\times10^{-2}t^{0.48}$	Thick plate (Clh)

TABLE 13.4

Final diameter and mass of snow crystals which had fallen from a level of −20°C to a level of 0°C while growing by diffusion in a water vapor saturated environment of temperature lapse rate of 6.5°C km^{-1}. The crystals are assumed to keep their original shape. (Based on data of Mason, 1994.)

Type	d_{crystal} (μm)	m_{crystal} (μg)	d_{drop} (μm)
frozen drop	420	35	400
simple plate	1980	160	670
sectar plate	4600	415	925
stellar dendrite	5300	545	1000

For the sake of convenience, we have included empirical relationships in Table 13.3 for the time dependence of the crystal mass and dimensions along the a and c axes, as a crystal grows at a particular temperature level between −3 and −22°C.

It is quite instructive to compute the mass gained by an ice crystal while falling from a level of −20°C to the 0°C level in a water saturated environment with a temperature lapse rate of 6.5°C km^{-1}. Such a computation was carried out by Mason (1994), who assumed that the crystal retains its shape during the entire fall. Using various empirical relationships for $\bar{f}_v, \rho_c, C$, and for the fall velocity of the ice particles, he arrived at the values given in Table 13.4. He deduced from his results that the more complex shapes achieve a greater mass while falling between the considered temperature levels, partly because they fall more slowly and therefore grow for a longer time. Consequently, when they melt below the 0°C level, they produce larger raindrops which, in turn, may grow even larger by accretion of cloud droplets, and will suffer less evaporation as they fall through unsaturated air below the cloud base. The more complex shapes are therefore more efficient in releasing precipitation, provided the cloud lasts long enough. From Table 13.4, Mason (1994) further concluded that no single crystal, even if it were able to retain its original shape during growth, could produce a raindrop of sufficient size to account for the drop sizes observed to fall from layer clouds, where for moderate rainfall rates of 2 mm hr^{-1}, the median volume drop diameter is 1.2 mm (Mason, 1972).

From our discussion on fogs and stratus (see Section 13.2.2.2), we infer that the growth and evaporation of cirrus cloud layers also will be affected by radiation. Ice is more absorbing of solar radiation than is water (Hobbs, 1974), so that the growth and evaporation of ice crystals in cirrus clouds is more sensitive to the influence of radiation than is the case for water drops. In addition, high-level cirrus clouds generally have an ice content which is much lower than that of lower-level clouds. The low water content and the consequent reduction in optical path, imply that the radiative effects in cirrus will be spread through a greater depth of cloud than is the case in water clouds.

The effects of radiative processes on the development and structure of cirrus clouds have been studied by various authors using numerical models which incorporate both microphysical and radiative processes. Thus, Starr and Cox (1985a,b)

and Starr (1987) concentrated largely on the effect of radiation on cloud structure, while Ramaswami and Detwiler (1986) were concerned more with the interaction between radiation and microphysical properties. In Figure 13.37, the overall radiative effects computed by Starr and Cox (1985b) on the ice content of modeled cirrus clouds for midday and night-time conditions are given. We notice that long wave cooling enhances the ice content of cirrus clouds.

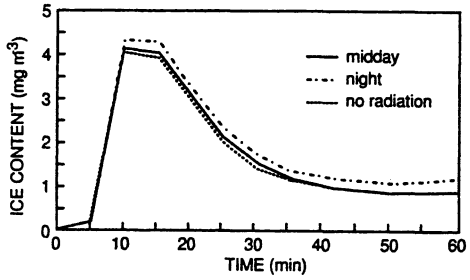


Fig. 13-37: Effects of radiation on the behavior of the domain ice content in modeled cirrus clouds at a height of 7 km. (From Starr and Cox, 1985b, with changes.)

According to Jonas (1989), radiative effects on the growth and evaporation of cirrus cloud crystals depend crucially on the presence of upper and lower cloud decks. For the case of a thin layer of cirrus with a clear sky above and a thick layer of cloud below, Jonas (1989) estimated a maximum cooling of 50 Watt per square meter of ice crystal surface. Using this cooling rate, he estimated that the supersaturation separating evaporation and growth of a crystal would be reduced by 5% for needle-shaped crystals of an equivalent radius of 200 μm, and by about 10% for plate-like snow crystals. This result verified the earlier calculations of Braham (1967) and Braham and Spyers-Duran (1967), which implied that cirrus cloud crystals survive over considerable fall distances.

Computations of the survival distance of cirrus crystals have been made by Hall and Pruppacher (1977) using (13-91), crystal fall velocities according to Heymsfield (1972), and the dimensional relations for the crystal shapes given by Heymsfield and Knollenberg (1972) and Auer and Veal (1970). By using maximum and minimum limits for the upward and downward radiation fluxes at cirrus cloud levels, and by considering the emission and absorption properties of ice, they concluded that radiative heat transfer affects the survival distance of columnar snow crystals falling from cirrus clouds by less than 10% if the relative humidity of the environmental air is less than 70%. From a consideration of these radiative effects and a wide range of values for the initial size and bulk density of the ice particle, they showed that snow crystals falling from cirrus clouds can survive fall distances of up to 2 km when the relative humidity is below 70% in a typical midlatitude atmosphere. Larger survival distances are possible only if the ambient air has a relative humidity larger than 70%. A comparison of their theoretical results with a field study by Heymsfield (1973) of the survival distance of cirrus ice particles is shown in Figure 13.38. Note that the theoretical predictions for $\rho_c = 0.75$ g cm^{-3} and $\rho_c = 0.9$ g cm^{-3} agree

satisfactorily with the lowest level (sample base) at which cirrus ice particles were detected.

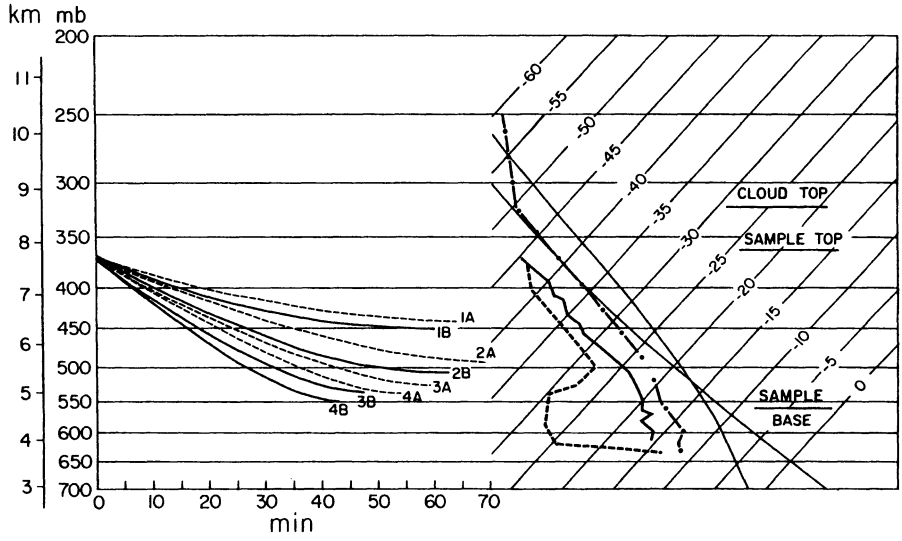


Fig. 13-38: Comparison between the survival distance of cirrus ice particles theoretically computed by Hall and Pruppacher (1977), and observed by Heymsfield (1973) on March 4, 1972 above Salem (Illinois). On right: $-.-.-.$ radiosonde data of Salem, — temperature, $- - -$ dew point, measured by aircraft in situ. On left: computed fall distances, (1) ρ_c = 0.3 g cm^{-3}, (2) ρ_c = 0.5 g cm^{-3}, (3) ρ_c = 0.75 g cm^{-3}, (4) ρ_c = 0.9 g cm^{-3}; (A) column, initial size 800 × 164 μm, (B) sphere, initial radius 160 μm; α_d = 0.014. (From Hall and Pruppacher, 1976; by courtesy of Am. Meteor. Soc., and the authors.)

Hall and Pruppacher also determined the final length of columnar crystals, of given length and width, which make an isobaric and isothermal excursion of 200 m out of a cirrus cloud into air of −32.7°C and 400 mb, for various relative humidities. As would be expected, the results given in Figure 13.39 are qualitatively similar to those shown in Figure 13.27 for the case of isobaric and isothermal excursions of water drops. Thus, for the stated conditions, the initial crystal lengths must be greater than 210, 320, 410, and 480 μm in order to survive the 200 m distance if the relative humidities are 90, 70, 50, and 30%, respectively.

Considering how fragile snow crystals are, one might wonder whether evaporating snow crystals would not break up into smaller fragments. Oralty and Hallett (1989) studied this problem in a wind tunnel and found that evaporating crystal plates and columns would not break up while evaporating. Also, dendritic snow crystals did not break up as long as the relative humidity was above 70%. However, at relative humidities below 70% , ice dendrites would break up, producing up to 50 ice splinters per crystal of 5 mm diameter.

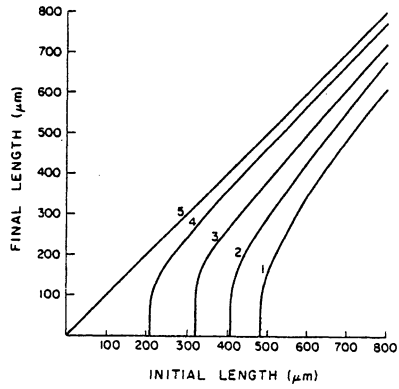


Fig. 13-39: Final length of columnar ice crystals of given initial length after an isobaric and isothermal excursion of 200 m into air of (1) 30 %, (2) 50 %, (3) 70 %, (4) 90 % relative humidity, at $-32.7°$C and 400 mb, for $\alpha_d = 0.1$, (5) limiting case of no evaporation; crytal width w and length L are related by $w = 0.0627\ L^{0.53}$. (From Hall and Pruppacher, 1976; by courtesy of Am. Meteor. Soc., and the authors.)

13.3.3 Growth Rate of Snow Crystal Faces - Snow Crystal Habit Change

The fact that the theoretical framework for crystal growth given by (13-91) and, for example, (13-88), is incomplete without a specification of $C = C(T, s_{v,i})$ indicates clearly that a consideration of vapor and heat exchange between the crystal and its environment cannot provide by itself a complete description of crystal growth mechanisms. The reason for this is that, in addition to the driving forces of vapor and heat gradients, there are also crystal surface forces which control the incorporation of water molecules into the ice lattice. From the observed changes in crystal growth habit with temperature, these latter forces are evidently sensitive functions of temperature, and are different for different crystal faces.

The extent to which the surface forces alone control the growth habit of ice crystals has been studied experimentally by Lamb and Hobbs (1971). They measured the 'linear' growth rates of the basal and the prism faces of ice crystals under conditions which ensured that the growth of the crystals was controlled by molecular events taking place at the crystal surface, and not by the rate of supply of water molecules from the vapor phase or by the rate at which latent heat of deposition was removed. For this purpose, the measurements were carried out in pure water vapor at a constant excess vapor pressure of 1.3×10^{-2} mb; such low pressures reduce the vapor and heat gradients to negligible levels. The results of this study are shown in Figure 13.40, where it can be seen that the growth rates of the prism and basal faces vary strongly with temperature, decreasing rapidly at first with decreasing temperature, and subsequently increasing sharply to a maximum followed by a monotonic decrease with a further decrease in temperature. Note also that the growth rate curves are shifted with respect to each other, crossing at -5.3 and

$-9.5°$C. At temperatures from 0 to $-5.3°$C and at temperatures from -9.5 to near $-22°$C, the linear growth rate of the prism face is larger than that of the basal face, implying a-axis growth and thus the development of plate-like ice crystals. On the other hand, at temperatures between -5.3 and $-9.5°$C and at temperatures below about $-22°$C, the basal face has a linear growth rate which is larger than that of the prism face, implying c-axis growth and thus the development of columnar ice crystals. These results are in reasonable agreement with the observed growth habit behavior of snow crystals in air under natural conditions, which demonstrates the dominance of surface kinetic effects in controlling the basic growth habit.

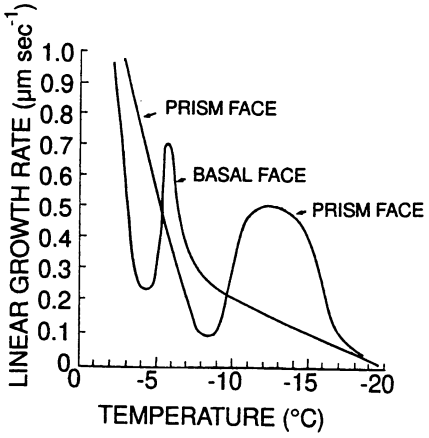


Fig. 13-40: Best fit curves to experimental measurements of the linear growth rates on the basal and prism faces of ice, at constant vapor pressure excess of 1.3×10^{-2} mb. (From Lamb and Hobbs, 1971, with changes.)

Given the linear growth rates G_B and G_P of the basal and prism faces, the mass growth rate of the crystal can evidently be determined from the relation

$$\frac{\mathrm{d}m}{\mathrm{d}t} = \rho_c[G_B(T)\Omega^{(B)} + G_P(T)\Omega^{(P)}]\,, \tag{13-93}$$

where ρ_c is the density of the crystal and $\Omega^{(B)}$ and $\Omega^{(P)}$ are the total respective areas of the basal and prism faces. From Figure 5.10, we easily find $\Omega^{(B)} = 4\sqrt{3}a'^2$ and $\Omega^{(P)} = 4\sqrt{3}a'H$, where H is the height of the hexagonal prismatic snow crystal, and a' is the radius of the circle inscribed in the hexagonal base of the ice prism. Since, in an environment of pure water vapor, the linear growth rates are constant with time at any one temperature, $a' = G_P(T)t$ and $H = 2G_B(T)t$. On combining these relations with (13-93), we obtain

$$\frac{\mathrm{d}m}{\mathrm{d}t} = 12\sqrt{3}\rho_c G_P^2 G_B t^2\,. \tag{13-94}$$

The growth rate described by (13-94) was referred to by Lamb and Hobbs (1971) as 'inherent', since it is governed by kinetic processes on the surface of ice and not

by diffusion of water vapor or heat through air. With their experimental values of G_P and G_B, Lamb and Hobbs evaluated (13-94) and obtained the results shown in Figure 13.41. We see that the 'inherent' growth rate attains peak values near -6 and $-12°C$, which are separated by a minimum near $-8°C$. Since these results are quite similar to those for a crystal growing at water saturation in air, we again conclude that surface kinetic effects must largely control the growth habit of snow crystals.

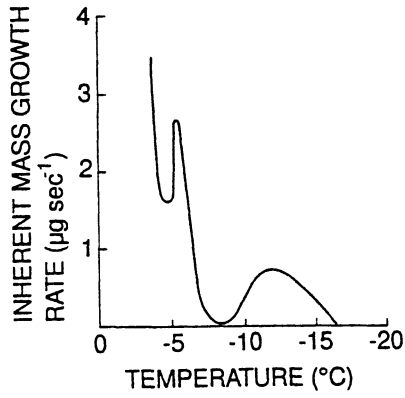


Fig. 13-41: 'Inherent' mass growth rate of ice after 1000 sec as a function of temperature at constant excess vapor pressure of 1.3×10^{-2} mb, based on the linear growth rates given in Figure 13-32. (From Lamb and Hobbs, 1971; by courtesy of Am. Meteor. Soc., and the authors.)

As for the modifications expected from the effects of finite vapor and heat gradients, we may first note that the second maximum near $-12°C$ in Figure 13.41 should be enhanced relative to the first by virtue of the fact that $e_{sat,w} - e_{sat,i}$ attains a maximum value for $T \approx -12°C$ (see Figure 4.5). Also, once the crystal habit has been decided by surface kinetic effects at an early stage of crystal development, the vapor flux to the crystal will not significantly alter its geometry, at least for low to moderate vapor density excess, since the excess water mass arriving at the corners and edges of the crystal can be effectively redistributed by surface diffusion. However, at a sufficiently high vapor density excess, surface diffusion will no longer suffice to compensate for the large non-uniform vapor deposition. Growth will then occur preferentially at the corners (where the liberated latent heat is also most effectively dissipated), and this will result in the formation of sector plates, dendrites, stellars, etc.

In attributing the characteristics of the mass growth of an ice crystal to the characteristics of the linear growth rate of its crystallographic faces, we of course have really done nothing more than exchanged one problem for another. Thus, for a further understanding of the mass growth rate behavior of ice crystals, we must attempt to gain further insight into the linear growth rate mechanism. For this purpose, we may note the experimental results of Hallett (1961) and Kobayashi (1967), who determined the rate of propagation of steps at the surface of snow

crystals. They found that steps of heights between 200 to 1000 Å have propagation velocities which are inversely proportional to the step height. Furthermore, the propagation velocities increase with increasing excess vapor density, and exhibit at constant excess vapor density a characteristic variation with temperature. If the results of Kobayashi are corrected for the effect of heating of the crystal surface by latent heat release (according to Ryan and Macklin (1969)), the measurements of Hallett and of Kobayashi agree with each other in suggesting that, at constant excess vapor pressure, the step propagation velocity on the basal face of a snow crystal decreases with increasing temperature in the interval 0 to $-4°C$ to reach a minimum near $-4°C$, then sharply increases in the interval -4 to $-6°C$ to reach a maximum near $-6°C$, and subsequently decreases monotonically towards $-20°C$. This behavior is indicated in Figure 13.42. Note, from a comparison of this figure with Figure 13.40, that the temperature variation of the step propagation velocity on the basal face of ice is practically identical to that of the linear growth rate of the basal face. Unfortunately, no similar experimental study is available for the step propagation velocity on the prism face of ice.

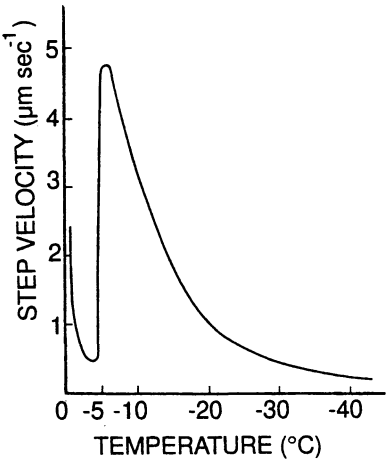


Fig. 13-42: Variation with temperature of the propagation velocity of steps 250×10^{-8} cm high on the basal face of ice; excess vapor density 0.25×10^{-6} g cm^{-3}. (From Hallett, 1961; by courtesy of *Phil. Mag.*, and the author.)

It is reasonable to find that the linear growth rate G of a crystallographic face of ice is proportional to the step propagation velocity v_0 on that face, since the rate at which the face grows depends directly on how fast the successive molecular layers can be formed. On the other hand, this argument implicitly assumes that there is no time lag in the initiation of each new successive layer. Since rapid step regeneration by nucleation is improbable at the low supersaturations prevailing under natural conditions, another mechanism must be responsible. Perhaps the most likely candidate is that of Frank (1949), who proposed the emergence of screw dislocations at the crystal surface (recall Figure 5.11). If we assume now

that a step is part of a screw dislocation, and that the latter can be represented by an Archimedes spiral, i.e., $r(\theta) = K\theta$, where K is a constant and $\vec{r} = \vec{r}(r, \theta)$ is the radius vector from the dislocation center to any point on the spiral, then for each full rotation of the spiral, another step will be released without delay from the spiral center and allowed to propagate across the crystal face. Furthermore, in this case, the frequency of step regeneration will be $f = \omega/2\pi$, where $\omega = \mathrm{d}\theta/\mathrm{d}t = K^{-1}\mathrm{d}r/\mathrm{d}t = v_0/K$; hence, the linear growth rate of the crystals face will be

$$G = f\mathsf{h} = \frac{v_0\mathsf{h}}{2\pi K}\,, \tag{13-95}$$

where h is the step height. Thus, we find $G \propto v_0$ for a screw dislocation growth process, and also that the spacing between the steps is given by $\Delta x = 2\pi K$.

Hallett (1961) interpreted his finding that $v_0 \propto \mathsf{h}^{-1}$ as an indication that steps grow largely by surface diffusion, using arguments similar to those presented in Section 5.7.3 for estimating the bunching time of monolayers on an ice surface. Thus, if d_S is the average migration distance which adsorbed water molecules travel by surface diffusion before re-evaporating, then it is reasonable to assume that a step of height h and unit length will receive material by surface diffusion at the rate $2\mathrm{w}_{\mathrm{net},i}d_S$ and by direct deposition from the vapor at the rate $\mathrm{w}_{\mathrm{net},i}\mathsf{h}$ where $\mathrm{w}_{\mathrm{net},i}$, given by (5-55), is the net flux to the surface (assumed to be uniform over the surface). Hence, if ρ_i is the density of ice, the velocity of the step is

$$v_0 = \frac{\mathrm{w}_{\mathrm{net},i}}{\mathsf{h}\rho_i}(2d_S + \mathsf{h})\,. \tag{13-96}$$

Hence, if $d_S \gg \mathsf{h}$ the step will grow by surface diffusion such that $v_0 \propto \mathsf{h}^{-1}$, which is consistent with Hallett's measurements. Also, given this result, we find from (13-95) that the growth rate has the form $G \approx \mathrm{w}_{\mathrm{net},i}d_S/\pi K$ i.e., it is independent of the step height and velocity, and the migration distance d_S emerges as the key surface parameter.

Mason *et al.* (1963) estimated d_S as one half of the critical separation for which the velocity of approach of two neighboring growth layers slows down (see Section 5.7.3). If their measured values are corrected for crystal surface heating from latent heat release (Ryan and Macklin, 1969), excellent agreement among the temperature variations of $d_S^{(B)}$, $v_0^{(B)}$, and G_B for the basal plane is found.

Unfortunately, no experiments have yet been carried out to determine $d_S^{(P)}$ on the prism plane of ice. Physical reasoning suggests, however, a similar agreement among the temperature variations of $d_S^{(P)}$, $v_0^{(P)}$, and G_P for this plane. If verified, plate-like crystals would then be expected to form preferentially in those temperature intervals in which the inequalities $d_S^{(P)} > d_S^{(B)}$, $v_0^{(P)} > v_0^{(B)}$ and $G_P > G_B$ hold. Similarly, columnar crystals would form preferentially in the temperature intervals in which one finds $d_S^{(B)} > d_S^{(P)}$, $v_0^{(B)} > v_0^{(P)}$, and $G_B > G_P$.

In order to estimate the imigration distance $d_S^{(P)}$ on the prism face of ice, Mason (1994) considered a hexagonal prism whose height is $2c$ and whose edge length of

the basal face is a. The growth rates of the crystal faces can then be written as

$$\left(\rho_i \frac{\mathrm{d}V}{\mathrm{d}t}\right)_{a=\text{const}} = 2\Omega_B F_B + 12a(d_S^{(P)} F_P - d_S^{(B)} F_B)\,, \tag{13-97}$$

$$\left(\rho_i \frac{\mathrm{d}V}{\mathrm{d}t}\right)_{c=\text{const}} = 6\Omega_P F_P + 12a(d_S^{(B)} F_B - d_S^{(P)} F_P)\,, \tag{13-98}$$

where V is the crystal volume, F_B and F_P are the vapor fluxes to the basal and prism faces, respectively, $d_S^{(B)}$ and $d_S^{(P)}$ are the migration distances on the basal and prism faces, respectively, and ρ_i is the density of ice. The second term in each equation represents the net fluxes of molecular migration from the neighboring faces within a distance $d_S^{(B)}$ and $d_S^{(P)}$, respectively, to their edges of total length $12a$. For $(\mathrm{d}V/\mathrm{d}t)_{a=\text{const}} = 3a^2\sqrt{3}(\mathrm{d}c/\mathrm{d}t)$ with $2\Omega_B = 3a^2\sqrt{3}$, and $(\mathrm{d}V/\mathrm{d}t)_{c=\text{const}} = 12ac(\mathrm{d}a/\mathrm{d}t)$ (with $\sqrt{3}/2 \approx 1$), Mason finds

$$\left(\rho_i \frac{\mathrm{d}c}{\mathrm{d}t}\right)_{a=\text{const}} = F_B + \frac{4}{a\sqrt{3}}(d_S^{(P)} F_P - d_S^{(B)} F_B)\,, \tag{13-99}$$

$$\left(\rho_i \frac{\mathrm{d}a}{\mathrm{d}t}\right)_{c=\text{const}} = F_P + \frac{1}{c}(d_S^{(B)} F_B - d_S^{(P)} F_P)\,. \tag{13-100}$$

Combining (13-99) and (13-100), Mason (1993) obtained

$$\frac{\mathrm{d}c}{\mathrm{d}a} = \frac{\gamma - \frac{4}{a\sqrt{3}}(\gamma d_S^{(B)} - d_S^{(P)})}{1 + \frac{1}{c}(\gamma d_S^{(B)} - d_S^{(P)})}\,, \tag{13-101}$$

with $\gamma = F_B/F_P$, so that for $a \gg d_S^{(B)}$ and $c \gg d_S^{(P)}$, $(\mathrm{d}c/\mathrm{d}a) \to \gamma$. In order to evaluate $d_S^{(P)}$ from (13-101), Mason (1994) made use of his earlier empirical results (Mason, 1953) and those of Shaw and Mason (1955) and Kobayashi (1961), which showed that the aspect ratio (c/a) of a small growing snow crystal whose shape is largely determined by the values of $d_S^{(B)}$ and $d_S^{(P)}$ tends to approach a limiting value for a given temperature when the long dimension of the crystal exceeds about $200\,\mu$m (see Figure 13.43a). Assuming that a crystal grows from a small isometric nucleus (e.g. a frozen drop) with $a_0 = c_0 = 20\,\mu$m, Mason numerically integrated (13-101) to determine the values of $d_S^{(P)}$ which allow the crystals to reach the limiting values of (c/a) shown in Figure 13.43a. As constraints for this integration, Mason assumed $d_S^{(P)} = d_S^{(B)}$ at -3°C, -8°C, and -25°C (where the observed habit changes occur). The values for $d_S^{(P)}$ thus obtained are plotted in Figure 13.43b. We notice that Mason's curve has the expected shape and is supported in the temperature range -12 to -20°C by solutions to (13-101) using the experimental values of Kobayashi (pers. comm. to Mason) for c, a, and $\mathrm{d}c/\mathrm{d}a$.

Of course, Mason's (1994) results have not brought us any closer to the problem we need to solve. By explaining the temperature dependence of the ice crystal habit on the basis of a temperature variation of the migration distance of water molecules on both ice crystal surfaces, we have merely again only exchanged one problem for

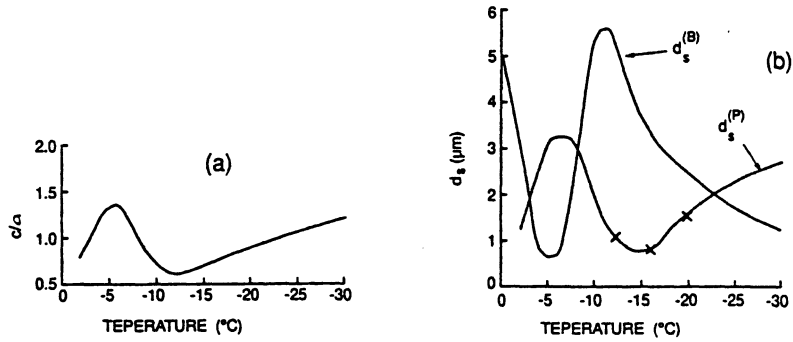


Fig. 13-43: (a): Variation with temperature of the limiting axis ratio c/a for small ice crystals. (b): Mean surface migration distance d_S as a function of temperature for the basal face d_S and prism face $d_S^{(P)}$; $d_S^{(B)}$ derived from observation, $d_S^{(P)}$ derived from (13-101); ($\times$) values derived from observations of c, a , and dc/da of Kobayashi. (From Mason, 1994, with changes.)

another, as no physical explanation is available for the reason why the migration distance of water molecules should have the indicated temperature variation. In earlier research, Mason *et al.* (1963), Hobbs and Scott (1965), and Lamb and Scott (1974) attempted to relate d_S to the energy of adsorption and desorption of water molecules on ice. However, this did not lead to a better understanding of the problem either, since even now no knowledge is available on the reason for the temperature dependence of these energies.

Similarly, the detailed studies of Kuroda (1982, 1984), Kuroda and Gonda (1984), and Yokoyama and Kuroda (1988) on the growth of kinetics of snow crystals in terms of two-dimensional nucleation after Hillig (1966), or in terms of the spiral growth steps after Burton *et al.* (1951), or in terms of adsorbed layers of water molecules after Cabrera and Levine (1956), or and in terms of the pseudo-liquid layer on the ice surface, could not pinpoint the reason for the temperature variation of the snow crystal shape. This is so, since no exact temperature variation of any of these mechanisms could be found. Thus, it appears that at present the basic mechanism which controls the characteristic temperature variation of the shape of snow crystals still needs to be resolved.

CHAPTER 14

CLOUD PARTICLE INTERACTIONS

In Chapter 10, we discussed the behavior of isolated cloud particles in some detail. Now we shall consider their hydrodynamic interactions, with a view to providing a quantitative assessment of the processes of particle growth by collision and coalescence, and of collisional breakup. We shall first treat the collision problem for drops of radii less than about 500 μm which, in accordance with our previous description of drop distortion in Section 10.3.2, may be regarded as rigid spheres (at least when falling in isolation). This will be followed by a discussion of the phenomena of drop coalescence and breakup. Finally, we shall consider water drop-ice crystal and ice crystal-ice crystal interactions, which lead to the formation of graupel, hail, and snow flakes.

14.1 The Basic Model for Drop Collisions

In any cloud, the effectiveness of the drop interaction process will be determined in part by such factors as uplift speed and entrainment, droplet charge and external electric field, and turbulence. For simplicity, we shall consider first the basic problem of determining the interaction of droplets falling through otherwise calm air under the influence of gravity and the hydrodynamic forces associated with their motion. Turbulence-enhanced gravitational collision is briefly discussed in Sections 14.5.2 and 17.4.2.4, while the effects of electric fields and charges are discussed in Chapter 18.

Although in principle the collision problem is a many-body problem, droplet concentrations in natural clouds are low enough so that only the interactions of pairs of droplets need be considered. This is supported by arguments presented in Section 2.1.5 and Appendix 2.1.5. It is clear that such interactions must occur extensively if rain is to form. From Chapter 13, we know that the initial stage of droplet growth by vapor diffusion produces a fairly uniform distribution, with droplets generally of 1 to 10 μm radius, thus possessing only 10^{-6} or so of the mass of a typical 1 mm diameter raindrop. Further broadening of the spectrum toward precipitation-sized droplets (conveniently defined as those with radii $\geq 100\,\mu$m) is possible only when conditions in the cloud are such that droplets can collide and coalesce.

In order to avoid excessive mathematical complications, we shall also assume that interacting drops which are spherical in shape when falling in isolation, remain so for all separations of their surfaces. As we shall see, the reasonableness of this assumption is borne out by the general good agreement between the resulting predicted and observed effective collision cross sections. The shape-distortions

which may occur when the drops are in close proximity may thus be considered of secondary importance in most cases of interest.

In consequence of these simplifying assumptions, the basic physical model for the collision problem reduces to one of two rigid spheres, initially with a large vertical separation, falling under gravity in an otherwise undisturbed and unbounded fluid.

14.2 Definition of Collision Efficiency

The essential piece of information to be extracted from a study of the collision model described above is the effective cross-section for the collision of the two spheres. Thus, the goal is to find y_c, the initial horizontal offset of the center of the lower (smaller) sphere of radius a_2, from the vertical line through the center of the upper (larger) sphere of radius a_1 such that a grazing trajectory will result (see Figure 14.1). Then, y_c/a_1 , called the *linear collision efficiency*, is a simple dimensionless measure of the tendency for collision. Another measure is the *collision efficiency*, E, defined here to be the ratio of the actual collision cross-section πy_c^2 to the geometric cross-section $\pi(a_1 + a_2)^2$:

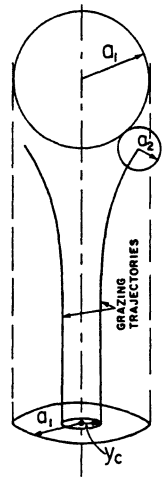


Fig. 14-1: Schematic representation of the hydrodynamic interaction of a pair of spheres; y_c is the critical, horizontal offset for a grazing trajectory of the small sphere.

$$\mathrm{E} \equiv \frac{y_c^2}{(a_1 + a_2)^2} \,. \tag{14-1}$$

Thus, on introducing the size ratio $p \equiv a_2/a_1$, we have the simple relationship

$$y_c/a_1 = (1 + p)\mathrm{E}^{1/2} \,. \tag{14-2}$$

Equation (14-2) assumes rotational symmetry, which means that it strictly applies only to flow past a sphere for $N_{\mathrm{Re}} < 300$. Also, (14-2) cannot be used for comparing the collision efficiency of differently shaped collectors, since columnar

or plate-like, crystals, for example, are not uniquely characterized by their radii. Wang (1983) has therefore suggested a more general definition in terms of the gravitational collision kernels (see Equation 11-85):

$$\mathrm{E} \equiv K/K^* , \tag{14-3}$$

where K and K^* are the effective and geometric volumes, respectively, swept out by the collector per unit time. Thus, two collectors of the same K^* sweep out equal volumes of air in unit time, even if their shapes are different. In this sense, they have also the same opportunity to collide with smaller bodies in their path. For rotational symmetry involving the collision of two spheres $K^* = \pi(a_1+a_2)^2(U_{\infty,1} - U_{\infty,2})$ and $K = \pi y_c^2(U_{\infty,1} - U_{\infty,2})$, which leads back to give (14-1).

Let us now consider the dependence of E on the physical parameters characterizing the problem. The initial vertical separation z_0 for unequal droplets is taken to be large enough so that they fall independently in the beginning; thus E will not depend on z_0. For equal droplets, this condition must be altered slightly, and we start with a vertical separation such that interaction is at a threshold. We can repeat trials with varying separation, and look for the limiting value of E as the separation increases. In practice, it has been found that E is generally insensitive to z_0 if $z_0 \geq 10^2 a_1$ for any size ratio a_2/a_1. In fact, most of the collision efficiency calculations, to be subsequently discussed, have been carried out for $z_0 = 50a_1$, following the conclusions of Hocking (1959) and Lin and Lee (1975) that no significiant differences in collision efficiency were found by setting $z_0 = 100a_1$ or $z_0 = 50a_1$.

Therefore, assuming we start with a large enough z_0, the only independent parameters which could possibly play a role in the interaction process are a_1, a_2, the kinematic viscosity ν and density ρ of the fluid (air), the density ρ' of the spheres (water), the acceleration g of gravity, and y, the initial horizontal offset. A collision ($y = y_c$) may therefore be described by some relation of the form $f_1(a_1, a_2, \nu, g, \rho, \rho', y_c) = 0$. By applying the π-theorem of dimensional analysis (which states that in an equivalent dimensionless formulation of a physical problem, the number of independent dimensionless parameters equals the number of independent dimensional parameters occurring in the original problem, less the number of dimensions involved - see, for example, Kline (1965)), this relationship may be expressed equivalently in terms of four dimensionless combinations of the seven parameters. For example, we may write $f_2(\mathrm{E}, a_2/a_1, \rho/\rho', ga_1^3/\nu^2) = 0$; or, explicitly in terms of E,

$$\mathrm{E} = \mathrm{E}(a_2/a_1, \rho/\rho', ga_1^3/\nu^2) . \tag{14-4}$$

Since $\rho/\rho', g$, and ν are fixed in the case of water droplets falling in air, we have in this case

$$\mathrm{E} = \mathrm{E}(a_2/a_1, a_1) . \tag{14-5}$$

In other words, the collision process for cloud droplets in air can be described by a one-parameter set of curves. The usual display is of E versus a_2/a_1, with a_1 as the curve label. (Of course, ν and ρ' will vary with height and this will also affect the value of E. For example, de Almeida (1977) calculated a 22% increase in E for a change in ambient conditions from 995 mb, 14°C to 800 mb, 25°C.)

One may anticipate the qualitative shape of the curves described by (14-5). The tendency for the small sphere to move with the flow around the large sphere is depicted schematically in Figure 14.1. As a consequence of this tendency for deflection by viscous forces from a collision trajectory, one can anticipate that generally $E < 1$ (except possibly for $a_2/a_1 \to 1$; see below). Since the forces of deflection must become less effective as the inertia of the spheres increases, E should be a monotonic increasing function of a_1. For the same reason, E also should be a monotonic increasing function of a_2/a_1 at least for $a_2/a_1 \ll 1$. However, the situation for a_2/a_1 approaching unity is not obvious. For example, as $a_2/a_1 \to 1$ the relative velocity of approach decreases so that small forces of deflection have a relatively long time to operate and, hence, prevent a collision. This effect tends to reduce E. On the other hand, there is the possibility of 'wake capture' as the trailing sphere falls into the wake of the leading sphere, and thus encounters less resistance to motion than the latter. This effect tends to increase E. (Another form of 'wake capture' for the case of $a_2/a_1 \ll 1$ is discussed in Chapter 17.) The overall result can be determined only by elaborate calculations, and as we shall see below, there is not yet complete agreement, even as to the qualitative outcome. However, since the strength and size of the wake increases with the Reynolds number, one at least may expect the wake capture effect to increase strongly with increasing a_1. In summary then, we may expect to find $E \ll 1$ for sufficiently small a_1 and for $a_2/a_1 \ll 1$ with arbitrary a_1. Also, E should increase with a_1 for fixed a_2/a_1 and there is a possibility of a greater than geometric cross-section ($E > 1$) by wake capture as $a_2/a_1 \to 1$ for sufficiently large a_1.

Note that if one hopes to simulate the collision process in the laboratory (which is desirable since it is difficult to observe the collision of small droplets in air), it is sufficient that $a_2/a_1, \rho/\rho'$, and a_1^3/ν^2 have the same values in the laboratory as in the natural cloud. Unfortunately, it has not been possible to model this way. To be a useful operation, the simulation should employ easily observable (large) spheres, and high viscosities in order to achieve low velocities. But then the density ratio ρ/ρ' cannot be preserved; whereas in clouds this ratio is about 10^{-3}, in model experiments it is generally larger than about 5×10^{-2}. However, we shall see later there is some evidence that practical similitude may be achieved so long as $\rho/\rho' \lesssim 10^{-1}$ in the laboratory, and this less severe modeling constraint can be met.

From (10-142) and (10-144), it can be seen that the parameter ga_1^3/ν^2 is a function only of ρ/ρ' and the terminal velocity Reynolds number $N_{\mathrm{Re},1}$ of sphere a_1 in isolation. Therefore, an expression equivalent to (14-5) for E is

$$\mathrm{E} = \mathrm{E}(a_2/a_1, \rho/\rho', N_{\mathrm{Re},1}) \,. \tag{14-6}$$

This is the more usual way of describing the dependence of E.

14.3 The Superposition Method

An account of the two sphere problem which directly incorporates results from the theory of flow past a single sphere obviously would be desirable. Such a scheme is known as the method of superposition, according to which each sphere is assumed to move in a flow field generated by the other sphere falling in isolation. More

explicitly, if spheres 1 and 2 move with the instantaneous velocities $\vec{v}_1$ and $\vec{v}_2$, respectively, the force $\vec{F}_{1,\text{sup}}$ on sphere 1 is assumed to have the form (cf. (10-40) and (10-143))

$$\vec{F}_{1,\text{sup}} = -6\pi a_1 \eta \left(\frac{C_D N_{\text{Re}}}{24} \right)_1 (\vec{v}_1 - \vec{u}_2) , \tag{14-7}$$

where $\vec{u}_2$ is the velocity field, due to the motion of sphere 2, which would exist at the location of the center of sphere 1 if it were absent. The corresponding expression for the force on sphere 2 is obtained by interchanging 1 and 2 in (14-7). The quantity $(C_D N_{\text{Re}}/24)_1$, a function only of the Reynolds number for sphere 1, evidently should be based on the relative velocity $(\vec{v}_1 - \vec{u}_2)$, although sometimes it is based instead on $U_{\infty,1}$, the terminal velocity of sphere 1 in isolation.

As would be expected, and as is demonstrated in the example presented in Appendix A-14.3 on the use of the superposition method in the Stokes regime, superposition does not give a very accurate account of the interaction for close separations. However, if the relative velocity of the spheres is sufficiently large, they may pass through the region of close proximity so rapidly that the inaccurate description of the forces acting there is of little consequence. In general, the method of superposition becomes increasingly accurate with decreasing a_2/a_1.

Langmuir (1948) was one of the first to adopt the superposition scheme to the collision problem. He restricted his investigation to small values of a_2/a_1 so that sphere 2 could be regarded as a mass point moving in the flow around sphere 1. Two extreme cases for the flow past sphere 1 were considered, namely potential flow for large $N_{\text{Re},1} = 2a_1 U_{\infty,1}/\nu$, and Stokes flow for small $N_{\text{Re},1}$. A recent calculation of a similar nature is that of Beard and Grover (1974), who used the method to determine E for small raindrops colliding with micron-sized particles. They employed the numerical solution of Le Clair *et al.* (1970) for the flow field past an isolated sphere.

The method also has been used to investigate the interaction of spheres of comparable size by Pearcey and Hill (1956), Shafrir and Neiburger (1963), Plumlee and Semonin (1965), Neiburger (1967), Shafrir and Gal-Chen (1971), Lin and Lee (1975), and Schlamp *et al.* (1976). For the single sphere flow field, Pearcey and Hill chose Goldstein's (1929) complete solution for Oseen flow. Shafrir and Neiburger, like Langmuir, employed two different Reynolds number regimes: (a) Stokes flow for $N_{\text{Re},1} \leq 0.4 (a_1 \leq 30\,\mu\text{m})$, and (b) a modified form of Jenson's (1959) numerical solution for $N_{\text{Re},1} > 0.4$. Plumlee and Semonin used the second approximation to the inner expansion of the flow field obtained by Proudman and Pearson (1957). Shafrir and Gal-Chen used a numerical solution by Rimon and Cheng (1969), Lin and Lee used their own numerical solution (Lin and Lee, 1973), and Schlamp *et al.* (1976) used Le Clair's (1970) solution.

Let us consider briefly the form of the equations of motion for the droplets. Assuming the method of superposition correctly describes the hydrodynamic forces, Newton's second law for sphere 2 of mass m_2 becomes

$$m_2 \frac{\mathrm{d}\vec{v}_2}{\mathrm{d}t} = m_2 \vec{g}^* + \vec{F}_2 , \tag{14-8}$$

where $\vec{g}^*[= (\rho' - \rho)\vec{g}/\rho']$ is the gravitational acceleration corrected for buoyancy, and $\vec{F}_2$ is given by (14-7) (with subscripts 1 and 2 interchanged). It is convenient to render these equations dimensionless by using a_1 for the unit of length, and the terminal velocity of sphere 1, $U_{\infty,1}$, as the unit of velocity; i.e., we introduce the following dimensionless quantities:

$$\vec{v}_2' \equiv \vec{v}_2/U_{\infty,1}\,, \qquad \vec{u}_1' \equiv \vec{u}_1/U_{\infty,1}\,, \qquad t' \equiv tU_{\infty,1}/a_1\,. \tag{14-9}$$

Then, in place of (14-8), we have

$$\frac{d\vec{v}_2'}{dt'} = \frac{\hat{g}^*}{N_{\mathrm{Fr}}} - \frac{\vec{v}_2' - \vec{u}_1'}{N_S}\,, \tag{14-10}$$

where $N_{\mathrm{Fr}} \equiv U_{\infty,1}^2/g^*a_1$, is the *Froude number* for sphere 1, $\hat{g}^*$ is a unit vector in the direction of gravity, and

$$N_S = \frac{2a_2^2\rho' U_{\infty,1}}{a_1\eta}\left(\frac{24}{C_D N_{\mathrm{Re}}}\right)_2\,. \tag{14-11}$$

The quantity N_S often is called the *inertia parameter* or *Stokes number.* It provides a measure of the ability of sphere 2 to persist in its state of motion in a viscous fluid. For example, in the limit of zero Reynolds number it is directly proportional to the 'range' or penetration distance of sphere 2 injected with its Stokes terminal velocity, $U_{S,2}$, into a fluid at rest (the law governing the deceleration of sphere 2 is assumed to be the obvious one involving the steady state Stokes drag):

$$-6\pi a_2\eta v_2 = m_2\frac{dv_2}{dt} = m_2 v_2\frac{dv_2}{dx}\,, \tag{14-12}$$

so that the 'range' x_s is

$$x_s = \frac{m_2 U_{S,2}}{6\pi a_2\eta}\,. \tag{14-13}$$

Then, since $U_{S,2} = p^2 U_{S,1}$, where $p \equiv a_2/a_1$, we have the relationship

$$\frac{x_s}{a_1} = \frac{2a_2^2 p^2\rho' U_{S,1}}{9a_1\eta} = \lim_{N_{\mathrm{Re},1}\to 0} p^2 N_S\,. \tag{14-14}$$

Other related parameters which often are employed in the collision problem are $q \equiv N_S^{-1}$ (Shafrir and Neiburger, 1963), $N_S^* \equiv x_s/a_1$ (Klett and Davis, 1973), and I (Hocking, 1959; Hocking and Jonas, 1970), where

$$I = \lim_{N_{\mathrm{Re},1}\to 0}\frac{N_S}{p^2} = \frac{4\rho'^2 a_1^3 g^2}{81\eta^2}\,. \tag{14-15}$$

From the definition of N_S , we may expect increasing viscous deflection of sphere 2 from a collision trajectory with sphere 1 (and thus decreasing values for E) for decreasing N_S, I, N_S^*, or increasing q.

Also, by rewriting N_S as

$$N_S = \frac{1}{9}p^2 \left(\frac{\rho'}{\rho}\right) N_{\mathrm{Re},1} \left(\frac{24}{C_D N_{\mathrm{Re}}}\right)_2 , \tag{14-16}$$

and assuming that $(24/C_D N_{\mathrm{Re}})_2$ is calculated according to the terminal velocity of sphere 2, we see that

$$N_S = N_S(p, \rho'/\rho, N_{\mathrm{Re},1}) , \tag{14-17}$$

since there is a unique relation between sphere size and Reynolds number for a given viscosity and density ratio. Similary for the Froude number, we have

$$N_{\mathrm{Fr}} = \frac{U_{\infty,1}^2}{g^* a_1} = I \left(\frac{C_D N_{\mathrm{Re}}}{24}\right)_1^2 = N_{\mathrm{Fr}}(p, \rho'/\rho, N_{\mathrm{Re},1}) . \tag{14-18}$$

Consequently, from (14-10) we infer the dimensionless sphere trajectories depend on the values of $p, \rho'/\rho$, and $N_{\mathrm{Re},1}$. This is consistent with (14-6) for the dependence of E.

14.4 The Boundary Value Problem Approach

14.4.1 The Quasi-Stationary Assumption

Since two interacting spherical cloud drops generally fall with unequal velocities, the flow must be intrinsically unsteady. The method of superposition simply ignores this difficulty by employing steady state flow fields for a single sphere. Even more rigorous formulations of the two sphere problem, which attempt to take into consideration the no slip boundary conditions on both spheres, must likewise ignore the fluid unsteadiness in order to avoid overwhelming mathematical difficulties. The general boundary value formulation deals with the unsteadiness of the flow as follows: The conditions of fall are assumed to be such that the motion is 'quasi-stationary', meaning the instantaneous velocities of the spheres at any moment define boundary values for the velocity field generated by the steady state equation of motion.

This quasi-stationary assumption would be unrealistic if the spheres experienced very large accelerations, for then the past history of the flow field would become important. As an extreme example, if the spheres were suddenly stopped in their motion, the assumption would immediately predict zero velocity everywhere in the fluid, which obviously would be incorrect. Since one would expect the acceleration of a falling sphere to vary inversely with its inertia relative to a similar volume of fluid, the quasi-stationary assumption should be applicable when $\rho/\rho' \ll 1$.

Hocking (1959) has given a somewhat different argument leading to the same conclusion by considering the order of magnitude of terms in the Stokes equation for the case of an accelerating spherical particle in a fluid otherwise at rest. Suppose the particle has radius a, velocity U, and density ρ'. Then, as we have seen, the viscous force on the particle will be of order $\rho\nu U a$ for N_{Re} of the order of unity or smaller. Therefore, by Newton's second law, the acceleration of the particle will be of order $\rho\nu U/\rho' a^2$ or smaller. The local acceleration of the fluid, $\partial\vec{u}/\partial t$, will

therefore be of this order or smaller. But the fluid viscous acceleration, $\nu\nabla^2\vec{u}$, is of order $\nu U/a^2$. Consequently, we find $|\,\partial\vec{u}/\partial t\,|\,/\,|\,\nu\nabla^2\vec{u}\,|\leq \rho/\rho'$, so that the time derivative term in the equation of motion may be neglected if $\rho/\rho' \ll 1$. A similar argument may be made for the case $N_{\mathrm{Re}} \gg 1$. Then, the force on the particle will be of order $\rho C_D a^2 U^2$, and the local acceleration of the fluid of order $\rho C_D U^2/\rho' a$ or less. Hence, we find in this case $|\,\partial\vec{u}/\partial t\,|\,/\,|\,\vec{u}\cdot\nabla\vec{u}\,| \lesssim C_D\rho/\rho'$, and again the term $\partial\vec{u}/\partial t$ becomes relatively unimportant if $\rho/\rho' \ll 1$.

We conclude the quasi-stationary assumption may be used to calculate theoretical collision efficiences for water droplets in air, since $\rho/\rho' \approx 10^{-3}$ in that case. Also, on the basis of the fairly good agreement obtained between theoretical and experimental trajectories of pairs of equal spheres falling along their line of center for $\rho/\rho' \approx 10^{-1}$ (see Section 14.4.4), it appears that the quasi-stationary assumption should remain valid for the relatively large density ratios one encounters in model simulations of cloud droplet interactions.

14.4.2 Two Spheres in Steady Stokes Flow

From the preceding discussion, it appears reasonable to apply time-independent Stokes flow theory to the collision problem for Reynolds numbers which are small compared to unity. Traditionally, such treatment has been assumed valid for droplet radii less than 30 microns, corresponding to $N_{\mathrm{Re}} \leq 0.4$. Strictly speaking, of course, the Stokes theory applies rigorously only for $N_{\mathrm{Re}} = 0$, and becomes progressively more inaccurate with increasing N_{Re}.

Assuming steady Stokes flow, the equations to be solved are

$$\nabla p = \eta\nabla^2\vec{u}, \tag{14-19}$$

$$\nabla\cdot\vec{u} = 0. \tag{14-20}$$

The velocity must vanish at infinity and match that of the spheres on their surfaces. In general, the spheres will have velocity components along and perpendicular to their line of centers. The latter components will create shears causing the spheres to rotate with angular velocity vectors perpendicular to the plane containing the direction of gravity and the line of centers. The flow will maintain symmetry with respect to that plane.

As the governing equations are linear, the complete solution may be built up out of special cases which are easier to treat. For example, the problem of general motion for two spheres may be considered solved when solutions to the following three special problems are available: problem-1 when one sphere is stationary, while the other moves toward or away from it along the line of centers; problem-2 when neither sphere translates, but one rotates about a diameter perpendicular to the line of centers; problem-3 when one sphere is stationary while the other moves perpendicular to the line of centers. Of course, this decomposition of the general problem is not unique. Historically, the first 2-sphere problem to be solved was that for equal parallel velocities along the line of centers by Stimson and Jeffery (1926). Later, the case of antiparallel motion along the line of centers was treated by Maude (1961) and Brenner (1961). These two axisymmetric problems are equivalent to case-1 above.

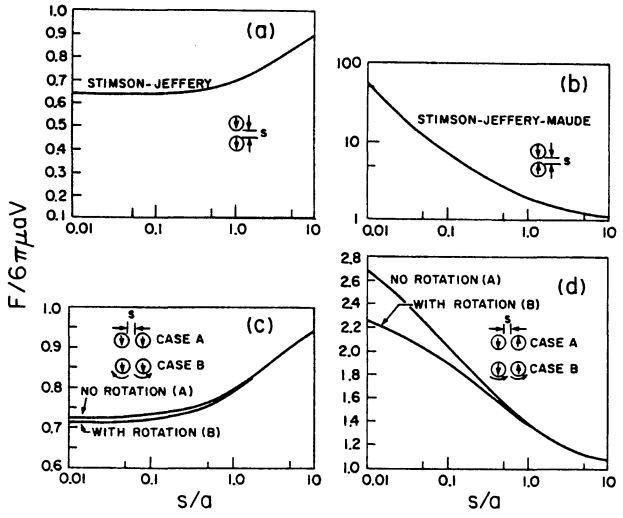


Fig. 14-2: Theoretical resistance coefficients for equal sized spheres in Stokes flow. (a) Parallel motion along the line of sphere centers, (b) antiparallel motion along the line of sphere centers, (c) parallel motion perpendicular to the line of sphere centers, (d) antiparallel motion perpendicular to the line of sphere centers. (From M.H. Davis, 1966, with changes.)

The solution to problem-1 leads to the results plotted in Figures 14.2a and 14.2b, which show the drag forces on identical spheres moving with equal parallel and antiparallel velocities along their line of centers. The forces are normalized with respect to the single sphere Stokes drag, so that they approach unity for large separations. For equal parallel motion, the forces on the spheres are identical, which is indicative of the absence of any wake in Stokes flow. For equal antiparallel motion, the forces are equal and opposite, and become singular like s^{-1} as the separation s between their surfaces approaches zero. This is generally true for any size ratio, and means that rigid spheres cannot be brought into contact according to the continuum theory of viscous flow. Physically, of course, the continuum theory will break down as the separation approaches the mean free path of air molecules. The effect of this breakdown on the collision problem is discussed in the next section.

The solutions for problems 2 and 3 lead to the results plotted in Figures 14.2c and 14.2d. Figure 14.2c shows the drag forces experienced by equal spheres falling with equal parallel velocities perpendicular to their line of centers with and without rotation. The angular velocities of the spheres for the case of rotation are determined by the condition that the spheres experience no torque. Similarly, Figure 14.2d shows the drag forces for equal antiparallel motion perpendicular to the line of centers, with and without rotation. Note, the forces for antiparallel motion appear to become singular with vanishing separation, as in the case of axisymmetric motion. In fact, O'Neil (1964) has shown that they do become singular, like

$\log s$, for $s \to 0$.

14.4.3 The Slip-Flow Correction in Stokes Flow

As we mentioned above, droplet collisions are theoretically impossible in Stokes flow, since the resistance to the approach of the spheres varies inversely with the gap between them, for separations small compared to their radii. Therefore, in the collision efficiency calculations which are based on rigorous Stokes flow (Davis and Sartor, 1967; Hocking and Jonas, 1970), it is assumed that a collision has occurred if the computed gaps become less than a given small fraction, $s' \equiv s/a_1$ of the radius of the larger droplet. Of course, such an approach can be useful only if the computed collision efficiencies are relatively insensitive to the choice of s'. This turns out to be the case for $a_1 \geq 30\,\mu$m. However, for smaller sizes, the choice of s' noticeably affects the results.

This uncertainty brought about by the arbitrary choice of a collision criterion has been removed by Davis (1972), Jonas (1972), and Hocking (1973), through application of the theory of slip-flow. The assumption that the air gap between the droplets is a continuum will break down progressively as the separation becomes of the order of ten times the mean free path of air molecules or less. The relevant manifestation of the onset of non-continuum flow will be that the effective viscosity will tend to decrease as the Knudsen number based on the separation of the droplets becomes larger than about 0.1. (This effect applies only to the component of antiparallel motion, which causes the air to be squeezed out from between the droplets.) The theory of slip-flow enables one to determine approximately the form of the effective viscosity.

According to slip-flow theory, the tangential component of the fluid velocity at a body surface is less than the surface velocity, with the velocity difference being proportional to the local tangential stress in the fluid. The factor of proportionality between the velocity slip and the local stress, the 'coefficient of external friction', β, then can be related to the mean free path. This leads directly to a new boundary condition, which must replace the continuum boundary condition of no slip.

The analysis of Davis (1972) yields forces which are functions of the dimensionless parameter $C \equiv \eta/\beta c$, where c is the length scale factor appearing in the transformation from cylindrical to bispherical coordinates. It is necessary to provide representative values of C to complete the force description. It is also of interest to determine the dependence of C on the mean free path λ. For the case of low pressure gas flow through glass capillaries, Davis found that good agreement between experimental data and the slip-flow analysis could be obtained by setting $\eta/\beta = A\lambda$, where A is a number in the range 1.3 to 1.5. Therefore, by analogy, he conjectured the dependence $C = A(\lambda/c)$. Then, for purposes of presenting results, a new quantity k was defined as $k \equiv C(c/a_2) = A(\lambda/a_2)$. The advantage of k over C is that the former is fixed for a given pair of spheres; while the latter varies with separation. Since the cross-over in dominance from Brownian to gravitational coagulation occurs for radii of a few microns, we see it is sufficient to evaluate the forces for $k < 0.1$.

TABLE 14.1

Effect of slip on the forces of interaction between equal size spheres in Stokes flow; equal parallel motion along the line of centers for $s'' = 0.01$. (From M. H. Davis, 1972; by courtesy of *Am. Meteor. Soc.*, and the author.)

	$a_1/a_2 = 1.0$	$a_1/a_2 = 5.0$	
k	$(F_1/F_{S,1})$	$(F_1/F_{S,1})$	$(F_2/F_{S,2})$
0.01	0.992	0.998	0.992
0.02	0.985	0.996	0.984
0.05	0.961	0.991	0.966

TABLE 14.2

Effect of slip on the forces of interaction between equal sized sphers in Stokes flow; equal anti-parallel motion along line of centers. (From M. H. Davis, 1972; by courtesy of *Am. Meteor. Soc.*, and the author.)

	$s'' = 0.10$		$s'' = 0.01$		$s'' = 0.001$	
k	$(F_1/F_{S,1})$	f	$(F_1/F_{S,1})$	f	$(F_1/F_{S,1})$	f
0.002	0.985	0.980	0.754	0.833	0.260	0.333
0.005	0.944	0.952	0.586	0.667	0.152	0.167
0.010	0.888	0.909	0.451	0.500	0.097	0.091
0.020	0.804	0.833	0.329	0.333	0.061	0.048

Over a wide range of separations and size ratios, the calculations produce the following results: 1) the effect of slip on forces for equal parallel motion along the line of centers is, as expected, insignificant for $k < 0.1$ (see Table 14.1; F_S is Stokesian value); 2) forces on two spheres in equal antiparallel motion along the line of centers are reduced significantly at close separations $\mathrm{s}'' \equiv \mathrm{s}/a_2$ for finite k. Further, if $F_{S,i}$, denotes the Stokesian value for sphere i, then an approximate representation of the forces is as follows:

$$F_i \approx F_{S,i} f\,, \tag{14-21}$$

where

$$f = \left(1 + \frac{k}{\mathrm{s}''}\right)^{-1} = \left(1 + A\frac{\lambda'}{\mathrm{s}''}\right)^{-1}, \tag{14-22}$$

and $\lambda' = \lambda/a_2$. Table 14.2 shows this representation (which of course has the familiar form of the Cunningham slip-correction factor; cf. Section 10.3.6 is reasonably good over a wide range of parameter values).

It can be seen that the form of f is such that the s^{-1} behavior of the Stokesian force coefficients for approaching spheres at close separations is eliminated. Therefore, if the force components that refer to antiparallel motion along the line of centers, are each multiplied by the factor f to allow for gas kinetic effects in the

region between the droplets, the need for imposing an arbitrary minimum gap in collision efficiency calculations is eliminated.

A related problem which has not yet been solved is the determination of the slip-flow modification of forces experienced by two spheres moving with antiparallel velocities perpendicular to their line of centers at close separations. However, Davis (1972) conjectured that the resulting corrections would have little effect on droplet trajectories. We agree because, as we discussed in the previous section, the forces in question become singular at a slower rate with vanishing s (like log s) than those for antiparallel line of centers motion.

14.4.4 Two Spheres in Modified Oseen Flow

We have seen that great mathematical complications attend the basic collision model in the theory of accretion growth of cloud droplets. This is true primarily because of the non-linearity of the convective acceleration terms in the governing Navier-Stokes equations, and because of the problem of satisfying the flow boundary conditions on two separate surfaces. The superposition method provides a means of estimating the effects of non-linear inertial accelerations in the fluid even for quite large Reynolds numbers, but only at the cost of completely avoiding the boundary value problem. On the other hand, as we have seen, the Stokes equations are just simple enough to permit a complete boundary analysis of the problem, but their use implies the complete omission of all fluid inertial effects.

Unfortunately, there is evidence that the applicable range of the Stokes flow model may be less than is often assumed. We have said that traditionally the model has been assumed valid for $a_1 \lesssim 30\,\mu$m, corresponding to $N_{\mathrm{Re}} \lesssim 0.4$. But while it is true that for single spheres of such radii the Stokes drag closely approximates the actual drag, for two spheres the effect of inertial accelerations in the fluid can cause a significant differential rate of fall even for considerably smaller sizes. This is especially true for spheres of comparable size. For example, Steinberger *et al.* (1968) observed the motion of pairs of equal spheres falling along their line of centers (for which case any relative motion is due entirely to non-Stokes behavior of the fluid), and found a significant acceleration effect, even for Reynolds numbers as small as 0.05, corresponding to droplet radii of $15\,\mu$m. Similar behavior has been observed in the model experiments of Pshenai-Severin (1957, 1958), Schotland (1957), Telford and Cottis (1964), and Horguani (1965).

From the foregoing, it would appear useful to obtain an analysis of the collision problem which does not assume that either the superposition scheme or the Stokes approximation is adequate to describe the flow. We now outline such a treatment, due to Klett and Davis (1973). It is an approximate boundary value analysis, based on the Oseen equations of motion as modified by Carrier (see Section 10.2.4).

For the two-sphere problem, Carrier's method must be generalized somewhat, since four variable Reynolds numbers are involved: with sphere $\ell(\ell = 1, 2)$ there are associated two characteristic Reynolds numbers, one (R_ℓ) based on its velocity U_ℓ and radius a_ℓ, and the other (R'_ℓ) on U_ℓ and the center-to-center distance d to the other sphere. The latter Reynolds number is the one involved in the inertial correction to the force on a given sphere due to the presence of the other sphere.

Typically, it will vary over an order of magnitude for those separations which give rise to a significant hydrodynamic interaction.

The analysis proceeds by first selecting for each sphere a primitive solution to an Oseen governing equation. For each such equation, the constant velocity appearing in the acceleration term is taken to be the velocity of the respective sphere through the fluid. Next, the sum of the two fields is made to satisfy the no-slip condition on the average over the surface of the spheres. The expressions for the forces are then obtained from this approximate solution, and these are modified further by making the replacements $R_\ell \to C_\ell R_\ell$ and $R'_\ell \to C'_\ell R'_\ell$, where

$$\begin{aligned} C_\ell &= 1 - 0.08 \log(1 + 50 R_\ell), \qquad R_\ell \leq 2, \\ C_\ell &= 0.43. \end{aligned} \tag{14-23}$$

The 'Carrier constants' C_ℓ ensure agreement to within 1% between the numerically determined drag values of Le Clair *et al.* (1970) and the Carrier-Oseen drag on sphere ℓ falling in isolation for $R \leq 2 (N_{\mathrm{Re}} \leq 4)$. The constants C'_ℓ have the value suggested originally by Carrier.

Some results of the computations are plotted in Figure 14.3, where the velocity difference between two equal spheres falling along their line of centers is given as a function of the distance d between the sphere centers. Also, a comparison is made with the theoretical predictions of Oseen (1927) and Stimson and Jeffery (1926), and with the experimental results of Steinberger *et al.* (1968), which covered the Reynolds number interval $0.06 \leq N_{\mathrm{Re},2} \leq 0.216$ ($N_{\mathrm{Re},2} = 2R_2$), corresponding roughly to cloud droplets from 15-22 μm in radius. In all cases observed by Steinberger *et al.*, both spheres continually accelerated as they fell, and the upper sphere fell faster and accelerated more rapidly than the lower one. Because the velocities changed as each experimental run proceeded, a range of values of $N_{\mathrm{Re},2}$ was generated. They grouped their results according to the ranges $0.060 \leq N_{\mathrm{Re},2} \leq 0.086$, $0.086 \leq N_{\mathrm{Re},2} \leq 0.150$, and $0.170 \leq N_{\mathrm{Re},2} \leq 0.216$.

We note from Figure 14.3 that the model of Stimson and Jeffery is obviously the most deficient, predicting zero velocity difference independently of separation and Reynolds number. Of course, this unrealistic result is due to the symmetry of the Stokes flow field (there is no wake), which yields equal forces on the spheres. The Klett-Davis formulation is seen to be the most successful of the three in predicting the magnitude of the velocity difference and its trend toward higher values with both increasing Reynolds number and decreasing separation. Oseen's model (essentially equivalent to the superposition method applied with single sphere Oseen flow fields) seriously overestimates these trends.

Another noteworthy feature of the motion observed by Steinberger *et al.*, but not revealed in Figure 14.3, is that the drag force for each sphere has a Reynolds number dependence. This is in agreement with the Klett-Davis formulation, but is at odds with Oseen's model, which predicts no such dependence for the upper sphere. Of course, in the Stimson-Jeffery model, all Reynolds numbers are effectively equal to zero.

The experiments of Steinberger *et al.* were conducted with both steel and tungsten carbide spheres in oil, for which the density ratios were $\rho/\rho' = 0.11$ and 0.06,

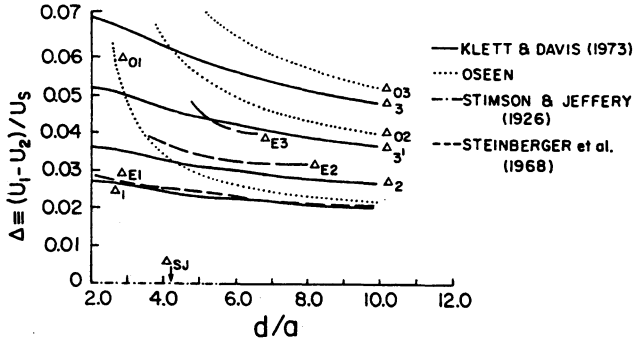


Fig. 14-3: Velocity difference between two spheres of equal size falling along their line of centers, according to Klett and Davis 1973 ($\Delta_1, \Delta_2, \Delta_3, \Delta_3'$), Oseen ($\Delta_{01}, \Delta_{02}, \Delta_{03}$), Stimson and Jefferey 1926 (Δ_{SJ}), and the experiments of Steinberg *et al.* 1968 ($\Delta_{E1}, \Delta_{E2}, \Delta_{E3}$). $\Delta_1 : 0.060 \leq N_{Re} \leq 0.086$, $\Delta_2 : 0.082 \leq N_{Re} \leq 0.0118$, $\Delta_3' : 0.120 \leq N_{Re} \leq 0.174$, $\Delta_3 : 0.168 \leq N_{Re} \leq 0.240$; $\Delta_{01} : 0.060 \leq N_{Re} \leq 0.086$, $\Delta_{02} : 0.082 \leq N_{Re} \leq 0.124$, $\Delta_{03} : 0.170 \leq N_{Re} \leq 0.250$; Δ_{SJ}:Stokes flow, $\Delta_{E1} : 0.060 \leq N_{Re} \leq 0.086$, $\Delta_{E2} : 0.080 \leq N_{Re} \leq 0.150$, $\Delta_{E3} : 0.170 \leq N_{Re} \leq 0.216$. (From Klett and Davis, 1973; by courtesy of Am. Meteor. Soc., and the authors.)

respectively. They found that for a given Reynolds number range, the results were independent of the kind of spheres used. Therefore, one can conclude that the density ratio was small enough not to play a noticeable role in the evolution of trajectories. This means the results shown are relevant to the case of water drops in air.

Additional comparisons between theory and experiment are made in the following section, where we discuss collision efficiencies.

14.5 Collision of Water Drops with Water Drops

14.5.1 The Case of Calm Air

Let us consider first the non-turbulent collision efficiencies E of small droplets with radii of 30 μm or less. As we discussed in the previous sections, it is this realm which has been treated most rigorously through application of the model of slip-corrected Stokes flow (Davis, 1972; Jonas, 1972; Hocking, 1973). Hence, the resultant values of E should be the best available, subject to the proviso that the radius ratio $p \equiv a_2/a_1 \lesssim 0.6$ so that fluid inertial effects, and especially the wake capture phenomenon, will be of negligible importance. Slip-flow corrected values of E computed by Jonas (1972) are shown in Figure 14.4, where they are compared with a representative example of computations (Hocking and Jonas, 1970) based on continuum Stokes flow and the assumption that a collision occurs whenever the separation of the sphere surfaces becomes less than $10^{-4}a_1$. The effect of slip is seen to be considerable for $a_1 \lesssim 20\,\mu$m, but to have little effect on drops as large as 30 μm.

Figure 14.4 also includes the corresponding values of E obtained by setting all

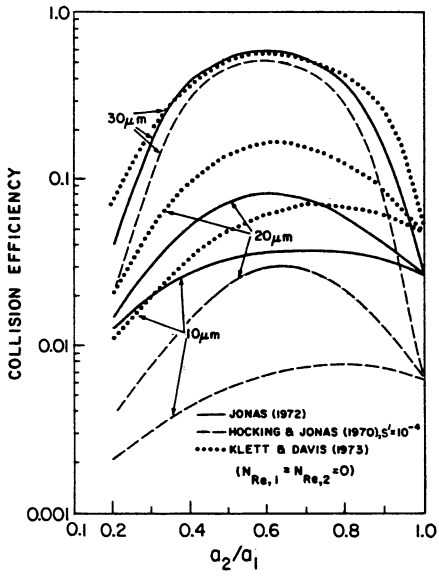


Fig. 14-4: Theoretically computed collision efficiencies of interacting spheres in Stokes flow, and in modified Oseen flow (zero Reynolds number limit) for spheres of various radii (given by label of each curve). (From Jonas, 1972, with changes.)

Reynolds numbers equal to zero in the modified Oseen flow model of Klett and Davis (1973). This provides a measure of the accuracy of the purely viscous forces according to their formulation. It can be seen that the Klett-Davis values agree better with the slip-corrected E's than do those that follow from the continuum Stokes flow model.

Computations for a given zero-Reynolds number model show that for $p = 1$, E is independent of the size of the spheres. This behavior can be seen in Figure 14.4 by the tendency of each set of curves to converge to a single point near $p = 1$. This (unphysical) behavior may be explained by noting that in the limit $p \to 1$, the sphere accelerations become vanishingly small, since no fluid inertial effects are permitted. Hence, dynamical effects vanish and so geometric similarity implies dynamic similarity as well, no matter what the absolute size of the equal spheres may be.

An indication of the importance of wake capture and other fluid inertial effects is provided by Figure 14.5, where the collision efficiencies derived from the Stokes flow model of Jonas (1972) are compared with those computed from the Klett-Davis model with non-zero Reynolds numbers, and with those following from the superposition models of Lin and Lee (1975) and Schlamp *et al.* (1976). It can be seen that the effect of fluid inertia on drop collisions is most pronounced for p-ratios near unity, where there is a marked tendency for an increase in E due to wake capture.

The trends of the collision efficiency curves in Figure 14.5 for all three of the most

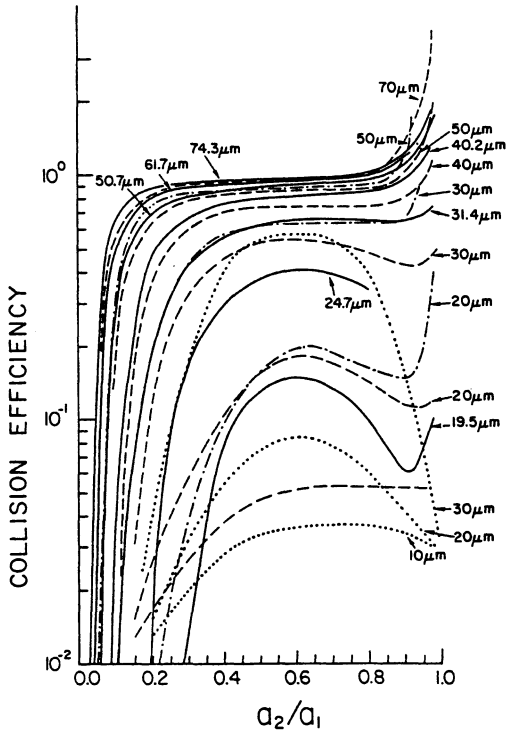


Fig. 14-5: Theoretical collision efficiencies of spherical water drops in calm air as a function of p-ratio and of collector drop radius (given by the label of each curve); — Schlamp *et al.* (1976), – – – – – Klett and Davis (1973), -.-.-.- Lin and Lee (1975), ... Jonas (1972).

recent models which include inertial effects are in accord with what was anticipated qualitatively in Section 14.2. Quantitatively, however, the agreement among the values of E computed by these models is only fair. In particular, the E values deriving from the superposition approach are somewhat larger than those computed from the approximate boundary value analysis of Klett and Davis, for $a_1 \gtrsim 30\,\mu$m and all p-ratios. The differences, which are especially large for p near unity, are most likely due to the following inherent deficiencies of the superposition model (cf., Klett, 1976): Since, under superposition, the individual flow fields do not interact, the strength of wake formation behind the leading sphere of two spheres falling in close proximity will be overestimated. This effect will be enhanced also by the underestimation of the strength of the viscous interaction between the spheres. This leads to spuriously low drag, hence higher velocities, and hence stronger wakes. In short, the deficiencies of superposition lead one to expect overestimated wake capture, and underestimated deflection by viscous forces from collision trajectories.

Finally, Figure 14.6 depicts some representative results in another fashion with E plotted as a function of the collected drop radius a_2, for various collector drop radii a_1. This manner of presentation shows clearly that E is near unity for $a_1 \gtrsim 40\,\mu$m

and $a_2 \gtrsim 15\,\mu$m, unless $a_1 \approx a_2$, in which case E> 1.

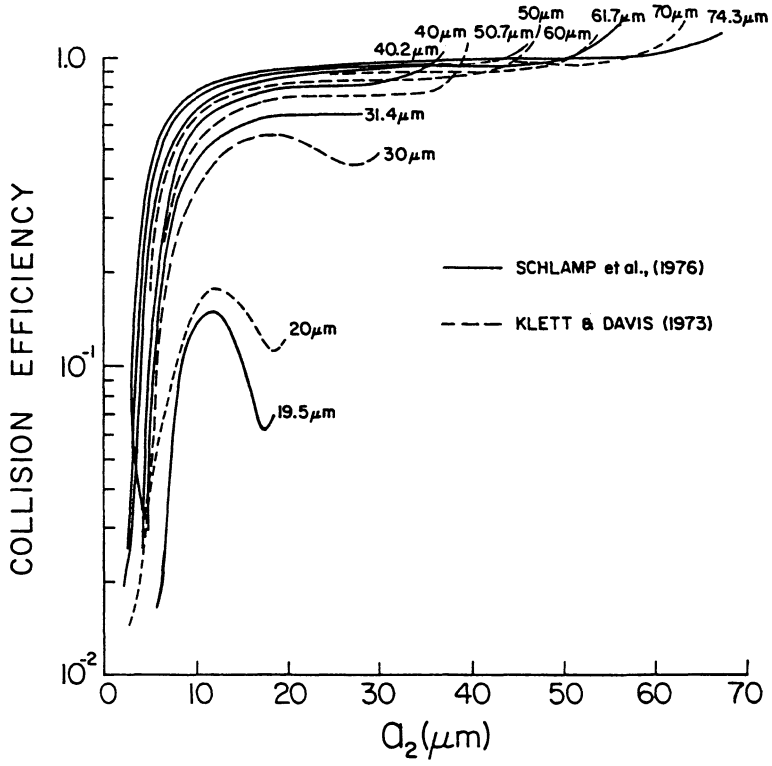


Fig. 14-6: Theoretical collison efficiencies of spherical water drops in calm air as a function of small drop radius and of large drop radius (given by label of each curve).

14.5.2 The Case of Turbulent Air

Since some degree of turbulence is always present in clouds, it is important to consider its effect on the collision process. A major problem of this class is to determine how the intensity of turbulence in young clouds affects the early stages of the evolution of droplet spectra through the enhancement (or suppression) of gravitational collection.

As briefly mentioned in Section 11.6.2, the intensity of turbulence in clouds varies widely, depending on the type of cloud and their age. Thus, Mazin *et al.* (1984, 1989) observed in stratus clouds $\varepsilon \approx 10$ cm^2 sec^{-3} as compared to $\varepsilon \approx 100$ cm^2 sec^{-3} in small cumuli. Ackermann (1967, 1968) found $3 \leq \varepsilon \leq 114$ cm^2 sec^{-3} under various conditions in cloudy air, a median value of 207 cm^2 sec^{-3} in well-developed cumuli. MacPherson and Isaac (1976) found, at various locations in 17 cumuli, $10 \lesssim \varepsilon \leq 450$ cm^2 sec^{-3}. In deep cumuli, Panchev (1971) quotes a typical value of $\varepsilon \approx 700$ cm^2 sec^{-3}. Weil *et al.* (1989), Aleksandrov *et al.* (1969)

and Rhyne and Steiner (1964) observed in heavy cumulonimbi, values for ε up to 2×10^3 cm^2 sec^{-3}. A plot of observed values for the turbulent spectral energy density inside and outside atmospheric clouds is given in Figure 14.7.

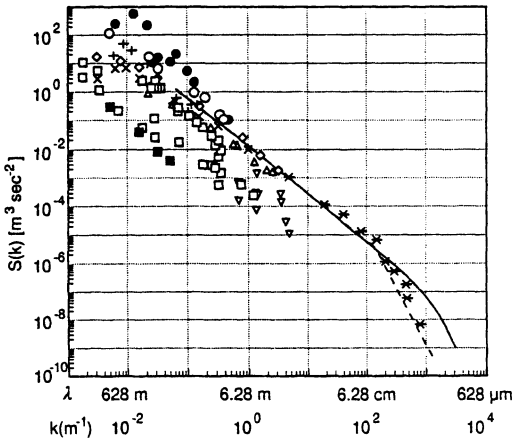


Fig. 14-7: Turbulent spectral energy density S as a function of wave number k and wave length λ, for vertical velocity inside and outside atmospheric clouds. $*$ Boston and Burling (1972), cloudless boundary layer, $\epsilon = 46$ cm^2 sec^{-3}; $\triangledown$ Merceret (1976a,b), below cloud; ■ Smith and Jonas (1995) cumulus clouds; □ Quante and Brown (1992) cirrus clouds, $\epsilon = 2$ cm^2 sec^{-3}; •, ○ McPherson and Isaac (1976), $\epsilon = 191$ cm^2 sec^{-3} and 92 cm^2 sec^{-3}, respectively; +, △ Kitchen and Caughey (1961) in cloud, $\epsilon = 15$ cm^2 sec^{-3} and below cloud, $\epsilon = 9$ cm^2 sec^{-3}, respectively; × Kaimal and Lenchow (1984), tower measurements. Continuous line given by $S(k) = 0.53\ \epsilon^{2/3}k^{-5/3}$ for $k \leq 0.13\ k_K$ and $S(k) = 4.54 \text{ x } 10^{-3}\epsilon^{5/4}\nu^{-7/4}k^{-4}$ for $k > 0.13\ k_K$(Townsend, 1976); dashed line $S(k) = \alpha\epsilon^{2/3}k^{-5/3}\exp(-\frac{3}{2}\alpha\nu\epsilon^{-1/3}k^{4/3})$ (Pao, 1965), both for $\epsilon = 46$ cm^2 sec^{-3} and α =0.5. (From Vohl 1995, pers. comm.)

Arenberg (1939, 1941) was perhaps the first to point out that turbulence in clouds may possibly affect the collision of drops. However, he confined himself in his theoretical studies to simple sinusoidal motions, a model also used later by Gabilly (1949). East and Marshall (1954) and East (1957b) extended Gabilly's work by incorporating in their treatment the random character of turbulent motion, neglecting, however, the spatial variability of the flow. Saffmann and Turner (1956) accounted for a local flow relative to that of drops, and also improved on the characterization of the turbulence field; their model best applies to the behavior of nearly equal size drops. A subsequent effort along the same lines can be found in the work of Levin and Sedunov (1966).

In the more recent literature, four main mechanisms have been identified by which atmospheric turbulence may contribute to the collisional growth of cloud drops. Unfortunately, none of these mechanisms is sufficiently complete and cannot successfully withstand criticism. Nevertheless, we shall briefly sketch them since they may provide a basis for more complete models.

A *first mechanism* considers the fact that drops of different sizes respond differently to fluctuations in a turbulent velocity field. This problem was treated by Grover and Pruppacher (1985). Using a one-dimensional model, they studied the effects of vertical velocity fluctuations on the efficiency with which spherical particles of radii between 0.5 and 5 μm and density 2 g cm^{-3}, moving with the air, are collected by water drops of radii between 42 and 310 μm. In this model, it was assumed that collector drops, while falling through turbulent air, would encounter eddies of various size scales. In some critical-sized eddies, the drops were assumed to reach terminal velocity after they had entered the new eddy with a velocity given by the intrinsic velocity difference between the eddy they entered and the eddy they left. These velocity differences were assumed to be Gaussian distributed with a standard deviation given by the integral over the turbulent energy spectrum of these eddies. From their entry velocity into the new eddy and their velocity variation within the new eddy, the drop velocity distribution with respect to the critical size eddy was computed. Eddies smaller than the critical size were assumed to have no effect on the drop's motion but only on the variation of the drop-air relative velocity. These velocity differences were also assumed to be given by a Gaussian distribution of mean value zero and standard deviation given by the integral over the turbulent energy spectrum of these eddies. Assuming that the drop velocity distribution with respect to the critical size eddies and the intrinsic velocity distribution of the smaller eddies were statistically independent, the drop velocity distribution with respect to the turbulent air was computed by superimposing the two distributions. Since the model considered only vertical turbulent velocity variations which affect the collision process with interaction distances of less than a few centimeters, the turbulent air characteristics were assumed to be described by the empirical, one-dimensional, longitudinal energy spectrum of Townsend (1976) for the viscous subrange (see Figure 14.7), continuous line). For computing the efficiency with which a drop collides with a smaller particle, Gover and Pruppacher assumed that the air flow in the immediate vicinity of the drop is laminar, although its pattern changes in time as the drop accelerates and decelerates relative to the turbulent air. In addition, these changes were considered to be sufficiently slow so that, during the trajectory of any given particle relative to the drop, the laminar flow could be assumed to be steady with its pattern and strength given by the average velocity of the drop during the particles' trajectory. The collision efficiency was then computed from the trajectory method of Beard and Gover (1974) for colliding particles of small p-ratio, using for the local air flow velocity the value derived from a solution of the Navier-Stokes equation of motion for steady, axisymmetric flow around the sphere of a Reynolds number which corresponded to the actual drop-air relative velocity. The results of these computations showed negligible effects of air turbulence on the collision efficiency for drop radii larger than 50 μm, even if the turbulent energy dissipation ε was as large as 10^3 cm^2 sec^{-3}. For drop radii smaller than 50 μm, however, a significant enhancement of the collision efficiency was found for $\varepsilon \gtrsim 10$. Although Grover and Pruppacher considered the turbulent energy spectrum in the range which is appropriate for the scales involved in a drop-particle collision (of the order of centimeter or less), their assumption of laminar steady flow around a drop at each instant of the particles' trajectory, and their neglect of

the randomness imparted by turbulence to the trajectory itself, make their results unconvincing and certainly not complete.

A *second mechanism* is related to the eddy structure of a turbulent velocity field. At any given time, cloud drops may be contained in two spatially separated turbulent eddies. It then might happen that, at a later stage, these two eddies will overlap. By random displacement fluctuations, the positions of the drops may be altered such that some of the drops in the combined eddy will be in a collision position. This problem was studied by Reuter *et al.* (1988), who formulated a model for computing the collection kernel of cloud drops of radii 50 to 800 μm colliding with smaller drops of radii 10 to 50 μm in turbulent air of $1 \leq \varepsilon \leq 10^3$ cm^2 sec^{-3} as a result of overlapping eddies, assuming $E_c = 1.0$ and the terminal velocities of the drops as given by Gunn and Kinzer (1949). Their model is based on stochastic diffusion equations with 'white noise' terms which describe the random turbulent displacements. The size of the random displacements was assumed to be characterized by a constant turbulent diffusion coefficient which was computed from the Richardson (1926)-Obukov (1954) relation to be 3×10^{-1} cm^2 sec^{-1}. The associated initial boundary value problem for the partial differential equation of the Fokker-Planck type was solved numerically by a finite difference method. From their results, Reuter *et al.* deduced that, for drops of radii larger than 100 μm, the enhancement of the collision kernel due to overlapping turbulent eddies is negligible, even for an energy dissipation rate of as large as 10^3 cm^2 sec^{-3}. However, for drops of $a_L \approx 50\,\mu$m, the collision kernel was found to be enhanced by a factor of 2.5.

The model of Reuter *et al.* (1988, 1984) was criticized by Cooper and Baumgardner (1989), who argued that it overestimates the turbulence effects on the collision kernel due to a number of shortcomings in the model: (1) The calculations do not consider the turbulence effects on the collision efficiency and the fall velocity of the drops. (2) The assumption of a constant diffusion coefficient neglects correlations between the motions of droplets which result from their proximity. (3) In using the Richardson-Obukov formula, which applies to the inertial subrange of the turbulent energy distribution, the model becomes based on an inertial subrange scaling applying to interactions which actually take place in the viscous subrange. (4) The model assumption that the drops instantaneously react to the fluctuations in the ambient flow is not consistent with observations which indicate that drops need time to adjust to the flow.

A *third mechanism* (de Almeida, 1975, 1977, 1979a,b) is based on the fact that a turbulent, unsteady flow imparts a degree of randomness to the drop trajectories as the drops interact hydrodynamically. Thus, whereas in the non-turbulent case, a collison is assured if the initial horizontal offset distance y satisfies $y \leq y_c$ and is impossible for $y > y_c$ (recall Figure 14.1), in the present case there is a finite probability $P(y)$ for a collision at any y. This distinction between the previous deterministic and present probabilistic problem is illustrated in Figure 14.8.

Evidently, $P(y)$ can be determined only by the laborious procedure of carrying out repeated trials for a given set of initial conditions. Thus, de Almeida obtained $P(y)$ as follows:

$$P(y) = \frac{n(y)}{T}\,. \tag{14-24}$$

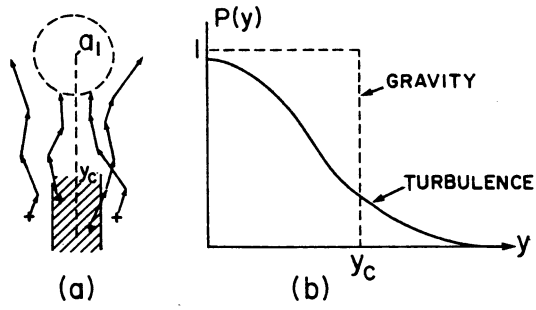


Fig. 14-8: (a) Typical drop-droplet relative trajectories in turbulent air, (b) collision probability curve (solid line) compared with a typical deterministic case (dashed line). (From de Almeida, 1975; by courtesy of the author.)

Here, $n(y)$ denotes the number of successes (collisions) out of T trials for a pair of spheres starting their motion with a given off-center horizontal separation y. After experimenting with various values of T, de Almeida decided on the choice $T = 200$ for his entire set of computations.

A somewhat analogous procedure is involved, even in the non-turbulent case, since a sequence of trials is required to produce a converging sequence of estimates of y_c. In this case, the error in the collision efficiency E is, from (14-2),

$$\Delta \mathrm{E} = \frac{2 y_c \Delta y}{(a_1 + a_2)^2} \leq \frac{2 \Delta y_c}{a_1 + a_2}, \tag{14-25}$$

where y_c is the error in the trial and error solution for the critical horizontal separation y_c. (As we have discussed in Section 14.2, and as we shall see further below, the inequality in (14-25) may break down for $a_2/a_1 \to 1$, due to the wake effect.)

Given $P(y)$, the total effective cross-section for collisions is just $\int_0^\infty 2\pi y P(y) \mathrm{d}y$. Therefore, the appropriate generalization of E to include the case of turbulence is

$$\mathrm{E} = \frac{2}{(a_1 + a_2)^2} \int_0^\infty y P(y)\, \mathrm{d}y\,. \tag{14-26}$$

Based on the work of Basset (1910) and Tchen (1947), de Almeida formulated the equations of motion for a pair of spherical droplets interacting hydrodynamically while falling under gravity in turbulent air. The drag on a drop was assumed to be given by the Klett and Davis (1973) forces for relative motion $(\vec{\mathrm{v}} - \vec{\mathrm{u}})$. To simulate the random vector $\vec{\mathrm{u}}$, a Monte Carlo method was employed and a numerical differential operator was used to obtain $\mathrm{d}\vec{\mathrm{u}}/\mathrm{d}t$. As constraints on the components of the random vector $\vec{\mathrm{u}}$, de Almeida formulated a velocity correlation applicable to the inertial subrange. With this model, he determined the probability $P(y)$ for a collision to take place at a given offset y after T trials, considering drops of $10 \leq a_L \leq 40\,\mu\mathrm{m}$ which were assumed to collide with smaller drops of $0.2 \leq p \leq 0.9$ in air of $\varepsilon = 0, 1$ and 10 $\mathrm{cm}^2\ \mathrm{sec}^{-3}$. The results of his computations indicate that at

turbulence energy dissipation rates as small as 10 cm^2 sec^{-3}, the collision efficiency becomes significantly enhanced.

Some erroneous features of de Almeida's model were pointed out by us earlier (see Pruppacher and Klett, 1978), and by Grover and Pruppacher (1985). One is that the Klett-Davis forces used in the model should have led to collision efficiencies for $\varepsilon = 0$ which agreed over the whole size range with the efficiencies given by Klett and Davis in Figure 14.4. Instead, for $a_L \leq 25\,\mu$m, the efficiencies of de Almeida were significantly smaller. Another feature which is likely to be more serious is that the basic governing form used for the equation of motion of the drops is not valid in principle for situations like the one of interest, in which the particles in the turbulent medium have a density large compared to that of the medium. The violation of this condition probably implies that the effect of turbulence on drop collisions is overestimated, since the drop's resistance to turbulent entrainment is apparently underestimated. Thirdly, it is necessary to note that the scale size of cloud droplets is generally smaller by at least one order of magnitude than the Kolmogorov microscale of the small eddies (see Section 11.6.2). This implies that the effect of turbulence on the interaction of neighboring droplets should be governed primarily by motions on a scale less than λ_k. In violation of this consideration, de Almeida applied an inertial subrange scaling to turbulent velocity correlations and, hence, drop interactions, which actually take place in the viscous subrange.

A *fourth and most recent mechanism* was formulated by Khain and Pinsky (1995a,b) and Pinsky and Khain (1995a,b) who considered the relative velocities between the drops and the surrounding air which arise due to a drop's inertia in a turbulent atmosphere. In this study, approximate equations of the motion for drops falling in turbulent air were formulated and used as a basis for estimating the statistical characteristics of drop motions in terms of the statistical properties of the turbulence. In a first attempt, only turbulent fluctuations of strictly horizontal flow were considered, and the fluctuations were assumed to be a function of height only. The model led to the conclusion that, due to drop inertia, large drop velocities relative to the ambient air can arise. The effect on the drop collection rate was estimated by forming a collision kernel wherein the conventional factor of the difference in fallspeeds of a pair of interacting drops was replaced by the root-mean-square drop velocity difference. This approach led to a stronger turbulence-included drop spectral broadening than had been found by previous investigators.

In a second attempt, three-dimensional turbulence was considered, which was assumed to be stationary, homogeneous, and isotropic. The turbulence provided a stochastic forcing function for the drop motions, and no feedback effect of the drop motions on the local turbulence structure was allowed. Both the inertial and viscous subranges of the turbulence were accounted for by choosing a plausible interpolation form for the structure function, as suggested by Batchelor (1951). The theoretical machinery of linear spectral transformation of stationary random processes (e.g., Monin and Yaglom, 1971) was then invoked to find once again the relationships between the stochastic behavior of the drops in terms of the stochastics to the turbulence. To complete this process, a closure hypothesis was

used, namely that the second and fourth moments of the air velocity distribution are related as in the case of a normal distribution; the validity of this hypothesis is supported by observations (e.g., Monin and Yaglom, 1971).

In a third attempt, the same methods of analysis, as described above, were applied but this time to determine the stochastics of the relative velocities of pairs of drops falling in three-dimensional turbulence. As in the first attempt, the results were used to calculate drop spectral evolution, as before the collison kernels were formulated by replacing the factor containing the difference of terminal velocities with the root-mean-square difference of drop relative velocities. Also, as in the first attempt, it was found that cloud turbulence significantly increases the generation rate of large drops. For example, the formation of rain drops with radii of about 100 μm starting from an inertial narrow droplet spectrum centered at about 10 μm, was found to take only 12 min for $\varepsilon = 200$ cm^2 sec^{-3}, and about 24 min for $\varepsilon = 50$ cm^2 sec^{-3}. In contrast, for the case of zero turbulence, essentially no large drops were formed during this same time period.

Although these results are encouraging in the sense that they are consistent with observations that rapid drop spectral broadening often takes place within cloudy regions of enhanced turbulence, they do not by themselves confirm the validity of the analysis of drop velocity fluctuations in response to turbulence forcing. In fact, as with the other turbulence collection efficiency models discussed already, there are a number of questionable features of the Khain and Pinsky analysis. First of all, as acknowledged by the authors themselves, there is no attempt to take into account how the hydrodynamic interaction of the drops is affected by the turbulence; in particular, collision efficiencies are taken to be the same as they would be in still air. Also, the replacement in the collection kernel of the drop terminal velocity difference by the root-mean-square drop velocity difference for non-interacting drops doesn't have a strong physical basis. A somewhat more realistic approach was taken by de Almeida (1975), who replaced the usual relative terminal velocity difference factor by the average velocity difference determined over the collision trajectory.

More seriously, the basic analysis of the turbulence appears questionable in some respects. For example, the authors find that velocity structures smaller than about 1 cm do not seem to contribute to the shear spectrum; this is at odds with the heuristic reasoning presented in Section 11.6.2, where it was shown, on the basis of dimensional arguments, that the shear strength in the inertial subrange increases with decreasing eddy size down to a microscale length, and that it remains roughly constant near its maximal value for smaller eddy sizes in the viscous subrange. They further find that relative drop velocities are established at separation distances of 1-2 cm, and not by turbulent fluctuations lying within the viscous subrange. This again conflicts with the heuristic analysis of the effects of turbulence fluctuations. Also, their estimate of turbulent inertial accelerations appears too large. For example, they estimate the inertial accelerations as $(\langle V_a \rangle^2 \varepsilon / 3\nu_a)^{1/2}$, where V_a is the characteristic velocity of ambient air. On the other hand, from (11-75) the acceleration is estimated to be $v_k(\varepsilon/\nu_a)^{1/2}$, where v_k is the microscale velocity. The authors assume $(\langle V_a^2 \rangle)^{1/2} = 1$ m sec^{-1}, whereas typically $v_k \approx 1$ cm sec^{-1}. Accordingly, their estimate of inertial acceleration in the turbulent flow appears

to be as much as two orders of magnitude too large. The inferred enhancement of drop collection rates by turbulence appears therefore to be overestimated. Unfortunately, at present, no laboratory studies are available to confirm or reject the results of the four theoretical studies described above.

Before closing these two sections on theoretical determinations of E, we should comment on the problem of extending the calculations to larger drop sizes. In general, for large falling drops with $N_{\mathrm{Re}} \gg 1$, the strong non-linearity of their hydrodynamic interaction makes the superposition method the only mathematically feasible approach known for estimating E. However, even this method has its limitations in implementation. We recall from Chapter 10 that for suffciently large drops, such complications as wake oscillations, eddy shedding, and shape deformations occur. Since there are no numerical solutions in existence for flows past single drops which reproduce these features, one must resort instead to the use of steady state numerical flows past rigid spheres or oblate spheroids. Since such flows become increasingly artificial for $N_{\mathrm{Re}} \geq 10^2 (a_0 \geq 300\,\mu\mathrm{m})$, one must expect the same for the corresponding estimates of E.

14.5.3 Experimental Verification

The many uncertainties inherent in the theoretical models for determining collision efficiencies make it especially important to check the computations against measurements. Unfortunately, however, the experimental approach is also beset with great difficulties. One major obstacle lies in the fact that in reality there is no clean conceptual division between the processes of 'collision' and 'coalescence'. When a pair of drops is allowed to interact, generally what is observed is either a coalescence or a non-coalescence event; in the latter case, it is usually not possible to say whether the drops actually collided but did not coalesce, or whether they simply experienced a 'near miss'. Thus, the experimentally accessible quantity is the *collection efficiency*, E_c, which is the ratio of the actual cross-section for drop coalescence to the geometric cross-section. This may be regarded as equivalent to the collision efficiency, as we have defined it, only if coalescence necessarily follows whenever the center-to-center separation of the two interacting drops becomes less than the sum of their (undistorted) radii (see Plate 17).

To determine E_c , one may either observe (usually photographically) the trajectories of interacting drops or measure the rate at which a drop grows as it falls through a cloud of smaller drops. Suppose, for example, that a drop of radius a_1 and fall speed $U_{\infty,1}$ grows by collecting drops each of radius a_2 and fall speed $U_{\infty,2}$; then, we have $\mathrm{E}_c = (\mathrm{d}m/\mathrm{d}t)/\pi(a_1 + a_2)^2(U_{\infty,1} - U_{\infty,2})\mathrm{w}_L$, where $\mathrm{d}m/\mathrm{d}t$ is the mass growth rate of the drop, and w_L is the liquid water content of the cloud of a_2-drops. Unfortunately, it is experimentally quite difficult to determine accurately drop sizes, trajectories, growth rates, and fall speeds, and to produce a homogeneous cloud of known liquid water content. Hence, experimental values of E_c are commonly subject to errors of 10 to 20%.

Telford *et al.* (1955), Telford and Thorndike (1961), Woods and Mason (1965, 1966), Beard and Pruppacher (1968), and Abbott (1974) have experimentally determined the collection efficiency of pairs of water drops in air with p-ratios close

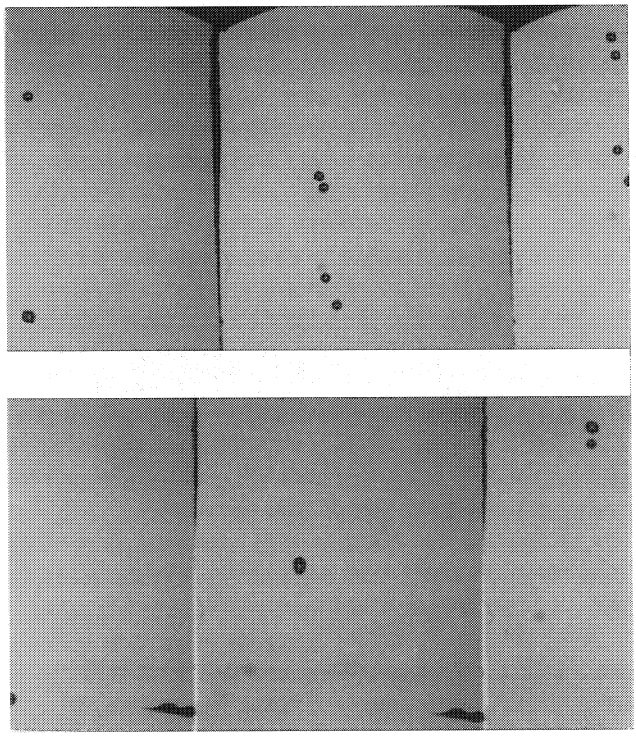


Plate 17.

to unity, while Kinzer and Cobb (1958), Picknet (1960), Woods and Mason (1964), and Beard and Pruppacher (1971b) determined E_c for drop pairs of low p-ratios. A few experimental results are also available for pairs of small drops with intermediate p-ratios (Jonas and Goldsmith, 1972).

A comparison between theoretical collision efficiencies and the experimental collection efficiencies of Abbot (1974), Telford *et al.* (1955), Woods and Mason (1965) and Beard and Pruppacher (1968) for $p \approx 1$ allows no clear conclusions, most probably because, for nearly equal drops, coalescence following a collision turns out to be a strong function of the size of the two interacting drops. On the other hand, for $p \ll 1$ a clearer picture arises. Thus, comparison between the critical collision efficiencies and experimental collection efficiencies for small p-ratios is made in Figure 14.9. The computed values of Klett and Davis (1973) appear to be in good agreement with experiment. Considering the relatively large experimental errors, we may apply the same conclusion to the computed values of Schlamp *et al.* (1976). The agreement between theory and experiment implies that, at least for small p-ratios, each collision is followed by a coalesence event.

While no direct measurements of collection efficiencies in turbulent clouds have been made, some related experiments which bear on the problem have been carried out (Woods *et al.*, 1972; Jonas and Goldsmith, 1972). Both groups measured E_c

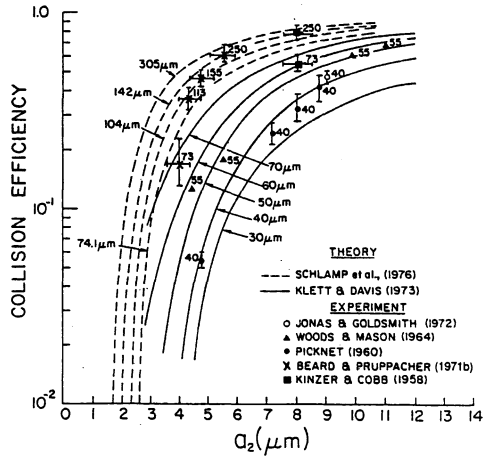


Fig. 14-9: Comparison of theoretical collision efficiencies with experimentally determined collection efficiencies, for water drop pairs of small p-ratio. Label of each curve and data point gives large drop radius in μm.

for drops in an approximately steady, laminar shear flow. As we discussed in Section 11.6.2, small aerosol particles interact on such small length and time scales that the effects of any turbulence which may be present can be modeled roughly through replacement of the turbulent velocity field by a much simpler linear shear field. This same basic modeling approach, including the selection of a representative shear strength near the Kolmogorov microscale value, is thought to be reasonable also for the problem of small droplet collisions in a turbulent cloud (see, for example, Tennekes and Woods, 1973).

Woods *et al.* and Jonas and Goldsmith measured the effect of shear on E_c for drops of $10 \lesssim a_1 \lesssim 40\,\mu$m colliding with drops of $9 \lesssim a_2 \lesssim 9.5\,\mu$m, and for linear shears in the horizontal wind varying up to 27 sec^{-1}. Since the results for the case of no shear appear somewhat low, we shall only discuss the qualitative trends which were observed. It was found that E_c values for drops of radius $a_1 \lesssim 25\,\mu$m are much larger in shear flows than in still air, while for larger drops, the effects of shear were much weaker. The effects were most pronounced for drops of comparable size. The experiments also indicated that E_c due to shear increases approximately linearly, once a threshold value of shear has been exceeded.

A theoretical treatment by Jonas and Goldsmith of the effect of shear flow on small droplet collisions failed to reveal any significant enhancement in E_c for shears of the magnitude of those employed in the experiments. This failure of the theory may be due to the fact that Stokes flow was assumed. An effect of shear is to induce a flux of droplets past one another. As suggested by Manton (1974), this indicates the possibility that some droplets might therefore be expected to intersect the wakes of neighboring ones and, hence, experience wake capture. Of course, such a possible mechanism for the enhancement of E_c is precluded by the assumption of Stokes flow, wherein no wakes can occur.

The plausibility of shear-induced wake capture is supported by measurements of the distance z_c of the wake interaction region behind falling drops of comparable size. For example, in the model experiments of Steinberger *et al.* (1968), discussed in Section 14.4.4, it was found that $z_c \gtrsim 12$ radii, even for a Reynolds number as low as 0.06 (equivalent to a drop of $a \approx 15\,\mu$m). Not surprisingly, z_c is observed to increase strongly with N_{Re}. Thus, Eaton (1970) found $z_c \gtrsim 20a$ for roughly equal-sized drops of $a = 150$ to $250\,\mu$m falling in air. Cataneo *et al.* (1971) observed much larger values of $z_c \gtrsim 2 \times 10^2 a$ and $3 \times 10^2 a$ for equal water drops of $a = 57.5$ and $350\,\mu$m, respectively. Finally, List and Hand (1971) found a maximum value of $z_c \approx 2.7 \times 10^3 a$ for drops of $a = 1.45$ mm.

Manton (1974) has provided a theoretical description of shear-induced wake capture which agrees with the qualitative features found in the experiments. However, his model is rather artificial, and greatly oversimplifies the hydrodynamics of the problem. For example, the wake interaction region is assumed to be undisturbed by the shear, and the interaction of the drops in close proximity is assumed independent of the shear.

14.5.4 Coalescence of Water Drops in Air

It is well-known that not all drop collisions result in a permanent union by coalescence. Rather, there are two additional possibilities with which we must be concerned: (1) The drops may bounce apart before surface contact is made, owing to the presence of an air film trapped between their surfaces. (2) The drops may disrupt following temporary coalescence; as we shall see, this latter behavior may be explained satisfactorily in terms of the relative magnitudes of the surface energy and the rotational kinetic energy of the coalesced drop pair.

Unfortunately. the drop coalescence problem is in general quite complex, and not nearly so well in hand as the collision problem. For example, there are no theoretical treatments which incorporate accurately the large amplitude surface distortions which may occur, and thereupon inhibit the rate of air film drainage between the drops. Similarly, it has proven very difficult to conduct experiments which can faithfully reflect natural conditions, and at the same time provide sufficient control and resolution for the parameters of interest.

A wide variety of experimental arrangements have been employed in the coalescence problem. For example, Lindblad (1964) and Semonin (1966) studied the coalescence between 2 mm-size water drops, artificially held quasi-fixed at the end of capillaries which could be moved at a variable relative velocity; Magono and Nakamura (1959), Schotland (1960), and Jayaratne and Mason (1964) studied the conditions for coalescence between drops of $29\,\mu\mathrm{m} \leq a_0 \leq 400\,\mu$m and a very large stationary, plane or hemispherical water surface; Whelpdale and List (1971), Whelpdale (1970), List and Whelpdale (1969), and Levin and Machness (1977) observed coalescences between a moving $35\,\mu$m radius drop and stationary larger drops of 500 to $1750\,\mu$m radius; Prokhorov (1951, 1954), Nakamura (1964), Adam *et al.* (1968), and Park (1970) studied the coalescence of freely moving drops of 3.1 mm to $25\,\mu$m radius colliding with each other at various imparted relative velocities; Montgomery (1971), Nelson and Gokhale (1973), and Spengler

and Gokhale (1973a,b) studied the coalescence of mm-size drops in a wind tunnel where the drops could be freely suspended in the vertical air stream of the tunnel, while Neiburger *et al.* (1972) and Levin *et al.* (1973) used a wind tunnel to infer the coalescence efficiency of water drops with radii between 45 and 120 μm from their growth rates. Brazier-Smith *et al.* (1973) studied the coalescence of nearly equal sized drops at impact speeds considerably in excess of those occurring in atmospheric clouds.

Unfortunately, most of these experiments were not carried out under natural conditions. For a proper simulation, both interacting drops should fall freely at the relative velocities following from their size difference, or from wake capture effects. Only in this way can the flows controlling drop deformations and relative trajectories for close separations be represented accurately. For this reason, experiments with fixed large drops should best be regarded as primarily exploratory and qualitative in nature. The use of stationary flat water targets is even less realistic, except possibly for the case of very small radius ratios, as film drainage rates and the forces resisting deformation can be expected to depend strongly on drop curvature. Serious shortcomings are also inherent in those studies which involve the measurement of drop growth rates, since it is difficult to ensure that no mass gain or loss occurs by diffusional growth or evaporation.

These experimental difficulties are exacerbated by the sensitivity of the coalescence phenomenon to such influences as turbulence, surface contaminants, and electric fields and charges. Because of these problems, our discussions in this section are limited primarily to just the qualitative trends which can be gleaned from the studies which appear to be the most comprehensive, and which yield the most mutually consistent results. The effects of turbulence and contaminants are not considered. Some discussion of the effects of electric fields and charges is presented in Chapter 18.

14.5.4.1 *The Rebound Problem*

It is now widely recognized that coalescence, if only temporary, will proceed once the drop surfaces make contact, since surface energy is lowered by the destruction of surface area (some apparent exceptions to this consensus include Gunn (1965) and Cotton and Gokhale (1967)). Therefore, the drop rebound problem is primarily the problem of air film drainage. Many experiments have confirmed that this drainage is hindered particularly when the two approaching drops are large enough to deform easily. Then, local flattening of their surfaces can strongly impede the expulsion of the intervening air. In addition to a dependence on drop size, the rate of air film drainage is also controlled by the relative velocity $\vec{v}_r$ of the drop pair, and by the impact angle θ between $\vec{v}_r$ and their line of centers at impact. Finally, many experiments have shown that the probability of coalescence rises sharply once the air film has thinned locally to a thickness $s \lesssim 0.1\,\mu$m. At such distances, attractive van der Waal's forces vary like s^{-3} (e.g., Adamson, 1960), and will likely be of sufficient strength to induce coalescence, especially with the help of small, random surface perturbations. While the early experimental studies of the coalescence efficiency were plagued by a variety of problems, most of all by both

incorrectly modeling the relative velocity of the two impacting drops as well as by not sufficiently controlling electrical effects, the more recent measurements of Beard and Ochs (1984), and of Ochs and Beard (1984) for drops of $1.6 \leq a_S \leq 31.6\,\mu$m colliding with drops of $50 \leq a_L \leq 501\,\mu$m give a relatively consistent picture. The results show that, for a given a_S, $\mathrm{E_{coal}}$ decreases with increasing a_L, while, for given a_L, $\mathrm{E_{coal}}$ decreases with increasing a_S. In agreement with our conclusions drawn from Figure 14.9, the coalescence studies of Beard and Ochs (1984) and Ochs and Beard (1984) show that for $1 \leq a_S \leq 5$ and $50 \leq a_L \leq 500\,\mu$m, $90 \leq \mathrm{E_{coal}} \leq 100\%$. The following parameterization of the experimental results was suggested by Beard (1994, pers. comm.) for $1 \leq a_S \leq 32\,\mu$m and $50 \leq a_L \leq 500\,\mu$m:

$$\frac{\mathrm{E_{coal}}}{100} = x + 0.459\,, \tag{14-27}$$

with $x = (a-b)^{1/3} - (a+b)^{1/3}$, $a = (b^2 + 0.00441)^{1/2}$, $b = 0.0946\beta - 0.319$, and $\beta = \ln a_S + 0.44\ln(a_L/200)$, with a_S and a_L in μm.

The coalescence of drops of $100 \leq a_L \leq 500\,\mu$m and $0.5 \leq p \leq 0.95$ was studied by Ochs *et al.* (1986, 1991), Czys (1987), and by Schaufelberger (1990). Their experimental results can be parameterized by the relation

$$\mathrm{E_{coal}} = 1 - 8.20x^{0.704}\,, \tag{14-28}$$

with $x = N_{\mathrm{We}}^{1/2} f(p)$ and $f(p) = p^4/[6(1+p^2)/(1+p^3)]$. Equation (14-28) shows that for these drops the coalescence efficiency is controlled by the Weber number $N_{\mathrm{We}} = \rho_{\mathrm{w}} a_S (U_\infty - u_\infty)^2/\sigma_{\mathrm{w/a}}$, which characterizes the deformation tendency of a drop pair. It simply compares the specific surface energy with the specific kinetic energy due to impaction of the small drop. We notice from (14-28) that $\mathrm{E_{coal}}$ decreases as N_{We} increases, which is a result of coalescence being impeded by increased drop deformation. A plot of (14-28) is provided in Figure 14.10a.

The most comprehensive investigation of drop coalescence involving larger drops has been carried out by Low and List (1982a). The five drop pairs studied involved drops of sizes $1.8\,\mathrm{mm} \leq a_L \leq 4.4$ mm and $395\,\mu\mathrm{m} \leq a_S \leq 1000\,\mu$m. Using their own data as well as those obtained by McTaggart-Cowan and List (1975), Low and List proposed the following parameterization of their experimental results:

$$\mathrm{E_{coal}} = A\left[\frac{D_{0,L}}{D_{0,L} + D_{0,s}}\right]^2 \exp\left[-\frac{B\sigma_{\mathrm{w/a}}\mathrm{E}_T^2}{S_c}\right]\,, \tag{14-29}$$

for drop diameters $D_{0,S} \geq 250\,\mu$m, $D_{0,L} \geq 500\,\mu$m and for $\mathrm{E}_T \leq 5.0\,\mu$ joule; otherwise, $\mathrm{E_{coal}} = 0$. In (14-29) $A = 0.778$, $B = 2.61 \times 10^6$ joule^{-2}m^2, $\mathrm{E}_T = CKE + \Delta S_\sigma$, $\Delta S_\sigma = S_T - S_c$, $S_T = \pi\sigma_{\mathrm{w/a}}(D_{0,L}^2 + D_{0,S}^2)$, and where CKE is the collision kinetic energy. The variation of $\mathrm{E_{coal}}$ with diameters $D_{0,S}$ and $D_{0,L}$ is given in Figure 14.10b. We notice from this figure that for given $D_{0,S} < 600\,\mu$m, $\mathrm{E_{coal}}$ increases with increasing $D_{0,L}$ while, for a given $D_{0,L}$, $\mathrm{E_{coal}}$ decreases with increasing $D_{0,S}$. For $D_{0,S} \approx 600\,\mu$m, $\mathrm{E_{coal}} \approx 0.3$ for all values of $D_{0,L}$. For $D_{0,S} > 600\,\mu$m, the coalescence behavior is complicated, but generally $\mathrm{E_{coal}}$ decreases with increasing $D_{0,L}$ for a given $D_{0,S}$.

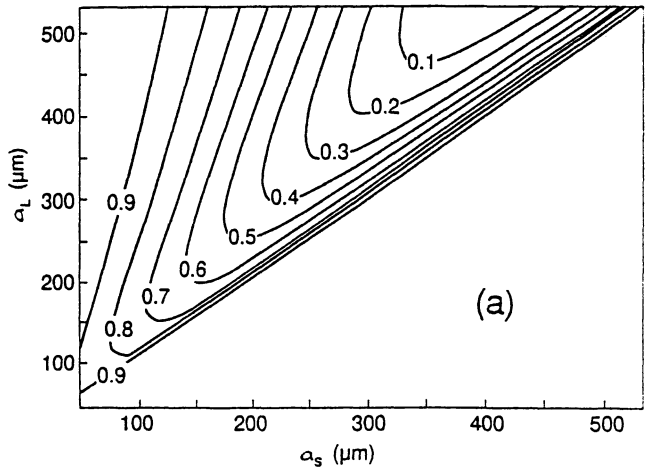


Fig. 14-10: a. Values for the parameterized coalescence efficiency of medium sized water drops colliding in air. $a_L(a_S)$ radius of large (small) drops. Based on Equation (14-29) and data of Ochs *et al.* (1986, 1991), Czys (1987) and Shaufelberger (1990). (From Beard, priv. comm., by courtesy of the author.)

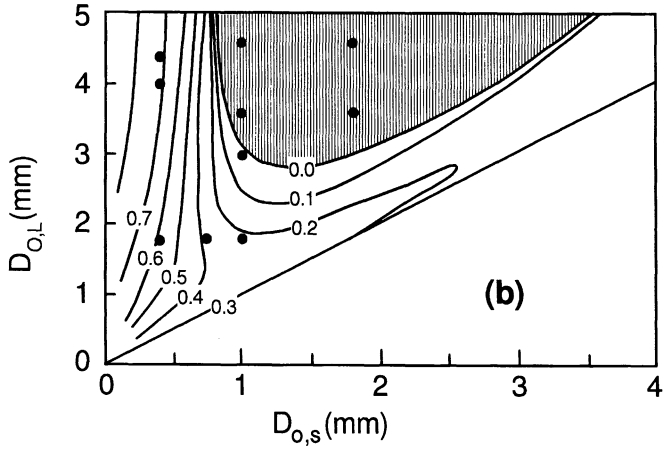


Fig. 14-10: b. Values for the parameterized coalescence efficiency of large water drops colliding in air. $D_{o,L}(D_{o,S})$ equivalent diameter of large (small) drop. The experimentally studied drop pairs are indicated by dots. The line $D_{o,L} = D_{o,S}$ corresponds to a value $E_{coal} = 0.19$. (From Low and List, 1982a; by courtesy of the author and the Am. Meteor. Soc.)

14.5.4.2 *Disruption Following Collision*

Drop breakup following the collision of two drops has been studied experimentally in vertical wind tunnels (Blanchard, 1948, 1949, 1950, 1962; Cotton and Gokhale, 1967; Spengler and Gokhale, 1973a,b; Montgomery, 1971), by directing droplet jets at each other (Magono and Nakamura, 1959; Gunn, 1965; Schneider *et al.*, 1965; Adam *et al.*, 1968; Brazier-Smith *et al.*, 1972, Whelpdale and List, 1971; Park 1970), and in long fall shafts (Nakamura, 1964; McTaggart-Cowan and List, 1975; Bradley and Stow, 1974, 1977, 1978, 1979; Low and List, 1982a,b). These experiments have demonstrated that during the early stages of coalescence, the coalescing drop-drop system is often highly unstable and may break up. Mainly four breakup modes were identified: neck or filament-type, sheet-type, disc-type and bag-type. *Neck* or *filament breakup* results from a glancing contact during which a water neck forms joining the two drops. As the drops separate, the neck breaks typically into two main drops and about five satellite drops. *Sheet breakup* occurs when a small drop hits the larger drop in such a position that it tears off one side of the large drop. This is followed by the bulk of the large drop rotating about the point of impact, while a film or sheet of water forms from the impact area. By disintegration of the sheet, about eight satellite drops of the size of the original small drop form. *Disc breakup* occurs when the small drop hits the large drop near the center. During their temporary coalescence, a disc forms, extending from the point of impact where the small drop becomes incorporated. Subsequently, the outer portion of the disc sheds drops. Eventually, the whole disc disintegrates into a large number of drops. *Bag breakup* occurs in a similar fashion as disc breakup except that now a toroid forms with a thin film of water at its center. Subsequently, the film blows up into a bag which eventually shatters into a large number of drops.

The most detailed study of drop breakup resulting from the collision of two drops has been carried out by Low and List (1982a,b). In their work, they defined E_{coal} as the fraction of colliding drops which coalesce completely into one single drop. A breakup due to collision is said to occur when either the drops bounced or when, immediately after collision, a temporarily combined pair of drops break into two or more fragment drops giving a fragment distribution $Q(m; m', m'')$, where m' and m'' are the original masses of the colliding drops producing fragment drops of mass m. Values for $Q(m; m', m'')$ were determined by Low and List using a fall shaft experiment. The results were parameterized in terms of a sum of the contributions from three major breakup types: filament-, sheet-, and disc-breakup given by

$$Q(D_0)_{D_0',D_0''} = R_f Q_f(D_0)_{D_0',D_0''} + R_s Q_s(D_0)_{D_0',D_0''} + R_d Q_d(D_0)_{D_0',D_0''}\,, \quad (14\text{-}30)$$

where $Q_{f,s,d}(D_0)_{D_0',D_0''}$ is the fragment number distribution for a particular breakup type per size interval and per collision of a D_0' with a D_0'' drop, and $R_{f,s,d}$ is the ratio of the number of breakups of type f, s, d to the total number of colliding drops which break up. The breakup probability $P(D_0', D'')$ is assumed to be given by the fraction $(1 - E_{coal})_{D_0',D_0''}$. A detailed parametrization for describing the drop fragment distribution is found in Low and List (1982b), with corrections given in List *et al.* (1987a).

14.6 Collision of Snow Crystals with Water Drops

14.6.1 Collision of Large Snow Crystals with Small Drops

In clouds with temperatures lower than 0°C, supercooled water drops as well as snow crystals may be present. In this case, two different types of hydrodynamic interaction may occur, depending on whether the flow past the snow crystal or past the drop dominates. We shall discuss both in sequence. Let us begin by considering the collision of large snow crystals with small cloud drops.

Due to the complicated shapes of snow crystals, the simple approach of the superposition method has proven to be the only feasible means for describing the interactions between drops and ice crystals. For example, Pitter and Pruppacher (1974), and Martin *et al.* (1981) have used the method to study the collisions of small supercooled drops with simple hexagonal ice plates. A numerical solution for the flow past a thin oblate spheroid was used as an approximation to the actual flow past the crystal. Similarly, Schlamp *et al.* (1975) used numerical flows past infinite cylinders in conjunction with superposition to estimate collision efficiencies of drops colliding with hexagonal columnar ice crystals. In both studies, the flow past the drop was assumed to be given by the numerical solution of Le Clair *et al.* (1970) for the flow past a liquid sphere, including the effects of internal circulation. For the drop-planar crystal problem, the form of (14-7) remains valid, it being understood that the radius a_1 now refers to the semi-major axis of the oblate spheroid. For the drop-columnar crystal problem, we see from (10-28) that the required modification of (14-8) is $\vec{F}_1 = -\rho_a v_1 C_{D,1} \mathsf{L} a_1 (\vec{v}_1 - \vec{u}_2) = 0.5 \mathsf{L} \eta_a C_{D,1} N_{\mathrm{Re},1} (\vec{v}_1 - \vec{u}_2)$, where L and a_1 are the crystal length and radius, respectively.

Earlier, less accurate computations by Wilkins and Auer (1970) and Ono (1969) were based on the computations of Ranz and Wong (1952) for inviscid flow past disks, and on the results of Davies and Peetz (I956), who studied the interaction between small droplets and an infinite cylinder in Oseen flow for $N_{\mathrm{Re}} \leq 0.2$, and in flow numerically determined by Thom (1933) for $N_{\mathrm{Re}} = 10$. Unfortunately, the use of inviscid flow is not well justified since, as we know from Chapter 10, ice crystals typically have $N_{\mathrm{Re}} \lesssim 100$. Also, the early numerical computations of Thom cannot be considered reliable.

Pitter and Pruppacher (1974) and Pitter (1977) computed collision efficiencies for drops of $1 \leq a_2 \leq 55\,\mu$m colliding with oblate spheroidal ice plates of axis ratio $b_1/a_1 = 0.05$ and of $147 \leq a_1 \leq 404\,\mu$m, corresponding to $2.0 \leq N_{\mathrm{Re}} \leq 20$ for air of -10°C and 700 mb. These computations were extended by Martin *et al.* (1981), who used an improved collision criterion to cover the size range $51 \leq a_2 \leq 639\,\mu$m corresponding to $0.1 \leq N_{\mathrm{Re}} \leq 50$. More accurate computations have recently been carried out by Ji (1991) and Wang and Ji (1992), who used a three-dimensional solution to the Navier-Stokes equation of motion (see Section 10.5.1) for flow past a simple hexagonal plate and a broad-branched crystal in conjunction with a collision criterion which includes the effects of the double rim of a crystal of finite thickness. The results of these computations are given in Figures 14.11 and 14.12. We notice from these figures that the collision efficiency increases with increasing crystal size and at first with increasing drop size, reaching a maximum which becomes increasingly broad as the size of the collecting crystal becomes larger. The reason for

the maximum and the subsequent decrease of the collision efficiency with further increase in drop size is due to the fact that, with increasing size, the drop's fall velocity rapidly approaches the fall velocity of a given crystal, thus inhibiting collision. We further notice that a broad-branched crystal of given Reynolds number has a considerably lower collision efficiency than a simple hexagonal plate of the same Reynolds number. This is most likely due to the smaller effective sweepout area of the broad-branched crystal. The collision efficiency decreases to zero as the collector crystal decreases to a critical size. This implies that a crystal has to grow by vapor diffusion to the critical size before riming may commence. This cut-off diameter for a type Pla crystal was found to be about $110\,\mu$m ($N_{\mathrm{Re}} = 0.1$), while for a Plc type crystal $d_c \approx 200\,\mu$m. The former critical size is in good agreement with the value inferred from the computations of Martin *et al.* (1981). However, in contrast to Martin *et al.*, Ji's collision efficiencies are somewhat larger, particularly those for small crystal plates.

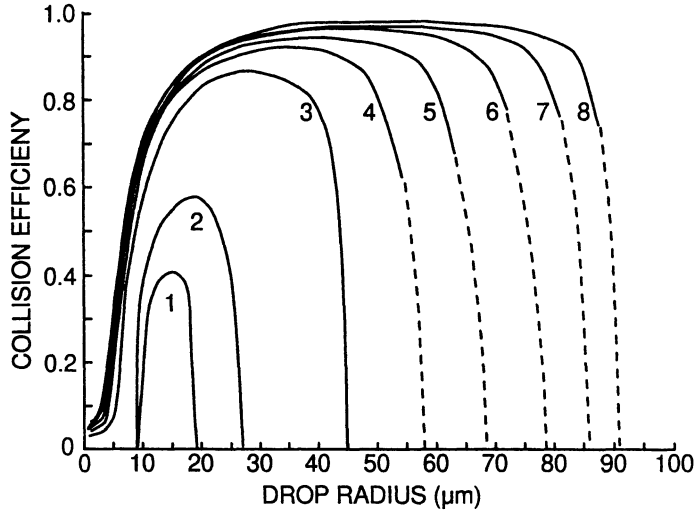


Fig. 14-11: Efficiencies with which simple hexagonal plate crystals collide with water drops of various sizes for various Reynolds numbers of the crystals. (1) $N_{\mathrm{Re}} = 1$, $d = 160$ μm, h = 18 μm; (2) $N_{\mathrm{Re}} = 2$, $d = 226.5$ μm, h = 20 μm; (3) $N_{\mathrm{Re}} = 10$, $d = 506.5$, h = 32 μm; (4) $N_{\mathrm{Re}} = 20$, $d = 716.3$ μm, h = 37 μm; (5) $N_{\mathrm{Re}} = 35$, $d = 947.6$ μm, h = 41 μm; (6) $N_{\mathrm{Re}} = 60$, $d = 1240$ μm, h = 45 μm; (7) $N_{\mathrm{Re}} = 90$, $d = 1500$ μm, h = 48 μm; (8) $N_{\mathrm{Re}} = 120$, $d = 1700$ μm, h = 49 μm. (From Wang & Ji, 1992, with changes.)

Let us now turn to the case of supercooled drops colliding with columnar ice crystals. In the theoretical study referred to earlier, Schlamp *et al.* (1975) computed collision efficiencies for drops of $2 \leq a_2 \leq 134\,\mu$m colliding with circular cylindrical ice crystals of length L and radius a_1, where $67.1 \leq \mathsf{L} \leq 2440\,\mu$m and $23.5 \leq a_1 \leq 146.4\,\mu$m ($0.2 \leq N_{\mathrm{Re}} \leq 20$). As we have said, the flow past the crystal was taken to be that past an infinite cylinder. This assumption is justified (at least for the lower half of the falling cylinder) by the observations of Ono (1969), Zikmunda and Vali (1972), and by Iwai (1973) who showed that, in contrast to

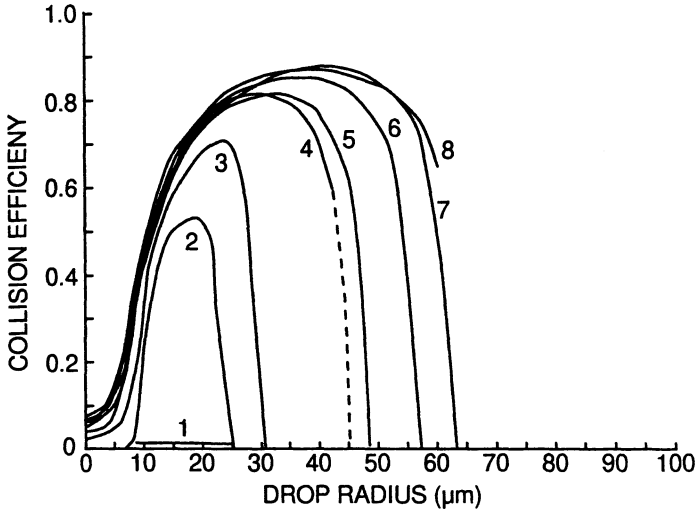


Fig. 14-12: Efficiencies with which broad-branched snow crystals collide with water drops of various sizes, for various Reynolds numbers of the crystals. (1) $N_{\mathrm{Re}} = 1$, $d = 200$ μm, h = 15 μm; (2) $N_{\mathrm{Re}} = 2$, $d = 250$ μm, h = 18 μm; (3) $N_{\mathrm{Re}} = 10$, $d = 700$ μm, h = 32 μm; (4) $N_{\mathrm{Re}} = 20$, $d = 1000$ μm, h = 40 μm; (5) $N_{\mathrm{Re}} = 35$, $d = 1500$ μm, $d = 50$ μm; (6) $N_{\mathrm{Re}} = 60$, $d = 2000$ μm, h = 60 μm; (7) $N_{\mathrm{Re}} = 90$, $d = 2500$ μm, h = 65 μm; (8) $N_{\mathrm{Re}} = 120$, $d = 3100$ μm, h = 73 μm. (From Wang & Ji, 1992, with changes.)

plate-like ice crystals, columnar crystals rime quite uniformly over their surface (see Plate 5). However, in an effort to minimize the errors from neglecting 'end effects', Schlamp *et al.* employed drag coefficients determined experimentally for finite cylinders (Jayaweera and Cottis, 1969; Kajikawa, 1971), rather than theoretical ones based on infinite cylinder calculations.

In a recent study, Ji (1991) and Wang and Ji (1992) computed more realistic collision efficiencies by applying their three-dimensional solutions of the Navier-Stokes equation of motion (see Section 10.4.2) to the flow past columnar crystals of finite length. The results of these computations are illustrated in Figure 14.13. We notice from this figure that, in analogy to the planar crystals, the collision efficiency of columnar crystals increases with increasing Reynolds number and a corresponding increase in the columnar crystal's length and width. For a given crystal Reynolds number, the efficiency also first increases with increasing drop size, and then reaches a maximum beyond which the efficiency decreases with further increasing drop size. The efficiency decreases to zero for drops whose fall velocity approaches the fall velocity of the crystal. Extrapolation of the results of Ji (1991) to lower Reynolds numbers shows that columns need to grow by vapor diffusion to a critical width of about 35 μm before riming may commence. In reasonable agreement with this value, Schlamp *et al.* (1975) computed a critical width of 47 μm.

Only a few laboratory studies are available on the efficiency with which planar

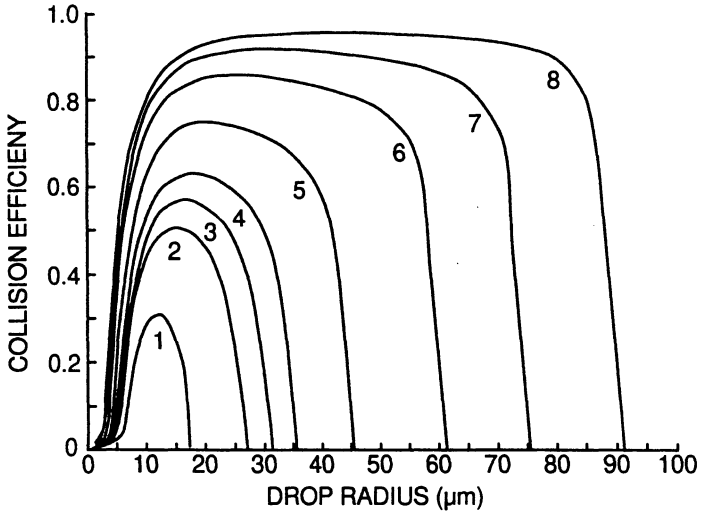


Fig. 14-13: Efficiencies with which hexagonal columns of finite lengths collide with water drops of various sizes for various Reynolds number of the crystals. (1) $N_{\mathrm{Re}} = 0.2$, L = 67.1 μm, $d = 47.0$ μm; (2) $N_{\mathrm{Re}} = 0.5$, L = 93.3, d = 65.4 μm; (3) $N_{\mathrm{Re}} = 0.7$, L = 112.6 μm, $d = 73.2$ μm; (4) $N_{\mathrm{Re}} = 1$, L = 128.3 μm, $d = 83.0$ μm; (5) $N_{\mathrm{Re}} = 2$, L = 237.4 μm, $d = 106.8$ μm; (6) $N_{\mathrm{Re}} = 5$, L = 514.9 μm, $d = 154.4$ μm; (7) $N_{\mathrm{Re}} = 10$, L = 1067 μm, $d = 213.4$ μm; (8) $N_{\mathrm{Re}} = 20$, L = 2440 μm, $d = 292.8$ μm. (From Wang & Ji, 1992, with changes.)

ice crystals collect supercooled water drops. Sasyo (1971) and Sasyo and Tokune (1973) made model experiments to determine the trajectory of water drops carried by an air stream past a rigidly fixed hexagonal bluff body, and to determine the efficiency with which such a body collects water drops. Unfortunately, the target sizes did not correspond to the air stream velocities chosen to represent the air flow past an ice crystal of a given size at terminal velocity. Also, the Reynolds numbers at which the study was carried out were larger than 100, implying that the model had an unsteady wake due to shedding of the eddy at the downstream side of the target. The same shortcomings characterize the model experiments of Kajikawa (1974), although he more realistically allowed his models to fall freely. Fortunately, Kajikawa also carried out experiments with natural plate like snow crystals which settled with $N_{\mathrm{Re}} < 100$ at their terminal velocity through a cloud of supercooled water drops of radius 2.5 to 17.5 μm. The results of this study confirm the theoretical efficiencies of Ji (1991) for crystals with $20 \leq N_{\mathrm{Re}} \leq 30$ and drops of $10 \leq a \leq 20\,\mu$m. For smaller drop sizes, the experimental errors were too large to give a clear trend of the variation of the collision efficiency with changing crystal size. Nevertheless, the experimental results of Kajikawa indicate that for $N_{\mathrm{Re}} \lesssim 10$ the collision efficiency does not decrease to zero but remains finite, even for drops as small as $a = 2.5\,\mu$m, in excellent agreement with the theoretical predictions of Ji (1991) (see Figure 14.11 and 14.12). This result contrasts with the earlier computations of Pitter and Pruppacher (1974), Pitter (1977), and Martin

TABLE 14.3
Critical dimensions of snow crystals necessary for the onset of riming. Based on data of : (1) Auer *et al.* (1970), (2) Bruntjes *et al.* (1987), (3) Reinking (1979).

Type	Major dimension (μm)			Width (μm)		
	(1)	(2)	(3)	(1)	(2)	(3)
N1a	100	-	220	30	-	41
N1c	-	-	185	-	-	46
N1e	100	-	-	30	-	-
C1e,c,f	100	-	125	40	-	40
C1g	50	75	-			
P1a	-	-	150			
P1b,P1c	-	275	240			
P7a,b	-	-	320			
CP1a	-	75	115			

et al. (1981), whose model predicted a collision efficiency cut-off at $a \approx 5\,\mu$m. This prediction was erroneously thought to be substantiated by the observations of Harimaya (1975) (see Figure 2.54), Wilkins and Auer (1970), Kikuchi and Uyeda (1979), and d'Enrico and Auer (1978), who observed that the number of drops frozen on planar crystals becomes very small if $a_2 < 5\,\mu$m. On the other hand, theoretical as well as experimental results, to be discussed in Chapter 17, indicate that aerosol particles as small as $0.5\,\mu$m radius have been observed to deposit on planar snow crystals by inertial impaction. This suggests that the riming cut-off observed in clouds is a result of the microstructure of clouds rather than a result of an actual decrease to zero of the collision efficiency.

Another noteworthy feature of the riming process of snow crystals is the evidence that there is a minimum crystal size below which drops, whatever their size, cannot be collected. The earlier computations of Pitter and Pruppacher (1974) and Pitter (1977) underestimated the collision efficiency of planar snow crystals and predicted a cut-off crystal diameter of about $300\,\mu$m, which apperared to be in agreement with the observations of Harimaya (1975), Wilkins and Auer (1970), and Ono (1969), see Figure 2.53. However, as mentioned earlier, the more realistic computations of Martin *et al.* (1981), of Ji (1991), and of Wang and Ji (1992) predict for crystals of Pla type and Plc type a cut-off diameter of 110 and $200\,\mu$m, and for columnar crystals, a cut-off width of $35\,\mu$m. These values are in excellent agreement with the more recent field studies listed in Table 14.3.

The pattern of rime deposited on a planar snow crystal was studied by Pitter and Pruppacher (1974). The study shows that there is often a circular region concentric with the crystal center where no drop collisions can occur. The portion of the crystal on which collisions may occur was thus predicted to have an annular shape. This result is in excellent agreement with the field observation of Wilkins and Auer (1970), Zikmunda and Vali (1972), Hobbs *et al.* (1972), and Knight and Knight (1973a,b), who observed that lightly rimed, natural planar snow crystals preferentially rime near the crystal edges (see Plate 4). This behavior was explained by Pitter and Pruppacher in terms of an 'air pillow' beneath the central portion of the falling ice crystal plate, inside of which drops may accelerate to the terminal

fall velocity of the ice plate before they collide with it, giving the viscous forces an opportunity to move the drop around the falling crystal.

Snow flakes may be considered essentially as falling plates with holes (see Plate 3). It is obvious that such objects may exhibit collision efficiencies which are considerably different from those of solid crystal plates, since the flow of air containing small cloud drops is directed *through* as well as *around* the porous flake. Using a vertical wind tunnel, Lew *et al.* (1986a,b) studied the efficiency with which supercooled cloud drops are collected by snow flake models which consisted of circular discs of given porosity. The results of this study were compared with the riming behavior of solid discs and of laboratory grown and natural snow flakes. The supercooled cloud studied had a liquid water content of 0.5 to 3 g m^{-3}, and consisted of drops of radius between 3 and 6 μm. The porous discs and snow flakes had diameters ranging between 0.6 and 1.1 cm. The results, summarized in Figure 14.14, show that the collection efficiency of snow flakes and of discs of known porosity is larger by one to two orders of magnitude than the efficiency of solid discs. A photographic study showed that the enhanced collection was due to the collection of drops on the rim of the various holes. The results of Lew *et al.* (1986a,b) were subsequently confirmed by experiments of Matsuo (1987).

It should be stressed at this point that the collision efficiencies discussed above only apply to ice crystals in their initial stages of riming, i.e., as long as their shape is still that assumed for the computations. During later stages, the shape changes from that of a planar or columnar hexagonal crystal into that of a spherical, conical, or irregular graupel particle and eventually, if riming proceeds further, into that of a hailstone. As might be expected, there are no theoretical values of E available for such irregular shapes, not only because of the complicated surface geometry, but also because such particles often fall with spinning and tumbling motions.

Some representative experiments have been carried out by Pflaum *et al.* (1978), and Pflaum and Pruppacher (1979), who studied the growth of graupel particles freely suspended in the vertical air stream of a wind tunnel. Their results indicated that under 'dry-growth' conditions (see Section 16.1), rimed spherical ice particles, which generally have a rough surface texture and exhibit various oscillatory-, spinning-, and helical motions (Section 10.5.3), have a collision efficiency which is considerably lower than that of a smooth sphere falling straight.

Using the wind tunnel results of Pflaum *et al.* (1978) and of Pflaum and Pruppacher (1979), Rasmussen and Heymsfield (1985) and Heymsfield and Pflaum (1985) established that the efficiency with which graupel collides with small supercooled drops may be computed from the trajectory model of Beard and Grover (1974) after replacing the Stokes number in (14-10) by the mixed Froude number. This method, originally suggested by Hall (1980), involves a slightly different non-dimensionalization than that used in Section 14.3 to obtain (14-10). Assuming that the flow field past a small cloud drop does not affect its trajectory around the graupel, (14-8) may be written for the small drop, after dividing through by m_d,

$$\frac{d\vec{v}_d}{dt} = \vec{g}^* - \frac{6\pi a_d \eta_a (C_D N_{Re}/24)_d}{m_d}(\vec{v}_d - \vec{u}_d)\,. \tag{14-31}$$

Considering the force balance $6\pi a_d \eta_a U_{\infty,d}(C_D N_{Re}/24)_d = m_d g$ and making (14-

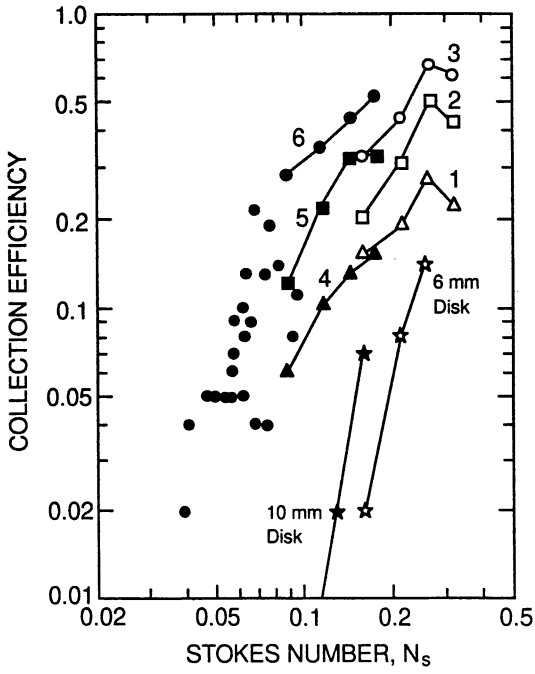


Fig. 14-14: Efficiencies with which supercooled drops are collected by synthetic ice aggregates (•) and porous or non-porous disk models (lines), for various Stokes numbers $N_S = 4U_\infty a_d \rho_w / 9\mu_a d_c$. Porosity (open area/total area of model) = 16.5 (1), 36.3 (2), 47.2 (3), 172 (4), 31.5 (5), 49.1 (6). Model diameters 0.6 to 1.1 cm. (From Lew *et al.*, 1986b, with changes.)

31) dimensionless by setting $\vec{v}'_d/(U_{\infty,g} - U_{\infty,d})$, $\vec{u}'_g = \vec{u}_g/(U_{\infty,g} - U_{\infty,d})$, and $t' = t(U_{\infty,g} - U_{\infty,d})/a_g$, the equation for the trajectory of the small drop becomes, in agreement with Hall (1980),

$$\frac{d\vec{v}'_d}{dt} = \frac{\hat{g}}{N'_{Fr}} - \frac{\vec{v}'_d - \vec{u}'_g}{N''_{Fr}} . \tag{14-32}$$

In this equation, $N'_{Fr} = (U_{\infty,g} - U_{\infty,d})^2/ga_g$ and $N''_{Fr} = (U_{\infty,g} - U_{\infty,d})U_{\infty,d}/ga_g$ constitute the 'mixed' Froude numbers. The collision efficiency may then be computed, using the model of Beard and Grover (1974), from

$$E = (y_{c,0} + p)^2/(1 + p)^2 , \tag{14-33}$$

where $y_{c,0} = y_c(p = 0) = (2/\pi)\tan^{-1}(H)$, $H = B_0 + B_1 Z + B_2 Z^2 + B_3 Z^3$, with $Z = \ln(N''_{Fr}/K_0)$, $K_0 = \exp G$, $G = B_4 + B_5 F + B_6 F^2$, $F = B_7 + B_8 x + B_9 x^2 + B_{10} x^3$, $x = \ln(C_D N^2_{Re})$, $C_D N^2_{Re} = (32/3)a_1^3(\rho_g - \rho_a)\rho_a g/\eta_a^2$, and where $B_0 = 0.1465$, $B_1 = 1.302$, $B_2 = -0.607$, $B_3 = 0.293$, $B_4 = -0.1007$, $B_5 = -0.358$, $B_6 = 0.0261$, $B_7 = -3.39$, $B_8 = 1.156$, $B_9 = -0.0430$, $B_{10} = 0.001206$.

Unfortunately, the largest graupel particles which Pflaum and Pruppacher (1979) and Pflaum *et al.* (1978) were able to grow in their wind tunnel were about 1 mm in diameter, corresponding to maximum Reynolds numbers between 100 and 200. With the foregoing parametrization, one may therefore only compute the collision efficiency of graupel in their initial stages of growth. Recently, Cober and List (1993) determined from their wind tunnel experiments the collection efficiency of rigidly suspended conical graupel of diameters between 1.5 and 6 mm. The graupel were growing in the dry growth regime (see Section 16.1) at air temperatures between -4 and $-21°C$, and in a cloud of 0.5 to 3 g m^{-3} liquid water content with a cloud droplet median volume radius of 12 to 21 μm. The cloud drops were moving with a velocity of 1.1 to 3 m sec^{-1}. Cober and List (1993) found that the average bulk collection efficiency could be parameterized by the relation

$$E = 0.55 \log(2.51 N_S), \tag{14-34}$$

where $N_S = 2a_d^2 \rho_w U_{\infty,g} / 9\eta_a a_g$. These results were found to be in good agreement with the earlier laboratory studies of Mossop (1976) and showed that the collision efficiency of graupel is up to 25% lower than the theoretical collision efficiencies of droplets colliding with a smooth sphere (Langmuir and Blodgett, 1946). Cober and List, as well as Mossop (1976) and Pflaum and Pruppacher (1979), attributed this reduction to changes in the air flow pattern caused by the roughness of the graupel surface.

In closing this section, we must briefly touch upon the retention efficiency of drops which collide with ice crystals. Since cloud drops which come into contact with an ice particle are supercooled, they immediately begin their transformation to ice. In the dry-growth regime (see Section 16.1), in which an ice particle acquires drops sufficiently slowly for all the acquired water to freeze, the collected drops tend to be retained by the ice particle. Earlier wind tunnel studies by List (1959, 1960a,b) indicated that also in the spongy or wet-growth regime (see Section 16.1), in which an ice particle acquires drops too fast for all of the water to freeze immediately, up to 70% of the unfrozen water is accommodated and retained in the dendritic ice mesh of the spongy ice deposit, implying that little, if any, of the water collected by the ice particle will be lost through shedding. However, experiments of Bailey and Macklin (1968a), of Carras and Macklin (1973), Joe (1975), and of List *et al.* (1976) appear to give some evidence that, at sufficiently high impact velocities of drops on riming cylinders and artificial hailstones, water retention is limited and water may be shed by drop bouncing, detachment of water sheets, or by splashing of impacting drops.

14.6.2 Collision of Large Drops with Small Snow Crystals

Having discussed so far the collision between relatively large snow crystals and small cloud drops, we shall now turn to the reverse case and discuss the capture of relatively small snow crystals by large cloud drops and small raindrops. This problem has been studied by Lew and Pruppacher (1983), who computed the efficiencies with which columnar snow crystals of $15 \leq d_c \leq 600\,\mu$m are captured in three orientations by drops of $100 \leq a_d \leq 600\,\mu$m, in air of 500 and 900 mb and

-6 and $-10°$C. The results of this study are summarized in Figure 14.15a,b for *columnar* crystals colliding in orientation (1). We notice that E decreases: with increasing L_c/d_c for given length L_c and density ρ_c, with decreasing ρ_c for given L_c/d_c and L_c, and with decreasing L_c for given L_c/d_c and ρ_c. For all L_c/d_c and ρ_c, E ≈ 1 if $L_c \gtrsim 200\,\mu$m. Somewhat unexpectedly, the dependence of E on drop size and orientation of the columnar crystals was found to be negligible.

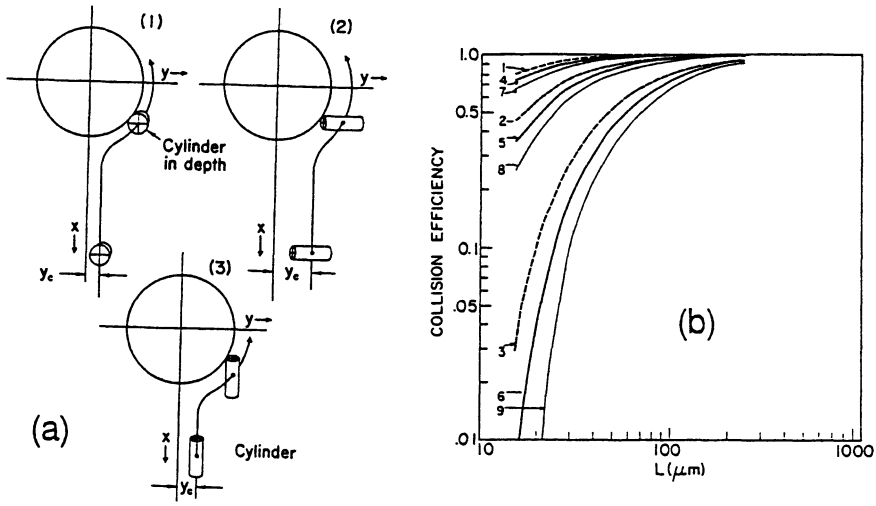


Fig. 14-15: Collision of small columnar crystals with large water drops. (a) Ice crystal orientations assumed for computing the trajectory of columnar ice crystals around a large water drop. (b) Efficiency with which a water drop of radius 416 μm ($N_{\mathrm{Re}} = 200$) collides in air with a columnar ice crystal as a function of its length L, its length-to-diameter ratio L/D, its bulk density ρ_c , and as a function of the pressure and temperature of the air, for crystal orientation (1). Curves 1,2,3 are for $\rho_c = 0.92$ g cm^{-3}, 900 mb, $-6°$ C; curves 4,5,6 are for $\rho_c = 0.5$ g cm^{-3}, 500 mb, $-10°$ C; curves 7,8,9 are for $\rho_c = 0.5$ g cm^{-3}, 900 mb, $-6°$ C. (From Lew and Pruppacher, 1983; by courtesy of the authors and the Am. Meteor. Soc.)

The capture of small *planar* crystals by large cloud drops and small raindrops was studied by Lew *et al.* (1985) for crystals of $10 \leq d_c \leq 100\,\mu$m, $\rho_c = 0.9$ g cm^{-3}, and $AR = 0.05$, allowed to be captured by drops of $530 \leq a_d \leq 760\,\mu$m in air of 400 mb and $-12°$C at various impact angles. The result of these computations are summarized in Figures 14.16a,b. We notice that, for given d_c, E decreases with decreasing values of tilt angle α due to increasing drag on the crystal. For a given value of α, E increases with increasing d_c and decreasing ρ_c. We also note that the collision efficiency for a planar crystal is lower than that for a sphere of corresponding mass, as a result of the smaller drag on the sphere.

14.7 Collision of Snow Crystals with Snow Crystals

The crystal aggregation mechanism which forms snow flakes is known to be a strong function of air temperature. For example, Dobrowolski (1903) observed 283

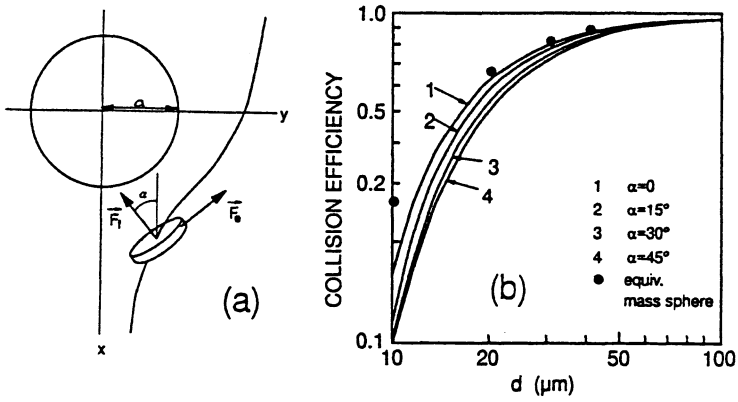


Fig. 14-16: Collision of small plate-like ice crystals with large water drops. (a) Ice crystal orientation to compute the trajectory of a plate-like crystal around a water drop. $\vec{F}_f$ and $\vec{F}_e$ are the face-wise and edge-wise components of the drag force. (b) Efficiency with which a drop of 530 μm radius collides in air with plate-like crystals of various diameters, d and tilt angles α ; for 400 mb and $-12°$ C, and crystal bulk density of 0.9 g cm^{-3}. Dots represent theoretical values for solid ice spheres of the same mass and density as those of a plate of given diameter d. (From Lew *et al.*, 1985, with changes.)

aggregation snowfall episodes, of which 83% occurred between +1 and $-5°$C, 9% between -5 and $-10°$C, and only 8% at temperatures less than $-10°$C. Similarly, Magono (1953, 1960) found that snow flakes had their largest dimensions at temperatures near $-1°$C, and that aggregation was mostly confined to temperatures warmer than -8 to $-10°$C. These observations were confirmed by Hobbs *et al.* (1974b) and Rogers (1974a,b), who also found a second snow flake diameter maximum at temperatures between -12 and $-17°$C, in addition to the main maximum near 0°C (see Figure 14.17). The field observations of Hobbs *et al.* and of Jiusto and Weickmann (1973) demonstrate that most snow flakes are aggregates of planar snow crystals with dendritic habit features. However, aggregates (bundles) of needles are also observed. Aggregates of simple, thick ice-plates and short columnar ice crystals are rare.

Observations show that, on contact, ice crystals 'stick' to each other by forming an ice bond across the surface of contact if the air temperature is relatively close to 0°C, or interlock with each other if the crystals have dendritic features. The 'interlocking mechanism' is expected to occur preferentially at temperatures between -12 and $-17°$C and at relatively high ice supersaturations (Ohtake, 1970b,c), since under these conditions, dendritic features are most favored (recall Section 2.2). The 'sticking mechanism' is most efficient at temperatures near 0°C where a quasi-liquid film is present to promote the formation of an ice neck between the particles (recall Section 5.7.3). Hobbs (1965) concluded, from a study of the sintering of ice spheres, that the rate of ice-neck formation is sufficiently fast for ice crystal aggregation to occur in clouds at temperatures as low as $-20°$C.

At present, no theoretically derived efficiencies are available for the collision

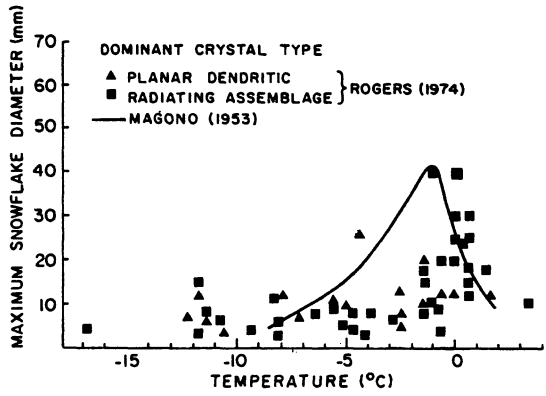


Fig. 14-17: Maximum observed snowflake diameters as a function of air temperature for two types of snowflake composition. (From Rogers, 1974b; by courtesy of the author.)

of snow crystals with other crystals. Although flow fields around Pla and Plc type crystals are now available, serious difficulties arise in defining an appropriate collision criterion.

Unfortunately, there are also only a very few experimental studies of the efficiency with which snow crystals are collected by other snow crystals, and most of these considered only the interactions between small crystals and fixed, large ice targets (Hallgren and Hosler, 1960; Hosler and Hallgren, 1960; Latham and Saunders, 1970; Keith and Saunders, 1989). Only Rogers (1974b) considered the collection efficiency of freely falling snow crystals. These efficiencies were inferred from a comparison of the observed number of component crystals in a flake and the number of component crystals computed with a continuous growth model, assuming $E_c = 1$. The results of these and other studies are plotted in Figure 14.18. We notice the large scatter in the data, suggesting perhaps only a general increase of the collection efficiency with increasing temperature. All data suffer mostly from the undetermined dependence of the collection efficiency on the size and shape of the colliding crystals. Keith and Saunders (1989) attempted to shed some light on this problem by considering the collision of a fixed cylindrical ice target with planar snow crystals as a function of their size. They found that the efficiency with which planar snow crystals are collected by a cylindrical target at $-11°C$ varied as a function of a Stokes-type parameter defined by $\Psi = 10 U_{\infty,c} d_c / D_c$ where $U_{\infty,c}$ in m sec^{-1} is the impact speed of the crystals given by the fall velocity of the larger crystal, d_c in μm is the size of the smaller snow crystal, and D_c in μm is the size of collector crystal. This function has been plotted by Keith and Saunders (1989) in their Fig. 10. Assuming that the relationship for Ψ also applies to planar crystals of $D_c = 1$ mm ($U_{\infty,c} = 50$ cm sec^{-1}) colliding with smaller planar crystals of $d_c = 50$, 30 and 20 μm, one finds from their graph $E_c = 0.83, 0.53, 0.31$, respectively, applying to $-11°C$. These efficiencies are larger than those shown in Figure 14.18, but are consistent with computations of Mitchell (1988) and Rauber (1987), who found that agreement between field observations and the results of their stochastic crystal

aggregation model required $E_c \approx 0.4$ in the temperature range -10 to $-20°C$.

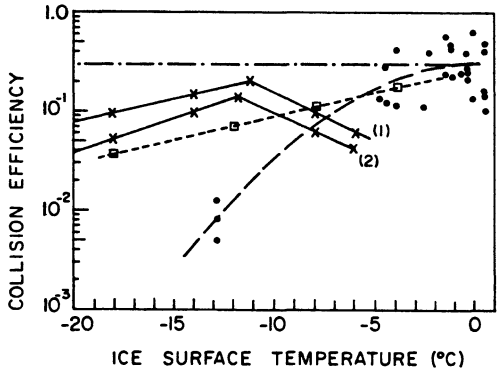


Fig. 14-18: Experimentally determined efficiency with which snow crystals and ice spheres collect micron sized ice crystals, as a function of temperature of collector ice particle. (-.-.) Latham and Saunders (1970), $a = 1000$ μm, spheres; (— — —) Rogers (1974b), $a = 500$ μm, snowflake; (– – –) Hallgren & Hosler (1960), $a = 85$ μm ice sphere; (×) Hosler & Hallgren (1960), $a = 180$ μm (1), $a = 63.5$ μm (2), ice spheres.

14.8 Orientation Model for Particles in Turbulence

As we have discussed in Chapter 10, for some hydrodynamic conditions non-spherical particles may adopt a preferred orientation of fall in quiet air. However, under virtually all atmospheric conditions there will be background turbulence as well, and this might be of sufficient intensity to significantly disrupt whatever orientational order the particles would otherwise possess. It is obvious, for example, that sufficiently small particles will be completely entrained by turbulent eddies and, hence, will experience a tumbling motion with no preferred orientation. Larger particles may tend to remain in a stable fall mode, but will nevertheless be buffeted by the turbulence so that a wobbling motion will be superimposed on their quasi-steady fall.

This problem is highly intractable, as are most turbulence problems. Partly for this reason, even relatively recent studies of the effects of ice crystals on cloud radiative properties continue to assume either i) random orientations (e.g., Takano *et al.*, 1992), or ii) some *ad hoc* ordered state (e.g., crystals with their long axis randomly oriented in the horizontal plane (Stephens, 1980), or parameterized Gaussian orientation distributions (Matrosov, 1991)).

In an analysis of the problem, Cho *et al.* (1981) concluded that "... turbulence is unable to destroy the preferred orientation of falling ice crystals." This qualitative outcome was obtained by a comparison of characteristic length and velocity scales of ice crystals and turbulent eddies. The essence of the argument was that eddies of sizes comparable to the reorientation length scale of a perturbed crystal have associated velocities that are much smaller than the crystal fall velocities, so that the crystals should remain relatively undisturbed as they fall through the eddies.

These arguments and conclusions are essentially qualitative, and are based primarily on kinematical considerations. We shall now describe a more recent model (Klett, 1995) that provides a quantitative estimate of the effects of turbulence.

14.8.1 Turbulence Model

As was done by Cho *et al.*, the turbulence is modeled by assuming a spectrum of eddies within or below the inertial subrange. Below the subrange, the velocity fluctuations are linearly related to the corresponding eddy sizes, as described in Section 11.6.2.1. If the maximum particle dimension, $d_{\max}$, is less than the microscale length λ_k, a condition we have found likely to be satisfied in the atmosphere (see Section 11.6.2.), then the velocity fluctuations affecting the particle will vary linearly with eddy size λ. Hence, the velocity fluctuation over the full extent of the particle, which is expected to be most effective for inducing rotational perturbations, will be of order $d_{\max}/\tau_k$, since τ_k^{-1} is the relevant characteristic shear rate in this linear regime.

The form of the most effective fluctuating turbulent velocities can therefore be consolidated as follows, where a normalization by microscale quantities has been carried out, and an interpolation has been used to smooth out the transition from one flow regime to the other:

$$\frac{v_\lambda(d_{\max})}{v_k} \approx \left(\frac{d_{\max}}{\lambda_k}\right)^{\alpha}, \tag{14-35}$$

where $\alpha = S(x-1,10) + S(1-x,10)/3$. In this equation S is the sigmoid function, i.e., $S(x,y) = (1+e^{xy})^{-1}$, and $x = d_{\max}/\lambda_k$. The choice of $y = 10$ provides smoothing measured by a deviation $\Delta\alpha = \pm 0.18$ from the limit values of 1/3 and 1 for $d_{\max}/\lambda = 1.1$ or 0.9, respectively. Smaller values of y give more smoothing of the step function, and vice versa for larger values.

14.8.2 Orientation of Spheroids in Turbulent Air

For a spheroid of small eccentricity, e, and for flow characterized by a small Reynolds number, N_{Re}, Cox (1965) solved for the magnitude Γ_c of the torque acting on the spheroid, assumed to be translating without rotation through the fluid with terminal velocity U_∞ to first order in e and N_{Re}. The result may be expressed as follows:

$$\frac{\Gamma_c}{6\pi\eta_a U_\infty c^2} = -\frac{29}{40} N_{\mathrm{Re}} e \sin\theta\cos\theta \tag{14-36}$$

In this equation, θ is the angle between the direction of fall and the symmetry axis of the rotationally symmetric spheroid. Cox defines the eccentricity in such a way that to O(e) the diameter of the spheroid is $2c(1-e)$ and the length of a prolate spheroid ($e > 0$) or the thickness of an oblate spheroid ($e < 0$) is $2c(1+e)$. Here c is a characteristic length scale for the spheroid, in terms of which its volume is $4\pi c^3/3$. The Reynolds number is based on this length also, i.e., $N_{\mathrm{Re}} = U_\infty c/\nu_{\mathrm{a}}$.

Next, we consider the dependence of some measure of tilting, such as the root-mean-square tilt angle, σ, on the physical parameters characterizing the problem for the case that turbulence dominates thermal fluctuations. Then, for a particle size and shape defined by two lengths a and b, we expect a functional relationship of the form $\sigma = f_1(\rho_a, \rho_p, g, \nu_a, a, b, \varepsilon)$, where ρ_p is the particle density. Using arguments applied in Section 14.2, an equivalent dimensionless relationship is

$$\sigma = f_2(e, v_\lambda(d_{\max})/U_\infty, N_{\mathrm{Re}})\,. \tag{14-37}$$

For $\theta \ll 1$, the equation of motion for the vertical tilting of the spheroid is given by:

$$I\ddot{\theta} + 2Q\theta + 8\pi c^3 \eta \dot{\theta} = \Gamma_t\,, \tag{14-38}$$

where $Q = 87\pi c^3 U_\infty \mid e \mid /40$, and where Γ_t represents the random torque caused by turbulence and thermal fluctuations, I is the moment of inertia for vertical tilting, and the dots represent time derivatives. The third term on the left-hand side is the viscous relaxation torque that attenuates $\dot{\theta}$.

Next, we perform a Langevin average similar to that described previously in Section 11.1: multiply (14-38) by θ and note that $\theta\ddot{\theta} = d(\dot{\theta}\theta)/\mathrm{d}t - \dot{\theta}^2$, and $2\theta\dot{\theta} = \mathrm{d}(\theta^2)/\mathrm{d}t$. Then, if we take an ensemble average (denoted by angular brackets) and assume a state of dynamic equilibrium so that $\langle\theta^2\rangle =$ constant, we conclude that $\langle\theta\dot{\theta}\rangle = 0$ and $\langle\theta\ddot{\theta}\rangle = -\langle\dot{\theta}^2\rangle$. If we further assume there is no correlation on average between the tilt angle and random torques, then also $\langle\Gamma_t\theta\rangle = 0$. As a result, the ensemble average of θ times (14-38) reduces to:

$$Q\langle\theta^2\rangle = \frac{I}{2}\langle\dot{\theta}^2\rangle. \tag{14-39}$$

Finally, the instantaneous angular velocity is separated into components due to Brownian motion and turbulence, i.e., $\dot{\theta} = \dot{\theta}_{\mathrm{therm}} + \dot{\theta}_{\mathrm{turb}}$. There should be negligible correlation between the two random processes so that $\langle\dot{\theta}_{\mathrm{therm}}\dot{\theta}_{\mathrm{turb}}\rangle = 0$. Therefore, we obtain $\langle\dot{\theta}^2\rangle = \langle\dot{\theta}^2_{\mathrm{therm}}\rangle + \langle\dot{\theta}^2_{\mathrm{turb}}\rangle$. But by the law of equipartition, we also have the relation $I\langle\dot{\theta}^2_{\mathrm{therm}}\rangle = kT$. On substituting this into (14-39), the result is:

$$Q\langle\theta^2\rangle = \frac{kT}{2} + \frac{I}{2}\langle\dot{\theta}^2_{\mathrm{turb}}\rangle \tag{14-40}$$

Equation (14-40) expresses the variance, $\langle\theta^2\rangle$, of the probability distribution for small tilt angles in terms of the variance of the turbulence-induced angular velocity fluctuations. Although the exact form of the distribution for $\theta \ll 1$ remains unknown, it is likely very close to Gaussian, given the random nature of the torques that drive it. Also, a study by Sassen (1987) on light pillars (vertical columns of light seen at night above bright localized light sources during light snowfall or ice fog) supports a normal distribution of tilt angles of falling disk-like snow crystals. Hence, it is here to be Gaussian, and the information accumulated so far is used to complete the specification of its variance. (On a historical note, a somewhat analogous procedure was adopted, in a classic paper on drop collisions in turbulent flow, by Saffman and Turner (1955).)

If we allow both positive and negative tilt angles, the Gaussian distribution will have the form:

$$p_G(\theta) = e^{-\beta\theta^2} Z_G^{-1}(\beta)\,, \tag{14-41}$$

with $Z_G(\beta) = \int_{-\pi/2}^{\pi/2} e^{-\beta\theta'^2}\,\mathrm{d}\theta' = (\pi/\beta)^{1/2}\mathrm{erf}(\pi\sqrt{\beta}/2)$. The parameter β is related to the variance by $\langle\theta^2\rangle = -\partial \ln Z_G/\partial\beta$. For $\beta \gg 1$ the error function factor is essentially unity, so that $\lim_{\beta\gg1}\langle\theta^2\rangle = 1/2\beta$. From this and (14-40), we have

$$\beta = \frac{Q}{kT + I\langle\dot{\theta}^2_{\mathrm{turb}}\rangle}\,. \tag{14-42}$$

With this expression for β , it can be seen that the orientation distribution given by (14-41) is consistent with a Boltzmann distribution for $\theta \ll 1$ and for the case of no turbulence; such a distribution was first described by Fraser (1979). Furthermore, (14-38) suggests that a reasonable evaluation of the turbulent kinetic term in (14-42) is:

$$I\langle\dot{\theta}^2_{\mathrm{turb}}\rangle = m' v_\lambda^2(d_{\max})\,, \tag{14-43}$$

where $m' = 87\pi\rho c^3/40$, and in terms of which $Q = \mid e \mid m' U_\infty^2$. With this form, we now obtain

$$\lim_{N_{\mathrm{Re}}\le 1} \sigma = \left(\frac{kT + m' v_\lambda^2(d_{\max})}{2 \mid e \mid m' U_\infty^2}\right)^{1/2}\,, \tag{14-44}$$

and for the case that turbulence is dominant, this satisfies (14-37), the lack of any explicit dependence on N_{Re} notwithstanding.

14.8.3 Generalized Orientation Distribution

Heuristic generalizations can now be used to eliminate restrictions on tilt angles, aspect ratios, and Reynolds numbers. To extend (14-41) to all tilt angles, we let $\theta \to \sin\theta$, which leads to the new orientation distribution $p(\theta,\beta) \sim e^{-\beta\sin^2\theta}$. The rationale for this change is simply that it ensures agreement with the Fraser (1979) distribution for all θ for the limiting case of $\varepsilon \to 0$.

It is also necessary to modify the orientation weighting function description to properly account for the fact that, in applications, averages will be taken over solid angles. If we consider a spherical polar coordinate system with the direction of gravity taken along the negative z direction, then for falling disk-like objects, the tilt angle, or angle of deviation from the stable mode, will be just the polar angle, θ, while for cylinder-like objects, it will be $\pi/2 - \theta$. Therefore, on introducing the differential element of solid angle $\mathrm{d}\Omega' = \mathrm{d}\phi' \sin\theta'\,\mathrm{d}\theta'$, where ϕ' is the azimuthal angle, the probability distribution will be of the form:

$$p(\theta,\beta) = \begin{cases} \dfrac{\sqrt{\beta}e^{-\beta\sin^2\theta}}{4\pi F(\sqrt{\beta})}\,, & \text{disks, oblates, plates,} \\ \dfrac{\sqrt{\beta}e^{-\beta\cos^2\theta}}{2\pi^{3/2}\mathrm{erf}(\sqrt{\beta})}\,, & \text{cylinders, prolates, columns,} \end{cases} \tag{14-45}$$

where $F(x)$ is Dawson's integral:

$$F(x) = e^{-x^2} \int_0^x e^{t^2}\, \mathrm{d}t\,, \tag{14-46}$$

and $\mathrm{erf}(x)$ is the error function. (A concise algorithm for evaluating $F(x)$ is given in Press *et al.* (1992).)

For an oblate spheroid or a disk of thickness H and diameter D, the aspect ratio is $y_D \equiv H/D$. The same definition would apply for plate-like ice crystals as well, with D representing the maximum (circumscribed) diameter. Similarly, for a prolate spheroid, finite cylinder, or columnar crystal of length L and diameter D, the aspect ratio is $y_C \equiv D/\mathsf{L}$. With these definitions, e is replaced as follows:

$$|\, e \,| \rightarrow \begin{cases} \frac{1-y_D}{2+y_D}\,, & \text{disks, oblates, plates,} \\ \frac{1-y_C}{1+2y_C}\,, & \text{cylinders, prolates, columns} \end{cases} \tag{14-47}$$

By using this equation for arbitrary aspect ratios, one in effect assumes that the first-order dependence of restoring torque on aspect ratio remains a good approximation for all aspect ratios. Similarly, the dependence of m' on aspect ratio can be summarized as:

$$m' = \frac{87\pi}{320}\rho \begin{cases} y_D D^3\,, & \text{disks, oblates, plates} \\ y_C^2 \mathsf{L}^3\,, & \text{cylinders, prolates, columns} \end{cases} \tag{14-48}$$

The extension of the model to moderate Reynolds numbers is based on the plausible notion that the hydrodynamic torque on the particle may be expressed approximately as $\Gamma = \Gamma_c(1 + N_{\mathrm{Be}})$, where N_{Be} is the Best number. The resulting composite orientation distribution is then given by (14-45) with

$$\beta = \frac{|\, e \,|\, m'(1 + 10^{-B_0/B_1} N_{\mathrm{Re}}^{1/B_1}) U_\infty^2}{kT + m'(1 + 10^{-B_0/B_1} N_{\mathrm{Re},t}^{1/B_1}) v_\lambda^2(d_{\max})}\,. \tag{14-49}$$

In this expression, $N_{\mathrm{Re},t}$ is the Reynolds number of turbulent eddies of scale size equal to the maximum particle dimension, and B_0 and B_1 are coefficients in an empirical fit of Best number to Reynolds number, as described in Section 10.4.

For particles large enough to satisfy $N_{\mathrm{Re}} \gg 1$, and for which buffeting by turbulence dominates Brownian impulses, the limiting form of β is:

$$\lim_{\substack{N_{\mathrm{Re}} \gg 1 \\ \frac{m' v_\lambda^2 |_{d_{\max}}}{kT} \gg 1}} \beta = \begin{cases} \left(\frac{1-y_D}{2+y_D}\right) \left(\frac{U_\infty}{v_\lambda(D)}\right)^{2+\frac{1}{B_1}}\,, & \text{disks, oblates, plates,} \\ \left(\frac{1-y_C}{1+2y_C}\right) y_C^{1/B_1} \left(\frac{U_\infty}{v_\lambda(\mathsf{L})}\right)^{2+\frac{1}{B_1}}\,, & \text{cylinders, prolates, columns} \end{cases} \tag{14-50}$$

From this equation we see, for example, that for the case of weak tilting, corresponding to the particle terminal velocity being much larger than the turbulence velocity fluctuations effective for particle tilting, the rms tilt angle is proportional

to the factor $\sqrt{(v_\lambda(d_{\max})/U_\infty)^{2+B_1^{-1}}}$. Since typically $B_1 \approx 1$, the rms tilt angle thus varies approximately as $(v_\lambda(d_{\max})/U_\infty)^{3/2}$. A naive argument for the case $N_{\mathrm{Re}} \gg 1$ would be to state that the tilt angle should be proportional to the ratio of main flow stress to turbulent stress, which from Bernoulli's law should result in an rms tilt angle of $(v_\lambda(d_{\max})/U_\infty)^2$. The reason the former estimate differs from this is that in the Reynolds number regime for which stable fall modes are found to exist falls short of the Bernoulli limit; i.e., the drag coefficient is not constant, because the Reynolds number is not large enough.

An application to the problem of ice pillar formation is shown in Figure 14.19a,b. Sassen (1980) related the width of ice pillars to characteristic ice crystal tilt angles. In this case, the inferred tilt angles are very small, being just a few degrees or less. For one of the snow flake types investigated, namely plates of the order of a millimeter in diameter, some independent empirical information from Section 10.5 on the fall speed and aspect ratios as a function of size can be used to obtain a somewhat more accurate description, namely $y_D \doteq 0.01 D^{-0.6}$ and $U_\infty \doteq 300 D^{0.824}$, with D in cm. This information can be substituted directly into (14-49) to improve the description. (In the absence of such an equation for fall speed, one can make use of the previously described empirical relationships between N_{Be} and N_{Re} for various particle geometries, and from them construct a simple algorithm for U_∞.) It can be seen from Figure 14.19b that tilt angles reasonably consistent with the measurements can be predicted by the present model using plausibly weak levels of turbulence. In this case, the angles plotted are maximal in the sense that only 1% of tilt angles are larger than those shown; they correspond roughly to two standard deviations from the equilibrium orientation.

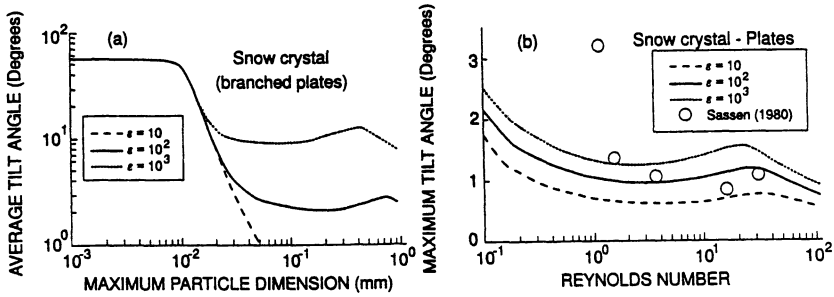


Fig. 14-19: (a) Average of positive tilt angles versus maximum particle dimension for plate type ice crystals, for various turbulence energy dissipation rates per unit mass. (b) Maximum tilt angles ($\geq$ 99 % of all tilt angles) versus particle Reynolds number for plate-type ice crystals. The results for weak levels of turbulence are consistent with the measurements of tilt angles in light pillars by Sassen (1980), except for the measured value near 3°. Curves based on (14-46). (From Klett, 1995; by courtesy of the author and the Am. Meteor. Soc.)

Figure 14.19a describes the tilting behavior of branched plates for a somewhat broader range of conditions than were encountered in the ice pillar study of Sassen (1980). We see the small crystal regime of random orientations due to Brownian

motion gives way rapidly to ordered fall with increasing crystal size, and the increasing interference with this transition caused by increasing levels of turbulence. It is also seen that there is a range of sizes such that, for moderate to strong turbulence, the tilt angles actually increase again with size, achieve a maximum, and then begin to fall off with further size increases. The increase in tilt angle with size occurs in the submicroscale turbulence regime of linear velocity fluctuations, which cause the velocity fluctuations over the size scale of the particles to increase faster than the particle terminal velocities. The tilt angle maximum and subsequent dropoff with increasing size comes about as the particles begin to exceed the Kolmogorov microscale length, since beyond that size scale, the velocity functions increase more weakly with size than do the terminal velocities. The fact that the Kolmogorov length increases with decreasing turbulence intensity accounts also for the fact that the maximum tilt angle location shifts to larger sizes with decreasing turbulence.

CHAPTER 15

GROWTH OF CLOUD DROPS BY COLLISION, COALESCENCE AND BREAKUP

As we have already learned from our brief historical review in Chapter 1, it has long been established that the presence of ice is not always necessary for precipitation formation in clouds. In more recent times, radar observations have confirmed this early conclusion. In such cases, the flow of water up the spectrum from small droplets to rain must occur by the process of collision and coalescence of drops. This is often referred to as the collection process, and sometimes erroneously as the 'warm rain' process. The latter designation is somewhat inappropriate, since collection growth also occurs in clouds colder than 0°C (Braham, 1964).

In this chapter, we shall discuss quantitatively the evolution of drop spectra by collection growth. We shall first consider the *continuous growth model*, according to which all large drops of the same size grow at the same continuous rate. This relatively simple model was the first to be applied to the problem of precipitation development and is capable of reasonable accuracy in describing some aspects of collection growth. It also is still used to describe the growth of graupel and hailstones at the expense of much smaller drops. However, the model generally overestimates the time required to form rain as a result of drops colliding with drops, since it does not account for the fact that a small fraction of larger drops will experience by chance a greater than average frequency of collection events, and will thus grow faster than the continuous model predicts. We shall therefore devote most of our attention to the *stochastic growth model*, which takes this probabilistic aspect of collection growth into account. We shall also show in Chapter 17 that it is only through the stochastic growth process that the observed redistribution of chemical compounds inside the cloud water may be explained.

15.1 Continuous Model for Collection Growth

We have already briefly introduced the continuous growth model in Section 14.5.3, where we discussed its application to the experimental problem of determining the collection efficiency E_c by measurement of drop growth rates. Thus, if a drop of radius a_1, fall speed $U_{\infty,1}$, and mass m_1 falls through a cloud of liquid water content w_L, containing uniform drops of radius $a_2 < a_1$, and fall speed $U_{\infty,2}$, then according to the continuous growth model, the growth rate of the large drop is

$$\frac{\mathrm{d}m_1}{\mathrm{d}t} = \mathrm{E}_c\pi(a_1 + a_2)^2(U_{\infty,1} - U_{\infty,2})\mathrm{w}_L = K(a_1, a_2)\mathrm{w}_L\,, \tag{15-1}$$

where

$$K(a_1, a_2) = \mathrm{E}_c\pi(a_1 + a_2)^2(U_{\infty,1} - U_{\infty,2})\,, \tag{15-2}$$

is the collection kernel for hydrodynamic capture (cf. (11-85)). Equation (15-1) follows from the assumption that the water associated with the small drops is distributed continuously and uniformly. Furthermore, if more than one a_1-drop falls through the homogeneous cloud, each one is assumed to grow at the rate specified by (15-1).

In Section 15.2, it is shown that K varies approximately as a_1^6 for $10 \leq a_1 \leq 50\,\mu$m, and as a_1^3 for $a_1 > 50\,\mu$m. On comparison with the weaker size dependence $\mathrm{d}m/\mathrm{d}t \sim a$, found for the diffusion growth of a small drop (Section 13.2), we conclude that the relative importance of collection growth increases sharply with drop size. In fact, a crossover in dominance from diffusion to collection growth generally occurs for $10 \lesssim a_1 \lesssim 20\,\mu$m.

We may easily generalize (15-1) to apply to a situation in which an a_1-drop falls through a polydisperse cloud of smaller drops, distributed in size according to the spectrum $n(a)$. Then, in place of (15-1), we have

$$\frac{\mathrm{d}m_1}{\mathrm{d}t} = \frac{4\pi\rho_\mathrm{w}}{3} \int K(a_1, a_2) n(a_2) a_2^3 \mathrm{d}a_2 \,. \tag{15-3}$$

Since $\mathrm{d}m_1/\mathrm{d}t = 4\pi\rho_\mathrm{w} a_1^2 \mathrm{d}a_1/\mathrm{d}t$, and assuming $\mathrm{E}_c = \mathrm{E} = y_c^2/(a_1 + a_2)^2$ (Equation (14-1)), then from (15-2) and (15-3) an alternative description in terms of the radius growth rate is

$$a_1^2 \frac{\mathrm{d}a_1}{\mathrm{d}t} = \frac{\pi}{3} \int y_c^2(a_1, a_2)[U_{\infty,1} - U_{\infty,2}] a_2^3 n(a_2) \mathrm{d}a_2 \,. \tag{15-4}$$

Several computations using (15-4) are in the literature (e.g., Mason, 1952b; Telford, 1955; Twomey, 1964; Braham, 1968; and Chien and Neiburger, 1972). Chien and Neiburger computed the drop growth rates in a cloud with a Khrgian-Mazin spectrum (Equation (2-3)), and in a monodisperse cloud with the same w_L and mean volume radius. The results, shown in Figure 15.1, demonstrate that the growth rate is significantly smaller in the monodisperse cloud, even though it is comprised of drops which are larger than three-quarters of those in the polydisperse cloud. This example shows that the growth rate is a sensitive function of the drop size distribution as well as the liquid water content. Braham (1968) also demonstrated this sensitivity by comparing the growth rate of drops in a typical maritime and continental cumuli. The result of Braham's computations is summarized in Figure 15.2 which shows that, in agreement with observations, precipitation sized drops develop much faster in maritime than in continental clouds due to the broader drop size distributions and larger liquid water contents of maritime clouds.

The continuous growth model also permits a simple assessment of the effect of an updraft on the development of precipitation. For example, assuming $a_2 \ll a_1$, (15-1) may be written in the form

$$\frac{\mathrm{d}a_1}{\mathrm{d}z} = \frac{\mathrm{E}_c U_{\infty,1} \mathrm{w}_L}{4\rho_\mathrm{w}} \,. \tag{15-5}$$

Now suppose there is an updraft of strength $W > U_{\infty,1}$, so that the upward velocity of the a_1-drop relative to the ground is $W - U_{\infty,1} = \mathrm{d}z/\mathrm{d}t$, where $z(t)$ measures

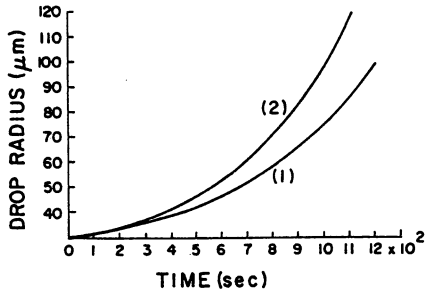


Fig. 15-1: Size variation of a drop of initial radius of 30 μm growing by collision and coalescence: (1) in a monodisperse cloud with a mean volume radius of 10 μm and w_L = 1 g m^{-3}; (2) in a cloud with a Khrgian Mazin drop size distribution, mean volume radius of 10 μm, and w_L = 1 g m^{-3}. (From Chien and Neiburger, 1972; by courtesy of Am. Meteor. Soc., and the authors.)

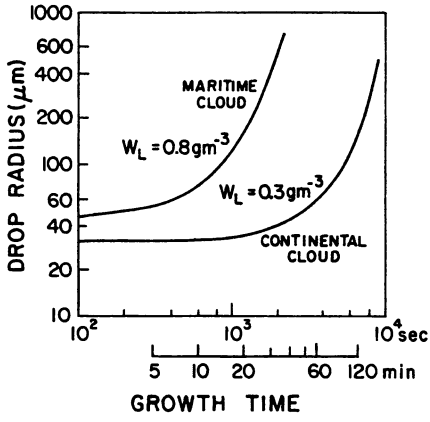


Fig. 15-2: Size variation of a drop growing by collision and coalescence in a maritime and a continental-type cloud. (From Braham, 1968; by courtesy of Am. Meteor. Soc., and the author.)

the height of the drop. Then, (15-5) may also be expressed as follows:

$$\frac{da_1}{dt} = \frac{E_c U_{\infty,1} w_L}{4\rho_w (W - V_{\infty,1})} . \tag{15-6}$$

For a constant updraft, the formal solution is

$$z(a_1) - z_0 = \frac{4\rho_w}{w_L} \left[W \int_{a_{1,0}}^{a_1} \frac{da_1}{U_{\infty,1}(a_1) E_c(a_1)} - \int_{a_{1,0}}^{a_1} \frac{da_1}{E_c(a_1)} \right] , \tag{15-7}$$

where $a_{1,0} = a_1(z_0)$. This equation has been the basis of several studies (e.g., Langmuir, 1948; Bowen, 1950; Ludlam, 1951; Mason, 1952b, 1959; and East, 1957). Figure 15.3 shows as an example some results obtained by Bowen. In this calculation, a drop, originating by the chance coalescence of two 10 μm radius cloud droplets near the cloud base, is assumed to grow further by collection of 10 μm radius drops in accordance with the collision efficiency, as given by Langmuir (1948). The figure demonstrates that strong updrafts reduce the growth time of drops considerably, and produce larger drops than weak updrafts.

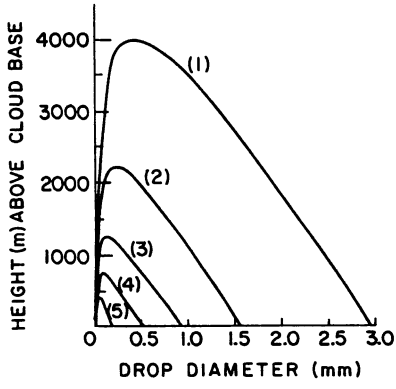


Fig. 15-3: Size variation of a drop of initial radius of 12.6 μm growing by collision and coalescence in clouds of various constant updraft speeds W: (1) 200, (2) 100, (3) 50, (4) 25, (5) 10 cm sec^{-1} and with drops of 10 μm radius and $w_L = 1$ g m^{-3}. Time to reach indicated size after return to cloud base is 60, 60, 70, 85, 115 min for (1), (2), (3), (4), and (5), respectively. (From Bowen, 1950; by courtesy of *Australian J. Sci. Res.*, and the author.)

15.2 Polynomial Approximations to the Gravitational Collection Kernel

It is obvious from (15-3) that the continuous growth equation, discussed in the previous section, as well as the stochastic growth equation to be discussed in the following section, can only be solved analytically for simple collection kernels (see

Section 15.3.2). The hydrodynamic collection kernel does not belong to this group of kernels, nor do the polynomial approximations to the collection kernel provided by Long (1974). Nevertheless, we shall briefly discuss Long's approximations, as they have proved to be useful in the numerical integration of the collection growth equations (Tzivion *et al.*, 1987).

The first step in obtaining the polynomial approximations is to evaluate the actual gravitational collection kernel K as accurately as possible. In the expression (15-2), for K we recall the collection efficiency E_c is the product of the collision efficiency E and the coalescence efficiency E_{coal}. Long (1974) assumes $E_{coal} = 1$ because evidence to the contrary (Woods and Mason, 1964; Whelpdale and List, 1971; Brazier-Smith *et al.*, I972) covers only a limited range of drop sizes (see Section 14.5.4.1). For $10 \leq a \leq 300\,\mu$m, Long uses the E values of Shafrir and Gal-Chen (1971) and Klett and Davis (1973). The terminal velocities are evaluated from the approximate formula developed by Long and Manton (1974), which is based on the data of Gunn and Kinzer (1949) and Beard and Pruppacher (1969) obtained at 1013 mb and 20°C. An altitude correction to the formula is made because the collision efficiencies were calculated for 900 mb and 0°C. For droplets of radii $< 15\,\mu$m, this correction is derivable from the Stokes terminal velocity formula, and is due to the change in viscosity of air with temperature. For radii $> 1690\,\mu$m Long uses the correction of Foote and du Toit (1969). For intermediate sizes, a linear interpolation with respect to the logarithm of the droplet radius is used.

In this manner, the curves of K vs. a_1 for various ratios a_2/a_1 are obtained as shown in Figure 15.4. The curves indicate a relatively weak dependence of K on a_2/a_1. The figure also shows that K varies roughly as v^2 for $a \lesssim 50\,\mu$m and as v for $a > 50\,\mu$m, where v is the drop volume. This is explained by the dependence of E and U_∞ on size: For small and intermediate sized-drops, the terminal velocity varies as a^2 and a, respectively. Similarly, for small drops and size ratios, $E \approx 4.5 \times 10^4 a^2$ (a in cm), while $E \approx$ constant for intermediate drop sizes.

These results provide the rationale for simple polynomial estimates for K of the form v or v^2 (or $(v+u)$ and $(v+u)^2$), where u and v are volumes of the interacting drops. The numerical coefficients selected by Long are those which give a minimum rms deviation between the logarithm of the approximating polynomial $P(v,u)$ and the logarithm of $K(v,u)$. The deviation between the logarithms of $P(v,u)$ and $K(v,u)$ rather than between the functions themselves, was chosen because of the large variation in K, and because of the presumed importance of representing K well in all size intervals. In this fashion, Long obtained the following polynomial estimates for K

$$P(v,u) = \begin{cases} 9.44 \times 10^9 (v^2 + u^2), & 10 \leq a \leq 50\,\mu\text{m} \\ 5.78 \times 10^3 (v + u), & a > 50\,\mu\text{m} \end{cases} \qquad (v > u) \qquad (15\text{-}8a)$$

and

$$P(v,u) = \begin{cases} 1.10 \times 10^{10} v^2, & 10 \leq a \leq 50\,\mu\text{m} \\ 6.33 \times 10^3 v, & a > 50\,\mu\text{m} \end{cases}. \qquad (v > u) \qquad (15\text{-}8b)$$

The merit of the approximations (15-8) has been tested by comparing numerical solutions based on them and the actual K; generally, the agreement is quite good.

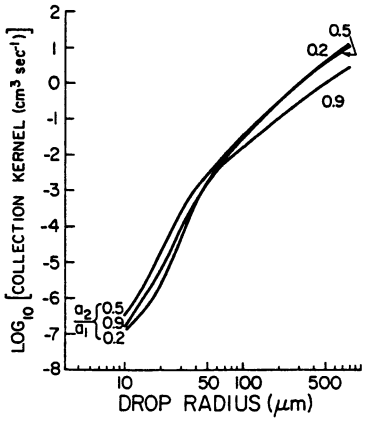


Fig. 15-4: Collection kernel $K\ (a_1, a_2)$ based on collision efficiencies of Shafrir and Gal-Chen (1971), and Klett and Davis (1973). (From Long, 1974; by courtesy of Am. Meteor. Soc., and the author.)

With this evidence of their accuracy, Long has suggested that an attempt should be made to find analytical solutions to the SCE based on either of them. Such solutions could then facilitate the simulation of droplet collection in, for example, multidimensional cloud models. Even if this proves impossible, (15-8) provides simple and concise, and therefore convenient, descriptions of the collection process (for the case of no turbulence) which may be of use in other applications. In passing, we note the restriction $a > 10\,\mu$m may be dropped without incurring significant errors (this was in fact done by Long in his computations).

15.3 Stochastic Model for Collisional Growth

One feature common to all the examples discussed in Section 15.1 is the prediction of growth times for precipitation-sized drops which are much longer (by a factor of two or more) than the times which are often observed to be necessary. As we indicated earlier, this fault arises from the neglect of the stochastic aspect of collection growth. Since raindrop concentrations are typically $10^5 - 10^6$ times smaller than cloud drop concentrations, one would expect that the fate of the 'favored' small fraction of drops which happen by chance to grow much faster than the average rate, should be quite important in the overall process of precipitation development. Many calculations have borne out this expectation.

To study this behavior, the kinetic coagulation equation, (11-53) or (11-56), is generally taken as the basic governing form for stochastic collection growth. (In the more recent literature on the subject, the coagulation equation is also variously referred to as the scalar transport equation, the kinetic equation, the collection equation, the stochastic coagulation equation, and the *stochastic collection equation* (SCE); henceforth, we shall employ this last abbreviated designation.) Telford (1955) was the first to introduce this approach to the drop collection problem,

using a version of the SCE which applies to an idealized cloud consisting initially of just two drop sizes, and for which the collision kernel is a constant. He showed that a small fraction of the large drops grows about 50 times faster than the rate predicted by the continuous model. This difference in growth rate between the stochastic and continuous model is exemplified in Figure 15.5 by computations carried out by Twomey (1964). For drop concentrations at the level of 100 $m^{-3}\mu m$, the growth rate in the stochastic mode is seen to be almost ten times faster than in the continuous mode. Similar conclusions were subsequently reached by Twomey (1966, 1976), Ryan (1974), Scott and Levine (1975a,b), Bartlett (1966, 1970) and Leighton and Rogers (1974). It is for this reason that, in the remainder of this chapter, we shall concern ourselves exclusively with the stochastic description of the collision-coalescence process.

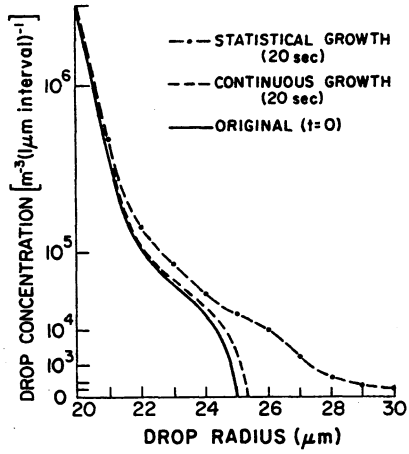


Fig. 15-5: Variation with time of a drop size distribution with time due to continuous- and stochasic growth of cloud drops by collision and coalescence; for a bell-shaped initial distribution between 10 and 22 μm radius, mode at 16 μm, and for $N = 135$ cm^{-3} and $w_L = 2.56$ g m^{-3}. (From Twomey, 1964; by courtesy of Am. Meteor. Soc., and the author.)

A systematic application of the SCE to the collection problem has occurred only relatively recently. In part, this reflects the rise of computer technology, which was requisite for coping with realistic collection growth problems. In the sequel, we shall consider in Section 15.3.1 the suitability of the SCE for the problem at hand. Having established the conditions under which its use is appropriate, we shall then develop and discuss in Section 15.3.2 some of the few known exact solutions. For the most part, these solutions do not correspond to very physical collection processes. Even so, they provide useful clues to the behavior in more realistic situations, and also serve as standards against which to judge the accuracy of various numerical integration schemes. We shall conclude Section 15.3 on stochastic collisional growth by a discussion of some of the most widely used approximation techniques for the SCE. In Section 15.4, we shall consider stochastic collisional breakup and formulate

the *stochastic breakup equation* (SBE). In the final Section 15.5, the SCE and the SBE are combined to describe the evolution of raindrop spectra.

15.3.1 Completeness of the SCE

Let us imagine an idealized cloud which is spatially homogeneous or 'well-mixed' at all times, and which contains drops whose masses are multiples of some unit mass. Let n_k be the number of drops per unit volume containing k units of mass, and let K_{ik} denote the collection kernel which describes the collection rate of i and k drops. Then, the discrete SCE for this situation has exactly the form of (11-53). If the cloud volume is V, then $N_k \equiv n_k V$ is the total number of drops of size k, and $A_{ik} \equiv K_{ik}/V$ is the probability per unit time of coalescences between, any pair of i and k drops (by the 'well-mixed' assumption). By introducing V into (11-53), we thus arrive at the SCE for $N_k(t)$:

$$\frac{\mathrm{d}N_k}{\mathrm{d}t} = \frac{1}{2}\sum_{i=1}^{k-1} A_{i,k-i} N_i N_{k-i} - N_k \sum_{i=1}^{\infty} A_{ik} N_i \,. \tag{15-9}$$

We would now like to determine whether (15-9) is suitable for studying the spectral evolution in our ideal cloud. As it happens, only a little reflection suffices to raise some doubts. For example, if we imagine several successive 'runs' or realization of the collection process for a given set of probabilities for binary interactions and a given initial distribution, we would expect to see at least slightly different outcomes for the spectrum from one to the next. However, (15-9) can only produce a unique spectrum once A_{ik} and $N_k(0)$ are specified. Thus, it is natural to suspect that (15-9) is not stochastically complete (i.e., does not describe the probabilities of all possible histories of drop growth), and that the solution to (15-9) must represent only some sort of average spectrum. Such stochastic incompleteness might well be expected to cause trouble, since for most applications in cloud physics we are primarily interested in the long tail of the spectrum where fluctuations are relatively strong, there being relatively few large particles in the system.

This problem of stochastic completeness has been debated extensively by Scott (1967, 1968), Berry (1967, 1968), Warshaw (1967, 1968), Slinn and Gibbs (1971), Long (1971); Chien and Neiburger (1972), Drake (1972b), Gillespie (1972, 1975a), Bayewitz *et al.* (1974), Pearson *et al.* (1984) and Valioulis and List (1984). We recommend Gillespie's (1972) paper as the most thorough and clear discussion of the general problem. Bayewitz *et al.* (1974) present what is apparently the only known rigorous solution to the full stochastic model which allows for spectrum fluctuations, accomplished under the assumption of a constant collection kernel. Their work provides an interesting concrete example of the extent of the incompleteness of the SCE, and is presented below in Section 15.3.2. Valioulis and List (1984) employ Gillespie's (1975b) Monte Carlo algorithm for stochastic collection in a numerical study that verifies Gillespie's predictions regarding stochastic completeness. Their work is summarized briefly in Section 15.3.1.3. But first we shall outline Gillespie's (1975b) analysis of the problem, which appears to us to delineate very well the salient features with a minimum of effort.

15.3.1.1 *Three Models for Collection Growth*

Let us further simplify our well-mixed cloud so that at time $t = 0$ it consists entirely of N 'drops' each having mass m_0 and N' 'droplets' each of mass μ. We further assume the conditions $m_0 > \mu$ and $N \ll N'$, and that coalescences are possible only between drops and droplets. Thus, the masses of the drops are increasing, but the number N of drops remains constant. Because of the condition $N \ll N'$, we assume the number N' of droplets also remains constant. (This is the cloud model used by Telford (1955).)

Our goal is to describe the growth of the N drops. For this purpose we need the collection kernel, which in the present case can be a function only of the drop mass m: $A_{ik} \to A(m)$. Gillespie (1975a) shows that three growth models are possible, depending upon the physical interpretation given the quantity $A(m)N'\mathrm{d}t$, where $\mathrm{d}t$ is an infinitesimal time interval. These models are:
(1) the *continuous model*, in which

$$A(m)N'\mathrm{d}t = \text{number of droplet which any drop of mass } m \text{ will collect in } \mathrm{d}t; \tag{15-10}$$

(2) the *quasi-stochastic model*, in which

$$A(m)N'\mathrm{d}t = \text{fraction of the drops of mass } m \text{ which will collect a droplet in } \mathrm{d}t; \tag{15-11}$$

(3) the *pure stochastic model*, in which

$$A(m)N'\mathrm{d}t = \text{probability that any drop of mass } m \text{ will collect a droplet in } \mathrm{d}t. \tag{15-12}$$

We shall now proceed to explore the consequences of each of these models under the assumption $A(m) = A$, a constant.

Since in the continuous model all drops start with the same mass m_0 and grow at the same rate, the state of the drops may be specified very simply by the function $M(t) \equiv$ mass of any drop at time t. From (15-10), we have $\mathrm{d}M = \mu AN'\mathrm{d}t$, so that

$$M(t) = m_0 + \mu AN't\,. \tag{15-13}$$

According to the quasi-stochastic model, only a certain fraction of the m-drops will collect a droplet in $\mathrm{d}t$. Thus, the m-drops do not grow in unison, and the definition of $M(t)$ given above no longer applies. Instead, for the quasi-stochastic model, we define the function $N_m(t) \equiv$ number of m-drops at time t, where $m = m_0, m_0 + \mu, \ldots$. Simple bookkeeping enables us to write down the governing equation for $N_m(t)$: From (15-10), in time $(t, t + \mathrm{d}t)$ exactly $N_{m-\mu}(t)AN'\mathrm{d}t$ drops of mass $m - \mu$ will each collect a droplet and so become drops of mass m, while exactly $N_m(t)AN'\mathrm{d}t$ m-drops will each collect a droplet and so become drops of mass $m + \mu$. Therefore, $\mathrm{d}N_m = (N_{m-\mu} - N_m)AN'\mathrm{d}t$, or

$$\frac{\mathrm{d}N_m}{\mathrm{d}t} = AN'(N_{m-\mu} - N_m)\,. \tag{15-14}$$

This is just the SCE as it appears for our simple drop-droplet cloud; it is also the equation considered by Telford (1955).

The solution to (15-14) may be obtained by noting it comprises a set of coupled, linear, first-order differential equations. These may be solved sequentially, subject to the initial condition $N_m(0) = N'$ if $m = m_0$, and 0 if $m \neq m_0$. The result, which may be verified by direct substitution, is

$$N_{m_0+k\mu}(t) = \frac{N(AN't)^k \exp(-AN't)}{k!}, \quad k = 0, 1, 2, \ldots . \tag{15-15}$$

Thus, the quasi-stochastic model yields a discrete mass spectrum. The average drop mass $M_1(t)$ at time t is, letting $x \equiv AN't$,

$$M_1(t) \equiv \frac{1}{N} \sum_{m=m_0}^{\infty} mN_m(t) = \sum_{k=0}^{\infty} (m_0 + k\mu)x^k e^{-x}/k! = M(t) . \tag{15-16}$$

This is what we would expect: The average drop mass coincides with the mass of every drop in the continuous model. Another quantity of interest is the width $\Delta(t)$ of the distribution, as measured by the root-mean-square (rms) deviation: $\Delta(t) \equiv [M_2(t) - M_1^2(t)]^{1/2}$, where M_2 denotes the second moment of the distribution. A simple calculation yields $\Delta(t) = \mu(AN't)^{1/2}$, which contrasts with the zero width in the continuous model.

The continuous model requires each m-drop to collect a definite number of droplets in a given time interval. As we have seen, the quasi-stochastic model requires only that all m-drops together collect droplets at a definite rate. But this is still too restrictive: by the probabilistic nature of the collection process, there should be fluctuations in the number of droplets collected by any group of drops as well as by any individual drop. Such fluctuations are permitted in the pure stochastic model. In consequence, we cannot predict exactly how many drops of a particular size there will be at any time t, so that the definition of the spectrum given above for $N_m(t)$ no longer applies. However, from (15-12), we have a means of predicting the probability of finding a given number of m-drops at time t. Therefore, an appropriate state function in the pure stochastic model is

$$\begin{aligned} P(n, m; t) \quad \equiv \quad & \text{probability that exactly } n \text{ drops} \\ & \text{have mass } m \text{ at time } t, \end{aligned} \tag{15-17}$$

where $n = 0, 1, \ldots, N$ and $m = m_0, m_0 + \mu, \ldots$.

In order to calculate $P(n, m; t)$, consider first the probability $\mathscr{P}(k, t)$ that any given drop will collect exactly k droplets in time t; this is just the familiar Poisson distribution (see Gillespie (1975a) or Feller (1967) for details):

$$\mathscr{P}(k, t) = \frac{(AN't)^k \exp(-AN't)}{k!} . \tag{15-18}$$

Then, since each drop collects droplets independently of the other drops, the probability that a particular selection of n drops will each collect exactly k droplets

in time t while the remaining $N-n$ drops will not is $\mathscr{P}^n(k,t)[1-\mathscr{P}(k,t)]^{N-n}$. And, since the number of distinct ways of selecting two groups of n drops and $N-n$ drops from a set of N drops is $\binom{N}{n} = N![n!(N-n)!]^{-1}$, the probability that exactly n of the N drops will collect exactly k droplets in time t is just $\binom{N}{n}\mathscr{P}^n(k,t)[1-\mathscr{P}(k,t)]^{N-n}$. Therefore, we obtain

$$P(n, m_0 + k\mu; t) = \frac{N!}{n!(N-n)!}\mathscr{P}^n(k,t)[1-\mathscr{P}(k,t)]^{N-n}, \tag{15-19}$$

where $n = 0, 1, \ldots, N$ and $k = 0, 1, \ldots$. Equations (15-18) and (15-19) constitute the solution for $P(n,m;t)$ for the simple drop-droplet cloud.

The first moment of $P(n,m;t)$ with respect to n has the physical meaning of being the average number $N_1(m;t)$ of m-drops in the cloud at time t:

$$\begin{aligned} N_1(m;t) \equiv \sum_{n=0}^{N} nP(n,m;t) &= \sum_{n=1}^{N} \frac{nN!}{n!(N-n)!}\mathscr{P}^n(k,t)[1-\mathscr{P}(k,t)]^{N-n} \\ &= N\mathscr{P}(k,t) = N_m(t). \end{aligned} \tag{15-20}$$

So, for our simple cloud, the average spectrum as defined above coincides with the solution to the SCE. Also of interest is the expected uncertainty associated with $N_1(m;t)$; i.e., we would like to know to what extent the actual number of m-drops in a particular realization can be expected to deviate from $N_m(t)$. In analogy with our previous choice of $\Delta(t)$ as the width of the SCE spectrum, we now choose the rms deviation of $P(n,m;t)$ with respect to n: $\Delta(m;t) \equiv [N_2(m;t) - N_1^2(m;t)]^{1/2}$, where $N_2(m;t)$ is the second moment of $P(n,m;t)$ with respect to n. A straightforward calculation gives the result $\Delta(m;t) = [N_1(m;t)]^{1/2}[1 - N_1(m;t)/N]^{1/2}$. As the second factor on the right side approaches unity for $t \to \infty$, we conclude we may reasonably expect to find roughly between

$$N_m(t) - [N_m(t)]^{1/2} \quad \text{and} \quad N_m(t) + [N_m(t)]^{1/2} \tag{15-21}$$

drops of mass in the cloud at time t. Thus, in the present simple case, the solution to the SCE provides not only the mean spectrum but also a measure of the fluctuations about the mean.

The result (15-21) shows that for the simple 'drop-droplet' cloud, the SCE is more 'stochastically complete' than its usual derivation via the quasi-stochastic interpretation would suggest. The important question arises as to whether or not the same holds true in the more realistic case in which the collection kernel is size dependent and drops of all sizes are present. A partial answer is provided in Gillespie's (1972) study of the general problem, in which it is shown that if (1) certain correlations can be neglected, and (2) coalescences between drops of the same size are prohibited, then the SCE does indeed determine the mean spectrum $N_1(m;t)$. Also,the function $P(n,m;t)$ then tends to the Poisson form

$$P(n,m;t) \overset{t\to\infty}{\longrightarrow} \frac{N_1^n(m;t)\mathrm{e}^{-N_1(m;t)}}{n!}, \tag{15-22}$$

and, in particular, $\Delta(m;t) \to \sqrt{N_1(m;t)}$, so that the result (15-21) still holds. Gillespie's analysis also provides a simple estimate of the time interval $\tau(m)$ after which the result (15-21) may be assumed applicable. This is given by the implicit relation

$$\int_0^{\tau(m)} \sum_{m'=1}^{\infty} N_{m'}(t) A_{mm'} \mathrm{d}t = \ln 2 . \tag{15-23}$$

The same general conclusion that (15-21) is a valid estimate of the spectrum fluctuations was arrived at earlier by Scott (1967); however, his analysis erroneously implies the equivalent of assuming $\tau(m) = 0$.

However, without assumptions (1) and (2) the situation is unclear. This is so primarily because, in general, the state of a cloud in the pure stochastic model cannot be determined completely by just the function $P(n, m; t)$. The existence of particle correlations means that various conditional probabilities must be specified also, such as the probability that n drops of mass m are present, given that there are also n' drops of mass m', etc. Such correlations are bound to occur in real clouds, partly because they are not well-mixed, as we have assumed for the 'drop-droplet' cloud: as droplets in a given region coalesce, there will be a corresponding decrease in the number available in that region for further coalescence. In addition, measurements show strong spatial, inhomogeneities in cloud liquid water content.

Some indication of the effect of particle correlations is included in the study of Bayewitz *et al.* (1974), to which we now turn.

15.3.1.2 *Correlations in a Stochastic Coalescence Process*

Bayewitz *et al.* consider a well-mixed cloud containing N_k drops of size k. The probability per unit time of coalescences between any pair of drops is taken as a constant, $A_{ik} = A$, as in the previous section. The authors proceed to set up and solve the governing equation which describes all possible histories of drop growth over the full range of drop sizes (an outline of the analysis is given in Appendix A-15.3.1.2). The results show the SCE produces total particle counts in excellent agreement with the true stochastic averages, even for very small initial populations, at least for collection kernels which are not strongly size dependent.

As we have noted, real clouds are not well-mixed. Bayewitz *et al.* go on to consider the consequences of poor mixing by adopting the following approach: A hypothetical large cloud is imagined to be partitioned into many small compartments of volume V_0 with the understanding that drops can coalesce only if they occupy the same compartment. By making V_0 sufficiently small, correlations are introduced which are perhaps similar to those occurring in a real cloud. The effects of poor mixing as simulated by this partitioning model are as follows: (1) If we are interested only in the total number of drops, and not their size distribution, then we find that for initial populations of as few as ten drops, the results of the SCE match the true stochastic averages. (2) If we focus instead on the size distribution of the coalescing drops, we find that either for small populations or for systems partitioned into small isolated compartments, the results of the SCE may differ significantly from the true stochastic averages, especially in the large-particle tail

of the distribution. Additionally, Bayewitz *et al.* make the plausible conjecture that the correlation effects which produce these differences would be enhanced by a more realistic size-dependent collection kernel.

15.3.1.3 *Monte Carlo Study of Stochastic Correlation*

The most comprehensive numerical treatment of the problem of stochastic completeness has been given by Valioulis and List (1984), who based their numerical study on the work of Gillespie (1975b). Gillespie outlined a rigorous Monte Carlo simulation of the stochastic coalescence process which avoids all of the assumptions included in the kinetic coagulation equation (15-9). A description of Gillespie's algorithm is given in Appendix A-15.3.1.3. However, nine years had to pass until Gillespie's technique was applied by Valioulis and List (1984) to actual collision functions. These authors compared the predictions of Gillespie's (1975b) Monte Carlo algorithms with numerical solutions to the kinetic coagulation equation (15-9) which they numerically integrated using Gear's (1971) modification of Adam's multistep variable-order predictor-corrector method.

The comparison was carried out for a Brownian diffusion-, a fluid shear-, and a differential sedimentation collision kernel. The results of this simulation showed that for isolated volumes of fluid, (15-9) produced an average size-spectrum of the coagulating population of particles that matched well the true stochastic average spectrum, provided that the total number of particles per unit volume was large. In agreement with Gillespie's conclusions, they found that with decreasing concentration of the total number of particles, the distributions predicted by the kinetic model increasingly differed from the true stochastic average spectrum, due to increasing particle property correlation. In contrast, (15-9) overestimates particle concentrations at the large end of a drop spectrum with a low total drop concentration, relative to the Monte Carlo technique. Valioulis and List also noted that for small total number concentrations of particles, the difference between the models was larger for Brownian-induced coagulation than for shear coagulation, since for Brownian coagulation, the coalescence between particles of equal size is relatively more important in determining the shape of the particle size distribution. This observation is in agreement with Gillespie's (1972) conclusion that the solution from the kinetic equation will approach the true stochastic average provided the coalescence of particles of equal size is prohibited.

Since precipitation formation is an example of a collection process in an aerosol which is not well-mixed, and in which particles in the tail of the distribution generally appear to play a major, if not the dominant role, it is tempting to infer that the standard SCE probably does not simulate the production of rain with a high degree of accuracy, and that it may be better in some instances to turn to other simulation techniques, particularly the Monte Carlo method. On the other hand, it also seems plausible that in some cases the flow rate of water up the spectrum toward rain is controlled predominantly by the self-collection of cloud droplets in the mid-range of the spectrum, in which case the SCE may be used with confidence. Some light has been shed on this problem by Berry and Reinhardt (1974a,b,c), who showed, based on solutions to the SCE, that the self-collection of cloud droplets

('auto-conversion') is less important than the self-collection of large drops ('large hydrometeor self-collection') and the collection of small droplets by large drops ('accretion'). This tends to support the notion that the SCE is not suitable for very accurate simulations of rain formation. Obviously, this is an area where further research is needed.

15.3.2 Exact Solutions to the SCE

In this section we shall be concerned with the continuous and dimensionless version of the SCE given by (11-95)

$$\frac{\partial f(x,\tau)}{\partial \tau} = \frac{1}{2}\int_0^x \alpha(x-y,y)f(x-y,\tau)f(y,\tau)\mathrm{d}y - f(x,\tau) \times \int_0^\infty \alpha(x,y)f(y,\tau)\mathrm{d}y\,. \tag{15-24}$$

The only known exact solution to the discrete SCE which has any practical value, in the sense of simulating real coagulation processes, is just that of Smoluchowski (1916), (11-52), for the case of a constant collection kernel. (Another solution (McLeod, 1962) has been found for the case $K_{ij} \sim ij$, but this choice of kernels appears quite unrealistic (see the discussion below on the xy kernel).) Also, in the steady state, there is an exact solution (Klett, 1975) to the continuous SCE enhanced by a particle source term, for $\alpha = x^\beta y^\beta (\beta < 1)$. This solution has already been discussed in Section 11.7.5.

All the known solutions to (15-24) correspond to special cases of the following kernel:

$$\alpha(x,y) = A + B(x+y) + Cxy\,. \tag{15-25}$$

In our development and/or discussion of these solutions, we shall follow the work of Drake (1972a) and Drake and Wright (1972). In the latter paper, families of exact solutions are constructed for the following sub-classes of (15-25). (1) $C = 0$ and $B = \mathrm{a}A$ for arbitrary a on the interval $0 \leq \mathrm{a} \leq \infty$, (2) $A = 0$ and $C = 2\mathrm{a}B$ for $0 \leq \mathrm{a} \leq \infty$, (3) $A = 1$, $B = \mathrm{a}$, and $C = \mathrm{a}^2$ for $0 \leq \mathrm{a} \leq \infty$. Here we shall consider only the first sub-class, because of the unphysical behavior associated with the presence of the xy term.

Before going ahead with the construction of solutions, let us consider briefly the essential difficulty with the choice $C \neq 0$: it is that solutions based on the xy kernel can exist only for a finite time interval (McLeod, 1964). This behavior is easily demonstrated by use of the moment equation (11-97). For example, for $\alpha = Cxy$, the equation for the zeroth moment is $\mathrm{d}M_0/\mathrm{d}\tau = -C/2$, so that $M_0(\tau) = 1 - C\tau/2$. Thus, collision apparently stops at least by $\tau = \tau_{\max} = 2C^{-1}$. Similarly, the equation for the second moment is $\mathrm{d}M_2/\mathrm{d}\tau = CM_2^2$, so that $M_2(\tau) = M_2(0)[1 - CM_2(0)\tau]^{-1}$. Therefore, the second moment becomes infinite when $\tau = \tau_\infty = [CM_2(0)]^{-1}$, a time which depends on the initial spectrum, $f(x,0)$. Let us assume, for example, that $f(x,0) = \delta(x-1)$; then $M_2(0) = 1$ and

$\tau_\infty = C^{-1} = \tau_{\max}/2$. The singularity occurs sooner if the initial spectrum is more spread out; thus, if $f(x,0) = \mathrm{e}^{-x}$, then $M_2(0) = 2$ and $\tau_\infty = (2C)^{-1} = \tau_{\max}/4$. These examples should suffice to illustrate how the xy kernel leads to unreasonable behavior in a finite time, such as the occurrence of an infinite radar reflectivity ($\Sigma n a^6 \sim M_2$), followed by the apparent collapse of the spectrum.

The solution of (15-24) and (15-25) with $C = 0$ is facilitated by introducing another time variable (Martynov and Bakonov, 1961):

$$T \equiv 1 - M_0(\tau)\,. \tag{15-26}$$

As coagulation proceeds, M_0 slowly decreases from unity to zero. Thus, corresponding to $0 \leq \tau < \infty$, we have $0 \leq T \leq 1$, which makes T a natural measure of the progress of coagulation. Let us define also

$$\mathrm{g}(x,T) \equiv f(x,\tau)\,, \tag{15-27}$$

so that

$$\frac{\partial f}{\partial \tau} = \frac{\partial \mathrm{g}}{\partial T}\frac{\mathrm{d}T}{\mathrm{d}\tau} = -\frac{\partial \mathrm{g}}{\partial T}\frac{\mathrm{d}M_0}{\mathrm{d}\tau}\,. \tag{15-28}$$

Then, from (15-24) and the moment eqation for $M_0(\tau)$, the governing equation for $\mathrm{g}(x,T)$ is found to be

$$\begin{aligned} D(T)\frac{\partial \mathrm{g}(x,T)}{\partial T} &= -2\mathrm{g}(x,T)\int_0^\infty \alpha(x,y)\mathrm{g}(y,T)\,\mathrm{d}y \\ &\quad + \int_0^x \alpha(x-y,y)\mathrm{g}(x-y,T)\mathrm{g}(y,T)\,\mathrm{d}y\,, \end{aligned} \tag{15-29}$$

where

$$D(T) = \int_0^\infty\int_0^\infty \alpha(x,y)\mathrm{g}(y,T)\mathrm{g}(x,T)\,\mathrm{d}x\,\mathrm{d}y\,. \tag{15-30}$$

On substitution of (15-25) with $C = 0$ into (15-29) and (15-30), we obtain

$$D(T)\frac{\partial \mathrm{g}}{\partial T} = -2\mathrm{g}(A+Bx)(1-T) - 2B\mathrm{g} + (A+Bx)\mathrm{g}*\mathrm{g}\,, \tag{15-31}$$

where

$$D(T) = A(1-T)^2 + 2B(1-T)\,, \tag{15-32}$$

and $\mathrm{g}*\mathrm{g} \equiv \int_0^x \mathrm{g}(x-y)\mathrm{g}(y)\,\mathrm{d}y$. The appearance of the convolution from $\mathrm{g}*\mathrm{g}$ in (15-31) indicates the feasibility of a solution via Laplace transforms. Therefore, let us introduce the Laplace transform of $\mathrm{g}(x,T)$:

$$L[\mathrm{g}(x,T)] \equiv \int_0^\infty \mathrm{g}(x,T)\mathrm{e}^{-sx}\,\mathrm{d}x \equiv \Phi(s,T)\,. \tag{15-33}$$

The inverse transform is

$$L^{-1}[\Phi(s,T)] \equiv \frac{1}{2\pi i}\int_{\gamma-i\infty}^{\gamma-i\infty} \Phi(s,T)e^{sx}\,ds = g(x,T)\,, \tag{15-34}$$

where γ is any number such that $g(x,T)e^{-\gamma x} \to 0$ as $x \to \infty$. Then, on taking the Laplace transform of (15-31) and using the well-known properties $L(f * g) = L(f)L(g)$ and $L(xf) = -d[L(f)]/ds$, we obtain the transformed equation for Φ:

$$D\frac{\partial \Phi}{\partial T} = -2A(1-T)\Phi + 2B(1-T)\frac{\partial \Phi}{\partial s} - 2B\Phi + A\Phi^2 - B\frac{\partial}{\partial s}\Phi^2\,. \tag{15-35}$$

Finally, in terms of a new dependent variable, $\eta(s,T)$, defined as follows:

$$\eta(s,T) \equiv \frac{2\Phi(s,T)}{D(T)}\,, \tag{15-36}$$

(15-35) simplifies to

$$\frac{\partial \eta}{\partial T} = \frac{A}{2}\eta^2 - B\eta\frac{\partial \eta}{\partial s} + \frac{2(1-T)}{D}B\frac{\partial \eta}{\partial s}\,. \tag{15-37}$$

We shall now construct the solutions for $g(x,T)$ in terms of the Laplace transform $G(s)$ of the initial spectrum, for the two special cases $A = 1$, $B = 0$, and $A = 0$, $B = 1$.

(1) $A = 1$, $B = 0 (\alpha(x,y) = 1)$. The equation for η is

$$\frac{\partial \eta}{\partial T} = \frac{\eta^2}{2}\,. \tag{15-38}$$

Therefore,

$$\eta(s,T) = \frac{\eta(s,0)}{1-\eta(s,0)T/2} = \frac{2G(s)}{1-G(s)T}\,. \tag{15-39}$$

Since $T \le 1$ and $G(s) = \int_0^\infty e^{-sx}g(x)\,dx \le g(x)\,dx = 1$, (15-39) may be expanded in a geometric series to yield

$$\eta(s,T) = 2\sum_{k=0}^{\infty} T^k G^{k+1}(s)\,. \tag{15-40}$$

Finally, since $L^{-1}[\eta(s,T)] = 2g(x,T)/(1-T)^2$, we have (Scott, 1968):

$$g(x,T) = (1-T)^2\sum_{k=0}^{\infty} T^k L^{-1}[G^{k+1}(s)]\,. \tag{15-41}$$

(2) $A = 0$, $B = 1 (\alpha(x,y) = x + y)$. The equation for η is

$$\frac{\partial \eta}{\partial T} + (\eta - 1)\frac{\partial \eta}{\partial s} = 0\,. \tag{15-42}$$

The equation is a 'quasi-linear' first-order partial differential equation, and can be solved in the following manner (e.g., Ames, 1965, p. 50): If the form of the differential equation is

$$P\frac{\partial\eta}{\partial T} + Q\frac{\partial\eta}{\partial s} = R\,, \tag{15-43}$$

where P, Q, and R are functions of s, T, and η, the general solutions is $f(u,v) = 0$, where F is an arbitrary, sufficiently differentiable function and $u(s,T,\eta) = \mathrm{a}$ and $v(s,T,\eta) = \mathrm{b}$ form independent solutions of the Lagrange system

$$\frac{\mathrm{d}T}{P} = \frac{\mathrm{d}s}{Q} = \frac{\mathrm{d}\eta}{R}\,. \tag{15-44}$$

In the present application, this leads to the implicit solution $\eta = F[s - (\eta - 1)T]$. From the initial condition $\eta(s,0) = F(s) = G(s)$, we find $F = G$:

$$\eta(s,T) = G[s - (\eta - 1)T]\,. \tag{15-45}$$

Now, on substitution of (15-34) and (15-36) into this last result, we have

$$\mathrm{g}(x,T) = \frac{(1-T)}{2\pi\mathrm{i}}\int_{\gamma-\mathrm{i}\infty}^{\gamma+\mathrm{i}\infty} \mathrm{e}^{sx}G[s - (\eta-1)T]\,\mathrm{d}s\,, \tag{15-46}$$

or, on letting $\sigma = s - (\eta - 1)T = s - [G(\sigma) - 1]T$,

$$\begin{aligned}\mathrm{g}(x,T) &= \frac{(1-T)}{2\pi\mathrm{i}}\int_{\gamma-\mathrm{i}\infty}^{\gamma+\mathrm{i}\infty} \mathrm{e}^{\sigma s + GTx - Tx}G\left(1 + \frac{\mathrm{d}G}{\mathrm{d}\sigma}T\right)\mathrm{d}\sigma \\ &= (1-T)\mathrm{e}^{-Tx}\left(\sum_{k=0}^{\infty}\frac{(Tx)^k}{k!}L^{-1}[G^{k+1}] + \frac{1}{2\pi\mathrm{i}}\right. \\ &\quad \left.\times\int_{\gamma-\mathrm{i}\infty}^{\gamma+\mathrm{i}\infty}\mathrm{e}^{\sigma x}\sum_{k=0}^{\infty}\frac{(Tx)^k}{k!}G^{k+1}T\frac{\mathrm{d}G}{\mathrm{d}\sigma}\,\mathrm{d}\sigma\right)\,.\end{aligned} \tag{15-47}$$

The last term may be integrated by parts, so that finally we have (Scott, 1968):

$$\mathrm{g}(x,T) = (1-T)\mathrm{e}^{-Tx}\sum_{k=0}^{\infty}\frac{(Tx)^k}{(k+1)!}L^{-1}[G^{k+1}(s)]\,. \tag{15-48}$$

In Appendix A-15.3.2, the general solutions (15-41) and (15-48) are evaluated for two particular choices of the initial spectrum. For the choice $\mathrm{g}(x,0) = \delta(x-1)$ (a monodisperse cloud), the results are as follows:

$$\mathrm{g}(x,T) = (1-T)^2\sum_{k=0}^{\infty}T^k\delta(x-k-1)\,,(\alpha=1)\,, \tag{15-49}$$

(Melzak, 1953), and

$$g(x,T) = (1-T)e^{-Tx}\sum_{k=0}^{\infty}\frac{(Tx)^k}{(k+1)!}\delta(x-k-1)\,,(\alpha = x+y)\,, \tag{15-50}$$

(Golovin, 1963).

The solution (15-49) must be completely equivalent to Smoluchowski's (11-52), since it is based on a constant collection kernel and the initial condition of a homogeneous aerosol. It is not difficult to demonstrate this equivalence. Thus, the discrete spectrum $g_n(T)$ which counts the number of n-tuple particles composed of n unit-sized (v_0) particles per unit aerosol volume, normalized by $N(0)$, the initial particle density (recall the normalization in (11-92)), is $g_n(T) = \int_{n-\varepsilon}^{n+\varepsilon} g(x,T)\,dx$ for integral n and $\varepsilon < 1$, so that

$$g_n(T) = (1-T)^2T^{n-1}\,. \tag{15-51}$$

The dimensionless time τ may be recovered from T through the relationship $dT/d\tau = -dM_0/d\tau = D(T)/2$, or

$$\tau = 2\int_0^T \frac{dT}{D(T)}\,. \tag{15-52}$$

In the present instance with $D = (1-T)^2$, this gives $T = \tau/2(1+\tau/2)^{-1}$. Therefore, we find

$$g_n(T) = f_N(\tau) = \frac{(\tau/2)^{n-1}}{(1+\tau/2)^{n+1}}\,, \tag{15-53}$$

which is the Smoluchowski solution (11-52), allowance being made for the fact that τ as defined in (11-94) is just twice the value which appears in (11-52).

For our second choice of the initial spectrum, we take the family of gamma distributions: $g(x,0) = f(x,0) = J(x)$, where $J(x)$ is given by (11-108). In passing, we note that the observations of Levin (1954) led him to conclude that (11-108) with $p = 8/3$ gives a satisfactory description of many fog droplet spectra. Also, as Scott (1968) has pointed out, if the initial droplet distribution is nearly Gaussian in radius, then, as a distribution in volume, it may be approximated very well by some function of the form of (11-108). Given the distribution (11-108), we find that the mean value of x (or the first moment) is $M_1 = 1$, the most probable value is $p/(p+1)$, and the relative rms dispersion (the square root of the relative variance, var x) is $(M_2 - M_1^2)^{1/2}/M_1 = (1+p)^{-1/2}$. Finally, we note again that (11-108) contains the limiting forms of a monodisperse distribution ($p \to \infty$) and an exponential distribution ($p \to 0$).

The solutions for this choice of initial distribution are as follows:

$$g(x,t) = x^p(1-p)^2(p+1)^{(p+1)}e^{-(p+1)x}\sum_{k=0}^{\infty}\frac{T^k(p+1)^{k(p+1)}x^{k(p+1)}}{\Gamma[(p+1)(k+1)]}\,,(\alpha = 1), \tag{15-54}$$

(Martynov and Bakanov, 1961), and

$$g(x,T) = x^p(1-T)(p+1)^{(p+1)}e^{-(T+p+1)x}\sum_{k=0}^{\infty}\frac{(Tx)^k(p+1)^{k(p+1)}x^{k(p+1)}}{(k+1)!\Gamma[(p+1)(k+1)]}, (\alpha = x+y), \tag{15-55}$$

(Scott, 1968). This last solution is probably the most realistic for the drop collection problem, since the collection kernel for drop radii $\gtrsim 50\,\mu$m is similar to the sum-of-volumes form (see Section 15.2). A plot of (15-55) for various T and $p = 0$, 10 is given in Figure 15.6. The 'wiggles' in the curves for $p = 10$ and x near unity reflect the narrowness of the initial spectrum. Similar behavior occurs in the steady state case of a reinforeed aerosol (see Figure 11.10). The curves indicate that for $xT \leq 1$ the form of the evolving spectrum is strongly influenced by the initial spectra, and that the influence is lost for $xT \gg 1$. Also, it turns out that the influence of the initial spectra is retained for larger xT for the sum-of-volumes kernel than for the constant kernel.

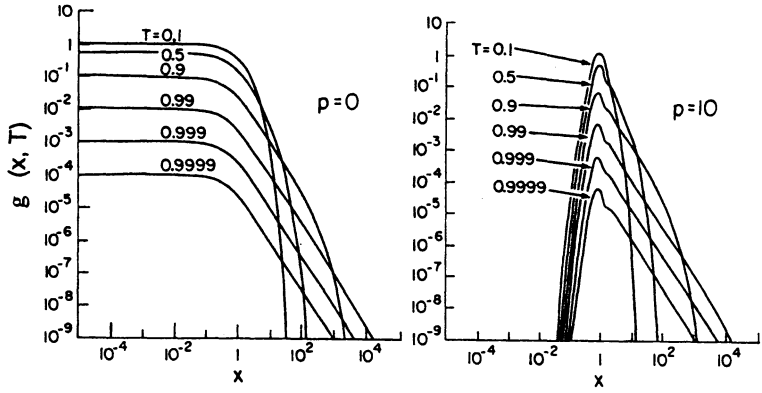


Fig. 15-6: Plots of the evolving drop size spectrum $g(x,T)$ for the kernel $\alpha(x,y) = x + y$. The initial spectrum $f(x,0)$ is a gamma distribution characterized by the parameter p (Equation (11-108). (From Drake and Wright, 1972; by courtesy of Am. Meteor. Soc., and the authors.)

Some corresponding curves for the dimensionless liquid water content $xg(x,T)$ are shown in Figure 15.7. The curves, taken from Scott (1968), are labeled with values of dimensional time t (in seconds). From (11-92), we see that this implies a particular choice of K_0 and $N(0)$. Scott assumed the collection kernel has the value 1.80×10^{-4} cm^3 sec^{-1}, when the drop volumes are $u_1 = 4.189 \times 10^{-9}$ cm^3 (radius of 10 μm) and $v_1 = 1.131 \times 10^{-7}$ cm^{-3} (radius of 30 μm). This was done to ensure agreement with the collection kernel value found by using the Shafrir and Neiburger (1963) collision efficiency for a 30 and 10 μm radius droplet pair. The liquid water content was taken as 1 g m^{-3}, and the initial mean particle volume was assumed to be $v_0 = 4.189 \times 10^{-9}$ cm^3; therefore, $N(0) = 10^{-6}v_0 - 1 = 239$ droplets per cm^3. For the constant collection kernel case, $K_0 = 1.80 \times 10^{-4}$ cm^3 sec^{-1} and so

$\tau = N(0)K_0 t = 0.0429t$. For the sum-of-volumes kernel, $K_0 = 1.80 \times 10^{-4} v_0(u_1 + v_1)^{-1}$ cm^3 sec^{-1}, so that $\tau = 0.00153t$ in Figure 15.7.

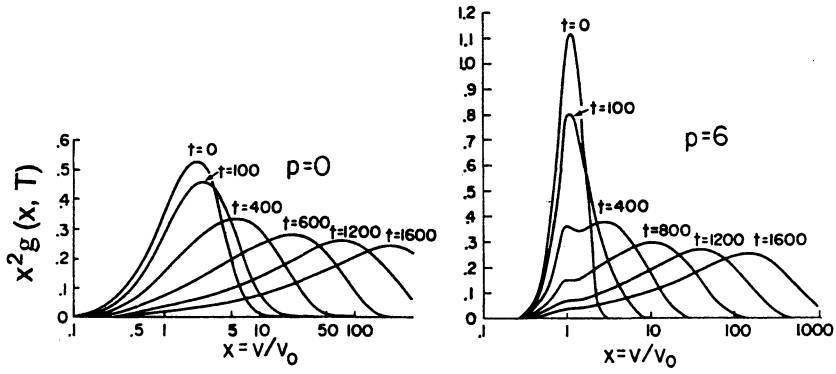


Fig. 15-7: Distribution of dimensionless liquid water content for the kernel $\alpha(x, y) = x + y$, and an initial distribution given by (11-110). (From Scott, 1968; by courtesy of Am. Meteor. Soc., and the author.)

As we have mentioned before, the SCE applies in the conservative situation in which there are no mechanisms available to transport particles in or out of volumes of aerosol. Consequently, we have the constraint $M_1(\tau) = \int_0^x xg(x, T)\,dx = 1$, so that the area under the curves of xg versus x is constant in time. This desirable property of equal areas, which clearly shows how the water content is distributed along the range of droplet sizes, may be preserved in a semi-logarithmic plot by noting that $xg\,dx = x^2 g\,d\ln x$; thus, in Figure 15.7, the ordinate is linear in the quantity $x^2 g(x, T)$.

15.3.3 Numerical and Approximation Techniques for the SCE

Considering the limitations under which exact solutions to the SCE can be obtained, we shall now turn to some numerical and approximation techniques. Numerous such techniques have been devised: the interpolation methods of Berry (1967), Reinhardt (1972), Berry and Reinhardt (1974a), and Kovetz and Okund (1969); the Markovian analysis of Valdez and Young (1985); the finite element method of Gelbard and Seinfeld (1978) and of Gelbard *et al.* (1980); and the method of moments formulated in various ways, by Golovin (1963b, 1965), Enukashvili (1964a,b, 1980), Wang (1966), Pick *et al.* (1970), Bleck (1970), Cohen and Vaughan (1971), Danielsen *et al.* (1972), Drake (1972a), Soong (1974), List and Gillespie (1976), Gillespie and List (1978), Srivastava (1978), Ochs and Yao (1978), Brown (1986, 1987, 1988, 1989, 1991), Tzivion *et al.* (1987, 1989), Feingold *et al.* (1988), and of Hu and Srivastava (1992). Considering the wealth of attempts to find solution algorithms for the SCE, it is of course impossible to summarize each one. Here we shall merely discuss the two currently most used methods.

15.3.3.1 *The Method of Berry (1967) and Reinhardt (1972)*

Numerical integration of the SCE generally requires replacing the integrals in the continuous version by finite sums, or truncating the infinite summation in the discrete version. In either case, the time derivatives are replaced by some suitable finite difference form so that the resulting finite system of non-linear algebraic equations may be numerically 'stepped along' in time. The drop size distribution function is solved at the grid points which separate the drop size classes. Berry (1967) and Reinhardt (1972) interpolate the distribution function between grid points using a six point Lagrange interpolation formula (see, e.g., Collatz, 1960). Although this method ensures exact solutions at the grid points, it does not ensure conservation of the physical moments of the drop size distribution; i.e., it neither conserves the number concentration (the zeroth moment) nor the liquid water content (the first moment) of the distribution, since moments are integral characteristics of a continuous spectrum and are not defined for a discrete spectrum. Nevertheless, Berry and Reinhardt's detailed interpolation scheme, together with a sufficiently fine resolution of the size distribution using a large (> 40) number of size categories (Silverman and Glass, 1973), allows one to compute a realistic evolution of a drop spectrum without numerically-induced artificial spreading. A three-dimensional display of the evolution of two initial drop size distributions computed by the scheme of Berry and Reinhardt is given in Figures 15.8a,b. The figures demonstrate that the evolution of the drop spectrum by collision and coalescence depends sensitively on the initial drop spectrum.

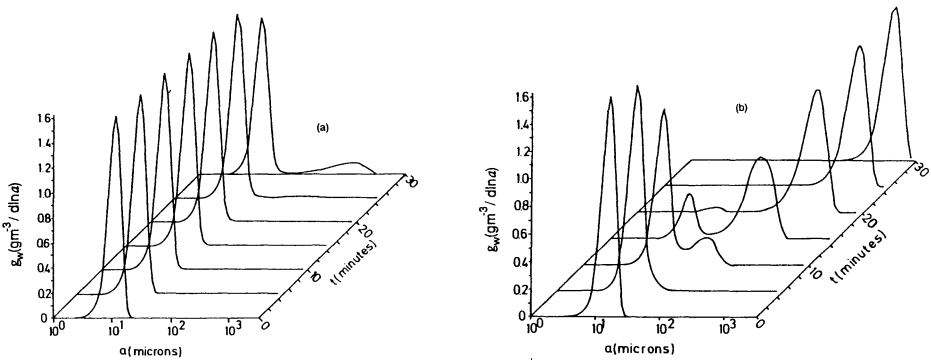


Fig. 15-8: Three-dimensional display of the time evolution of the drop mass distribution function as a function of drop radius, for an assumed initial spectrum of drops growing by collision and coalescence: (a) $\overline{a} = 9$ μm, $N_d = 237$ cm^{-3}, $w_L = 1$ g m^{-3}; (b) $\overline{a} = 13$ μm, $N_d = 108$ cm^{-3}, $w_L = 1$ g m^{-3}. Based on the Berry Reinhardt method. (From Flossmann *et al.*, 1985, with changes.)

For the continuous version of the SCE, the basic procedure is as follows: one discretizes the continuous mass (or volume) axis into 'bins' of width $\Delta m_k, k = 1, 2, \ldots$, and each bin is characterized by some resentative mass $m_k (m_1 < m_2 < \ldots)$. One then calculates $\partial n(m_k, t)/\partial t$ at $t = 0$ by numerical evaluation of the integrals on the right side of the SCE, wherein the initial spectrum $n(m_k, 0)$ is

inserted. The corresponding spectrum at time t is then written as

$$n(m_k, \Delta t) = n(m_k, 0) + \left.\frac{\partial n(m_k, t)}{\partial t}\right|_{t=0} \Delta t\,. \tag{15-56}$$

The process can be repeated to obtain the spectrum for every $t > 0$.

A key practical problem which arises is how to subdivide the volume axis into a manageable (small) number of bins, while maintaining adequate resolution over the broad size range of interest (from a few microns to a few millimeters). An effective solution is that of Berry (1965, 1967), who employed an exponential subdivision in which the drop radius a is written as a function of the integer J as follows:

$$a(J) = a_0 \mathrm{e}^{(J-1)/J_0}\,, \tag{15-57}$$

$J = 1, 2, \ldots, J_{\max}$; J_0 = unspecified number. The corresponding mass is given by

$$m(J) = m_0 \mathrm{e}^{3(J-1)/J_0}\,. \tag{15-58}$$

Here $4\pi\rho_{\mathrm{w}} a_0^3/3 \equiv m_0$ is the smallest mass considered and replaces the lower limit zero in the SCE.

To facilitate the discussion slightly, let us now rewrite the SCE given by (15-9) in the following form:

$$\left(\frac{\partial n(m)}{\partial t}\right)_C = \int_0^{m/2} K(m_c, m')n(m_c)n(m')\,\mathrm{d}m' - n(m)\int_0^{\infty} K(m, m')n(m')\,\mathrm{d}m'\,, \tag{15-59}$$

where $m_c \equiv m - m'$. The symmetry of K permits a change in form of the first (gain) integral. Also, for brevity, we have suppressed the dependence of n on time. In terms of the transformation (15-58), the upper limit $m/2$ in the gain integral is specified by the integer J_{up} where $m(J_{\mathrm{up}}) = m(J)/2$, or $J_{\mathrm{up}} = J - (J_0 \ln 2)/3$. Since by construction J_{up} is an integer, so too must be $J_0 \ln 2/3 \equiv J_R$. This reduces (15-58) to a geometric progression of sizes, with each drop mass being $2^{1/J_R}$ times the preceding one:

$$m(J) = m_0 2^{(J-1)/J_R}\,. \tag{15-60}$$

For example, if $J_R = 2$ the mass doubles every second category. The transformation results in a new distribution function $n(J)$ which is related to $n(m)$ by $n(J)\,\mathrm{d}J = n(m)\,\mathrm{d}m$,

$$n(J) = \frac{\ln 2}{J_R} m n(m)\,. \tag{15-61}$$

Also, from $m_c = m - m'$ and (15-61), we find the number J_c (generally not an integer) which corresponds to m_c is

$$J_c = J + \frac{J_R}{\ln 2} \ln[1 - 2^{(J'-J)/J_R}]\,. \tag{15-62}$$

With these changes, the form of (15-59) for the function $n(J)$ is

$$\frac{\partial n(J)}{\partial t} = m(J) \int_1^{J-J_R} \frac{K(J_c, J')}{m(J_c)} n(J_c) n(J') \, \mathrm{d}J' - n(J) \int_1^{J_{\max}} K(J, J') n(J') \, \mathrm{d}J' , \tag{15-63}$$

where now $J_{\max}$ replaces the upper limit of infinity for the loss integral.

For the physical and graphical reasons we have already discussed, there is some advantage in working directly with the distribution of liquid water content per unit $\ln a$ interval, $\mathrm{g}(\ln a)$, which is related to $n(m)$ by $\mathrm{g}(\ln a)\mathrm{d}(\ln a) = mn(m)\mathrm{d}m$, or $\mathrm{g}(\ln a) = 3m^2 n(m)$. Then, on defining $G(J) \equiv \mathrm{g}(\ln a)$, we have

$$G(J) = J_0 m n(J) . \tag{15-64}$$

From (15-63) and (15-64), the governing equation for $G(J)$ follows immediately (Reinhardt, 1972; Berry and Reinhardt, 1974a):

$$\frac{\partial G(J)}{\partial t} = \frac{m(J)}{J_0} \left(m(J) \int_1^{J-J_R} \frac{K(J_c, J') G(J_c) G(J')}{m^2(J_c) m(J')} \, \mathrm{d}J' - \frac{G(J)}{m(J)} \times \int_1^{J_{\max}} \frac{K(J, J') G(J')}{m(J')} \, \mathrm{d}J' \right) . \tag{15-65}$$

In Reinhardt's computations, a value of G below 10^{-70} g cm^{-3} per unit $\ln a$ is defined as zero.

Two types of numerical operations must be carried out in order to evaluate $\partial G/\partial t$ from (15-65). First, since J_c is generally not an integer, the value of $G(J_c)$ must be interpolated. Second, the indicated integrations must be carried out by some suitable process of numerical quadrature. The numerical schemes devised by Reinhardt (1972) are able to accomplish these tasks with considerable accuracy and speed.

A comparison of the Berry-Reinhardt scheme with the Monte Carlo simulation algorithm of Gillespie (1975b) for the stochastic growth of drops by collision using a hydrodynamic kernel, has been provided by Seeszelberg (1996). The results of this comparison are given in Figure 15.9, where $M(J)\,\mathrm{d}J$ is the mass of water per unit volume at time t, involving drops with masses between $m(J)$ and $m(J + \mathrm{d}J)$. Note the excellent agreement between the integration scheme of Berry and Reinhardt and Gillespie's stochastic simulation algorithm. Unfortunately, the Berry-Reinhardt scheme is limited to the description of the collisional drop growth, and is not suitable to handle the empirical collisional drop breakup functions which were derived by Low and List (1982a,b) (see Section 14.5.4.2).

15.3.3.2 *The Method of Moments*

This method is a widely used technique for solving the SCE. In our discussion, we shall first consider the *one-moment approximation* introduced by Bleck (1970)

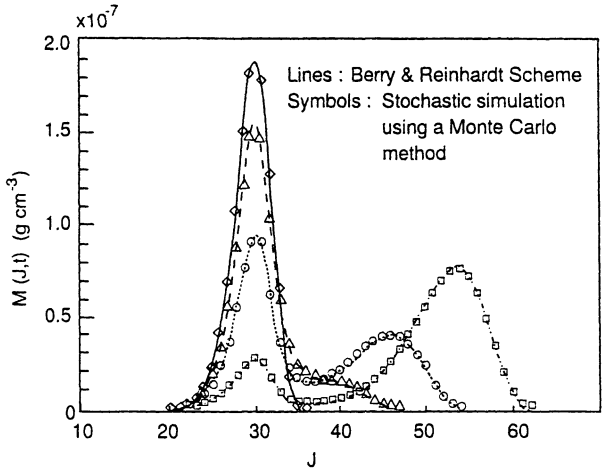


Fig. 15-9: The function $M(J,T)$ versus J at different times t for the hydrodynamic collision kernel. The lines are the result of the Berry and Reinhardt integration scheme. The solid (long-dashed, dashed-dotted, dashed) line corresponds to time $t = 0$ sec ($t =$ 600 sec, $t = 900$ sec, $t = 1200$ sec). The symbols are obtained from a simulation using a Monte Carlo method. Rhombs, triangles, circles, squares correspond to time $t = 0$ sec, $t =$ 600 sec, $t = 900$ sec, $t = 1200$ sec; for $N_d = 87$ cm^{-3}, w_L =1 g m^{-3} (FromSeesselberg *et al.*, 1996, with changes).

and Danielsen *et al.* (1972). Subsequently, we shall look at the more complete *two-moment approximation* formulated by Tzivion *et al.* (1987).

In both approximations, the drop spectrum is subdivided as in (15-60) into separate mass categories according to

$$m_{k+1} = p_k m_k \,, \tag{15-66}$$

with k being the number of the category, m_k and m_{k+1} being the lower and upper mass boundary of the category, and p_k a parameter designating the category width. Normally p_k takes on the values of $2^{1/J_R}$.

For applying the one-moment approximation to the SCE, Bleck (1970) and Danielsen *et al.* (1972) suggested solving (15-59) in sub-categories of the spectrum by assuming a mass weighted mean value for the drop number density in each mass category, expressed by

$$\begin{aligned} \bar{n}_k(t) &= \int_{m_k}^{m_{k+1}} n(m,t) m \, \mathrm{d}m \left[\int_{m_k}^{m_{k+1}} m \, \mathrm{d}m \right]^{-1} \\ &= \frac{2}{m_{k+1}^2 - m_k^2} \int_{m_k}^{m_{k+1}} n(m,t) m \, \mathrm{d}m \,. \end{aligned} \tag{15-67}$$

Considering (15-67), an equation for $\partial\bar{n}_k/\partial t$ can be obtained by multiplying both sides of (15-59) with $m\,\mathrm{d}m$ and integrating the result between m_k and m_{k+1}, to get

$$\left(\frac{\partial\bar{n}_k(t)}{\partial t}\right)_C = \frac{2}{m_{k+1}^2 - m_k^2}\left[\int_{m_k}^{m_{k+1}} m\,\mathrm{d}m \int_0^{m/2} K(m-m',m') \times n(m-m',t)n(m',t)\,\mathrm{d}m' - \int_{m_k}^{m_{k+1}} m\,\mathrm{d}m \int_0^{\infty} K(m,m')n(m,t)n(m',t)\,\mathrm{d}m'\right]. \quad (15\text{-}68)$$

On introducing the definition $C(m,t) \equiv (\partial n(m,t)/\partial t)_C$, we also have:

$$\left(\frac{\partial\bar{n}_k(t)}{\partial t}\right)_C = \frac{2}{m_{k+1}^2 - m_k^2}\int_{m_k}^{m_{k+1}} C(m,t)m\,\mathrm{d}m. \quad (15\text{-}69)$$

On the right-hand side of (15-68), Bleck introduced the approximation $n(m,t) = \bar{n}_k(t)$, where k is chosen such that $m_k \le m \le m_{k+1}$. By this step, he replaced the continuous size distribution on the right-hand side of (15-68) by a piecewise constant function with discontinuities at $m_k (k = 0, 1, 2, \ldots)$. By means of a graphical method, Bleck (1970) showed that the term between the square brackets of (15-69) may be approximated by

$$\int_{m_k}^{m_{k+1}} C(m,t)m\,\mathrm{d}m \approx \sum_{j=k-1}^{k}\sum_{i=1}^{k-1} a_{ijk}\bar{n}_j\bar{n}_i - \bar{n}_k\sum_{i=1}^{I} b_{ik}\bar{n}_i\,, \quad (15\text{-}70)$$

so that

$$\left(\frac{\partial\bar{n}(t)}{\partial t}\right)_C \approx \frac{2}{m_{k+1}^2 - m_k^2}\sum_{j=k-1}^{k}\sum_{i=1}^{k-1} a_{ijk}\bar{n}_j\bar{n}_i - \bar{n}_k\sum_{i=1}^{I} b_{ik}\bar{n}_i\,, \quad (15\text{-}71)$$

where I is the total number of categories. Expressions for the collection coefficients a_{ijk} and b_{ik} have been given by Danielsen *et al.* (1972) and Brown (1983, 1985).

The one moment approximation has been applied to the SCE by Bleck (1970), Danielsen *et al.* (1972), Soong (1974), Gillespie (1977), List and Gillespie (1976), Gillespie and List (1978), Srivastava (1978), Brown (1985, 1986, 1987, 1988, 1989, 1991), and Hu and Srivastava (1992). Despite its wide useage, the one moment approximation has received severe criticism. Bleck (1970) was also aware of some of the limitations of this method. Although the method conserves the first moment, $M_k' = \int_{m_k}^{m_{k+1}} mn(m)\,\mathrm{d}m$, i.e., the liquid water content, since the equations are normalized by the mass density distribution function, the method does not conserve any additional physical moments.

A comparison of the one-moment technique with the analytical solution of the SCE involving Golovin's sum of masses kernel has been worked out by Enukashvili (1980) and Tzivion *et al.* (1987). The comparison shows that the one-moment solution deviates significantly from the analytical solution due to an anomalous acceleration of the collisional drop growth toward the large end of the drop spectrum. According to Tzivion *et al.* (1987), this artifice is inherent in any one-moment approximation, since it prescribes that the average mass of the drops in each category be independent of time. In reality, however, the average mass in each drop size category changes with time, particularly in the large drop categories which broaden because of the logarithmically increasing mass scale. In addition, the one moment approximation assumes that the actual average mass of the drops in each category is given by the mass of the category center. In consequence, during collisional growth, the actual average mass of the drops which had entered a category, progressively lags behind the assumed average mass at the category center, thereby leading to anomalous growth acceleration. Although by using a constant kernel or a Golovin's kernel, it could be shown that the deviation from the analytical solution became less by increasing the number of mass categories, the spreading problem could not be alleviated satisfactorily. Such considerations led Bleck (1970) and Soong (1974) to introduce special weighting functions of the type $n_k(m,t) = \kappa m^{-1}$, where the constant κ was determined from the requirement of conservation of liquid water content. Such functions were able to shift the position of the average mass; however, its position is still constant in time. Despite the deficiencies of the one moment approximation in its application to the SCE, we shall find in the following section that it gives useful results when applied to the stochastic *breakup* process, and, if the *growth* process is described, e.g., by the Berry-Reinhardt method, also to the complete rain formation process.

Fortunately, the problems which arise in conjunction with the one-moment approximation to the SCE are circumvented by using a *two-moment approximation method.* In this method, the average mass of the drops in each size category is not constrained to be constant in time. We will therefore briefly outline this method. Following Tzivion *et al.* (1978), the ν^{th} moment of the distribution function $n(m,t)$ in category k can be expressed as

$$M_k^\nu = \int_{m_k}^{m_{k+1}} m^\nu n(m,t)\,\mathrm{d}m\,. \tag{15-72}$$

Applying the operator $\int_{m_k}^{m_{k+1}} m^\nu\,\mathrm{d}m$ to both sides of (15-59), we obtain a system of equations with respect to the moments in each category

$$\begin{aligned}\frac{\partial M_k^\nu(t)}{\partial t} &= \frac{1}{2}\int_{m_k}^{m_{k+1}} m^\nu\,\mathrm{d}m \int_{m_0}^{m} K(m-m',m')n(m-m',t)n(m',t)\,\mathrm{d}m' \\ &\quad -\sum_{i=1}^{I}\int_{m_k}^{m_{k+1}} m^\nu n_k(m,t)\,\mathrm{d}m \int_{m_i}^{m_{i+1}} K(m,m')n_i(m',t)\,\mathrm{d}m', \end{aligned}\tag{15-73}$$

where I is again the total number of categories and m_0 is the mass in the lowest class considered. Following Bleck (1970), Danielsen *et al.* (1972), and Soong (1974), the first double integral in (15-73) is now transformed by dividing the area of integration into separate sub-areas (i, k) in which the functions in the integrand belong to a certain category k. Tzivion *et al.* (1987) showed that this leads to the following set of equations for the special case of doubling the mass in each subsequent category, i.e., $p_k = 2(J_R = 1)$:

$$\begin{aligned}
\frac{\partial M_k^\nu(t)}{\partial t} &= \sum_{i=1}^{k-1} \int_{m_i}^{m_{i+1}} n_i(m',t)\,\mathrm{d}m' \int_{m_k}^{m_{k+1}-m'} (m+m')^\nu K_{k,i}(m,m') n_k(m,t)\,\mathrm{d}m \\
&\quad + \sum_{i=1}^{k-2} \int_{m_i}^{m_{i+1}} n_i(m',t)\,\mathrm{d}m' \int_{m_k-m'}^{m_k} (m+m')^\nu \\
&\quad \times K_{k-1,i}(m,m') n_{k-1}(m,t)\,\mathrm{d}m \\
&\quad + \frac{1}{2} \int_{m_{k-1}}^{m_k} n_{k-1}(m',t)\,\mathrm{d}m' \int_{m_{k-1}}^{m_k} (m+m')^\nu n_{k-1}(m,t) \\
&\quad \times K_{k-1,k-1}(m,m')\,\mathrm{d}m \\
&= \sum_{i=1}^{I} \int_{m_k}^{m_{k+1}} m^\nu n_k(m,t)\,\mathrm{d}m \int_{m_i}^{m_{i+1}} n_i(m',t) K_{k,i}(m,m')\,\mathrm{d}m' , \qquad (15\text{-}74)
\end{aligned}$$

where K is the collection kernel. Two problems must be overcome before this set of equations can be solved: First, the set of equations is not closed even for the special case of $K_{k,i}$ = constant, since moments of order larger than ν appear in (15-74). Second, the first and second terms in (15-74) cannot be expressed in terms of moments because the domain of integration does not span the whole category. Consequently, an approximation is required.

In order to overcome the first problem, Tzivion *et al.* expressed the collection kernel $(K_{k,i})$ in terms of Long's (1974) polynomial approximation (see Section 15.2). Closure of the equations was then achieved by expressing moments of order larger than ν in terms of moments of order not exceeding ν. To accomplish this, a non-dimensional parameter ξ_p was introduced:

$$\xi_p = \frac{\int_{m_k}^{m_{k+1}} m^{\nu+1} n_k(m,t)\,\mathrm{d}m \int_{m_k}^{m_{k+1}} m^{\nu-1} m_k(m,t)\,\mathrm{d}m}{\left[\int_{m_k}^{m_{k+1}} m^\nu n_k(m,t)\,\mathrm{d}m\right]^2} , \qquad (15\text{-}75)$$

with $1 \le \xi_p \le (p_k+1)^2/4p_k$. Using the mean value of $\xi_p(\bar{\xi}_p)$, the relationship between three neighboring moments of the distribution function could be expressed in the form

$$M_k^{\nu+1} = \bar{\xi}_p \bar{m}_k^\nu M_k^\nu , \qquad (15\text{-}76)$$

with $\bar{m}_k^\nu = M_k^\nu / M_k^{\nu-1}$. In order to remove the second problem, integrals over incomplete category intervals of the form $\int_{m_{k+1}-m'}^{m_{k+1}} m^\nu n_k(m,t)\,\mathrm{d}m$ were represented by approximating the integral by a linear distribution function.

Formulating (15-74) in terms of the first moment ($M_k^0 = N_k$) and the second moment $M_k = M_k(\mathrm{w}_L)$, Tzivion *et al.* (1987) found

$$\begin{aligned}
\frac{\partial N_k(t)}{\partial t} = & \left[\frac{1}{2}\int_{m_{k-1}}^{m_k} n_{k-1}(m',t)\,\mathrm{d}m' \int_{m_{k-1}}^{m_k} K_{k-1,k-1}(m,m')n_{k-1}(m,t)\,\mathrm{d}m\right. \\
& \left. + \sum_{i=1}^{k-2} n_i(m',t)\,\mathrm{d}m' \int_{m_k-m'}^{m_k} K_{k-1,i}(m,m')n_{k-1}(m,t)\,\mathrm{d}m\right] \\
& - \left[\frac{1}{2}\int_{m_k}^{m_{k+1}} n_k(m',t)\,\mathrm{d}m' \int_{m_k}^{m_{k+1}} K_{k,k}(m,m')n_k(m,t)\,\mathrm{d}m\right. \\
& \left. + \sum_{i=1}^{k-1} \int_{m_i}^{m_{i+1}} n_i(m',t)\,\mathrm{d}m' \int_{m_{k+1}-m'}^{m_{k+1}} K_{k,i}(m,m')n_k(m,t)\,\mathrm{d}m\right] \\
& - \left[\frac{1}{2}\int_{m_k}^{m_{k+1}} n_k(m',t)\,\mathrm{d}m' \int_{m_k}^{m_{k+1}} K_{k,k}(m,m')n_k(m,t)\,\mathrm{d}m\right. \\
& \left. + \sum_{i=k+1}^{I} \int_{m_i}^{m_{i+1}} n_i(m',t)\mathrm{d}m' \int_{m_k}^{m_{k+1}} K_{k,i}(m,m')n_k(m,t)\mathrm{d}m\right], \quad (15\text{-}77a)
\end{aligned}$$

$$\begin{aligned}
\frac{\partial M_k(t)}{\partial t} = & \left[\frac{1}{2}\int_{m_{k-1}}^{m_k} n_{k-1}(m',t)\mathrm{d}m' \int_{m_{k-1}}^{m_k} (m+m')K_{k-1,k-1}(m,m')n_{k-1}(m,t)\mathrm{d}m\right. \\
& \left. + \sum_{i=1}^{k-2} \int_{m_i}^{m_{i+1}} n_i(m',t)\mathrm{d}m' \int_{m_k-m'}^{m_k} (m+m')K_{i,k-1}(m,m')n_{k-1}(m,t)\mathrm{d}m\right] \\
& - \left[\frac{1}{2}\int_{m_k}^{m_{k+1}} n_k(m',t)\,\mathrm{d}m' \int_{m_k}^{m_{k+1}} (m+m')K_{i,k}(m,m')n_k(m,t)\,\mathrm{d}m\right. \\
& \left. + \sum_{i=1}^{k-1} \int_{m_i}^{m_{i+1}} n_i(m',t)\,\mathrm{d}m' \int_{m_{k+1}-m'}^{m_{k+1}} (m+m')K_{i,k}(m,m')n_k(m,t)\,\mathrm{d}m\right] \\
& + \left[\sum_{i=1}^{k-1} \int_{m_i}^{m_{i+1}} m' n_i(m',t)\,\mathrm{d}m' \int_{m_k}^{m_{k+1}} K_{i,k}(m,m')n_k(m,t)\,\mathrm{d}m\right.
\end{aligned}$$

$$- \sum_{i=k+1}^{I} \int_{m_i}^{m_{i+1}} n_i(m',t)\mathrm{d}m' \int_{m_k}^{m_{k+1}} mK_{i,k}(m,m')n_i(m,t)\mathrm{d}m \Bigg] , \quad (15\text{-}77\text{b})$$

where K is again the collection kernel. In (15-77a), the first two terms represent auto-conversion of particles to interval k as a result of the coagulation between particles in category $k-1$ with one another (term 1), and with those in categories less than $k-1$ (term 2). Terms 3 and 4 describe the auto-conversion from class k to class $k+1$ as a result of coagulation between particles in category k with one another (term 3), and with those in categories less than k (term 4). The last two terms represent the decrease in the number of particles in category k with one another (term 5), and with those in categories larger than k (term 6). The terms in (15-77b) are analogous to those in (15-77a) except that they represent mass transfer rather than number transfer.

In order to test the accuracy of the two-moment approximation, Tzivion *et al.* (1987) solved the SCE analytically by using Golovin's kernel $K(m,m') = 1500(m+m')$ $\mathrm{cm^3 sec^{-1}}$, and compared the result with that obtained from the two-moment method using the same kernel. Excellent agreement was obtained.

A comparison between the one-moment method with the two-moment method is given in Figure 15.10. We notice that the one-moment method exhibits the anomalous acceleration mentioned at the beginning of this section, making the method of one-moment unsuitable for computing the stochastic collisional growth of drops.

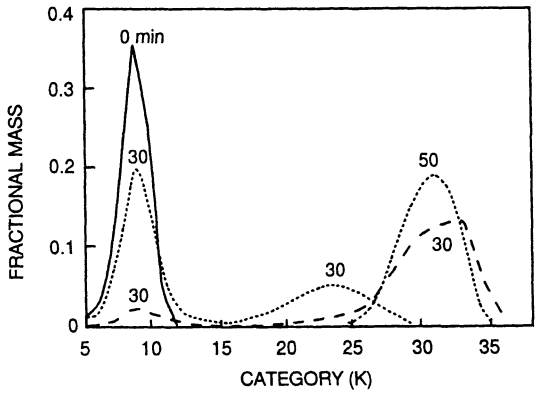


Fig. 15-10: Comparison of the one-moment method (long dashed curve) with the two-moment method (short dashed curve) for drop growth by collision and coalescence without breakup. Continuous line: initial distribution. (From Tzivion *et al.* 1987; by courtesy of Am. Meteor. Soc., and the author.)

15.4 Stochastic Model for Drop Breakup

An unrealistic feature of solutions to the SCE is that they predict a continual flow of water mass to larger and larger drop sizes. This is not a serious flaw when we

wish only to estimate the time required for the first few precipitation-sized drops to form. However, we cannot expect to obtain realistic theoretical descriptions of quasi-steady state rain spectra, such as exponential distributions of the Marshall-Palmer type (Equation (2-15)), unless we take into account the spectral shaping due to drop breakup as well as coalescence. Such considerations prompted Langmuir, as early as 1948, to suggest that 'warm' rain develops by means of a chain-reaction involving drops which grow by collision and, subsequently, break up into fragments. These, in turn, would have the opportunity also to grow and eventually break up too, and so on.

Fragmentation of large drops may be induced by the collision of drops with each other ('collisional breakup', see Section 14.5.4.2), or by hydrodynamic instabilities of drops ('spontaneous breakup', see Section 10.3.5). Cloud models in which spontaneous drop breakup is considered, have been developed and evaluated by Srivastava (1971), Young (1975), Danielsen *et al.* (1972), Hall (1980), Flossmann *et al.* (1985, 1987), Flossmann and Pruppacher (1988), Flossmann (1991, 1994), and Kogan (1991).

For the condition of hydrodynamic breakup of single drops, the stochastic breakup equation (SBE) can be expressed by the relation

$$\left(\frac{\partial n(m,t)}{\partial t}\right)_B = \int_0^\infty Q(m,m')P(m')n(m',t)\,\mathrm{d}m' - n(m,t)P(m)\,, \qquad (15\text{-}78)$$

where $P(m)$ is the probability for a drop of mass m to spontaneously breakup, and $Q(m,m')$ represents the number density function for the drop fragments formed by the breakup of a parent drop of mass m'. Recalling Section 10.3.5, one may set (after Hall, 1980; and Danielsen *et al.*, 1972) $P(m) = 1$ for $a_0(m) \geq a_{0,\mathrm{crit}} = 2580\,\mu\mathrm{m}$, and $P(m) = 0$ for $a_0(m) < a_{0,\mathrm{crit}}$. The fragment distribution, $Q(m,m')$, is then given in Table 10.2. Alternatively, one may follow Srivastava (1971) and describe $P(m)$ by (10-134) and $Q(m,m')$ by (10-135). The first term on the right of (15-78) represents the gain term and describes the generation of m-drops as a result of the spontaneous breakup of drops with mass $m' > m$. The second term on the right of (15-78) represents the loss-term and describes the decrease in the number of m-drops as a result of their spontaneous breakup.

One advantage of considering spontaneous drop breakup lies in the fact that one may solve (15-78) simultaneously with the SCE (15-72) by applying Berry and Reinhardt's (1974a,b,c) method of solution (Section 15.3.3.1). Observations show, however, that in atmospheric clouds, drops large enough to enter the realm of spontaneous breakup (diameter $\gtrsim 5$ mm) are very rare. Indeed, model calculations by Young (1975), in which both breakup modes were included, showed that spontaneous breakup is negligible. Furthermore, the spectral shape produced by a balance between spontaneous breakup and coalescence is unrealistically flat, i.e., there is too great a bias toward the larger drop sizes (Srivastava, 1971; Tsias, 1996).

As we have reported in Section 14.5.4.2, laboratory studies have shown that drops do break up in collision. Computations of the collisional, stochastic breakup of drops have been carried out by List and Gillespie (1976), Gillespie and List

(1978), and Srivastava (1978). They used the experimental results of McTaggart-Cowan and List (1975) for specifying the breakup probability and the size distribution of the fragment drops. Subsequently, Brown (1983, 1985, 1986, 1987, 1988), Tzivion *et al.* (1987, 1989), Feingold *et al.* (1988), and Hu and Srivastava (1992) employed the more accurate experimental results of Low and List (1982a,b).

Collisional breakup is described by the following form of the SBE:

$$\begin{aligned}\left(\frac{\partial n(m,t)}{\partial t}\right)_B &= \frac{1}{2}\int_0^\infty n(m',t)\,\mathrm{d}m' \int_0^\infty K(m',m'')[1-E_{\mathrm{coal}}(m',m'')] \\ &\quad \times Q(m;m',m'')n(m'')\,\mathrm{d}m'' \qquad (0 \le m \le m'+m'') \\ &\quad -n(m,t)\int_0^\infty \frac{n(m'',t)K(m,m'')[1-E_{\mathrm{coal}}(m,m'')]}{m+m''}\,\mathrm{d}m'' \\ &\quad \times \int_0^{m+m''} m'Q(m';m,m'')\,\mathrm{d}m' \qquad (0 \le m \le \infty)\,. \quad (15\text{-}79)\end{aligned}$$

An equivalent form is (see, e.g., List and Gillespie, 1976):

$$\begin{aligned}B(m,t) \equiv \left(\frac{\partial n(m,t)}{\partial t}\right)_B &= \int_0^\infty n(m',t)\,\mathrm{d}m' \int_0^{m'} K(m',m'')[1-E_{\mathrm{coal}}(m',m'')] \\ &\quad \times Q(m;m',m'')n(m'')\,\mathrm{d}m'' \\ &\quad -n(m,t)\int_0^\infty \frac{n(m'',t)K(m,m'')[1-E_{\mathrm{coal}}(m,m'')]}{m+m''}\,\mathrm{d}m'' \\ &\quad \times \int_0^{m+m''} m'Q(m';m,m'')\,\mathrm{d}m'\,, \qquad (15\text{-}80)\end{aligned}$$

where $K(m',m'')$ is the collision kernel for the collision of an m'-drop with an m''-drop, and $E_{\mathrm{coal}}(m',m'')$ is the coalescence efficiency for an m'-drop that collides with an m''-drop. The term $[1-E_{\mathrm{coal}}(m,m'')] = P(m,m'')$ represents the breakup probability for an m-drop that collides with an m''-drop. The term $Q(m;m',m'')$ specifies the mean number of fragments of mass m per collision and subsequent breakup of masses m' and m''. The first term on the right side of (15-79) describes the gain of m-drops created by the collisional breakup of all masses m' and m'', whereby the factor $1/2$ prevents counting the same pair (m',m'') twice. The second term represents the loss of m-drops resulting from collision and subsequent breakup of drops of mass m and m''. Mass conservation requires $\int_0^{m'+m''} mQ(m;m',m'')\,\mathrm{d}m = m'+m''$.

In order to apply Bleck's (1970) one-moment approximation to the SBE, we may proceed, as pointed out by List and Gillespie (1976), in a manner analogous to that

used for solving the SCE. Thus, the mass coordinate is discretized by subdividing it into separate mass bins according to (15-66). Equation (15-80) is then solved in sub-categories of the spectrum by assuming a mass weighted mean value for the drop number density in each mass category as expressed by (15-67). Applying the operator $\int_{m_k}^{m_{k+1}} m\,\mathrm{d}m$ to both sides of (15-80), we obtain, analogously to (15-69),

$$\left(\frac{\partial \bar{n}_k}{\partial t}\right)_B = \frac{2}{m_{k+1}^2 - m_k^2}\left[\int_{m_k}^{m_{k+1}} B(m,t) m\,\mathrm{d}m\right]. \tag{15-81}$$

Applying Bleck's method to (15-81) as it was applied before to (15-69), List and Gillespie (1976) approximated the term in the square bracket of (15-81) by

$$\int_{m_k}^{m_{k+1}} B(m,t) m\,\mathrm{d}m \approx \sum_{j=1}^{I}\sum_{i=1}^{j} p_{ijk}\bar{n}_j\bar{n}_i - n_k \sum_{i=1}^{I} q_{i,k}\bar{n}_i\,; \tag{15-82}$$

therefore, in analogy to (15-71), we obtain:

$$\left(\frac{\partial \bar{n}_k(t)}{\partial t}\right)_B = \frac{2}{m_{k+1}^2 - m_k^2}\sum_{j=1}^{I}\sum_{i=1}^{j} p_{ijk}\bar{n}_j\bar{n}_i - n_k \sum_{i=1}^{I} q_{i,k}\bar{n}_i\,. \tag{15-83}$$

Expressions for the breakup coefficients $p_{ijk}, q_{i,k}$ have been given by List and Gillespie (1976) and Brown (1983).

Feingold *et al.* (1988) have generalized this approach by taking multiple moments of the SBE. As in the treatment of the SCE, the operator $\int_{m_k}^{m_{k+1}} m^\nu \mathrm{d}m$ was applied to both sides of (15-79) to obtain a set of moment equations:

$$\begin{aligned}\frac{\partial M_k^\nu(t)}{\partial t} &= \frac{1}{2}\int_{m_k}^{m_{k+1}} m^\nu\,\mathrm{d}m \int_0^\infty n(m',t)\,\mathrm{d}m' \int_0^\infty K(m',m'')[1 - E_{\mathrm{coal}}(m',m'')] \\ &\quad \times Q(m;m',m'')n(m'')\,\mathrm{d}m'' \\ &\quad - \int_{m_k}^{m_{k+1}} n(m,t)m^\nu\,\mathrm{d}m \int_0^\infty \frac{n(m'',t)K(m,m'')[1 - E_{\mathrm{coal}}(m,m'')]}{m+m''}\,\mathrm{d}m'' \\ &\quad \times \int_0^{m+m''} m' Q(m';m,m'')\,\mathrm{d}m'\,. \end{aligned} \tag{15-84}$$

A Bleck-type transformation of this equation yields

$$\frac{\mathrm{d}M_k^\nu(t)}{\mathrm{d}t} = \sum_{i=1}^{I}\sum_{j=1}^{i-1} \int_{m_i'}^{m_{i+1}'} n_i(m',t)\,\mathrm{d}m' \int_{m_j'}^{m_{j+1}'} n_j(m'',t)K_{i,j}(m',m'')$$

$$\times[1 - E_{\text{coal}}(m', m'')]\,\mathrm{d}m'' \int_{m'_k}^{m'_{k+1}} m^\nu Q_{k,i,j}(m; m', m'')\,\mathrm{d}m$$

$$+\frac{1}{2}\sum_{i=1}^{I} \int_{m'_i}^{m'_{i+1}} n_i(m', t)\,\mathrm{d}m' \int_{m'_i}^{m'_{i+1}} n_i(m'', t) K_{i,j}(m', m'')$$

$$\times[1 - E_{\text{coal}}(m', m'')]\,\mathrm{d}m'' \int_{m'_k}^{m'_{k+1}} m^\nu Q_{k,i,i}(m; m', m'')\,\mathrm{d}m$$

$$-\sum_{i=1}^{I}\sum_{j=1}^{k} \int_{m'_k}^{m'_{k+1}} m^\nu n_k(m, t)\,\mathrm{d}m \int_{m'_j}^{m'_{j+1}} \frac{n_j(m'', t) K_{k,j}(m, m'')}{(m + m'')}$$

$$\times[1 - E_{\text{coal}}(m, m'')]\,\mathrm{d}m'' \int_{m'_i}^{m'_{i+1}} m' Q_{i,k,j}(m'; m, m'')\,\mathrm{d}m'$$

$$-\sum_{i=1}^{I}\sum_{j=k+1}^{I} \int_{m'_k}^{m'_{k+1}} m^\nu n_k(m, t)\,\mathrm{d}m \int_{m'_j}^{m'_{j+1}} \frac{n_j(m'', t) K_{j,k}(m'', m)}{(m + m'')}$$

$$\times[1 - E_{\text{coal}}(m'', m)]\,\mathrm{d}m'' \int_{m'_i}^{m'_{i+1}} m' Q_{i,j,k}(m'; m'', m)\,\mathrm{d}m'\,, \quad (15\text{-}85)$$

$$Q(m; m', m'') = 0 \quad \text{for} \quad m > m' + m''\,,\; Q(m'; m, m'') = 0 \quad \text{for} \quad m' > m + m''\,,$$

which again may be separated into the first ($\nu = 0$) and second ($\nu = 1$) moments. We note from (15-85) that, in contrast to the SCE, all integrals cover complete categories so that the method of moments can be implemented without approximating n_k. To close the moment equations, the kernels are again approximated by polynomials, so that higher order moments can be related to lower ones using (15-76).

In order to test the accuracy of the one- and two-moment approximations for breakup only, Feingold *et al.* chose a fragment distribution of the form $Q(m; m', m'') = \gamma^2(m' + m'')\exp(-\gamma m)$. This permits an analytic solution of (15-79), with $\gamma = nN_0/M_0$, where n is a positive integer that characterizes the fragment concentration, and where N_0 and M_0 are the drop number concentration and liquid water content of the initial spectrum. The breakup kernel was set to be constant. Excellent agreement between the analytical solution and the solution obtained with the method of two-moments was found (see Figure 15.11). Somewhat surprising at first sight was the fact that application of the one-moment method to the SBE produced a result which agreed well with the analytical as well as with the two-moment

solution (see Figure 15.11). In order to explain this finding, we must consider that, in contrast to *collisional growth* where the drop mass is 'forward' distributed into progressively *broader* drop size classes with the effect of increasingly larger deviation between the actual average drop mass and the mass of the category center, in *drop breakup* the drop fragment mass is distributed 'backward' into progressively *narrower* size classes with the effect of rapidly decreasing differences between the actual average mass and the mass of the category center. It appears, therefore, that the one-moment method is useful in handling stochastic collisional breakup.

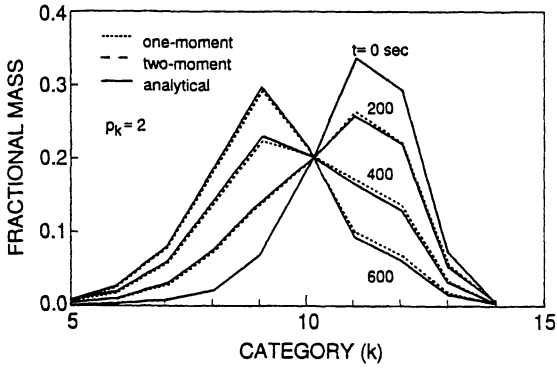


Fig. 15-11: Comparison of the one-moment and two-moment methods with the analytical solution described in Section 15.4 for collision-breakup only; w_L =2.2 g m^{-3}, N_d = 3900 m^{-3}. (From Feingold *et al.*, 1988; by courtesy of the Am. Meteor. Soc., and the author.)

15.5 Stochastic Drop Growth in Combination with Stochastic Drop Breakup

Telford's (1955) early calculation of drop growth by stochastic collection in an idealized warm cloud was followed by numerous studies which considered more realistic initial drop size distributions, mass dependent collection kernels, and breakup following collision. In current models, the evolution in time of a drop spectrum due to collisional growth and breakup is determined from the relation

$$\frac{\partial n(m,t)}{\partial t} = C(m,t) + B(m,t)\,, \tag{15-86}$$

where $C(m,t)$ and $B(m,t)$ are the collection and breakup rates given by (15-59) and (15-80), respectively. Solutions to (15-86) show that a given initial drop size distribution, evolving by collisional growth and breakup, approaches a steady state size distribution given sufficient time (in a box model), or sufficient height of fall (in a shaft model). This behavior is illustrated in Figures 15.12 and 15.13. These summarize computations of Tsias (1996) who combined the Berry-Reinhardt scheme for collisional drop growth with the method of one-moment for collisional drop breakup. We notice from Figure 15.12 that an originally MP-type drop distribution narrows in time due to fragmentation of large drops. In contrast, an assumed

initial gamma drop size distribution (Figure 15.13) broadens with time due to the formation of large drops resulting from the collection of drop fragments caused by drop breakup. Comparison of the final drop size distributions shows that, after 20 minutes, both spectra exhibit the same slope of $\Lambda = 63$ cm^{-1}. This result substantiates the earlier theoretical finding of List *et al.* (1987a) that, at steady state, equilibrium rain drop distributions are independent of the distribution the drops had initially, and can be described by multiples of each other (see (15-91)).

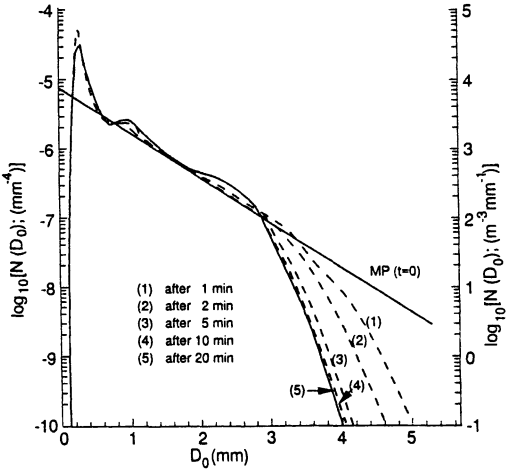


Fig. 15-12: Variation with time of an initial Marshall Palmer (MP) raindrop size distribution during growth of drops by collision and coalescence (using the method of Berry & Reinhardt), and by collisional breakup (using the 1-moment method with $p_k = 2^{1/3}$); box model, for $R = 100$ mm hr^{-1}. (From Tsias, 1996, by courtesy of the author.)

A detailed look at the raindrop spectra, computed from (15-86) by using the fragment distribution and collisional breakup kernel of Low and List (1982a,b), reveals that, on approaching steady state, one primary and two secondary maxima develop. The primary maximum of such a three-peaked equilibrium distribution (3 PED) appears at drop diameters between 0.22 and 0.27 mm. The two secondary maxima appear at drop diameters 0.7 to 0.9 mm and 2.0 to 2.5 mm, respectively. These peaks are noticeable in Figures 15.12 and 15.13. According to Brown (1988) and List and McFarquhar (1990a), the maxima are caused by the three main breakup modes observed by Low and List (1982a,b). An analysis of the contributions of the individual breakup mechanism to the overall drop size distribution is given in Figure 15.14 (see also Brown, 1988). The computations of List and McFarquhar (1990a) and of Brown (1988) show that filament breakup (see Chapter 14) is mainly responsible for the primary maximum in the drop size distribution. The sheet and disk breakup mechanism are chiefly responsible for the middle of the three modes, while all three breakup modes contribute to the third maximum.

List and McFarquhar (1990b) and McFarquhar and List (1991a) found that maxima in the computed raindrop spectra also appear in non-steady raindrop dis-

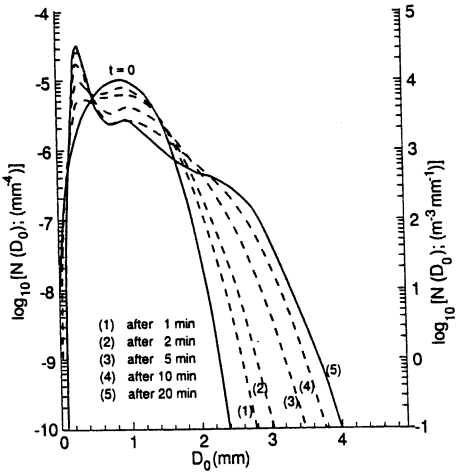


Fig. 15-13: As in Figure 15-12 but for an initial gamma distribution. (From Tsias, 1996, by courtesy of the author.)

tributions, modeled by a pulsed input of raindrop packages at the top of a rain shaft. They showed that the three peak distributions (3 PD's) resemble 3 PED's the more frequent and the shorter the pulses.

We mentioned in Chapter 2 that considerable debate has arisen in the literature as to whether 3 PED's are found in natural raindrop spectra. It appears from current field observations that data, taken with carefully calibrated raindrop spectrometers, do not exhibit distinct secondary maxima except at high rainfall rates. This fact does not imply that the theoretical results are incorrect, since the existence of collisional breakup modes acting in definite drop size intervals has experimentally been well established. However, it may well be that turbulent motions, raindrop sorting, and condensation and evaporation processes at small rainfall rates may completely or partly mask the breakup maxima.

Raindrop spectra computed from (15-86) also show that steady state distributions take time to develop. This fact has already been pointed out earlier by Srivastava (1971), List *et al.* (1980, 1987a), and Valdez and Young (1985), who stressed that the time to reach steady state increases with decreasing rainfall rate. This is illustrated by Figures 15.15a,b derived from computations of Tsias (1996). In these computations, a rainshaft model was used in which it was assumed that the top of the computational grid coincided with the cloud base where the drop size distribution remained constant in time. We notice from Figure 15.15a that the largest drops reach the ground first, followed in time by progressively smaller drops which are, in part, resulting from broken up large drops. We also notice that, with increasing time, collision and breakup lead to increasingly narrower drop size spectra with increasingly steeper slopes at the large drop size end of the spectrum, as less and less large drops survive their fall, and that, with increasing time, the secondary maxima become increasingly distinct. Figure 15.15b shows

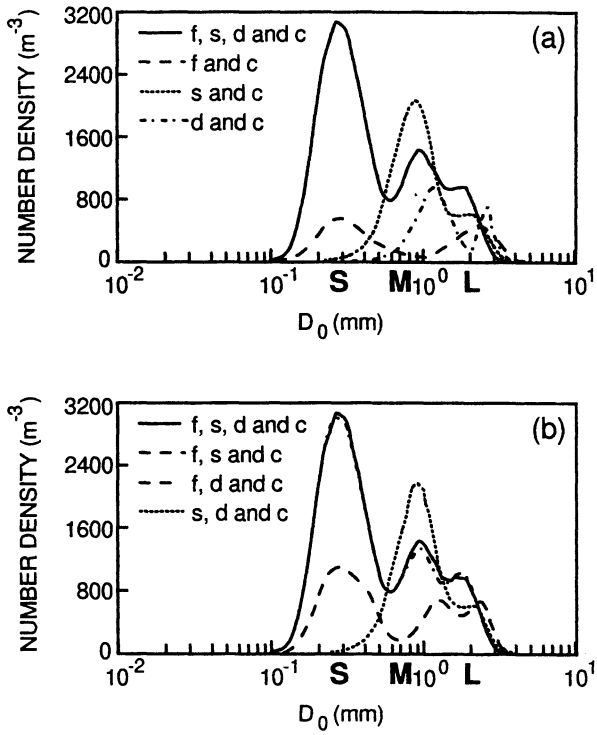


Fig. 15-14: Number density per logarithm diameter interval for equilibrium distributions of drops grown by collision and coalescence and Low & List breakup: f: filament breakup, s: sheet breakup, d: disk breakup. Size distribution evolved from a MP distribution with $R = 54.0$ mm hr^{-1}. Based on the method of Gelbard & Seinfeld (1978) with $p_k = 2^{1/2}$. (From List & McFarquhar, 1990a, with changes.)

that 40 minutes are needed for a steady state raindrop size distribution to develop at the ground, assumed to be 4 km below cloud base. Of course, within this time span the drop size distribution has also become steady state at 3, 2, 1 and 0.4 km below cloud base. Since natural clouds often do not provide these times or fall distances, natural raindrop spectra often have slopes considerably flatter and with less distinct secondary maxima than those of equilibrium distributions pertaining to the same rainfall rate. This is verified by consulting Figure 2.31, which shows that, for $R = 100$ mm hr^{-1} , Λ typically varies between 15 and 37 cm^{-1}, in contrast to $\Lambda \approx 63$ cm^{-1} for the steady state drop distribution given in Figures 15.12 and 15.13, and $\Lambda = 30.1, 45.5, 57, 62$, and 63 cm for curves 1 to 5, respectively, in Figure 15.15b.

It is obvious from the preceding paragraphs that the fundamental quantity which underlies the evolution of raindrop spectra is the rate at which drops collide with one another. Unless this rate is sufficiently high, an equilibrium spectrum cannot be established in a realistic time period. Although solutions to the stochastic collection equation embody the collision rate, this quantity is usually not explicitly

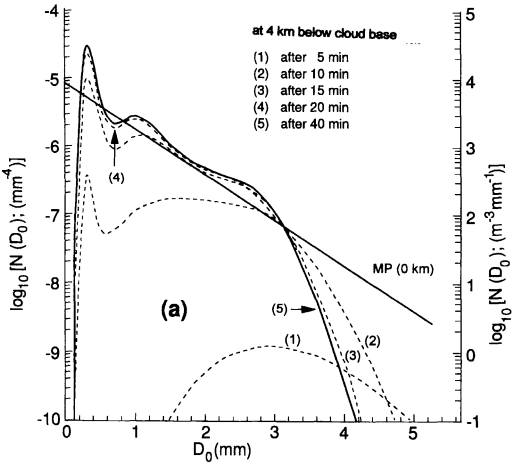


Fig. 15-15: a. Variation with time of the raindrop size distribution resulting from collison and coalescence (using the method of Berry & Reinhard) and from collisional breakup (using the 1-moment method with $p_k = 2^{1/3}$) of rain drops, observed in a shaft at 4 km below cloud base; for $R = 100$ mm hr^{-1} and a constant in time MP drop sprectrum at the top of the shaft. (From Tsias, 1996, by courtesy of the author.)

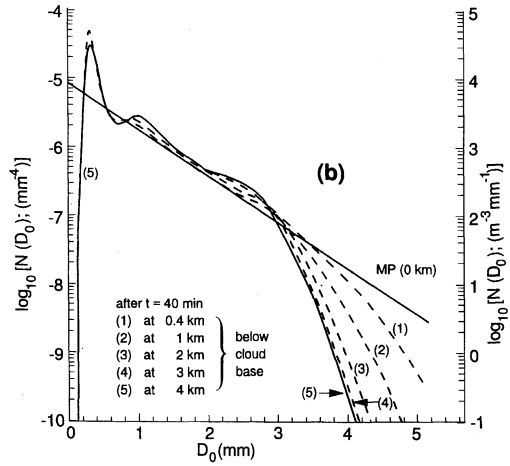


Fig. 15-15: b. Steady state rain drop size distribution resulting after 40 minutes from collison and coalescence (using the method of Berry & Reinhard) and from collisional breakup (using the 1-moment method with $p_k = 2^{1/3}$) of raindrops, observed in a shaft at various distances below cloud base; for $R = 100$ mm hr^{-1} and a constant in time MP drop sprectrum at the top of the shaft. (From Tsias, 1996, by courtesy of the author.)

solved for. In view of this, we shall now follow the analytical approach of List *et al.* (1970), Beard *et al.* (1986), Rogers (1989), and McFarquhar and List (1991b) to estimate the collision rate from the mean time between collisions for some simple model drop spectra. This estimate will show that, in contrast to expectations, the collision rate, and therefore the opportunity for collisional breakup, is quite low, except in very heavy rain. This result implies that equilibrium drop size distributions will indeed be slow in emerging.

Consider drops of diameter $D_{0,L}$ in concentration N_L falling in a rain shaft through a region containing smaller drops of diameter $D_{0,S}$ in concentration N_S. By elementary arguments, if the N_L-drops move a distance $\mathrm{d}x$ relative to N_S-drops, the change in their concentration will be given approximately by $\mathrm{d}N_L = -N_L[\mathrm{E}\pi(D_{0,L} + D_{0,S})^2 N_S/4]\,\mathrm{d}x$, where E is the collision efficiency. For a small time interval, we have $\mathrm{d}x = U_{\infty,L} - U_{\infty,S})\,\mathrm{d}t$, assuming the relative velocity of approach is given by the difference in terminal velocities. Hence, the mean free time between collisions is

$$\tau = [\mathrm{E}\pi(D_{0,L} + D_{0,S})^2 N_S(U_{\infty,L} - U_{\infty,S})/4]^{-1}\,, \tag{15-87}$$

and the mean free distance $\lambda = U_{\infty,L}\tau$ between collisions is

$$\lambda = \frac{4U_{\infty,L}}{\mathrm{E}\pi(D_{0,L} + D_{0,S})^2 N_S(U_{\infty,L} - U_{\infty,S})}\,. \tag{15-88}$$

For the case that the smaller drops do not have uniform size but rather are sizes distributed according to $n(D_0)\,\mathrm{d}D_0$, the time between collision and the mean free distance become, respectively,

$$\tau(D_{0,L}, D_0) = \left(\frac{1}{4}\int_{D_{0,S}}^{D_{0,L}} n(D_0)\mathrm{E}\pi[U_{\infty,L} - U_\infty(D_0)](D_{0,L} + D_0)^2\,\mathrm{d}D_0\right)^{-1}\,, \tag{15-89}$$

and

$$\lambda(D_{0,L}, D_0) = \frac{4U_{\infty,L}}{\int_{D_{0,S}}^{D_{0,L}} n(D_0)\mathrm{E}\pi[U_{\infty,L} - U_\infty(D_0)](D_{0,L} + D_0)^2\,\mathrm{d}D_0}\,, \tag{15-90}$$

for $D_{0,S} \le D_0 \le D_{0,L}$, and where U_∞ is the terminal velocity of raindrops of diameter D_0.

For equilibrium distributions, List *et al.* (1987a) and List (1988) showed that

$$n(D_0, R) = R\Psi_n(D_0)\,, \tag{15-91}$$

where R is the rainfall rate and $\Psi_n(D_0)$ is the shape function for the number concentration, which is uniquely determined for an equilibrium distribution evolving from the coalescence and breakup of raindrops. Hence, the denominator in (15-90) has only a linear dependence on R, since all other factors in this equation

depend only on the diameter of the colliding drops. Therefore, for an equilibrium distribution, τ and λ may be expressed approximately by

$$\tau(D_{0,L}, D_0) = \frac{\Psi_n(D_{0,L}, D_{0,S})}{U_{\infty,L} R}; \tag{15-92a}$$

$$\lambda(D_{0,L}, D_0) = \frac{\Psi_n(D_{0,L}, D_{0,S})}{R}; \tag{15-92b}$$

for $D_S \leq D_0 \leq D_{0,L}$ and where $\Psi_n(D_{0,L}, D_{0,S})$ depends only on those raindrops in the size interval $(D_{0,L}, D_{0,S})$ which are geometrically swept out by the drop of size $D_{0,L}$.

Equations (15-89) and (15-90) were evaluated by List *et al.* (1970), List and Gillespie (1976), Rogers (1989) and McFarquhar and List (1991b). The results of the computations of McFarquhar and List (1991b) for a MP distribution and for a three-peak equilibrium distribution (3 PED) are summarized in Figure 15.16 for various rainfall rates, E = 1, and two values for $D_{0,L}$. In these figures, the mean free path length and mean free time between collisions of a raindrop of size $D_{0,L}$ with smaller drops having diameters larger than $D_{0,S}$, is given as a function of $D_{0,S}$. We note that τ and λ increase with decreasing rainfall rate R, as expected from (15-92). On the other hand, τ and λ decrease with decreasing $D_{0,S}$, i.e., with an increasing range of drops with which the large drop collides and, hence, with an increasing value for the integral in the denominator of (15-90). The rate C at which the $D_{0,L}$ drop collides with all drops larger than $D_{0,S}$ is given from (15-89) by

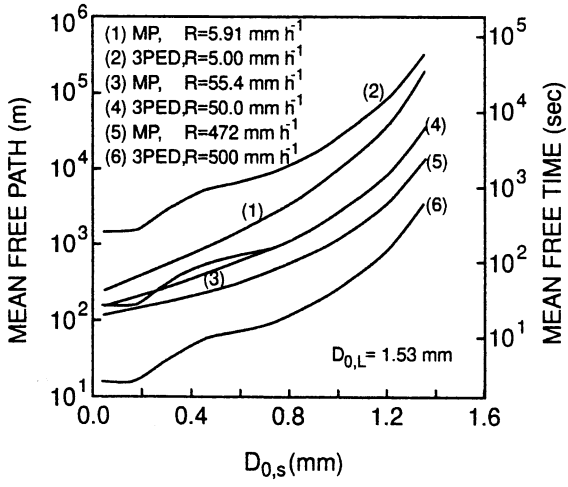


Fig. 15-16: Mean free path and mean free time between collisions of raindrops of diameter $D_{0,L}$ with raindrops having diameters larger than $D_{0,S}$, for different rain rates, and for MP and 3PED distributions. (From McFarquhar and List, 1991b, with changes.)

TABLE 15.1

Mean free distance λ , mean free time τ and collision rate C as a function of rainfall rate and large drop size, for $D_{o,s} \geq 1$ mm and a 3 PED. (From data of McFarquhar & List, 1991b.)

R (mm hr^{-1})	τ (sec)	λ (m)	C (sec^{-1})	$D_{O,L}$ (mm)
5	235	2×10^3	4.3×10^{-3}	
50	23.5	2×10^2	4.3×10^{-2}	3.43
500	2.35	2×10^1	4.3×10^{-1}	
5	4000	2×10^4	2.5×10^{-4}	
50	400	2×10^3	2.5×10^{-3}	1.53
500	40	2×10^2	2.5×10^{-2}	

$$C = \frac{1}{\tau} = \frac{1}{4} \int_{D_{0,S}}^{D_{0,L}} n(D_0) \mathrm{E} \pi [U_{\infty,L} - U_\infty(D_0)](D_{0,L} + D_0)^2 \, \mathrm{d}D_0 \qquad (15\text{-}93)$$

(see Equation 10-118). A few representative values derived from Figure 15.16 are listed in Table 15.1. We notice from this table that a 3.43 mm diameter drop with a fall velocity of 8 m sec^{-1} in rain of 5 mm hr^{-1} would experience only one collision during the fall from a cloud whose base is 2000 m above ground, and only ten collisions in a rain of 50 mm hr^{-1}. For a raindrop of 1.53 cm diameter the collision rate is even lower. Since only a fraction of all the collisions experienced by a drop results in breakup by any of the four major modes, the improbability of achieving breakup-controlled equilibrium distributions in realistic times is underscored, except perhaps in very intense rain.

Another conclusion may also be drawn from Table 15.1 and Figure 15.16. Due to the low collision rates at small rain rates, it may become possible for drops larger than 3 mm in diameter to survive their fall from cloud to ground without experiencing a collision if the concentration of smaller raindrops is low. This has been verified by Beard *et al.* (1986) for a drop size spectrum observed during a rain with $R = 17$ mm hr^{-1} in Hilo, Hawaii (Figure 2.28). The observed concentration of drops with diameter between 1 and 2 mm was 30 m^{-3}. Considering (15-93), a 5 mm diameter drop would experience under these conditions and for E = 1 a collision rate of only 3.6×10^{-3} sec^{-1}, or one collision every 4.6 minutes. Since a 5 mm diameter drop falls with a velocity of 9.1 m sec^{-1}, a 2.5 km fall distance would be required for such a drop to experience one collision with drops in the size range of 1 to 2 mm in diameter. It is therefore not surprising that Beard *et al.* (1986) collected drops larger than 3 mm in clouds near Hilo, Hawaii, since the distance of fall available in this case was less than 2 km.

Another instructive result is obtained if the total collision rate involving collisions between drops of all sizes occurring in a unit volume of rainshaft is considered.

Instead of (15-93), we then have

$$C_t = \frac{1}{4} \int_0^{\infty} \int_0^{D_{0,L}} n(D_{0,L}) n(D_{0,S}) \mathrm{E}\pi [U_{\infty,L} - U_{\infty,S}](D_{0,L} + D_{0,S})^2 \, \mathrm{d}D_{0,L} \, \mathrm{d}D_{0,S} \,, \tag{15-94}$$

where the integration is performed over all possible pairs of drop collisions. Considering (15-91), we may rewrite (15-94) as

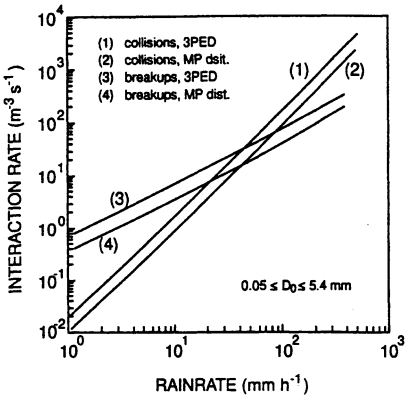


Fig. 15-17: Total collision and breakup rate for raindrops of sizes D_0 between 0.05 and 5.4 mm for different rain rates, and for MP and 3 PED distributions. (From McFarquhar and List, 1991b, with changes.)

$$C_t = \frac{1}{4} R^2 \int_0^{\infty} \int_0^{D_{0,L}} \Psi_n(D_{0,L}) \Psi_n(D_{0,S}) \mathrm{E}\pi [U_{\infty,L} - U_{\infty,S}](D_{0,L} + D_{0,S})^2 \, \mathrm{d}D_{0,L} \, \mathrm{d}D_{0,S} \,, \tag{15-95}$$

which shows that, for an equilibrium rain drop size distribution, the total collision rate increases with the square of the rainrate. Equation (15-95) has been numerically analyzed for E = 1 by McFarquhar and List (1991b) for a 3 PED and a MP size distribution. The breakup rate was determined from (15-94) after multiplying the right-hand side with $[1 - \mathrm{E}_{\mathrm{coal}}(D_{0,L}, D_{0,S})]$. The results of this analysis are summarized in Figure 15.17. This figure shows that, on taking into account all interactions between drops of 0.05 to 5.4 mm diameter, about 50% of the collisions result in breakup.

CHAPTER 16

GROWTH OF ICE PARTICLES BY ACCRETION AND ICE PARTICLE MELTING

In Chapter 13, we discussed the growth of snow crystals by vapor diffusion, and in Chapter 14, we described the manner with which snow crystals interact with other snow crystals and with drops. In this chapter, we shall look closer at the growth of ice particles by the accretion of supercooled drops, at the formation of snow flakes by the collision of snow crystals, and also consider the physics of melting of individual ice particles.

16.1 Growth of Ice Particles by Accretion of Supercooled Drops

16.1.1 Growth Mode and Structure of Rimed Ice Particles, Graupel, and Hailstones

Ice particles which grow by collisions with supercooled drops have a surface temperature which is higher than that of the air surrounding them, owing to the release of latent heat during the freezing process. This heating-up of the ice particle is counteracted and, at steady state, just balanced by the transfer of heat to the environmental air by conduction, and by evaporation if the air is water vapor subsaturated. As long as the latent heat of freezing is dissipated from the growing ice particle in such a way that its temperature remains below 0°C, all accreted cloud water must freeze on the ice particle. The particle is then considered to grow in the so-called *dry growth regime* (Ludlam, 1958). With increasing liquid water content of the cloud, increasing drop size, and increasing frequency of collision between drops and the ice particle, the temperature of the growing particle gradually rises. This rise in temperature generally comes to an end when the surface temperature of the ice particle approaches 0°C. Under such growth conditions, not all accreted water is converted to ice, the amount of ice formed being determined by the rate at which heat is dissipated from the particle. The ice particle is now considered to grow in the *wet growth regime* (Ludlam, 1958). The critical conditions for which all the accreted water freezes on the ice particle and acquires a temperature of 0°C in the solid phase, is known as the *Schumann-Ludlam Limit* (SLL); the SLL thus marks the boundary between the two growth regimes.

Schumann (1938) and Ludlam (1958) studied the thermodynamics of the wet growth regime under the assumptions that the growing ice particle would remain solid and shed all excess water acquired as a liquid film over its surface. However, the wind tunnel studies of List (1959, 1960a,b) and Macklin (1961) demonstrated that often little or no shedding occurs in the wet growth regime. Furthermore, the

assumption of impervious ice particles was found to be incorrect; rather, they were found to consist of a dense ice framework whose capillaries are filled with water and air bubbles, termed *spongy ice* by List (1965). Such spongy ice may either form directly if the heat exchange between the growing ice deposit and the surroundings is insufficient to freeze all accreted water (the latter being retained in a mesh of ice dendrites), or by intake of unfrozen water into porous ice (termed *soaking*) formed beforehand during growth of the ice particle in the dry growth regime.

Spongy ice has been subject to numerous investigations. The sponginess of some natural hailstones was measured by Gitlin *et al.* (1968) and Browning *et al.* (1968). Knight and Knight (1968a,b, 1973b) looked for evidence of sponginess in natural hailstones which had become completely frozen. The sponginess of laboratory grown icing accretions was examined by List (1959), Macklin (1961), Bailey and Macklin (1968a,b), Goyer *et al.* (1966), Roos and Pum (1974), and Ashworth and Knight (1978). Water shedding has been investigated by Carras and Macklin (1973), Joe *et al.* (1976) and List (1977). Lesins (1980), Lesins *et al.* (1980), Joe (1982), and Lesins and List (1986) determined shedding rates and shed drop size distributions from wind tunnel experiments with rotating ice cylinders and spheroidal hailstone models. They found that both shedding and sponginess depended critically on the icing conditions, on the rotation rate of the ice cylinder, and on the nutation precession rate of the ice spheroid (see Chapter 10).

Microphotographs of rimed ice cylinders (Macklin and Payne, 1968), and of rimed ice crystals and graupel freely floating in a wind tunnel (Pflaum *et al.*, 1978), show that at low temperatures of the ice deposit and for relatively small drop impact velocities and sizes, supercooled drops tend to freeze rapidly as individual ice spheres, forming loosely woven chains with densities as low as 0.1 to 0.3 g cm^{-3}. At higher deposit temperatures and for larger drop impact velocities and sizes, the drops become increasingly distorted on impact and tend to pack more closely.

The spreading of supercooled water drops impacting on ice surfaces has been studied by Brownscombe and Hallett (1967) and Macklin and Payne (1969). Macklin and Payne considered air temperatures between -11 and $-22°C$, surface temperatures of the ice deposit between -3 and $-20°C$, cloud drops of radii between 17 and 511 μm, and impact speeds between 5 and 30 m sec^{-1}. They found that the spreading factor, defined as the final maximum drop radius to the initial radius, varied between 1.3 and 6, depending primarily on impact speed and deposit temperature. Only at the lowest impact speeds and lowest deposit temperatures studied did the drops freeze as hemispheres or truncated spheres. With an increase in either of these parameters, the drops became increasingly flattened. They concluded that the final drop shape is a function of several compensating factors. Three of these are: (1) the kinetic energy which the drop possesses at impact and which acts to distort it, (2) the surface tension of the drop which acts to retain its spherical shape, and (3) the rate at which the drop freezes and thus terminates deformation.

The density ρ_R of rime deposits has been studied by Macklin (1962) and Macklin and Payne (1968). Their observations showed that ρ_R is related to the surface temperature T_s of the ice substrate, and to the radius a and impact velocity U_{imp} of the cloud drops. For deposit temperatures ranging between -5 and $-20°C$,

impact speeds between 2 and 12 m sec^{-1}, drop radii between 11 and 32 μm, and for cloud liquid water contents between 1 and 7 g m^{-3}, Macklin (1962) found the relation

$$\rho_R = A\left(-\frac{aU_{\rm imp}}{T_{\rm s}}\right)^B , \tag{16-1}$$

with $T_{\rm s}$ (°C), $U_{\rm imp}$ (m sec^{-1}), a (μm), and, ρ_R (g cm^{-3}). Macklin (1962) and Bain and Gayet (1983) found $A = 0.11$ and $B = 0.76$; other results include: Pflaum and Pruppacher (1979), $A = 0.26$, $B = 0.38$; Prodi *et al.* (1986), $A = 0.33$, $B = 0.6$; Prodi *et al.* (1991), $A = 0.23$, $B = 0.44$; and Levi *et al.* (1991), $A = 0.28$ and $B = 0.6$. Equation (16-1) predicts, for example, that $\rho_R = 0.19$ g cm^{-3} for $a = 20\,\mu$m, $U_{\rm imp} = 2$ m sec^{-1}, and $T_{\rm s} = -20$°C; similarly $\rho_R = 0.86$ g cm^{-3} for $a = 30\,\mu$m, $U_{\rm imp} = 5$ m sec^{-1}, and $T_{\rm s} = -10$°C. (For comparison, we may note that the density of a structure composed of regularly packed spheres of individual density 0.9 g cm^{-3} is 0.67 g cm^{-3}, while the corresponding figure for randomly packed spheres is 0.57 g cm^{-3}.) If such low density rime becomes soaked with water, its density obviously increases and assumes values between the bulk density of ice and that of water.

From a detailed study, Heymsfield and Pflaum (1985) suggested the following parameterization of the density of rime deposited at the surface of a graupel of radius a_g:

$$\begin{aligned} \rho_R(a_g, a) &= AY^{B_1}, \quad \text{for} \begin{cases} T_{\rm s} \le -5°\text{C} \\ T_{\rm s} > -5°\text{C}, \quad Y < 1.60 \end{cases} \\ \rho_R(a_g, a) &= \exp(B_2 + B_3 Y + B_4 Y^2 + B_5 Y^3), \quad \text{for } T_{\rm s} \ge -5°\text{C}, Y > 1.60, \end{aligned} \tag{16-2}$$

with $Y = -aU(a_g, a)/T_{\rm s}(a_g)$, and with $A = 0.30$ and $B_1 = 0.44$, $B_2 = -0.03115$, $B_3 = -1.7030$, $B_4 = 0.9116$, $B_5 = -0.1224$.

Rasmussen and Heymsfield (1985) argued that the impact velocity averaged over the entire rime deposit would be seriously overestimated if one would set $U_{\rm imp} = U_0$, where U_0 is the impact velocity at the stagnation point of the falling graupel. They instead suggested computing $U_{\rm imp}$ according to the following parameterization:

$$\frac{U_{\rm imp}}{U_{\infty,g}} = B_0 + B_1 X + B_2 X^2 + B_3 X^3 + B_4 X^4 , \tag{16-3}$$

where $X = \log N_s$, $N_s = 4N_{{\rm Re},g}\rho_{\rm w} a_{\rm d}^2/9\rho_{\rm a} d_g^2$ is the Stokes number (see (14-12)), $U_{\infty,g}$ is the terminal fall velocity of the riming graupel, $a_{\rm d}$ is the radius of the impacting drops, and d_g is the diameter of the riming graupel for an oblate spheroidal ice particle. For $N_{\rm Re} = 300$ and $0.1 \le N_s \le 10.0$, $B_0 = 0.356$, $B_1 = 0.4738$, $B_2 = -0.1233$, $B_3 = -0.1618$ and $B_4 = 0.08087$; for $N_s < 0.1$, $U_{\rm imp}/U_{\infty,g} = 0$; for $N_s > 10$, $U_{\rm imp}/U_\infty = 0.636$. For $N_{\rm Re} = 100$ and $0.1 \le N_s \le 10$, $B_0 = 0.372$, $B_1 = 0.4907$, $B_2 = -0.09452$, $B_3 = -0.1906$, $B_4 = 0.07105$; $N_s < 0.1$, $U_{\rm imp}/U_{\infty,g} = 0$; $N_s > 10$, $U_{\rm imp}/U_{\infty,g} = 0.61$. For $N_{\rm Re} = 30$ and $0.1 \le N_s \le 10$, $B_0 = 0.2927$, $B_1 = 0.5085$, $B_2 = -0.03453$, $B_3 = 0.2184$, $B_4 = 0.03595$; $N_s < 0.1$, $U_{\rm imp}/U_{\infty,g} = 0$; $N_s > 10$, $U_{\rm imp}/U_{\infty,g} = 0.59$. For $N_{\rm Re} = 10$ and $0.1 \le N_s \le 10$,

$B_0 = 0.1701$, $B_1 = 0.7246$, $B_2 = 0.2257$, $B_3 = -1.13$, $B_4 = 0.5756$; $N_s < 0.4$, $U_{\text{imp}}/U_\infty = 0$; $N_s > 10$, $U_{\text{imp}}/U_{\infty,g} = 0.57$.

In Section 2.2.2, we described in some detail the characteristic layer structure of rimed ice crystals, graupel, and hailstones, due to a varying concentration and size of trapped air bubbles. From their studies of hailstones produced in a wind tunnel, List and Agnew (1973) concluded that it is the cloud liquid water content which controls both the air bubble concentration and size. On the other hand, Carras and Macklin (1975) inferred from their experiments that a more fundamental determinant is the rate at which the collected water freezes. They found that in both the dry and wet growth regimes, the bubble concentration increases with increasing freezing rate which is governed in the dry growth regime by the temperature of the ice deposit and by the size and impact speed of the accreted droplets and, in wet growth regime, by the rate of heat transfer by forced convection away from the riming ice particle. This finding is understandable if we consider that for smaller freezing rates more dissolved air can escape by diffusion and more bubbles can migrate to the surface of the accreting ice particle. Therefore, small freezing rates lead to relatively clear ice, and large freezing rates to relatively opaque ice. Thus, Carras and Macklin typically found bubble concentrations of 10^5 to 10^6 cm^{-3} in the wet growth regime with small freezing rates, and 10^6 to 10^8 cm^{-3} in the dry growth regime with relatively large freezing rates.

In a similar way, the freezing rate controls the size of the bubble, by limiting its growth; thus, the smaller the freezing rate, the larger the bubble size. In the dry growth regime, this trend is counteracted somewhat in that, at increasingly warm deposit temperatures, given the relatively slow growth rate and the considerable spreading of the drops on the accreting ice surface, an increasingly larger amount of air is allowed to diffuse away and so to become unavailable for bubble growth. Typically, Carras and Macklin found bubble sizes of 10 to 50 μm radius in the wet growth regime and of 1 to 4 μm radius in the dry growth regime.

Thin sections of rimed ice crystals, graupel, and hailstones viewed in polarized light reveal alternating layers of large concentrations of small ice crystallites and of smaller concentrations of larger ice crystallites. Wind tunnel studies of Aufdermauer *et al.* (1963), Levi and Aufdermauer (1970), Levi *et al.* (1970a,b), Macklin and Rye (1974), and Rye and Macklin (1975) showed that in the dry growth regime the mean length of ice crystallites generally decreases from $\sim$ 8000 to $\sim$ 250 μm, and the mean width from $\sim$ 1000 to $\sim$ 200 μm, as the air temperature (i.e., the temperature of the accreted drops) decreases from -5 to -30°C. At air temperatures colder than -15°C, the crystallite size also depends on the temperature of the ice deposit such that, for each air temperature, a critical deposit temperature exists at which the crystallite size rather abruptly decreases to below 50 μm. More recently, Levi and Prodi (1978) and Prodi *et al.* (1982) found that, in the dry growth regime, the areal size σ of ice crystallites decreases exponentially for a given air temperature T_a with decreasing temperature T_d of the ice deposit. The areal size also decreases for a given T_d with decreasing air temperature T_a. Thus, for $T_a = -12$°C and $T_d = -2$°C, $\sigma = 1$ mm^2; for $T_a = -12$°C, and $T_d = -15$°C, $\sigma = 2 \times 10^{-3}$ mm^2; and for $T_a = -25$°C and $T_d = -2$°C, $\sigma = 0.1$ mm^2.

Levi and Lubart (1991), Levi and Prodi (1983), Levi *et al.* (1970a,b), and Levi

and Aufdermauer (1970) showed that ice crystallites exhibit preferred orientations with respect to their c-axis and the radial growth direction of the accreting ice particle. Thus, they found that, in the dry growth regime, the crystallographic c-axis of individual crystallites tends to be oriented normal to the growing ice surface, i.e., parallel to the radial growth direction of the hailstone, while in the wet growth regime, the c-axis tends to be parallel to the growing ice surface, i.e., normal to the radial growth direction of the accreting ice particle. In terms of the frequency distribution of orientation angles α (see Figure 16.1), a distinct maximum in the dry growth regime was thus found near $\alpha = 0°$ for air temperatures warmer than $-18°$C, shifting to $\sim 45°$C as the air temperature decreased below $-20°$C.

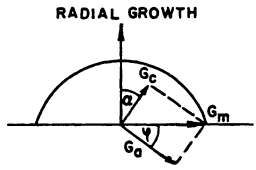


Fig. 16-1: Schematic relation between non-rational dendrite growth velocity G_m, its component growth velocity G_a along the basal plane, and its component growth velocity G_c perpendicular to the basal plane of ice. Also shown is the orientation angle α between the radial growth direction of ice and G_c, and the 'splitting angle' between G_m and G_a.

The orientation and size of the crystallites in the spongy or wet growth regime has been studied by Macklin and Rye (1974) and Prodi *et al.* (1982). For $25°\text{C} \leq T_\text{a} < -9°\text{C}$, most of the c-axes of the crystallites were oriented at angles α which ranged between 60 and 90°C. An analysis of the areal size σ of the crystallites in the wet growth regime showed that σ is considerably smaller than in the dry growth regime for the same T_a and T_d (which is about 0°C in the wet growth regime). Thus, for $T_\text{a} = -12°\text{C}$, $\sigma = 3 \times 10^{-2}$ mm^2 (as compared to 1 mm^2 in the dry growth regime), and for $T_\text{a} = -24°\text{C}$, $\sigma = 3 \times 10^{-2}$ mm^2 (as compared to 2×10^{-1} mm^2 in the dry growth regime). The maximum length of the crystallites at $T_\text{a} = -12°\text{C}$ was found to be 1 mm, and 2×10^{-1} mm at $T_\text{a} = -24°\text{C}$. The maximum width of the crystallite was 2.0 to 2.5×10^{-1} mm, independent of temperature.

It is obvious that information concerning the structural features of ice particles, such as discussed above, is very useful for purposes of interpreting the growth history of natural graupel and hailstones. Attempts to determine the growth history of fallen hailstones in this manner have been made by Knight and Knight (1968a,b), Levi *et al.* (1970a,b), Macklin *et al.* (1970), and by Macklin *et al.* (1976). Some physical concepts needed for a better understanding of the preferred orientation of ice crystallites in ice deposits of riming ice particles are provided at the end of the following section.

16.1.2 Structure and Growth Mode of Ice in Supercooled Water

The structure and growth mode of ice in supercooled water has been studied experimentally by Kumai and Itagaki (1953), Lindenmeyer (1959), Hallett (1960, 1964), Macklin and Ryan (1965, 1966), Knight (1966), and Pruppacher (1967a,b). Most

experiments were carried out with relatively large supercooled water bodies nucleated by single ice crystals which had a temperature close to 0°C. It was found that, at supercoolings less than 0.9°C, ice crystals, nucleated with their c-axis normal to the surface of the water, develop as thin, almost circular disks. On the other hand, crystals with their c-axis parallel to the water surface grow as long surface needles. Each of these consists of a dendritic portion which is co-planar with the seed crystal and grows into the water, and of a rib-like portion which grows along the water surface boundary. At supercoolings between about 0.9 and 2.5°C, ice crystals grow as plane stellar dendrites or dendritic sheets co-planar with the seed crystal, i.e., parallel to the seed crystal's basal plane. At supercoolings larger than about 2.5°C, ice crystals no longer grow co-planar with the seed crystal, but rather split into two symmetrical, hollow, hexagonal pyramidal segments joined together at their apices (Figure 16.2 and Plate 18). With increasing supercooling, the angle between these segments increases. According to Macklin and Ryan (1966), the angle φ between a primary growth segment and the basal plane of ice (which is one half of the angle between the two primary growth segments) increases from $\varphi \approx 4°$ at $\Delta T = 2°C$ to $\varphi \approx 20°C$ at $\Delta T = 7°C$. At supercoolings larger than about 5.5°C, secondary and higher order splitting takes place on the major growth planes, causing the formation of complex, three-dimensional structures favored by the presence of salts dissolved in water (Pruppacher, 1967b). Primary, secondary, and higher order splitting leads to non-rational growth, i.e., growth in directions which cannot be described by rational crystallographic indices (see Chapter 3). Lindenmeyer (1959), Hallett (1964), and Macklin and Ryan (1965, 1966) suggested that this non-rational growth of ice in supercooled water can be explained, as illustrated in Figure 16.3, on the basis of a step growth mechanism analogous to the explanation of the hopper structure of ice crystals grown from the vapor (see Section 5.7.3). Here two growth components, G_a, and G_c, are involved. The component G_a is the growth velocity of ice parallel to the crystallographic a-axis of ice (i.e., the growth velocity of the crystallographic prism plane of ice), while G_c is the growth velocity of ice parallel to the crystallographic c-axis of ice (i.e., the growth velocity of the basal plane of ice). Observations discussed in Section 16.1.3 show $G_a > G_c$ at all water supercoolings. Note from Figure 16.3 that the angle of splitting is determined by the ratio of the height of the growth step to the distance between the steps, i.e., by the ratio of the growth velocities parallel and perpendicular to the c-axis. Since observations show that G_c increases more rapidly with supercooling than G_a, the angle φ between a primary growth segment and the basal plane must increase with increasing supercooling as has been observed. Another implication of such a mechanism is that one would expect the non-rational ice structures to be single crystals. This expectation was confirmed by Lindenmeyer (1959), who used X-rays to analyze ice structures grown in water, and by Macklin and Ryan (1965, 1966) who noted that all the secondary growth features are aligned parallel to the primary growth features.

Additional support for this conclusion was given by Hallett (1963, 1964), who found that when millimeter size water drops were frozen by contact with an ice single crystal of a temperature near 0°C, they developed into single crystals with the crystal orientation of the substrate, irrespective of the temperature of the drop.

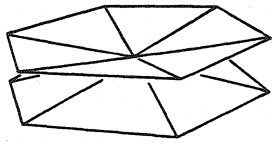


Fig. 16-2: Schematic representation of ice structures formed in water supercooled by about 5° C. (From Macklin and Ryan, 1965; by courtesy of Am. Meteor. Soc., and the authors.)

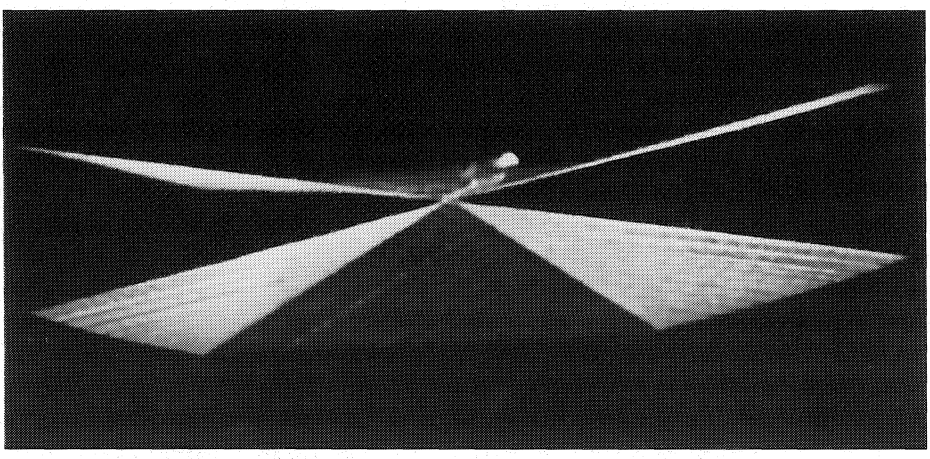


Plate 18. Ice structure formed in supercooled water at −5.2° C. (From Macklin & Ryan, 1965; by courtesy of the *Am. Meteor. Soc.*, and the authors.)

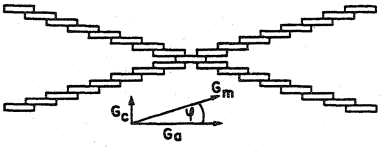


Fig. 16-3: Schematic representation of the stepped growth mechanism considered to be responsible for explaining the ice structures formed in supercooled water. (From Macklin and Ryan, 1965, with changes.)

This occurred also when the temperatures of both the drop and ice surface were warmer than $-5°C$ (Figure 16.4). If the temperatures of the drop and the surface were below $-5°C$, the drop froze into polycrystalline ice, the polycrystallinity apparently being due to the existence of more than one point of nucleation. Additional studies of the conditions required for drops to freeze polycrystalline when brought into contact with an ice single crystal were carried out by Magono and Aburukawa (1968), Aufdermauer and Mayes (1965), Brownscombe and Hallett (1967), Rye and Macklin (1975), Takahashi (1979), Mizuno and Wakashima (1983), Levi *et al.* (1980) and Nasello *et al.* (1980). The results of these studies all agree well with line (2) of Figure 16.4 if drop freezing occurs on the basal face of ice. For freezing on a prism face, the transition to polycrystallinity was found to take place at temperatures several degrees below the critical temperature for freezing on the basal face. The critical conditions for polycrystallinity of water drops freely falling in air was studied by Parungo and Weickmann (1973) and by Pitter and Pruppacher (1973). In contrast to nucleation of drops on an ice surface, the freezing mode of a drop of given size surrounded by air is not determined by a unique temperature, but varies depending on the nuclei which initiated the ice phase. Thus, Pitter and Pruppacher (1973) used distilled and deionized water to obtain curve (1) in Figure 16.4, while Parungo and Weickmann (1973) used AgI particles to nucleate the drops giving curve (3), and singly distilled water to produce curve (4). However, all investigators found that whether or not a drop became a polycrystalline ice particle depended critically on the size and supercooling of the drop before freezing and on the thermal conductivity of the medium into which the latent heat of freezing dissipated (see Figure 16.4). The critical drop radius a_c was found to be related to the drop's supercooling by a relation of the form

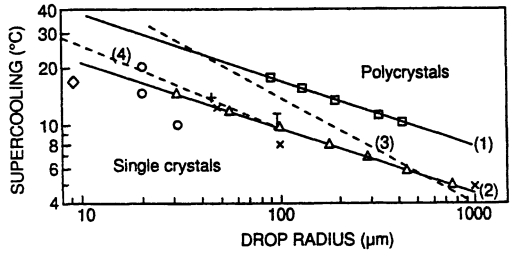


Fig. 16-4: Variation with supercooling of the polycrystallinity of drops frozen under various conditions during laboratory experiments. □ and (1) drops of distilled, deionized water in air, line fitted to Equation (16-4) for $k = k_{air}$, from of Pitter & Pruppacher, 1973); (3) drops of singly distilled water in air (Parungo & Weickmann, 1973); (4) water drops in air nucleated by AgI (Parungo & Weickmann, 1973); (△) and (2) pure water drops frozen on the surface of an ice single crystal, line fitted to Equation (16-4) for $k = k_{ice}$, from Pitter & Pruppacher (1973); × Hallett (1963b, 1964), Brownscombe & Hallett (1967); I Rye & Macklin (1975); ○ Magono & Aburukawa (1968); + Aufdermauer & Mayes (1965).

$$a_c = \left(\frac{\beta}{\Delta T}\right)^C, \quad \text{with} \quad \beta = Ak_m^B, \tag{16-4}$$

where for curves (1) and (2) $A = 23$, $B = -1/8$, and $C = 3$, k_m (cal $\text{cm}^{-1}\text{sec}^{-1}\,^\circ\text{C}^{-1}$) is the heat conductivity of the medium in contact with the drop, and a_c is in μm. If we now recall Figure 2.33, which shows that most atmospheric clouds have glaciated before they have cooled to $-20°$C, and Figures 2.8a,b,c, which show that most cloud drops are found in the size range less than 60 μm, we conclude from Figure 16.4, curves 1 and 3, that most cloud drops freeze as single crystals. Each of these can then grow by vapor diffusion into a hexagonal shaped ice single crystal after sufficient time for growth. Hexagonal ice crystals in atmospheric clouds may therefore be the result either of nucleation in the depositon mode or in the freezing mode.

Experiments show that the polycrystallinity of ice grown in supercooled water is a result of c-axis reorientation during the epitaxial overgrowth of ice on ice in an environment of supercooled water. According to Hallett (1964) and Rye and Macklin (1975), a most common reorientation is one in which the c-axis of the nucleated ice makes an angle of 90° with the c-axis of the substrate ice. Other common reorientations of small misfits to the basal plane of ice have been determined by Higuchi and Yoshida (1967), Magono and Suzuki (1967), Aburakawa and Magono (1972) and Lee (1972).

Following Levi (1970), Levi and Aufdermauer (1970), Rye and Macklin (1973), and Macklin and Rye (1974), we finally may suggest some reasons for the preferred orientation of ice crystallites in ice deposits grown by riming. We recall that the c-axis of these crystallites is preferentially oriented at an angle α of 0° and 90° to the radial growth direction of the riming ice deposit in the dry growth and wet growth regimes, respectively. This can be understood if we consider that, in the dry growth regime in which the cloud drops collide with a relatively cold substrate, the latent heat of freezing is preferentially lost to the substrate. Since heat is more efficiently conducted along the crystallographic c-axis of ice than along other directions (Hobbs, 1974; the effect arises from the greater lineal density of molecules along the c-axis, making this the preferred direction for the propagation of thermal fluctuations; see Section 5.7.1 and Figure 3.3), growth of those ice dendrites which nucleate by chance with their a-axis parallel to the surface of the accreting ice deposit, is facilitated as compared to dendrites which nucleate in other orientations. Thus, in this growth regime, ice crystallites assume preferentially an orientation in which the c-axis of the ice crystallites is oriented perpendicular to the accreting ice surface, i.e., parallel to the radial growth direction of the surface. On the other hand, in the wet growth regime, the ice substrate is relatively warm and latent heat of freezing is dissipated mainly by conduction and convection into the surrounding air. Consequently, the growth of those ice dendrites which nucleate by chance with their a-axes perpendicular to the accreting ice surface is facilitated as compared to growth of ice dendrites nucleated in other directions. Thus, in this growth regime, the ice crystallites preferentially assumed an orientation in which their c-axis is oriented parallel to the acccreting ice surface, i.e., perpendicular to the radial growth direction of the surface.

TABLE 16.1

Experimentally derived laws for the variation of the growth rate G of ice in water supercooled by ΔT_∞ degrees. G_m is the non-rational dendrite growth velocity, G_c is the component growth velocity perpendicular to the basal plane of ice, G_a is the component growth velocity along the basal plane of ice.

Lindenmeyer (1959)	$G_m = 0.023\ (\Delta T_\infty)^{2.39}$	$2 \leq \Delta T_\infty \leq 6.5°\text{C}$
Hallett (1964), max. values	$G_m = 0.08\ (\Delta T_\infty)^{1.9}$	$1 \leq \Delta T_\infty \leq 10°\text{C}$
Pruppacher (1967d)	$G_m = 0.035\ (\Delta T_\infty)^{2.22}$	$0.5 \leq \Delta T_\infty \leq 9°\text{C}$
Macklin and Ryan (1968)	$G_a = 0.015\ (\Delta T_\infty)^{2.49}$	$2 \leq \Delta T_\infty \leq 10°\text{C}$
	$G_c = 9 \times 10^{-4}\ (\Delta T_\infty)^{3.35}$	$2 \leq \Delta T_\infty \leq 10°\text{C}$
Gokhale and Lewinter (1971)	$G_m = 0.044\ (\Delta T_\infty)^{2.3}$	$5 \leq \Delta T_\infty \leq 10°\text{C}$

The temperature dependence of the angular orientation of the ice crystallites is a result of the non-rational growth of ice dendrites in supercooled water, as illustrated in Figure 16.1. Thus, since the non-rational growth angle φ increases with increasing supercooling (see Section 16.1), while in the dry growth regime G_m tends to be oriented parallel to the growing ice surface, the orientation angle α also will increase with increasing supercooling. An analogous argument holds for the wet growth regime in which G_m tends to be oriented perpendicular to the growing ice surface.

16.1.3 Growth Rate of Ice in Supercooled Water

Most studies of the growth rate of ice crystals in supercooled water have dealt with ice growth in narrow tubes and capillaries (for a review of some of the earlier work, see Pruppacher, 1967c). It is obvious that such measurements have very limited application to the growth rate of ice in supercooled water drops, since these are not affected by the proximity of heat conducting walls. The so-called free growth rate G_m of ice crystals in supercooled bulk water and in supercooled drops has been studied by Lindenmeyer (1959), Hallett (1964), Pruppacher (1967d), Macklin and Ryan (1968), Ryan and Macklin (1968), Ryan (1969), and Gokhale and Lewinter (1971). Their results are summarized in Table 16.1 and Figure 16.5. Note from this figure and table that the growth rate G_m of ice in supercooled water varies nearly as the square of the bath supercooling $T_\infty = T_0 - T_\infty$ for $0 \leq \Delta T_\infty \lesssim 10°\text{C}$, where $T_0 = 273°\text{K}$ (0°C) and where T_∞ is the temperature far away from the growing ice crystal surface. Note also that the component growth rate of ice parallel to its crystallographic a-axis, $G_a = G_m \cos\varphi$ (see Figure 16.3), shows a similar dependence on supercooling because of the smallness of angle φ. On the other hand, the component growth rate of ice parallel to the crystallographic c-axis, $G_c = G_m \sin\varphi$, is considerably smaller than G_a and varies approximately as the third power of ΔT_∞. At $9 \lesssim \Delta T_\infty \lesssim 12°\text{C}$, a discontinuity in G is observed which is characterized by little change in growth rate with decrease in ΔT_∞. From Figure 16.5, this discontinuity is evidently a manifestation of a transition from a higher to a lower power growth law as, at $\Delta T_\infty > 12°\text{C}$, the growth rate appears to vary nearly linearly with ΔT_∞.

The effect of water soluble salts on the growth rate of ice has been studied by

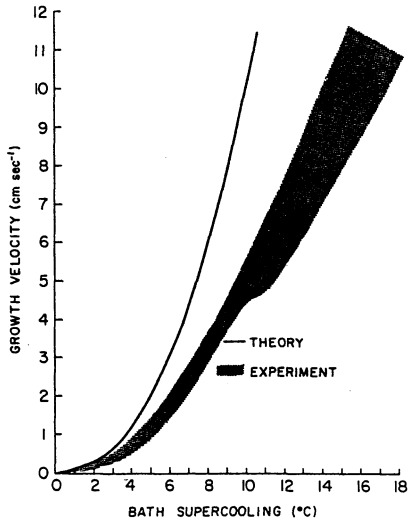


Fig. 16-5: Variation of the free growth velocity of ice in supercooled water. Theory is due to Bolling and Tiller (1961) for $\Delta T_s = 0$. Experimental results are due to Lindenmeyer (1959), Hallett (1964), Pruppacher (1967a,d), and Macklin and Ryan (1968). (From Pruppacher, 1967e, with changes.)

Pruppacher (1967d), Ryan and Macklin (1968), Macklin and Ryan (1968), and Ryan (1969). These studies show that the growth rate of ice in supercooled aqueous solutions remains unaffected until the salt concentration becomes greater than about 10^{-2} mole l^{-1}. At larger concentrations, the growth rate is progressively retarded by the salt. Fluorides, however, behave exceptionally in that they invariably enhance the growth rate at concentrations between 10^{-3} and 10^{-2} mole l^{-1}. Such growth rate enhancement was also noted by Michaels *et al.* (1966) and Pruppacher (1967c). The effects of dissolved salts on the growth rate of ice were attributed by the above authors: (1) to a change of the thermal conductivity of water by the presence of salt ions, thus affecting the rate at which latent heat is dissipated by conduction from the ice water interface; (2) to a concentration buildup of salt rejected at the ice-water interface, thus lowering the local equilibrium freezing temperature; (3) to adsorption of salt ions at growth steps on the ice surface, thus inhibiting the incorporation of water molecules at these locations; (4) to a change of the mobility and therefore also the diffusivity of water molecules through water by the presence of salt ions, thus affecting the rate at which water molecules can reach the ice-water interface and the rate at which the salt ions can diffuse away from the surface into the solution under the effect of the concentration gradient at the ice-water interface; (5) to a formation of additional dislocations in the growing ice crystal lattice by ions incorporated into the ice lattice, thus causing additional strain and stresses in the lattice; and (6) to the development of relatively large, local electric fields at the ice-water interface due to differential incorporation of ions into the ice crystal lattice (see Section 5.10), thus affecting the local structure

of water.

It is obvious that mechanisms (2) and (3) will impede the rate of ice crystal propagation, since the experiments of Eigen (1952) and Kauptinskii and Razanin (1955) show that most salts decrease the heat conductivity of water, and since the experiments of Wang and Miller (1952), Wang (1954), and McCall and Douglas (1965) show that most salts reduce the self-diffusion coefficient of water, increasingly so with increasing salt concentration. Little is known about the effects of mechanisms (5) and (6). However, from our discussions of the effect of surface dislocations on ice nucleation (see Section 9.2.3.5), and on the growth rate of ice from the vapor (see Section 13.3), one would expect that an increase in the number density of dislocations and, consequently, an increase in the number density of surface steps on a growing ice crystal would facilitate the incorporation of water molecules into the ice crystal lattice. Also, Ryan (1969) has argued that the electric fields which tend to build up at the ice-aqueous solution interface would also facilitate the incorporation of water molecules into the ice crystal lattice. Thus, while mechanisms (1) to (4) appear to explain the generally observed growth rate retardation of ice crystals in salt solutions, mechanisms (5) and (6) may conceivably be responsible for the growth rate enhancement of ice crystals in the aqueous solutions of fluoride salts.

In order to interpret the experimentally found variation of the growth rate of ice in supercooled water as a function of supercooling, we shall consider first the simple case of a planar ice face propagating into supercooled water. We shall assume that the face contains no steps due to emerging dislocations, but nevertheless is molecularly rough. The latter assumption implies that any site at the surface is a potential site for attachment of water molecules. Such a case has been studied by Wilson (1900) and Frenkel (1932) through use of the simple theory of reaction rates. If μ_i is the chemical potential of ice and $\mu_{w,\ell}$, is that of water one mean molecular jump distance ℓ away from the ice-water interface, the thermodynamic driving force responsible for the advance of the crystal face is $(\mu_{w,\ell} - \mu_i)/\ell$. The rate of advance of the ice crystal face is then given by the product of this driving force and the mobility $D_w/\mathscr{R}T_s$ of the water molecules, where T_s is the temperature of the ice-water interface (Glasstone *et al.*, 1941). Thus,

$$G = \frac{D_w}{\mathscr{R}T_s}\frac{(\mu_{w,\ell} - \mu_i)}{\ell}, \tag{16-5}$$

where D_w is the diffusivity of water molecules in water, given in Chapter 3. Since $(\partial F/\partial T)_p = -S$, where S is the entropy and F the Helmholtz free energy of the system $\Delta F_{vol} = -\int_0^{\Delta T_s} S_{vol} d(\Delta T) \approx \overline{-\Delta S_{vol}} T_s$, where $\Delta T_s = T_0 - T_s$. From (7-18) we have, on the other hand, $\Delta F_{vol} = n_i(\mu_i - \mu_{w,\ell})$. We therefore find that

$$\mu_{w,\ell} - \mu_i = \frac{\overline{\Delta S_{vol}}\Delta T}{n_i} = \overline{\Delta S_{vol}}\Delta T = \frac{\overline{\mathscr{L}_m}}{\bar{T}}\Delta T_s, \tag{16-6}$$

where $\overline{\mathscr{L}_m}$ is the molar latent heat of fusion taken at the mean temperature $\bar{T} \approx (T_s + T_0)/2$. On combining (16-5) with (16-6), we find that the rate of advance of

the molecularly rough ice crystal face is given by

$$G = \frac{D_w \mathscr{L}_m}{\ell \mathscr{R} T_s \bar{T}} \Delta T_s \approx \frac{D_w \overline{\mathscr{L}_m}}{a_0 \mathscr{R} T_0^2} \Delta T_s \,, \tag{16-7}$$

where we have now assumed ℓ to be of the order of the molecular spacing a_0 in ice, and $T_s \bar{T} \approx T_0^2$. Note that this model predicts a growth rate which is linear in ΔT_s. Crystals exhibiting such a growth law are said to grow in the 'continuous growth regime', as their faces advance continuously without involving a lateral spreading of surface steps.

Frank (1949) and Burton *et al.* (1951) pointed out that many crystal surfaces are not perfect on a microscopic scale (i.e., molecularly rough), but contain steps due to emerging lattice dislocations. By assuming an abrupt step which advances laterally by addition of single molecules from the liquid through a diffusion jump mechanism, Hillig and Turnbull (1956) derived an expression for the growth rate of such a crystal in its supercooled melt. The starting point for their development is a modified form of the simple Wilson-Frenkel growth law. Instead of assuming that every site on the ice surface is available for molecular attachment, they assumed that only sites on the growth spirals of emerging screw dislocations can be used for molecular attachment. An approximate equation for such a growth spiral, considered nearly Archimedean, was given by Burton *et al.* (1951). Applied to a growth spiral on an ice surface in supercooled water, the equation can be expressed as

$$r = 2\theta a_g \,, \tag{16-8}$$

where r and θ are polar coordinates describing the spiral and a_g is the radius of a two-dimensional ice germ on an ice surface in supercooled water at temperature T_s. To determine an expression for a_g , we rewrite (9-10) for the energy of i-mer formation of a cylindrical ice embryo of molecular height a_0 on an ice substrate, including a contribution from line tension, interpreted here as the step energy per unit length, as

$$\Delta F_{i,s} = \pi a_i^2 a_0 \Delta f_{vol} + \sigma_{i,i} \Omega_{i,i} + 2\pi\lambda a_i \,. \tag{16-9}$$

From (7-18) and (7-19), $\Delta f_{vol} = -(\mu_w - \mu_i)/v_i$, where v_i is the mole volume of ice. Considering that the ice embryo forms on an ice substrate, the second term on the right side of (16-9) is zero. Instead of (9-15), we then obtain for a_g (by setting $\partial(\Delta F_{i,s})/\partial a_i = 0$):

$$a_g = -\frac{\lambda}{a_0 \Delta f_{vol}} = -\frac{\lambda v_i}{a_0(\mu_w - \mu_i)} \,, \tag{16-10}$$

where λ is the step energy per unit length. With (16-10), one finds from (16-8) and (16-6) that

$$r = 2\theta \frac{\lambda v_i \bar{T}}{a_0 \overline{\mathscr{L}_m} \Delta T_s} \approx 2\theta \frac{\lambda v_i T_0}{a_0 \overline{\mathscr{L}_m} \Delta T_s} \,. \tag{16-11}$$

The change in r as θ advances by one revolution, i.e., by 2π, is thus

$$\Delta r = \frac{4\pi\lambda v_i T_0}{a_0 \overline{\mathscr{L}_m} \Delta T_s} \,. \tag{16-12}$$

The fraction $\alpha a_0/\Delta r$ of surface sites available for molecular attachment is therefore

$$\alpha = \frac{a_0^2 \overline{\mathscr{L}_m} \Delta T_s}{4\pi\lambda v_i T_0}, \tag{16-13}$$

if attachment of molecules to the step occurs only within a distance a_0 of the step. The growth rate of a surface advancing by lateral spreading of steps is therefore

$$G = \frac{3\alpha D_w \overline{\mathscr{L}_m} \Delta T_s}{a_0 \mathscr{R} T_0^2} = \frac{3 D_w \overline{\mathscr{L}_m}^2 a_0}{4\pi\lambda v_i \mathscr{R} T_0^3} (\Delta T_s)^2, \tag{16-14}$$

in place of (16-7), assuming that three molecules are available for attachment at a given step site. (Note that this number is somewhat smaller than the number of nearest-neighbors (namely 4.4) to a given water molecule in bulk water (see Section 3.4.1). Assuming further that λ may be estimated from $\lambda = a_0\sigma_{i/w}$ (e.g., Cahn *et al.*, 1964), Hillig and Turnbull (1956) found

$$G = \frac{3 D_w \overline{\mathscr{L}_m}^2}{4\pi\sigma_{i/w} v_i \mathscr{R} T_0^3} (\Delta T_s)^2 . \tag{16-15}$$

Note that (16-15) predicts a parabolic growth law ('classical growth regime').

In deriving (16-15), Hillig and Turnbull assumed that the ice-water interface is sharp, i.e., that ordering of the water molecules at the growth front occurs within a distance $\ell \approx a_0$ of a step by a monomolecular transport process characterized by a diffusion constant D_w, with three molecules available for attachment at a given step. Cahn (1960) and Cahn *et al.* (1964) criticized this assumption by pointing out that the interface is not sharp but diffuse, the transition from the liquid to the solid phase occurring over several molecular layers. To correct for this feature, they introduced a parameter g which is a measure of the diffuseness of the interface, and which depends on the number n of molecular layers comprising the transition zone. From a theoretical study of surface energy, they found $g \approx (\pi^4/8)n^3 \exp(-\pi^2 n/2)$. For a sharp interface $g \approx 1$; g decreases rapidly toward zero with increasing interface diffuseness ($g \approx 0.01$ for $n = 2$). Instead of the traditionally assumed estimate for the step energy per unit length, namely that $\lambda = a_0\sigma_{i/w}$, Cahn *et al.* argued that $\lambda = a_0\sigma_{i/w} g^{1/2}$. They also conjectured that the number of molecules in position to jump into a growth site is given by $2 + g^{-1/2}$, which reduces to 3 (the value assumed by Hillig and Turnbull), when g approaches 1. For $g \approx 0.01$, the number of molecules in position to jump into a growth site is ~ 10. In addition, Cahn *et al.* proposed that an accommodation coefficient β should be introduced as a measure for the difficulty molecules have in moving to a step and in assuming an orientation suitable for incorporation into the ice lattice. With these corrections introduced into (16-14), Cahn *et al.* estimated the rate at which a crystal grows by a screw dislocation mechanism to be

$$G = \frac{\beta(1 + 2g^{1/2})}{4\pi g} \frac{D_w \overline{\mathscr{L}_m}^2}{\sigma_{i/w} v_i \mathscr{R} T_0^3} (\Delta T_s)^2 , \tag{16-16}$$

and that the corresponding rate at which a crystal grows in the continuous growth regime is

$$G = \frac{\beta D_w \overline{\mathscr{L}_m}}{a_0 \mathscr{R} T_0^2} \Delta T_s . \tag{16-17}$$

Obviously, the growth rate of ice in supercooled water is not exclusively controlled by kinetic processes at the ice-water interface, as was assumed above, but by heat transport processes as well. Two distinct points of view commonly exist regarding the relative effect of these two mechanisms which influence crystal growth. The first point of view assumes that the growth rate is an interface-controlled, material-transport process determined mainly by the molecular mobility at the interface and by the temperature, crystallographic perfection, and crystallographic orientation of the interface. The second point of view assumes that there is no effective transport barrier at the interface between the crystal and its melt, and that the growth rate of the crystal is therefore predominantly controlled by the rate at which latent heat of solidification is removed from the growing interface.

In actuality, of course, these two points of view are only limiting cases since the temperature T_s of the interface is not exactly the bath temperature T_∞, or the heat of solidification could obviously not be extracted; nor is it exactly the equilibrium temperature T_0 or T_e (the latter being the equilibrium temperature of a curved ice-water interface), or there would be no driving force for freezing. Rather, in steady state growth T_s adjusts itself such that the rate of liberation of heat corresponding to the rate of molecular incorporation just balances the rate of heat dissipation from the interface. Thus, the supercooling $T_e - T_s$ of the curved ice interface controls the rate of deposition of water molecules, while the supercooling $T_s - T_\infty$ controls the rate of heat dissipation from the ice-water interface (note that $T_\infty < T_s < T_e < T_0 = 273°\text{K} = 0°\text{C}$). Experiments show that $T_e - T_\infty$ for ice growing in supercooling water is only a small fraction of $T_s - T_\infty$. This implies that the growth rate of ice in supercooled water is heat dissipation limited (as is the growth rate of ice in supersaturated vapor (Section 13.3)). This result was confirmed by Lindenmeyer *et al.* (1957), who found that the larger the heat conductivity of the walls encasing a sample of supercooled water, the larger the growth rate of ice in the water sample.

The rate of heat dissipation from an ice dendrite tip growing in supercooled water has been studied theoretically by Bolling and Tiller (1961), Horvay and Cahn (1961), and Holzman (1970), all of whom idealized the growing dendrite tip by an isothermal prolate spheroid and assumed $\Delta T_s = 0$. Values for the growth rate determined by Bolling and Tiller are plotted in Figure 16.5. The plotted curve fits the equation $G = 0.049 \Delta T_\infty^{2.3}$ (for $\Delta T_s = 0$). On the other hand, Horvay and Cahn found $G = (\Delta T_\infty)^{1.3}/r$, where r is the curvature of the dendrite tip. According to Fisher and Hillig (1959), and Bolling and Tiller (1961), however, r is proportional to $(\Delta T_\infty)^{-1}$. Therefore, the result of Horvay and Cahn implies $G \propto (\Delta T_\infty)^{2.3}$, in good agreement with the result derived by Bolling and Tiller.

On comparing the observed values of G in Figure 16.5 with those computed for the case that $\Delta T_s = 0$, we notice that G is not completely thermally determined; i.e., for each value of G some value ΔT_s must be added to bring the theoretical pre-

diction into agreement with experiment. Such comparison yields $G = G(\Delta T_s)$, i.e., the growth rate of ice is a function of interface supercooling. From the maximum observed values for G , one finds approximately for $1 \lesssim T_\infty 10°C$ that $G \approx 1.0(\Delta T_s)^2$, while for $\Delta T_\infty > 10°C$, $G \approx 2.3\Delta T_s$. From a comparison of the experimentally observed growth laws with (16-16) and (16-17), one finds that with $\delta = 3 \times 10^{-8}$ cm, we have $\beta \approx 1$ and $g \approx 4 \times 10^{-3}$, which implies a diffuseness of about 3 molecular layers (Cahn *et al.*, 1964). Comparison of the experimental growth laws with (16-16) and (16-17) further suggests that growth of ice in supercooled water proceeds via the lateral spreading of steps at $1 \leq T_\infty \lesssim 10°C$, and via the continuous growth mechanism at $\Delta T_\infty > 10°C$, i.e., when $G > 5$ cm sec^{-1} (Pruppacher, 1967e; Macklin and Ryan, 1969). There is no obvious reason for the observed large scatter of data for $\Delta T_\infty > 10°C$.

In addition to the classical and continuous growth regimes, Cahn (1960) and Cahn *et al.* (1964) considered the existence of a transitional growth regime in which growth continues to proceed by lateral spreading of steps but which also progressively deviates from the simple parabolic growth law which characterizes the classical regime. Through theoretical arguments involving the free energy per unit volume ΔF_{vol} which acts as the driving force for crystal growth in a melt, they found that for the transitional regime $\sigma g/a_0 \lesssim -\Delta F_{vol} \lesssim \pi\sigma g/a_0$ where σ is the interface energy between the crystal and its melt. Thus, $\Delta F_{vol} < \sigma g/a_0$ characterizes the classical regime, while $-\Delta F_{vol} > \pi\sigma g/a_0$ characterizes the continuous growth regime. If we recall from Section 7.11.3 that ΔF_{vol} is proportional to the supercooling of the melt, we see that $\pi\Delta T_s^*$ will mark the supercooling onset of the continuous growth regime if ΔT_s^* marks the supercooling limit of the classical regime. From their experimental growth studies on ice, Pruppacher (1967e) and Macklin and Ryan (1969) suggested that $\pi\Delta T_\infty^* \approx 9$ to 10°C, from which it follows from Bolling and Tiller's theory (Figure 16.5) that $\pi\Delta T_s^* \approx 2°C$ and therefore $T \approx 0.6°C$, giving $\Delta T_\infty^* \approx 2.7°C$. This latter supercooling has some physical significance in that it closely agrees with the supercooling required for the onset of non-rational growth of ice in supercooled water, discussed in Section 16.1.2.

16.1.4 Freezing Time of Water Drops

Observations show that following the collision of an ice particle with a supercooled drop, solidification of the supercooled water proceeds in two major stages. The first stage, controlled by the intrinsic rate of ice propagation in water, is completed within a relatively short time span. During this stage, only a very small portion of the liberated latent heat of freezing is transferred to the drop environment, most of the heat being absorbed instead by the water of the liquid portion of the drop, and warming the latter quickly towards 0°C. In fact, one may readily show that for a drop supercooling of ΔT , only a fraction of about $\Delta T/80$ of the drop becomes converted to ice in stage one. Thus, if m_i and m_w, respectively, denote the masses of ice and water in the drop at the end of stage one, the heat balance for the drop is, assuming no heat loss to the environment,

$$m_i L_m = (m_w c_w + m_i c_i)\Delta T\,, \tag{16-18}$$

where c_w and c_i are the specific heats of water and ice, and L_m is the latent heat of melting. First, we may note that for no realizable supercooling will the drop freeze entirely during this adiabatic stage; in fact, we see from (16-18) with $m_w = 0$ that the supercooling ΔT which would be required for this to occur is $\Delta T = L_m/c_i \approx 160°C$, with $L_m \approx 80$ cal g^{-1} and $c_i \approx 0.5$ cal g^{-1}°C^{-1}. Hence, we have $m_i c_i \ll m_w c_w$, and so from (16-2),

$$\frac{m_i}{m_w} \approx \frac{c_w \Delta T}{L_m} \approx \frac{\Delta T}{80} . \tag{16-19}$$

The initial stage of freezing is followed by a second stage during which the remainder of the water is frozen. The freezing rate during this stage is one to several orders of magnitude smaller than during the first stage and is controlled partly by the rate at which heat is conducted into the underlying ice surface, and partly by the rate at which heat is dissipated by forced convection into the environment. Although it is clear that the two freezing stages overlap, the total time it takes to freeze a drop may be regarded approximately as the sum of the initial freezing time t_1 and the subsequent freezing time t_2.

Macklin and Payne (1967, 1968) estimated t_1 and t_2 by assuming that the ice substrate surrounded by air is a sphere of radius a and has an initial temperature T_d. In their model, every impinging drop is assumed to spread uniformly over the ice substrate into a thin layer of water of thickness δa. The latent heat of freezing is considered to flow in a radial direction only. A crude estimate of the initial freezing time t_1, can then be made from

$$t_1 \approx \delta a / G , \tag{16-20}$$

where G is the growth rate of ice dendrites in supercooled water. (Note we have not used even a fraction (m_i/m_w) of the total thickness δa in this estimate; this is because the layer δa does not become solid ice in time t_1 but only a mixture of ice crystals and water.) Using observed values for G for growth parallel to the basal plane of ice, and assuming that growth proceeds perpendicular to the water layer, Macklin and Payne determined that for $T = -20°C$, $t_1 \approx 1 \times 10^{-6}$, 1×10^{-5}, 7.5×10^{-5}, 2×10^{-4} sec, for $\delta a = 0.2$, 2, 15, 40 μm, respectively.

To determine t_2 Macklin and Payne (1967, 1968) considered first the heat flow into the spherical ice substrate of radius a. Assuming that during t_1, the initial temperature T_d of the ice substrate is raised instantaneously to $T_0 = 273$ K (0°C), and using expressions derived by Carslaw and Jaeger (1959), Macklin and Payne found the amount of heat conducted into the sphere ($T_d < T_0$) as a function of time to be given by

$$q(t) \approx \frac{4\pi}{3} a^3 \rho_i c_i \left[\frac{6(T_0 - T_d)(\kappa_i t)^{1/2}}{a\pi^{1/2}} - \frac{3(T_0 - T_d)\kappa_i t}{a^2} \right] , \tag{16-21}$$

where κ_i is the thermal diffusivity of ice, which was assumed constant in order to obtain (16-21). (For the purpose of the calculation, this is a valid assumption, though it should be noted that $\kappa_i = k_i/\rho_i c_i$ actually depends on temperature

through the temperature dependence of ρ_i and c_i (recall Chapter 3), and also of the thermal conductivity k_i, which for the range $-50 \leq T \leq 0°C$ obeys the empirical relation

$$k_i = (537.4 - 1.48T + 0.028T^2) \times 10^{-5}\,, \tag{16-22}$$

with k_i in cal $cm^{-1}sec^{-1}{}^{\circ}C^{-1}$. This expression for k_i fits the experimental data of Ratcliff (1962) to an accuracy of $\pm 0.5 \times 10^{-5}$ cal $cm^{-1}sec^{-1}{}^{\circ}C^{-1}$.) The amount of heat $\hat{q}_{in}$ conducted per unit area into the sphere during the freezing time t_2 is then

$$\hat{q}_{in} = \rho_i c_i (T_0 - T_d)\left[2\left(\frac{\kappa_i t_2}{\pi}\right)^{1/2} - \frac{\kappa_i t_2}{a}\right]. \tag{16-23}$$

Secondly, Macklin and Payne considered the amount of heat transferred by forced convection and evaporation to the environmental air. For a smooth spherical ice substrate of surface temperature T_0, the average amount of heat $\hat{q}_{out}$ transferred per unit area during time t_2 by these two mechanisms is (from (13-67))

$$\hat{q}_{out} = t_2[k_a(T_0 - T_\infty)\bar{f}_h + L_e D_v(\rho_{v,a} - \rho_{v,\infty})\bar{f}_v]/a\,, \tag{16-24}$$

where $\bar{f}_h$ and $\bar{f}_v$ are the mean ventilation coefficients for heat and vapor transport in air, D_v is the diffusivity of water vapor in air, k_a is the heat conductivity of air, T_∞, $\rho_{v,\infty}$ are the temperature and water vapor density in air far away from the ice sphere, and $T_a (= T_0)$, $\rho_{v,a}$ are the temperature and water vapor density of air at the surface of the water layer. Considering that the amount of heat to be removed per unit area is $\rho_w \delta a[L_m - c_w(T_0 - T_\infty)]$, where ρ_w is the density of water, t_2 is found as the solution of the equation

$$\hat{q}_{out} + \hat{q}_{in} = \rho_w \delta a[L_m - c_w(T_0 - T_\infty)]\,, \tag{16-25}$$

where $\hat{q}_{out}$ and $\hat{q}_{in}$ are given by (16-23) and (16-24). For small values of t_2, i.e., at relatively low deposit temperature, $\hat{q}_{out}$ $\hat{q}_{in}$ and $(\kappa_i t_2/a) \ll (\kappa_i t_2/\pi)^{1/2}$, so that approximately

$$t_2 \approx \frac{\pi \rho_w^2 (\delta a)^2 [L_m - c_w(T_0 - T_\infty)]^2}{4 k_i \rho_i c_i (T_0 - T_d)^2}\,. \tag{16-26}$$

From (16-26), Macklin and Payne determined that for $T_\infty = -20°C$ and $T_d = -10°C$, $t_2 \approx 1 \times 10^{-5}$, 1×10^{-3}, 5×10^{-2} sec, for $\delta a = 0.2$, 2, 15 μm, respectively. Similarly, for $T_\infty = -10°C$ and $\delta a = 2\,\mu$m, $t_2 \approx 1$ and 10^{-3} sec, for $T_d = 0°C$ and $-10°C$, respectively. These results demonstrate that t_2 is strongly dependent on the thickness δa of the water layer and on the deposit temperature T_d, and that it is considerably longer than t_1, except for very thin water layers.

Observations show that the model used above is highly idealized, since drops colliding with the ice surface do not spread such as to form a liquid layer over the entire underlying ice particle, except perhaps at large accretion rates when the surface temperature of the ice surface is raised to near 0°C. At other deposit temperatures, the observations described in Section 16.1.1 show that drops freeze onto the ice deposit in a more or less 'chain-like' manner. In order to estimate the freezing time of stage two for more realistic conditions, Macklin and Payne assumed

that the drop and substrate could be considered as a half hemisphere attached to the end of an ice rod. For this model, the total amount of heat conducted from the ventilated hemisphere of area $2\pi a^2$ and temperature T_0 to air of T_∞ is then approximately

$$q_{\text{out}} = 2\pi a t_2 [k_{\text{a}}(T_0 - T_\infty)\bar{f}_{\text{h}} + L_{\text{e}} D_{\text{v}}(\rho_{\text{v},a} - \rho_{\text{v},\infty})\bar{f}_{\text{v}}], \tag{16-27}$$

and the total amount of heat conducted into the rod is (from Carslaw and Jaeger, 1959)

$$q_{\text{in}} = (T_0 - T_d) k_i a^2 \left(\frac{\pi t_2}{\kappa_i}\right)^{1/2}. \tag{16-28}$$

Considering that the heat to be removed is $(2\pi/3)a^3\rho_{\text{w}}[L_m - c_{\text{w}}(T_0 - T_\infty)]$, t_2 is found as the solution of the equation

$$q_{\text{out}} + q_{\text{in}} = \frac{2\pi}{3} a^3 \rho_{\text{w}} [L_m - c_{\text{w}}(T_0 - T_\infty)], \tag{16-29}$$

where q_{out} and q_{in} are given by (16-27) and (16-28). For $T_\infty = -20°\text{C}$ and $a = 10\,\mu\text{m}$, Macklin and Payne found $t_2 \approx 5\times10^{-3}$ sec and 5×10^{-2} sec, for $T_d = -10°\text{C}$ and $-2°\text{C}$, respectively. These results suggest again that the subsequent freezing time t_2 is considerably longer than the initial freezing time t_1. Macklin and Payne also showed that, for the same values of T_∞, a, and T_d, the ratio of t_2 computed by assuming no loss of heat to the ice surface, to t_2 computed by assuming no loss of heat to the air, is 8.2 and 1.4, respectively. This indicates that the rate of heat conduction into the ice substrate plays a much more important role in the drop freezing process than does heat flow into the air, substantiating the suggestions of Brownscombe and Hallett (1967), and of Macklin and Payne (1967).

It is instructive to compare the freezing times computed above for drops in contact with an ice surface with those for drops freely falling in air (Section 13.2.3). Due to the relative ineffectiveness of air in removing the latent heat released during freezing, we expect that these latter freezing times will be considerably longer. This expectation has been verified by Dye and Hobbs (1968), Johnson and Hallett (1968), and Murray and List (1972) in independent treatments. The essentials of these are summarized below.

Consider a water drop supercooled to the temperature T_∞ of the environment. When the drop is nucleated at time $t = 0$, ice crystals grow rapidly through the drop, completing the initial growth in a relatively short time, to be neglected here, while heating the drop to a temperature close to 0°C. At this stage the drop consists of a mixture of water and ice, with a fraction $(1 - c_{\text{w}}\Delta T/L_m)$ of the drop volume yet to freeze. Subsequent freezing occurs at a much slower rate through the transfer of heat by conduction and evaporation to the environment. Assuming that the heat transfer is spherically symmetric, a spherical shell of ice will form with internal radius r at time t. According to Hallett (1964), the ice shell thickens at the small rate of $\simeq 10^{-2}$ cm sec^{-1}, and the local supercooling at the ice-water interface is about 0.2°C. For the present computations, we shall neglect this supercooling and assume that the ice-water interface is at $T_0 = 273$ K (0°C). Then, for a quasi-steady state, the rate of release of latent heat of freezing is equal to the rate of

heat conduction through the ice shell, which in turn is equal to the rate of heat loss by evaporation and conduction to the environmental air. These balance conditions are expressed by the relations

$$4\pi\rho_{\mathrm{w}}L_m r^2\frac{\mathrm{d}r}{\mathrm{d}t}\left(1-\frac{c_{\mathrm{w}}\Delta T}{L_m}\right) = \frac{4\pi k_i a r[T_0-T_a(r)]}{a-r}, \tag{16-30}$$

$$\frac{4\pi k_i a r(T_0-T_a(r))}{a-r} = 4\pi a k_{\mathrm{a}}[T_a(r)-T_\infty]\bar{f}_{\mathrm{h}}+4\pi a L_s D_{\mathrm{v}}(\rho_{\mathrm{v},a}-\rho_{\mathrm{v},\infty})\bar{f}_{\mathrm{v}}, \tag{16-31}$$

where from Section 13.2.3, we have

$$\begin{aligned}\rho_{\mathrm{v},a}-\rho_{\mathrm{v},\infty} &= \rho_{\mathrm{v,sat}}(T_a)-\rho_{\mathrm{v},\infty} \\ &= (1-\phi_{\mathrm{v}})\rho_{\mathrm{v,sat}}(T_\infty)+[T_a(r)-T_\infty]\left(\overline{\frac{\mathrm{d}\rho_{\mathrm{v}}}{\mathrm{d}T}}\right)_{\mathrm{sat},i},\end{aligned} \tag{16-32}$$

and where $T_a(r)$ is the surface temperature of the freezing drop, L_s is the latent heat of sublimation, ϕ_{v} is the fractional relative humidity of the air, and $\overline{(\mathrm{d}\rho_{\mathrm{v}}/\mathrm{d}T)}_{\mathrm{sat},i}$ is the mean slope of the ice saturation vapor density curve over the interval from $T_a(r)$ to T_∞. From (16-30), we find the freezing time t_f may be expressed as

$$t_f = \frac{\rho_{\mathrm{w}}L_m(1-c_{\mathrm{w}}\Delta T/L_m)}{ak_i}\int_a^0 \frac{r(a-r)}{T_0-T_a(r)}\,\mathrm{d}r, \tag{16-33}$$

where $T_a(r)$ is given by (16-31).

We may obtain an approximate solution by assuming for simplicity that the air has a relative humidity of 100%, i.e., $\phi_{\mathrm{v}}=1$, and that $\bar{f}_{\mathrm{h}}\approx\bar{f}_{\mathrm{v}}=\bar{f}$ (see Section 13.2.3); then, (16-31) reduces to

$$\frac{k_i r[T_0-T_a(r)]}{a-r} = \bar{f}[T_a(r)-T_\infty]\left[k_{\mathrm{a}}+L_s D_{\mathrm{v}}\left(\overline{\frac{\mathrm{d}\rho_{\mathrm{v}}}{\mathrm{d}T}}\right)_{\mathrm{sat},i}\right]. \tag{16-34}$$

Eliminating $T_a(r)$ between (16-34) and (16-30), we find,

$$3t_0\frac{\mathrm{d}y}{\mathrm{d}t} = -\frac{1}{(1-m)y^2+my}, \tag{16-35}$$

where $y=r/a$, and

$$t_0 = \frac{\rho_{\mathrm{w}}L_m a^2[1-(T_0-T_\infty)c_{\mathrm{w}}/L_m]}{3\bar{f}(T_0-T_\infty)\left[k_{\mathrm{a}}+L_s D_{\mathrm{v}}\left(\overline{\frac{\mathrm{d}\rho_{\mathrm{v}}}{\mathrm{d}T}}\right)_{\mathrm{sat},i}\right]}, \tag{16-36}$$

$$m = \frac{\bar{f}\left[k_{\mathrm{a}}+L_s D_{\mathrm{v}}\left(\overline{\frac{\mathrm{d}\rho_{\mathrm{v}}}{\mathrm{d}T}}\right)_{\mathrm{sat},i}\right]}{k_i}. \tag{16-37}$$

Integrating (16-35) together with (16-36) and (16-37) from $t = 0$, $y = r/a = 1$ to $t = t_f$, $y = 0(r = 0)$, we find

$$t_f = t_0 \left(1 + \frac{m}{2}\right) . \tag{16-38}$$

Since, for water drops in air, $m/2 \ll 1$,

$$t_f \approx t_0 , \tag{16-39}$$

with t_0 given by (16-36). For $(T_0 - T_\infty) = 10°\text{C}$, $L_m = 74.5$ cal g^{-1}, $L_s = 677.5$ cal g^{-1}, $k_a = 5.63 \times 10^{-5}$ cal cm^{-1}sec^{-1}°C^{-1}, $D_v = 0.196$ cm^{2}sec^{-1} and $\overline{(\mathrm{d}\rho_v/\mathrm{d}T)}_{\mathrm{sat},i} = 1.8 \times 10^{-7}$ g cm^{-3}, we find for a drop of 500 μm radius ($\bar{f} = 5$) a freezing time of $t_f \approx 13$ sec. Similarly, for a drop of 2 mm equivalent radius ($\bar{f} = 14$), we obtain a freezing time of $t_f \approx 80$ sec. Both of these estimates are in good agreement with values determined by Murray and List (1972) from laboratory observations.

16.1.5 Growth Rate of Graupel and Hailstones

Graupel and hailstones are very sparely populated in atmospheric clouds. Their growth at the expense of supercooled cloud drops can be therefore adequately computed from the continuous growth equation, discussed in Section 15.1. Computations involving this equation have been carried out by List and Dessault (1967), List *et al.* (1968), Musil (1970), Charlton and List (1972a,b), Dennis and Musil (1973), Harrimaya (1981), Heymsfield (1982) and Johnson (1987). In the present context, we shall follow the more recent experimental and theoretical studies of Lesins and List (1986) and of Cober and List (1993), who based their formulations on experiments with gyrating hailstones.

Assuming that the size and fall velocity of cloud drops can be neglected in comparison to the size and fall velocity of a graupel or hailstone we may write the continuous growth equation of a graupel or hailstone as

$$\frac{\mathrm{d}m_{\mathrm{accr}}}{\mathrm{d}t} = \mathrm{E}_c \bar{A}_H(t) \mathrm{w}_L U_{\infty,H} , \tag{16-40}$$

where, for an oblate spheroidal hailstone falling with its major axis in a fixed orientation perpendicular to the fall direction, $\bar{A}_H(t) = A_H = (\pi/4)d_H^2$, with $d_H^2 = (6m_H/\pi(AR)\rho_H)^{2/3}$ and (AR) being the axis ratio of the oblate spheroid. For a gyrating hailstone $\bar{A}_H(t) = (\pi/4)\kappa d_1(t)d_2(t)$, where $\kappa = 1.0793$ is the gyration factor for a spheroid obtained after intergrating $A(t)$ over one gyration period (considering a nutation/precession amplitude of 30°, an inclination angle of 90°, and an aspect ratio of 0.67), and where d_1 and d_2 are the major and minor diameters of the hailstone. In (16-40), $U_{\infty,H}$ is the terminal fall velocity of the hailstone, w_L is the liquid water content of the supercooled water cloud, $\mathrm{E}_c = \mathrm{EE}_{\mathrm{ret}}$ is the collection efficiency of the hailstone, and $\mathrm{E}_{\mathrm{ret}}$ is the hailstone's retention efficiency, i.e. the fraction of the cloud drops which, after collision, is retained by the hailstone. The collection efficiency E_c is a priori not known due to both the hailstone's complicated

shape as well as to the unknown fraction of liquid which is shed from the still unfrozen accreted cloud water.

For non-shedding hailstone growth, Cober and List (1993) determined E_c experimentally for a variety of conditions. Their parameterization for E_c is given in (14-35). With E_c known, $(dm/dt)_{accr}$ may be determined for the dry growth regime from (16-40). For computing the total growth rate of the hailstone, we must also include its growth by vapor deposition:

$$\frac{dm}{dt} = \left(\frac{dm}{dt}\right)_{accr} + \left(\frac{dm}{dt}\right)_{diff}, \tag{16-41}$$

For the dry growth regime this rate is given by

$$\left(\frac{dm}{dt}\right)_{diff} = \frac{\Omega_H D_v M_w \bar{N}_{Sh}}{d_H \mathscr{R}} \left(\frac{e_\infty}{T_\infty} - \frac{e_s}{T_s}\right), \tag{16-42}$$

where $\Omega_H = 0.789 d_H$ is the surface area of a gyrating spheroidal hailstone of aspect ratio 0.67, $\bar{N}_{Sh}$ is the Sherwood number (Section 13.2.3), e_∞ and T_∞ are the vapor pressure and temperature, respectively, in the environment, and $e_s = e_{sat,i}(T_s)$, T_s being the temperature at the surface of the growing stone. Cober and List (1993) used an infrared radiometer to determine T_s by remote sensing while the hailstone was growing in an icing tunnel. Depending on the growth condition, T_s was found to be 0.3 to 2.0°C warmer than the ambient air.

In order to evaluate (16-42), it is further necessary to estimate $\bar{N}_{Sh}$. For this purpose, one generally assumes $\bar{N}_{Sh} \approx \bar{N}_{Nu}$ (Section 13.2.3). Relevant heat transfer studies have been carried out by List (1960b), Macklin (1963, 1964a,b), List *et al.* (1965), Bailey and Macklin (1968b), Schüepp and List (1969a,b), Joss and Aufdermauer (1970), and Schüepp (1971), who expressed their findings in terms of the relation $\bar{N}_{Nu} = B N_{Re}^{1/2} N_{Pr,v}^{1/3}$. As N_{Re} increased from 1×10^4 to 2×10^5, B typically increased for spherical hailstones from 0.74 to 2.5. The reason for the increase of B with N_{Re} lies in the fact that two physically distinct processes determine the heat transfer from a spherical particle, namely, transfer through the laminar boundary layer on the upstream side of the sphere, and transfer through the turbulent wake on the downstream side; B increases because the latter becomes increasingly important as the Reynolds number increases. The coefficient B is also a function of the roughness of the hailstone. Thus, for a spherical body with a roughness (ratio of height to diameter of the roughness elements) of 8%, Joss and Aufdermauer found $B = 0.88$ at $N_{Re} = 4 \times 10^3$, and $B = 1.9$ at $N_{Re} = 7 \times 10^4$. With increasing turbulence of the air stream, B was found to increase, reaching a value of $B \approx 1.26$ at $N_{Re} = 7 \times 10^4$ for a smooth sphere, and $B \approx 2.02$ for a sphere of 8% roughness. In a more realistic experiment, Cober and List (1993) found for a gyrating hailstone

$$\bar{N}_{Nu} = 2.24 N_{Re}^{0.41} N_{Pr,v}^{1/3}. \tag{16-43}$$

Once T_s and $\bar{N}_{Nu}$, i.e. $\bar{N}_{Sh}$ are known, the total growth rate of the stone in the dry growth regime may be determined from (16-41).

If T_s cannot be measured, it may be obtained indirectly from the heat balance for the hailstone and a known rate of growth by accretion and diffusion:

$$\left(\frac{dq}{dt}\right)_{fr} + \left(\frac{dq}{dt}\right)_{diff,m} + \left(\frac{dq}{dt}\right)_{accr} = \left(\frac{dq}{dt}\right)_{diff,h} . \tag{16-44}$$

Considering the dry growth regime, the first term on the left represents the heating rate due to release of latent heat during the freezing of the accreted water:

$$\left(\frac{dq}{dt}\right)_{fr} = L_f \left(\frac{dm}{dt}\right)_{accr} = L_f E_c \bar{A}_H w_L U_{\infty,H} , \tag{16-45}$$

where L_f is the latent heat of freezing. The second term on the left represents the heating rate due to vapor deposition:

$$\left(\frac{dq}{dt}\right)_{diff,m} = \frac{L_s \Omega_H D_v M_w \bar{N}_{Sh}}{d_H \mathscr{R}} \left(\frac{e_\infty}{T_\infty} - \frac{e_s}{T_s}\right) . \tag{16-46}$$

The third term on the left represents the rate at which heat is extracted from the hailstone in order to warm the accreted cloud water from T_∞ to T_s:

$$\left(\frac{dq}{dt}\right)_{accr} = -c_w (T_s - T_\infty)(dm/dt)_{accr} . \tag{16-47}$$

The term on the right of (16-44) represents the rate at which heat is dissipated through the air:

$$\left(\frac{dq}{dt}\right)_{diff,h} = \frac{\Omega_H k_a \bar{N}_{Nu} (T_s - T_\infty)}{d_H} . \tag{16-48}$$

Inserting (16-45) to (16-48) into (16-44), we thus obtain an equation implicit in T_s

$$T_s = \frac{L_s (dm/dt)_{diff} + (L_f + c_w T_\infty)(dm/dt)_{accr} + (\Omega_h k_a \bar{N}_{Nu}/d_H) T_\infty}{(\Omega_H k_a \bar{N}_{Nu}/d_H) + c_w (dm/dt)_{accr}} , \tag{16-49}$$

where $(dm/dt)_{diff}$ and $(dm/dt)_{accr}$ are given by (16-42) and (16-40), respectively. Equation (16-49) reduces to (13-63) for the surface temperature of an evaporating drop if we set $(dm/dt)_{accr} = 0$ and $L_s = L_e$.

If a hailstone grows in the wet or spongy growth regime and sheds all excess liquid water, its growth rate is given by the rate at which the collected cloud water can be frozen, i.e., by the rate at which the released latent heat is dissipated. Thus, from the heat balance equation (16-44), we find together with (16-45) to (16-48), with L_e instead of L_s, and with T_0 instead of T_s due to the wet hailstone surface:

$$\left(\frac{dm}{dt}\right)_{accr} = \frac{(\Omega_H k_a \bar{N}_{Nu}/d_H)(T_0 - T_\infty) + L_e \Omega_H D_v \bar{N}_{Sh}/d_H)(\rho_{v,s} - \rho_{v,\infty})}{L_f - c_w (T_0 - T_\infty)} . \tag{16-50}$$

However, under most conditions, not all the excess water collected by the hailstone in the wet growth regime is shed, but rather a fraction I_f is retained unfrozen on the growing hailstone. Instead of (16-45), we then have

$$\left(\frac{dq}{dt}\right)_{fr} = I_f L_f E_c \bar{A}_H w_L U_{\infty,H} . \tag{16-51}$$

If, after collision with the hailstone, a fraction E_{shed} of the drops is shed (termed *shedding efficiency*), we must include in (16-47) the heat which is extracted from the hailstone by the shed water:

$$\left(\frac{dq}{dt}\right)_{accr} = -\bar{A}_H w_L U_{\infty,H}[E_c c_w(T_s - T_\infty) + EE_{shed} c_w(T_w - T_0)], \qquad (16\text{-}52)$$

where T_w is the temperature of the water shed, and where $E_{shed} = 1 - E_{ret}$, from which $EE_{shed} = E - E_c$ is the fraction of the drop mass in the geometrically swept out path of the hailstone which is shed.

By applying the experimental conditions obtained in an icing tunnel to (16-44), (16-51), (16-46), (16-52), and (16-48), Lesins and List (1986) identified five distinct growth regimes for a hailstone experiencing a nutation/precession and spin frequency of 5 Hz. These are identified in Figure 16.6a in terms of a diagram for w_L as a function of T_∞. At high rotation rates (> 20 Hz), all unfrozen accreted water becomes shed from the hailstone surface by centrifugal forces, producing a dry, non-spongy deposit of solid ice. At these frequencies, a sixth growth regime was identified, which is described in Figure 16.6b.

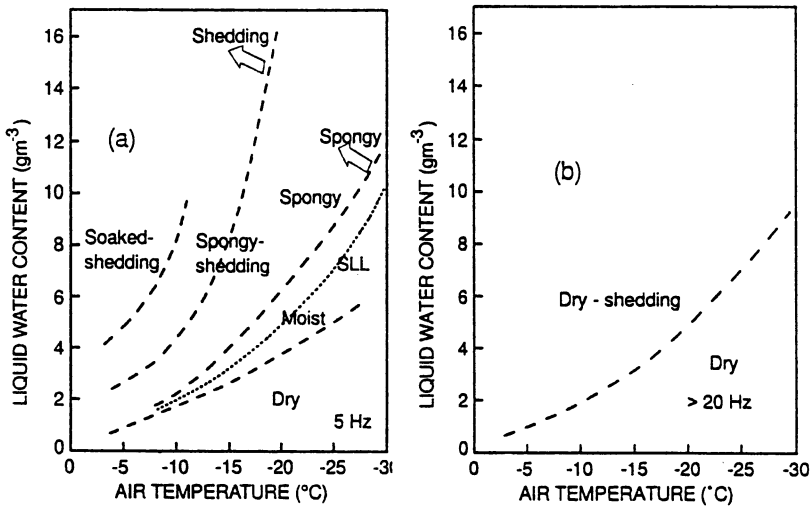


Fig. 16-6: Hailstone growth regimes as a function of liquid water content and air temperature; from laboratory experiments: (a) for a nutation-precession and spin frequency of 5 Hz; the dotted line is the theoretically derived Schumann Ludlam limit (SLL), (b) for a nutation-precession and spin frequency of > 20 Hz. (From Lesins & List, 1986, with changes.)

In the spongy regime without shedding, the heat transfer is insufficient to freeze all the accreted water. Some of this becomes trapped in the deposit while another portion remains as a mobile water skin on the surface of the hailstone. The water film in this growth regime was studied by List (1990) and List *et al.* (1987b, 1989). Unexpectedly, they found large temperature gradients of up to 6°C across the water

skin, a film thickness of up to 1 mm, and a film surface temperature which was below 0°C. In the spongy regime with shedding, water is shed as millimeter-sized drops from a torus-shaped water bulge near the line of flow separation. About 90% of the shed water is carried into the wake of the stone, while about 10% is recaptured by rear collision (Joe *et al.*, 1980). Shedding and recapture depends in general on the nutation/precession rate, the air temperature, and the liquid water content. In the soaked regime with shedding, all water beyond a minimum fraction of $I_f = 0.5$ was shed.

Using the continuous growth equation, Johnson (1987) made an instructive comparison between the growth of a frozen drop by riming in the dry regime, and the growth by collision and coalescence of a liquid water drop of originally the same mass. The results of this comparison are shown in Figure 16.7. We note that the graupel follows a trajectory which is higher than that of the drop. Consequently, the graupel requires a longer time to fall out. Details of this computation showed that after 10 minutes growth time the water drop had, in fact, become 8% heavier than the graupel, limiting its growth time in the atmosphere to 30 minutes. On the other hand, at the time of falling through the melting level (after 47 minutes of growth), the graupel had reached a mass which was about 13 times larger than that of the water drop.

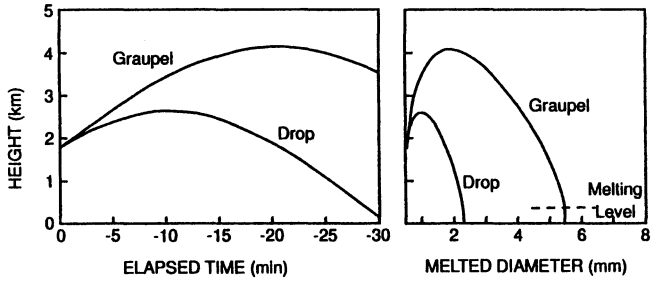


Fig. 16-7: Growth trajectories for drops and graupel particles growing by collision and coalescence and by riming, respectively, in a cold base cloud (cloud base temperature 2° C) and in a uniform updraft of 5 m sec^{-1}. Two water drops of $a_L = 250$ μm diameter were introduced at the −8° C level with one of them being allowed to freeze instantaneously; $N_d = 600$ cm^{-3}, $w_L = 0.6$ g m^{-3}, a_S : 13 to 14 μm; graupel assumed to be smooth spheres. (From Johnson, 1987, with changes.)

Based on the different growth regimes mentioned, Pflaum *et al.* (1978) and Pflaum (1980, 1984) suggested that hailstone growth may be a result of 'microphysical recycling' by which hailstones grow alternately in the dry and wet growth regimes. In the dry growth regime, in which low density rime is deposited, the hailstone exhibits a relatively large hydrodynamic drag to the air flow, and therefore requires a relatively small vertical air velocity to be carried upward. If, during subsequent growth, the hailstone enters a high liquid water content zone so that it grows in the wet growth regime, in which the collected water soaks into the previously acquired porous rime, freezing will produce a dense ice particle which may fall with respect to the updraft until it enters anew into a dry growth zone. Pflaum

(1980) suggests that such a two-stage process lessens the dynamic requirement on a cloud to produce large hailstones.

While it is justifiable to use the continuous growth equation to determine the growth of ice particles which are relatively large compared to the cloud drops, the growth problem must be treated as a stochastic process (see Chapter 15) if the ice particles and drops have similar sizes. The evolution of a size distribution of spherical ice particles growing by a stochastic riming process has been considered by Ryan (1973), and by Beheng (1978, 1980). Ryan used a simple stochastic model in which changes in the ice particle spectrum were studied without considering simultaneous changes in the drop size distribution, and without considering the feedback of these changes on ice particle riming. In addition, Ryan assumed relatively unrealistic collision efficiencies for the supercooled drops and ice crystals, and he further imposed the artificial condition that all the ice crystals appear in the cloud at one given time. In Beheng's more comprehensive study, the evolution of an ice particle size spectrum of originally plate like and columnar crystals was computed for the case of stochastic growth of drops colliding with other drops, and drops colliding with snow crystals. Unfortunately, Beheng's model was not embedded in a dynamic framework, and required the assumption of initial drop and crystal size distributions. Also, the diffusional growth of drops and crystals was not considered. Diffusional growth has been included in the more recent computations of Alheit *et al.* (1990), who used a parcel model to make an *ab initio* computation of the growth of drops, snow crystals, and graupel in an environment of stochastically growing cloud drops. The growth of snow crystals by collision with other crystals was neglected.

Following Alheit *et al.* (1990), we may consider the simple parcel model of Chapter 12, but extend (12-38) now to include the growth of crystals by diffusion of water vapor and by collision with supercooled drops, assuming that ice particles appear by drop freezing only. The time rate of change of the drop number density distribution function $n_{\rm d}$ is then given by:

$$\frac{\partial n_{\rm d}(m)}{\partial t} = -\mu n_{\rm d}(m)W + \left.\frac{\partial n_{\rm d}(m)}{\partial t}\right|_{\rm act/deact} + \left.\frac{\partial n_{\rm d}(m)}{\partial t}\right|_{\rm con/eva} + \left.\frac{\partial n_{\rm d}(m)}{\partial t}\right|_{\rm d,coal} + \left.\frac{\partial n_{\rm d}(m)}{\partial t}\right|_{i,\rm rim} + \left.\frac{\partial n_{\rm d}(m)}{\partial t}\right|_{g,\rm rim} + \left.\frac{\partial n_{\rm d}(m)}{\partial t}\right|_{\rm d,fd}. \tag{16-53}$$

Analogously, the time rate of change of the snow crystal number distribution function n_i may be written as

$$\frac{\partial n_i(m_i)}{\partial t} = -\mu n_i(m_i)W + \left.\frac{\partial n_i(m_i)}{\partial t}\right|_{\rm d,fd} + \left.\frac{\partial n_i(m_i)}{\partial t}\right|_{i,\rm dep/subl} + \left.\frac{\partial n_i(m_i)}{\partial t}\right|_{\rm act/deact} + \left.\frac{\partial n_i(m_i)}{\partial t}\right|_{i,\rm rim} + \left.\frac{\partial n_i(m_i)}{\partial t}\right|_{\rm conv}, \tag{16-54}$$

and for the graupel

$$\frac{\partial n_g(m_g)}{\partial t} = -\mu n_g(m_g)W + \left.\frac{\partial n_g(m_g)}{\partial t}\right|_{\rm d,fd} + \left.\frac{\partial n_g(m_g)}{\partial t}\right|_{g,\rm dep,subl}$$

$$+ \left.\frac{\partial n_g(m_g)}{\partial t}\right|_{g,\mathrm{rim}} + \left.\frac{\partial n_g(m_g)}{\partial t}\right|_{\mathrm{conv}} . \tag{16-55}$$

The corresponding mass density distribution functions are $g_w(m) = m n_d(m)$, $g_i(m_i) n_i(m_i)$, and $g_g(m_g) = m_g n_g(m_g)$. The second, third, and fourth terms on the right of (16-53) are given by (12-37), (12-38), (12-40), and (13-42), respectively. The fifth, sixth, and seventh terms on the right of (16-53) are given in

$$\left.\frac{\partial n_d(m)}{\partial t}\right|_{i,\mathrm{rim}} = -n_d(m) \int_0^\infty n_i(m_i) K_i[a_i(m_i), a(m)]\, \mathrm{d}m_i , \tag{16-56}$$

$$\left.\frac{\partial n_d(m)}{\partial t}\right|_{g,\mathrm{rim}} = -n_d(m) \int_0^\infty n_g(m_g) K_g[a_g(m_g), a(m)]\, \mathrm{d}m_g , \tag{16-57}$$

where K_i is the collection kernel for the collision of drops with snow crystals (Section 14.6.1) with K_g now being the collection kernel for the collision of drops with graupel, and for the following (16-58), a Bigg drop freezing mechanism (Equation (9-50)) is assumed:

$$\left.\frac{\partial n_d(m)}{\partial t}\right|_{\mathrm{d,fd}} = -n_d(m) B \frac{m}{\rho_m} \exp[a(T_0 - T)] \tag{16-58}$$

Before expressing the individual terms in (16-54) and (16-55), we first must make some assumptions concerning the division between rimed snow crystals and graupel. As a working hypothesis, Altheit *et al.* assumed that frozen drops of radii larger than 100 μm can be assigned to the category of graupel, while smaller frozen drops were considered planar snow crystals which could grow further only by vapor deposition. Rimed snow crystals whose axis ratio $(b_i/a_i) > 0.25$ were considered graupel, while those of smaller axis ratio were assumed to remain in the category of 'snow crystals'. Of course, these conditions require transforming the mass growth rate equations into equations which follow the change in radius of the ice particles. However, in the present context, we shall keep the mass scale, and write for the individual terms in (16-54):

$$\left.\frac{\partial n_i(m_i)}{\partial t}\right|_{\mathrm{d,fd}} = -\left.\frac{\partial n_d(m)}{\partial t}\right|_{\mathrm{d,fd}} \quad \text{for } a(m) < 100\,\mu\mathrm{m} , \tag{16-59}$$

$$\left.\frac{\partial n_i(m_i)}{\partial t}\right|_{\mathrm{act}} = \frac{1}{\Delta t}\left(N_{iN} - \left[\int_0^\infty n_i(m_i)\, \mathrm{d}m_i + \int_0^\infty n_g(m_g)\, \mathrm{d}m_g\right]\right) , \tag{16-60}$$

where N_{iN} is the number of ice forming nuclei given as a function of temperature (see Chapter 9), and Δt is the numerical time step;

$$\left.\frac{\partial n_i(m_i)}{\partial t}\right|_{\mathrm{deact}} = -\left.\frac{\partial n_{AP,a}(m_{AP,i})}{\partial t}\right|_{\mathrm{deact}} , \tag{16-61}$$

where $m_{AP,i}$ is the mass of the aerosol particle set free when a snow crystal has completely evaporated;

$$\left.\frac{\partial n_i(m_i)}{\partial t}\right|_{i,\mathrm{dep/subl}} = -\frac{\partial}{\partial m_i}\left[\left(\frac{\mathrm{d}m_i}{\mathrm{d}t}\right)_{\mathrm{dep/subl}} n_i(m_i)\right], \tag{16-62}$$

where $(\mathrm{d}m_i/\mathrm{d}t)_{\mathrm{dep/subl}}$ is given by (13-91);

$$\left.\frac{\partial n_i(m_i)}{\partial t}\right| i,\,\mathrm{rim} = -\frac{\partial}{\partial m_i}\left[\left(\frac{\mathrm{d}m_i}{\mathrm{d}t}\right)_{i,\mathrm{rim}} n_i(m_i)\right], \tag{16-63}$$

with

$$\left.\frac{\mathrm{d}m_i}{\mathrm{d}t}\right|_{i,\mathrm{rim}} = \int_0^{m_{\max}} m n_{\mathrm{d}}(m) K_i[a_i(m_i), a(m)]\,\mathrm{d}m\,, \tag{16-64}$$

and where $m_{\max}$ is the maximum drop size which contributes to the riming of a snow crystal (see Section 14.6.1).

The individual terms in (16-55) are given by

$$\left.\frac{\partial n_g(m_g)}{\partial t}\right|_{\mathrm{d,fd}} = -\left.\frac{\partial n_{\mathrm{d}}(m)}{\partial t}\right|_{\mathrm{d,fd}} \quad \text{for } a(m) \geq 100\,\mu\mathrm{m}\,, \tag{16-65}$$

$$\left.\frac{\partial n_g(m_g)}{\partial t}\right|_{g,\mathrm{dep/subl}} = -\frac{\partial}{\partial m_g}\left[\left(\frac{\mathrm{d}m_g}{\mathrm{d}t}\right)_{\mathrm{dep/subl}} n_g(m_g)\right], \tag{16-66}$$

where $(\mathrm{d}m_g/\mathrm{d}t)_{\mathrm{dep/subl}}$ is again given by (13-91);

$$\left.\frac{\partial n_g(m_g)}{\partial t}\right|_{g,\mathrm{rim}} = -\frac{\partial}{\partial m_g}\left[\left(\frac{\mathrm{d}m_g}{\mathrm{d}t}\right)_{g,\mathrm{rim}} n_g(m_g)\right], \tag{16-67}$$

where

$$\left.\frac{\mathrm{d}m_g}{\mathrm{d}t}\right|_{g,\mathrm{rim}} = \int_0^{\infty} m n_{\mathrm{d}}(m) K_g[a_g(m_g), a(m)]\,\mathrm{d}m\,; \tag{16-68}$$

and finally the conversion of snow crystals to graupel given by

$$\left.\frac{\partial n_g(m_g)}{\partial t}\right|_{\mathrm{conv}} = -\left.\frac{\partial n_i(m_i)}{\partial t}\right|_{\mathrm{conv}}, \quad \text{for } \frac{b_i}{a_i} \geq 0.25\,. \tag{16-69}$$

The above set of equations was solved by Alheit *et al.* (1990) who started their computations on a rural background aerosol (see Chapter 8) and assumed that the vertical temperature and humidity distribution is given by that of 17 April 1986, 00 UTC over Essen (FRG), when graupel showers were observed on the ground. One of their results is illustrated in Figures 16.8a,b,c for aerosol particles with a water soluble fraction of $\varepsilon_m = 0.15$. We notice from Figure 16.8c that graupel had developed by 1200 sec model time, reaching millimeter size by

1600 sec. Snow crystals appeared after 800 sec model time, reaching a size of several hundred microns by 1600 seconds. We also note that the drop spectrum is strongly affected by the appearance of snow crystals and graupel. The drop spectrum begins broadening by collision and coalescence after 800 seconds model time, and exhibits the typical double maximum by 1600 seconds. However, after that it suddenly collapses due to the removing of drops by riming. These model results were found to agree well with observations.

16.1.6 Snow Crystal Multiplication by Riming

In Section 9.2.6 and in Figures 2.42 and 2.43, we have pointed out that, in atmospheric clouds, the ice particle concentration may be up to several orders of magnitude larger than the concentration of ice forming nuclei. Several mechanisms were discussed which may be responsible for this observation. Among these, the Hallett-Mossop mechanism has received most attention in the literature and has been widely used in current cloud models.

Koenig (1977), Beheng (1982, 1987), Cotton *et al.* (1986), Harris-Hobbs and Cooper (1987), and Aleksic *et al.* (1989) have included the rate of ice crystal production P_c due to the Hallett-Mossop splinter mechanism by means of the following relation:

$$P_c(\text{sec}^{-1}) = 35 \times 10^4 \left(\frac{\mathrm{d}m}{\mathrm{d}t}\right)_{\text{rim}} f(T_p)\,, \tag{16-70}$$

where $(\mathrm{d}m/\mathrm{d}t)_{\text{rim}}$ (g sec^{-1}) is the riming rate of an ice crystal or graupel, T_p is the surface temperature of the riming particle, and the function $f(T_p)$ is given by

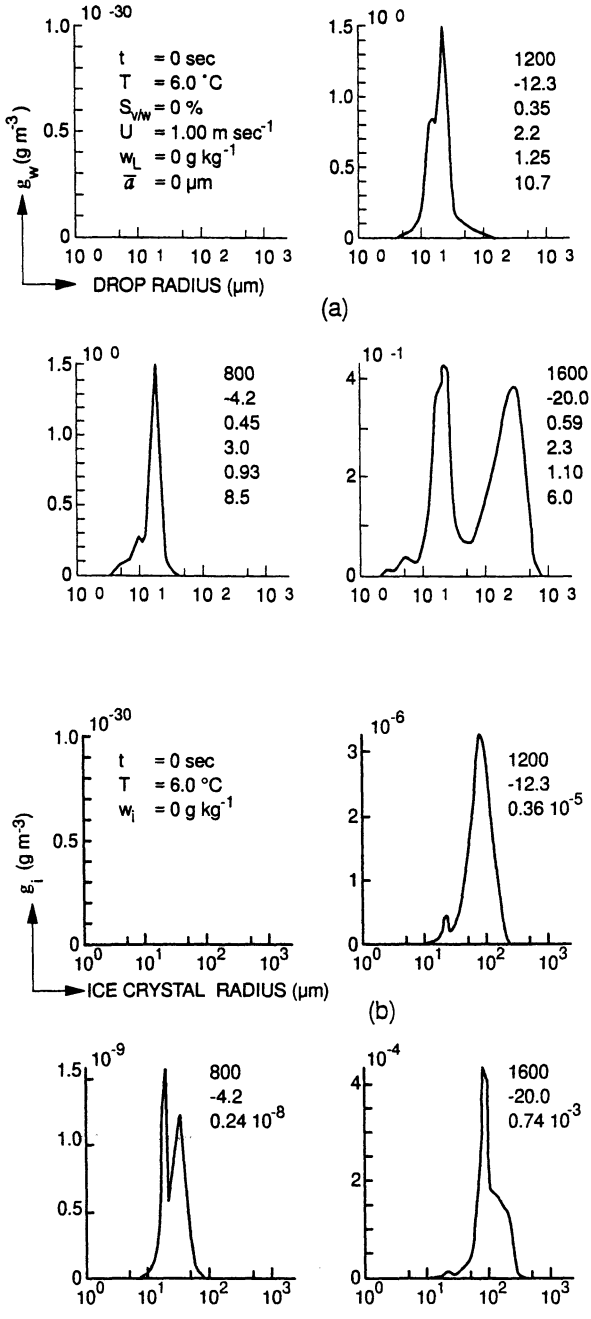
$$f(T_p) = \begin{cases} 0 & T_p > 270.16 \text{ K} \\ (270.16 - T_p)/2 & 270.16 \geq T_p \geq 268.16 \text{ K} \\ (T_p - 265.16)/3 & 268.16 \geq T_p \geq 265.16 \text{ K} \\ 0 & T_p < 265 \text{ K} \end{cases} \tag{16-71}$$

Equation (16-70) accounts for the observed fact that approximately 350 ice splinters are produced for every 10^{-3} g of rime accreted by a graupel at $-5°$C. Alternatively, one may use the relation

$$P_c = \frac{1}{250}\frac{\pi d_g^2}{4} U_g \mathrm{E}_g(a_g, a_{12}) N_{12} f(T_p)\,, \tag{16-72}$$

where $\mathrm{E}_g(a_s, a_{12})$ is the efficiency for collision between a graupel of radius a_g and cloud drops of $a \geq 12\,\mu$m, and N_{12} is the number concentration of cloud drops larger than $12\,\mu$m in radius. Equation (16-72) includes the observed fact that approximately one ice splinter is produced per 250 drops larger than $12\,\mu$m radius ($24\,\mu$m diameter) accreted onto a graupel at $-5°$C.

Beheng (1982, 1987) studied the implication of the Hallett-Mossop splinter mechanism on the glaciation behavior of a cloud whose drops grow by collision and coalescence, and by collision with ice crystals, choosing a modified gamma function for the initial drop size distribution, and a Gaussian distribution function for the columnar snow crystals. Drops larger than $100\,\mu$m radius were allowed to collide


10 -30
t = 0 sec
T = 6.0 °C
$S_{v/w}$ = 0 %
U = 1.00 m sec^{-1}
w_L = 0 g kg^{-1}
$\bar{a}$ = 0 μm
g_w (g m^{-3})
DROP RADIUS (μm)
10 0
1200
-12.3
0.35
2.2
1.25
10.7
(a)
10 0
800
-4.2
0.45
3.0
0.93
8.5
10 -1
1600
-20.0
0.59
2.3
1.10
6.0
10^{-30}
t = 0 sec
T = 6.0 °C
w_i = 0 g kg^{-1}
g_i (g m^{-3})
ICE CRYSTAL RADIUS (μm)
10^{-6}
1200
-12.3
0.36 10^{-5}
(b)
10^{-9}
800
-4.2
0.24 10^{-8}
10^{-4}
1600
-20.0
0.74 10^{-3}

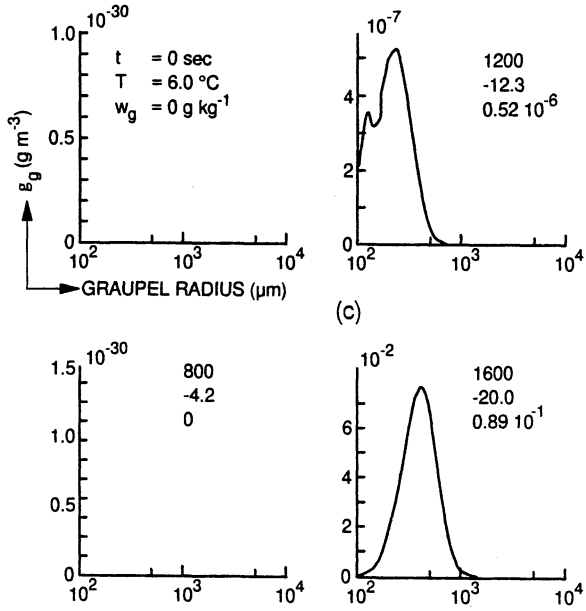


Fig. 16-8: Evolution with time of the mass density distribution function: for cloud drops (a), cloud snow crystals (b), and graupel (c), per logarithm radius interval. Cloud drops evolve on a rural background aerosol (Jaenicke, 1988) of $(NH_4)_2SO_4$ particles with $\epsilon_m = 0.15$, and grow by condensation and collision and coalescence; parcel model; ice formation by drop freezing. (From Alheit *et al.*, 1990, with changes.)

with the columnar crystals with an efficiency given by Lew and Pruppacher (1983) (see Section 14.6.2). Riming of the ice columns proceeded with efficiencies given by Schlamp *et al.* (1975), and frozen drops were assumed to turn into lump graupel growing by collision with drops at a rate given by the scheme of Heymsfield and Pflaum (1985). At model times between 450 and 1750 seconds, the results agreed well with the observations of Mossop (1985a,b) in small winter cumuli, if a splinter rate of 4×10^{-3} to 5×10^{-3} splinters per drop was assumed, as suggested by Mossop (1976), and if drops of diameters larger than $24\,\mu$m were present in the cloud. Beheng (1987) also found that the time interval Δt required for increasing the number of ice particles by a factor of 10^4 in a cloud was related to N_0, the initial number of the crystals per liter, by $\Delta t = A/N_0 B$, where $A = 11.7$, and $B = 0.313$. For $N_0 = 10^{-2}$ liter^{-1} Beheng found $\Delta t = 50$ minutes, a reasonable value considering the observations of Mossop *et al.* (1970, 1972).

16.2 Growth of Snow Crystals by Collision with other Snow Crystals

Many continental snow storms contain little supercooled water so that changes in the ice mass concentration are primarily the result of the diffusional growth of snow crystals from ice-supersaturated vapor, followed by aggregation resulting from the

collision of snow crystals with other snow crystals. The variation of the number density distribution functions for snow crystals growing by vapor deposition, aggregation and breakup has been studied by Passarelli (1978a,b, 1987), Passarelli and Srivastawa (1979), Lo and Passarelli (1982), and by Mitchell (1988), assuming drops to be absent and assuming that the initial ice crystal spectrum is given. The change in the number density distribution function may then be expressed by the relation

$$\frac{\partial n_i(m_i)}{\partial t} = \left.\frac{\partial n_i(m_i)}{\partial t}\right|_{i,\text{dep/subl}} + \left.\frac{\partial n_i(m_i)}{\partial t}\right|_{i,\text{aggr}} + \left.\frac{\partial n_i(m_i)}{\partial t}\right|_{i,\text{break}}, \tag{16-73}$$

where the first term on the right of (16-73) is due to the diffusional growth of snow crystals given by (16-62). The second term on the right is given by the stochastic collision rate of snow crystals which can be expressed by the relation (see Chapter 15).

$$\begin{aligned}\left.\frac{n_i(m_i,t)}{\partial t}\right|_{\text{aggr}} = {} & \frac{1}{2}\int_0^{m_i} K_i(m_i - m_i', m_i')n_i(m_i', t)n_i(m_i - m_i', t)p(T) \\ & \times \mathrm{E}_{st}(m_i - m_i', m_i')\,\mathrm{d}m_i' - n_i(m_i,t)\int_0^{\infty} K_i(m_i, m_i')n_i(m_i', t)p(T) \\ & \times \mathrm{E}_{st}(m_i, m_i')\,\mathrm{d}m_i', \end{aligned} \tag{16-74}$$

where the first term on the right of (16-74) represents the production of ice aggregates of mass m_i due to aggregation of crystals having mass $m_i - m_i'$ and m_i', and the second term on the right of (16-74) represents the depletion of aggregates of mass m_i due to aggregation with particles of mass m_i'. The function $p(T)$ represents a weighing factor for the collision efficiency to correct for the temperature variation of the crystal shape. The factor $\mathrm{E}_{st}(m_i, m_i')$ represents the sticking efficiency of the colliding crystals. K_i is the collision kernel for snow crystals colliding with other crystals (Section 14.7). Finally, the third term on the right of (16-73) may be expressed by the relation (see Chapter 15)

$$\begin{aligned}\left.\frac{\partial n_i(m_i,t)}{\partial t}\right|_{i,\text{break}} = {} & \int_0^{\infty}\int_0^{m_i'} K_i(m_i', m_i'')[1 - \mathrm{E}_{st}(m_i', m_i'')]n_i(m_i', t)n_i(m_i'', t) \\ & \times Q(m_i; m_i', m_i'')\,\mathrm{d}m_i'\,\mathrm{d}m_i'' - n_i(m_i,t)\int_0^{\infty} K_i(m_i, m_i') \\ & \times [1 - \mathrm{E}_{st}(m_i, m_i')]n_i(m_i', t)\,\mathrm{d}m_i'. \end{aligned} \tag{16-75}$$

The first term on the right of (16-75) is due to the production of particles of mass m_i due to collisions between particles of m_i and m_i'', $Q(m_i; m_i', m_i'')$ is the number of fragments with masses between m_i and $m_i + \mathrm{d}m_i$ when particles with mass m_i and m_i'' collide and break up, and $(1 - \mathrm{E}_{st})$ is the breakup efficiency of the colliding

fragments m_i' and m_i''. The second term on the right of (16-75) represents the depletion of particles of mass m_i due to collisional breakup with particles of mass m_i'.

Unfortunately, at present a quantitative description of the breakup mechanism of aggregating snow crystals is not available, so that the last term in (16-73) must be ignored. On further setting the sticking efficiency $E_{st} = 1$, and assuming that the aggregation efficiency E_c is given by the temperature corrected collision efficiency $Ep(T)$, Mitchell (1988) computed the change of a size spectrum of snow crystals as a function of time, with the size distribution constrained to be exponential. The theoretically predicted values for the size distribution parameters N_0 and Λ was compared to values observed by Lo and Passarelli (1982) in cyclonic storms for aggregating particles of diameter 300 to 4500 μm. The temperature and humidity profiles, as well as the snowfall rate at some reference level near the cloud top, were taken from observation. In addition, the snowfall rate was assumed to follow an exponential distribution with height, E was assumed to be unity, and $p(T)$ was arbitrarily set to the values 0.25 ($T < -20°C$), 0.40 ($-20 \leq T \leq -17°C$), 1.0 ($-17 \leq T < -12.5°C$), 0.40 ($-12.5 < T < -9°C$), 0.10 ($-9 \leq T < -6°C$), 0.60 ($-6 \leq T < -4°C$), and 0.10 ($T \geq -4°C$). Results of these computations are given in Figures 16.9a,b. We note the computed values of $\Lambda(t)$ and $N_0(t)$ agree well with those observed. We also note from these figures that the size spectrum of particles which grow by diffusion, only evolves in a significantly different manner from a spectrum which is controlled at the same time by snow crystal aggregation.

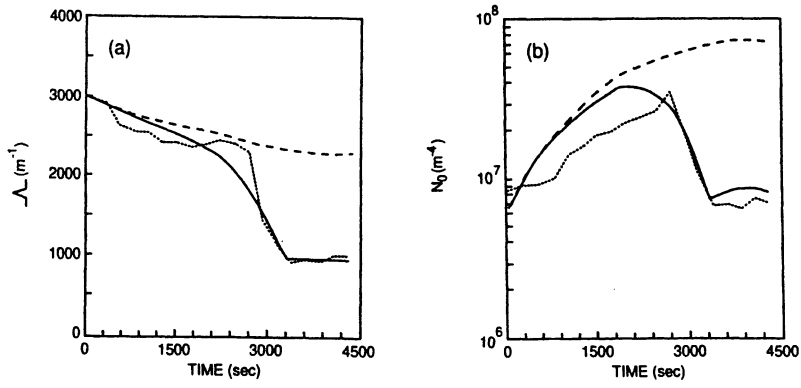


Fig. 16-9: Time evolution of the parameters Λ (a) and N_0 (b) for a snow crystal size distribution growing by aggregation. (—) theoretically predicted by parcel model, (.....) observed, (– – –) theoretically predicted for growth by diffusion of water vapor only. (From Mitchell, 1988, with changes.)

16.3 Melting of Ice Particles

When ice particles fall through the 0°C level in the atmosphere, they commence melting. Obviously, such melting is not instantaneous due to the finite rate at which heat can be supplied to provide for the necessary latent heat of melting. Due to their

smaller mass-to-area ratio, smaller sized ice particles melt quicker than do larger ones. Because of this and the difference in fall speeds, generally only very large particles of the size of hailstones can survive the fall from a cloud base above 0°C to ground. In this section, we shall briefly discuss the quantitative details of such behavior, following the work of Mason (1956), Macklin (1963, 1964a,b), Drake and Mason (1966), and Bailey and Macklin (1968), Rasmussen and Pruppacher (1982), Rasmussen *et al.* (1982, 1984a,b), Rasmussen and Heymsfield (1987a,b,c), Matsuo and Sasyo (1981a,b), and Mitra *et al.* (1990c).

16.3.1 Melting of Graupel and Hailstones

The simplest model for describing the melting process of a graupel or hailstone obviously involves a spherical ice particle of radius a_d falling at terminal velocity in air of constant humidity and constant temperature $T_\infty > T_0$, where $T_0 = 273$ K. Since $T_\infty > T_0$, the ice particle melts and therefore consists at time t of a spherical ice core of radius a_i surrounded by a layer of water of thickness $a_\mathrm{d} - a_i$, assumed to be uniform and concentric with the ice core (Figure 16.10). We also shall assume that there is no internal circulation in the meltwater and that $a_\mathrm{d} =$ constant. The latter assumption implies that no meltwater is lost by shedding or evaporation, although we will consider the effect of evaporative cooling on the melting process. Assuming a steady state and no internal circulation in the meltwater, the rate of release of latent heat of melting must then be balanced by the rate at which heat is transferred through the water layer, so that

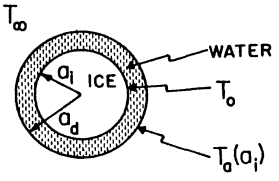


Fig. 16-10: Auxiliary figure to illustrate theory of Mason (1956) for idealized melting of an ice sphere.

$$4\pi\rho_\mathrm{i} L_m a_i^2 \frac{\mathrm{d}a_i}{\mathrm{d}t} = \frac{4\pi a_\mathrm{d} a_i k_\mathrm{w}[T_0 - T_a(a_i)]}{a_\mathrm{d} - a_i}\,, \tag{16-76}$$

where k_w is the thermal conductivity of water (Mason, 1956). In (16-76), T_a is the temperature at the surface of the liquid layer and T_0 is the temperature at the ice-water interface.

From (16-76), we thus find the time t_m for complete melting of the ice sphere to be given by

$$t_m = \frac{L_m \rho_i}{k_\mathrm{w} a_\mathrm{d}} \int_a^0 \frac{r(a_\mathrm{d} - a_i)\,\mathrm{d}r}{T_0 - T_a(a_i)}\,, \tag{16-77}$$

with T in K. This equation was first evaluated by Drake and Mason (1966). Since, for a steady state, the rate of heat transfer through the water layer to the ice core

must be balanced by the rate at which heat is transferred through the air to the surface of the melting particle by forced convection of heat and by evaporation (condensation), we must also require that

$$\frac{4\pi k_w[T_a(a_i)-T_0]a_d a_i}{(a_d-a_i)} = 4\pi a_d k_a[T_\infty - T_a(a_i)]\bar{f}_h + 4\pi a_d D_v \frac{L_e M_w}{\mathscr{R}}\left[\frac{e_\infty}{T_\infty} - \frac{e_a}{T_a(a_i)}\right]\bar{f}_v, \tag{16-78}$$

where D_v is the diffusivity of water vapor in air, k_a is the heat conductivity of air, $e_\infty = \phi_v e_{sat,w}(T_\infty)$, $e_a = e_{sat,w}[T_a(a_i)]$, $\mathscr{R}$ is the universal gas constant, ϕ_v is the fractional relative humidity of air, and $\bar{f}_v$ and $\bar{f}_h$ are the ventilation coefficients for mass and heat transfer. For given T_∞, ϕ_v, and a_d one may determine $T_a(a_i)$ from (16-78), which then permits the determination of t_m in (16-77) and da_i/dt from (16-76).

Evaporative cooling of the surface of a melting ice sphere falling through subsaturated air reduces the rate of melting and therefore the time and distance for complete melting. In addition, the onset of melting may be considerably delayed. The critical air temperature T_{crit} at which melting begins is found by setting $T_a(a_i) = T_0$. Assuming further that $\bar{f}_v = \bar{f}_h$, we have, from (16-78),

$$T_{crit} = T_0 + \frac{D_v L_e M_w}{k_a \mathscr{R}}\left[\frac{e_{sat,w}(T_0)}{T_0} - \frac{\phi_v e_{sat,w}(T_\infty)}{T_\infty}\right]. \tag{16-79}$$

Equation (16-79) was experimentally verified by Rasmussen and Pruppacher (1982), showing that, with decreasing relative humidity, the onset of melting shifts to temperatures above 0°C. Thus, at a relative humidity of 50%, e.g., melting begins at +4°C.

Equations (16-76) and (16-77) were experimentally verified by Rasmussen *et al.* (1984b) for the case of ice particles of diameter between 5 and 9 mm ($3.0 \times 10^3 \leq N_{Re} \leq 6 \times 10^3$) (see Figure 16.11d). For these ice particles, the meltwater exhibited no internal circulation. The rate of melting of the ice core can therefore be determined from (16-76) and (16-77), which assume heat transport by conduction only. These equations also assume a concentrically located ice core which contradicts observation (see Figure 16.11d). However, Rasmussen *et al.* (1982, 1984) showed that by solving the heat transfer equation in a bispherical coordinates, the corrections to the concentric location of the ice core can be neglected.

Melting ice particles of sizes smaller than 5 mm exhibit a vigorous internal circulation in the meltwater, as shown schematically in Figures 16.11e,f. Unfortunately, a complete solution to the heat transfer equation, including the effects of circulation in the meltwater, is not available for the appropriate geometry. However, a solution was provided by Rasmussen *et al.* (1982) under assumption of creeping flow in the meltwater, and with an eccentrically located ice core. Unfortunately, the melting rates thus determined were much too small compared to those observed. This suggests that the internal circulation in the meltwater is not laminar but turbulent. For the agreement of theory with experiment, it is in fact necessary to set $T_a(a_i) = T_0$, so that now for particles of this size

$$-\frac{dm_i}{dt} = \frac{4\pi a_d}{L_m}\left(k_a(T_\infty - T_0)\bar{f}_h + \frac{D_v L_e M_w}{\mathscr{R}}\left[\frac{e_\infty}{T_\infty} - \frac{e_a}{T_0}\right]\bar{f}_v\right), \tag{16-80}$$

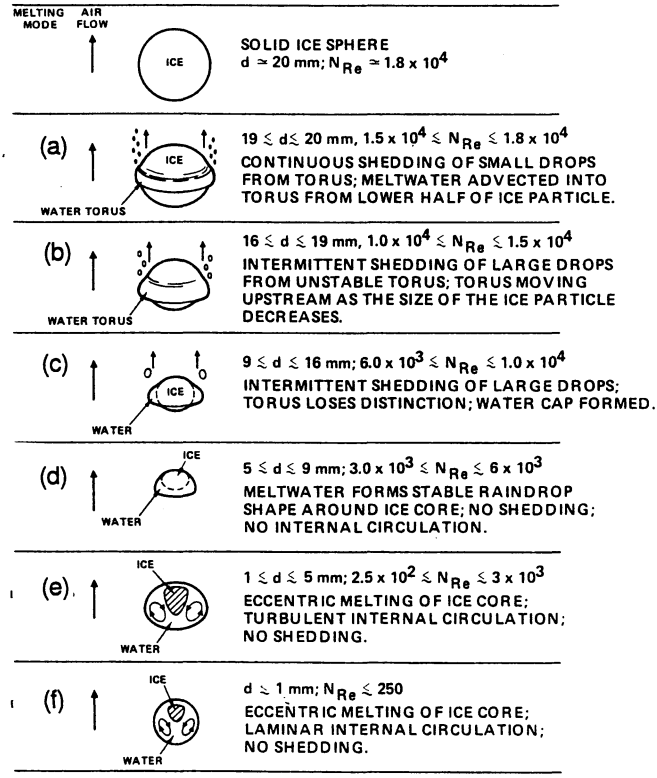


Fig. 16-11: Schematic of melting modes of ice spheres of various sizes and Reynolds number derived from wind tunnel experiments; arrow indicates direction of air flow. (From Rasmussen *et al.*, 1984b, with changes.)

where $e_a = e_{sat,w}(T_0)$. Wind tunnel experiments of Rasmussen *et al.* (1984a,b) and Rasmussen and Pruppacher (1982) have verified that (16-80) for ice particles of $d < 1$ mm ($N_{\mathrm{Re}} < 250$), and ice particles of $1 \leq d \leq 5$ mm ($2.5 \times 10^2 \leq N_{\mathrm{Re}} \leq 3 \times 10^3$).

Thus far, we have considered that the meltwater remains attached to the melting ice sphere and does not shed. However, wind tunnel studies of Rasmussen *et al.* (1984b) showed that melting ice spheres of $9 \leq d \leq 16$ mm ($6 \times 10^3 \leq N_{\mathrm{Re}} \leq 1 \times 10^4$) exhibited intermittent shedding of large drops from a stable torus near the equator, while melting ice spheres of $16 \leq d \leq 19$ mm ($1 \times 10^4 \leq N_{\mathrm{Re}} \leq 2 \times 10^4$) exhibited intermittent shedding of large drops from a highly unstable torus which moves downstream as melting proceeds. In contrast, ice spheres of $d < 19$ mm ($N_{\mathrm{Re}} < 2 \times 10^4$) exhibited continuous shedding of small drops from the torus and turbulent boundary layer (Figures 16.11a,b,c). To describe the melting rate of spherical hailstones of $9 \leq d \leq 19$ mm ($6 \times 10^3 \leq N_{\mathrm{Re}} \leq 2 \times 10^4$), Rasmussen and Heymsfield (1987a) suggested using an equation due to Macklin (1963, 1964) based on his experiments with ice spheroids. For the case that most of the meltwater is

shed, Macklin found

$$-\frac{\mathrm{d}m_i}{\mathrm{d}t} = \frac{\chi A}{2a_i L_m} N_{\mathrm{Re}}^{1/2} \left[N_{\mathrm{Pr,a}}^{1/3} k_{\mathrm{a}} (T_\infty - T_0) + \frac{N_{\mathrm{sc,v}}^{1/3} D_{\mathrm{v}} L_{\mathrm{e}} M_{\mathrm{w}}}{\mathscr{R}} \left(\frac{\mathrm{e}_\infty}{T_\infty} - \frac{\mathrm{e}_a}{T_0} \right) \right], \tag{16-81}$$

where $\mathrm{e}_a = \mathrm{e}_{\mathrm{sat,w}}(T_0)$, and where the effect of ventilation on melting is given by $\bar{f}_{\mathrm{v}} = \chi N_{\mathrm{Re}}^{1/2} N_{\mathrm{Pr,a}}^{1/3}/2$ and $\bar{f}_{\mathrm{h}} = \chi N_{\mathrm{Re}}^{1/2} N_{\mathrm{sc,v}}^{1/3}/2$, χ being the heat (mass) transfer coefficient, and A being the surface area of the ice spheroid. For $6 \times 10^3 \leq N_{\mathrm{Re}} \leq 2 \times 10^4$, Macklin gave $\chi = 0.76$. For $N_{\mathrm{Re}} < 2 \times 10^4$, Bailey and Macklin (1968b) suggested $\chi = 0.57 + 9.0 \times 10^{-6} N_{\mathrm{Re}}$.

In order to estimate the mass of meltwater shed by melting hailstones of $d >$ 9 mm, Rasmussen and Heymsfield (1987a) analyzed the wind tunnel data of Rasmussen *et al.* (1984b) to find that the critical water mass on the ice core of the melting hailstone just before shedding is related to the mass of the ice core by

$$m_{\mathrm{w,crit}} = 0.268 + 0.1389 m_i. \tag{16-82}$$

This equation implies that for non-tumbling hailstones there is a maximum amount of water which can be retained on the surface of a given ice core before shedding occurs. If the amount of water exceeds this maximum amount, shedding of all the excess water occurs.

Rasmussen and Heymsfield (1987b) applied the melting and shedding rate equations to an atmospheric case in which it was assumed that a hailstone was falling through cloud free air of various relative humidity, with a linear temperature profile given by 24°C at the ground (0.8 km MSL, 920 mb) and 0°C at 5.2 km (525 mb). From their model, they determined the variation with height of the hailstones size, the terminal velocity, the density, and the shedding behavior. The results of this study are given in Figures 16.12a,b,c,d. We notice from Figure 16.12a that a hailstone of $\rho_H = 0.91$ g cm^{-3} and 1 cm diameter survives the 5.2 km fall to the ground, reaching it as a 0.2 cm diameter ice particle, while a same-sized hailstone with $\rho_H = 0.45$ g cm^{-3} is completely melted at 1.3 km above the ground. In Figure 16.12d, the variation with height of the hailstone's mean density is given. We notice that the density of a hailstone of initial density 0.45 g cm^{-3} increases with decreasing altitude due to the soaking of meltwater. During soaking, the particles terminal velocity increases (16-12b). A particle of initial density 0.9 g cm^{-3} does not soak meltwater but rather accumulates it on its surface, causing a water torus to build up around its equator. This results in a decrease of the particle's terminal velocity (Figure 16.12b). Shedding of meltwater for the 0.9 g cm^{-3} particle begins at about 2.3 km below the 0°C level (Figure 16.12c). Soaking of the 0.45 g cm^{-3} particle delays shedding which begins 0.9 km below shedding from the 0.9 g cm^{-3} particle. As expected, the study of Rasmussen and Heymsfield (1987b) also showed that melting and shedding are both very sensitive functions at the relative humidity of the air. Thus, their computations showed that a 2 cm diameter hailstone of density 0.45 g cm^{-3} melts during its fall due to evaporative cooling to a 1.2 cm stone in an environment of 50% relative humidity, but melts completely at 100% relative humidity.

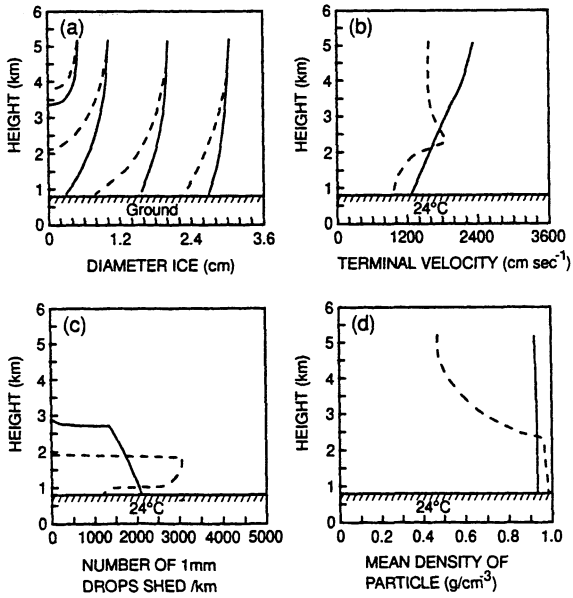


Fig. 16-12: Melting and shedding behavior of spherical ice particles falling through cloud free, still air of given temperature and humidity; for $T = 24°$ C and relative humidity = 60 % at the ground and $T = 0°$ C and 100 % at 5.2 km. (– – –) initial density of ice particle density = 0.45 g cm^{-3}, (—) initial density of ice particle = 0.9 g cm^{-3}. Variation with height of: ice particle diameter (a), terminal velocity of ice particle (b), number of melt water drops shed (c), and mean density of ice particle (d). (From Rasmussen & Heymsfield, 1987b, with changes.)

Before concluding this section, a few consequences with practical implications should be pointed out: (1) The melting rate equations show that the amount of water mass melted per unit time in a population of small ice spheres is larger than the water mass melted per unit time in a population of large ice spheres, given the same total initial ice mass in each population. This implies that the smaller stones will be more effective in extracting heat from the environment, and therefore be more effective in cooling the environmental air. Also, smaller hailstones spend more time in the air due to their smaller fall velocity. The assumption, made above, of equal ice mass in a given size interval, may be justified by considering that a typical size distribution of hailstones consists of about 20 stones per 100 m^3 air for 1 cm diameter stones, and about 2 stones per 100 m^3 air for 2 cm diameter stones. Thus, the number of 1 cm stones is about 10 times as large as the number of 2 cm stones. However, the mass of a 1 cm stone is about 1/8 of the mass of a hailstone of 2 cm in diameter, which implies that the mass of ice in each size interval is nearly the same. (2) By melting, the terminal fall velocity of a hailstone is lowered due to the meltwater torus which increases the cross-sectional area and therefore the drag on the falling particle. Shedding lessens the fall velocity further by reducing the particle mass. A reduction in terminal fall velocity, in turn, implies that the

particle spends a longer time in the cloud. Shedding also significantly affects the distribution of liquid water in a cloud, and the raindrop size distribution below the cloud.

16.3.2 Melting of Snow Flakes

The basic concepts developed in the previous section may also be applied to describe the melting behavior of snow flakes. However, before we formulate the necessary equations, we shall first point out some of the differences between melting hailstones and melting flakes, considering the field observations made by Knight (1979) and Fujiyoshi (1986), the laboratory observations with stationary snow flakes made by Matsuo and Sasyo (1981a), and the wind tunnel observations of Mitra *et al.* (1990c) with freely falling flakes. These show that, during melting of snow flakes, the meltwater does not form a coat around the flake as in the case of melting graupel and hailstones, but rather flows from the flake periphery to the linkages of the snow flake branches where it accumulates, leaving the ice skeleton of the flake essentially uncovered with water. Thus, the melting rate may be computed without considering an intermediate water film through which heat has to be conducted to melt the ice. In agreement with each other, all observations suggest the following four stages of melting:

During *Stage-1*, small drops of meltwater appear at the tips of the crystal branches. During *Stage-2*, the meltwater flows from the periphery to the linkages of the crystal branches as a result of capillary forces or surface tension effects which attempt to minimize the total surface energy of the system. As a result, the ice skeleton surface is essentially uncovered by meltwater. Although somewhat reduced in diameter, the main ice skeleton remains intact. During *Stage-3*, ice branches in the flake's interior begin to melt. This results in a structural rearrangement during which some branches bulge out and some flip inward. The crystal mesh changes from one with many small openings to one with only a few large ones. During *Stage-4*, the main ice frame suddenly collapses. The remaining unmelted ice portions become embedded inside the meltwater which pulls itself together to form a drop.

In agreement with Fukuta *et al.* (1986), Mitra *et al.* (1990c) showed that, during melting, freely falling snow flakes exhibit breakup and meltwater shedding only if the flakes have a very asymmetric structure and the relative humidity remains below about 70%. These results are in agreement with those of Matsuo and Sasyo (1981a), who found no breakup during the melting of flakes in air of relative humidity of 94%, and with those of Oralty and Hallett (1989), who found that melting dendrites did not breakup as long as the relative humidity was above 70%. However, breakup and drop shedding did occur at relative humidities below 70%. Snow crystals of plate-shape showed no shedding or breakup under any of the investigated conditions.

Assuming no shedding or breakup and considering that the snow flake remains at 0°C once melting had begun, Mitra *et al.* (1990c) suggest expressing the rate of

melting by a relation analogous to (16-80):

$$-\frac{\mathrm{d}m_i}{\mathrm{d}t} = \frac{4\pi C_i f_{L^*}}{L_m}\left(k_a[T_\infty(t) - T_0] + \frac{D_v L_e M_w}{\mathscr{R}}\left[\frac{\phi_v e_{sat,w}(T_\infty, t)}{T_\infty(t)} - \frac{e_{sat,w}(T_0)}{T_0}\right]\right), \tag{16-83}$$

where we assumed $\bar{f}_v = \bar{f}_h = f_{L^*}$, given by (13-88) and (13-89), and $L^* = \Omega_i/P_i$ ((13-81)). Mitra *et al.* (1990c) assumed the flake to have the shape of a thin oblate spheroid of axis vario $(AR)_i$ with $P_i = 2\pi a_i$, $\Omega_i = \pi a_i^2(2+\pi(AR)_i\varepsilon^{-1}\ln[(1+\varepsilon)/(1-\varepsilon)])$, $\varepsilon = [1-(AR)_i^2]^{1/2}$, $(AR)_i = b_i/a_i$, $a_i = [3m_i/4\pi(AR)_i\rho_i]^{1/3}$, $C_i = 0.8C_{i,0}$, and $C_{i,0} = a_i\varepsilon/\sin^{-1}\varepsilon$, where C_i is the capacitance of the flake. The density of the flake was assumed to vary linearly with m_w/m_F, where m_w is the mass of meltwater in the flake and m_F is the mass of the flake, with $\rho_i = 0.02$ g cm^{-3} for $m_w/m_F = 0$, and $\rho_i = \rho_w = 1$ g cm^{-3} for $m_w/m_F = 1$. The axis ratio was assumed to vary linearly with m_w/m_F, between $(AR)_i = 0.3$ for $m_w/m_F = 0$ and $(AR)_i = 1$ for $m_w/m_F = 1$. The relative capacitance $C_i/C_{i,0}$ was assumed to vary linearly with m_w/m_F, between $C_i/C_{i,0} = 0.8$ for $m_w/m_F = 0$ and $C_i/C_{i,0} = 1$ for $m_w/m_F = 1$. The variation of the fall velocity of a melting snow flake was empirically determined.

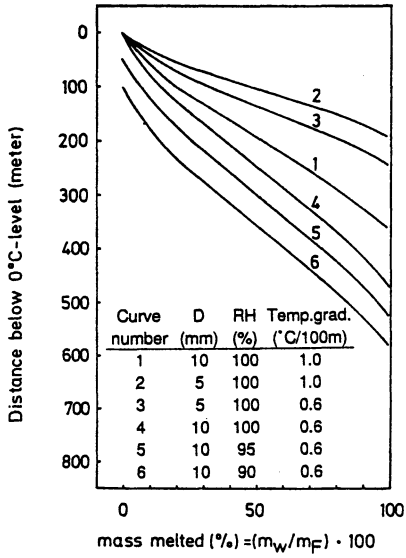


Fig. 16-13: Variation with distance below the 0°C level of the fractional mass melted for snowflakes of various diameters falling in still air of various relative humidities, and temperature gradients. (From Mitra *et al.*,1990, with changes.)

Some results of the computations of Mitra *et al.* (1990c) are given in Figure 16.13 in terms of snow crystal trajectories. We notice from this figure that, inside clouds of 100% relative humidity and a lapse rate of 0.6°C/100 m, 99% of the ice mass of a snow flake of 10 mm in diameter melts within a fall distance of 450 m. This fall distance is about 100 m longer if the relative humidity is only 90%. These results are consistent with radar observations, which show that typically the bright

band extends between 0 and 5°C and encompasses several hundred meters (see Figure 2.50). The results of Mitra *et al.* (1990c) are also consistent with the conclusions of Matsuo and Sasyo (1981b) derived from experiments with stationary snow flakes.

CHAPTER 17

CLOUD CHEMISTRY

In Chapter 8, we have shown that air contains a great variety of solid and liquid particles other than water drops and ice particles. We also know from our discussions in Chapters 6 and 9 that a considerable fraction of those serve as cloud condensation and ice forming nuclei, whereby they become incorporated into the cloud drops, raindrops and snow crystals. This removal process is usually referred to as *nucleation scavenging.* From our discussion in Chapters 10 and 14, we further expect that, in addition to nucleation scavenging, aerosol particles will be removed from the atmosphere by collision with cloud drops, raindrops and ice particles. This mechanism is referred to as *impaction scavenging.* We also have shown in Chapter 8 that, in addition to particles, air contains a great variety of gases other than water vapor and the permanent gases listed in Table 8.1. Since most of these have a finite solubility in water, they are expected to contribute further to the load of chemical species in cloud and precipitation water. The uptake of gases by cloud and precipitation particles is referred to as *gas scavenging.* Gases which particularly contribute to gas scavenging are the chemically reactive species such as CO_2, SO_2, NO_2, HNO_3, NH_3, HCl, H_2O_2, O_3, organic gaseous acids such as HCOOH (formic acid), CH_3COOH (acetic acid), and aldehydes such as HCHO (formaldehyde), as well as radicals such as OH, HO_2, NO_3, NO, Cl. Gases are not only scavenged by cloud and raindrops but also by snow crystals which adsorb them on their surface.

A detailed description of the physical and chemical processes which take place in the gas phase, inside water drops, and on the surface of ice particles, would go far beyound the scope of the present book. In the present chapter, we shall instead concentrate only on three major topics of cloud chemistry: (1) the chemical constituents found in cloud and rain water, and in the meltwater of snow, (2) the mechanisms by which these constituents enter the cloud and precipitation particles, both inside and below a cloud, referred to as *in-cloud* and *below-cloud scavenging,* and (3) the mechanisms by which these constituents are deposited on the ground. For a more indepth treatment of cloud and clear air chemistry, the reader is referred to the excellent texts of Junge (1963), Finlayson and Pitts (1986), Seinfeld (1986), and Warneck (1988) on atmospheric chemistry, and to the texts of Stumm and Morgan (1961), and Snoeyink and Jenkins (1980) on water chemistry. Also, in the present chapter, we have to refrain from discussing the numerous cloud-dynamic models in which chemical processes are considered. For information on these models, the reader is referred to the current literature, since no summary texts are available.

17.1 Concentrations of Water Soluble Compounds in Bulk Cloud and Rain Water, and in Bulk Water of Melted Snow

Most salts which are contained in atmospheric aerosol particles dissociate in water into ions. Ion formation also occurs if certain reactive gases such as CO_2, SO_2, HNO_3, NH_3, and HCl are dissolved in water. Chemical analysis of cloud and rain water, and of water of melted snow substantiates the presence of such ions. Ions typically found are: H^+, NH_4^+, Na^+, K^+, Ca^{2+}, Mg^{2+}, Cl^-, NO_2^-, NO_3^-, SO_4^{2-}, HSO_3^-, HSO_4^-, SO_3^{2-}, CO_3^{2-}, and HCO_3^-. Over the past several years, a large number of observations has been made on the chemical composition of bulk cloud and rain water, and bulk water of melted snow. It would be an impossible task to list all these observations and give credit to the respective observers. Therefore, we are forced to select from a wealth of information only a small set of what appears to us as a meaningful sample of observations across the world. Thus, in Table 17.1, ion concentrations are given for rain water collected in urban areas (a), maritime areas (b), and rural and remote areas (c). Table 17.2 lists the acidity of rain water collected in urban areas. In Table 17.3, selected values for the ion concentration in meltwater of fresh snow are listed. A comparison between ion concentrations in the meltwater of fresh snow and meltwater of rimed particles collected at the same location is made in Table 17.4. Selected values for the ion concentration in cloud and fog water are given in Table 17.5. Acidities of cloud and fog water are listed in Table 17.6, and a comparison between the composition of cloud water in different types of clouds and between cloud water and rain water is made in Tables 17.7 and 17.8. We shall see in a later section that hydrogen peroxide (H_2O_2) plays a significant role in cloud chemistry. We have therefore listed in Table 17.9 selected values for the concentration of H_2O_2 in cloud and rain water. For all undissociated species, the concentration is given in 10^{-6} mole liter^{-1}(μ mole liter^{-1}), while for all dissociated species the concentration is given in micro equivalent liter^{-1}(μ eq liter^{-1})$= 10^{-6}/z$ mole liter^{-1}, where z is the valency of the ion in the water.

The following general trends can be deduced from Tables 17.1 to 17.8: (1) Over land, the ion content, generally, is highest in rain which had fallen over urban areas and lowest in rain sampled on mountains. (2) Over land, the most prominent ions in rain water are NH_4^+, SO_4^{2-} and NO_3^-, with Cl^- and Na^+ contributing in proportion to a station's exposure to air trajectories from the ocean. (3) Over the ocean, the total ion content in rain water is higher than that over land. (4) Close to the ocean's surface, the prominent ions in rain water are Na^+, Cl^-, Mg^{2+}, with SO_4^{2-}, NH_4^+ and NO_3^- playing a lesser role. This finding is expected considering that sea salt particles in air are most prominent in the lower 2 to 3 km over the ocean, while sulfate particles dominate higher up. (5) Cloud water in nonprecipitating clouds whose drops are relatively small has a higher ion concentration than cloud water in precipitating clouds whose drops are relatively large. (6) Cloud water, particularly from stratus clouds, and fog water have ion concentrations which are larger than the ion concentration in precipitation water. (7) Most rain appears to be acidic. An exception to this are rains in certain parts of China and India where scavenged

TABLE 17.1a

Concentration of various salt ions in rain (the upper and lower numbers represent the range of concentrations observed, otherwise mean values); for: urban areas.

Location	Concentration (μeq liter^{-1})						Observer
	Na^+	Mg^{2+}	NH_4^+	Cl^-	NO_3^-	SO_4^{2-}	
Frankfurt a.M (Germany)	48	-	178	111	45	85	Georgii (1965)
Athens (Greece)	68	31	22	94	24	100	Dikaiakos *et al.* (1990)
Sao Paulo (Brazil)	21	-	44	27	45	13	Forti *et al.* (1990)
Long Island (N.Y.)	32	-	18	37	28	25	Lee *et al.* (1986)
Beijing (China)	77	-	224	59	81	337	Zhao *et al.* (1988)
Pasadena (Calif.)	25	7	33	29	75	60	Liliestrand & Morgan (1978)
Dhaharan (S. Arabia)	30	9	33	17	9	37	Ahmed *et al.* (1990)
	1026	288	125	1220	227	700	

TABLE 17.1b

As in Table 17-1a but for maritime areas.

Location	Concentration (μeq liter^{-1})						Observer
	Na^+	Mg^{2+}	NH_4^+	Cl^-	NO_3^-	SO_4^{2-}	
S. Indian Ocean	225	50	2	262	1.5	32	Vong (1990)
(Amsterdam Is.)	1467	322	28	1618	9	178	Likens *et al.* (1987) Keene *et al.* (1986) Galloway *et al.* (1982)
Bermuda	105	23	3	135	4	26	Keene *et al.* (1986)
	1071	250	55	1255	41	202	Galloway *et al.* (1989) Church *et al.* (1982)
Atlantic	100	-	-	58	11	15	Parungo *et al.* (1986a,b)
(20° - 30°N)	1086			1000	62	416	
Atlantic	38	10	9	37	19	14	Galloway *et al.* (1983)
(E. of US)	315	60	trace	333	trace	41	
Virginia Key (Florida, US Samoa)	84	-	-	-	8.2	3.9	Savoie *et al.* (1987)

TABLE 17.1c

As in Table 17-1a but for rural and remote areas.

Location	Concentration (μeq liter^{-1})						Observer
	Na^+	Mg^{2+}	NH_4^+	Cl^-	NO_3^-	SO_4^{2-}	
Rocky Mts. (3000m) (Colorado)	13	2	13	4	19	7	Grant & Lewis (1982)
Kilauea Mt. (1200 m) (Hawaii)	-	-	-	6 25	0.3 1.3	18 72	Harding & Miller (1982)
Kl. Feldberg (800 m) (Germany)	48	-	83	51	37	26	Georgii (1965)
Zugspitze (2966 m) (Germany)	48	-	48	46	13	11	Georgii (1965)
NW England	57	15	55	79	28	89	Harrison & Pio (1983)
Big Lake (Minnesota)	-	-	-	0.3 93	3 165	2 348	Guiang *et al.* (1984)
Poker Flat (Alaska)	0.5	0.1	1.3	2.7	1.9	7.2	Dayan *et al.* (1985)
Waga-Waga (S.E. Australia)	10.5	1.2	13	18	10	3.5	Ayres & Manton (1991)
Lake Ozette (Washington)	79	18	2	98	3	15	Vong (1990)
Katherine	7	2	2	12	4	6	Vong (1990), Galloway
(Australia)	65	15	19	85	21	25	*et al.* (1982)
San Carlos	2	0.5	2	3	3	3	Likens *et al.* (1987)
(Venezuela)	7	3	13	12	15	7	
Langen (Germany)	48	-	217	191	42	80	Georgii (1965)

TABLE 17.2

Acidity of rain water observed at various locations (range, or mean values).

Location	$pH = -\log [H^+]$	Observer
Albany (N.Y.)	4.2	Khwaja & Hussain (1990)
Sao Paulo (Brazil)	2.7 - 6.3	Forti *et al.* (1990)
Long Island (N.Y.)	4.3	Lee *et al.* (1986)
Beijing (China)	6.7	Zhao *et al.* (1988)
Pasadena (Calif.)	4.06	Liljestrand & Morgan (1978)
Dhaharan (S. Arabia)	5.1 - 7.2	Ahmed *et al.* (1990)
Sydney (Australia)	4.25 - 5.08	Ayers & Gilett (1984)
Big Lake (Minnesota)	4.83	Guyang *et al.* (1984)
Mt. Kilauea (1200 m) (Hawaii)	3.6	Harding & Miller (1984)
India (various stations)	5.5 - 9.0	Verma (1989)

TABLE 17.3

Concentration of various salt ions in the melt water of fresh snow observed at various locations, (the upper and lower numbers represent the range of concentration observed, otherwise mean values).

Location	Concentration (μeq liter^{-1})						Observer
	Na^+	Mg^{2+}	NH_4^+	Cl^-	NO_3^-	SO_4^{2-}	
E. Antarctica	0.2	0.1	0.1	0.4	0.2	0.2	Legrand &
	10.2	2.4	0.2	12.1	1.1	1.8	& Delmas (1985)
S. Calif. Mts.	trace	trace	trace	trace	1.5	trace	Gunz &
	115.7	9.9	8.1	128.2	15.8	17.2	Hoffmann (1990)
Scottish Highlands (Scotland)	76	18	-	111	41	55	Tranter *et al.* (1986)
Kl. Feldberg (Germany)	87	-	222	114	73	125	Georgii (1965)
Kashmir (India)	17	-	23	26	21	31	Kapoor & Paul (1980)
Hokkaido (Japan)	65	7	15	117	-	23	Takahashi (1963)
Abisho	13	-	6	15	1	0.5	Noone &
(Sweden)	141		22	164	15	9	Clarke (1988)
Hokkaido dendritic	65	7	15	117	trace	23	Takahashi
(Japan) collumnar	18	3	3	31	trace	8	(1963)

TABLE 17.4

Comparison between the concentration of various salt ions in the melt water of snow with the concentration in the melt water of graupel, (the upper and lower numbers represent the range of concentration observed, otherwise mean values).

Location	Concentration (μeq liter^{-1})					Observer
	Na^+	NH_4^+	Cl^-	NO_3^-	SO_4^{2-}	
Sierra Nevada (U.S.A.)						
fresh snow	2	1	1	1	1	Mitchell &
	21	13	15	14	8	Lamb (1989)
rimed ice part.	7	1	8	4	2	
	20	47	24	43	15	
California Mts.						
fresh snow	4.1	-	3.3	3.9	2.6	Berg *et al.*
rimed ice part.	10.3	-	9.5	16.7	10.5	(1991)
Hokuriku, sea level (Japan)						
fresh snow	174	7	194	-	-	Isono *et al.*
rimed ice part.	1217	28	1417	-	-	(1966)

TABLE 17.5a

Concentration of various salt ions in cloud water, observed at various locations; (the upper and lower numbers represent the range of concentration observed, otherwise mean values).

Location	Concentration (μeq liter^{-1})						Observer
	Na^+	Mg^{2+}	NH_4^+	Cl^-	NO_3^-	SO_4^{2-}	
Luquillo Mts.	-	9	-	154	-	18	Lazrus *et al.* (1970)
		103		2000		47	
over Charleston	2	-	24	<15	62	21	Daum *et al.* (1984)
(S. Carolina)	18		328	19	197	98	
White Face Mt.	4	3	32	2	69	52	Mohnen (1989)
(1620 m) N.Y.	11	4	89	5	110	140	
Mt. Mitchel	-	-	1.8	-	0.3	0.4	Clairborn &
(2006 m) N. Carolina			2039		2118	1709	Aneja (1991)
2 km above Hawaii	200	-	-	100	50	10	Parungo *et al.*
	400			700	200	40	(1982)
over Holland and	-	-	12	16	8	9	Römer *et al.*
Belgium			1055	475	860	200	(1985, 1983)
over cities of ETU	63	6	337	119	17	21	Petrenchuk &
	330	117	1594	1205	197	220	Drozdova (1966)
over ETU remote	30	4	33	60	2	3	Petrenchuk &
	104	21	100	180	13	46	Selezneva (1970)
Mt. Noribura	45	-	115	75	50	230	Okita (1968)
(Japan)	165	-	260	230	350	1250	

TABLE 17.5b

As in Table 17-5a but for fog water.

Location	Concentration (μeq liter^{-1})						Observer
	Na^+	Mg^{2+}	NH_4^+	Cl^-	NO_3^-	SO_4^{2-}	
Po-Valley	7	3	700	27	290	350	Fuzzi *et al.* (1988)
(Italy)	170	120	8100	1700	8200	6300	
Central plateau			101	63	44	20	Joos & Baltenberg
(Switzerland)			9215	4316	4420	859	(1991)
Sea fog (Japan)	165	38	-	129	-	66	Miyake (1948)
Albany	10	6	57	18	11	21	Fuzzi *et al.* (1984)
(N.Y.)	101	47	425	176	218	1360	
Zurich	11	2	1014	113	286	88	Johnson *et al.* (1987)
(Switzerland)	35	33	2793	11549	1293	225	
Los Angeles	12	7	370	56	130	62	Waldman *et al.* (1982)
(California)	5200	1380	9750	1100	10660	5060	& Munger *et al.*(1983)

TABLE 17.5c

Concentration of formic and acetic acid in rain water.

Location	Concentration μmole liter^{-1}		Observer
	$HCOO^-$	CH_3COO^-	
Amsterdam Isld.	3.8 - 19.6	0.8 - 9	Galloway *et al.* (1987)
San Carlos (Venezuela)	7.3 - 21.1	0.8 - 4.4	"
Katherine (Australia)	16.6 - 25.8	5.9 - 7.8	"
Hubbard Brook (New Hamp.)	0.2	2.8	Likens *et al.* (1983)
Ithaca (New York)	2.4	1.1	"
Bermuda	2.2	1.3	Galloway *et al.* (1989)
New Zealand	1.0	1.2	
Big Lake (Michigan)		1.5 - 5.2	Guiang *et al.* (1984)
Round Lake (Michigan)	<0.43 - 56	<0.83 - 33	Chapman *et al.* (1986)

TABLE 17.6

Acidity of cloud and fog water observed at various locations (range of values).

Location	$pH = -\log [H^+]$	Observer
Stratus over Los Angeles	2.4 - 3.6	Richards *et al.* (1983)
Fog, Carolina coast	3.4 - 5.2	Barrie *et al.* (1989)
Cloud, Mt. Mitchell (2038 m)	2.2 - 5.5	Kim & Aneja (1992)
Fog, Central plateau, Switzerland	2.9 - 7.1	Joos & Baltenberger (1991)
Cloud, 2 km over Hawaii	4.2 - 4.7	Parungo *et al.* (1982)
Fog, Albany, N.Y.	4.3 - 6.2	Fuzzi *et al.* (1984)
Fog, Zurich, Switzerland	2.1 - 6.0	Johnson *et al.* (1987)
Fog, Los Angeles	2.25 - 5.78	Waldmann *et al.* (1982)
Cloud over ETU	4.7 - 5.3	Petrenchuk & Drozdova (1966)

TABLE 17.7

Chemical composition of cloud and rain water as a function of cloud type (based on data of Petrenchuk & Drozdova (1966) and Petrenchuk & Selezneva (1970) over the Soviet Union (mean values).

Cloud type	Concentration (μeq liter^{-1})				
	Na^+	NH_4^+	Cl^-	NO_3^-	SO_4^{2-}
St, Sc (Over Kiev)	78	1367	222	196	476
St, Sc (rural)	30	133	63	16	59
Ns	30	50	57	6	28

TABLE 17.8

Comparison between the chemical composition of cloud water and the chemical composition of rain water. Based on data of Petrenchuk & Drozdova (1966) and Petrenchuk & Selezneva (1970) over the European territory of the Soviet Union (mean values).

	Concentration (μeq liter^{-1})					
	Na^+	Mg^{2+}	NH_4^+	Cl^-	NO_3^-	SO_4^{2-}
Non-precipitating cloud	48	50	94	51	10	63
Precipitation from clouds with frontal rain	13	17	28	23	2	16

TABLE 17.9a

Concentration of H_2O_2 in cloud water (range of values).

Location	Concentration (μmole liter^{-1})	Observer
Holland, at:		
2000-3000 m	9 - 59	Römer *et al.* (1983)
1500-2000 m	32 - 44	
1100-1400 m	< 1.2 - 45	
White Top Mt. (1689 m) (Tennessee)		
Summer	2.4 - 247	Olszyna *et al.* (1988)
Winter	0.3 - 130	
Los Angeles	11 - 142	Richards *et al.* (1983)
Great Dunfell Mt. (England)	1.2 - 110	Dollard *et al.* (1988) Radojevic *et al.* (1990)
Mt. Mitchell (2006 m) (N.Carolina)	0.2 - 219	Claiborn & Aneja (1991)
over Carolina coast	0.3 - 112	Barth *et al.* (1989)
Eastern US	< 1 - 127	Daum *et al.* (1984), Kelly *et al.* (1985)

TABLE 17.9b

As in Table 17-9a but for rain water.

Location	Concentration (μmole liter^{-1})	Observer
White Top Mt. (1689 m) (Tennessee)		
Summer	6.7 - 15.8	Olszyna *et al.* (1988)
Fall	<0.04 - 21.2	
Japan		
Summer	1.5 - 7.6	Yoshizumi *et al.* (1984)
Fall	0.8 - 1.2	
Clermont (California)	0.03 - 46.8	Kok (1980)
Dortmund (Germany)	2.8 - 32.8	Jacob *et al.* (1986)
Los Angeles area	0.01 - 145	Sakugawa *et al.* (1993)

clay particles dissolve OH^- ions into the cloud and rainwater. The lowest pH values are found in nonprecipitating clouds over cities and in city fogs. (8) The same ions which are found in cloud and rain water are also found in the meltwater of snow, graupel and hail with ion concentrations not significantly different from those in cloud and rain water. (9) Among the various snow crystal shapes, the highest salt concentrations are found in the meltwater of dendritic snow crystals as a result of their high collection efficiency for aerosol particles by impaction scavenging. (10) Rimed ice particles have generally higher salt contents than snow flakes or single snow crystals, due to the salt contributed by the cloud drops frozen on them. This finding has been confirmed by Borys *et al.* (1988), Colette *et al.* (1990), and by MacGregor *et al.* (1991). (11) Comparison between salt concentrations in rain water and in the meltwater of fresh snow made by Raynor and Hayes (1983), Dash (1987), Cadle *et al.* (1990), Reynolds (1983), Nagamoto *et al.* (1983), and Topol (1986) show that at a given location and time the concentration of NO_3^- in the meltwater of fresh snow often is found to be larger by a factor 1.5 to 2.5 than its concentration in rain; the reverse behavior was found for SO_4^{2-}.

17.2 Concentration of Water Insoluble Particles in Bulk Cloud and Rain Water and Bulk Water of Melted Snow

Rosinski (1966, 1967a), Rosinski and Kerrigan (1969), and Rosinski *et al.* (1970) studied the number concentration and size of water-insoluble particles in rain water, in individual raindrops, and in ice particles. Most frequently, the particles had diameters much less than 40 μm, but rain water collected from severe storms contained appreciable numbers of particles with even larger diameters. The particle concentration in rain water depended strongly on the collection time during the life cycle of the storm. Highest particle concentrations were always found at the onset of precipitation. Typical values are given in Table 17.10. Unfortunately, no counts were taken of particles with diameters less than 1 μm. Using a power law of the type $N \sim r^{-3}$, Vali (1968a) estimated by extrapolation that particles with diameters of 0.01 μm may be present in rain water in concentrations of 10^{10} to 10^{11} cm^{-3}. Also, Rosinski *et al.* (1970) observed that even at the cirrus cloud level, the number of water-insoluble particles in water from melted crystals is appreciable, ranging in their samples from 7.4×10^3 cm^{-3} to 8.4×10^6 cm^{-3} for particles with diameters larger than 2 μm. Particles designated as magnetic spherules were also present in water from melted cirrus ice crystals, and appeared in concentrations of 5 to 8000 cm^{-3}.

Ishizaka (1972, 1973) has made a detailed study of the amount and type of solid, water-insoluble material contained in rain and snow water collected in Japan. Water from melted snow which fell during the NW monsoon contained 4.6 mg of solid material per liter of snow water. Of this material, 70% by weight consisted of α-quartz, feldspar, illite, chlorite, kaolinite, halloysite, montmorillonite, and talc. Rain water from a storm which originated in central China, contained 1.3 $mg\ell^{-1}$ of solid material, of which about 20% consisted of α-quartz, feldspar, illite, chlorite, kaolinite, and vermiculite. Rain water collected during Typhoon 7002 was relatively clean and contained small amounts of α-quartz, α-crystobalite, and pyroxene, while

TABLE 17.10

Concentration (number of particles cm^{-3}) of water-insoluble particles in rain water and in water of melted graupel and hail, as a function of particle-size. (Based on data of Rosinski, 1966, 1967a; and of Rosinski and Kerrigan, 1969.)

Diameter of particle (μm)	1.5 to 3	3 to 15	15 to 50	50 to 100	100 to 200
Concentration (number cm-3)	2.6×10^4 to 2.7×10^6	7.4×10^3 to 2.5×10^5	2.1×10^2 to 1.2×10^4	9 to 1100	2 to 520

TABLE 17.11

Concentration of particulate carbon in rain water (Ducret & Cachier), and in snow (Noone & Clarke); observed at various locations (range of values).

Location	Concentration ranges (μg liter^{-1}) total carbon	black carbon	Observer
Swedish Arctic		4 - 60	Noone & Clarke (1988)
Savannah (Ivory Coast)	33 - 727	20 - 197	Ducret & Cachier (1992)
Equat. Forest (Congo)			"
Nov.- March	265 - 745	75 - 258	"
May - Oct.	34 - 430	11 - 75	"
Paris (France)	69 - 5868	27 - 1348	"
Mace Head (Ireland)	47 - 323	9 - 94	"
Seattle (Washington)	28 - 130	28 - 130	"
Sweden	20 - 600	20 - 600	"

rain water from a storm which had a relatively long trajectory over Japan contained large amounts of amorphous carbon and other oreanic material. Measurements of the particulate carbon content of rain water, made at various locations, are summarized in Table 17.11.

Measurements of the size distribution of water insoluble aerosol particles in rain water have been reported by Schütz and Krämer (1987), and Brinkmann (1994), who analyzed the water insoluble content of rain water collected at Mainz (Germany). They found that the aerosol particles in the size range 0.1 to 100 μm followed a Junge power law, $-\mathrm{d}N/\mathrm{d}\log r \propto 1/r^2$, as illustrated in Figure 17.1. Consistent with these observations, Malyschew *et al.* (1994) found that in rains over Darmstadt (Germany), $r = 4 \times 10^{-2}$ μm was the most frequent radius of water insoluble particles consisting mainly of calcium-silicate.

As expected from their capacity for nucleating snow crystals (see Section 9.2), water insoluble aerosol particles are found also in the meltwater of snow crystals. Those responsible for ice nucleation are usually found at or near the center of the snow crystal. Inspection of the surface of snow crystals by microscopy shows, however, that snow crystals scavenge during their life time a large number of additional particles by impacting them on their surface. Such studies have been carried out by Magono *et al.* (1974, 1975a,b, 1979). An example for the size distribution of such particles is given in Figure 17.2.

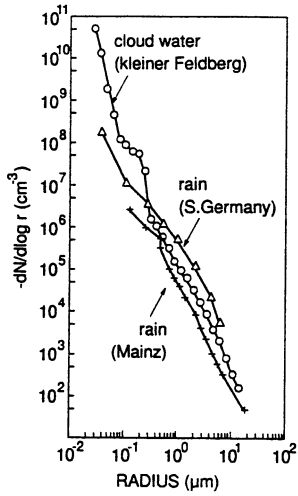


Fig. 17-1: Size distribution of water insoluble particles in rain water and cloud water, sampled at various locations. (From Brinkman, 1994, with changes.)

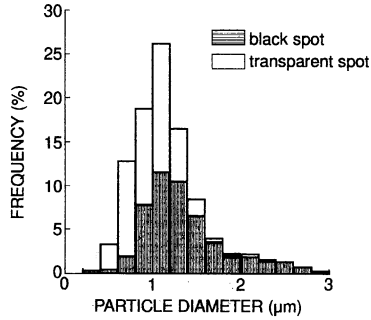


Fig. 17-2: Size distribution of aerosol particles observed on snow crystals, sampled in Sapporo, Japan. (From Magono *et al.*, 1975a,b, with changes.)

17.3 Concentration of Water Soluble Compounds in Individual Cloud and Raindrops

Until recently, not much has been known about the chemical constitution of individual cloud and raindrops. This is understandable considering the smallness of drops in atmospheric clouds, and the fact that chemical analysis typically requires a minimum sample volume much larger than a single drop. Fortunately, however, recent technology such as capillary zone electrophoresis (see Bächmann *et al.*, 1991, 1993a, 1992a; Bächmann and Steigerwald, 1993) has provided new methods by which chemical analysis of raindrops can be carried out with considerable accuracy on drop volumes down to a few nanoliters (a 100 μm radius drop has a volume of 4.2×10^{-9} liters).

Early attempts to study the chemical compositions of cloud and fog drops dealt with the residue of evaporated drops. These studies suggested a direct correlation between drop size and the size of the aerosol particles upon which they grew (Kuroiwa, 1951, 1956; Ogiwara and Okita, 1952; Isono, 1957; Naruse and Maruyama, 1971). The observations imply that large cloud drops develop by condensation from large salt particles, while small drops grow from small salt particles, thus supporting the results from the Köhler theory for equilibrium growth (see Table 6.2).

Chemical analysis of drop residues is exemplified in Table 17.12. We notice from this table that salt particles and particles derived from combustion together account for more than 50% of the residue left by evaporated cloud and fog drops. Again, sea salt is found to be more abundant near or over the ocean, while combustion products are more abundant inland. Similar results have been obtained by Ogiwara and Okita (1952). In addition, Naruse and Maryama (1971) have found that about 95% of all cloud and fog drops with diameters between 5 and 50 μm contain residue masses between 8×10^{-14} g and 9×10^{-13} g. The largest residue observed had a mass of 831×10^{-13} g. More quantitative results on the composition of cloud drops have become available through the field experiments of Gieray *et al.* (1993), Ogren *et al.* (1989, 1992), Heintzenberg *et al.* (1989), and Noone *et al.* (1988, 1989). Based on their field studies, the latter authors formulated a schematic which conceptually relates the salt concentration in cloud drops to their size. This schematic is illustrated in Figure 17.3. Cloud model studies of Flossmann *et al.* (1985, 1987), Flossmann and Pruppacher (1988), Flossmann (1991, 1994), Baumgarten (1990), Ahr (1988), and Roeloffs (1992) confirm this conceptual model (see Figure 17.4).

We notice from Figure 17.3 that the variation of salt concentrations in drops as a function of drop size can be subdivided characteristically into four size intervals:

In *size interval I*, the drop growth process involves drops typically between 1 and 10 μm radius. In this size range, the salt concentration decreases sharply with increasing size. This size interval involves drops which just have been activated. Therefore, the salt concentration in these drops reflects the salt concentration in the drops near the critical saturation ratio S_c given in Table 6.2. This table shows that, at S_c , the salt concentration varies inversely with drop size. Since new aerosol particles continuously enter the cloud by entrainment, this variation of the salt concentration with drop size will be maintained across this drop size interval

TABLE 17.12
Chemical composition of the residues from cloud and fog drops, observed at various locations.

	Kuroiwa (1951, 1953) (%)	Yamamoto and Ohtake (1953, 1955) (%)	(%)	Isono (1957, 1959a) (%)
sea salt	13	16	23	54
combustion products	51	36	30	22
soil material	28	23	20	14
unknown	8	25	27	10
Total	100	100	100	100

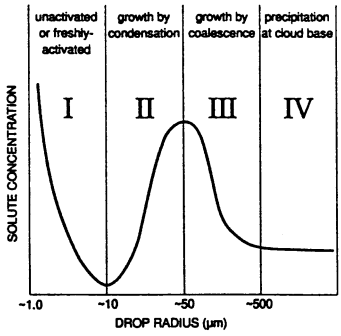


Fig. 17-3: Conceptual model for the variation with drop size of the salt concentration in cloud drops. (After Ogren *et al.*, 1992, with changes.)

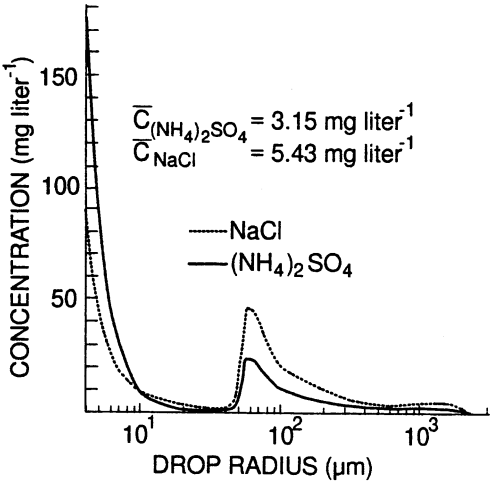


Fig. 17-4: Variation with drop radius of the concentration of NaCl and $(NH_4)_2SO_4$ in cloud drops, after 21 minute cloud life 500 m above cloud base near the cloud center. Based on a two-dimensional cloud model applied to case GATE-261 in the S. Atlantic. (From Flossmann, 1993 pers. comm., by courtesy of the author.)

at all the levels inside a cloud at which entrainment plays a role.

In *size interval II*, the drop growth process involves drops typically between 10 and 50 μm radius. In this size range, the salt concentration rises with increasing drop size. This size interval involves drops which, after their activation, continue to grow by vapor diffusion. For a given supersaturation and temperature, and for a given mass of salt in the drop, we may rewrite (13-28) as

$$\frac{\mathrm{d}V_{\mathrm{w}}}{\mathrm{d}t} = 4\pi a \frac{s_{\mathrm{v,w}} - y}{A + B}\,, \tag{17-1}$$

where V_{w} is the drop volume, y is given by (13-27), and A and B are constants as given in (13-28). If the salt mass in the drop is m_s, the variation of the salt concentration is readily found to be

$$-\frac{\mathrm{d}}{\mathrm{d}t}\left(\frac{m_s}{V_{\mathrm{w}}}\right) = -\frac{\mathrm{d}c_s}{\mathrm{d}t} = \frac{3}{a^2}\left(\frac{s_{\mathrm{v,w}} - y}{A + B}\right) c_s\,. \tag{17-2}$$

Since $c_s = 3m_s/4\pi a^3$, we find that $(-\mathrm{d}c_s/\mathrm{d}t) \propto 1/a^5$. This shows that the larger the drop size, the less rapid is its dilution. Since, generally, larger drops also have started off on larger salt particle masses (Kuroiwa, 1951, 1956; Ogiwara and Okita, 1952; Isono, 1957; Naruse and Maruyama, 1971) their salt concentration will be larger during diffusional growth than the salt concentration in smaller drops.

In *size interval III*, the drop growth process involves drops typically between about 50 and 500 μm radius. In this size range, drop growth is dominated by the collision and coalescence process which causes the higher concentrated drops to become diluted by collision with lower concentrated drops. Since large drops have a higher collision efficiency than small drops, their rate of dilution is larger so that during this growth stage the solute concentration in drops decreases with increasing drop size.

Size interval IV involves precipitation sized drops of a few hundred microns and larger inside clouds. Across this size interval, the salt concentration is rather uniform. This is due to the numerous collision and coalescence events which are necessary to form precipitation sized drops, yielding a rather well-mixed cloud water. This behavior has been confirmed by the observations of Bächmann *et al.* (1995) who studied the variation of the salt ion content with drop size at cloud base and at the ground, and by the cloud model studies of Flossmann (1993) (see Figure 17.4 for $200 \leq a_0 \leq 2000\,\mu$m).

In addition to the four size intervals which pertain to drops inside a cloud, we must distinguish a 'fifth' interval (see Figure 17.5) pertaining to drops which have sizes as those in interval IV but whose salt concentration is additionally determined by mechanisms which take place below the cloud. During their fall from cloud base to ground, drops experience an increase in solute concentration due to evaporation and below cloud scavenging of particle and gases. We shall show in Sections 17.4.2 and 17.5 that, in this size range, the efficiency with which particles and gases are scavenged by drops decreases with increasing drop size. In addition, evaporations of falling rain mainly effects the smallest drops. Thus, one expects that the solute concentration in raindrops which reach the ground decreases with

increasing drop size. This general trend has been verified by the field studies of Georgii and Wötzel (1970), Adams *et al.* (1986), Turner (1955), and by the cloud model studies of Flossmann (1994), and of Tsias (1996) (see Figure 17.6, curve a, assuming spontaneous drop breakup).

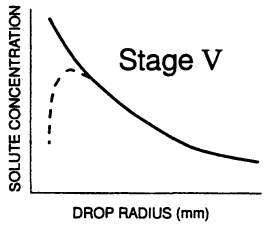


Fig. 17-5: Conceptual model for the variation with drop size of the salt concentration in raindrops observed on the ground.

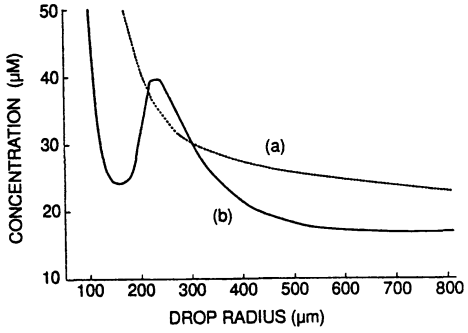


Fig. 17-6: Variation of the salt concentration in raindrops with drop size on the ground: (a) assuming spontaneous breakup of drops for $a_0 > 2.6$ mm, (b) assuming collisional breakup of drops after Low & List (1982a,b); using a $1\frac{1}{2}$-dimensional cloud model including condensation on a remote continental aerosol of $(NH_4)_2SO_4$, growth by collision and coalescence and drop breakup at a model time of 2400 sec. (Tsias, 1996, by courtesy of the author.)

In contrast to these, the field studies of Bächmann *et al.* (1992b, 1993b) showed that, during a precipitation event, the salt concentration across the raindrop spectrum evolves in time, and often develops a concentration maximum in drops of 200 to 300 μm radius (see Figure 17.7). Cloud model studies of Tsias (1996) show that this maximum is a indirect result of collisional breakup of large raindrops. During such a breakup, small fragment drops are formed which have the same low concentration as their larger parent drops. Since many of these fragment drops evade further capture, they produce a concentration minimum in the range $100 \leq a_0 \leq 200\,\mu$m (see Figure 17.6, curve b, where collisional breakup was included in the stochastic drop growth process). The relative concentration maximum thus occurs for slightly larger drops, which are not affected by this 'dilution'

mechanism. An additional effect causing a maximum in the variation of soluble concentration with rain drop size will be discussed at the end of Section 17.4.2.5.

Cloud model studies and field observations show that not only the salt concentration but also the chemical composition of cloud water is a function of drop size. Thus, Naruse and Maruyama (1971) showed that larger droplets contained sea salt particles, while the smaller drops contained $(NH_4)_2SO_4$. More recently, Munger *et al.* (1989), who analyzed two drop size fractions of California stratus clouds, found that the fraction consisting of the larger drop mostly contained Na^+, Cl^{2+} and Mg^{2+}, while the fraction with the smaller drops contained SO_4^{2-}, NO_3^-, and NH_4^+. The concentration of Cl^- was nearly equal in both size fractions. A similar result was predicted by the cloud model of Flossmann (1991), who demonstrated that an aerosol size distribution consisting of $(NH_4)_2SO_4$ in the small particle size range and NaCl in the large size range produced small drops which contained mainly $(NH_4)_2SO_4$, and larger drops which contained mostly NaCl.

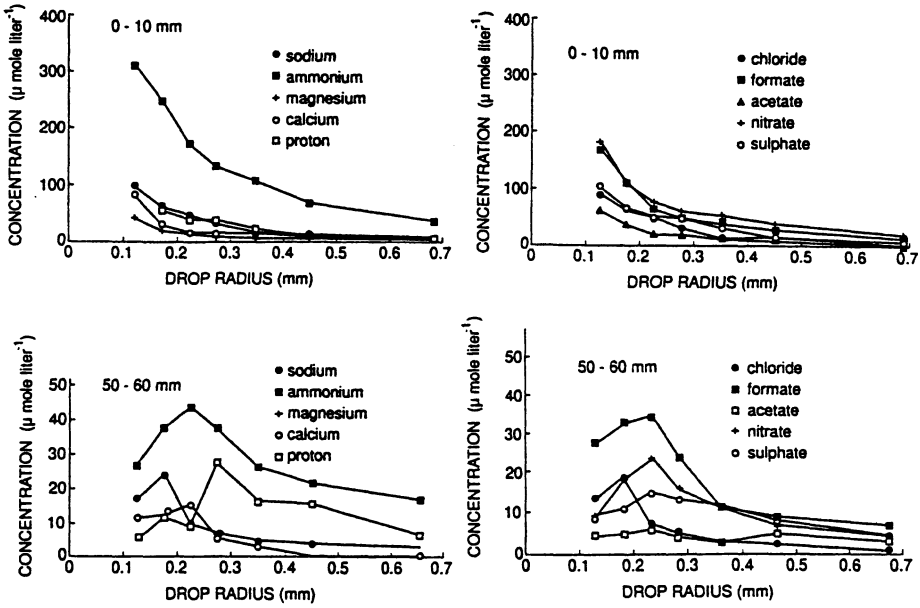


Fig. 17-7: Observed concentration of salt ions inside raindrops as a function of raindrop size and amount of rainfall, observed during rain on 31. May, 1992 at Darmstadt, Germany. (From Bächmann *et al.*, 1992b, 1993b, with changes.)

17.4 Scavenging of Aerosol Particles by Cloud Drops, Raindrops and Ice Particles

As noted earlier, aerosol particles become incorporated into cloud drops by the mechanisms of nucleation and impaction scavenging. Cloud modeling demonstrates that, together, both mechanisms remove a substantial fraction of the aerosol particle population and incorporate it into the cloud water. This is illustrated by

Figure 17.8 for a maritime aerosol subjected to nucleation and impaction scavenging inside a rising, entraining air parcel. We note from this figure that after 27 minutes of model time, about 94% of the total original aerosol particle number concentration has become scavenged. The aerosol particles remaining unscavenged, called the *cloud-interstitial aerosol*, are those with radii typically less than 0.1 μm.

Once incorporated in cloud water, the scavenged aerosol mass becomes redistributed inside the cloud water due to collision and coalescence between drops. This process is illustrated in Figure 17.9 for the same maritime aerosol for which Figure 17.8 was obtained. We note from this figure that the distribution function $g_{AP,d}$ for the aerosol mass inside the drops per m^3 air follows closely the distribution function g_w (see Section 13.2.2) for the cloud water. This implies that the scavenged aerosol mass becomes redistributed inside the cloud water in such a fashion that the main scavenged aerosol mass remains associated with the main water mass. Since the latter encompasses the precipitation sized drops, the precipitation efficiency of a cloud (given by the fraction of cloud water which formed by condensation eventually arrives as rain on the ground) will eventually control the fraction of the scavenged aerosol mass which will become returned to the ground.

In the following sections, we shall attempt to describe the mechanisms which are responsible for aerosol particle scavenging. Our discussion of the first mechanism, nucleation scavenging, will be relatively brief, since we have already considered heterogeneous drop and ice crystal formation in Chapters 6, 9, and 13. The section on nucleation scavenging will then be followed by a longer discussion on the mechanisms which are responsible for impaction scavenging.

17.4.1 Nucleation Scavenging

Field experiments (Georgii *et al.*, 1971; Schumann *et al.*, 1986; Hudson, 1993, a.o.) have demonstrated that the concentration of aerosol particles in the atmosphere become drastically reduced at the levels where clouds form. This indirectly verified the involvement of aerosol particles in the process of cloud drop nucleation. As mentioned in the introduction to this chapter, this mode of aerosol removal is therefore termed *nucleation scavenging.*

The contribution of nucleation scavenging to the total uptake of aerosol particles by a cloud can be conveniently computed by a detailed formulation of the condensation process which tracks the evolution of the aerosol size spectrum in the air and the aerosol particle mass in the cloud drops. This procedure has been followed in numerous cloud model studies (Flossmann *et al.* 1985, 1987; Flossmann, Pruppacher, 1988; Flossmann, 1991, 1994; Baumgarten, 1990; Ahr, 1988). A more recent computation (Wurzler *et al.*, 1994) is illustrated in Figure 17.8. Since nucleation scavenging completely dominates impaction scavenging at the beginning of cloud formation, we notice that after 200 seconds (Figure 17.8b), nucleation scavenging had removed about 75% of the aerosol particle population present in the air. Subsequent rise in supersaturation affected by further cooling as well as by collision and coalescence between drops, had removed another 20% of the aerosol particle population within 1400 seconds. In this manner, the 'cut-off' in the aerosol particle spectrum is shifted from about 0.3 μm radius to about 0.08 μm radius. Ahr

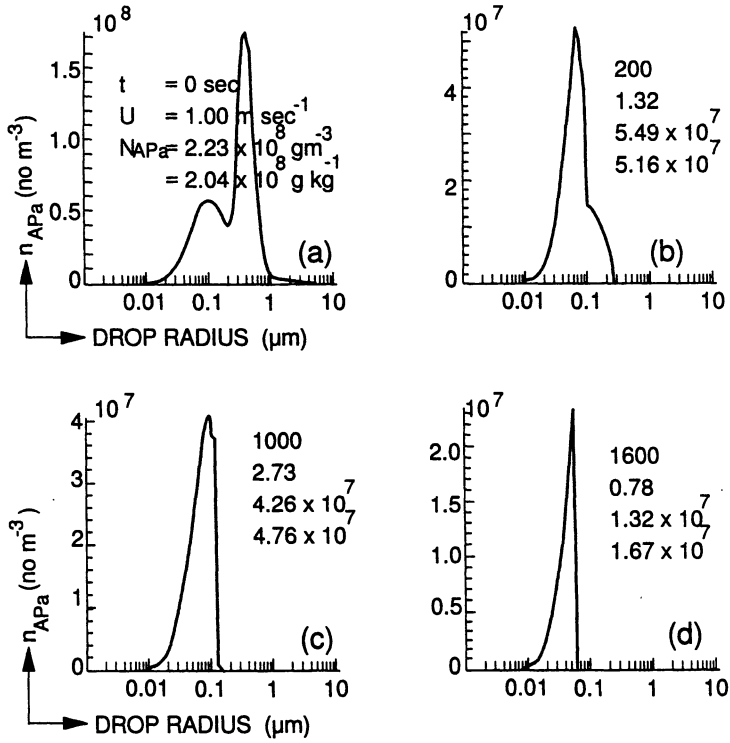


Fig. 17-8: Variation with time of the aerosol particle size distribution in air per logarithm radius interval during cloud formation. (a) original size distribution in air; (b), (c), (d) time evolution of the cloud interstitial aerosol spectum. For the maritime spectrum of Figure 8-28a, curve 4; first mode: $(NH_4)_2SO_4$, 2^{nd} mode 10 % $NaNO_3$, 90 % NaCl; $N_{AP,a}$ = 223 cm^{-3}; air parcel model. (From Wurzler, 1995, with changes.)

et al. (1989) showed that the cut-off of 'wet' aerosol particles (i.e., aerosol particles at the critical supersaturation) is independent of the chemical composition of the particles and depends only on the prevailing supersaturation in the cloud. However, with respect to the original spectrum of 'dry' aerosol particles, the cut-off becomes diffuse and depends on the prevailing supersaturation as well as on the chemical composition of the particles. This is so because aerosol particles of different chemical composition may have the same activation radius (see Figure 17.10). Thus, increasing chemical heterogeneity of the condensing aerosol will cause the cut-off to become less distinct. This effect has been verified by the field observations of Noone *et al.* (1992b) in fogs formed in heavily polluted air. Their observations are illustrated in Figure 17.11, which shows that particles with radii less than 0.15 μm were essentially not affected by nucleation scavenging. With increasing size, the scavenged fraction increased gradually to about 50% for particles of radius less than 0.25 μm, to 100% for particles less than 0.4 μm.

Additional field studies of nucleation scavenging and the cloud interstitial aerosol

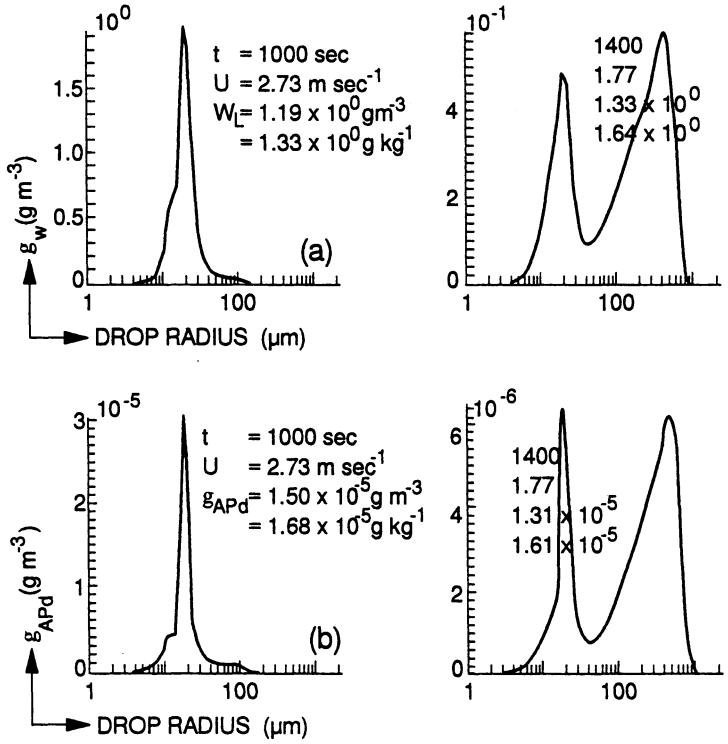


Fig. 17-9: Variation with time: (a) of the cloud drop mass distribution function, and (b) of the distribution function for the aerosol mass inside the cloud water, per logarithm drop radius interval, for the case defined in Figure 17-8. (From Wurzler, 1995, with changes.)

have been carried out by Scott and Laulinen (1979), Knollenberg (1981), Radke (1983), Sievering *et al.* (1984), Hudson (1984, 1993), Hegg *et al.* (1984), Leaitch *et al.* (1986), Brink *et al.* (1987), Daum (1988), Hallberg *et al.* (1992), and Martinsohn *et al.* (1992). These studies confirm the existence of a 'cut-off' in the aerosol particle spectrum inside a cloud and an associated cloud interstitial aerosol. Such a cut-off was found to be particularly distinct in clouds with relatively large updraft, and associated large supersaturations, and a relatively small number concentration of aerosol particles of rather uniform chemical composition. In such clouds, 75 to 90% of the original AP number concentration were found to be depleted by nucleation scavenging.

The effects of nucleation scavenging by snow crystals has not been studied in the field. On the other hand, some cloud model results of Alheit *et al.* (1990) show convincingly that, in mixed clouds, scavenging by ice nucleation can be neglected in comparison to drop nucleation scavenging.

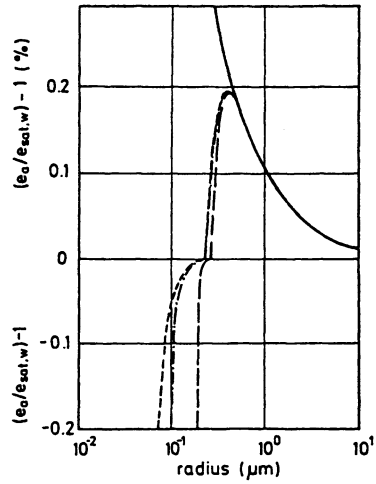


Fig. 17-10: Equilibrium growth curves (Köhler curves) with the same activation radius for salt solution drops evolving from $(NH_4)_2SO_4$ particles: short dashed line for $\epsilon_m = 0.5$, $r_N = 0.052$ μm, long dashed line for $\epsilon_m = 0.01$, $r_N = 0.187$ μm, dash-dot line for $\epsilon_m = 0.1$, $r_N = 0.089$ μm; continuous line: Kelvin curve. (From Ahr *et al.*, 1989b, with changes.)

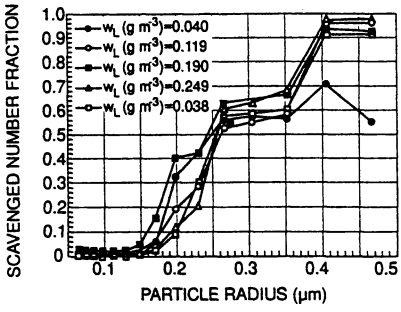


Fig. 17-11: Fraction of aerosol particles scavenged by nucleation scavenging during a fog event in the Po Valley, Italy. (From Noone *et al.*, 1992, with changes.)

17.4.2 Impaction Scavenging

We shall now turn our attention to the various wet-removal processes by which aerosol particles become attached to drops and ice particles due to collision. In our discussion, we shall consider the attachment mechanisms of (1) convective Brownian diffusion, (2) thermophoresis and diffusiophoresis, (3) turbulent shear and turbulent inertial capture, and (4) gravitational or 'inertial' capture.

From (11-58), we see that the loss rate of aerosol particles of radius r per unit volume of air by virtue of impaction scavenging by cloud drops is given by

$$-\frac{\partial n(r,t)}{\partial t} = n(r,t)\int_0^\infty K(r,a)n_{\mathrm{d}}(a,t)\,\mathrm{d}a\,, \tag{17-3}$$

where a denotes drop radius, and $n_{\mathrm{d}}(a,t)\,\mathrm{d}a$ is the number of drops per unit volume of air at time t in the size interval a to $a+\mathrm{d}a$. The fractional depletion rate of the aerosol concentration by scavenging is called the *scavenging coefficient*, Λ. From (17-3), we thus have

$$-\frac{1}{n}\frac{\partial n(r,t)}{\partial t} \equiv \Lambda(r,t) = \int_0^\infty K(r,a)n_{\mathrm{d}}(a,t)\,\mathrm{d}a\,. \tag{17-4}$$

The scavenging problem is therefore basically one of determining the collection kernel $K(r,a)$ for the various attachment processes of interest. If the drop distribution does not vary with time, then, Λ becomes constant in time, and we have the simple result that

$$n(r,t) = n(r,0)\exp[-\Lambda(r,t)]\,. \tag{17-5}$$

17.4.2.1 *Scavenging by Convective Brownian Diffusion*

Stationary drops capture particles by simple Brownian diffusion. The discussion of Section 11.5 is therefore directly applicable to this process. From (11-37), we then find that the loss rate of aerosol particles due to Brownian collision with a stationary drop is given by the flux of particles to the drop, i.e., opposite to the radial coordinate

$$-\left(\frac{\mathrm{d}N}{\mathrm{d}t}\right)_B = -J_0 = 4\pi a D_p n_\infty\,, \tag{17-6}$$

where n_∞ is the concentration of particles far from the drop. Often, however, the fall velocity of a drop is large enough so that there is a significant enhancement of the diffusion rate caused by the convection of particles relative to the drop. We shall therefore briefly discuss the mechanism of scavenging by forced convective diffusion.

Suppose particles in concentration n are transported by Brownian motion and by virtue of being suspended in a medium moving with velocity $\vec{\mathrm{u}}$. The particle current density is

$$\vec{j} = -D_p\nabla n + n\vec{\mathrm{u}}\,, \tag{17-7}$$

so that, for the case of a steady state and constant diffusivity, the condition of particle continuity ($\nabla \cdot \vec{j} = 0$) yields the following governing equation for n:

$$\vec{u} \cdot \nabla n = D_p \nabla^2 n \,. \tag{17-8}$$

This is the steady state convective diffusion equation. To obtain (17-8), we have assumed the flow to be incompressible.

Let us now discuss the use of this equation in estimating the rate of attachment of small aerosol particles to a spherical drop of radius a falling with velocity $\vec{U}_\infty$. If we adopt the usual point of view of a reference frame moving with the drop (regarded as a rigid sphere), the boundary conditions for the problem are $\vec{U}|_{\text{drop}} = 0$, $\vec{u}|_\infty = -\vec{U}_\infty$, $n|_{\text{drop}} = 0$, and $n|_\infty = n_\infty$, where n_∞ is the concentration of particles far from the drop. On using the same simple scaling arguments which demonstrated the significance of the Reynolds number in Section 10.2.1, we find the relative strengths of the particle diffusion and convective transport processes are measured by the dimensionless Péclet number, N_{Pe}:

$$\frac{|\, \vec{u} \cdot \nabla n \,|}{|\, D_p \nabla^2 n \,|} \propto \frac{U_\infty n_\infty / d}{D n_\infty / d^2} = \frac{U_\infty d}{D_p} \equiv N_{\text{Pe},p} \,, \tag{17-9}$$

where $d = 2a$ is the drop diameter. (Although the radius a would be a more natural choice for the characteristic length in (17-9), we use d in order to conform with the conventional definition of N_{Pe} without having to keep track of factors of two.) Also, the Péclet number may be expressed in terms of the Reynolds number and the particle Schmidt number, $N_{\text{Sc},p}$:

$$N_{\text{Pe},p} = N_{\text{Sc},p} N_{\text{Re}} \,, \quad \text{with} \quad N_{\text{Sc},p} \equiv \frac{\nu_a}{D_p} \,. \tag{17-10}$$

As can be seen from Table 11.1, the Schmidt number for aerosols is generally quite large. Therefore, the Péclet number for convective diffusion of aerosols will be large for essentially all cloud droplets, even though they may have very small Reynolds numbers. We recall from Section 10.2.2.3 that, for $N_{\text{Re}} \gtrsim 1$, there is a *momentum boundary layer* of characteristic thickness $\delta_u \sim N_{\text{Re}}^{-1/2}$. From the analogous definitions of N_{Re} and N_{Pe} (from (17-9) and (17-10) we see N_{Pe} is the Reynolds number for particle diffusion) and the fact that $N_{\text{Sc},p} \gg 1$, we can anticipate finding a *diffusion boundary layer*, whose characteristic thickness δ_D is a monotonic decreasing function of N_{Pe}. At distances from the drop surface smaller than δ_D, diffusion dominates, while beyond δ_D convection controls the particle concentration.

Let us now use scaling arguments to find the form of δ_D for the case of small drops, with $N_{\text{Re}} \ll 1$. The procedure consists simply of exploring the consequences of the fact that both sides of (17-8) have comparable magnitudes at a distance δ_D from the drop surface. Consider a small region of the flow where δ_D is assumed to be well-defined, letting x denote distance along the drop surface in the direction of the local flow, and y denote distance normal to the surface. Then, we may write $\vec{u} \cdot \nabla n = u_x \partial n / \partial x + u_y \partial n / \partial y$. Both terms on the right side are of comparable

magnitude, by the condition $\nabla \cdot \vec{u} = 0$. So it suffices to estimate the term $u_x \partial n/\partial x$ at $y = \delta_D$. For small N_{Re} flow, u_x will scale up to the free stream value in a characteristic distance $y \sim d$, so that, if $\delta_D \ll d$, we expect $u_x(y = \delta_D) \approx U_\infty(\delta_D/d)$, i.e., the velocity shear is linear for small y. On the other hand, the characteristic length for the gradient in x is just d. So we estimate $u_x \partial n/\partial x \sim U_\infty n_\infty \delta_D/d^2$ at $y = \delta_D$. For the right side of (17-8), we have the obvious estimate $D_p \nabla^2 n \approx D_p \partial^2 n/\partial y^2 \sim D_p n_\infty/\delta_D^2$ at $y = \delta_D$. On equating these estimates, we find $\delta_D^3 \sim D_p d^2/U_\infty$, or

$$\frac{\delta_D}{d} \sim N_{\mathrm{Pe},p}^{-1/3}, \quad N_{\mathrm{Re}} \ll 1. \tag{17-11}$$

According to (17-11), the concentration gradient in the neighborhood of the droplet and, hence, the particle flux to it, will be enhanced by a factor proportional to $N_{\mathrm{Pe},p}^{1/3}$ over the magnitude due to pure diffusion, for $N_{\mathrm{Pe},p} \gg 1$. Therefore, an interpolation formula which gives a fairly good approximation to the total convective Brownian diffusion flux $J_{CD} = \int_s \vec{j}_{CD} \cdot \mathrm{d}\vec{S}$ for arbitrary $N_{\mathrm{Pe},p}$ and $N_{\mathrm{Re}} \ll 1$ is

$$J_{CB} = J_0(1 + A N_{\mathrm{Pe},p}^{1/3}), \quad N_{\mathrm{Re}} \ll 1, \tag{17-12}$$

where J_0 is the pure steady state diffusive flux given by (17-4) assuming $r \ll a$ and A is a dimensionless positive constant. The analyses of convective diffusion to a sphere in Stokes flow by Friedlander (1957), Baird and Hamielec (1962), Levich (1962), and Ruckenstein (1964) have resulted in the estimates $A = 0.45$, 0.50, 0.50, and 0.52, respectively.

For larger droplets with $N_{\mathrm{Re}} > 1$, the results are modified somewhat. For this case there exists a momentum boundary layer as well as the diffusion boundary layer. The relevant inequalities are $\delta_u \ll d$ and $\delta_D \ll \delta_u$, the latter one arising from $N_{\mathrm{Sc}} \gg 1$. Therefore, in estimating the convective term $u_x \partial n/\partial x$, we note that u_x scales up to U_∞ in a distance $y \sim \delta$, rather than $y \sim d$ as before, so that $u_x \partial n/\partial x \sim U_\infty n_\infty \delta_D/d\delta_u$ at $y = \delta_D$. The diffusion term in (17-8) is still characterized by $D_p \nabla^2 n = D_p n_\infty/\delta_D^2$, which, on being set equal to the convective term, leads to $U\delta_D/d\delta \sim D_p/\delta_D^2$, or

$$\frac{\delta_D}{\delta_u} \sim N_{\mathrm{Sc},p}^{-1/3}, \quad \text{(17-13a)} \qquad \frac{\delta_D}{d} \sim N_{\mathrm{Sc},p}^{-1/3} N_{\mathrm{Re}}^{-1/2}. \tag{17-13b}$$

It is thus seen that for aerosol particle diffusion, δ_D is typically less than one-tenth the thickness of the momentum boundary layer. The corresponding interpolation formula for the total convective particle flux to a falling drop has the form

$$J_{CB} = J_0(1 + B N_{\mathrm{Re}}^{1/2} N_{\mathrm{Sc},p}^{1/3}), \qquad N_{\mathrm{Re}} \gg 1. \tag{17-14}$$

Unfortunately, no experiments are available to verify the low Reynolds number result (17-12) and the constants of proportionality determined by Friedlander, Baird and Hamielec, Levich, and Ruckenstein. On the other hand, experiments carried out at high Reynolds numbers by Steinberger and Treybal (1960), Rowe *et al.* (1965) and Gilbert *et al.* (1972) showed that, over limited Reynolds number

ranges, one indeed may express the convection effect in accordance with (17-14) for $0.6 \leq N_{\mathrm{Sc},p} \leq 3 \times 10^3$, the value of B ranging between 0.25 and 0.50 due to experimental scatter. Slinn and Hales (1971) and Young (1974) have used the value $B = 0.30$, which derives from the correlation of data presented by Ranz and Marshall (1952) (also in Bird *et al.*, 1960). In Young's study, aerosol collection rates for $10\,\mu$m droplets are presented. This corresponds to the case $N_{\mathrm{Re}} \ll 1$, so that, in principle, it would have been better to use an expression of the form of (17-12) rather than (17-14). However, the quantitative differences are probably not significant.

Numerical computations of convective diffusion to a sphere have been carried out bv Woo (1971) for $1 \leq N_{\mathrm{Re}} \leq 300$ and $0.25 \leq N_{\mathrm{Sc},p} \leq 5$. Woo found a flux enhancement factor of $J_{CB}/J_0 \approx \mathrm{a}N_{\mathrm{Sc},p}^{\mathrm{b}}$ where $\mathrm{a} = 1.552 + 3.41 \times 10^{-2} N_{\mathrm{Re}} - 1.17 \times 10^{-4} N_{\mathrm{Re}}^2 + 1.83 \times 10^{-7} N_{\mathrm{Re}}^3$ and $\mathrm{b} = 0.198 N_{\mathrm{Re}}^{0.096}$. Unfortunately, Woo did not extend his calculations to higher values of $N_{\mathrm{Sc},p}$.

We have mentioned in Chapter 13 that it is customary in cloud physics literature to describe the enhancement of the water vapor flux due to the motion of the air around a falling drop in terms of the mean ventilation coefficient $\bar{f}_v$ given by (13-60) and (13-61). In the present context, the mean ventilation coefficient $\bar{f}_p$ for the particle flux is simply the ratio J_{CB}/J_0. Due to the lack of reliable values for $\bar{f}_p$ for the particle size range of atmospheric interest ($0.01 \leq r \leq 10\,\mu$m, i.e., $9.5 \times 10^2 \leq N_{\mathrm{Sc},p} \leq 1.2 \times 10^7$ (see Table 11.1), it has become customary to assume without further proof that $\bar{f}_p \approx \bar{f}_v$. We nevertheless shall continue to use $\bar{f}_p$ in all the forthcoming equations. Supposing that the drops follow the size distribution $n_d(a,t)$, the scavenging coefficient and collection kernel for convective Brownian diffusion may thus be written as

$$\Lambda_{C,B}(r,t) = 4\pi D_p \bar{f}_p \int_0^\infty a n_d(a,t)\,\mathrm{d}a\,, \tag{17-15}$$

and

$$K_{CB}(r,a) = 4\pi D_p \bar{f}_p a\,. \tag{17-16}$$

As a simple example, we shall obtain an approximate expression for Λ_{CB} assuming $r \ll a$, negligible convective enhancement of Brownian diffusion, and assuming the Khrgian-Mazin drop spectrum (see Section 2.1.4). The result is

$$\Lambda_{CB} = 4\pi D_p \int a n_{\mathrm{d}}(a)\,\mathrm{d}a \approx \frac{1.35 \mathrm{w}_L D_p}{\bar{a}^2}\,, \tag{17-17}$$

where w_L is the liquid water content of the cloud in g cm^{-3}, and a is average drop radius in cm (Sax and Goldsmith, 1972). Considering (17-5), we see that the corresponding half-life of the aerosol particles (the time $t_{1/2}$ such that $n(t_{1/2}) = n_\infty/2$ is

$$t_{1/2} \approx \frac{(\ln 2)\bar{a}^2}{1.35 \mathrm{w}_L D_p}\,. \tag{17-18}$$

For example, for $\mathrm{w}_L = 10^{-6}$ g cm^{-3}, $\bar{a} = 10\,\mu$m, and $D_p = 2.3 \times 10^{-4}$ cm^2 sec^{-1} (corresponding to $r = 0.01\,\mu$m, $T = -5°$, and $p = 600$ mb), we get $t_{1/2} \approx 38$ min;

for 15°C and 1000 mb, $D_p = 1.6 \times 10^{-4}$ cm^2 sec^{-1} and $t_{1/2} \approx 55$ min. Thus, if we assume that the total concentration of Aitken particles is typically about 10^4 cm^{-3}, a number of this magnitude is predicted to be scavenged by the cloud per cm^3 of cloud air, corresponding to $O(10^{10})$ particles absorbed per cm^3 of cloud water, within the span of one hour. These estimates are consistent with the field observations of Rosinski (1966, 1967a) as extrapolated to small particles by Vali (1968a).

17.4.2.2 *Scavening by Thermophoresis and Diffusiophoresis*

The phenomena of thermo- and diffusiophoresis were predicted by Stefan (1873) and subsequently observed by Facy (1955, 1958, 1960). Quantitative studies using various experimental techniques have been carried out by Goldsmith *et al.* (1963), Goldsmith and May (1966), Waldmann and Schmitt (1966), and Vittori and Prodi (1967). The theoretical aspects of these mechanisms have been discussed in detail by Waldmann and Schmitt (1966), Slinn and Shen (1970), Slinn and Hales (1971), and Derjaguin and Yamalov (1972).

Thermophoresis is the name given to the motion of particles caused by a kind of thermally induced (radiometric) force, which arises from the non-uniform heating of particles due to temperature gradients in the suspending gas. This phenomenon naturally depends strongly on the Knudsen number of the particles. For $N_{\mathrm{Kn}} \gg 1$ the mechanism of thermophoresis is relatively simple: The temperature gradients cause the gas molecules to deliver a greater net impulse on the 'warm' side of the particle than on the 'cold' side, thus driving it in the direction of colder gas temperatures. For $N_{\mathrm{Kn}} \ll 1$, the organization of this mechanism is somewhat more involved. In this limit, we consider a portion of the aerosol particle surface layer, large compared to λ over which a temperature gradient is established. The layer of gas closest to this surface will acquire a temperature gradient which conforms approximately to that of the surface, which means that gas molecules from the hotter direction will impart a greater impulse to the surface locally than those from the colder direction. Thus, the entire particle can experience a force along the temperature gradient in the gas.

The mechanism of thermophoresis involves gas motion relative to the particle surface, which means theoretical models for the case $N_{\mathrm{Kn}} \ll 1$ must abandon the usual hydrodynamic boundary condition of no slip. What is often done for this case is to assume the flow is described by continuum hydrodynamics with slip-flow boundary conditions. An analysis of this type, which appears to yield results of widest application, is due to Brock (1962), who obtained the following approximate expression for the thermophoretic force $\vec{F}_{\mathrm{Th}}$ on a particle of radius r in air:

$$\vec{F}_{\mathrm{Th}} = -\frac{12\pi\eta_{\mathrm{a}} r(k_{\mathrm{a}} + c_t k_p N_{\mathrm{Kn}})k_{\mathrm{a}}\nabla T}{5(1 + 3c_m N_{\mathrm{Kn}})(k_p + 2k_{\mathrm{a}} + 2c_t k_p N_{\mathrm{Kn}})p}, \tag{17-19}$$

where p and $-\nabla T$ denote gas pressure and temperature gradient, k_{a} and k_p are the air and particle thermal conductivities, η_{a} is the dynamic viscosity of air, and c_m and c_t are phenomenological coefficients known as the 'isothermal slip' coefficient and the 'temperature jump' coefficient. These coefficients depend on T as well

as air and surface properties. Comparison with other theories and experiments indicates that (17-19), which includes friction slip, is fairly accurate through the entire inter $0 < N_{\mathrm{Kn}} < \infty$, except for a high conductivity aerosol. Further details may be found in Waldmann and Schmitt (1966) and Hidy and Brock (1970).

For a quasi-steady state, the thermophoretic velocity is easily obtained by setting $\vec{F}_{\mathrm{Th}}$ equal to the slip-flow corrected Stokes drag, $6\pi\eta_{\mathrm{a}} r\vec{\mathrm{v}}_{\mathrm{th}}(1+\alpha N_{\mathrm{Kn}})^{-1}$, acting on the particle. Therefore, the thermophoretic velocity of a particle in air may be written as

$$\vec{\mathrm{v}}_{\mathrm{Th}} = -\frac{Bk_{\mathrm{a}}\nabla T}{p}\,, \tag{17-20a}$$

where

$$B = \frac{0.4(1+\alpha N_{\mathrm{Kn}})(k_{\mathrm{a}} + 2.5k_p N_{\mathrm{Kn}})}{(1+3N_{\mathrm{Kn}})(k_p + 2k_{\mathrm{a}} + 5k_p N_{\mathrm{Kn}})}\,, \tag{17-20b}$$

and where α is given by (11-16). In (17-20b), the values $c_t = 2.5$ and $c_m = 1.0$ have been adopted, following Brock (1962). Note that $\vec{\mathrm{v}}_{\mathrm{Th}}$ is proportional to and in the direction of the heat flux vector, $\vec{j}_h = -k_{\mathrm{a}}\nabla T$ (see Section 13.1.2).

With these results, we may write down the thermophoretic flux of particles in concentration n_∞ to a stationary evaporation drop of radius a. Since the thermophoretic particle flux vector is $\vec{j}_{\mathrm{Th}} = n_\infty \vec{\mathrm{v}}_{\mathrm{Th}}$, the total particle flux J_{Th} to a stationary, evaporating or growing drop, becomes, considering the radial symmetry of the problem,

$$J_{\mathrm{Th}} = \int_s \vec{j}_{\mathrm{Th}} \cdot \mathrm{d}\vec{\mathrm{S}} = \frac{4\pi a^2 n_\infty B}{p} j_{h,a}\,. \tag{17-21}$$

From (13-16), $j_{h,a} = k_{\mathrm{a}}(T_a - T_\infty)/a$, so that

$$J_{\mathrm{Th}} = -\frac{4\pi a n_\infty B k_{\mathrm{a}}}{p}(T_\infty - T_a)\,. \tag{17-22}$$

The loss rate of particles by thermophoresis is then

$$-\left(\frac{\mathrm{d}N}{\mathrm{d}t}\right)_{\mathrm{Th}} = -J_{\mathrm{Th}} = \frac{4\pi a n_\infty B k_{\mathrm{a}}}{p}(T_\infty - T_a)\,, \tag{17-23}$$

where N is the total number of particles. Applying this result to ventilated drops of size distribution $n_{\mathrm{d}}(a,t)$, we obtain the following scavenging coefficient and collection kernel for thermophoresis:

$$\Lambda_{\mathrm{Th}}(r,t) = \frac{4\pi B k_{\mathrm{a}} \bar{f}_p}{p}(T_\infty - T_a)\int_0^\infty a n_{\mathrm{d}}(a,t)\,\mathrm{d}a \tag{17-24}$$

and

$$K_{\mathrm{Th}}(r,a) = \frac{4\pi B k_{\mathrm{a}} \bar{f}_p a}{p}(T_\infty - T_a)\,, \tag{17-25}$$

for an evaporating drop ($T_a < T_\infty$). Since Λ_{Th} and K_{Th} cannot be negative, $\Lambda_{\mathrm{Th}} = 0$ and $K_{\mathrm{Th}} = 0$ for $T_\infty < T_a$.

Diffusiophoresis refers to aerosol particle motion induced by concentration gradients in a gaseous mixture. Unlike the case of thermophoresis, both continuum and non-continuum effects contribute to this phenomenon. The continuum contribution is due to *Stephan flow*, which can be regarded as a hydrodynamic flow of the medium which compensates for a diffusive flow of some constituent(s) (such as water vapor). The non-continuum contribution arises from gas slippage along a particle surface due to concentration gradients in some constituent(s); this mechanism is thus analogous to the processes responsible for thermophoresis.

For detailed discussions of diffusiophoresis, see Waldmann and Schmitt (1966) and Hidy and Brock (1971). For our purposes here, we merely quote from Waldmann and Schmitt (p. 151) the following approximate result for the diffusiophoretic velocity $\vec{v}_{Df}$ of a particle in stagnant air through which water vapor is diffusing:

$$\vec{v}_{Df} = -\frac{M_w^{1/2}}{(x_v M_w^{1/2} + x_a M_a^{1/2})} \frac{D_v}{x_a} (\nabla x_v)_\infty , \tag{17-26a}$$

for $N_{Kn} \gtrsim 1$ ($r \lesssim \lambda_a$) and

$$\vec{v}_{Df} = -(1 + \sigma_{va} x_a) \frac{D_v}{x_a} (\nabla x_v)_\infty , \tag{17-26b}$$

for $N_{Kn} < 1$ ($r > \lambda_a$). The experiments of Schmitt and Waldmann (1960), Schmitt (1961), and Goldsmith and May (1966) showed that the values for $\vec{v}_{Df}$ computed from (17-26) agree well with observed values for particles of $r \lesssim \lambda_a$. For particles of $r > \lambda_a$, the experiments suggested that $\vec{v}_{Df}$ has to be computed from (17-26b) with $\sigma_{va} \approx -0.26$, i.e., $(1 + \sigma_{va} x_a) \approx 0.74$ for $x_v \leq x_a \approx 1$. This value of σ_{va} is supported by the earlier studies of Kramers and Kistenmacher (1943) who proposed on theoretical grounds that, for large articles in air through which water vapor diffuses, $\sigma_{va} = (M_w^{1/2} - M_a^{1/2})/(x_v M_w^{1/2} - x_a M_a^{1/2}) \approx -0.21$, from which $1 + \sigma_{va} x_a \approx 0.79$ for $x_a \approx 1$. Thus, we may tentatively conclude that one may use (17-26b) with $\sigma_{va} \approx -0.3$ to -0.2.

The diffusiophoretic force $\vec{F}_{Df}$ exerted on an aerosol particle by water vapor diffusing through stagnant air may be obtained by inserting (17-26b) for the diffusiophoretic velocity into the slip flow corrected Stokes drag, $6\pi\eta_a \vec{v}_{Df} r (1 + \alpha N_{Kn})^{-1}$, and setting this drag equal to $\vec{F}_{Df}$. One then finds the diffusiophoretic force on an aerosol particle may be expressed approximately as

$$\vec{F}_{Df} = -\frac{6\pi\eta_a r (1 + \sigma_{va} x_a) D_v (\nabla x_v)_\infty}{(1 + \alpha N_{Kn}) x_a} . \tag{17-27}$$

Since $x_v = n_v/(n_v + n_a)$ and therefore $(\nabla x_v)_\infty / x_a = \nabla n_v / n_a = (M_a/M_w) \Delta\rho_v / \rho_a$, we obtain from (17-26b) with $\sigma_{va} \approx -0.26$ and $(M_a/M_w) = 1.61$, and for $x_v \leq x_a \approx 1$,

$$\vec{v}_{Df} = -1.2 \frac{D_v}{\rho_a} \nabla \rho_v = 1.2 \vec{j}_v / \rho_a , \tag{17-28}$$

where $\vec{j}_v = -D_v \nabla \rho_v$ is the water vapor mass flux vector. Note that the direction of motion induced by diffusiophoresis is the same as that of the vapor flux. Since

the diffusiophoretic particle flux vector is $\vec{\jmath}_{\mathrm{Df}} = n_\infty \vec{v}_{\mathrm{Df}}$, the total particle flux to a stationary drop becomes, after using (17-28),

$$J_{\mathrm{Df}} = \int_S \vec{\jmath}_{\mathrm{Df}} \cdot \mathrm{d}\vec{S} = \frac{4.8\pi a^2 n_\infty}{\rho_{\mathrm{a}}} j_{\mathrm{v},a} \,. \tag{17-29}$$

Then, with $j_{\mathrm{v},a} = D_{\mathrm{v}}(\rho_{\mathrm{v},a} - \rho_{\mathrm{v},\infty})/a$ (cf. (13-7)), we obtain

$$J_{\mathrm{Df}} = -\frac{4.8\pi a n_\infty D_{\mathrm{v}}}{\rho_{\mathrm{a}}} (\rho_{\mathrm{v},\infty} - \rho_{\mathrm{v},a}) \,. \tag{17-30}$$

The loss rate of particles by diffusiophoresis is then

$$-\left(\frac{\mathrm{d}N}{\mathrm{d}t}\right)_{\mathrm{Df}} = -J_{\mathrm{Df}} = \frac{4.8\pi a n_\infty D_{\mathrm{v}}}{\rho_{\mathrm{a}}} (\rho_{\mathrm{v},\infty} - \rho_{\mathrm{v},a}) \,. \tag{17-31}$$

Assuming ventilated drops of size distribution $n_{\mathrm{d}}(a,t)$ we find for the scavenging coefficient and collection kernel for diffusiophoresis:

$$\Lambda_{\mathrm{Df}}(r,t) = \frac{4.8\pi D_{\mathrm{v}} \bar{f}_p}{\rho_{\mathrm{a}}} (\rho_{\mathrm{v},\infty} - \rho_{\mathrm{v},a}) \int_0^\infty a n_{\mathrm{d}}(a,t)\, \mathrm{d}a \,, \tag{17-32}$$

and

$$K_{\mathrm{Df}}(r,a) = \frac{4.8\pi D_{\mathrm{v}} \bar{f}_p a}{\rho_{\mathrm{a}}} (\rho_{\mathrm{v},\infty} - \rho_{\mathrm{v},a}) \,, \tag{17-33}$$

for a condensing drop ($\rho_{\mathrm{v},\infty} > \rho_{\mathrm{v},a}$). Since Λ_{Df} and K_{Df} cannot be negative, $\Lambda_{\mathrm{Df}} = 0$, $K = 0$ for $\rho_{\mathrm{v},\infty} < \rho_{\mathrm{v},a}$. We see from (17-33) and (17-25) that thermophoresis and diffusiophoresis have opposing effects on the scavenging behavior of drops.

Young (1974) has carried out a numerical evaluation of expressions similar to (17-16), (17-25), and (17-33) for various atmospheric conditions. His results for the case of a water drop of 10 μm radius evaporating at 98% relative humidity, 600 mb, and -5°C, and for a drop growing at a supersaturation of 0.3%, 600 mb, and -5°C, are displayed in Figure 17.12. Note that in both cases the effects of thermophoresis overpower those of diffusiophoresis if $r < 1\,\mu$m. This agrees also with the predictions of Slinn and Hales (1971). Note also that both phoretic scavenging processes depend only slightly on the particle size, if $0.01 \leq r \leq 1\,\mu$m, and that above a certain particle size, the phoretic effects dominate Brownian motion. The net effect of all three processes on the scavenging rate of aerosol particles has been computed by Young on the assumption that the individual collection kernels may simply be added together. It is questionable whether this assumption is justifiable in the light of the coupling which exists between Brownian diffusion of particles and particle motion due to phoretic forces. On the other hand, the experiments of Goldsmith and May (1966) and the theoretical considerations of Annis and Mason (1975) show that, for water vapor diffusing in air under atmospheric conditions, for which $x_{\mathrm{v}} \ll x_{\mathrm{a}}$, the thermo- and diffusiophoretic forces are additive, i.e., thermo- and diffusiophoretic effects are not coupled.

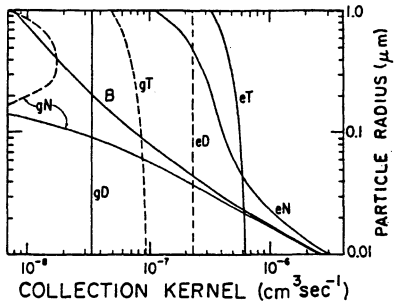


Fig. 17-12: Collection kernel (cm^3 sec^{-1}) for a water drop of $a = 10$ μm in air of 600 mb and $-5°C$, collecting aerosol particles by Brownian diffusion (B), thermophoresis (T), or diffusiophoresis (D); (N) is net effect: for 0.3% supersaturation (g), 98% relative humidity (e). (From Young, 1974; by courtesy of Am. Meteor. Soc., and the author.)

The results of Young, displayed in Figure 17.13, show that by considering convective Brownian diffusion and phoretic effects only, the collection kernel and, hence, the scavenging efficiency of a cloud drop of given size, decreases with increasing particle size; also, for an aerosol particle of given size, the scavenging efficiency increases with increasing drop size. The values shown in Figure 17.13 indicate that, for particles of $r \gtrsim 1\,\mu$m in concentrations of 10 cm^{-3} and in air of 600 mb, $-5°C$, and 98% relative humidity, 10^2 to 10^5 aerosol particles are scavenged by water drops of 10 to 1000 μm radius within 10 min, in fair agreement with the field observations of Rosinski. However, these estimates do not include the effects of inertial impaction and, thus, most likely underestimate the number of aerosol particles scavenged.

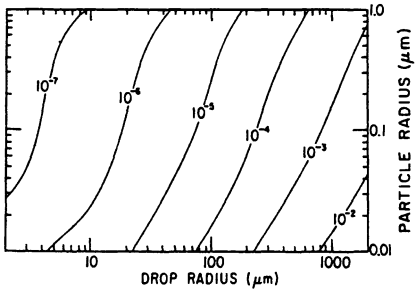


Fig. 17-13: Collection kernel (cm^3 sec^{-1}) for a water drop in air collecting aerosol particles by Brownian diffusion and phoretic forces as a function of aerosol and drop radii for drops evaporating at 600 mb, $-5°C$ and 98% relative humidity. (From Young, 1974; by courtesy of Am. Meteor. Soc., and the author.)

The discussion on the phoretic and Brownian capture of aerosol particles by drops once more takes us back to our earlier treatment of contact nucleation (Section 9.2.3.5). Such nucleation depends on the contact rate between supercooled cloud drops and aerosol particles. Phoretic forces are certainly candidates for caus-

ing such collisions near the periphery of clouds where, through evaporative cooling, the drops are somewhat colder than the ambient air. This has been verified by field experiments already some time ago. For example, from wet bulb temperatures observed on days when relatively warm cloud glaciation was observed in clouds over Missouri, Koenig (1965b) determined that drops at the periphery of clouds could have cooled by as much as 6°C below the ambient temperature. Similarly, Mossop *et al.* (1968) determined a maximum wet bulb depression of 4°C for drops at the periphery of a cumulus cloud, located off the southern coast of Australia, which glaciated at −4°C. Evidence for the effectiveness of ice formation by contact nucleation has been given by the wind tunnel studies of Gokhale and Spengler (1972) and Pitter and Pruppacher (1973), who showed that clay and soil particles of diameters between 0.1 and 30 μm nucleate supercooled water drops at temperatures as warm as −3 to −4°C.

The number of ice crystals produced by contact nucleation may be estimated from the study of Young (1974), who determined the relative collection rate, i.e., the number of collection events per cubic centimeter per second, for evaporating drops capturing aerosol particles by Brownian diffusion, diffusiophoresis, and thermophoresis. On the basis of Young's computations (see Figure 17.13), one finds that, in a cloud at 600 mb where the temperature is assumed to be −5°C and where the relative humidity is 98%, an ice crystal concentration of 30 to 300 m^{-3} will be produced within 5 min if 10 μm radius drops are present in a concentration of 100 cm^{-3}, assuming that the drops are nucleated by contact nuclei with a radius of 0.03 μm and that the concentration of contact nuclei at −5°C ranges between 1 and 10 $liter^{-1}$. Considering that at temperatures between −5 and −10°C, the observed concentration of snow crystals is of the order of several hundred per liter, we must conclude that contact nucleation cannot be responsible for the observed snow crystal concentration. Although one could argue with Gokhale and Goold (1968) that the ability of an aerosol particle to act as a contact ice nucleus increases with increasing aerosol particle size, a computation similar to the one carried out above but for contact nuclei of radius 0.5 μm and a concentration of 100 $liter^{-1}$, captured within 5 minutes by drops of radius 10 μm and with a concentration of 100 cm^{-3}, leads from Figure 17.13 to an ice crystal concentration of only 900 m^{-3}. Thus, in order to explain the observed number of snow crystal in clouds by contact ice nucleation, the number of contact nuclei would have to be of the order of a few tens per cm^3. This requirement is not met under atmospheric conditions, considering the observations given in Figure 9.19, the observations of Blanchard (1957) who estimated the concentration of contact nuclei to be 0.01 $liter^{-1}$ at −4°C and 0.1 $liter^{-1}$ at −8°C, and the observations of Vali (1974), who estimated a concentration of 2 $liter^{-1}$ at −16°C, and of Cooper (1980) who found on the order of 1 $liter^{-1}$ at −10°C (see Figure 19.19). In addition, computations of the type made above assume that drops which capture contact nuclei by Brownian and phoretic forces do not change their size during the capture, whereas, in fact, they become smaller due to evaporation. This fact has recently been considered by Baker (1991) to show that the assumption of a drop size spectrum which is constant in time leads to a considerable overestimate of the role of contact nucleation in the ice crystal budget of a cloud.

17.4.2.3 *Scavenging by Gravitational or Inertial Impaction*

Thus far, we have considered the scavenging of aerosol particles which are relatively small, so that there was no need to take their inertia into account. We shall now drop this assumption and consider particles which are large enough so that neither Brownian motion nor phoretic forces affect their collection. We also shall assume that all particles which collide with a collector drop or crystal will stick to it. For collector drops, this is consistent with the experiments of Weber (1968, 1969), who found that the collection efficiency problem reduces to that of determining the collision efficiency $\mathrm{E}(r, a)$. (Whether a captured insoluble particle remains on the surface of a drop or becomes completely immersed, depends on the contact angle, defined in Section 5.5 (see McDonald (1963b) for a theoretical study of this effect). Since, generally, we have $r \ll a$, $\mathrm{E}(r, a)$ may be determined by using the superposition scheme of hydrodynamic interaction (see Sections 11.6.3 and 14.3). Of course, once $\mathrm{E}(r, a)$ is known, the corresponding collection kernel K_G may be obtained from (11-87).

The first theoretical estimates of $\mathrm{E}(r, a)$ were made by Langmuir and Blodgett (1946) and Langmuir (1948). Their computations were later extended and improved by Mason (1957) and Fonda and Herne (in Herne, 1960). The method used by these authors is based on a scheme which allows interpolating between potential flow, assumed to characterize the flow past a large collector drop, and Stokes flow, assumed to characterize the flow past a small collector drop. The flow past aerosol particles was considered to have negligible effect. Beard and Grover (1974) have computed improved values of $\mathrm{E}(r, a)$ by using the numerically determined flow fields of Le Clair *et al.* (1970) (see Section 10.2.2.5) for spherical drops of $1 \leq N_{\mathrm{Re}} \leq 400$, corresponding to $40 \lesssim a \lesssim 600\,\mu\mathrm{m}$. Their formulation involves the standard superposition scheme, described in detail in Section 14.3, and they also include the refinement of invoking the slip-flow correction (11-15) for the drag on the aerosol particle. Thus, their equation of motion for a particle of mass m and velocity $\vec{\mathrm{v}}$ is

$$m\frac{\mathrm{d}\vec{\mathrm{v}}}{\mathrm{d}t} = m\vec{\mathrm{g}}^{*} - \frac{6\pi\eta_{\mathrm{a}} r}{1 + \alpha N_{\mathrm{Kn}}}(\vec{\mathrm{v}} - \vec{\mathrm{u}})\,, \tag{17-34}$$

where $\vec{\mathrm{g}}^{*} = \vec{\mathrm{g}}(\rho_P - \rho_{\mathrm{a}}/\rho_P)$ is the buoyancy-corrected acceleration of gravity, and $\vec{\mathrm{u}}$ is the flow field past the drop, evaluated at the location of the particle. Beard and Grover worked with a dimensionless form of this equation, given by (14-10). In the latter equation, the 'inertia parameter' or Stokes number N_S acquires the form $N_S = p^2 \rho_P N_{\mathrm{Re}}(1 + \alpha N_{\mathrm{Kn}})/9\eta_{\mathrm{a}}$, where $p = r/a$.

The values of $\mathrm{E}(r, a)$ found by Beard and Grover for particle radii $r \gtrsim 1\,\mu\mathrm{m}$, subject to $r/a \lesssim 0.1$, are intermediate to previously calculated values for the potential and Stokes flow limits, but do not follow the Langmuir interpolation formula mentioned above. For the particle sizes considered, $\mathrm{E}(r, a)$ was found to increase monotonically with increasing r for $1 \leq N_{\mathrm{Re}} \leq 400$. However, a later extension of these computations down to $r \approx 0.1\,\mu\mathrm{m}$ by Beard (1974b) revealed a minimum in the curve of $\mathrm{E}(r, a)$ versus r, near $r \approx 0.5\,\mu\mathrm{m}$ for $N_{\mathrm{Re}} \gtrsim 20$ and $\rho_P = 1\ \mathrm{g\ cm^{-3}}$. Beard's computations for rigid spheres were extended by Grover (1978) to spherical water drops with internal circulation ($1 \leq N_{\mathrm{Re}} \leq 200$), and to particles with

$\rho_P = 2$ g cm^{-3}. The results of Grover, shown in Figure 17.14, agree with Beard's computations in revealing a minimum in $E(r, a)$ for $0.3 \lesssim r \lesssim 0.5\,\mu$m, and for drops with $N_{Re} = 100$ and 200. Although the decrease in E with decreasing r is readily understandable on considering the effects of particle inertia, the increase in E for decreasing r less than $r = r(E_{min})$ may seem strange at first sight. Beard suggested that, for drops with $N_{Re} \gtrsim 20$, the latter finding may be explained on the basis of small particle capture by the standing eddy on the downstream side of the drop, which is aided by gravity pulling the particle towards the rear of the drop (*wake capture*). (Note this form of wake capture is quite distinct from another type which involves falling drops of comparable size. In the latter situation, the trailing drop becomes drawn into the wake of the leading one and eventually collides with it). The effectiveness of the rear-capture process should obviously increase with decreasing particle inertia and with increasing eddy size, thus explaining the shape of the collision efficiency curves in Figure 17.14 for $N_{Re} > 30$. Grover's (1978) more refined computations generally support the notion of the existence of a rear-capture process; however, his results indicate that its onset occurs for N_{Re}, since for $20 \leq N_{Re} \leq 30$, the strength of the eddy in the rear of a drop is still too weak to affect particle collection. Note that the curves (4) and (5) cross over curves (1), (2), and (3), indicating that in a narrow particle size range, drops with $N_{Re} = 4$ and 10 exhibit a slightly larger collision efficiency than drops of $N_{Re} = 30$, 100, and 200. This result is a reflection of the 'interception effect' discussed in Section 11.6.3, where we showed that, for interacting particles of suffciently small size, the collision efficiency is controlled by the p-ratio ($p = r/a$), and increases with increasing p-ratio (i.e., with decreasing drop size for given r).

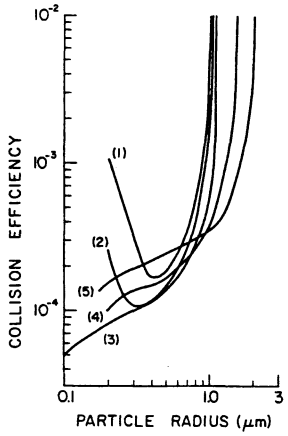


Fig. 17-14: Numerically computed efficiency with which water drops collide by inertial impaction with aerosol particle in air of 10°C and 900 mb; (1) $N_{Re} = 200$ ($a = 438\,\mu$m), (2) $N_{Re} = 100$ ($a = 310\,\mu$m), (3) $N_{Re} = 30$ ($a = 173\,\mu$m), (4) $N_{Re} = 10$ ($a = 106\,\mu$m), (5) $N_{Re} = 4$ ($a = 72\,\mu$m). (From Grover, 1978; by courtesy of the author.)

Theoretical values of E for $N_{Re} \gtrsim 400$ have not been computed since numerical solutions for flow fields past drops exclude the phenomena of eddy shedding and

drop oscillations which are known to occur for such sizes.

17.4.2.4 *Scavenging by Turbulence*

The approximate descriptios of turbulent shear and turbulent inertial coagulation given in Section 11.6.2 and the comparison of these effects with Brownian and gravitational coagulation in Figure 11.6 for spherical particles of $0.1 \lesssim r \lesssim 10\,\mu$m, should apply also to the problem of turbulent scavenging of aerosol particles by small drops of radii $\lesssim 10\,\mu$m. For larger drops with significant fall speeds, one must account also for the possible convective enhancement of the particle flux. Although no rigorous treatment of this problem exists, several simple and plausible approaches suggest themselves. For example, we may attribute the turbulent shear collection kernel (11-73) to a process of diffusion characterized by the constant diffusion coefficient D_{TS}. By comparing the forms of the collection kernels for Brownian diffusion, (11-56), and turbulent shear, we find $D_{\mathrm{TS}} \approx a^2(\varepsilon/\nu)^{1/2}/4\pi$, for the case $r \ll a$. Then, by assuming the independence of Brownian and turbulent diffusion, we may represent the net effect of both by the diffusion coefficient $D_{\mathrm{net}} = D_{\mathrm{TS}} + D$. From (17-16), the corresponding collection kernel for convection-enhanced turbulent-shear and Brownian diffusion scavenging is estimated to be $K_{\mathrm{net}} \approx 4\pi a D_{\mathrm{net}} \bar{f}(D_{\mathrm{net}})$. An approach of this kind has been followed by Williams (1974) and Greenfield (1957).

In this procedure, it is tacitly assumed that the collection kernel for the various scavenging processes is given by the sum of the collector kernels for the individual processes in isolation. A variation on this scheme has been provided by Saffmann and Turner (1956), whose model results suggest that the resultant kernel is best represented by taking the square root of the sum of the squares of the individual kernels. In principle, a more rigorous approach, which has been followed to some degree by various researchers, is to superpose the various forces acting simultaneously on a particle. Unfortunately though, in this more recent work, the effects of turbulence have not been considered. It further turns out that the modeled forces could not be included in one single scavenging model. Instead, two complementary models have been employed, each of which covers a specific aerosol particle size range. The results of both models are then joined in the size range in which both are approximately valid.

17.4.2.5 *Combined Force Effects: the Trajectory and Flux Models*

The trajectory model. For particles with $r \geq 0.2\,\mu$m, the trajectory method of Beard and Grover (1974) was extended by Grover *et al.* (1977) to include the thermo- and diffusiophoretic forces. In doing so, the effects of Brownian diffusion were neglected. For particles with $r < 0.2\,\mu$m, the concept of the convective Brownian particle flux was extended by Wang and Pruppacher (1980a) and Wang *et al.* (1978) to include the effects of the thermo-and diffusiophoretic forces. Due to the smallness of the particles considered in this latter model, the effects of inertial impaction were neglected. Martin *et al.* (1980a,b), Wang and Pruppacher (1980b), and Miller and Wang (1989) applied the same concepts to particle scavenging by snow crystals, modeled as oblate spheroids and cylinders.

To formulate the trajectory model, we shall follow Grover *et al.* (1977), and consider a simple extension of (17-34) which leads to the equation for a particle's trajectory past a falling, evaporating or condensing drop:

$$m\frac{\mathrm{d}\vec{v}}{\mathrm{d}t} = m\vec{g}^{*} - \frac{6\pi\eta_{\mathrm{a}}r}{1+\alpha N_{\mathrm{Kn}}}(\vec{v}-\vec{u}) + \vec{F}_{\mathrm{Df}} + \vec{F}_{\mathrm{Th}}\,, \tag{17-35}$$

where $\vec{F}_{\mathrm{Th}}$ and $\vec{F}_{\mathrm{Df}}$ are given by (17-19) and (17-27), respectively, and where $\vec{u}$ is the flow field around a drop or snow crystal. The values for $\mathrm{E}(r,a)$ and $K(r,a)$ are found from the trajectory at which the particle just makes grazing contact with the drop (see Figure 14.1). Examples of such trajectories around a drop are given in Figures 17.15a,b,c, and around a planar snow crystal in Figure 17.16. We note from Figures 17.15a,b,c that relatively large particles may be captured on the upstream (lower) side of a falling drop, while relatively small particles are captured on the drop's rear side. From Figure 17.16, we note that, analogously to the deposition of rime (Plate 4), aerosol particles become scavenged preferentially at the rim of plate-like snow crystals (Plate 19). This is chiefly due to the strong, local horizontal flow component just underneath a falling snow crystal plate.

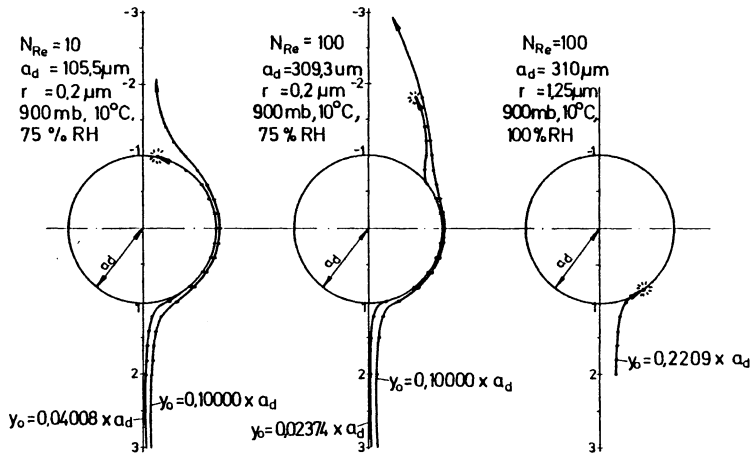


Fig. 17-15: Theoretically computed trajectories of aerosol particles around drops falling in air of 10°C and various relative humidity. (From Lew, 1982, pers. comm., by courtesy of the author.)

The flux model. To formulate the flux model, we shall follow Wang *et al.* (1978), Wang and Pruppacher (1980a,b), Martin *et al.* (1980a), and Wang (1985, 1989), and recall (11-19), which we extend to include the thermo- and diffusiophoretic force:

$$\vec{v}_{\mathrm{Drift}} = B_p\vec{F}_{\mathrm{ext}} = B(m\vec{g}^{*} + \vec{F}_{\mathrm{Df}} + \vec{F}_{\mathrm{Th}}). \tag{17-36}$$

The particle flux is therefore

$$\vec{J} = nB_p(m\vec{g}^{*} + \vec{F}_{\mathrm{Df}} + \vec{F}_{\mathrm{Th}}) - D_p\nabla n\,, \tag{17-37}$$

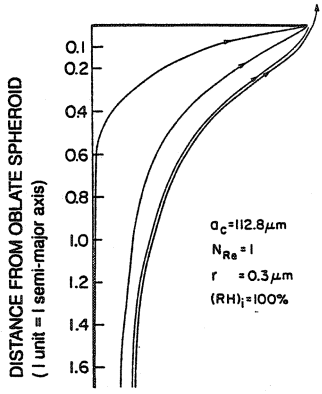


Fig. 17-16: Theoretically computed trajectories of an aerosol particle of $r = 0.3$ μm around a planar snow crystal of $N_{\mathrm{Re}} = 1$ ($a_c = 112.8$ μm), falling in ice saturated air at $-10°$C and 700 mb. (From Martin *et al.*, 1980a, with changes.)

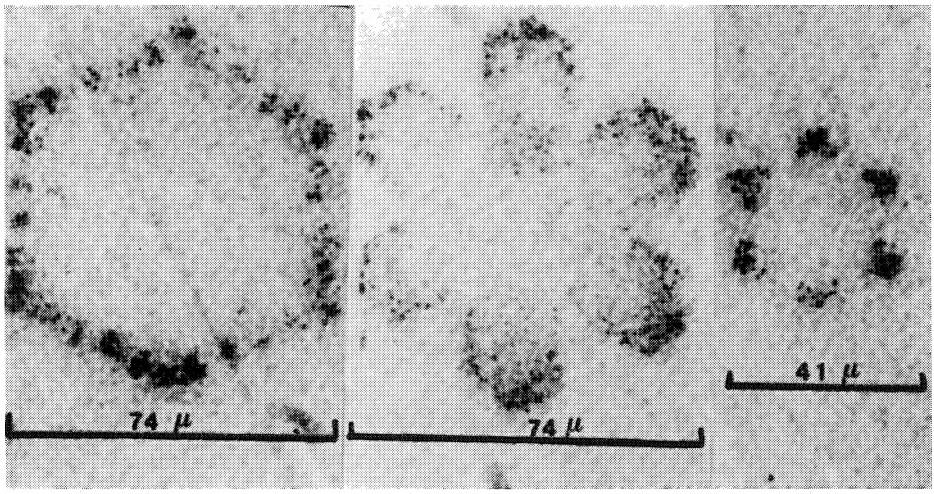


Plate 19. Distribution of aerosol particles scavenged by planar snow crystals while freely falling through a chamber filled with aerosol particles of $0.1 \leq r \leq 1.0$ μm. (Reproduced by courtesy of Prof. F. Prodi, Institute FISBAT, Bologna, Italy, 1976.)

where n is the concentration of the particles, and the particle mobility B_p is given by (11-20). In the flux model, we assume that for particles with $r < 0.2\,\mu$m the term $m\vec{g}^*$ may be neglected in comparison to the other terms in the parentheses of (17-37). With this assumption, the flux density of particles to a falling ventilated drop may be expressed as

$$\vec{J} = nB(\bar{f}_h\vec{F}_{\mathrm{Th}} + \bar{f}_v\vec{F}_{\mathrm{Df}}) - D_p\bar{f}_p\nabla n\,. \tag{17-38}$$

To simplify (17-38), we shall assume that the ventilated heat and vapor density fields around the drop are spherically symmetric inverse square fields; i.e., $\bar{f}_h\vec{F}_{\mathrm{Th}} = C_{\mathrm{Th}}\hat{R}/R^2$ and $\bar{f}_v\vec{F}_{\mathrm{Df}} = C_{\mathrm{Df}}\hat{R}/R$, where R is the radial distance from the drop center, $\hat{R}$ is the unit vector in the radial direction, and where from (17-19) and (17-27) we have

$$C_{\mathrm{Th}} = -\frac{12\pi\eta_a r(k_a + 2.5k_pN_{\mathrm{Kn}})k_a a(T_\infty - T_a)\bar{f}_h}{5(1+3N_{\mathrm{Kn}})(k_p + 2k_a + 5k_pN_{\mathrm{Kn}})p} \tag{17-39a}$$

and

$$C_{\mathrm{Df}} = -6\pi\eta_a r\frac{0.74D_vM_a a(\rho_{v,\infty} - \rho_{v,a})\bar{f}_v}{(1+\alpha N_{\mathrm{Kn}})M_w\rho_a}\,. \tag{17-39b}$$

For the above-defined fields we have $\nabla\cdot(\bar{f}_h\vec{F}_{\mathrm{Th}} + \bar{f}_v\vec{F}_{\mathrm{Df}}) = 0$. Assuming a steady state, $\partial n/\partial t = 0$, the condition of particle continuity ($\nabla\cdot\vec{j} = 0$) leads to

$$B(\bar{f}_h\vec{F}_{\mathrm{Th}} + \bar{f}_v\vec{F}_{\mathrm{Df}})\cdot\nabla n - D_p\bar{f}_p\nabla n = 0\,. \tag{17-40}$$

Equation (17-40) was solved by Wang *et al.* (1978), subject to the boundary conditions $n = 0$ for $R = a$ and $n = n_\infty$ for $R \to \infty$. They found for spherical drops:

$$n(R) = n_\infty\left[\frac{\exp[(BC_{\mathrm{Ph}}/D_p\bar{f}_r a)(1-\frac{a}{R})] - 1}{\exp[BC_{\mathrm{Ph}}/D_p\bar{f}_p a] - 1}\right], \tag{17-41}$$

with $C_{\mathrm{Ph}} = C_{\mathrm{Th}} + C_{\mathrm{Df}}$. The total particle flux is then

$$J = \int_S D_p\bar{f}_p\nabla n\cdot\mathrm{d}\vec{S}\,, \tag{17-42}$$

from which follows the collection kernel $K = J/n_\infty$, or

$$K = \frac{4\pi BC_{\mathrm{Ph}}}{\exp[BC_{\mathrm{Ph}}/D_p\bar{f}_p a] - 1}\,; \tag{17-43a}$$

and the collection efficiency

$$\mathrm{E} = \frac{K}{\pi(a+r)^2(U_{\infty,a} - U_{\infty,r})}\,. \tag{17-43b}$$

For snow crystals whose shape can be expressed in terms of a capacitance C (see Section 13.3), we may simply replace a by C in (17-43), and in (17-39a,b), while replacing $\pi(a+r)^2$ in (17-43b) by the cross-sectional area of the crystal.

An interesting result is obtained when the effects of various scavenging mechanisms are combined. For scavenging processes in the atmosphere, this was first done by Greenfield (1957), who considered Brownian diffusion, turbulent shear diffusion, and inertial impaction. He found that the overall scavenging coefficient exhibited a strong broad minimum for aerosol particles between about 0.1 and 1.0 μm radius. In the literature, this minimum is therefore often referred to as the 'Greenfield gap'. It is the result of Brownian diffusion dominating particle capture for $r < 0.1\,\mu$m, and of inertial impaction dominating capture for $r > 1\,\mu$m. Later investigators (e.g., Slinn and Hales, 1971; Dingle and Lee 1973; Crandall *et al.* 1973; Pilat and Prem, 1976; Wang *et al.*, 1978; Martin *et al.*, 1980a) who included also the phoretic effects, obtained similar results. The results of Wang *et al.* (1978) for the overall efficiency with which aerosol particles are collected by water drops are exhibited in Figure 17.17. Similar computations were carried out by Martin *et al.* (1980a) for planar snow crystals modeled as thin oblate spheroids, and by Miller and Wang (1989) for columnar crystals modeled as cylinders. These latter results are given in Figure 17.18 and 17.19, respectively. Note the pronounced minimum in the collection efficiency for $N_{\mathrm{Re}} > 5$, as expected from Greenfield's earlier results. We also notice that, for drops and crystals, the phoretic forces tend to 'fill the gap', particularly at low relative humidities, but it remains distinct nonetheless (see Figure 17.18a). For crystals of $5 \leq N_{\mathrm{Re}} \leq 1$, the collision efficiency assumes a maximum near $r \approx 1\,\mu$m, to decrease sharply to zero with a further increase in particle radius. This is a result of the rapidly decreasing relative velocity between crystal and aerosol particle so that the horizontal forces in the flow field past the crystal have sufficient time to carry the particle around the crystal, and thus prevent collision (see Figure 17.18b). For crystals of $N_{\mathrm{Re}} \leq 1$, an additional abrupt change in collision behavior takes place in that at these low Reynolds numbers, the ice crystals regain their capability to capture aerosol particles of radius larger than 1 μm. The reason for this behavior lies in the rapid decrease of the velocity field around the crystal and the associated rapid decrease of the horizontal deflection force such that, despite the small relative velocity, the particle cannot escape collision. The effect of electric charges will be discussed in Chapter 18.

Until recently, flow fields around drops and snow crystals were available only for Reynolds numbers which apply to axisymmetric flow. Because of this restriction, computations of the scavenging efficiency of aerosol particles by drops, planar snow crystals, and columnar snow crystals were restricted to flow fields with $N_{\mathrm{Re}} \leq 300$, $N_{\mathrm{Re}} \leq 50$, and $N_{\mathrm{Re}} \leq 20$, respectively. For columnar crystals, the additional unrealistic assumption had to be made that the collision was not affected by the finite length of the crystal. Recently, however, three-dimensional flow fields around falling hydrometeors have become available through numerical solutions of the primitive Navier-Stokes equation of motion (see Chapter 10). With these flow fields, it is now possible to extend the presently available collision efficiencies to larger collector bodies.

Unfortunately, experimental verfication of the scavenging behavior of drops and snow crystals have proven to be quite difficult, so that only few data are available for comparison with theory. Four main experimental requirements have caused these difficulties: (1) uniform particle size, (2) high and uniform particle concentration

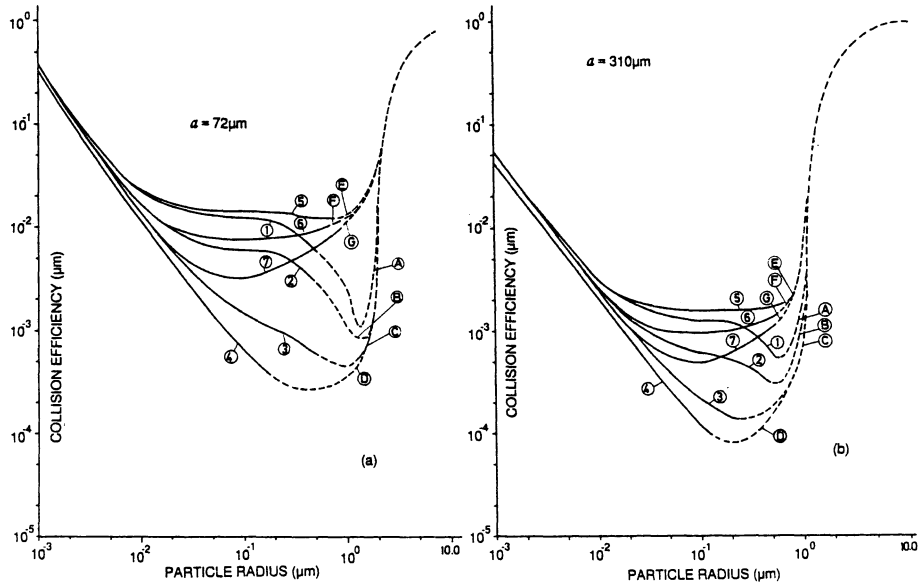


Fig. 17-17: Effect of relative humidity and electric charge on the efficiency with which aerosol particles of $\rho_P = 2$ g cm^{-3} and of various sizes collide by impaction scavenging with water drops of (a) 310 μm radius, and (b) 72 μm radius in air of 10°C and 900 mb. Combination of trajectory model (dashed lines) with flux model (continuous lines); curves 1,2,3,4 and A,B,C,D are for $\hat{Q}_a = Q_a/a^2 = 0$, $\hat{Q}_r = Q_r/r^2 = 0$, and RH = 50, 75, 95 and 100%, respectively. Curves 5,6,7, and E,F,G are for $\hat{Q}_a = \pm 2.0$ e.s.u. cm^{-2}, $\hat{Q}_r = \mp 2.0$ e.s.u. cm^{-2} and RH = 50, 75, 95%,, respectively. (From Wang *et al.*, 1978, with changes.)

over the collector's fall distance, (3) controlled electric charge on collector and particles, and (4) collectors freely falling at their terminal fall velocity in air of well-defined temperature and humidity.

Despite these difficulties, the presently available experimental results have given considerable support to the predictions of theoretical models. The experiments of Oaks (1960) with oil droplets, paraffin particles, and ammonium chloride particles of 0.5 to 3.7 μm diameter, of Starr and Mason (1966) and Starr (1967) with pollen of 4 to 12 μm diameter, of Adam and Semonin (1970) with rod-shaped spores of 0.7 μm diameter and 1.2 μm length, of Dana (1970) with dye particles of 0.4 to 7.5 μm diameter, and of Hampl *et al.* (1971), Kerker and Hampl (1974), and of Lai *et al.* (1978) with silver chloride particles of 0.15 to 1.2 μm diameter, indicate qualitatively that the efficiency with which these particles are collected by water drops larger than about 600 μm, equivalent radius decreases with increasing drop size. Toulcova and Podzimek (1968) and Beard (1974b) conjectured that this may indicate the existence of a maximum for E. The existence of such a maximum has been verified by Starr and Mason (1966) and by Wang and Pruppacher (1977b). The former experimentally studied the efficiency with which particles of 2.25, 2.6

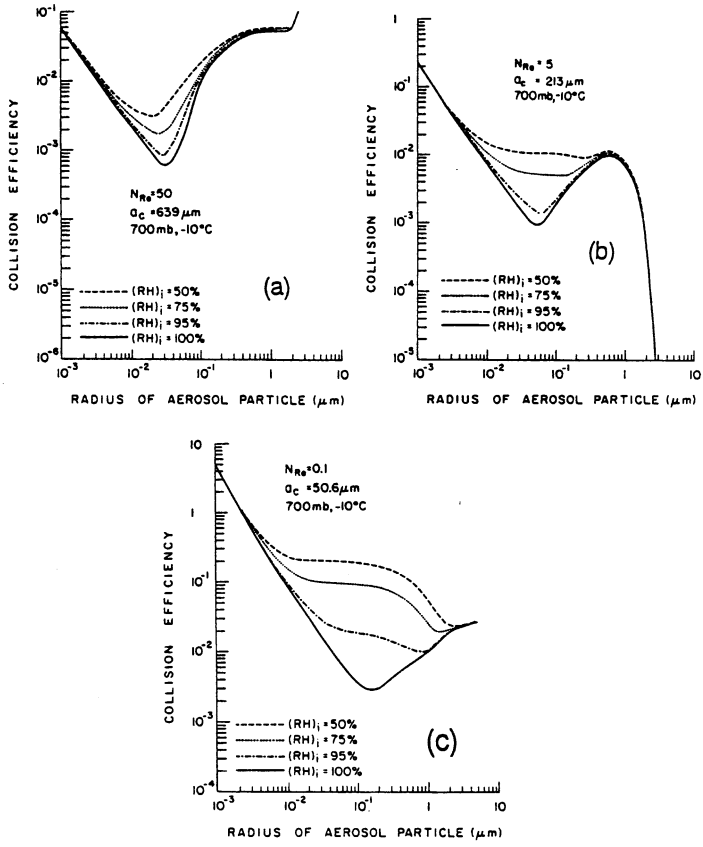


Fig. 17-18: Efficiency with which aerosol particles of $\rho_P = 2$ g cm^{-3} collide with planar snow crystals idealized by an oblate spheroid of 0.05 axis ratio in air of $-10°$ C and 700 mb at various relative humidities with respect to ice. (a) $a_c = 639$ μm, (b) $a_c = 213$ μm, (c) $a_c = 50.6$ μm. (From Martin *et al.*, 1980a; by courtesy of the Am. Meteor. Soc., and authors.)

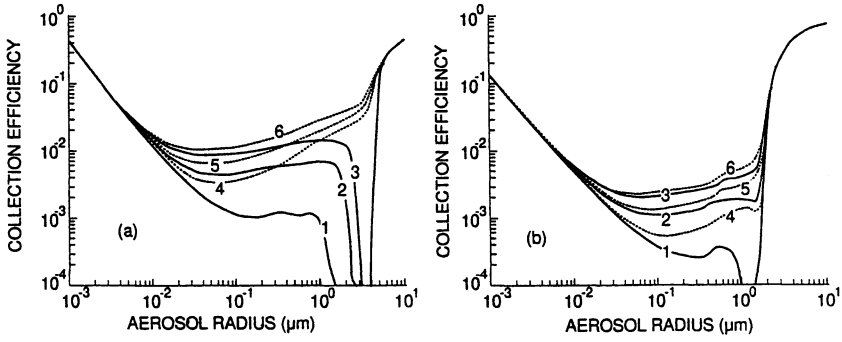


Fig. 17-19: Effect of relative humidity and electric charge on the efficiency with which aerosol particles of various sizes collide by impaction scavenging with columnar snow crystals of: (a) $N_{\mathrm{Re}} = 1$ ($a_c = 41.5\ \mu$m, $\mathrm{L_c} = 138.3\ \mu$m), and (b) $N_{\mathrm{Re}} = 10$ ($a_c = 106.7\ \mu$m, $\mathrm{L_c} = 1067\ \mu$m), in air of $-20°$ C and 600 mb. Combination of trajectory model with flux model. Curves 1,2,3 are for zero charge and 95, 75 and 50 % relative humidity, respectively. Curves 4,5,6 are for $\hat{Q}_c = -3.445\times\ 10^{-5}$ e.s.u./cm (a), and $\hat{Q}_c = -2.277\times\ 10^{-4}$ e.s.u./cm (b), and 95, 75 and 50% relative humidity, respectively. (From Miller and Wang, 1989, with changes.)

and 6.4 μm radius are captured by drops of $100 \leq a \leq 1400\,\mu$m radius, the latter determined the efficiency with which aerosol particles of 0.25 μm radius were captured by drops of $100 \leq a \leq 2500\,\mu$m falling through an aerosol chamber in which the relative humidity was 23% and the temperature was 22°C. The attainment of terminal velocity by the drops was assured by allowing the largest of them to fall through an enclosed 33 m long shaft. A maximum near $a = 500\,\mu$m was found in Starr and Mason's and Wang and Pruppacher's experiment.

The results of Wang and Pruppacher's experiments are plotted in Figure 17.20a. Note from this figure (curve 1 to 3) that E exhibits a minimum not only in a plot of E vs. r for a given a but also in a plot of E vs. a for a given r. The good agreement between the experimental results of Wang and Pruppacher (1977b) and the theoretical predictions of Grover *et al.* (1977) allows one to conclude that the increase of E with decreasing drop size for $a < a(\mathrm{E_{min}})$ is a result of the increasingly pronounced phoretic effects as the flow field past the drop becomes weaker, while the increase of E with increasing drop size for $a > a(\mathrm{E_{min}})$ is a result of the increasingly pronounced hydrodynamic effects which allow particles to be captured by the growing, standing eddy in the rear of the drop. Note also that E rapidly decreases for drops of radii larger than about 500 μm. Toulcova and Podzimek (1968) and Beard (1974) conjecture that this decrease is a result of eddy shedding which sets-in for drops with $a > 500\,\mu$m. Indeed, one would expect that with increasing unsteady flow in the wake of a falling drop, rear capture of aerosol particles would become less likely. A more convincing suggestion, however, has been made by Mitra *et al.* (1990) on the basis of the dimensionless equation of motion (14-10) for a particle past a falling drop. Recall that the controlling parameter for the particle trajectory around a drop is the Stokes number N_S.

As N_S decreases, the effective inertia of the particle and, hence, its likelyhood of collision with the drop, decreases as well. A careful inspection of Figure 10.25 shows that the terminal velocity of drops with radii larger than 500 μm varies as $U_{\infty,a} \sim a^{\alpha}$, with $\alpha < 1$. This causes N_S and, hence, E to decrease with increasing a, as is observed for drops of $a > 500\,\mu$m.

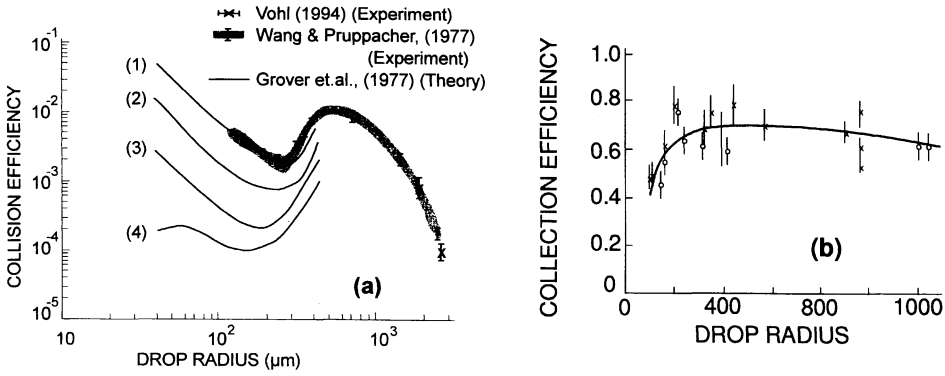


Fig. 17-20: (a) Comparison of theoretically computed and experimentally measured values for the efficiency with which uncharged aerosol particles of r= 0.25 μm and ρ_P = 2 g cm^{-3} collide with uncharged water drops of various sizes in air. Solid lines: trajectory model for RH = 20% (1), 75% (2), 95% (3), 100% (4). Hatched area experimental results: $\vdash\!\dashv$ (Wang & Pruppacher, 1977b), × Vohl (pers. comm. 1994). (From Wang & Pruppacher, 1977b, with changes). (b) Experimental collison efficiency for water drops of various sizes colliding with aerosol particles of r= 6.4 μm; (From Starr and Mason, 1966, with changes.)

The observed dependence of the particle collection efficiency on drop size provides us with an alternative explanation for the observed salt concentration found in rain drops of different size (see Figure 17.7 and text in Section 17.3). Thus, for $E > E_{max}$, the salt concentration due to capture of salt particles is expected to increase with decreasing drop size due to increasing collection efficiency and due to the decreasing drop volume. In the range $E_{min} \leq E \leq E_{max}$, however, two opposing effects are present, since the collection efficiency as well as the drop volume are decreasing with decreasing drop size. Thus, if the collection efficiency for salt particles of given size decreases less with decreasing drop size than does the drop volume, one would expect that the salt concentration in a drop would continue to increase with a future decrease in size. If, on the other hand, the collection efficiency decreases more with decreasing drop size than does the drop volume, the collection effect would rapidly overpower the volume effect so that at a specific drop size the salt concentration in a drop becomes maximum. The former scenario is precisely that expected from the variation of E with drop radius observed by Starr and Mason (1966) for particles with radii of a few microns, while the latter scenario is that expected from the observation of Wang and Pruppacher (1977b) for particles with radii of a few tenths of microns. A very recent field verification of both scenarios has been provided by Bächmann *et al.* (1996), who observed

by artificially dispersing water soluble aerosol particles of different radii that the solute concentration inside raindrops continuously increased with decreasing drop size when micron particles were captured, while exhibiting a maximum in drops of about 200 μm radius when submicron particles were captured.

Some verification of the flux model of Wang *et al.* (1978) came through the experiments of Deshler (1985), who found that the scavenging efficiency of small aerosol particles with $0.03 \leq r \leq 0.13\,\mu$m by drops of $1.2 \leq a \leq 1.3$ mm at relative humidities between 60 and 95% agreed with the theoretical values within a factor of two. Some verification of the trajectory model of Grover (1978) and Grover *et al.* (1977) was provided by the experiments of Leong *et al.* (1982), who studied drops of radius near 70 μm colliding with aerosol particles of $0.1 \leq r \leq 3\,\mu$m. Comparison of their experimental values with theory is made in Figure 17.21.

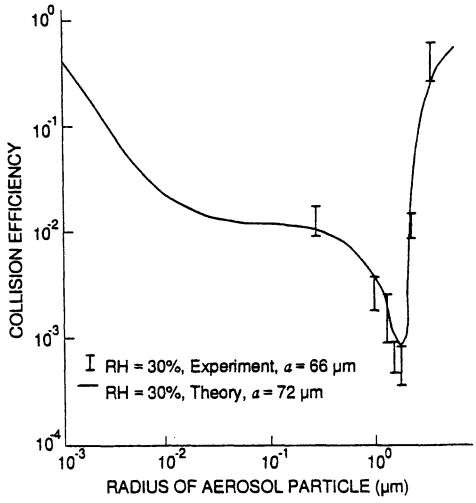


Fig. 17-21: Efficiency with which drops of $a \approx 70$ μm radius collide with aerosol particles of various sizes in air of 30% relative humidity and 20°C. Experiment: for $a = 66$ μm (From Leong *et al.*, 1982, with changes). Trajectory model: for $a = 72$ μm (from Grover, 1983, pers. comm.)

A considerable number of experimental observations are available to demonstrate the capacity of snow crystals to capture AP. The first observations were due to Facy (1955, 1958, 1960), who observed that evaporating crystals or drops develop a particle-free space adjacent to their surface. This effect, later confirmed by Goldsmith *et al.* (1963), Vittori and Prodi (1967), and Vittori (1973), was explained in terms of phoretic effects. However, it is obvious from our discussions in Section 17.4.2.2 that thermo- and diffusiophoresis have opposite effects on particle capture by a hydrometeor. This had previously been pointed out by Slinn and Hales (1971), and was demonstrated quantitatively by Martin *et al.* (1980) for planar snow crystals in Figure 17.22. We notice that the magnitude of the two phoretic forces become equal for AP with $2 < r < 3\,\mu$m. This result implies, e.g., that in

the case of a crystal growing by vapor diffusion, thermophoresis keeps the crystal free of particles and diffusiophoresis contributes to scavenging only if $r > 3\,\mu$m. This prediction has been verified experimentally by Prodi (1983), who showed that crystals, growing by vapor diffusion in an environment containing carnauba wax particles of $r \approx 0.17\,\mu$m, remained free of particles.

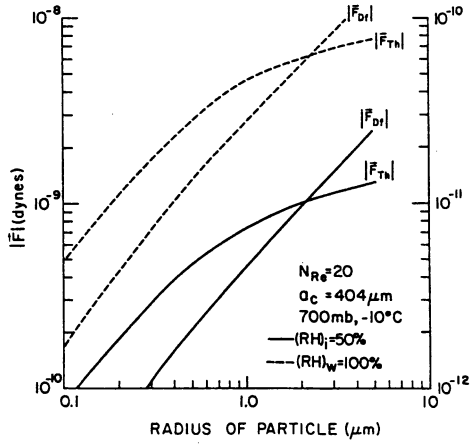


Fig. 17-22: Thermophoretic and diffusiophoretic force on aerosol particles of various sizes and $\rho_P = 2$ g cm^{-3} , moving around a planar snow crystal of a_c= 404 μm in air of $(RH)_i$ = 100% and 50% at -10°C and 700 mb. (From Martin *et al.*, 1980a; by courtesy of the Am. Meteor. Soc., and the authors.)

Experimental studies to determine the scavenging efficiency of aerosol particles by millimeter-sized snow crystals and snow flakes were carried out by Sood and Jackson (1969, 1970), Knutson *et al.* (1967), Prodi (1976, 1983), Murakami *et al.* (1981, 1983, 1985a,b,c), Sauter and Wang (1989), Mitra *et al.* (1990), and Bell and Saunders (1991). Snow crystal models rather than actual crystals were used by Stavitskaya (1972), Starr and Mason (1966), and Prodi *et al.* (1981). All these studies show that the scavenging efficiency of crystals larger than 1 mm in diameter decreases rapidly with increasing crystal size (see Figure 17.23). In fact, a combination of the computations of Martin *et al.* (1980) with the observations of Knutson *et al.* (1967), results in an efficiency maximum near a crystal diameter of 1 mm (see Figure 17.23), in analogy to the maximum exhibited in Figure 17.20 for drops. The decrease in E with increasing crystal size was explained by Mitra *et al.* (1990) in the same way as was done for drops; i.e., the fall velocity of most snow crystals increases with increasing size at less than a proportional rate, so that N_S and, hence, E decrease with increasing crystal size, as is observed.

A rather interesting deviation from this behavior, noted originally by Sood and Jackson (1969, 1970), has recently been confirmed by Mitra *et al.* (1990). They showed that snow crystal aggregates (flakes) of diameter 6 to 30 mm exhibit a scavenging efficiency which is larger than that of single crystals, and which does not decrease with increase size (Figure 17.24). Mitra *et al.* suggest that this effect

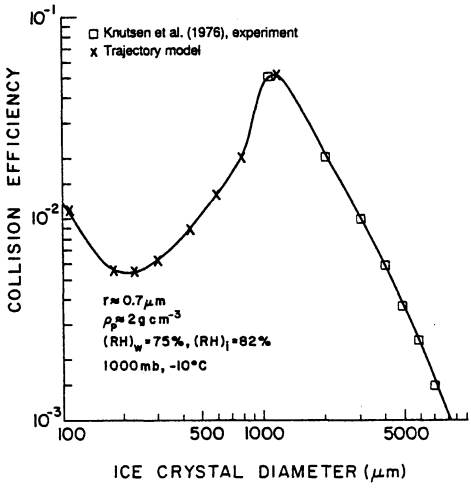


Fig. 17-23: Efficiency of aerosol particles of $r = 0.7$ μm and $\rho_P = 2$ g cm^{-3} colliding with planar snow crystals in air of $-10°$ C, 1000 mb and $(\mathrm{RH})_i = 82\%$. ($\times$) Trajectory model, ($\square$) Experiments of Knutson *et al.* (1976). (From Martin *et al.*, 1980a, with changes.)

is due to particle-filtering by the 'holes' in the crystal mesh of the snow flakes. Such a mechanism depends on the flow through the aggregates rather than around the crystal. To substantiate their arguments, Mitra *et al.* cited the theoretical work of Redkin (1973), who studied the scavenging behavior of a porous sphere exposed to Stokes flow, and found that its scavenging efficiency for particles of $0.2 \leq r \leq 2\,\mu$m was 5 to 8 times larger than the efficiency of an impervious sphere.

The scavenging efficiency of snow crystals of 1 to 5 mm in diameter was experimentally studied by Murakami *et al.* (1981, 1985a,b,c). Their results are plotted in Figures 17.25a,b. Although their observations could not resolve the actual location of the Greenfield gap, the decrease of E with decreasing particle radius is clearly noticeable. We also note from the data of Murakami that the surface roughness induced by the riming of snow crystals causes a significant increase in the efficiency with which aerosol particles are collected. Unfortunately, neither Murakami's nor Knutson's field studies can be used for comparison with the theoretical results of Martin *et al.* (1980), since the crystals studied in the field were considerably larger than those used in the theoretical model and since neither temperature nor the relative humidity which control the phoretic forces was measured. Also, the recent laboratory studies of Bell and Saunders (1991) are not suitable for comparison with theory, due to various experimental uncertainties. Thus, the authors gave no information regarding possible electric charges on the crystals and aerosol particles produced, and on the relative humidity at the scavenging site of their chamber. Also, no test was made on the possible growth of the sodium chloride particles in the vapor field of the evaporating ice crystals. These effects could have been responsible for the relatively large collision efficiencies found. Finally, surface roughness of the crystals and an uneven fall pattern due to an uneven mass loading make it

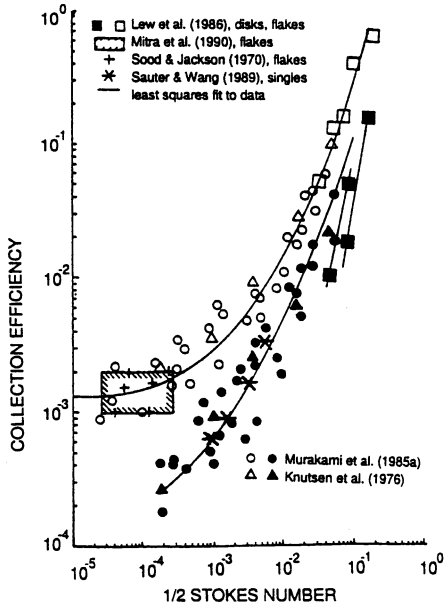


Fig. 17-24: Efficiency with which aerosol particles of diameter larger than 0.2 μm collide with planar snow crystals and with snow flakes of diameter larger than 1 mm in air of -2 to -10°C at ice saturation. (From Mitra *et al.*, 1990c, with changes.)

very difficult to compare experimentally derived collection efficiencies with those derived from theory for idealized bodies of smooth surface and even fall attitude.

In closing this section, we shall recall that it has been pointed out by McDonald (1964) that the atmosphere does provide a mechanism to 'bridge the Greenfield gap', in that the aerosol particles of radii between 0.1 and 1 μm are precisely those which most readily serve as cloud condensation and ice nuclei. As such, they may be removed from the atmosphere if cloud formation is followed by precipitation. It also seems likely that turbulence and electrical effects will tend to fill in the gap. Thus, Grover *et al.* (1977) and Wang *et al.* (1978) demonstrated this filling-in effect for the case of scavenging by Brownian diffusion, inertial- and phoretic forces, and because of the presence of electric charges and external electric fields. These results will be dicussed in Chatper 18. However, at the present time no definitive assessment of the overall problem including turbulence exists.

17.5 Scavenging of Gases by Cloud Drops, Raindrops and Ice Particles

Most gases and vapors present in the atmosphere exhibit a finite solubility in water, ranging from very low solubility for O_2, N_2, CO and CS_2 to very high solubility for NH_3, HNO_3 and HCl. The uptake of a gas by a water drop or ice crystal proceeds essentially in two stages. These will now be summarized briefly.

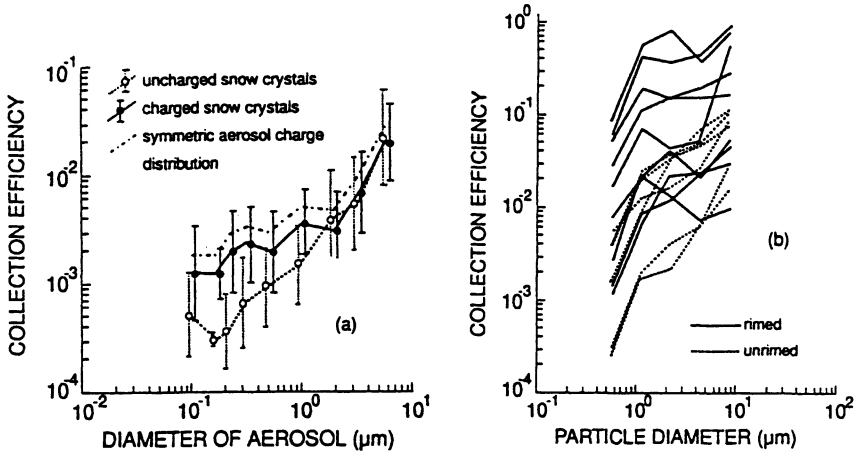


Fig. 17-25: Experimentally determined efficiency with which aerosol particles of various sizes are collected by various planar snow crystals of 1 to 5 mm diameter at ice saturation. (a) Uncharged vs. charged snow crystals (from Murakami, 1985c, with changes), (b) rimed vs. unrimed snow crystals. (From Murakami *et al.*, 1981, with changes).

During the *first stage*, the gas diffuses through the air to the surface of the hydrometeor. This stage is described by the laws of molecular or convective diffusion discussed for water vapor in Chapter 13. These laws can be applied to any gas if the appropriate molecular diffusivity D_g is used. Diffusivities for selected gases in air are listed in Table 17.13. Models which describe the diffusion of a gas species to a water drop will be discussed in Section 17.5.1.2.

During the *second stage*, the gas enters the hydrometeor. If the hydrometeor is a drop, the gas molecules become dissolved in the water while surrounding themselves with water molecules. Gases such as H_2, He, Ne, Ar, Kr, Xe, N_2, O_2, and O_3 molecularly disolve in water, while gases, such as SO_2 and NH_3, dissociate into ions, after having been dissolved in water. Once inside the drop, the dissolved gas molecules and ions spread through the drop by molecular diffusion. Such diffusion is significantly enhanced by the laminar or turbulent flow present in internally circulating drops (see Section 10.3.1). Molecular diffusivities D_l for various species in water range typically between 1×10^{-5} to 2×10^{-5} cm^2 sec^{-1} (Himmelblau, 1964; Broeker and Peng, 1974; Barrie, 1978; Carmichael and Peters, 1979; Worsnop *et al.*, 1989). We shall see in Section 17.5.1.2 that molecular diffusivities may be used to describe the diffusion process if the motion inside the drop can be completely modeled. Unfortunately, this is not possible anymore for drops of millimeter-size. In Section 10.3.1, we have already pointed out that drops of such size exhibit an internal flow which alternates rapidly between a laminar circulation and a completely turbulent flow. In fact, laboratory experiments of Diehl (1989) showed that in millimeter-size drops, the laminar circulation remains for about 0.75 seconds, after which a completely turbulent interior takes over, lasting for about 0.25 seconds. Thus, for a correct description of the gas uptake by such drops, a model

TABLE 17.13
Diffusivity of various gases in air.

Gas	Diffusivity (cm^2 sec^{-1})	Observer
H_2O_2	0.243 (in H_2O vap.), 0.22 (in Ar), 0.61 (in He)	Leaist(1984)
	0.166	Kumar (1985)
	0.186	Durham *et al.* (1984)
CO_2	0.16 - 0.17	Sherwood *et al.* (1975)
O_3	0.157	Durham *et al.* (1984)
NH_3	0.218	Kumar (1985)
N_2O_5	0.122 (in He + H_2O vap)	Van Doren *et al.* (1990)
HNO_3	0.127 (in He + H_2O vap)	Van Doren *et al.* (1990)
SO_2	0.136 + 5.64 (T-T_0)	Barrie (1978)
	0.126 820 °C), 0.12 (0°C)	Beilke & Gravenhorst (1978)
	0.124 (in H_2O vap), 0.099 (in Ar), 0.43 (in He)	Leaist (1984)
	0.130	Kumar (1985)
HCOOH	0.095 (in H_2O vap), 0.083 (in He)	Jayne *et al.* (1990)
	0.153	Lugg (1968)
CH_3COOH	0.528 (in H_2O vap), 0.378 (in He)	Lugg (1968)
HCHO	0.172	Kumar (1985)

which assumes that the drop is well-mixed during its turbulent stage must be alternated with a laminar convective diffusion model. Such a procedure is quite computer intensive. Fortunately, wind tunnel studies of Walcek *et al.* (1984), Waltrop *et al.* (1991), Mitra *et al.* (1993), and Hannemann *et al.* (1995) suggest that such an alternating application of two diffusion models to drops of millimeter-size may be parameterized by introducing a modified diffusivity $D_l^* = B(a_0)D_l$, where $B(a_0) \approx 25$, for $a_0 = 2$ mm.

If the hydrometeor is an ice particle, the gas becomes adsorbed on the surface of the ice particle if the temperature is sufficiently low. At temperatures close to 0°C, the gas becomes dissolved in the quasi-liquid layer. Unfortunately, the solubility of gases in such a layer is not known. Following its uptake on the ice surface, the gas may diffuse into the ice particles along grain boundaries if the ice particle is polycrystalline, or along dislocations if the particle is a single crystal. Unfortunately, no theoretical framework is available at present to describe the diffusional uptake of gases by ice particles. We shall, therefore, return to our discussion of the gas uptake by a liquid body.

Experiments show that, after a sufficiently long time, a solubility equilibrium becomes established between the gas in the gas phase and the gas dissolved in water. For small water drops, this equilibrium is very rapidly established and involves the whole drop. With increasing drop size, the time to reach equilibrium lengthens until eventually it is longer than the times over which significant changes in the gas phase concentration take place in the drop's evironment. Drops of these sizes will not come into complete solution equilibrium with the environment. Also, no solution equilibrium will be established if the gas entering a drop becomes converted into solute species which do not participate in the solution equilibrium. Nevertheless, it turns out that in many cases the concept of solution equilibrium may at least be applied to the surface layer of the drop in terms of a 'local equilibrium' between the

gas in the gas phase and the gas dissolved in the surface layer (see Section 17.5.3).

The equilibrium between a gas in the gas phase and the gas dissolved in water is described by Henry's law. In order to illustrate this law, we consider a gas species A to be in complete solution equilibrium, i.e.,

$$(A)_g \rightleftharpoons (A)_{aq} \tag{17-44}$$

where $(A)_{aq}$ denotes the hydrated gas species. Henry's law expresses the experimental observation that the concentration of a gas in water is proportional to the partial pressure of this gas in the gas phase. This may be expressed by the relation

$$[A]_{aq} = K_H p_A \,, \tag{17-45a}$$

or

$$[A]_{aq} = k_H [A]_g \,, \tag{17-45b}$$

where the square brackets indicate concentration, K_H is Henry's law coefficient in M atm^{-1}, with M in mole liter^{-1}, and k_H is the dimensionless Henry's law coefficient, so that $k_H = K_H \mathscr{R} T$. We must note that (17-45a,b) are only applicable to gases which do not dissociate in water into ions. For gases which dissociate in water, a modified Henry's law coefficient, given by the symbol K_H^*, has to be introduced which involves the dissociation constants. Also, (17-45a,b) are only applicable if the uptake of the gas leads to a low or moderate concentration of the gas in water. For computing the uptake of gases by highly concentrated thin water films, present, e.g., at the surface of aerosol particles, one must replace the concentration of the gas in water by the activity of the gas in water (see Chapter 4).

Many of the gases, relevant to cloud chemistry, dissociate in one or more stages into ions, thereby establishing equilibrium between the dissociated and undissociated species. These dissociation equilibria follow the mass action law of Guldberg and Waage (see current text books in physical chemistry). To illustrate this law, we consider the gas species A and B which dissociate into ion species C and D according to the equilibrium

$$\alpha A + \beta B \rightleftharpoons \gamma C + \delta D \,. \tag{17-46}$$

The constant for dissociation equilibrium may then be found from

$$K = \frac{[C]^\gamma [D]^\delta}{[A]^\alpha [B]^\beta} \,, \tag{17-47}$$

where α, β, γ and δ indicate the number of molecules involved in the dissociation reaction.

Henry's law coefficient K_H and the dissociation constants K are temperature dependent. This dependency may be expressed by van't Hoff's relation $\mathrm{d} \ln K / \mathrm{d}T = \Delta H / \mathscr{R} T^2$, where ΔH is the increase in enthalpy when the reaction takes place from left to right in (17-46), $\mathscr{R}$ is the universal gas constant, T is temperature, and K is the equilibrium constant. Over a small temperature range, one may assume that ΔH is approximately independent of temperature. Integrating the van't Hoff

TABLE 17.14

Henry's constant K_H(M atm^{-1}) for various gases in air in equilibrium with water. To compute the dimensionless k_H consider $k_H = K_H \mathscr{R} T$, with $\mathscr{R} = 0.82$ atm M^{-1} K^{-1} and M = mole liter $^{-1}$.

Gas	$K_{H,298}$ (M atm^{-1})	$\Delta H_{298}/\mathscr{R}$ (K)	Observer
H_2O_2	9.7×10^4	-6600	Chameides (1984)
	7.4×10^4	-6600	Lind and Kok (1986)
	7.1×10^4	-6800	Martin & Damschen (1981)
HO_2	2.0×10^3	-6600	Schwartz (1984a,b)
OH	25	-5200	Klanning *et al.* (1985)
O_3	1.15×10^{-2}	-2560	NBS/Johnson & Isaksen (1993)
	1.13×10^{-2}	-2300	Kosak & Helz (1983)
	1.10×10^{-2}	-2400	Hoffmann & Calvert (1985)
CO_2	3.4×10^{-2}	-2440	Stumm & Morgan (1981)
	3.1×10^{-2}	-2423	Chameides (1984)
HCl	1.1	-2020	Marsch & McElroy (1985)
HNO_2	49	-4800	Schwartz & White (1981)
HNO_3	2.1×10^5	-8700	Schwartz & White (1981)
NO	1.9×10^{-3}	-1480	Schwartz & White (1981)
NO_2	6.4×10^{-3}	-2500	Lee & Schwartz (1981)
NH_3	75	-3400	Hales & Drewes (1979)
	58	-4085	NBS/Chameides (1984)
SO_2	1.2	-3135	Hoffmann & Calvert (1985)
	$\log K_H = (1376/T)$ -4.521		Maahs (1982)
HCOOH	5.5×10^3	-5736	Helas *et al.* (1992)
CH_3COOH	8.7×10^{-3}	-6391	Winniwater *et al.* (1988)

relation with this assumption from $T = 298$ K to another arbitrary temperature T one finds

$$K(T) = K_{298} \exp\left[\frac{\Delta H_{298}}{\mathscr{R}}\left(\frac{1}{298} - \frac{1}{T}\right)\right]. \tag{17-48}$$

Values for $K_{H,298}$, K_{298}, and the respective values for ΔH_{298} are listed for some pertinent gases in Tables 17.14 and 17.15a,b, with K in mole liter^{-1} and $\Delta H/\mathscr{R}$ in K. Applying (17-48) to K_H and considering the values in Table 17.14, one finds that for the gases listed, K_H increases as T decreases, reflecting a greater solubility of the gas at lower temperatures. Solution and dissociation equilibria for some pertinent gases will be discussed in Section 17.5.1.1. Note that these equilibria pertain to bulk water only. No knowledge is available on effects of drop volume on the dissociation mechanism. Also, values for the given constants are only available for temperatures above 0°C. Any extrapolation to below 0°C has to be carried out with great caution.

While diffusing, some of the dissociated species may undergo chemical reactions with other species present. The rate at which such reactions proceed are described by empirically derived rate equations. Examples for such reactions and their rates are listed in Table 17.16, again only for temperatures above 0°C

TABLE 17.15
Dissociation constants for various chemical species in water.

Gas	K_{298} (M)	$\Delta H_{298}/\mathscr{R}$ (K)	Observer
H_2O	$K_w = 1.0 \times 10^{-14}$	+6716	NBS, Johnson & Isaksen (1993)
	$K_w = 1.0 \times 10^{-14}$	+6670	Hoffman & Calvert (1985)
	$K_w = 1.0 \times 10^{-14}$	+6710	Smith & Martell (1976)
CO_2	$K_1 = 4.3 \times 10^{-7}$	+ 913	Chameides (1984)
	$K_1 = 4.3 \times 10^{-7}$	+ 919	Stumm & Morgan (1981)
	$K_1 = 4.4 \times 10^{-7}$	+1000	Hoffman & Calvert (1985)
	$K_2 = 4.7 \times 10^{-11}$	+1787	Stumm & Morgan (1981)
HNO_2	$K_1 = 5.1 \times 10^{-40}$	+1260	Schwartz & White (1981)
	$K_1 = 5.9 \times 10^{-4}$	+1760	NBS(1965), Chameides (1984)
HNO_3	$K_1 = 15.1$	-8700	Schwartz & White (1981)
HCl	$K_1 = 1.7 \times 10^{6}$	-6900	Marsch & McElroy (1985)
SO_2	$K_1 = 1.23 \times 10^{-2}$	-2010	Smith & Martell (1976)
	$K_1 = 1.7 \times 10^{-2}$	-2090	Chameides (1984)
	$K_1 = 1.3 \times 10^{-2}$	-2000	Hoffman & Calvert (1985)
	$K_2 = 6.6 \times 10^{-8}$	-1510	Smith & Martell (1976)
	$K_2 = 6.3 \times 10^{-8}$	-1495	Hoffman & Calvert (1985)
	$\log K_1 = (853.0/T)-4.740$		Maahs (1982, 1983)
	$\log K_2 = (621.9/T)-9.278$		
	$K_3 = 1.0 \times 10^{-2}$	-2720	Smith & Martell (1976)
NH_3	$K_1 = 1.71 \times 10^{-5}$	+4325	Hoffmann & Calvert (1985)
	$K_1 = 1.75 \times 10^{-5}$	+4325	Smith & Martell (1976)
HO_2	$K_1 = 2.05 \times 10^{-5}$		Bielski (1978)
	$K_1 = 3.5 \times 10^{-5}$		Perrin (1982)
H_2O_2	$K_1 = 1.58 \times 10^{-12}$	+3700	Hoffmann & Calvert (1985)
HCOOH	$K_1 = 1.8 \times 10^{-4}$	- 151	Helas *et al.* (1992)
CH_3COOH	$K_1 = 1.7 \times 10^{-5}$	- 50	Winiwater *et al.* (1988)

17.5.1 Scavenging of Gases by Water Drops

17.5.1.1 *Solution and Dissociation Equilibria*

In the present section, we shall describe the solution and dissociation equilibria for a few of the gases and vapors relevant to cloud chemistry.

1. Water, H_2O

Water is perhaps the most simple example for which to demonstrate a dissociation equilibrium. In pure water, a water molecule is slightly dissociated into hydrogen ions H^+ and hydroxyl ions OH^- according to the equilibrium relation

$$H_2O \rightleftharpoons H^+ + OH^- . \tag{17-49}$$

According to the mass action law, this equilibrium can be expressed by the relation

$$K_1 = \frac{[H^+][OH^-]}{[H_2O]} = \frac{k_w}{[H_2O]} \quad (17\text{-}50a); \qquad k_w = [H^+][OH^-] . \tag{17-50b}$$

TABLE 17.16

Oxidation rate of S(IV) to S(VI) in water: R (M sec^{-1}) = - d [S(IV)]/dt = d [S(VI)]/dt; (a) oxidation by H_2O_2, (b) Oxidation by O_3, (c) oxidation by O_2 in presence of metal ions (Fe^{2+}, Fe^{3+}, Mn^{2+}).

	Observer
(a) $R(\text{M sec}^{-1}) = \frac{k_1[\text{H}^+][\text{H}_2\text{O}_2]_{aq}[\text{S(IV)}]}{1+B[\text{H}^+](1+\frac{[\text{H}^+]}{K_1})}$	Gunz & Hoffmann (1990)
k_1 (M^{-2} sec^{-1}) = 7.45×10^{-7} exp[4430($\frac{1}{298} - \frac{1}{T}$)]	McArdle & Hoffmann (1983)
B (M^{-1}) = 13 (16)	Hoffmann & Calvert (1985)
$R(\text{M sec}^{-1}) = \frac{k_2[\text{H}_2\text{O}_2][\text{SO}_2]_{aq}}{1+B[\text{H}^+]}$	Martin (1983, 1984)
k_2 (M^{-1} sec^{-1}) = $(8 \pm 2) \times 10^5$ exp[3650($\frac{1}{298} - \frac{1}{T}$)]	Martin & Dahmshen (1981)
B (M^{-1}) = 10	
(b) $R(\text{M sec}^{-1}) = (k_1 + k_2\ 10^{\text{pH}})$ [S(IV)][O_3]aq	
k_1 (M^{-1} sec^{-1}) = 4.39×10^{11} exp($-4131/T$)	Maahs (1983)
k_2 (sec^{-1}) = 2.56×10^3 exp($-966/T$)	
$10^{\text{pH}} = 1/[\text{H}^+]$	
$R(\text{M sec}^{-1}) = (k_0\alpha_0 + k_1\alpha_1 + k_2\alpha_2)$ [S(IV)][O_3]aq	
$\alpha_0 = [(SO_2)_{aq}]/[\text{S(IV)}]$	
$\alpha_1 = [HSO_3^-]/[\text{S(IV)}]$	
$\alpha_2 = [SO_3^{2-}]/[\text{S(IV)}]$	
k_0 (M^{-1} sec^{-1}) = 2.4×10^4 Hoffmann $=(2 \pm 0.29 \times 10)^4$	Hoigné *et al.*
k_1 (M^{-1} sec^{-1}) = 3.7×10^5 (1986) $=(3.2 \pm 0.2) \times 10^5$	(1985)
k_2 (M^{-1} sec^{-1}) = 1.5×10^9 $=(1.0 \pm 0.2) \times 10^9$	
(c) $R(\text{M sec}^{-1}) = 620\ [Fe^{2+}]^{0.5}[\text{H}^+]^{0.5}\ [\text{S(IV)}]^2$	Ibusuki *et al.* (1990)
$R(\text{M sec}^{-1}) = k\ [Fe^{3+}][SO_3^{2+}]$	Hoffmann & Calvert (1985)
$k(M^{-1}\ sec^{-1}) = 1.2 \times 10^6$	
$R(\text{M sec}^{-1}) = k$ [Fe(III)][S(IV)]	
$k(\mu\text{g ml sec}^{-1}) = 3.6 \times 10^{-2}$	Grgic *et al.* (1991,1992)
$R(\text{M sec}^{-1}) = k\ [Fe^{3+}][\text{H}^+]^{-1}$ [S(IV)]	Martin & Hill (1987)
$k(sec^{-1}) = k_0 \times 10^{-2.0}\ I^{1/2}/(1+I^{1/2})$	
k_0 (sec^{-1}) = 6.0; I = ionic strength	
$R(\text{M sec}^{-1}) = k\ [Mn^{2+}][HSO^-_3]$	Hoffmann & Calvert (1985)
$k(M^{-1}\ sec^{-1}) = 3.4 \times 10^3$	
$R(\text{M sec}^{-1}) = k\ [\text{Mn(II)}][\text{S(IV)}]^{0.65}$	Grgic *et al.* (1991)
$k(\mu g^{-0.65}\ ml^{0.65}\ sec^{-1}) = 2.5 \times 10^{-2}$	

TABLE 17.16 (continued)

$R(\text{M sec}^{-1}) = k\,[\text{Mn}^{2+}][\text{S(IV)}]$ $k(\text{M}^{-1}\text{ sec}^{-1}) = k_0 \times 10^{-4.07\, I^{1/2}/(1+I^{1/2})}$ $k_0(\text{M}^{-1}\text{ sec}^{-1}) = (1000 \pm 50)$	Martin & Hill (1987)
$R(\text{M sec}^{-1}) = (k_1\,[\text{Fe(III)}] + k_2\,[\text{Mn(II)}] + k_3\,[\text{Fe(III)Mn(II)}])[\text{S(IV)}]$ $k_1(\text{M}^{-1}\text{ sec}^{-1}) = 2600$ $k_2(\text{M}^{-1}\text{ sec}^{-1}) = 750$ $k_3(\text{M}^{-2}\text{ sec}^{-1}) = 1.0 \times 10^{10}$	Martin & Good (1991)

Since in pure water $[H^+] = [OH^-]$, it follows from Table 17.15 that $[H^+] = [OH^-] = 1.0 \times 10^{-7}$ mole liter^{-1} (25°C). It is common to express the acidity of a solution in terms of the concentration of the hydrogen ions $[H^+]$ in solution, and to introduce as a measure for the acidity the so-called pH, defined by the relation

$$\text{pH} = -\log[H^+]\,. \tag{17-51}$$

Thus, we find from Table 17.15 that, for pure water, pH= 7. Solutions whose pH< 7 are called acidic, solutions with pH> 7 are called basic or alkaline.

2. Hydrogen Peroxide, H_2O_2

The solution and dissociation equilibria for this gas can be described by the relations

$$(H_2O_2)_g \rightleftharpoons (H_2O_2)_{aq}\,, \tag{17-52a}$$

$$(H_2O_2)_{aq} \rightleftharpoons HO_2^- + H^+\,. \tag{17-52b}$$

The constants which characterize these equilibria are

$$K_H = \frac{[H_2O_2]_{aq}}{p_{H_2O_2}} \quad (17\text{-}53a)\,, \qquad K_1 = \frac{[H^+][HO_2^-]}{[H_2O_2]_{aq}}\,. \tag{17-53b}$$

3. Carbon dioxide, CO_2

The solution and dissociation equilibria for CO_2 can be expressed by the relations:

$$(CO_2)_g \rightleftharpoons (CO_2)_{aq}\,, \tag{17-54a}$$

$$(CO_2)_{aq} + H_2O \rightleftharpoons H^+ + HCO_3^-\,, \tag{17-54b}$$

$$HCO_3^- \rightleftharpoons H^+ + CO_3^{2-}\,. \tag{17-54c}$$

The constants which characterize these equilibria are

$$K_H = \frac{[(CO_2)_{aq}]}{p_{CO_2}} \quad (17\text{-}55a)\,, \qquad K_1 = \frac{[H^+][HCO_3^-]}{[(CO_2)_{aq}]} \quad (17\text{-}55b)\,, \qquad K_2 = \frac{[H^+][CO_3^{2-}]}{[HCO_3^-]}\,. \tag{17-55c}$$

From a combination of these equations, we find for the equilibrium concentration of each species in water:

$$[(CO_2)]_{aq} = K_H p_{CO_2}\,, \tag{17-56a}$$

$$[HCO_3^-] = \frac{K_1[(CO_2)_{aq}]}{[H^+]} = \frac{K_H K_1}{[H^+]} p_{CO_2}\,, \tag{17-56b}$$

$$[CO_3^{2-}] = \frac{K_2[HCO_3^-]}{[H^+]} = \frac{K_H K_1 K_2}{[H^+]^2} p_{CO_2}\,. \tag{17-56c}$$

The total concentration of all carbon species, dissociated and undissociated, is

$$[(CO_2)_{aq}] + [HCO_3^-] + [CO_3^{2-}] = K_H \left(1 + \frac{K_1}{[H^+]} + \frac{K_1 K_2}{[H^+]^2}\right) p_{CO_2}\,. \tag{17-57}$$

It has become customary to define a modified Henry's law coefficient K_H^* by including the effects of dissociation.

$$K_H^* = K_H \left(1 + \frac{K_1}{[H^+]} + \frac{K_1 K_2}{[H^+]^2}\right). \tag{17-58}$$

The ions in solution obey the condition of electroneutrality. This implies

$$[H^+] = [OH^-] + [HCO_3^-] + 2[CO_3^{2-}]. \tag{17-59}$$

Considering that $[OH^-] = k_w/[H^+]$, one finds that the equilibrium concentration of hydrogen ions can be computed from

$$[H^+]^3 - (k_w + K_H K_1 p_{CO_2})[H^+] - 2K_H K_1 K_2 p_{CO_2} = 0\,. \tag{17-60}$$

The pH of a solution can then be evaluated from (17-53). For typical atmospheric conditions, we may assume $[CO_2]_g \approx 330$ ppm, which implies from (17-60) that in the absence of other pollutant gases cloud and rain water in equilibrium with atmospheric CO_2 has a pH$\approx$ 5.6.

4. Sulfur dioxide, SO_2

The solution and dissociation equilibrium for this gas can be expressed by the relations

$$(SO_2)_g \rightleftharpoons (SO_2)_{aq}\,, \tag{17-61a}$$

$$(SO_2)_{aq} + H_2O \rightleftharpoons H^+ + HSO_3^-\,, \tag{17-61b}$$

$$HSO_3^- \rightleftharpoons H^+ + SO_3^{2-}\,. \tag{17-61c}$$

The constants which characterize these equilibria are

$$K_H = \frac{[(SO_2)_{aq}]}{p_{SO_2}}\ (17\text{-}62a)\,, K_1 = \frac{[H^+][HSO_3^-]}{[(SO_2)_{aq}]}\ (17\text{-}62b)\,, K_2 = \frac{[H^+][SO_3^{2-}]}{[HSO_3^-]}. (17\text{-}62c)$$

From a combination of these equations, we find for the concentration of each species in water

$$[(SO_2)_{aq}] = K_H p_{SO_2}\,, \tag{17-63a}$$

$$[HSO_3^-] = \frac{K_1[(SO_2)_{aq}]}{[H^+]} = \frac{K_H K_1}{[H^+]} p_{SO_2}\,, \tag{17-63b}$$

$$[SO_3^{2-}] = \frac{K_2[HSO_3^-]}{[H^+]} = \frac{K_H K_1 K_2}{[H^+]^2} p_{SO_2}\,. \tag{17-63c}$$

The total concentration of the S(IV) species is then

$$[S(IV)] = [(SO_2)_{aq}] + [HSO_3^-] + [SO_3^{2-}] = K_H^* p_{SO_2}\,, \tag{17-64}$$

where K_H^* is the modified Henry's law coefficient as defined by (17-58) for a two-stage dissociation. The ions in solution follow the law of electroneutrality, which is

$$[H^+] = [OH^-] + [HSO_3^-] + 2[SO_3^{2-}]\,. \tag{17-65}$$

Substituting (17-50) for $[OH^-]$ and using (17-63b) and (17-63c), we may compute the equilibrium hydrogen ion concentration from

$$[H^+]^3 - (k_w + K_H K_1 p_{SO_2})[H^+] - 2K_H K_1 K_2 p_{SO_2} = 0\,, \tag{17-66}$$

which determines the pH of the solution. Often it is more convenient to determine $[H^+]$ from the total concentration of S(IV), the 4-valenced sulfur in solution. For this purpose, we replace p_{SO_2} in (17-66) by $[S(IV)]/K_H^*$ from (17-64) and disregard k_w in comparison to $K_H K_1 p_{SO_2}$ to obtain

$$[H^+]^3 + K_1[H^+]^2 + (K_1 K_2 - K_1[S(IV)])[H^+] - 2K_1 K_2[S(IV)] = 0\,. \tag{17-67}$$

Considering (17-63a) to (17-63c) together with (17-64), we obtain for the mole fractions of the various S(IV) species:

$$x_{SO_2 \cdot H_2O} = \frac{[(SO_2)_{aq}]}{[S(IV)]} = \left[1 + \frac{K_1}{[H^+]} + \frac{K_1 K_2}{[H^+]^2}\right]^{-1}; \tag{17-68a}$$

$$x_{HSO_3^-} = \frac{[HSO_3^-]}{[S(IV)]} = \left[1 + \frac{[H^+]}{K_1} + \frac{K_2}{[H^+]^2}\right]^{-1}; \tag{17-68b}$$

$$x_{SO_3^{2-}} = \frac{[SO_3^{2-}]}{[S(IV)]} = \left[1 + \frac{[H^+]}{K_2} + \frac{[H^+]^2}{K_1 K_2}\right]^{-1}. \tag{17-68c}$$

The variation of the mole fraction of these species is plotted as a function of pH in Figure 17.26. We note from this figure that, for $pH \lesssim 5.5$, which is typical for cloud and rain water in most regions of the Earth, the concentration of SO_3^{2-} can be considered sufficiently small so that it may be neglected in comparison to the concentration of $SO_2 \cdot H_2O$ and HSO_3^-. Neglecting $[OH^-]$ and $[SO_3^{2-}]$ in comparison with $[HSO_3^-]$ in (17-65), the condition for electroneutrality becomes

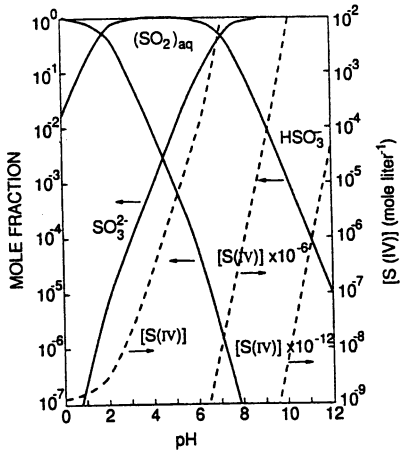


Fig. 17-26: Equilibrium mole fraction and concentration of the three dissolved S(IV) species: $(SO_2)_{aq}$, HSO_3^-, and SO_3^{2-}, as a function of pH at 25°C and $p_{so_2} = 10^{-9}$ atm (1 ppbv). (From Seinfeld, 1986, with changes.)

$$[H^+] = [HSO_3^-], \tag{17-69}$$

from which we obtain, instead of (17-63b), (17-64), (17-66) and (17-67):

$$[HSO_3^-] = (K_H K_1 p_{SO_2})^{1/2}; \tag{17-70}$$

$$[S(IV)] = K_H \left(1 + \frac{K_1}{[H^+]}\right) p_{SO_2} = K_H p_{SO_2} + (K_H K_1 p_{SO_2})^{1/2}; \tag{17-71}$$

$$[H^+]^2 - K_H K_1 p_{SO_2} = 0; \tag{17-72}$$

$$[H^+]^2 + K_1[H^+] - K_1[S(IV)] = 0. \tag{17-73}$$

If we assume that the water drop contains an oxidizing agent which is able to convert the 4-valenced sulfur S(IV) to the 6-valenced sulfur S(VI), at a known rate we must consider the presence of HSO_4^- and SO_4^{2-} in the solution. Considering that the S(IV) species is virtually fully dissociated, we have

$$HSO_4^- \rightleftharpoons H^+ + SO_4^{2-}, \tag{17-74}$$

with the equilibrium constant

$$K_3 = \frac{[H^+][SO_4^{2-}]}{[HSO_4^-]}. \tag{17-75}$$

The total concentration of S(VI) is then

$$[S(VI)] = [HSO_4^-] + [SO_4^{2-}], \tag{17-76}$$

so that the concentration of the ion species in (17-76) as a function of S(VI) becomes

$$[SO_4^{2-}] = \frac{K_3[S(VI)]}{[H^+] + K_3} \quad (17\text{-}77), \qquad [HSO_4^-] = \frac{[H^+][S(VI)]}{[H^+] + K_3}. \tag{17-78}$$

For pH$\leq$ 5.5 , the condition for electroneutrality is

$$[H^+] = [HSO_3^-] + [HSO_4^-] + 2[SO_4^{2-}]. \tag{17-79}$$

Considering (17-77), (17-78) and (17-63b), we may compute the equilibrium hydrogen ion concentration from

$$\begin{aligned} [H^+]^3 + \{(K_1 + K_3) - [S(VI)]\}[H^+]^2 \\ +\{K_1K_3 - [S(IV)]K_1 - [S(VI)](K_1 + 2K_3)\}[H^+] \\ -K_1K_3\{[S(IV)] + 2[S(VI)]\} \quad = \quad 0. \end{aligned} \tag{17-80}$$

If, in addition, a drop contains dissolved ammonium sulfate, $(NH_4)_2SO_4$, we must consider also NH_4^+ in the equation for electroneutrality. Assuming complete dissociation of the salt, the equation for electroneutrality is then

$$[NH_4^+] + [H^+] = [HSO_3^-] + [HSO_4^-] + 2[SO_4^{2-}]. \tag{17-81}$$

The equilibrium hydrogen ion concentration is found from

$$\begin{aligned} [H^+]^3 + \{(K_1 + K_3) - [S(VI)] + [NH_4^+]\}[H^+]^2 + \{K_1K_3 \\ -([S(IV)] - [NH_4^+])K_1 - [S(VI)](K_1 + 2K_3) + [NH_4^+]K_3\}[H^+] \\ -K_1K_3\{[S(IV)] + 2[S(VI)] - [NH_4^+]\} = 0. \end{aligned} \tag{17-82}$$

5. Ammonia, NH_3

The solution and dissociation equilibria for NH_3 can be expressed by the relations

$$(NH_3)_g \rightleftharpoons (NH_3)_{aq}, \tag{17-83}$$

$$(NH_3)_{aq} \rightleftharpoons NH_4^+ + OH^-. \tag{17-84}$$

The constants which characterize these equilibria are

$$K_H = \frac{[(NH_3)_{aq}]}{p_{NH_3}} \quad (17\text{-}85a), \qquad K_1 = \frac{[NH_4^+][OH^-]}{[(NH_3)_{aq}]}. \tag{17-85b}$$

From a combination of these equations, we find for the concentration of each species:

$$[(NH_3)_{aq}] = K_H p_{NH_3}, \tag{17-86a}$$

$$[NH_4^+] = \frac{K_1[(NH_3)_{aq}]}{[OH^-]} = \frac{K_H K_1[H^+]}{k_w} p_{NH_3}. \tag{17-86b}$$

The total concentration of all N(III)-species present in this reaction is

$$[\mathrm{N(III)}] = [(\mathrm{NH_3})_{aq}] + [\mathrm{NH_4^+}] = K_H \left(1 + \frac{K_1[\mathrm{H^+}]}{k_\mathrm{w}}\right) p_{\mathrm{NH_3}} = K_H^* p_{\mathrm{NH_3}}\,, \quad (17\text{-}87)$$

where K_H^* is the modified Henry's law coefficient. For $[\mathrm{H^+}] \ll [\mathrm{OH^-}]$, the condition for electroneutrality is

$$[\mathrm{NH_4^+}] = [\mathrm{OH^-}]\,. \quad (17\text{-}88)$$

Inserting (17-50b) and (17-86b) into (17-88), we find the equilibrium concentration of the hydrogen ions from

$$[\mathrm{H^+}] = \frac{k_\mathrm{w}}{(K_H K_1 p_{\mathrm{NH_3}})^{1/2}}\,; \quad (17\text{-}89)$$

or, in terms of [N(III)] after substituting for $p_{\mathrm{NH_3}}$ in (17-89) using (17-87),

$$K_1[\mathrm{N(III)}][\mathrm{H^+}]^2 - K_1 k_\mathrm{w}[\mathrm{H^+}] - k_\mathrm{w}^2 = 0\,. \quad (17\text{-}90)$$

6. Nitric acid, HNO_3

The solution and dissociation equilibria for HNO_3 can be expressed by the relations

$$(\mathrm{HNO_3})_g \rightleftharpoons (\mathrm{HNO_3})_{aq}\,, \quad (17\text{-}91a)$$

$$(\mathrm{HNO_3})_{aq} \rightleftharpoons \mathrm{H^+} + \mathrm{NO_3^-}\,. \quad (17\text{-}91b)$$

The constants which characterize the equilibria are

$$K_H = \frac{[(\mathrm{HNO_3})_{aq}]}{p_{\mathrm{HNO_3}}}\,; \quad (17\text{-}92a) \qquad K_1 = \frac{[\mathrm{H^+}][\mathrm{NO_3^-}]}{[\mathrm{HNO_3}]_{aq}}\,. \quad (17\text{-}92b)$$

From a combination of these equations, we find the concentration of each species in the water from

$$[(\mathrm{HNO_3})_{aq}] = K_H p_{\mathrm{HNO_3}}\,, \quad (17\text{-}93a)$$

$$[\mathrm{NO_3^-}] = \frac{K_1 K_H}{[\mathrm{H^+}]} p_{\mathrm{HNO_3}}\,. \quad (17\text{-}93b)$$

The total concentration of all N(V) nitrogen species present is

$$[\mathrm{N(V)}] = [(\mathrm{HNO_3})_{aq}] + [\mathrm{NO_3^-}] = K_H \left(1 + \frac{K_1}{[\mathrm{H^+}]}\right) p_{\mathrm{HNO_3}}\,. \quad (17\text{-}94)$$

Unfortunately, K_H and K_1 are not well-known by themselves. Instead, the overall equilibrium coefficient $K_{oa} = K_H K_1 = 3.3 \times 10^6 \exp(-8700[(1/298) - (1/T)])$ $(\mathrm{M^2 atm^{-1}})$ has been determined for the overall reaction $(\mathrm{HNO_3})g \rightleftharpoons \mathrm{H^+} + \mathrm{NO_3^-}$. Since $K_1 \approx 15$ M at 298 K (see Table 17.15), and considering that in cloud water $[\mathrm{H^+}] \ll 15$ M, we may assume $([\mathrm{H^+}]/K_1) \ll 1$, and therefore approximate (see Wurzler *et al.*, 1995)

$$[\mathrm{N(V)}] \approx \frac{K_{oa}}{[\mathrm{H^+}]} p_{\mathrm{HNO_3}}\,. \quad (17\text{-}95)$$

The condition of electroneutrality is

$$[H^+] = [NO_3^-]\,. \tag{17-96}$$

From (17-93b), the equilibrium concentration of the hydrogen ions follows:

$$[H^+] = (K_{oa} p_{HNO_3})^{1/2}\,, \tag{17-97}$$

or alternatively in terms of [N(V)], after substituting for p_{HNO_3} in (17-97) by inserting (17-95):

$$[H^+] \approx [N(V)]. \tag{17-98}$$

17.5.1.2 *Diffusion Models for Gases*

We shall now proceed to formulate a theoretical framework with which to describe the rate at which a drop absorbs a specific gas present in its environment. For this purpose, we must recall the laws of diffusion discussed in Chapter 13, as well as the equilibrium formulations given in the previous section.

1. The perfect sink model

The simplest model for describing the uptake of a gas by a drop assumes that the drop is at rest and has an infinite capacity to accommodate the particular gas species, i.e., the drop behaves as a perfect sink. We, therefore, can completely disregard the drop's interior and consider only the diffusion of the species in the gas phase. The convective diffusion equation for gas (g) diffusing through air can then be written in analogy to the laws of diffusion of water vapor (see Section 13.1):

$$\frac{\partial c_g}{\partial t} + \vec{u}_g \cdot \nabla c_g = D_g \nabla^2 c_g\,, \tag{17-99}$$

where c_g is the concentration of the gas in the gas phase. For the case of a spherical drop at rest (i.e., $\vec{u}_g = 0$), we may assume that the diffusion field is radially symmetric, so that (17-99) becomes

$$\frac{\partial c_g}{\partial t} = D_g \left(\frac{\partial c_g}{\partial r^2} + \frac{2}{r} \frac{\partial c_g}{\partial r} \right)\,, \tag{17-100}$$

where r is the radial distance from the center of the drop. Since the drop is assumed to behave as a perfect sink, the concentration c_l of the species inside the drop can be considered to be zero at all times. This does not imply that the concentration $c_{g,a}$ of the species at the drop surface in the gas phase can also be set equal to zero. In fact, at steady state, with c_l remaining zero at all times, we expect (see Equation (17-114)) a small but finite gas concentration at the drop's surface, as required by the Hertz-Knudsen equation. However, without sacrificing significant

accuracy in the transient behavior to reach steady state, we may set $c_{g,a} = 0$. The boundary conditions for the present case are

$$\begin{aligned} c_g(r, t = 0) &= c_{g,\infty} \quad ; \quad r > a, t = 0 \\ c_g(r = \infty, t) &= c_{g,\infty} \quad ; \quad r \to \infty, t > 0 \\ c_g(r = a, t) &= c_{g,a} = 0 \end{aligned} \tag{17-101}$$

With these boundary conditions, (17-100) has the solution (see Equation (13-4) and Seinfeld, 1986)

$$\frac{c_g(r,t)}{c_{g,\infty}} = \left[1 - \frac{a}{r} + \frac{a}{r}\text{erf}\left(\frac{r-a}{2(D_g t)^{1/2}}\right)\right], \tag{17-102a}$$

or

$$\frac{c_g(r,t)}{c_{g,\infty}} = 1 - \frac{a}{r}\left[1 - \frac{2}{\sqrt{\pi}}\int_0^{(r-a)/2\sqrt{D_g t}} e^{-\xi^2}\, d\xi\right], \tag{17-102b}$$

where ξ is the integration variable. Evaluating the integral in (17-102b), one finds

$$\frac{c_g(r,t)}{c_{g,\infty}} = 1 - \frac{a}{r}\left[1 - \frac{2}{\sqrt{\pi}} e^{-\frac{(r-a)^2}{4D_g t}} \sum_{n=0}^{\infty} \frac{2^n u^{2n+1}}{1 \cdot 3 \ldots (2n+1)}\right], \tag{17-103}$$

where $u = (r-a)/2(D_g t)^{1/2}$. From (17-102a), we find for the radial flux density at the drop surface

$$(j_{g,r})_{r=a} = -D_g\left(\frac{\partial c_g(r,t)}{\partial r}\right)_{r=a} = -\frac{D_g c_{g,\infty}}{a}\left(1 + \frac{a}{(\pi D_g t)^{1/2}}\right). \tag{17-104}$$

For the overall flux to the drop, we have

$$J_g(r = a) = \int_S (j_{g,r})_{r=a}\, dS = -4\pi a D_g c_{g,\infty}\left(1 + \frac{a}{(\pi D_g t)^{1/2}}\right). \tag{17-105}$$

Equation (17-105) suggests selecting a characteristic time, (τ_{dg}), for the diffusion process in the gas phase such that the flux J_g of the gas to the drop is twice the flux $J_{g,\infty}$ at steady state, where $J_{g,\infty} = -4\pi a D_g c_{g,\infty}$. This characteristic time is $(\tau_{dg})_1 = a^2/\pi D_g$, with a in cm, D_g in cm^2 sec^{-1} and τ_{dg} in sec. Following Seinfeld (1986), one may alternatively define a characteristic time $(\tau_{dg})_2$ in terms of the time necessary for the gas concentration profile to relax to steady state. We notice from (17-103) that the response of the concentration to a change at $r = a$ depends on terms of the form $\exp[-(r-a)^2/4D_g t]$. This implies that the characteristic time for the concentration profile to relax to steady state increases with increasing r. Considering the concentration change at a distance a from the drop surface (i.e., at $r = 2a$), Seinfeld (1986) finds $(\tau_{dg})_2 = a^2/4D_g$, with $(\tau_{dg})_2$ in sec, and a in cm. Values for $(\tau_{dg})_1$, and $(\tau_{dg})_2$ are given in Table 17.17.

TABLE 17.17

Characteristic times for the diffusion of SO_2 in air and inside a water drop; for $p_{g,\infty} = 50$ ppbv, $D_g = 0.13$ cm^2 sec^{-1}, $D_l = 1.66 \times 10^{-5}$ cm^2 sec^{-1}, 15°C, 1000 mb. The values given in parentheses pertain to $D_l^* = 25D_l$.

Characteristic time (sec)	$a(\mu m)$ 10^3	10^2	10^1
$(\tau_{dg})_1 = a^2/\pi D_g$	2.4×10^{-2}	2.4×10^{-4}	2.4×10^{-6}
$(\tau_{dg})_2 = a^2/4D_g$	1.9×10^{-2}	1.9×10^{-4}	1.9×10^{-6}
$(\tau_{dl})_1 = a^2/\pi^2 D_l$	51	5.1×10^{-1}	5.1×10^{-3}
$(\tau_{dl})_2 = 0.056\ a^2/D_l$	28 (1.1)	2.8×10^{-1}	2.8×10^{-3}
$(\tau_{\text{circ}})_{\text{KB}} = 5 \times 10^{-4}/\ a$	5×10^{-3}	5×10^{-2}	5×10^{-1}
$(\tau_{dl})_{\text{KB}} = 0.022\ a^2/D_l$	11 (0.4)	1.1×10^{-1}	1.1×10^{-3}
$(\tau_{\text{abs}})_{\text{diss}} = a^2(K_H K_1/\ C_{g,\infty})^{1/2}/6D_g^* f_g$	19.7	1.4	2.2×10^{-2}

The rate at which gas is absorbed by a stationary drop is, from (17-105),

$$\left(\frac{dm}{dt}\right)_{0,l} = -J_g = 4\pi a D_g c_{g,\infty}\left(1 + \frac{a}{(\pi D_g t)^{1/2}}\right), \tag{17-106}$$

and the total mass of gas taken up by the drop at rest after a time t is (Seinfeld, 1980)

$$[m_g(t)]_l = 4\pi a D_g c_{g,\infty}\left(t + \frac{2a\sqrt{t}}{(\pi D_g)^{1/2}}\right). \tag{17-107}$$

Equation (17-103) has been evaluated for SO_2 by Beilke and Gravenhorst (1978), Baboolal *et al.* (1981), and Seinfeld (1980). Their results are illustrated in Figure 17.27 in terms of concentration profiles immediately adjacent to a drop of 10 μm. We note that the steady state concentration profile in the gas phase just outside the drop is rapidly established and, after 10^{-3} sec, has nearly reached the steady state concentration profile for which $c_g/c_{g,\infty} = 0.5$ at $r = 2a$ and $t \to \infty$, as predicted by (17-103). In addition, we find from (17-103) that for $t = \tau_{dg} = 10^{-4}$ sec $c_g/c_{g,\infty} = 0.92$, and for $t = 10^{-4}$, $c_g/c_{g,\infty} = 0.56$.

2. The well-mixed sink model

In order to make the foregoing model more realistic, we shall assume that the drop's capacity for gas uptake is limited and determined by Henry's law. Instead of line 3 in (17-101), we have as the boundary condition $c_g(r = a, t) = c_{g,a}$ which we consider constant. The solution to (17-100) for a drop at rest now becomes

$$c_g(r,t) = c_{g,\infty} + (c_{g,a} - c_{g,\infty})\frac{a}{r}\left[1 - \text{erf}\left(\frac{r-a}{2(D_g t)^{1/2}}\right)\right], \tag{17-108a}$$

and for steady state

$$c_g(r) = c_{g,\infty} + (c_{g,a} - c_{g,\infty})\frac{a}{r}. \tag{17-108b}$$

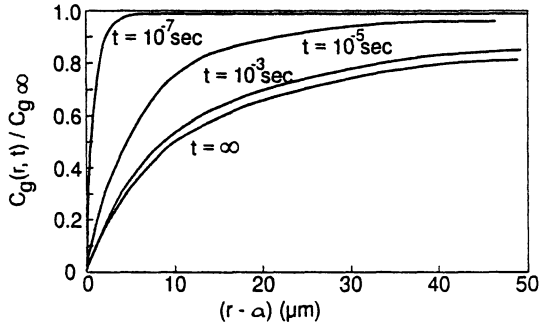


Fig. 17-27: SO_2 concentration profile normal to the surface of a water drop of a= 10 μm, caused by molecular diffusion assuming the drop to be a perfect-sink. (From Beilke & Gravenhorst, 1978, with changes.)

In order to determine $c_{g,a}$, we follow the arguments in Section 13.1.1, applied to the diffusion of water vapor, and assume that the gas diffusion is continuous only in the region $r \geq a + \Delta_g$, where $\Delta_g \approx \lambda_a$ is the gas jump length. Within the region $a \leq r \leq a + \Delta_g$, on the other hand, the gas transport is considered to occur according to the laws of gas kinetics. Analogous to (13-11), the equation to solve for steady state diffusion is

$$c_g(r) = c_{g,\infty} + \frac{B}{r} . \tag{17-109}$$

To determine B , we proceed as in Section 13.1.1. If we assume that the drop remains well-mixed all the time, i.e., that $c_{l,a} = c_l$, the net gas flux through the layer $a \leq r \leq a + \Delta_g$ is given by

$$J_g(r = a) = \pi a^2 \alpha_g \bar{v}_g \left[\frac{c_l}{K_H^* \mathscr{R} T} - c_g(a + \Delta_g) \right] , \tag{17-110}$$

where c_l is the uniform species concentration in the drop. Equation (17-110) is another form of the Hertz-Knudsen boundary condition (5-54) discussed in Section 5.11. At steady state, (17-110) is equal to the flux $J_g(a + \Delta_g)$ at $r = a + \Delta_g$. To determine $J_g(a + \Delta_g)$, we find, analogously to (13-12b) for total flux

$$J_g(r = a + \Delta_g) = -4\pi(a + \Delta_g)^2 D_g \left(\frac{\partial c_g}{\partial r} \right)_{a+\Delta_g} = 4\pi D_g B , \tag{17-111}$$

with $(\partial c_g / \partial r)_{a+\Delta_g} = -B/(a + \Delta_g)^2$. Equating now (17-110) and (17-111), and considering from (17-109) that $c_g(r = a + \Delta_g) = c_{g,\infty} + [B/(a + \Delta_g)]$, the constant B is found to be

$$B = \frac{a \left(\frac{a}{K_H^* \mathscr{R} T} - c_{g,\infty} \right)}{\frac{a}{a+\Delta_g} + \frac{4 D_g}{a \alpha_g \bar{v}_g}} . \tag{17-112}$$

Inserting (17-112) into (17-109), we obtain for $\Delta_g \ll a$ and a steady state

$$c_g(r) = c_{g,\infty} + \frac{a}{r}\left[\frac{1}{1+\frac{4D_g}{a\alpha_g \bar{v}_g}}\right]\left(\frac{c_l}{K_H^* \mathscr{R} T} - c_{g,\infty}\right), \tag{17-113}$$

analogously to (13-15). For $r = a$

$$c_{g,a} = c_{g,\infty} + \left[\frac{1}{1+\frac{4D_g}{a\alpha_g \bar{v}_g}}\right]\left(\frac{c_l}{K_H^* \mathscr{R} T} - c_{g,\infty}\right), \tag{17-114}$$

leading to

$$\frac{c_{g,a}}{c_l/K_H^* \mathscr{R} T} = 1 + \frac{[c_{g,\infty}/(c_l/K_H^* \mathscr{R} T)] - 1}{[a\alpha_g \bar{v}_g/4D_g] + 1}. \tag{17-115}$$

From (17-115), it follows that Henry's equilibrium across the drop's interface ('local equilibrium') is only fullfilled if $(c_l/K_H^* \mathscr{R} T) = c_{g,\infty}$, i.e., if the system is in complete thermodynamic equilibrium or, from (17-114), if alternatively $(4D_g/a\alpha_g \bar{v}_g) \ll 1$, which requires $a \to \infty$.

Considering (17-113), we now find for the gas flux density

$$(j_{g,r})_{r=a} = -D_g\left(\frac{\partial c_g(r)}{\partial t}\right)_{r=a} = \frac{D_g^*}{a}\left(\frac{c_l}{K_H^* \mathscr{R} T} - c_{g,\infty}\right), \tag{17-116}$$

where for $\Delta_g \ll a$

$$D_g^* = \frac{D_g}{1+\frac{4D_g}{a\alpha_g \bar{v}_g}}. \tag{17-117}$$

For the overall gas flux to the drop at rest follows

$$J_g = 4\pi a D_g^*\left(\frac{c_l}{K_H^* \mathscr{R} T} - c_{g,\infty}\right). \tag{17-118}$$

The rate of gas uptake then becomes

$$\left(\frac{\mathrm{d}m_g}{\mathrm{d}t}\right)_{0,l} = -J_g = 4\pi a D_g^*\left(c_{g,\infty} - \frac{c_l}{K_H^* \mathscr{R} T}\right). \tag{17-119}$$

With $c_l = m_{g,l}/(4\pi a^3/3)$, we obtain, for the time rate of change of the concentration inside the drop at steady state and at rest,

$$\left(\frac{\mathrm{d}c_l}{\mathrm{d}t}\right)_0 = \frac{3D_g^*}{a^2}\left(c_{g,\infty} - \frac{c_l}{K_H^* \mathscr{R} T}\right). \tag{17-120}$$

If the drop is not at steady state, the right-hand side of (17-120) has to be multiplied by the term $1 + [a/(\pi D_g t)^{1/2}]$ (see (13-5)). Considering this, Seinfeld (1986) obtained for the rate of change of the mass of gas in a drop at rest

$$[m_g(t)]_l = [m_g(t=\infty)]_l\left\{1 - \exp\left[\left(-\frac{3D_g^*}{a^2 K_H^* \mathscr{R} T}\right)\left(t + \frac{2a\sqrt{t}}{(\pi D_g)^{1/2}}\right)\right]\right\}, \tag{17-121a}$$

with

$$[m_g(t=\infty)]_l = (4\pi a^3/3)K_H^*\mathscr{R}Tc_{g,\infty}\,. \tag{17-121b}$$

Equation (17-121a) has been evaluated by Beilke and Gravenhorst (1978) for the case of SO_2 diffusing into a drop of 10 μm radius and given pH. Their results are plotted in Figure 17.28 together with an evaluation of (17-107). Both equations were made dimensionless by (17-121b). We notice from this figure that, for a drop acting as a perfect sink, the sulfur loading for $t \to \infty$ is reached in less than one second for pH< 6. On the other hand, when the effect of dissolved SO_2, accumulation is accounted for in a complete mixing model, we find that the time to reach total loading at equilibrium is considerably longer than that for a perfect sink model, and increases with increasing drop radius.

In a final comment on Figure 17.28, we should point out that in Beilke and Gravenhorst's analysis, the pH was held constant. In actuality, however, the pH of the drop varies with time during the uptake of SO_2, and has to be computed as a function of time from (17-80), with S(IV) and S(VI) also to be determined as a function of time.

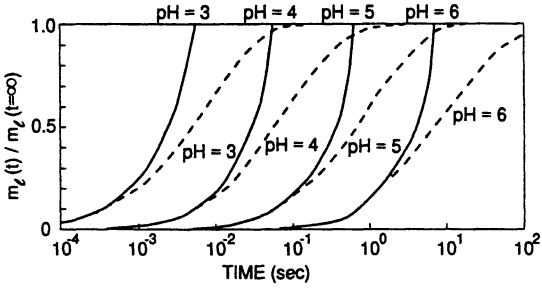


Fig. 17-28: Vartiation with time of the dimensionless suflur mass entering a water drop of a= 10 μm by diffusion of SO_2, for various pH in the drop. (—) perfect sink model, (– – –) complete mixing model. (From Beilke & Gravenhorst, 1978, with changes.)

In our derivation, so far we had assumed that the drop remains at rest and has a spherically symmetric diffusion field around it. However, in atmospheric clouds, drops are falling and have a diffusion field around them which is strongly affected by the flow of the air past the drop. In order to determine the effects of air flow on the diffusion of a gas to a falling drop, we may proceed in a manner analogous to that used for determining the convective diffusion of water vapor to a falling drop (see Chapter 13). As a measure for this ventilation effect, we shall therefore introduce a mean Sherwood number, $\bar{N}_{\mathrm{Sh},g}$, for the particular gas. Considering (13-55), this quantity may be calculated from

$$\bar{N}_{\mathrm{Sh},g} = \frac{a}{(c_{g,\infty} - c_{g,a})} \int_0^\pi \left[\frac{\partial c_g(\theta)}{\partial r}\right]_{r=a} \sin\theta \, \mathrm{d}\theta\,, \tag{17-122}$$

with $[\partial c_g(\theta)/\partial r]_{r=a}$ to be determined from a numerical solution of (17-99) together with the appropriate boundary conditions. This was done by Baboolal *et al.* (1981)

for a number of gases in air with Schmidt numbers, $N_{\mathrm{Sc},g} = \nu_a/D_g$, varying betwen 0.1 to 5.0 and for drops with Reynolds numbers up to 300. Their results showed that the ventilation factor $\bar{f}_g = 1/2\bar{N}_{\mathrm{Sh},g}$ is not a strong function of $N_{\mathrm{Sc},g}$, so that for all practical purposes, $\bar{f}_g$ may be computed from the theoretically and experimentally well-established relation (13-60) and (13-61) for water vapor. Therefore, (17-120) for a falling drop must now be written

$$\left(\frac{\mathrm{d}c_l}{\mathrm{d}t}\right) = \bar{f}_g \left(\frac{\mathrm{d}c_l}{\mathrm{d}t}\right)_0 = \frac{3\bar{f}_g D_g^*}{a^2}\left(c_{g,\infty} - \frac{c_l}{K_H^* \mathscr{R} T}\right), \tag{17-123}$$

assuming a steady state diffusion field.

It is customary in the literature to write (17-122) in terms of the *mean mass transfer coefficient* $\bar{k}_g = D_g^* \bar{f}_g / a$ (see Equation (13-51)) or the *mean mass transfer rate coefficient* $\bar{k}_{m,t} \equiv 3\bar{k}_g/a\bar{f}_g = 3D_g^*/a^2$. In terms of the latter, (17-123) becomes

$$\frac{\mathrm{d}c_l}{\mathrm{d}t} = \bar{k}_{m,t}\bar{f}_g \left(c_{g,\infty} - \frac{c_l}{K_H^* \mathscr{R} T}\right), \tag{17-124a}$$

where

$$\bar{k}_{m,t} = \frac{3D_g}{a^2}\left(1 + \frac{4D_g}{a\alpha_g \bar{v}_g}\right)^{-1} = \left(\frac{a^2}{3D_g} + \frac{4a}{3\alpha_g \bar{v}_g}\right)^{-1}. \tag{17-124b}$$

3. Diffusion inside a drop

In the previous two sections, we have assumed that the main resistance to diffusion of the foreign gas lies in the gas phase, and required that the drop is a perfect sink or well-mixed. Although we shall show later that the well-mixed assumption is justifiable for a number of gases of typical atmospheric gas concentrations, we cannot assume that this assumption holds in general, since a gas may find considerable resistance to diffusion also inside the drop. In order to obtain an expression for the diffusion of a gas species inside a drop, we shall consider a spherical water drop initially free of solute. At the time $t = 0$, the solute concentration at the drop surface shall be raised to a concentration $c_{l,a}$, which is assumed to remain constant with time. The solute will then be allowed to diffuse into the drop. If the drop is falling and therefore internally circulating, the equation to be solved is

$$\frac{\partial c_l}{\partial t} + \vec{u}_l \cdot \nabla c_l = D_l \nabla^2 c_l, \tag{17-125}$$

where $\vec{u}_l$ is the flow field due to the internal circulation and D_l is the molecular diffusivity of the diffusing species in water. For a spherical drop at rest, $\vec{u}_l = 0$ and therefore the equation to be solved is:

$$\frac{\partial c_l}{\partial t} = D_l\left(\frac{\partial^2 c_l}{\partial r^2} + \frac{2}{r}\frac{\partial c_l}{\partial r}\right). \tag{17-126}$$

The boundary conditions for the present case are

$$\begin{aligned} c_l(r, t=0) &= 0 \quad ; \quad 0 \le r \le a\,, \\ (\partial c_l/\partial r) &= 0 \quad ; \quad r = 0, t > 0\,, \\ c_l(r,t) &= c_{l,a} \quad ; \quad r = a, t > 0\,. \end{aligned} \tag{17-127}$$

The solution to (17-126) is (Carlslaw and Jaeger, 1947; Seinfeld, 1980, 1986)

$$\frac{c_l(r,t)}{c_{l,a}} = 1 + \frac{a}{r}\sum_{n=1}^{\infty}(-1)^n\left(\frac{2}{n\pi}\right)\sin\left(\frac{n\pi r}{a}\right)\exp\left(-\frac{n^2\pi^2 D_l t}{a^2}\right)\,. \tag{17-128}$$

We note that, for $t \to \infty$, $c_l(r, t \to \infty) \to c_{l,a}$, which implies that after a sufficiently long time, the concentration inside the drop will reach the surface concentration. The total flux of solute into the drop is (Seinfeld, 1986)

$$4\pi a^2 D_l\left(\frac{\partial c_l}{\partial r}\right)_{r=a} = 8\pi a D_l c_{l,a}\sum_{n=1}^{\infty}\exp\left(-\frac{n^2\pi^2 D_l t}{a^2}\right)\,, \tag{17-129}$$

and the total amount of solute which has entered the drop after a time t is (Seinfeld, 1986)

$$m_l(t) = 8\pi a D_l c_{l,a}\int_0^t\sum_{n=1}^{\infty}\exp\left(-\frac{n^2\pi^2 D_l t''}{a^2}\right)\,dt''\,, \tag{17-130}$$

where $m_l(t \to \infty) = m_{l,\text{sat}} = 4\pi a^3 c_{l,a}/3$. Therefore, Seinfeld (1980, 1986) finds:

$$\frac{m_l(t)}{m_{l,\text{sat}}} = 1 - \frac{6}{\pi^2}\sum_{n=1}^{\infty}\frac{1}{n^2}\exp\left(-\frac{n^2\pi^2 D_l t}{a^2}\right)\,. \tag{17-131}$$

By considering the dominating term in the exponential of solution (17-128), Seinfeld (1986) obtained as characteristic time for aqueous phase diffusion $(\tau_{dl})_1 = a^2/\pi^2 D_l$, with a in cm, D_l in cm^2 sec^{-1} and τ_{dl} in sec. Kronig and Brink (1950), on the other hand, followed Carlslaw and Jaeger (1948) and determined the time required for $m_l(t)$ in (17-131) to reach 63% of $m_{l,\text{sat}}$, which is $(\tau_{dl})_2 = 0.056a^2/D_l$, again with a in cm, D_l in cm^2 sec^{-1} and τ_{dl} in sec. Values for $(\tau_{dl})_1$, and $(\tau_{dl})_2$ for various drop sizes are also given in Table 17.17.

Equation (17-131) was analyzed by Beilke and Gravenhorst (1978) for the case when S(IV) diffuses inside a water drop with a diffusivity of $D_l = 1.15\times10^{-5}$ cm^2 sec^{-1}. The results of this analysis are shown in Figure 17.29. We note that drops with radius $a \le 20\,\mu$m become saturated in less than 0.2 seconds.

4. Coupled diffusion inside and outside a drop falling at terminal velocity

We shall proceed now to consider the uptake of a gas from its environment as a coupled process between diffusion outside and inside the drop. At the same time, we shall assume that the drop is falling. Such a study has been carried out by

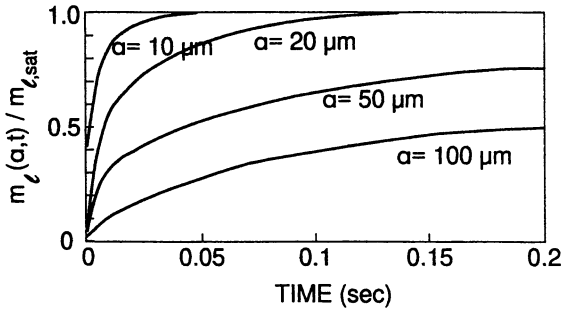


Fig. 17-29: Variation with time of the dimensionless sulfur mass entering drops of various radii by diffusion of SO_2, for a given drop surface concentration $c_{l,s}$ and c_l (r,t = 0) = 0. (From Beilke & Gravenhorst, 1978, with changes.)

Walcek and Pruppacher (1984a) for the case that the flow fields inside and outside the drop are axially symmetric. For these conditions, (17-99) and (17-125) may be written in dimensionless form as

$$\frac{\partial c'_g}{\partial t'} = D' \left[\left(\frac{\partial^2 c'_g}{(\partial R)^2} + \frac{1}{R^2} \frac{\partial^2 c'_g}{(\partial \theta)^2} \right) + \left(\frac{2}{R} - \frac{N_{Pe,g}}{2} u'_{r,g} \right) \frac{\partial c'_g}{\partial R} + \left(\frac{\cot\theta}{R^2} - \frac{N_{Pe,g}}{2R} u'_{\theta,g} \right) \frac{\partial c'_g}{\partial \theta} \right], \tag{17-132}$$

$$\frac{\partial c'_l}{\partial t'} = \left(\frac{\partial^2 c'_l}{(\partial R)^2} + \frac{1}{R^2} \frac{\partial^2 c'_l}{(\partial \theta)^2} \right) + \left(\frac{2}{R} - \frac{N_{Pe,l}}{2} u'_{r,l} \right) \frac{\partial c'_l}{\partial R} + \left(\frac{\cot\theta}{R^2} - \frac{N_{Pe,l}}{2R} u'_{\theta,l} \right) \frac{\partial c'_l}{\partial \theta}, \tag{17-133}$$

where $R = r/a$ and θ are the radial and angular coordinates, respectively, $D' = D_g/D_l$, $t' = D_l t/a^2$, $N_{Pe,l} = 2U_\infty a/D_l$, $c'_g = c_g/c_{g,\infty}$, $c'_l = c_l/c_{l,\text{sat}}$, $N_{Pe,g} = 2U_\infty a/D_g$, $u'_{\theta,g} = u_{\theta,g}/U_\infty$, $u'_{r,g} = u_{r,g}/U_\infty$, $u'_{\theta,l} = u_{\theta,l}/U_\infty$, $u'_{r,l} = u_{r,l}/U_\infty$, and where the flow fields $\vec{u}_g$ and $\vec{u}_l$ were determined from solutions to the Navier-Stokes equation of motion (see Chapter 10). The boundary conditions necessary to solve (17-132) and (17-133) are

$$\begin{aligned} t' = 0: \quad & 0 \le R \le 1; \quad 0 \le \theta \le \pi; \quad c'_l = 0 \\ & 1 \le R \le R_\infty; \quad 0 \le \theta \le \pi; \quad c'_g = 1.0 \\ t' > 0: \quad & R = R_\infty; \quad 0 \le \theta \le \pi; \quad c'_g = 1.0\,. \end{aligned} \tag{17-134a}$$

In order order to prevent mass accumulation at the phase boundary, we must further require mass conservation, which, using dimensional units, requires

$$D_l \left(\frac{\partial c_l}{\partial r} \right)_{r=a^-} = D_g \left(\frac{\partial c_g}{\partial r} \right)_{r=a^+}, \tag{17-134b}$$

where a^+ and a^- mean that the derivative is evaluated approaching from the gas side and from the liquid side, respectively. To simplify the computations, Walcek and Pruppacher further assumed that Henry's law is fulfilled locally across the drop/air interface, i.e.,

$$(c_g)_{r=a} = \frac{(c_l)_{r=a}}{K_H^* \mathscr{R} T} . \tag{17-134c}$$

Assuming that the diffusing species is SO_2, then $D_g = D_{SO_2}$ and $D_l = D_{S(IV)}$, $c_g = [SO_2]_g$ and $c_l = [S(IV)]_l$ Walcek and Pruppacher (1984a) solved (17-132) coupled to (17-133) subject to (17-134) and determined the rate at which S(IV) enters drops of various sizes. The results of this computation are given in Figure 17.30. We notice that even at gas concentrations as high as 10% by volume, saturation is reached only after several seconds, while tens of seconds are required for the same drop if $[SO_2]_{g,\infty} = 200$ ppbv. The drop size and gas concentration dependence is further illustrated in Figure 17.31 for drops up to 2 mm radius and $10 \leq [SO_2]_{g,\infty} \leq 10^8$ ppbv. We notice that, at typical atmospheric concentrations of a few ppbv, millimeter-sized drops require up to 150 seconds to come within 63% of saturation. We further note from this figure that the time to reach saturation decreases with increasing gas concentration. In Figure 17.32, the distribution of S(IV) inside a falling drop of $a = 316\,\mu$m is given during the initial stages of SO_2 uptake. We notice that SO_2 fills the drop from its rear due to the internal circulation which transports the S(IV) very quickly to the downstream side of the drop. Filling then proceeds across the streamlines of the internal circulation, keeping the lines of equal concentration S(IV) concentric with the streamlines.

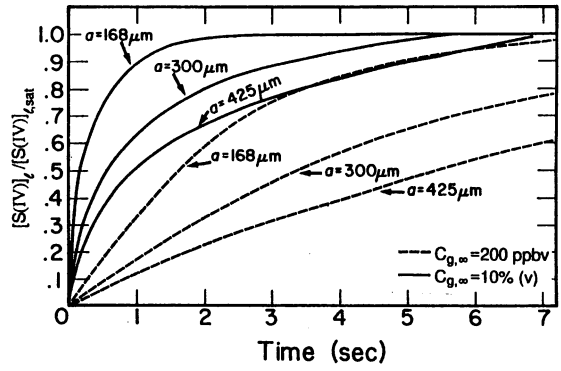


Fig. 17-30: Variation with time of the average concentration of S(IV) inside water drops of various radii during the uptake of SO_2. Based on a solution of equations (17-132) to (17-134). (From Walcek & Pruppacher, 1984a, with changes.)

In a more rigorous approach, the boundary condition (17-134c) must be replaced by a relation which equates the kinetic flux at the phase boundary to the flux in the continuous diffusional flow regime, i.e., equating

$$(j_g)_{r=a} = \frac{\alpha_g \bar{v}_g}{4} \left[\frac{(c_l)_{r=a}}{K_H^* \mathscr{R} T} - c_g(a + \Delta g) \right] , \tag{17-134d}$$

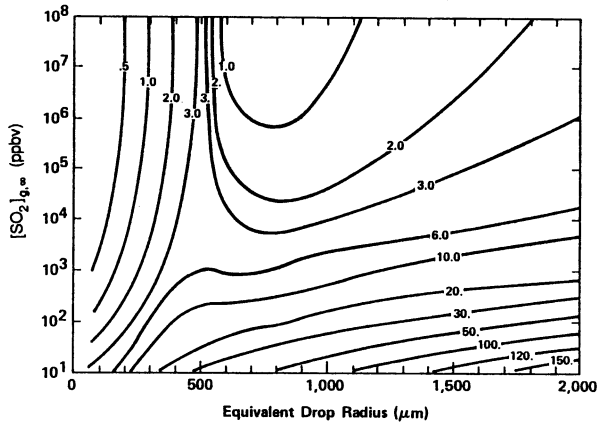


Fig. 17-31: Time taken by drops of various radii falling through air with given SO_2 concentration to reach within 63% of saturation. Curves are labeled in seconds. Based on a solution of equations (17-132) to (17-134). (From Walcek & Pruppacher, 1984a, with changes.)

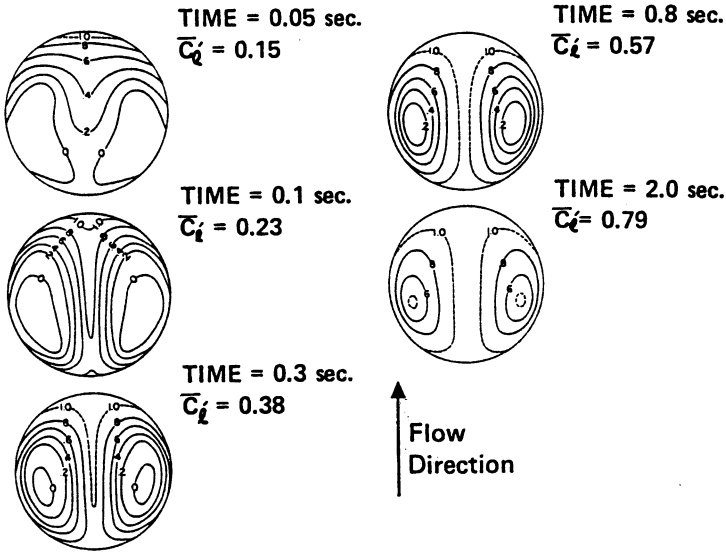


Fig. 17-32: Variation with time of the contours for equal dimensionless concentration inside a water drop of a= 316 μm during the uptake of SO_2 from air with $[SO_2]_{g,\infty}$ = 10%(v). $c_l' = [S(IV)]_l$ / $[S(IV)]_{l,sat}$, $\overline{c_l'}$ is the volume averaged dimensionless concentration. (From Walcek & Prupacher, 1984a, with changes.)

from (17-110), to

$$(j_g)_{r=a+\Delta g} = -D_g \left(\frac{\partial c_g}{\partial r}\right)_{a+\Delta_g}, \tag{17-134e}$$

from 17-111), in order to relate the numerically determined values for $\partial c_g/\partial r$ and c_g to c_l.

The computation of Walcek and Pruppacher (1984a) shows that solving the coupled Equations (17-132) and (17-133) is a computer intensive undertaking. In search of a less laborious but still accurate diffusion model, Walcek and Pruppacher (1984a) showed that, with satisfactory accuracy, the complete theory for coupled diffusion outside and inside a falling drop can be simplified according to a suggestion of Kronig and Brink (1950). These authors assumed that the streamlines inside a drop follow approximately those given by the Hadamard (1951) solution of flow, an assumption which was verified by Le Clair *et al.* (1972) who applied the complete Navier-Stokes equation to the interior of a drop. The Kronik and Brink model further assumes that along the streamlines the solute concentration remains constant, so that the transport of solute species takes place only across the streamlines from 'layer to layer' in a direction perpendicular to them. In terms of a coordinate ξ which is coincident with the Stokes flow streamlines, and a coordinate ζ which is perdendicular to these streamlines, Walcek and Pruppacher (1984a) obtained for the diffusion inside the drop:

$$\frac{\partial c_l}{\partial t} = \frac{16 D_l}{a^2} \frac{1}{q(\xi)} \frac{\partial}{\partial \xi}\left(p(\xi)\frac{\partial c_l}{\partial \xi}\right), \tag{17-135}$$

where

$$p(\xi) = \int \frac{(2R^2-1)\sin^3\theta}{R\cos^3\theta}\,\mathrm{d}\zeta, \tag{17-136a}$$

$$q(\xi) = \int \frac{(2R^2-1)^2}{4R^3\cos^3\theta[(1-R^2)\cos^2\theta + (2R^2-1)^2\sin^2\theta]}\,\mathrm{d}\zeta, \tag{17-136b}$$

where $R = r/a$, $\xi = 4R^2(1-R^2)\sin^2\theta$, and $\zeta = (R^4\cos^4\theta)/(2R^2-1)$.

In order to obtain a complete description for the diffusion of a gas species into a drop, Walcek and Pruppacher (1984a) considered that, at the drop interface, the Kronig-Brink parameterization for diffusion inside the drop is coupled to the diffusion of the gas species outside the drop by the condition of local mass flux continuity:

$$D_g\left(\frac{\partial c_g}{\partial R}\right)_{R=1} = D_l\left(\frac{\partial c_l}{\partial R}\right)_{R=1} = D_l\left(\frac{\partial c_l}{\partial \xi}\right)_{\xi=0}\left(\frac{\partial \xi}{\partial R}\right)_{R=1}, \tag{17-137}$$

with $(\partial\xi/\partial R)_{R=1} = -8\sin^2\theta$. In order to remove the unfortunate angle dependence Walcek and Pruppacher considered an average mass flux. Averaging the left-hand side of (17-137) over all angles yields $2D_g(\overline{\partial c_g/\partial R})_{R=1}$, while averaging the right-hand side of (17-137) yields $-(32/3)\times D_l(\overline{\partial c_l/\partial \xi})_{\xi=0}$. Instead of

(17-137) for the condition of mass flux continuity, one then obtains

$$D_g \left(\overline{\frac{\partial c_g}{\partial R}}\right)_{R=1} = -\frac{16}{3} D_l \left(\overline{\frac{\partial c_l}{\partial \xi}}\right)_{\xi=0} . \tag{17-138}$$

Since

$$\left(\overline{\frac{\partial c_g}{\partial R}}\right)_{R=1} = \frac{1}{2}\int_0^{\pi} \left(\frac{\partial c_g}{\partial R}\right)_{R=1} \sin\theta \, d\theta , \tag{17-139}$$

we obtain by comparison with (17-122) for the left-hand side of (17-138)

$$D_g \left(\overline{\frac{\partial c_g}{\partial R}}\right)_{R=1} = \frac{1}{2} D_g (c_{g,\infty} - c_{g,a}) \bar{N}_{\mathrm{Sh}} = (D_g)(c_{g,\infty} - c_{g,a}) \bar{f}_g . \tag{17-140}$$

If $c_{g,\infty}$ and $\bar{f}_g$ are known, $c_l(\xi, t)$ may then be obtained by solving (17-135) to (17-140) by substituting $c_{g,a}$ by $c_{l,a}/K_H^* \mathscr{R} T$, and using the accommodation factor corrected gas phase diffusivity D_g^* in place of D_g. Values for the mean gas concentration $\overline{c_l}(t)$ may subsequently be computed by simply averaging $c_l(\xi, t)$ inside the drop. In Figure 17.33, the results of such computations are compared with the results of a numerical solution to (17-132) to (17-134). We notice that the Kronig-Brink model satisfactorily approximates the results from the complete coupled convective diffusion model.

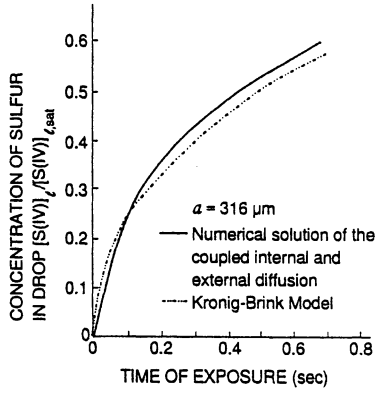


Fig. 17-33: Variation with time of the dimensionless concentration of sulfur in a drop of a= 316 μm exposed to SO_2 in air, for $[SO_2]_{g,\infty}$ = 10% (v). Comparison of solutions (17-132 to 17-134) with the Kronig Brink model. (From Walcek *et al.*, 1984, with changes.)

Considering its assumptions, the Kronik-Brink model is applicable only if the time $(\tau_{\mathrm{circ}})_{KB}$, required by a fluid particle to make a complete loop on a given stream line, is much shorter than the characteristic time for gas diffusion; i.e., the time during which $m_l(t)$ has reached 63% of $m_{l,\mathrm{sat}}$ for the case of gas uptake, or the time required for the dissolved gas concentration to decrease to $1/e$ (37%) of its original value for the case of gas desorption. Kronik and Brink (1950) found from

their model $(\tau_{\text{circ}})_{KB} = 5 \times 10^{-4}/a$, with a in cm and τ in sec. Values for $(\tau_{\text{circ}})_{KB}$ pertaining to selected drop sizes are given in Table 17.17. For comparison, Kronik and Brink found from their model that the characteristic time for diffusion through a fluid circulating with a Hadamard-Rybczinski flow (see Section 10.3.1) is given by $(\tau_{dl})_{KB} = 0.022a^2/D_l$, with a in cm and τ in sec. Values for $(\tau_{dl})_{KB}$ are also given in Table 17.17. Comparison of $(\tau_{\text{circ}})_{KB}$ with $(\tau_{dl})_2$ and $(\tau_{dl})_{KB}$ show that $(\tau_{\text{circ}})_{KB}$ is shorter than $(\tau_{dl})_{KB}$ and $(\tau_{dl})_2$ as long as $a \gtrsim 70\,\mu$m.

Of course, for drops of $a_0 > 1$ mm, one has to consider that the flow inside a drop is turbulent. As mentioned earlier, this may be done by applying the Kronig-Brink model and the well-mixed model alternatingly in succession during 0.25 and 0.75 sec, respectively, or by setting $D_l^* = 25D_l$ (see the beginning of Section 17.5).

In order to compare the contribution of the diffusion of a species outside a drop to the overall uptake of this species by the drop, Walcek and Pruppacher (1984a) solved the Kronig-Brink model for a variety of conditions. The results of this analysis are given in Figure 17.34 in terms of the resistance ρ to diffusion in the gas phase as a percentage of the total resistance to diffusion. The quantity ρ was defined by $\rho \equiv \tau_0/(\tau_i + \tau_0)$, where τ_0 and τ_i are the characteristic times for a drop to reach saturation assuming that diffusion is controlled completely by diffusion outside and inside the drop, respectively. Thus, e.g., if $\tau_0 = 10\tau_i$, then $\rho = 0.9$, which implies that 90% of the resistance to diffusion lies in the gas phase outside the drop. If, on the other hand, $\tau_0 = \tau_i$, then the gas phase outside the drop and the drop interior contribute equally to the diffusion of the species.

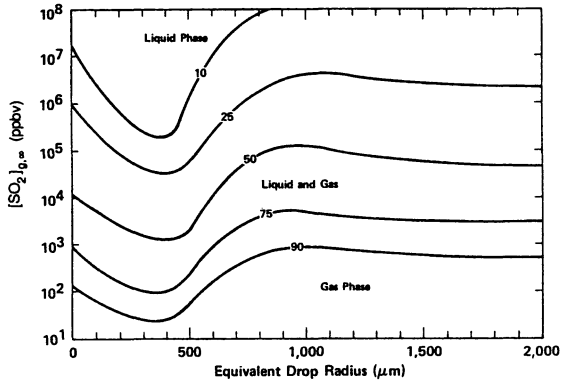


Fig. 17-34: Contribution of the gas phase diffusion of SO_2 to the total uptake of SO_2 as a function of drop size and concentration of SO_2 in the air. Lines given in terms of the resistance to diffusion $\rho(\%) \equiv 100\ \tau_0/(\tau_i+\tau_0)$, where τ_0 and τ_i are the characteristic times for a drop to reach equilibrium for the case that diffusion is controlled solely by diffusion outside and inside the drop, respectively. From a solution of the Kronig Brink model, Equations (17-133) to (17-142). (From Walcek & Pruppacher, 1984a, with changes.)

Thus, we note from Figure 17.34 that, for $[SO_2]_{g,\infty} < 10^2$ ppbv, the SO_2 uptake by a water drop is completely controlled by the diffusion of SO_2 through the air. At these gas concentrations, diffusion of SO_2 through the drop plays only a negligible role, and one may assume that the drop is well-mixed all the time. However,

at industrial SO_2 concentrations, of 500 ppbv and higher, diffusion through the liquid phase must be considered by applying the Kronig-Brink model. This is also illustrated by Figures 17.35 and 17.36.

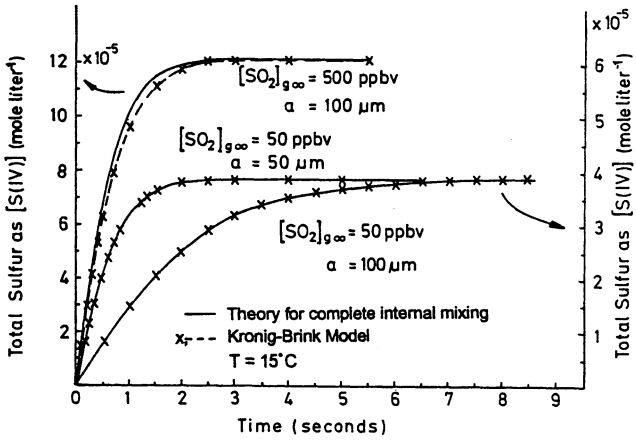


Fig. 17-35: Uptake of SO_2 by water drops of various sizes, assuming various concentrations of SO_2 in air. Comparison of the well-mixed model with the Kronig Brink model for $D_l^* = 25\ D_l$. (From Mitra *et al.*, 1992b, with changes.)

The applicability of the well-mixed diffusion model to the uptake of a gas by a water drop may be demonstrated further by integrating (17-123) for the case that the gas entering the well-mixed drop is completely dissociated in water, so that from (17-58), $k_H^* = k_H K_1/c_l$, for $[H^+] \ll K_1$ and $[H^+] \approx c_l$. Equation (17-123) then becomes

$$\frac{dc_l}{dt} = \frac{3D_g^* \bar{f}_g}{a^2}\left(c_{g,\infty} - \frac{c_l^2}{k_H K_1}\right) . \tag{17-141}$$

This equation has the solution (Hannemann, 1995)

$$c_l(t) = c_{g,\infty}\frac{(1 + c_0/c_{l,\text{sat}})\exp(2kc_{g,\infty}t/c_{l,\text{sat}}) - (1 - c_0/c_{l,\text{sat}})}{(1 + c_0/c_{l,\text{sat}})\exp(2kc_{g,\infty}t/c_{l,\text{sat}}) + (1 - c_0/c_{l,\text{sat}})} , \tag{17-142a}$$

with $c_{l,\text{sat}} = (k_H K_1 c_{g,\infty})^{1/2}$. If $c_l(t = 0) \equiv c_0 = 0$, (17-142a) becomes

$$c_l(t) = c_{l,\text{sat}} \tanh\left(\frac{kc_{g,\infty}}{c_{l,\text{sat}}}t\right) = \begin{cases} kc_{g,\infty}t , & \text{for } t \to 0; \\ c_{l,\text{sat}}[1 - \exp(-2kc_{g,\infty}t/c_{l,\text{sat}})] , & \text{for } t \to \infty \end{cases} , \tag{17-142b}$$

with $k = 3D_g^* \bar{f}_g/a^2$. From (17-142b), it follows that the characteristic time $(\tau_{\text{abs}})_{\text{diss}}$ required for the transport of the gas species through air to the drop is $(\tau_{\text{abs}})_{\text{diss}} = c_{l,\text{sat}}/2kc_{g,\infty} = a^2(k_H K_1/c_{g,\infty})^{1/2}/6D_g^* \bar{f}_g$. Values for $(\tau_{\text{abs}})_{\text{diss}}$ pertaining to selected drop sizes are given in Table 17.17 for $p_{g,\infty} = p_{SO_2,\infty} = 50$ ppbv. We notice from this table that $(\tau_{\text{abs}})_{\text{diss}} > (\tau_{dl})_{KB}$ for drops of 10 and 100 μm radius, as predicted by the numerical solution of Walcek and Pruppacher (1984a)

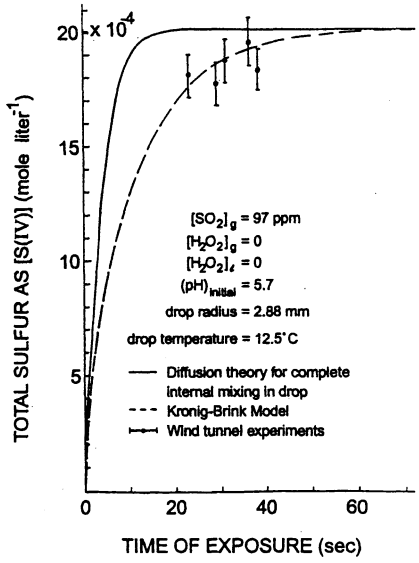


Fig. 17-36: Uptake of SO_2 by a water drop of 2.88 mm radius, assuming $[SO_2]_{g,\infty} = 97$ ppmv. Comparison of well-mixed model with Kronig Brink model for $D_l^* = 25\ D_l$, and with wind tunnel observations. (From Mitra *et al.* 1992b, with changes.)

which is given in Figure 17.34. This inequality is particularly pronounced for the case of an intermittently turbulent drop interior so that we may conclude that, for $p_{SO_2} \leq 50$ ppbv, more than 90% of the total resistance to diffusion lies in the gas phase, justifying the application of the well-mixed model. Of course, (17-142) depends strongly on the solubility of the gas in water and its concentration in the gas phase, so that the conditions for the applicability of the well-mixed model has to be tested separately for each gas and its concentration in air.

Thus far, we assumed that a water drop absorbs only one single gas. However, observations show that the uptake of a gas may significantly be strongly affected by the presence of other gases (Figure 17.37). Experimental verification for the applicability of the well-mixed model to the uptake of SO_2 by water drops in the presence of H_2O_2 has been provided by the wind tunnel results of Mitra *et al.* (1992b) and Waltrop *et al.* (1991). Their results are plotted in Figure 17.38 . We note that, for an unlimited supply of H_2O_2, the uptake of SO_2 is strongly enhanced, while the sulfur content in the drop continuously rises with time. The reason for this lies in the fact that S(VI) formed from the available S(IV) does not contribute to the gas-liquid equilibrium. A similar experimental verification of the well-mixed model has been provided by the wind tunnel studies of Hannemann *et al.* (1995) for the uptake of NH_3 in the presence of CO_2 (Figure 17.39a) and for the uptake of SO_2 in the presence of NH_3 and CO_2 (Figure 17.39b), and by Waltrop *et al.* (1991) for the variation with time of the pH inside a drop during the uptake of SO_2 in the presence of H_2O_2 (Figure 17.40).

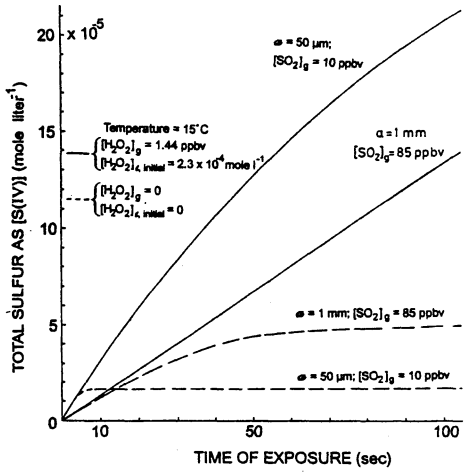


Fig. 17-37: Effect of H_2O_2 inside water drops on the uptake of SO_2, for various SO_2 concentrations in air, and for various drop sizes; based on the well-mixed model.

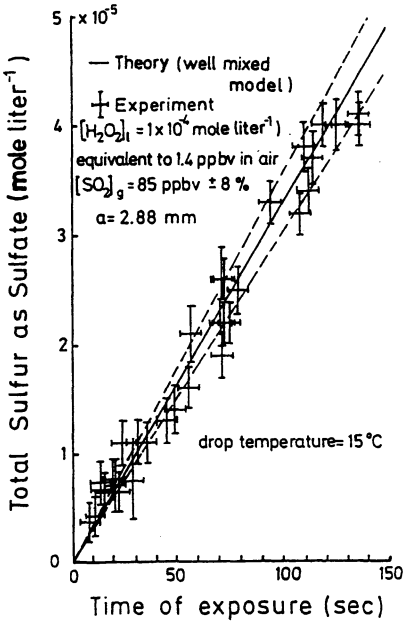


Fig. 17-38: Uptake of SO_2 by a water drop of 2.88 mm radius containing H_2O_2 inside the drop. Comparison of the well-mixed model with wind tunnel experiments. (From Mitra *et al.*, 1992b, with changes.)

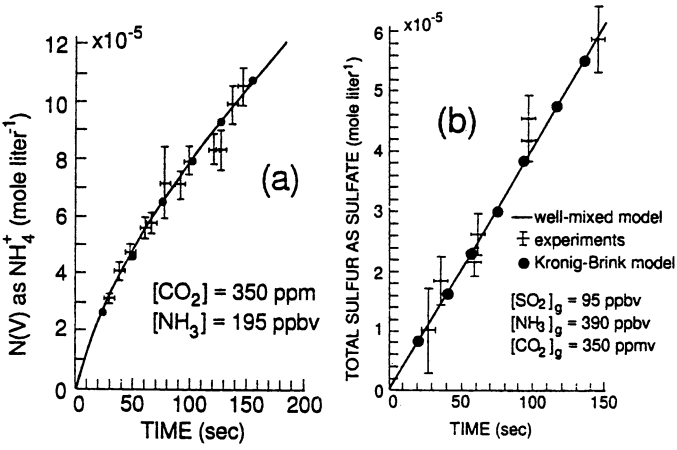


Fig. 17-39: Uptake of NH_3 by a water drop of 2.88 mm radius. (a) In the presence of CO_2, for $[NH_3]_{g,\infty}$ = 195 ppbv, $[CO_2]_{g,\infty}$ = 350 ppmv. (b) In the presence of CO_2 and SO_2, for $[NH_3]_{g,\infty}$ = 390 ppbv, $[SO_2]_{g,\infty}$ = 95 ppbv, $[CO_2]_{g,\infty}$ = 350 ppmv. Comparison of the well-mixed model with the Kronig Brink model for D_l^* = 25 D_l, and with wind tunnel experiments. (From Hannemann *et al.* 1995, and Hannemann, 1995, with changes.)

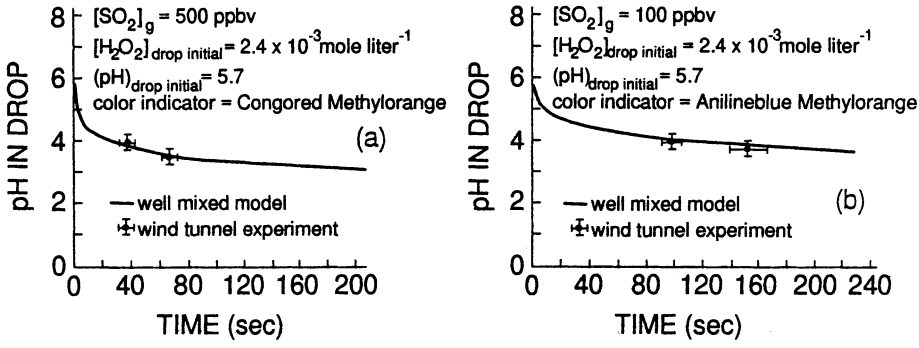


Fig. 17-40: Variation with time of the pH inside a drop of 2.88 mm radii containing H_2O_2 during the uptake of SO_2, for : (a) $[SO_2]_{g,\infty}$ = 500 ppbv, (b) $[SO_2]_{g,\infty}$ = 100 ppbv. Comparison of well-mixed model with wind tunnel experiments. (From Waltrop *et al.*, 1991, with changes.)

17.5.2 Asymmetry between Absorption and Desorption of Gases

Following our discussion on the uptake of foreign gases by water drops, in the present section we shall now consider the reverse process: gas desorption. For this purpose, we shall assume that a drop, which has absorbed some gas, is exposed to air which is devoid of that gas, or contains it in less than the equilibrium concentration. Under these conditions, the absorbed gas will desorb.

From a detailed study, Hannemann (1995) confirmed the earlier conclusions of Barrie (1978) that a gas which dissociates in water will not desorb at the same rate at which it had been absorbed. This behavior is in contrast to a gas which does not dissociate in water. Considering first the latter type of gas, we may integrate (17-123) for $k_H^* = k_H$ to give

$$c_l(t) = (c_0 - k_H c_{g,\infty}) \exp(-kt/k_H) + k_H c_{g,\infty} , \tag{17-143a}$$

for $k = 3D_g^* \bar{f}_g / a^2$. For desorption with $c_{g,\infty} = 0$ and for absorption with $c_0 = 0$, we obtain

$$c_l(t) = c_0 \exp(-kt/k_H) , \tag{17-143b}$$

$$c_l(t) = k_H c_{g,\infty} [1 - \exp(-kt/k_H)] , \tag{17-143c}$$

respectively. We notice from (17-143b,c) that, for a gas which does not dissociate in water, absorption and desorption can be described by symmetric functions with the same time constant $(\tau_{\text{abs,des}})_{\text{non-diss}} = k_H a^2 / 3D_g^* \bar{f}_g$.

An intirely different situation is found for a gas which dissociates in water. From (17-142a), we find for desorption with $c_{g,\infty} = 0$

$$c_l(t) = \frac{c_0}{1 + c_0 (k/k_H K_1) t} . \tag{17-144}$$

A comparison of (17-142b) with (17-144) shows that absorption of a strongly dissociating gas proceeds exponentially in time while the desorption of such a gas varies as $1/t$ and, thus, considerably slower than absorption. This result is exemplified in Figure 17.41, where, using the Kronig-Brink model, the uptake and desorption of SO_2 are compared for initial conditions which are completely equivalent to each other.

Comparisons between theoretical prediction and experiment have been provided by Mitra and Hannemann (1993). These are illustrated in Figures 17.42 and 17.43 for drops of 251 μm and 2.2 mm radius, respectively. We notice that, for both drops, the rate of desorption is significantly overestimated by the well-mixed model, while the Kronig-Brink model shows excellent agreement with observation. A surprising agreement with the Kronig-Brink model and the well-mixed model was found if the right-hand side of the well-mixed model (17-120) is multiplied by a correction factor which depends only on the drop size (see Figures 17.42 and 17.43). The results in these figures imply that desorption of a gas is significantly affected by the diffusion process in the drop's interior.

Garland (1978), Overton *et al.* (1979), and Walcek and Pruppacher (1984b) combined the mechanisms of absorption and desorption to obtain the net amount

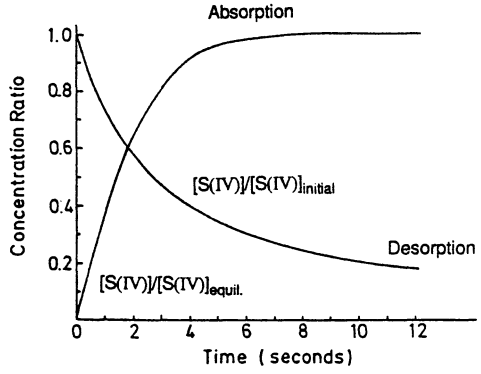


Fig. 17-41: Comparison of the rate of absorption with the rate of desorption of SO_2, for a drop of 100 μm radius. For absorption: $[SO_2]_{g,\infty} = 50$ ppbv. For desorption: $[S(IV)]_{initial} = 3.75 \times 10^{-5}$ mole liter^{-1} in equilibrium with $[SO_2]_{g,\infty} = 50$ ppbv. Based on the well-mixed model. (From Mitra & Hannemann, 1993, with changes.)

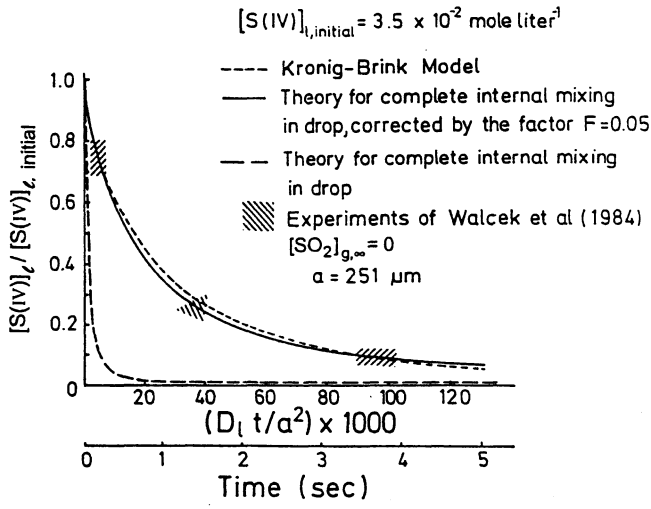


Fig. 17-42: Variation of the concentration of S(IV) inside a drop of 251 μm radius during desorption, for $[SO_2]_{g,\infty} = 0$. Comparison of the complete-mixing model with the Kronig Brink model for $D_l^* = 25\ D_l$, and with wind tunnel experiments. (From Mitra & Hannemann, 1993, with changes.)

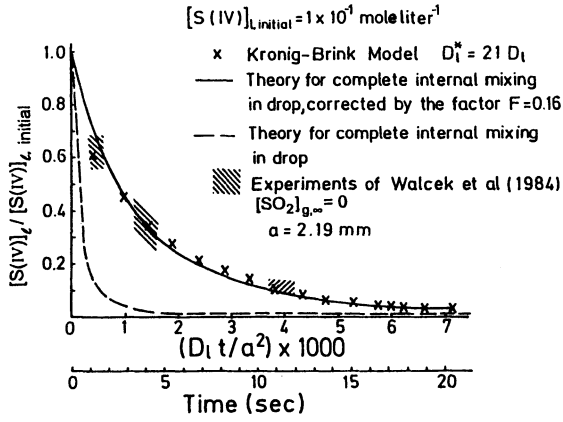


Fig. 17-43: As in Figure 17-42 but for a drop of 2.2 mm radius. (From Mitra & Hannemann, 1993, with changes.)

of a gas taken up by a drop while falling through a pollution layer. Thus, Walcek and Pruppacher assumed that the pollution layer consisted of a Gaussian SO_2 plume centered a few hundred meters above ground. Applying the Kronig-Brink model and assuming that no oxidation takes place inside the drops, they found (see Figure 17.44a) that, during a rainfall, the plume becomes 'washed down' and is reduced in strength as the rain progresses. In contrast, Hannemann (1995) showed that, in the presence of NH_3, an SO_2 polution plume is reduced in strength, but does not become washed down by falling rain. This is understandable if we consider that through the uptake of NH_3 the pH of a drop rises drastically which, in turn, increases the solubility of SO_2 (see Figure 17.26). From Figure 17.45, we see that drops which have fallen through the assumed SO_2 plume exhibit sulfur concentrations at the ground which vary significantly with drop size. Thus, large drops, which fall relatively fast through the plume, take up little gas and, accordingly, have little to lose by desorption. Small drops which fall relatively slowly are able to take up much gas but, accordingly, lose also much due to desorption. Consequently, drops of an intermediate size ($a_0 \approx 1$ mm) arrive at the ground with concentrations higher than both larger and smaller drops.

Of course, alsc the presence of oxidants significantly affect the desorption of SO_2 from a drop. This has been verified by Mitra and Hannemann (1993), who showed that the desorption of SO_2 becomes significantly reduced if H_2O_2 is simultaneously taken up by a drop from the gas phase.

17.5.3 Deviations from Equilibrium

In the previous section, we have pointed out that the concept of local equilibrium (117-134c) is unacceptable in a rigorous description of the gas uptake by a drop, and that it has to be replaced by a boundary condition which involves flux kinetics across the drop's interface (117-134d,e). A measure of the amount of deviation

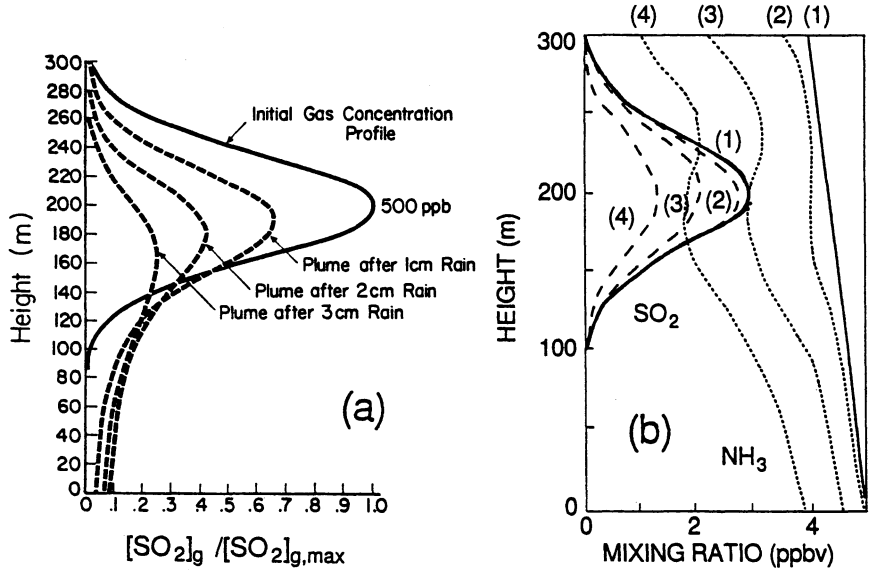


Fig. 17-44: (a) Variation with time of the SO_2 concentration in a pollution plume after various amounts of rain had fallen through the plume. For $R = 25$ mm hr^{-1}, and a drop size distribution according to Best (1950). (From Walcek & Pruppacher, 1984b, with changes.) (b) Variation with time of the SO_2 concentration in a pollution plume in the presence of a background concentration of NH_3, after various amounts of rain had fallen through, for $R = 50$ mm hr^{-1}. (1) original concentration profile; (2), (3), and (4) after 0.1, 0.5 and 1.0 cm of rain had fallen through the plume. (From Hannemann, 1995, with changes.)

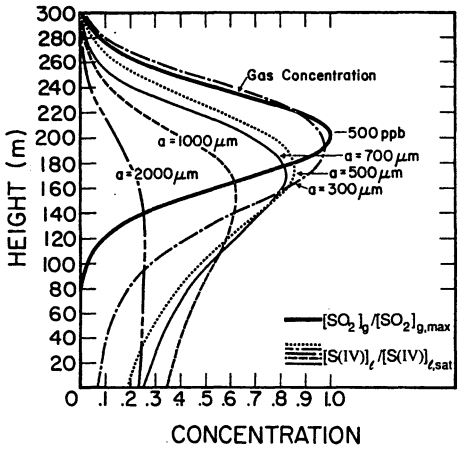


Fig. 17-45: Concentration of S(IV) inside raindrops of various sizes after they had fallen through a pollution plume of SO_2. (From Walcek & Pruppacher, 1984b, with changes.)

TABLE 17.18
Accomodation coefficient α_g for various gases on a water surface.

Gas	α_g	Observer
SO_2	0.03 ± 0.02	Schweighofer (1989)
	0.11 ± 0.02	Worsnop *et al.* (1989)
	$> (5.4 \pm 0.6) \times 10^{-2}$	Gardner *et al.* (1987)
	$> 2 \times 10^{-2}$	Tang & Lee (1987)
	0.15 ± 0.06	Ponche *et al.* (1993)
H_2O_2	0.18 ± 0.02	Worsnop *et al.* (1989)
HO_2	> 0.2	Mozurkevice *et al.* (1987)
NH_3	0.097 ± 0.009	Ponche *et al.* (1993)
NO2	$(6.3 \pm 0.7) \times 10^{-4}$	Lee and Tang (1988)
	$(1.5 \pm 0.8) \times 10^{-3}$	Ponche *et al.* (1993)
HNO_3	0.193	van Doren *et al.* (1990)
HCl	0.064	van Doren *et al.* (1990)
N_2O_5	0.040	van Doren *et al.* (1990)
CO_2	$(6 \text{ to } 20) \times 10^{-5}$	Bongartz & Schurath (1992)

from local equilibrium is given by (17-115) for the case that gas is taken up by a drop from an environment which has a steady state gas profile. It is instructive now to consider how this deviation changes with time. This problem has been treated by Danckwerts (1970), Schwartz (1984a,b, 1986, 1987, 1988), Freiberg and Schwartz (1981) and Seinfeld (1986). Seinfeld (1986) considered the time required to establish Henry's law equilibrium on the liquid side of the gas-liquid interface, after a step change in gas concentration has taken place on the gas side of the interface. He showed that, for a planar water/air interface, the characteristic time τ_{Ph} for a gas species to achieve interfacial phase equilibrium is given by

$$\tau_{\text{Ph},1} = D_l \left(\frac{4\mathscr{R}TK_H^*}{\alpha_g \bar{v}_g} \right)^2 , \tag{17-145a}$$

where D_l is the diffusivity of the species in water, α_g is the accommodation coefficient for a gas molecule at the water surface (see Table 17.18), and $\bar{v}_g = (8\mathscr{R}T/\pi M_g)^{1/2}$ is the average speed of the gas molecules. We note from (17-145a) that $\tau_{\text{Ph},1}$ depends on the square of K_H^*. This implies that $\tau_{\text{Ph},1}$ lengthens as the solubility of a gas increases. Equation (17-145a) also shows that $\tau_{\text{Ph},1}$ increases as the accommodation coefficient decreases.

For deriving (17-145a), Seinfeld (1986) assumed that the gas diffuses with molecular diffusivity into the water body of infinite volume. In actuality, a drop has a finite volume and, in most situations, the species is exposed to convective diffusion inside the drop. Assuming a fully mixed drop of radius a, Mitra (1994, pers comm.) equated the net flux of the gas molecules entering the water drop to the concentration rise inside the drop. For these conditions, the characteristic time $\tau_{\text{Ph},2}$ for interfacial phase equilibrium becomes

$$\tau_{\text{Ph},2} = \frac{aK_H^*(2\pi M_g \mathscr{R}T)^{1/2}}{3 \times 10^9 \alpha_g} , \tag{17-145b}$$

TABLE 17.19
Characteristic times to achieve interfacial phase equilibrium, for $D_l = 1.66 \times 10^{-5}$ cm sec^{-2}, for a drop of radius a in cm, and 25°C.

Gas	M_g (g mole^{-1})	α_g	K_H (M atm^{-1})	K_H^* (M atm^{-1})	$\tau_{ph,1}$ (sec)	$\tau_{ph,2}$ (sec)	pH
SO_2	64	0.1	1.22	16	4.2×10^{-6}	$1.7 \times 10^{-1} a$	3
	64	0.1	1.22	1.5×10^3	3.6×10^{-2}	$16\ a$	5
O_3	48	10^{-4}	1.0×10^{-2}		1.2×10^{-6}	$9 \times 10^{-2}\ a$	
H_2O_2	34	0.2	7.1×10^4		10.5	$270\ a$	
		1.0	7.1×10^4		0.4	$54\ a$	
CO_2	44	10^{-4}	3.4×10^{-2}	3.4×10^{-2}	1.2×10^{-5}	$2.9 \times 10^{-1}\ a$	5
NH_3	17	1.0	60	1×10^6	43	$1.7 \times 10^3\ a$	5
	17	1.0	60	1×10^3	4.8×10^{-5}	$1.8\ a$	8
HNO_3	63	0.2	2.2×10^5	2.2×10^5	181	$1.1 \times 10^3\ a$	4

with K_H^* in M atm^{-1} and a in cm. Due to the well-mixed assumption, $\tau_{Ph,2}$ is also the characteristic time for phase equilibrium with the entire drop. A numerical analysis of $\tau_{Ph,1}$ and $\tau_{Ph,2}$ is given in Table 17.19 for some selected conditions. We notice from this table that the validity of assuming instantaneous local phase equilibrium depends crucially on the type of gas involved, its Henry's law coefficient, and the time scales of the other processes occurring. Thus, Table 17.19 shows that for the less soluble gases such as SO_2, O_3 and CO_2 as well as for NH_3 at high pH, τ_{Ph} is sufficiently short to assume that local phase equilibrium is instantaneously established. However, instantaneous local phase equilibrium is not justified for the highly soluble gases H_2O_2, HNO_3 and for NH_3 at low pH. We further notice from Table 17.19 that, despite the assumption of a finite volume, (17-145b) does not lead to characteristic times which are smaller than those computed from (17-145a), simply because the time reduction due to assuming a finite drop volume is compensated for by assuming a convectively well-mixed drop.

Let us consider next the characteristic time for aqueous ionic equilibrium, using as an example the dissociation of SO_2 in water. The rate at which the equilibrium given by (17-61b) is established has been investigated by Eigen *et al.* (1964) who determined the rate constants for the reaction

$$(SO_2)_{aq} + H_2O \overset{k_{f,1}, k_{r,1}}{\rightleftharpoons} HSO_3^- + H^+ . \tag{17-146}$$

Eigen *et al.* found $k_{f,1} = 3.4 \times 10^6$ sec^{-1} and $k_{r,1} = 2 \times 10^8$ M^{-1} sec^{-1} for 25°. According to Seinfeld (1986), the characteristic time at which (17-61b) is established, is given by

$$\tau_i = \{k_{f,1} + k_{r,1}([H^+] + [HSO_3^-])\}^{-1} . \tag{17-147}$$

With the values for $k_{f,1}$ and $k_{r,1}$ given by Eigen *et al.* (1954), Seinfeld (1986) found for $p_{SO_2} = 1$ ppb and pH= 3, using (17-63b), $\tau_i = 2 \times 10^{-7}$ sec and $\tau_i = 1 \times 10^{-6}$ sec in order that 67 and 99% of the dissociation equilibrium is reached, respectively.

According to Erickson and Gates (1976) and Erickson *et al.* (1976), the second ionization equilibrium

$$HSO_3^- \overset{k_{f,2},k_{r,2}}{\rightleftharpoons} H^+ + SO_3^{2-} \tag{17-148}$$

is established even quicker, since $k_{f,2} = 1.0 \times 10^4$ sec^{-1} and $k_{r,2} = 1.0 \times 10^{11}$ sec^{-1}. Thus, we may safely assume that the characteristic times for aqueous dissociation involving SO_2 are very short when compared with the characteristic times involving gas phase and liquid phase diffusion of SO_2. Aqueous ionic equilibrium involving SO_2 may therefore be assumed to hold at all points inside a water drop. Of course, for each gas, a separate analysis of the type given above has to be made.

Thus, an entirely different situation is found for CO_2. According to Stumm and Morgan (1981),

$$(CO_2)_{aq} + H_2O \overset{k_1,k_{-1}}{\rightleftharpoons} H_2CO_3\,, \tag{17-149}$$

$$H_2CO_3 \overset{k_2,k_{-2}}{\rightleftharpoons} HCO_3^- + H^+\,, \tag{17-150}$$

with $k_1 = 3.0 \times 10^{-2}$ sec^{-1}, $k_{-1} = 11.9$ sec^{-1}, $k_2 = 8 \times 10^6$ sec^{-1}, and $k_{-2} = 4.7 \times 10^{10}$ M^{-1} sec^{-1}. If reactions (17-149) and (17-150) are combined, we obtain the overall reaction

$$(CO_2)_{aq} + H_2O \overset{k_f,k_r}{\rightleftharpoons} HCO_3^- + H^+\,, \tag{17-151}$$

for which $k_f = k_1$ and $k_r = (k_{-2}k_{-1})/(k_{-1} + k_2)$. According to Stumm and Morgan,

$$k_f(\text{sec}^{-1}) = 3 \times 10^{-2} \exp\left[7578\left(\frac{1}{298} - \frac{1}{T}\right)\right], \tag{17-152}$$

$$k_r(\text{M}^{-1}\ \text{sec}^{-1}) = 7 \times 10^4 \exp\left[6659\left(\frac{1}{298} - \frac{1}{T}\right)\right]. \tag{17-153}$$

Using these reaction rates, Stumm and Morgan found that, for $[CO_2] = 330$ ppm and pH= 5.6, $\tau_i \approx 20$ sec in order to reach 99% of dissociation equilibrium. This implies that, for a correct description of the uptake of CO_2 by water drops, one must consider the effects of reaction kinetics and must replace the equilibrium (17-54b) by (17-151).

According to Overton *et al.* (1979), we must consider further that for pH> 8

$$(CO_2)_{aq} + OH^- \overset{k'_f,k'_r}{\rightleftharpoons} HCO_3^-\,, \tag{17-154}$$

with $k'_f = 1.4 \times 10^4$ M^{-1} sec^{-1} and $k'_r = 1.0 \times 10^{-4}$ sec^{-1} at 25°. Considering (17-151) and (17-154), we have

$$\frac{d[(CO_2)_{diss}]}{dt} = -\frac{d[(CO_2)_{aq}]}{dt} = k_f[(CO_2)_{aq}] - k_r[HCO_3^-][H^+] + k'_f[OH^-][(CO_2)_{aq}] - k'_r[HCO_3^-]\,, \tag{17-155}$$

TABLE 17.20a
Characteristic times for aqueous oxidation of S(IV) to S(VI) by O_3 for the reaction: $-(1/[S(IV)])\,(d\,[S(IV)]\,/dt) = k^{(2)}\,[O_3]_{aq}$.

pH	$[O_3]_g$ (ppbv)	$[O_3]_{aq}$ (M)	$k^{(2)}$ (M^{-1} sec^{-1})	$\tau_{r,l}$ (sec)
4	50	5×10^{-10}	10^6	2×10^3
5	50	5×10^{-10}	10^7	2×10^2

where

$$[(CO_2)_{diss}] \equiv [HCO_3^-] + [CO_3^{2-}]\,. \tag{17-156}$$

Assuming that equilibrium (17-54c) is almost instantaneously established, we find, together with (17-156), (17-55c) and (17-56c), that

$$[HCO_3^-] = \frac{[(CO_2)_{diss}]}{1 + (K_2/[H^+])}\,, \qquad [CO_3^{2-}] = \frac{[(CO_2)_{diss}]}{1 + ([H^+]/K_2)}\,, \tag{17-157}$$

which may be substituted in (17-155) to solve for $d[(CO_2)_{diss}]/dt$. For determining the pH, we find instead of (17-60)

$$[H^+] = \frac{k_w}{[H^+]} + [(CO_2)_{diss}]\,\frac{[H^+] + 2K_2}{[H^+] + K_2}\,. \tag{17-158}$$

Hannemann (1995) compared the kinetic description of the CO_2 uptake by a drop during a simultaneous uptake of NH_3 with the uptake based on an equilibrium description for the CO_2 uptake. This comparison shows that, by assuming equilibrium, the NH_3 uptake is significantly overestimated, a result quantitatively verified by her wind tunnel results.

Once a chemical species has entered a water drop, chemical reactions between the various species present may take place. Of particular interest in cloud chemistry are the reactions which evolve during the oxidation of S(IV) to S(VI) by H_2O_2 and O_3, or by O_2 in the presence of metal ions such as Fe^{2+}, Fe^{3+} and Mn^{2+}. A selection of expressions for the rates at which these reactions proceed is given in Table 17.16. Using first-order kinetics, the characteristic time τ_{rl} for the conversion of S(IV) to S(VI) is given by

$$\frac{1}{\tau_{rl}} = -\frac{1}{[S(IV)]}\,\frac{d[S(IV)]}{dt}\,. \tag{17-159}$$

Some characteristic times evaluated from (17-159) for the aqueous oxidation of S(IV) to S(VI) by O_3 and H_2O_2 are listed in Tables 17.20a,b. We notice that the characteristic times for the reactions involving SO_2 are long in comparison to the characteristic times for the dissociation equilibrium and interfacial phase equilibrium.

TABLE 17.20b
As in Table 17-20a but for oxidation by H_2O_2 for the reaction: - (1/[S(IV)] (d[S(IV)] /dt) = $k^{(2)}$ $[H_2O_2]_{aq}$.

pH	$[H_2O_2]_g$ (ppbv)	$[H_2O_2]_{aq}$ (M)	$k^{(2)}$ (M^{-1} sec^{-1})	$\tau_{r,l}$ (sec)
4	10	7×10^4	10^4	0.15
5	10	7×10^4	10^3	1.5

17.5.4 Scavenging of Gases by Ice Particles

Until recently, it has been assumed that gas scavenging in the atmosphere is not significantly affected by falling ice hydrometeors. However, as we have shown in Section 5.8, Sommerfeld and Lamb (1986), Valdez *et al.* (1989), Mitra *et al.* (1990), Conklin *et al.* (1993), Diehl *et al.* (1995), Dominé and Thiebert (1995), among others, have experimentally shown that ice particles are actively involved in the gas scavenging process. At temperatures 0 to −40°C, SO_2, HCl and HNO_3 become adsorbed on the surface of ice spheres and snow crystals at gas concentrations in the ppbv range. This uptake was attributed to 3 causes: (1) to monolayer and multi-layer adsorption, (2) to the solution and subsequent clathrate formation of the gas in the intrinsic quasi-liquid layer on the ice surface and (3) to the solution of the gas in the quasi-liquid surface layer enhanced by surface melting of ice. The mechanisms operating were found to depend strongly on the type of gas, the concentration of the gas in the gas phase, and on temperature. Diehl *et al.* (1995) and Dominé and Thiebert (1995) also demonstrated that portions of adsorbed gas penetrate the ice via diffusion along grain boundaries in polycrystalline ice and via diffusion along dislocations in single crystalline ice. Mitra *et al.* (1990), Valdez *et al.* (1989), and Diehl *et al.* (1995) showed further that an additional uptake mechanism must be operating during the growth of snow crystals from water vapor. They found that during such growth, HCl, HNO_3 and SO_2 in the presence of H_2O_2, are scavenged in proportion to the mass of water vapor converted to ice.

In addition to the uptake of gas directly from the gas phase, ice particles may scavenge gases indirectly by collision with drops which contain absorbed gas. The experiments of Lamb and Blumenstein (1987) showed, however, that during riming of an ice rod, only a small fraction of the gas contained in the drops become transferred to the riming ice particle. This fraction was found to increase with decreasing temperature. Thus, only about 19% of SO_2 in the drops was trapped by a riming ice particle near −30°C, and only 4% near −5°C. Their results could be expressed in terms of a retention coefficient $\Gamma = c/c_0$, where c_0 is the original concentration of the species in the drops and c is the concentration of the species retained in the frozen drops. Lamb and Blumenstein found for S(IV) $\Gamma = 0.012 + 0.0058T_s$, where $T_s = T_0 - T$ and $T_0 = 273$ K. The retention coefficient determined by Iribarne *et al.* (1983, 1990) for the same species was considerably larger and followed the relation $\Gamma = 0.25 + 0.012T_s$ for drops freezing under gravity and for

the riming of an ice target, $\Gamma \approx 0.62$. The retention coefficient for H_2O_2, HCl and HNO_3 were found to be near unity (Iribarne and Pyshnov, 1990).

Unfortunately, no theoretical formulations are presently available to describe the gas uptake by ice particles.

17.6 The Scavenging Parameters

Field experiments generally do not allow one to directly derive scavenging efficiencies of aerosol particles and gases by individual cloud and precipitation particles. Instead, the scavenging characteristics of a particular cloud or precipitation event are usually described by parameters which are accessible during field experiments. One such parameter we have already introduced during our discussion of aerosol particle scavenging, the *scavenging coefficient* Λ_{AP}, is defined for impaction scavenging of aerosol particle by (17-4). In analogy to Λ_{AP} for aerosol particle scavenging, one may define the scavenging coefficient Λ_g for gases by

$$\Lambda_g \equiv -\frac{1}{c_g}\frac{\partial c_g}{\partial t}\,, \tag{17-160}$$

where (17-160) refers to the relative decrease of the gas concentration during the cloud and precipitation event. Considering the results of numerous authors, McMahon and Denison (1979) have compiled a list of values for Λ_{AP} determined from field observations. From these, we notice that generally $1 \times 10^{-5} \leq \Lambda_{AP} \leq 1 \times 10^{-3}$ sec^{-1}. These values are consistent with the more recent data of Huebert *et al.* (1983), Schumann (1989), Schumann *et al.* (1988), and of Jylhä (1991). Of course, we notice from (17-2) that Λ_{AP} depends on the drop size distribution and, thus in turn, on the rain fall rate. For a given drop size distribution, Λ_{AP} is a function of the collection kernel which, in turn, is a function of the efficiency with which aerosol particles collide with the drops. In Figures 17.17 and 17.18, we have shown that the collision efficiency of aerosol particles with drops and planar crystals assumes a minimum near a particle radius of 0.1 μm. Figure 17.46 shows that the scavenging coefficients for rain and snow determined during field experiments exhibit the expected trend of Λ_{AP} with decreasing particle radius, although the minimum in the scavenging coefficient was not resolved. Note also the typical shoulder in the curve for snow, as expected from Figure 17.18a.

Scavenging coefficients Λ_g for SO_2 have been obtained by Beilke (1970) from laboratory data and by Makhon'ko (1967), Hales *et al.* (1970), and Dana *et al.* (1975) from field observations. Field measurements of Huebert *et al.* (1983) and of Shimshock and de Pena (1989) provided data for Λ_{HNO_3} and Λ_{NH_3}. For SO_2, one finds $5 \times 10^{-6} \leq \Lambda_g \leq 6 \times 10^{-5}$ sec^{-1}, while for the more soluble gases NH_3 and HNO_3, one obtains $1 \times 10^{-4} \leq \Lambda_g \leq 3 \times 10^{-4}$ sec^{-1}.

Before leaving the subject of scavenging, we shall briefly address the controversy which has arisen in the literature on the proper way to determine Λ_{AP}. Thus, Davenport and Peters (1978), Schumann (1989), and Graedel and Franey (1975) found that Λ_{AP}, evaluated from field observations by using the left-hand side of (17-4), was consistently higher by about one order of magnitude than Λ_{AP} evaluated from the right hand side of (17-4), using literature values for the collision efficiency

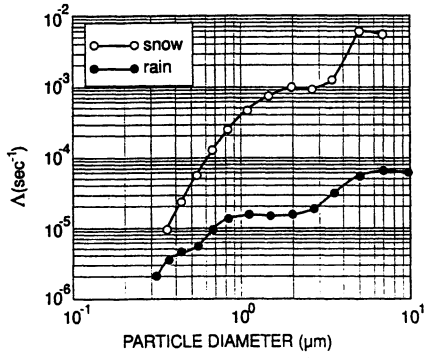


Fig. 17-46: Variation with aerosol particle size of the scavenging coefficient for rain and snow according to observation taken on Mt. Rigi (Switzerland), for an equivalent precipitation rate of 1.3 mm hr^{-1}. (From Schumann, 1989, with changes.)

for dry aerosol particles. This controversy has recently been resolved by Floßmann (1991), who used the literature values for E_{AP} in a two-dimensional cloud model with detailed microphysics and a detailed computation of the flow- and moisture field to obtain values for Λ_{AP} which agreed well with observed values. This study indirectly verified the collision efficiencies available in the literature, and showed that the field-derived values for Λ_{AP} determined from the left-hand side of (17-4) can only be compared with the values determined from the right-hand side of (17-4) if also the changes in the aerosol particle size caused by humidity variations in the cloud are considered.

The *scavenging ratio* W (sometimes termed 'washout ratio') is a second parameter which is used to characterize the efficiency with which pollutants are scavenged by clouds and precipitation from the atmosphere. This parameter is defined as the ratio of the concentration of pollutant X in the rain water to the concentration of X in the air according to

$$W \equiv \frac{[\mathrm{X}]_{\mathrm{rain}}}{[\mathrm{X}]_{\mathrm{air}}}, \tag{17-161}$$

with $[\mathrm{X}]_{\mathrm{rain}}$ in g liter^{-1} and $[\mathrm{X}]_{\mathrm{air}}$ in g m^{-3}. A literature survey of earlier measurements of is to be found in McMahon and Danison (1979). From their data, it appears that typically $10^2 \leq W \leq 10^6$, which is consistent with the newer measurements of Barrie (1985b), Wolff *et al.* (1987), Jaffrezo and Colin (1988), and Cadle *et al.* (1981). Field studies of Gatz (1976), Hicks and Shannon (1979), and Barrie (1985a) showed that $W \propto P^{-\alpha}$, where P is the precipitation amount in millimeters and $0.24 \leq \alpha \leq 0.36$.

The *scavenging factor* F is a third parameter used in the literature to describe scavenging. F is defined as the ratio of the concentration of the scavenged pollutant X in the rain or cloud water per unit volume of air to the concentration of X in the air:

$$F \equiv \frac{[\mathrm{X}]_{\mathrm{rain,cloud}} \times \mathrm{w}_L}{[\mathrm{X}]_{\mathrm{air}}}, \tag{17-162}$$

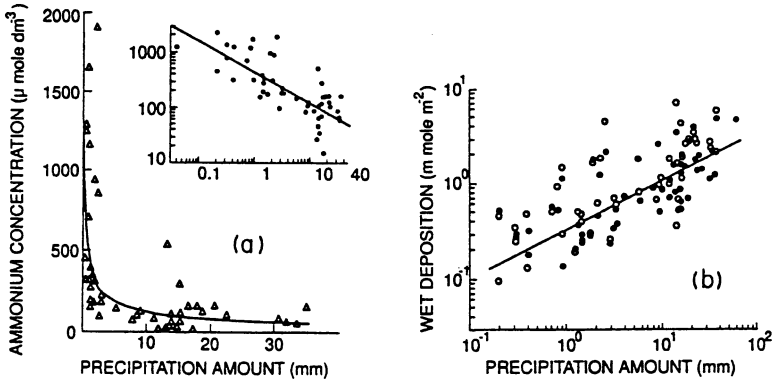


Fig. 17-47: Variation with precipitation amount: (a) of the concentration of NH_4^+ in rain, (b) of the wet deposition of NH_4^+ (•) and NO_3^- (○). Precipitation observed over the West Baltic. (From Fieldler, 1990, with changes.)

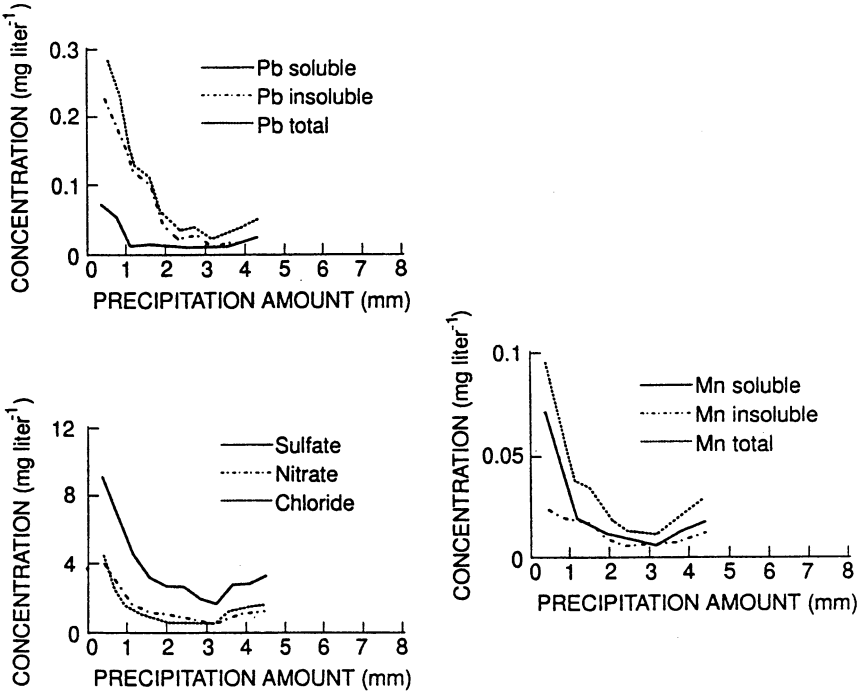


Fig. 17-48: Variation with precipitation amount of the concentration of various salt ions and metals in rain water. Precipitation observed over Frankfurt (Germany). (From Kins, 1982a,b, with changes.)

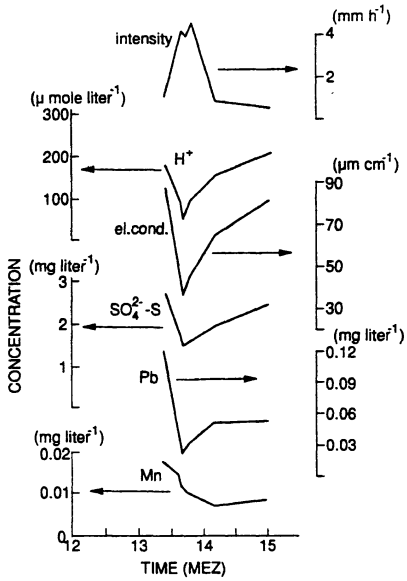


Fig. 17-49: Variation with time of the precipitation intensity and of the concentration of various salt ions and metals in rain water. Precipitation observed during a shower over Frankfurt (Germany). (From Kins, 1982a, b, with changes.)

with $[X]_{rain}$, cloud in $\mu g/g$ water, w_L in g water/m^3 air, and $[X]_{air}$ in $\mu g/m^3$ air. Hegg *et al.* (1984, 1986) and Hegg and Hobbs (1988) have shown that for sulfate and nitrate particles $0.4 \leq F \leq 0.9$.

17.7 Wet Deposition

Field studies have shown that only a relatively small fraction of the gaseous and particulate air pollutant mass which has been scavenged at cloud level eventually arrives in rain on the ground. This fraction depends on the amount of gas and particles originally scavenged by the cloud, the amount of gas lost from the falling rain by desorption below the cloud, and the amount of gas and particles scavenged by the falling rain below cloud level. However, the fraction depends foremost on the efficiency with which cloud water is converted to rain water reaching the ground. In fact, cloud model studies have shown that the deposition efficiency E_D of a pollutant type X, defined by

$$E_D \equiv \frac{\text{cumulative mass of X in rain on the ground}}{\text{cumulative mass of X scavenged}}, \tag{17-163}$$

is given within a few percent by the precipitation efficiency E_P, defined by

$$E_P \equiv \frac{\text{cumulative rain mass on the ground}}{\text{cumulative vapor mass converted to cloud water}}. \tag{17-164}$$

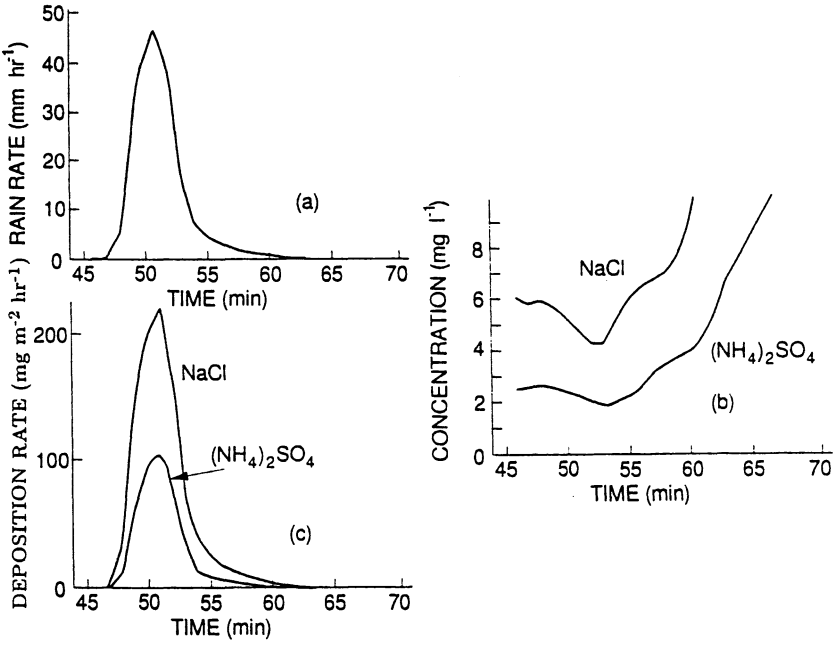


Fig. 17-50: Variation with time of: (a) the precipitation rate, (b) the concentration of NaCl and $(NH_4)_2SO_4$ in rain and (c) the deposition rate of NaCl and $(NH_4)_2SO_4$. Based on computations with a two-dimensional cloud model for the case of GATE-261 over S. Atlantic. (From Flossmann, 1991, with changes.)

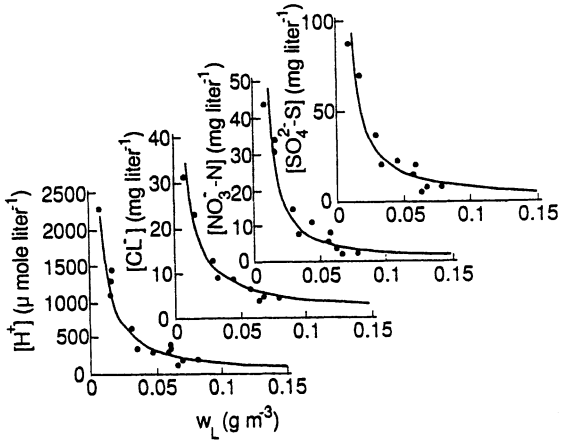


Fig. 17-51: Variation with liquid water content of the concentration of various salt ions and H^+ inside fog water. During a fog event on Kl. Feldberg (Germany). (From Schmitt, 1986, with changes.)

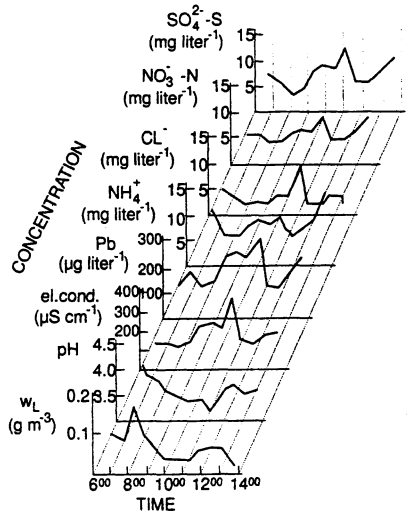


Fig. 17-52: Variation with time of the liquid water content and of the concentration of various salt ions, metals and the pH inside fog water. During a fog event on Kl. Feldberg (Germany). From Schmitt, 1986, with changes.)

Depending on the convective vigor of a cloud, the precipitation efficiency of a convective cloud has been found to range from a few percent to a few tens of a percent (Floßmann and Pruppacher, 1988; Floßmann, 1991; Browning, 1977; Marwitz, 1972).

A number of additional parameters have been defined in the literature to characterize the efficiency with which air pollutants are deposited on the ground. The *deposition* D_P is used as a measure for the amount of pollutants deposited on the ground by rain per unit area, after a given amount of rain has fallen. This parameter is defined by

$$D_P \equiv cP\,, \tag{17-165}$$

where the concentration c of the pollutant in the rain water is given in mg liter^{-1}, the precipitation amount P in mm, and the deposition D_P in mg m^{-2}. Georgii and Weber (1960), Junge (1963), Dawson (1978), Kins (1982a,b), Lindberg (1982), Zimmermann (1986) and Fiedler (1990) found, from field observations, that

$$c \propto P^{-b}\,, \text{ and } \quad D_P \propto P^{1-b}\,, \tag{17-166}$$

with $0.2 \leq b \leq 0.6$ depending on the type of pollutant in the rain water. The variation of c and D_P with P is illustrated in Figures 17.47a,b. We note that, generally, at the beginning of a rain event, the pollution concentration in the rain on the ground decreases sharply with increasing rain amount. The reason for this is that, at the beginning of a rain event, the concentration of the pollutant in the air and the evaporation rate of the drops, are still relatively high. As the rain progresses, the amount of pollutant available for scavenging, as well as

drop evaporation, decrease, causing the concentration in the rain to level out. Nevertheless, the concentration in the rain often rises again at the very end of a precipitation event (see Figure 17.48). This may be due to a decrease in relative humidity and an associated increase in the drop evaporation rate, due to advected pollution, or due to rain drops which originated on cloud drops at the periphery of the cloud where they had a longer life time and, consequently, also had taken up more pollutants than the drops at the cloud center.

Of course, during any particular rain event, the rain intensity varies. Field observations show that the concentration of a pollutant in the rain water on the ground is often inversely related to the rain intensity. This correlation is exemplified in Figure 17.49, based on observations taken during a rain event over Frankfurt (Germany), and in Figures 17.50a,b, based on model cloud studies over the South Atlantic. To explain the inverse correlation between precipitation rate and the concentration of the pollutant content in the rain water, we must recall from Chapter 2 that a high precipitation rate is associated with large drops, which generally have a much lower solute content than small drops. The *deposition rate* r_D, defined by the relation

$$r_D \equiv cR, \tag{17-167}$$

with c in mg liter^{-1}, R in mm hr^{-1}, and r_D in mg m^{-2}hr^{-1}, is, as expected, positively correlated with the rain rate. This is exemplified in Figures 17.50a,c by the model cloud study of Flossmann (1991). Note that the maxima in the deposition rate for NaCl and $(NH_4)_2SO_4$ coincide with the maximum in the rain rate. We also note that the deposition rate during a short but intense local shower may be considerably higher than the annual average deposition rate. Over urban areas, annual average deposition rates range typically between 1 and 7 g m^{-2}yr^{-1} for SO_4^{2-}, NO_3^- and NH_4^+ (Raynor and Hayes, 1982; Shaw, 1982; Georgii *et al.*, 1984; Fay *et al.*, 1985; Bilonick, 1985; Stohlgras and Parsons 1987; Mosello *et al.*, 1988; Harrison and Allen, 1991; Yamaguchi *et al.*, 1991). For rains over remote continental areas (East Africa; Nigeria; San Carlos, Venezuela; Amazon Basin; Catherine, Australia), Galloway (1985) deduced from numerous observations global average deposition rates of 0.45 to 0.84 g m^{-2}yr^{-1} for SO_4^{2-}, 0.22 to 1.01 g m^{-2}yr^{-1} for NO_3^-, and 0.014 to 0.66 g m^{-2}yr^{-1} for NH_4^+. For marine areas, these values range between 0.09 to 1.2 g m^{-2}yr^{-1} for SO_4^{2-}, 0.04 to 0.03 g m^{-2}yr^{-1} for NO_3^-, and 0.014 to 0.10 g m^{-2}yr^{-1} for NH_4^+. For Greenland and the Antarctica, the corresponding values are 0.0024 to 0.042 g m^{-2}yr^{-1} for SO_4^{2-}, 0.0014 to 0.0078 g m^{-2}yr^{-1} for NO_3^-, and 0.0024 to 0.0052 g m^{-2}yr^{-1} for NH_4^+.

Finally, a comment is in order concerning wet deposition from fogs. Obviously, we expect that these rates must be very small due to the small drops in a fog, and their associated small settling rates. Nevertheless, the results of fog models show that drop deposition must be considered to explain quantitatively the water and chemical budget of a fog. Observations of Schmitt (1986) demonstrated that in (17-167)

$$c \propto w_L^b, \tag{17-168}$$

with c in mg liter^{-1} or μg liter^{-1} and w_L in g water per m^3 air, and where b is a constant. This behavior is illustrated in Figure 17.51, where the concentration of four ions in fog water is plotted as a function of the fog's liquid water content. We note that the pollution concentration decreases rapidly as the liquid water content of the fog increases. Therefore, we expect that the pollution content of the cloud water and the liquid water content of a fog vary inversely with time. This is exemplified by Figure 17.52 for a fog on the Kl. Feldberg in Germany.

CHAPTER 18

CLOUD ELECTRICITY

The subject of cloud electricity is quite massive and complex in its own right and has in addition many controversial aspects. Consequently, we shall make no attempt here to provide a comprehensive treatment of the entire subject; rather, we shall restrict ourselves primarily to summaries of some observed electrical properties of clouds and the particles contained within them, to an outline of the major cloud charging mechanisms, and to a consideration of electrical effects on cloud microphysical processes. The topics of lightning, current budgets, and measurement techniques are omitted altogether.

Useful general references on atmospheric and cloud electricity include Israel (1970, 1973), Coroniti and Hughes (1969) Chalmers (1967), and Twomey (1977). Lightning is treated in detail by Uman (1969) and Golde (1977) and, to some extent, by Mason (1971). Summaries of the electrical state of clouds and the mechanisms which lead to cloud charging have been given by Latham (1981), Proctor (1983), Illingworth (1985), Beard and Ochs (1986), Krehbiel *et al.* (1986), Levin and Tzur (1986), Williams (1985, 1989), Saunders (1988), and Mason (1972, 1988).

18.1 Electrical State of the Cloudless Atmosphere

In this section, we shall first briefly summarize the main features of the 'fair weather' electrical state in order to establish the background conditions to which an isolated cloud is exposed, at least in the early stages of development. A list of characterisitc values which describe the fair weather electric state has recently been given by Roble and Tzur (1986, Table 15.1). In the sequel, we shall make use of these data in the appropriate paragraphs.

Under clear sky conditions, flat portions of the conducting Earth carry a negative surface charge density σ_0 which is approximately $\sigma_0 = -3.4 \times 10^{-4}$ e.s.u. cm^{-2}, or -1.1×10^{-9} C m^{-2} (1 e.s.u. of charge (1 statcoulomb)$\approx 1/3 \times 10^{-9}$ C (coulombs)$\approx 2 \times 10^{9}$e (elementary charges)). Assuming a surface area of 5×10^{14} m^2, the total fair weather charge on the Earth is therefore about 5.1×10^5 C (Roble and Tzur, 1986).

By Gauss's law, there is a corresponding, downward-directed surface electric field of magnitude $E_0 = 4\pi\sigma_0$ (e.s.u.)$= \sigma_0/\epsilon_0$ (m.k.s.) $\approx$ 130 V m^{-1}, where ϵ_0 (m.k.s.) $= 8.85 \times 10^{-12}$ farad m^{-1} (1 e.s.u. of field strength (1 Statvolt cm^{-1}) $\approx 3 \times 10^4$ V m^{-1}). The surface electric field varies significantly with location, assuming a typical value of 120 V m^{-1} at the equator, 155 V m^{-1} at 60° latitude, 71 V m^{-1} at the South Pole, and 300 to 400 V m^{-1} in polluted industrial areas (Roble and Tzur, 1986).

Given the existence of σ_0, one might expect the field strength in the atmosphere to vary with height in accordance with Coulomb's law (i.e., as d^{-2}, where d denotes distance from the center of the Earth). However, the rate of attenuation is much greater than this, owing to the existence of positive space charge which rapidly 'screens out' the surface field with increasing height. The main cause of this space charge is cosmic radiation, which provides an essentially continuous source of oppositely charged small ion pairs. Roughly speaking, the positive ions drift in the field toward the ground and encounter increasing resistance (decreasing atmospheric conductivity) as the air and aerosol density increase with decreasing height. This conductivity gradient leads to a 'traffic-jam' effect of space charge buildup with decreasing height.

An approximate empirical description of the variation of electric field strength with height is

$$E(\mathrm{Vm}^{-1}) = 81.8\exp(-4.52z) + 38.6\exp(-0.375z) + 10.27\exp(-0.121z)\,, \quad (18\text{-}1)$$

where z is in km (Gish, 1944). The integral of this expression from the surface to a great height yields a potential difference between Earth and space of about 2×10^5 V. This is within the range of ionospheric potential estimates of 1.50 to 6.0×10^5 V (Roble and Tzur, 1986). From Gauss's law

$$\nabla \cdot \vec{\mathrm{E}} = \rho/\epsilon_0\,, \quad (18\text{-}2)$$

the corresponding positive space charge density ρ (elementary charges cm^{-3}) is

$$\rho = 20.4\exp(-4.52z) + 0.8\exp(-0.375z) + 0.069\exp(-0.121z)\,. \quad (18\text{-}3)$$

Thus, at ground level, the charge density is about 21 e cm^{-3}, while the average over the first kilometer of the atmosphere is about 5 e cm^{-3}.

The conduction current densityor flux vector of charge due to ionic drift in the electric field is

$$\vec{\mathrm{J}}_{q,\mathrm{cond}} = \sum_i n_i q_i \vec{\mathrm{v}}_i\,, \quad (18\text{-}4)$$

where n_i, q_i, and $\vec{\mathrm{v}}_i$ respectively denote the number density, charge, and drift velocity of ion species i. The drift velocity due to the electric field is customarily expressed in the form

$$\vec{\mathrm{v}}_i = \frac{q_i}{\mid q_i \mid} B_i \vec{\mathrm{E}}\,, \quad (18\text{-}5)$$

where B_i is the ionic mobility. (Note, this definition for mobility differs slightly from the one (B_i') introduced in (11-19): Since the force on the ion is $q_i\vec{\mathrm{E}}$, (11-19) becomes $\vec{\mathrm{v}}_i = q_i B_i' \vec{\mathrm{E}}$, so that $B_i = \mid q_i \mid B_i'$.) From (11-21), the corresponding ionic diffusion coefficient is

$$D_i = \frac{B_i \mathrm{k} T}{\mid q_i \mid} \text{ (18-6a),,} \qquad D_i = \frac{B_i \mathrm{k} T}{e}\,, \quad (18\text{-}6\mathrm{b})$$

for ions of charge q_i and one single elementary charge e, respectively.

The small ions produced by cosmic rays and radioactive substances are generally singly charged molecules. They may become 'large' ions by attaching themselves to much larger aerosol particles. Since the mobilities of the large ions are usually 10^{-2} to 10^{-4} times less than those of the small ions, they contribute relatively little to the total ion current. Measurements show that the representative mobilities B_- of the small negative ions are greater than the corresponding mobilities B_+ of the positive ions; according to Bricard (1965), negative ions have a mobility which is about 25 to 40% higher than that of positive ions. He gives as the mean mobilities $B_+ = 1.4\ \mathrm{cm^2 V^{-1}\ sec^{-1}}$ and $B_- = 1.9\ \mathrm{cm^2 V^{-1}\ sec^{-1}}$ at STP. An extrapolation of these values to altitudes $z \leq 10$ km in the standard atmosphere has been given by Shreve (1970):

$$B_+ = 1.4\exp(0.14z)\,, \qquad B_- = 1.9\exp(0.14z)\,, \tag{18-7}$$

where z is in km. Shreve also obtained expressions for the variation with altitude of the corresponding diffusivities (in $\mathrm{cm^2\ sec^{-1}}$):

$$D_+ = 3.6\times 10^{-2}\exp(0.092z)\,, D_- = 4.8\times 10^{-2}\exp(0.092z) \tag{18-8}$$

The values for $z = 0$ were obtained by substituting the corresponding mobilities and $T = 273$ K into (18-6).

On substituting (18-5) into (18-4) for the case of small ions present in concentrations n_+ and n_-, we have

$$\vec{J}_{q,\mathrm{cond}} = \Lambda\vec{E} = (\Lambda_+ + \Lambda_-)\vec{E}\,, \tag{18-9}$$

where Λ is the total conductivity and

$$\Lambda_+ = en_+B_+\,, \qquad \Lambda_- = en_-B_- \tag{18-10}$$

are the polar conductivities. The conductivities $\Lambda_\pm \geq 0$ both contribute in the same way to Λ, since oppositely charged ions move in opposite directions in the electric field. The constant air-to-Earth conduction current density normally varies between 2 and 4×10^{-12} Amp $\mathrm{m^{-2}}$ according to Chalmers (1967), while Gish (1944) gives a value of 2.7×10^{-12} Amp $\mathrm{m^{-2}}$. Regional values include 1×10^{-12} Amp $\mathrm{m^{-2}}$ over industrialized areas, 2.4×10^{-12} Amp $\mathrm{m^{-2}}$ over deserts and vegetated ground, and 2.5×10^{-12} Amp $\mathrm{m^{-2}}$ over the South Pole (Roble and Tzur, 1986). Assuming a global average value of $\vec{J}_{q,\mathrm{cond}} = 3\times 10^{-12}$ Amp $\mathrm{m^{-2}}$, we obtain from the fair weather current to the Earth's surface a value of about 1500 Amp.

From (18-9) and the above global average $\vec{J}_{q,\mathrm{cond}}$, we can estimate the fair weather sea level conductivity to be $\Lambda_0 \approx 3\times 10^{-12}/130 \approx 2.3\times 10^{-14}\ \mathrm{Ohm^{-1}m^{-1}} = 2.1\times 10^{-4}$ e.s.u. (1 $\mathrm{Ohm^{-1}m^{-1}} = 9\times 10^9$ e.s.u.) The conductivity at other levels may be estimated from the relation $\Lambda = 130\Lambda_0/E$ where E is given by (18-1). These estimates are similar to those of Roble and Tzur (1986), who report $\Lambda = \mathrm{O}(10^{-14})\ \mathrm{Ohm^{-1}m^{-1}}$ at sea level, increasing to $\mathrm{O}(10^{-13})\ \mathrm{Ohm^{-1}m^{-1}}$ at the tropopause.

An interesting exercise is to calculate the time which would be required for $j_{q,\text{cond}}$ to reduce the fair weather surface charge density σ_0 to zero if no charging mechanisms existed to maintain σ_0. The governing equation for this situation is

$$\frac{\partial \sigma_0}{\partial t} = -j_{q,\text{cond}} = -\Lambda_0 E_0 = -\frac{\Lambda_0}{\epsilon_0}\sigma_0 \,, \tag{18-11}$$

so that $\sigma_0(t) = \sigma_0(0)\exp(-t/\tau_c)$, where $\tau_c = \epsilon_0/\Lambda_0 \approx 385$ sec ≈ 6.5 min. This short discharge time implies the existence of a very active Earth-charging mechansim. Observations indicate that thunderstorms world-wide collectively fulfill this role of serving as the 'battery' which maintains σ_0 near a constant value.

Williams (1989) suggests that the global lightning flash rate during thunderstorms is larger than 100 sec^{-1}, perhaps as much as 250 sec^{-1}, 20% of which, i.e., 50 sec^{-1}, involve cloud to ground discharges. Assuming that per flash approximately 30 C are transported to the ground (Mason, 1971), we obtain a global current from thunderstorms of 1500 Amp, capable of compensating the fair weather current. Assuming a thunderstorm cell lasts for about 25 minutes (i.e., 1500 sec), we find that each thunderstorm cell generates a current of about 1 Amp. Flights with U-2 planes above thunderstorms (Blakeslee and Christian, 1989) have verified this figure by observing currents of 0.09 to 3.7 Amp, with an average of 1.7 Amp above thunderstorms. Stergis (1957) estimated much earlier a current of 1.3 Amp. From other literature sources, Roble and Tzur (1986) have similarly suggested that the current per thunderstorm cell ranges between 0.5 and 1 Amp, and the total global current between 750 and 2000 Amp, implying that 1500 to 2000 thunderstorms act at any one time.

Finally, we shall estimate the fair weather small ion concentration from Λ. Since the ions are produced in pairs, it is reasonable to assume $n_- \approx n_+ = n \gg (n_+ - n_-)$ (this is justified a posteriori). Thus, we may write $n \approx \Lambda/2eB_+$; at $z = 0, 3,$ and 8 km this gives $n \approx 5 \times 10^2$, 6×10^2 and 8×10^2 cm^{-3}, respectively, with $e = 1.6 \times 10^{-19}$ C. Although, in principle, similar estimates may be made by solving directly for the steady state balance between ion production and loss rates (see also Section 18.3.3), some of the relevant quantities, and especially the ionization rate, have not been measured or calculated to a high degree of accuracy (Israel, 1970).

18.2 Electrical State of the Atmospheric Aerosol

Aerosol particles acquire charge through Brownian deposition of ions. In turn, such charged particles experience Brownian coagulation which is enhanced or suppressed by electrostatic forces. We may formulate this problem using a slight generalization of the model of Section 11.5. Consider the relative motion of charged particles of volume v_2 toward a charged particle of volume v_1. We write the v_2-particle flux vector toward the v_1-particle as the sum of contributions due to diffusion and conduction, ignoring gas kinetic (finite mean free path) effects:

$$\vec{j}_q = -D_{12}\nabla n_2 + \frac{q_2}{\mid q_2 \mid} B_{12}\vec{\text{E}}_{12} n_2 \,, \tag{18-12}$$

where q_2 is the v_2-particle charge, and $\vec{\text{E}}_{12}$ is the electric field acting on a v_2-particle due to particle v_1. On using (18-6) and writing $q_2\vec{\text{E}}_{12} = -\nabla\Phi_{12}$, where Φ_{12} is the

electrostatic interaction potential, (18-12) may also be expressed in the form

$$\vec{J}_q = -D_{12} \exp(-\Phi_{12}/kT) \nabla [n_2 \exp(\Phi_{12}/kT)] . \tag{18-13}$$

If we now make the reasonable assumptions (1) that Φ_{12} is a function only of the center-to-center distance $r \geq r_{12}$ and (2) that there is a steady state, then the constant v_2-particle flux J_q into any spherical surface $S = 4\pi r^2$ concentric with the v_1-particle is

$$J_q = -\int_S \vec{J}_q \cdot d\vec{S} = 4\pi D_{12} r^2 \exp(-\Phi_{12}/kT) \frac{d}{dr} n_2 \exp(\Phi_{12}/kT) . \tag{18-14}$$

On integrating this equation and imposing the conditions $n_2(r_{12}) = 0$ and $\Phi_{12}(\infty) = 0$, we find

$$J_q = 4\pi D_{12} n_2(\infty) \left[\int_{r_{12}}^{\infty} \frac{\exp(\Phi_{12}/kT)}{r^2} dr \right]^{-1} . \tag{18-15}$$

Therefore, the generalization of the Brownian collection kernel K_{ij} of (11-54) which includes the effects of particle charge is

$$K'_{ij} = K_{ij} Q_{ij} , \quad Q_{ij} = \left[r_{ij} \int_{r_{ij}}^{\infty} \frac{\exp(\Phi_{ij}/kT)}{r^2} dr \right]^{-1} \tag{18-16}$$

(Fuchs, 1934).

Let us now use (18-16) to estimate the effect of charging on the coagulation rate. Under fair weather conditions, aerosol charging is approximately symmetrical, since small ions are created in pairs and have roughly equal mobilities. Therefore, in equilibrium, particles of any size have a charge distribution approximately symmetrical about zero charge, so that for every v_j-particle bearing charge $q_j > 0$, another has charge $-q_j$. For such particles coagulating with a v_i-particle of charge $q_i > 0$, the appropriate (Coulomb) interaction potential is

$$\Phi_{ij}(\text{e.s.u.}) = \pm \frac{q_i q_j}{r} . \tag{18-17}$$

This expression ignores induced (image) charges, which are insignificant in the present context (e.g., see Fuchs, 1964, p.307). On substituting (18-17) into (18-16), we find the effect of electrostatic repulsion is a decrease in the coagulation rate of v_i and v_j-particles measured by the factor

$$Q_{ij}^{+} = \frac{\tau}{\exp(\tau) - 1} , \quad \tau = \frac{q_i q_j}{r_{ij} kT} . \tag{18-18a}$$

Similarly, electrostatic attraction enhances the coagulation rate by the factor

$$Q_{ij}^{-} = \frac{\tau}{1 - \exp(-\tau)} . \tag{18-18b}$$

Because of the symmetry of the charging process, the overall effect may be estimated by the arithmetic mean of Q_{ij} and Q_{ij}, viz.,

$$\bar{Q}_{ij} = \frac{\bar{\tau}[\exp(\bar{\tau}) + 1]}{2[\exp(\tau) - 1]} \geq 1 , \tag{18-19}$$

where $\bar{\tau}$ is the average value of τ. The coagulation rate of a symmetrically charged aerosol is thus higher than that of a neutral one. However, the effect turns out to be quite small: If we regard particle charge as providing an extra degree of freedom in the particle's energy budget, then by the equipartition theorem, we have $\overline{q_i q_i}/r_{ij} = \mathrm{k}T/2$ (e.g., Keefe *et al.*, 1959). Then $\bar{\tau} = 1/2$ and $Q_{ij} \approx 1.02$, implying the charge carried by natural aerosols should have a negligible influence on their coagulation rate. This conclusion has been borne out by many experiments (e.g., see Devir, 1967).

Besides acquiring charge through ionic diffusion, aerosol particles polarize in the fair weather electric field and thereby receive an additional ionic drift current. This problem is discussed in Section 18.3.1 for the case of charged drops. It can be dismissed in the present context in the following way: the energy acquired by an ion moving in the background field E over the characteristic length (the radius) r of an aerosol particle is small compared to the thermal energy $\mathrm{k}T$. For example, for $r = 1\,\mu\mathrm{m}$, $E = 1$ V cm^{-1}, and $T = 273$ K, we have $eEr/\mathrm{k}T \approx 4 \times 10^{-3}$. Consequently, Brownian diffusion of ions completely dominates under ordinary circumstances. Then, the estimate $\bar{\tau} = 1/2$ remains good, which says that aerosol particles carry few, if any, charges on the average. Therefore, particle mobility in the field E remains low, so that the relative particle motion (and, hence, the coagulation rate) is changed only slightly by the presence of the field. For example, drift velocities of particles of 0.1 and $1\,\mu\mathrm{m}$ radius carrying one elementary charge in a field of 1 V cm^{-1} are roughly 10^{-4} and 10^{-5} cm sec^{-1}, respectively. Such small ordered velocities are insignificant compared to ambient air motions and sedimentation velocities.

The argument above which led to $\bar{\tau} = 1/2$ also implies a normal (Boltzmann) charge distribution centered about zero charge. Thus, if $n(r, p)$ denotes the concentration of aerosol particles of radius r bearing p elementary charges, then $n(r, p) \sim n(r, 0) \exp(p^2 e^2/2r\mathrm{k}T)$ and the width (standard deviation) of the distribution is $\sigma = (r\mathrm{k}T)^{1/2}/e$ Also, the average number of charge of either sign is given by

$$\overline{|\,p(r)\,|} = \int_0^\infty pn(r, p)\,\mathrm{d}p \left[\int_0^\infty n(r, p)\,\mathrm{d}p\right]^{-1} = \frac{1}{e}\left(\frac{2r\mathrm{k}T}{\pi}\right)^{1/2} \approx 300 r^{1/2} , \tag{18-20}$$

for 0°C and r in cm (see also Section 18.3.2). These predictions are generally consistent with observations: For example, Whitby and Liu (1966) found that aerosol particles of $1\,\mu\mathrm{m}$ diameter carry an average absolute charge of about $e/2$. Similarly, Israel (1973) quotes measurements which showed that $\overline{|\,p\,|} \approx 7$ and 14 for particles of radius 5 and $20\,\mu\mathrm{m}$, respectively; also, the distributions, were found to broaden with increasing r, as expected.

18.3 Electrical Conductivity in Clouds

Cloud charging mechanisms are opposed by field-driven leakage currents. Hence, the degree of electrification achieved will depend in part on the cloud conductivity, Λ_c. In this section, we shall explore the dependence of Λ_c on field strength, ionization rates, and microphysical properties such as cloud particle concentrations, sizes, and charge states.

18.3.1 Diffusion and Conduction of Ions to Cloud Drops

The electrical conductivity in clouds is controlled by the local balance of ion sources and sinks. The dominant sinks are the cloud particles, which efficiently adsorb ions through diffusion and conduction. The rate of ion attachment by diffusion alone has been treated in the previous section. Thus, from (18-16) to (18-18), we see that the positive and negative ion currents to a stationary drop of charge $Q = pe > 0$ in a region of negligible electric field and where the ambient concentration of positive and negative ions are $n_+(\infty) = n_-(\infty)$ are, respectively,

$$J_D^+(p) = \frac{4\pi aeD_+n_+(\infty)pc}{\exp(pc) - 1}, \tag{18-21a}$$

$$J_D^-(p) = \frac{4\pi aeD_-n_-(\infty)pc}{1 - \exp(-pc)}, \tag{18-21b}$$

where $pc = pe^2/akT = Qe/akT$, with $c = e^2/akT \approx 6 \times 10^{-6}/a$, $D = BkT/e$, for 0°C and a in cm (Fuchs, 1934; Pluvinage, 1946; Bricard, 1949; Gunn, 1954). For the case that $Q < akT/e$, i.e., $pc \ll 1$ and therefore $\exp(pc)/pc \approx 1$, we find for pure ionic diffusion

$$J_+ = 4\pi aeD_+n_+(\infty) \quad J_- = 4\pi aeD_-n_-(\infty). \tag{18-21c}$$

If the magnitude of the background electric field is E, the relative strengths of the conduction and diffusion ion current are measured by the ratio

$$\frac{|\, B_\pm \nabla n_\pm \cdot \vec{\mathrm{E}}\,|}{|\, D_\pm \nabla^2 n_\pm\,|} \propto \frac{eEa}{\mathrm{k}T} \equiv \gamma, \tag{18-22}$$

using (18-6) and applying usual scaling arguments (cf. Section 17.4.2.1). From the analogy between (17-9) and (18-22), the parameter γ can be described as an 'electric' Péclet number. Conduction is clearly negligible when $\gamma \ll 1$, and it is for this case that (18-21) applies. Since γ $(m.k.s.) = 42.5Ea$ at 0°C, we see that for a typical fair weather situation ($a = 10\,\mu$m, $E = 10^2$ V m^{-1}, $\gamma \approx 0.04$), (18-21) provides a good estimate for the ion attachment rates.

Unfortunately, a general solution for simultaneous diffusion and conduction at higher field strengths is not available. However, a solution to first order in γ has been obtained by the method of matched asymptotic expansions (Klett, 1971b). (A description of this method is given in example 4 of Section 10.2.2.3). The resulting modified ion attachment rates are given by

$$J_{D+C}^{\pm}(p) = \left(1 \pm \frac{\gamma pc}{2[1 - \exp(\pm pc)]}\right) J_D^{\pm}(p), \tag{18-23}$$

where $J_D^{\pm}(p)$ are the rates expressed in (18-21).

For highly electrified clouds with $\gamma \gg 1$, the ion loss rate due to conduction, surpasses that from diffusion. This situation can be modeled by calculating the conduction currents to the polarized drop, assuming the ambient ion concentrations prevail right up to the drop surface. Let us proceed with this formulation by considering a drop of radius a and charge $Q > 0$ in a region where the background electric field is $\vec{\mathrm{E}} = E\hat{\mathrm{e}}_z$. Then, the electric field in the vicinity of the drop may be expressed in spherical coordinates (and in e.s.u.) as

$$\vec{\mathrm{E}} = \frac{Q}{r^2}\hat{\mathrm{e}}_r + E\hat{\mathrm{e}}_z + \frac{Ea^3}{r^3}(2\cos\theta\hat{\mathrm{e}}_r + \sin\theta\hat{\mathrm{e}}_\theta)\,, \tag{18-24}$$

where θ is the polar angle measured from the direction of $\hat{\mathrm{e}}_z$. The last term in (18-24) is the dipole field induced by the conducting drop. The radial field at the drop surface is therefore $(E_r,)_{r=a} = 3E\cos\theta + Q/a^2$, and can be seen to switch sign as θ passes through $\theta_0 = \cos^{-1}(-Q/3Ea^2)$. Consequently, negative ions are conducted to the drop for $0 \le \theta \le \theta_0$, while positive, ions flow to the surface where $\theta_0 < \theta \le \pi$. Therefore, the positive and negative ion currents to the drop are

$$J_c^+ = 2\pi a^2\Lambda_+ \int_{\theta_0}^{\pi} (E_r)_{r=a}\sin\theta\,\mathrm{d}\theta = \frac{\pi\Lambda_+}{3Ea^2}(Q - 3Ea^2)^2\,, \tag{18-25a}$$

and

$$J_c^- = 2\pi a^2\Lambda_- \int_{0}^{\theta_0} (E_r)_{r=a}\sin\theta\,\mathrm{d}\theta = \frac{\pi\Lambda_-}{3Ea^2}(Q_2 + 3Ea^2)^2\,. \tag{18-25b}$$

For an unchanged drop, these currents reduce to

$$J_{c,0}^+ = -3\pi e n_+ B_+ E a^2\,, \tag{18-25c}$$

$$J_{c,0}^- = 3\pi e n_- B_- E a^2\,. \tag{18-25d}$$

In equilibrium $J_c^+ = J_c^-$, which results in an expression for the drop charge as a function of radius, field strength, and polar conductivity ratio:

$$Q(\text{e.s.u.}) = 3Ea^2\left[\frac{(\Lambda_+/\Lambda_-)^{1/2} - 1}{(\Lambda_+/\Lambda_-)^{1/2} + 1}\right] \tag{18-26}$$

(Pauthenier and Moreau-Hanot, 1931; Gunn, 1956). We thus find that the maximum charge attainable through conduction charging is $Q_{\max} = \pm 3Ea^2$. This limiting value of charge on a polarized drop has been verified experimentally in a discharge tube by Panthenier and Guillien (1932).

18.3.2 Conductivity in Weakly Electrified Clouds

For the case $\gamma \ll 1$, we may assume the ion attachment rates per drop are adequately described by (18-21). However, to obtain the overall ion loss rate using

this formulation, we evidently need to know the distribution of drop charge which arises from diffusion charging. Fortunately, it turns out that only a small error is introduced if we assume that every drop carries the average charge of the distribution (assuming equal sized drops). To show this simplification is possible, we must first determine the stationary drop charge distribution function. Although, as we have indicated in Section 18.2, this is given to a good approximation by a Boltzmann distribution, it is of some interest to determine it more exactly. As emphasized by Fuchs (1964), the actual distribution differs in principle from a Boltzmann distribution since ions, once captured by a drop, are unable to leave it.

Let the fractional concentration of equal sized drops bearing charge pe be denoted by $n(p)$. We can determine $n(p)$ by the principle of detailed balancing, according to which the steady state rate at which drops of charge pe capture positive ions is equal to the rate at which drops of charge $(p+1)e$ capture negative ions. Thus, we have

$$n(p)J_D^+(p) = n(p+1)J_D^-(p+1)\,, \tag{18-27}$$

or

$$n(p) = \frac{(p-1)(1-\mathrm{e}^{-pc})\Lambda_+}{p(\mathrm{e}^{(p-1)c}-1)\Lambda_-}n(p-1)\,, \tag{18-28}$$

from (18-21). This recursion relation is easily solved by writing $n(p-1)$ in terms of $n(p-2)$, etc., and noting that $1+2+\ldots+(p-1) = p(p-1)/2$; the result is

$$n(p) = n(0)\left(\frac{\Lambda_+}{\Lambda_-}\right)^p \frac{\sinh(\frac{pc}{2})}{\frac{pc}{2}}\mathrm{e}^{-p^2c/2} \tag{18-29}$$

(Pluvinage, 1946; Sal'm, 1971).

In order to explore the implications of (18-29), let us first consider the special situation for which $\Lambda_+ = \Lambda_-$ Then, if the total drop concentration is $N = \sum_p n(p)$, the average positive ion flux per drop, $\overline{J_D^+}$, may be expressed as

$$N\overline{J_D^+} = \sum_{p=-\infty}^{\infty} J_D^+(p)n(p) = 2\sum_{p=0}^{\infty} J_D^+(p)n(p)\,, \tag{18-30}$$

using (18-27) and the symmetry conditions $n(-p) = n(p)$ and $J_D^+(-p) = J_D^-(p)$. On substituting (18-21a) and (18-29) with $\Lambda_+ = \Lambda_-$ into (17-30), we obtain

$$N\overline{J_D^+} = 2n(0)J_D^+(0)\sum_{p=0}^{\infty}\mathrm{e}^{[p(p+1)c]/2} \approx \left(\frac{\pi}{2c}\right)^{1/2} J_D^+(0)n(0)\mathrm{e}^{c/8}\left[1-\mathrm{erf}\left(\frac{1}{2}\sqrt{\frac{c}{2}}\right)\right]. \tag{18-31}$$

The last form on the right side has been obtained by approximating the sum over p by an integral. Since $c = e^2/akT < 10^{-2}$ for $a > 1\,\mu$m at $T = 273$ K, (18-29) reduces approximately to $n(p) = n(0)\exp(-p^2c/2)$, so that $N \approx (\pi/2c)^{1/2}n(0)$. Therefore, (17-31) becomes

$$\overline{J_D^+} \approx J_D^+(0)\left[1-\sqrt{\frac{c}{2\pi}}+\frac{c}{8}+\mathrm{O}(c^{3/2})\right], \tag{18-32}$$

which is the desired result, namely that to within an error of a few percent, we may calculate the total ion flux to the drops by assuming each carries the average (zero) charge. Furthermore, for this case the charge distribution is close to a Gaussian (Boltzmann) form, symmetric about zero charge.

Now let us suppose the average drop charge $\bar{Q} = \bar{p}e$ is not zero. From the nature of diffusion charging, we might well expect the physics to be largely unchanged in this generalization, the only difference being a new reference level of average charge. Thus, we would expect $n(p)$ to be given approximately by a Gaussian distribution centered about $\bar{p}$, viz.,

$$n(p) \approx \frac{N}{(2\pi)^{1/2}\sigma} e^{-[(p-\bar{p})^2]/2\sigma^2}, \quad \sigma^2 = \frac{1}{c} = \frac{akT}{e}, \tag{18-33}$$

and that the total ion flux to the drops may be determined with sufficient accuracy by assuming each carries the average charge.

It is easy to show that these expectations are consistent with the more rigorous form of $n(p)$ given by (18-29). Thus, if we assume the average positive ion flux per drop is now $\overline{J_D^+} = J_D^+(\bar{p})$ (cf. (18-32)), and that similarly the average negative ion flux is $\overline{J_D^-} = J_D^-(\bar{p})$, then on setting these two rates equal for a steady state, we find from (18-21) that

$$\bar{p} = \sigma^2 \ln \frac{\Lambda_+}{\Lambda_-} = \frac{akT}{e^2} \ln \frac{\Lambda_+}{\Lambda_-} \tag{18-34}$$

(Gunn, 1954, 1955). Now from (18-34), we find $\Lambda_+/\Lambda_- = \exp(\bar{p}c)$ which, on substitution into (18-29), produces a charge distribution of the form

$$n(p) = n(0)e^{\bar{p}^2 c/2} \frac{\sinh \frac{pc}{2}}{\frac{pc}{2}} e^{-[(p-\bar{p})^2 c]/2} \approx n(0)e^{-[(p-\bar{p})^2 c]/2}, \tag{18-35}$$

which is equivalent to (18-33).

With an electric field present, the assumption of a Gaussian charge distribution is still reasonable if the energy acquired by an ion in moving a mean free path λ_a in the field direction is small compared with its thermal energy; i.e., if $eE\lambda_a \ll kT$ or $E \ll 2 \times 10^3$ V cm^{-1} for typical cloud conditions. The corresponding constraint on γ for 10 μm radius drops is $\gamma \ll 80$. Hence, for $\gamma \lesssim 1$, the expression (18-23) may be used (with p replaced by $\bar{p}$) in conjunction with (17-33) to determine the first-order effect of γ on $\bar{p}$:

$$\bar{p} = \left(1 + \frac{\gamma}{2}\right) \frac{akT}{e^2} \ln \frac{\Lambda_+}{\Lambda_-}. \tag{18-36}$$

Let us now use these results to explore the behavior of conductivity and the disposition of space charge in weakly electrified clouds. Within the cloud, the attachment rates of ions to drops are much greater than the loss rates arising from ionic recombination. Therefore, if the local ionization rate is I(= number per unit volume of ions of either sign created per unit time), then, for a steady state balance between the generation and loss rates, we have to a good approximation

from (18-21) and (18-23):

$$I = 4\pi a N D_+ n_+ \left(1 - \frac{\bar{p}c}{2} + \frac{\gamma}{2}\right) = 4\pi a N D_- n_- \left(1 + \frac{\bar{p}c}{2} + \frac{\gamma}{2}\right), \tag{18-37}$$

where we have made the assumption, justified above, that each of the N drops per unit volume of radius a carries the average charge $\bar{p}e$. To obtain (18-37), we have also retained just the first-order term in $\bar{p}c$ from (18-21) and (18-23). From the preceding discussions, we may expect this simplification to yield sufficient accuracy for $\bar{p} \lesssim 10^2$ under typical conditions (with $a \approx 10\,\mu$m).

We see from (18-6), (18-10), and (18-37) that the total cloud conductivity Λ_c has, to $O(\bar{p}c)$ and $O(\gamma)$, the form

$$\Lambda_c \approx \Lambda_{co}\left(1 - \frac{\gamma}{2}\right), \quad \Lambda_{co}\ (\text{e.s.u.}) = \frac{Ic}{2\pi N} = \frac{eIB}{2\pi a N D}. \tag{18-38}$$

The quantity Λ_{co} is the estimate of total conductivity, due to Pluvinage (1946), for the case of uncharged drops (here B and D may be regarded as the average of the mobilities and diffusivities of the positive and negative ions). Equation (18-38) shows that the ambient field lowers the total conductivity, but that drop charge has no first-order effect. Numerical evaluation with $I = 10$ cm^{-3} sec^{-1} shows that Λ_c is typically 1/40 to 1/3 the clear air value at the same level, in good agreement with observations (e.g., Pluvinage, 1946; Israel and Kasemir, 1952; Allee and Phillips, 1959).

We may also use (18-37) to estimate the net ionic space charge in a region of charged drops. The ionic space charge density is $(n_+ - n_-)e$, while the drop charge density is $N\bar{p}e$; from (18-37), the ratio of these densities is

$$\frac{n_+ - n_-}{N\bar{p}} \approx \frac{Ic}{4\pi a N^2 D}. \tag{18-39}$$

For typical conditions with $I = 10$ cm^{-3} sec^{-1}, $a = 10\,\mu$m, and $N = 10^2$ cm^{-3}, we find the drop charge density is about 10^2 times greater than the ionic space charge density. Thus, for practical purposes, the charge in a region of cloud may be assumed to reside on the drops. Equation (18-39) also justifies a posteriori an assumption we have implicitly made in all of our models for calculating ion attachment rates to drops, namely that the ionic space charge is too dilute to have any noticeable screening effect on the Coulomb field of the charged drops. Finally, we see from (18-34) or (18-37) that the polar conductivity ratio is near unity ($\Lambda_+/\Lambda_- \approx 1 + \bar{p}c$) in weakly electrified clouds; hence, the inequality $n_+ - n_- \ll n_+ \approx n_-$ ($\approx I/4\pi a N D$) holds, just as for the case of a clear atmosphere.

18.3.3 Conductivity in Strongly Electrified Clouds

The results of the previous section indicate that, for a monodisperse cloud with average drop charge $\bar{Q}$, a good approximation to the equilibrium concentration of positive ions n_+ may be obtained by solving the following equation:

$$I = \alpha n_+ n_- + 4\pi a N D_+ n_+ + \frac{\pi B_+ n_+ N}{3Ea^2}(3Ea^2 - \bar{Q})^2. \tag{18-40}$$

We have included in the first term on the right side an expression for the loss rate due to ionic recombination, the quantity $\alpha(\approx 1.6 \times 10^{-6}$ cm^3 sec$^{-1})$ being the recombination coefficient for small ions. Outside the cloud, we thus have $n_+ \approx n_- \approx \sqrt{I/\alpha}$. To first-order in γ and $\bar{p}c$ ($\bar{Q} = \bar{p}e$) the diffusion and conduction terms in (17-40) reduce to $4\pi aND_+n_+(1-\bar{p}c/2+3\gamma/4)$, which is fairly close to (18-37); for $\gamma \gg 1$, the ion loss rate will be controlled by the last (conduction) term on the right side of (18-40). Hence, (18-40) is reasonably accurate in both the low and high field limits.

Phillips (1967) used (18-40), along with its obvious counterpart for the negative ion concentration, to show that cloud conductivity is reduced sharply with increasing field strength and liquid water content, and more moderately with decreasing drop size for a given water content. The explanation for this last mentioned trend is simply that a given quantity of water presents an absorbing surface area which increases as it achieves a more finely divided state. (Incidentally, it is for this reason that we may safely ignore the effects of drop motion on ion capture rates. Ventilation effects are significant only for $a > 50\,\mu$m (see Section 13.2.3), and the drops in that fraction of the spectrum contribute negligibly to the total surface area of the cloud water, at least in the early stages of cloud development when electrification is weak. In the later stages, an increase in electrification will generally accompany any shift in the spectrum to larger drop sizes, so that ion drift velocities will grow faster than representative drop terminal velocities. Hence, in-cloud drop motions probably never exert a significant influence on ion capture rates.) For example, for a cloud with $w_L = 1$ g m^{-3} and $E = 0$, the cloud conductivity is less than the fair weather value at the same altitude by factors of about 40 and 10 for $a = 10$ and $20\,\mu$m, respectively. If $E = 300$ V/cm (1 e.s.u.) and the other condition remains unchanged, the reduction factors become 500 and 200. Changes in w_L alone produce proportionate changes in the reduction factor.

Similar calculations were carried out by Griffiths *et al.* (1974), who considered an extension of (18-40) to three different cloud types: cumulus congestus, stratocumulus, and fog. They also considered the effects of ion emission due to corona discharge from hydrometeors for the case of high electric fields. The decrease of the electrical conductivity in these clouds was found to be sensitive to variations in the liquid water content and the electric field but only slightly affected by changes in altitude, particle charge, and the manner in which the charge is distributed over the size spectrum. When a secondary source of ion production, resulting from corona currents emitted from ice particles under the influence of a strong electric field, was introduced into the calculations, a large increase in conductivity was predicted. However, since the critical electric fields for onset of corona (5.4 kV cm^{-1} for snow flakes and 7.2 kV cm^{-1} for hailstones), measured by Griffiths and Latham (1974), are much larger than the observed values of electric fields in clouds (see Section 18.4.1), we may expect that cloud conductivities are generally very small, and that it is probably unnecessary to account for ionic leakage currents in calculations of electric field growth in clouds. Some workers have argued that effective cloud conductivities are often quite large, perhaps as much as 20 times the fair weather value, on the basis of the observed rapid recovery times of sudden electric field changes associated with thunderstorms (e.g., Freier, 1962; Colgate, 1969).

However, a more convincing explanation for this behavior is that there is a rearrangement of charge over a large region of the atmosphere outside the cloud in response to the abrupt field change, so that recovery times (generally measured at the ground) are close to the short clear air relaxation times at higher elevations (Illingworth, 1971).

The difference between clear air and cloud conductivities causes a layer of space charge to form at cloud boundary regions, if a component of the electric field is normal to the boundary. For example, if we consider an idealized layer-type cloud with a boundary location given by $z = z_B$, then in the steady state, the vertical conduction current must be continuous across the boundary, which leads to the relation $\Lambda_c E_c = \Lambda_0 E_0$ at $z = z_B$, the subscripts 0 and c referring to the values outside and within the cloud, respectively. Then, from Gauss's law (18-2), we find the boundary charge density is ρ (m.k.s.) $\approx \epsilon_0(E_c - E_0)/\Delta z = \epsilon_0 E_c(1 - \Lambda_c/\Lambda_0)/\Delta z$, where Δz is the characteristic depth over which the charge is distributed. A crude estimate for Δz for the case of large fields ($\gamma \gg 1$) is that it is given by the conduction mean free path of ions, ℓ, in a cloud of uncharged drops. From (18-40) or (18-41), we see that the rate of depletion of ions by conductive attachment to charged drops is measured by $dn/dt = v_{\text{drift}} dn/dz = -3\pi B N E_c a^2 n$; since $v_{\text{drift}} = BE_c$ we obtain $\Delta z \approx \ell = (3\pi N a^2)^{-1}$ (typically, $5 \lesssim \ell \lesssim 50$ m), and so $\rho \approx \epsilon_0 E_c/\ell$ with $\Lambda_c/\Lambda_0 \ll 1$. The corresponding charge per drop is

$$\bar{Q}(\text{boundary layer}) \approx 3\pi\epsilon_0 E_c a^2 (\text{m.k.s.}) = \frac{3E_c a^2}{4} (\text{e.s.u.}) . \tag{18-41}$$

This generally large value of drop charge suggests our estimate for Δz is not very accurate. (Another source of error we have completely ignored is turbulent mixing at the cloud boundary, which can establish a characteristic cloud conductivity gradient and, hence, a different characteristic value for Δz.) Nevertheless, our simple calculation suffices to illustrate how large drop charge densities can form from ion currents which enter clouds. (More detailed studies of the formation and structure of charge screening layers around clouds may be found in Brown *et al.* (1971), Hoppel and Phillips (1971, 1972), and Klett (1972).)

18.4 Charge Distribution in Clouds

18.4.1 Weakly Electrified Clouds

Let us consider first the extent to which the preceding descriptions of charging by ion attachment can provide at least a qualitative basis for understanding the charge distributions observed in fair weather clouds. Since clouds are poor conductors, we would expect the fair weather electric field to deposit negative ions in the base of a newly formed cloud. We would further expect that this charge, essentially all of which will reside on the cloud particles, to be carried along in any updraft, so that the cloud should tend to develop a negatively charged core. On the other hand, the regions of the cloud near the upper surface should be positively charged from the positive ion current entering the cloud from above.

The above picture is in accord with most observations of fair weather clouds. For example, the field studies of Reiter (1964, 1969) showed that electrified strato-

cumulus, altocumulus, and convective cumulus clouds which contain neither ice nor precipitation-sized particles are electrically bi-polar with a pronounced negatively charged base and a positively charged upper portion. Also, Takahashi (1972, 1975, 1978a, 1982) observed predominantly negatively charged drops in the bases of warm clouds in Hawaii. On the other hand, Twomey (1956) found a net positive charge in the bases of stratus and stratocumulus clouds. Krasnogorskaya (1969) observed predominantly negative charge in cumuli and stratified cumuli generally less than 1 km thick, but the location of the measurements relative to the cloud boundaries was not reported.

Although the observed overall pattern of charges in fair weather clouds is usually in agreement with what we would expect from the action of ion capture processes, the same cannot be said for the quantitative details of the distribution of charge among individual cloud particles. In particular, the observed particle charges are usually much larger than what would follow from diffusion and conduction charging alone. The best case of agreement with the theory of diffusion charging was provided by Phillips and Kinzer (1958), who measured the size and charge of drops in stratocumulus clouds with 'near normal' fair weather electric fields. They found the observed charge distributions were represented moderately well by (18-33) with $\bar{p} = 0$. For this case, the mean absolute charge is given by (18-20); for example, a 10 μm radius drop carried about 10 elementary charges on the average, irrespective of sign. However, much larger drop charges were reported by Twomey (1956) under apparently similar conditions (unfortunately, the field strength was not stated). As noted above, Twomey found mainly positively charged drops; for these, the charge versus size relation could be expressed as $\bar{Q}$ (e.s.u.) $\approx 0.3a^2$ (cm). According to this result, for example, a 10 μm radius drop usually carried about 6×10^2 positive elementary charges, in striking contrast to the observations of Kinzer and Phillips. (As we have seen, conduction charging produces a quadratic dependence of charge on radius also. However, under fair weather conditions, we would generally expect the magnitude of charge to be somewhat less than that found by Twomey. If, for example, we were to suppose that he measured drop charges acquired through conduction charging in the boundary layer, then, from (18-43), we see that the cloud electric field would have to have been about 10^2 V cm^{-1} which implies $\Lambda_c/\Lambda_0 \approx 10^{-2}$. But for stratocumulus, it is doubtful that the liquid water content would be large enough to achieve such a low cloud conductivity.) Krasnogorskaya (1969) reported two characteristic types of distributions in stratocumuli, a near Gaussian distribution centered about zero mean charge, and an asymmetrical distribution displaced toward negative charge values. In general, the mean absolute charge could be expressed as $\overline{|Q|} = ca^2$, with $0.28 \leq c(\text{e.s.u. cm}^{-2}) \leq 1.6$, the exact value of c depending on the cloud shape and stage of development. Electric field values up to 30 V cm^{-1} were present. Colgate and Romero (1970) measured charges on small drops ($a \leq 12\,\mu$m) in the lower few hundred meters and at an early stage of a forming thunderstorm. They expressed their results in e.s.u. as $\overline{|Q|} = 1.72a^2$, and reported in addition an average negative charge of about 4×10^2 elementary charges at each of several drop sizes. The electric field was not measured.

It should be emphasized that although Twomey, Krasnogorskaya, and Colgate

and Romero were all able to fit their data to a quadratic charge versus size relation, their respective measurements are really quite different, since Twomey found an average strong positive drop charge, Krasnogorskaya an average weak negative charge, and Colgate and Romero an average strong negative charge. In the literature, such differences have often been minimized or overlooked altogether, with the result that it has often been considered reasonable, for purposes of modeling cloud electrification processes, to assume that all small cloud drops carry positive charge in proportion to their surface area (e.g., Colgate, 1972; Pringle *et al.*, 1973). Further discussion of this point may be found in Illingworth (1973).

18.4.2 Strongly Electrified Clouds

Field studies of the electrical structure of strongly electrified clouds which produce lightening show that mechansims other than diffusion and conduction charging must be responsible for the observed electric fields and for the observed charges carried on cloud and precipitation particles.

A summary of earlier observed values of the charge on cloud drops up through precipitation size for both strong and weak cloud electrification has been compiled by Takahashi (1973c) and is shown in Figure 18.1. More recent field studies of charges on drops in thunderstorm rains support this figure. Thus, Christian *et al.* (1980) observed charges up to ± 250 pC ($1\,\text{pC} = 1 \times 10^{-12}$ C $= 3 \times 10^{-3}$ e.s.u. $\approx 6 \times 10^{6}$ elementary charges) on raindrops during New Mexico storms, Chauzy and Despeau (1980) observed mean charges of ± 5 to 100 pC on raindrops during storms in France, and Holden *et al.* (1980) and Marshall and Winn (1982) found charges ranging between 10 and 400 pC on solid and liquid precipitation particles of 1 to 3 mm in diameter in New Mexico storms. Similarly, Dye *et al.* (1986) found charges up to 50 pC on precipitation particles in Montana thunderstorms. These values are sharply contrasted by the much lower charges ranging between -70 to $+60 \times 10^{-14}$ C, observed on raindrops during monsoon rains in India by Kamra and Sathe (1983).

The maximum charge that it is physically possible for a drop to carry is given by the *Rayleigh limit* Q_R for disruption (Rayleigh, 1882). This expresses the condition that mechanical instability occurs when the surface electrostatic stress equals the surface tension stress, i.e., when $E^2/8\pi = 2\sigma/a$; with $E = Q_R/a^2$, we thus have

$$Q_R(\text{e.s.u.}) = (16\pi\sigma a^3)^{1/2}\,. \tag{18-42}$$

This result is plotted as curve 1 in Figure 18.1, and indicates that drops in clouds are generally far from the Rayleigh limit. On the other hand, the Rayleigh limit has been reached in the laboratory by the controlled evaporation of charged drops on the size interval $30 \leq a \leq 170\,\mu$m (Doyle *et al.*, 1964; Abbas and Latham, 1967; Roulleau and Desbois, 1972; and Dawson, 1973). (On reaching the Rayleigh limit, the drops were observed to undergo explosive mass disjection, the extent of which varied in the experiments from a mass loss of only a few percent (Roulleau and Desbois, 1972; Dawson, 1973) to up to 30% (Abbas and Latham, 1969; Doyle *et al.*, 1964)). It is therefore conceivable that the Rayleigh limit may be reached on

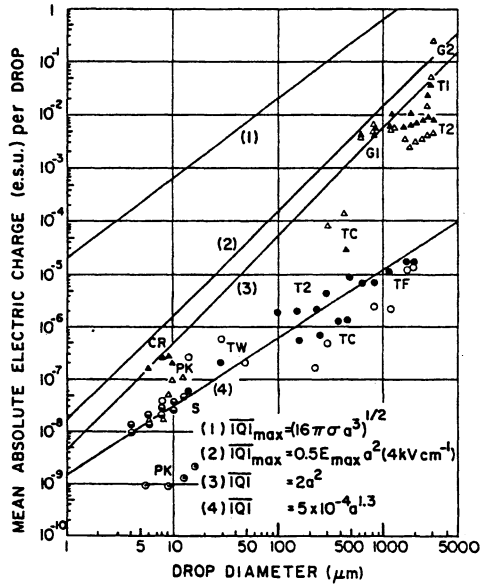


Fig. 18-1: Mean absolute electric charge on cloud and raindrops. Round symbols indicate warm cloud cases, triangular symbols indicate thunderstorm cases; solid symbols indicate negative charge, open symbols indicate positve charge. PK Phillips and Kinzer (1958), S. Sergieva (1959) (1959), CR Colgate and Romero (1970), TW Twomey (1956), TC Takahashi and Craig (1973), T1 Takahashi (1965), T2 Takahashi (1972), TF Takahashi and Fullerton (1972), G1 Gunn (1949), G2 Gunn (1950). (Adapted with changes from Takahashi, 1973c.)

occasion by evaporating drops at the edges of clouds, assuming that ionic leakage currents are relatively ineffective.

Various empirical fits have been tried to express the observed variation with size of the electric charge on cloud and precipitation particles. A fair approximation for the larger values of charge (in e.s.u.) is given by curve 3 in Figure 18.1, which is a plot of the relationship

$$\overline{|Q|} = 2a_0^2 , \tag{18-43}$$

where a_0 (cm) is the equivalent drop radius. Similarly, an approximate fit of the data over the full drop spectrum for warm clouds (with no ice phase and of generally weak electrification) is

$$\overline{|Q|} = 5 \times 10^{-4} a_0^{1.3} , \tag{18-44}$$

which is plotted as curve 4 in Figure 18.1.

We have already mentioned the fact that, for the case of small drops, different workers have reported different prevailing charge signs. The same variability extends to larger drops as well. Thus, according to Takahashi (1972) and Takahashi and Craig (1973), drizzle drops falling from warm clouds appear to carry predominantly negative charge, while from thunderstorm clouds they are predominantly

positively charged. Also, the charge sign for rain may depend on drop size. For example, Takahashi and Fullerton (1972) found that raindrops from warm clouds were predominantly negatively charged if $a_0 \lesssim 850\,\mu$m, and mainly positively charged for larger sizes. Just the opposite charge-sign versus size relationship has been observed for thunderstorms by Smith (1955) and Takahashi (1972). Their data appear consistent with a predominance of negatively charged drops for $a_0 \gtrsim 800\,\mu$m, and positively charged drops for smaller sizes. Other trends have been reported by Takahashi (1973c), and by Christian *et al.* (1980) and Chauzy and Despeau (1980). These results can hardly be attributed to an inconsistency among the observations. Rather, we must assume that the charge sign observed on a precipitation particle on the ground is affected not only by the charge it had assumed at its origin in the cloud, but also by the ions in the air and the charges on the drops with which it had collided on its trajectory to the ground.

Similarly, ice particles collected on the ground appear to have electric charges of both signs. Thus, Isono *et al.* (1966), Magono and Orikasa (1966), Kikuchi (1973, 1975) found that dendrites, plate, and sector plate snow crystals were predominantly negative, while columnar crystals, side planes, large snow flakes, and bullets were predominantly positive. In contrast, Magono and Iwabuchi (1972) observed that columns were predominantly negatively charged. Kikuchi *et al.* (1979) and Magono *et al.* (1983) found graupel to be predominantly positively charged. Kikuchi *et al.* (1979), Magono *et al.* (1982) and Takahashi (1983) attempted to explain the sign of the charge on the snow crystals on the basis of a mirror image relation to the external electric field present, whereby a negative precipitation current (negatively charged particles are falling) is related to a positive electric field (positive space charge above the location of observation). Magono *et al.* (1982), and Takahashi (1983) found charges up to 0.1 e.s.u. on snow crystals, while the snow crystals studied by Burrows and Hobbs (1970) carried a charge less than $Q_{99\%}$, where $10^{-3} \leq Q_{99\%} \leq 10^{-2}$ e.s.u.

Numerous field observations of electric field charges associated with lightning discharges (see, for example, Chalmers, 1967; and Mason, 1971) indicate that the charge distribution in a typical thunderstorm is roughly like that shown in Figure 18.2. This figure implies field strengths as large as $(4\pi\epsilon_0)^{-1} \times 80 \times (3 \times 10^3)^{-2} \approx 10^5$ V m^{-1} may occur between the main positive and negative charge centers. Field strengths required to produce local dielectric breakdown of air and, hence, lightning may be perhaps one order of magnitude larger than this representative average maximum value. Thus, from aircraft, Gunn (1948) measured mean maximum storm field intensities of 1.3×10^5 V m^{-1}. On one occasion, a field strength of 3.4×10^5 V m^{-1} was observed just before lightning struck the aircraft. Fitzgerald and Byers (1962) observed fields up to 2.3×10^5 V m^{-1}, while Kasemir and Holitza (1972) reported fields up to 3×10^5 V m^{-1}. Using instrumented rockets, Winn *et al.* (1974) observed a field of 4×10^5 V m^{-1} on one occasion, while peak values of 10^5 V m^{-1} were encountered 10% of the time. More recent studies of the electric field strengths in thunderstorms have not altered the earlier picture. Thus, Marshall and Rust (1991) observed, in New Mexico storms, maximum field strengths of $(96 \pm 28) \times 10^3$ V m^{-1}, with an extreme case of 146×10^3 V m^{-1}. In other storms, Christian *et al.* (1980) observed strengths up to 100×10^3 V m^{-1}. In

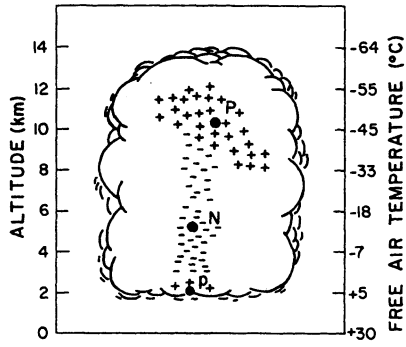


Fig. 18-2: Probable distributions of the thundercloud charges, P, N, and p for a South African thundercloud according to Malan (1952, 1963); solid black circles indicate locations of effective point charges, typically P = +40 C, N = -40 C, and p = +10 C, to give observed electric field intensity in the vicinity of the thundercloud. (From *Lightning* by M.A. Uman, copyrighted by McGraw-Hill Book Co., 1969.)

Montana storms, Dye *et al.* (1986) observed field strengths up to 15×10^3 V m^{-1}.

It is interesting to note that none of these values is close to the so-called 'dielectric strength of air', $E_s = 3 \times 10^7$ V m^{-1}, which represents the approximate field strength required to initiate breakdown between plane parallel electrodes in dry air at STP. In clouds, the large surface curvature of some cloud particles can apparently cause sufficient local field enhancement and ion emission to initiate large-scale breakdown when the ambient field is only about one percent of E_s.

It is of some interest to use the observed maximum values of electric field to estimate the corresponding maximum drop charge which would occur by conduction charging. This is approximately given from (18-26) by $0.5E_{\max}a_0^2$ assuming $(\Lambda_+/\Lambda_-)_{\max} \approx 2$, in accordance with the conductivity study of Griffiths *et al.* (1974). On substituting the value $E_{\max} \approx 4 \times 10^5$ V m^{-1} (Winn *et al.*, 1974), we thus estimate $\overline{|Q|}_{\max} \approx 7a_0^2$. This result, plotted as curve 2 in Figure 18.1, lies only slightly higher than many observed drop charge values under thunderstorm conditions. It therefore seems likely that the average magnitude of charge carried by particles of a given size in highly electrified clouds is fairly close to the equilibrium value arising from conduction charging in the ambient electric field. This estimate is also consistent with the experiments of Barker *et al.* (1983), who carried out a laboratory study of the charging of drops in positive corona streamers. He found that, in an external electric field of 4.1×10^5 V m^{-1}, the maximum charge on the drops followed the equation $Q_{\max} = 0.5Ea_0^2$.

The tri-polar structure of thunderstorms, suggested early on by Simpson and Scrase (1937), Simpson and Robinson (1941), and by Malan (1952, 1963), has been documented also by more recent studies. A negative charge center is found to be present between -15 to -20°C. This charge center appears to remain near that temperature level during the entire life time of the storm (Krehbiel *et al.*, 1984, 1979; Brook *et al.*, 1980; Krehbiel, 1981; Proctor, 1983). On the other hand, the upper positve charge center, located above the -20°C temperature level, moves

upward with time. In an interesting comparison, Krehbiel (1986) showed (see Figure 18.3) that the negative charge centers for cloud to ground lightning are at similar temperature levels in the New Mexico and Florida thunderstorms, even though the latter often had much greater extent of cloud and precipitation both below and above the 0°C level. The negative charge centers of intra-cloud lightning are also at these altitudes and temperatures. Winterstorms in Japan show that the negative charge is at a lower altitude than that of the two summer storms; however it does reside at a temperature level comparable to the New Mexico and Florida storms.

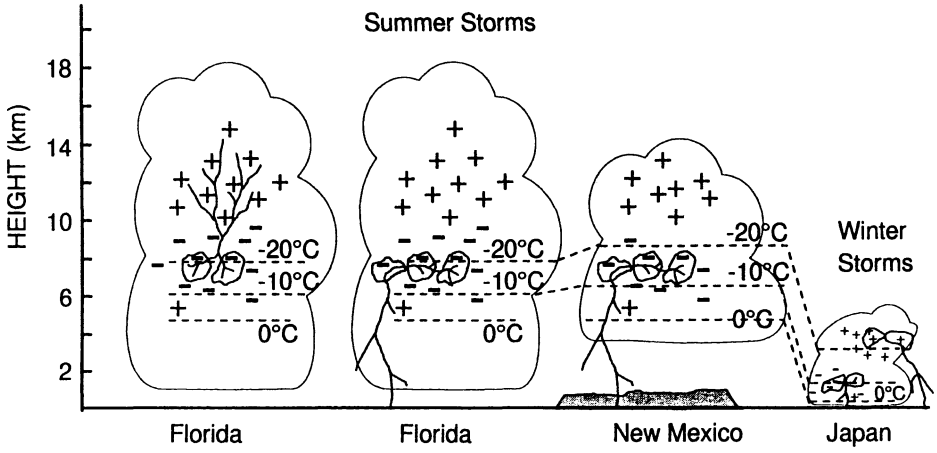


Fig. 18-3: Negative and positive charge centers in thunderstorm clouds at various locations. (From Krehbiel, 1986, based on data of Jacobson & Krider, 1976; Krehbiel *et al.*, 1979; Krehbiel, 1981; Brook *et al.*, 1982.)

The lower positive charge center appears near the 0°C level but is not bound to be related to the melting level. Although we shall see in the following section that several charging mechanisms can positively charge melting precipitation particles, recent studies give evidence of positively charged precipitation particles at temperature levels between 0 and −10°C due to a sign reversal of the charge on the graupel particles.

Although the question of precedence concerning the formation of electric charge centers and associated electric fields and the appearance of precipitation particles in a cloud was an issue of considerable debate for many years, sufficient evidence is now available (Dye *et al.*, 1986, 1988, 1989; Breed and Dye, 1989; Williams *et al.*, 1988) to show that the build up of electric fields lags the first development of precipitation sized particles by approximately 8 to 15 minutes. Thus, in the New Mexico and Montana thunderstorms, the electric field does not appear to exceed a few hundred volts per meter until the radar reflectivity, indicating the presence of precipitation-sized particles, has exceeded 35 to 45 dBZ, depending on the location of the storm.

Since there appears to be no rule without its exceptions, we conclude this section by mentioning also the findings of Marshall and Rust (1991), who studied 12 thunderstorms in Oklahoma, Alabama, and New Mexico. None of these storms appeared to fit the traditional tri-polar structure. Instead, four to ten electric charge regions were present in the clouds which generally had positive anvils with a negative screening layer at the upper boundary (Byrne *et al.*, 1989; Marshall *et al.*, 1989).

18.5 Cloud Charging Mechanisms

18.5.1 Requirements for a Cloud Charging Mechanism

Based on the observational evidence given in the previous sections, we may follow Mason (1971, 1972, 1988), Gardiner *et al.* (1985), and Latham and Dye (1989) by listing some of the major requirements a cloud charging mechanism has to fulfill: (1) A single mechanism has to produce a tri-polar electric cloud structure with a negative charge center at a temperture level near $-20°C$, a positive charge center above that level (i.e., below this temperature), and a positive charge center at a temperature level between -10 and $0°C$. (2) Alternatively, if the mechanism only produces a di-polar structure involving the two upper charge centers, a separate mechanism is required to explain the lower charge center. (3) Sufficient electric charge has to be generated and separated so that a thunderstorm cell maintains a cloud to ground current of 1 Ampère during 25 minutes, requiring that within this time about 1500 C are produced and separated. Assuming a cloud volume of 60 km^3, this is eqivalent to a charging rate $dQ/dt \approx 1$ C $km^{-3}min^{-1}$. Since about 30 C are destroyed per lightning flash, a flash rate of 2 min^{-1} has to be maintained during 25 minutes (this value is consistent with our estimate in Section 18.1 which suggests a global flash rate of ~ 50 sec^{-1} and 1500 storms maintaining the electric charge on the Earth's surface over time). (4) Sufficient electric charge has to be generated and separated to produce a breakdown electric field of 100 to 400 kV m^{-1} within about 20 minutes. The electric field is to grow slowly initially but explosively if $E \gtrsim 1$ kV m^{-1}. (5) The regions with strong electric fields have to coincide with regions of high radar reflectivity and thus with regions of precipitation sized particles. The development of precipitation particles has to precede any significant growth of the electric field by several minutes. (6) The precipitation particles involved in significant electric activity have to be solid, consisting of ice crystals and graupel present in regions with significant amounts of supercooled water. (7) The regions with a high electric field generally should have a charge density of 1 to 10 C km^{-3}. (8) The electric charges carried by precipitation particles of 1 to 3 mm diameter must range between 10 and 100 pC and be present in concentrations of about 100 m^{-3}. Particles inside the upper positive cloud region must consist of positively charged ice crystals, particles inside the lower negative charge regions consist of negatively charged graupel, and particles inside the lower positive cloud regions consist of positively charged graupel or raindrops.

18.5.2 The Major Cloud Charging Mechanisms

We shall now briefly describe the major charging mechanisms of atmospheric clouds. Most of the mechanisms are illustrated schematically in Figure 18.4.

18.5.2.1 *Charging by Diffusion of Ions*

We have shown in Section 18.3.2 that generally diffusion charging win weakly electrified clouds leads to a symmetric charge distribution on cloud droplets which is centered near zero charge with $\bar{Q} \approx 0$, and that the individual charges of either sign on the drops is small. Thus, from (18-20) $\mid p \mid = 30$ and, therefore, $\overline{\mid Q \mid} = 14 \times 10^{-9}$ e.s.u. ($\approx 5 \times 10^{-18}$ C $= 5 \times 10^{-6}$ pC) for $a = 100\,\mu$m and 0°C. In order to estimate the magnitude attained in diffusion charging, Beard and Ochs (1986) considered the root-mean-square charge, which for a zero centered distribution is $\mid (\bar{p}^2)^{1/2} \mid = \frac{1}{e}(2akT)^{1/2}$. This result was interpreted by Beard and Ochs as a balance between the stored electric energy on a droplet ($= (1/2)Q^2/a$) and the thermal motion energy of the ions (kT). For these conditions $\mid p_{\text{rms}} \mid = 35$ and $\mid Q \mid_{\text{rms}} = 25 \times 10^{-9}$ e.s.u. ($\approx 8 \times 10^{-18}$ C), a very small charge considering the observed charges in strongly electrified clouds.

Initially, the rate of charging $J_D = \mathrm{d}Q/\mathrm{d}t$ of a drop by ion diffusion is given by (18-21c,d). Soon thereafter, when the charge on the drop must be considered, the rate of charging is given by (18-21a,b). At equilibrium, $J_D^+ = J_D^-$ so that from (18-34) we have, for the mean charge of the distribution, $\bar{Q}_D = (akT/e)\ln(\Lambda_+/\Lambda_-)$. The charge distribution is symmetric about zero charges if $\Lambda_+ = \Lambda_-$. For $(\Lambda_+/\Lambda_-) \approx 2$, $a = 100\,\mu$m and 0°C the mean charge of the distribution at equilibrium is $\bar{Q}_D = 5 \times 10^{-7}$ e.s.u. ($\approx 2 \times 10^{-16}$ C). For the case that Λ_+ is not too different from Λ_-, Gunn (1954) obtained an approximate expression for $J_D^+ - J_D^-$ from which he determined that the charge on a drop as a function of time t is given by $\bar{Q}(t) = \bar{Q}_0[1 - \exp(-4\pi\Lambda t)]$. In other words, the characteristic time t after which 63% of $\bar{Q}_0$ has been reached is $\tau = 1/4\pi\Lambda$. Thus, for $\Lambda \approx 2 \times 10^{-4}$ e.s.u., $\tau = 400$ sec at the Earth's surface, showing that the equilibrium charge is reached fairly rapidly.

Although the magnitude of diffusion charge on drops is small and can only account for the charges at the very early stages of cloud development, we have pointed out in Section 18.4.1 that charging by diffusion of ions does indeed lead to the usual observed electric polarity of weakly electrified clouds.

18.5.2.2 *Convection Charging*

Grenet (1974) and, independently, Vonnegut (1955) proposed that a convective cloud may operate as an electrostatic energy generator according to the following scenario. Initially, an updraft carries positive space charge from the lowest levels of the troposphere into the growing cloud; the electrified cloud soon acquires a negative charge screening layer at its top and edges due to cloud particle capture of negative ions drifting from the conducting clear air to the cloud under the influence of the main positive charge; finally, downdrafts are envisioned to carry the negative charge close to the cloud base, thereby enhancing the (reversed) electric field at the

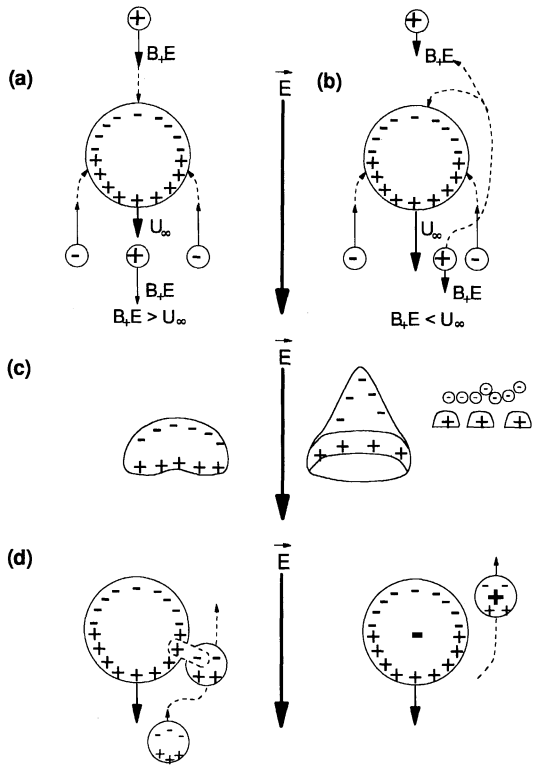
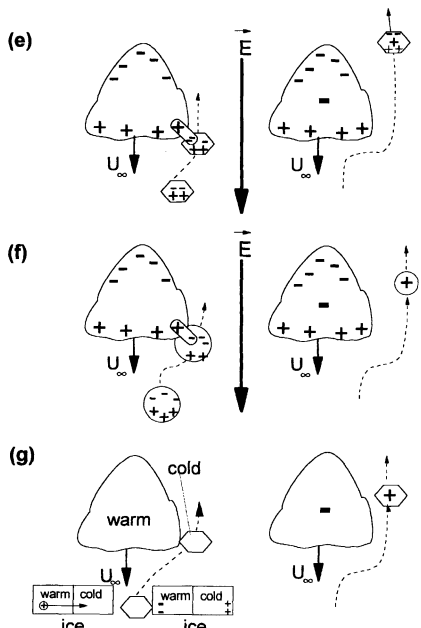


Fig. 18-4: Schematic representation of the major cloud charging mechanism, (a, b) selective ion capture, (c) drop breakup in electric field, (d) drop rebound during collision of drops in electric field, (e) ice particle rebound during collision of ice particles in electric field, (f) drop rebound during collision of drops with ice particle, (g) thermoelectric effect, (h) contact potential effect, (i) Workman Reynolds effect, (k) splintering during freezing of singe drops, (l) splintering during riming, (m) drop breakup, (n) melting of ice particle.



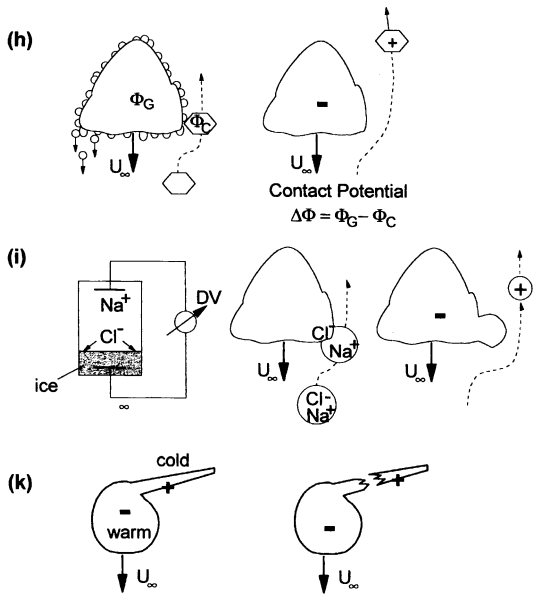


Fig. 18-4 continued

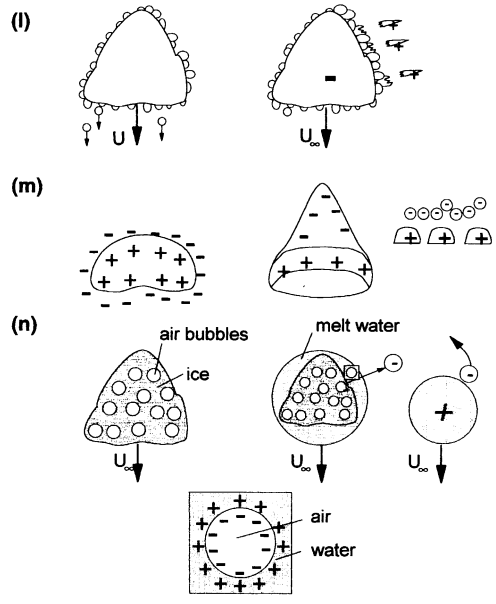


Fig. 18-4 continued

Earth sufficiently to initiate positive point discharge which enhances the positive charge entering the cloud via updraft. The continuance of this positive feedback cycle can thus provide for the strong buildup of electrostatic energy at the expense of organized cloud convective motions.

We see that, according to the above picture, the cloud in its early stages is predicted to have a positively charged base and core, which is in conflict with the reasoning and the bulk of the the evidence presented in Section 18.4.1. The cause of the disagreement is evident: In Section 18.4.1, we ignored the expected upward covection current of positive space charge; on the other hand, the convection model ignored the net upward conduction current of negative charge. However, a simple estimate shows that the latter should dominate the former. Thus, if we assume fair weather conditions, the negative conduction current density is approximately $j_{q,\mathrm{cond}}/2 \approx 1.5 \times 10^{-12}$ Amp m^{-2} from Section 18.1. Assuming a cloud base at 1 km altitude, we have from (18-3) an expected positive charge density of $\rho_+ \approx 1\, e$ cm^{-3}. Therefore, even with a rather strong updraft speed of $W \approx 1$ m sec^{-1}, the ratio of convection to conduction current densities is $\rho_+ W/0.5 j_{q,\mathrm{cond}} \approx 10^{-1}$. Hence, it appears that the neglect of the field driven deposition of negative ions into the base of a young cloud constitutes a significant flow in the convection charging model.

This conclusion is supported by numerical simulations of the convective electrification process (Ruhnke, 1970, 1972; Chiu and Klett, 1976). These studies show that, for usual conditions of cloud formation, a charge distribution in general qualitative agreement with that discussed in Section 18.4.1 is produced, namely a negatively charged cloud core capped by a relatively thin positively charged upper layer. However, Chiu and Klett also found that convective transport of positive charge may dominate the conductive transport of negative charge, and thus produce a cloud of polarity opposite to the usual case, if the cloud forms near ground level. This happens primarily because higher concentrations of positive space charge are then available to be carried aloft into the cloud. (Incidentally, this last result may conceivably have some bearing on the fact that drop charge measurements such as Twomey's (1956), which were taken on a mountain summit imbedded in the base of stratocumulus clouds, have often revealed a predominance of positive charge.)

Additional unrealistic features of the convective charging theory under later stages of cloud development have been pointed out by Latham (1981), Beard and Ochs (1986), and Williams (1989). Thus, based on recent measurements (Standler and Winn, 1979), it appears that earlier estimates of the point discharge current from the Earth's surface beneath thunderstorms were substantially exaggerated. According to Standler and Winn (1979), the total current may be less than 100 mA and is small in comparison with the (time-integrated) lightning current. Furthermore, observations by Standler and Winn (1979), Chauzy and Raisonville (1983), do not show a deep vertical column of positive space charge from the Earth's surface, as required for convective transport, but rather a layer confined to the Earth's surface with 100 to 200 m thickness. It has not yet been established whether this finite thickness is the result of the capture of small ions by aerosol particles or charge relaxation in the finitely conductive atmosphere, or some other cause. Earlier theoretical studies (Moore *et al.*, 1983) had already identified the problem of the long transport time of the convected positive charge in accounting for the first

lightning in a developing cloud.

Another flaw in the convective charging mechanism is related to the negative charge transport downward from the cloud top, invoked by Vonnegut (1953) and Wagner and Telford (1981). Thus, there are reasons to question whether this negative charge descends to levels of the cloud where the main negative charge is consistently observed. According to Wagner and Telford (1981), the negative charge descends within the central portion of the cloud; this seems unlikely in light of Doppler radar observations showing upward air and particle motions throughout the central region of the cloud during the early stage of development and into the mature stage (Lhermitte and Williams, 1985; Comez and Krehbiel, 1986). According to Vonnegut (1953), the negative charge is carried down in screening layers at the cloud boundary. While negative screening layers around the upper portions of clouds appear to be commonplace (Winn *et al.*, 1978; Byrne *et al.*, 1983), there is some question as to whether their descent can account for the apparent 'pancake' shape of the main negative charge.

In addition, updrafts and downdrafts may disorganize their associated charges through mixing. In their study, Chiu and Klett (1976) showed that single cell convection with eddy diffusion diminishes the electric field within a cloud. Thus, if one pictures cloud turrets as convective cells with interspersed updrafts and downdrafts, a disorganization by mixing between adjacent charge regions would appear probable.

18.5.2.3 *Inductive Charging Mechanisms*

In Section 18.1, we have pointed out that our atmosphere is characterized by a permanent fair weather electric field (18-1). Under the influence of this field, cloud particles become polarized such that a positive charge is induced on the lower hemisphere of a cloud particle and a corresponding negative charge on the particle's upper hemisphere. This polarization effect is the basis for several cloud charging mechanisms.

1. Charging by selective ion capture (Figures 18.4a,b)

Wilson (1929) described how an electrically polarized cloud particle may selectively capture ions of one sign as it falls. This happens because, while the lower surface of the particle may attract and capture ions which carry a sign opposite to the local surface charge, the upper surface is not as effective in this respect, since ions attracted to it must first catch up with it in order to be captured. The net effect of this selective process is a large-scale separation of charge, due to the sedimentation of the charged cloud particles. This reinforces the existing field, so that its occurrence in clouds would cause a field enhancement in qualitative agreement with what is expected for thunderstorms (recall Figure 18.3).

A mathematical model for the 'Wilson process', based on spherical particles in Stokes flow (and thus of restricted validity), has been worked out by Whipple and Chalmers (1944). As might be expected, the equilibrium charge for this process is proportional to the ambient field strength and particle surface area.

The fundamental condition for selective ion capture, and thus for cloud charging, is given by the inequality $U_\infty > B_+E$, where U_∞ is the terminal fall velocity of the drop and B_+ is the mobility of the positively charged ions. Would it be otherwise, i.e., $B_+E > U_\infty$ (see Figure 18.4a), the fast positive, downward-moving ions would become attached to the rear of the drop, while the slow and fast upward moving ions would become attached to the lower (front) side of the drop. Therefore, little net charging would result. However, if $B_+E < U_\infty$ (Figure 18.4b), the positive ions in the rear of the drop will not catch up with the drop, and will be repulsed by the positive induced charge on the lower side of the drop. In contrast, both the fast and slow negative ions will be attracted to the lower side of the drop, imparting to the drop a net negative charge. An experimental verification of the condition for selective ion capture has been provided by Gott (1933) who showed that when drops fall through a region of ions of both sign in an external electric field, selective ion capture occurs only if $E < U_\infty/B_+$. Setting $B_+ \approx 1.4\ \text{cm}^2\text{V}^{-1}\ \text{sec}^{-1}$ and an upper value of 8 m sec^{-1} for the terminal fall velocity of a drop, we find that selective capture can only occur if $E < 5.7 \times 10^2\ \text{V cm}^{-1}$, which is still considerably below characterisitic values for the initiation of lightning in thunderstorms.

2. Drop breakup charging (Figure 18.4c)

From (18-24), we see that an uncharged drop polarized in the fair weather electric field carries a surface charge density σ (e.s.u.) $= (4\pi)^{-1}(E_r)_{r=a} = (3/4\pi)E\cos\theta$, θ being the polar angle measured from the lowest point on the drop. Thus, the lower hemisphere carries a positive charge of $Q = 2\pi a^2(3E/4\pi)\int_0^{2\pi} \cos\theta \sin\theta\, \mathrm{d}\theta = 3Ea^2/4$, and an equivalent negative charge on the upper hemisphere. Thus, if a drop of radius 3 mm were sliced at the equator on breakup in an external field of 500 V cm^{-1}, each fragment would carry a charge of about 0.1 e.s.u., or a charge density of about 1 e.s.u. per gram of ruptured water. This is equivalent to a cloud charge density of about 1 C km^{-3}, assuming a large liquid water content of 5 g m^{-3}. In verification of this, Matthews and Mason (1964) studied the charging of single drops, breaking up in the bag breakup mode in vertical external electric fields up to 1.5 kV cm^{-1}. They found that with increasing field, the average charge on the drops increased also, reaching 5.5 e.s.u. per gram of ruptured water. They concluded that drop breakup in external electric fields could contribute significantly to the charging of the lower positive charge pocket of a cloud, because the large drop fragments were found to carry positive charge while the smaller drops carried negative charge. However, a severe criticism of this mechanism is the simple observation that large drops generally do not break up as envisioned above but rather as a result of collision with other drops (see Section 14.5.4.2). The various drop breakup modes involved in collisional breakup obviously do not provide an ideal partitioning as considered above for the bag breakup mode of single drops, and so they result in a much lower charge separation. Unfortunately, no studies on this problem have been carried out.

3. Particle Rebound Charging (Figures 14d-f)

Collisions between polarized cloud particles and their subsequent bounce may provide an additional mechanism for cloud charging. Thus, if such a cloud particle were to experience on its lower hemisphere a momentary electrical contact with, and subsequent separation from, a similarly polarized smaller cloud particle in a fair weather field, there would result a net negative charge on the larger particle, and a net positive charge of equal magnitude on the smaller one. Separation of these charges under gravity would serve to reinforce the existing field leading to a positively charged upper portion and a negatively charged lower portion of the cloud. The actual amount of charge transferred depends on the contact angle relative to the direction of the external electric field, the contact time, the separation probability, the charge relaxation time, the net charge on the drops, and the magnitudes of the polarization charge.

Elster and Geitel (1913) were the first to point out that such a process of inductive charge transfer, occurring throughout a cloud and followed by the large scale separation of charge through relative sedimentation under gravity, would serve to increase the in-cloud electric field in the sense normally observed in thunderstorms.

Elster and Geitel also provided a simple estimate of the maximum charge transfer that could occur for the case of a sphere of radius a_2 which contacts the lowest point ($\theta = 0$) of a sphere of radius $a_1 \gg a_2$. In this case, the smaller sphere will acquire a charge with average density equal to $\pi^2/6$ times the density of the charge on the larger sphere at the point of contact, since the curvature of the larger sphere can be ignored (the capacitance of the small sphere in contact with a conducting plane is $C_2 = a_2(\pi^2/6)$; see also Appendix A-18.6.3). Thus, the maximum charge than can be acquired by the small sphere is approximately $(\pi^2/6)(4\pi a_2^2) \times (3E/4\pi) = \pi^2 E a_2^2/2 \approx 5Ea_2^2$. This is generally a very large charge (for example, it is ten times larger than the equilibrium charge expected from ion attachment by conduction under conditions of strong electrification (recall Section 18.3.3 and Figure 18.1)), and suggests that induction charging may be powerful enough to produce strong cloud electrification.

However, any quantitative assessment of the efficacy of induction charging must take into account several other factors as well. For example, let us first consider the more realistic situation where contact occurs for $\theta \neq 0$ and the drops initially carry charges Q_1 and Q_2. Then, by a simple extension of the arguments given above, the charges after contact and separation will be Q_1' and Q_2', where $Q_2' = (\pi^2/6)a_2^2(3E\cos\theta + Q_1'/a_1^2)$. On writing $Q_2' = Q_2 + \Delta Q$ and $Q_1' = Q_1 - \Delta Q$, we thus find that the charge transferred is given by

$$\Delta Q = \frac{\pi^2}{2} E a_2^2 \cos\theta + \frac{\pi^2}{6} p^2 Q_1 - Q_2 \,, \tag{18-45}$$

where $p \equiv a_2/a_1 \ll 1$ (the problem of finding ΔQ for arbitrary p on the interval $0 \leq p \leq 1$ is discussed in Appendix A-18.6.3). This expression shows that induction discharging may also occur; i.e., ΔQ may be negative for sufficiently large θ and $Q_2 > 0$. Since θ represents the polar angle between the point of contact and the electric field, and since the latter may have a large horizontal component in some

cloud regions (recall Figure 18.1), we see that even collisions restricted to the lower hemisphere of the large drop may result in $\Delta Q < 0$.

On the other hand, if we use (18-45) to estimate the equilibrium charge $\langle Q_1 \rangle$ to be expected on the larger sphere after many induction charging events with smaller spheres of radius a_2, we find, by setting $\Delta Q = 0$ for equilibrium and neglecting Q_2 relative to $\langle Q_1 \rangle$, that $\langle Q_1 \rangle \approx -3a_1^2 \langle E \cos\theta \rangle$ (here $\langle E \cos\theta \rangle$ denotes the expected value of $E \cos\theta$ under the assumed equilibrium conditions). This rough calculation implies the equilibrium charge on the large drop will have a large negative value, in spite of possibly frequent discharging events, if $\langle E \cos\theta \rangle$ is sufficiently large.

Consideration of the expected value of the electrical contact angle brings several additional problems into focus (assuming they have not been obvious from the outset!). Thus, to find $\langle E \cos\theta \rangle$ we must in effect solve the fairly difficult collision efficiency problem with the inclusion of electrostatic forces (see Section 18.6.5). Furthermore, we must determine the θ-dependence of the probability that separation actually occurs after contact is made. From our discussion in Chapter 14, we expect that coalescence generally follows a collision between drops of radii less than $100\,\mu$m even if the drops are uncharged and no external electric field is present. Collisions between drops of opposite electric charge, or collisions in external electric fields should reduce the separation efficiency even more. Thus, we suspect that the effectiveness of inductive charge transfer must be quite small for colliding water drops. We also expect a tendency for this charge separation mechanism to be 'shorted out' as large drops rapidly acrete smaller, oppositely charged droplets (e.g., Colgate, 1972; Moore, 1975a,b).

An even more severe rebound problem appears during the collision of ice particles and supercooled drops (Paluch and Sartor, 1973; Moore, 1975a,b; Colgate *et al.*, 1977; Sartor, 1981). Thus, laboratory experiments showed that only glancing collisions will result in separation of cloud drop and ice particle (Aufdermauer and Johnson, 1972; Shewshuk and Iribarne, 1974; Gaskell, 1979, 1981; Gaskell and Illingworth, 1980).

On the other hand, the experiments of Latham and Mason (1962), Scott and Levin (1970), Buser and Aufermauer (1977), Takahashi (1978), and Gaskell (1981) demonstrated that significant inductive charging occurs during collisions between ice particles, since for these the separation probability is high, except at temperatures near 0°C where the quasi-liquid layer on an ice surface tends to bond two colliding crystals together.

Nevertheless, during the interaction between such ice particles, an additional physical barrier to charge separation occurs, namely the relatively long relaxation time for charge conduction through ice. Gross (1982) determined the relaxation time for ionic charge transfer during an ice-ice contact as a function of impurities in ice. He found for pure ice (impurity concentration of 10^{-8} mole liter^{-1}) a value of about 2×10^{-3} sec near -20°C, increasing to 7×10^{-3} sec near -50°C. Sartor (1970) gives a value of 6.8×10^{-3} sec near -10°C and 2.8×10^{-2} sec near -19°C. According to Gross (1982), impurities in ice shorten the relaxation time considerably, decreasing it at -20°C to 5×10^{-5} sec for an impurity concentration of 3×10^{-6} mole liter^{-1}, and to 2×10^{-6} sec for an impurity concentration of 1×10^{-3} mole liter^{-1}. These relaxation times have to be compared with the contact

times of two colliding ice particles, which turn out to be rather short (Buser, 1976; Latham and Miller, 1965; Scott and Levin, 1970; Tabor, 1951; Gaskell, 1979; Sartor, 1970; Caranti and Illingworth, 1980). According to these observations, the contact time for a particle which collides with a much larger target decreases with increasing particle size, and ranges between 10^{-4} and 10^{-7} sec for a particle of 1 cm radius and 100 μm radius, respectively. Thus, for smaller particles, it appears that a substantial charge transfer seems possible only if the ice particles are considerably contaminated or a liquid surface is involved. Since efficient charge transfer has been observed experimentally during the collision of relatively pure ice particles, a transfer mechanism other than the one envisioned above, must have been operating. One possible mechanism involves the transfer of electrons across surface states with a relaxation time of less than 10^{-7} sec.

Considering now that not all the available charge is transferred during contact, because the contact time t_c may be shorter than the relaxation time τ_Q for charge transfer, we must extend (18-45) and write

$$\Delta Q_1 = [\gamma_1 E a_2^2 \cos\theta + A Q_1 - B Q_2] \left[1 - \exp\left(-\frac{t_c}{\tau_Q}\right)\right] , \tag{18-46}$$

where Q_1 and Q_2 are the initial charges on the two colliding particles of radius a_1 and a_2, respectively, and γ_1, and γ_2 are given (Chiv, 1978) by

$$A = \frac{\gamma_2 (a_2/a_1)^2}{1 + \gamma_2 (a_2/a_1)^2} \text{ (18-47a)}, \qquad B = \frac{1}{1 + \gamma_2 (a_2/a_1)^2} ; \tag{18-47b}$$

and γ_1 and γ_2 are positive numerical constants depending on a_1/a_2 (Paluch and Sartor, 1973; Latham and Mason, 1962; Davis, 1964a,b; see also Appendix 18.6.3). For $(a_1/a_2) \ll 1$, $\gamma_1 = \pi^2/2$ and $\gamma_2 = \pi^2/6$, as given in (18-45). An experimental test of (18-46) has been carried out by Latham and Mason (1962). Excellent agreement between theory and experiment was found.

Assuming $\tau_Q \ll t_c$, $(a_2/a_1) \ll 1$, and $(Q_2/Q_1) \ll 1$, we find for the rate of charging of the large particle

$$\frac{\mathrm{d}Q_1}{\mathrm{d}t} = -\mathrm{E}_{\mathrm{coll}} \mathrm{E}_{\mathrm{reb}} \pi a_1^2 (U_{\infty,1} - U_{\infty,2}) n_2 a_2^2 \left[\frac{\pi^2}{2} E \cos\theta + \frac{\pi^2}{6} \frac{Q_1}{a_1^2}\right] , \tag{18-48}$$

where E_{coll} is the collision efficiency, E_{reb} is the fraction of colliding particles which rebound, θ is the angle between the electric field and the line of centers between the two colliding particles, and n_2 is the number concentration of small particles. From (18-48), it follows after integration that

$$Q_1(t) = -3 E a_1^2 \cos\theta [1 - \exp(-t/\tau)] , \tag{18-49a}$$

with

$$\tau = \left[\frac{\pi^3}{6} \mathrm{E}_{\mathrm{coll}} \mathrm{E}_{\mathrm{reb}} (U_{\infty,1} - U_{\infty,2}) n_2 a_2^2\right]^{-1} . \tag{18-49b}$$

Therefore, as $\tau \to \infty$, $Q_1 \to Q_{1,\max} = 3 E a_1^2 \cos\theta$.

For the case $t_c \ll \tau_Q$, the charge ΔQ_2 transferred to the smaller particle is simply $\Delta Q_2 = \Delta Q_1$. Therefore,

$$\Delta Q_2(t) = \left[\frac{\pi^2}{2} E \cos\theta + \frac{\pi^2}{6} \frac{Q_1(t)}{a_1^2}\right] a_2^2 , \tag{18-50}$$

if it is assumed that each small particle during its life time makes only one contact with the large particle.

18.5.2.4 *Non-Inductive Charging Mechanisms Involving the Collision between Particles*

Numerous experimental studies have shown that electric charging of cloud particles may occur without the intervention of an external electric field. Some of the more important charging mechanisms of this type are described briefly in this section.

The non-inductive electric charge transferred to a large particle during impact with a smaller particle can be formulated analogously to (18-46), except that now the inductive term $(\gamma_1 E \cos\theta a_2^2)$ is replaced by the observed charge $\Delta Q'$ separated per collision. Various mechanisms may cause such a charge transfer.

1. The thermo-electric effect (Figure 18.4g)

Reynolds *et al.* (1957) obtained laboratory evidence that a hail pellet may become charged as a result of collisions with ice crystals having a temperature different from that of a pellet. The physical basis of the charge transfer was suggested as being due to the diffusion of hydrogen ions down the temperature gradient existing in the region of momentary contact (Brook, 1958). Thus, since H^+ ions have a greater mobility in the ice lattice than OH^- ions, a temperature gradient maintained across a piece of ice will result in an excess of positive charge on the colder portion. Mason (in Latham and Mason, 1961a) formulated a one-dimensional model for this process on the basis of an ideal ice structure. Assuming a steady state temperature gradient across the ice species, he computed the steady state potential difference between the cold and warm ends of the specimen. Using values given in the literature for the mobilities of H^+ and OH^- ions and for the activation energy for dissociation of a water molecule into H^+ and OH^- ions, he found

$$-\frac{\mathrm{d}V}{\mathrm{d}T} = 1.9\,\mathrm{mV/°C}\,. \tag{18-51}$$

This relation has been verified experimentally by Latham and Mason (1961b). (A more complex expression for the thermoelectric power which reduces to (18-51) for pure ice was derived by Jaccard (1963).) Considering that the separated space charge in the ice specimen could be regaded as equivalent to a surface density of charge σ on the ends of the specimen (18-51), Latham and Mason (1961a) found

$$\sigma = \frac{\epsilon}{4\pi} \frac{\mathrm{d}V}{\mathrm{d}x} = 5 \times 10^{-5} \frac{\mathrm{d}T}{\mathrm{d}x}\,, \tag{18-52}$$

where ϵ is the static dielectric constant of ice. For two ice rods which are only temporarily in contact with each other, Latham and Mason (1961a) found, for a contact time of $t_c \approx 10^{-2}$ sec,

$$\sigma = \sigma_{\max} = 3 \times 10^{-3} \Delta T \quad \text{e.s.u./cm}^{-3}. \tag{18-53}$$

For shorter contact times, σ was less due to insufficient time for charge exchange, while for longer contact times, σ was less due to temperature equalization. Applying this result to the collision of a small, cold ice crystal of temperature T_c, grown by vapor diffusion, and a large, warm graupel particle of temperature T_G, grown by riming, we find from (18-53) that the negative charge imparted to the graupel, and the positive charge imparted to the snow crystal is given by

$$\Delta Q = 3 \times 10^{-3} (T_G - T_c) \times \text{contact area}. \tag{18-54}$$

Setting $\Delta T \approx 5°\text{C}$ and assuming that the contact area is $(1/10)\pi a_c^2$, where $a_c = 10\,\mu\text{m}$ is the radius of the crystal, we obtain $\Delta Q \approx 5 \times 10^{-9}$ e.s.u. $\approx 1.5 \times 10^{-18}$ C per collision, in agreement with the charges observed on ice crystals of the same size forced to collide with a probe coated with ice and heated 5°C above the temperature of the surrounding air (Latham and Mason, 1961b). Although these values substantiate the theoretically derived one, they are considerably smaller than the values observed during the collision of ice crystals with graupel acquiring supercooled drops by riming. Latham and Stow (1965) therefore suggested that perhaps one must include in (18-53) a dependence on the impact velocity by multiplying the right-hand side of (18-53) by $(1 + 10v)$, where v is the impact velocity. However, one readily finds that the impact velocities, temperature differences, and contact areas would have to be unrealistically large in order for the thermoelectric effect to account for observed charges up to 10^{-4} e.s.u. It follows that thermoelectric charging, although leading, via gravitational sedimentation, qualitatively to the observed cloud polarity, cannot account quantitatively for the cloud charging.

2. The contact potential effect (Figure 18.4h)

Laboratory experiments of Marshall *et al.* (1978), Magono and Takahashi (1973a,b), Takahashi (1978), Buser and Aufdermauer (1977), Hallett and Saunders (1979), Caranti and Illingworth (1980, 1983), Gaskell and Illingworth (1980), Jayaratne *et al.* (1983), Illingworth (1985), Jayaratne and Saunders (1985), Baker *et al.* (1987), Saunders and Zhang (1987), Kumar and Saunders (1989), Caranti *et al.* (1985), Saunders *et al.* (1985), Baker and Dash (1989), and Dong and Hallett (1992), showed that the early experiments of Reynolds *et al.* (1957) should not be interpreted in terms of charging due to ice temperature differences only, but rather in terms of differences in electric surface potential between the two colliding particles. This conclusion was based on two experimental facts: (1) the ice surface acquires a positive charge during diffusional growth and a negative charge during evaporation, except at temperatures between -3 and 0°C. Charges of opposite sign were found for condensing and evaporating liquid water surfaces. (2) The charge separated during the collision of an ice crystal with an ice particle growing by collision with

supercooled drops was found to range between 1 and 5×10^{-14} C (3×10^{-5} to 2×10^{-4} e.s.u.) per collision, and was not directly correlated to the temperature difference between the target and the ice crystals. (3) The riming target was found to become negatively charged below a temperature of -15 to -20°C, and positively charged above -5 to -10°C, implying that one and the same mechanism can be made responsible for the observed negative charge center as well as for the observed lower and upper positive charge centers in clouds. One may also readily verify that an observed charge of $(\Delta Q)_G \approx 10^{-4}$ e.s.u., transferred during the collision of an ice crystal with a graupel, would lead to a volume charging rate of

$$\left(\frac{\mathrm{d}Q}{\mathrm{d}t}\right)_{\mathrm{vol}} = \left(\frac{\mathrm{d}Q}{\mathrm{d}t}\right)_G n_G = \mathrm{E}_{\mathrm{coll}} \pi a_G^2 U_{\infty,G} n_c n_G (\Delta Q)_G \,, \tag{18-55}$$

for $U_{\infty,c} \ll U_{\infty,G}$, and $a_c^2 \ll a_G^2$. With $\mathrm{E}_{\mathrm{coll}} = 1$, $a_G = 2$ mm, $n_c = 100$ liter^{-1}, $U_G = 5$ m sec^{-1}, $n_G = 100$ m^{-3}, $\rho_G = 0.5$ g cm^{-3}, and $(\Delta Q)_G = 10^{-4}$ e.s.u./collision, we obtain $\mathrm{d}Q/\mathrm{d}t \approx 1$ C km^{-3}min^{-1}.

Unfortunately, no comprehensive theory is available at present to describe quantitatively the charging mechanism by means of surface potential differences, as these depend in a complicated manner on the surface texture of the riming graupel, the impact velocity, impact angle, and temperature difference between the colliding particles. Nevertheless, Fletcher (1968) showed that such a contact potential is to be expected. Considering that some water dipoles are aligned at the surface of ice, he calculated an equilibrium charge carrier density of $\sim 5 \times 10^{-2}$ C m^{-2} as a result of free ions. An area of 1 μm^2 would therefore carry a charge of 5×10^{-14} C. Due to differences in the surface states of the charge carriers on the two surfaces in contact, a contact potential between the two colliding bodies must result.

3. The Workman-Reynolds effect (Figure 18.4i)

In Section 5.10, we have mentioned that during freezing of dilute aqueous solutions, large potential differences occur at the ice/solution interface due to selective ion incorporation into the ice lattice. Sign and magnitude of the interface potential was found to be a sensitive function of the concentration of the ions in solution, the freezing rate, and the type of ions in solution. Since the interface potential disappeared once the freezing process was completed, any charge separation mechanism involving the Workman-Reynolds effect must involve either a shedding of the still unfrozen solution or a tearing-off of unfrozen solution, by splashing during the collision with large drops. In a limited manner, shedding of unfrozen liquid is possible from hailstones growing in the wet regime (see Chapter 16). The splashing mechanism was studied by Latham and Warwicker (1980) and was found to cause only very small charges to be separated. In addition, the strong dependence of the Workman-Reynolds effect on the concentration of the ions in solution and on the type of ions, (e.g., NH_4^+ in solution would charge the ice positively, while Cl^- in solution would charge the ice negatively) make the mechanism unlikely to contribute to cloud electrification. The experiments of Shewschuk and Iribarne (1971) and Crabb (1973) showed further that the presence of salt ions in the surface of a graupel does not significantly affect its surface potential.

18.5.2.5 *Non-Inductive Charging Mechanisms Involving the Breakup of Precipitation Particles*

1. Breakup of a freezing drop (Figure 18.4k)

Experiments of Mason and Maybank (1960), Evans and Hutchinson (1963), Dye and Hobbs (1968), Johnson and Hallett (1968), Kolomeychuk *et al.* (1975), and Pruppacher and Schlamp (1975) showed that freezing drops may produce an ice shell which fractures or produce spikes which splinter. If fragmentation of some type occurred, charges of either sign were observed, although the main ice particle was often negatively charged and the ice splinters positively. The magnitude of the charge on the main ice particle ranged between 1×10^{-5} and 1×10^{-3} e.s.u. Considering that the outer portion of the ice shell can be assumed to have the temperature of the air, while the drop inside is at 0°C, Mason (1971) attempted to explain the charging on the basis of the thermoelectric effect. Writing (18-54) as $\sigma = 5 \times 10^{-5}(T_{\text{in}} - T_{\text{out}})/\Delta x$, where Δx is the thickness of the ice shell, and setting $T_{\text{in}} = 0°\text{C}$, $T_{\text{out}} = -15°\text{C}$, $\Delta x = (1/10)a_{\text{d}}$, where $a_{\text{d}} = 1$ mm is the drop radius, and assuming that only 1/100 of the shell fragments, he obtained a charge of about 1×10^{-4} e.s.u. produced on the ice residue of the shattered drop, in agreement with the observed charges. However, we have already pointed out in Section 9.2.6 that only a small and highly unpredictable proportion of freezing drops shatters or produces spikes which fracture, and that only drops larger than 50 μm diameter were observed to show any tendency to fragment at all. Furthermore, the thickness of the fragmenting shell as well as the proportion of the shell which disintegrates are unknown and most likely highly variable. Breakup of freezing drops is therefore not likely to be a major cause of organized cloud charging.

2. Splintering during riming (Figure 18.4l)

Experiments of Latham and Mason (1961b) showed that small drops of 20 to 90 μm diameter, impacting on an ice sphere of 5 mm diameter, eject positively charged ice splinters while the riming ice sphere becomes negatively charged. A charge of 4×10^{-6} e.s.u. per drop was found to be acquired by the graupel. Considering this value and a volume charging rate of $(\text{d}Q/\text{d}t)_{\text{vol}} = \text{E}_{\text{coll}}\pi a_G^2 U_{\infty,G} n_{\text{d}} n_G (\Delta Q)_G$, Mason (1971) found $(\text{d}Q/\text{d}t)_{\text{vol}} = 0.5$ C km^{-3}min^{-1}, for $(\Delta Q)_G = 4 \times 10^{-6}$ e.s.u., $a_G = 2$ mm, $U_{\infty,G} = 5$ m sec^{-1}, $n_{\text{d}} = 1$ cm^{-3}, and $n_G = 100$ m^{-3}, where a_G, n_G, $U_{\infty,G}$ are the radius, number concentration, and fall velocities of the graupel particles, and n_{d} is the number concentration of drops. We notice from this result that this mechanism does provide for the observed polarity of a cloud, but contributes only a fraction of the required charging rate. More seriously, however, later studies of Hallett and Mossop (1974), Mossop (1976, 1978), and Hallett and Saunders (1979) showed (see Sections 9.2.6 and 16.1.6) that splintering during riming is limited to the temperature range between −5 and −8°C and requires the presence of drops with a radius of 25 μm impacting at a critical impact speed. Therefore, this mechanism likely contributes only in a very limited manner to cloud charging.

3. Drop breakup (Figure 18.4m)

In Sections 10.3.5 and 14.5.4.2, we have shown that drops may break up by hydrodynamic instability or by collision. Elster and Geitel (1885), and Lenard (1892) observed that the small drops produced by a water fall were negatively charged. Later experiments of Simpson (1909, 1927), Lenard (1921), Zeleny (1933), and Chapman (1952) confirmed the early observation and showed that drop breakup causes electrification. During drop breakup, electrons are stripped-off and attached to air molecules, leaving the main body of water positively charged. Typically, 2×10^{-2} e.s.u. per gram of broken up water was found to be separated. It is obvious from the charge sign on the drops and on the air molecules that this mechanism could account only for the positively charged region in the lower portions of a cloud. However, even if a cloud liquid water content of 4 g m^{-3} is assumed, and the entire liquid water mass were to breakup three times within a span of 10 minutes, a volume charging rate of only about 1×10^{-2} C $km^{-3}min^{-1}$ could be achieved (Mason, 1971). This value is too small to account for the charging rates observed in clouds.

4. Graupel melting (Figure 18.4n)

Experiments of Dinger and Gunn (1946) showed that ice which contains air bubbles (such as found in graupel particles and hailstones) acquires a positive charge on melting. This finding was later confirmed by Chalmers (1956), Magono *et al.* (1963, 1965), Kikuchi (1965), MacCready and Proudfit (1965), Dinger (1965), Drake and Mason (1966), Iribarne and Mason (1967), Drake (1968), and Martin and Hutchinson (1977). Dinger and Gunn (1946), Blanchard (1963), and Iribarne and Mason (1967) showed that the charging is due to the ejection of negatively charged minute droplets produced by air bubbles bursting at the surface of the meltwater. The charging was found to be a function of the radius of the escaping air bubbles, the bubble content of the ice, and the ion content of the meltwater. The mechanism of charging is assumed to be associated with an electric double layer at a water/air interface of the air bubble cavity, with an excess of negative ions near the air/water interface and a diffuse positive space charge extending into the meltwater. Shearing of the electric double layer during the escape of the air bubble transfers negative charge to the drops from the bursting bubble cap. Electric charges between a few tenths and about 7 e.s.u. per gram of melted ice was found, depending mostly on the bubble content of the melting ice specimen. Mason (1972) assumed a value of 2 e.s.u. per gram resulting from the melting of millimeter-sized graupel particles, and an ice water content of 2 g m^{-3} to obtain a spatial charge concentration of approximately 1 C km^{-3}, sufficient to explain the positive space charge often found near the 0°C level in a cloud. However, the mechanism cannot explain the positive space charge often found, even above the melting level (MacCready and Proudfit, 1965; Marshall and Winn, 1982; Marshall and Marsh, 1986).

18.5.2.6 *Growth of the Electric Field*

In order to test the importance of each of the cloud charging mechanisms just discussed, numerous cloud modeling studies have been performed by which the time rate of change of the cloud electric field is computed. Some of the early studies (Latham and Mason, 1962, later used again by Mason, 1971, 1972, 1988; Müller-Hillebrand, 1954, 1955; Ziv and Levin,1974; Scott and Levin, 1975a,b) were based on a one-dimensional or parallel plate capacitor cloud geometry. Considering the local current density of falling, charged precipitation particles, given by $j_Q = -4\pi \sum_k n_k U_{\infty,k} Q_k(t)$, where the summation is taken over k particle categories, and a total leakage current density $j_L = \lambda E + i$, where i represents current densities which are non-linear in the electric field (e.g., point discharge currents), the time rate of change of the electric field is given by

$$\frac{\mathrm{d}E}{\mathrm{d}t} = -4\pi \sum_k n_k U_{\infty,k} Q_k(t) - 4\pi j_L \,. \tag{18-56}$$

From measurements of point discharge currents, Mason (1971) has suggested an empirical representation of the total leakage current density of the form $j_L = 10^{-3}[\exp(0.2E) - 1]$. Evaluating (18-56) for the case of two particle types, namely large graupel particles and small ice crystals charging by induction during their collision in the growing electric field, and assuming a constant concentration of small ice crystals of 50 liter^{-1} of radius 50 μm, a fall velocity difference of 5 m sec^{-1} between the large and small particles, a collision and separation efficiency of unity, and a graupel precipitation rate initially of 1 mm hr^{-1} and reaching 37 mm hr^{-1} after 540 sec, Mason (1971) found that the electric field grew exponentially and reached a value of 4.4 kV cm^{-1} after 9 minutes.

Illingworth and Latham (1975), however, pointed out that real clouds of finite extent could not be as easily electrified. The parallel plate capacitor cloud also completely ignores the effects of the air-motions in a cloud. Therefore, in later cloud electrification models (Tzur and Levin, 1981; Helsdon, 1980; Chiu, 1978; Chiu and Orville, 1976; Takahashi, 1978c, 1979, 1983a, 1984; Kuettner *et al.*, 1981; Illingworth and Latham, 1977; Dye *et al.*, 1986; Rawlins, 1982; Asama and Kikuchi, 1987; Helsdon and Farley, 1987; Ziegler *et al.*, 1991; Norville *et al.*, 1991), the cloud charging mechanisms were embedded in two- and three-dimensional cloud models. It would lead us much too far afield should we venture to discuss these various models in detail, including their advantages and disadvantages, and the results derived from them. The models are also not strictly comparable, since not all of them considered the same charging mechanisms. In addition, many different approaches are used to describe cloud microphysical processes, some of which are heavily parameterized.

Nevertheless, from the more recent model studies, a few pertinent conclusions can be drawn: (1) All cloud charging mechanisms mentioned above appear to contribute to some degree at some time to the charging of a cloud. Among these, however, the non-inductive mechanism involving the collision of graupel with snow crystals in the presence of supercooled water, dominates all others and is able to explain the tripolar charge distribution often observed. A secondary, but never-

theless significant role is played by the inductive mechanism involving the collision of polarized ice particles with smaller snow crystals. Drop-drop interactions, on the other hand, tend to produce electric fields which grow little and reach sizeable values only if heavy precipitation is sustained and large separation efficiencies are assumed. (2) While the non-inductive ice-ice mechanism tends towards a steady state electric field, as the same charge is separated during each collision, the inductive ice-ice mechanism causes a continuously building electric field and explains the often observed exponential increase of the field with time. (3) Both ice-ice mechanisms together appear to produce, within 20 minutes, an electric field of up to 1-4 kV cm^{-1}, a tripolar cloud structure with net negative and positive charge centers of 1 to 10 C km^{-3} and peak charging rates of 10 C $km^{-3}min^{-1}$, the negative charge center appearing near $-20°C$, an upper positive charge center appearing at considerably lower temperatures, and a lower positive charge center between -10 and $0°C$. These findings meet the major requirements listed in Section 18.5.1.

18.6 Effect of Electric Fields and Charges on Microphysical Processes

We shall now describe some observed and/or predicted modifications in the behavior of isolated and interacting cloud particles in consequence of the presence of ions, particle charges, and ambient electric fields.

18.6.1 Drop and Ice Crystal Nucleation

Many expansion chamber experiments (for a summary, see Mason, 1971; and Rathje and Stranski, 1955) have shown that, in the presence of singly charged, negative small ions, the onset of an appreciable rate of drop formation ($J = 1$ in the notation of Chapter 7) in otherwise clean moist air, requires critical saturation ratios $(S_{v,w})_c$ of 3.7 to 4.2, i.e., critical supersaturations $(S_{v,w})_c$ of 270 to 320%. For positive ions, the corresponding critical saturation ratio is $(S_{v,w})_c \approx 6$. Both results apply to temperatures between -5 and $-8°C$. Note by comparison with Figure 7.5 that, for the same temperature interval, homogeneous nucleation at the rate $J = 1$ occurs for $4.6 \lesssim (S_{v,w}) \lesssim 4.9$. Thus, we see that the presence of negative ions decreases the supersaturation required for drop nucleation below the value required under homogeneous conditions, while positive ions raise the critical supersaturation. This electric sign effect was qualitatively explained by Loeb *et al.* (1938). They argued that embryonic water drops are in a pseudo-crystalline state in which the molecules assume a definite structural arrangement. In order to minimize the surface energy of such an arrangement, the water molecules at the surface tend to be oriented with their oxygen atoms outward, since the polarizability of an oxygen atom is considerably larger than that of a hydrogen atom. Thus, the capture of negatively charged ions will enhance the original tendency of the embryonic drops to orient approaching water molecules with their hydrogen atoms inward and thereby facilitate drop nucleation; by the same argument, positive ions will hinder nucleation. However, the small differences due to sign aside, the main point to be made is that since supersaturations in clouds rarely exceed a few percent (see Figure 2.1), small ions cannot affect the nucleation rate under natural conditions. Studies of

the effect of net electric charges on aerosol particles and of external electric fields on heterogeneous drop nucleation are not available in the literature.

Work carried out prior to 1963 suggested qualitatively that electric fields and charges enhance ice nucleation (Pruppacher, 1963b). Subsequent more quantitative experimental studies confirmed these effects, but indicated that, under atmospheric conditions, only charges are likely to affect ice nucleation. Gabarashvili and Gliki (1967) and Gabarashvili and Kartsivadze (1968, 1969) found that supercooled drops containing particles of quartz or napthalene were nucleated to ice at significantly warmer temperatures when the particles carried a net negative charge than when they were neutral or carried a net positive charge. Abbas and Latham (1969a) and Morgan and Langer (1973) observed that charged nuclei produced during corona discharges or by sparks promoted ice nucleation of supercooled drops. The effect of charge sign was not reported. Pruppacher (1973b) found that the freezing temperature of supercooled water drops of 100 to 350 μm radius, freely suspended in the air stream of a wind tunnel, was considerably raised when contacted by predominantly negatively charged amorphous sulfur particles which, when uncharged are known to be poor ice forming nuclei.

The effect of external electric fields on ice nucleation has been studied under essentially two different experimental conditions. Pruppacher (1963c) observed in laboratory experiments that millimeter-sized drops, forced in an external electric field to deform and thus to rapidly spread over a solid surface, froze at temperatures up to 10°C warmer than when the drops were unaffected by the field. These results are consistent with the observations of Doolittle and Vali (1975), who found that an electric field had no effect on the freezing of supercooled drops if they remained motionless with respect to the supporting surface. Other studies have dealt with drops in free fall. For example, Dawson and Cardell (1973) observed millimeter-sized drops suspended in the air stream of a wind tunnel at temperatures of -8 to -15°C and detected no electrofreezing effect for external fields up to 4 kV cm^{-1}. Coalescence between drops did not alter this outcome. In contrast to these studies, however, Abbas and Latham (1969a) and Smith *et al.* (1971) found that millimeter-sized drops falling in air of -5 to -12°C through intense fields froze if disruptions caused small filaments to be drawn out from or between drops.

18.6.2 Diffusional Growth of Ice Crystals

Numerous laboratory studies suggest that both the growth mode and the growth rate of ice crystals are significantly affected by external electric fields. Studies prior to 1973 have been reviewed by Evans (1973) and by Crowther and Saunders (1973). From their summaries, it appears that in intense electric fields ice crystals tend to assume the shape of a needle or spike, independently of temperature, which is oriented in the direction of the field lines. To understand this behavior, we may consider a corner of an ice crystal pointing in the direction of the field lines: The local field enhancement caused by the large curvature of the corner causes the formation of ions in its neighborhood. Some of these ions are captured by the polar water molecules, which then move in the field to enhance the vapor flux to the crystals corner. As the corner grows into a needle or spike, the process is self-

propagating as side branches which might compete for water vapor are suppressed. The growth rate of the crystal is further increased by the field enhancement of the migration distance of water molecules at the ice surface. Both effects have been observed to enhance the growth rate of an ice crystal by factors of 10 to 1000 over the rate in the absence of electric fields. For such significant effects to occur, the field strength has to reach several kV cm^{-1}. No growth enhancement has been observed if $E \lesssim 500$ V cm^{-1}.

18.6.3 Drop Deformation, Disruption and Corona Production

It is well-known that a drop in an electric field will elongate along the field direction, due to the interaction of the field and the polarization charge induced on the drop. For situations in which gravitational and aerodynamic forces are negligible, the distorted shape is approximately prolate spheroidal, with an eccentricity which increases with increasing field strength until, finally, disruption occurs at a critical field value. Zeleny (1915, 1917) was the first to observe that drops raised to a critical electric potential would disintegrate if held fixed at the end of a glass capillary. He pointed out that the disintegration begins as a hydrodynamic instability rather than the formation of ion currents. Taylor (1954) modeled this situation theoretically for an uncharged drop by assuming a spheroidal shape, and then setting up equations of equilibrium between surface tension and electrical stresses at the poles and equator of the drop. As a result of this analysis, he estimated the critical field E_{cr} for disruption (in e.s.u.) to be given by

$$E_{cr} = X_{cr} \left(\frac{\sigma_{w/a}}{a_0} \right)^{1/2}, \tag{18-57}$$

where a_0 is the undeformed radius of the drop in cm, $\sigma_{w/a}$ is its surface tension, and $X_{cr} = 1.625$. In a more refined numerical study, Brazier-Smith (1971) abandonned the constraining assumption of a spheroidal shape by formulating an iterative method in which the critical electric field for drop instability was computed in a succession of stages. The drop shape at each stage was based on the deformation imposed by the external electric field on the shape it had in the previous stage. In this way, Brazier-Smith found $X_{cr} = 1.603$, showing that the spheroidal assumption of Taylor was a good approximation to the true behavior. However, it must be pointed out that neither Taylor (1964) nor Brazier-Smith (1971) included in their theory the very important contribution of aerodynamic forces which, as we have seen in Section 10.3.2, control the shape of a falling drop in the absence of a field. We are therefore not surprised that the values found experimentally for X_{cr} deviate somewhat from the calulated one. Thus, Wilson and Taylor (1925), experimenting with soap bubbles, found $X_{cr} = 1.61$, while Nolan (1926), Macky (1931), Abbas and Latham (1969b), and Griffiths and Latham (1972), experimenting with drops falling through an intense vertical electric field, observed $X_{cr} = 1.61$, 1.51, 1.60, and 1.81, respectively. The experiments of Latham (1965) and of Mathews (1967) showed that the deviations found result not only from a neglect of the aerodynamic effects in the theoretical models, but also from differing experimental conditions. Thus, the drops fell through fields of very limited vertical extent, and allowance

was generally not made for observations showing that the mass loss of a drop in an intense electric field was found to increase with increasing time of exposure to the field.

More realistic experiments were carried out by Dawson and Richards (1970), Richards and Dawson (1971), and by Rasmussen *et al.* (1985), who floated drops at their terminal velocity in the vertical air stream of a wind tunnel in which the drops were allowed to oscillate freely while being exposed to a vertical electric field. These studies showed that the electrical instability ensues at the drop's upper surface and that X_{cr} is not constant but increases with increasing drop size. Thus, X_{cr} was found to increase from 1.63 ($D_0 = 2.5$ mm) to 1.92 ($D_0 = 6$ mm) and from 1.67 ($D_0 = 3.4$ mm) to 1.80 ($D_0 = 5$ mm), according to Richards and Dawson (1971), and Rasmussen *et al.* (1985), respectively.

Richards and Dawson's (1971) values for the critical electric field for onset of instability in charged water drops falling in air at terminal velocity are shown in Figure 18.5. We see that, for $a_0 \lesssim 1.5$ mm, the wind tunnel results are in good agreement with the simple Taylor limit of (18-57), plotted as curve (1) in the figure. However, for larger sizes, (18-57) progressively underestimates E_{cr}. The principal reason for this growing difference is that aerodynamic forces tend to flatten the drops into shapes resembling oblate spheroids, the more so as the size increases (recall Section 10.3.2), thereby stabilizing the drops against the vertical field.

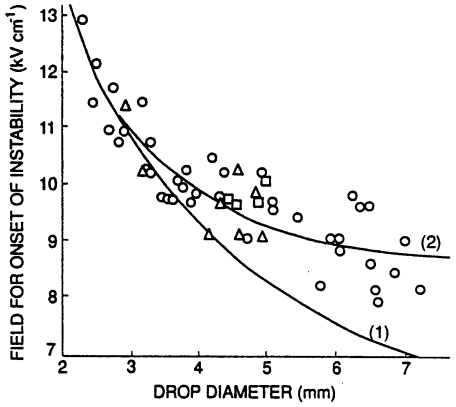


Fig. 18-5: Effect of the electric field on drop instability as a function of drop radius, for uncharged water drops in air; (1) theory of Taylor (1964), (2) best fit to experiment, □ slow increase of field, pos.; ○ slow increase of field, neg.; △ impulse, pos. (From Richards and Dawson, 1971, with changes.)

It is also interesting to note from Figure 18.5 that, for drops of $a_0 \gtrsim 2.5$ mm, the critical field for breakup remains nearly constant at about 9 kV cm^{-1}. This result is consistent with the observations of Griffiths and Latham (1972), who showed that at 1000 mb the onset of corona discharge (which accompanies instability) from water drops of $a_0 = 2.7$ mm in air at 1000 mb occurs in a vertical field of (9 ± 0.5) kV cm^{-1}, decreasing to about 5.5 kV cm^{-1} at 500 mb.

The experimental and theoretical studies discussed above show that the critical electric fields necessary for the disintegration of a single drop, and thus necessary for dielectric breakdown in clouds, are considerably larger than the maximum electric fields observed in natural clouds. This conclusion is not altered if the results of experiments with horizontal instead of verticle electric fields are considered. Thus, Ausmann and Brook (1967) derived $X_{cr} = 1.56$ from experiments with drops falling through a horizontal electric field of limited extent. Kamra *et al.* (1993) studied drops suspended freely for long periods of time in the vertical air stream of a wind tunnel, and found $X_{cr} = 1.0$. This rather low value was explained in terms of the previously mentioned experimental results of Latham (1965) and Mathews (1967). Using this result, one finds $E_{cr} = 5.1$ and 4.4 kV cm^{-1} for drops of $D_0 = 5$ and 6.6 mm, respectively. These values are still larger than the maximum electric fields observed in atmospheric clouds.

Of course, one may argue that drops in strong electric fields will generally also carry net charges, which can be expected to affect their stability as well. A combined theoretical and experimental study of the more general problem of charged drops falling through an electric field was first carried out by Abbas and Latham (1969b), who attempted to extend Taylor's analysis by including drop charge and some terms representing hydrostatic and aerodynamic effects. From their computations (also reported in Latham and Meyers (1970)), they obtained the following relationship between the critical field for disruption and the drop charge Q (in e.s.u.):

$$E_{cr}\left(\frac{a_0}{\sigma}\right)^{1/2} = 1.6\left(1 - \frac{1.5Q}{Q_R}\right), \tag{18-58}$$

where Q_R is the Rayleigh charge limit given by (17-46). They also found that (18-58), their experimental results, and the experiments of Ausman and Brook showed agreement to within 3% for $0.1 \leq a_0 \leq 0.17$ cm and $0 \leq Q/Q_R \leq 0.15$.

It is interesting to note that (18-58) does not yield the Rayleigh limit $Q = Q_R$ for $E_{cr} = 0$; however, (18-58) was not intended to be applicable for $Q/Q_R > 0.15$. On the other hand, (18-58) does closely approximate the Taylor limit, (18-57), for $Q = 0$. Levine obtained a result similar to (18-58), but with the coefficient 1.5 multiplying Q/Q_R replaced by 1.0, in order to achieve the Rayleigh limit for zero field.

It is obvious from (18-58) that a drop charge lowers the critical field for instability. For example, from (18-58) we find $E_{cr} = 6$ kV cm^{-1} for $D_0 = 4$ mm, $Q = 2$ e.s.u. and $\sigma = 76$ erg cm^{-2}. The study of Brazier-Smith (1972), in which the constraining assumption of a spheroidal shape is abandoned (but which does not include aerodynamic effects), yields $E_{cr} \approx 5.5$ kV cm^{-1} for the same conditions. Despite the rather unrealistically large charge assumed in the previous example, we note that the critical field strengths required for drop instability are still considerably larger than those typically observed in thunderstorms.

Thus far, we have considered only the instability of single drops. One would expect that pairs of drops in close proximity would behave quite differently. In this case, a strong enhancement of the field between the drops is expected due to the mutual interaction of the polarization charges. This effect will be particularly

strong if the field is nearly parallel to the line of centers of the drops. A theoretical and experimental study of this problem was performed by Latham and Roxburgh (1966). They employed the basic calculational procedure of Taylor (1964), described above, along with the theoretical values of Davis (1964a,b) for the local field enhancement in the gap between two spheres situated in an electric field. (Davis's analysis is discussed in Appendix A-18.6.3.) The computations of Latham and Roxburg showed that the field required to initiate instability in one of a pair of closely separated drops may be several orders of magnitude less than that needed to disrupt either drop in isolation. The calculated critical fields for $a_0 \approx 1$ mm were also found to agree well with their experimental values.

On the other hand, Brazier-Smith (1971) applied the same numerical method used for single drops to this problem, and obtained critical field values consistently higher (by about a factor of 2 for close separations of equal drops, decreasing to a factor of about 1.1 for a separation of $2a_0$) than those found by Latham and Roxburgh. Brazier-Smith explained the agreement between the theoretical and experimental results of Latham and Roxburgh by noting that both actually dealt with the problem of supported drops, rather than of free drops as proposed and as studied by Brazier-Smith.

The relevance of these studies to pairs of drops falling under natural conditions may be somewhat limited, since hydrodynamic forces were ignored. By analogy with the previous case of studies on isolated drops, we might expect that hydrodynamic forces would tend to suppress the onset of electrical instability for interacting drop pairs. However, the effect is probably not as great in the present instance, since the deformations and instabilities occur in the vicinity of closely adjacent surfaces where air-flow effects may be relatively unimportant.

Crabb and Latham (1974) have made measurements on the critical field required to produce corona from a pair of water drops, of radii 2.7 mm and 0.65 mm, colliding with a relative velocity of 5.8 m $\sec^{-1}$, which is similar to their difference in terminal velocities. The critical field ranged from about 5 kV cm^{-1} for head-on collisions to about 2.5 kV cm^{-1} for glancing collisions; these values are, of course, considerably less than those required to produce corona from single drops, and suggest that corona from colliding raindrops may be capable of triggering lightning. Similar results and conclusions follow from the experiments of Griffiths and Latham (1974) on corona production from ice crystals or hailstones. They found that the critical field for sustained positive or negative corona depends on the size, shape, and surface features of the particle, but may be as low as 4 kV cm^{-1} at pressures corresponding to those where lightning is initiated.

In the previous paragraphs, we have been concerned with the electric field at which a drop becomes distorted to such an extent that disruption follows. We shall now briefly consider the distortion which a drop experiences when exposed to external electric fields less than critical. Values for the ratio of the minor to the major axis b/a of a drop in an external electric field have been computed as a function of $E(a_0/\sigma_{\text{w,a}})$ by O'Konski and Thatcher (1953), Taylor (1964), Abbas and Latham (1969a,b), Brazier-Smith (1971), Brazier-Smith *et al.* (1971), and Zrnic *et al.* (1984). With the exception of Brazier-Smith, all authors assumed that a drop retains its spheroidal shape while being deformed. Also, none of the

computations included aerodynamic effects.

In Section 10.3.2, we have shown that hydrodynamic forces acting on a falling drop induce on it an oblate spheroidal shape with a b/a value that is smaller the larger the drop. This effect obviously counteracts the prolate spheroidal deformation produced by the electrostatic stress $E^2/8\pi$ of a vertical external electric field. As long as the electric field is relatively small, the flow around the drop and the surface tension stress will dominate drop shape. This situation is expected to change drastically as the electrostatic stress begins to dominate the other stresses. Thus, large drops with a small value for $(2\sigma_{w/a})/a$ are expected to yield more readily to the deforming electrostatic stress, and vice versa. The first expectation has been verified experimentally by Kamra and Ahire (1993), who found that oscillating drops of $3.5 \leq D_0 \leq 6.6$ mm changed their shape (given by the time averaged axis ratio $(b/a)_t$) only relatively little for $0 \leq E \leq 5$ kV cm^{-1}. Unfortunately, no larger electric fields were applied. The second expectation has been verified theoretically by Chuang and Beard (1990), who computed the equilibrium shape of a drop exposed to an external electric field by means of an extension of the hydrodynamic drop shape model of Beard and Chuang (1987) (see Section 10.3.2). Their results are exhibited in Figure 18.6. We note that, as expected, the curves for (b/a) vs. E and for $D_0 =$ constant tend to cross each other when the fields become sufficiently large, hence, causing larger drops to become more deformed. However, a comparison of these theoretical results with the observed values for the electric fields for breakup, also shown in Figure 18.5, demonstrates that the theoretical predictions significantly overestimate the electric field required to achieve critical drop deformation. This discrepancy is a result of the fact that the theoretical model disregards drop oscillations and assumes all forces on the drop to be in equilibrium all the time. Freely falling drops oscillate, however, generally in a prolate/oblate mode (see Section 10.3.3). Since, for a given external electric field, the induced charge on the drop's upper-side is the same in both modes, the charge on a prolate deformed drop is distributed over a much smaller area than on an oblate deformed drop, causing the electric force per unit area of the drop to be much larger in its prolate mode than in its oblate mode, and also larger than in its equilibrium shape. Oscillating drops are therefore expected to deform in an external electric field more readily than a drop which is prevented from oscillating and is forced to keep an equilibrium shape. In order to demonstrate the expected drop deformation for an oscillating drop, we have included in Figure 18.6 the dashed curves which, for low values of E , are consistent with the computations of Chuang and Beard (1990) and the experiments of Kamra and Ahire (1993), and for large values of E, are consistent with the critical electric fields observed by Richards and Dawson (1971). Note the dashed curves deviate considerably from the equilibrium curves.

The effects of electric charges on drop shape in the absence of an external electric field, determined by Chuang and Beard (1990), are exhibited in Figure 18.7. We note that increasing charges enhance the oblate drop deformation, as expected from (18-58).

It is, of course, expected that electric fields and charges also affect the oscillation frequency of a drop. This has been verified theoretically by Brazier-Smith *et al.* (1971), and recently by detailed theoretical modeling of Feng and Beard (1990,

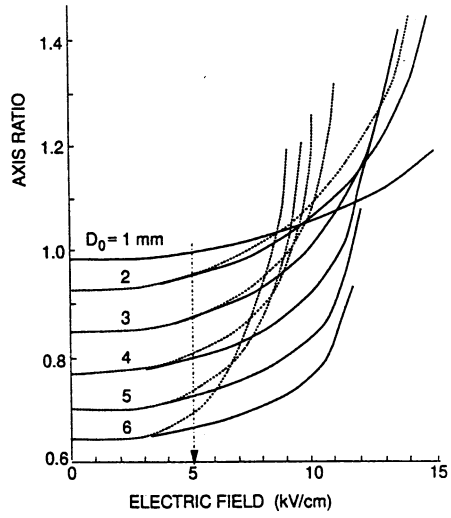


Fig. 18-6: Axis ratio of uncharged millimeter-sized drops at terminal velocity in air as a function of the intensity of an external electric field. (—) based on computations of Chuang & Beard (1990) for equilibrium shape; (– – –) based on observed time-mean axis ratios of oscillating drops derived from wind tunnel observations of Rasmussen *et al.* (1985) and from the critical electric field of Richards & Dawson (1971) in Figure 18-5.

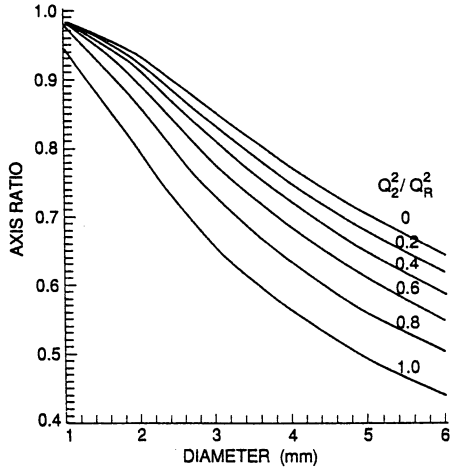


Fig. 18-7: Axis ratio of electrically charged drops at terminal velocity in air as a function of drop size and magnitude of electrical charge ratio $Q_2{}^2/Q_R{}^2$, where Q_R is the Rayleigh limit computed for drop equilibrium shapes. (From Chuang and Beard, 1990, with changes.)

TABLE 18.1

Terminal fall velocities (cm sec^{-1}) of water drops of radius a and $Q = 2Ea^2$ (e.s.u.) falling in air in a vertical positive electric field of field strength E. Drops of radius less than 50 μm are assumed to carry positve charges while larger ones carry negative charges. The minus sign signifies upward motion of the drop. For 20° C and 1013 mb. (Based on data given by Gay *et al.*, 1974, in their Table 2.)

E	$a(\mu m)$			$a(\mu m)$	
(kV/cm)	10	20	50	100	300
0	1.2	4.6	25.6	71.0	245
0.5	2.8	7.7	19.3	63.4	237
1.0	7.4	16.8	-2.4	38.4	214
1.5	15.1	31.2	-35.1	-20.8	173
2.0	25.9	49.7	-70.8	-79.2	102
2.5	39.2	72.1	-110	-133	-57.8
3.0	55.1	97.8	-151	-189	-178
3.4	73.2	125	-193	-248	-278
4.0	92.8	155	-238	-309	-373

1991a,b). These studies show that the oscillation frequency is reduced by charges and fields.

Weinheimer and Few (1987) showed that electrical fields may also affect the fall of snow crystals. On comparing the aerodynamic torques due to Stokes flow, using the solutions of Jeffreys (1922) with the electric torques on falling snow crystals using the formulations of Stratton (1941) and McCormick and Hendry (1977), they found that snow crystals with dimensions of 200 to 1000 μm align in an external electric field of 100 kV m^{-1}. In fields of 10 kV m^{-1}, only crystals with diameters of less than 50 μm would align. Columnar crystals were found to align more easily than plates, except for dendrites.

18.6.4 Drop Terminal Velocities

A drop of mass m bearing charge of magnitude Q and falling in a vertical electric field E , will experience a combined gravitational and electrical force of $mg \pm QE$. If the drop is small enough to retain a spherical shape, the computational schemes of Section 10.3.6 for spherical drops may be used to determine its terminal velocity, the only modification required being merely the replacement of mg by $mg \pm QE$. Table 18.1 gives some selected values for drop terminal velocities computed in this manner by Gay *et al.* (1974) for water drops in air. Note the pronounced increase in terminal velocity which charged drops experience in an external electric field. Experiments carried out by Gay *et al.* for the same range of drop sizes, drop charges, and external electric fields, yielded terminal velocities which were in good agreement with those theoretically predicted.

For deformed drops, the computational schemes of Section 10.3.6 cannot be used unless the drop deformation is known as a function of drop size, charge, and field strength. Unfortunately, there are at present no satisfactory experimental or theoretical descriptions of this functional relationship. However, some information concerning the electric field dependence of terminal velocities of large uncharged

drops falling in vertical fields has been obtained by Dawson and Warrender (1973). As we know from the previous section, a vertical field tends to counter the oblate spheroidal deformation of large falling drops, induced by hydrodynamic forces. Therefore, we would expect to see an increase in terminal velocity with increasing field strength, owing to the resulting decrease in the drop cross-section presented to the flow. The extent of the increase found by Dawson and Warrender for millimeter-sized drops was rather small: typically, $\delta U_\infty/\delta E = 0.1$ m sec^{-1} (kV cm^{-1})$^{-1}$; for example, for a drop of $a_0 = 2.1$ mm they found $\Delta U_\infty = 1.3$ m sec^{-1} if E was increased from 0 to 10 kV cm^{-1}.

18.6.5 Collisional Growth Rate of Cloud Particles

We would also expect to see a significant change in the collision and coalescence (or sticking) efficiencies of cloud particles which are subjected to electrostatic forces of magnitude comparable to the acting hydrodynamic and gravitational forces. Several theoretical and experimental investigations of the possible electrostatic influences have been carried out. For example, in a field experiment Latham (1969) found that the growth rate of 130 μm radius drops colliding with 15 μm diameter drops (all carrying negligible charge) was enhanced if the external electric field strength exceeded 150 V cm^{-1}. At field strengths of 500 V cm^{-1}, the growth rate was about 20% higher than for the case of no field. No further enhancement was noted until the field reached 1200 V cm^{-1}; in larger fields, the growth rate rapidly increased again, achieving for 1600 V cm^{-1} a 100% increase over the rate for zero field. Qualitatively similar results were obtained in laboratory investigations by Phan Dong and Dinh-Van (1973). They showed that the number of collection events for a given time period in a cloud of uncharged drops in air was affected only by field strengths exceeding 400 V cm^{-1}. The collection rate increased linearly with further increasing field strength.

Some effects of drop charge on growth by collision and coalescence have been studied by Woods (1965). In the absence of an external electric field, oppositely charged drops of $a \lesssim 40\,\mu$m required a charge $Q > 5 \times 10^{-5}$ e.s.u. for a discernible increase in growth. Above this threshold, the number of collection events increased approximately linearly with increasing charge. Drops of $a > 40\,\mu$m exhibited a similar trend, but no clear threshold for the onset of a charge effect could be detected. Charges of equal sign reduced the number of collection events below that occurring for uncharged drops if $a > 40\,\mu$m, and inhibited collection completely if $a \lesssim 40\,\mu$m.

Similar electrostatic effects on the growth rate of ice crystals colliding with ice crystals have been observed by Latham (1969), Latham and Saunders (1970), Crowther and Saunders (1973), and Saunders and Wahab (1975). In these experiments, threshold fields of 100 to 600 V cm^{-1} were required for a discernible effect. For larger fields, the growth rate increased rapidly, reaching values 80 to 100% larger than for the zero field case if $E \approx 1500$ V cm^{-1}. In the absence of a field, only about 10% of the ice crystals were aggregated, the aggregates consisting of up to 6 component crystals. In fields of near 1500 V cm^{-1}, 100% of the ice crystals were aggregated, each consisting of up to 10 crystals. In addition, Saunders and

Wahab (1975) found that aggregation in electric fields was most efficient at temperatures near −8°C, i.e., in the temperature region where columnar crystals are the favored growth habit. At this temperature, the crystal aggregates consisted of short columns joined at their basal or prism planes.

The effect of electric fields on the growth rate of ice crystals growing by collision with supercooled drops was studied by Latham (1969). He found a threshold field of ~ 900 V cm^{-1} for a discernible effect. In the presence of larger fields, the growth rate increased rapidly, reaching about 150% at 1500 V cm^{-1} and about 200% near 2000 V cm^{-1}, of the growth rate in the absence of a field. No studies on the effect of charges on the growth rate of ice crystals colliding with other ice crystals are available in the literature.

Several theoretical studies of the effect of electrostatic forces on the collision efficiency of water drops in air have been carried out. For most cases of interest, very complex hydrodynamic and electrostatic interactions are involved, and the solutions can be obtained only through numerical integration procedures. However, a few approximate analytical solutions are also available for special combinations of drop mass, charge, and electric fields. Two of these asymptotic estimates of collision efficiencies are especially simple and helpful in providing some additional physical insight into the more complex situations, and so we shall now turn to a discussion of them, following Atkinson and Paluch (1968) (similar results appear in Paluch, 1970).

First, let us consider the case of large drops bearing large charges. If a pair of such drops has a sufficiently large initial relative velocity, the relative motion can be described adequately within the theoretical framework of the classical two-body problem, in which two particles approach each other in a frictionless medium and are subjected to an inverse square law mutual attraction. The solution of this problem is well-known (e.g., see Goldstein, 1965), and may be expressed as $(y_p/r_a)^2 = 1 + (E_e/E_k)$, where y_p is the impact parameter of the encounter, r_a is the apsidal (orbital turning point) distance, E_k is the kinetic energy of the relative motion for large separations, and E_e is the decrease in electrical energy that occurs as the particles are brought from infinity to the minimal separation r_a at the turning point of the orbit. Considering the definition of the collision efficiency E (Section 14.4.2), we may view $(y_p/r_a)^2$ for $r_a = a_1 + a_2$ and $y_p = y_c$ as the collision efficiency for two point particles which approach to within the drop collision distance $a_1 + a_2$. In this manner we obtain the estimate

$$\mathrm{E} \approx 1 + z\,, \quad z = \frac{-Q_1 Q_2}{(a_1 + a_2)} \left(\frac{m_1 m_2}{(m_1 + m_2)} \right) \frac{\Delta U_\infty^2}{2}\,, \tag{18-59}$$

where ΔU_∞ is the initial relative velocity, Q_i is the drop charge in e.s.u., and $z \gtrsim 0$. Numerical computations of the trajectories which evolve when the effects of polarization (image) charges and drag are included, produce results which can be fitted within a few percent to the relationship

$$\mathrm{E} = 1 + 1.4z\,, \tag{18-60}$$

for the ranges $0 \leq z \leq 5$, $100 \leq a_1 \leq 1000\,\mu$m, and $K \geq 4$, where $K = -Q_1Q_2/a_1^2a_2^2$. Thus, we see that the simple two-body model and (18-61) describe the essential behavior for this class of interactions.

The other approximate analytical result applies to the case of highly (and oppositely) charged small drops in the Stokes regime ($a_i \lesssim 30\,\mu$m). The model in this case involves the assumptions of negligible drop inertia and hydrodynamic interaction, so that the Stokes drag on each drop just balances the applied forces from gravity, the Coulomb interaction, and the external electric field $\vec{E}$; thus, for drop 1, we write

$$6\pi a_1 \eta \vec{v}_1 = m_1 \vec{g}^* + Q_1 \vec{E} + \frac{Q_1 Q_2}{r^2} \hat{e}_r \,, \tag{18-61}$$

where r is the center to center distance between the drops and $\hat{e}_r$ is the unit vector along the line of centers from drop 1 to drop 2 ($Q_1Q_2 < 0$). On subtracting (18-61) from the similar equation for drop 2 and letting both gravity and the external field act in the positive x-direction, we find the velocity of drop 2 relative to drop 1 has the components

$$\frac{dx}{dt} = \Delta V_\infty + \frac{(B_1 + B_2)Q_1Q_2x}{r^3} \,, \quad \frac{dy}{dt} = \frac{(B_1 + B_2)Q_1Q_2y}{r^3} \,, \tag{18-62}$$

where $r = (x^2+y^2)^{1/2}$ and $B_i = (6\pi a_1 \eta)^{-1}$ is the mobility of drop i. On eliminating time from (18-62), the governing equation for the relative trajectories is obtained:

$$\frac{dx}{dy} = \frac{x}{y} + \frac{C(x^2 + y^2)^{3/2}}{y} \,, \quad C = -\frac{\Delta U_\infty}{Q_1Q_2(B_1 + B_2)} \,. \tag{18-63}$$

Integration of this equation yields the family of trajectories $x/r = Cy^2/2 + C_1$, where C_1 is the integration constant. We may determine C_1, in terms of the impact parameter y_p by noting that $y = y_p$ for $x \to \infty$. Furthermore, inspection of the resulting trajectories reveals that collisions ($y_p = y_c$) will occur only for those trajectories which approach the origin from the $-x$ direction: i.e., the criterion for $y_p = y_c$ is that $x/r \to -1$ as x and r approach zero. Therefore, we obtain $y_c^2 = 4/C$, or

$$\mathrm{E} = \frac{4}{C(a_1 + a_2)^2} = \frac{2Q_1Q_2}{3\pi\eta a_1 a_2 (a_1 + a_2)\Delta U_\infty} \,. \tag{18-64}$$

For highly charged drops, (18-64) predicts collision efficiencies two to three orders of magnitude larger than the geometric value of unity. For example, (18-64) gives $\mathrm{E} = 1.3 \times 10^3$ for $a_1 = 25\,\mu$m $a_2 = 20\,\mu$m, $Q_1 = 3.4 \times 10^{-4}$ e.s.u., and $Q_2 = -1.9 \times 10^{-4}$ e.s.u.; and $\mathrm{E} = 3.3 \times 10^2$ for $a_1 = 14\,\mu$m, $a_2 = 12\,\mu$m, $Q_1 = 2.6 \times 10^{-5}$ e.s.u., $Q_2 = -2.9 \times 10^{-5}$ e.s.u. Laboratory experiments by Krasnogorskaya and Neizvestnyy (1973) and Abbott (1975) have shown (18-64) to be within the range of experimental scatter for $\mathrm{E} > 2 \times 10^2$. However, for smaller E, Abbott found that (18-64) progressively underestimates the experimental values. From the numerical examples given above, we see that $\mathrm{E} > 2 \times 10^2$ typically corresponds to drop charges much larger than those found in clouds (recall Figure 17.1). Therefore, for small drops and realistic charges, it is necessary to employ a more complete physical-mathematical model and numerical methods of solution.

A complete description of the electrostatic forces acting on a pair of drops is available from the work of Davis (1964a,b), who solved the boundary value problem of two charged conducting spheres subjected to a background electric field. (A description of this solution is given in Appendix A-18.6.3.) For the hydrodynamic forces, the various flow fields and flow-interaction descriptions discussed in Chapter 14 may be used. The two types of forces may then be superposed and the drop trajectories integrated numerically to determine the extent of electrostatic influences on the collision efficiency problem.

Such studies have been carried out by Sartor (1960), Davis (1965), and Krasnogorskaya (1965) using Stokes flow, and by Lindblad and Semonin (1963), Plumlee and Semonin (1965), and in and Plumlee (1966) using Proudman and Pearson flow (see Section 10.2.2.3). In all studies, except that of Krasnogorskaya, the electric force expressions of Davis were used. The results of these studies, applicable to collector drops of low Reynolds number only, show that for a given charge or field, the effect on the collision efficiency increases with decreasing size of the collector drop, and that for a given collector drop, the effect increases with decreasing size of the collected drop. Furthermore, for a given drop pair, a critical charge and/or field is generally found to be necessary for electrostatic effects to be noticeable. For example, Davis (1965) concluded that in the absence of electric fields and for $a_1 \gtrsim 20\,\mu$m, the threshold charge is $Q_c(\text{e.s.u.}) \gtrsim 0.1a^2$, with a in cm. Similarly, Krasnogorskaya found $Q_c \gtrsim 10^{-7}$ e.s.u. for $a_1 \gtrsim 10\,\mu$m. Semonin and Plumlee found $3 \times 10^{-1} \lesssim Q_c \lesssim 3 \times 10^{-6}$ e.s.u. for $30 \leq a_1 \leq 50\,\mu$m and $5 \leq a_2 \leq 10\,\mu$m. Lindblad and Semonin and Semonin and Plumlee found that the threshold vertical field for a noticeable enhancement of the collision efficiency for uncharged drops was $E_{\text{cr}} = 200$ V cm^{-1} for $a_1 = 30\,\mu$m and $a_2 = 5\,\mu$m, $E_{\text{cr}} = 500$ V cm^{-1} for $a_1 = 30\,\mu$m and $a_2 = 15\,\mu$m, $E_{\text{cr}} = 400$ V cm^{-1} for $a_1 = 40\,\mu$m and $a_2 = 5\,\mu$m, and $E_{\text{cr}} = 1$ kV cm^{-1} for $a_1 = 40\,\mu$m and $a_2 = 15\,\mu$m.

In order to determine the effect of electric fields and charges on the collision efficiency of larger drops, Schlamp *et al.* (1976, 1979) employed the superposition scheme (see Section 14.3) in conjunction with numerically determined flow fields around drops (see Section 10.2.2.4) and Davis expressions for the electrostatic forces. The equation of motion for the a_1-drop was thus written as

$$m_1 \frac{\mathrm{d}\vec{v}_1}{\mathrm{d}t} = m_1 \vec{g}^* - \frac{\pi}{4} C_{D,1} N_{\text{Re},1} a_1 \eta_a (\vec{v}_1 - \vec{u}_2) + \vec{F}_{e,1}\,, \tag{18-65}$$

with an analogous equation for the a_2-drops. The electric forces $\vec{F}_e$ were those given by the Davis relations (A. 18-2 to A. 18-4). The computations were carried out for $11.4 \leq a_1 \leq 74.3\,\mu$m and $1 \leq a_2 \leq 118\,\mu$m, for the case that the external electric field was assumed to be parallel to gravity pointing downward due to a net positive charge in the upper part of the cloud, and for the case that the a_1-drop was positively charged and initially above the smaller, negatively charged a_2-drop (Schlamp *et al.*, 1976). The case where the a_1-drop was negatively charged and either above or below the positively charged a_2-drop was treated by Schlamp *et al.* (1979). The electric fields assumed ranged between 0 and 3529 V cm^{-1}, while the charge on the drops was assumed to be given by a relation of the form $Q = \hat{Q}a^2$ (see Equation 18.43) with $0 \leq \hat{Q} \leq 2.0$, implying $0 \leq Q \leq 2.8 \times 10^{-4}$ e.s.u.).

Selected results from the collision efficiency study of Schlamp *et al.* (1976) for the case of a positively charged a_1-drop above a negatively charged a_2-drop in a negative electric field (Q_1E negative) are shown in Figures 18.8a,b,c, with legends given in Tables 18.2 to 18.4.

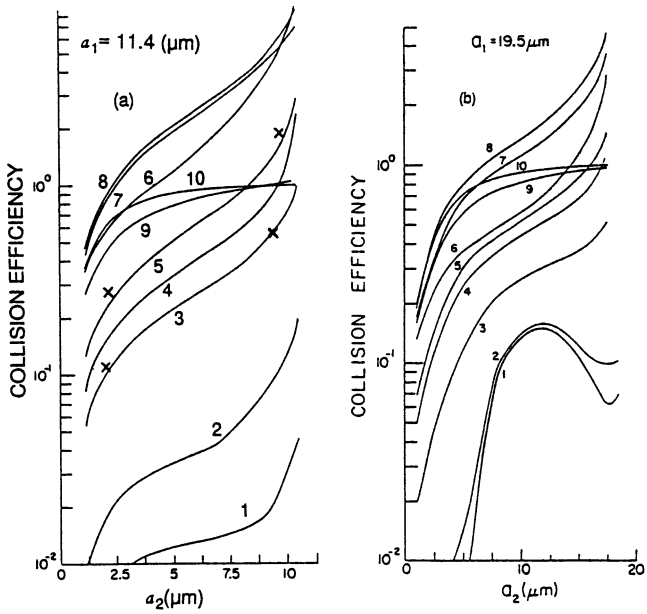


Fig. 18-8: Effect of electric charges and electric fields on the collision efficiency of cloud drops. (a) Collector drop radius 11.4 μm, explanation of curve labels in Table 18-2. (*) from List and Freire (1981), (from Schlamp *et al.*, 1976, with changes). (b) Collector drop radius 19.5 μm, explanation of curve labels given in Table 18-3; (c) collector drop radius 74.3 μm, explanation of curve labels in given in Table 18-4; (b) and (c) from Schlamp *et al.* 1976; by courtesy of the Am. Meteor. Soc., and the authors.)

From these figures, we note that the collision efficiency of small highly charged drops in thunderstorm fields may be up to 10^2 times larger than the corresponding efficiency for the same drop pairs in weakly electrified clouds. Therefore, studies of cloud electrification via precipitation charging mechanisms should obviously account for the electrostatic influence on the collision efficiency. On the other hand, the figures also suggest that the weak charges and fields present in young clouds will probably not significantly promote the early stages of drop spectral evolution by collision and coalescence. However, because of the complex non-linear nature of the collection growth problem, the actual quantitative importance of any colloidal destabilization induced by electrostatic forces can only be determined by comprehensive simulations of the collection process which include the full coupling between changes in electrification and in the drop spectrum.

Figures 18.8a,b,c show further that the influence of electrostatic effects decreases with increasing a_1 becoming negligible, even in the presence of the highest electric

TABLE 18.2
Legend for curves in Figure 18-8a.

$a_1 = 11.4\mu$m Curve	$\hat{Q}_1$ (esu cm^{-2})	$\hat{Q}_2$ (esu cm^{-2})	E (V cm^{-1})
1	0.0	0.0	0.0
2	$\pm$ 0.2	$\mp$ 0.2	0.0
3	0.0	0.0	$\mp$ 500
4	0.0	0.0	$\mp$ 706
5	0.0	0.0	$\mp$ 1000
6	$\pm$ 2.0	$\mp$ 2.0	0.0
7	0.0	0.0	$\mp$ 2847
8	0.0	0.0	$\mp$ 3000
9	$\pm$ 2.0	$\mp$ 2.0	$\mp$ 706
10	$\pm$ 2.0	$\mp$ 2.0	$\mp$ 2847

TABLE 18.3
Legend for curves in Figure 18-8b.

$a_1 = 19.5\mu$m Curve	$\hat{Q}_1$ (esu cm^{-2})	$\hat{Q}_2$ (esu cm^{-2})	E (V cm^{-1})
1	0.0	0.0	0.0
2	$\pm$ 0.2	$\mp$ 0.2	0.0
3	0.0	0.0	$\mp$ 500
4	0.0	0.0	$\mp$ 1000
5	0.0	0.0	$\mp$ 1236
6	$\pm$ 2.0	$\mp$ 2.0	0.0
7	0.0	0.0	$\mp$ 2504
8	0.0	0.0	$\mp$ 3000
9	$\pm$ 2.0	$\mp$ 2.0	$\mp$ 1236
10	$\pm$ 2.0	$\mp$ 2.0	$\mp$ 2504

TABLE 18.4
Legend for curves in Figure 18-8c.

$a_1 = 74.3\mu$m Curve	$\hat{Q}_1$ (esu cm^{-2})	$\hat{Q}_2$ (esu cm^{-2})	E (V cm^{-1})
1	0.0	0.0	0.0
	$\pm$ 0.2	$\mp$ 0.2	0.0
	0.0	0.0	$\mp$ 500
2	0.0	0.0	$\mp$ 705
	0.0	0.0	$\mp$ 1000
3	$\pm$ 2.0	$\mp$ 2.0	0.0
4	0.0	0.0	$\mp$ 2960
	0.0	0.0	$\mp$ 3000
5	$\pm$ 2.0	$\mp$ 2.0	$\mp$ 705
6	$\pm$ 2.0	$\mp$ 2.0	$\mp$ 2960

fields and charges observed in clouds if $a_1 \gtrsim 70\,\mu$m. Also, as expected, for a given drop pair, the effect of electric fields and charges on the collision efficiency generally increases with increasing drop charge in the absence of an external field, and with increasing field strength in the absence of charges. For a given a_1 , the effect on the collision efficiency of either electric charges or an external electric field depends on the drop size ratio $p = a_2/a_1$, the effect being largest for $p \ll 1$, least for intermediate p, and increasing again for $p \approx 1$. We also note that, for a given a_1 the collision efficiency generally increases with increasing radius of the a_2-drop, i.e., with increasing p, and thus decreasing relative velocity between the drops.

The collision efficiencies computed by Schlamp *et al.* (1979) for the case of a negatively charged a_1-drop colliding with a positively charged a_2-drop in a negative electric field (i.e., Q_1E positive), were found to differ considerably from the values for a positively charged a_1-drop, computed by Schlamp *et al.* (1976). This is due mainly to the fact that the relative velocity difference of the drops and, hence, their interaction time are significantly different for the two cases. In addition, in some cases, collisions were found to occur both on the front as well as the rear hemisphere of the a_1-drop, or on the rear hemisphere only. Such rear collisions are examplified in Figure 18.9. In contrast, collisions with a positively charged drop in a negative field occurred only on the front hemisphere of the a_1-drop. These results lead to the conclusion (Schlamp *et al.*, 1979) that, in the latter case, the electrostatic forces dominate collision, while in the former case, collision is controlled by the hydrodynamic forces, which merely become enhanced by the electrostatic forces.

Unfortunately, no experimental verification is available for the collision efficien-

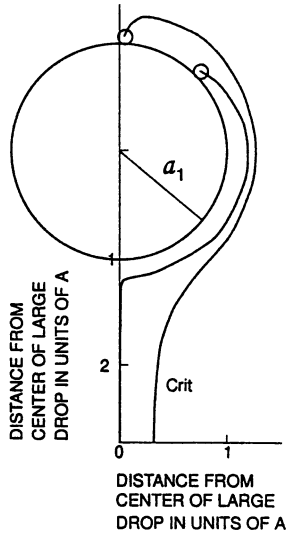


Fig. 18-9: Trajectories for a cloud drop of $a_2 = 2.4\ \mu$m moving past a larger drop of $a_1 = 40.2\ \mu$m for the case $\hat{Q}_1$ = -2 e.s.u. cm^{-2} = $-\hat{Q}_2$, E = -659 Volt cm^{-1}. The grazing trajectory is labelled Crit. (From Schlamp *et al.* 1979, with changes.)

cies computed by Schlamp *et al.* (1976, 1979), except for the study of Barker *et al.* (1983) who determined the collection efficiency of a_1-drops of 40 to 120 μm radius colliding with a_2-drops of 12 μm radius. The small drops were uncharged while the drops of radii between 40 and 80 μm and between 80 and 120 μm were either uncharged or carried a charge of 2×10^{-3} and 9×10^{-3} e.s.u, respectively. While the collision efficiency obtained with uncharged drops was near 0.8, agreeing well with the values computed by Schlamp *et al.*, the efficiencies obtained with charged a_1-drops were up to twice as large as those for uncharged a_1-drops. Unfortunately, Schlamp *et al.* (1979, 1976) did not apply their model to the case of charged a_1-drops and uncharged a_2-drops, so that no comparison with theory can be made. Some quantitative support for curves 3 and 5 in Figure 18.8a was provided by the analytical study of List and Freire (1981).

In addition to increasing the collision efficiency, electric fields and charges may raise the growth rate of cloud drops by increasing the fraction of 'colliding' drops which coalesce. In Section 14.5.4.1, we pointed out that drops of $a > 100\,\mu$m are likely to rebound from each other rather than coalesce, due to the presence of an air film temporarily trapped between their deformed surfaces as they collide. We would expect that this barrier to coalescence would be weakened by the forces of electrostatic attraction, and also by the local surface deformations which may result. These expectations have been verified by Lindblad (1964) and Semonin (1966), who found that, for millimeter-sized drops, the apparent delay time between collision and coalescence was strongly reduced if the potential difference across the colliding drops was raised to several Volts. Also, Goyer *et al.* (1960) observed that $\sim 34\%$ of 50 μm radius drops colliding with 300 to 400 μm radius drops coalesced if the electric field across them was raised to ~ 3 V cm^{-1}, while 95% of the colliding drops coalesced if the field was raised to ~ 40 V cm^{-1}. Jayaratne and Mason (1964) found that a critical electric field of ~ 100 V cm^{-1} was required to affect the coalescence of 150 μm radius drops impacting on a large essentially flat water target. Freier (1960) observed that the probability of coalescence between 2.5 μm drops began to be affected when the electric field exceeded ~ 300 V cm^{-1}. In agreement with this result, Jennings (1975) found that colliding drops always coalesced if $E > 250$ V cm^{-1}. Generally, the studies performed so far show that the larger the colliding drops, the higher the field required to enhance the efficiency with which the drops coalesce. This is expected from our discussion in Section 14.5.4.1, where we pointed out that the larger the colliding drops, the more pronounced is the deformation which the drops experience on collision, and thus the more extensive the air film trapped between the drops.

The effect of charges of opposite sign on the coalescence of water drops in air has been studied by Jayaratne and Mason (1964), Park (1970), Whelpdale and List (1971), and by Brazier-Smith *et al.* (1972). From these studies, it appears that for drops of $150 \lesssim a \lesssim 2000\,\mu$m, coalescence is affected only if the charge on the drops is larger than $\sim 10^{-4}$ e.s.u. For charges of magnitude 10^{-2} to 10^{-1} e.s.u., the two colliding drops were found always to coalesce.

A very detailed study with freely falling drop pairs of $a_1 = 340\,\mu$m and $a_2 = 190\,\mu$m were carried out by Czys and Ochs (1988) with drops charged to 2×10^{-15} C$\leq Q_1 \leq 2 \times 10^{-12}$ C and $Q_2 \approx 2 \times 10^{-14}$ C. Their study showed that,

regardless of charge, collisions which occurred at impact angles less than 43° always resulted in coalescence. Coalescence at larger impact angles depended critically on $|Q_1 - Q_2|$. For $|Q_1 - Q_2| \lesssim 7 \times 10^{-14}$ C ($\approx 2 \times 10^{-4}$ e.s.u.) no coalescence occurred. For 7×10^{-14} C$\leq |Q_1 - Q_2| \leq 2 \times 10^{-12}$ C temporary coalescence was observed. Coalescence occurred always if $|Q_1 - Q_2| \gtrsim 2 \times 10^{-12}$ C ($\approx 6 \times 10^{-3}$ e.s.u.). A glance at Figure 18.1 shows us that the charge requirement for 100% coalescence is met only in highly electrified thunderclouds. In all other clouds, the charge residing on drops of $a > 100\,\mu$m is probably less than that required for no rebound.

Unfortunately, no theoretical studies of the electrostatic enhancement of ice particle collision efficiencies are available in the literature. However, some related studies have been carried out. For example, the force expressions of Davis (1964a,b) for the case of two electrically conducting spheres have been extended by Hall and Beard (1975) and by Grover (1976a) to include the case of electrical interaction between a conducting sphere and a dielectric sphere, and by Davis (1969) for the case of electrical interaction between a conducting plate and a dielectric sphere. The results of these studies show that the calculated force constants are not sensitive to the dielectric constant ϵ of the sphere if $\epsilon > 80$, and agree essentially with the values found for $\epsilon = 10^8$, taken to represent a conducting sphere. Only for sphere separations smaller than $0.01a_1$ are there noticeable deviations from the conducting case. According to Halmbey and Harrott (1956), the static dielectric constant ϵ_w for water as a function of temperature is given by

$$\epsilon_w = 87.740 - 0.4008T + 9.398 \times 10^{-4}T^2 - 1.410 \times 10^{-6}T^3\,, \qquad (18\text{-}66)$$

with T in °C, for $0 \leq T \leq 100$°C ($\epsilon_w = 106.3 \pm 2$ at -35°C, according to Hodge and Angell, 1978). The static dielectric constant ϵ_i of ice has been determined by Gränicher (1963). His values are plotted in Figure 18.10. Since, for 0°C $\epsilon_w = 87.7$ and $\epsilon_i = 105$ (parallel to the c-axis), the conducting sphere assumption and thus the solution of Davis (1964a,b) may be taken to represent reasonably well the forces of interaction between either charged water spheres or charged ice spheres in an external electric field.

The effect of ice crystal shape on the force of interaction has been studied experimentally by Latham *et al.* (1965), and Latham and Saunders (1970) for the case of two uncharged metallic ice crystal models of various shapes arranged in various configurations. The measured forces could be made to agree closely with the force expressions of Davis merely by introducing a simple shape factor γ, which was essentially independent of the direction and strength of the background field, and of the separation of the crystals. Depending on the combination of crystal shapes, γ was found to range between ~ 0.5 and ~ 6; thus, in most cases, the forces between ice crystals are greater than between drops of the same volume as the crystals and separated by the same distance. Shape factors for the electrical interaction between a sphere and an ice crystal-shaped body were not determined. If charge resided on the crystal model, no corresponding simple modification of the Davis expressions was found to be adequate, since then the shape factor depended in an undetermined manner on the amount of charge present.

Martin *et al.* (1981) considered the effects of electric charges on the efficiency with which supercooled drops collide with planar snow crystals, which they ideal-

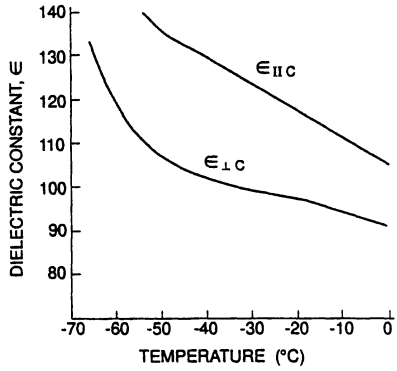


Fig. 18-10: Variation with temperature of the dielectric constant of ice perpendicular and parallel to the crystallographic c-axis. (From Gränicher, 1963, with changes.)

ized as thin oblate spheroids. Using the trajectory method, they solved

$$m_{\rm d}\frac{{\rm d}\vec{\rm v}_{\rm d}}{{\rm d}t} = m_{\rm d}\vec{\rm g}^{*} - \frac{\pi}{4}C_{\rm D,d}N_{\rm Re,d}a_{\rm d}\eta_{\rm a}(\vec{\rm v}_{\rm d} - \vec{\rm u}_c) + \vec{\rm F}_{e,{\rm d}}\,, \qquad (18\text{-}67)$$

to determine the trajectory of a drop around the crystal, and by switching the subcripts d and c to determine the trajectory of a crystal around the drop. The flow fields $\vec{\rm u}_c$ and $\vec{\rm u}_{\rm d}$ around the crystal and drop, respectively, were numerically determined (see Section 10.2.2.4). The electric force $\vec{\rm F}_{e,{\rm d}} = Q_d\vec{\rm E}$, acting on a drop was assumed to result from an interaction between the charge $Q_{\rm d}$ on the drop and the electric field $\vec{\rm E}$ around the ice crystal carrying a surface electric charge Q_c. They assumed the ice crystal is a perfect electric conductor satisfying the condition $\vec{\rm E} = -\nabla\Phi_c$, where Φ_c is the electric potential for the crystal. Taking this potential to be zero far away from the crystal and assuming no background electric field and no electric charges outside the ice spheroid, they solved $\nabla^2\Phi_c = 0$ in oblate spheroidal coordinates (see Happel and Brenner, 1965, p. 513) to determine Φ_c and, thus, $\vec{\rm E}$ and $\vec{\rm F}_{e,{\rm d}}$. The force $\vec{\rm F}_{e,c}$ exerted on the crystal by the spherical symmetric charge on the drop was assumed to be given by the Coulomb force $\vec{\rm F}_{e,c} = (Q_cQ_{\rm d}/R^2)\hat{\rm R}$, where R is the center to center distance between the interacting drop and crystal, and $\hat{\rm R}$ is the unit vector along this line. In determining the trajectories, it was assumed that the effects due to mutally induced charges could be neglected, and that the electric force on the crytal would not tip the crystal so that its largest dimension was always oriented horizontally. Computations were carried out for $51 \le a_c \le 639\,\mu$m, $1 \le a_{\rm d} \le 85\,\mu$m. $Q_{\rm d} = \hat{Q}_{\rm d}a_{\rm d}^2$, with $\mid \hat{Q}_{\rm d} \mid = 2.0$, and for $Q_c = \hat{Q}_ca_c^2$, with $\mid \hat{Q}_c \mid = 2.0$, equivalent to $5.2\times10^{-5} \le Q_c \le 8.2\times10^{-3}$ e.s.u., and $2\times10^{-8} \le Q_{\rm d} \le 14\times10^{-4}$ e.s.u. The results of this computation are displayed in Figure 18.11. We note from this figure that electric charges of opposite sign on drops and crystals considerably enhance the efficiency with which a planar crystals collide with drops. Of course, this enhancement becomes more pronounced the larger the charges on the drop and crystal.

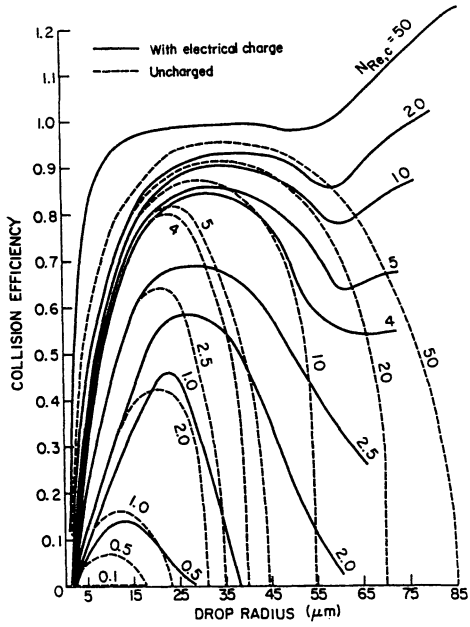


Fig. 18-11: Effect of electric charges on the efficiency with which supercooled drops are collected by simple plate-like snow crystals idealized as oblate spheroids of 0.05 axis ratio, for $-10°$C and 700 mb. (From Martin *et al.*, 1981; by courtesy of the Am. Meteor. Soc., and the authors.)

18.6.6 Scavenging of Aerosol Particles

As would be expected from the discussions of the previous sections, the efficiency with which aecosol particles are scavenged by cloud and raindrops can be strongly enhanced by the presence of drop charge and external electric fields. Grover and Beard (1975) and Grover (1976b) demonstrated this behavior through theoretical studies of the effect of charges and fields on the inertial impaction of aerosols. Grover *et al.* (1977) have carried out similar computations, including also the effect of phoretic forces. They studied the efficiency of scavenging of aerosol particles by water drops in air by means of the particle trajectory method discussed in Section 17.4.2.3, using an expanded version of (17-35), viz.,

$$m\frac{\mathrm{d}\vec{\mathrm{v}}}{\mathrm{d}t} = m\vec{g} - \frac{6\pi\eta_{\mathrm{a}}r}{1+\alpha N_{\mathrm{Kn}}}(\vec{\mathrm{v}}-\vec{\mathrm{u}}) + \vec{\mathrm{F}}_e + \vec{\mathrm{F}}_{\mathrm{Df}} + \vec{\mathrm{F}}_{\mathrm{Th}}\,, \tag{18-68}$$

where the thermophoretic force $\vec{\mathrm{F}}_{\mathrm{Th}}$, and the diffusiophoretic force $\vec{\mathrm{F}}_{\mathrm{Df}}$ were computed from (17-19) and (17-27), respectively, using numerically determined vapor density and temperature fields around evaporating water drops in air, and where the electric force $\vec{\mathrm{F}}_e$ on the aerosol particle due to the charge Q_{d} on the drop of radius a_1 was determined from the Davis (1964a,b) expressions in (A.18-3) and (A.18-4). The dynamic and electric effects of the aerosol particle on the drop were neglected.

As we have already pointed out in Chapter 17, the trajectory method can only be used to determine the efficiency with which relatively large particles of $r \geq 0.2\,\mu$m are captured by cloud drops, since effects due to Brownian diffusion are not included in this method. Wang *et al.* (1978) extended the 'particle flux' described in Section 17.4.2.5 to the case for electrically charged drops and aerosol particles. Although this method includes the capture due to Brownian diffusion and phoretic forces, it neglects particle capture by inertial impaction. Including the electric force, the current density of aerosol particles moving toward a stationary water drop is then, from (17-37),

$$\vec{\mathrm{J}} = nB_p(\vec{\mathrm{F}}_e + \vec{\mathrm{F}}_{\mathrm{Th}} + \vec{\mathrm{F}}_{\mathrm{Df}}) - D_p\nabla n\,, \tag{18-69}$$

where n, D_p, B_p are the number concentration, diffusivity and mobility of the aerosol particles, respectively, and where $\vec{\mathrm{F}}_{\mathrm{Th}}$ and $\vec{\mathrm{F}}_{\mathrm{Df}}$ are given by (17-19) and (17-27). For simplicity, Wang *et al.* (1978) assumed $\vec{\mathrm{F}}_e = (Q_aQ_r/R^2)\hat{\mathrm{R}}$, where R is the center to center distance between drop and aerosol particle. Analogously to (17-43a), the collision kernel for a moving drop becomes

$$K = \frac{4\pi B_p C_{\mathrm{Ph}}}{\exp(B_pC_{\mathrm{Ph}}/D_p\bar{f}_pa) - 1}\,; \tag{18-70}$$

however, now $C_{\mathrm{Ph}} = C_e + C_{\mathrm{Th}} + C_{\mathrm{Df}}$ with $C_e = Q_rQ_a$, and $\mathrm{E}_c = K/\pi(a+r)^2(U_{\infty,a} - U_{\infty,r})$.

A combination of the flux model and the trajectory model of Grover *et al.* (1977) has been given by Wang *et al.* (1978), assuming a variety of radii for the aerosol particles and drops. As an example, the collision efficiency as a function of particle-size is given for drops of radii $a = 72\,\mu$m ($Q_a \approx 3.3 \times 10^{-14}$ C) and $a = 310\,\mu$m ($Q_a \approx 6.4 \times 10^{-13}$ C) in Figures 17.17a,b. We note that the flux and trajectory method combined give a consistent description of the Greenfield gap, and the sensitivity of the depth, width, and position of this gap to phoretic and electric forces. We note that the presence of opposite electric charges on drop and aerosol particles causes a pronounced filling-in of the gap, while the effects of electric charges on particle capture becomes negligible for $r \gtrsim 1.0\,\mu$m and $r \lesssim 0.02\,\mu$m. We also note that a complete 'bridging' of the Greenfield gap is achieved neither through the effect of phoretic forces at typical atmospheric humidity nor through the effects of electric forces due to electric charges, as they are found in thunderstorm conditions. The results given in Figures 17.17a,b also show that, for given a, r and relative humidity, the collision efficiency increases with increasing electric charge (for drops and particles bearing charge of opposite sign). Also, for given r and relative humidity, the electrostatic influence on the collision efficiency increases with decreasing drop radius. Similarly, for $r \lesssim 0.1\,\mu$m, a given drop radius and relative humidity, the efficiency increases with decreasing particle radius.

These theoretical trends were confirmed experimentally by Wang *et al.* (1983), who showed that the collision efficiency increased: (1) as Q_r increased from 1.6×10^{-19} C to 2.2×10^{-18} C for $Q_a = 3.36 \times 10^{-11}$, $a = 250\,\mu$m, $r = 0.1\,\mu$m, (2) as a decreased from 300 to $50\,\mu$m for $Q_a = 4.18 \times 10^{-12}$ C, $Q_r = 1 \times 10^{-18}$ C,

TABLE 18.5

Effect of electical charges on the efficiency with which aerosol particles are captured by cloud drops. Comparison of values theoretically computed by Grover (1977 pers. comm.), based on the model of Grover *et al.* (1977), with the experimental values of Wang & Pruppacher (1977b).

a (μm)	r (μm)	Q_a (C)	Q_r (C)	E_{exp}	E_{theor}
170	0.25	4×10^{-13}	2.4×10^{-18}	1.8×10^{-2}	
174	0.25	4×10^{-13}	2.4×10^{-18}		1.6×10^{-2}
174	0.25	8×10^{-14}	1.4×10^{-18}		5.3×10^{-3}
180	0.25	8×10^{-14}	1.4×10^{-18}	5.0×10^{-3}	
310	0.25	1.1×10^{-12}	2.4×10^{-18}	5.6×10^{-3}	
312	0.25	1.1×10^{-12}	2.4×10^{-18}		8.1×10^{-3}
312	0.25	2.6×10^{-3}	1.4×10^{-18}		3.0×10^{-3}
340	0.25	2.6×10^{-13}	1.4×10^{-18}	3.6×10^{-3}	

$r = 0.1\,\mu$m, and (3) as r decreased from 0.10 to 0.03 μm for $Q_a = 2.77 \times 10^{-11}$ C, $a = 250\,\mu$m, and $Q_r = 1.6 \times 10^{-19}$ C.

A quantitative verification of the predictions of the trajectory model of Grover *et al.* (1977) was given by Wang and Pruppacher (1977b) for a few selected drop sizes and charges and aerosol particle of radius 0.25 μm carrying charges of either 1.4×10^{-18} C or 2.4×10^{-18} C. Their results are tabulated in Table 18.5.

Additional experiments have been carried out by Byrne and Jennings (1993), Barlow and Latham (1983), Lai *et al.* (1978), and Adam Semonin (1970). Unfortunately, most of these experiments were carried out for a variety of combinations of Q_a, Q_r, a, and r so that a quantitative comparison is neither possible among the experimental results themselves nor between the experimental and theoretical results. We nevertheless found it instructive to follow Barlow and Latham (1983) and plot the experimentally determined collision efficiencies available in one graph for $150 \leq a \leq 600\,\mu$m, $3 \times 10^{-15} \leq Q_a \leq 2 \times 10^{-11}$ C, and for submicron particles of opposite charge. This is illustrated in Figure 18.12 which demonstrates that the collision efficiency increases with increasing drop charge, although with a wide scatter of values being the result of the wide range of combinations of Q_a, Q_r, a and r. An additional reason for the scatter lies in the fact that for electrically charged drops and aerosol particles, rear collision are possible, and may or may not have been considered in computing the experimental collision efficiency (see Figure 18.13).

In evaluating the trajectory method (Grover and Beard, 1975), one may assume that the electric interaction between drop and aerosol particle is given by a simple Coulomb force between point charges rather than by the Davis (1964a,b) forces. In dimensionless form, (18-67) is then given by

$$\frac{d\vec{v}'}{dt} = \frac{\hat{z}}{N_{Fr}} - \frac{1}{N_S}(\vec{v}' - \vec{u}') - \frac{F_e'}{N_{Fr}}\hat{R}, \tag{18-71}$$

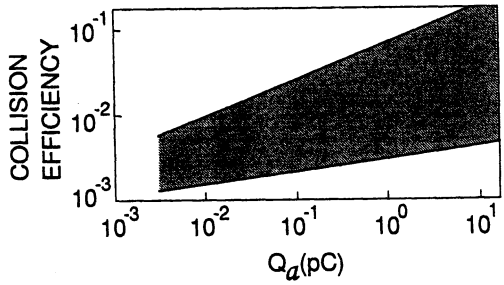


Fig. 18-12: Efficiency with which aerosol particles are captured by electrically charged drops. Based on observation of Barlow & Latham (1983), Lai *et al.* 1978), Adam & Semonin (1970), Wang & Pruppacher (1977b), Wang *et al.* (1983), Byrne & Jennings (1993), for drops of $150 \leq a \leq 600$ μm and submicron particles of opposite charge. (Based on Barlow and Latham, 1983, with changes.)

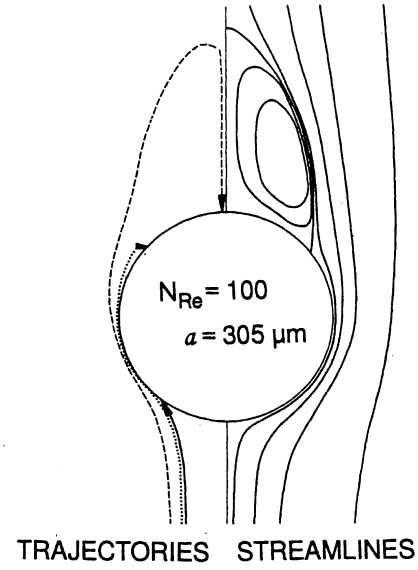


Fig. 18-13: Streamlines (on the right-hand side) and trajectories of aerosol particles (on the left-hand side) past a water drop of $a_1 = 305$ μm, for $r = 2.2$ μm. Solid trajectory $F_E = 0$, dotted trajectory F_E = -29, dashed trajectory F_E = -145. (From Grover & Beard, 1975, with changes.)

where $N_{\rm Fr}$ and $N_{\rm S}$ are given by $2U_\infty\rho_{\rm w}r^2(1+\alpha N_{\rm w})/9\eta_{\rm a}a$ and U_∞^2/g^*a, respectively, $t' = tU_\infty/a_1$, $\vec{v}' = \vec{v}/U_\infty$ and $\vec{u}' = \vec{u}/\vec{U}_\infty$, $F_e' = F_e/mg^*$, $F_e = Q_aQ_r/R^2$, R being the center to center distance between the interacting drop and aerosol particle, and where $\vec{g}^* = \vec{g}^*\hat{z}$, with $g^* = g(\rho_{\rm w} - \rho_{\rm a})/\rho_{\rm w}$. According to Grover and Beard (1975), we may define the electric force by

$$F_e \equiv Q_aQ_rN_S^{1/2}/a^2mg^*\,, \tag{18-72}$$

so that (18-71) becomes

$$\frac{{\rm d}\vec{v}'}{{\rm d}t} = \frac{\hat{z}}{N_{\rm Fr}} - \frac{1}{N_S}(\vec{v}' - \vec{u}') - \frac{F_e}{N_{\rm Fr}N_S^{1/2}}\frac{\hat{R}}{(R')^2}\,, \tag{18-73}$$

where $R' = R/a$. Grover and Beard (1975) analyzed (18-73) and compared the results with those obtained by using the Davis (1964a,b) forces. The comparison showed that the point charge model is sufficiently accurate for the charges found in atmospheric clouds as long as $a_1 \gtrsim 104\,\mu$m.

Kraemer and Johnstone (1955) defined a dimensionless Coulomb force parameter by the relation

$$K_e = \frac{F_eN_S^{1/2}}{N_{\rm Fr}} = \frac{Q_aQ_r(1+\alpha N_{\rm Kn})}{6\pi\eta_{\rm a}ra^2U_{\infty,a}}\,. \tag{18-74}$$

Assuming free streaming flow all the way to the drop surface, Kraemer and Johnston found that the efficiency with which charged drops collide with charged aerosol particles is given approximately by $4K_e$. This prediction was experimentally verified by Wang *et al.* (1983) for $50 \le a \le 300\,\mu$m, $4\times10^{-12} \le Q_a \le 3\times10^{-11}$ C, $0.03 \le r \le 0.10\,\mu$m, and $1.6\times10^{-19} \le Q_r \le 2.2\times10^{-18}$ C.

Martin *et al.* (1980c) applied the trajectory method of Grover *et al.* (1977) and the flux method of Wang *et al.* (1978) to plate-like snow crystals which were idealized by thin oblate spheroids of axis ratio b_c/a_c. Using the flow fields around thin oblate spheroids, Martin *et al.* (1980c) analyzed the trajectories of aerosol particles by determining the electric force on the particle from $\vec{F}_e = Q_r\vec{E}$, where $\vec{E} = -\nabla\Phi_c$, and Φ_c is the electric potential around the crystal computed in oblate spheroidal coordinates. In Figure 18.14, a plot of typical trajectories is given. We note that aerosol particles are preferentially deposited near the rim of falling plate-like snow crystals. In fact, we notice that rim deposition is even possible in the rear of the crystal. Using the flux model, Martin *et al.* (1980c) found for the collision kernel

$$K = \frac{4\pi B_pCa_c{\rm sech}[\tanh^{-1}(AR)]}{\left[\frac{\pi}{2} - \sin^{-1}(AR)\right]\left[\exp\left(\frac{B_pc}{D_p\bar{f}_p}\right) - 1\right]}\,, \tag{18-75}$$

where $C = C_{\rm Th} + C_{\rm Df} + C_e$, and

$$C_e = \frac{Q_cQ_r\sin^{-1}([1-(AR)^2]^{1/2})}{a_c[1-(AR)^2]^{1/2}}. \tag{18-76}$$

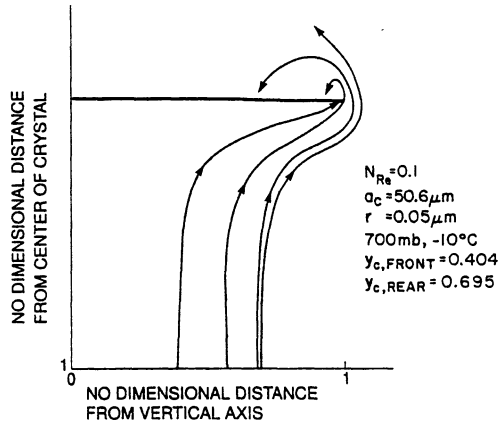


Fig. 18-14: Trajectories of an electrically charged particle of $r = 0.05$ μm past an electrically charged planar snow crystal of $a_c = 50.6$ μm falling at terminal velocity in air of $-10°$C and 700 mb, for $\hat{Q}_r = +2.0$ e.s.u. cm^{-2}, and $\hat{Q}_a = -2.0$ e.s.u. cm^{-2}. (From Martin *et al.*, 1980c, with changes.)

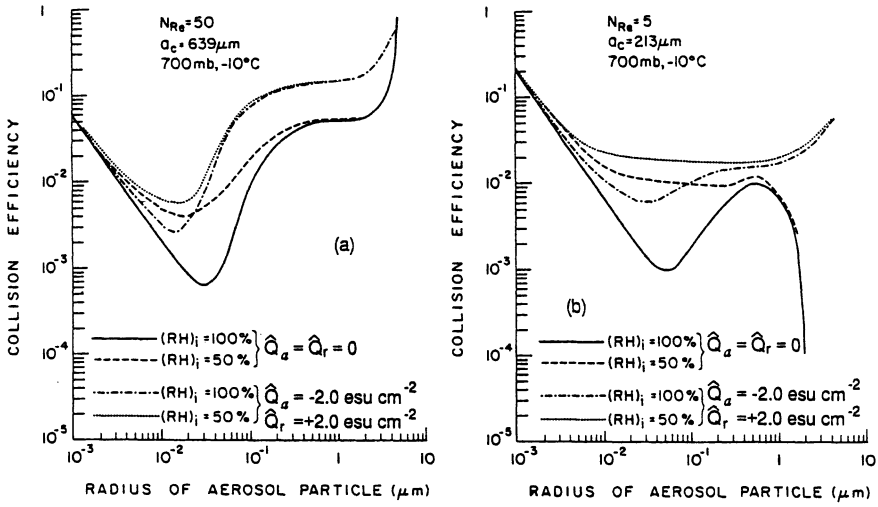


Fig. 18-15: Effect of electrical charge on the efficiency with which aerosol particles collide with a plate-like snow crystal idealized by an oblate spheroid of 0.05 axis ratio, in air of $-10°$C and 700 mb, and of various relative humidities with respect to ice, for $\rho_P = 2$ g cm^{-3}; (a) $a_c = 639$ μm, (b) $a_c = 213$ μm. (From Martin *et al.*, 1980c, with changes.)

From (18-75), the collision efficiency $E_c = K/\pi(a_c + r)^2(U_{\infty,c} - U_{\infty,r})$ may be found. Examples for the variation of the collision efficiency with particle radius are given in Figures 18.15a,b where the results of the trajectory and flux models have been combined. We note from these figures that electrical charges on crystal and aerosol particle significantly raise the collision efficiency above their uncharged values. Particularly, we note that electrical effects allow collision between crystals and particles, even for crystals which are sufficiently small, so that they are not able to capture aerosol particles above a certain size by hydrodynamic effecs alone.

Miller and Wang (1989) extended the model of Martin *et al.* (1980c) to columnar snow crystals. Their results are given in Figure 17.19 in the previous chapter. We note again the significant increase of the collision efficiency due to the effect of charges.

A qualitative experimental verification of the results of Martin *et al.* (1980c) has been given by Murakami *et al.* (1985c) who studied the effect of electric charges on planar snow crystals of 1.3 mm diameter. Their results are given in Figure 17.25a in the previous chapter. We note that electric charges on the snow crystals raise the collection efficiency by up to one order of magnitude above the efficiency observed for uncharged crystals.

APPENDICES

APPENDIX TO CHAPTER 2

A-2.1.5 Nearest Neighbor Distance Between Cloud Drops

Let $p(r)dr$ be the probability that the nearest neighbor to a given drop is located between a distance r and $r + dr$ from it. This probability is simply the product of the probability of no nearest neighbor between 0 and r, which is $1 - \int_0^r p(r)\,dr$, and the probability of a drop occurring between r and $r + dr$, which is $4\pi r^2 n dr$, where n is the average number concentration of drops. Therefore, we obtain the relation

$$p(r) = 4\pi r^2 n \left(1 - \int_0^r p(r)dr\right). \tag{A.2-1}$$

From this we find $dg/g = -4\pi r^2 n dr$, where $g = p/4\pi r^2 n$; hence $g = g_0 \exp(-4\pi r^3 n/3)$. From the condition $\int_0^\infty p(r)dr = 1$, we see that $g_0 = 1$, and so

$$p(r) = 4\pi r^2 n \exp\left(-4\pi r^3 \frac{n}{3}\right). \tag{A.2-2}$$

From A.2-2 the average nearest neighbor distance is

$$\overline{d} = \int_0^\infty r p(r)dr = \left(\frac{3}{4\pi n}\right)^{1/3} \int_0^\infty x^{1/3} e^{-x} dx, \tag{A.2-3}$$

in which we have set $x = 4\pi r^3 n/3$. The integral is $\Gamma(4/3)$, where Γ is the *gamma function*, so that finally we obtain

$$\overline{d} = \frac{0.554}{n^{1/3}}. \tag{A.2-4}$$

(Hertz, 1909; Underwood, 1969). In terms of the liquid water content, $w_L = 4\pi a^3 n/3$, where a is the characteristic drop radius, the result is

$$\frac{\overline{d}}{a} = \frac{\Gamma(4/3)}{w_L^{1/3}} = \frac{0.893}{w_L^{1/3}}. \tag{A.2-5}$$

The simple estimate of (2-10) is this seen to be quite accurate.

APPENDIX TO CHAPTER 4

A-4.8 Convenient Formulations for Determining the Saturation Vapor Pressure Over Water and Ice

(a) According to Lowe and Ficke (1974) and Lowe (1981 pers. comm.)

$$e_{sat} = a_0 + T(a_1 + T(a_2 + T(a_3 + T(a_4 + T(a_5 + Ta_6))))), \quad \text{(A.4-1)}$$

with T(°C) and e_{sat} in mb.

for water	*for ice*
$a_0 = 6.107799961$	$a0 = 6.10690449$
$a_1 = 4.436518521 \times 10^{-1}$	$a_1 = 5.02660639 \times 10^{-1}$
$a_2 = 1.428945805 \times 10^{-2}$	$a_2 = 1.87743264 \times 10^{-2}$
$a_3 = 2.650648471 \times 10^{-4}$	$a_3 = 4.13476180 \times 10^{-4}$
$a_4 = 3.031240396 \times 10^{-6}$	$a_4 = 5.72333773 \times 10^{-6}$
$a_5 = 2.034080948 \times 10^{-8}$	$a_5 = 4.71651246 \times 10^{-8}$
$a_6 = 6.136820929 \times 10^{-11}$	$a_6 = 1.78086695 \times 10^{-10}$

Range of validity: -50 to +50°C for water, -50 to 0°C for ice.

(b) According to the Magnus equation (Herbert, in: Landolt-Börnstein, New Series, Volume 4a, 1987)

- for water:

$$e_{sat,w} = e_{sat,w}(T_0) \exp\left[\frac{A_w(T - T_0)}{T - B_w}\right], \quad \text{(A.4-2)}$$

with $e_{sat,w}$ in hPa, T in °K, $e_{sat,w}(T_0) = 6.1070$ hPa.
$A_w = 17.15$ and $B_w = 38.25$ °K

- for ice:

$$e_{sat,i} = e_{sat,i}(T_0) \exp\left[\frac{A_i(T - T_0)}{T - B_i}\right], \quad \text{(A.4-3)}$$

with $e_{sat,i}$ in hPa, T in °K, $e_{sat,i}(T_0) = 6.1064$ hPa.
$A_i = 21.88$ and $B_i = 7.65$ °K

APPENDIX TO CHAPTER 7

A-7.1 Relations From Statistical Mechanics

Our purpose here is primarily to summarize relations from statistical mechanics which are used in this chapter. Where possible in the limited space available, we have also sketched in relevant

derivations. Of course, detailed treatments are available in any good reference on the subject (e.g., Landau and Lifshitz, 1958; Huang, 1963, Morse, 1969).

We need connecting links between thermodynamics and statistical mechanics. The most fundamental of these is the basic postulate, first stated by Boltzmann, which relates the entropy S for a thermodynamic macrostate of a system to the microstate distribution function f_ν:

$$S = -k \sum_\nu f_\nu \ln f_\nu. \tag{A.7-1}$$

The macrostate corresponds to an ensemble of systems with different microstates, and f_ν measures the probability that a system selected at random from the ensemble is in the microstate characterized by quantum numbers $(\nu_1, \nu_2, \ldots, \nu_\phi) \equiv \nu$, where ϕ is the number of degrees of freedom of the system. Of course, f_ν is subject to the normalization condition

$$\sum_\nu f_\nu = 1. \tag{A.7-2}$$

Canonical Ensemble

Consider a thermodynamic macrostate described by a system of N particles held at constant temperature T and volume V. The ensemble corresponding to this thermodynamic situation must be comprised of systems which also have constant T, V, and N. The energy E_ν of each system need not be constant, but the mean energy for the ensemble must satisfy the constraint

$$\sum_\nu f_\nu E_\nu = U = F + TS, \tag{A.7-3}$$

where U and F are respectively the internal energy and Helmholtz function for the thermodynamic system.

By the use of Lagrange multipliers one may readily solve for the f_ν which satisfies (A.7-1) and is subject to the constraints (A.7-2) and (A.7-3). On realizing that F is the thermodynamic function which is minimized for equilibrium at constant T and V (see (4-7)), and that S is maximized, the proper identification of the multipliers is straightforward and the following results are obtained:

$$f_\nu = Q^{-1} e^{-E_\nu/kT}, \tag{A.7-4}$$

where

$$Q = \sum_\nu e^{-E_\nu/kT} = e^{-F/kT}. \tag{A.7-5}$$

The ensemble corresponding to this distribution is called the *canonical ensemble*, and Q is called the *canonical partition function*. The result (A.7-5) provides another important link between thermodynamics and statistical mechanics.

If the interparticle forces in the system are negligible, the system energy will then be the sum of the separate energies of the individual particles, each depending only on its own set of quantum numbers. Then the sum in (A.7-5) will become a product of N factors, each of which will be a single-particle partition function. However, if the particles are indistinguishable, we must be careful to avoid counting the system microstates which are the same except for a reshuffling of the quantum numbers among the particles; rather, these must be regarded as the same microstate, which therefore is to be counted only once. For the cases of interest to us this bookkeeping problem can be resolved merely by dividing the product of N factors by N!. Thus, for example, the canonical partition function for a perfect gas of N molecules has the form

$$Q = q^N/N!, \tag{A.7-6}$$

where q is the partition function per molecule, i.e.,

$$q = \sum_j e^{-\varepsilon_j/kT} = e^{-\dot{F}/kT}, \tag{A.7-7}$$

where the sum runs over the allowed energies ε_j of the molecule, and $\dot{F}$ is the free energy per molecule.

The same process of factorization may be continued if the molecular energy can be written as the sum of separate contributions due to translation, rotation, etc.; then we can also write, in obvious notation,

$$q = q_T q_R \cdots . \tag{A.7-8}$$

Let us calculate the translational partition function q_T for a molecule in the volume V. For the classical context of interest to us, the energy levels are closely spaced and we may, for the sake of computational convenience, replace the indicated sum over energy levels by an integral over the Hamiltonian $H = p^2/2\,m$, where p is the momentum of the molecule, and m is its mass. For this purpose we must also take into account the fact that there are $h^{-\phi}(dV)_{ph}$ microstates corresponding to the phase space volume element $(dV)_{ph}$ where h is Planck's constant; this follows directly from the Heisenberg uncertainty principle. Thus we have, using Cartesian coordinates,

$$q_T = \frac{1}{h^3}\int_V dx\,dy\,dz \int_{-\infty}^{+\infty} dp_x\,dp_y\,dp_z e^{-p^2/2\,mkT} = V(2\,\pi mkT/h^2)^{3/2}. \tag{A.7-9}$$

In the same way one may obtain the rotational partition function for a molecule having the principal moments of inertia I_1, I_2, I_3:

$$q_R = \delta^{-1}(\pi I_1 I_2 I_3)^{1/2}(8\,\pi^2 kT/h)^{3/2}, \tag{A.7-10}$$

where δ is called the rotation symmetry number, and counts the number of physically indistinguishable orientations of the molecule.

Grand Canonical Ensemble

Let us now devise an ensemble (the *grand canonical ensemble*) in which we drop the requirement that the number of particles be fixed; instead, we require only that the average number of particles be specified as $\bar{N}$. In other respects the ensemble is to be chosen as before. A microstate for this ensemble is then specified by both the number of particles N the selected sample system has, and the quantum numbers $\nu_1, \nu_2, \ldots, \nu_{3N}$ which will determine its energy $E_{N,\nu}$. Thus for an equilibrium macrostate the distribution function $f_{N,\nu}$ must satisfy the following conditions:

$$\begin{aligned} &S = -k\sum_{N,\nu} f_{N,\nu} \ln f_{N,\nu} \quad \text{is maximum} \\ &\sum_{N,\nu} f_{N,\nu} = 1; \qquad \sum_{N,\nu} N f_{N\nu} = \bar{N} \\ &\sum_{N,\nu} E_{N,\nu} f_{N,\nu} = U = TS + \bar{N}\mu + \Omega, \end{aligned} \tag{A.7-11}$$

where μ is the chemical potential per particle, and $\Omega \equiv F - \mu\bar{N}$ is the *grand potential*, whose differential is

$$d\Omega = -S\,dT - \bar{N}\,d\mu - p\,dV. \tag{A.7-12}$$

The solution to (A.7-11) may be obtained via Lagrange multipliers as in the previous case; the results are:

$$f_{N,\nu} = \mathcal{Q}^{-1} \exp\left(\frac{\mu N - E_{N,\nu}}{kT}\right), \tag{A.7-13}$$

where the *grand canonical partition function* $\mathcal{Q}$ is

$$\mathcal{Q} = \sum_{N,\nu} \exp\left(\frac{\mu N - E_{N,\nu}}{kT}\right) = e^{-\Omega/kT}. \tag{A.7-14}$$

We see that $\mathcal{Q}$ is the sum of the canonical partition functions Q(N) for ensembles with different

values of N, each weighted by the factor $e^{\mu N/kT}$:

$$\mathcal{Q} = \sum_{N=0}^{\infty} e^{\mu N/kT} Q(N),$$
$$Q(N) = \sum_{\nu} e^{-E_{N,\nu}/kT}. \tag{A.7-15}$$

The relation (A.7-14) provides still another very useful connection between thermodynamics and statistical mechanics.

APPENDIX TO CHAPTER 10

A-10.1 Equation of Fluid Flow

The following is a somewhat descriptive development of the pertinent governing equations of fluid flow. More complete derivations may be found elsewhere (e.g., Landau and Lifshitz, 1959; Batchelor, 1967; White, 1974).

1. *Continuity Equation*

Consider a fluid of density ρ moving with velocity $\vec{u}$, both functions of position $\vec{r}$ and time t. If we follow a small fluid element of volume δV and mass $\delta m = \rho \delta V$ in its motion, the principle of conservation of mass tells us that

$$\frac{d\delta m}{dt} = \frac{d\rho}{dt}\delta V + \rho \frac{d\delta V}{dt} = 0,$$

where d/dt denotes differentiation following the moving element. The rate of change of δV is evidently given by the flux of $\vec{u}$ out of the surface δS enclosing δV. Therefore, from the divergence theorem we have to first order in δV (or, more concisely, simply from the definition of the divergence),

$$\frac{d\delta V}{dt} = \int_{\delta S} \vec{u} \cdot \hat{n}\, dS = \nabla \cdot \vec{u} \delta V,$$

where $\hat{n}$ is the unit outward normal associated with the surface element dS. The principle of mass conservation therefore becomes

$$\frac{d\rho}{dt} + \rho \nabla \cdot \vec{u} = 0, \tag{A.10-1}$$

which is known as the *continuity equation.* If $d\rho/dt = 0$, then $\nabla \cdot \vec{u} = 0$ and the flow is termed *incompressible.*

The first order change in any function $f(\vec{r}, t)$ due to changes in time dt and position $d\vec{r} = \vec{u}\, dt$ is

$$df = f(\vec{r} + \vec{u}\, dt; t + dt) - f(\vec{r}, t) = \vec{u} \cdot \nabla f\, dt + \frac{\partial f}{\partial t} dt,$$

which allows us to express d/dt as

$$\frac{d}{dt} = \frac{\partial}{\partial t} + \vec{u} \cdot \nabla. \tag{A.10-2}$$

Using (A.10-2), we can obtain another form of the continuity equation, involving the local time derivative $\partial/\partial t$:

$$\frac{\partial \rho}{\partial t} + \nabla \cdot (\rho \vec{u}) = 0. \tag{A.10-3}$$

2. *Navier-Stokes Equation*

An interior volume V of fluid with boundary surface S may be accelerated by external body forces, and by surface forces exerted on S by the fluid outside V. If we denote the external force per unit mass acting on volume element dV by $\vec{f}$, and the surface stress acting on surface element dS with outward normal $\hat{n}$ by $\vec{T}(\hat{n})$, the equation of motion of the fluid volume is

$$\frac{d}{dt}\int_V \rho\vec{u}\,dV = \int_V \rho\vec{f}\,dV + \int_S \vec{T}(\hat{n})\,dS. \tag{A.10-4}$$

In terms of the usual suffix notation, where suffices i, j take the values 1, 2, 3 corresponding to the components of vectors and second rank tensors along the x, y, z axes, respectively, the equation of motion is

$$\frac{d}{dt}\int_V \rho u_i\,dV = \int_V \rho f_i\,dV + \int_S T(\hat{n})_i\,dS. \tag{A.10-5}$$

If the volume V has a characteristic dimension ℓ, then $V \sim \ell^3$ and $S \sim \ell^2$. Consequently, if we let $\ell \to 0$ while preserving the shape of the volume, (A.10-5) reduces to the condition of local equilibrium:

$$\lim_{\ell\to 0}\left[(1/\ell^2)\int_S T(\hat{n})_i\,dS\right] = 0. \tag{A.10-6}$$

If (A.10-6) is applied to a small tetrahedron whose slant face has unit normal n_i and whose other faces are parallel to the coordinate planes, we easily find

$$T(\hat{n})_i = T_{ij}n_j, \tag{A.10-7}$$

where T_{ij} is the stress in the x_i direction acting on a surface element whose normal is in the x_j direction, and we have used the usual convention of summation over a double index. Since $T(\hat{n})_i$ and n_i are vectors, the quantities T_{ij} are components of a second rank tensor $\bar{T}$, called the *stress tensor*, which describes completely the system of stresses in a fluid.

It is also easy to show that $\bar{T}$ is symmetric, i.e.,

$$T_{ji} = T_{ij}. \tag{A.10-8}$$

This is an immediate consequence of applying the condition that there must be zero net torque on a small cube of fluid whose faces are parallel to the coordinate planes.

The effect of pressure $p(\vec{r}, t)$ in the fluid is to contribute an inward (compressional) normal stress on any surface element. Thus we may write

$$T_{ij} = -p\delta_{ij} + T''_{ij}, \tag{A.10-9}$$

where δ_{ij} (Kronecker delta symbol) is unity for $i = j$ and zero otherwise, and where T''_{ij} includes the stress contribution due to the viscosity of the fluid. For ordinary (Newtonian) fluids, of which air and water are examples, the viscous stress is proportional to the amount of relative motion taking place near the point in question. Thus, at least for small velocity gradients, T''_{ij} must be a linear function of the derivatives $\partial u_i/\partial x_j$. By also imposing the conditions that T''_{ij} must be symmetric and that $T''_{ij} = 0$ for pure rotation, in which case no internal friction can arise in the fluid, one obtains

$$T''_{ij} = \eta\left(\frac{\partial u_i}{\partial x_j} + \frac{\partial u_j}{\partial x_i}\right), \tag{A.10-10}$$

for an incompressible fluid. The factor η is called the *dynamic viscosity*. For the problems of interest to us η may be assumed constant.

On substituting (A.10-7) into (A.10-5), and using the divergence theorem to transform the surface integral into a volume integral, we obtain

$$\frac{d}{dt}\int_V \rho u_i\,dV = \int_V \left(\rho f_i + \frac{\partial T_{ij}}{\partial x_j}\right)dV. \tag{A.10-11}$$

Furthermore, if we use the mass continuity principle in the form $d\delta m/dt = 0$, we can write

$$\frac{d}{dt}\int_V u_i(\rho\, dV) = \int_V \frac{du_i}{dt}(\rho\, dV).$$

If this last result is substituted into (A.10-11) we obtain, in view of the arbitrariness of the choice of volume V,

$$\rho\frac{du_i}{dt} = \rho f_i + \frac{\partial T_{ij}}{\partial x_j}. \tag{A.10-12}$$

In vector notation, this (*Navier-Stokes*) equation of motion for the fluid is

$$\frac{\partial \vec{u}}{\partial t} + \vec{u}\cdot\nabla\vec{u} = -\frac{\nabla p}{\rho} + \vec{f} + \nu\nabla^2\vec{u}, \tag{A.10-13}$$

where ν , is the *kinematic viscosity*, and we have assumed the flow is incompressible.

A-10.2.2 Stream Function Formulation for Axisymmetric, Incompressible Flow

Consider steady incompressible flow past a fixed axisymmetric body. Let us describe the flow in terms of a right-handed, orthogonal, curvilinear coordinate system with its origin at the center of the body, and with coordinates (q_1, q_2, ϕ), where q_1 and q_2 describe position in any meridian plane. We may express the velocity field in this system as $\vec{v} = (u_1, u_2, 0)$. The condition $\nabla\cdot\vec{u} = 0$ then becomes

$$\frac{\partial}{\partial q_1}(h_2h_3u_1) + \frac{\partial}{\partial q_2}(h_1h_3u_2) = 0, \tag{A.10-14}$$

where the h's are the scale factors associated with the coordinates; i.e., $h_i\, dq_i$ is the element of arc length associated with dq_i. This equation is satisfied by choosing

$$h_2h_3u_1 = -\frac{\partial\psi}{\partial q_2}, \quad h_1h_3u_2 = \frac{\partial\psi}{\partial q_1}, \tag{A.10-15}$$

where ψ is the *stream function*. For example, in cylindrical coordinates $(z, \bar{\omega}, \phi)$ we have $h_1 = 1$, $h_2 = 1$, $h_3 = \bar{\omega}$, so that

$$u_z = -\frac{1}{\bar{\omega}}\frac{\partial\psi}{\partial\bar{\omega}}, \quad u_{\bar{\omega}} = \frac{1}{\omega}\frac{\partial\psi}{\partial z}. \tag{A.10-16}$$

Similarly, in spherical coordinates (r, θ, ϕ) we have $h_1 = 1$, $h_2 = r$, $h_3 = r\sin\theta$, so that

$$u_r = -\frac{1}{r^2\sin\theta}\frac{\partial\psi}{\partial\theta}, \quad u_\theta = \frac{1}{r\sin\theta}\frac{\partial\psi}{\partial r}. \tag{A.10-17}$$

It is easy to see that ψ = constant along a streamline by writing (A.10-15) in the form

$$\nabla\psi = -h_3\hat{e}_\phi\times\vec{u}, \tag{A.10-18}$$

where $\hat{e}_\phi$ is the unit vector in the ϕ direction. Therefore, we have $\nabla\psi\cdot\vec{u} = \vec{u}\cdot(\hat{e}_\phi\times\vec{u}) = \hat{e}_\phi\cdot(\vec{u}\times\vec{u}) = 0$. Since $\nabla\psi$ is normal to the line ψ = constant in any meridian plane, this line must be parallel to u everywhere.

Using the vector identities $\nabla^2\vec{u} = \nabla(\nabla\cdot\vec{u}) - \nabla\times(\nabla\times\vec{u})$ and $\vec{u}\cdot\nabla\vec{u} = 1/2\,\nabla u^2 - \vec{u}\times(\nabla\times\vec{u})$, the steady state Navier-Stokes equation becomes

$$(\nabla\times\vec{u})\times\vec{u} = -\nabla\left(\frac{u^2}{2} + \frac{p}{\rho}\right) - \nu\nabla\times(\nabla\times\vec{u}). \tag{A.10-19}$$

On taking the curl of this equation, we obtain

$$\nabla\times[(\nabla\times\vec{u})\times\vec{u}] = -\nu\nabla\times[\nabla\times(\nabla\times\vec{u})]. \tag{A.10-20}$$

In the system (q_1, q_2, ϕ) we have

$$\nabla \times \vec{u} = \frac{\hat{e}_\phi}{h_1 h_2}\left[\frac{\partial}{\partial q_1}(h_2 u_2) - \frac{\partial}{\partial q_2}(h_1 u_1)\right]. \tag{A.10-21}$$

Using (A.10-15) this becomes

$$\nabla \times \vec{u} = \frac{\hat{e}_\phi}{h_3} E^2\psi, \tag{A.10-22}$$

where

$$E^2 \equiv \frac{h_3}{h_1 h_2}\left[\frac{\partial}{\partial q_1}\left(\frac{h_2}{h_1 h_3}\frac{\partial}{\partial q_1}\right) + \frac{\partial}{\partial q_2}\left(\frac{h_1}{h_2 h_3}\frac{\partial}{\partial q_2}\right)\right]. \tag{A.10-23}$$

After carrying out all the indicated differentiations in (A.10-20), using (A.10-18) and (A.10-21) to (A.10-23), we obtain the governing equation for the flow in terms of the stream function:

$$\left[\nabla\psi \times \nabla\left(\frac{E^2\psi}{h_3^2}\right)\right] \cdot \hat{e}_\phi = \frac{\nu E^4}{h_3}, \tag{A.10-24}$$

where $E^4 \equiv E^2(E^2)$. In spherical coordinates, (A.10-24) becomes

$$\sin\theta\left[\frac{\partial\psi}{\partial r}\frac{\partial}{\partial\theta} - \frac{\partial\psi}{\partial\theta}\frac{\partial}{\partial r}\right]\left(\frac{E^2\psi}{r^2\sin^2\theta}\right) = \nu E^4\psi, \tag{A.10-25}$$

where

$$E^2 = \frac{\partial^2}{\partial r^2} + \frac{\sin\theta}{r^2}\frac{\partial}{\partial\theta}\left(\frac{1}{\sin\theta}\frac{\partial}{\partial\theta}\right). \tag{A.10-26}$$

For Stokes flow, the pressure may be easily recovered from the stream function by noting that

$$\nabla p = \frac{1}{\eta}\nabla^2\vec{u} = -\nabla \times (\nabla \times \vec{u}) = \frac{\hat{e}_\phi \times \nabla(E^2\psi)}{r\sin\theta}, \tag{A.10-27}$$

where $r\sin\theta$ is the radial distance from the symmetry axis.

A-10.3.3 Drop Oscillations

We follow here the treatment given in §61 of Landau and Lifshitz (1959). Assuming potential flow within the drop, the velocity potential Φ satisfies $\nabla^2\Phi = 0$. To solve this equation, the shape of the deformed drop must be specified. Since the shape is governed by (10-80), we must determine the sum $R_1^{-1} + R_2^{-1}$ for a slightly deformed sphere. To accomplish this, first note that the area of a surface $r = r(\theta, \phi)$ given in spherical coordinates (r, θ, ϕ) is

$$S = \int_0^{2\pi}\int_0^{\pi}\left[r^2 + \left(\frac{\partial r}{\partial\theta}\right)^2 + \frac{1}{\sin^2\theta}\left(\frac{\partial r}{\partial\phi}\right)^2\right]^{1/2} r\sin\theta\, d\theta\, d\phi. \tag{A.10-28}$$

Assuming $r = a_0 + \xi$ with $\xi \ll a_0$, (A.10-28) becomes

$$S = \int_0^{2\pi}\int_0^{\pi}\left\{(a_0+\xi)^2 + \frac{1}{2}\left[\left(\frac{\partial\xi}{\partial\theta}\right)^2 + \frac{1}{\sin^2\theta}\left(\frac{\partial\xi}{\partial\phi}\right)^2\right]\right\}\sin\theta\, d\theta\, d\phi. \tag{A.10-29}$$

Therefore, the variation in S due to a variation $\delta\xi$ is

$$\delta S = \int_0^{2\pi}\int_0^{\pi}\left\{2(a_0+\xi)\delta\xi + \frac{\partial\xi}{\partial\theta}\frac{\partial(\delta\xi)}{\partial\theta} + \frac{1}{\sin^2\theta}\frac{\partial\xi}{\partial\phi}\frac{\partial(\delta\xi)}{\partial\phi}\right\}\sin\theta\, d\theta\, d\phi \tag{A.10-30}$$

$$= \int_0^{2\pi}\int_0^{\pi}\left\{2(a_0+\xi) - \frac{1}{\sin\theta}\frac{\partial}{\partial\theta}\left(\sin\theta\frac{\partial\xi}{\partial\theta}\right) - \frac{1}{\sin^2\theta}\frac{\partial^2\xi}{\partial\phi^2}\right\}\delta\xi\sin\theta\, d\theta\, d\phi, \tag{A.10-31}$$

This last result has been obtained by integrating the second and third terms in (A.10-30) by parts with respect to θ and ϕ, respectively.

Another expression for δS is available from (10-78) and (10-79), viz.,

$$\delta S = \int \delta \, dS = -\int \frac{(p_e - p_i)}{\sigma} \delta\xi \, dS = \int \left(\frac{1}{R_1} + \frac{1}{R_2}\right) \delta\xi \, dS, \tag{A.10-32}$$

where the integral is taken over the closed surface. In spherical coordinates, $dS = r^2 \sin\theta \, d\theta \, d\phi = a_0(a_0 + 2\xi) \sin\theta \, d\theta \, d\phi$ to first order in ξ. Therefore, on comparing (A.10-31) and (A.10-32) we obtain the result

$$\frac{1}{R_1} + \frac{1}{R_2} = \frac{2}{a_0} - \frac{2\xi}{a_0^2} - \frac{1}{a_0^2}\left[\frac{1}{\sin^2\theta}\frac{\partial^2\xi}{\partial\phi^2} + \frac{1}{\sin\theta}\frac{\partial}{\partial\theta}\left(\sin\theta\frac{\partial\xi}{\partial\theta}\right)\right]. \tag{A.10-33}$$

For small amplitude potential flow, the Navier-Stokes equation reduces to $\partial\vec{u}/\partial t = -\nabla p/\rho_w$. Therefore, in terms of the velocity potential

$$\rho_w \frac{\partial\Phi}{\partial t} + p = p_e, \tag{A.10-34}$$

where p_e is the constant exterior pressure (gravity effects are ignored). Then from (10-80), (A.10-33), and (A.10-34), the boundary condition at $r = a_0$ for Φ is

$$\rho_w \frac{\partial\Phi}{\partial t} + \sigma\left\{\frac{2}{a_0} - \frac{2\xi}{a_0^2} - \frac{1}{a_0^2}\left[\frac{1}{\sin^2\theta}\frac{\partial^2\xi}{\partial\phi^2} + \frac{1}{\sin\theta}\frac{\partial}{\partial\theta}\left(\sin\theta\frac{\partial\xi}{\partial\theta}\right)\right]\right\} = 0. \tag{A.10-35}$$

To eliminate reference to ξ, we differentiate (A.10-35) with respect to time, and note that $\partial\xi/\partial t = u_r = \partial\Phi/\partial r$. The result at $r = a_0$ is

$$\rho_w \frac{\partial^2\Phi}{\partial t^2} - \frac{\sigma}{a_0^2}\left\{2\frac{\partial\Phi}{\partial r} + \frac{\partial}{\partial r}\left[\frac{1}{\sin^2\theta}\frac{\partial^2\Phi}{\partial\phi^2} + \frac{1}{\sin\theta}\frac{\partial}{\partial\theta}\left(\sin\theta\frac{\partial\Phi}{\partial\theta}\right)\right]\right\}. \tag{A.10-36}$$

If we seek a solution in the form of a stationary wave, then $\Phi = e^{i\omega t}\psi$, where $\nabla^2\psi = 0$. In spherical coordinates, therefore, the velocity potential is of the form

$$\Phi = Ae^{i\omega t} r^n P_n^m(\cos\theta) e^{im\phi}, \tag{A.10-37}$$

where $P_n^m(\cos\theta)$ is the associated Legendre function. Finally, on substituting (A.10-37) into (A.10-36), and using the fact that $Y_{nm} \equiv P_n^m(\cos\theta)e^{im\phi}$ satisfies

$$\frac{1}{\sin\theta}\frac{\partial}{\partial\theta}\left(\sin\theta\frac{\partial Y_{nm}}{\partial\theta}\right) + \frac{1}{\sin^2\theta}\frac{\partial^2 Y_{nm}}{\partial\phi^2} + n(n+1)Y_{nm} = 0,$$

we find a discrete set of allowed angular frequencies, namely

$$\omega_n^2 = \frac{n(n-1)(n+2)\sigma}{\rho_w a_0^3}. \tag{A.10-38}$$

Since ω_n is independent of m, there are $2n+1$ different oscillatory modes ($m = 0, \pm 1, \ldots, \pm n$) corresponding to each ω_n. Thus the asymmetric modes have the same frequencies as the axisymmetric modes of the same n.

A-10.3.5 Rayleigh-Taylor Instability of Two Superposed Fluids

We consider the stability of two superposed inviscid fluids in a vertical circular cylinder, following the treatment given in Chapter 4 of Yih (1965).

Denote the lower fluid density by ρ and the upper by ρ' ($\rho' > \rho$). Let the axis of the cylinder be along the vertical z-axis. Assume potential flow, and let the velocity potentials be Φ and Φ'.

The boundary conditions at the cylinder wall are that the radial velocities must vanish, so that in cylindrical coordinates (r, θ, z) we have

$$\frac{\partial\Phi}{\partial r} = \frac{\partial\Phi'}{\partial r} = 0 \quad \text{at} \quad r = a. \tag{A.10-39}$$

The kinematic condition at the fluid interface is that the vertical velocity is continuous, or

$$\frac{\partial \Phi}{\partial z} = \frac{\partial \Phi'}{\partial z} = \frac{\partial \xi}{\partial t} \quad \text{at} \quad z = \xi, \tag{A.10-40}$$

where ξ is the displacement of the interface. (When there is no motion, the interface is at $z = 0$.) If p and p′ denote the perturbation pressures associated with the potential flow, then from arguments parallel to those used in deriving (A.10-33) we have the following dynamic boundary condition at the interface:

$$p' - p = \sigma \left(\frac{\partial^2 \xi}{\partial r^2} + \frac{1}{r}\frac{\partial \xi}{\partial r} + \frac{1}{r^2}\frac{\partial^2 \xi}{\partial \theta^2} \right). \tag{A.10-41}$$

Assuming the upper fluid extends to $z \to +\infty$ and the lower fluid to $z \to -\infty$, and recognizing that $\nabla^2 \Phi = \nabla^2 \Phi' = 0$, suitable particular solution forms for the velocity potentials are

$$\begin{aligned} \Phi &= c \exp(\alpha t + k_m z) \cos n\theta J_n(k_m r), \\ \Phi' &= c' \exp(\alpha t - k_m z) \cos n\theta J_n(k_m r), \end{aligned} \tag{A.10-42}$$

where J_n is the Bessel function of the n^{th} order. The eigenvalues k_m are roots of the equation

$$J_n'(kr) = dJ_n(kr)/dr = 0 \quad \text{at} \quad r = a.$$

These solutions thus satisfy the conditions (A.10-39).

To satisfy (A.10-40), we set

$$\xi = a e^{\alpha t} \cos n\theta \, J_n(kr), \tag{A.10-43}$$

and find

$$ck = -c'k = \alpha a, \tag{A.10-44}$$

by imposing (A.10-40) at $z = 0$ (ξ is regarded as an infinitesimal disturbance).

For small amplitude inviscid flow, the Navier-Stokes equation in the presence of gravity reduces to $\partial \tilde{u}/\partial t = -\rho^{-1}\nabla p - \nabla(gz)$, so that the pressures can be found from the (Bernoulli) equations

$$\frac{p}{\rho} = -\frac{\partial \Phi}{\partial t} - g\xi \quad \text{and} \quad \frac{p'}{\rho'} = -\frac{\partial \Phi}{\partial t} - g\xi. \tag{A.10-45}$$

On substituting (A.10-42), (A.10-43), and (A.10-45) into (A.10-41) for $z = 0$, we obtain

$$\rho(-\alpha c + ga) - \rho'(-\alpha c' + ga) = \sigma k^2 a. \tag{A.10-46}$$

Finally, by eliminating c, c′, and a from (A.10-44) and (A.10-46), the value of α is determined in terms of the physical parameters ρ, ρ', and σ, and the eigenvalue k:

$$\alpha^2 = \frac{g(\rho' - \rho)k}{\rho + \rho'} - \frac{\sigma k^3}{\rho + \rho'}. \tag{A.10-47}$$

Therefore, if

$$k < k_c = \left[\frac{g(\rho' - \rho)}{\sigma} \right]^{1/2}, \tag{A.10-48}$$

the fluid is unstable, since then the amplitude of the disturbance will grow exponentially in time. It is noteworthy that this result is valid for any cross-sectional shape, which only affects the eigenvalues of k. In particular, (A.10-48) holds for the case $a \to \infty$, i.e., two semi-infinite fluids with an interface.

APPENDIX TO CHAPTER 11

A-11.4 Mutal Sedimentation and Diffusion of Aerosol Particles

The solution to (11-24) is facilitated by making the change of variable from n to n', where

$$n(z,t) = n'(z,t) \exp\left(-\frac{V_s z}{2D} - \frac{V_s^2 t}{4D} \right). \tag{A.11-1}$$

Substitution of (A.11-1) into (11-24) reduces the latter to the standard diffusion equation for n':

$$\frac{\partial n'}{\partial t} = D\nabla^2 n'. \tag{A.11-2}$$

From the initial and boundary conditions specified in Section 11.4, namely that $n(z,0) = n_0 =$ constant and $n(0,t) = 0$, we find the corresponding conditions on n': $n'(z,0) = n_0 \exp(V_s z/2D)$ and $n'(0,t) = 0$. This problem may be reduced to one without boundary conditions by extending the solution to include the region $z < 0$, where we assume an initial distribution which simulates the actual boundary condition at $z = 0$ for all $t > 0$. This can be accomplished by choosing $n'(z,0) = -n'(-z,0)$, so that for the extended region the initial condition is

$$n'(z,0) = \begin{cases} n_0 \exp(V_s z/2D), & z > 0 \\ -n_0 \exp(-V_s z/2D), & z < 0 \end{cases} \tag{A.11-3}$$

Our problem is now one of solving the diffusion equation for a specified initial distribution in an unbounded medium. This can be accomplished by expanding the desired solution as a Fourier integral:

$$n'(z,t) = \int_{-\infty}^{+\infty} \Phi(k,t) e^{ikz} \mathrm{d}k, \tag{A.11-4}$$

$$\Phi(k,t) = \frac{1}{2\pi} \int_{-\infty}^{+\infty} n'(z',t) e^{-ikz'} \mathrm{d}z'. \tag{A.11-5}$$

On substituting (A.11-4) into (A.11-2) we find $\partial\Phi/\partial t + k^2 D\Phi = 0$; the solution is $\Phi(k,t) = \Phi(k,0)e^{-k^2 Dt}$, where $\Phi(k,0)$ is obtained by substituting the initial distribution for n' into (A.11-5). Therefore, (A.11-4) may be expressed as an integral over the specified initial distribution as follows:

$$n'(z,t) = \frac{1}{2\pi} \int_{-\infty}^{+\infty} \int_{-\infty}^{+\infty} n'(z',0) e^{-k^2 Dt} e^{ik(z-z')} \mathrm{d}z' \, \mathrm{d}k. \tag{A.11-6}$$

The integration over k is easily carried out, when the solution for n' becomes

$$n'(z,t) = \frac{1}{(4\pi Dt)^{1/2}} \int_{-\infty}^{+\infty} n'(z',0) \exp[-(z-z')^2/4Dt] \mathrm{d}z'. \tag{A.11-7}$$

The solution may now be completed by substituting (A.11-3) into (A.11-7) and integrating. The result in terms of $n(z,t)$ is given by (11-25), where $\mathrm{erf}(x) \sim (2/\pi^{1/2}) \int_0^x e^{-x^2} \mathrm{d}x$.

APPENDIX TO CHAPTER 14

A-14.3 Superposition Method for Stokes Flow

As an illustration of the use of the superposition method, we shall consider the special case of two spheres falling in the x-direction in Stokes flow. The situation is depicted in Figure A.14-1. For the velocity field $\vec{u}_1$ generated by sphere-1 we write $\vec{u}_1 = \vec{u}_1(r_1, \theta_1)$, where θ is the polar angle between $\vec{r}_1$ and the x_1-axis. Then according to (14-7) the hydrodynamic forces on the two spheres are

$$\vec{F}_1 = -6\pi a_1 \eta[\vec{v}_1 - \vec{u}_2(d, \Theta + \pi)], \tag{A.14-6a}$$

$$\vec{F}_2 = -6\pi a_2 \eta[\vec{v}_2 - \vec{u}_1(d, \Theta)], \tag{A.14-6b}$$

where $\vec{v}_1 = v_1 \hat{e}_x$, $\vec{v}_2 = v_2 \hat{e}_x$, d is the separation of the sphere centers, and Θ is the angle between the line of centers and the direction of fall. The unit vectors $\hat{e}_r$, $\hat{e}_\theta$, $\hat{e}_x$ and $\hat{e}_y$ satisfy the following

relations: (a) along the line of centers, $\hat{e}_{r,1} = -\hat{e}_{r,2}$, $\hat{e}_{\theta,1} = -\hat{e}_{\theta,2}$; (b) $\hat{e}_{r,1} = \hat{e}_x \cos\Theta + \hat{e}_y \sin\Theta$, $\hat{e}_{\theta,1} = -\hat{e}_x \sin\Theta + \hat{e}_y \cos\Theta$. Therefore the forces may be expressed as

$$-\frac{\vec{F}_1}{6\pi a_1 \eta v_1} = \Lambda_1 \hat{e}_x + \Gamma_1 \hat{e}_y, \tag{A.14-7a}$$

$$-\frac{\vec{F}_2}{6\pi a_2 \eta v_2} = \Lambda_2 \hat{e}_x + \Gamma_2 \hat{e}_y, \tag{A.14-7b}$$

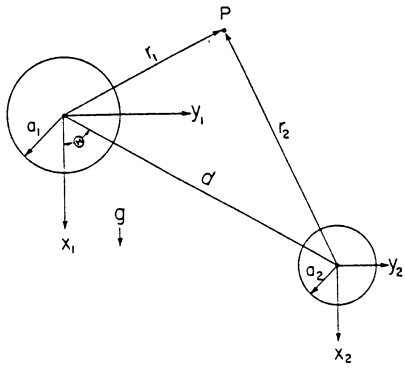


Fig. A.14-1. Geometrical relations for the two sphere problem.

where

$$\Lambda_1 = 1 + \frac{u_{r,2}(d, \Theta+\pi)\cos\Theta - u_{\theta,1}(d, \Theta+\pi)\sin\Theta}{v_1}, \tag{A.14-8}$$

$$\Gamma_1 = \frac{u_{r,2}(d, \Theta+\pi)\sin\Theta + u_{\theta,2}(d, \Theta+\pi)\cos\Theta}{v_1}, \tag{A.14-9}$$

$$\Lambda_2 = 1 + \frac{u_{\theta,1}(d, \Theta)\sin\Theta - u_{r,1}(d, \Theta)\cos\Theta}{v_2}, \tag{A.14-10}$$

$$\Gamma_2 = \frac{-u_{r,1}(d, \Theta)\sin\Theta - u_{\theta,1}(d, \Theta)\cos\Theta}{v_2}. \tag{A.14-11}$$

Assuming Stokes flow, from (10-35) and (A.10-17) we have

$$\frac{\tilde{u}_1}{v_1} = \frac{\cos\theta_1}{2}\left(\frac{3a_1}{d} - \frac{a_1^3}{d^3}\right)\hat{e}_{r,1} - \frac{\sin\theta}{4}\left(\frac{3a_1}{d} + \frac{a_1^3}{d^3}\right)\hat{e}_{\theta,1}, \tag{A.14-12}$$

and similarly for $\tilde{u}_2$. As a result the dimensionless forces are

$$\Lambda_1 = 1 - \frac{v_2}{v_1}\left[(3\beta - \beta^3)\frac{\cos^2\Theta}{2} + (3\beta + \beta^3)\frac{\sin^2\Theta}{4}\right], \tag{A.14-13}$$

$$\Gamma_1 = -\frac{3v_2}{4v_1}\beta(1+\beta^2)\sin\Theta\cos\Theta, \tag{A.14-14}$$

$$\Lambda_2 = 1 - \frac{v_1}{v_2}\left[(3\alpha - \alpha^3)\frac{\cos^2\Theta}{2} + (3\alpha + \alpha^3)\frac{\sin^2\Theta}{4}\right], \tag{A.14-15}$$

$$\Gamma_2 = -\frac{3v_1}{4v_2}\alpha(1+\alpha^2)\sin\Theta\cos\Theta, \tag{A.14-16}$$

where $\alpha = a_1/d$ and $\beta = a_2/d$.

According to (A.14-13) and (A.14-15), the dimensionless drag (x-component) force acting on either

sphere of an equal pair falling side by side ($\Theta = \pi/2$) is

$$\Lambda_1 = \Lambda_2 = 1 - \frac{3}{4}\alpha - \frac{\alpha^3}{4}. \tag{A.14-17}$$

For motion along the line of centers ($\Theta = 0$), the result is

$$\Lambda_1 = \Lambda_2 = 1 - \frac{3}{2}\alpha + \frac{\alpha^3}{2}. \tag{A.14-18}$$

For touching spheres ($\alpha = 1/2$) we have $\Lambda = 0.313$ for $\Theta = 0$ and $\Lambda = 0.594$ for $\Theta = \pi/2$. These values compare rather poorly with the known rigorous results $\Lambda = 0.645$ for $\Theta = 0$ and $\Lambda = 0.725$ for $\Theta = \pi/2$ (see Appendix A-14.4.2), showing the superposition scheme to be indeed rather inaccurate for spheres of comparable size in close proximity. (If the spheres are free to rotate as they fall side by side, a slight reduction in drag results: $\Lambda = 0.715$.) Note spheres falling side by side experience a greater resistance than when falling along their line of centers, in agreement with intuition since the latter configuration is the more streamlined of the two.

We also see from (A.14-4) and (A.14-16) that there are no transverse (lift) forces acting on spheres falling side by side in Stokes flow: $\Gamma_1 = \Gamma_2 = 0$ for $\Theta = \pi/2$. This result happens to be true rigorously for Stokes flow.

APPENDIX TO CHAPTER 15

A-15.3.1.2 Correlations in a Stochastic Coalescence Process (Bayewitz *et al.*, 1974)

1. *Formulation of the Stochastic Model*

Suppose that at time $t + dt$ the aerosol contains N_k droplets of size k, for $k = 1, 2, \ldots, L$. Suppose also that the aerosol is well-mixed, and that the probability per unit time of coalescences between any pair of droplets is a constant, $A_{ik} = A$. Let N denote the total number of droplets present: $N = \Sigma_k N_k$. For notational purposes it is convenient to describe the state as an ordered list, $N, N_1, N_2, \ldots, N_L$. This facilitates the description of neighboring states; e.g., $N, N_1, N_2 + 1, \ldots, N_L$ is meant to denote another state, identical to the first except for an additional double droplet.

Now we pose the following question: From what states could the distribution at $t + dt$ have evolved in time dt, assuming that at most one coalescence could occur in the entire system during the interval? The answer is that there are three possible routes: (1) a coalescence occurs between two droplets of the same size; (2) a coalescence occurs between two droplets of different size; (3) no coalescence occurs.

We now consider the first route. If the system is to reach the desired distribution at $t + dt$ through a coalescence of two droplets of size m, it must be, at time t, in the state $N + 1, N_1, N_2, \ldots, N_m + 2, \ldots, N_{2m} - 1, \ldots, N_L$. Let the probability of this state be denoted by $v(N + 1, N_1, N_2, \ldots, N_m + 2, \ldots, N_{2m} - 1, \ldots, N_L; t)$. Since the probability that any two droplets will coalesce in dt is A dt, the probability that any two droplets of size m will coalesce in the interval $(t, t + dt)$ is just $\binom{N_m+2}{2}$A dt. Accordingly, the product of these probabilities, summed over m to account for all the possible mutually exclusive outcomes, gives the total transition probability in dt for route 1):

$$\sum_m v(N + 1, N_1, N_2, \ldots, N_m + 2, \ldots, N_{2m} - 1, \ldots, N_L; t)\binom{N_m + 2}{2} A\, dt. \tag{A.15-1}$$

Similarly, if the system is to reach the desired distribution through a coalescence of droplets of size m and n, it must be, at time t, in the state $N + 1, N_1, N_2, \ldots, N_m + 1, \ldots, N_n + 1, \ldots, N_{m+n} - 1, \ldots, N_L$. The probability of coalescence of two particles of sizes m and n in the interval $(t, t + dt)$ is $(N_m + 1)(N_n + 1)$A dt. Hence the desired transition probability for route 2) is

$$\sum_{m<n}\sum v(N + 1, N_1, N_2, \ldots, N_m + 1, \ldots, N_n + 1, \ldots, N_{m+n} - 1, \ldots, N_L; t) \times (N_m + 1)(N_n + 1) A\, dt. \tag{A.15-2}$$

The condition $m<n$ is included to avoid counting the same coalescence event twice. The transition

probability for the desired distribution at time t and no coalescence between t and $t + dt$ is

$$v(N, N, N_2, \ldots; t)\left[1 - \binom{N}{2} A\, dt\right]. \tag{A.15-3}$$

The probability $v(N, N_1, N_2, \ldots, t + dt)$ of having the desired distribution at time $t + dt$ is just the sum of the three mutually exclusive probabilities assembled above. From this mathematical statement one immediately obtains the fundamental equation for the stochastic description:

$$\frac{dv}{dt}(N, N_1, N_2, \ldots; t) = A \sum_{m<n} \sum v(N+1, N_1, N_2, \ldots, N_m + 1, \ldots, N_n + 1, \ldots,$$

$$N_{m+n} - 1, \ldots; t)(N_m + 1)(N_n + 1) + A \sum_m v(N+1, N_1, N_2, \ldots,$$

$$N_{m+2}, \ldots, N_{2m} - 1, \ldots, t)\binom{N_m + 2}{2} - Av(N, N_1, N_2, \ldots; t)\binom{N}{2}. \tag{A.15-4}$$

2. *Total Number of Particles*

The probability $v_N(t)$ of having N droplets of arbitrary size at time t is evidently just

$$v_N(t) = \sum_{\text{over all } N_m} \cdots \sum v(N, N_1, N_2, \ldots; t). \tag{A.15-5}$$

Therefore, summing over (A.15-4) leads to the equation governing v_N:

$$\frac{dv_N}{dt} = A\binom{N+1}{2} v_{N+1} - A\binom{N}{2} v_N. \tag{A.15-6}$$

[This equation may also be arrived at more directly. Thus, the probability of having N + 1 droplets of arbitrary size is v_{N+1}, and the number of ways of producing a set of N droplets of arbitrary size from the set of N + 1 arbitrary droplets via binary coalescences is $\binom{N+1}{2}$. Therefore, the 'rate of production' of the probability v_N associated with the set of N droplets of arbitrary size is just the first term on the right side of (A.15-6). Similar arguments account also for the second (loss rate) term on the right side.]

The coupled, linear equation set contained in (A.15-6) may be solved sequentially. For the initial conditions $v_N(0) = 0$ for $N \neq N_0$ and $v_N(0) = 1$ for $N = N_0$, the solution to (A.15-6) is

$$v_N(t) = \sum_{k=N}^{N_0} \frac{(-1)^{k+N}(2k-1)(k+N+2)!}{N!(N-1)!(k-N)!} \prod_{\nu=0}^{k-1} \binom{N_0 - \nu}{N_0 + \nu} e^{-A\binom{k}{2}t}. \tag{A.15-7}$$

Therefore, the mean number of droplets at time t is

$$\langle N \rangle = \sum_N N v_N = \sum_{k=N}^{N_0} (2k-1) \prod_{\nu=0}^{k-1} \binom{N_0 - \nu}{N_0 + \nu} e^{-A\binom{k}{2}t}. \tag{A.15-8}$$

It is of interest to compare (A.15-8) with the corresponding result from the SCE. As we have seen, the SCE arises from the quasi-stochastic model in which N is uniquely determined. For the present situation in which every pair of the N droplets has the same coalescence probability, the equation governing N is evidently given by $dN/dt = -A\binom{N}{2} = -AN(N-1)/2$. The solution for $N(0) = N_0$ is

$$N(t) = \frac{N_0}{N_0 - (N_0 - 1)e^{-At/2}}. \tag{A.15-9}$$

[This is the result obtained by Bayewitz *et al.* (though in a slightly different manner), and they refer to it as following from the SCE. However, this is not quite so: on summing the discrete SCE over the index k, we get $dN/dt = -AN^2/2$; thus the solution for $N(0) = N_0$ is $N(t) = N_0(1 + N_0At/2)^{-1}$. However, the two expressions for N differ very little except in the limit of large t (i.e., $t \gg A^{-1}$); then (A.15-9) predicts $N \to 1$, while the SCE yields $N \to 0$. In general, the SCE approximates the coalescence rate of droplets of size k, $A_{kk}N_k(N_k - 1)/2$, by the expression $A_{kk}N_k^2/2$. Fortunately, the resulting error is unimportant.]

Evaluation of (A.15-8) and (A.15-9) shows that N(t) according to the SCE is an excellent approximation to the true mean $\langle N \rangle$, even for droplet counts as small as $N_0 = 10$. Therefore, it appears the SCE theory produces total particle counts in excellent agreement with the true stochastic averages, even for very small initial populations, at least for collection kernels which are not strongly size dependent.

3. *Size Spectrum*

For an initial population of N_0 droplets of unit size, there is a surprisingly simple solution for (A.15-4) in terms of $v_N(t)$:

$$v(N, N_1, N_2, \ldots ; t) = \phi(N_1, N_2, \ldots, N_{N_0}/N) v_N(t), \tag{A.15-10}$$

where ϕ is the probability of having a specified distribution given that there are N droplets. The expression for ϕ is

$$\phi(N_1, N_2, \ldots, N_{N_0}/N) = \binom{N}{N_1, N_2, \ldots, N_0} \Big/ \binom{N_0 - 1}{N - 1}. \tag{A.15-11}$$

The numerator is the multinomial coefficient which counts the number of ways a specified (N_1, N_2, etc.) distribution of N_0 units of mass in N droplets can be obtained, and the denominator counts the total number of ways of distributing N_0 units of mass in N droplets. (The form of the denominator may be explained in the following manner: Imagine the N_0 units of mass in a row, so that there are $N_0 - 1$ spaces between them. A particular distribution of N droplets may be achieved by partitioning the row in $N - 1$ places. At least one mass unit is to go in each segment of the row ($N_0 \geq N$). Therefore, the number of possible distributions is the number of ways of selecting any $N - 1$ of the $N_0 - 1$ spaces as partition locations.)

Bayewitz *et al.* demonstrate that (A.15-11) is the solution to (A.15-4) by direct substitution into the differential equation, followed by numerical evaluation in simple cases which verifies uniqueness of the solution.

It is now possible to determine the function P(n, m; t) defined by (15-16):

$$P(n, m, t) = \sum_{N} \sum_{N_1} \sum_{N_2} \cdots \sum_{\text{except } N_m} v(N, N_1, N_2, \ldots, N_m = n, \ldots ; t). \tag{A.15-12}$$

Numerical evaluation in a few cases ($m = 2, 5$; $N_0 = 20$) indicates that as time increases P(n, m; t) approaches a Poisson distribution. As we discussed in Section 15.2.1.1, Gillespie (1972) showed this to be true also for a variable collection coefficient in the absence of correlations.

4. *Correlations in Poorly-Mixed Systems*

As we have noted, real clouds are not well-mixed, and this can be expected to give rise to correlation problems. Bayewitz *et al.* have considered the consequences of poor mixing by partitioning the cloud into small, isolated compartments of volume V_0. This approach has the merit of dictating only slight changes in the mathematics.

Let us now compare the descriptions of droplet growth in each compartment as provided by the SCE and the full stochastic equations. From (A.15-9) with A replaced by KV_0^{-1}, where K is the constant collection kernel, one may obtain the mean stochastic droplet concentration in any compartment, viz. $\langle f \rangle \equiv \langle N \rangle V_0^{-1}$. Similarly, from (A.15-9) we have the corresponding droplet concentration according to the SCE: $f \equiv N V_0^{-1}$. Computations show that for N_0 as small as 10, f exceeds $\langle f \rangle$ only slightly. Thus the results indicate the total droplet concentration is rather insensitive to poor mixing as simulated by the partitioning model.

Now let us consider the size spectrum in the partitioned system. Let $\langle \gamma_m(t) \rangle$ be the mean fraction of the total mass of any compartment consisting of particles of mass m. With N_0 being the total mass in each compartment (recall $N(0) = N_0$ droplets of unit mass), we have

$$\langle \gamma_m(t) \rangle = \frac{m \langle N_m(t) \rangle}{N_0}, \tag{A.15-13}$$

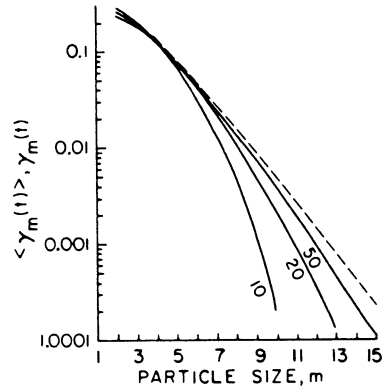


Fig. A.15-1. Mass fraction distribution at Kt = 0.002. —— $\langle\gamma_m(t)\rangle$ for $N_0 = 10, 20, 50$; $-\cdot-\cdot-$ $\gamma_m(t)$. (From Bayewitz *et al.*, 1974; by courtesy of Amer. Meteor. Soc., and the authors.)

where

$$\langle N_m(t)\rangle = \sum_n nP(n, m; t). \tag{A.15-14}$$

The corresponding mass fraction from the SCE is $\gamma_m(t) = mN_m(t)/N_0$. In the present case of an initially homogeneous aerosol and a constant collision kernel, $N_m(t)$ is just the Smoluchowski solution (12-43); therefore,

$$\gamma_m(t) = m\left(\frac{f_0Kt}{2}\right)^{m-1}\Big/\left(\frac{1+f_0Kt}{2}\right)^{m+1}. \tag{A.15-15}$$

In this expression f_0 is the concentration of droplets of unit mass at t = 0.

Figure A.15-1 compares $\langle\gamma_m(t)\rangle$ and $\gamma_m(t)$ at Kt = 0.02 and with $f_0 = 100$. For small N_0 (small V_0), there are seen to be substantial differences between the spectra predicted by the full stochastic model and the SCE, especially in the tails of the spectra. These differences decrease sharply with increasing V_0, and more moderately with time.

A-15.3.2 Particular Solutions to the SCE

Our purpose here is to evaluate the general solutions (15-40) and (15-47) for two choices of the initial spectrum. First, let us assume $g(x, 0) = \delta(x - 1)$. Then $G(s) = e^{-s}$, so that

$$L^{-1}[G^{k+1}(s)] = \frac{1}{2\pi i}\int_{\gamma-i\infty}^{\gamma+i\infty} e^{sx}e^{-s(k+1)}\,ds = \frac{1}{2\pi}\int_{-\infty}^{+\infty} e^{iy(x-k-1)}\,dy = \delta(x-k-1). \tag{A.15-16}$$

Substitution of this result into (15-40) and (15-47) leads to the solutions (15-48) and (15-49), respectively.

For our second choice of the initial spectrum we choose the family of gamma distributions given by (12-129). The Laplace transform of the initial spectrum is therefore

$$G(s) = \frac{(p+1)^{p+1}}{\Gamma(p+1)}\int_0^\infty x^p e^{-(s+p+1)x}\,dx = \frac{(p+1)^{p+1}}{(s+p+1)^{p+1}}, \tag{A.15-17}$$

using the defining equation

$$\Gamma(p) \equiv \int_0^\infty e^{-x}x^{p-1}\,dx, \quad p > 0 \tag{A.15-18}$$

for $\Gamma(P)$. Therefore,

$$L^{-1}[G^{k+1}(s)] = \frac{(p+1)^{(p+1)(k+1)}}{2\pi i} \int_{\gamma-i\infty}^{\gamma+i\infty} \frac{e^{sx}\,ds}{(s+p+1)^{(p+1)(k+1)}}. \tag{A.15-19}$$

This integral may be evaluated by means of the well known residue theorem (e.g., Morse and Feshbach, vol. I, 1953), according to which the integral of a function of the complex variable z around a closed contour C is equal to $2\pi i$ times the sum of the residues of the function at its singular points within C. It is assumed that the function is analytic except at the singular points. The residue at an isolated singular point z_0 is just the coefficient of $(z-z_0)^{-1}$ in an expansion of the function in powers of $(z-z_0)$. From (A.15-19) we thus see that what is called for is an expansion of e^{sx} about $s_0 = -(p+1)$, so that the integrand may be expressed as

$$e^{-(p+1)x} \sum_{\ell=0}^{\infty} \frac{x^{\ell}}{\ell!} (s+p+1)^{\ell-(p+1)(k+1)}.$$

Assuming integral p (the result holds for all $p > 0$), the residue occurs for $\ell = (p+1)(k+1)-1$, and the contour may be closed in the left half of the s plane, for negative real s. Therefore, we obtain

$$L^{-1}[G^{k+1}(s)] = \frac{(p+1)^{(p+1)(k+1)} e^{-(p+1)x} x^{p+k(p+1)}}{\Gamma[(p+1)(k+1)]}. \tag{A.15-20}$$

Substitution of this result into (15-40) and (15-47) leads to the solutions (15-53) and (15-54), respectively.

A-15.3.1.3 A monte Carlo Algorithm for Stochastic Coalescence

Our purpose here is to present Gillespie's (1975b) exact simulation algorithm. This requires focusing not on the average drop volume spectrum function which appears in the SCE, but rather on a quantity $P(\tau, i, j)$ which Gillespie calls the 'coalescence probability density function.' An explicit expression for $P(\tau, i, j)$ in terms of the basic probability of coalescence of a pair of drops with labels i and j in time dt can be derived, and the derivation is rigorous in that it is free of any no-correlation assumptions. A Monte Carlo simulation procedure is then based on $P(\tau, i, j)$ to calculate the stochastic evolution of a set of drops.

1. *Coalescence Probability Density Function*

Consider a well-mixed cloud containing N drops at time t. Label these drops in any convenient way by the index i ($i = 1, 2, \ldots, N$), and let V_i denote the volume of drop i. We define the 'coalescence probability density function' $P(\tau, i, j)$ by the following statement:

$$\begin{aligned} P(\tau, i, j)\, d\tau \equiv\ & \text{probability at time t that the next coalescence} \\ & \text{will occur in the time interval } (t+\tau, t+\tau+d\tau), \\ & \text{and will be the coalescence of droplets i and j } (i<j). \end{aligned} \tag{A.15-21}$$

Now let us define also the set of numbers $A_{k\ell}$ as follows:

$$\begin{aligned} A_{k\ell}\, d\tau \equiv\ & \text{probability that droplets k and } \ell \text{ will coalesce} \\ & \text{in the next infinitesimal time interval } d\tau. \end{aligned} \tag{A.15-22}$$

(As in Section 15.2.1, $A_{k\ell} = K_{k\ell} V^{-1}$, where $K_{k\ell}$ is the collection kernel and V is the volume of the well-mixed cloud.) An expression for (A.15-21) in terms of the quantities (A.15-22) can be derived as follows: The probability in (A.15-21) is the product of: (1) the probability that none of the droplets coalesce in the time interval $(t, t+\tau)$; times (2) the probability that droplets i and j coalesce in the next differential time interval $(t+\tau,\ t+\tau+d\tau)$; times (3) the probability that no other droplets coalesce in that same differential time interval.

To calculate the probability (1), imagine the time interval $(t, t+\tau)$ to be divided into m subintervals of equal length $\delta = \tau/m$. For small δ, the probability that drops k and ℓ $(k < \ell)$ will not coalesce in the first δ-interval is $(1 - A_{k\ell}\delta)$; hence the probability that all drop pairs will not coalesce in any of the m δ-intervals is

$$\left[\prod_{k=1}^{N-1} \prod_{\ell=k+1}^{N} (1 - A_{k\ell}\delta)\right]^m.$$

We now obtain (1) by taking the limit of this expression as our subdivision of $(t, t+\tau)$ becomes infinitesimally fine:

$$(1) \qquad = \lim_{m\to\infty}\left[\prod_{k=1}^{N-1}\prod_{\ell=k+1}^{N}(1-A_{k\ell}\delta)\right]^m = \prod_{k=1}^{N-1}\prod_{\ell=k+1}^{N}\lim_{m\to\infty}\left[1-\frac{A_{k\ell}\tau}{m}\right]^m$$

$$= \prod_{k=1}^{N-1}\prod_{\ell=k+1}^{N}\exp(-A_{k\ell}\tau) = \exp\left[-\sum_{k=1}^{N-1}\sum_{\ell=k+1}^{N}A_{k\ell}\tau\right]. \qquad \text{(A.15-23)}$$

From (A.15-22) the probabilities (2) and (3) immediately follow:

$$(2) \qquad = A_{ij}\,d\tau, \qquad \text{(A.15-24)}$$

and

$$(3) \qquad = \prod_{\substack{k=1\\ k\ell\neq ij}}^{N-1}\prod_{\ell=k+1}^{N}(1-A_{k\ell}\,d\tau). \qquad \text{(A.15-25)}$$

Therefore, on setting (A.15-21) equal to the product of (A.15-23)–(A.15-25) and dividing through by $d\tau$, we obtain

$$P(\tau, i, j) = A_{ij}\exp\left[-\sum_{k=1}^{N-1}\sum_{\ell=k+1}^{N}A_{k\ell}\tau\right]. \qquad \text{(A.15-26)}$$

This result holds for $0 \leq \tau < \infty$ and $1 \leq i < j \leq N$; otherwise, $P(\tau, i, j) = 0$.

2. *Basic Simulation Algorithm*

The simulation algorithm based on $P(\tau, i, j)$ is as follows:

Step 0: Set $t = 0$. Specify initial values for the N drop volumes $V_1, V_2, \ldots, V_N$, and calculate the corresponding $N(N-1)/2$ matrix elements $A_{k\ell}$. Specify a series of sampling times $t_1 < t_2 < \cdots$, and also a stopping time t_{stop}.

Step 1: By employing suitable Monte Carlo techniques (see next section), generate a random triplet (τ, i, j) distributed according to the joint probability density function $P(\tau, i, j)$.

Step 2: Using the values τ, i, and j obtained in Step 1, advance the time variable t by τ, remove drops i and j, and insert a new drop of volume $(V_i + V_j)$. Adjust the drop numbering scheme in any convenient way to reflect the fact that the cloud now contains one less drop than before, and make whatever rearrangements and recalculations of the matrix elements $A_{k\ell}$ are required.

Step 3: If t has just been advanced through one of the sample times t_i, display the drop volume spectrum at time t_i as a frequency histogram of the current V_i values. If $t \geq t_{stop}$ (or if only one drop remains), terminate the calculation: otherwise, return to Step 1.

By carrying out this algorithm from time 0 to time t, one realization of the stochastic collection process is obtained. Several such realizations, starting from the same initial data, must be carried out to get a statistically complete picture. Let

$$N_k(v, \delta v; t) = \text{number of drops found in run k at time t with volumes between v and } v + \delta v. \qquad \text{(A.15-27)}$$

Then for k runs the average number of drops at time t with volumes between v and $v + \delta v$ is

$$\bar{N}(v, \delta v; t) \approx \frac{1}{K}\sum_{k=1}^{K}N_k. \qquad \text{(A.15-28)}$$

(The expression becomes exact in the limit $k \to \infty$.) Similarly, the rms fluctuation about this average is

$$\Delta(v, \delta v; t) \approx \left[\frac{1}{K}\sum_{k=1}^{K}N_k^2 - \left(\frac{1}{K}\sum_{k=1}^{N}N_k\right)^2\right]^{1/2}. \qquad \text{(A.15-29)}$$

If $\Delta/\bar{N} \ll 1$, then the results found in separate runs will be nearly identical. If $\Delta/\bar{N} \geq 1$, then an accurate estimate of $\bar{N}$ is not really necessary; of more interest is the scatter of N_k for several trials. Probably $k \leq 10$ should provide an adequate picture of the state of the spectrum in general. Finally, the connection between $\bar{N}(v, \delta v; t)$ and the usual average spectrum function $n(v, t)$ belonging to the

SCE is as follows: Let

$$N(v, t) \equiv Vn(v, t). \tag{A.15-30}$$

Then

$$N(v, t) = \lim_{\substack{\delta v \to 0 \\ k \to \infty}} \frac{\bar{N}(v, \delta v, t)}{\delta v}. \tag{A.15-31}$$

3. *Implementing the Monte Carlo Step*

Gillespie provides three Monte Carlo methods for implementing Step 1 of the simulation algorithm. Here we shall summarize only one of these, the 'first-coalescence' method, because of its intuitive appeal and relative simplicity. However, it is probably not as efficient as the other two methods.

Consider any two cloud drops k and ℓ ($k < \ell$) at time t. From (A.15-22) it is easy to show that

$$\mathscr{P}_{k\ell}(\tau)\, d\tau = e^{-A_{k\ell}\tau} A_{k\ell}\, d\tau \tag{A.15-32}$$

would be the probability for k and ℓ to coalescence in the time interval $(t + \tau, t + \tau + d\tau)$, were it not for the fact that k or ℓ might coalesce with some other drop prior to time $t + \tau$. This being the case, Gillespie generates a *tentative* coalescence time $\tau_{k\ell}$ for the drop pair (k, ℓ) according to (A.15-32) (in a manner described below). This is done for all (k, ℓ) pairs, and of these $N(N-1)/2$ tentative next coalescences, the one which occurs first is chosen as the actual next coalescence. Thus, we put

$$\begin{aligned} \tau &= \text{smallest } \tau_{k\ell} \text{ for all } (k, \ell) \text{ pairs}, \\ (i, j) &= (k, \ell) \text{ for which } \tau_{k\ell} \text{ is smallest.} \end{aligned} \tag{A.15-33}$$

This procedure is a physically plausible way to pick values for τ, i, and j. Gillespie proves that it is, in fact, the correct way; i.e., if we let $\mathscr{P}'(\tau, i, j)\, d\tau$ be the probability that the procedure just described will result in the next coalescence being between drops i and j and occurring in the time interval $(t + \tau, t + \tau + d\tau)$, then it can be shown that $\mathscr{P}'(\tau, i, j) = \mathscr{P}(\tau, i, j)$.

We now consider the problem of generating the numbers $\tau_{k\ell}$. The goal is to generate a sequence of random numbers $\{\tau\}$ distributed according to some given probability density function $\mathscr{P}(\tau)$; in the present case $\mathscr{P}(\tau)$ has the exponential form (A.15-32). One way to accomplish this by means of the so-called 'method of inversion' (e.g., Gillespie, 1975c), which can be described in the following manner: For $\mathscr{P}(\tau)$ defined on the interval $[a, b]$, consider the corresponding probability distribution function

$$F(\tau) \equiv \int_a^\tau \mathscr{P}(\tau')\, d\tau', \quad a \leq \tau \leq b. \tag{A.15-34}$$

Then to generate τ distributed according to $\mathscr{P}(\tau)$, we simply draw a random number r from a uniform random number generator (a source of pseudorandom numbers distributed uniformly on [0, 1]), and then choose for τ that value which satisfies $F(\tau) = r$; i.e., we take

$$\tau = F^{-1}(r). \tag{A.15-35}$$

As applied to (A.15-32), this procedure yields the sequence of numbers

$$\tau_{k\ell} = A_{k\ell}^{-1} \ln (1/r_{k\ell}), \tag{A.15-36}$$

where $r_{k\ell}$ is on the interval [0, 1] and $k = 1, \ldots, N-1$; $\ell = k+1, \ldots, N$.

APPENDIX TO CHAPTER 18

A-18.6.3 Two Charged Conducting Spheres in a Background Electric Field

Here we summarize the work of Davis (1964a, b), who solved the boundary value problem of two electrically conducting spheres of given radii and charges, separated by a given distance and situated in an external electric field of given uniform strength far away from the spheres. Figure A.14-1

depicts the geometry of this problem, if we now assume that Θ describes the angle between the background field $\vec{E}_0$ and the line of centers of the spheres (i.e., if we replace $\vec{g}$ by $\vec{E}_0$ in the figure). To solve this problem the electrostatic potential function Φ must be determined which satisfies the boundary conditions (1) that at large distances from the spheres the potential corresponds to that of the uniform field, and (2) that the two spheres are equipotential surfaces carrying charges Q_1 and Q_2, respectively. The governing equation for Φ is Laplace's equation, $\nabla^2\Phi = 0$, which Davis solved in bispherical coordinates (a description of this system is given in Appendix A-14.4.2).

Given the solution for Φ, the force $\vec{F}_e$ (in e.s.u.) acting on either sphere may then be obtained by integrating the electrical stress over its surface:

$$\vec{F}_e \cdot \hat{\ell} = \frac{\varepsilon}{8\pi} \int_S \left(\frac{\partial \Phi}{\partial n}\right)^2 \hat{\ell} \cdot \hat{n}\, dS, \tag{A.18-1}$$

where $\hat{\ell}$ is an arbitrary unit vector, $\hat{n}$ the unit normal to the surface element dS, and ε is the dielectric constant of the medium in which the conducting spheres are imbedded. The forces on the two spheres must of course satisfy the relation

$$\vec{F}_e(a_1) + \vec{F}_e(a_2) = (Q_1 + Q_2)\vec{E}_0, \tag{A.18-2}$$

so that the integration in (A.18-1) need be carried out for only one of the spheres. Referring to Figure A.14-1, the components of the electrical force on sphere 2 along and at right angles to the line of centers were found by Davis to be given respectively by

$$\begin{aligned} F_{e,r}(a_2) = {} & \varepsilon a_2^2 E_0^2 (F_1 \cos^2\Theta + F_2 \sin^2\Theta) + E_0 \cos\Theta (F_3 Q_1 + F_4 Q_2) \\ & + \frac{1}{\varepsilon a_2^2}(F_5 Q_1^2 + F_6 Q_1 Q_2 + F_7 Q_2^2) + E_0 Q_2 \cos\Theta, \end{aligned} \tag{A.18-3}$$

and

$$F_{e,\Theta}(a_2) = \varepsilon a_2^2 E_0^2 F_8 \sin 2\Theta + E_0 \sin\Theta (F_9 Q_1 + F_{10} Q_2) + E_0 Q_2 \sin\Theta, \tag{A.18-4}$$

where the coefficients $F_1, F_2, \ldots, F_{10}$ are complicated functions, tabulated in Davis (1964a, b), of the distance between the spheres and of $p = a_2/a_1$. The corresponding force components in the x and y directions of Figure A.14-1 are then given by

$$\begin{aligned} F_{e,x}(a_2) &= F_{e,r}(a_2)\cos\Theta - F_{e,\Theta}(a_2)\sin\Theta, \\ F_{e,y}(a_2) &= F_{e,r}(a_2)\sin\Theta + F_{e,\Theta}(a_2)\cos\Theta. \end{aligned} \tag{A.18-5}$$

Davis's solution may also be used to calculate the charge transferred between the two spheres if they make electrical contact. Most convenient for this purpose are the following expressions from Davis (his Eq. (24) from 1964b):

$$\begin{aligned} V_1 &= P_{11}(Q_1 - Q_1^\dagger) + P_{12}(Q_2 - Q_2^\dagger), \\ V_2 &= P_{12}(Q_1 - Q_1^\dagger) + P_{22}(Q_2 - Q_2^\dagger), \end{aligned} \tag{A.18-6}$$

where $V_1 = \Phi(a_1)$ and $V_2 = \Phi(a_2)$ are the potentials of the two spheres, the P_{ij} are the calculated coefficients of induction ($P_{12} = P_{21}$ by the Reciprocation Theorem; e.g., see §2.12 of Smythe (1950)), and $Q_1^\dagger$, $Q_2^\dagger$ are the calculated charges which the spheres would have if they were at zero potential (i.e., grounded). Note that the only place $\vec{E}_0$ enters into (A.17-6) is in the functional dependence of the effective charges $Q_1^\dagger$ and $Q_2^\dagger$.

Now suppose the spheres touch, so that $V_1 = V_2 = V$, and the original charges Q_1, Q_2 become Q_1', Q_2'. Then from (A.18-6) we have

$$Q_1' = \frac{-(P_{11} - P_{12})Q_1^\dagger + (P_{12} - P_{22})(Q_T - Q_2^\dagger)}{2P_{12} - P_{11} - P_{22}}, \tag{A.18-7}$$

where $Q_T = Q_1 + Q_2 = Q_1' + Q_2'$. A similar expression may be written down for Q_2'. The charge transferred is then given by $\Delta Q = Q_1' - Q_1 = Q_2 - Q_2'$.

Of course, another way to evaluate ΔQ is by setting the electric field equal to zero at the point of contact. From Eq. (31) of Davis, the field strength at the near surface point of sphere 2 is

$$E_{2,r} = \frac{(E_1Q_1 + E_2Q_2)}{\varepsilon a_2^2} + E_3E_0 \cos \Theta, \tag{A.18-8}$$

where E_1, E_2, and E_3 are functions of separation distance and a_2/a_1, tabulated by Davis. From A.18-8) with $E_{2,r} = 0$ we therefore immediately find also that

$$\Delta Q = Q_1' - Q_1 = \frac{E_1Q_1 + E_2Q_2 + \varepsilon a_2^2 E_3 E_0 \cos \Theta}{(E_2 - E_1)}. \tag{A.18-9}$$

REFERENCES

Abbas, M. A., and Latham, J., 1967:*J. Fluid. Mech.* **30**, 663.
Abbas, M. A., and Latham, J., 1969a:*J. Meteor. Soc. Japan* **47**, 65.
Abbas, M. A., and Latham, J., 1969b:*Quart. J. Roy. Meteor. Soc.* **95**, 63.
Abbott, C. E., 1974:*J. Geophys. Res.* **79**, 3098.
Abbott, C. E., 1975:*J. Appl. Meteor.* **14**, 87.
Abel, N. *et al.*, 1969:*Meteor. Rundschau* **22**, 158.
Abraham, F. F., 1968:*J. Atmos. Sci.* **25**, 47.
Abraham, F. F., 1974a:*J. Chem. Phys.* **61**, 1221.
Abraham, F. F., 1974b:*Homogeneous Nucleation Theory*, Academic Press.
Abramowitz, M., and Segun, I. A., 1968:*Handbook of Mathematical Functions*, Dover.
Aburukawa, H., and Magono, C., 1972:*J. Meteor. Soc. Japan* **50**, 166.
Achenbach, E., 1972:*J. Fluid. Mech.* **54**, 565.
Achenbach, E., 1974:*J. Fluid Mech.* **62**, 209.
Ackerman, B., 1959:*J. Meteor.* **16**, 191.
Ackerman, B., 1963:*J. Atmos. Sci.* **20**, 288.
Ackerman, B., 1967:*J. Appl. Meteor.* **6**, 61.
Ackerman, B., 1968:*Preprints Cloud Phys. Conf.*, Toronto, Canada, p. 564, Univ. of Toronto Press, Toronto.
Acrivos, A., and Taylor, T. D., 1962:*Phys. Fluids* **5**, 387.
Adam, J. R., and Semonin, R. G., 1970:*Precipitation Scavenging, 1970*, AEC Symposium, Richland, Washington, p.151, U.S. Dept. of Commerce, Springfield, Virginia.
Adam, J. R., Lindblad, N. R., and Hendricks, C. D., 1968:*J. Appl. Phys.* **39**, 5173.
Adams, F. *et al.*, 1977:*Atmos. Environ.* **11**, 629.
Adams, S. J. *et al.*, 1986:*Nature* **321**, 842.
Adamson, A. W., 1960:*Physical Chemistry of Surface*, Interscience Publ., Inc.
Adamson, A. W., Dormant, L. M., and Orem, M. W., 1967:*J. Coll. Interface Sci.* **25**, 206.
Admirat, P., 1962:*Bull. Obs. Puy de Dome* **2**, 87.
Admirat, P., and Grenier, J. C., 1975:*J. de Rech. Atmos.* **9**, 97.
Agee, E. M., and Asai, T., 1982:*Cloud Dynamics*, D. Reidel.
Ahmed, A. F., Singh, R. P., and Elmubarah, A. H., 1990:*Atmos. Environ.* **24A**, 2927.
Ahr, M., 1988:*Diploma Thesis*, Inst. f. Atmos. Phys., Univ. Mainz, Mainz.
Ahr, M., Flossmann, A. I., and Pruppacher, H. R., 1989a:*Beitr. Phys. Atmos.* **62**, 321.
Ahr, M., Flossmann, A. I., and Pruppacher, H. R., 1989b:*J. Atmos. Chem.* **9**, 465.
Akoy, E., 1971:*M.S. Thesis*, Brown University, Providence, Rhode Island.
Al-Naimi, R., and Saunders, C. P. R., 1985:*Atmos. Environ.* **19**, 1871.
Aleksic, N. M., Farley, R. D., and Orville, H. D., 1989:*Atmos. Res.* **23**, 1.
Alexandrov, U. S., Silayeva, V. I., and Schmeter, S. M., 1969:*Air Force Cambridge Res. Labs., Report AFCRL-69-0178, Translation No. 45*, Hanscom AFB, Bedford, Massachusetts (NTIS AD-687342).
Alheit, R. R., Flossmann, A. I., and Pruppacher, H. R., 1990:*J. Atmos. Sci.* **47**, 870.
Allard, E. F., and Kassner, J. L., 1965:*J. Chem. Phys.* **42**, 1401.
Allee, P. A., 1970:*Preprints Conf. on Weather Mod.*, Santa Barbara, California, p. 244, Am. Meteor. Soc., Boston.
Allee, P. A., and Phillips, B. B., 1959:*J. Meteor.* **16**, 405.
Allen, L. B., and Kassner, J. L., 1969:*J. Coll. and Interface Sci.* **30**, 81.
Alofs, D. J. *et al.*, 1979:*J. Appl. Meteor.* **18**, 1106.
Alofs, D. J., Hagen, D. E., and Trueblood, M. B., 1989:*J. Appl. Meteor.* **28**, 126.
Alty, T., 1931:*Proc. Roy. Soc.* **A131**, 554.
Alty, T., 1933:*Phil. Mag.* **15**, 82.
Alty, T., and Mackay, C. A., 1935:*Proc. Roy. Soc. London* **A149**, 104.
Alty, T., and Nicole, F. H., 1931:*Can. J. Res.* **4**, 547.

Alusa, A. L., 1975:*J. de Rech. Atmos.* **9**, 1.
Alusa, A. L., and Blanchard, D. C., 1973:*J. de Rech. Atmos.* **7**, 1.
Ambe, Y., and Nishikawa, M., 1986:*Atmos. Environ.* **20**, 1931.
Ames, W. F., 1965:*Nonlinear Partial Differential Equations in Engineering*, Academic Press.
Anderson, J., and Hallett, J., 1976:*J. Atmos. Sci.* **33**, 822.
Anderson, P. A., Tannehill, J. C., and Pletcher, R. H., 1984:*Computational Fluid Mechanics and Heat Transfer*, McGraw-Hill.
Anderson, R. J. *et al.*, 1980:*J. Atmos. Sci.* **37**, 2508.
Andreae, M. O. *et al.*, 1985:*J. Geophys. Res.* **90**, 12891.
Andreae, M. O., 1983:*Science* **220**, 1148.
Andreae, M. O., and Raemdonck, H., 1983:*Science* **221**, 744.
Andreae, M. O., Beresheim, H., and Andreae, T. W., 1988:*J. Atmos. Chem.* **6**, 149.
Andsager, K., Beard, K. V., and Laird, N. F., 1999: *J. Atmos. Sci.* **56**, 2673.
Angell, C. A., 1982:*Water* F. Frank, Ed.,, **Vol. 7**, p. 1, Plenum.
Angell, C. A., Guni, M. O., and Sichina, W. J., 1982:*J. Phys. Chem.* **86**, 998.
Annis, B. K., and Mason, E. A., 1975:*Aerosol Science* **6**, 105.
Antonoff, G., 1907:*J. Chem. Phys.* **5**, 372.
Aoi, T., 1955:*J. Phys. Soc. Japan* **10**, 119.
Arenberg, D. L., 1941:*Bull. Am. Meteor. Soc.* **22**, 113.
Arenberg, D., 1939:*Bull. Am. Meteor. Soc.* **20**, 444.
Aris, R., 1962:*Vectors, Tensors, and the Basic Equations of Fluid Mechanics*, Prentice-Hall, Englewood Cliffs, New Jersey.
Arlander, D. W. *et al.*, 1990:*J. Geophys. Res.* **95**, 16391.
Arnold, F. *et al.*, 1989:*Nature* **342**, 493.
Arnold, F., and Fabian, R., 1980:*Nature* **283**, 55.
Arnold, F., Fabian, R., and Joos, W., 1981:*Geophys. Res. Lett.* **8**, 293.
Artemov, I. S., 1946:*J. Phys. Chem.*, U.S.S.R. **20**, 553.
Asai, T., and Kasahara, A., 1967:*J. Atmos. Sci.* **24**, 487.
Asuma, Y., and Kikuchi, K., 1987:*J. Meteor. Soc. Japan* **65**, 973.
Atkinson, R., Winer, A. M., and Pitts, J. N., 1986:*Atmos. Environ.* **20**, 331.
Atkinson. W. R., and Paluch, I., 1968:*J. Geophys. Res.* **73**, 2035.
Atlas, D. *et al.*, 1969:*Quart. J. Roy. Meteor. Soc.* **95**, 544.
Auer, A. H. *et al.*, 1970:*Final Rept.*, University of Wyoming, Laramie, Wyoming.
Auer, A. H., 1966:*J. de Rech. Atmos.* **3**, 289.
Auer, A. H., 1970:*J. de Rech. Atmos.* **4**, 145.
Auer, A. H., 1971:*J. Atmos. Sci.* **28**, 285.
Auer, A. H., 1972a:*J. Atmos. Sci.* **29**, 311.
Auer, A. H., 1972b:*Monthly Weather Rev.* **100**, 325.
Auer, A. H., and Veal, D. L., 1970:*J. Atmos. Sci.* **27**, 919.
Auer, A. H., Veal, D. L., and Marwitz, J. D., 1969:*J. Atmos. Sci.* **26**, 1342.
Aufdermauer, A. and Johnson, D. A., 1972:*Quart. J. Roy. Meteor. Soc.* **98**, 369.
Aufdermauer, A. and Joss, J., 1967:*Z. Angew. Math. und Phys.* **18**, 852.
Aufdermauer, A. and Mayes, W. C., 1965:*Preprints Cloud Phys. Conf.*, Tokyo, Japan, p. 281, Meteor. Soc., Japan, Tokyo.
Aufdermauer, A., 1963:*Schweiz. Z. f. Obst und Weinbau* **72**, 434.
Aufdermauer, List, R., and Mayes, W. C., 1963:*Z. Angew. Math. und Phys.* **14**, 574.
Aufm Kampe, B. J., Weickmann, H.K. and Kelley, J. J., 1951:*J. Meteor.* **8**, 168.
Ausman, E. L., and Brook, M., 1967:*J. Geophys. Res.* **72**, 6131.
Austin, J. M., and Fleisher, A., 1948:*J. Meteor.* **5**. 240.
Austin, P. H. *et al.*, 1985:*J. Atmos. Sci.* **42**, 1123.
Austin, P. M., and Bemis, H. C., 1950:*J. Meteor.* **7**, 145.
Ayers, G. P., and Gillette, R. W., 1984:*Atmos. Environ.* **2**, 25.
Ayers, G. P., and Gras, J. L., 1991:*Nature* **352**, 834.
Ayres, G. P., and Manton, M. S., 1991:*Tellus* **43B**, 379.
Baboolal, L. B., Pruppacher, H. R., and Topalian, J. H., 1981:*J. Atmos. Sci.* **38**, 856.
Bach, W., 1976:*Rev. Geophys. Space Phys.* **14**, 429.
Bächmann, K. *et al.*, 1991:*Fresenius. J. Anal. Chem.* **340**, 548.
Bächmann, K. *et al.*, 1992a:*Int. J. Environ. Anal. Chem.* **49**, 87.
Bächmann, K. *et al.*, 1993a:*J. Chromatography* **643**, 191.
Bächmann, K. *et al.*, 1995:*Atmos. Environ.* **30**, 1019, 1027.
Bächmann, K., and Steigewald, K., 1993:*Fresenius J. Anal. Chem.* **346**, 410.
Bächmann, K., Haag, I., and Röder, A., 1993b:*Atmos. Environ.* **27A**, 1951.

Bächmann, K., Röder, A., and Haag, I., 1992b:*Atmos. Environ.* **26A**, 1795.
Bader, M. *et al.*, 1974:*Quart. J. Roy. Meteor. Soc.* **100**, 420.
Bader, R. F., and Jones, G. A., 1963:*Canad. J. Chem.* **41**, 586.
Bagnold, R. A., 1965:*The Physics of Blown Sand Desert Dunes*, Methuen.
Bailey, I. H. *et al.*, 1984:*Geophys. Res. Lett.* **11**, 397.
Bailey, I. H., and Macklin, W. C., 1968a:*Quart. J. Roy. Meteor. Soc.* **94**, 1.
Bailey, I. H., and Macklin, W. C., 1968b:*Quart. J. Roy. Meteor. Soc.* **94**, 93.
Baird. M. H., Hamielec, A. E., 1962:*Canad. J. Chem. Eng.* **40**, 119.
Baker, B. A., 1991a:*J. Atm. Sci.* **48**, 1545.
Baker, B. A., 1991b:*J. Atm. Sci.* **48**, 1904.
Baker, M. B. *et al.*, 1982:*Quart. J. Roy. Meteor. Soc.* **108**, 899.
Baker, M. B. *et al.*, 1984:*J. Atmos. Sci.* **41**, 299.
Baker, M. B. *et al.*, 1987:*Quart. J. Roy. Meteor. Soc.* **113**, 1193.
Baker, M. B., 1991:*J. Atmos. Sci.* **48**, 1904.
Baker, M. B., 1992:*J. Atmos. Sci.* **49**, 387.
Baker, M. B., and Dash, J. G., 1989:*J. Crys. Growth* **97**, 770.
Baker, M. B., and Latham, J., 1979:*J. Atmos. Sci.* **36**, 1612.
Baker, M. B., and Latham, J., 1982:*Quart. J. Roy. Meteor. Soc.* **108**, 871.
Baker, M. B., Corbin, R. G., and Latham, J., 1980:*Quart. J. Roy. Meteor. Soc.* **106**, 581.
Baker, P. W., and Hudson, M. C., 1985:*J. Clim. and Appl. Meteor.* **24**, 4951.
Bakhanova, R. A., and Kiselev, V. I., 1972:*Colloid J., U.S.S.R.* **34**, 481.
Bakhanova, R. A., and Kiselev, V. I., 1974:*Colloid J., U.S.S.R.* **36**, 680.
Balakrishnan, N., and Zrnic, D. S., 1990:*J. Atmos. Sci.* **47**, 565.
Bandy, A. R. *et al.*, 1981:*Geophys. Res. Lett.* **8**, 1180.
Bansil, R., Akenten, J. W., and Taafe, J. L., 1982:*J. Chem. Phys.* **76**, 2221.
Baramaev, M. K., 1939:*Zhurnal Fiz. Khim.* **13**, 1635.
Barchet, W. R., 1971:*Ph. D. Thesis*, Colorado State University, Fort Collins, Colorado (also: Atmos. Sci., Paper No. 168, Dept. of Atmos. Sci., Colorado State University).
Barchet, W. R., and Corrin, M. L., 1972:*J. Phys. Chem.* **76**, 2280.
Barge, L. G., and Isaac, G. A., 1973:*J. de Rech. Atmos.* **7**, 11.
Barger, W. R., and Garrett, W. D., 1970:*J. Geophys. Res.* **75**, 4561.
Barger, W. R., and Garrett, W. D., 1976:*J. Geophys. Res.* **81**, 3151.
Barker, J. A., and Watts, R. O., 1969:*Chem. Phys. Lett.* **3**, 144.
Barklie, R. H. D., and Gokhale, N. R., 1959:*Scientific Report, MW-30*, Stormy Weather Group, McGill University, Montreal.
Barlow, A. K., and Latham, J., 1983:*Quart. J. Roy. Meteor. Soc.* **109**, 763.
Barnaal, J., and Slotfeld-Ellingsen, D., 1983:*J. Phys. Chem.* **87**, 4321.
Barnard, A. J., 1953:*Proc. Roy. Soc. London* **A220**, 132.
Barnard, A. J., 1954:*Ph.D. Thesis, Glasgow University*, Glasgow, Scotland.
Barnard, W. R. *et al.*, 1982:*J. Geophys. Res.* **87**, 8787.
Barrie, L. A. *et al.*, 1981:*Atmos. Environ.* **15**, 1407.
Barrie, L. A. *et al.*, 1987:*Atmos. Environ.* **21**, 1133.
Barrie, L. A., 1978:*Atmos. Environ.* **12**, 407.
Barrie, L. A., 1981:*Atmos. Environ.* **15**, 31.
Barrie, L. A., 1985a:*J. Atmos. Chem.* **3**, 139.
Barrie, L. A., 1985b:*J. Geophys. Res.* **90**, 5789.
Barrie, L. A., 1986:*Atmos. Environ.* **20**, 643.
Barrie, L. A., and Georgii, H. W., 1976:*Atmos. Environ.* **10**, 743.
Barrie, L., Beilke, S., and Georgii, H. W., 1974:*Precipitation Scavenging - 1974*, p. 151, Techn. Info. Center, US. Dept. of Commerce, Springfield, Virginia.
Barth, M. C. *et al.*, 1989:*Tellus* **41B**, 61.
Barthakur, N., and Maybank, J., 1963:*Nature* **200**, 866.
Barthakur, N., and Maybank, J., 1966:*J. de Rech. Atmos.* **2**, 475.
Bartlett, J. T., 1966:*Quart. J. Roy. Meteor. Soc.* **92**, 93.
Bartlett, J. T., 1968:*Preprints Cloud Phys. Conf.*, Toronto, p. 515, Am. Meteor. Soc., Boston.
Bartlett, J. T., 1970:*Quart. J. Roy. Meteor. Soc.* **96**, 730.
Bartlett, J. T., and Jonas, P. R., 1972:*Quart. J. Roy. Meteor. Soc.* **98**, 150.
Bashforth, F., and Adams, J. C., 1883:*An Attempt to Test the Theory of Capillary Action*, Cambridge Univ. Press.
Bashkirova, G. M., and Pershina, T. A., 1956:*Trudy Glav. Geofiz. Observ.* **57**, 19.

Bashkirova, G. M., and Pershina, T. A., 1964a:*Trudy Glav. Geofiz. Observ.* **165**, 83.
Bashkirova, G. M., and Pershina, T. A., 1964b:*Trudy Glav. Geofiz. Observ.* **165**, 90.
Basset, A. B., 1910:*Quart. J. Pure Appl. Math.* **41**, 369.
Batchelor, G. K., 1953:*The Theory of Homogeneous Turbulence*, Cambridge Univ. Press, London.
Batchelor, G. K., 1967:*Fluid Dynamics*, Cambridge University Press, London.
Bates, T. S. *et al.*, 1987:*J. Geophys. Res.* **92**, 2930.
Bates, T. S., Calhoun, J. A., and Quinn, P. K., 1992:*J. Geophys. Res* . **97**, 9859.
Battan, L. J., 1973:*Radar Observations of Atmospheric Clouds*, University of Chicago Press.
Battan, L. J., 1977:*J. Appl. Meteor.* **16**, 595.
Battan, L. J., and Braham, R. R., 1956:*J. Meteor.* **13**, 587.
Battan, L. J., and Reitan, C. H., 1957:*Artificial Stimulation of Rain*, p. 184, Pergamon.
Baumgarten, U., 1990:*Diploma Thesis*, Inst. f. Atmos. Phys., Univ. Mainz, Mainz.
Baumgärtner, F., Zanier, A., and Krebs, K., 1989:*J. Atmos. Sci* . **20**, 883.
Bayardelle, M., 1955:*C. R. Acad. Sci.* **240**, 2553.
Bayewitz, M. H. *et al.*, 1974:*J. Atmos. Sci.* **31**, 1604.
Bayne, M., and Gayet, J. F., 1983:*Annals. Glaciol.* **4**, 19.
Beaglehole, D., and Nason, D., 1980:*Surface Science* **96**, 357.
Beard, K. V., 1974:*J. Atmos. Sci.* **31**, 1595.
Beard, K. V., 1976:*J. Atmos. Sci.* **33**, 851.
Beard, K. V., 1980:*J. Atmos. Sci.* **37**, 1363.
Beard, K. V., 1984a:*Radio Sci.* **19**, 67.
Beard, K. V., 1984b:*J. Atmos. Sci.* **41**, 1765.
Beard, K. V., and Chuang, C., 1987:*J. Atmos. Sci.* **44**, 1509.
Beard, K. V., and Grover, S. N., 1974:*J. Atmos. Sci.* **31**, 543.
Beard, K. V., and Heymsfield, A. J., 1988:*J. Atmos. Sci.* **45**, 3515.
Beard, K. V., and Jameson, A. R., 1983:*J. Atmos. Sci.* **40**, 448.
Beard, K. V., and Johnson, D. B., 1984:*Geophys. Res. Lett.* **11**, 65.
Beard, K. V., and Kubesch, R. J., 1991:*J. Atmos. Sci.* **48**, 2245.
Beard, K. V., and Ochs, H. T., 1984:*J. Geophys. Res.* **89**, 7165.
Beard, K. V., and Ochs, H. T., 1986:*The Earth Electrical Environment*, Studies in Geophysics, p. 114, National Academic Press, Washington D.C.
Beard, K. V., and Pruppacher, H. R., 1968:*J. Geophysics* **73**, 6407.
Beard, K. V., and Pruppacher, H. R., 1969:*J. Atmos. Sci.* **26**, 1060.
Beard, K. V., and Pruppacher, H. R., 1971a:*J. Atmos. Sci.* **28**, 1455.
Beard, K. V., and Pruppacher, H. R., 1971b:*Quart. J. Roy. Meteor. Soc.* **97**, 242.
Beard, K. V., and Tokay, A., 1991:*Geophys. Res. Lett.* **18**, 2257.
Beard, K. V., Feng, J. Q., and Chuang, C., 1989:*J. Atmos. Sci.* **46**, 2404.
Beard, K. V., Johnson, D. B., and Baumgardner, D., 1986:*Geophys. Res. Lett.* **13**, 991.
Beard, K. V., Johnson, D. B., and Jameson, A. R., 1983:*J. Atmos. Sci.* **40**, 455.
Beard, K. V., Kubesch, R. J., and Ochs, H. T., 1991:*J. Atmos. Sci.* **48**, 698.
Beard, K. V., Ochs, H., and Feng, J. Q., 1989:*Nature* **342**, 408.
Beauville, C. A. *et al.*, 1988:*J. Atmos. Sci.* **45**, 3320.
Becker, R., and Döring, W., 1935:*Ann. d. Phys.* **24**, 719.
Beheng, K. D., 1978:*J. Atmos. Sci.* **35**, 683.
Beheng, K. D., 1980:*Pure and Appl. Geophys.* **119**, 820.
Beheng, K. D., 1987:*Quart. J. Roy. Meteor. Soc.* **113**, 1377.
Beheng, K., 1982:*Beitr. Phys. Atmos.* **55**, 201.
Beilke, S., 1970:*Prec. Scav. 1970*, p. 261, Proc. Symp., Richland, Wash. Natl. Techn. Info. Service, US. Dept. Commerce, Springfield, Virginia.
Beilke, S., and Gravenhorst, G., 1978:*Atmos. Environ.* **12**, 231.
Bell, D. A., and Saunders, C. P. R., 1991:*Atmos. Environ.* **25A**, 801.
Belvayev, V. I., 1961:*Izv. Akad. Nauk., U.S.S.R., Geofis. Ser.* **8**, 1209.
Ben-Naim, A., 1972:*Water*, F. Franks, Ed., Vol.1, p. 413, Plenum.
Ben-Naim, A., 1974:*Water and Aqueous Solutions*, Plenum.
Ben-Naim, A., and Stillinger, F. H., 1972:*Water and Aqueous Solutions*, R. A. Horne, Ed., p. 295, Wiley-Interscience.
Bennett, D. A., and Ouldridge, M., 1984:*Quart. J. Roy. Meteor. Soc.* **110**, 85.
Benson, G. C., and Shuttleworth, R., 1951:*J. Chem. Phys.* **19**, 130.
Bentley, W. A., and Humphreys, W. J., 1931:*Snow Crystals*, McGraw-Hill, (Dover Publ., 1962).

Berezinski, N. A., Stepanov, G. V., and Khorguami, V. S., 1988:*Atmos. Aerosol and Nucleation*, Lecture Notes in Physics, P. E. Wagner, G. Vali, Eds., **309**, p. 709, Springer.
Berg, N., Dunn, P., and Fenn, M., 1991:*Atmos. Environ.* **25A**, 915.
Bernal, J. D., and Fowler, R. H., 1933:*J. Chem. Phys.* **1**, 515.
Berry, E. X., 1965:*Ph.D. Thesis*, University of Nevada, Reno.
Berry, E. X., 1967:*J. Atmos. Sci.* **24**, 688.
Berry, E. X., 1968:*J. Atmos. Sci.* **25**, 151.
Berry, E. X., and Pranger, M. R., 1974:*J. Appl. Meteor.* **13**, 108.
Berry, E. X., and Reinhardt, R. L., 1974a:*J. Atmos. Sci.* **31**, 1814.
Berry, E. X., and Reinhardt, R. L., 1974b:*J. Atmos. Sci.* **31**, 1825.
Berry, E. X., and Reinhardt, R. L., 1974c:*J. Atmos. Sci.* **31**, 2118.
Berry, E. X., and Reinhardt, R. L., 1974d:*J. Atmos. Sci.* **31**, 2127.
Best, A. C., 1947:*Meteor. Res. Comm.*, Air Ministry, Great Britain, M.R.P. 330.
Best, A. C., 1950a:*Quart. J. Roy. Meteor. Soc.* **76**, 16.
Best. A. C., 1950b:*Quart. J. Roy. Meteor. Soc.* **76**, 302.
Best, A. C., 1951a:*Quart. J. Roy. Meteor. Soc.* **77**, 418.
Best, A. C., 1951b:*Quart. J. Roy. Meteor. Soc.* **77**, 241.
Best, A. C., 1952:*Quart. J. Roy. Meteor. Soc.* **78**, 28.
Betts, A. K., 1982a:*J. Atmos. Sci.* **39**, 1484.
Betts, A. K., 1982b:*J. Atmos. Sci.* **39**, 2182.
Betts, A. K., 1985:*J. Atmos. Sci.* **42**, 2751.
Bielski, B. H., 1978:*Photochem. Photobiol.* **28**, 645.
Bigg, E. K., 1953a:*Quart. J. Roy. Meteor. Soc.* **79**, 510.
Bigg, E. K., 1953b:*Proc. Phys. Soc., B.* **66**, 688.
Bigg, E. K., 1955:*Quart. J. Roy. Meteor. Soc.* **81**, 478.
Bigg, E. K., 1963:*Nature* **197**, 172.
Bigg, E. K., 1965:*Preprints Cloud Phys. Conf.*, Tokyo, p.137, Meteor. Soc. of Japan, Tokyo.
Bigg, E. K., 1967:*J. Atmos. Sci.* **24**, 226.
Bigg, E. K., 1975:*J. Atmos. Sci.* **32**, 910.
Bigg, E. K., 1977:*J. Appl. Meteor.* **16**, 262.
Bigg, E. K., 1980:*J. Appl. Meteor.* **19**, 521.
Bigg, E. K., 1986:*Atmos. Res.* **20**, 75.
Bigg, E. K., and Giutronich, J., 1967:*J. Atmos. Sci.* **24**, 46.
Bigg, E. K., and Hopwood, S. C., 1963:*J. Atmos. Sci.* **20**, 185.
Bigg, E. K., and Miles, G. T., 1963:*Tellus* **15**, 162.
Bigg, E. K., and Miles, G. T., 1964:*J. Atmos. Sci.* **21**, 396.
Bigg, E. K., and Stevenson, C., 1970:*J. de Rech. Atmos.* **4**, 41.
Bigg, E. K., Kriz, Z., and Thompson, W. J., 1971:*Tellus* **23**, 247.
Bigg, E. K., Kriz, Z., and Thompson, W. J., 1972:*J. Geophys. Res.* **77**, 3916.
Bigg, E. K., Miles, G. T., and Heffernan, K. J., 1961:*J. Meteor.* **18**, 804.
Bigg, E. K., Ono, A., and Thompson, W. J., 1970:*Tellus* **22**, 550.
Bikerman, J. J., 1970:*Physical Surfaces*, Academic Press.
Bilham, E. G., and Relf, E. F., 1937:*Quart. J. Roy. Meteor. Soc.* **63**, 149.
Billings, J. J., and Holland, D. F., 1969:*J. Geophys. Res* . **74**, 6881.
Bilonick, R., 1985:*Atmos. Environ.* **19**, 1829.
Bingham, E. C., and Jackson, R. F., 1918:*Bull. US Bur. Stand.* **14**, p. 59.
Bird, R. B., Stewart, W. E., and Lightfoot, E. L., 1960:*Transport Phenomena*, Wiley.
Birstein, S. J., 1954:*Geophys. Res. Papers 32*, Atmos. Phys. Lab., Geophys. Res. Dir., Air Force Cambridge Res. Center, Bedford, Massachusetts.
Birstein, S. J., 1955:*J. Meteor.* **12**, 324.
Birstein, S. J., 19S6:*J. Meteor.* **13**, 395.
Birstein, S. J., and Anderson, C. E., 1955:*J. Meteor.* **12**, 68.
Bjerrum, N., 1951:*K. Danske Vidensk., Selsk., Skr.* **27**, 1.
Black, R. A., and Hallett, J., 1986:*J. Atmos. Sci.* **43**, 802.
Blackman, M., and Lisgarten, N. D., 1957:*Proc. Roy. Soc. London* **A239**, 93.
Blake, D. F., and Kato, K., 1995:*J. Geophys. Res.* **100**, 7195.
Blakeslee, R. J., and Christian, H. J., 1989:*J. Geophys. Res.* **94**, 13, 135.
Blanchard, D. C., 1948:*Occasional. Rept. 7*, Project Cirrus, General Electric Res. Labs. Schenectady, New York.
Blanchard, D. C., 1949:*Occasional. Rept. 17*, Project Cirrus, General Electric Res. Labs. Schenectady, New York.

Blanchard, D. C., 1950:*Trans. Am. Geophys. Union* **31**, 836.
Blanchard, D. C., 1953:*J. Meteor.* **10**, 457.
Blanchard, D. C., 1954:*Nature* **174**, 470.
Blanchard, D. C., 1955:*J. Meteor.* **12**, 91.
Blanchard, D. C., 1957:*Artificial Stimulation of Rain*, p. 233, Pergamon.
Blanchard, D. C., 1962:*J. Atmos. Sci.* **19**, 119.
Blanchard, D. C., 1963:*Progr. in Oceanogr.* **1**, 71.
Blanchard, D. C., 1964:*Science* **146**, 396.
Blanchard, D. C., 1968:*Preprints Cloud Phys. Conf.*, Toronto, p. 25. University of Toronto Press.
Blanchard, D. C., 1969:*J. de Rech. Atmos.* **4**, 1.
Blanchard, D. C., 1971:*J. Atmos. Sci.* **28**, 645.
Blanchard, D. C., 1971b:*J. Atmos. Sci.* **28**, 811.
Blanchard, D. C., and Spencer, A. T., 1957:*Tellus* **9**, 541.
Blanchard, D. C., and Spencer, A. T., 1964:*J. Atmos. Sci.* **21**, 182.
Blanchard, D. C., and Spencer, A. T., 1970:*J. Atmos. Sci.* **27**, 101.
Blanchard, D. C., and Syzdek, L. D., 1974:*J. de Rech. Atmos.* **8**, 529.
Blanchard, D. C., and Woodcock, A. E., 1980:*Ann., N.Y. Acad. Sci.* **338**, 330.
Blanchard, D. C., and Woodcock, A. H., 1957:*Tellus* **9**, 145.
Blanchard, D. C., Woodcock, A. H., and Cipriano, R. J., 1984:*Tellus* **36**, 118.
Bleck, R., 1970:*J. Geophys. Res.* **75**, 5165.
Blecker, W., Dansgaard, W., and Lablaus, N. V., 1966:*Tellus* **18**, 773.
Blottner, F. G., and Ellis, M. A., 1973:*Computers and Fluids* **1**, 133.
Blumenstein, R. *et al.*, 1987:*J. Clim. and Appl. Meteor.* **26**, 1363.
Blyth, A. M. *et al.*, 1980:*Quart. J. Roy. Meteor. Soc.* **106**, 821.
Blyth, A. M., and Latham, J., 1984:*Quart. J. Roy. Meteor. Soc.* **110**, 773.
Blyth, A. M., and Latham, J., 1985:*Quart. J. Roy. Meteor. Soc.* **111**, 773.
Blyth, A. M., and Latham, J., 1990:*Quart. J. Roy. Meteor. Soc.* **116**, 1405.
Blyth, A. M., Cooper, W. A., and Jensen, J. B., 1988:*J. Atmos. Sci.* **45**, 3944.
Boatman, J. F., and Auer, A. H., 1983:*J. Atmos. Sci.* **40**, 1517.
Bodhaine, B. A. *et al.*, 1981:*Atmos. Environ* . **15**, 1375.
Bodhaine, B. A. *et al.*, 1986:*Tellus* **38B**, 233.
Bolling, G. F., and Tiller, W. A., 1961:*J. Appl. Phys.* **32**, 2587.
Bollinger, M. J. *et al.*, 1984:*J. Geophys. Res.* **89**, 9623.
Bonacci, I. C. *et al.*, 1976:*Chem. Eng. Sci.* **31**, 609.
Bongartz, A., and Schuhrath, U., 1992:*Proc. Eurotrac. Symposium*, p. 29.
Bonsang, B. *et al.*, 1980:*J. Geophys. Res.* **85**, 7410.
Borovikov, A. M. *et al.*, 1963:*Cloud Physics*, p. 65. Transl. by Israel Program f. Scientific Translation, U.S. Dept. Commerce, Washington, D.C.
Borrmann, S., and Jaenicke, R., 1987:*Atmos. Environ.* **21**, 1891.
Borrmann, S., Jaenicke, R., and Neumann, P., 1993:*Atmos. Res.* **29**, 229.
Borrmann, S. *et al.*, 1993:*Geophys. Res. Lett.* **20**, 2559.
Borys, R. D. 1983:*Precipitation Scavenging, Dry Deposition and Resuspension*, Pruppacher *et al.*, Eds., p. 1281, Elsevier.
Borys, R., and Rahn, K. A., 1981:*Atmos. Environ.* **15**, 1491.
Borys, R., Hindman, E. E., and DeMott, P. J., 1988:*J. Atmos. Chem.* **7**, 213.
Bos, R., 1980:*J. Air Poll. Control Assoc.* **30**, 1222.
Bosio, L., Teixeira, J., and Stanley, H. E., 1981:*Phys. Rev. Lett.* **46**, 597.
Boston, N. E., and Burling, R. W., 1972:*J. Fluid. Mech.* **55**, 473.
Bott, A., 1991:*Boundary-Layer Meteor.* **56**, 1.
Bott, A., Sievers, V., and Zdunkowski, W., 1990:*J. Atmos. Sci.* **47**, 2153.
Bourot, J. M., 1969:*C. R. Acad. Sci. de Paris* **A269**, 1017.
Bowdle, D. A., Hobbs, P. V., and Radke, L. F., 1985:*J. Clim. and Appl. Meteor.* **24**, 1370.
Bowen, E. G., 1950:*Austral. J. Sci. Res.* **A3**, 193.
Bowen, E. G., 1956a:*J. Meteor.* **13**, 142.
Bowen, E. G., 1956b:*Tellus* **8**, 394.
Bowen, E. G.,1953:*Austral. J. Phys.* **6**, 490.
Bower, K. N., and Choularton, T. W., 1988:*Quart. J. Roy. Meteor. Soc.* **114**, 1411.
Bowers, R., 1953:*Phil Mag.* **44**, 467.
Bradley, S. G., and Stow, C. C., 1974:*J. Appl. Meteor.* **13**, 131.
Bradley, S. G., and Stow, C. D., 1977:*J. Appl. Meteor.* **16**, 1206.

Bradley, S. G., and Stow, C. D., 1978:*Phil. Trans. Prog. Soc. London* **287**, 66.
Bradley, S. G., and Stow, C. D., 1979:*J. Atmos. Sci.* **36**, 497.
Braham, R. R., 1963:*J. Appl. Meteor.* **2**, 498.
Braham, R. R., 1964:*J. Atmos. Sci.* **21**, 640.
Braham, R. R., 1967:*J. Atmos. Sci.* **24**, 311.
Braham, R. R., 1968:*Bull. Am. Meteor. Soc.* **49**, 343.
Braham, R. R., 1974:*Bull. Am. Meteor. Soc.* **55**, 100.
Braham, R. R., 1990:*J. Appl. Meteor.* **29**, 200.
Braham, R. R., and Spyers-Duran, P., 1967:*J. Appl. Meteor.* **5**, 1058.
Braham, R. R., and Spyers-Duran, P., 1975:*J. Appl. Meteor.* **13**, 940.
Braham, R. R., and Squires, P., 1974:*Bull. Am. Meteor. Soc.* **55**, 543.
Brasseur, G., and Solomon, S., 1984:*Aeronomy of the Middle Atmosphere*, D. Reidel.
Brazier-Smith, Jennings, S. G., and Latham, J., 1973:*Quart. J. Roy. Meteor. Soc.* **99**, 260.
Brazier-Smith, P. R. *et al.*, 1971:*Proc. Roy. Soc. London* **A322**, 523.
Brazier-Smith, P. R., 1971:*Phys. of Fluids* **14**, 1.
Brazier-Smith, P. R., 1972:*Quart. J. Roy. Meteor. Soc.* **98**, 434.
Brazier-Smith, P. R., Jennings, S. G., and Latham, J., 1972:*Proc. Roy. Soc. London* **A326**, 393.
Breach, D. R., 1961:*J. Fluid Mech.* **10**, 306.
Breed, D. W., and Dye, J. E., 1989:*J. Geophys. Res.* **94**, 14841.
Breeding, R. J. *et al.*, 1973:*J. Geophys. Res.* **78**, 7057.
Brenner, H., 1961:*Chem. Eng. Sci.* **16**, 242.
Brenner, H., 1963:*Chem. Eng. Sci.* **18**, 109.
Brenner, H., and Cox, R. G., 1962:*J. Fluid Mech.* **13**, 561.
Bricard, J., 1949:*J. Geophys. Res.* **54**, 39.
Bricard, J., 1965:*Problems of Atmospheric and Space Electricity*, S. C. Coronity, Ed., p. 82, Elsevier.
Bricard, J., Billard, F., and Madelaine, G., 1978:*J. Geophys. Res.* **73**, 4487.
Bricard, J., Cabane, M., and Madelaine, G., 1971:*J. Aerosol. Sci.* **2**, 275.
Bridgeman, P. W., 1929:*Int. Crit. Tables* **4**, 11.
Bridgeman, P. W., 1931:*Dimensional Analysis*, Yale Univ. Press, New Haven, Connecticut.
Briggs, G. A., 1968:*Monthly Weather Rev.* **96**, 1744.
Brill, R., and Ender, H., 1955:*Nature* **174**, 925.
Brill, R., and Tippe, A., 1967:*Acta Cryst.* **23**, 343.
Brink-ten, H. M., Schwartz, S. E., and Daun, P. H., 1987:*Atmos. Environ.* **21**, 2035.
Brinkmann, J., 1994:*Ph. D. Thesis*, Inst. f. Atmos. Phys., Univ. Mainz, Mainz.
Broadwell, J. E., and Breidenthal, R. E., 1982:*J. Fluid. Mech.* **125**, 397.
Brock, C. A. *et al.*, 1995:*Science* **270**, 1650.
Brock, J. R., 1962:*J. Coll. Sci.* **17**, 768.
Brock, J. R., 1971:*Atmos. Environment* **5**, 833.
Broll, A. *et al.*, 1984:*Phys. Chem. Behavior of Atmos. Pollutants*, p. 390, B. Versino and G. Angeletti, Eds., D. Reidel.
Brook, M. *et al.*, 1980:*Preprints Conf. Atmos. Electr.*, L. H. Ruhnke and J. Latham, Eds., p. 365, A. Deepak, Hampton, Virginia.
Brook, M. *et al.*, 1982:*J. Geophys. Res.* **87**, 1207.
Brook, M., 1958:*Recent Advances in Thunderstorm Electricity*, L. G. Smith, Ed., p. 383, Pergamon.
Brook, M., and Latham, J. D.. 1968:*J. Geophys. Res.* **73**, 7137.
Broto, F., and Clausse, D., 1976:*J. Phys. Chem., Solid State* **9**, 4251.
Brown, E. N., and Braham, R. R., 1959:*J. Meteor.* **16**, 609.
Brown, K. A. *et al.*, 1971:*J. Geophys. Res.* **76**, 2825.
Brown, P. S., 1983:*J. Clim. and Appl. Meteor.* **22**, 693.
Brown, P. S., 1985:*J. Comput. Phys.* **58**, 417.
Brown, P. S., 1986:*J. Clim. and Appl. Meteor.* **25**, 313.
Brown, P. S., 1987:*J. Atmos. Sci.* **44**, 242.
Brown, P. S., 1988:*J. Atmos. Sci.* **45**, 712.
Brown, P. S., 1989:*J. Atmos. Sci.* **46**, 1186.
Brown, P. S., 1991:*J. Atmos. Sci.* **48**, 200.
Brown, R., 1980:*Quart. J. Roy. Meteor. Soc.* **106**, 781.
Brown, R., and Roach, W. T., 1976:*Quart. J. Roy. Meteor. Soc.* **102**, 335.

Brown, S., 1970:*Atmospheric Sciences Paper 170*, Dept. Atmos. Sci., Colorado State University, Fort Collins, Colorado.
Browning, K. A. *et al.*, 1968:*J. Appl. Meteor.* **7**, 603.
Browning, K. A., 1966:*Quart. J. Roy. Meteor. Soc.* **92**, 1.
Browning, K. A., 1977:*Meteorol. Monographs* **38**, p. 1., G. B. Foote, C. A. Knight, Eds., Am. Meteor. Society.
Browning, K. A., and Beimers, J. G., 1967:*J. Appl. Meteor.* **6**, 1075.
Brownscombe, J. L., and Goldsmith, P., 1972:*Preprints Cloud Phys. Conf.*, London, p. 27, Roy. Meteor. Soc., London.
Brownscombe, J. L., and Hallett, J., 1967:*Quart. J. Roy. Meteor. Soc.* **93**, 455.
Brownscombe, J. L., and Thorndyke, N. S. C., 1968:*Nature* **220**, 687.
Brunauer, S., Copeland. L. E., and Cantro, D. L., 1967:*The Solid-Gas Interface*, E. A. Flood, Ed., p. 71, Marcel Dekker.
Brunauer, S., Emmett, P. H., and Teller, E. J., 1938:*J. Atmos. Chem. Soc.* **60**, 309.
Bruntjes, R. T., Heymsfield, A. J., and Krauss, T. W., 1987:*J. Atmos. Sci.* **44**, 1331.
Bryant, G. W., and Mason. B. J., 1960:*Phil. Mag.* **5**, 1221.
Bryant, G. W., Hallett, J., and Mason, B. J., 1959:*J. Phys. Chem. Solids* **12**, 189.
Bucaro, J. A., and Litovitz, T. A., 1971:*J. Chem. Phys.* **54**, 3846.
Buff, F. P., 1951:*J. Chem. Phys.* **19**, 1591.
Buff, F. P., 1955:*J. Chem. Phys.* **23**, 419.
Buijs, K, and Choppis, G., 1963:*J. Chem. Phys.* **39**, 2035.
Bullemer, B., and Riehl, N., 1966:*Solid State Commun.* **4**, 447.
Bullrich, K. *et al.*, 1966:*Final Techn. Rept.*, Contract No. DA-91-591-EUC-3458, University of Mainz, Mainz.
Bürgermeister, S., 1984:*Diploma Thesis*, Meteor. Inst., Univ. Frankfurt, Frankfurt.
Burley, G., 1963:*J. Chem. Phys.* **38**, 2807.
Burley, G., 1964:*J. Phys. Chem. Solids* **25**, 629.
Burrows, D. A., and Hobbs, P. V., 1970:*J. Geophys. Res.* **75**, 4499.
Burton, W. K., Cabrera, N., and Frank, F. C., 1951:*Phil. Trans. Roy. Soc., London* **243A**, 299.
Buser, O., 1976:*Mitteilung 33*, Swiss Fed. Inst. f. Snow and Avelanche Res., Davos, Switzerland.
Buser, O., and Aufdermauer, A. N., 1977:*Electrical Processes in the Atmosphere*, H. Dolezalek, R. Reiter, p. 294, Eds. Steinkopff.
Businger, J. A., 1973:*Workshop in Micrometeorology*, p. 67, D. A. Hanger, Ed., Am. Meteor. Soc., Boston.
Butcher, S. S., and Charlson, R. J., 1972:*An Introduction to Air Chemistry*, Academic Press.
Butorin, G. T., and Skripov, V. P., 1972:*Kristallografiya* **17**, 379.
Byers, H. R., 1965:*Elements of Cloud Physics*, University of Chicago Press, Chicago.
Byers, H. R., and Braham, R. R., 1949:*The Thunderstorm Project*, U.S. Gov. Printing Office, Washington D. C.
Byers, H. R., and Hull, E. C., 1949:*Bull. Am. Meteor. Soc.* **30**, 90.
Byers. H. R., Sievers, J. R., and Tufts, B., 1957:*Artificial Stimulation of Rain*, p. 47, Pergamon.
Byrne, G. J., Few, A. A., and Lueber, M. E., 1983:*Geophys. Res. Lett.* **10**, 39.
Byrne, G. J., Few, A. A., and Stewart, M. F., 1989:*J. Geophys. Res.* **94**, 6297.
Byrne, M. A., and Jennings, S. G., 1993:*Atmos. Environ.* **27A**, 2099.
Cabrera, N., and Levine, N. M., 1956:*Phil. Mag.* **1**, 450.
Cachier, H., Bremond, M. P., and Buat-Menard, P., 1990:*Preprints*, Conf. on Global Atmos. Chem., Beijing, p. 241, Brookhaven Natl. Labs. Press.
Cadle, R. D., 1972:*Trans. Am. Geophys. Union* **53**, 812.
Cadle, R. D., 1973:*Chemistry of the Lower Atmosphere*, S. I. Rasool, Ed., p. 69, Plenum.
Cadle, R. D., and Langer, G., 1975:*Geophys. Res. Lett.* **2**, 329.
Cadle, R. D., and Powers, J. W., 1966:*Tellus* **18**, 176.
Cadle, S. H. *et al.*, 1990:*Atmos. Environ.* **24A**, 2981.
Cadle, S. H., 1985:*Atmos. Environ.* **19**, 181.
Cadle, S. H., Countess, R. J., and Kelly, N. A., 1982:*Atmos. Environ.* **16**, 2501.
Cadle, S., Countess, R. J., and Kelly, N. A., 1982:*Atmos. Environ.* **19**, 181.
Cahn, J. W., 1960:*Acta Metallurgica* **8**, 554.
Cahn, J. W., Hillig, W. B., and Sears, G. W., 1964:*Acta Metallurgica* **12**, 1421.

Cameron, A. G. W., 1981:*Essays in Nuclear Astrophysics*, C. A. Barnas, D. D. Clayton, D. N. Schramm, Eds., Cambridge University Press, London.
Campbell, E. S., 1952:*J. Chem. Phys.* **20**, 1411.
Caranti, J. M. and Illingworth, A. J., 1983:*J. Phys. Chem.* **87**, 4125.
Caranti, J. M., and Illingworth, A. J., 1980:*Nature* **284**, 44.
Caranti, J. M., Illingworth, A. J., and Marsh, S. J., 1985:*J. Geophys. Res.* **90**, 6041.
Carlslaw, K.S. *et al.*, 1994:*Geophys. Res. Lett.* **21**, 2479.
Carras, J. N., and Macklin, W. C., 1973:*Quart. J. Roy. Meteor. Soc.* **99**, 639.
Carras, J. N., and Macklin, W. C., 1975:*Quart. J. Roy. Meteor. Soc.* **101**, 127.
Carrier, G. F., 1953:*Final Rept., Office of Naval Res., Contract No.-653-00/1.*
Carroll, M. A., 1985:*J. Geophys. Res.* **90**, 10483.
Carslaw, H. S., and Jaeger, J. C., 1948:*Conduction of Heat in Solids*, Oxford, University Press.
Carslaw, H. S., and Jaeger, J. C., 1959:*Heat and Mass Transfer*, McGraw-Hill.
Carstens, J. C. *et al.*, 1966:*J. de Rech. Atmos.* **2**, 95.
Carstens, J. C., 1972:*J. Atmos. Sci.* **29**, 588.
Carstens, J. C., and Kassner, J. L., 1968:*J. de Rech. Atmos.* **3**, 33
Carstens,1. C., Podzimek, J., and Saad, A., 1974:*J. Atmos. Sci.* **31**, 592.
Carte, A. E., 1956:*Proc. Phys. Soc., London* **69**, 1028.
Carte, A. E., 1959:*Proc. Phys. Soc., London* **73**, 324.
Carte, A. E., and Kidder, R. E., 1966:*Quart. J. Roy. Meteor. Soc.* **92**, 382.
Carte, A. E., and Mossop, S. C., 1960:*Bull. Obs. Puy de Dome* **4**, 137.
Carter, A. E., and Kidder, R. E., 1961:*Quart. J. Roy. Meteor. Soc.* **92**, 382.
Cataneo, R., Adam, J. R., and Semonin, R. G., 1971:*J. Atmos. Sci.* **28**, 416.
Cataneo, R., and Stout, G. E., 1968:*J. Appl. Meteor.* **7**, 90.
Caton, P. G., 1966:*Quart. J. Roy. Meteor. Soc.* **92**, 15.
Cerwinski, N., and Pfisterer, W., 1972:*J. de Rech. Atmos.* **6**, 89.
Chagnon, C. W., and Junge, C. E., 1961:*J. Meteor.* **18**, 746.
Chalmers, B., 1964:*Principles of Solidification*, p. 62, Wiley.
Chalmers, J. A., 1967:*Atmospheric Electricity, 2nd edn.*, Pergamon.
Chalmes, J. A., 1956:*J. Atmos. Terr. Phys.* **9**, 311.
Chamberlain, A. C., 1953:*Rep.* British Atomic Energy Res. Establ., AERE-HPIl2-1261.
Chameides, W. L., 1984:*J. Geophys. Res.* **89**, 4739.
Chandrasekhar, S., 1943:*Rev. Mod. Phys.* **15**, 1.
Chandrasekhar, S., 1961:*Hydrodynamic and Hydromagnetic Stability*, Oxford University Press.
Chandrasekhar, V., Cooper, W. A., and Bringi, V. N., 1988:*J. Atmos. Sci.* **45**, 1323.
Chang, B., and Hill, R. C., 1980:*Atmos. Environ.* **14**, 803.
Chapman, E. G., Sklarew, D. S., and Flickinger, J. S., 1986:*Atmos. Environ.* **20**, 1717.
Chapman, S., 1952:*Cornell Alo. Lab. Rept.*, No. VC 603-P-1, Ithaca, New York.
Chappell, C. F., Magzainer, E. L., and Fritsch, J. M., 1974:*J. Appl. Meteor.* **13**, 726.
Charlesworth, D. H., and Marshall, W. R., 1960:*Am. Inst. Chem. Engs.* **6**, 9.
Charlson, R. *et al.*, 1987:*Nature* **326**, 655.
Charlton, R. B., and List, R., 1972a:*J. de Rech. Atmos.* **6**, Nos. 1-3, 55
Charlton, R. B., and List, R., 1972b:*J. Atmos. Sci.* **29**, 1182.
Chauzy, S., and Despiau, S., 1980:*J. Atmos. Sci.* **37**, 1619.
Chauzy, S., and Raisonville, P., 1983:*Preprints Conf. Atmos. Electr.*, L. H. Ruhnke and J. Latham, Eds., p. 184, A. Deepak, Hampton, Virginia.
Chen, C. S., 1971:*Ph.D. Thesis*, Dept. Meteor., Univ. of California, Los Angeles.
Chen, J. P., and Crutzen, P. J., 1994:*J. Geophys. Res.* **99**, 18, 847.
Cheng, L., and English, M., 1983:*J. Atmos. Sci.* **40**, 204.
Cheng, R. J., 1988:*The Generation of Secondary Marine Aerosols*, Lecture Notes in Physics, p. 589, Springer.
Cheng, R. J., Blanchard, D. C., and Cipriano, R. J., 1988:*Atmos. Res.* **22**, 15.
Cheng, Y. *et al.*, 1988b:*Aerosol Sci. and Techn.* **8**, 199.
Cheng, Y., Yeh, H., and Allen, M. D., 1988a:*Aerosol Sci. and Techn.* **8**, 109.
Cheng. L., English, M., and Wong, R., 1985:*J. Clim. and Appl. Meteor.* **24**, 1059.
Chepil, W. S., 1951:*Soil Sci.* **72**, 387.
Chepil, W. S., 1957:*Am. J. Sci.* **225**, 12, 206
Chepil, W. S., 1965:*Meteor. Monographs* **6**, 123.
Chepil, W. S., and Woodruff, N. P., 1957:*Am. J. Sci.* **225**, 104.
Chepil, W. S., and Woodruff, N. P., 1963:*Adv. Agronomy* **15**, 211.

Chernov, A. A., and Melnikova, A. M., 1971:*Soviet Physics (Crystallography)* **16**, 404.
Chess, J. P., and Crutzen, P. J., 1994:*J. Geophys. Res.* **99**, 18, 847.
Chester, R., and Johnson, L. R., 1971:*Nature* **229**, 105.
Chester, W., and Breach, D. R., 1969:*J. Fluid Mech.* **37**, 75
Chien, E. H. C., and Neiburger, M., 1972:*J. Atmos. Sci.* **29**, 718.
Chilekuri, R., 1987:*Trans. Am. Soc. Mech. Eng.* **109**, 166.
Chiu, C. S., 1978:*J. Geophys. Res.* **83**, 5025.
Chiu, C. S., and Klett, J. D., 1976:*J. Geophys. Res.* **81**, 1111.
Cho, H. R., Iribarne, J. U., and Richards, W. G., 1981:*J. Atmos. Sci.* **38**, 1111.
Chodes, N., Warner, J., and Gagin, A., 1974:*J. Atmos. Sci.* **31**, 1351.
Choularton, T. W. *et al.*, 1986:*Quart. J. Roy. Meteor. Soc.* **112**, 131.
Choularton, T. W., Griggs, D. D., and Hunood, Y., 1980:*Quart. J. Roy. Meteor. Soc.* **106**, 367.
Christian, H. *et al.*, 1980:*Quart. J. Roy. Meteor. Soc.* **106**, 159.
Chruch, T. M. *et al.*, 1982:*J. Geophys. Res.* **870**, 11013.
Chu, L. T., Leu, M. T., and Keyser, L. F., 1993:*J. Phys. Chem.* **97**, 7779.
Chu, T. S., 1974:*Bull. Syst. Tech. J.* **53**, 1557.
Chylek, P. *et al.*, 1987:*J. Geophys. Res.* **92**, 9801.
Cipriano, R. J. *et al.*, 1983:*J. Atmos. Sci.* **40**, 469.
Cipriano, R. J., and Blanchard, D. C., 1981:*J. Geophys. Res.* **86**, 8085.
Claiborn, C. S., and Aneja, V. P., 1991:*J. Geophys. Res.* **96**, 18, 771.
Claiborn, C. S., and Aneja, V. P., 1991:*J. Geophys. Res.* **96**, 18, 787.
Clapsdale, C., and Lamb, D., 1989:*Geophys. Res. Lett.* **16**, 1173.
Clark, A., 1970:*The Theory of Adsorption and Catalysis*, Academic Press.
Clark, T. L., 1973:*J. Atmos. Sci.* **30**, 857.
Clarke, A. D., 1989:*Aerosol Sci. Techn.* **10**, 1148.
Clarke, A. D., Ahlquist, N. C., and Covert, D. S., 1987:*J. Geophys. Res.* **92**, 4179.
Clementi, E., Kistenmacher, H., and Popkie, H., 1973:*J. Chem. Phys.* **58**, 2460.
Cleveland, W. S., Graedel, T. E., and Kleiner, B., 1977:*Atmos. Environ.* **11**, 357.
Clift, R., Grace, J. R., and Weber, M. E., 1978:*Bubbles, Drops and Particles*, Academic Press.
Cobb, A. W., and Gross, G. W., 1969:*J. Electrochem. Soc.* **116**, 796.
Cober, S. G., and List, R., 1993:*J. Atmos. Sci.* **50**, 1591.
Cohen, E. R., and Vaughn, E. U., 1971:*J. Coll. Interface Sci.* **35**, 612.
Cohen, M. D., Flanagan, R. C., and Seinfeld, J. H., 1987:*J. Phys. Chem.* **91**, 4583.
Cohen, N. V. *et al.*, 1962:*Trans. Farad. Soc.* **58**, 490.
Cohen, R. E., 1970:*J. Stat. Phys.* **2**, 147.
Colgate, S. A., 1972:*J. Geophys. Res.* **72**, 479.
Colgate, S. A., and Romero, J. M., 1970:*J. Geophys. Res.* **75**, 5873.
Colgate, S. A., Levin, Z., and Petschek, A. G., 1977:*J. Atmos. Sci.* **34**, 1433.
Collatz, L., 1960:*The Numerical Treatment of Differential Equations*, 3rd edn., Springer.
Collett, J. L. *et al.*, 1991:*Envir. Sci. and Techn.* **25**, 782.
Comez, R., and Krehbiel, P., 1986:*Preprints 23rd Conf. on Radar Meteor.*, Snowmass, Colorado, p. 12, Am. Meteor. Soc.
Compaan, K., and Haven, Y., 1956:*Trans. Faraday Soc.* **52**, 786.
Conklin, M. H. *et al.*, 1993:*Atmos. Environ.* **27A**, 159.
Conklin, M. H., and Bales, R. C., 1993:*J. Geophys. Res.* **98**, 16, 851.
Cooper, W. A., 1974:*J. Atmos. Sci.* **31**, 1832.
Cooper, W. A., 1980:*Preprints Cloud Phys. Conf.*, Clermont-Ferrand, p. 665, Blaise Pascal University, Aubière, France.
Cooper, W. A., and Baumgardner, D., 1989:*J. Atmos. Sci.* **46**, 1165.
Coriel, S. R., Hardy, S. C., and Sekerka, R. F., 1971:*J. Crystal Growth* **11**, S3.
Corn, M., 1966:*Aerosol Science*, C. N. Davies, Ed., p. 359, Academic Press
Coroniti, S. C., and Hughes, J., Eds., 1969:*Planetary Electrodynamics*, Gordon and Breach.
Corrin, M. L., 1975:*Proc. Symposium on Hail*, Section IV, NCAR, Boulder, Colorado.
Corrin, M. L., and Nelson, J. A., 1968:*J. Phys. Chem.* **72**, 643.
Corrin, M. L., Edwards, H. W., and Nelson, J. A., 1964:*J. Atmos. Sci.* **21**, S65.
Corrin, M. L., Moulik, S. P., and Cooley, B., 1967:*J. Atmos. Sci.* **24**, 530.
Corrsin, S., 1964:*Phys. Fluids* **7**, 1156.
Cotton, W. R. *et al.*, 1986:*J. Clim. and Appl. Meteor.* **25**, 1658.

Cotton, W. R., 1972:*Monthly Weather Rev.* **100**, 764.
Cotton, W. R., 1975:*J. Atmos. Sci.* **32**, 548.
Cotton, W. R., and Anthes, R. A., 1989:*Storm and Cloud Dynamics*, Academic Press.
Cotton, W. R., and Gokhale, N. R., 1967:*J. Geophys. Res.* **72**, 4041.
Cotton, W. R., and Tripoli, G. J., 1978:*J. Atmos. Sci.* **35**, 1503.
Coulter, L. V., and Candela, G. A., 1952:*Z. Elektrochem.* **56**, 449.
Covert, D. S., 1992:*Personal Communication*, Prof. Hobbs, Univ. Washington, Seattle.
Covert, D. S. *et al.*, 1992:*J. Geophys. Res.* **97**, 20, 581.
Cox, R. A., and Penkett, S. A., 1970:*Atmos. Environment* **4**, 425.
Cox, R. G., 1965:*J. Fluid. Mech.* **23**, 625.
Crabb, J. A., 1973:*Ph. D. Thesis*, University of Manchester.
Crabb, J. A., and Latham, J., 1974:*Quart. J. Roy. Meteor. Soc.* **100**, 191.
Cram, D. J., and Hammond, G. S., 1955:*Organic Chemistry*, McGraw-Hill.
Crowther, A. G., and Saunders, C. P. R., 1973:*J. Meteor. Soc. Japan* **51**, 490.
Crutzen, P. J., 1976:*Geophys. Res. Lett.* **3**, 73.
Cunningham, E., 1910:*Proc. Roy. Soc. London* **A83**, 357.
Cunningham, R. M., 1947:*J. Meteor.* **4**, 163.
Cwilong, B. M., 1947:*Proc. Roy. Soc. London* **A190**, 137.
Czerwinski, N., and Pfisterer, W., 1972:*J. de Rech. Atmos.* **6**, 89.
Czys, R. R., 1987:*Ph. D. Thesis*, University of Illinois, Urbana, Illinois.
Czys, R. R., and Ochs, H. T., 1988:*J. Atmos. Sci* . **45**, 3161.
D'Almeida, F. C., 1975:*Research Rept.* 75-2, Dept. Meteor., University of Wisconsin, Madison, Wisconsin.
D'Almeida, F. C., 1976:*J. Atmos. Sci.* **33**, 571.
D'Almeida, F. C., 1977:*J. Atmos. Sci.* **34**, 1286.
D'Almeida, F. C., 1979a:*J. Atmos. Sci.* **36**, 1557.
D'Almeida, F. C., 1979b:*J. Atmos. Sci.* **36**, 1564.
D'Almeida, G. A., and Schütz, L., 1983:*J. Clim. and Appl. Meteor.* **22**, 233.
D'Arrigo, G. *et al.*, 1981:*J. Chem. Phys.* **75**, 4264.
D'Enrico, R. E., and Auer, A. H., 1978:*Preprints Cloud Phys. Conf.*, Issaquah, p. 114, Am. Meteor. Soc.
Dana, M. T., Hales, J. M., and Wolff, M. A., 1975:*J. Geophys. Res.* **80**, 4119.
Danckwerts, P. U., 1970:*Gas-liquid Reactors*, McGraw-Hill.
Danford, M. D., and Levy, 1962:*J. Am. Chem. Soc.* **84**, 3965.
Danielsen, E. F., Bleck, R., and Morris, D. A., 1972:*J. Atmos. Sci.* **29**, 135.
Darzi, M., and Winchester, J. W., 1982:*J. Geophys. Res.* **87**, 1251.
Dasch, J. M., 1987:*Atmos. Environ.* **21**, 137.
Dasch, J. M., 1987:*The Chemistry of Acid Rain*, R. W. Johnson *et al.*, Eds., ACS. Symp. Ser. 349, p. 242, Am. Chem. Soc., Washington D.C.
Daum, P. H. *et al.*, 1984:*Atmos. Environ.* **18**, 2671.
Daum, P. H. *et al.*, 1987:*J. Geophys. Res.* **92**, 8426.
Daum, P. H., 1988:*Acid Deposition at High Elevation Sites*, M. A. Unsworth, D. Fowler, Eds., p. 139, Kluwer.
Daum, P. H., Schwartz, S. E., and Newman, L., 1984:*J. Geophys. Res.* **89**, 1447.
Davenport, H. M., and Peters, L. K., 1978:*Atmos. Environ.* **12**, 997.
Davies, C. N., 1945:*Proc. Phys. Soc.* London, **57**, 259.
Davies, C. N., 1966:*Aerosol Science*, Academic Press.
Davies, C. N., and Peetz, C. V., 1956:*Proc. Roy. Soc. London* **A234**, 269.
Davies, J. T., and Rideal, E. K., 1961:*Interfacial Phenomena*, Academic Press.
Davies, T. D., 1983:*Atmos. Environ.* **17**, 797.
Davis, B. L., Johnson, L. R., and Moeng, F. J., 1975:*J. Appl. Meteor.* **14**, 891.
Davis, C. I., 1974:*Ph.D. Thesis*, Dept. Environ. Sci., University of Wyoming, Laramie, Wyoming.
Davis, C., and Litovitz, T., 1965:*J. Chem. Phys.* **42**, 2563.
Davis, E. J. *et al.*, 1987:*Aerosol Sci. Technol.* **6**, 273.
Davis, M. H., 1964a:*Res. Rept., RM-3860-PR*, The RAND Corp., Santa Monica, California.
Davis, M. H., 1964b:*Quart. J. Mech. and Appl. Math.* **17**, 499.
Davis, M. H., 1965:*Preprints Cloud Phys. Conf.*, Tokyo and Sapporo, p. 118, Meteor. Soc. Japan, Tokyo.
Davis, M. H., 1966:*J. Geophys. Res.* **71**, 3101.
Davis, M. H., 1969:*Am. J. Phys.* **37**, 26.

Davis, M. H., 1972:*J. Atmos. Sci.* **29**, 911.
Davis, M. H., and Sartor, J. D., 1967:*Nature* **215**, 1371.
Davy, J. G., and Somorjai, G. A., 1971:*J. Chem. Phys.* **55**, 3624.
Dawson, G. A., 1973:*J. Geophys. Res.* **78**, 6364.
Dawson, G. A., 1978:*Atmos. Environ.* **12**, 1991.
Dawson, G. A., and Cardell, S. R., 1973:*J. Geophys. Res.* **78**, 8864.
Dawson, G. A., and Farmer, J. C., 1988:*J. Geophys. Res.* **93**, 5200.
Dawson, G. A., and Richards, C. N., 1970:*J. Geophys. Res.* **75**, 4589.
Dawson, G. A., and Warrender, R. A., 1973:*J. Geophys. Res.* **78**, 3619.
Day, G. J., 1955:*Geofys. Pura e Appl.* **31**, 169.
Day, J. A., 1964:*Quart. J. Roy. Meteor. Soc.* **90**, 72.
Day, J. A., 1965:*Natural History*, Jan. issue.
Dayan, V. *et al.*, 1985:*Atmos. Environ.* **19**, 651.
De Beauville, C. A. *et al.*, 1988:*J. Atmos. Sci.* **45**, 3320.
de Micheli, S. M., and Iribarne, J. V., 1963:*J. de Chim. Phys.* **48**, 767.
Dean, W. R., and O'Neill, M. E., 1963:*Mathematika* **10**, 13.
Deardorff, J. W., 1980:*J. Atmos. Sci.* **37**, 131.
Defay, R. *et al.*, 1966:*Surface Tension and Adsorption*, Wiley.
Deirmendjian, D., 1969:*Electromagnetic Scattering on Spherical Polydispersions*, Elsevier.
Delaney, L. J., Houston, R. W., and Eagleton, L. C., 1964:*Chem. Engr. Sci.* **19**, 105.
Delany, A. C. *et al.*, 1967:*Geochim. Cosmo. Chim. Acta* **31**, 885.
Demas, R. *et al.*, 1980:*J. Geophys. Res.* **85**, 4468.
DeMott, P. J., 1990:*J. Appl. Meteor.* **29**, 1072.
DeMott, P. J., and Grant, L. O., 1984:*Preprints Cloud Phys. Conf.*, Tallin, p. 191, Estonian Acad. Sci., SSR.
DeMott, P. J., and Rogers, D. C., 1990:*J. Atmos. Sci.* **47**, 1056.
DeMott, P. J., Meyers, M. P., and Cotton, W. R., 1992:*Preprints Cloud Phys. Conf.*, Montreal, p. 492, McGill University.
DeMott, P. J., Meyers, M. P., and Cotton, W. R., 1994:*J. Atmos. Sci.* **51**, 77.
Dennis, A. S., and Musil, D. J., 1973:*J. Atmos. Sci.* **30**, 278.
Dennis, S. C. R., and Shimshoni, M., 1964:*Current Paper No. 797*, Aero. Res. Counc.
Derjaguin, B. V., and Yamalov, Yu. I., 1972:*Reviews in Aerosol Phys. and Chem.*, G. M. Hidy and J. R. Brock, Eds., Vol. 3, p. 3, Pergamon.
Derjaguin, B. V., Fedoseyev, U. A., and Rosenzweig, L. A., 1966:*J. Coll. Interface Sci.* **22**, 45.
Derjaguin, L. A., and Fedoseyev, U. A., 1971:*J. Coll. Interface Sci.* **37**, 484.
Desalmand, F., 1987:*Atmos. Res.* **21**, 13.
Deshler, T., 1982:*Ph. D. Thesis*, Dept. Phys. Astronomy, University of Wyoming, Laramie, Wyoming.
Dessens, H., 1946:*C. R. Acad. Sci.* **223**, 915.
Dessens, H., 1947:*La Météorologie*, Oct. - Dec., 321.
Dessens, H., 1949:*Quart. J. Roy. Meteor. Soc.* **75**, 23.
Detwiler, A. G., Smith, P. L., and Stith, J. L., 1992:*Preprints Cloud Phys. Conf.*, Montreal, p. 260, McGill Univ. Press.
Deutsch, P. W. *et al.*, 1983a:*J. Chem. Phys.* **78**, 5103.
Deutsch, P. W. *et al.*, 1983b:*J. Phys. Chem.* **87**, 4309.
Devir, S. E., 1963:*J. Colloid. Sci.* **18**, 744.
Devir, S. E., 1966:*J. Coll. Interface Sci.* **21**, 9.
Diehl, C., 1989:*MS Thesis*, Inst. f. Atmos. Phys., Univ. Mainz, Mainz.
Diehl, C., Mitra, S. K., and Pruppacher, H. R., 1995:*Atmos. Environ.* **29**, 975.
Diem, M., 1968:*Arch. Meteor. Geophys. Biokl.* **B16**, 347.
Diem, M., and Strantz, R., 1971:*Meteor. Rundschau* **24**, 23.
Dihajakos, I. G. *et al.*, 1990:*Atmos. Environ.* **24B**, 171.
Dinger, J. E., 1965:*J. Atmos. Sci.* **22**, 162.
Dinger, J. E., and Gunn, R., 1947:*Terr. Magn. Atmos. Electr.* **51**, 477.
Dinger, J., Howell, H. B., and Wojciechowski, T. H., 1970:*J. Atmos. Sci.* **27**, 1791.
Dingle, A. N., and Lee, Y., 1972:*J. Appl. Meteor.* **11**, 877.
Dobrowolski, A. B., 1903:*Rapports Scientifiques (Resultats du Voyage de S. Y. Belgica, 1897-1899)*, 3/4 (Meteorology), pt. 3: La neige et le givre, J. E. Buschman, Anvers (Belgium).
Dodd, K. N., 1960:*J. Fluid Mech.* **9**, 175.

Dominé, F., and Thibert, E., 1995:*Biogeochemistry of Seasonally Snow-Covered Catchments*, IAHS Publ. No. 228, 3.
Dong, Y., and Hallett, J., 1992:*J. Geophys. Res.* **97**, 20361.
Doolittle, J. B., and Vali, G., 1975:*J. Atmos. Sci.* **32**, 375.
Dorsch, R. G., and Boyd, B., 1951:*NACA*, Techn. Note, 2532.
Dorsch, R. G., and Hacker, P., 1950:*NACA*, Techn. Note, 2142.
Dorsch, R. G., and Hacker, P., 1951:*NACA*, Techn. Note, 2510.
Dorsey, N. E., 1940:*Properties of Ordinary Water Substance*, Reinhold Publ. Co., New York.
Doskey, P. V., and Andren, A. W., 1986:*Atmos. Environ.* **20**, 1735.
Douglas, R. H., 1960:*Nubila* **3**, No. 1, 5.
Douglas, R. H., 1964:*Preprints 11th Weather Radar Conf.*, p. 146, Boulder, Colorado, Am. Meteor. Soc., Boston.
Dowling, D. R., and Radke, L. F., 1990:*J. Appl. Meteor.* **29**, 970.
Doyle, A., Moffet, D. R., and Vonnegut, B., 1964:*J. Coll. Sci.* **19**, 136.
Draginis, M., 1958:*J. Meteor.* **15**, 481.
Drake, J. C., 1968:*Quart. J. Roy. Meteor. Soc.* **94**, 176.
Drake, J. C., and Mason, B. J., 1966:*Quart. J. Roy. Meteor. Soc.* **92**, 500.
Drake, R. L., 1972a:*J. Atmos. Sci.* **29**, 537.
Drake, R. L., 1972b:*Topics in Current Aerosol Research*, G. M. Hidy and G. R. Brock, Eds., Vol. 3, p. 201, Pergamon.
Drake, R. L., and Wright, T. J., 1972:*J. Atmos. Sci.* **29**, 548.
Dreiling, V., 1992:*Ph. D. Thesis*, Inst. f. Atmos. Phys., Univ. Mainz, Mainz.
Droessler, E. G., 1964:*J. Atmos. Sci.* **21**, 201.
Droessler, E. G., and Heffernan, K. J., 1965:*J. Appl. Meteor.* **4**, 442.
Drost-Hansen, W., 1967:*J. Coll. Interface Sci.* **25**, 131.
Du Toit, P. S., 1967:*J. Appl. Meteor.* **6**, 1087.
Duce, R. A., 1972:*Science* **176**, 161.
Duce, R. A., 1978:*Pure and Appl. Geophys.* **116**, 244.
Duce, R. A. *et al.*, 1983:*Geophys. Space Phys.* **21**, 921.
Ducret, J., and Cachier, H., 1992:*J. Atmos. Chem.* **15**, 55.
Dufour, L., 1965a:*Report*, Publ. Ser. B, 46, Inst. Roy. Meteor. de Belgique, Brussels.
Dufour, L., 1965b:*Report*, Bull. de l'Acad. Royale de Belgique (Classes des Sciences) Ser. 5, 60, 298.
Dufour, L., and Defay, R., 1963:*Thermodynamics of Clouds*, Academic Press.
Dumas, J. P., and Broto, F., 1974:*Compte. Rend. Acad. Sci.*, Paris 279, Ser. B., 415.
Duncan, A. B., and Pople, J. A., 1953:*Trans. Farad. Soc.* **49**, 217.
Dundon, M. L., and Mack, E., 1923:*J. Am. Chem. Soc.* **45**, 2479, 2650.
Dunham, S. B., 1966:*J. de Rech. Atmos.* **2**, 231.
Dunning, W. J., 1955:*Chemistry of the Solid State*, W. E. Garner, Ed., p.159, Butterworths.
Dunning, W. J., 1967:*The Solid-Gas Interface*, E. A. Flood, Ed., Vol.1, p. 271, Marcel Dekker.
Dunning, W. J., 1969:*Nucleation*, A. C. Zettlemoyer, Ed., Marcel Dekker.
Durbin, N. G., 1959:*Tellus* **11**, 202.
Durham, J. L., Barnes, H. M., and Overton, J. H., 1984:*Chemistry of Particles, Fogs and Rain*. J. L. Durham, Ed., Chapter 5, p. 197, Butterworths.
Duynkerke, P. G., and Driedonks, A. G., 1988:*J. Atmos. Sci.* **45**, 2343.
Dye, J. E. *et al.*, 1986:*J. Geophys. Res.* **91**, 1231.
Dye, J. E. *et al.*, 1988:*Quart. J. Roy. Meteor. Soc.* **114**, 1271.
Dye, J. E. *et al.*, 1992:*J. Geophys. Res.* **97**, 8015.
Dye, J. E., and Hobbs, P. V., 1966:*Nature* **209**, 464.
Dye, J. E., and Hobbs, P. V., 1968:*J. Atmos. Sci.* **25**, 82.
Eadie, W. J., 1971:*Ph.D. Thesis*, Dept. of Geophys. Sciences, University of Chicago. (Also Techn. Note No. 40, Cloud Phys. Lab., Univ. of Chicago.)
East, T. W. R., 1957a:*Quart. J. Roy. Meteor. Soc.* **83**, 61.
East, T. W. R., 1957b:*Quart. J. Roy. Meteor. Soc.* **83**, 121.
East, T. W. R., and Marshall, J. S., 1954:*Quart. J. Roy. Meteor. Soc.* **80**, 26.
Easter, R. C., and Hobbs, P. V., 1974:*J. Atmos. Sci.* **31**. 1586.
Easter, R. C., and Peters, L.K., 1994:*J. Appl. Meteor.* **33**, 775.
Eaton, L., 1970:*Preprints Cloud Phys. Conf.*, Fort Collins, Col., p. 137, Am. Meteor. Soc., Boston.

Edwards, G. R., and Evans, L. F., 1960:*J. Atmos. Sci.* **17**, 627.
Edwards, G. R., and Evans, L. F., 1968:*J. Atmos. Sci.* **25**, 249.
Edwards, G. R., and Evans, L. F., 1971:*J. Atmos. Sci.* **28**, 1443.
Edwards, G. R., and Evans, L. F., and La Mer, V. K., 1962:*J. Coll. Sci.* **17**, 749.
Edwards, G. R., and Evans, L. F., and Zipper, A. F., 1970:*Trans. Farad. Soc.* **66**, 220.
Egner, H., and Erikson, E., 1955:*Tellus* **7**, 134.
Ehhalt, D. H., 1973:*J. Geophys. Res.* **78**, 7076.
Eichel, C., 1995:*Diploma Thesis*, Inst. f. Phys. of Atm., Univ. of Mainz, Mainz.
Eichmann, R. *et al.*, 1979:*Atmos. Environ.* **13**, 587.
Eigen, M. *et al.*, 1964:*Progr. in Reaction Kinetics*, Vol. 2, p. 287, G. Porter, Ed., MacMillan.
Eigen, M., 1952:*Z. f. Elektrochemie* **56**, 176.
Einstein, A., 1905:*Ann. d. Physik* **17**, 549.
Eisenberg, D., Kauzmann, W., 1969:*The Structure and Properties of Water*, Oxford University Press.
Eisner, H. S., Quince, B. W., and Slack, C., 1960:*Disc. Farad Soc.* **30**, 86.
El Ghandour *et al.*, 1983:*Atmos. Environ.* **17**, 573.
Eldrige, R. G., 1957:*J. Meteor.* **14**, 55.
Eldrup, M. Morgensen, O. E., and Bilgram, J. H., 1978:*J. Glaciol.* **21**, 101.
Eldrup, M., 1976:*J. Chem. Phys.* **64**, 5283.
Elgroh, M. W., and Hobbs, P. V., 1979:*Atmos. Environ.* **13**, 953.
Elster, J., and Geitel, H., 1913:*Phys. Z.* **14**, 1287.
Elster, J., and Geitel, H., 1985:*Ann. Phys. Chem.* **25**, 121.
Emanuel, K., 1981:*J. Atmos. Sci.* **38**, 1541.
Engelmann, R. J., 1970:*Scavenging - 1970*, p. 475, U.S. Atmos. Energy Commission, Techn. Info Service, U.S. Dept. of Commerce, Springfield, Virginia.
Enukashvili, I. M., 1964a:*Bull. Acad. Sci., U.S.S.R., Geophys. Ser.*, **10**, 944.
Enukashvili, I. M., 1964b:*Bull. Acad. Sci., U.S.S.R., Geophys. Ser.*, **11**, 1043.
Enukashvili, I. M., 1980:*J. Atmos. Sci.* **37**, 2521.
Erickson, R. E. *et al.*, 1977:*Atmos. Environ.* **11**, 813.
Erickson, R. E., and Yates, L. M., 1976:*Report*, Dept. No. EPA-600/3-76-089, US. Env. Protect Agency.
Erikson, D. J., Merril, J. T., and Duce, R. A., 1986:*J. Geophys. Res.* **91**, 1067.
Erikson, E., 1959:*Tellus* **11**, 375
Evans, D. G., and Hutchinson, W. L., 1963:*Quart. J. Roy. Meteor. Soc.* **89**, 370.
Evans, L. F., 1965:*Nature* **206**, 822.
Evans, L. F., 1966:*Nature* **211**, 281.
Evans, L. F., 1967a:*Nature* **213**, 384.
Evans, L. F., 1967b:*Trans. Farad. Soc.* **63**, 1.
Evans, L. F., 1970:*Preprints Conference Cloud Phys.*, Fort Collins, Col., p. 14, Am. Meteor. Soc., Boston.
Evans, L. F., 1973:*J. Atmos. Sci.* **30**, 1657.
Eyring, H., and Jhon, M. S., 1969:*Significant Liquid Structures*, Wiley.
Facy, L., 1951:*J. Sci. de la Météorologie* **3**, 62.
Facy, L., 1955:*Arch. Meteor. Geophys. and Biokl.* **A8**, 229.
Facy, L., 1958:*C. R. Acad. Sci., Paris*, **246**, 3161.
Facy, L., 1960:*Geofys. Pura e Appl.* **46**, 201.
Fage, A., 1934:*Proc. Roy. Soc. London* **A144**, 381
Fage, A., 1937a:*Aero Res. Comm., Repts. and Mem.* 1765.
Fage, A., 1937b:*Aero Res. Comm., Repts. and Mem.* 1766.
Fahey, D. W. *et al.*, 1989:*J. Geophys. Res.* **94**, 11299.
Fall, R. R., and Schnell, R. C., 1984:*Preprints 11th Conf. on Aerosols, Condensation and Ice Nuclei*, Budapest, p. 79, Hungarian Meteor. Soc.
Faraday, M., 1860:*Proc. Roy. Soc. London* **10**, 440.
Farkas, L., 1927:*Z. Phys. Chem.* **A125**, 236.
Farley, F. J., 1952:*Proc. Roy. Soc. London* **A212**, 530.
Farquhar, G. M., and List, R., 1992:*Preprints Cloud Phys. Conf.*, Montreal, p. 165, McGill University.
Fay, J. A., Colomb, D., and Kumar, S., 1985:*Atmos. Environ.* **19**, 1773.
Federer, B., 1968:*Z. Angew Math Phys.* **19**, 637.
Federer, B., and Waldvogel, A., 1975:*J. Appl. Meteor.* **14**, 91.
Federer, B., and Waldvogel, A., 1978:*Quart. J. Roy. Meteor. Soc.* **104**, 69.

Feingold, G., and Levin, Z., 1986:*J. Clim. and Appl. Meteor.* **25**, 1346.
Feingold, G., Tzivion, S., and Levin, Z., 1988:*J. Atmos. Sci.* **45**, 3387.
Feller, W., 1967:*An Introduction to Probability Theory and its Application*, Vol. l, Wiley.
Feng, J. Q., and Beard, K. V., 1991a:*J. Atmos. Sci.* **48**, 1856.
Feng, J. Q., and Beard, K. V., 1991b:*J. Fluid. Mech.* **227**, 429.
Ferguson, W. S., Griffin, J. J., and Goldberg, E. D., 1970:*J. Geophys. Res.* **75**, 1137.
Ferm, M., 1979:*Atmos. Environ.* **13**, 1385.
Ferry, G. U. *et al.*, 1989:*J. Geophys. Res.* **94**, 16459.
Fidleris, V., and Whitmore, R. L., 1961:*British J. Appl. Phys.* **12**, 490
Fiedler, R. P., 1990:*Atmos. Environ.* **24A**, 3061.
Finger, J. E., and Wendling, P., 1990:*J. Atmos. Sci.* **47**, 1351.
Finlayson, B. J., and Pitts, J. N., 1986:*Atmospheric Chemistry*, Wiley.
Finn, R. K., 1953:*J. Appl. Phys.* **24**, 771.
Fischer, K., and Hänel, G., 1972:*'Meteor.', Forschg. Ergebn.*, Ser. B., No. 8, p. 59.
Fishman, J., and Crutzen, P. J., 1978:*Nature* **274**, 432.
Fitzgerald, D., and Byers, H. R., 1962:*Research Rept.*, AF 19(604)2189, Dept. Meteorology, University of Chicago.
Fitzgerald, J. W., 1970:*J. Atmos. Sci.* **27**, 70.
Fitzgerald, J. W., 1972:*Ph.D. Thesis*, Dept. of Geophys. Sci., Univ. of Chicago. (Also Techn. Note, No. 44, Cloud Phys. Lab., Univ. of Chicago.)
Fitzgerald, J. W., 1973:*J. Atmos. Sci.* **30**, 628.
Fitzgerald, J. W., 1974:*J. Atmos. Sci.* **31**, 1358.
Fitzgerald, J. W., 1991:*Atmos. Environ.* **25A**, 533.
Flachsbart, O., 1927:*Phys. Z.* **28**, 461.
Flanagan, V. P., and Tayler, P., 1967:*Atmos. Environ.* **1**, 327.
Fletcher, A. N., 1972:*J. Appl. Meteor.* **11**, 988.
Fletcher, N. H., 1958:*J. Chem. Phys.* **29**, 572.
Fletcher, N. H., 1959a:*J. Meteor.* **16**, 173.
Fletcher, N. H., 1959b:*J. Chem. Phys.* **31**, 1136.
Fletcher, N. H., 1959c:*J. Chem. Phys.* **30**, 1476.
Fletcher, N. H., 1960:*Austral. J. Phys.* **13**, 408.
Fletcher, N. H., 1962a:*Physics of Rain Clouds*, Cambridge University Press, London.
Fletcher, N. H., 1962b:*Phil. Mag.* **7**, 255.
Fletcher, N. H., 1963:*Phil. Mag.* **8**, 1425.
Fletcher, N. H., 1968:*Phil. Mag.* **18**, 1287.
Fletcher, N. H., 1969:*J. Atmos. Sci.* **26**, 1266.
Fletcher, N. H., 1970a:*The Chemical Physics of Ice*, Cambridge University Press, London.
Fletcher, N. H., 1970b:*J. Atmos. Sci.* **27**, 1098.
Fletcher, N. H., 1973:*Preprints*, Conf. Phys. and Chem. of Ice, Ottawa, p. 132, Roy. Soc of Canada, Ottawa.
Fletcher, N., 1961:*Science* **134**, 361.
Flohn, H., 1973:*Globale Energiebilanz und Klimaschwankungen*, Bonner Meteor. Abhandlg., Sonderheft, Westdeutscher Verlag, Bonn.
Flood, E. A., Ed., 1967:*The Solid-Gas Interface*, p. 11, Marcel Dekker.
Flossmann, A. I., 1991:*Tellus* **43B**, 301.
Flossmann, A. I., 1993:*Tellus* **45B**, 34.
Flossmann, A. I., 1994:*Atmos. Res.* **32**, 233.
Flossmann, A. I., and Pruppacher, H. R., 1988:*J. Atmos. Sci.* **45**, 1857.
Flossmann, A. I., Hall, W. D., and Pruppacher, H. R., 1985:*J. Atmos. Sci.* **42**, 583.
Flossmann, A. I., Pruppacher, H. R., and Topalian, J. H., 1987:*J. Atmos. Sci.* **44**, 2912.
Flower, W. I., 1928:*Proc. Phys. Soc.* **A40**, 167.
Flubacher, P., Leadbetter, A. J., and Morrison, J. A., 1960:*J. Chem. Phys.* **33**, 1751.
Fonda, H., and Herne, H., 1957:*Rept. No. 2068.*, Natl. Coal Board Min., Res. Est.
Fonselius, S., 1954:*Tellus* **6**, 90.
Foote, G. B., and Brazier-Smith, P. R., 1972:*J. Geophys. Res.* **77**, 1695.
Foote, G. B., and du Toit, P. S., 1969:*J. Appl. Meteor.* **8**, 249.
Forkel, R., Sievers, U., and Zdunkowski, W., 1987:*Beitr. Phys. Atmos.* **60**, 340.
Forrest, J. *et al.*, 1982:*Atmos. Environ.* **15**, 2273.
Forrest, J. *et al.*, 1982:*Atmos. Environ.* **16**, 1473.
Forslind, E., 1952:*Acta Polytechn. Scand.* **3**, No. 5.
Forti, M. C. *et al.*, 1990:*Atmos. Environ.* **24B**, 355.
Fournier d'Albe, E. M., 1949:*Quart. J. Roy. Meteor. Soc.* **75**, 1.

Fournier d'Albe, E. M., and Hidayetulla, M. S., 1955:*Quart. J. Roy. Meteor. Soc.* **81**, 610.
Frank, F. C., 1949:*Disc. Farad. Soc.* **5**, 45.
Frank, F. C., 1958a:*Growth and Perfection of Crystals*, R. H. Doremus *et al.*, Eds., p. 411, Wiley.
Frank, H. S., 1958:*Proc. Roy. Soc.* **A247**, 481.
Frank, H. S., and Quist, A. S., 1961:*J. Chem. Phys.* **34**, 604.
Frank, H. S., and Wen, W. Y., 1957:*Disc. Farad. Soc.* **24**, 133.
Franks, F., Ed., 1972:*Water,* Vol. 1, Plenum.
Franks, F., Ed., 1973:*Water,* Vol. 3, Plenum.
Fraser, A. B., 1979:*J. Opt. Soc. Am.* **69**, 420.
Freier, G., 1960:*J. Geophys. Res.* **65**, 3979.
Freier, G., 1962:*J. Geophys. Res.* **67**, 4683.
Frenkel, J., 1932:*Phys. Z., Sowietunion* **1**, 498.
Frenkel, J., 1946:*Kinetic Theory of Liquids,* Oxford University Press.
Fresch, R. W., 1973:*Res. Rept.,* AR-106, Dept. of Atmos. Resources, University of Wyoming, Laramie, Wyoming.
Freundlich, H., 1926:*Colloid and Capillary Chemistry,* Methuen and Co., Ltd., London.
Frey, F., 1941:*Z. f. Phys. Chemie* **B49**, 83.43.
Friedlander, S. K., 1960a:*J. Meteor.* **17**, 373.
Friedlander, S. K., 1960b:*J. Meteor.* **17**, 479.
Friedlander, S. K., 1961:*J. Meteor.* **18**, 753.
Friedlander, S. K., 1965:*Proc. Conf. on Aerosols*, Liblice, K. Spurny, Ed., p. 115, Czechoslovak Acad. Sci., Prague.
Friedlander, S. K., 1977:*Smoke, Dust and Haze,* Wiley.
Friedlander, S. K., and Hidy, G. M., 1969:*Proc. Int. Conf. on Condensation and Ice Nuclei*, Prague and Vienna, p. 21, Czechoslovak Acad. of Sci., Prague.
Friedlander, S. K., and Wang, C. S., 1966:*J. Colloid. Interface Sci.* **22**, 16.
Friend, J. P., 1966:*Tellus* **18**, 465.
Frisinger, H. H., 1977:*The History of Meteorology to 1800,* Science History Publications, New York.
Fromm, J., Clementi, E., and Watts, R. O., 1975:*J. Chem. Phys.* **62**, 1388.
Frossling, N., 1938:*Gerlands Beitr. z. Geophysik* **52**, 170.
Fuchs, N, 1951:*Dokl. Akad. Nauk, SSSR* **81**, 1043.
Fuchs, N. A., 1964:*The Mechanics of Aerosols,* Pergamon.
Fuchs, N., 1934:*Z. f. Physik* **89**, 736.
Fuchs, N., 1959:*Evaporation and Droplet Growth in Gaseous Media,* Pergamon.
Fuchs, N., 1964:*The Mechanics of Aerosols,* Pergamon.
Fujikawa, S. *et al.*, 1983:*Appl. Sci. Res.* **38**, 363.
Fujiyoshi, Y., 1986:*J. Atmos. Sci.* **43**, 307.
Fukuta, N. *et al.*, 1986:*Preprints Cloud Phys. Conf.*, Snow Mass, Vol. 3, p. 280, Colorado, Am. Meteor. Soc., Boston.
Fukuta, N., 1958:*J. Meteor.* **15**, 17.
Fukuta, N., 1963:*Nature* **199**, 475.
Fukuta, N., 1966:*J. Atmos. Sci.* **23**, 191.
Fukuta, N., 1969:*J. Atmos. Sci.* **26**, 522.
Fukuta, N., 1975a:*J. Atmos. Sci.* **32**, 1597.
Fukuta, N., 1975b:*J. Atmos. Sci.* **32**, 2371.
Fukuta, N., 1985:*Scientia Sinica, Ser. B.,* **28**, 979.
Fukuta, N., and Armstrong, P. A., 1974:*Preprints Cloud Phys. Conf.*, Tucson, Arizona, p. 46, Am. Meteor. Soc., Boston.
Fukuta, N., and Mason, B. J., 1963:*J. Phys. Chem. Solids* **24**, 715.
Fukuta, N., and Walter, L. A., 1970:*J. Atmos. Sci.* **27**, 1160.
Fukuta, N., Sano, I., and Asaoka, M., 1959:*J. Meteor. Soc. Japan* **37**, 274.
Fung, K. H., Tang, I. N., and Munkelwitz, H. R., 1987:*Appl. Optics* **26**, 1282.
Furukawa, Y., 1982:*J. Meteor. Soc. Japan* **60**, 535.
Furukawa, Y., Yamamoto, M., and Kuroda, T., 1987:*J. Crys. Growth* **82**, 665.
Fushimi, K., and Miyake, Y., 1980:*J. Geophys. Res.* **85**, 7533.
Fuzzi, S. *et al.*, 1984:*J. Geophys. Res.* **89**, 7159.
Fuzzi, S. *et al.*, 1985:*J. Atmos. Chem.* **3**, 289.
Fuzzi, S. *et al.*, 1988:*J. Geophys. Res.* **93**, 11141.
Fuzzi, S. *et al.*, 1992:*Tellus* **44B**, 448.

Gabarashvili, T. G., and Gliki, N. V., 1967:*Izv. Acad. Sci., U.S.S.R., Atmos. and Ocean. Phys.* **3**, 324.
Gabarashvili, T. G., and Kartsivadze, A. I., 1968:*Preprints Conf. Cloud Phys.*, Toronto, p. 188, Univ. of Toronto Press.
Gabarashvili, T. G., and Kartsivadze, A. I., 1969:*Proc. Conf. on Condensation and Ice Nuclei.*, Prague-Vienna, p. 220, Czechoslovak. Acad. Sci., Prague.
Gabilly, A., 1949:*Ann. Geophys.* **5**, 233.
Gagin, A., 1965:*Preprints Cloud Phys. Conf.*, Tokyo, p. 155, Meteor. Soc. of Japan, Tokyo.
Gagin, A., 1971:*Preprints Conf. on Weather Mod.*, Canberra, p. 5, Am. Meteor. Soc., Boston.
Gagin, A., 1972:*J. de Rech. Atmos.* **6**, 175.
Gagin, A., and Nozyce, H., 1984:*J. de Rech. Atmos. 18, 119.*
Gal-Or, B., and Waslo, S., 1968:*Chem. Eng. Sci.* **23**, 1431.
Galasyn, J. F., Tschudy, K. L., and Huebert, B. J., 1987:*J. Geophys. Res.* **92**, 3105.
Gallily, I., and Michaeli, G., 1976:*Nature* **259**, 110.
Galloway, N. J. *et al.*, 1982:*J. Geophys. Res.* **87**, 8771.
Galloway, N. J. *et al.*, 1989:*Tellus* **41B**, 427.
Galloway, N. J., 1985:*Biochemical Cycling of Sulfur and Nitrogen.* NATO ASI Series C, Math. Phys. Sci., J. N. Galloway *et al.*,Eds., Vol. 159, p. 143, D. Reidel.
Gandrud, B. W. *et al.*, 1989:*J. Geophys. Res.* **94**, 11, 285.
Gardiner, J. *et al.*, 1985:*J. Geophys. Res.* **90**, 6079.
Gardiner, J. *et al.*, 1987:*J. Geophys. Res.* **92**, 10887.
Garland, J. A., 1971:*Quart. J. Roy. Meteor. Soc.* **97**, 483.
Garland, J. A., 1978:*Atmos. Environ.* **12**, 349.
Garner, F. H., and Lane, J. J., 1959:*Trans. Inst. Chem. Eng.* **37**, 167.
Garner, F. H., Skelland, A. H., and Haycook, P. J., 1954:*Nature* **173**, 1239.
Garner, F. H.. and Lihou, D. A., 1965:*DECHEMA Monographien* **55**, 155.
Garnier, J. P., Ehrhard, P., and Mirabel, P., 1987:*Atmos. Res.* **21**, 41.
Garret, W. D., 1965:*Linnology and Oceanography* **10**, 602.
Garret, W. D., 1967:*Deep-Sea Res.* **14**, 221.
Garret, W. D., 1969:*Ann. d. Meteor. N.F.* **4**, 25.
Garret, W. D., 1971:*J. Atmos. Sci.* **28**, 816.
Garret, W. D.,1970:*Preprints Cloud Phys. Conf.*, Fort Collins, p. 131, Am. Meteor. Soc., Boston.
Garten, V. H., and Head, R. B., 1964:*Nature* **201**, 573.
Gaskell, W. A., 1979:*Ph. D. Thesis,* University of Manchester, England.
Gaskell, W. A., 1981:*Quart. J. Roy. Meteor. Soc.* **107**, 955.
Gaskell, W. A., Illingworth, A. J., 1980:*Quart. J. Roy. Meteor. Soc.* **106**, 841.
Gatz, D. F., 1976:*Great Lakes Res.* **2**, Suppl., p. 21.
Gay, M. J. *et al.*, 1974:*Quart. J. Roy. Meteor. Soc.* **100**, 682.
Gayet, J. F., Jarmuszynski, M., and Soulage, G., 1978:*Preprints Cloud Phys. Conf.*, Issaquah, p. 318, Am. Meteor. Soc., Boston.
Gear, C. W., 1971:*Numerical Initial Value Problems in Ordinary Differential Equations,* Prentice-Hall.
Gearay, R. *et al.*, 1993:*Atmos. Res.* **30**, 263.
Gelbard, F., and Seinfeld, J. H., 1978:*J. Comput. Phys.* **28**, 357.
Gelbard, F., Tambour, Y., and Seinfeld, J. H., 1980:*J. Coll. Interface Sci.* **76**, 541.
Gentile, A. L., and Drost-Hansen, W., 1956:*Naturwissenschaften* **43**, 274.
Georgii, H. W., 1959a:*Ber. Deutsch. Wetter Dienst, U.S. Zone,* **8**, No. 58.
Georgii, H. W., 1959b:*Geofysica Pura e Appl.* **44**, 249.
Georgii, H. W., 1960:*Geofysica Pura e Appl.* **47**, 155.
Georgii, H. W., 1963:*Z. Angew. Math. Phys.* **14**, 503.
Georgii, H. W., 1965:*Ber. Deutsch. Wetter Dienst,* U.S. Zone, No. 100.
Georgii, H. W., 1970:*J. Geophys. Res.* **75**, 2365.
Georgii, H. W., 1982:*Chemistry of the Unpolluted and Polluted Troposphere,* p. 295, H. W. Georgii, W. Jaeschke, Eds., D.Reidel.
Georgii, H. W., and Gravenhorst, G., 1972:*Meteor. Rundschau* **25**, 180.
Georgii, H. W., and Jost, D., 1964:*Pure and Appl. Geophys.* **59**, 217.
Georgii, H. W., and Keller, 1970:*Ber. Inst. Meteor. u. Geophys.* No. 21, University of Frankfurt, Frankfurt.
Georgii, H. W., and Kleinjung, E., 1967:*J. de Rech. Atmos.* **3**, 145.

Georgii, H. W., and Kleinjung, E., 1968:*Pure and Appl. Geophys.* **71**, 181.
Georgii, H. W., and Lenhard, U., 1978:*Pure and Appl. Geophys.* **116**, 385.
Georgii, H. W., and Metnieks, A. L., 1958:*Geofysica. Pura e Appl.* **41**, 159.
Georgii, H. W., and Müller, W. J., 1974:*Tellus* **26**, 180.
Georgii, H. W., and Pankrath, J., 1982:*Deposition of Atmospheric Pollutants,* 9-43, D. Reidel.
Georgii, H. W., and Weber, E., 1960:*Techn. Note*, Contract, AF 61(052)-249, July, 1960, University Frankfurt, Frankfurt.
Georgii, H. W., and Wötzel, D., 1970:*J. Geophys. Res.* **75**, 1727.
Georgii, H. W., Jost, D., and Vitze, W., 1971:*Ber. Inst. Meteor. u. Geophys.* No. 23, University of Frankfurt, Frankfurt.
Georgii, H. W., Perseke, C., and Rohbok, E., 1984:*Atmos. Environ.* **18**, 581.
Gerber, H. E., 1980:*J. Appl. Meteor.* **19**, 1196.
Gerber, H. E., 1981:*J. Atmos. Sci.* **38**, 454.
Gerber, H. E., Hoppel, W. A., and Wojcieckowski, T. A., 1977:*J. Atmos. Sci.* **34**, 1836.
Gerber, H., 1972:*J. Atmos. Sci.* **29**, 391.
Gerhard, E. R., and Johnstone, H. R., 1955:*Ind. Eng. Chem.* **47**, 972.
Giauque, W. F., and Stout, J. W., 1936:*J. Am. Chem. Soc.* **58**, 1144.
Gilbert, H., Couderc, J. P., and Angelina, H., 1972:*Chem. Eng. Sci.* **27**, 45.
Gill, P. S., Graedell, T. E., and Weshler, C. J., 1983:*Rev. Geophys.* **21**, 903.
Gillen, K. T., Douglass, D. C., and Hoch, M. J. R., 1972:*J. Chem. Phys.* **57**, 5117.
Gillespie, D. T., 1972:*J. Atmos. Sci.* **29**, 1496.
Gillespie, D. T., 1975a:*J. Atmos. Sci.* **32**, 600.
Gillespie, D. T., 1975b:*J. Atmos. Sci.* **32**, 1977.
Gillespie, J. R., 1977:*Ph. D. Thesis,* Dept. Phys., University Toronto.
Gillespie, J. R., and List, R., 1978:*Pure a. Appl. Geophys.* **117**, 599.
Gillette, D. A., 1978a:*Atmos. Environ.* **12**, 1735.
Gillette, D. A., 1978b:*Atmos. Environ.* **12**, 2309.
Gillette, D. A., and Blifford, I. H., 1971:*J. Atmos. Sci.* **28**, 1199.
Gillette, D. A., and Walker, T. R., 1977:*Soil Science* **123**, 97.
Gillette, D. A., Blifford, I. H., and Fenster, C. R., 1972:*J. Appl. Meteor.* **11**, 977.
Gillette, D. A., Blifford, I. H., and Fryrear, D. W., 1974:*J. Geophys. Res.* **79**, 4068.
Ginnings, D. C.. and Corrucini, R. J., 1947:*J. Res. Nat. Bur. Stand.* **38**, 583.
Gish, O. H., 1944:*Terr. Magn. Atmos. Electr.* **49**, 159.
Gitlin, S. N., Goyer, G. G., and Henderson, T. J., 1968:*J. Atmos. Sci.* **25**, 97.
Gittens, G. J., 1969:*J. Coll. Interface Sci.* **30**, 406.
Glass, M., and Carlson, T. N., 1963:*J. Atmos. Sci.* **20**, 397.
Glasstone, S., 1959:*Physical Chemistry,* Van Nostrand, Co., Inc.
Glasstone, S., Laidler, K. J.. and Eyring, H., 1941:*The Theory of Rate Processes,* McGraw-Hill.
Goddard, J. W., and Cherry, S. M., 1984:*Radio Sci.* **19**, 201.
Goetz, A., 1965:*Preprints Cloud Phys. Conf.*, Tokyo, p. 42, Meteor. Soc. of Japan, Tokyo.
Goff, J. A., 1942:*Trans. Am. Soc. Heating and Vent. Engr.* **48**, 299.
Goff, J. A., 1949:*Trans. Am. Soc. Mech. Engs.* **71**, 903.
Goff, J. A., 1957:*Trans. Am. Soc. Heat, Air Cond. Eng.* **63**, 347.
Goff, J. A., 1965:*Humidity and Moisture,* A. Wexler, Ed., Vol. 3, p. 289, Reinhold Publ. Co.
Goff, J. A., and Gratch, S., 1945:*Trans. Am. Soc. Heating and Vent. Engr.* **51**, 125.
Goff, J. A., and Gratch, S., 1946:*Trans. Am. Soc. Heating and Vent. Engr.* **52**, 95.
Gok, M. C. *et al.*, 1988:*J. Phys. Chem.* **92**, 5074.
Gokhale, N. R., and Goold, J., 1968:*J. Appl. Meteor.* **7**, 870.
Gokhale, N., and Goold, J., 1969:*J. Geophys. Res.* **74**, 5374.
Gokhale, N., and Lewinter, O., 1971:*J. Appl. Meteor.* **10**, 469.
Gokhale, N., and Spengler, J. I., 1972:*J. Appl. Meteor.* **11**, 157.
Gold, L. W., and Power, B. A., 1952:*J. Meteor.* **9**, 447.
Gold, L. W., and Power, B. A., 1954:*J. Meteor.* **11**, 35.
Goldburg, A., and Florsheim, B. H., 1966:*Phys. Fluids* **9**, 45.
Golde, R. H., Ed., 1977:*Lightning,* Academic Press.
Goldsmith, P., and May, F. G., 1966:*Aerosol Science,* C. N. Davies, Ed., p. 163, Academic Press.

Goldsmith, P., Delafield, H. J., and Cox, L. C., 1963:*Quart. J. Roy. Meteor. Soc.* **89**, 43.
Goldstein, H., 1965:*Classical Mechanics,* Addison-Wesley.
Goldstein, S., 1929:*Proc. Roy,. Soc. London* **A123**, 216.
Goleki, I., and Jaccard, C., 1978:*J. Chem. Phys.* **11**, Solid State Phys., 4229.
Gollup, J. P., Chabay, I., and Flygave, W. H., 1974:*J. Chem. Phys.* **61**, 2139.
Golovin, A. M., 1963a:*Izv. Geophys.* **5**, 482.
Golovin, A. M., 1963b:*Izv. Geophys.* **9**, 880.
Golovin, A. M., 1965:*Izv. Atmos. Oceanic Phys.* **1**, 422.
Goodall, F., 1976:*Ph. D. Thesis,* University of Bradford, Bradford, UK.
Gordon, G. L., and Marwitz, J. D., 1983:*J. Atmos. Sci.* **43**, 1087.
Gori, E. G., and Joss, J., 1980:*J. de Rech. Atmos.* **14**, 289.
Gott, J. P., 1933:*Proc. Roy. Soc. London* **A142**, 248.
Goyer, G. G. *et al.*, 1960:*J. Meteor.* **17**, 442.
Graedel, T. E., and Franey, J. P., 1975:*Geophys. Res. Lett.* **2**, 325.
Gränicher, H. *et al.*, 1957:*Disc. Farad. Soc.,* **23**, 50.
Gränicher, H., 1958:*Z. f. Kristallogr.* **11O**, 432.
Gränicher, H., 1963:*Phys. d. kondens. Materie* **1**, 1.
Grant, L. O., 1968:*Preprints Cloud Phys. Conf.*, Toronto, p. 305, University of Toronto Press, Toronto.
Grant, M. C., and Lewis, W. M., 1982:*Tellus* **34**, 74.
Gras, J. L., 1983:*Atmos. Environ.* **17**, 815.
Gras, J. L., 1989:*J. Atmos. Chem.* **11**, 89.
Gras, J. L., 1990:*Geophys. Res. Lett.* **17**, 1565.
Gravenhorst, G., and Corrin, M. L., 1972:*J. de Rech. Atmos.* **6**, 205.
Green, A. W., 1975:*J. Appl. Meteor.* **14**, 1578.
Green, H. L. and Lane, R. L., 1964:*Particulate Clouds,* E.a.F.N. Spon. Ltd., London.
Greenberg, L., and Jacobs, M. B., 1956:*Ind. Eng. Chem.* **48**, 1517.
Greenfield, S. M., 1957:*J. Meteor.* **14**, 115.
Gregocy, P. H., 1961:*The Microbiology of the Atmosphere,* Leonard Hill Publ. Co., London.
Gregory, P. H., 1967:*Science Progr.* **55**, 613.
Gregory, P. H., 1978:*Pure and Appl. Geophys.* **116**, 309.
Grenet, G., 1947:*Extrait des Ann. Geophys.* **3**, 306.
Gretz, R. D., 1966c:*J. Chem. Phys.* **45**, 3160.
Grgic, I. *et al.*, 1991:*Atmos. Environ.* **25A**, 1591.
Grgic, I. *et al.*, 1992:*Atmos. Environ.* **26A**, 571.
Griffin, F. O., 1972:*M.S. Thesis,* Dept. Chem. Eng., University of British Columbia, Vancouver.
Griffiths, R. F., and Latham, J., 1972:*J. Meteor. Soc. Japan* **50**, 416.
Griffiths, R. F., and Latham, J., 1974:*Quart. J. Roy. Meteor. Soc.* **100**, 163.
Griffiths, R. F., Latham, J., and Myers, V., 1974:*Quart. J. Roy. Meteor. Soc.* **100**, 181.
Griggs, D. D., and Choularton, T. W., 1983:*Quart. J. Roy. Meteor. Soc.* **109**, 243.
Griggs, D. J., and Choularton, T. W., 1986:*Quart. J. Roy. Meteor. Soc.* **1120**, 1254.
Grim, R. E., 1953:*Clay Mineralogy,* McGraw-Hill.
Grosch, M. L., 1978:*Ber. Inst. Meteor.* **36**, University Frankfurt.
Grosjean, D., Swanson, R., and Ellis, C., 1983:*Sci. Total Envir* . **29**, 65.
Gross, B., 1954:*Phys. Rev.* **94**, 1545.
Gross, G. W., 1965:*J. Geophys. Res.* **70**, 2291.
Gross, G. W., 1965:*J. Geophys. Res.* **87**, 7170.
Gross, G. W., 1967:*J. Coll. Interface Sci.* **25**, 270.
Gross, G. W., 1968:*Adv. Chem. Ser.* **73**, 27.
Gross, G. W., 1971:*J. Atmos. Sci.* **28**, 1005.
Gross, G. W., Gutjahr, A., and Caylor, K., 1987:*J. Phys. Chem.* **58**, 527.
Gross, G. W., Wu, C., and McKee, C., 1975:*J. Chem. Phys.* **62**, 3085.
Grosse, G., and Stix, E., 1968:*Ber. Deutsch. Bot. Gesellsch.* **81**, 528.
Grovenhort, G., 1975:*Ber. Inst. Meteor.* **29**, University Frankfurt, Germany.
Grover, S. N., 1976a:*Pure and Appl. Geophys.* **114**, 521.
Grover, S. N., 1978:*Ph.D. Thesis,* Dept. Atmos. Sci., University of California, Los Angeles.
Grover, S. N., and Pruppacher, H. R., 1985:*J. Atmos. Sci.* **42**, 2305.
Grover, S. N., Pruppacher, H. R., and Hamielec, A. E., 1977:*J. Atmos. Sci.* **34**, 1655.

Grover, S. N.. 1976b:*Pure and Applied Geophys.* **114**, 509.
Grover, S. N.. and Beard, K. V., 1975:*J. Atmos. Sci.* **32**, 2156.
Grunow, J.. 1960:*Geophys. Monograph* **5**, p. 130, Am. Geophys. Union, Washington, D.C.
Gudris, N., and L. Kulikova, L., 1924:*Z. Phys.* **24**, 121.
Guenadiev, N., 1970:*J. de Rech. Atmos.* **4**, 81.
Guenadiev, N., 1972:*Pure and Appl. Geophys.* **99**, 251.
Guiang, S. F., Krupa, S. U., and Pratt, G. C., 1984:*Atmos. Environ.* **18**, 1677.
Guilder, L., Johnson, D. P., and Jones, F. E., 1975:*Science* **191**, 1261.
Gunn, R., 1948:*Phys. Res.* **71**, 181.
Gunn, R., 1949:*J. Geophys. Res.* **54**, 57.
Gunn, R., 1950:*J. Geophys. Res.* **55**, 171.
Gunn, R., 1952:*J. Meteor.* **11**, 339.
Gunn, R., 1956:*J. Meteor.* **13**, 283.
Gunn, R., 1965:*Science* **150**, 695.
Gunn, R., and Kinzer, G. D., 1949:*J. Meteor.* **6**, 243.
Gunn, R., and Marshall, J. S., 1958:*J. Meteor.* **15**, 452.
Gunz, D. W., and Hoffmann, M. R., 1990:*Atmos. Environ.* **24A**, 1601.
Gupalo. Y. P., and Ryazantsev, Y. S., 1972:*Chem. Eng. Sci.* **27**, 61.
Gurikov, Yu., V., 1960:*Zh. Strukt. Khim.* **1**, 286.
Gurikov, Yu., V., 1965:*Zh. Strukt. Khim.* **6**, 817.
Haaf, W., and Jaenicke, R., 1980:*J. Aerosol Sci.* **11**, 321.
Hadamard, J., 1911:*C. R. Acad. Sci., Paris* **152**, 1735.
Hagen, D. E. *et al.*, 1989a:*J. Atmos. Sci.* **46**, 803.
Hagen, D. E. *et al.*, 1994:*Atmos. Res.* **31**, 123.
Hagen, D. E., 1973:*Bull. Am. Phys. Soc.* **18**, 609.
Hagen, D. E., Anderson, R. J., and Kassner, J. L., 1981:*J. Atmos. Sci.* **38**, 1236.
Hagen, D. E., Kassner, J. L., and Miller, R. C., 1982:*J. Atmos. Sci.* **39**, 1115.
Hagen, D. E., Trueblood, M. B., and White, D. R., 1989b:*Aerosol Sci. and Techn.* **10**, 63.
Haggis, G. H., Hasted, J. B., and Buchanan, T. J., 1952:*J. Chem. Phys.* **20**, 1452.
Hahn, J., 1980:*Ann. N.Y. Acad. Sci.* **338**, 359.
Hale, B. N. *et al.*, 1980:*J. Chem. Phys.* **84**, 1473.
Hale, B. N. *et al.*, 1981:*J. Chem. Phys.* **75**, 1991.
Hale, B. N., and Kiefer, J., 1980:*J. Chem. Phys.* **73**, 923.
Hale, B. N., and Plummer, P. L., 1974a:*J. Chem. Phys.* **61**, 4012.
Hale, B. N., and Plummer, P. L., 1974b:*J. Atmos. Sci.* **31**, 1615.
Hales, J. M., and Drewes, D. R., 1979:*Atmos. Environ.* **13**, 1133.
Hales, J. M., Thorp, J. M., and Wolff, M. A., 1970:*Precipitation Scav. - 1974,* Proc. Symp., Champaign, Illinois, Natl. Techn. Info. Service, US. Dept. of Commerce, Springfield, Virginia.
Hall, W. D., 1980:*J. Atmos. Sci.* **37**, 2486.
Hall, W. D., and Beard, K. V., 1975:*Pure and Appl. Geophys.* **113**, 515.
Hall, W. D., and Pruppacher, H. R., 1976:*J. Atmos. Sci.* **33**, 1995.
Hallberg, A. *et al.*, 1992:*Tellus* **44B**, 545.
Haller, W., and Duecker, H. C., 1960:*Nat. Bur. Stand., J. Res.* **A64**, 527.
Hallett, J. *et al.*, 1978:*Quart. J. Roy. Meteor. Soc.* **104**, 631.
Hallett, J. *et al.*, 1986*Preprints Cloud Phys. Conf.*, Snow Mass, Colorado, Vol. 2, p. 9, Am. Meteor. Soc., Boston.
Hallett, J., 1960:*J. Glaciol.* **3**, 698.
Hallett, J., 1961:*Phil. Mag.* **6**, 1073.
Hallett, J., 1963a:*Proc. Phys. Soc., London* **82**, 1046.
Hallett, J., 1963b:*Meteor. Monogr.* **5**, p. 168, Am. Meteor. Soc., Boston.
Hallett, J., 1964:*J. Atmos. Sci.* **21**, 671.
Hallett, J., 1965:*J. de Rech. Atmos.* **2**, 81.
Hallett, J., and Mason, B. J., 1958:*Proc. Roy. Soc. London* **A247**, 440.
Hallett, J., and Mossop, S. C., 1974:*Nature* **249**, 26.
Hallett, J., and Saunders, C. P. R., 1979:*J. Atmos. Sci.* **36**, 2230.
Hallett, J., and Shrivastava, S. K., 1972:*J. de Rech. Atmos.* **6**, 223.
Hallett, J., Hudson, J. G., and Rogers, C. F., 1989:*Aerosol Sci. and Techn.* **10**, 70.
Hallgren, R. E., and Hosler, C. L., 1960:*Geophys. Monogr.* **5**, p. 257, Am. Geophys. Union, Washington, D.C.

Halsey, G. D., 1948:*J. Chem. Phys.* **16**, 931.
Haltenroth, H., and Klinger, J., 1969:*Physics of Ice,* N. Riehl, B. Buellemer, H. Engelhardt, Eds., p. 579, Plenum.
Hamielec, A. E., and Raal, J. D., 1969:*Phys. Fluids* **12**, 11.
Hamielec, A. E., Hoffmann, J. W., and Ross, L., 1967:*A.I.Ch.E. Journal* **13**, 212.
Hammeke, K., and Kappler, E., 1953:*Z. Geophys.* **19**, 181.
Hampl, B., Kerker, M., Cooke, D. D., and Matijevic, E., 1971:*J. Atmos. Sci.* **28**, 1211.
Handa, B. K., 1969:*Tellus* **21**, 95.
Hänel, G., 1970:*Beitr. z. Phys. d. Atmos.* **43**, 119.
Hänel, G., 1972a:*Ph.D. Thesis,* Meteor. Inst., Univ. of Mainz, Mainz.
Hänel, G., and Thudium, J., 1977:*Pure and Appl. Geophys.* **115**, 799.
Hannemann, A., 1995:*Ph. D. Thesis,* Inst. f. Atmos. Phys., Univ. Mainz, Mainz.
Hannemann, A., Mitra, S. K., and Pruppacher, H. R., 1995:*J. Atmos. Chem.* **21**, 293.
Hansen, A. D., and Rosen, H., 1984:*Geophys. Res. Lett.* **11**, 381.
Hansen, A. D. *et al.*, 1988:*Geophys. Res. Lett.* **15**, 1193.
Hanson, D. R., and Mauersberger, K., 1988a:*Geophys. Res. Lett.* **15**, 855.
Hanson, D. R., and Mauersberger, K., 1988b:*Geophys. Res. Lett.* **15**, 1507.
Hanson, H. P., 1995:*J. Atmos. Sci.* **41**, 1226.
Happel, J., and Brenner, H., 1965:*Low Reynolds Number Hydrodynamics,* Prentice-Hall, Englewood Cliffs, New Jersey.
Harding, D., and Miller, J. M., 1982:*J. Geophys. Res.* **87**, 1225.
Hardy, J. T., 1982:*Progr. Oceanogr.* **11**, 307.
Hare, D. E., and Sörensen, C. M., 1987:*J. Chem. Phys.* **87**, 4840.
Hare, D. E., and Sörensen, C. M., 1990:*J. Chem. Phys.* **93**, 28.
Harimaya, T., 1975:*J. Meteor. Soc. Japan* **52**, 384.
Harimaya, T., 1976:*J. Meteor. Soc. Japan* **54**, 42.
Harimaya, T., 1981:*J. Fac. Sci.* Hakkaido University, Ser. VII, 121.
Harries, J. E., 1976:*Rev. Geophys. and Space Phys.* **14**, 565.
Harris-Hobbs, R. L., and Cooper, W. H., 1987:*J. Atmos. Sci.* **44**, 1071.
Harrison, L. P., 1965a:*Humidity and Moisture,* A. Wexler, Ed., Vol. 3, p. 3, Reinhold Publ. Co.
Harrison, L. P., 1965b:*Humidity and Moisture,* A. Wexler, Ed., Vol. 3, p. 105, Reinhold Publ. Co.
Harrison, R. M., and Allen, A. G., 1991:*Atmos. Environ.* **25A**, 1719.
Harrison, R. M., and McCartney, H. A., 1980:*Atmos. Environ.* **14**, 233.
Harrison, R. M., and Pio, C. A., 1983:*Atmos. Environ.* **17**, 2539.
Harvey, M. J. *et al.*, 1991:*Atmos. Environ.* **25A**, 509.
Haste, D. R. *et al.*, 1988:*Atmos. Environ.* **22**, 2381.
Hasted, J. B., 1961:*Processes in Dielectrics,* J. B. Birks, J. Hart, Eds., Vol. 3, p. 101, Wiley.
Hasted, J. B., 1972:*Water,* F. Franks, Ed., Vol. 1, Chapter 5, p. 255, Plenum.
Hauff, Th., 1995:*DLR-Rept.,* 1625, Inst. f. Atmos. Phys., KLR, Oberpfaffenhofen, Germany.
Hayami, S., and Toba, Y., 1958:*J. Oceanographical Soc., Japan* **14**, 145.
Head, R. B., 1961a:*Bull. Obs. de Puy de Dome* **1**, 47.
Head, R. B., 1961b:*Nature* **191**, 1058.
Head, R. B., 1962a:*J. Phys. Chem. Solids* **23**, 1371.
Head, R. B., 1962b:*Nature* **196**, 736.
Heath, D. F., and Linnett, J., 1948:*Trans. Farad. Soc.* **44**, 556.
Hedlin, C. P., and Trofimenkoff, F. N., 1965:*Humidity and Moisture,* A. Wexler, Ed., Vol. 3, p. 519, Reinhold Publ. Co.
Heffernan, K. J., and Bracewell, R. N., 1959:*J. Meteor.* **16**, 337.
Hegg, D. A. *et al.*, 1991b:*J. Geophys. Res.* **96**, 13, 189.
Hegg, D. A., and Hobbs, P. V., 1988:*J. Atmos. Chem.* **7**, 325.
Hegg, D. A., and Kober, P. U., 1986:*Atmos. Environ.* **20**, 901.
Hegg, D. A., Hobbs, P. V., 1992:*Nucleation and Atmospheric Aerosols,* N. Fukuta and P. E. Wagner, Eds., p. 181, A. Deepak, Hampton, Virginia.
Hegg, D. A., Hobbs, P. V., and Radke, L. F., 1980:*J. de Rech. Atmos.* **14**, 217.
Hegg, D. A., Hobbs, P. V., and Radke, L. F., 1984:*Atmos. Environ.* **18**, 1939.
Hegg, D. A., Radke, L. F., and Hobbs, P. U., 1990:*J. Geophys. Res.* **95**, 13917.
Hegg, D. A., Radke, L. F., and Hobbs, P. V., 1991a:*J. Geophys. Res.* **96**, 18727.
Hegg, D. A., Covert, D. S., and Kapustin, V. N., 1992: *J. Geophys. Res.* **97**, 9851.

Heikes, B. G., 1992:*J. Geophys. Res.* **97**, 18001.
Heinmetz, F., 1962:*Trans. Farad. Soc.* **58**, 788.
Heintzenberg, J. *et al.*, 1989:*Atmos. Res.* **24**, 89.
Heintzenberg, J., 1982:*Atmos. Environ.* **16**, 2461.
Heintzenberg, J., 1987:*Tellus* **39B**, 374.
Heintzenberg, J., 1989:*Tellus* **41B**, 149.
Heintzenberg, J., and Covert, D. S., 1984:*Science of the Total Environment* **36**, 289.
Heintzenberg, J., Hansson, H. E., and Lannefors, H., 1981:*Tellus* **33**, 162.
Heist, R. H., and Reiss, H., 1973:*J. Chem. Phys.* **59**, 665.
Helas, G., 1989:*Promet* **3/4**, 95.
Helas, G., Andreae, M. O., and Hartmann, W. R., 1992:*J. Atmos. Chem.* **15**, 101.
Heldson, J. H., and Farley, R. D., 1987:*J. Geophys. Res.* **92**, 5661.
Helsdon, J. H., 1980:*J. Appl. Meteor.* **19**, 1101.
Herrmann, J., and Jaeschke, W., 1984:*J. Atmos. Chem.* **1**, 111.
Hertz, P., 1909:*Math. Ann.* **67**, 387.
Herzegh, P. H., and Hobbs, P. V., 1985:*Quart. J. Roy. Meteor. Soc.* **111**, 463.
Hess, S. L., 1959:*Introduction to Theoretical Meteorology,* H. Holt and Co., New York.
Heverly, J. R., 1949:*Trans. Am. Geophys. Union* **30**, 205.
Heymsfield, A. J., 1975a:*J. Atmos. Sci.* **32**, 799.
Heymsfield, A. J., 1975b:*J. Atmos. Sci.* **32**, 820.
Heymsfield, A. J., 1977:*J. Atmos. Sci.* **34**, 367.
Heymsfield, A. J., 1982:*J. Atmos. Sci.* **39**, 2867.
Heymsfield, A. J., 1986:*J. Atmos. Sci.* **43**, 851.
Heymsfield, A. J., and Hiemfelt, M. R., 1984:*J. Atmos. Sci.* **41**, 2811.
Heymsfield, A. J., and Kajikawa, M., 1987:*J. Atmos. Sci.* **44**, 2088.
Heymsfield, A. J., and Miloskevich, L. M., 1993:*J. Atmos. Sci.* **50**, 2335.
Heymsfield, A. J., and Mossop, S. C., 1984:*Quart. J. Roy. Meteor. Soc.* **110**, 765.
Heymsfield, A. J., and Pflaum, J. C., 1985:*J. Atmos. Sci.* **42**, 2264.
Heymsfield, A. J., and Platt, C. M., 1984:*J. Atmos. Sci.* **41**, 846.
Heymsfield, A. J., and Sabin, R. M., 1989:*J. Atmos. Sci.* **46**, 2252.
Heymsfield, A. J., Johnson, P. N., and Dye, J. E., 1978:*J. Atmos. Sci.* **35**, 1589.
Heymsfield, A. J., Knight, C. H., and Dye, J. E., 1979:*J. Atmos. Sci.* **36**, 2216.
Heymsfield, A. J., Miller, K. M., and Spinhirne, J. D., 1990:*Monthly Weather Rev.* **118**, 2313.
Heymsfield, A. K. *et al.*, 1991:*J. Atmos. Sci.* **48**, 923.
Heymsfield, A., 1972:*J. Atmos. Sci.* **29**, 1348.
Heymsfield, A., 1973:*Ph.D. Thesis,* p. 111, Dept. Geophys. Sci., University of Chicago, Chicago.
Heymsfield, A., 1975a:*J. Atmos. Sci.* **32**, 799.
Heymsfield, A., 1975b:*J. Atmos. Sci.* **32**, 809.
Heymsfield, A., 1975c:*J. Atmos. Sci.* **32**, 820.
Heymsfield, A., and Knollenberg, R. E., 1972:*J. Atmos. Sci.* **21**, 1358.
Heymsfield, G. M., 1979:*J. Atmos. Sci.* **36**, 2093.
Hicks, B. B., 1984:*Depositions, Both Wet and Dry,* Butterworth.
Hicks, B. B., and Shannon, J. D., 1979:*J. Appl. Meteor.* **18**, 1415.
Hidy, G. M., 1965:*J. Colloid. Sci.* **20**, 123.
Hidy, G. M., 1973:*Chemistry of the Lower Atmosphere,* S. I. Rasool, Ed., Plenum.
Hidy, G. M., 1984:*Aerosols,* Academic Press.
Hidy, G. M., and Brock, J. R., 1970:*The Dynamics of Aerocolloidal Systems,* Internat. Reviews in Aerosol Phys. and Chem., Vol. I, Pergamon.
Hidy, G. M., and Brock, J. R., 1971:*Topics in Current Aerosol Research,* Internat. Rev. in Aerosol Phys. and Chem., Vol. 2, Pergamon.
Hidy, G. M., and Brock, J. R., 1972:*Topics in Current Aerosol Research,* Internat. Rev. in Aerosol Phys. and Chem., Vol. 3, Pergamon.
Hidy, G. M., Ed., 1972:*Aerosols and Atmospheric Chemistry,* Academic Press.
Higuchi, K., 1958:*Acta Metallurgica* **6**, 363.
Higuchi, K., 1961:*J. Meteor. Soc. Japan,* **39**, 237.
Higuchi, K., 1962a:*J. Meteor. Soc. Japan,* **40**, 65.
Higuchi, K., 1962b:*J. Meteor. Soc. Japan,* **40**, 73.
Higuchi, K., 1962c:*J. Meteor. Soc. Japan,* **40**, 266.
Higuchi, K., and Wushiki, H., 1970:*J. Meteor. Soc. Japan* **48**, 248.

Higuchi, K., and Yoshida, T., 1967:*Proc. Conf. on Low Temp. Sci.,* Vol. 1, p. 79, Inst. of Low Temp. Sci., Hokkaido University, Sapporo, Japan.
Hill, M. A., 1894:*Phil. Trans. Roy. Soc., London* **A185**, 213.
Hill, T. A., and Choularton, T. W., 1985:*Quart. J. Roy. Meteor. Soc.* **111**, 517.
Hill, T. L., 1946:*J. Chem. Phys.* **14**, 263.
Hill, T. L., 1947:*J. Chem. Phys.* **15**, 767.
Hill, T. L., 1949:*J. Chem. Phys.* **17**, 580, 668.
Hill, T. L., 1952:*Adv. in Catalysis 4,* Academic Press.
Hillig, W. B., 1966:*Acta Metallurgica* **14**, 1868.
Hillig, W. B., and Turnbull, D., 1956:*J. Chem. Phys.* **24**, 1956.
Himmelblau, P. M., 1964:*Chem. Rev.* **64**, 527.
Hinze, J. O., 1959:*Turbulence,* McGraw-Hill.
Hirschfelder, J. O., Curtiss, C. F., and Bird, R. B., 1954:*Molecular Theory of Gases and Liquids,* Wiley.
Hirth, J. P., and Pound, G. M., 1963:*Condensation and Evaporation,* Pergamon.
Hobbs, P. V. *et al.*, 1971a:*Res. Rept. VI,* Dept. of Atmospheric Sciences, University of Washington, Seattle, Washington.
Hobbs, P. V. *et al.*, 1972:*Res. Rept. VII,* Dept. Atmos. Sci., University of Washington, Seattle, Washington.
Hobbs, P. V. *et al.*, 1974b:*Res. Rept. VIII,* Cloud Physics Group, Dept. Atmospheric Sci., University of Washington, Seattle, Washington.
Hobbs, P. V. *et al.*, 1978:*Res. Rept. XIII,* Dept. Atmos. Sci., Univ. Washington.
Hobbs, P. V. *et al.*, 1982:*J. Geophys. Res.* **87**, 11062.
Hobbs, P. V., 1965:*J. Atmos. Sci.* **22**, 296.
Hobbs, P. V., 1969:*J. Atmos. Sci.* **26**, 315.
Hobbs, P. V., 1971:*Quart. J. Roy. Meteor. Soc.* **97**, 263.
Hobbs, P. V., 1974:*Ice Physics,* Oxford University Press.
Hobbs, P. V., and Alkezweeny, A. J., 1968:*J. Atmos. Sci.* **25**, 881.
Hobbs, P. V., and Atkinson, D. G., 1976:*J. Atmos. Sci.* **33**, 1362.
Hobbs, P. V., and Burrows, D. A., 1966:*J. Atmos. Sci.* **23**, 757.
Hobbs, P. V., and Farber, J., 1972:*J. de Rech. Atmos.* **6**, 245.
Hobbs, P. V., and Ketcham, W. M., 1969:*Proceedings Conf. on Phys. of Ice,* Munich, p. 95, Plenum.
Hobbs, P. V., and Locatelli, J. D., 1969:*J. Appl. Meteor.* **8**, 833.
Hobbs, P. V., and Locatelli, J. D., 1970:*J. Atmos. Sci.* **27**, 90.
Hobbs, P. V., and Mason, B. J., 1964:*Phil. Mag.* **9**, 181.
Hobbs, P. V., and Radke, L. F., 1967:*J. Glaciol.* **6**, 879.
Hobbs, P. V., and Radke, L. F., 1969:*Science* **1163**, 279.
Hobbs, P. V., and Radke, L. F., 1970:*J. Atmos. Sci.* **27**, 81.
Hobbs, P. V., and Rangno, A. L., 1985:*J. Atmos. Sci.* **42**, 2523.
Hobbs, P. V., and Rangno, A. L., 1990:*J. Atmos. Sci.* **47**, 2710.
Hobbs, P. V., and Scott, W. D., 1965:*J. Geophys. Res.* **70**, 5025.
Hobbs, P. V., Bluhm, G. C., and Ohtake, T., 1971b:*Tellus* **23**, 28.
Hobbs, P. V., Bowdle, D. A., and Radke, L. F., 1985:*J. Clim. and Appl. Meteor.* **24**, 1358.
Hobbs, P. V., Chang, S., and Locatelli, J. D., 1974a:*J. Geophys. Res.* **79**, 2199.
Hobbs, P. V., Fullerton, C. M., and Bluhm, G. C., 1971c:*Nature (Phys. Sci)* **2311**, 90.
Hobbs, P. V., Hess, D. A., and Radke, L. F., 1983:*J. Geophys. Res.* **88**, 3919.
Hobbs, P. V., Politovich, M. K., and Radke, L. F., 1980:*J. Appl. Meteor.* **19**, 645.
Hocking, L. M., 1959:*Quart. J. Roy. Meteor. Soc.* **85**, 44.
Hocking, L. M., 1973:*J. Engr. Math.* **7**, 207.
Hocking, L. M., and Jonas, P. R., 1970:*Quart. J. Roy. Meteor. Soc.* **96**, 722.
Hodge, I. M., and Angell, C. A., 1978:*J. Chem. Phys.* **68**, 1363.
Hodson, M. C., 1986:*J. Clim. and Appl. Meteor.* **25**, 1070.
Hoff, R. M. *et al.*, 1983:*J. Geophys. Res.* **88**, 10947.
Hoffer, T. E., and Bowen, J., 1972:*J. de Rech. Atmos.* **6**, 259.
Hoffer, T. E., and Mallen, S. C., 1970:*J. Atmos. Sci.* **27**, 914.
Hoffer, T., 1960:*Techn. Note 22,* Cloud Phys. Lab., Dept. of Meteorology, University of Chicago, Chicago.
Hoffer, T., 1961:*J. Meteor.* **18**, 766.
Hoffmann, E. J., and Duce, R. A., 1974:*J. de Rech. Atmos.* **8**, 676.
Hoffmann, E. J., and Duce, R. A., 1977:*Geophys. Res. Lett.* **4**, 449.

Hoffmann, H. E., and Roth, R., 1988:*Preprints Cloud Phys. Conf.*, Bad Homburg, p. 175, Deutscher Wetterdienst, Offenbach.
Hoffmann, M. R., 1986:*Atmos. Environ.* **20**, 1145.
Hoffmann, M. R., and Calvert, J. G., 1985:*The Chemical Transformation Module for Eulerian and Deposition Models,* Vol II., The Aqueous Phase Chemistry, NCAR, Rept.
Hofmann, D. J. *et al.*, 1975:*J. Atmos. Sci.* **32**, 1446.
Hofmann, D. J. *et al.*, 1975:*J. Atmos. Sci.* **32**, 1446.
Hofmann, D. J. *et al.*, 1990:*Geophys. Res. Lett.* **17**, 1279.
Hofmann, D. J., 1990a:*Geophys. Res. Lett.* **17**, 357.
Hofmann, D. J., 1990b:*Science* **248**, 996.
Hofmann, D. J., and Deshler, T., 1989:*Geophys. Res. Lett.* **16**, 1429.
Hofmann, D. J., and Deshler, T., 1991:*J. Geophys. Res.* **96**, 2897.
Hofmann, D. J., and Rosen, J. M., 1981a:*Geophys. Res. Lett.* **8**, 1231.
Hofmann, D. J., and Rosen, J. M., 1981b:*J. Atmos. Sci.* **38**, 168.
Hofmann, D. J., and Rosen, J. M., 1982:*J. Geophys. Res.* **87**, 11, 039.
Hofmann, D. J., and Rosen, J. M., 1983:*Geophys. Res. Lett.* **10**, 313.
Hofmann, D. J., and Rosen, J. M., 1984:*J. Geophys. Res.* **89**, 4883.
Hofmann, D. J., Rosen, J. M., and Gringel, W., 1985:*J. Geophys. Res.* **90**,2341.
Hofmann, D. J., Rosen, J. M., and Kiernan, J. M., 1976:*J. Atmos. Sci.* **33**, 1782.
Hogan, A. W., 1968:*J. de Rech. Atmos.* **3**, 53.
Hogan, A. W., 1975:*J. Appl. Meteor.* **14**, 550.
Hogan, A. W., Barnard, S., and Portiniak, J., 1979:*Geophys. Res. Lett.* **6**, 845.
Hoigne, J. *et al.*, 1985:*Water Res.* **19**, 993.
Hollomon, J. H., and Turnbull, D., 1953:*Progr. Metal Phys.* **4**, B. Chalmers, Ed., p. 333, Wiley-Interscience.
Holroyd, E. W., 1964:*J. Appl. Meteor.* **3**, 633.
Holton, J. R., 1973:*Monthly Weather Rev.* **101**, 201.
Holzman, E. G., 1970:*J. Appl. Phys.* **41**, 1460, 4769.
Homan, F., 1936:*Forschg. auf d. Gebiete d. Ing. Wesens* **7**, 1.
Hooper, I. E. N., and Kippax, A. A., 1950:*Quart. J. Roy. Meteor. Soc.* **76**, 125.
Hoppel, W. A. *et al.*, 1990:*J. Geophys. Res.* **95**, 3659.
Hoppel, W. A. *et al.*, 1994:*Aerosol Sci. and Techn.* **20**, 1.
Hoppel, W. A., 1979:*J. Atmos. Sci.* **36**, 2006.
Hoppel, W. A., 1987:*Atmos. Environ.* **21**, 2703.
Hoppel, W. A., and Frick, G. M., 1990:*Atmos. Environ.* **24A**, 645.
Hoppel, W. A., and Phillips, B. B., 1971:*J. Atmos. Sci.* **28**, 1258.
Hoppel, W. A., and Phillips, B. B., 1972:*J. Atmos. Sci.* **29**, 1218.
Hoppel, W. A., Dinger, J. E., and Ruskin, R. E., 1973:*J. Atmos. Sci.* **30**, 1410.
Hoppel, W. A., Fitzgerald, J. W., and Larson, R. E., 1985:*J. Geophys. Res.* **90**, 2365.
Hoppel, W. A., Frick, G. M., and Larson, R. E., 1986:*Geophys. Res. Lett.* **13**, 125.
Hoppel, W. A., Gerber, H. E., and Wojcieckowski, T. A., 1981:*Preprints Int. Conf. on Aerosols, Condensation Nuclei and Ice Nuclei*, Galway, Ireland, A. F. Roddy, T. C. O. Connor, Eds., p. 193, Galway, Univ. Press.
Horguani, V. G., 1965:*Izv. Acad. Sci., SSSR,* Atmos. Ocean, Phys., Ser. 1, No. 2, 208.
Horne, R. A., Ed., 1972:*Water and Aqueous Solutions,* Wiley-Interscience.
Horvath, L. *et al.*, 1981:*Tellus* **33**, 382.
Horvath, L., 1974:*Staub* **34**, 251.
Horvath, L., 1979:*J. Aerosol Sci.* **10**, 309.
Horvay, G., and Cahn, J. W., 1961:*Acta Metallurgica* **9**, 695.
Hosler, C. L., 1951:*J. Meteor.* **8**, 326.
Hosler, C. L., and Hallgren, R. E., 1960:*Trans. Farad. Soc.*, **30**, 200.
Hosler, C. L., and Spalding, G. R., 1957:*Artificial Stimulation of Rain,* p. 369, Pergamon.
Hosler, C. L., Jensen, D. C., and Goldshlak, 1957:*J. Meteor.* **14**, 415.
Houghton, H. G., 1933:*Physics* **4**, 419.
Houghton, H. G., 1950:*J. Meteor.* **7**, 363.
Houghton, H. G., 1972:*J. de Rech. Atmos.* **6**, 657.
Houghton, H. G., and Radford, W. H., 1938:*MIT Papers in Phys. Oceanogr. and Meteor.* **6**, No. 4.
Houze, R. A. *et al.*, 1979:*J. Atmos. Sci.* **36**, 156.
Houze, R. A., 1993:*Cloud Dynamics,* Academic Press.
Howell, W. E., 1949:*J. Meteor.* **6**, 134.

Hu, Z., and Srivastava, R. C., 1992:*Preprints Cloud Phys. Conf.*, Montreal, p. 60, McGill University Press.
Huan, Mei-Yuan, 1963:*Izv. Akad. Nauk., SSSR,* Ser. Geofiz, No. 2, 362.
Huang, K., 1963:*Statistical Mechanics,* Wiley.
Huang, W. S., and Kintner, R. S., 1969:*Am. Inst. Chem. Eng. J.* **15**, 735.
Hudson, J. G., 1980:*J. Atmos. Sci.* **37**, 1854.
Hudson, J. G., 1983:*Optical Engineering* **22**, 063.
Hudson, J. G., 1984:*J. Clim. and Appl. Meteor.* **23**, 42.
Hudson, J. G., 1993:*J. Geophys. Res.* **98**, 2693.
Hudson, J. G., and Frisbie, P. R., 1991:*J. Geophys. Res.* **96**, 20, 795.
Hudson, J. G., Hallett, J., and Rogers, C. F., 1991:*J. Geophys. Res.* **96**, 10847.
Huebert, B. J. *et al.*, 1983:*Prec. Scav., Dry Depos. and Resusp.*, H. B. Prinak, R. Semonin, and W. G. Slinn, Eds., p. 293, Elsevier.
Huebert, B. J., 1980:*Geophys. Res. Lett.* **7**, 325.
Huebert, B. J., and Lazrus, A. L., 1980a:*J. Geophys. Res.* **85**, 7337.
Huebert, B. J., and Lazrus, A. L., 1980b:*J. Geophys. Res.* **85**, 7322.
Huffman, P. J., 1973a:*J. Appl. Meteor.* **12**, 1080.
Huffman, P. J., 1973b:*Research Rept. AR 108*, Dept. of Atmospheric Resources, University of Wyoming, Laramie, Wyoming.
Humphreys, W. J., 1937:*Weather Rambles,* Williams and Wilkins, Baltimore, Maryland.
Humphreys, W. J., 1942:*Ways of the Weather,* A Cultural Survey of Meteorology, Lancaster, Pennsylvania.
Hussain, K., and Saunders, C. P. R., 1984:*Quart. J. Roy. Meteor. Soc.* **110**, 75.
Ibusuki, T., Ohsawa, M., and Takeuchi, K., 1990:*Atmos. Environ.* **24A**, 1325.
Ichimura, I., Fujiwara, M., and Yanase, T., 1980:*J. Meteor. Soc. Japan* **58**, 403.
Ikegami, K. *et al.*, 1978:*Seppyo* **40**, 50.
Illingworth, A. J., 1985:*J. Geophys. Res.* **90**, 6026.
Illingworth, A. J., and Latham, J., 1975:*J. Atmos. Sci.* **32**, 2206.
Illingworth, A. J., and Latham, J., 1977:*Quart. J. Roy. Meteor. Soc.* **103**, 231.
Illingworth, A., 1971:*Quart. J. Roy. Meteor. Soc.* **97**, 440.
Illingworth, A., 1973:*J. Geophys. Res.* **78**, 3628.
Illingworth, A., 1988:*Nature* **33b**, 754.
Imai, I., 1950:*Geophys. Mag. (Tokyo)* **21**, 244.
Inmann, R. L., 1969:*J. Appl. Meteor.* **8**, 155.
Inn, E. C., Vedder, J. F., and O'Hara, D., 1981:*Geophys. Res. Lett.* **8**, 5.
Iribarne, J. V., 1972:*J. de Rech. Atmos.* **6**, 265.
Iribarne, J. V., and Godson, W. L., 1973:*Atmospheric Thermodynamics,* D. Reidel.
Iribarne, J. V., and Mason, B. J., 1967:*Trans. Farad. of Soc.* **163**, 2234.
Iribarne, J. V., and Pyshnov, T., 1990:*Atmos. Environ.* **24A**, 383.
Iribarne, J. V., Barrie, L. A., and Iribarne, A., 1983:*Atmos. Environ.* **17**, 1047.
Iribarne, J. V., Pyshnov, T., and Naik, B., 1990:*Atmos. Environ.* **24A**, 389.
Isaac, G. A. *et al.*, 1978:*Preprints Cloud Phys. Conf.*, Issaquah, p. 363, Am. Meteor. Soc.
Isaac, G. A., and Daum, P. H., 1987:*Atmos. Environ.* **21**, 1587.
Isaac, G. A., and Schemenauer, R. S., 1979:*J. Appl. Meteor.* **18**, 1056.
Isaka, C., 1972:*Ph.D. Thesis,* Université de Clermont-Ferrand, Dept. Nat. Sciences, Clermont Ferrand, France.
Ishizaka, Y., 1972:*J. Meteor. Soc. Japan* **50**, 362.
Ishizaka, Y., 1973:*J. Meteor. Soc. Japan* **51**, 325.
Isono, K, and Tanaka, T., 1966:*J. Meteor. Soc. Japan* **44**, 255.
Isono, K. *et al.*, 1970:*NWAP Rept.*, 70-R Water Resoucces Lab., Nagoya University, Nagoya, Japan.
Isono, K., 1955:*J. Meteor.* **12**, 456.
Isono, K., 1957:*Geofysica. Pura e Appl.* **36**, 156.
Isono, K., 1959a:*Japan J. Geophys.* **2**, No. 2.
Isono, K., 1959b:*Nature* **183**, 317.
Isono, K., 1965:*Preprints Cloud Phys. Conf.*, Tokyo, p. 150, Meteor. Soc. of Japan, Tokyo.
Isono, K., and Ikebe, Y., 1960:*J. Meteor. Soc. Japan* **38**, 213.
Isono, K., and Ishizaka, Y., 1972:*J. de Rech. Atmos.* **6**, 283.
Isono, K., and Komabayasi, M., 1954:*J. Meteor. Soc. Japan* **32**, 29.
Isono, K., Komabayasi, M., and Ono, A., 1959:*J. Meteor. Soc. Japan* **37**, 211.

Isono, K., Komabayasi, M., and Takahashi, T., 1966:*J. Meteor. Soc. Japan* **44**, 227.
Isono, K., Tanaka, T., and Iwai, K., 1966:*J. de Rech. Atmos.* **3**, 341.
Israel, H., and Kasemir, H. W., 1952:*Arch. Meteor. Geophys. Biokl.* **A5**, 71.
Israel, H.. 1970:*Atmospheric Electricity,* Vol. 1, Akad. Verlags-Gesellschaft, Leipzig.
Israel, H., 1973:*Atmospheric Electricity,* Vol. 2, Akad. Verlags-Gesellschaft, Leipzig.
Itagaki, K., 1967:*J. Coll. Interface Sci.* **25**, 218.
Ito, T. Morita, Y., and Iwasaka, Y., 1986:*Tellus* **38B**, 214.
Ito, T., 1985:*J. Atmos. Chem.* **3**, 69.
Itoo, K., 1957:*Tokyo Papers in Meteor. and Geophys.* **8**, 20.
Iwabuchi, T., and Magono, C., 1975:*J. Meteor. Soc. Japan* **53**, 393.
Iwai, K., 1971:*J. Meteor. Soc. Japan* **49**, 516.
Iwai, K.. 1973:*J. Meteor. Soc. Japan* **51**, 458.
Jaccard, C., 1963:*Phys. d. Kondens. Materie* **2**, 143.
Jaccard, C., 1971:*Water and Aqueous Solutions,* R. A. Horne, Ed., p. 25, Wiley-Interscience.
Jaccard, C., and Levi, L., 1961:*Z. Angew. Math. und Phys.* **12**, 70.
Jaccard, C.. 1967:*Proc. Conf. on Phys. of Snow and Ice,* Sapporo, Vol. 1, p. 173, University of Hokkaido, Sapporo, Japan.
Jacob, P., and Klockow, D., 1992:*J. Atmos. Chem.* **15**, 353.
Jacob, P., Tavares, T. M., and Klockow, D., 1986:*Fresenius Z. Anal. Chem.* **325**, 359.
Jacobson, B., 1953:*Nature* **172**. 666.
Jacobson, E. A., and Krider, E. P., 1976:*J. Atmos. Sci.* **33**, 103.
Jaenicke, R., 1978a:*Atmos. Environ.* **12**, 161.
Jaenicke, R., 1978b:*Pure and Appl. Geophys.* **116**, 283.
Jaenicke, R., 1978c:*Ber. Bunsen Gesellsch. f. Phys. Chemie* **82**, 1198.
Jaenicke, R., 1982:*Chemistry of the Polluted and Unpolluted Troposphere,* H. W. Georgii, W. Jaeschke, Eds., p. 341, D. Reidel.
Jaenicke, R., 1988:*Landolt Börnstein, Numerical Data and functional Relationships in Science and Technology,* New Series Vol. 4, Meteorology Sub. Vol. b, Physical and Chem. Properties of Air, p. 391, G. Fischer, Ed., Springer.
Jaenicke, R., 1992:*Nucleation and Atmospheric Aerosol,* N. Fukuta, P. E. Wagner, Eds., p. 417, Deepak Publ., Hampton, Virginia.
Jaenicke, R., and Junge, C. E., 1967:*Beitr. z. Phys. d. Atmos.* **40**, 129.
Jaenicke, R., Junge, C. E., and Kanter, H. J., 1971:*'Meteor.' Forschg. Ergebn.,* Ser. B, No. 7, p. 1.
Jaeschke, W. *et al.*, 1978:*Pure and appl. Geophys.* **116**, 465.
Jaeschke, W. H., and Herrmann, G. J., 1987:*The Chemistry of Acid Rain,* ACS Smposium Series 349, R. W. Johnson *et al.*, Eds., Chapter 17, p. 142, Am. Chem. Soc., Washington D. C.
Jaeschke, W., 1978:*Atmos. Environ.* **12**, 715.
Jaffrezo, J. J., and Colin, J. L., 1988:*Atmos. Environ.* **22**, 929.
Jameson, A. R., 1983:*J. Atmos. Sci.* **40**, 1792, 1803.
Jameson, A. R., and Beard, K. V., 1982:*J. Appl. Meteor.* **21**, 257.
Jamieson, D. T., 1964:*Nature* **202**, 583.
Jarvis, N. L., and Scheiman, M. A., 1967:*NRL Report,* Naval Res. Labs. Dept. No. 6583.
Jaw Jeou-Jang, 1966:*Tellus* **18**, 722
Jayaratne, E. R., and Saunders, C. P. R., 1985:*J. Geophys. Res.* **90**, 13063.
Jayaratne, E. R., Saunders, C. P. R., and Hallett, J., 1983:*Quart. J. Roy. Meteor. Soc.* **109**, 609.
Jayaratne, O. W., and Mason, B. J., 1964:*Proc. Roy. Soc.* **A280**, 545.
Jayaweera, K. O. L. F., 1971:*J. Atmos. Sci.* **28**, 728.
Jayaweera, K. O. L. F., 1972a:*Preprints Cloud Phys. Conf.*, London, p. 48, Roy. Meteor. Soc., London.
Jayaweera, K. O. L. F., 1972b:*J. Atmos. Sci.* **29**, 596.
Jayaweera, K. O. L. F., and Cottis, R. E., 1969:*Quart. J. Roy. Meteor. Soc.* **95**, 703.
Jayaweera, K. O. L. F., and Mason, B. J., 1965:*J. Fluid Mech.* **22**, 709.
Jayaweera, K. O. L. F., and Mason, B. J., 1966:*Quart. J. Roy. Meteor. Soc.* **92**, 151.
Jayaweera, K. O. L. F., and Ohtake, T., 1974:*J. Atmos. Sci.* **31**, 280.
Jayaweera, K. O. L. F., and Ryan, B. F., 1972:*Quart. J. Roy. Meteor. Soc.* **98**, 193.
Jayne, J. T. *et al.*, 1990:*J. Phys. Chem.* **94**, 6041.
Jeffrey, G. B., 1922:*Proc. Roy. Soc. London* A102, 161.
Jeffreys, H., 1918:*Phil. Mag.* **35**, 270.
Jellinek, H. H., 1967:*J. Coll. Interface Sci.* **25**, 192.

Jennings, S. G., 1975:*Quart. J. Roy. Meteor. Soc.* **101**, 227.
Jennings, S. G., McGovers, F. M., and Cooke, W. F., 1993:*Atmos. Environ.* **27A**, 1229.
Jensen, J. B. *et al.*, 1985:*J. Atmos. Sci.* **42**, 173.
Jenson, V. G., 1959:*Proc. Roy. Soc. London* **A249**, 346.
Jhon, M. S. *et al.*, 1966:*J. Chem. Phys.* **44**, 1465.
Ji, W., 1991:*Ph. D. Thesis*, Dept. Meteor., Univ. of Wisconsin, Madison, Wisconsin.
Ji, W., and Wang, P. K., 1990:*Atmos. Res.* **25**, 539.
Ji, W., and Wang, P. K., 1991:*Theor. Comput. Fluid Dynamics* **3**, 43.
Jindal, B. K., and Tiller, W. A., 1972:*J. Coll. Interface Sci.* **39**, 339.
Jiusto, J. E., 1967:*Tellus* **19**, 359.
Jiusto, J. E., and Bosworth, G. E., 1971:*J. Appl. Meteor.* **10**, 1352.
Jiusto, J. E., and Kocmond, W. C., 1968:*J. de Rech. Atmos.* **3**, 101.
Jiusto, J. E., and Lala, G. G., 1980:*J. de Rech. Atmos.* **14**, 391.
Jiusto, J. E., and Lala, G. G., 1982:*Preprints Cloud Phys. Conf.*, Chicago, p. 300, Am. Meteor. Soc., Boston.
Jiusto, J. E., and Weickmann, H. K., 1973:*Bull. Am. Meteor. Soc.* **54**, 1148.
Jiusto, J. E.,1966:*J. de Rech. Atmos.* **2**, 245.
Jiusto, J. E.,1971:*J. de Rech. Atmos.* **5**, 69.
Joe, P. I. *et al.*, 1976:*Preprints Cloud Phys. Conf.*, Boulder, p. 264, Am. Meteor. Soc., Boston.
Joe, P. I., 1975:*M.S. Thesis*, Dept. Physics, University of Toronto, Toronto.
Joe, P. I., 1982:*Ph. D. Thesis*, University Toronto.
Joe, P. I., List, R., and Lesins, G. B., 1980:*J. de Rech. Atmos.* **14**, 357.
Johnson, C. A., Sigg, L., and Zobrist, J., 1987:*Atmos. Environ.* **21**, 2365.
Johnson, D. A., 1982:*J. Atmos. Sci.* **39**, 448.
Johnson, D. A., and Hallett, J., 1968:*Quart. J. Roy. Meteor. Soc.* **94**, 468.
Johnson, D. B., 1981:*J. Atmos. Sci.* **38**, 215.
Johnson, D. B., 1987:*J. Atmos. Sci.* **44**, 1671.
Johnson, D. B., and Beard, K. V., 1984:*J. Atmos. Sci.* **41**, 1235.
Johnson, D. B., and Cooke, R. C., 1979:*J. Geophys. Res.* **84**, 3761.
Johnson, D. B., Beard, K. V., and Baumgardner, D., 1986:*Preprints Cloud Phys. Conf.*, Snowmass Colorado, p. 48, Am. Meteor. Soc., Boston.
Jonas, P. R., 1972:*Quart. J. Roy. Meteor. Soc.* **98**, 681.
Jonas, P. R., 1989:*Atmos. Res.* **23**, 259.
Jonas, P. R., and Goldsmith, P., 1972:*J. Fluid Mech.* **52**, 593.
Jonas, P. R., and Mason, B. J., 1974:*Quart. J. Roy. Meteor. Soc.* **100**, 286.
Jones, B. M. R., Cox, R. A., and Penkett, S. A., 1983:*J. Atmos. Chem.* **1**, 65.
Jones, D. M., 1959:*J. Meteor.* **16**, 504.
Jones, G., and Ray, W. A., 1937:*J. Am. Chem. Soc.* **59**, 187.
Jonson, J. E., and Isaksen, I. S. A., 1993:*J. Atmos. Chem.* **16**, 99.
Joos, F., and Baltenberger, V., 1991:*Atmos. Environ.* **25A**, 217.
Joshi, P. V., 1988:*Lecture Notes in Physics*, P. E. Wagner, G. Vali, Eds., **308**, p. 134, Springer.
Joss, J., and Aufdermauer, A. N., 1970:*Internat. J. Heat and Mass. Transfer* **13**, 213.
Joss, J., and Gori, E. G., 1978:*J. Appl. Meteor.* **17**, 1054.
Joss, J., and Waldvogel, A., 1969:*J. Atmos. Sci.* **26**, 566.
Joss, J., Thams, J. C., and Waldvogel, A., 1968:*Preprints Cloud Physics Conference*, Toronto, p. 369, University of Toronto Press, Toronto.
Jost, D., 1974:*Tellus* **26**, 206.
Junge, C. E., 1936:*Gerlands Beitr. z. Geophys.* **46**, 108.
Junge, C. E., 1950:*Ann. Meteor.* **3**, 128.
Junge, C. E., 1952a:*Ann. Meteor.* **5**, Beiheft.
Junge, C. E., 1952b:*Ber. Deutsch. Wett. D. U.S. Zone* **35**, 261.
Junge, C. E., 1952c:*Arch. Meteor. Geophys. Biokl.* **5**, 44.
Junge, C. E., 1953:*Tellus* **5**, 1.
Junge, C. E., 1954:*J. Meteor.* **11**, 323.
Junge, C. E., 1955:*J. Meteor.* **12**, 13.
Junge, C. E., 1956:*Tellus* **8**, 127.
Junge, C. E., 1957a:*Artificial Stimulation of Rain,* p. 3, Pergamon.
Junge, C. E., 1957b:*Artificial Stimulation of Rain,* p. 24, Pergamon.
Junge, C. E., 1961:*J. Meteor.* **18**, 501.
Junge, C. E., 1963a:*Air Chemistry and Radioactivity,* Academic Press.

Junge, C. E., 1963b:*J. de Rech. Atmos.* **1**, 185.
Junge, C. E., 1969a:*Preprints Conference on Condensation and Ice Nuclei*, Prague and Vienna, p. 31, Czechoslovak Akad. of Sci., Prague.
Junge, C. E., 1969b:*J. Atmos. Sci.* **26**, 603.
Junge, C. E., 1972a:*Quart. J. Roy. Meteor. Soc.* **98**, 711.
Junge, C. E., 1972b:*J. Geophys. Res.* **77**, 5183.
Junge, C. E., 1972c:*Koll. Z. and Z. Polymere* **250**, 628.
Junge, C. E., and Abel, N., 1965:*Final Tech. Rept.,* No. DA9I-591 EVC-3484, University of Mainz, Mainz
Junge, C. E., and Jaenicke, R., 1971:*J. Aerosol Sci.* **2**, 305.
Junge, C. E., and Manson, J. E., 1961:*J. Geophys. Res.* **66**, 2163.
Junge, C. E., and McLaren, E., 1971:*J. Atmos. Sci.* **28**, 382.
Junge, C. E., Chagnon, C. W., and Manson, J. E., 1961a:*J. Meteor.* **18**, 81.
Junge, C. E., Chagnon, C. W., and Manson, J. E., 1961b:*Science* **133**, 1478.
Junge, C. E., Robinson, E., and Ludwig, F. L., 1969:*J. Appl. Meteor.* **8**, 340.
Jurica, G. M., and Frey, D. S., 1989:*WMO Conf. Rept.* No. 12, p. 35, Weather Mod. Conf. Beijing, China, World Meteor. Org., Geneva, Switzerland.
Jylhä, K., 1991:*Atmos. Environ.* **25A**, 263.
Kachurin, L. G., Zaiceva, N. A., and Lomanooa, S. I, 1956:*Izv. Akad. Nauk., SSSR, Ser. Geog.* **7**, 857.
Kajikawa, M., 1971:*J. Meteor. Soc. Japan* **49**, 367.
Kajikawa, M., 1972:*J. Meteor. Soc. Japan* **50**, 577.
Kajikawa, M., 1973:*J. Meteor. Soc. Japan* **51**, 263.
Kajikawa, M., 1974:*J. Meteor. Soc. Japan* **52**, 328.
Kajikawa, M., 1975a:*J. Meteor. Soc. Japan* **53**, 476.
Kajikawa, M., 1975b:*J. Meteor. Soc. Japan* **53**, 267.
Kajikawa, M., 1976:*J. Meteor. Soc. Japan* **54**, 276.
Kajikawa, M., 1982:*J. Meteor. Soc. Japan* **60**, 797.
Kajikawa, M., 1989:*J. Meteor. Soc. Japan* **67**, 731.
Kajikawa, M., 1992:*J. Meteor. Soc. Japan* **70**, 1.
Kajikawa, M., and Heymsfield, A. J., 1989:*J. Atmos. Sci.* **46**, 3108.
Kamra, A. K., and Ahire, D. V., 1989:*Atmos. Res.* **23**, 117.
Kamra, A. K., and Sathe, A. B., 1983:*Arch. Met. Geophys. Biok., Ser.* **A 32**, 145.
Kamra, A. K., Bhalwankar, R. V., and Sathe, A. B., 1991:*J. Geophys. Res.* **96**, 17159.
Kamra, A. K., Bhalwankar, R. V., and Sathe, A. B., 1993:*J. Geophys. Res.* **98**, 12901.
Kapoor, R. K., and Paul, S. K., 1980:*Tellus* **32**, 38.
Kappler, E., and Hammeke, K., 1955:*Forschg. Ber. Wirtsch. u. Verkehr, N. Rhein Westf.* **3**, 125.
Kaselau, K. H., 1975:*Staub-Reinhalt Luft* **35**, 101.
Kasemir, H. W., and Holitza, F. D., 1972:*EOS Trans., AGU* **53**, 1001.
Kassander, A. R., Sims, L. L., and McDonald, J. E., 1957:*Artificial Stimulation of Rain,* p. 233, Pergamon.
Kassner, J. L. *et al.*, 1971:*Preprints Conf. on Weather Mod.*, Canberra, Australia, p. 51, Amer. Meteor. Soc., Boston, Massachusetts.
Kassner, J. L., Carstens, J. C., and Allen, L. B., 1968a:*J. Atmos. Sci.* **25**, 919.
Kassner, J. L., Carstens, J. C., and Vietti, M. A., 1968b:*J. de Rech. Atmos.* **3**, 45.
Katz, J. L., and Ostermier, B. J., 1967:*J. Chem. Phys.* **47**, 478.
Katz, U., 1960:*Z. Angew. Math. Phys.* **11**, 237.
Katz, U., 1962:*Z. Angew. Math. Phys.* **13**, 333.
Katz. U., 1961:*Z. Angew. Math. Phys.* **12**, 76.
Katzoff, S., 1934:*J. Chem. Phys.* **2**, 1841.
Kauptinskii, A. F., and Razanin, I. I., 1955:*Zhur. Fiz. Khim.* **29**, 222.
Kavanau, J. L., 1964:*Water and Solute-Water Interactions,* Holden-Day, Inc., San Francisco.
Kawaguti, M., 1953:*J. Phys. Soc., Japan* **8**, 747.
Kawaguti, M., and Jain, P., 1966:*J. Phys. Soc., Japan* **21**, 2055.
Keefe, D., Noland, P. J., and Rich, T. A., 1959:*Proc. Roy. Irish Acad.* **A60**, 27.
Keene, W. C. *et al.*, 1986:*J. Geophys. Res.* **91**, 6647.
Keith, W. D., and Saunders, C. P. R., 1989:*Atmos. Res.* **23**, 83.
Kell, G. S., 1972a:*Water,* Vol. 1, p. 363, F. Franks, Ed., Plenum.
Kell, G. S., 1972b:*Water and Aqueous Solutions,* p. 331, R. A. Horne, Ed., Wiley-Interscience.

Kell, G. S., McLauring, G. E., and Whalley, E., 1968: *J. Chem. Phys.* **48**, 3805.
Keller, H. B., and Takami, H., 1966:*Proceedings Sympos. on Numerical Solutions of Nonlinear Differential Equations*, p. 115, D. Greenspan, Ed., Wiley.
Kelly, K. K. *et al.*, 1993:*J. Geophys. Res.* **98**, 8713.
Kelly, T. J., Daum, P. H.and Schwartz, S. E., 1985:*J. Geophys. Res.* **90**, 7861.
Kennard, E. H., 1938:*Kinetic Theory of Gases,* McGraw-Hill.
Kerker, M., and Hampl, B., 1974:*J. Atmos. Sci.* **31**, 1368.
Kern, C. W., and Karplus, M., 1972:*Water,* F. Franks, Vol. 1, p. 21, Ed., Plenum.
Kestin, J., and Whitelaw, J. H., 1965:*Humidity and Moisture,* A. Wexler, Ed., p. 301, Reinhold.
Ketcham, W. M., and Hobbs, P. V., 1968:*Phil. Mag.* **18**, 659.
Ketcham, W. M., and Hobbs, P. V., 1969:*Phil. Mag.* **19**, 1161.
Ketseridis, G. *et al.*, 1976:*Atmos. Environment* **10**, 603.
Ketseridis, G. *et al.*, 1976a:*J. Phys. Chem.* **75**, 3870.
Ketseridis, G. *et al.*, 1976b:*Atmos. Environ.* **10**, 603.
Ketseridis, G., and Eichmann R., 1978:*Pure and appl. Geophys.* **116**, 274.
Khain, A. P., and Pinsky, M. B., 1995a:*J. Atmos. Sci.* **52**, 196.
Khain, A. P., and Pinsky, M. B., 1995b:*Preprints Cloud Physics Conference*, Dallas, p. 122, Amer. Meteorology Society.
Khalil, M. A. K., and Rasmussen, R. H., 1984:*Atmos. Environ.* **18**, 1805.
Khorguany, U. G., Myakonky, G. U., and Stepanov, G. V., 1980:*Proceedings Conf. on Atmospheric Aerosols and Nuclei*, Galway, A. F. Roddy, T. C. O'Connor, Eds., p. 399, Galway University Press.
Khwaja, H. A., and Husain, L., 1990:*Atmos. Environ.* **24A**, 1869.
Kidder, R. E., and Carte, A. E., 1964:*J. de Rech. Atmos.* **1**, 169.
Kiefer, J., and Hale, B. N., 1977:*J. Chem. Phys.* **67**, 3206.
Kientzler, C. F. *et al.*, 1954:*Tellus* **6**, 1.
Kikuchi, K. *et al.*, 1979:*J. Fac. Sci., Hokkaido Univ., Ser.* **7**, 6, 31.
Kikuchi, K., 1968:*J. Meteor. Soc. Japan* **46**, 128.
Kikuchi, K., 1970:*J. Meteor. Soc. Japan* **48**, 243.
Kikuchi, K., 1971:*J. Meteor. Soc. Japan* **49**, 20
Kikuchi, K., 1972a:*J. Meteor. Soc. Japan* **50**, 142.
Kikuchi, K., 1972b:*J. Meteor. Soc. Japan* **50**, 131.
Kikuchi, K., 1973:*J. Meteor. Soc. Japan* **51**, 337.
Kikuchi, K., 1975:*J. Meteor. Soc. Japan* **53**, 322.
Kikuchi, K., and Inatsu, K., 1979:*J. Fac. Sci., Hokkaido Univ. Ser.* **7**, 6, 21.
Kikuchi, K., and Ishimoto, K., 1974:*J. Fac. Sci., Hokkaido University, Ser.* **7**, 4, 69.
Kikuchi, K., and Uyeda, N., 1978:*Snow Crystals in the Arctic Canada,* C. Magno, Ed., p. 83, Hokkaido University Press.
Kikuchi, K., and Yanai, K. 1971:*Antarctic Record,* **41**, 34, Polar Res. Center, Tokyo.
Kikuchi, K., Murakami, M., and Sanuhi, Y., 1982:*Memoires, Nat. Inst. Polar Ras.,* Spec. Issue 24, p. 157.
Kim, D. S., and Aneja, U. P., 1992:*Tellus* **44B**, 41.
Kingery. W. D., 1960a:*J. Glaciol.* **3**, 577.
Kingery, W. D., 1960b:*J. Appl. Phys.* **31**, 833.
Kins, L., 1982a:*Diploma Thesis.* Inst. Meteor., University of Frankfurt.
Kins, L., 1982b:*Depos. of Atm. Pollutants,* H. W. Georgii, and J. Pankrath, Eds., p. 87, D. Reidel.
Kinzer, G. D., and Cobb, W. E., 1958:*J. Meteor.* **15**, 138.
Kinzer, G. D., and Gunn, R., 1951:*J. Meteor.* **8**, 71.
Kirkwood, J. G., and Buff, F. P., 1949:*J. Chem. Phys.* **17**. 338.
Kirkwood, J. G., and Oppenheim, I., 1961:*Chemical Thermodynamics,* McGraw-Hill.
Kiryukhin, B. V., and Pevzner, S. I., 1956:*Trudy Glavnui Geofiz. Obs.* **57**, 101.
Kiryukhin, B. V., and Plaude, N. O., 1965:*Studies of Clouds, Precipitation and Thunderstorm Electricity,* N. I. Vulfson and L. M. Levin, Eds., p. 29, Am. Meteor. Soc., Boston.
Kistenmacher, H. *et al.*, 1974a:*IBM Research Report,* RJ 1334, IBM Res. Lab., San Jose, California.
Kistenmacher, H. *et al.*, 1974b:*IBM Research Report,* RJ 1335, IBM Res. Lab., San Jose, California.
Kistler, A. L., and Verbalovich, T., 1966:*J. Fluid. Mech.* **26**, 37.
Kitchen, M., and Caughey, S. J., 1981:*Quart. J. Roy. Meteor. Soc.* **107**, 853.

Klaassen, W., 1988:*J. Atmos. Sci.* **45**, 3741.
Klanning, U. R., Sehesfed, K., and Holaman, J., 1985:*J. Phys. Chem.* **89**, 760.
Klett, J. D., 1971a:*J. Atmos. Sci.* **28**, 646.
Klett, J. D., 1971b:*J. Atmos. Sci.* **28**, 78.
Klett, J. D., 1972:*J. Geophys. Res.* **77**, 3187.
Klett, J. D., 1975:*J. Atmos. Sci.* **32**, 380.
Klett, J. D., 1976:*J. Atmos. Sci.* **33**, 870.
Klett, J. D., 1977:*J. Atmos. Sci.* **34**, 551.
Klett, J. D., 1995:*J. Atmos. Sci.* **52**, 2276.
Klett, J. D., and Davis, M. H., 1973:*J. Atmos. Sci.* **30**, 107.
Kley, D. *et al.*, 1979:*J. Atmos. Sci.* **36**, 2513.
Kley, D. *et al.*, 1982:*Geophys. Res. Lett.* **9**, 617.
Kline. D. W., 1963:*Monthly Weather Rev.* **91**, 681.
Kline. S. J., 1965:*Similitude and Approximation Theory,* McGraw-Hill.
Knelman, F., Dombrowski, N., and Newitt, D. M., 1954:*Nature* **173**, 261.
Knight, C. A., 1966:*J. Meteor. Soc. Japan* **37**, 568.
Knight, C. A., 1979:*J. Atmos. Sci.* **36**, 1123.
Knight, C. A., and Knight, N. C., 1968a:*J. Atmos. Sci.* **25**, 445.
Knight, C. A., and Knight, N. C., 1968b:*J. Atmos. Sci.* **25**, 458.
Knight, C. A., and Knight, N. C., 1970a:*J. Atmos. Sci.* **27**, 667.
Knight, C. A., and Knight, N. C., 1970b:*J. Atmos. Sci.* **27**, 659.
Knight, C. A., and Knight, N. C., 1970c:*J. Atmos. Sci.* **27**, 672.
Knight, C. A., and Knight, N. C., 1973a:*J. Atmos. Sci.* **30**, 118.
Knight, C. A., and Knight, N. C., 1973b:*J. Atmos. Sci.* **30**, 1665.
Knight, C. A., and Knight, N. C., 1974:*J. Atmos. Sci.* **31**, 1174.
Knight, C. A., and Knight, N. C., 1976:*Preprints Cloud Phys. Conf.*, Boulder, Colo., p. 222, Am. Meteor. Soc., Boston.
Knight, C., and Heymsfield, A. J., 1983:*J. Atmos. Sci.* **40**, 1510.
Knight, N. C., 1981:*J. Appl. Meteor.* **20**, 750.
Knight, N. C., 1986:*J. Clim. and Appl. Meteor.* **25**, 1956.
Knight, N. C., and Knight, C. A., 1981:*J. Appl. Meteor.* **20**, 750.
Knollenberg, R. G., 1981:*Clouds: Their Formation, Optical Properties and Effects,* P. H. Hobbs, and A. Deepak, Eds., p. 15, Academic Press.
Knudsen, M., and Weber, S., 1911:*Ann. Physik* **36**, 982.
Knutson, E. O., Sood, S. K., and Stockham, J. D., 1976:*Atmos. Environ.* **10**, 395.
Kobayashi, T. *et al.*, 1976:*J. Cryst. Growth* **35**, 262.
Kobayashi, T., 1957:*J. Meteor. Soc. Japan,* 75th Anniversary Volume, 38.
Kobayashi, T., 1958:*J. Meteor. Soc. Japan* **36**, 193.
Kobayashi, T., 1961:*Phil. Mag.* **6**, 1363.
Kobayashi, T., 1965a:*J. Meteor. Soc. Japan* **43**, 359.
Kobayashi, T., 1965b:*Contrib. of Inst. Low Temp. Sci.,* Ser. A, 20, Hokkaido University, Sapporo, Japan.
Kobayashi, T., 1967:*Preprints* Conf. on Low Temp. Science, Sapporo, Vol.1, p. 95, Institute of Low Temp. Sci., Hokkaido University, Sapporo, Japan.
Kocmond, W. C., 1965:*Res. Rept.* RM-1788-p9, p. 36, Cornell Aeronaut. Lab.. Buffalo, New York.
Kocmond, W. C., Garrett, W. D., and Mack, E. J., 1972:*J. Geophys. Res.* **77**, 3221.
Koenig, F. O., 1950:*J. Chem. Phys.* **18**, 449.
Koenig, L. R., 1963:*J. Atmos. Sci.* **20**, 29.
Koenig, L. R., 1965b:*Preprints Cloud Phys. Conf.*, Tokyo, Japan, p. 242, Meteor. Soc. of Japan, Tokyo.
Koenig, L. R., 1971:*J. Atmos. Sci.* **28**, 226.
Kogan, Y. L., 1991:*J. Atmos. Sci.* **48**, 1160.
Köhler, H., 1921a:*Meteor. Z.* **38**, 168.
Köhler, H., 1921b:*Geofysiske Publ.* **2**, No. 1.
Köhler, H., 1922:*Geofysiske Publ.* **2**, No. 6.
Köhler, H., 1927:*Geofysiske Publ.* **5**, No. 1.
Köhler, H., 1936:*Trans. Farad. Soc.* **32**, 1152.
Kojima, K., Ono, T., and Yamaii, K., 1952:*Teion-Kagaku,* Hokkaido University 4, p. 223.
Kok, G. L., 1980:*Atmos. Environ.* **14**, 653.
Kolmogorov, A. N., 1941:*Doklady Acad. Sci.,* SSSR 32, 16.
Kolmogorov, A. N., 1949:*Doklady Akad. Nauk.,* SSSR 66, 825.

Kolomeychuk, R. J., McKay, D. C., and Iribarne, J. U., 1975:*J. Atmos. Sci.* **32**, 974.
Komabayasi, M., and Ikebe, Y., 1961:*J. Meteor. Soc. Japan, Ser.* **11**, 39, 82.
Komabayasi, M., Gonda, T., and Isono, K., 1964:*J. Meteor. Soc. Japan* **32**, 330.
König, R. L., 1977:*Quart. J. Roy. Meteor. Soc.* **1030**, 585.
Koros, R. B. *et al.*, 1966:*Chem. Engr. Sci.* **21**, 941.
Korson, L., Drost-Hausen, W., and Millero, F. J., 1969:*J. Phys. Chem.* **730**, 34.
Kortüm, G., 1972:*Einführung in die Chemische Thermodynamik,* 6th edn., Vandenhoeck & Rupprecht, Göttingen.
Kosak, L. F., and Helz, G. R., 1983:*Environ. Sci. Technol.* **17**, 145.
Kosarev, A. L., Mazin, I. P., and Nezrov, U. S., 1978:*Some Problems in Cloud Physics,* p. 113, Hydrometeorol. Press.
Koutsky, J. A., Walton, A. G., and Baer, 1965:*Surface Science* **3**, 165.
Kovetz, A., and Olund, B., 1969:*J. Atmos. Sci.* **26**, 1060.
Kozikowska, A., Heman, K., and Supronowicz, J., 1984:*Quart. J. Roy. Meteor. Soc.* **110**, 65.
Kraemer, H. F., and Johnstone, H. F., 1955:*Ind. Eng. Chem.* **47**, 2426.
Kramers, H. A., and Stemerding, S., 1951:*Appl. Sci. Res.* **A3**, 73.
Krasnogorskaya, N. V., 1965:*Izv. Acad. Sci., S.S.S.R., Atmos. and Oceanic Phys.* **1**, 200.
Krasnogorskaya, N. V., 1969:*Planetary Electrodynamics,* S. C. Coroniti and J. Hughes, Eds., Vol. 1, p. 427, Gordon and Breach.
Krasnogorskaya, N. V., and Neizvestnyy, A. I., 1973:*Izv. Atmos. Ocean Phys.* **9**, 220.
Krastanow, L., 1940:*Meteor. Z.* **58**, 37.
Krastanow. L., 1943:*Meteor. Z.* **60**, 15.
Krehbiel, P. R. *et al.*, 1984:*Preprints 7th Int. Conf. Atmos. Electr.*, p. 279, Am. Meteor. Soc., Boston.
Krehbiel, P. R., 1981:*Ph.D. Thesis.* University of Manchester, England.
Krehbiel, P. R., 1986:*The Earth Electrical Environment,* Studies in Geophysics, p. 90, National Academic Press, Washington D.C.
Krehbiel, P. R., Brook, M., and McCroy, R. A., 1979:*J. Geophys. Res.* **84**, 2432.
Kreidenweiss, S. M., Seinfeld, J. H., 1988:*Atmos. Environ.* **22**, 283.
Krestov, G. A., 1964:*Zh. Struct. Khim.* **5**, 909.
Krishnan, P. N., and Solomon, R. E., 1989:*J. Phys. Chem.* **73**, 2680.
Kronig, R., and Brink, J. C., 1950:*J. Appl. Sci. Res.* **A2**, 142.
Kry, P. R., and List, R., 1974a:*Phys. Fluids* **17**, 1093.
Kry, P. R., and List, R., 1974b:*Phys. Fluids* **17**, 1087.
Kubelka, P., 1932:*Z. Elektrochemie* **38**, 611.
Kubelka, P., and Prokscha, R., 1944:*Koll. Z.* **109**, 79.
Kubesch, R. J., and Beard, K. V., 1993:*J. Atmos. Sci.* **50**, 1089.
Kuczynski, 1949:*J. Meteor.* **1**, 169.
Kuettner, J., 1950:*J. Meteor.* **7**, 322.
Kuhns, I., 1968:*J. Atmos. Sci.* **25**, 878.
Kuhns. I. E., and Mason, B. J., 1968:*Proc. Roy. Soc. London* A302, 437.
Kumai, M., 1951:*J. Meteor.* **8**, 151.
Kumai, M., 1957:*Geofys. Pura e Appl.* **36**, 169.
Kumai, M., 1961:*J. Meteor.* **18**, 139.
Kumai, M., 1965:*CRREL Rept.* 150.
Kumai, M., 1966a:*J. Meteor. Soc. Japan* **44**, 18S.
Kumai, M., 1966b:*J. Geophys. Res.* **71**, 3397.
Kumai, M., 1968:*J. Glaciol.* **7**, 95.
Kumai, M., 1969a:*CRREL Rept.* 235.
Kumai, M., 1969b:*CRREL Rept.* 245.
Kumai, M., 1976:*J. Atmos. Sci.* **33**, 833.
Kumai, M., 1982:*J. Appl. Meteor.* **21**, 579.
Kumai, M., and Francis, K. E., 1962a:*CRREL Rept.* 100.
Kumai, M., and Francis. M., 1962b:*J. Atmos. Sci.* **19**, 434.
Kumai, M., and Itagaki, K., 1953:*J. Fac. Sci., Ser.* **2**, 4, 235, Hokkaido University.
Kumar, P. P., and Saunders, C. P. R., 1989:*J. Geophys. Res.* **94**, 13099.
Kumar, S., 1985:*Atmos. Environ.* **19**, 769.
Kunkel, B. A., 1982:*Res. Rept.*, 767, AFGL-TR-82-0026, Meteor. Div. Air Force Geophys. Lab., Hanscomb A713, Massachusetts.
Kuroda, T., 1982:*J. Meteor. Soc. Japan* **60**, 520.

Kuroda, T., 1984:*J. Meteor. Soc. Japan* **62**, 552.
Kuroda, T., and Gonda, T., 1984:*J. Meteor. Soc. Japan* **62**, 563.
Kuroda, T., and Lacmann, R., 1982:*J. Cryst. Growth* **56**, 189.
Kuroiwa, D., 1953:*Rept.* 349, Hokkaido University
Kuroiwa, D., 1956:*J. Meteor.* **13**, 408.
Kuroiwa, D., 1961:*Tellus* **13**, 252.
Kuroiwa, D., 1962:*CRREL Rept.* 86.
Kuroiwa. D., 1951:*J. Meteor.* **8**, 157.
Küttner, J. P., Levin, Z., and Sartor, J. D., 1981:*J. Atmos. Sci.* **38**, 2470.
Kuwata, K. *et al.*, 1983:*Anal. Chem.* **55**, 2013.
Kvajuc, G., and Brajovic, V., 1971:*J. Crystal Growth* **11**, 73.
Kvlividze, V. I., Kiselev, V. F., and Ushakova, L. A., 1970:*Dok. Phys. Chem. S.S.S.R.* **191**, 307.
La Mer, V. K., and Gruen, R., 1952:*Trans. Farad. Soc.* **48**, 410.
La Placa, S., and Post, B., 1960:*Acta Cryst.* **13**, 503.
Lacman, R., and Stranski, I. N., 1972:*J. Cryst. Growth* **13/14**, 236.
Ladla, S. H. *et al.*, 1990:*Atmos. Environ.* **24A**, 2981.
Lagford, J., 1961:*Bull. Obs. du Puy de Dome No.* **2**, 87.
Lagourette, B., Boned, C., and Royer, R., 1976:*J. Physique* **37**, 955.
Laird, S. K., and Sommerfeld, R. A., 1995:*Geophys. Res. Lett.* **22**, 921.
Laktinov, A. G., 1972:*Izv. Atmos. Ocean Phys.* **8**, 443.
Lamb, D., and Blumenstein, R., 1987:*Atmos. Environ.* **21**, 1765.
Lamb, D., and Scott, W. D., 1974:*J. Atmos. Sci.* **31**, 570.
Lamb, D., Hallett, J., and Sax, R. I., 1981:*Quart. J. Roy. Meteor. Soc.* **107**, 935.
Lamb, D.. and Hobbs. P. V., 1971:*J. Atmos. Sci.* **28**, 1506.
Lamb, H., 1911:*Phil. Mag.* **21**, 112.
Lamb, H., 1945:*Hydrodynamics,* Dover Publications.
Landau, L., and Lifshitz, E. M., 1958:*Statistical Physics,* Pergamon.
Landau, L., and Lifshitz, E. M., 1959:*Fluid Mechanics,* Pergamon.
Landry, C. R., and Hardy, K. R., 1970:*Preprints 14th Conference on Radar Meterol.*, Tucson, Am. Meteor. Soc., Boston.
Landsberg, H., 1938:*Ergebnisse d. Kosm. Physik* **3**, 155.
Lane, W. R., 1951:*Ind. Eng. Chem.* **43**, 1312.
Lanes, W. R., and Green, H. L., 1956:*Surveys in Mechanics,* p. 162, Cambridge University Press.
Langer, G., 1968:*Preprints Conf. on Weather Mod.*, Albany, p. 220, Am. Meteor. Soc., Boston.
Langer, G., and Rodgers, J., 1975:*J. Appl. Meteor.* **14**, 560.
Langer, G., and Rosinski, J., 1967:*J. Appl. Meteor.* **6**, 114.
Langer, G., Rosinki, J., and Bernsen, S., 1963:*J. Atmos. Sci.* **20**, 557.
Langham, E. J., and Mason, B. J., 1958:*Proc. Roy. Soc.* **A247**, 493.
Langleben, M. P., 1954:*Quart. J. Roy. Meteor. Soc.* **80**, 174.
Langmuir, I., 1918:*J. Am. Chem. Soc.* **40**, 1361.
Langmuir, I., 1944:*Research Rept.* RL-223, General Electric Labs., Schenectady, New York.
Langmuir, I., 1948:*J. Meteor.* **5**, 175.
Langmuir, I., and Blodgett, K. B., 1946:*Techn. Rept.* 5418.40, U.S. Army and Air Force Command, Wright Field, Dayton, Ohio.
Laplace P., 1806:*Traite de Mecanique Celeste* **4**, Suppl. to book 10, Courcier, Paris.
Laranti, J. M., and Illingworth, R. J., 1983:*J. Phys. Chem.* **87**, 4078.
Latham, J., 1965:*Quart. J. Roy. Meteor. Soc.* **91**, 87.
Latham, J., 1969:*Quart. J. Roy. Meteor. Soc.* **95**, 349.
Latham, J., 1981:*Quart. J. Roy. Meteor. Soc.* **107**, 277.
Latham, J., and Dye, J. E., 1989:*J. Geophys. Res.* **94**, 13141.
Latham, J., and Mason, B. J., 1961b:*Proc. Roy. Soc. London* A260, 537.
Latham, J., and Mason, B. J., 1962:*Proc. Roy. Soc. London* A266, 387.
Latham, J., and Mason, B. J., 196la:*Proc. Roy. Soc. London* A260, 523.
Latham, J., and Miller, A. H., 1965:*J. Atmos. Sci.* **22**, 505.
Latham, J., and Myers, V., 1970:*J. Geophys. Res.* **75**, 515.
Latham, J., and Reed, R. L., 1977:*Quart. J. Roy. Meteor. Soc.* **103**, 297.
Latham, J., and Roxburgh, I. W., 1966:*Proc. Roy. Soc. London* A295, 84.
Latham, J., and Saunders, C. P. R., 1970:*Quart. J. Roy. Meteor. Soc.* **96**, 257.

Latham, J., and Stow, C. D., 1965:*Quart. J. Roy. Meteor. Soc.* **91**, 462.
Latham, J., and Warwicker, R., 1980:*Quart. J. Roy. Meteor. Soc.* **106**, 559.
Latham, J., Mystrom, R. E., and Sartor, J. D., 1965:*Nature* **206**, 1344.
Laws, J. O., 1941:*Trans. Am. Geophys. Union* **22**, 709.
Laws, J. O., and Parsons, D. A., 1943:*Trans. Am. Geophys. Union* **24**, 452.
Lazarev, P. P., 1912:*Annal. d. Physik* **37**, 233.
Lazrus, A. L., and Ferek, R. J., 1984:*Geophys. Res. Lett.* **11**, 417.
Lazrus, A. L., and Gandrud, B. W., 1974:*J. Geophys. Res.* **79**, 3424.
Lazrus, A. L., Baynoton, H. W., and Lodge, J. P., 1970:*Tellus* **22**, 106.
Lazrus, A. L., Gandrud, B. W., and Cadle, R. D., 1971:*J. Geophys. Res.* **75**, 8083.
Le Clair, B. P. *et al.*, 1972:*J. Atmos. Sci.* **29**, 728.
Le Clair, B. P., 1970:*Ph.D. Thesis,* Dept. Chem. Eng., McMaster University, Hamilton, Canada.
Le Clair, B. P., Hamielec, A. E., and Pruppacher, H. R., 1970:*J. Atmos. Sci.* **27**, 308.
Le Compte, J., and Grant, L. O., 1976:*Preprints Cloud Phys. Conf.*, Boulder, Colorado, p. 176, Am. Meteor. Soc., Boston.
Leaist, D. G., 1984:*J. Chem. Eng. Data* **29**, 281.
Leaitch, W. R. *et al.*, 1984:*J. Clim. and Appl. Meteor.* **23**, 916.
Leaitch, W. R. *et al.*, 1986:*J. Geophys. Res.* **91**, 11821.
Leary, C. a., and Houze, R. A., 1979:*J. Atmos. Sci.* **36**, 669.
Lee, C. W., 1972:*J. Meteor. Soc. Japan* **50**, 171.
Lee, C. W., and Magono, C., 1967:*J. Meteor. Soc. Japan* **45**, 343.
Lee, C., and Leith, D., 1989:*J. Aerosol Sci.* **20**, 503.
Lee, I. Y., and Pruppacher, H. R., 1977:*Pure and Appl. Geophys.* **115**, 523.
Lee, I. Y., Hänel, G., and Pruppacher, H. R., 1980:*J. Atmos. Sci.* **37**, 1839.
Lee, J. H., and Tang, I. N., 1988:*Atmos. Environ.* **22**, 1147.
Lee, J. K., Abraham, F. F., and Pound, G. M., 1973:*Surface Sci.* **34**, 745.
Lee, R. N., and Busness, K. M., 1989:*EOS Trans. AGU* **70**, 1030.
Lee, Y. N. *et al.*, 1986:*Water, Air, Soil Poll.* **30**, 143.
Lee, Y. N., and Schwartz, S. E., 1981:*J. Phys. Chem.* **85**, 840.
Lee, Y. N., and Schwartz, S. E., 1983:*Prec. Scav. Dry Depos. and Resusp.,* H. R. Pruppacher, R. G. Semonin, W. G. N. Slinn, Eds., Vol. 1, p. 453, Elsevier.
LeFebre, V., 1967:*J. Coll. Interface Sci.* **25**, 263.
Legrand, M., and Delmas, R. J., 1985:*Ann. Glaciol.* **7**, 20.
Leighton, H. G., and Rogers, R. R., 1974:*J. Atmos. Sci.* **31**, 271.
Lenard, P., 1887:*Ann. Phys. Chem.* **30**, 209.
Lenard, P., 1892:*Ann. Phys.* **46**, 584.
Lenard, P., 1904:*Meteor. Z.* **21**, 249.
Lenard, P., 1921:*Ann. Phys.* **65**, 659.
Lenhard, U., 1977:*Diploma Thesis.* Meteor. Institute, University of Frankfurt.
Leong, K. H., 1987a:*J. Aerosol. Sci.* **12**, 417.
Leong, K. H., 1987b:*J. Aerosol. Sci.* **18**, 511.
Leong, K. H., Beard, K. V., and Ochs, H. T., 1982:*J. Atmos. Sci.* **39**, 1130.
Lesins, G. B., and List, R., 1986:*J. Atmos. Sci.* **43**, 2813.
Lesins, G. B., List, R., and Joe, P. I., 1980:*J. de Rech. Atmos.* **14**, 347.
Letey, J., Osborn, J., and Pelishek, R. E., 1962:*Soil Science* **93**, 149.
Levi, L., 1970:*J. Glaciol.* **9**, 109.
Levi, L., Achaval, E. M., and Aufdermauer, A. N., 1970b:*J. Atmos. Sci.* **27**, 512.
Levi, L., Achaval, E. M., and Lubart, L., 1970a:*J. Cryst. Growth* **22**, 303.
Levi, L., and Aufdermauer, A. N., 1970:*J. Atmos. Sci.* **27**, 443.
Levi, L., and Lubart, L., 1991:*Atmos. Res.* **26**, 191.
Levi, L., and Prodi, F., 1978:*J. Atmos. Sci.* **35**, 2181.
Levi, L., and Prodi, F., 1983:*J. Atmos. Sci.* **40**, 1281.
Levi, L., Nasello, O. B., and Prodi, F., 1991:*Quart. J. Roy. Meteor. Soc.* **117**, 761.
Levi, L., Nasello, O., and Achaval, E. M., 1980:*J. Crys. Growth* **48**, 121.
Levich, V., 1954a:*Dokl. Akad. Nauk,* SSSR 99, 809.
Levich, V., 1954b:*Dokl. Akad. Nauk,* SSSR 99, 1041.
Levich, V., 1962:*Physico-Chemical Hydrodynamics,* Prentice-Hall Inc., Englewood Cliffs, New Jersey.
Levin, L. M., 1954:*Dokl. Akad. Nauk,* SSSR 94, 1045.
Levin, L. M., and Sedunov, Y. S., 1966:*J. de Rech. Atmos.* **2**, 425.

Levin, Z. *et al.*, 1980:*Preprints Cloud Phys. Conf.*, Clermont-Ferrand, p. 45, Blaise Pascal Université, Aubière, France.
Levin, Z., 1976:*J. Atmos. Sci.* **33**, 1756.
Levin, Z., and Machnes, B., 1977:*Pure and appl. Geophys.* **115**, 845.
Levin, Z., and Tzur, I., 1986:*The Earth Electrical Environment,* Studies in Geophysics, p. 263, National Academic Press, Washington D.C.
Levin, Z., and Yankowski, S. A., 1983:*J. Clim. and Appl. Meteor.* **22**, 1964.
Levin, Z., Neiburger, M., and Rodriquez, L., 1973:*J. Atmos. Sci.* **36**, 944.
Levine, J., 1950:*NACA, Techn. Note,* 2234.
Levine, J., 1959:*J. Meteor.* **16**, 653.
Levine, N. E., 1971:*J. Geophys. Res.* **76**, 5097.
Levine, N. E., 1973:*J. Geophys. Res.* **78**, 6266.
Levkov, L., 1971:*J. de Rech. Atmos.* **5**, I33.
Lew, J. K. *et al.*, 1986a:*J. Atmos. Sci.* **43**, 2392.
Lew, J. K. *et al.*, 1986b:*J. Atmos. Sci.* **43**, 2410.
Lew, J. K., and Pruppacher, H. R., 1983:*J. Atmos. Sci.* **40**, 139.
Lew, J. K., Kingsmill, D. E., and Montague, D. C., 1985:*J. Atmos. Sci.* **42**, 857.
Lewis, G. N., and Randall, M., 1961:*Thermodynamics,* 2nd edn., McGraw-Hill.
Lezberg, E. A. *et al.*, 1982:*J. Geophys. Res.* **87**, 3123.
Lhermitte, R. M., and Williams, E. R., 1985:*J. Geophys. Res.* **90**, 6071.
Likens, G. E. *et al.*, 1987:*J. Geophys. Res.* **92**, 13299.
Likens, G. E., Edgarton, E. S., and Galloway, J. N., 1983:*Tellus* **35B**, 16.
Liliestrand, H. M., and Morgan, J. J., 1980:*Envir. Sci. Technol.* **15**, 333.
Lilly, D. K., and Gal-Chen, T., 1982:*Mesoscale Meteorology.* NATO ASI Series C, Matter and Phys. Sci. 114, D. Reidel.
Lin, C. L., and Lee, S. C., 1973:*Computer and Fluids* **1**, 235.
Lin, C. L., and Lee, S. C., 1975:*J. Atmos. Sci.* **32**, 1412.
Lin, Sin-Shong, 1973:*Rev. Sci. Instruments* **44**, 516.
Lind, J. A. *et al.*, 1987:*EOS Trans. AGU* **68**, 1212.
Lind, J. A., and Kok, G. L., 1986:*J. Geophys. Res.* **91**, 7889.
Lindberg, S., 1982:*Atmos. Environ.* **16**, 1701.
Lindblad, N. R., 1964:*J. Coll. Sci.* **19**, 729.
Lindblad, N. R., and Semonin, R. G., 1963:*J. Geophys. Res.* **68**, 1051.
Lindenmeyer, C. S., 1959:*Ph.D. Thesis,* Harvard University, Cambridge.
Lindenmeyer, C. S., Orrok, G. T., and Jackson, K. A., 1957:*J. Chem. Phys.* **27**, 822.
Lipari, F., Dasch, J. M., and Seruggs, W. F., 1984:*Environ. Sci. a. Technol.* **19**, 70.
List, R. *et al.*, 1969:*Preprints Conference on Severe and Local Storms*, Chicago, p. 267, Am. Meteor. Soc., Boston.
List, R. *et al.*, 1973:*J. Atmos. Sci.* **30**, 653.
List, R. *et al.*, 1976:*Preprints Cloud Phys. Conf.*, Boulder, p. 233, Am. Meteor. Soc., Boston.
List, R. *et al.*, 1987b:*J. Atmos. Ocean Techn.* **4**, 454.
List, R., 1958a:*Z. Angew. Math. Phys.* **9a**, 180.
List, R., 1958b:*Z. Angew. Math. Phys.* **9a**, 217.
List, R., 1959:*Z. Angew. Math. Phys.* **10**, 143.
List, R., 1960a:*Geophys. Monograph 5,* p. 317, Am. Geophys. Union, Washington, D.C.
List, R., 1960b:*Z. Angew. Math. Phys.* **11**, 273.
List, R., 1961:*Bull. Am. Meteor. Soc.* **42**, 452.
List, R., 1965:*Preprints Cloud Phys. Conf.*, Tokyo, p. 481, Meteor. Soc. of Japan, Tokyo.
List, R., 1977:*J. Glaciol.* **19**, 451.
List, R., 1988:*J. Atmos. Sci.* **45**, 3564.
List, R., 1990:*J. Atmos. Sci.* **47**, 1919.
List, R., and Agnew, T. A., 1973:*J. Atmos. Sci.* **30**, 1158.
List, R., and Dussault, J. G., 1967:*J. Atmos. Sci.* **24**, 522.
List, R., and Freire, E., 1988:*J. Atmos. Sci.* **38**, 2257.
List, R., and Gillespie. J. R., 1976:*J. Atmos. Sci.* **33**, 2007.
List, R., and McFarquhar, G. M., 1990a:*J. Atmos. Sci.* **47**, 2274.
List, R., and McFarquhar, G. M., 1990b:*J. Atmos. Sci.* **47**, 2996.
List, R., and Schemenauer. R. S., 1971:*J. Atmos. Sci.* **28**, 110.
List, R., and Whelpdale, D. M., 1969:*J. Atmos. Sci.* **26**, 305.
List, R., Cantin, J.. and Farland, M. G., 1970:*J. Atmos. Sci.* **27**, 1080.
List, R., Donaldson, N. R., and Stewart, R. E., 1987a:*J. Atmos. Sci.* **44**, 362.

List, R., Garcia, F., and Greenan, B., 1989:*Atmos. Res.* **24**, 83.
List, R., Low, T. B., and Donaldson, N., 1980:*Preprints Cloud Phys. Conf.*, Clermont-Ferrand, p. 165, Blaise Pascal Université, Aubière, France.
List, R., MacNeil, C. F., and McTaggart-Cowan, J. D., 1970:*J. Geophys. Res.* **75**, 7573.
List, R., Schuepp, P. H., and Method, R. G., 1965:*J. Atmos. Sci.* **22**, 710.
List, R.. and Hand, M. J., 1971:*Physics of Fluids* **14**, 1648.
List, R.. Charlton, R. B., and Buttuls, P. I., 1968:*J. Atmos. Sci.* **25**, 1061.
List, R.. Murray, W. A., and Dyck, C., 1972:*J. Atmos. Sci.* **29**, 916.
Litvinov, I. V., 1956:*Iz. Akad. Nauk., SSSR, Ser. Geofiz.* **7**, 853.
Liu, B. Y. H., 1976:*Fine Particles,* Academic Press.
Liu, B. Y., and Whitby, K., 1968:*J. Coll. Interface Sci.* **26**, 161.
Liu, S. C. *et al.*, 1983:*J. Geophys. Res.* **88**, 1360.
Lo, K. K., and Liu, C. M., 1990:*J. Geophys. Res.* **95**, 20417.
Lo, K. K., and Passarelli, R. E., 1982:*J. Atmos. Sci.* **39**, 697.
Locatelli, J. D., and Hobbs. P. V., 1974:*J. Geophys. Res.* **79**, 2185.
Lodge, J. P., 1955:*J. Meteor.* **12**, 493.
Lodge, J. P., and Baer, F., 1954:*J. Meteor.* **11**, 420.
Lodge, J. P., and Pate. J. B., 1966:*Science* **153**, 408.
Lodge, J. P., Baker, M. L., and Pierrard, J. M., 1956:*J. Chem. Phys.* **24**, 716.
Loeb, L. B., Kip, A. F., and Einarsson, A. W., 1938:*J. Chem. Phys.* **6**, 264.
Long, A. B., 1971:*J. Atmos. Sci.* **28**, 210.
Long, A. B., 1974:*J. Atmos. Sci.* **31**, 1040.
Long, A. B., and Manton, M. J., 1974:*J. Atmos. Sci.* **31**, 1053.
Lonsdale, K., 1958:*Proc. Roy. Soc. London* A247. 424.
Lovett, R. F., 1978:*Tellus* **30**, 358.
Low, R. D. H., 1975:*J. de Rech. Atmos.* **9**, 23.
Low, R. D. H., Duncan, L. D., and Hsiao. Y. Y., 1979:*Research. Rept.* ASL-TR-DO34.
Low, R. D., 1969a:*J. Atmos. Sci.* **26**, 608.
Low, R. D., 1969d:*Research Rept.* AD 691700, ECOM-5249, Atmos. Sci. Lab., White Sands Missile Range, New Mexico.
Low, T. B., and List, R., 1982a:*J. Atmos. Sci.* **39**, 1591.
Low, T. B., and List, R., 1982b:*J. Atmos. Sci.* **39**, 1607.
Low. R. D., 1969b:*J. de Rech. Atmos.* **4**, 65.
Low. R. D., 1969c:*J. Atmos. Sci.* **26**, 1345.
Low. R. D., 1971:*Research and Develop. Techn. Rept.* ECOM-5358, U.S. Army Electronics Command, Fort Monmouth, New Jersey.
Lowe, D. C., and Schmidt, U., 1983:*J. Geophys. Res.* **88**, 1084.
Lowe, P. R., and Ficke, J. M., 1974:*Techn. Paper* 4-74, Environmental Prediction Res. Facility, Naval Post Grad. School, Monterey, California.
Lozowski, E. P., and Beattle, A. G., 1979:*Quart. J. Roy. Meteor. Soc.* **105**, 453.
Luck, W. H. P., 1962:*Z. f. Elektrochemie* **66**, 766.
Luck, W. H. P., 1963:*Z. f. Elektrochemie* **67**, 186.
Luck, W. H. P., 1965:*Z. f. Elektrochemie* **69**, 626.
Luck, W. H. P., 1967:*Discuss. Ferad. Soc.,* **43**, 115, 132.
Ludlam, F. H., 1951:*Quart. J. Roy. Meteor. Soc.* **77**, 402.
Ludlam, F. H., 1958:*Nubila* **1**, 12.
Ludlam, F. H.., 1950:*Quart. J. Roy. Meteor. Soc.* **76**, 52.
Lugg, G. A., 1968:*Anal. Chem.* **40**, 1072.
Maa, J. R., 1967:*Ind. Eng. Chem. Fundam.* **6**, 504.
Maahs, H. G., 1982:*Heterogeneous Atmospheric Chemistry,* Geophys. Monogr. 26, p. 187, D. R. Schryer, Ed., Am. Geophys. Union, Washington D.C.
Maahs, H. G., 1983a:*Atmos. Environ.* **17**, 341.
Maahs, H. G., 1983b:*J. Geophys. Res.* **88**, 10721.
Mac Cready, P. B., and Proudfit, A., 1965:*Quart. J. Roy. Meteor. Soc.* **91**, 44.
Mac Gregor, L. *et al.*, 1990:*Atmos. Environ.* **24A**, 2247.
Mac Pherson,J. I., and Isaac, G. A., 1977:*J. Appl. Meteor.* **16**, 81.
Mack, E. J. *et al.*, 1980:*Rept.* AFGL-TR-80-0340, Airforce Geophys. Res. Lab., Hanscom AFB. Massachusetts.
Macki, L. R., and Willoughby, K. J., 1978:*J. Appl. Meteor.* **17**, 1049.
Macklin, W. C., 1960:*Nubila* **3**, 30.
Macklin, W. C., 1961:*Quart. J. Roy. Meteor. Soc.* **87**, 413.
Macklin, W. C., 1962:*Quart. J. Roy. Meteor. Soc.* **88**, 30.

Macklin, W. C., 1963:*Quart. J. Roy. Meteor. Soc.* **89**, 360.
Macklin, W. C., 1964a:*J. Atmos. Sci.* **21**, 227.
Macklin, W. C., 1964b:*Quart. J. Roy. Meteor. Soc.* **90**, 84.
Macklin, W. C., and Bailey, I. H., 1968:*Quart. J. Roy. Meteor. Soc.* **94**, 393.
Macklin, W. C., and Ludlam, F. H., 1961:*Quart. J. Roy. Meteor. Soc.* **87**, 72.
Macklin, W. C., and Payne, G. S., 1967:*Quart. J. Roy. Meteor. Soc.* **93**, 195.
Macklin, W. C., and Payne, G. S., 1968:*Quart. J. Roy. Meteor. Soc.* **94**, 167.
Macklin, W. C., and Payne, G. S., 1969:*Quart. J. Roy. Meteor. Soc.* **95**, 724.
Macklin, W. C., and Ryan, B. F., 1965:*J. Atmos. Sci.* **22**, 452.
Macklin, W. C., and Ryan, B. F., 1966:*Phil. Mag.* **14**, 847.
Macklin, W. C., and Ryan, B. F., 1968:*Phil. Mag.* **17**, 83.
Macklin, W. C., and Ryan, B. F., 1969:*J. Chem. Phys.* **50**, 551.
Macklin, W. C., and Rye, P. J., 1974:*J. Atmos. Sci.* **31**, 849.
Macklin, W. C., Carras, J. N., and Rye, P. J., 1978:*Quart. J Roy. Meteor. Soc.* **102**, 25.
Macklin, W. C., Merlivat, L., and Stevenson, C. M., 1970:*Quart. J. Roy. Meteor. Soc.* **96**, 472.
Macklin, W. C., Strauch, E., and Ludlam, F. H., 1960:*Nubila* **3**, 12.
Macky, W. A., 1931:*Proc. Roy. Soc. London* A133, 565.
Madonna, L. A. *et al.*, 1961:*Proc. Phys. Soc., London* A78, 1218.
Maeno, N., 1973:*Proceedings Conf. Phys. Chem. of Ice*, Ottawa, p. 140, Roy. Soc., Canada, Ottawa.
Magarvey, R. H., and Bishop, R. L., 1961a:*Phys. Fluids* **4**, 800.
Magarvey, R. H., and Bishop, R. L., 1961b:*Canad. J. Phys.* **39**, 1418.
Magarvey, R. H., and Geldart, J. W., 1962:*J. Atmos. Sci.* **19**, 107.
Magarvey, R. H., and McLatchey, C. S., 1965:*Canad. J. Phys.* **43**, 1649.
Magarvey, R. H., and Taylor, B. H., 1956:*J. Appl. Phys.* **27**, 1129.
Magono, C. *et al.*, 1974:*J. Meteor. Soc. Japan* **52**, 407.
Magono, C. *et al.*, 1975a:*J. Fac. Sci.,* Hokkaido Univ. Ser. VII, 4, 93.
Magono, C. *et al.*, 1975b:*J. Fac. Sci.,* Hokkaido Univ. Ser. VII, 4, 103.
Magono, C. *et al.*, 1979:*Tellus* **31**, 102.
Magono, C., 1951:*J. Meteor.* **8**, 199.
Magono, C., 1953:*Science Rept.,* Yokohama Natl. University, Sect. I, 2, 18, Yokohama, Japan.
Magono, C., 1954a:*J. Meteor.* **11**, 77.
Magono, C., 1954b:*Science Rept.,* Yokohama Natl. University, Sect. I, 3, 33, Yokohama, Japan.
Magono, C., 1960:*Geophys. Monograph,* 5, p. 142, Am. Geophys. Union, Washington, D.C.
Magono, C., and Aburukawa, H., 1968:*J. Fac. Sci.,* Ser. 7, 3, 85, Hokkaido University, Sapporo, Japan.
Magono, C., and Arai, B., 1954:*J. Meteor. Soc. Japan* **32**, 336.
Magono, C., and Iwabuchi, T., 1972:*Arch. Met. Geophys. Biok.,* Ser. A. 21, 287.
Magono, C., and Kikuchi, K., 1961:*J. Meteor. Soc. Japan* **39**, 258.
Magono, C., and Lee, C. W., 1966:*J. Fac. Sci.,* Hokkaido University, Ser. 7, 2, No. 4.
Magono, C., and Lee, C. W., 1973:*J. Meteor. Soc. Japan* **51**, 176.
Magono, C., and Nakamura, T., 1959:*J. Meteor. Soc. Japan* **37**, 124.
Magono, C., and Nakamura, T., 1965:*J. Meteor. Soc. Japan* **43**, 139.
Magono, C., and Orikasa, K., 1966:*J. Meteor. Soc. Japan* **44**, 260, 280.
Magono, C., and Suzuki, S., 1967:*J. Fac. Sci.,* Hokkaido University, Ser. 7, 3, 27.
Magono, C., Endoh, T., and Shigeno, T., 1983:*J. Meteor. Soc. Japan* **61**, 325.
Magono, C., Endoh, T., and Tanoguchi, T., 1982:*J. Meteor. Soc. Japan* **60**, 1188.
Magono, C., Kikuchi, K., and Kimura, T., 1959:*J. Fac. Sci.,* Hokkaido University, Ser. 7, 1, 195.
Magono, C., Kikuchi, K., and Kimura, T., 1960:*J. Fac. Sci.,* Hokkaido University, Ser. 7, 1, 267.
Magono, C., Kikuchi, K., and Kimura, T., 1962:*J. Fac. Sci.,* Hokkaido University, Ser. 7, 1, 373.
Magono, C., Kikuchi, K., and Kimura, T., 1963:*J. Fac. Sci.,* Hokkaido University, Ser. 7, 2, 49.
Magono, C., Kikuchi, K., and Kimura, T., 1965:*J. Fac. Sci.,* Hokkaido University, Ser. 7, 2, 123.

Magono, C., Kikuchi, K., and Kimura, T., 1966:*J. Foc. Sci.,* Hokkaido University, Ser. 7, 2, 287.
Magono, C., Kikuchi, K., and Yamami, N., 1971:*J. Meteor. Soc. Japan* **49**, 179.
Mahata, P. C., and Alofs, D. J., 1975:*J. Atmos. Sci.* **32**, 116.
Mahrous, M. A., 1954:*Quart. J. Roy. Meteor. Soc.* **80**, 99.
Maidique, M. A., Hippel, A. V., and Westphal, W. B., 1971:*J. Chem. Phys.* **54**, 150.
Makhonko, K. P., 1967:*Tellus* **19**, 467.
Malan, D. J., 1952:*Ann. Geophys.* **8**, 385.
Malan, D. J., 1963:*Physics of Lightning,* The English University Press, Ltd., London.
Malkus, D. S., 1960:*Cumulus Dynamics,* Pergamon.
Malkus, J. S., 1954:*J. Meteor.* **11**, 220.
Malkus, J. S., and Scorer, R. S., 1955:*J. Meteor.* **12**, 43.
Malmberg, C. G., and Mariott, A. A., 1956:*J. Res. Nat. Bur. Stand.* **56**, 1.
Malyschew, A. *et al.*, 1994:*Atmos. Environ.* **28**, 1575.
Mamane, Y., and Mehler, M., 1987:*Atmos. Environ.* **21**, 1984.
Manley, R., and Mason, S., 1952:*J. Colloid Sci.* **7**, 354.
Manton, M. J., 1974:*Geophys. Fluid Dyn.* **6**, 83.
Mantovani, S. *et al.*, 1980:*J. Chem. Phys.* **72**, 4077.
Markowitz, A. H., 1976:*J. Appl. Meteor.* **15**, 1029.
Maroulis, D. J., and Bandy, A. R., 1974:*Science* **196**, 647.
Maroulis, P. J., and Bandy, A. R., 1980:*Geophys. Res. Lett.* **7**, 681.
Marreno, T. R., and Mason, E. A., 1972:*J. Phys. Chem.,* Ref. Data 1, 1.
Marsh, A. R., and McElroy, W. J., 1985:*Atmos. Environ.* **19**, 1075.
Marshall, B. J., Latham, J., and Saunders, C. P. R., 1978:*Quart. J. Roy. Meteor. Soc.* **104**, 163.
Marshall, I. S., and Gunn, K. L. S., 1952:*J. Meteor.* **9**, 322.
Marshall, I. S., and Marsh, S. J., 1986:*EOS Trans.* 67, 890, Am. Geophys. Union.
Marshall, J. S., and Palmer, W. M., 1948:*J. Meteor.* **5**, 165.
Marshall, T. C. *et al.*, 1989:*J. Geophys. Res.* **94**, 2171.
Marshall, T. C., and Rust, W. D., 1991:*J. Geophys. Res.* **96**, 22, 297.
Marshall, T. C., and Winn, W. P., 1982:*J. Geophys. Res.* **87**, 7141.
Marshall, T. C., Latham, J., and Saunders, C. P. R., 1978:*Quart. J. Roy. Meteor. Soc.* **104**, 163.
Martell, E. A., 1970:*Advances in Chem. Series,* **93**, 138.
Martell, E. A., 1971:*Man's Impact on the Climate,* Mathews *et al.*, Eds., p. 421, MIT Press, Cambridge, Massachusetts.
Martell, E. A., and Moore, H. E., 1974:*J. de Rech. Atmos.* **8**, 903.
Martin, A., and Barber, F. R., 1985:*Atmos. Environ.* **19**, 1091.
Martin, J. J. *et al.*, 1980b:*Pure and Appl. Geophys.* **118**, 1109.
Martin, J. J. *et al.*, 1981:*J. Atmos. Sci.* **38**, 2462.
Martin, J. J., Wang, P. K., and Pruppacher, H. R., 1980a:*J. Atmos. Sci.* **37**, 1628.
Martin, J. J., Wang, P. K., and Pruppacher, H. R., 1980c:*J. Coll. Interface Sci.* **78**, 44.
Martin, J. J., Wang, P. K., and Pruppacher, H. R., 1981:*J. Atmos. Sci.* **38**, 2462.
Martin, L. R., 1983:*Acid Precipitation. J. G. Lamberts, Ed., Ann. Arbor. Science.*
Martin, L. R., 1984:*SO_2, NO, and NO_2 Oxidation Mechanisms,* J. S. Calvert, Ed., Chapter 2, p. 63, Butterworths.
Martin, L. R., and Dahmschen, D. E., 1981:*Atmos. Environ.* **15**, 1615.
Martin, L. R., and Good, T. W., 1991:*Atmos. Environ.* **25A**, 2395.
Martin, L. R., and Hill, M. W., 1987:*Atmos. Environ.* **21**, 1487.
Martin, P. F., and Hutchinson, W. C. A., 1977:*Electrical Processes in Atmosphere,* H. Dolezahlek, R. Reiter, Eds., p. 302, Steinkopff.
Martin, R. T., 1959:*Clays and Clay Minerals, Monograph* No. 2, Earth Sci. Series, p. 259, Pergamon.
Martinsson, B. *et al.*, 1992:*Tellus* **44B**, 593.
Marty, J. C., Aliot, A., 1979:*J. Geophys. Res.* **84**, 5707.
Martynov, G. A., and Bakanov, S. P., 1961:*Surface Forces,* B. Derjaguin, Ed., p. 182.
Maruyama, M., and Kitagawa, T., 1967:*J. Meteor. Soc. Japan* **65**, 126.
Marwitz, J. D., 1972:*J. de Rech. Atmos.* **6**, 367.
Marwitz, J. D., 1974:*J. Appl. Meteor.* **13**, 450.
Marwitz, J. D., 1987a:*J. Atmos. Sci.* **44**, 174.
Marwitz, J. D., 1987b:*J. Atmos. Sci.* **44**, 159.
Masliyah, J. H., 1972:*Phys. Fluids* **15**, 1144.

Masliyah, J. H., and Epstein, N., 1971:*Proceedings Symp. on Two Phase Systems*, Haifa, Israel.
Masliyah. J. H., and Epstein, N., 1970:*J. Fluid. Mech.* **44**, 493.
Mason, B. J., 1952a:*Quart. J. Roy. Meteor. Soc.* **22**, 78.
Mason, B. J., 1952b:*Quart. J. Roy. Meteor. Soc.* **78**, 377.
Mason, B. J., 1953:*Quart. J. Roy. Meteor. Soc.* **79**, 104.
Mason, B. J., 1954a:*J. Meteor.* **11**, 514.
Mason, B. J., 1954b:*Nature* **174**, 470.
Mason, B. J., 1955:*Quart. J. Roy. Meteor. Soc.* **81**, 262.
Mason, B. J., 1956:*Quart. J. Roy. Meteor. Soc.* **82**, 209.
Mason, B. J., 1957a:*Physics of Clouds*, Oxford University Press.
Mason, B. J., 1957b:*Geofysica Pura e Appl.* **36**, 148.
Mason, B. J., 1959:*Tellus* **2**, 216.
Mason, B. J., 1960a:*Quart. J. Roy. Meteor. Soc.* **86**, 552.
Mason, B. J., 1960b:*J. Meteor.* **17**, 459.
Mason, B. J., 1971:*The Physics of Clouds*, Oxford University Press.
Mason, B. J., 19*Proc. Roy. Soc. London* A327, 433.
Mason, B. J., 1975:*Quart. J. Roy. Meteor. Soc.* **101**, 178.
Mason, B. J., 1988:*Proc. Roy. Soc. London*, A 415, 303.
Mason, B. J., 1993:*Proc. Roy. Soc. London*, A 441, 3.
Mason, B. J., 1994:*Quart. J. Roy. Meteor. Soc.* **120**, 849.
Mason, B. J., and Andrews, J. B., 1960:*Quart. J. Roy. Meteor. Soc.* **86**, 346.
Mason, B. J., and Chien, C. W., 1962:*Quart. J. Roy. Meteor. Soc.* **88**, 136.
Mason, B. J., and Jonas, P. R., 1974:*J. Meteor. Soc.* **100**, 23.
Mason, B. J., and Maybank, J., 1958:*Quart. J. Roy. Meteor. Soc.* **84**, 235.
Mason, B. J., and Maybank, J., 1960:*Quart. I. Roy. Meteor. Soc.* **86**,176.
Mason, B. J., and Shaw, D., 1955:*J. Meteor.* **12**, 93.
Mason, B. J., and van den Heuvel, H. P., 1959:*Proc. Phys. Soc. London* A74, 744.
Mason, B. J., Bryant, G. W., and van den Heuvel, H. P., 1963:*Phil. Mag.* **8**, 505.
Mastenbrook, H. J., 1968:*J. Atmos. Sci.* **25**, 299.
Mastenbrook, H. J., 1974:*Can. J. Chem.* **52**, 1527.
Mathews, J. B., 1967:*J. Geophys. Res.* **72**, 3007.
Mathews, J. B., and Mason, B. J., 1964:*Quart. J. Roy. Meteor. Soc.* **90**, 275.
Matrosov, S. Y., 1991:*J. Atmos. Sci.* **48**, 1062.
Matson, R. J., and Huggins, A. W., 1980:*J. Atmos. Sci.* **37**, 1107.
Matsubara, K., 1973:*J. Meteor. Soc. Japan* **51**, 54.
Matsumoto, M., and Kataoke, Y., 1988:*J. Chem. Phys.* **88**, 3233.
Matsuo, T., 1987:*J. Meteor. Soc. Japan* **65**, 635.
Matsuo, T., and Sasyo, Y., 1981a:*J. Meteor. Soc. Japan* **59**, 1.
Matsuo, T., and Sasyo, Y., 1981b:*J. Meteor. Soc. Japan* **59**, 10.
Mattauch, J., 1925:*Z. Phys.* **32**, 439.
Matthews, J. B., and Mason, B. J., 1963:*Quart. J. Roy. Meteor. Soc.* **89**, 376.
Matthias, S., 1992:*Ph. D. Thesis.* Inst. f. Atmos. Phys., Univ. Mainz, Mainz.
Matveev, L. T., 1984:*Cloud Dynamics*, D. Reidel.
Maude, A. D., 1961:*Brit. J. Appl. Phys.* **12**, 293.
Maxwell, J. C., 1890:*The Scientific Papers of James Clerk Maxwell*, Vol. 2, p. 636, Dover Publ.
Maxworthy, T., 1965:*J. Fluid Mech.* **23**, 369.
May, D. R., and Kolthoff, I. M., 1948:*J. Phys. Chem.* **52**, 836.
Maybank,1., and Mason, B. J., 1959:*Proc. Phys. Soc.*, London 74, 11.
Mazin, I. P., 1965:*Moscow Cent. Aerosl. Obs. Trudy* **64**, 57.
Mazin, I. P., Khrgian, A. K., and Imyanitov, I. M., 1989:*Handbook of Clouds and Cloudy Atmospheres*, Hydro-Meteor. Service, Leningrad.
Mazin, I. P., Silaeva, V. I., and Strunin, M. A., 1984:*Izv. Atmos. Oceanic Phys.* **20**, 6.
Mazzega, E. *et al.*, 1976:*J. Chem. Phys.* **64**, 1028.
McArdle, J. U., and Hoffmann, M. R., 1983:*J. Phys. Chem.* **87**, 5425.
McCall, D. W., and Douglass, D. C., 1965:*J. Phys. Chem.* **69**, 2001.
McCarthy, J., 1974:*J. Atmos. Sci.* **31**, 1028.
McCormick, G. C., and Hendry, A., 1974:*J. de Rech. Atmos.* **8**, 175.
McCormick, G. C., and Hendry, A., 1977:*Electron. Lettr.* **13**, 83.
McCormick, M. P., and Swissler, T. J., 1983:*Geophys. Res. Lett.* **10**, 877.
McCormick, M. P. *et al.*, 1981:*Science* **214**, 328.

McDonald, J. E., 1953a:*J. Meteor.* **10**, 68.
McDonald, J. E., 1953b:*J. Meteor.* **10**, 416.
McDonald, J. E., 1954:*J. Meteor.* **11**, 478.
McDonald, J. E., 1958:*Advances in Geophys.* **5**. 223.
McDonald, J. E., 1962:*Am. J. Phys.* **30**, 870.
McDonald, J. E., 1963a:*Am. J. Phys.* **31**, 31.
McDonald, J. E., 1963b:*Z. Angew. Math. Phys.* **14**, 610.
McDonald, J. E., 1964:*J. Atmos. Sci.* **21**, 109.
McElroy, W. J., 1986:*Atmos. Environ.* **20**, 427.
McFarquhar, G. M., and List, R., 1991a:*J. Atmos. Sci.* **48**, 1587.
McFarquhar, G. M., and List, R., 1991b:*J. Atmos. Sci.* **48**, 1999.
McKenzie, A. R.*et al.*, 1995:*J. Geophys. Res.* **100**, 11275.
McKinnon, D., Morewood, H. W., 1970:*J. Atmos. Sci.* **37**, 483.
McLeod, J. B., 1962:*Quart. J. Math., Oxford,* **13**, 119.
McLeod, J. B., 1964:*Proc. Math. Soc. London* 14, 445.
McLeod, J. C., 1976:*Preprints Cloud Phys. Conf.*, Boulder, Colorado, p. 326, Am. Geophys. Union, Washington D.C.
McMahon, T. A., and Denison, P. J., 1979:*Atmos. Environ.* **13**, 571.
McMurry, P. H., and Stolzenburg, M. R., 1989:*Atmos. Environ.* **23**, 497.
McPerson, J. I., and Isaac, G. A., 1977:*J. Appl. Meteor.* **16**, 81.
McPortland, I., Super, A., and Holroyd, E., 1977:*Preprints Conf. on Weather Mod.*, Urbana, Illinois, p. 351, Am. Meteor. Soc., Boston.
McTaggart-Cowan, J. D., and List, R., 1975:*J. Atmos. Sci.* **32**, 1401.
Meanhaut, W. *et al.*, 1979:*J. Geophys. Res.* **84**, 2421.
Mecke, K., 1933:*Z. Phys.* **81**, 313.
Meetham, A. R., 1959:*Geophys. Monogr.* 3, p. 115, Am. Geophys. Union, Washington D.C.
Meigs, R., 1953:*Rev. of Res. on Arid Zone Hydrology,* Vol. 1, p. 203, UNESCO.
Meischner, P., and Bögel, W., 1988:*Tellus* **40B**, 189.
Meissner, F., 1920:*Z. Anorg. Allg. Chemie* **110**. 169.
Meixner, F. X. *et al.*, 1985:*Physico-chem. Behavior of Atmos. Pollutants,* F. de Leeuw and N. U. Egmond, Eds., p. 103, D. Reidel.
Meixner, F., 1981:*Ber. Inst. Meteor.* 45, University of Frankfurt.
Melissinos, A. C., 1966:*Experiments in Modern Physics,* Academic Press.
Melzak, Z. A., 1953:*Quart. Appl. Math.* **11**, 231.
Merceret, F. J., 1976a:*J. Atmos. Sci.* **33**, 1739.
Merceret, F. J., 1976b:*J. Appl. Meteor.* **15**, 482.
Meszaros, A., 1965:*J. de Rech. Atmos.* **2, 53.**
Mészaros, A., 1984:*Science of the Total Environment* **36**, 283.
Mészaros, A., and Mészaros, E., 1989:*Aerosol Sci. and Technol.* **10**, 337.
Meszaros, A., and Vissy, K., 1974:*J. Aerosol Sci.* **5**, 101.
Meszaros, E., 1968:*Tellus* **211**, 443.
Meszaros, E., 1969:*Ann. d. Meteor.* **4**, 132.
Meyer, L., 1958:*Z. Phys. Chem.* **16**, 333.
Meyer, M. B., Jiusto, J. E., and Lala, G. G., 1980:*J. Atmos. Sci.* **37**, 622.
Meyers, M. P., DeMott, P. J., and Cotton, W. R., 1992:*J. Appl. Meteor.* **31**, 708.
Michaels, A. S., Brian, P. L., and Sperry, P. R., 1966:*J. Appl. Phys.* **37**, 4649.
Middleton, J. R., 1971:*Research Rept,* AR 101, Dept. of Atmos. Resources, University of Wyoming, Laramie, Wyoming.
Middleton, W. E., 1965:*A History of the Theories of Rain and Other Forms of Precipitation,* Oldbourne, London.
Mihara, Y., 1966:*Nature* **212**, 602.
Miller, N. L., and Wang, P. K., 1989:*J. Atmos. Sci.* **46**, 1656.
Miller, R. C. *et al.*, 1983:*J. Chem. Phys.* **78**, 3204.
Miller, T., and Young, K. C., 1979:*J. Atmos. Sci.* **36**, 458.
Miller-Hildebrand, D., 1954:*Tellus* **6**, 367.
Miller-Hildebrand, D., 1955:*Ark. Geofis.* **2**, 395.
Millikan, R. A., 1923:*Phys. Rev.* **21**, 217.
Millikan, R. A., 1924:*Phys. Rev.* **22**, 1.
Mills, R., 1971:*Ber. Bunsengesellschaft* **75**, 195.
Mills, R., 1973:*J. Phys. Chem.* **77**, 685.
Mirabel, P., and Chavelin, J. L., 1978:*J. Chem. Phys.* **68**, 5020.

Mirabel, P., and Katz, J. L., 1974:*J. Chem. Phys.* **60**, 1138.
Mitchell, D. L., and Lamb, D., 1989:*J. Geophys. Res.* **94**, 1431.
Mitchell, D. L., Zhang, R., and Pitter, R. L., 1990:*J. Appl. Meteor.* **29**, 153.
Mitchell, D., 1988:*J. Atmos. Sci.* **45**, 3431.
Mitra, S. K. *et al.*, 1990c:*J. Atmos. Sci.* **47**, 584.
Mitra, S. K. *et al.*, 1992b:*Precipitation Scavenging and Atmosphere-Surface Exchange*, S. E. Schwartz, W. G. N. Slinn, Eds., Vol. 1, p. 123, Hemisphere.
Mitra, S. K., and Hannemann, A. U., 1993:*J. Atmos. Chem.* **16**, 201.
Mitra, S. K., Barth, S., and Pruppacher, H. R., 1990a:*Atmos. Environ.* **24A**, 2307.
Mitra, S. K., Barth, U., and Pruppacher, H. R., 1990b:*Atmos. Environ.* **24A**, 1247.
Mitra, S. K., Brinkmann, J., and Pruppacher, H. R., 1992a:*J. Aerosol. Sci.* **23**, 245.
Miyake, Y., 1948:*Geophys. Mag. Japan* **16**, 64.
Miyamoto, S., and Letey, J., 1971:*Proc. Soil Science Soc. of America* **35**, 856.
Mizuno, Y., and Hanafusa, N., 1987:*J. de Phys., Coll.* C1, Suppl. No. 3, 48, C1-511.
Mizuno, Y., and Wakashima, G., 1983:*J. Phys. Chem.* **87**, 4161.
Mocdy, W. A., 1959:*Tellus* **11**, 16.
Mockros, L. F., Quon, J. E., and Hjelmfelt, A. T., 1967:*J Coll. Sci.* **23**, 90.
Mocris, T. R., 1957:*J. Meteor.* **14**, 281.
Mohnen, V. A., 1970:*J. Geophys. Res.* **75**, 7117.
Mohnen, V. A., 1971:*Pure and Appl. Geophys.* **84**, 141.
Mohnen, V. A., and Lodge, J. P., 1969:*Preprints Conf. on Cloud Nuclei*, Prague and Vienna, 69, Czechoslovak Akad. Sci., Prague.
Mohnen, V., 1989:*Tellus* **41B**, 79.
Moller, W., 1938:*Phys. Z.* **39**, 57.
Monahan, E. C., 1968:*J. Geophys. Res.* **73**, 1127.
Monahan, E. C., 1969:*J. Atmos. Sci.* **26**, 1026.
Monahan, E. C., 1971:*J. Phys. Oceanogr.* **1**, 139.
Monin, A. S., and Yaglom, A. M., 1971:*Statistical Fluid Mechanics,* MIT Press, Cambridge, Massachusetts.
Montgomery, D. N., 1971:*J. Atmos. Sci.* **28**, 291.
Moore, C. B., 1975:*J. Atmos. Sci.* **32**, 608.
Moore, C. B., 1975b:*J. Geophys. Res.* **80**, 2658.
Moore, C. B., 1976a:*Quart. J. Roy. Meteor. Soc.* **102**, 225.
Moore, C. B., 1976b:*Quart. J. Roy. Meteor. Soc.* **102**, 935.
Moore, C. B., Winn, W. P., and Cooper, A. S., 1983:*Preprints Atmos. Electr. Conf.*, L. H. Ruhnke, J. Latham, A. Deepak, Eds., Hampton, p. 267, Virginia.
Moore, D. J., and Mason, B. J., 1954:*Quart. J. Roy. Meteor. Soc.* **80**, 583.
Moore, H. E., Poet, S. E., and Martell, E. A., 1973:*J. Geophys. Res.* **78**, 7065.
Moore. D. J., 1952:*Quart. J. Roy. Meteor. Soc.* **78**, 596.
Morariu, V. V., and Mills, R., 1972:*Z. Phys. Chem.* **79**, 1.
Morgan, G. M.. and Langer, G., 1973:*Quart. J. Roy. Meteor. Soc.* **99**, 387.
Morgan, J., and Warren, B. E., 1938:*J. Chem. Phys.* **6**, 666.
Morgensen, O. E., Eldrup, M., 1978:*J. Glaciol.* **21**, 85.
Morris, T. R., and Braham, 1968:*Preprints Conference on Weather Mod.*, Albany, p. 306, Am. Meteor. Soc., Boston.
Morse, M. D., and Rice, S. A., 1982:*J. Chem. Phys.* **76**, 650.
Morse, P., 1969:*Thermal Physics,* W. A. Benjamin, Inc., New York.
Morse, P., and Feshbach, H., 1953:*Methods of Theoretical Physics,* Vol. I, McGraw-Hill.
Morton, B. R., 1957:*J. Fluid. Mech.* **2**, 127.
Morton, B. R., Taylor, G., and Turner, J. S., 1*Proc. Roy. Soc. London* 234, 1.
Morton, B.R., 1959:*J. Fluid. Mech.* **5**, 151.
Mosello, R., Marchetto, A., and Tartari, G. A., 1988:*Water, Air, Soil Poll.* **42**, 137.
Moss, S. J., and Johnson, D. W., 1992:*Preprints Cloud Phys. Conf.*, Montreal, Canada, p. 211, McGill University Press.
Mossop, S. C., 1955:*Proc. Phys. Soc.* **B68**, 193.
Mossop, S. C., 1956:*Proc. Phys. Soc.* **B69**, 165.
Mossop, S. C., 1963a:*Nature* **199**, 325.
Mossop, S. C., 1963b:*Z. Angew. Math. Phys.* **14**, 4S6.
Mossop, S. C., 1965:*Geochim. et Cosmochim. Acta* **29**. 201.
Mossop, S. C., 1970:*Bull. Am. Meteor. Soc.* **51**, 474.
Mossop, S. C., 1971:*Weather* **26**, 222.
Mossop, S. C., 1972:*J. de Rech. Atmos.* **6**, 377.

Mossop, S. C., 1976: *Quart. J. Roy. Meteor. Soc.* **102**, 45.
Mossop, S. C., 1978: *Quart. J. Roy. Meteor. Soc.* **104**, 323.
Mossop, S. C., 1985a: *Quart. J. Roy. Meteor. Soc.* **111**, 1113.
Mossop, S. C., 1985b: *Quart. J. Roy. Meteor. Soc.* **111**, 183.
Mossop, S. C., 1985c: *Bull. Am. Meteor. Soc.* **66**, 264.
Mossop, S. C., and Hallett, J., 1974: *Science* **186**, 632.
Mossop, S. C., and Jayaweera, K. O. L. F., 1969: *J. Appl. Meteor.* **8**, 241.
Mossop, S. C., and Ono, A., 1969: *J. Atmos. Sci.* **26**, 130.
Mossop, S. C., Cottis, R. E., and Bartelett, B. M., 1972: *Quart. J. Roy. Meteor. Soc.* **98**, 105.
Mossop, S. C., Ono, A., and Heffernan, K. J., 1967: *J. de Rech. Atmos.* **3**, 45.
Mossop, S. C., Ono, A., and Wishart, E. R., 1970: *Quart. J. Roy. Meteor. Soc.* **96**, 487.
Mossop, S. C., Ruskin, R. E., and Heffernan, K. J., 1968: *J. Atmos. Sci.* **25**, 889.
Mossop, S. C.. and Kidder, R. E., 1964: *Nubila* **6**, 74.
Mozurkewich, M. *et al.*, 1987: *J. Geophys. Res.* **92**, 4163.
Mozurkewich, M., 1986: *Aerosol Science and Technology* **5**, 223.
Mucray, F. W., 1967a: *J. Appl. Meteor.* **6**, 203.
Mueller, E. A., and Sims, A. L., 1966: *Tech. Rev.*, ECOM-00032-F, Illinois State Water Survey, Urbana.
Mueller, E. M., 1966: *Ph. D. Thesis,* University of Chicago.
Munger, J. W. *et al.*, 1983: *J. Geophys. Res.* **88**, 5109.
Munger, J. W. *et al.*, 1989a: *Atmos. Environ.* **23**, 2305.
Munger, J. W. *et al.*, 1989b: *Tellus* **41B**, 230.
Munzah, T., 1960: *Tellus* **12**, 282.
Murakami, M. *et al.*, 1983: *J. Meteor. Soc. Japan* **61**, 346.
Murakami, M., Hiramatsu, C., and Magono, C., 1981: *J. Meteor. Soc. Japan* **59**, 763.
Murakami, M., Kikuchi, K., and Magono, C., 1985a: *J. Meteor. Soc. Japan* **63**, 119.
Murakami, M., Kikuchi, K., and Magono, C., 1985b: *J. Meteor. Soc. Japan* **63**, 130.
Murakami, M., Kikuchi, K., and Magono, C., 1985c: *J. Meteor. Soc. Japan* **63**, 1127.
Murgatroyd, R. J., Garrod, M. P., 1957: *Quart. J. Roy. Meteor. Soc.* **83**, 528.
Murray, F. W., 1970: *Research Report,* D-19910-ARPA, The RAND Corp. Santa Monica, California.
Murray, J. D., 1967: *J. Math. and Phys.* **46**, 1.
Murray, W. A., and List, R., 1972: *J. Glaciol.* **11**, 415.
Murty, A. S. R., and Murty, B. V. R., 1972: *Tellus* **24**, 581.
Murty, Bh. V., 1969: *J. Meteor. Soc. Japan* **47**, 219.
Musil, D. J., 1970: *J. Atmos. Sci.* **27**, 474.
Musil, D. J., and Smith, P. L., 1989: *Atmos. Res.* **24**, 149.
Nagamoto, C. T. *et al.*, 1983: *Atmos. Environ.* **17**, 1073.
Nagle, J. F., 1966: *J. Math. Phys.* **7**, 1484.
Nakamura, T., 1964: *J. Meteor. Soc. Japan* **42**, 65.
Nakaya, U., 1954: *Snow Crystals,* Harvard University Press.
Nakaya, U., and Higuchi, K., 1960: *Geophys. Monograph* 5, p. 118, Am. Geophys. Union, Washington, D.C.
Nakaya, U., and Matsumoto, A., 1953: *Research Paper 4*, Snow, Ice and Permafrost, Res. Establ., U.S. Army .
Nakaya, U., and Matsumoto. A., 1954: *J. Coll. Sci.* **9**, 41.
Nakaya, U., and Tereda, T., 1935: *J. Fac. Sci.,* Hokkaido Univ., Ser. II, 1, 191.
Namiot, A. Yu., 1961: *Zh. Stnict. Khim.* **2**, 476.
Narten, A. H., and Levy, H. A., 1969: *Science* **165**, 447.
Narten, A. H., and Levy, H. A., 1970: *Science* **167**, 1521.
Narten, A. H., and Levy, H. A., 1971: *J. Chem. Phys.* **55**, 2263.
Narten, A. H., and Levy, H. A., 1972: *Water,* F. Franks, Ed., p. 311, Plenum
Narten, A. H., Danford, M. D., and Levy, H. A., 1967: *Disc. Farad. Soc.* **43**, 97.
Narusawa, M., and Springer, G. S., 1975: *J. Coll. Interface Sci.* **50**, 392
Naruse, H., and Maryama, H., 1971: *Papers in Meteor. and Geophys.* **22**, 1. Nasello, O. *et al.*, 1980: *J. de Rech. Atmos.* **14**, 365.
Neiburger, M., 1949: *J. Meteor.* **6**, 98.
Neiburger, M., 1967: *Monthly Weather Rev.* **95**, 917.
Neiburger, M., and Chien, C. W., 1960: *Meteor. Monographs,* 5, p. 191. Am. Geophys. Union, Washington, D.C.
Neiburger, M., and Wurtele, M. G., 1949: *Chem. Rev.* **44**, 21.

Neiburger, M., Levin, Z., and Rodriguez, L., 1972:*J. de Rech. Atmos.* **6**, 391.
Neitzert, V., and Seiler, W., 1981:*Geophys. Res. Lett.* **8**, 79.
Neizvestnyy, A. I., Kotov, G. B., and Onischenko, L. I., 1979:*Izv. Atm. Ocean. Phys.* **15**, 47.
Nelson, A. R., and Gokhale, N. R., 1972:*J. Geophys. Res.* **77**, 2724.
Nelson, A. R., and Gokhale, N. R., 1973:*J. Geophys. Res.* **78**, 1472.
Nemethy, G. and Scheraga, H. A., 1962a:*J. Chem. Phys.* **36**, 3382.
Nemethy, G., and Scheraga, H. A., 1962b:*J. Phys. Chem.* **66**, 1773.
Nemethy, G., and Scheraga, H. A., 1964:*J. Chem. Phys.* **41**, 680.
Newmann, G. H., Fonselius, S., and Wahlman, 1959:*Intl. J. Air Poll.* **2**, 132.
Nguyen, B. C. *et al.*, 1978:*Nature* **237**, 452.
Nguyen, B. C., Bonsang, B., and Lambert, G., 1974:*Tellus* **26**, 241.
Nguyen, B., Bousang, B., and Gandry, A., 1983:*J. Geophys. Res.* **88**, 10903.
Nicholls, S., 1987:*Quart. J. Roy. Meteor. Soc.* **113**, 1141.
Nishioka, M., and Sato, H., 1974:*J. Fluid Mech.* **65**, 97.
Nix, N., and Fukuta, N., 1974:*J. Atmos. Sci.* **31**, 1334.
Nolan, J. J., 1926:*Proc. Roy. Irish Acad.* **37**, 28.
Noll, G., 1969:*Physics of Ice,* N. Riehl *et al.*,Eds., p. 113, Plenum.
Noll, K. E., and Pilat, M. J., 1971:*Atmos. Environment* **5**, 527.
Noone, K. J. *et al.*, 1988:*J. Geophys. Res.* **93**, 9477.
Noone, K. J. *et al.*, 1992:*Tellus* **44B**, 489.
Noone, K. J., Ogren, J. H., and Heintzenberg, J., 1990:*Atmos. Res.* **25**, 3.
Noone, K., and Clarke, A. D., 1988:*Atmos. Environ.* **22**, 2773.
Norville, K., Baker, M., and Latham, J., 1991:*J. Geophys. Res.* **96**, 7463.
Noxon, J. F., 1981:*Geophys. Res. Lett.* **8**, 1223.
O'Brien, F. E., 1948:*J. Sci. Instruments* **25**, 73.
O'Connell, J. P.et al., 1969:*J. Phys. Chem.* **73**, 2000.
O'Konski, C. T., and Thatcher, H. C., 1953:*J. Phys. Chem.* **57**, 955.
O'Neil, M. E., 1964:*Ph.D. Thesis,* University of London, London.
O'Neil, M. E., and Majundar, S. R., 1970a:*Z. Angew. Math. und Phys.* **21**, 164.
O'Neil, M. E., and Majundar, S. R., 1970b:*Z. Angew. Math. und Phys.* **21**, 180.
Oakes, B., 1960:*Intl. J. Air Poll.* **3**, 179.
Oberbeck, A., 1876:*Crelle's J. Math.* **81**, 62.
Obukov, A. M., 1954:*Math. J.* **6**, 77.
Ocampo, J., and Klinger, J., 1982:*J. Coll. Interface Sci.* **86**, 377.
Ocampo, J., and Klinger, J., 1983:*J. Phys. Chem.* **87**, 4167.
Ochs, H. T., 1978:*J. Atmos. Sci.* **35**, 1959.
Ochs, H. T., and Beard, K. V., 1984:*J. Atmos. Sci.* **40**, 863.
Ochs, H. T., and Gatz, D. F., 1980:*Atmos. Environ.* **14**, 615.
Ochs, H. T., and Yao, C. S., 1978:*J. Atmos. Sci.* **35**, 1947.
Ochs, H. T., Czys, P. R., and Beard, K. V., 1986:*J. Atmos. Sci.* **43**, 225.
Ochs, H. T., Schaufelberger, D. E., and Feng, J. Q., 1991:*J. Atmos. Sci.* **48**, 946.
Ockelmann, G., 1988:*Ber. Inst. Meteor.,* No. 75, University Frankfurt.
Ockendon, J. R., and Evans, G. A., 1972:*J. Aerosol Sci.* **3**, 237.
Ogiwara, S., and Okita, T., 1952:*Tellus* **4**, 233.
Ogren, J. H. *et al.*, 1989:*Tellus* **41B**, 24.
Ogren, J. H. *et al.*, 1992:*Tellus* **44B**, 570.
Ogren, J. H., and Charlson, R. J., 1992:*Tellus* **44B**, 208.
Ohta, S., 1951:*Bull. Am. Meteor. Soc.* **82**, 30.
Ohtake, T., 1967:*Preprints Conf. Low Temp. Sci.*, Sapporo, Vol. l, p. 105, Institute of Low Temp. Sci., Hokkaido University, Sapporo, Japan.
Ohtake, T., 1968:*Preprints Cloud Phys. Conf.*, Toronto, p. 285, University of Toronto Press, Toronto.
Ohtake, T., 1969:*J. Atmos. Sci.* **26**, 545.
Ohtake, T., 1970a:*J. Atmos. Sci.* **27**, 509.
Ohtake, T., 1970b:*Final Rept. Ap-100449,* Geophys. Institute, University of Alaska, Fairbanks, Alaska.
Ohtake, T., 1970c:*J. Atmos. Sci.* **27**, 804.
Okada, K., 1983a:*J. Meteor. Soc. Japan* **61**, 727.
Okada, K., 1983b:*J. Aerosol Sci.* **14**, 301.
Okita, T. *et al.*, 1986:*J. Atmos. Chem.* **4**, 343.
Okita, T., 1958:*Sci. Rept.,* Tohoku University, 5th Ser., Geofys., 10, No. 1.

Okita, T., 1962a:*J. Meteor. Soc. Japan* **40**, 39.
Okita, T., 1968:*J. Meteor. Soc. Japan* **46**, 120.
Okuyama, M., and Zung, J. T., 1967:*J. Chem. Phys.* **46**, 1580.
Oliver, D. A., and Chung, J. N., 1987:*J. Fluid. Mech.* **177**, 1.
Oliver, D. A., Lewellen, W. S., and Williamson, G. S., 1978:*J. Atmos. Sci.* **35**, 301.
Olszyna, K. J., Meagher, J. F., and Bailey, S. M., 1988:*Atmos. Environ.* **22**, 1699.
Ono, A., 1969:*J. Atmos. Sci.* **26**, 138.
Ono, A., 1970:*J. Atmos. Sci.* **27**, 649.
Ono, A., 1971:*J. Meteor. Soc. Japan* **45**, 845.
Ono, A., 1972:*J. de Rech. Atmos.* **6**, 399.
Ono, A., Ito, T., and Iwai, K., 1981:*Memoirs Nat. Inst. Polar Res.,* Special Issue 19, p. 141.
Ono, S., and Kondo, S., 1960:*Handbuch der Physik,* S. Flügge, Ed., Vol.10, p.134, Springer.
Oralty, R. G., and Hallett, J., 1989:*Atmos. Res.* **24**, 169.
Oralty, R. G., and Hallett, J., 1990:*J. Aerosol Sci.* **21**, Suppl., 263.
Orem, M. W., and Adamson, A. W., 1969:*J. Coll. Interface Sci.* **31**, 278.
Orr, C., Hurd, F. K., and Hendrix, W. P., 1958:*J. Meteor.* **15**, 240.
Osborne, N. S. , Stimson, H. F., and Ginnings, D. C., 1939:*J. Res. Nat. Bur. Stand.* **23**, 197, 643.
Oseen, C. W., 1910:*Ark. Math. Astron. Fys.* **6**, No. 29.
Oseen, C. W., 1915:*Archiv., Math. Phys., Ser.* **3**, 24, 108.
Oseen, C. W., 1927:*Hydrodynamik,* Akad. Verlagsgesellschaft, Leipzig.
Osipov, Y. A. *et al.*, 1977:*Zh. Fiz. Kem.* **51**, 1264.
Osipow, L. I., 1962:*Surface Chemistry,* Reinhold.
Ostwald, W., 1900:*Z. Phys. Chem.* **34**, 495.
Ostwald, W., 1902:*Lehrbuch der Allgem. Chemie,* Verlag W. Engelmann, Leipzig.
Otani, Y., and Wang, C. S., 1984:*Aerosol Sci. and Techn.* **3**, 155.
Overton, J. H., Aneja, U. P., and Durham, J. L., 1979:*Atmos. Environ.* **13**, 355.
Owen, P. R., 1964:*J. Fluid Mech.* **20**, 225.
Pai, S-I., 1956:*Viscous Flow Theory,* Vol. I: Laminar Flow, Van Nostrand, Publ.
Palmer, L. S., 1952:*Proc. Phys. Soc., London* **65**, 674.
Paluch, D. R., and Breed, D. W., 1984:*J. Atmos. Sci.* **41**, 1008.
Paluch, I., 1970:*J. Geophys. Res.* **75**, 1633.
Paluch, I., 1979:*J. Atmos. Sci.* **36**, 2467.
Paluch, I., 1980:*J. Atmos. Sci.* **43**, 1984.
Paluch, I., and Baumgardner, D., 1989:*J. Atmos. Sci.* **46**, 261.
Paluch, I., and Knight, C., 1984:*J. Atmos. Sci.* **41**, 1801.
Paluch, I., and Sartor, J. D., 1973:*J. Atmos. Sci.* **30**, 1166.
Panchev, S., 1971:*Random Functions and Turbulence,* Pergamon.
Pandis, S. N., Seinfeld, J. H., and Pilinis, C., 1990:*Atmos. Environ.* **24A**, 1957.
Pao, Y. H., 1965:*Phys. Fluids* **8**, 1063.
Park, R. W., 1970:*Ph.D. Thesis,* Dept. Chem. Engr., University of Wisconsin, Madison, Wisconsin.
Parker, B. C., 1968:*Nature* **219**, 617.
Parkin, D. W. *et al.*, 1970:*J. Geophys. Res.* **73**, 1782.
Parkin, D. W., Phillips, D. R., Sullivan, R. A., 1972:*Quart. J. Roy. Meteor. Soc.* **98**, 798.
Parkinson, W. C., 1952:*J. Geophys. Res.* **57**, 314.
Parrish, D. D. *et al.*, 1986:*J. Geophys. Res.* **91**, 5379.
Parungo, F. *et al.*, 1979:*Tellus* **31**, 521.
Parungo, F. P. *et al.*, 1982:*J. Geophys. Res.* **87**, 8805.
Parungo, F. P. *et al.*, 1986b:*J. Atmos. Chem.* **4**, 199.
Parungo, F. P. *et al.*, 1990:*Atmos. Environ.* **24A**, 109.
Parungo, F. P., Ackermann, E., and Prouex, H., 1976:*J. de Rech. Atmos.* **10**, 45.
Parungo, F. P., and Pueschel, R. F., 1980:*J. Geophys. Res.* **85**, 4507.
Parungo, F. P., and Weickmann, H. K., 1973:*Beitr. Phys. Atmos.* **46**, 289.
Parungo, F. P., Nagamoto, C. T., and Harris, J. M., 1986a:*Atmos. Res.* **20**, 23.
Parungo, F., and Lodge, J. P., 1965:*J. Atmos. Sci.* **22**, 309.
Parungo, F., and Lodge, J. P., 1967a:*J. Atmos. Sci.* **24**, 274.
Parungo, F., and Lodge, J. P., 1967b:*J. Atmos. Sci.* **24**, 439.
Parungo, F., and Weickmann, H. K., 1973:*Beitr. z. Phys. der Atmosphäre* **46**, 289.
Parungo, F., and Wood, J., 1968:*J. Atmos. Sci.* **25**, 154.

Pasqualuci, F., 1982:*Geophys. Res. Lett.* **9**, 839.
Pasquill, F., 1962:*Atmospheric Diffusion,* Van Norstrand.
Passarelli, R. E., 1978a:*J. Atmos. Sci.* **35**, 882.
Passarelli, R. E., 1978b:*J. Atmos. Sci.* **35**, 118.
Passarelli, R. E., 1982:*J. Atmos. Sci.* **39**, 697.
Passarelli, R. E., and Srivastava, R. C., 1979:*J. Atmos. Sci.* **36**, 484.
Pasternak, I. S., and Gauvin, W. H., 1960:*Canad. J. Chem. Eng.* **38**, 35.
Patterson, H. S., and Cawood, W., *Proc. Roy. Soc. London* A136, 538.
Patterson, M. P. and Spillane, K. T., 1967:*J. Atmos. Sci.* **24**, 50.
Patterson, M. P., and Spillane, K. T., 1969:*Quart. J. Roy. Meteor. Soc.* **95**, 526.
Pattlock, F., and Tränkle, E., 1984:*J. Am. Opt. Soc.* **1**, 520.
Patton, A. J., and Springer, G. S., 1969:*Rarefied Gas Dynamics,* L. Trillin and H. Y. Wachman Eds., Vol. 2, p. 1947, Academic Press.
Pauling, L., 1935:*J. Am. Chem. Soc.* **57**, 2680.
Pauling, L., 1959:*Hydrogen Bonding,* D. Hadzi, H. W. Thompson, Eds., Pergamon.
Pauling, L., 1960:*The Nature of the Chemical Bond,* 3rd edn., Cornell University Press, Ithaca, New York.
Pauthenier, M., and Moreau-Hanot, M., 1931:*C. R. Acad. Sci.,* Paris 13, 1068.
Pawlow, P., 1910:*Z. Phys. Chem.* **74**, 562.
Pearcey, T., and Hill, G. W., 1956:*Quart. J. Roy. Meteor. Soc.* **83**, 77.
Pearcey, T., and McHugh, B., 1955:*Phil. Mag. 46, Ser.* **7**, 783.
Pearson, H. J., Vilioulis, I. A., and List, E. J., 1984:*J. Fluid. Mech.* **143**, 367.
Pena, J. A., and Pena, R. G., 1970:*J. Geophys. Res.* **75**, 2831.
Pena, J. A., Pena. R. G., and Hosler, C. L., 1969:*J. Atmos. Sci.* **26**, 309.
Penndorf, R., 1954:*Geophys. Res. Papers,* 25, 1, Air Force Cambridge Res. Center, Cambridge, Massachusetts.
Peppler, W., 1940:*Forschg. u. Erfahrung,* Reichsamt f. Wetterdienst. B., No. 1.
Perrin, D. D., 1982:*Ionization Constants of Inorganic Acids and Bases in aqueous Solutions.* Pergamon.
Perry, J., 1950:*Chem. Eng. Handbook,* 3rd edn., p. 1017, McGraw-Hill.
Peterson, J. T., and Junge, C. E., 1971:*Man's Impact on the Climate,* Matthews *et al.*, Eds., p. 310, MIT Press, Cambridge, Massachusetts.
Peterson, S. W., and Levy, H. A., 1957:*Acta Cryst.* **10**, 70.
Petrenchuk, O. P. and Selezneva, E. S., 1970:*J. Geophys. Res.* **75**, 3629.
Petrenchuk, O. P., and Drozdova, V. M., 1966:*Tellus* **18**, 280.
Peyret, R., and Taylor, T. D., 1983:*Computational Methods for Fluid Flow.* Springer.
Pflaum, J. C., and Pruppacher, H. R., 1979:*J. Atmos. Sci.* **36**, 680.
Pflaum, J. C., 1980:*J. Atmos. Sci.* **37**, 160.
Pflaum, J. C., 1984:*Bull. Am. Meteor. Soc.* **65**, 583.
Pflaum, J. C, Martin, J., and Pruppacher, H. R., 1978:*Quart. J. Roy. Meteor. Soc.* **104**, 179.
Phan-Cong, L., and Dinh-Van, P., 1973:*Tellus* **25**, 63.
Phillips, B. B., 1967:*Monthly Weather Rev.* **95**, 854.
Phillips, B. B., and Kinzer, G. D., 1958:*J. Meteor.* **15**, 369.
Pich, J., Friedlander, S. K., and Lai, F. S., 1970:*Aerosol Sci.* **1**, 115.
Pick, W. H., 1929:*Quart. J. Roy. Meteor. Soc.* **55**, 305.
Pick, W. H., 1931:*Quart. J. Roy. Meteor. Soc.* **57**, 288.
Picknett, R. G., 1960:*Int. J. Air Pollution* **3**, 160.
Pierce, C., 1960:*J. Phys. Chem.* **64**, 1184.
Pilié, R. J. *et al.*, 1975:*J. Appl. Meteor.* **14**, 364.
Pilié, R. J., 1966:*Res. Rept., CR 368,* Cornell Aeron. Lab., Buffalo, New York.
Pinnick, R. G., and Auvermann, H. J., 1979:*J. Atmos. Sci.* **10**, 55.
Pinnick, R. G., Jennings, S. G., and Fernandez, G., 1987:*J. Atmos. Sci.* **44**, 562.
Pinsky, M. B., and Khain, A. P., 1996a:*Atmos. Res.*
Pinsky, M. B., and Khain, A. P., 1996b:*Geophys. and Astr. Fluid Dynamics.*
Pitchford, M. Hudson, J. S., and Hallett, J., 1991:*J. Geophys. Res.* **96**, 20787.
Pitter, R. L., 1977:*J. Atmos. Sci.* **34**, 684.
Pitter, R. L., and Pruppacher, H. R., 1973:*Quart. J. Roy. Meteor. Soc.* **99**, 540.
Pitter, R. L., and Pruppacher, H. R., 1974:*J. Atmos. Sci.* **31**, 551.
Pitter, R. L., Pruppacher, H. R., and Hamielec, A. E., 1973:*J. Atmos. Sci.* **30**, 125.
Pitter, R. L., Pruppacher, H. R., and Hamielec, A. E., 1974:*J. Atmos. Sci.* **31**, 1058.
Pitzer, K. S., and Polissar, J., 1956:*J. Phys. Chem.* **60**, 1140.

Platt, C. M. R., 1978:*J. Atmos. Sci.* **26**, 482.
Plumlee, H. R., and Semonin, R. G., 1965:*Tellus* **17**, 356.
Plummer, P. L., 1973:*Phys. and Chem. of Ice,* E. Whalley, S. J. Jones, and L. W. Gold, Eds., p. 109, Roy. Soc. Ottawa.
Plummer, P. L., and Hale, B. N., 1972:*J. Chem. Phys.* **56**, 4329.
Pluvinage, P., 1946:*Ann. d. Geophys.* **2**, 31.
Pocza, J.F., Barna, A., and Barna, P. B., 1969:*J. Vac. Sci. Techn.* **6**, 242.
Podzimek, J., 1965:*Preprints Cloud Phys. Conference*, Tokyo, p. 224, Meteor. Soc. of Japan, Tokyo.
Podzimek, J., 1966:*Studia Geophys. et Geodet.* **10**, 235.
Podzimek, J., 1968:*Preprints Cloud Phys. Conf.*, Toronto, p. 295, University of Toronto Press, Toronto.
Podzimek, J., 1969:*Docent Thesis,* Charles University, Prague.
Podzimek, J., 1984:*Preprints Cloud Phys. Conf.*, Tallin, p. 173, Estonian Acad. Sci., Tallin.
Podzimek, J., and Cernoch, I., 1961:*Geofysica Pura e Appl.* **50**, 96.
Podzimek, J., Haberl, J. B., and Sedlacek, W. A., 1975:*Proceedings 4th Conference on Climatic Impact Assessment Program*, U.S. Dept. of Transportation, Cambridge, Massachusetts.
Podzimek, J., Sedlacek, W. A., and Haberl, J. B., 1974:*Rept. of SANDS to U.S.* Dept. of Transportation.
Poellot, M. R., and Pflaum, J. C., 1989:*Atmos. Res.* **24**, 123.
Poet, S. E., Moure, H. E., and Martell, E. A., 1972:*J. Geophys. Res.* **77**, 6515.
Politovich, M. K., and Cooper, W. A., 1988:*J. Atmos. Sci.* **45**, 1651.
Politovich, M. K., and Vali, G., 1983:*J. Atmos. Sci.* **40**, 1300.
Ponche, J. L., George, Ch., and Mirabel, Ph., 1993:*J. Atmos. Chem.* **16**, 1.
Pontikis, C., Rigaud, A., and Hicks, E., 1987:*J. Atmos. Sci.* **44**, 2150.
Popkie, H., and Kistenmacher, H., and Clementi, E., 1973:*J. Chem. Phys.* **59**, 1325.
Pople, J. A., 1951:*Proc. Roy. Soc. London* A205, 163.
Pound, G. M., Madonna, L. A., and Sciulli, C. M., 1955:*Proceedings Conf. on Interfacial Phenomena and Nucleation*, H. Reiss, Ed., p. 85, U.S. Dept. of Commerce, Washington, D.C.
Pound, G. M., Simnad, M. T., and Yang, L., 1954:*J. Chem. Phys.* **22**, 1215.
Prandtl, L., 1904:*Verh. 3d Int. Math. Kongr.* Heidelberg, p. 484 (transcribed as NACA Tech. Mem. No. 452).
Press, W. H. *et al.*, 1992:*Numerical Recipies in Fortran,* Cambridge Univ. Press.
Price, S., and Pales, J., 1963:*Arch. Meteor. Geophys. Biokl.* **A.13**, 398.
Priestly, C. H. B., and Ball, F. K., 1955:*Quart. J. Roy. Meteor. Soc.* **81**, 144.
Prigogine, I., and Defay, R., 1967:*Chemical Thermodynamics,* 4th edn., Longmans and Green Co., London.
Pringle, J. E., Orville, H. D., and Stechmann, T. D., 1973:*J. Geophys. Res.* **78**, 4508.
Proctor, D. E., 1983:*J. Geophys. Res.* **88**, 5421.
Prodi, F. *et al.*, 1981:*Quart. J. Roy. Meteor. Soc.* **107**, 699.
Prodi, F. *et al.*, 1982:*J. Atmos. Sci.* **39**, 2301.
Prodi, F. *et al.*, 1991:*Quart. J. Roy. Meteor. Soc.* **117**, 783.
Prodi, F., 1970:*J. Appl. Meteor.* **9**, 903.
Prodi, F., 1976:*Preprints Cloud Phys. Conf.*, Boulder, p. 70, Am. Meteor. Soc., Colorado.
Prodi, F., 1983:*Prec. Scav., Dry Depos. and Resusp.,* H. R. Pruppacher, R. Semonin, and W. G. Slinn, Eds., p. 505, Elsevier.
Prodi, F., Levi, L., and Levizzani, V., 1986:*Quart. J. Roy. Meteor. Soc.* **112**, 1091.
Prodi, F., Santachiara, G., and Oliosi, F., 1983:*J. Geophys. Res.* **88**, 10957.
Prodi, F., Santachiara, G., and Prodi, V., 1979:*J. Aerosol Sci.* **10**, 421.
Prokhorov, P. S., 1951:*Doklady Akad. Nauk* S.S.S.R. 81, 637.
Prokhorov, P. S., 1954:*Disc. Farad. Soc.* **18**, 41.
Prospero, J. M. *et al.*, 1970:*Earth and Planetary Sci. Lett.* **9**, 287.
Prospero, J. M. *et al.*, 1985:*J. Geophys. Res.* **90**, 10, 568.
Prospero, J. M., 1968:*Bull. Am. Meteor. Soc.* **49**, 649.
Prospero, J. M., 1979:*J. Geophys. Res.* **84**, 725.
Prospero, J. M., and Bonatii E., 1969:*J. Geophys. Res.* **74**, 3362.
Prospero, J. M., and Carlson, T. N., 1972:*J. Geophys. Res.* **77**, 5225.
Prospero, J. M., Glaceum, R. A., and Nees, R. T., 1981:*Nature* **289**, 570.

Proudman, I., 1969:*J. Fluid Mech.* **37**, 759.
Proudman, I., and Pearson, J. R. A., 1957:*J. Fluid Mech.* **2**, 237.
Pruger, W., 1940:*Z. Phys.* **115**, 202.
Pruppacher, H. R., 1962:*Ph.D. Thesis,* Dept. Meteor., University of California, Los Angeles.
Pruppacher, H. R., 1963a:*J. Chem. Phys.* **39**, 1586.
Pruppacher, H. R., 1963b:*Z. Angew Math. und Phys.* **14**, 590.
Pruppacher, H. R., 1963c:*J. Geophys. Res.* **68**, 4463.
Pruppacher, H. R., 1967a:*Pure and Appl. Geophys.* **68**, 186.
Pruppacher, H. R., 1967b:*J. Glaciol.* **6**, 651.
Pruppacher, H. R., 1967c:*Z. f. Naturforschg.* **22a**, 895.
Pruppacher, H. R., 1967d:*J. Coll. Interface Sci.* **25**, 285.
Pruppacher, H. R., 1967e:*J. Chem. Phys.* **47**, 1807.
Pruppacher, H. R., 1972:*J. Chem. Phys.* **56**, 101.
Pruppacher, H. R., 1973:*Pure and Appl. Geophys.* **104**, 623.
Pruppacher, H. R., 1995:*J. Atmos. Sci.* **52**, 1924.
Pruppacher, H. R., and Beard, K. V., 1970:*Quart. J. Roy. Meteor. Soc.* **96**, 247.
Pruppacher, H. R., and Klett, D. J., 1978:*Microphysics of Clouds,* D. Reidel.
Pruppacher, H. R., and Neiburger, M., 1963:*J. Atmos. Sci.* **20**, 376.
Pruppacher, H. R., and Pflaum, J., 1975:*J. Coll. Interface Sci.* **52**, 543.
Pruppacher, H. R., and Pitter, R. L., 1971:*J. Atmos. Sci.* **28**, 86.
Pruppacher, H. R., and Rasmussen, R., 1979:*J. Atmos. Sci.* **36**, 1255.
Pruppacher, H. R., and Sänger, R., 1955:*Z. Angew Math. Phys.* **6**, 407.
Pruppacher, H. R., and Schlamp, R. J., 1975:*J. Geophys. Res.* **80**, 380.
Pruppacher, H. R., and Schlamp, R., 1975:*J. Geophys. Res.* **8**, 380.
Pruppacher, H. R., and Steinberger, E. H., 1968:*J. Appl. Phys.* **39**, 4129.
Pruppacher, H. R., Le Clair, B. P., and Hamielec, A. E., 1970:*J. Fluid Mech.* **440**, 781.
Pruppacher, H. R., Semonin, R. C., and Slinn, W. C., Eds., 1983:*Prec. Scav., Dry Depos. and Resusp.,* Vol. 2, Elsevier.
Pruppacher, H. R., Steinberger, E. H., and Wang, T. L., 1968:*J. Geophys. Res.* **73**, 571.
Pshenay-Severin, S. V., 1957:*Izvestyia Geophys. Ser.* **8**, 1054.
Pshenay-Severin, S. V., 1958:*Izvestyia Geophys. Ser.* **10**, 1254.
Pueschel, R. F. *et al.*, 1989:*J. Geophys. Res.* **94**, 11271.
Pueschel, R. F. *et al.*, 1992:*J. Geophys. Res.* **97**, 8105.
Pueschel, R. F., 1978:*J. Weather Mod.* **10**, No. 1, 9.
Pueschel, R. F., and Langer, G., 1973:*J. Appl. Meteor.* **12**, 549.
Puxbaum, H. *et al.*, 1988:*Atmos. Environ.* **22**, 2841.
Quante, M., and Brown, P. R., 1992:*Preprints Cloud Phys. Conf.*, Montreal, p. 510, McGill University, Montreal, Canada.
Quinn, P. K. *et al.*, 1990:*J. Geophys. Res.* **95**, 16, 405.
Quon, J. E., and Mockros, L. F., 1965:*Internat. J. Air and Waste Poll.* **9**, 279.
Qureshi, M. M., and Maybank, J., 1966:*Nature* **211**, 508.
Raasch, J., and Umhauer, H., 1991:*Part. Syst. Charact.* **6**, 13.
Radke, L. F. *et al.*, 1984:*Geophys. Res. Lett.* **11**, 393.
Radke, L. F., 1970:*Preprints Cloud Phys. Conf.*, Fort Collins, Colorado, p. 7, Am. Meteor. Soc., Boston.
Radke, L. F., 1970:*Preprints Cloud Phys. Conf.*, Fort Collins, Col., p. 7, Am. Meteor. Soc., Boston.
Radke, L. F., 1983:*Prec. Scav., Dry Depos. and Resusp.,* H. R. Pruppacher, Semonin, R., and G. Slinn, Eds., p. 71, Elsevier.
Radke, L. F., and Hegg, D., 1972:*J. de Rech. Atmos.* **6**, 447.
Radke, L. F., and Hobbs, P. V., 1969:*J. Atmos. Sci.* **26**, 281.
Radke, L. F., and Lyons, J. H., 1982:*Preprints Second Sympos. on the Composition of the non-urban Troposphere,* p. 159, Am. Meteor. Soc., Boston.
Radojevic, M. *et al.*, 1990:*Atmos. Environ.* **24A**, 323.
Rahman, A., and Stillinger, F. H., 1971:*J. Chem. Phys.* **55**, 3336.
Ramaswamy, U., and Detwiler, A., 1986:*J. Atmos. Sci.* **43**, 2289.
Ramseier, R. O., 1967:*Res. Rept.,* Coldregions Res. and Eng. Lab., Hannover, New Hempshire.
Randall, D. A., 1980:*J. Atmos. Sci.* **37**, 125.
Rangno, A. L. and Hobbs, P. V., 1991:*Quart. J. Roy. Meteor. Soc.* **117**, 207.
Rangno, A. L., and Hobbs, P. V., 1988:*Atmos. Environ.* **22**, 1.

Ranz, W. E., and Marshall, W. R., 1952:*Chem. Eng. Progr.* **48**, 141, 173.
Ranz, W. E., and Wong, J. B., 1952:*Ind. Eng. Chem.* **44**, 1371.
Rao, C. N. R., 1972:*Water,* F. Franks, Ed., p. 93, Plenum.
Rasmussen, D. H., 1972:*Water Structure at the Polymer Interface,* H. H. Jellinek, Ed., p. 126, Plenum.
Rasmussen, D. H., 1982:*J. Crys. Growth* **56**, 56.
Rasmussen, D. H., and Mac Kenzie, A. T., 1973:*J. Chem. Phys.* **59**, 5003.
Rasmussen, R. A., and Went, F. W., 1965:*Proc. Nat. Acad. Sci.* **53**, 215.
Rasmussen, R. M. *et al.*, 1985:*J. Atmos. Sci.* **42**, 1647.
Rasmussen, R. M., and Heymsfield, A. J., 1985:*J. Atmos. Sci.* **42**, 2275.
Rasmussen, R. M., and Heymsfield, A. J., 1987a:*J. Atmos. Sci.* **44**, 2754.
Rasmussen, R. M., and Heymsfield, A. J., 1987b:*J. Atmos. Sci.* **44**, 2764.
Rasmussen, R. M., and Heymsfield, A. J., 1987c:*J. Atmos. Sci.* **44**, 2783.
Rasmussen, R. M., and Pruppacher, H. R., 1982:*J. Atmos. Sci.* **39**, 152.
Rasmussen, R. M., Levizzani, V., and Pruppacher, H. R., 1982:*Pure and Appl. Geophys.* **120**, 702.
Rasmussen, R. M., Levizzani, V., and Pruppacher, H. R., 1984a:*J. Atmos. Sci.* **41**, 374.
Rasmussen, R. M., Levizzani, V., and Pruppacher, H. R., 1984b:*J. Atmos. Sci.* **41**, 381.
Rasool, S. I., Ed., 1973:*Chemistry of the Lower Atmosphere,* Plenum.
Rathje, W., and Stranski, I. N., 1955:*Proceedings Conf. on Interfacial Phenomena and Nucleation,* Vol. 1, H. Reiss, Ed., p. 1, Air Force Cambridge Res. Center, Cambridge, Mass.
Rau, W., 1950:*Z. f. Naturforschung* **5a**, 667.
Rauber, R. M., 1987a:*J. Clim. and Appl. Meteor.* **56**, 189.
Rauber, R. M., 1987b:*J. Clim. and Appl. Meteor.* **26**, 488.
Rauber, R. M., and Beard, K. V., 1991:*J. Atmos. Sci.* **48**, 1791.
Rauber, R. M., and Grant, L. O., 1986:*J. Clim. and Appl. Meteor.* **25**, 1189.
Rauber, R. M., and Tokay, A., 1991:*J. Atmos. Sci.* **48**, 1005.
Rauber, R. M., Beard, K. V., and Andrews, B. M., 1991:*J. Atmos. Sci.* **48**, 1791.
Rawlins, F., 1982:*Quart. J. Roy. Meteor. Soc.* **108**, 779.
Ray, J. D., Van Valin, C. C., and Boatmann, J. F., 1992:*J. Geophys. Res.* **97**, 2507.
Rayleigh, J. W. S., 1882:*Phil. Mag.* **14**, 184.
Raymond, D. J., and Blyth, A. M., 1986:*J. Atmos. Sci.* **43**, 2708.
Raynor, G. S., and Hayes, J. U., 1983:*Prec. Scav., Dry Depos. and Resusp.,* H. R. Pruppacher, R. Semonin, G. Slinn, Eds., p. 249, Elsevier.
Raynor, G. S., and Hayes, J. V., 1982:*Atmos. Environ.* **16**, 1647.
Reago, D. A., 1986:*Ph. D. Thesis.* Univ. of Missouri at Rolla, Missouri.
Redder, C. R., and Fukuta, N., 1989:*Atmos. Res.* **24**, 247.
Redkin, Y. N., 1973:*Hydrodynamics and Thermodynamics of Aerosols,* V. M. Voloshuk, and Y. S. Sedunov, Eds., p. 226, Wiley.
Reid, R. C., and Sherwood, T. K., 1966:*The Properties of Gases and Liquids,* Vol. 2, McGraw-Hill.
Reinhardt, R. L., 1972:*Ph.D. Thesis,* University of Nevada, Reno, Nevada.
Reinking, R. F., 1979:*J. Atmos. Sci. 36, 870.*
Reinking, R. F., and Lovill, J. E., 1971:*J. Atmos. Sci.* **28**, 812.
Reiquam, H., and Diamond, M., 1959:*CRREL Rept. 52.*
Reischel, M. T., 1972:*Research Rept. AR105,* Dept. of Atmos. Resources, University of Wyoming, Laramie, Wyoming.
Reischel, M. T., and Vali, G., 1975:*Tellus* **27**, 414.
Reiss, H., 1965:*Methods of Thermodynamics,* Blaisdell Publ. Co., Waltham, Massachusetts.
Reiter, R., 1964:*Felder, Ströme und Aerosole,* Dietrich Steinkopff Verlag, Darmstadt.
Reiter, R., 1969:*Planetary Electrodynamics,* S. C. Coroniti and J. Hughes, Eds., Vol.1, p. 59, Gordon and Breach.
Reiter, R., Sladovic, R., and Kanter, H. J., 1987:*Meteorology and Atmospheric Physics* **37**, 27.
Relf, E. F., and Simmons, L. F., 1924:*Repts. and Memoranda 917,* Great Britain Aeronaut. Res. Council
Resch, F., and Avellan, F., 1982:*Proceedings 2nd Int. Conf. on Drops and Bubbles,* Monterey, California, p. 182, JPL., Calif. Inst. of Techn., Pasadena, California.
Reuck, A. V. S., 1957:*Nature* **179**, 1119.
Reuter, G. W., de Villiers, R., and Yavin, Y., 1988:*J. Atmos. Sci.* **45**, 765.

Reuter, G. W., Wright, C. J., and Eyre, D., 1989:*J. Atmos. Sci.* **46**, 1407.
Rex, R. W., and Goldberg, E. D., 1958:*Tellus* **10**, 153.
Reynolds, B., 1983:*Atmos. Environ.* **17**, 1849.
Reynolds, O., 1876:*Nature* **15**, 163.
Reynolds, S. E., 1952:*J. Meteor.* **9**, 36.
Reynolds, S. E., Brook, M., and Gourley, M. F., 1957:*J. Meteor. Soc.* **14**, 426.
Rhyne, R. H., and Steiner, R., 1964:*NASA Techn. Note, J-2469.*
Rice, S. A., and Sceats, M. G., 1981:*J. Phys. Chem.* **85**, 1108.
Richards, C. N., and Dawson, G. A., 1971:*J. Geophys. Res.* **76**, 3445.
Richards, C. W. *et al.*, 1983:*Atmos. Environ.* **17**, 911.
Richards, T. W., and Carver, E. K., 1921:*J. Am. Chem. Soc.* **43**, 827.
Richardson, G. B. *et al.*, 1986:*Aerosol Sci. and Techn.* **5**, 103.
Richardson, L. F., 1926:*Proc. Roy. Soc.* A. 110.
Riehl, N., Bullemer, B., and Engelhardt, H., Eds., 1969:*Physics of Ice,* Plenum.
Rimmer, P. L., 1969:*J. Fluid Mech.* **32**, 1.
Rimon, Y., and Cheng, S. I., 1969:*Phys. Fluids* **12**, 949.
Rimon, Y., and Lugt, H. J., 1969:*Phys. Fluids* **12**, 2465.
Roach, T. *et al.*, 1976:*Quart. J. Roy. Meteor. Soc.* **102**, 313.
Roach, W. T., 1976:*Quart. J. Roy. Meteor. Soc.* **102**, 361.
Roberts, P., and Hallett, J., 1968:*Quart. J. Roy. Meteor. Soc.* **94**, 25.
Robertson, D., 1974:*J. Atmos. Sci.* **31**, 1344.
Robinson, R. A., and Stokes, R. H., 1970:*Electrolyte Solutions,* 2nd edn. Butterworths.
Roble, R. G., and Tzur, I., 1986:*The Earths Electrical Environment,* Studies in Geophysics, Chapter 15, p. 206, Natl. Acad. Sci. Press, Washington D.C.
Rodhe, H., 1972:*Tellus* **24**, 128.
Roelofs, G. J. H., 1992:*Atmos. Environ.* **26A**, 2309.
Rogers, C. F., and Squires, P., 1974:*Preprints Cloud Phys. Conf.*, Tucson, Arizona, p. 17, Am. Meteor. Soc., Boston.
Rogers, C. F., Hudson, G., and Kocmond, W. C., 1981:*Science* **211**, 824.
Rogers, D. C., 1974a:*Preprints Cloud Phys. Conf.*, Tuscon, Arizona, p. 108, Am. Meteor. Soc., Boston.
Rogers, D. C., 1974b:*Res. Rept. AR110*, Dept. of Atmos. Resources, University of Wyoming, Laramie, Wyoming.
Rogers, D. C., 1982:*Preprints Cloud Phys. Conf.*, Chicago, p. 115, Am. Meteor. Soc., Boston.
Rogers, D. P., Telford, J. W., and Chai, S. K., 1985:*J. Atmos. Sci.* **42**, 1846.
Rogers, L. N., 1971:*Bull. Am. Meteor. Soc.* **52**, 994.
Rogers, R. R., 1989:*J. Atmos. Sci.* **46**, 2469.
Römer, F. G. *et al.*, 1983:*Acid Deposition,* p. 195, S. Beilke, R. J., Elshout, Eds., D. Reidel.
Römer, F. G. *et al.*, 1985:*Atmos. Environ.* **19**, 1847.
Rood, M. J. *et al.*, 1989:*Nature* **337**, 537.
Roos, D. S., 1972:*J. Appl. Meteor.* **11**, 1008.
Roos, D., and Pum, H. D., 1974:*Quart. J. Roy. Meteor. Soc.* **100**, 640.
Rose, W. I., Chuan, R. L., and Woods, D. C., 1982:*J. Geophys. Res.* **87**, 4956.
Rosen, H., and Novakov, T., 1983:*Nature* **306**, 768.
Rosen, H., Novakov, T., and Bodhaine, B. A., 1981:*Atmos. Environ.* **15**, 137.
Rosen, J. M., 1969:*Space Sci. Rev.* **9**, 58.
Rosen, J. M., 1971:*J. Appl. Meteor.* **10**, 1044.
Rosen, J. M., 1974:*Final Rept.,* Contract N0001-70-A-0266-0011, University of Wyoming, Laramie, Wyoming.
Rosen, J. M., and Hofmann, D. J., 1975:*J. Atmos. Sci.* **32**, 1457.
Rosen, J. M., Hofmann, D. J., and Käselau, K. H., 1978:*J. Appl. Meteor.* **17**, 1737.
Rosen, J. M., Hofmann, G. J., and Laby, J., 1975:*J. Atmos. Sci.* **32**, 1457.
Rosenhead, L., Ed., 1963:*Laminar Boundary Layers,* Oxford Press.
Roshko, A., 1954:*NACA, Rept.* 1191.
Rosinski, J. *et al.*, 1970:*J. Geophys. Res.* **75**, 2961.
Rosinski, J. *et al.*, 1980:*Meteor. Rundschau* **33**, 97.
Rosinski, J. *et al.*, 1991:*Acta Meteor. Sinica* **5**, 497.
Rosinski, J., 1966:*J. Appl. Meteor.* **5**, 481.
Rosinski, J., 1967a:*J. Appl. Meteor.* **6**, 1066.
Rosinski, J., and Kerrigan, T. C., 1969:*J. Atmos. Sci.* **26**, 695.

Rosinski, J., and Snow, R. H., 1961:*J. Meteor.* **18**, 736.
Rosinski, J., Langer, G., and Nagamoto, C. T., 1981:*Proceedings Conf. on Atmos. Aerosols and Nuclei*, Galway, 1977, p. 372, Galway University Press.
Rosinski, J., Nagamoto, C. T., and Kerrigan, T. C., 1975:*J. de Rech. Atmos.* **9**, 107.
Rosinski,1., 1967b:*J. Atmos. Terrestr. Phys.* **29**, 1201.
Rösner, S., Flossmann, A. I., and Pruppacher, H. R., 1990:*Quart. J. Roy. Meteor. Soc.* **116**, 1389.
Rossini, F. C. *et al.*, 1952:*J. Res. Nat. Bur. Stand.*, Circular 500, p. 126.
Rossknecht, G. F., Elliott, W. P., and Ramsey, F. L., 1973:*J. Appl. Meteor.* **12**, 825.
Rossmann, F., 1950:*Ber. Deutsch Wett. D., U.S. Zone,* **15**, 1.
Rottner, D., and Vali, G., 1974:*J. Atmos. Sci.* **31**, 560.
Roulleau, M., 1958:*J. Sci. Meteor.* **10**, 12.
Roulleau, M., and Desbois, M., 1972:*J. Atmos. Sci.* **29**, S65.
Roussel, J. C., 1968:*J. de Rech. Atmos.* **3**, 253.
Rowe, P. N., Claxton, K. T., and Lewis, J. B., 1965:*Trans. Inst. Chem. Engrs.* **43**, T 14.
Rowlinson, J. S., 1949:*Trans. Farad. Soc.* **45**, 974.
Rowlinson, J. S., 1951:*Trans. Farad. Soc.* **47**, 120.
Rucklidge, J., 1965:*J. Atmos. Sci.* **22**, 301.
Rüden, H. *et al.*, 1978:*Pure and Appl. Geophys.* **116**, 335.
Ruepp, R., and Käss, M., 1969:*Proceedings Conf. of Phys. on Ice*, Munich, p. 555, Plenum.
Ruhnke, L. H., 1970:*J. Appl. Meteor.* **9**, 947.
Ruhnke, L. H., 1972:*Meteor. Res.* **25**, 38.
Ryan, B. F., 1969:*J. Crystal Growth* **5**, 284.
Ryan, B. F., 1973:*J. Atmos. Sci.* **30**, 824.
Ryan, B. F., 1974:*J. Atmos. Sci.* **31**, 1942.
Ryan, B. F., and Macklin, W. C., 1968:*J. Crystal Growth* **2**, 337.
Ryan, B. F., and Macklin, W. C., 1969:*J. Coll. Interface.* **31**, 566.
Ryan, B. F., and Scott, W. D., 1969:*J. Atmos. Sci.* **36**, 611.
Ryan, B. F., Wishart, E. R., and Holroyd, E. W., 1974:*J. Atmos. Sci.* **31**, 2136.
Ryan, B. F., Wishart, E. R., and Shaw, D. E., 1976:*J. Atmos. Sci.* **33**, 842.
Ryan, R. T. *et al.*, 1972:*J. Appl. Meteor.* **11**, 149.
Ryan, R. T., 1976:*J. Appl. Meteor.* **15**, 1571.
Rybczinski, W., 1911:*Bull. Acad.* Cracovie A, 40.
Ryde, J. W., 1946:*Meteor. Factors in Radio Wave Propagation,* Phys. Soc. London, p. 169.
Rye, P. J., and Macklin, W. C., 1973:*J. Atmos. Sci.* **30**, 1421.
Rye, P. J., and Macklin, W. C., 1975:*Quart. J. Roy. Meteor. Soc.* **101**, 207.
Saffman, P. G., 1968:*Topics in Nonlinear Physics,* N. J. Zabusky, Ed., Springer.
Saffman, P. G., and Turner, J. S., 1956:*J. Fluid Mech.* **1**, 16.
Sakugawa, H., and Kaplan, I. R., 1993:*Atmos. Environ.* **27B**, 203.
Sal'm, Ya., I., 1971:*Bull. (Izv.) Acad. Sci., SSSR, Atmos. Oceanic Phys.* **7**, 306.
Salk, S. H., Lutrus, C. K., and Hagen, D. E., 1988:*J. Atmos. Sci.* **45**, 2979.
Salzman, E. S. *et al.*, 1983:*J. Geophys. Res.* **88**, 10897.
Salzman, E. S., and Cooper, D. J., 1988:*J. Atmos. Chem.* **7**, 191.
Sambles, J. R., 1971:*Proc. Roy. Soc. London* A423, 339.
Sambles, J. R., Skinner, L. M., and Lisgarten, N. D., 1970:*Proc. Roy. Soc. London* A318, 507.
Samoilov, O. Ya., 1946:*Zh. Fiz. Khim* **20**, 1411.
Samoilov, O. Ya., 1957:*Zh. Fiz. Khim.* **31**, 537.
Samorjai, G. A., 1972:*Principles of Surface Chemistry,* Prentice-Hall, Inc., Englewood Cliffs, New Jersey.
Sandalls, F. J., and Penkett, S. H., 1977:*Atmos. Environ.* **11**, 197.
Sander, A., and Damkohler, G., 1943:*Naturwissenschaften* **3**, 460.
Sano, I., Fujitani, Y., and Maena, Y., 1960:*Memoirs* Kobe Marine Obs. 14, 1.
Sano. T., 1972:*J. Eng. Math.* **6**, 217.
Sartor, J. D., 1960:*J. Geophys. Res.* **65**, 1953.
Sartor, J. D., 1961:*J. Geophys. Res.* **66**, 831.
Sartor, J. D., 1967:*J. Atmos. Sci.* **24**, 601.
Sartor, J. D., 1970:*General Thunderstorm Electrification,* NCAR Rept., Boulder, Colorado.
Sartor, J. D., 1981:*J. Atmos. Sci.* **38**, 218.

Sartor, J. D., and Abbott, C. E., 1975:*J. Appl. Meteor.* **14**, 232.
Sassen, K., 1980:*J. Atmos. Sci.* **37**, 435.
Sassen, K., 1987:*J. Opt. Soc. Am.* **A4**, 570.
Sassen, K., and Dodd, G. C., 1988:*J. Atmos. Sci.* **45**, 1357.
Sassen, K., O'Starr, D., and Uttal, T., 1989:*J. Atmos. Sci.* **46**, 371.
Sasyo, Y., 1971:*Papers in Meteor. and Geophys.* **22**, 69.
Sasyo, Y., 1977:*Papers in Meteor. and Geophys.* **28**, 159.
Sasyo, Y., and Matsuo, T., 1980:*Papers in Meteor. and Geophys., Japan* **31**, 61.
Sasyo, Y., and Tokune, H., 1973:*Papers in Meteor. and Geophys., Japan* **24**, 1.
Sato, N., Kikuchi, K., 1989:*J. Meteor. Soc. Japan* **67**, 521.
Saunders, C. P. R. *et al.*, 1985:*J. Geophys. Res.* **90**, 6047.
Saunders, C. P. R., 1988:*Weather* **43**, 318.
Saunders, C. P. R., and Wahab, N. M. A., 1975:*J. Meteor. Soc. Japan* **53**, 121.
Saunders, C. P. R., and Zhang, C. C., 1987:*Atmos. Res.* **21**, 101.
Saunders, P. M., 1961:*J. Meteor.* **18**, 451.
Sauter, D. P., and Wang, P. K., 1989:*J. Atmos. Sci.* **46**, 1650.
Savic, P., 1953:*Res. Rept. NRC-MT-22,* Nat. Res. Council of Canada, Div. of Mech. Eng., Ottawa.
Savoie, D. L. *et al.*, 1989:*J. Atmos. Chem.* **8**, 391.
Savoie, D. L., and Prospero, J. M., 1982:*Geophys. Res. Lett.* **9**, 1207.
Savoie, D. L., Prospero, J. M., and Nees, R. T., 1987:*Atmos. Environ.* **21**, 103.
Sax, R. I., and Goldsmith, P., 1972:*Quart. J. Roy. Meteor. Soc.* **98**, 60.
Sax, R. I., and Hudson, J. G., 1981:*J. Atmos. Sci.* **38**, 1467.
Saxena, V. K., and Fukuta, N., 1976:*Preprints Cloud Phys. Conf.*, Boulder, p. 26, Am. Meteor. Soc., Boston.
Saxena, V. K., and Rathore, R. S., 1984:*Preprints 11th Int. Conf. on Atmos. Aerosol, Condensation and Ice Nuclei*, p. 292, Hungarian Meteor. Soc., Budapest.
Saxena, V. K., Burford, J. N., and Kassner, J. L., 1970:*J. Atmos. Sci.* **27**, 73.
SCEP, 1970:*Man's Impact on the Global Environment,* Rept. on the Study of Critical Environmental Problems, MIT Press, Cambridge, Massachusetts.
Schaefer, V. J., 1947:*Trans. Amer. Geophys. Union* **28**, 587.
Schaefer, V. J., 1950:*Occasional Rept. 20,* Project Cirrus, General Electric Res. Lab., Schenectady, New York.
Schäfer, K., 1932:*Z. f. Physik* **77**, 198.
Schaller, R. C., and Fukuta, N., 1979:*J. Atmos. Sci.* **36**, 1788.
Scharrer, L., 1939:*Ann. d. Physik* **35**, 619.
Schaufelberger, D. E., 1990:*MS. Thesis.* University of Illinois, Urbana.
Schedlovsky, J. P., and Paisley, S., 1966:*Tellus* **18**, 499.
Schiff, L., 1968:*Quantum Mechanics,* 3rd edn, McGraw-Hill.
Schiller, L., 1932: *Handbuch der Exp. Physik. Hydro- und Aerodyn.,* 2. Teil, Akad. Verlag. Ges., Leipzig.
Schlager, H. F. *et al.*, 1990:*Geophys. Res. Lett.* **17**, 1275.
Schlamp, R. J. *et al.*, 1976:*J. Atmos. Sci.* **33**, 1747.
Schlamp, R. J. *et al.*, 1979:*J. Atmos. Sci.* **36**, 339.
Schlamp, R. J., and Pruppacher, H. R., 1977:*Pure and Appl. Geophys.* **115**, 805.
Schlamp, R. J., Pruppacher, H. R., and Hamielec, A. E., 1975:*J. Atmos. Sci.* **32**, 2330.
Schlichting, H., 1968:*Boundary Layer Theory,* McGraw-Hill.
Schmidt, J., 1995:*Diploma Thesis.* Inst. f. Atmos. Phys., Univ. Mainz, Mainz.
Schmidt, M., 1972:*Pure and Appl. Geophys.* **97**, 219.
Schmidt, W., 1913:*Meteor. Z.* **30**, 456.
Schmiedel, J., 1928:*Phys. Z.* **29**, 593.
Schmitt, G., 1986:*Atmospheric Pollutants in Forest Areas,* p. 129, H. W. Georgii, Ed., D. Reidel.
Schmitt, K. H., 1961:*Z. f. Naturforschung* **16a**, 144.
Schmitt, K. H., and Waldmann, L., 1960:*Z. f. Naturforschung* **15a**, 843.
Schneider, J. M., Lindblad, N. R., and Hendricks, C. N., 1965:*J. Coll. Interface Sci.* **20**, 610.
Schneider-Carius, K., 1955:*Wetterkunde und Wetterforschung,* Karl Alber Verlag, Munich.
Schneider-Carius, K., 1962:*Linkes Meteorologishes Taschenbuch,* Vol. 1, 2nd edn., F. Bauer, Ed., Akad. Verlagsgesellschaft, Leipzig.
Schnell, R. C. *et al.*, 1980:*Geophys. Res. Lett.* **7**, 397.

Schnell, R. C., 1972:*Res. Rept. AR-102,* Dept. of Atmos. Resources, University of Wyoming, Laramie, Wyoming.
Schnell, R. C., 1974:*Res. Rept. AR-111,* Dept. of Atmos. Resources, University of Wyoming, Laramie, Wyoming.
Schnell, R. C., 1977:*J. Atmos. Sci.* **34**, 1299.
Schnell, R. C., and Vali, G., 1976:*J. Atmos. Sci.* **33**, 1554.
Schnell, R. C., Pueschel, P. F., and Wellmann, D. L., 1982:*J. Geophys. Res.* **87**, 11, 109.
Schotland, R. M., 1957:*J. Meteor.* **14**, 381.
Schotland, R. M., 1960:*Discuss. Farad., Soc.* **30**, 72.
Schrage, R. W., 1953:*Interphase Mass Transfer,* Columbia University Press, New York.
Schubert, B., Schmidt, U., and Erhalt, D., 1984:*Phys. Chem. Behavior of Atmos. Pollutants,* B. Versino and G. Angeletti, Eds., p. 44., D. Reidel.
Schuepp, P. H., 1971:*J. Appl. Meteor.* **10**, 1018.
Schuepp, P. H., and List, R., 1969a:*J. Appl. Meteor.* **8**, 254.
Schuepp, P. H., and List, R., 1969b:*J. Appl. Meteor.* **8**, 743.
Schuman, T. E., 1938:*Quart. J. Roy. Meteor. Soc.* **64**, 3.
Schuman, T. E., 1940:*Quart. J. Roy. Meteor. Soc.* **66**, 195.
Schumann, T., Zinder, B., and Waldvogel, A., 1986:*Aerosols: Formation and Reactivity,* p. 67, Pergamon.
Schumann, Th., 1989:*Ph. D. Thesis,* Lab. Atmos. Phys., Federal Inst. of Techn., Zürich.
Schumann, Th., Zinder, B., and Waldvogel, A., 1988:*Atmos. Environ.* **22**, 1443.
Schütz, L., 1971:*Diploma Thesis.* Inst. f. Atmos. Phys., Univ. Mainz, Mainz.
Schütz, L., 1980:*Ann., N.Y. Acad. Sci.* **338**, 515.
Schütz, L., 1989:*Paleoclimatology and Paleometeorology, Modern and past Patterns of Global Atmospheric Transport,* p. 359, M. Leinen, M. Sarnthein, Eds., Kluwer.
Schütz, L., and Jaenicke, R., 1974:*J. Appl. Meteor.* **13**, 863.
Schütz, L., and Krämer, M., 1987:*J. Atmos. Chem.* **5**, 173.
Schwartz, S. E., 1984a:*J. Geophys. Res.* **89**, 11589.
Schwartz, S. E., 1984b:*SO_2, NO, NO_2 Oxidation Mechanisms, Atmospheric Consideration,* p. 173, Butterworths.
Schwartz, S. E., 1987:*The Chemistry of Acid Rain,* ACS Symposium, R. W. Johnson *et al.*,Eds., Ser. 349, Chapter 8, p. 93, Am. Chem. Soc., Washington D.C.
Schwartz, S. E., 1988:*Atmos. Environ.* **22**, 249.
Schwartz, S. E., and Freiberg, J. E., 1981:*Atmos. Environ.* **15**, 1129.
Schwartz, S. E., and White, W. H., 1981:*Adv. Environ. Sci. Eng.* **4**, 11.
Schweighofer, S., 1989:*Diploma Thesis,* Inst. f. Phys. Chem., University of Bonn, Bonn.
Scorer, R. S., 1957:*J. Fluid. Mech.* **2**, 583.
Scorer, R. S., and Ludlam, F. H., 1953:*Quart. J. Roy. Meteor. Soc.* **79**, 94.
Scorer, R. S., and Ronne, C., 1956:*Weather* **11**, 151.
Scorer, R., 1972:*Clouds of the World,* Lothian Publ. Co., Melbourne.
Scorer, R., 1986:*Cloud Investigation by Satellite.* Ellis Horwood Ltd.
Scorer, R., and Wexler, H., 1967:*Cloud Studies in Colour,* Pergamon.
Scott, B. C., and Hobbs, P. V., 1977:*J. Atmos. Sci.* **34**, 812.
Scott, B. C., and Laulainen, N. S., 1979:*J. Appl. Meteor.* **18**, 138.
Scott, B. C., and Levin, Z., 1970:*J. Atmos. Sci.* **27**, 463.
Scott, W. D., and Hobbs, P. V., 1967:*J. Atmos. Sci.* **24**, 54.
Scott, W. D., and Levin, Z., 1975a:*J. Atmos. Sci.* **32**, 843.
Scott, W. D., and Levin, Z., 1975b:*J. Atmos. Sci.* **32**, 1814.
Scott, W. D., Lamb, D., and Duffy, D., 1969:*J. Atmos. Sci.* **26**, 727.
Scott, W. D., Levin, Z., 1970:*J. Atmos. Sci.* **27**, 463.
Scott, W. T., 1967:*J. Atmos. Sci.* **24**, 221.
Scott, W. T., 1968:*J. Atmos. Sci.* **25**, 54.
Searcy, J. Q., and Fenn, J. B., 1974:*J. Chem. Phys.* **61**, 5282.
Seary, C. A., and Houze, R. A., 1979:*J. Atmos. Sci.* **36**, 669.
Sedunov, Yu. S., 1960:*Izv. Geophys. Ser.* **5**, 792.
Sedunov, Yu. S., 1963:*Izv. Geophys. Ser.* **11**, 1747.
Sedunov, Yu. S., 1964:*Izv. Geophys. Ser.* **1**, 150.
Sedunov, Yu. S., 1965:*Izv. Akad. Nauk., Atm. Ocean. Phys.* **1**, 722.
Seigneur, C. *et al.*, 1986:*Aerosol Sci. and Techn.* **5**, 205.
Seigneur, C., and Saxena, P., 1988:*Atmos. Environ.* **22**, 101.
Seinfeld, J. H., 1980:*Lectures in Atmospheric Chemistry.* Am. Inst. of Chem. Engrs., Monograph Series, Vol. 76, Am. Inst. Chem. Engrs., New York.

Seinfeld, J. H., 1986:*Atmospheric Chemistry and Physics of Air Pollution.* Wiley.
Seinfeld, J. H., and Bassett, M., 1982:*Heterogeneous Atmospheric Chemistry,* D. R. Schryer, Ed., Geophys. Monographs 26, p. 6, Geophys. Union, Washington D.C.
Sekhorn, R. S., and Srivastava, R. C., 1971:*J. Atmos. Sci.* **28**, 983.
Sekhorn, R. S., and Srivastava, R. C., 1970:*J. Atmos. Sci.* **27**, 299.
Sekigawa, K., 1983:*J. Meteor. Soc. Japan* **61**, 359.
Selezneva, E. S., 1966:*Tellus* **18**, 525.
Semonin, R. G., 1966:*Proceedings 47th Annual AAAS and AMS Meeting*, Seattle, Washington.
Semonin, R. G., and Plumlee, H. R., 1966:*J. Geophys. Res.* **71**, 427.
Senior, W. A., and Varral, R. E., 1969:*J. Chem. Phys.* **73**, 4242.
Sergieva, A. P., 1959:*Izv. Akad. Nauk.* SSSR 7, 721.
Serpolay, R., 1958:*Bull. Obs. Puy de Dome* **No. 3**, 81.
Serpolay, R., 1959:*Bull. Obs. Puy de Dome* **No. 3**, 81.
Sesselberg, M., Trautman, T. and Thorn, M., 1996:*Atmos. Res.*
Seymour, M., and Stout, T., 1983:*Atmos. Environ.* **17**, 1483.
Shafrir, U., and Gal-Chen, T., 1971:*J. Atmos. Sci.* **28**, 741.
Shafrir, U., and Neiburger, M., 1963:*J. Geophys. Res.* **68**, 4141.
Shanks, D., 1955:*J. Math. Phys.* **34**, 1.
Shaw, D., and Mason, B. J., 1955:*Phil. Mag.* **46**, 249.
Shaw, G. E., 1988:*Rev. Geophys.* **26**, 89.
Shaw, M. A., and Rood, M. J.,1990:*Atmos. Environ.* **24A**, 1837.
Shaw, R. W., 1982:*Atmos. Environ.* **16**, 337.
Shaw, R. W., Stevens, R. K., and Bowermaster, J., 1982:*Atmos. Environ.* **16**, 2501.
Sheridan, P.J., Brock, C. A., and Wilson, J. C., 1994:*Geophys. Res. Lett.* **21**, 2587.
Sherwood, T. K., Pigford, R. L., and Wilke, C. R., 1975:*Mass Transfer,* McGraw-Hill.
Shettle, E. P., and Fenn, R. W., 1979:*Research Rept.* Project 17670, Airforce Geophys. Labs., Bedford, Massachusetts.
Shewchuk, S. R., and Iribarne, J. V., 1971:*Quart. J. Roy. Meteor. Soc.* **97**, 272.
Shewmon, P. G., 1963:*Diffusion in Solids.* McGraw-Hill.
Shewshuk, S. R., and Iribarne, J. U., 1974:*J. Atmos. Sci.* **31**, 777.
Shimazaki, T., 1985:*Minor Constituents in the Middle Atmosphere,* Terra Scientifica, Publ. Co., Tokyo and D. Reidel.
Shimshock, J. P., and de Pena, R. G., 1989:*Tellus* **41B**, 296.
Shirvaikar, V. V., Kutty, I. A., and Patil, M. S., 1981:*Meteor. Rundschau* **34**, 40.
Shutt, F. T., 1907:*Trans. Roy. Soc., Canada, Ser.* **3**, 1, 35.
Sievering, H. *et al.*, 1984:*Atmos. Environ.* **18**, 2685.
Silverman, B. A., and Glass, M., 1973:*J. Atmos. Sci.* **30**, 1620.
Simonett, B. R., and Mazurek, M. A., 1982:*Atmos. Environ.* **16**, 2139.
Simpson, G. C., 1909:*Phil. Trans. Roy. Soc.,* London, A 209, 379.
Simpson, G. C., 1927:*Phil. Roy. Soc.,* London, A 114, 376.
Simpson, G., and Robinson, G. D., 1941:*Proc. Roy. Soc. London*, A177, 281.
Simpson, G., and Scrase, F. G., 1937:*Proc. Roy. Soc. London*, A161, 309.
Simpson, J. *et al.*, 1965:*Rev. Geophys.* **3**, 387.
Simpson, J., 1976:*Advances in Geophys.* **19**, 1.
Simpson, J., and Wiggert, V. W., 1969:*Monthly Weather Rev.* **97**, 471.
Sinnarwalla, A. M., Alofs, D. J., and Carstens, D. J., 1975:*J. Atmos. Sci.* **32**, 592.
Skapski, A., 1959:*J. Chem. Phys.* **31**, 533.
Skapski, A., Billups, R., and Rooney, A., 1957:*J. Chem. Phys.* **26**, 1350.
Skatskii, V. I., 1965:*Izv. Atmos. Oceanic Phys.* **1**, 479.
Skelland, A. H., and Cornish, A. R., 1963:*A.I.Ch.E. Journal* **9**, 73.
Skinner, L. M., and Sambles, J. R., 1972:*Aerosol Science* **3**, 199.
Slingo, A., Brown, R., and Wrench, C. L., 1982:*Quart. J. Roy. Meteor. Soc.* **108**, 145.
Slinn, W. G., and Gibbs, A. G., 1971:*J. Atmos. Sci.* **28**, 973.
Slinn, W. G., and Hales; J. M., 1970:*J. Atmos. Sci.* **28**, 1465.
Slinn, W. G., and Shen, S. F., 1970:*J. Geophys. Res.* **75**, 2267.
SMIC, 1971:*Inadvertant Climate Modification,* Rept. on the Study of Man's Impact on Climates, MIT Press, Cambridge, Massachusetts.
Smith, A. M. O., and Clutter, D. W., 1963:*Am. Inst. Aeron. and Astron.* **1**, 2062.
Smith, L. G., 1955:*Quart. J. Roy. Meteor. Soc.* **81**, 23.
Smith, M. H., 1976:*J. Appl. Meteor.* **15**, 275.

Smith, M. H., Griffiths, R. R., and Latham, J., 1971:*Quart. J. Roy. Meteor. Soc.* **97**, 495.
Smith, P. L. *et al.*, 1976:*Preprints Cloud Phys. Conf.*, Boulder, Colo., p. 252, Am. Meteor. Soc., Boston.
Smith, P., Myers, C. G., and Orville, H. D., 1975:*J. Appl. Meteor.* **14**, 1156.
Smith, R. M., and Martell, A. E., 1976:*Critical Stability of Constants,* Vol. 4, Inorganic Complexes, Plenum.
Smith, S. H., and Jonas, P. R., 1995:*Quart. J. Roy. Meteor. Soc.* **121**, 1185.
Smoluchowski, M., 1916:*Physik Z.* **17**, 557.
Smoluchowski, M., 1917:*Z. Phys. Chem.* **92**, 129.
Smythe, W. R., 1950:*Static and Dynamic Electricity,* McGraw-Hill.
Snead, C. C., and Zung, J. T., 1968:*J. Coll. Interface Sci.* **27**, 25.
Snetsinger, K. G., *et al.*, 1987:*J. Geophys. Res.* **92**, 14, 761.
Snider, J. R., Montague, D. C., and Vali, G., 1992:*J. Geophys. Res.* **97**, 7569.
Snoeyink, V. L., and Kenkius, D., 1980:*Water Chemistry,* Wiley.
Sommerfeld, R. A., and Lamb, D., 1986:*Geophys. Res. Lett.* **13**, 349.
Son, J. S., and Hanratty, T. J., 1969:*J. Fluid. Mech.* **35**, 369.
Sood, S. K., and Jackson, M. R., 1966:*Proceedings Conf. on Condensation and Ice Nuclei,* Prague and Vienna, p. 299, Czechoslovak Acad. of Sci., Prague.
Sood, S. K., and Jackson, M. R., 1970:*Precipitation Scavenging, 1970,* AEC Symposium, Richland, p. 11, U.S. Dept. of Commerce, Springfield, Virginia.
Soong, S., 1974:*J. Atmos. Sci.* **35**, 108.
Soulage, G., 1955:*Arch. Meteor. Geophys., Biokl.* **8**, 211.
Soulage, G., 1957:*Ann. Geophys.* **13**, 103.
Soulage, G., 1961:*Nubila* **4**, 43.
Soulage, G., 1964:*Nubila* **6**, 43.
Soulage, G., 1966:*J. de Rech. Atmos.* **2**, 219.
Soulage. G., 1958:*Bull. Obs. Puy de Dome,* **4**, 121.
Spann, J. F., and Richardson, G. B., 1985:*Atmos. Environ.* **19**, 819.
Spells, K. E., 1952:*Proc. Phys. Soc.* **B65**, 541.
Spengler, J. D., and Gokhale, N. R., 1972:*J. Appl. Meteor.* **11**, 1101.
Spengler, J. D., and Gokhale, N. R., 1973a:*J. Geophys. Res.* **78**, 497.
Spengler, J. D., and Gokhale, N. R., 1973b:*J. Appl. Meteor.* **12**, 316
Spilhaus, A. F., 1948:*J. Meteor.* **5**, 108.
Spillane, M. C. *et al.*, 1986:*Oceanic White Caps.,* E. C. Monahan, and G. Mac Niocail, Eds., p. 167, D. Reidel.
Squires, P., 1952:*Australian J. Sci. Res.* **5**, 59, 473.
Squires, P., 1958a:*Tellus* **10**, 256.
Squires, P., 1958b:*Tellus* **10**, 372.
Squires, P., and Turner, J. S., 1962:*Tellus* **14**, 422.
Squires, P., and Twomey, S., 1958:*Tellus* **10**, 272.
Squires, P., and Twomey, S., 1966:*J. Atmos. Sci.* **23**, 401.
Srivastava, R. C., 1971:*J. Atmos. Sci.* **28**, 410.
Srivastava, R. C., 1971:*J. Atmos. Sci.* **28**, 410.
Srivastava, R. C., 1978:*J. Atmos. Sci.* **35**, 108.
Standler, R. B., and Winn, W. P., 1979:*Quart. J. Roy. Meteor. Soc.* **105**, 285.
Stanev, S., Moralijski, E., and Veltsev, K., 1987:*Z. Meteorol.* **37**, 39.
Stanley, H. E., and Teixeira, J., 1980:*J. Chem. Phys.* **73**, 3404.
Stansbury, E. J., and Vali, G., 1965:*Scientific Report MW-46,* Stormy Weather Group, McGill University, Montreal.
Starr, D. C., and Cox, S. K., 1985a:*J. Atmos. Sci.* **42**, 2663.
Starr, D. C., and Cox, S. K., 1985b:*J. Atmos. Sci.* **42**, 2682.
Starr, D., 1987:*J. Geophys. Res.* **92**, 3973.
Starr, J. R., 1967:*Ann. Occup. Hyg.* **10**, 349.
Starr, J. R., and Mason, B. J., 1966:*Quart. J. Roy. Meteor. Soc.* **92**, 490.
Stauffer, D., 1976:*J. Aerosol Sci.* **7**, 319.
Stavitskaya, A. V., 1972:*Izv. Atmos. Ocean Phys.* **8**, 768.
Stefan, J., 1873:*Wien Akad. Sci. Sitzungs Ber., Math. Naturw. Kl.* **68**, 2 Abt., 943.
Stein, D., and Georgii, H. W., 1982:*J. Hungarian Meteor. Soc.* **86**, 124.
Stein, D., and Georgii, H. W., 1983:*Meteor. Rundschau* **36**, 127.
Stein, D., Georgii, H. W., and Kramm, V., 1985:*Meteor. Rundschau* **38**, 15.
Steinberger, E. H., Pruppacher, H. R., and Neiburger, M., 1968:*J. Fluid Mech.* **34**, 809.

Steinberger, R. L., and Treybal, R. E., 1960:*A.I.Ch.E. Journal* **6**, 27.
Steiner, M., and Waldvogel, A., 1987:*J. Atmos. Sci.* **44**, 3127.
Stepanov, A. S. 1976:*Preprints Cloud Phys. Conf.*, Boulder, Colo. p. 27, Am. Meteor. Soc., Boston.
Stepanov, A. S., 1975:*Izv. Akad. Nauk.*, SSSR, FAO, 11, 267.
Stephens, G. L. *et al.*, 1990:*J. Atmos. Sci.* **47**, 1742.
Stergis, C. G., Revi, G. R., and Kangas, T., 1957:*J. Atmos. Terr. Phys.* **11**, 83.
Sterlyadkin, V. V., 1988:*Izv. Atmos. Oceanic Phys.* **24**, 6, 449.
Stevenson, C., 1968:*Quart. J. Roy. Meteor. Soc.* **94**, 35.
Stevenson, R. E., and Collier, A., 1962:*Lloydia* **25**, 89.
Stewart, R. E., and List, R., 1983:*Phys. Fluids* **26**, 920.
Stewart, R. E., Marwitz, I. D., and Pace, I. C., 1984:*J. Atmos. Sci.* **41**, 3227.
Stille, U., 1961:*Messen und Rechnen in der Physik,* Vieweg Verlag, Braunschweig.
Stillinger, F. H., 1970:*J. Phys. Chem.* **74**, 3677.
Stillinger, F. H., and Rahman, A., 1972:*J. Chem. Phys.* **57**, 1281.
Stillinger, F. H., and Rahman, A., 1978:*J. Chem. Phys.* **68**, 666.
Stimson, M., and Jeffrey, G. B., 1926:*Proc. Roy. Soc.* **A111**, 110.
Stinebaugh, W. H., Sparkin, D. M., and Kasper, J. L., 1980:*J. Phys. Chem.* **84**, 1469.
Stith, J. L., Hobbs, P. V., and Radke, L. F., 1978:*J. Geophys. Res.* **83**, 4009.
Stith, J. L., Radke, L. F., and Hobbs, P. V., 1981:*Atmos. Environ.* **15**, 73.
Stix, E., 1969:*Umschau in Wiss. Techn.* **19/69**, 620.
Stix, E., and Grosse, G., 1970:*Flora* **159**, 1.
Stockmayer, W. H., 1941:*J. Chem. Phys.* **9**, 398.
Stohlgren, T. J., and Parsons, D. J., 1987:*Atmos. Environ.* **21**, 1369.
Stokes, G. G., 1851:*Trans. Cambridge Phil. Soc.* **9**, 8.
Stokes, R. H., and Mills, R., 1965:*Viscosity of Electrolytes and Related Properties,* p. 74, Pergamon.
Stommel, H., 1947:*J. Meteor.* **4**, 91.
Stonehouse, B., 1986:*Arctic Air Pollution* Cambridge, Univ. Press.
Storebo, P. B., 1972:*Geofys. Publ.* **28**, 1.
Stott, D., and Hutchinson, W. C. A., 1965:*Quart. J. Roy. Meteor. Soc.* **91**, 80.
Strantz, R., 1971:*Meteor. Rundschau* **24**, 19.
Stratton, J. A., 1941:*Electromagnetic Theory.* McGraw-Hill.
Stringham, G. E., Simons, D. B., and Guy, H. P., 1969:*Geological Survey Paper,* 562-C, Government Printing Office, Washington, D.C.
Stumm, W., and Morgan, J. J., 1981:*Aquatic Chemistry,* 2nd edn., Wiley.
Suck, S. H., and Brock, J. R., 1979:*J. Aerosol Sci.* **10**, 581.
Summers, P. W., 1968:*Preprints Cloud Phys. Conf.*, Toronto, p. 455, University of Toronto Press, Toronto.
Sutton, O. G., 1*Proc. Roy. Soc. London* A135, 143.
Sutton, O. G., 1942:*Meteor. Res. Paper 40,* Chem. Defense Exp. Station, Porton, England.
Sutugin, A. G., and Fuchs, N. A., 1968:*J. Coll. Interface Sci.* **27**, 216.
Sutugin, A. G., and Fuchs, N. A., 1970:*J. Aerosol Sci.* **1**, 287.
Sutugin, A. G., Fuchs, N. A., and Kotsev, E. I., 1971:*J. Aerosol Sci.* **2**, 301.
Svenningsson, I. B. *et al.*, 1992:*Tellus* **44B**, 556.
Swift, D. L., and Friedlander, S. K., 1964:*J. Colloid. Sci.* **19**, 621.
Szymanski, W., and Wagner, P. E., 1983:*Atmos. Environ.* **17**, 2271.
Tabor, D., 1951:*The Hardness of Metals,* Clarendon, Oxford.
Takahashi, C., and Yamashita, A., 1969:*J. Meteor. Soc. Japan* **47**, 431.
Takahashi, C., and Yamashita, A., 1970:*J. Meteor. Soc. Japan* **48**, 373.
Takahashi, K., and Kasahara, M., 1968:*Atmos. Environ.* **2**, 441.
Takahashi, T. *et al.*, 1991:*J. Meteor. Soc. Japan* **69**, 15.
Takahashi, T., 1963:*J. Meteor. Soc. Japan* **41**, 327.
Takahashi, T., 1965:*J. Meteor. Soc. Japan* **43**, 206.
Takahashi, T., 1969a:*J. Atmos. Sci.* **26**, 1253.
Takahashi, T., 1969b:*J. Atmos. Sci.* **26**, 1259.
Takahashi, T., 1972:*J. Geophys Res.* **77**, 3869.
Takahashi, T., 1973a:*J. Atmos. Sci.* **30**, 249.
Takahashi, T., 1973b:*J. Atmos. Sci.* **30**, 1220.
Takahashi, T., 1973c:*Rev. of Geophys. and Space Phys.* **11**, 903.
Takahashi, T., 1975:*J. Atmos. Sci.* **32**, 132.

Takahashi, T., 1978a:*Monthly Weather Rev.* **106**, 1598.
Takahashi, T., 1978b:*J. Atmos. Sci.* **35**, 1536.
Takahashi, T., 1978c:*J. Atmos. Sci.* **35**, 1549.
Takahashi, T., 1979:*J. Atmos. Sci.* **36**, 2236.
Takahashi, T., 1982:*J. Meteor. Soc. Japan* **60**, 508.
Takahashi, T., 1983a:*J. Meteor. Soc. Japan* **61**, 656.
Takahashi, T., 1983b:*J. Phys. Chem.* **87**, 4122.
Takahashi, T., 1984:*J. Atmos. Sci.* **41**, 2541.
Takahashi, T., and Craig, T., 1973:*J. Meteor. Soc. Japan* **51**, 191.
Takahashi, T., and Fukuta, N., 1988a:*J. Atmos. Sci.* **45**, 3288.
Takahashi, T., and Fukuta, N., 1988b:*J. Meteor. Soc. Japan* **66**, 841.
Takahashi, T., and Fullerton, C. M., 1972:*J. Geophys. Res.* **77**, 1630.
Takami, H., and Keller, H. B., 1969:*Phys. of Fluids,* Suppl. II, **12**, 11.
Takano, Y., Liou, K. N., and Minnis, P., 1992:*J. Atmos. Sci.* **49**, 1487.
Takeda, T., 1968:*J. Meteor. Soc. Japan* **46**, 255.
Talbot, R. W. *et al.*, 1986:*J. Geophys. Res.* **91**, 5173.
Tammann, G., 1910:*Z. Phys. Chem.* **72**, 609.
Tammann, G., 1920:*Z. Anorg. Allg. Chemie* **110**, 166.
Tanaka, M., 1966:*Special Contrib.,* Geophys. Inst. No. 6, 45, Kyoto University, Kyoto, Japan.
Tanaka, T., 1980:*Papers in Meteor. and Geophys.* **31**, 153.
Taneda, S., 1956a:*Rept. Res. Inst. Appl. Mech.* **6**, 16, 99, Kyushu University, Hakozaki, Fukuoka, Japan.
Taneda, S., 1956b:*J. Phys. Soc.,* Japan 11, 302.
Tang, I. N., 1976:*J. Aerosol Sci.* **7**, 361.
Tang, I. N., and Lee, J. H., 1987:*Chemistry of Acid Rain,* Chapter 9, ACS Symps. Ser. 349, R. W. Johnson *et al.*,Eds., Am. Chem. Soc., Washington D.C.
Tang, I. N., and Munckelwitz, H. R., 1978:*J. Coll. Interface Sci.* **63**, 297.
Tang, I. N., and Munckelwitz, H. R., 1984:*J. Coll. Interface Sci.* **98**, 430.
Tang, I. N., and Munckelwitz, H. R., 1994:*J. Appl. Meteor.* **33**, 791.
Tang, I. N., Fung, K. H., and Munkelwitz, H. R., 1986a:*Aerosols: Formation and Reactivity,* p. 354, Pergamon.
Tang, I. N., Munkelwitz, H. R., and Wang, N., 1986b:*J. Coll. Interface Sci.* **114**, 409.
Taylor, G. I., 19*Proc. Roy. Soc. London* A280, 383.
Taylor, T. D., and Acrivos, A., 1964:*J. Fluid Mech.* **18**, 466.
Tazawa, S., and Magono, C., 1973:*J. Meteor. Soc. Japan* **51**, 168.
Tchen, C. M., 1947:*Ph.D. Thesis,* Den Haag, Holland.
Tcheurekdjian, N., Zettlemoyer, A. C., and Chessick, J.J., 1964:*J. Phys. Chem.* **68**, 773.
Telford, J. W., 1955:*J. Meteor.* **12**, 436.
Telford, J. W., 1960:*J. Meteor.* **17**, 86.
Telford, J. W., 1975:*Pure and Appl. Geophys.* **113**, 1067.
Telford, J. W., and Chai, S. K., 1980:*Pure and Appl. Geophys.* **119**, 720.
Telford, J. W., and Cottis, R. E., 1964:*J. Atmos. Sci.* **21**, 549.
Telford, J. W., and Thorndike, N. S., 1961:*J. Meteor.* **18**, 32.
Telford, J. W., Keck, T. S., and Chai S. K., 1984:*J. Atmos. Sci.* **41**, 3170.
Telford, J. W., Thorndike, N. S., and Bowen, E. G., 1955:*Quart. J. Roy. Meteor. Soc.* **81**, 241.
Tenekes, H., and Woods, J. D., 1973:*Quart. J. Roy. Meteor. Soc.* **99**, 758.
Tennekes, H., and Lumley, J. L., 1972:*A First Course in Turbulence,* MIT Press, Cambridge, Massachusetts.
Tennekes, H., and Woods, J. D., 1973:*Quart. J. Roy. Meteor. Soc.* **99**, 758.
Thaveau, B., Serpolay, R., and Piekarski, S., 1987:*Atmos. Res.* **21**, 83.
Thom, A., 1933:*Proc. Roy. Soc. London* **A141**, 651.
Thomas, D. T., 1971:*Radio Sci.* **6**, 833.
Thomson, J. J., 1888:*Application of Dynamics to Physics and Chemistry,* 1st edn., p. 165, Cambridge University Press, London.
Thomson, W. (Lord Kelvin), 1870:*Proc. Roy. Soc.,* Edinburgh 7, 63.
Thorpe, A. D., and Mason, B. J., 1966:*Brit. J. Appl. Phys.* **17**, 54.
Thudium, J., 1978:*Pure and Appl. Geophys.* **116**, 130.
Thuman, W. C., and Robinson, E., 1954:*J. Meteor.* **11**, I51.
Toba, Y., and Tanaka, M., 1968:*J. de Rech. Atmos.* **3**, 17.
Toba, Y.: 1965a:*Tellus* **17**, 131.

Toba, Y.: 1965b:*Tellus* **17**, 365.
Tokay, A., and Beard, K. V., 1996:*J. Appl. Meteor.* **35**, in press.
Tolman, R., 1949a:*J. Chem. Phys.* **17**, 118.
Tolman, R., 1949b:*J. Chem. Phys.* **17**, 333.
Tomotika, S., 1935:*Repts. and Memoranda,* 1678, Great Britain, Aero Res. Comm. 86.
Topol, L. E., 1986:*Atmos. Environ.* **20**, 347.
Torres, A. G., Goldby, A. B., and Bandy, A. R., 1980:*J. Geophys. Res.* **85**, 7357.
Toulcova, J., and Podzimek, J., 1968:*J. de Rech. Atmos.* **3**, 89.
Townsend, A. A., 1976:*The Structure of Turbulent Shear Flow,* Cambridge University Press, London.
Tranter, M. *et al.*, 1986:*Atmos. Environ.* **20**, 517.
Trinh, E. H., and Wang, T. G., 1982:*Proceedings 2nd Conf. on Drops and Bubbles*, p. 143, Monterey, NASA Publ.
Trinh, E., Zwern, A., and Wang, T., 1982:*J. Fluid. Mech.* **115**, 453.
Tritton, D. J., 1971:*J. Fluid. Mech.* **45**, 203.
Truby, F. K., 1955a:*Science* **121**, 404.
Truby, F. K., 1955b:*J. Appl. Phys.* **26**, 1416.
Tschudin, K., 1945:*Helvetica Phys. Acta* **19**, 91.
Tsias, A., 1996:*Ph.D. Thesis,* Dept. Atmos. Phys. Univ. of Mainz
Tsuji, M., 1950:*Geophys. Mag., Japan* **22**, 15.
Tsunogai, S., 1971:*Geochem. J., Japan* **5**, 57.
Tsunogai, S., and Fukuda, K., 1974:*Geochem. J., Japan* **8**, 141.
Tunitskii, N., 1946:*Zh. fiz. Khim.* **20**, 1136.
Turco, R. P., 1982:*Rev. Geophys.* **20**, 233.
Turco, R. P, Whitten, R. C., and Toon, O. B., 1982:*Rev. Geophys.* **20**, 233.
Turnbull, D., 1950:*J. Chem. Phys.* **18**, 769.
Turnbull, D., 1956:*Solid State Physics* **3**, 225.
Turnbull, D., and Fischer, J. C., 1949:*J. Chem. Phys.* **17**, 71.
Turnbull, D., and Vonnegut, B., 1952:*Industr. Eng. Chem.* **44**, 1292.
Turner, J. S., 1955:*Quart. J. Roy. Meteor. Soc.* **81**, 418.
Turner, J. S., 1962:*J. Fluid Mech.* **13**, 356.
Turner, J. S., 1963:*J. Fluid Mech.* **16**, 1.
Turner, J. S., 1969:*Ann. Rev. of Fluid Mech.* **1**, 29.
Turner, J. S., 1973:*Buoyancy Effects in Fluids,* Cambridge University Press, London.
Twomey, S,., 1954:*J. Meteor.* **11**, 334.
Twomey, S., 1953:*J. Appl. Phys.* **24**, 1099.
Twomey, S., 1955:*J. Meteor.* **12**, 81.
Twomey, S., 1956:*Tellus* **7**, 445.
Twomey, S., 1959a:*Geofys. Pura e Appl.* **43**, 227.
Twomey, S., 1959b:*J. Chem. Phys.* **30**, 941.
Twomey, S., 1959c:*Geofys. Pura e Appl.* **43**, 243.
Twomey, S., 1960:*Bull. Obs. de Puy de Dome* **1**, 1.
Twomey, S., 1963:*J. de Rech. Atmos.* **1**, 101.
Twomey, S., 1964:*J. Atmos. Sci.* **21**, 553.
Twomey, S., 1965:*J. de Rech. Atmos.* **2**, 113.
Twomey, S., 1966:*J. Atmos. Sci.* **23**, 405.
Twomey, S., 1968:*J. de Rech. Atmos.* **3**, 281.
Twomey, S., 1969:*J. de Rech. Atmos.* **4**, 179.
Twomey, S., 1971:*J. Atmos. Sci.* **28**, 377.
Twomey, S., 1972:*J. Atmos. Sci.* **29**, 318.
Twomey, S., 1976:*J. Atmos. Sci.* **33**, 720
Twomey, S., 1977:*Atmospheric Aerosols,* Elsevier.
Twomey, S., and Davidson, K. A., 1970:*J. Atmos. Sci.* **21**, 1056.
Twomey, S., and Davidson, K. A., 1971:*J. Atmos. Sci.* **28**, 1295.
Twomey, S., and McMaster, K. N., 1955:*Tellus* **7**, 458.
Twomey, S., and Severynse, G. T., 1964:*J. de Rech. Atmos.* **1**, 81.
Twomey, S., and Warner, J., 1967:*J. Atmos. Sci.* **24**, 702.
Twomey, S., and Wojciechowski, T. A., 1969:*J. Atmos. Sci.* **26**, 684.
Tzivion, S., Feingold, G., and Levin, Z., 1987:*J. Atmos. Sci.* **44**, 3139.
Tzivion, S., Feingold, G., and Levin, Z., 1989:*J. Atmos. Sci.* **46**, 3312.
Tzur, I., and Levin, Z., 1981:*J. Atmos. Sci.* **38**, 2444.
Uano, Y., and Sano, I., 1971:*Bull. Chem. Soc., Japan,* **44**, 908.

Uhlig, E. M., 1995:*Ph.D. Thesis,* Dept. of Atmos. Sci., University of Mainz.
Ulbrich, C. W., 1978:*Preprints 18th Radar Conf.*, p. 298, Am. Meteor. Soc., Boston.
Ulbrich, C. W., 1983:*J. Clim. and Appl. Meteor.* **22**, 1764.
Ulbrich, C. W., 1985:*J. Clim. and Appl. Meteor.* **24**, 581.
Uman, M. A., 1969:*Lightning,* McGraw-Hill.
Underwood, R. L., 1969:*J. Fluid Mech.* **37**, 95.
Uyeda, H., and Yagi, T., 1984:*J. Meteor. Soc. Japan* **62**, 917.
Valdez, M. P., and Young, K. C., 1985:*J. Atmos. Sci.* **42**, 1024.
Valdez, P., Dawson, G. A., and Bales, R. C., 1989:*J. Geophys. Res.* **94**, 1095.
Valencia, M. J., 1967:*Am. J. Sci.* **265**, 843.
Vali, G. *et al.*, 1976:*J. Atmos. Sci.* **33**, 1565.
Vali, G., 1968a:*Preprints Cloud Phys. Conf.*, Toronto, p. 232, University of Toronto Press
Vali, G., 1968b:*Sci. Rept. MW-58,* Stormy Weather Group, McGill University, Montreal.
Vali, G., 1971:*J. Atmos. Sci.* **28**, 402.
Vali, G., 1974:*Preprints Cloud Phys. Conf.*, Tuscon, Arizona, p. 34, Am. Meteor. Soc., Boston.
Vali, G., 1976:*Report, 3rd Internatl. Workshop on Ice Nuclei Measurement*, Laramie, Wyoming, p. 159.
Vali, G., 1980:*Preprints Cloud Phys. Conf.*, Clermont-Ferrand, p. 227, Blaise Pascal Université, Aubière, France.
Vali, G., 1992:*Preprints Cloud Phys. Conf.*, Montreal, p. 256, McGill University Press.
Vali, G., and Schnell, R. C., 1973:*Nature* **246**, 212.
Vali, G., and Stansbury, E. J., 1965:*Scientific Report MW-41,* Stormy Weather Group, McGill University, Montreal.
Vali, G., and Stansbury, E. J., 1966:*Canad. J. Phys.* **44**, 477.
Van den Heuvel, A. P., and Mason, B. J., 1963:*Quart. J. Roy. Meteor. Soc.* **89**, 271.
Van der Hage, J., 1972:*J. de Rech. Atmos.* **6**, 595.
Van Dyke, M., 1964:*Perturbation Methods in Fluid Mechanics,* Academic Press
Van Eck, C. L. P., Mendel, H., and Fahrenfort, 1958:*Proc. Roy. Soc. London* A247, 472.
Van Mieghem, J., and Dufour, L., 1948:*Thermodynamique de l'atmosphére,* Memoires, Vol. 30, Instit. Roy. Meteor. de Belgique.
Van-Doven *et al.*, 1990:*J. Phys. Chem.* **94**, 3265.
Vand, V., and Senior, W. A., 1965a:*J. Chem. Phys.* **43**, 1869.
Vand, V., and Senior, W. A., 1965b:*J. Chem. Phys.* **43**, 1878.
Vardiman, L., 1974:*Sci. Paper 230,* Dept. Atmos. Sci., Colorado State University.
Vardiman, L., and Grant, L. D., 1972a:*Preprints Cloud Phys. Conf.*, London, England, p. 22, Roy. Meteor. Soc., London.
Vardiman, L., and Grant, L. D., 1972b:*Preprints Conf. on Weather Mod.*, Rapid City, p. 113, Am. Meteor. Soc., Boston.
Varhelyi, G., and Gravenhorst, G., 1983:*J. Geophys. Res.* **88**, 6737.
Verma, S. S., 1989:*Atmos. Environ.* **23**, 747, 2723.
Verwey, E. J., 1941:*Rec. Trav. Chim. Pays Bas, Belg.* **60**, 887.
Vilioulis, I. A., and List, E. I., 1984:*J. Atmos. Sci.* **41**, 2516.
Vittore, O., 1973:*J. Atmos. Sci.* **30**, 321.
Vittori, A., and Prodi, V., 1967:*J. Atmos. Sci.* **24**, 533.
Vohl, O., 1989:*Diploma Thesis,* Inst. f. Atmos. Phys., Univ. Mainz, Mainz.
Vohra, K. G., and Nair, P. V., 1970:*J. Aerosol Sci.* **1**, 127.
Vohra, K. G., Ramu, S., and Vasudevan, K. N., 1969:*Atmos. Environ.* **3**, 99.
Vohra, K. G., Vasudevan, K. N., and Nair, P. V., 1970:*J. Geophys. Res.* **75**, 2951.
Volmer, M., 1939:*Kinetik der Phasenbildung,* Verlag Th. Steinkopff, Dresden.
Volmer, M., and Flood, H., 1934:*Z. Phys. Chem.* **A170**, 273.
Volmer, M., and Weber, A., 1926:*Z. Phys. Chem.* **A119**, 277.
Vong, R. J., 1990:*Atmos. Environ.* **24A**, 1007.
Vonnegut, B. *et al.*, 1966:*J. Atmos. Sci.* **23**, 764.
Vonnegut, B., 1953:*Bull. Am. Meteor. Soc.* **34**, 378.
Vonnegut, B., 1955:*Geophys. Res. Paper 42,* Air Force Cambridge Res. Center, Cambridge, Massachusetts.
Vulfson, N. I., and Levin, L. M., 1965:*Studies of Clouds, Precipitation, and Thunderstorm Electricity,* N. I. Vufson and L. M. Levin, Eds., p. 33, Am. Meteor. Soc., Boston.
Vulfson, N. I., Laktinov, A. G., and Skatskii, V. I., 1973:*J. Appl. Meteor.* **12**, 664.
Wagner, P. B., and Telford, J. W., 1981:*J. de Rech. Atmos.* **15**, 97.

Wagner, P. G., 1982:*Aerosol Microphysics II: Chem. Phys. of Micro Particles,* W. H. Marlow, Ed., p. 129, Springer.
Walcek, C. *et al.*, 1984:*J. Atmos. Chem.* **1**, 291.
Walcek, C., and Pruppacher, H. R., 1984a:*J. Atmos. Chem.* **1**, 269.
Walcek, C., and Pruppacher, H. R., 1984b:*J. Atmos. Chem.* **1**, 307.
Waldmann, J. M. *et al.*, 1982:*Science* **218**, 677.
Waldmann, L., and Schmitt, K. H., 1966:*Aerosol Science,* C. N. Davies, Ed., p. 137, Academic Press.
Waldvogel, A., 1974:*J. Atmos. Sci.* **31**, 1067.
Wallace, J. M, and Hobbs, P. V., 1977:*Atmospheric Sciences,* Academic Press.
Walrafen, G. E., 1966:*J. Chem. Phys.* **44**, 1546.
Walrafen, G. E., 1967:*J. Chem. Phys.* **47**, 114.
Walrafen, G. E., 1968a:*J. Chem. Phys.* **48**, 244.
Walrafen, G. E., 1968b:*Hydrogen Bonded Solvent Systems,* A. K. Covington and P. Jones, Eds., p. 9, Taylor and Francis.
Walrafen, G. E., 1972:*Water,* F. Franks, Ed., Vol. 1, Chapter 5, p. 151, Plenum.
Walter, H., 1973:*J. Aerosol Sci.* **4**, 1.
Waltrop, A. *et al.*, 1991:*J. Atmos. Chem.* **12**, 1.
Wang, C. S., 1966:*Ph.D. Dissertation,* California Inst. of Technology, Pasadena, California.
Wang, C. S., and Friedlander, S. K., 1967:*J. Colloid. Interface Sci.* **24**, 170.
Wang, H. C. *et al.*, 1983:*J. Aerosol Sci.* **14**, 703.
Wang, J. H., 1951a:*J. Am. Chem. Soc.* **73**, 510.
Wang, J. H., 1951b:*J. Am. Chem. Soc.* **73**, 4181.
Wang, J. H., 1952:*J. Am. Chem. Soc.* **74**, 466.
Wang, J. H., 1954:*J. Phys. Chem.* **58**, 686.
Wang, J. H., and Miller, S., 1952:*J. Am. Chem. Soc.* **74**, 1611.
Wang, J. Y., 1974:*J. Atmos. Sci.* **31**, 513.
Wang, K. C., 1970:*J. Fluid Mech.* **43**, 187.
Wang, P, K., Chang, C. H., and Miller, N. L., 1985:*J. Atmos. Sci.* **42**, 2371.
Wang, P. K., 1983:*J. Atmos. Sci.* **40**, 1051.
Wang, P. K., 1985:*J. de Rech. Atmos.* **19**, 185.
Wang, P. K., 1987:*J. Coll. Interface Sci.* **117**, 271.
Wang, P. K., 1989:*Atmos. Res.* **23**, 195.
Wang, P. K., and Denzer, S. M., 1983:*J. Atmos. Sci.* **40**, 1024.
Wang, P. K., and Ji, W., 1992:*Preprints Cloud Phys. Conf.*, p. 76, Montreal, McGill University.
Wang, P. K., and Pruppacher, H. R., 1977a:*J. Appl. Meteor.* **16**, 275.
Wang, P. K., and Pruppacher, H. R., 1977b:*J. Atmos. Sci.* **34**, 1664.
Wang, P. K., and Pruppacher, H. R., 1980a:*J. Coll. Interface Sci.* **75**, 286.
Wang, P. K., and Pruppacher, H. R., 1980b:*Pure and Appl. Geophys.* **118**, 1090.
Wang, P. K., Grover, S. N., and Pruppacher, H. R., 1978:*J. Atmos. Sci.* **35**, 1735.
Wanlass, F. M., and Eyring, H., 1961:*Adv. in Chem.* **33**, 140.
Ward, R. C., Hale, B. N., and Terrazas, S., 1983:*J. Chem. Phys.* **78**, 420.
Ward, R. C., Holdman, J. M., and Hale, B. N., 1982:*J. Chem. Phys.* **22**, 3198.
Warneck, P., 1988:*Chemistry of the Natural Atmosphere,* Academic Press.
Warner, J., 1955:*Tellus* **7**, 449.
Warner, J., 1968a:*J. de Rech. Atmos.* **3**, 233.
Warner, J., 1968b:*J. Appl. Meteor.* **7**, 247.
Warner, J., 1969a:*J. Atmos. Sci.* **26**, 1049.
Warner, J., 1969b:*J. Atmos. Sci.* **26**, 1272.
Warner, J., 1970a:*J. Atmos. Sci.* **27**, 682.
Warner, J., 1970b:*J. Atmos. Sci.* **27**, 1035.
Warner, J., 1972:*J. Atmos. Sci.* **29**, 218.
Warner, J., 1973:*J. Atmos. Sci.* **30**, 256.
Warner, J., 1975a:*J. Atmos. Sci.* **32**, 995.
Warner, J., 1975b:*Quart. J. Roy. Meteor. Soc.* **101**, 176.
Warner, J., and Twomey, S., 1967:*J. Atmos. Sci.* **24**, 704.
Warren, D. R., and Seinfeld, J. H., 1985a:*Aerosol Sci. and Technol.* **4**, 31.
Warren, D. R., and Seinfeld, J. H., 1985b:*J. Coll. Interface Sci.* **105**, 136.
Warshaw, M., 1967:*J. Atmos. Sci.* **24**, 278.
Warshaw, M., 1968:*J. Atmos. Sci.* **25**, 874.

Watson, J. D., and Crick, F. H., 1953:*Nature* **171**, 737.
Watson, P. A., and Arabi, M., 1973:*Proc. IEEE* **120**, 413.
Watts, R. G., and Farhi, I., 1975:*J. Atmos. Sci.* **32**, 1864.
Weber, R. J. *et al.*, 1995:*J. Atmos. Sci.* **52**, 2242.
Wedding, J. B., Kim, J. D., and Dennison, R. S., 1986:*Atmos. Environ.* **20**, 1039.
Weickman, H. K., 1945:*Beitr. Z. Phys. d. freien Atmosphäre* **28**, 12.
Weickman, H. K., 1949:*Ber. Deutsch. Wett. Dienst,* U.S. Zone, 6.
Weickman, H. K., 1953:*Thunderstorm Electricity,* H. R. Byers, Ed., p. 66, University of Chicago Press, Chicago.
Weickman, H. K., 1957a:*Artificial Stimulation of Rain,* p. 315, Pergamon.
Weickman, H. K., 1957b:*Artificial Stimulation of Rain,* p. 81, Pergamon.
Weickman, H. K., 1964:*Nubila* **6**, 7.
Weickman, H. K., 1972:*J. de Rech. Atmos.* **6**, 603.
Weickman, H. K., and Aufm Kampe, H. J., 1953:*J. Meteor.* **10**, 204.
Weickman, H. K., and Pueschel, R. F., 1973:*Beitr. z. Phys. d. Atmos.* **48**, 112.
Weil, J. C., Lawson, R. P., and Rodi, A. R., 1989:*J. Appl. Meteor.* **32**, 1055.
Weingärtner, E., Burtscher, H., and Baltensberger, V., 1993:*J. Aerosol Sci.* **24**, Suppl. 1, 5371.
Weinheimer, A. J., and Few, A. A., 1987:*J. Geophys. Res.* **92**, 14833.
Weissweiler, W., 1969:*Z. f. Meteor.* **21**, 108.
Welch, R. M., Ravichandran, M. G., and Cox, S. K., 1986:*J. Atmos. Sci.* **43**, 633.
Wen Ching-Sung, 1966:*Sci. Sinica* **15**, 870.
Went, F. W., Slemons, D. B., and Mozingo, H. N., 1967:*Proc. Nat. Acad. Sci.* **58**, 69.
Weyl, W. A., 1951:*J. Coll. Sci.* **6**, 389.
Whalley, E., Jones, S. J., and Gold, L. W., Eds., 1973:*Physics and Chemistry of Ice,* Roy. Soc. of Canada, Ottawa.
Whelpdale, D. M., 1970:*Ph.D. Thesis,* Dept. of Physics, University of Toronto, Toronto.
Whelpdale, D. M., and List, R., 1971:*J. Geophys. Res.* **76**, 2836.
Whipple, F. J. W., and Chalmers, J. A., 1944:*Quart. J. Roy. Meteor. Soc.* **70**, 103.
Whitby, K. T., 1978:*Atmos. Environ.* **12**, 135.
Whitby, K.T., and Liu, B. T., 1966:*Aerosol Science,* C. N. Davies, Ed., p. 59, Academic Press.
White, F. M., 1974:*Viscous Flow,* McGraw-Hill.
White, G. F., and Twinning, R. H., 1913:*American Chem. J.* **50**, 380.
Whitehead, A. N., 1889:*Quart. J. Math.* **23**, 143.
Whitehead, H. C., and Feth, J. H., 1964:*J. Geophys. Res.* **69**, 3319.
Whytlaw-Gray, R., 1935:*J. Chem. Soc.,* London, p. 268.
Whytlaw-Gray, R., and Patterson, H. S., 1932:*Smoke,* Edward Arnold, London.
Wieland, W., 1956:*Z. Angew. Math. Phys.* **7**, 428.
Wieselberger, C., 1922:*Phys. Z.* **23**, 219.
Wilkins, R. D., and Auer, A. H., 1970:*Preprints Cloud Phys. Conf.*, Fort Collins, Colorado, p. 81, Am. Meteor. Soc., Boston.
Wilkniss, P. E., and Bressan, D. J., 1972:*J. Geophys. Res.* **77**, 5307.
Williams, A. L., 1974:*Res. Rept.,* Univ. of California, UCRL-75897, Lawrence Livermore Lab., Livermore, California.
Williams, E. R., 1985:*J. Geophys. Res.* **90**, 6013.
Williams, E. R., 1989:*J. Geophys. Res.* **94**, 13151.
Williams, E. R., Weber, M. E., and Orville, R. E., 1988:*Preprints 8th Int. Conf. Atmos. Electr.*, p. 235, Am. Meteor. Soc., Boston.
Williams, G. L., 1970:*J. Atmos. Sci.* **27**, 1220.
Williamson, R. E., and McCready, P. B., 1968:*Final Report,* Contract No. 5-2-67, Meteor. Res. Inc., Altadena, California.
Willis, P. T., 1984:*J. Atmos. Sci.* **41**, 1648.
Willis, P. T., and Hallett, J., 1991:*J. Atmos. Sci.* **48**, 283.
Willis, P. T., and Heymsfield, A. J., 1989:*J. Atmos. Sci.* **46**, 2008.
Willis, P. T., and Tattelmann, P., 1989:*J. Appl. Meteor.* **28**, 3.
Willmarth, W. W., Hawk, N. E., and Harvey, R. L., 1964:*Phys. Fluids* **7**, 197.
Wilson, A. T., 1959:*Nature* **184**, 99.
Wilson, C. T. R., 1899:*Phil. Trans. Roy. Soc.* **A193**, 289.
Wilson, C. T. R., 1929:*J. Franklin Inst.* **208**, 1.
Wilson, C. T. R., and Taylor, G. I., 1925:*Proc. Cambridge Phil. Soc.* **22**, 728.
Wilson, H. A., 1900:*Phil. Mag. 50, Ser.* **5**, 238.

Wilson, J. C. *et al.*, 1990:*Geophys. Res. Lett.* **17**, 361.
Wilson, J. C. *et al.*, 1992:*J. Geophys. Res.* **97**, 7997.
Wilson, J. C. *et al.*, 1993:*Science* **261**, 1140.
Wilson, J. C., Lai, W. T., and Smitt, S. D., 1991:*J. Geophys. Res.* **96**, 17415.
Wilson, M. A., Pokorille, A., and Pratt, L. R., 1987:*J. Chem. Phys.* **91**, 4873.
Winklec, P., 1967:*Diploma Thesis,* Meteor. Inst., University of Mainz, Mainz.
Winkler, P., 1968:*Ann. Meteor.,* N.S. 4, 134.
Winkler, P., 1970:*Ph.D. Thesis,* Meteor. Inst., University of Mainz, Mainz.
Winkler, P., 1973:*Aerosol Sci.* **4**, 373.
Winkler, P., 1974:*Meteor. Rundschau* **27**, 129.
Winkler, P., 1988:*Physica Scripta* **37**, 223.
Winkler, P., and Junge, C. E., 1971:*J. Appl. Meleor.* **10**, 159.
Winkler, P., and Junge, C. E., 1972:*J. de Rech. Atmos.* **6**, 617.
Winn, W. P., and Byerley, L. G., 1975:*Quart. J. Roy. Meteor. Soc.* **101**, 979.
Winn, W. P., Moore, C. B., and Holmes, C. R., 1978:*J. Geophys. Res.* **83**, 3079.
Winn, W. P., Schwede, G. W., and Moore, C. B., 1974:*J. Geophys. Res.* **79**, 176.
Winniwater, W. *et al.*, 1988:*Tellus* **40B**, 348.
Wirth, E., 1966:*J. de Rech. Atmos.* **2**, 1.
Wisner, C., Orville, H. D., and Meyers, G. G., 1972:*J. Atmos. Sci.* **29**, 1160.
Wobus, H. B., Murray, F. W., and Koenig, L. R., 1971:*J. Appl. Meteor.* **10**, 751.
Wolff, E. W., Mulvaney, R., and Oates, K., 1989:*Geophys. Res. Lett.* **16**, 487.
Wolff, G. A., 1957:*Artificial Stimulation of Rain,* p. 332, Pergamon.
Wolff, G. *et al.*, 1987:*Atmos. Environ.* **21**, 2623.
Wolff, G. T. *et al.*, 1986:*Atmos. Environ.* **20**, 1229.
Wollan, E. O., Davidson, W. L., and Shull, C. G., 1949:*Phys. Rev.* **75**, 1348.
Woo, S., 1971:*Ph.D. Thesis,* Dept. Chem., Eng., McMaster University, Hamilton, Canada.
Woo, S., and Hamielec, A. E., 1971:*J. Atmos. Sci.* **28**, 1448.
Wood, G. R., and Walton, H. G., 1970:*J. Appl. Phys.* **41**, 3027.
Woodcock, A. H. *et al.*, 1953:*Nature* **173**, 1144.
Woodcock, A. H., 1953:*J. Meteor.* **10**, 362.
Woodcock, A. H., 1957:*Tellus* **9**, 521.
Woodcock, A. H., 1972:*J. Geophys. Res.* **77**, 5316.
Woodcock, A. H., 1978:*J. Atmos. Sci.* **35**, 657.
Woodcock, A. H., and Duce, A., 1972:*J. de Rech. Atmos.* **6**, 639.
Woodcock, A. H., and Jones, R. H., 1970:*J. Appl. Meteor.* **9**, 690.
Woodcock, A. H., Blanchard, D. C., and Jiusto, J. E., 1981:*J. Atmos. Sci.* **37**, 129.
Woods, J. D., 1965:*Quart. J. Roy. Meteor. Soc.* **91**, 353.
Woods, J. D., and Mason, B. J., 1964:*Quart. J. Roy. Meteor. Soc.* **90**, 373.
Woods, J. D., and Mason, B. J., 1965:*Quart. J. Roy. Meteor. Soc.* **91**, 35.
Woods, J. D., and Mason, B. J., 1966:*Quart. J. Roy. Meteor. Soc.* **92**, 171.
Woods, J. D., Drake, J. C., Goldsmith, P., 1972:*Quart. J. Roy. Meteor. Soc.* **98**, 135.
Woodward, B., 1959:*Quart. J. Roy. Meteor. Soc.* **85**, 144.
Workman, E. J., and Reynolds, S. E., 1949:*Bull. Am. Meteor. Soc.* **30**, 142.
Workman, E. J., and Reynolds, S. E., 1950:*Phys. Rev.* **78**, 254.
Workmann, E. J., 1969:*The Physics of Ice,* Riehl *et al.*, Eds., p. 594, Plenum.
Worley, J. D., and Klotz, I. M., 1966:*J. Chem. Phys.* **45**, 2868.
Worsnop, D. R. *et al.*, 1989:*J. Phys. Chem.* **93**, 1159.
Wronski, C. R., 1967:*Brit. J. Appl. Phys.* **18**, 1731.
Wu, I., 1981:*J. Geophys. Res.* **86**, 457.
Wu, T. H., 1964:*J. Geophys. Res.* **69**, 1083.
Wulff, G., 1901:*Z. Kristallogr.* **34**, 449.
Wurzler, S. *et al.*, 1995:*J. Atmos. Chem.*, **20**, 259.
Wurzler, S., 1995:*Ph. D. Thesis.* Dept. Meteor., University of Mainz, Mainz, Germany.
Wyckoff, R. W. G., 1963:*Crystal Structures,* 2nd Ed., Vol. 1, Interscience Publ.
Xu, J. L., 1983:*Bull. Am. Meteor. Soc.* **64**, 124.
Yamaguchi, K. *et al.*, 1991:*Atmos. Environ.* **25A**, 285.
Yamamoto, G., and Miura, A., 1949:*J. Meteor. Soc. Japan* **27**, 257.
Yamamoto, G., and Ohtake, T., 1953:*Sci. Rept.,* Tohoku University, Ser. 5, (Geophys.) 4, 141.
Yamamoto, G., and Ohtake, T., 1955:*Sci. Rept.,* Tohoku University, Ser. 5, (Geophys.) 7, 10.
Yamashita, A., 1969:*J. Meteor. Soc. Japan* **47**, 57.

Yamashita, A., 1971:*J. Meteor. Soc. Japan* **49**, 215.
Yamashita, A., 1973:*J. Meteor. Soc. Japan* **51**, 307.
Yankowski *et al.*, 1981:*J. Appl. Meteor.* **20**, 1013.
Yeh, Y., Bilgram, J. H., and Känzig, W., 1982:*J. Chem. Phys.* **77**, 2317.
Yih, C-S., 1965:*Dynamics of Nonhomogeneous Fluids,* Macmillan.
Yokoyama, E., and Kuroda, T., 1988:*J. Meteor. Soc. Japan* **66**, 927.
Yokoyama, T., 1985:*J. Meteor. Soc. Japan* **63**, 100.
Yokoyama, T., and Tanaka, H., 1984:*J. Meteor. Soc. Japan* **63**, 650.
Yoshizumi, K. *et al.*, 1984:*Atmos. Environ.* **18**, 395.
Young, K. C., 1974:*J. Atmos. Sci.* **31**, 768.
Young, K. C., 1974:*Preprints Cloud Phys. Conf.*, Tucson, Arizona, p. 95, Am. Meteor. Soc., Boston.
Young, K. C., 1975:*J. Atmos. Sci.* **32**, 965.
Young, K. C., and Warren, A. J., 1992:*J. Atmos. Sci.* **49**, 1138.
Young, R. G., and Browning, K. A., 1967:*J. Atmos. Sci.* **24**, 58.
Yue, G. K., 1979:*J. Aerosol Sci.* **10**, 75.
Yue, G. K., and Hamill, P., 1979:*J. Aerosol Sci.* **10**, 609.
Zaitsev, V. A., 1950:*Trudy Glavnoi Geofiz. Observ.* **19**, 122.
Zajac, A., 1958:*J. Chem. Phys.* **29**, 1324.
Zawadzki, I., and de Agostino, M., 1988:*J. Atmos. Sci.* **45**, 3452.
Zdunkowski, W. *et al.*, 1982:*Beitr. Phys. Atmos.* **55**, 215.
Zdunkowski, W. G., and Barr, A. E., 1972:*Boundary-Layer Meteor.* **2**, 152.
Zdunkowski, W. G., and Nielsen, B. C., 1969:*Pure and Appl. Geophys.* **75**, 278.
Zebel, G., 1956:*Z. f. Aerosol Forschg. und Therapie* **5**, 263.
Zehner, C., 1952:*Imperfection in Nearly Perfect Crystals,* Ch. 11, p. 306, Wiley.
Zeldovich, J., 1942:*Zh. Eksp. Theor. Fiz.* **12**, 525.
Zeleny, J., 1915:*Proc. Cambridge Phil. Soc.* **18**, 71.
Zeleny, J., 1917:*Phys. Rev.* **10**, 1.
Zeleny, J., 1933:*Phys. Rev.* **44**, 837.
Zettlemoyer, A. C., 1968:*J. Coll. Interface Sci.* **28**, 343.
Zettlemoyer, A. C., Ed., 1969:*Nucleation,* Marcel Dekker.
Zettlemoyer, A. C., Tcheurekdjian, and Hosler, C. L., 1963:*Z. Angew. Math. Phys.* **14**, 496.
Zettlemoyer, A. C., Tcheurekdjian, N., and Chessick, J. J., 1961:*Nature* **192**, 653.
Zhao, D. *et al.*, 1988:*Atmos. Environ.* **22**, 349.
Ziegler, C. L. *et al.*, 1991:*J. Geophys. Res.* **96**, 12833.
Ziegler, C. L., Ray, P. S., and Knight, N. C., 1983:*J. Atmos. Sci.* **40**, 1768.
Zikmunda, and Vali, G., 1972:*J. Atmos. Sci.* **29**, 1334.
Zikmunda, J., 1970:*J. de Rech. Atmos.* **4**, 7.
Zikmunda, J., 1972:*J. Atmos. Sci.* **29**, 1511.
Zimmermann, R., 1986:*Diploma Thesis,* Inst. Meteor. Geophys., University Frankfurt.
Ziv, A., and Levin, Z., 1974:*J. Atmos. Sci.* **31**, 1652.
Zoebell, C. E., and Matthews, H., 1936:*Proc. Nat. Acad. Sci.* **27**, 567.
Zrnic, D. S., Doviak, R. J., and Makapatra, P. R., 1984:*Radio Science* **19**, 75.

LIST OF PRINCIPAL SYMBOLS

a	radius of spherical drop, radius of rigid sphere, radius of circle circumscribed to basal plane of ice crystal, semi-major axis of oblate spheroid, radius of curvature of interface, radius of circular cylinder
$\bar{a}$	mean drop radius
a_0	equivalent radius of deformed drop, crystallographic lattice parameter in a-axis direction
a_L, a_S	radius of the large drop, of the small drop
a_c	critical radius of cloud drop during condensation
a_i, a_p	radius of spherical ice crystal, potential drop radius
a_i, a_{g}	radius of spherical embryo consisting of i molecules, of spherical germ consisting of g molecules
a_k	activity of component k in mixture
$\mathrm{a_w}, \mathrm{a_s}$	activity of water in aqueous solution, of solute in aqueous solution
A_c	cross-sectional area of body oriented perpendicular to viscous flow
A	virial coefficient
b	semi-minor axis of oblate spheroid
B_+, B_-	mobility of positive, negative ions
c_k	concentration of component k
$\dot{c}$	concentration of molecules
c	number of components
c_{w}, c_i	specific heat of water, of ice
$c_{\mathrm{pv}}, c_{\mathrm{pa}}$	specific heat of water vapor at constant pressure, of air at constant pressure
c_0	crystal lattice parameter in c-axis direction
c_i, c_1	equilibrium concentration of i-mers, of single molecules
C	electrostatic capacitance
C_D	hydrodynamic drag force coefficient
$C_{\mathrm{a}}, C_{\mathrm{v}}, C_{\mathrm{m}}$	compressibility factor for dry air, water vapor, moist air
$C_{\mathrm{w}}, C_i, C_{\mathrm{pv}}, C_{\mathrm{pa}}$	molar heat capacity of water, of ice, of water vapor at constant pressure, of air at constant pressure
c_{w}	number concentration of water molecules in water
$c_{\mathrm{sat,w}}, c_{\mathrm{sat},i}$	concentration of water molecules at saturation with respect to water, to ice
c_g, c_l	concentration of gas molecules of given species in the gas phase, in the liquid phase

d	diameter of spherical drop, of rigid sphere, of circle circumscribed to basal plane of ice crystal, of graupel, of hailstone
$\bar{d}$	average nearest neighbor distance between cloud drops
d_s	mean migration distance of water molecules by surface diffusion on ice
D	hydrodynamic drag on body in viscous medium, diffusivity of aerosol particles in air
D_v	diffusivity of water vapor in air
D_+, D_-	diffusivity of positive ions, of negative ions in air
D_0	equivalent diameter of raindrop
D_S	Stokes drag
D_w, D_i	self diffusivity of water molecules in water, in ice
e	partial pressure of water vapor in moist air, vapor pressure of pure water vapor
$\mathrm{e}_{a,\mathrm{w}}, \mathrm{e}_{a,i}$	water vapor pressure over spherically curved water surface, over spherically curved ice surface
$\mathrm{e}_{\mathrm{sat,w}}, \mathrm{e}_{\mathrm{sat},i}, \mathrm{e}_{\mathrm{sat},s}$	saturation vapor pressure over plane water surface, over plane ice surface, over plane aqueous solution surface
e	elementary electric charge
$\hat{e}$	unit vector
$\vec{\mathrm{E}}$	electric field vector
E	magnitude of electric field (electric field intensity)
E_ν	energy of system of quantum number
E	collision efficiency
E_c	collection efficiency
$\mathrm{E}_{\mathrm{coa}}$	coalescence efficiency
E_d	deposition efficiency
E_p	precipitation efficiency
E_m	energy per molecule for cleaving a crystal
E_H	hydrogen bond energy
E_L	lattice energy of ice
f	shedding frequency of vortices from rear of a rigid sphere
$f_\mathrm{w}, f_\mathrm{s}$	rational activity coefficient of water, of salt, in aqueous solution
f_i', f_i	unsteady, steady concentration of i-mers
f_v, f_h	mean ventilation coeficient for vapor diffusion, for heat diffusion
f_vol	bulk Helmholtz free energy change per unit volume
F	Helmholtz free energy of system, scavenging factor
$\vec{\mathrm{F}}, \vec{\mathrm{F}}_1, \vec{\mathrm{F}}_2$	force on body, hydrodynamic force on sphere-1, on sphere-2
F_e	electric force on body
$\vec{\mathrm{F}}_\mathrm{Th}, \vec{\mathrm{F}}_\mathrm{Df}$	thermophoretic, diffusiophoretic force on aerosol particle

$\Delta \mathrm{g}^{\ddagger}$	energy of activation for the diffusion of a water molecule across the ice-water interface, per mole
$\Delta G_{\mathrm{act}}, \Delta \mathrm{g}_{\mathrm{act}}$	activation energy for the diffusion of water molecules in bulk water and ice, per molecule, per mole
$\Delta \mathrm{F}_i, \Delta \mathrm{F}_g$	energy of i-mer formation, of germ formation
$\Delta G_{\mathrm{ad}}, \Delta G_{\mathrm{des}}$	energy of adsorption, of desorption, per molecule
ΔG_{sd}	activation energy for surface diffusion per molecule
$\vec{\mathrm{g}}, g$	acceleration of gravity, magnitude of acceleration of gravity
g_k	partial molar Gibbs free energy of component k in mixture
G	Gibbs free energy of system, linear growth rate of ice crystal face
h	thickness of planar ice crystal, thickness of quasi-liquid layer on ice, Planck's constant
h	molar enthalpy, enthalpy per unit mass
h_k	partial molar enthalpy of component k in mixture
$h_{\mathrm{w}}, h_{\mathrm{v}}$	partial molar enthalpy of water in aqueous solution, of water vapor in air
h_i	molar enthalpy of ice
h_{m}	molar enthalpy of mixing of water in aqueous solution
$h^{(P)}, h^{(B)}$	perpendicular distance from crystal center to prism plane, basal plane
H	enthalpy of system
H	height of prism
$(\Delta h)^f_{v,\mathrm{w}}, (\Delta h)^f_{v,i}$	molar activation enthalpy for vacancy formation in water, in ice
$(\Delta h)_{\mathrm{act,w}}, (\Delta h)_{\mathrm{act},i}$	molar activation enthalpy for self-diffusion in water, in ice
$(\Delta h)^m_{v,\mathrm{w}}, (\Delta h)^m_{v,i}$	molar activation enthalpy for vacancy migration in water, in ice
$(\Delta h)_e, (\Delta h)_m, (\Delta h)_s$	molar enthalpy of evaporation, of melting, sublimation
i	Van't Hoff coefficient for non-ideal aqueous salt solution
i	number of water molecules per embryo
I	moment of inertia
j	number of hydrogen bonds per molecule
$j_{\mathrm{Th}}, j_{\mathrm{Df}}, j_{\mathrm{CD}}$	current density of particles due to thermophoresis, due to diffusiophoresis, due to convective diffusion
j_{v}, j_h, j_q	mass flux density of water vapor, of heat, of electrical charge
$J, J_{\mathrm{Th}}, J_{\mathrm{Df}}, J_{\mathrm{CD}}$	nucleation rate, total particle flux due to thermophoresis, due to diffusiophoresis, due to convective diffusion

J_+, J_-	positive, negative ion current
k	Boltzmann constant, reaction rate constant, wave number
$k_\mathrm{v}, k_\mathrm{a}, k_\mathrm{w}, k_i$	heat conductivity of water vapor, of air, of water, of ice
$\bar{k}_\mathrm{v}$	mean mass transfer coefficient for water vapor in air
K	collection kernel
K_B, K_{ij}	collection kernel for Brownian coagulation
$K_\mathrm{Th}, K_\mathrm{Df}$	collection kernel for thermophoresis, for diffusiophoresis
K_G	collection kernel for gravitational collection
K_f	molar equilibrium freezing point depression
K_H	Henry's law constant (mole liter^{-1}atm^{-1})
k_H	Henry's law constant (dimensionless)
l	length
$L, \mathscr{L}$	latent heat of phase change per unit mass, per mole
$L_{\mathrm{e},0}, L_{m,0}, L_s$	latent heat of evaporation of pure water, of melting of ice, of sublimation of ice, per unit mass
$\mathscr{L}_{\mathrm{e},0}, \mathscr{L}_{m,0}, \mathscr{L}_s$	latent heat of evaporation of pure water, of melting of ice, of sublimation of ice, per mole
$\mathscr{L}_\mathrm{e}, \mathscr{L}_m$	molar latent heat of evaporation of water from an aqueous solution, of melting of ice in an aqueous solution
L	length of columnar snow crystal, angular momentum of coalesced drop pair
L^*	$= \Omega/P$
m_g	mass of gas
m, m'	mass of drops
$\dot{m}, \dot{m}_\mathrm{w}$	mass of molecule, mass of water molecule
m, m_d, m_c	mass of aerosol particle, of water drop, of snow crystal
m_N	mass of nucleus
m_0	mass of aerosol deposit
m_s	mass of salt particle, of salt deposit
$m_{i/\mathrm{v}}, m_{i/\mathrm{w}}$	compatibility parameter for ice on a solid substrate against water vapor, against water
$m_{\mathrm{w}/\mathrm{v}} \equiv \cos\theta$	compatibility parameter for water on a solid substrate
$m_{s,t}$	mass of water-soluble portion of aerosol deposit
m_u	mass of insoluble portion of aerosol particle, of aerosol deposit
$m_{\mathrm{v,ad}}$	mass of water vapor adsorbed on solid substrate
$m_\mathrm{v}, m_\mathrm{w}, m_\mathrm{a}, m_i$	mass of water vapor, of water, of air, of ice
M	molecular weight
$M_\mathrm{a}, M_\mathrm{w}, M_\mathrm{s}, M_\mathrm{m}$	molecular weight of air, of water, of salt, of moist air
$\mathfrak{M}$	molality of aqueous solution

$\hat{M}$	$M_{\mathrm{w}}/1000$
n_k	number of moles of component k in mixture
$n(a), n_{\mathrm{d}}(a)$	number of cloud drops of radius a per unit volume and per unit size interval
$n(D_0)$	number of raindrops of diameter D_0 per unit volume and per unit size interval
$n(r)$	number of aerosol particles of radius r per unit volume and per unit size interval
n_m	number of adsorption sites available on solid substrate
n_{ad}	number of vapor molecules adsorbed on solid substrate
$n_{\mathrm{v}}, n_{\mathrm{w}}, n_{\mathrm{s}}, n_{\mathrm{a}}$	number of moles of water vapor, of water, of salt, of air
$\hat{n}$	unit outward normal vector from surface element
n_+, n_-	number of positive ions, of negative ions, per unit volume of air
N	total number of particles in system
N_A	Avogadro number
N_{Re}	Reynolds number based on diameter
N_{Pe}	Péclet number
N_{Sc}	Schmidt number
N_{Sh}	Sherwood number
N_{Pr}	Prandtl number
N_{Nu}	Nusselt number
N_{Fr}	Froude number
N_{St}	Strouhal number
N_{We}	Weber number
N_{Bo}	Bond number
N_S	Stokes number
N_{Kn}	Knudson number
N_{Be}	Best number
N_{P}	Physical property number
N_{CCN}, N_{IN}	number of cloud condensation nuclei, of ice forming nuclei, per unit volume of air
$N_i, N_i^{(S)}$	number of i-mers in volume, on surface of substrate
N_1	total number of single water molecules in volume
$N_{\mathrm{sat,w}}, N_{\mathrm{sat},i}$	number of water molecules in gas phase, at water saturation, at ice saturation, in volume
N_c	number of water molecules in water contacting unit area of ice germ
N_j	number of j-bonded molecules
N_{w}	number of water molecules in unit volume of water
$N_{\mathrm{u}}, N_{\mathrm{f}}$	number of unfrozen drops, of frozen drops of drop population in volume
p	pressure, number of elementary charges, percentage of broken hydrogen bonds in water

p_k	partial pressure of component k in mixture
p_{a}	partial pressure of dry air in gas mixture, pressure of dry air
p_{w}	pressure of water inside a motionless water drop
p_∞	free stream pressure
p_s	static pressure
$p_{\mathrm{i}}, p_{\mathrm{e}}$	pressure inside, outside of a water drop
p_m	melting pressure of ice
p_0	frontal stagnation pressure on a sphere
P	perimeter of a body, precipitation amount
p	momentum of molecule
p-ratio	ratio of the small drop size to large drop size
q	heat
q_{v}	specific humidity of moist air
q_i, q_1	electric charge of ion species i, partition function of i-mer, of monomer
q_j	partition function of a j-bonded molecule
$Q(N_i)$	canonical partition function of gas of i-mers
$\mathscr{Q}$	grand canonical partition function of gas of i-mers
Q, Q_a, Q_r	electric charge, electric charge on drop of radius a, electric charge on aerosol particle of radius r
$\mathrm{d}Q$	amount of heat
$\vec{\mathrm{r}}$	position vector, radial distance
r	radius of aerosol particle, radial distance
r_N	radius of dry nucleus, radius of curvature of solid substrate
r_u	radius of water-insoluble portion of aerosol particle
r_D	deposition rate
R	precipitation rate, Reynolds number based on radius, radius of air bubble in water
R_M	maximum ice enhancement ratio
$R_{\mathrm{v}}, R_{\mathrm{a}}, R_{\mathrm{m}}$	specific gas constant for water vapor, for dry air, for moist air
$\mathscr{R}$	universal gas constant
R_1, R_2	principal radii of curvature
s	separation between the surfaces of two spheres
s	molar entropy, radius of aerosol particle
$\mathrm{s}_{\mathrm{v,w}}, \mathrm{s}_{\mathrm{v},i}$	supersaturation of moist air with respect to a plane water surface, with respect to a plane ice surface
S	entropy
S_0	zero-point entropy
S	surface area
$S_{\mathrm{v,w}}, S_{\mathrm{v},i}$	saturation ratio of moist air with respect to a plane water surface, with respect to a plane ice surface
t	time
T	absolute temperature

T_a	temperature at drop surface
T_∞	temperatuce of environment
T_e	equilibrium freezing temperature
T_v	virtual temperature of air
T_m	median freezing temperature of population of drops
T_s	$= T_0 - T$
T_{ij}	components of hydrodynamic stress tension
T_0	melting temperature of ice
T_S	surface temperature of ice crystal
T_tr	Tripole point temperature
$\vec{\mathrm{u}}, u$	flow velocity vector, magnitude of flow velocity
$u_\mathrm{v}, u_\mathrm{a}$	velocity of water vapor, of dry air
$u_{\mathrm{i},\theta}$	magnitude of internal velocity in falling drop
u	volume of aerosol particle, volume of drop
U	internal energy of system, interaction potential between molecules, vertical velocity of air
U_∞	free stream velocity of viscous flow, terminal fall velocity of particle
U_S	Stokes velocity
$\vec{\mathrm{v}}, v$	velocity, magnitude of velocity
v	mole volume
v_k	mole volume of component k in mixture
$v_{\mathrm{w},0}, v_{\mathrm{s},0}, v_i$	mole volume of pure water, of pure salt, of ice
$v_{\mathrm{v},0}, v_{\mathrm{a},0}, v_\mathrm{m}$	mole volume of pure water vapor, of dry air, of moist air
$v_\mathrm{w}, v_\mathrm{s}$	partial molar volume of water, of salt, in aqueous solution
v	volume of aerosol particle, volume of drop
$\dot{v}$	volume of molecule
v_0	propagation speed of steps on crystal surface
$\bar{\mathrm{v}}$	mean speed of gas molecules
V_i	volume of system, volume of i-mer
V_S	Stokes fall velocity of particle
V_uc	volume of crystallographic unit cell
V_s	volume of solution
V_d	liquid portion of drop condensed on mixed aerosol particle
V_c	volume of ice crystal
V_i	volume of i-mer
V_d	drop volume
w	variance of system
w_L	liquid water content of cloud
w_i	cloud ice content
w_v	mixing ratio of unsaturated moist air
$w_\mathrm{v,sat}$	mixing ratio of moist air saturated with water vapor
$w^\downarrow, w^\uparrow$	flux of molecules to and from a surface

W_c	work for cleaving a crystal
W	vertical velocity of air, number of distinguishable microstates in ice, scavenging ratio
x	length coordinate
x_k	mole fraction of component k in mixture
$x_\mathrm{v}, x_\mathrm{a}$	mole fraction of water vapor, of dry air, in moist air
$x_\mathrm{w}, x_\mathrm{s}$	mole fraction of water, of salt, in aqueous solution
y	length coordinate
y_c	linear collision efficiency
z	(vertical) length coordinate
Z	Zeldovich factor
α	angle, phase
α_c	condensation coefficient
α_d	deposition coefficient
α_T	thermal accommodation coefficient
$\gamma_\pm$	mean activity coefficient of salt ions in aqueous solution
$\Gamma_d, \Gamma_s, \Gamma_c, \Gamma'$	lapse rate: dry adiabatic, saturation adiabatic-, cloud-, in environment
γ_c	cooling rate
$\Gamma_k^{(\sigma)}, \Gamma_s^{(\mathrm{s/v})}, \Gamma_\mathrm{w}^{(\mathrm{s/v})}, \Gamma_\mathrm{w}^{(\mathrm{w/v})}$	Gibbs adsorption of component k at interface σ, of salt at solution/vapor interface, of water at solution/vapor interface, of water at water/vapor interface
Γ	shear rate
δ	crystallographic misfit
δ_u, δ_D	thickness of momentum boundary layer, of diffusion boundary layer
ε	ratio of molecular weight of water to molecular weight of air, average elastic strain produced inside ice germ, turbulent energy dissipation rate
$\varepsilon_v, \varepsilon_m$	volume-, mass fraction, of water-soluble substance in mixed aerosol particle
$\varepsilon_\mathrm{w}, \varepsilon_i$	dielectric constant of water, of ice
ξ	vorticity
$\eta, \eta_\mathrm{a}, \eta_\mathrm{w}$	dynamic viscosity of viscous medium, of air, of water
ϑ	angle
θ	contact angle for water on solid substrate, angular coordinate counted from foreward stagnation point on falling sphere
Θ	angle between the line of centers of interacting spheres and direction of fall
κ	compressibility of water
λ	wave length of waves on surface of water, mean free distance between collision of falling rain drops, step energy per unit length, eddy size

λ_a	mean free path of air molecules
Λ	electric conductivity, slope of Marshall-Palmer rain drop distribution, scavenging coefficient
μ	chemical potential, chemical potential of an i-mer, entrainment rate
μ_k	chemical potential of component k in mixture
$\mu_{v,0}, \mu_{w,0}, \mu_i$	chemical potential of pure water vapor, of pure water, of ice
μ_v, μ_w, μ_s	chemical potential of water vapor in air, of water in aqueous solution, of salt in aqueous solution
ν	number of ions into which a salt molecule dissociates in water, jump frequency of molecules, kinematic viscosity of viscous medium
ν_a, ν_w	kinematic viscosity of air, of water
ν_S	frequency of vibration of water molecule adsorbed on solid substrate
ν_0	frequency of oscillation of a water molecule
Π	spreading pressure
ρ	density of viscous medium, of moist air
$\rho_w, \rho_i, \rho_a, \rho_m, \rho_w$	density of water, of ice, of dry air, of moist air, of water vapor
ρ_c	bulk density of ice crystal
ρ_s''	density of aqueous salt solution
ρ_N, ρ_p	bulk density of nucleus, of aerosol particle
ρ_u, ρ_s	bulk density of water-insoluble, of water-soluble, portion of aerosol particle
σ	surface tension

TABLE OF PHYSICAL CONSTANTS

Absolute temperature of ice point	$T_0 = 273.15$ K
Gas constant for 1 mole of ideal gas	$\mathscr{R} = 8.3144 \times 10^7$ erg mole^{-1} (K)$^{-1}$
	$= 1.9858$ cal$_{IT}$ mole^{-1} (K)$^{-1}$
	$= 0.082$ atm mole^{-1} liter^{-1} (K)$^{-1}$
Gas constant for 1 g of dry air	$R_a = 2.8706 \times 10^6$ erg g^{-1} (K)$^{-1}$
	$= 6.8557 \times 10^{-2}$ cal$_{IT}$ g^{-1} (K)$^{-1}$
Gas constant for 1 g of water vapor	$R_v = 4.6150 \times 10^6$ erg g^{-1} (K)$^{-1}$
	$= 1.1023 \times 10^{-1}$ cal$_{IT}$ g^{-1} (K)$^{-1}$
Boltzman's constant	$k = 1.3804 \times 10^{-16}$ erg (K)$^{-1}$
Planck's constant	$h = 6.6252 \times 10^{-27}$ erg sec
Avogadro's number	$N_A = 6.02257 \times 10^{23}$ molecule mole^{-1}
Molecular weight of dry air	$M_a = 28.9644$
Molecular weight of water	$M_w = 18.0160$
$\epsilon = (R_a/R_v) = (M_w/M_a)$	$\epsilon = 0.6220$
NACA Standard Atmosphere	$p_{st} = 1013.250$ mb
(sea level values)	$\rho_{st} = 1.2250 \times 10^{-3}$ g cm^{-3}
	$T_{st} = 288.15$ K $= 15^\circ$ C
	$g_{st} = 980.665$ cm sec^{-2}
	$n_{st} = 2.5471 \times 10^{19}$ air molecule cm^{-3}
electronic charge	$e = 4.80298 \times 10^{-10}$ e.s.u. $= 1.60210 \times 10^{-19}$ C

INDEX

A

activation energy for self-diffusion and viscous flow, 96
activity, 109
adaptation time, 542–546
adiabat
  cloud, 492
  dry, 489
  reversible saturation, 492
  saturation pseudo, 492
  wet, 492
adsorption
  chemical, 137
  definition of, 128
  isotherm, 138
  of gases on ice surfaces, 155–157
  of salt, 132
  of water vapor on solid surfaces, 137–145
  physical, 137
aerosol particles, 225
  Brownian coagulation of, 454–463
  Brownian motion of, 447–449
  coagulation in turbulent flow of, 465
  diffusivity of, 449
  formation of by bulk to particle conversion, 240–247
    at the solid earth surface, 240
    at the surface of oceans, 243
    from extraterrestrial sources, 247
  formation of by drop to particle conversion, 233–236
  formation of by gas-to-particle conversion, 226–233
  large, giant, Aitken, 225
  mass concentration, 255
  mobility and drift velocity of, 450–451
  number concentration, 252
  of the accumulation mode, 225
  of the coarse mode, 225
  of the nuclei mode, 225
  rate of emission of paticulate matter, 248
  residence time of, 248
  sedimentation of, 451–454
  size distribution of, 261–269
  stratospheric and arctic aerosol, 260
  total mass and number concentration of, 252–261
  total mass and number concentration of particles, 260
  vertical variation, 270–286
  water-soluble fraction of, 251
air parcel model, 497–501
angle of contact, 135–137
Antonoff's rule, 160
aqueous solutions
  hydration in, 98
  structure of, 98–99
  structure-breaking effect in, 99
atomaric defects in ice, 80

B

Bernoulli's law, 375
Best number
  definition of, 417
bond number, 418
bubble-burst-mechanism, 244
bulk density, 50
bunching of monomolecular layers, 151

C

capacitances of various crystal forms, 548
charge distribution in clouds, 804–811
charging mechanisms in clouds, 811–827
chemical potential
  of water in aqueous solutions, 107–109

of water vapor in humid air, 107–109
cirrus clouds
ice water content of, 56
microstructure of, 55
size spectra for crystals, 56
snow crystals in, 55
Clausius-Clapeyron equation, 116
for bulk phases, 116
for phases with used interfaces, 169
cloud chemistry, 700
cloud condensation nuclei (CCN), 287
chemical composition of, 287–296
definition of, 287
mode of action and mixed CCN, 296–297
number concentration of, 287–296
cloud drops
theoretical formulation of, 24
Best distribution, 27
gamma distribution, 26
Khrgian-Mazin distribution, 26
lognormal distribution, 26
cloud-interstitial aerosol
definition of, 716
clouds
accumulation zones in, 23
bimodality of size distribution in, 18
consisting of ice particles, 38
drop concentration in, 15, 16
drop size distribution in, 15, 24
liquid water content of, 18, 23
mean distance between drops in, 27
microstructure of, 15
radar echo of, 24
radar studies of, 24
relative humidity of, 10
spatial distribution of the drop size in, 18
coagulation
Brownian, 454–463
effect of turbulence on, 465
gravitational, 463–472
laminar, 463–472
turbulence, 463–472
coalescence of water drops in air, 594–596
collection efficiency
definition of, 591
collision
basic model, 568–569
of large snow crystals with small water drops, 599–606
of small snow crystals with large water drops, 606–607
of snow crystals with snow crystals, 607–610
of snow crystals with water drops in air, 599–607
of water drops with water drops, 581–594
the superposition method, 571–574
collision efficiency, 470
definition of, 541–571
'compatibility parameter', 137
concentration of water insoluble particles
in bulk cloud and rain water, 708–709
in bulk water of melted snow, 708–709
concentration of water soluble compounds, 701–715
in bulk cloud and rain water, 701–708
in bulk water of melted snow, 701–708
in individual cloud and raindrops, 711–715
condensation coefficient, 164
condensation growth
in cumuliform clouds, 512–531
in stratiform clouds and fogs, 531–536
contact angle, 135
convective condensation level, 491
cooling of air, 485
adiabatic, 488–489

isobaric, 488
critical point, 122
critical radius, 173

D

Davies number
definition of, 417
defects in ice
atomaric, 80
Bjerrum defects, 81
chemical, 81
interstitial molecules, 81
ionized states, 81
molecular vacancies, 81
stacking faults, 81
Definition of
van't Hoff factor, 110
definition of
absolute humidity, 107
equilibrium freezing point depression, 124
equilibrium freezing temperature, 124
hygroscopic nature of salt, 112
mean activity coefficient, 111
mixing ratio, 107
molal coefficient, 111
molality, 110
mole fraction of water vapor, 107
practical osmotic coefficient, 111
relative humidity, 107
saturation ratio, 107
specific humidity, 107
supersaturation, 107
deposition coefficient, 165
desorption of gases, 775–777
diffusion
models for gases, 757–772
of heat, 507–509
of water vapor, 502–506
diffusion boundary layer, 721
diffusiophoresis, 726
diffusivity of water vapor, 503
direct interception
definition of, 470
dislocations, 150
edge, 150
screw, 150
drag, 367
on circular cylinders, 428
on circular disks and oblate spheroids, 422
on graupel, 433
on hailstones, 433
on rigid spheres, 367–369
on snow crystals, 433
on water drops in air, 388, 390
drag coefficient, 368
drop breakup
collisional, 598
hydrodynamic of single drops, 410–415
drop number concentration, 12, 13
drop oscillation
frequency of, 400
modes of, 400–404
drop shape, 393–399

E

effect of curvature on latent heat of phase change, 168
effect of electric fields and charges, 827–852
on collisional growth rate of cloud particles, 836–845
on diffusional growth of ice crystals, 828
on drop deformation, disruption and corona, 829–835
on drop terminal velocity, 835
on drops and ice crystal nucleation, 827–828
on scavenging of aerosol particles, 846–852
electrical conductivity in clouds, 798–804
conductivity in strongly electrified clouds, 802
conductivity in weakly electrified clouds, 799
energy of activation for diffusion of water molecules, 206

entrainment, 492–497
entrainment parameter, 499
entrainment rate, 493
equation of state, 105
equilibrium, 100, 127
between a pure water drop and humid air, 170–172
between an aqueous solution and humid air, 172–175
between bul aqueous salt solutions and ice, 123–125
between bulk aqueous salt solutions and water vapor, 109
between the bulk phases of water, ice and aequeous solutions, 100–125
conditions for ice particles, 178–184
crystal shape for ice, 148
experimental verification of various relationships, 184–190
for phases separated by a curved interface, 127, 167
general conditions for, 102–104
etch-pits, 150
etching
thermal, 150
evaporation
of snow crystals, 550–560
of water drops, 537–546

F

facetted surfaces, 151
fair weather electrical state, 792–797
conduction current density, 793
conductivity, 794
definition of, 792
electric field strength, 792–795
mobility and diffusivity of ions, 793
fall behavior
of conical modes and graupel, 444
of cylinders, 433
of drops, 409
of hailstones, 445
of oblate spheroids, 428
of rigid spheres, 384
of snow crystals, 444
flow past a sphere, 365
Carrier's modification for, 372
matched asymptotic expansion for, 372
Oseen, 370
potential flow and boundary layer theory, 374
Stokes, 369
fog
definition of condensation nuclei, 291
ice fog, 58
liquid water content of, 15
number concentration of, 15
relative humidity of, 10
fogs
drop size distribution in, 24
mean distance between drops in, 27
microstructure of, 12, 15
freezing potential, 162
freezing time
of water drops, 674–679
Froude number
definition of, 573

G

gaseous constituents
concentrations, 217
fast varying, 217
of the atmosphere, 216
quasi-constant, 216
slowly varying, 216
sources and sinks, 217
Gibbs adsorption isotherm, 131
Gibbs phase rule, 104
Gibbs-Duhem relation, 101
glaciation, 53
graupel
bubble concentration in, 662
bubble size in, 662
bulk density of, 58
dimensions of, 58
drag on, 433–437

fall pattern, 444–446
fall velocity of, 438–444
growth rate of, 679–687
ice crystallites in, 662
melting of, 692–697
number concentration of, 58
shape of, 58
thin sections of, 73
growth
dry growth regime
definition of, 659
numerical approximation techniques, 636–645
method of Berry and Reinhardt, 637–639
method of moments, 639–645
of aqueous solution drops by diffusion of water vapor, 509–536
of drops by collision, 617–658
continuous model, 617–620
stochastic model, 617, 622–645
of drops by collision (num. approx. techniques)
in combination with drop breakup, 650–658
of ice particles by accretion of supercooled drops, 659–689
of snow crystals by collision with other snow crystals, 689–691
of snow crystals by diffusion of water vapor, 546–567
of water drops by diffusion of water vapor, 502–536
wet growth regime
definition of, 659
growth of electric field in clouds, 826

H

hailstones
air bubbles in, 73
bubble concentration in, 662
bubble size in, 662
bulk density of, 58
crystallites, 73
definition of
spongy ice, 72
dimensions of, 58
drag on, 433–437
fall pattern, 444–446
fall velocity of, 438–444
growth rate of, 679–687
ice crystallites in, 662
melting of, 692–697
number concentration of, 58
shape of, 58
thin sections of, 73
Hawaiian rainbands
studies on, 31
Hertz-Knudsen equation, 165
heterogeneous nucleation, 287
'Hill's spherical vortex'
definition of, 390
holograms, 29
homogeneous nucleation, 191
hopper structure, 151
hydrodynamic behavior, 361
of rigid spheres, 364–383
of snow crystals, graupel and hailstones, 433–446
of water drops in air, 385–433
hydrophilic walls, 138
hydrophobic walls, 138
hygropause, 487
hysteresis loop, 186

I

ice, 145
activation energy to form a vacancy in, 84
activation enthalpy for a lattice vacancy to migrate in, 84
'aged' surface of, 146
aqueous solution interface, 161–163
atomaric defects in, 80
Bernal-Fowler (BF) rules for, 80
dielectric relaxation time for, 86
diffusivity in, 85
equilibrium crystal shape for, 148
'fresh' surface of, 146

growth mode of in supercooled water, 663–668
growth rate of ice in supercooled water, 668–674
hexagonal rings in, 79
hydrogen bond energy in, 83
hydrogen bonds in, 79
lattice energy of, 83
nearest neighbors in, 78
real surface of, 150
self-diffusion mechanism of H_2O through ice, 84
space group of, 78
specific heat of, 86
structure in supercooled water, 663–668
structure of, 78–86
sublimation energy of, 83
surface energy of, 145
symmetry of, 78
unit cell of, 79
valence angle in, 82
work of cohesion of, 145
zero-point entropy of, 81
ice clouds
definition of
aggregation, 39
clumping, 39
deposition, 39
graupel particle, 39
hailstones, 40
ice crystals, 39
rimed snow crystals, 39
riming, 39
sleet, 40
small-hail particle, 39
snow crystals, 39
snow pellet, 39
snowflakes, 39
soft hail particle, 39
type-a ice pellets, 40
type-b ice pellet, 39
microstructure of, 38
ice fog, 58
ice forming nuclei (IN), 287, 309–341
contact nucleation, 339
definition of disregistry, 330
definition of IN-storms, 310
main requirements for, 326
modes of action, 309
number concentration of, 309
sources and chemical composition of, 317
ice point, 104, 120
ice-vapor interface, 145
ice-water interface, 157–161
impact velocity
of drop on graupel, 661
impaction scavenging, 720–744
by convective Brownian motion, 720–724
by gravitational impaction, 730–732
by inertial impaction, 730
by thermo- and diffusiophoresis, 724–729
by turbulence, 732
the trajectory and flux models for, 732–744
inertia parameter
definition of, 573
inertial subrange, 467
interface
water-vapor, 129–135
interface energy between ice and supercooled water, 157

K

Kelvin equation, 170
Kirchoff's equations, 116
Knudsen number
definition of, 448
Köhler equations, 173
Kolmogorov microscale length
definition of, 466

L

Langevin equation
definition of, 447
Laplace formula, 128
lapse rate
dry adiabatic, 489

moist adiabatic, 489
saturation adiabatic, 492
latent heat of phase change, 115–116
definition of, 115
temperature dependence of, 116
level of free convection, 491
lifting condensation level, 490
liquid water contents, 12

M

Markoff process
definition of, 447
mass transfer coefficient
definition of
for snow crystals, 551
for water drops, 537
melting
of graupel and hailstones, 692–697
of ice particles, 691–699
of snow flakes, 697–699
melting pressure of ice, 120
meteor
definition of, 247
meteorid
definition of, 247
meteorites
definition of, 247
micrometeorites
definition of, 248
Mischkerne
definition of, 251
mixed particles
definition of, 251
mode of drop oscillation, 401

N

Navier-Stokes equation, 362
numerical approach, 378
nucleation, 287
definition of, 191
definition of embryos, 192
definition of germ, 192
heterogeneous, 287
homogeneous, 191
of ice
classical model, 341
discrepancy between concentrations of IN and ice particles, 355
enhancement factor, 355
extensions to the classical model, 344
of freezing of supercooled water drops, 347
secondary ice particles, 355
statistical mechanics model, 345
of ice in supercooled water, 205–215
classical model, 207
energy of germ formation, 207
molar activation energy, 209
molecular model, 207
nucleation rate, 205
of water drops, 297–305
experimental verification, 306
on a curved substrate, 302
on a planar substrate, 298
of water drops and ice crystals from water vapor, 192–205
classical description, 194
energy of germ formation, 198
experimental verification, 204
molecular model, 194
nucleation rate, 199
statistical mechanics description, 192
scavenging, 716–718
theory of heterogeneous ice, 341
Nusselt number
definition of, 541

O

oscillation frequency, 401
Ostwald's rule of stages, 203

P

Péclet number
definiton of, 721
partition coefficient, 162
Péclet number
definition of, 538

phase rule
for bulk phase, 104
phase rule for systems with curved interface, 128–129
'physical property' number, 418
polar stratospheric clouds
definition of, 283
polymorphy, 120
potential flow, 366
potential radius, 174
precipitation
consisting of ice particle, 38

Q

'quasi-liquid' layer, 153, 155
quasi-stationary distributions, 472
quasi-stationary self-preserving distributions, 480

R

radar, 23
rain
liquid water content of, 30
microstructure of, 30
rainfall rate of, 30
raindrops
breakup
by collision, 598, 645–650
hydrodynamic, 645–650
equilibrium spectrum of, 653
fit to the observed spectra of, 37
mean free distance between collisions, 655
mean free time between collisions, 655
'n_0-jump', 35
size distribution of, 30
Best, 34
Marshall-Palmer (MP), 34
rainfall rate, 30
Raoult's law, 108, 110
rational activity coefficient, 109
Rayleigh limit
definition of, 806
Rayleigh-Taylor instability
definition of, 411
retention coefficient, 162
Reynolds number
definition of, 364
rigid spheres, 361
rime deposits
density of, 660–661

S

saltation, 241
saturation vapor pressure
over ice, 117
over water, 117
scavenging, 700, 715–787
of aerosol particles by cloud drops, raindrops and ice particles, 715–744
of gases by cloud drops, raindrops and ice particles, 744–784
of gases by ice particles, 783–784
of gases by water drops, 749–782
scavenging coefficient, 720–787
definition of, 720
for aerosol particles, 723, 725, 727, 784–787
for convective Brownian diffusion, 723
for diffusiophoresis, 727
for gases, 784–787
for thermophoresis, 725
scavenging factor, 785
scavenging ratio, 785
Schumann-Ludlam limit, 659
segregation
coefficient, 162
process, 161
self-preserving distributions (SPD), 474
shedding efficiency
definition of, 682
Sherwood number
definition of, 551
for snow crystals, 551
for water drops, 537
singular hypothesis, 350
snow crystal
by diffusion of water vapor, 546–574

evaporation of, 550–560
growth by collision with other snow crystals, 689–692
growth by collision with supercooled drops, 684–687
growth rate of in a water saturated environment, 546–558
inherent growth rate of, 563
linear growth rate of faces, 561
migration distance on, 565
multiplication by riming, 687–689
step propagation velocity on, 564
surface diffusion on, 565
snow crystal habit change, 561–567
snow crystals
aggregates of, 58
bulk density of, 40, 50
definition of
bullet, 49
combination of bullets, 49
glaciation, 53
polycrystalline crystals, 49
rosette, 49
single ice crystals, 44
spatial crystals, 49
dimensional relations of, 50
dimensional relationships, 58
dimensions of, 50
drag on, 433–437
faces, 40
fall pattern, 444–446
fall velocity of, 438–444
flow field past, 433–437
habit change, 40–50
number concentrations of, 40
rimed and unrimed, 53
shape of, 40–50
size distribution of, 53
size-mass relationships for, 50
unrimed, planar, 444
snow flake
melting of, 697–699
snow flakes
fall pattern, 445
fall velocity, 440
snowflakes
'bright band', 61
bulk density of, 58
dimensional relationships, 58
dimensions of, 58
'melting layer', 61
number concentration of, 58
number of component crystals in, 59
shape of, 58
size distribution of, 59
soaking
definition of, 660
spongy ice
definition of, 660
spreading pressure, 141
Stephan flow, 726
stochastic hypothesis, 348
Stokes flow, 365
Stokes number
definition of, 573
Stokes terminal velocity, 416
stream function, 366
Strouhal number, 383
structure of aqueous solutions, 98–99
structure of ice, 78–86
structure of water, 86–97
structure of water molecule, 74–76
structure of water vapor, 77–78
surface
hydrophilic, 136
hydrophobic, 136
surface tension, 126
definition of, 126
effect of drop radius on, 133–135
effect of temperature on, 130
of an aqueous salt solution, 130–133
of water, 130

T

temperature scale, 118
terminal velocity
of graupel and hailstones, 439
of plate-like and columnar crystals, 438
of water drops in air, 415

tetrahedron, 78
thermal accommodation coefficient, 165
thermal conductivity of dry air and water vapor, 508
thermodynamic surface of water, 122
thermophoresis, 724
triple point, 104, 120
turbulence
  effect on fall mode of particles, 610–616
  effect on the collision of drops, 585–591
  energy dissipation rate in clouds, 584
  spectral energy density inside and outside clouds, 584

V

variance of a system, 104
ventilation coefficient
  for snow crystals, 550–554
  for water drops, 537–542
  ventilation coefficient
    definition of, 537

W

water
  activation energy for self-diffusion and viscous flow, 96
  density of, 86
  enthalpy of evaporation, 97
  enthalpy of melting of, 97
  singularity behavior of, 94
  specific heat, 92
  structure of, 86–97
  the self-diffusion coefficient of, 95
  viscosity of, 93
water drops
  break up of, 410–415, 598
  evaporation of, 537–546
  fall behavior of, 409–410
  freezing time, 674–679
  growth
    by diffusion of water vapor, 504–536
  internal circulation in, 385–393
  oscillation of, 400–408
  shape of, 393–399
  terminal fall velocity of, 415–421
water molecule, 74, 75
  bond length of, 74
  dipole moment of, 74
  electron configuration in, 75
  lone-pair hybrids of, 76
  structure of, 74–76
water vapor, 74, 75
  clusters in, 77
  specific heat of, 74
  structure of, 77–78
Weber number
  definition of, 405
wet deposition, 787–791
  deposition efficiency, 787
  deposition rate, 790
  precipitation efficiency, 787
wetbulb temperature, 490
'wetting coefficient', 137
Wulff's Theorem, 147–149

Y

Young's relation, 136

Z

Zeldovitch factor, 201